

21st Century COE Program
Evolution of Urban Earthquake Engineering

Second International Conference on Urban Earthquake Engineering



*Center for Urban Earthquake Engineering
Tokyo Institute of Technology*

Tokyo Tech
CUEE

21st Century COE Program
Evolution of Urban Earthquake Engineering

Second International Conference on Urban Earthquake Engineering

Center for Urban Earthquake Engineering
Tokyo Institute of Technology

Tokyo Tech
CUEE

PREFACE

I am very pleased to launch the 2nd International Conference on Urban Earthquake Engineering. This conference is organized by the Center for Urban Earthquake Engineering (CUEE), which was established at the Tokyo Institute of Technology in September 2003, to carry out the 21st Century Center of Excellence (COE) program entitled “Evolution of Urban Earthquake Engineering” sponsored by the Ministry of Education, Culture, Sport, and Technology (MEXT) for 5 years from 2003-2008. This COE program, currently at the end of the second year, aims not only to promote research for the overall earthquake risk reduction technology but also to strengthen the graduate education program as well as to launch international collaboration in research and education.

Since the first successful conference held in last March, CUEE has been working towards making various contributions in the areas of the following three major research topics:

- (1) *Advanced Technology for Earthquake Disaster Mitigation*
- (2) *Renovation Technology for Urban Earthquake Resilience*
- (3) *Strategic Plan for Urban Seismic Risk Reduction*

This second conference aims not only to exchange and discuss with experts in-depth information on these topics but also to promote collaboration and interaction with foreign and local research institutions, as well as government and non-government organizations.

The Niigata-Ken Chuetsu earthquake that hit Niigata prefecture on October 23, 2004, killed forty people and injured almost 3,000. Numerous landslides triggered by the earthquake damaged local communities that comprise a complicated web of people, lifeline facilities and natural eco-systems. The tragedy caused by the Sumatra Island earthquake and tsunami of December 26, 2004 has been really stunning and heartbreaking on the global scale. Reportedly more than 200,000 people were killed by the tsunami, and as many as one third of the total killed were children. These catastrophic disasters and the subsequent widespread disaster chain reinforce the pressing need for enhancing our R&D activities, especially in collaboration with foreign institutions. We would appreciate your kind participation, contributions and fruitful discussions during this conference.

Tatsuo Ohmachi

Director and Professor, Center for Urban Earthquake Engineering and
Program Leader, 21st Century Center of Excellence (COE) program entitled “Evolution of Urban Earthquake Engineering”

TABLE OF CONTENTS

Papers Presented in the Oral Sessions

Seismic Behavior and Design of Structures

Design for collapse safety	1
Zareian, F., Krawinkler, H. and Ibarra, L.	
Effect of phase spectrum uncertainties of earthquake motion on seismic fragility curve of steel bridge pier	9
Sato, T., Masmoto, M. and Yoshida, I.	
Strong motion records observed in the 2004 Niigata-ken-Chuetsu earthquake	21
Midorikawa, S. and Miura, H.	
Strong motion characteristics and structural damage potential	27
Kawase, H.	
Effectiveness of diaphragm wall in reducing the potential of soil liquefaction induced by earthquakes	36
Chen, H. and Chen, W.	
Safety of fill dams under level 2 earthquake motions: lessons from the 2004 Niigata-Chuetsu earthquake	44
Ohmachi, T.	

Bridge Structures and Response Control Technology

Experimental evaluation of seismic performance of SMA bridge restrainer	52
Maragakis, E., Saiidi, M., Johnson, R., DesRoches, R. and Padgett, J.	
Seismic performance of unbonded columns and isolator built-in columns based on cyclic loading tests	62
Kawashima, K. and Watanabe, G.	
Effect of near field ground motions on force reduction factor and residual displacement of structures	70
Watanabe, G., Kijima, K. and Kawashima, K.	
Seismic resistance verification of fatigue retrofitted steel bridge bents (A case study in the Metropolitan Expressway)	77
Miki, C., Sasaki, E. and Shimoizato, T.	

Building Structures and Response Control Technology

Energy distribution and power flow in passively controlled structures	85
Igusa, T.	
Experiment and analysis of a steel frame with visco-elasto-plastic damper	91
Kasai, K. and Minato, N.	

Shaking table test of passively controlled light-gage steel frames	99
Ooki, Y., Kasai, K., Wada, A., Midorikawa, M., Yokoyama, S. and Iwasaki, K.	
Proposal regarding seismic strengthening characteristics for more efficient earthquake disaster mitigation of wooden houses	107
Yoshikawa, Y., Ouchi, K. and Harada, M.	
Seismic retrofit of tower structures with buckling-restrained braces	116
Takeuchi, T.	

Concrete Structures and Components

Behavior of reinforced concrete walls with diagonal web reinforcement subjected to cyclic lateral loading	122
Shiangchin, S., Lukkunaprasit, P., Sittipunt, C. and Wood, S.	
Effect of active confinement on shear crack behaviors for R/C columns prestressed laterally	131
Shinohara, Y., Miyano, K., Inagaki, M. and Watanabe, H.	
Seismic performance of steel reinforced concrete members using light-weight aggregate concrete	139
Hsu, H., Chen, H. and Chen, J.	
Difference between static test results and real restoring force characteristics	146
Nishimura, K., Takiguchi, K. and Masaki, K.	
Column-to-beam strength ratio effect on seismic behavior of reinforced concrete buildings	152
Jalali, A. and Mostashari, A.	
Influence of joint concrete interfacial slip on the seismic response of non-ductile frames upgraded with RC jacketing	160
Wang, Y., Ho, W., Ko, R. and Ya, T.	
Lattice model analysis considering cyclic stress-strain relationships of concrete	167
Niwa, J., Suzuki, N. and Miki, T.	

Special Report

Tsunami damage in Sri Lanka due to the Sumatra earthquake of December 26, 2004 - preliminary reconnaissance	175
Wijeyewickrema, A., Inoue, S. and Sekiguchi, T.	

Geotechnical Earthquake Engineering

Overturning of buildings in Adapazari, during the 1999 Kocaeli earthquake	186
Gazetas, G., Anastasopoulos, I. and Gerolymos, N.	
Investigation on building damages caused by ground failure and their rehabilitation in Yuanlin after the Taiwan Chi-Chi earthquake	192
Lee, C., Hsiung, T., Wen, H. and Shia, C.	

Effects of inertial and kinematic interaction on seismic behavior of pile foundations based on large shaking table tests	200
Tokimatsu, K. and Suzuki, H.	

Engineering Seismology

Ground motion responses in the Taipei urban area	208
Wen, K., Chang, T. and Lin, C.	
Estimation of 3D S-wave velocity model of the Kanto basin, Japan, for prediction of long-period strong ground motion	219
Yamanaka, H., Komaba, N. and Yamada, N.	
Analytical investigation into BAM earthquake of 26 Dec 2003 - Iran	225
Ghanbari, E.	
An estimation of site effects during the 2004 Niigataken Chuetsu earthquake based on microtremor measurements	232
Motoki, K., Yamanaka, H., Seo, K., Yamada, N. and Fukumoto, S.	
A basic study on estimation of the phase velocities of microtremors using time-frequency analysis	238
Morikawa, H. and Udagawa, S.	

Planning and Policy for Seismic Hazard Mitigation

Recent activities in UNESCO related with urban disaster mitigation	246
Rouhban, B.	
Methodology to study the seismic risk to buildings in a modern high rise city in a region of moderate seismicity	252
Pappin, J., Free, M. and Vesey, D.	
Research activities on earthquake disaster mitigation in Armenia	270
Seo, K., Sasano, S. and Motoki, K.	
Development of an integrated GIS and space technology applications for seismic risk management and mitigation in urban planning in high seismic zones	277
Sarma, B. and Pathak, J.	

Papers Presented in the Poster Sessions

Engineering Seismology

Correlation between horizontal and vertical components of near-field strong motions	285
Shirai, K. and Ohmachi, T.	
Slope failure potential mapping in urban area using high-resolution digital elevation model	291
Miura, H. and Midorikawa, S.	

Paleoseismicity and newseismicity studies in Azerbaijan area and the necessity of microseismic zonation in Tabriz city and other seismic regions of Azerbaijan	297
Ghanbari, E.	

Geotechnical Engineering

Two dimensional modeling of piles subjected to liquefied ground.....	302
Dungca, J., Kuwano, J. and Takahashi, A.	
Estimation of effects of pore water pressure response on p-y behavior of pile group in liquefied ground	310
Suzuki, H. and Tokimatsu, K.	
P-delta effect of piles founded on laterally spreading and liquefiable soils.....	316
Bhattacharya, S. and Tokimatsu, K.	

Human Response

To help schoolteachers take appropriate action in the event of earthquake disaster	324
Hashimoto, K., Ohmachi, T. and Inoue, S.	
Questionnaire survey on drivers' reaction in the 2003 Sanriku-Minami earthquake	332
Maruyama, Y. and Yamazaki, F.	
Perception of earthquake hazard by urban children.....	338
Katayama, M., Ohno, R., Soeda, M. and Nara, S.	
Fundamental study on establishment of evaluation method for seismic resistance of floor finishing system	346
Yokoyama, Y. and Yokoi, T.	

RC Structure

An experimental study on the performance of RC columns subjected to cyclic flexural-torsional loading.....	354
Tirasit, P., Kawashima, K. and Watanabe, G.	
An experimental study on behavior of non - bond RC columns subjected to three-axial compulsory force.....	362
Hoang, N., Takiguchi, K. and Nishimura, K.	
Fiber element analysis of reinforced concrete C-bent columns	369
Nagata, S., Kawashima, K. and Watanabe, G.	
Simplified truss model for shear carrying capacity analysis of non-rectangular cross sectional PC slender beams.....	377
Lertsamattiyakul, M., Niwa, J., Tamura, S. and Hamada, Y.	
Research on weight reduction of composite PC beams using various UFC web members	385
Murata, H., Niwa, J., Chigira, E. and Kawaguchi, T.	

Damage process and collapse capacity of RC frame structure: - from the viewpoint of mechanism control	391
Nagae, T., Hayashi, S., Ibarra, L. and Krawinkler, H.	

Steel Structures

Experimental study on hysteresis behaviors of structural steel during multi-axial loadings ...	399
Chung, K., Matsumoto, Y. and Yamada, S.	
A study on bolted connections using concrete slab as the lateral force transfer	407
Kishiki, S., Yamada, S., Takeuchi, T., Suzuki, K., Sasaki, E. and Wada, A.	
Seismic performance of link-to-column connections in steel eccentrically braced frames	415
Okazaki, T. and Engelhardt, M.	
Nonlinear dynamic behaviour of structures due to near-field ground motions	423
Tehranizadeh, M. and Labafzadeh, M.	

Dynamic Response

Estimation of seismic demand of multi-story asymmetric buildings with bi-directional eccentricity	431
Fujii, K., Nakano, Y., Sanada, Y., Sakata, H. and Wada, A.	
Effects of near-field vertical ground motions on structural response	439
Tehranizadeh, M. and Labafzadeh, M.	

Passive Control and Base Isolation

Seismic response control of nonlinear isolated bridges with variable dampers	447
Lee, T. and Kawashima, K.	
A constitutive rule for viscoelastic material considering heat conduction and heat transfer ...	455
Kasai, K. and Sato, D.	

Bridge and Health Monitoring

Seismic performance of reinforced concrete bridge columns under bilateral excitation	463
Ogimoto, H., Kawashima, K., Watanabe, G. and Nagata, S.	
Seismic performance evaluation of beam-to-column connections with fatigue retrofitting	471
Tanabe, A., Miki, C. and Sasaki, E.	
Analysis of passive control systems for existing steel bridges in Japan	479
Kinoshita, K.	
Ultrasonic detection of defects by using the 3D ultrasonic phased array system	485
Rattanasuwannachart, N., Katsuyama, M. and Miki, C.	
Experimental rocking response of direct foundations of bridges	493
Sakellarakis, D., Watanabe, G. and Kawashima, K.	

DESIGN FOR COLLAPSE SAFETY

F. Zareian¹⁾, H. Krawinkler²⁾, and L.F. Ibarra³⁾

1) Ph.D Candidate, Department of Civil and Environmental Engineering, Stanford University, USA

2) Professor, Department of Civil and Environmental Engineering, Stanford University, USA

3) Senior Research Engineer, Southwest Research Institute, USA

farzin@stanford.edu, krawinkler@stanford.edu, libarra@cnwra.swri.edu

Abstract: Collapse prevention is a major constraint in the design decision process. Because of shortcomings in analytical modeling, collapse usually is assumed to be associated with an acceptable story drift. Recently, the introduction of realistic deterioration models has made it possible to predict structural response close to collapse. Evaluation of collapse capacity can be based on a measure called *relative intensity*, which is defined as the ratio of ground motion intensity to a structure strength parameter. Using this measure, the proposed approach for design for collapse safety consists of (a) specifying performance targets (e.g., tolerable probability of collapse at certain hazard level, mean annual frequency of collapse), and (b) deriving engineering parameters for system selection, using the relatively simple design decision support tools discussed in this paper. The proposed approach addresses the effects of aleatory and epistemic uncertainties on these engineering parameters. Application of this approach is illustrated through examples and discussions provided in the paper.

1. INTRODUCTION

Collapse in earthquake engineering implies loss of vertical (gravity) load carrying capacity of the structure during and after ground shaking. In modern structures in which brittle failure modes are prevented, collapse is usually triggered by large interstory drifts that are amplified by P- Δ effects (Bernal 1992, Gupta and Krawinkler 1999) and deterioration in strength and stiffness of structural elements (Ibarra 2003). In performance assessment, an already selected and proportioned structural system can be evaluated for its ability to resist ground motions without collapse, provided that reliable analytical models are available to predict behavior in the inelastic range up to collapse.

Design is different from performance assessment, by virtue of the fact that the building and its structural components and system first have to be created. Good designs are based on concepts that incorporate performance targets *up front* in the conceptual design process, so that subsequent performance assessment becomes more of a verification process of an efficient design rather than a design improvement process that may require radical changes.

Collapse prevention is one of the major constraints in the design decision process. Because of shortcomings in analytical modeling, collapse is usually assumed to be associated with an acceptable story drift. This approach does not permit redistribution of damage and does not account for the ability of the structural system to sustain deformations without collapse that are significantly larger than those associated with loss in resistance of individual elements. Ibarra (2003) has developed a methodology for evaluating structural collapse capacity for deteriorating structural systems. In Ibarra's study, the evaluation of collapse capacity is based on a measure called *relative intensity*, which is defined as the ratio of ground motion intensity to a structure strength parameter. The same measure will be used throughout this paper to address design for collapse safety.

This paper is concerned with conceptual design for collapse safety. The first task is to identify structural parameters that significantly affect the structure's collapse capacity and develop collapse capacity fragility curves associated with different combinations of these structural properties. The second task is to address the effects of uncertainties, both aleatory and epistemic, on the collapse capacity. The final task is to develop a process for estimating suitable structural properties that satisfy specified collapse performance targets. Conceptual design for collapse safety is greatly facilitated by focusing on discrete performance targets associated with discrete hazard levels, similar to the way it is being practiced in most of the performance-based guidelines presently in use. A more general approach is to define the performance target in the form of a tolerable mean annual frequency of collapse. Both options are pursued in the following discussion.

2. DOMAINS THAT CONTROL DESIGN FOR COLLAPSE SAFETY

Design for collapse safety comprises two domains; the *Hazard Domain*, and the *Structural System Domain* as illustrated in Figure 1. In conceptual design for collapse safety, the objective is to search for effective solutions at a time at which the details of the structural system are yet to be determined. In the following discussion the content of the two domains is summarized.

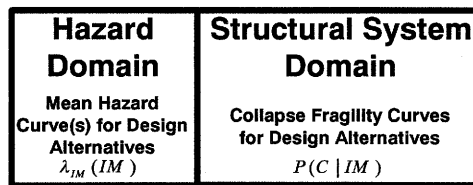


Figure 1: Domains controlling design for collapse safety

2.1 Hazard Domain

The hazard domain contains the return period dependent description of the ground motion intensity plus associated time history records. The intensity measure could be a scalar or a vector quantity (Baker and Cornell 2004), with the latter being of particular importance in the case of near-fault ground motions. In the numerical example presented later the spectral acceleration at the first mode period of the structural system ($S_a(T_1)$) is used as IM . The process of developing hazard curves involves many scientific assumptions (Kramer 1996). This means that there is *epistemic* uncertainty in the evaluation of a hazard curve. It has been shown by Jalayer (2003) that the *epistemic* uncertainty in the hazard is dealt with by using the *mean* hazard curve, denoted as $\bar{\lambda}_{IM}(IM)$, which reflects directly the *epistemic* uncertainty involved the process of developing hazard curves. It is important to note that the mean hazard curve changes with the first mode period of the explored structural system.

The records selected to represent the seismic input for specific IM values affect the collapse fragility curves contained in the structural system domain discussed in Section 2.2. The associated issues of ground motion scaling and near-fault effects have been and still are the subject of research and are not discussed further in this paper.

2.2 Structural System Domain

This domain contains collapse fragility curves, which portray, for a given structural system, the probability of collapse as a function of the intensity measure ($P(C|IM)$). Such curves can be obtained by subjecting deteriorating structural systems of specific properties to sets of ground motions representative of the range of IM s in which collapse is expected. If all component deterioration modes are adequately presented in the analytical model, it should be feasible to analytically trace structures till collapse by

incrementing the *IM* of the ground motion until a minute increment in *IM* leads to a very large increment in a global engineering demand parameter, *EDP* (such as maximum interstory drift), indicating dynamic instability.

Research has been performed recently on the “collapse capacity” of moment resisting frames, utilizing component hysteresis models that account for strength deterioration in the backbone curve (see Figure 2) and for cyclic deterioration in strength and stiffness (Ibarra 2003). The collapse capacity is defined as that value of the “relative intensity”, defined here as $[S_a(T_1)/g]/\gamma$ (γ = base shear strength coefficient V_y/W) at which dynamic instability occurs due to deterioration and P- Δ effects. It is noted that $[S_a(T_1)/g]/\gamma$ is equivalent to the ductility dependent strength reduction factor R_μ . The probability density function (assuming a lognormal distribution) of the collapse capacity is obtained as illustrated in Figure 3, and the corresponding cumulative distribution function represents the collapse fragility curve, $P(C|IM)$. Collapse fragility curves of the type shown in Figure 4 have been derived for regular and soft story frames subjected to a set of 40 ground motions. It has been concluded that the collapse fragility depends primarily on the component ductility capacity δ_c/δ_y (which is assumed to be the same for all components in the structure), the post-capping stiffness ratio α_c (see Figure 2), and the cyclic deterioration parameter $\gamma_{s,c,k,a}$. These parameters, together with the fundamental period T_1 and the base shear strength parameter $\gamma = V_y/W$, control the design for collapse safety.

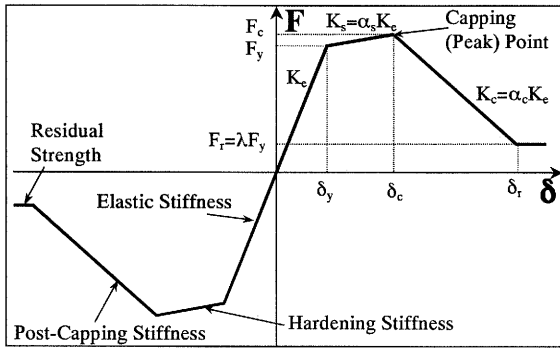


Figure 2. Backbone curve for deteriorating component hysteresis models (after Ibarra 2003)

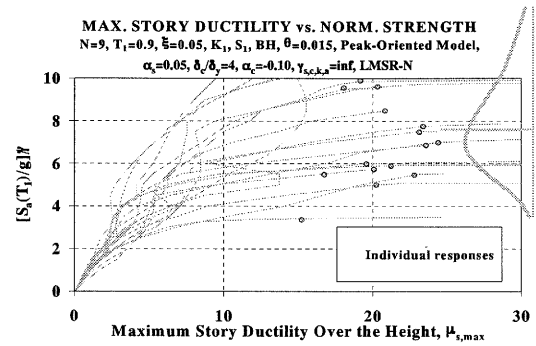


Figure 3: IDAs till collapse and distribution of collapse capacity (after Ibarra 2003)

The *aleatory* uncertainty due to the record-to-record variability is represented in the collapse fragility curve. If a lognormal distribution is considered for the probability of $[S_a(T_1)/g]/\gamma$ associated with collapse, its measure of dispersion (which is the standard deviation of the log of the data), β_{RC} (“Randomness in collapse Capacity”), is the representation of *aleatory* uncertainty. The *epistemic* uncertainty in the evaluation of collapse fragility curves, which has a number of sources, with lack of knowledge about the exact structural properties and inaccurate structural modeling being two major ones, affects the median estimate of $[S_a(T_1)/g]/\gamma$ associated with collapse but it is assumed to have no effect on β_{RC} . In other words, the lognormal distribution that was considered for collapse fragility curves has a random median value and a constant dispersion of β_{RC} . Detailed representation of *epistemic* uncertainty in the evaluation of collapse fragility curves is discussed in Section 3.2.

3. DECISION SUPPORT IN CONCEPTUAL DESIGN FOR COLLAPSE SAFETY

3.1 Design for Tolerable Probability of Collapse at a Specific Hazard Level

In most codes and guidelines it is assumed that adequate collapse safety is provided by limiting the maximum story drift at the design earthquake level to a specific value (e.g., a drift limit of 0.02 at the 10/50 hazard level). The drift at this hazard level is estimated from either an elastic analysis or an

inelastic time history analysis. But the latter usually is executed with the use of component hysteresis models that do not account for strength and stiffness deterioration. Thus, these *EDP* predictions provide no insight into the probability of collapse. With the advent of deterioration models that do account for important aspects of deterioration it is becoming possible to trace the response of structures to collapse (Ibarra 2003, Sivaselvan and Reinhorn 2000, Song and Pincheira 2000) and to be specific about a collapse performance target. Such a target could be expressed as a tolerable probability of collapse at a specific hazard level (say, 10% at the 2/50 hazard level), which could include a confidence statement (say, 10% at the 2/50 hazard level with 90% confidence) if epistemic uncertainty is accounted for. Figure 5 illustrates the design for collapse safety for a specific hazard level. The intersection of the line denoting the *IM* value at the specified hazard level with the line denoting the tolerable probability of collapse divides the design alternatives into a feasible and an unfeasible solution space.

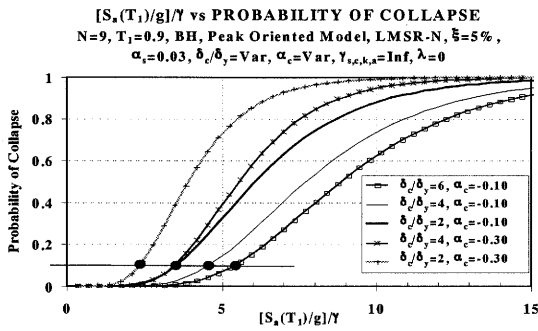


Figure 4. Collapse fragility curves for 9-story frame structures with $T_1 = 0.9$ s (after Ibarra 2003)

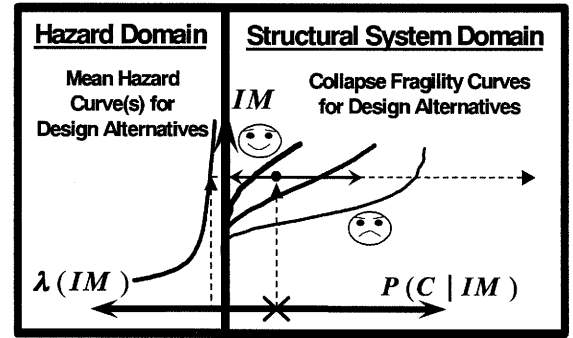


Figure 5: Conceptual design for collapse safety at discrete hazard levels

3.2 Design for Tolerable Mean Annual Frequency of Collapse

A different way to express desired collapse performance is to target a tolerable mean annual frequency (MAF) of collapse. If *epistemic* uncertainty is considered, a confidence level should be associated with the MAF, which then can be expressed as λ_c^x (e.g., tolerable mean annual frequency of collapse of 0.0004 with 90% confidence, $\lambda_c^{90\%} = 0.0004$). This performance target is more general (it permits the estimation of the probability of collapse over an expected life time), but it is more difficult to implement because the computation of a MAF requires integration over the hazard curve:

$$\lambda_c^x = \int_{Sa} P^x(C | sa) |d\bar{\lambda}_{sa}(sa)| \quad (1)$$

In Equation 1, $P^x(C | sa)$ is probability distribution function of the collapse capacity in terms of $Sa(T_1)$, or simply Sa , associated with collapse for confidence level x . The uncertainty in this probability distribution function, which has been accounted for in the calculation of MAF of collapse by introducing a confidence level x , is due to *epistemic* uncertainty. The other source of uncertainty is the *aleatory* uncertainty which has been discussed in Section 2.2. The *epistemic* uncertainty affects the estimate of the median of the collapse capacity, $\hat{\eta}_c$, and it is assumed that it has no effect on β_{RC} . The effect of *epistemic* uncertainty on $\hat{\eta}_c$ is described by β_{UC} (“Uncertainty in collapse Capacity”) which is the dispersion of the lognormal distribution fitted to the median estimates of $\hat{\eta}_c$. Jalayer (2003) has introduced a closed form solution, Equation 2, to estimate λ_c^x :

$$\lambda_c^x = \int_{Sa} P^x(C | sa) |d\bar{\lambda}_{sa}(sa)| = [\bar{\lambda}_{sa}(\hat{\eta}_c)] \left[\exp\left(\frac{1}{2} k^2 \beta_{RC}^2\right) \right] \left[\exp[K_x(k\beta_{UC})] \right] \quad (2)$$

The simplified expression on the right-hand side contains the MAF of the median collapse capacity, $\bar{\lambda}_{sc}(\hat{\eta}_c)$, and two terms that account, in an approximate manner, for the uncertainties inherent in the computation of the collapse capacity. The second term on the right hand side of Equation (2) accounts for the *aleatory* uncertainty and contains the slope of the hazard curve, k , at the referenced spectral acceleration value, and the dispersion, β_{RC} , due to record to record variability in the collapse fragility curve.. The dispersion β_{RC} in Equation (2) is found to be on the order of 0.4 to 0.5 (except for long period structures for which it is smaller because of the dominance of P-delta effects). The third term on the right hand side of Equation (2) accounts for the *epistemic* uncertainty. Pilot studies have shown that the dispersion due to *epistemic* uncertainty in the collapse fragility curve, β_{UC} , may be as large as or larger than that due to *aleatory* uncertainty (Ibarra 2003). For this reason, it is assumed that β_{UC} is 0.4 in the example described below. K_x is the standardized Gaussian variate associated with probability x of not being exceeded, and x is the confidence level that is sought for design.

4. EXAMPLE IMPLEMENTATION OF DECISION SUPPORT FOR COLLAPSE SAFETY

Providing collapse safety implies adherence to capacity design concepts, and it implies design for ductility. The latter is implicitly considered in present design approaches with the judgmental response modification (R) factor or behavior (q) factor. These factors are tied to component detailing (ductility) requirements, and in the design process they are used to reduce the strength design level to a fraction of the elastic demand associated with the spectral acceleration at the first mode period. To this date it is not known whether or not this R (or q) based design process provides a quantifiable, or for that matter even remotely consistent, factor of safety against collapse. Provided one can develop confidence in the collapse fragility curves of the type illustrated in Figure 3, the process illustrated conceptually in Section 3 can be utilized to perform designs that target a specific tolerable probability of collapse. This is illustrated next with an example.

The example addresses a 9-story office building, located in Southern California. Desired performance at the collapse prevention level could be expressed in terms of a tolerable probability of collapse at a specified hazard level or alternatively, a tolerable mean annual frequency of collapse. These two alternatives implicitly consider the *aleatory* uncertainty involved in the estimation of collapse capacity. The *epistemic* uncertainty can be dealt with by introducing confidence levels for design targets. These design targets could be expressed as a tolerable probability of collapse at a specified hazard level with a certain confidence statement, or a tolerable mean annual frequency of collapse with a certain confidence level.

4.1 Design for Tolerable Probability of Collapse at a Specific Hazard Level

In the example it was decided to use reinforced concrete moment-resisting frames as the primary structural system. Because of space constraints, only moment frames with $T_1 = 0.9$ and 1.8 sec. and with a base shear strength coefficient $\gamma = V_y/W = 0.1, 0.2$, and 0.3 are considered as alternatives. For the same reason the effect of *epistemic* uncertainty, which may be expressed in terms of a confidence statement, is ignored in this section. The site specific spectral acceleration hazard curves for the period of 0.9 sec. and 1.8 sec. are shown in the left portion of Figure 6. At the 2/50 hazard level, the collapse fragility curves for the structures with $T_1 = 0.9$ sec. and $\gamma = 0.1, 0.2, 0.3$, and $T_1 = 1.8$ sec. and $\gamma = 0.1, 0.2$, shown in the right portion of Figure 6 (which is magnified at the left hand side of the figure), indicate that the actual probability of collapse is greater than 0.1, rendering these solutions undesirable for collapse safety. Only for the $T_1 = 1.8$ sec. and $\gamma = 0.3$ structure, the collapse fragility curve in the right portion of Figure 6 indicates that the actual probability of collapse is smaller than 0.1 at 2/50 hazard level, rendering this solution desirable for collapse safety.

One could inspect collapse fragility curves for stronger structures, or, perhaps better from the perspective of behavior, take advantage of collapse capacity spectra of the type shown in Figures 7 and

8 (Ibarra 2003). These spectra show the relative intensity $[S_a(T_1)/g]/\gamma$ associated with a certain probability of collapse (10% in Figure 7, and 50% in Figure 8) for frame structures with $T_1 = 0.1N$ (N = number of stories) and several combinations of system parameters (see Figure 2). The spectra illustrate the effect of component ductility capacity (δ_c/δ_y) on the relative intensity, assuming $\alpha_c = -0.1$ and no cyclic deterioration ($\gamma_{s,c,k,a} = 8$). For a tolerable probability of collapse of 10% in a 2/50 event, data of the type shown in Figure 7 provides the necessary design decision support (similar spectra are available for other combinations of system parameters). For instance, if T_1 is selected as 0.9 sec. and the component ductility capacity is 4.0, the $[S_a(T_1)/g]/\gamma$ value for a 10% probability of collapse is 4.6, which for the 2/50 hazard of the example problem ($S_a(0.9) = 1.7g$) results in a required base shear strength coefficient of $\gamma = 1.7/4.6 = 0.37$. A larger ductility capacity (better detailing) or a more flexible structure can reduce the required strength. For instance, for $T_1 = 0.9$ sec. and $\delta_c/\delta_y = 6$, the $[S_a(T_1)/g]/\gamma$ value is 5.4, which would result in $\gamma = 1.7/5.4 = 0.31$. Alternatively, a more flexible structure could be selected. For $T_1 = 1.8$ sec. and $\delta_c/\delta_y = 4$, the $[S_a(T_1)/g]/\gamma$ value is 3.5, which for the 2/50 S_a value of 0.86g at 1.8 sec. results in a required base shear strength coefficient of $\gamma = 0.86/3.5 = 0.25$.

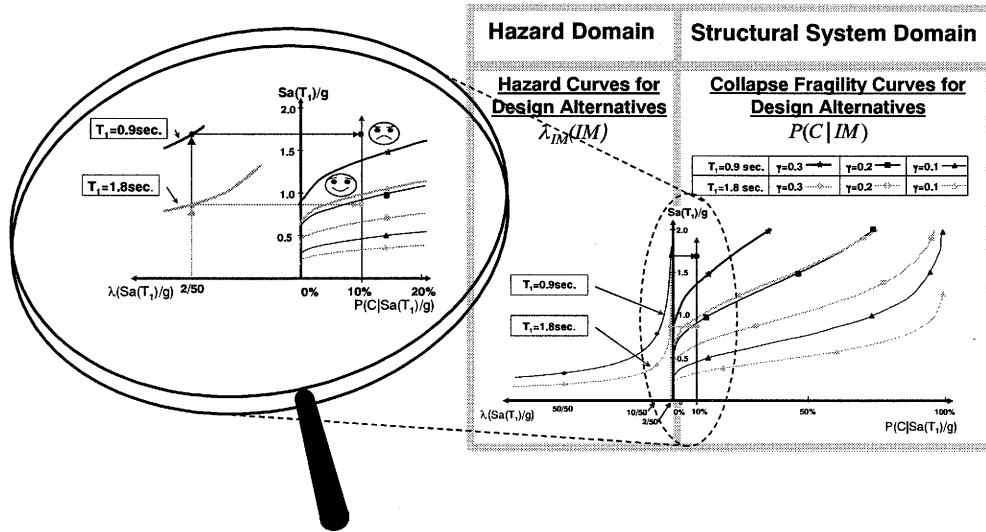


Figure 6: Example of conceptual design for collapse safety at discrete hazard levels

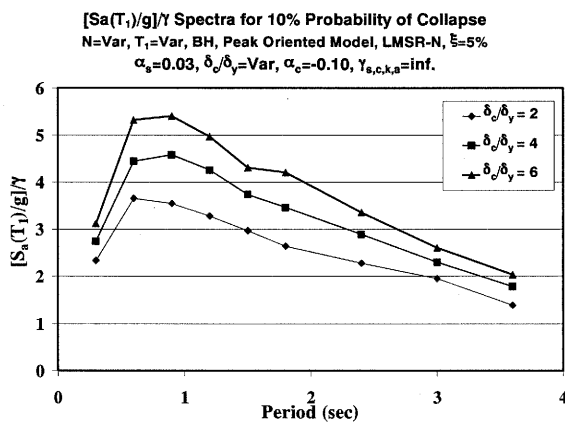


Figure 7. $[S_a(T_1)/g]/\gamma$ spectra for Beam-Hinge models associated with 10% probability of collapse

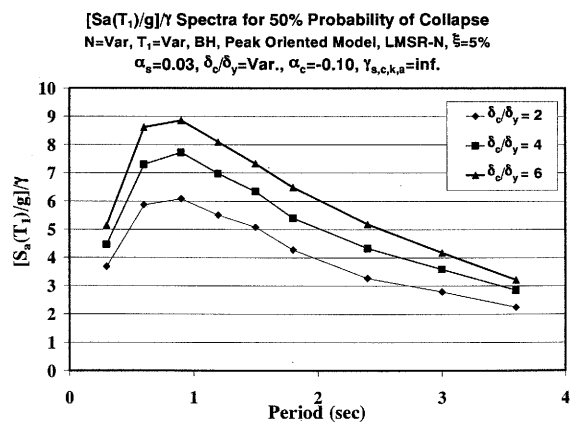


Figure 8. $[S_a(T_1)/g]/\gamma$ spectra for Beam-Hinge models associated with 50% probability of collapse

These are the kind of trade-offs that can be evaluated through the use of collapse probability spectra of the type shown in Figure 6, presuming that a tolerable probability of collapse is specified at a specific hazard level. It is important to note that the benefits of component ductility capacity and of flexibility are much smaller than anticipated from code design procedures. An increase in δ_c/δ_y by 50% (from 4 to 6) only led to a decrease in required base shear strength coefficient γ from 0.37 to 0.31, and an increase in T_I from 0.9 to 1.8 sec. only led to a decrease in required base shear strength coefficient γ from 0.37 to 0.25 even though the elastic strength demands would differ by a factor of 2.0 in the constant velocity region of design spectra.

4.2 Design for Tolerable Mean Annual Frequency of Collapse

Continuing the above example, let us target a tolerable mean annual frequency of collapse of 0.0002 (i.e., a tolerable probability of collapse of approximately $0.0002 \times 50 = 0.01$ in a 50 year life span) and for the time being ignore the *epistemic* uncertainty by not specifying a confidence level of this design target. For this case, Equation 2 reduces to

$$\lambda_c = [\bar{\lambda}_{Sa}(\hat{\eta}_c)] \left[\exp\left(\frac{1}{2} k^2 \beta_{RC}^2\right) \right] \quad (3)$$

The above collapse safety criterion could be used, together with $[S_a(T_I)/g]/\gamma$ spectra for a 50% probability of collapse (see Figure 8), to arrive at effective design solutions. Again using the example of the 9-story frame structure, the following design alternatives could be explored. If a period of 0.9 sec. and a component ductility capacity of $\delta_c/\delta_y = 4$ are targeted, then the median $[S_a(T_I)/g]/\gamma$ value from Figure 8 is 7.7. For the site specific hazard curve the slope of the S_a hazard curve in the neighborhood of a MAF of 0.0001 to 0.0004 is about 2.2, and the β_{RC} value is about 0.4 (Ibarra 2003). Thus, from Equation (3) the MAF of the S_a associated with the 50% probability of collapse, $\bar{\lambda}_{sa}(\hat{\eta}_c)$, is equal to $0.0002/\exp(0.5 \times 2.2^2 \times 0.4^2) = 0.000136$. From the S_a hazard curve for the site of the example problem, the corresponding S_a is 2.8g, and the corresponding γ value is $2.8/7.7 = 0.36$. Alternatives are to increase the component ductility capacity (if it is increased from 4 to 6, $[S_a(T_I)/g]/\gamma$ is 8.9, and for the same $\bar{\lambda}_{sa}(\hat{\eta}_c)$ of 0.000136 the γ value becomes $2.8/8.9 = 0.31$), or to increase the structure period. If, for instance, T_I is 1.8 sec., the $[S_a(T_I)/g]/\gamma$ value from Figure 8 is 5.4 (for $\delta_c/\delta_y = 4$), and, using the site specific k value of 2.4 for the $T = 1.8$ sec. hazard curve, $\bar{\lambda}_{sa}(\hat{\eta}_c)$ becomes 0.000126, the S_a value for this MAF is 1.4g, and the base shear strength parameter γ becomes $1.4/5.4 = 0.26$.

By including the *epistemic* uncertainty, one could target, for instance, a 90% confidence level for a mean annual frequency of collapse of 0.0004 (2% in 50 years). Using the process illustrated previously, if a period of 0.9 sec. and a component ductility capacity of $\delta_c/\delta_y = 4$ are assumed, then the median $[S_a(T_I)/g]/\gamma$ value from Figure 8 is 7.7. For the site specific hazard curve the slope of the S_a hazard curve in the neighborhood of a MAF of 0.001 to 0.004 is about 2.2, and the β_{RC} value is about 0.4. For the 90% confidence level, the K_x value is 1.28. Using $\beta_{UC} = 0.4$, the MAF of S_a at the median collapse capacity, $\bar{\lambda}_{sa}(\hat{\eta}_c)$, is computed from Equation (2) as $0.0004/[\exp(0.5 \times 2.2^2 \times 0.4^2) \cdot \exp(1.28 \times 2.2 \times 0.4)] = 0.000088$. From the S_a hazard curve the corresponding S_a is 3.4g, and the corresponding γ value is $3.4/7.7 = 0.44$. This is a large value that would control strength design. As before, alternatives are to increase the component ductility capacity (if it is increased from 4 to 6, $[S_a(T_I)/g]/\gamma$ is 8.9, and for the same $\bar{\lambda}_{sa}(\hat{\eta}_c)$ of 0.000088 [presuming that both β_{RC} & β_{UC} are insensitive to the ductility change] the γ value becomes $3.4/8.9 = 0.38$), or to increase the structure period. If, for instance, T_I is 1.8 sec., the $[S_a(T_I)/g]/\gamma$ value from Figure 8 is 5.4 (for $\delta_c/\delta_y = 4$), and, presuming that k is also about 2.4 for the $T = 1.8$ sec. hazard curve, the S_a value for a MAF of 0.000074 becomes 1.8g, and the base shear strength parameter γ becomes $1.8/5.4 = 0.33$.

The importance of including *epistemic* uncertainty and an associated confidence level can be quantified by computing the base shear strength coefficient γ for a targeted mean annual frequency of collapse of 0.0004 from Equation (3), i.e., by ignoring the *epistemic* uncertainty. In this case γ becomes 0.26 for $T_1 = 0.9$ sec. and $\delta_c/\delta_y = 4$, as compared to the value of 0.44 for the case including *epistemic* uncertainty and a high confidence level of 90%. This example demonstrates that *epistemic* uncertainty together with a high confidence level can indeed have a large effect on the target design strength of frame structures (the assumed value of $\beta_{UC} = 0.4$ is believed to be realistic).

5. CONCLUSIONS

This paper proposes two approaches to accomplish effective design for collapse safety and illustrates them conceptually and through examples. Conceptual design for collapse safety implies a decision process that leads to the selection of one or several effective design alternatives based on either a tolerable probability of collapse at discrete hazard levels or a tolerable mean annual frequency of collapse with or without a confidence statement, depending on the incorporation or exclusion of *epistemic* uncertainty. The implementation challenges are to identify structural parameters that significantly affect the structure's collapse capacity, to develop collapse fragility curves associated with different combinations of these structural properties, to quantify the effects of uncertainty, both *aleatory* and *epistemic*, on collapse fragility curves, and to develop a process for estimating structural properties that meet specified collapse performance targets. It was shown by example that increasing the flexibility (choosing a structure with larger natural period) or increasing the ductility capacity of structural members reduces the required strength for collapse safety – but by a smaller amount than anticipated based on present code design concepts. Uncertainties, both *aleatory* and *epistemic*, have a significant effect on the outcome of the conceptual design for collapse safety.

Acknowledgements:

This research was carried out as part of a comprehensive effort at Stanford's John A. Blume Earthquake Engineering Center to develop basic concepts for PBEE and supporting data on seismic demands and capacities. This effort is supported by the NSF sponsored Pacific Earthquake Engineering Research (PEER) Center.

References:

- Bernal, D. (1992), "Instability of Buildings Subjected to Earthquakes," *Journal of Structural Engineering*, **118**(8), 2239-2260.
- Gupta, A. and Krawinkler, H. (1999), "Seismic Demands for Performance Evaluation of Steel Moment Resting Frame Structures," Report 132. John A. Blume EERC, Stanford University.
- Ibarra, L.F. (2003), "Global Collapse of Frame Structures Under Seismic Excitations," *Ph.D. Dissertation*, Department of Civil Engineering, Stanford University.
- Cornell, A. and Krawinkler, H. (2000), "Progress and Challenges in Seismic Performance Assessment," *PEER News*, April 2000.
- Deierlein G. (2004), "Overview of a Comprehensive Framework for Earthquake Performance Assessment. *Proc. Int'l Workshop on Performance-Based Seismic Design – Concepts and Implementation*, Bled, Slovenia, 15-26.
- Krawinkler, H. and Miranda, E. (2004), "Performance-Based Earthquake Engineering," Chapter 9 of *Earthquake Engineering: From Engineering Seismology to Performance-based Engineering*, CRC Press.
- Jalayer, F. (2003), "Direct Probabilistic Seismic Analysis: Implementing Nonlinear Dynamic Assessments," *Ph.D. Dissertation*, Department of Civil Engineering, Stanford University.
- Baker, J. and Cornell, C. A. (2004), "Choice of a Vector of Ground Motion Intensity Measures for Seismic Demand Hazard Analysis," *Proceedings of 13th WCEE*, Vancouver, Canada, Paper No. 3384.
- Kramer, S. L. (1996), "Geotechnical Earthquake Engineering," *Prentice Hall*.
- Sivaselvan, M.V. and Reinhorn, A.M. (2000), "Hysteretic Models for Deteriorating Inelastic Structures," *Journal of Engineering Mechanics*, American Society of Civil Engineers, **126**(6), 633-640.
- Song, J. and Pincheira, J. (2000), "Spectral Displacement Demands of Stiffness and Strength Degrading Systems," *Earthquake Spectra*, **16**(4), 817-851.
- Cornell, C.A. (1996), "Calculating Building Seismic Performance Reliability; A Basis for Multi-Level Design Norms," *Proc. 11th WCEE*, Acapulco, Mexico.

EFFECT OF PHASE SPECTRUM UNCERTAINTIES OF EARTHQUAKE MOTION ON SEISMIC FRAGILITY CURVE OF STEEL BRIDGE PIER

T. Sato¹⁾, M. Masmoto²⁾ and I. Yoshida³⁾

1) Professor, Disaster Prevention Research Institute, Kyoto University, Japan

2) Graduate Student, Department of Urban Management, Kyoto University, Japan

3) Manager, Geotechnical & Structural Engineering Dept. Tokyo Electric Power Services Co., Ltd, Japan
sato@catfish.dpri.kyoto-u.ac.jp, masumoto@catfish.dpri.kyoto-u.ac.jp, dyoshida@tepsco.co.jp

Abstract: The earthquake resistant capacity of a structure with uncertainties is evaluated by fragility curves based on the probabilistic concept. We estimate fragility curves by using Monte Carlo simulation (MCS) and limit seismic intensity. For the effective estimation of the tail part, namely low conditional failure probability, we use the Subset simulation method. Samples are generated to search the failure region in each subspace by using Markov Chain Monte Carlo (MCMC). The effect of phase spectrum uncertainties on the fragility curve is also examined and a method to define a design earthquake motion eliminating phase uncertainties

1. INTRODUCTION

The necessity of effective method to estimate the low failure probability of structural system is increased from the standpoint of evaluation of life cycle cost, risk and probabilistic safety assessment (PSA). In seismic PSA, the seismic load and the strength of structure are often estimated separately. The former is modeled based on the probabilistic concept, a seismic hazard curve. On the other hand the structure strength with uncertainties is modeled by a fragility curve.

It is important to estimate the tail part of fragility curve, very low conditional failure probability of structural system, in order to compute the failure probability accurately. We propose an efficient method to estimate a fragility curve by using MCS and limit seismic intensity. Limit seismic intensity is defined as the minimum amplitude of an input motion causing damage to a structure, in other words, input motion level at where the safety factor of structural system becomes 1.0. In our research, we use the Subset simulation method proposed by Au and Beck (2002), in which samples in each subspace are generated by using MCMC (Gilks *et al.*, 1996).

In following section, we first explain the concept of limit seismic intensity and Subset simulation method, and then show results of numerical simulations in which fragility curves of a steel bridge pier are calculated by the proposed method. Effect of input motions to the fragility curves is also investigated to make clear importance of phase characteristic of earthquake motions.

2. ESTIMATION OF FAILURE PROBABILITY WITH LIMIT SEISMIC INTENSITY

In general a limit state function defines the failure region as follows,

$$g(S, \mathbf{x}_R) < z_0 \quad (1)$$

where, S is a structural parameter with uncertainty, which is sensitive to the limit state, \mathbf{x}_R and z_0 are the other uncertain parameters and threshold value to define the failure, respectively. The inverse

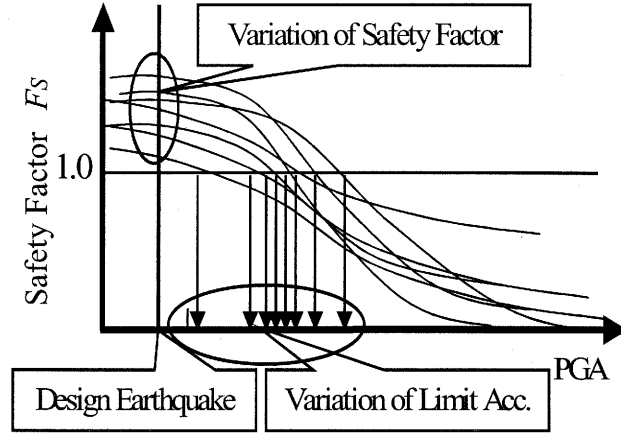


Fig. 1 Proposed method to evaluate a fragility curve by using
Limit Seismic Intensiv (Acceleration)

function $R(z_0, \mathbf{x}_R)$ is defined to calculate S which satisfies $g(S, \mathbf{x}_R) = z_0$. The R is defined as limit intensity. We assume $R < S$ for failure zone in following discussion. Assuming independence between S and the other parameters, the probability density function (hereafter referred as f or pdf) of parameters is expressed by,

$$f(S, \mathbf{x}_R) = f_S(S) f_{\mathbf{x}_R}(\mathbf{x}_R) \quad (2)$$

The failure probability can be obtained as follows,

$$\begin{aligned} P_f &= \int_{g < z_0} f(S, \mathbf{x}_R) dS d\mathbf{x}_R = \int_{R < S} f_S(S) f_{\mathbf{x}_R}(\mathbf{x}_R) dS d\mathbf{x}_R = \left(\int_{R < S} f_S(S) dS \right) f_{\mathbf{x}_R}(\mathbf{x}_R) d\mathbf{x}_R \\ &= \left(\int_{R(z_0, \mathbf{x}_R)}^{\infty} f_S(S) dS \right) f_{\mathbf{x}_R}(\mathbf{x}_R) d\mathbf{x}_R = \{1 - F_S(R(z_0, \mathbf{x}_R))\} f_{\mathbf{x}_R}(\mathbf{x}_R) d\mathbf{x}_R \end{aligned} \quad (3)$$

We can estimate a failure probability using a seismic hazard curve $1 - F_S(R(z_0, \mathbf{x}_R))$ and a probability density function of limit seismic intensity $f_{\mathbf{x}_R}$. The failure probability for S conditioned by $R < S$, which is equivalent to the fragility curve, can be expressed as

$$F_R(S) = \int_{R < S} f(S, \mathbf{x}_R) d\mathbf{x}_R = \int U(S - R(z_0, \mathbf{x}_R)) f_{\mathbf{x}_R}(\mathbf{x}_R) d\mathbf{x}_R \quad (4)$$

$U(x)$ is step function, which is equal to 1.0 when x is non-negative, otherwise 0.0. In this study MCS is used for the integration of Eq.(4). The probability density function of \mathbf{x}_R is approximated by using samples generated according to the $f(\mathbf{x}_R)$ and Dirac's delta function.

$$f_{\mathbf{x}_R}(\mathbf{x}_R) = \frac{1}{n} \sum_{j=1}^n \delta(\mathbf{x}_R - \mathbf{x}_R^{(j)}) \quad (5)$$

Substituting Eq.(5) into Eq.(4), Eq.(6) is derived to estimate fragility curve.

$$F_R(S) = \frac{1}{n} \sum_{j=1}^n U(S - R(z_0, \mathbf{x}_R^{(j)})) \quad (6)$$

The fragility curve is defined as conditional failure probability, provided seismic intensity as given in Eq.(4) or (6). A simple way to estimate a fragility curve is to perform MCS many times for several given S levels and count the number of samples dropping into a failure region but it needs a rather long computational time. The proposed method is illustrated in **Fig. 1**. In this method, we generate samples $\mathbf{x}_R^{(j)}$ ($j=1, \dots, n$) at the design earthquake motion level by MCS and limit seismic intensity $R(z_0,$

$\mathbf{x}_R^{(j)}$) is calculated for each generated $\mathbf{x}_R^{(j)}$ by binary search as to satisfy $g(S, \mathbf{x}_R)=z_0$ and then fragility curve is obtained by using Eq.(6). Although the estimation of $R(z_0, \mathbf{x}_R^{(j)})$ needs a longer computation time than to evaluate the ordinary limit state value $g(S, \mathbf{x}_R)$, the proposed method is more efficient in most cases because a fragility curve can be obtained by a single MCS samples.

3. SUBSET SIULATION

The procedure of Subset simulation (Au and Beck, 2002) is summarized as follows.

- 1) Generate n_t samples according to $pdf(\mathbf{x})$ and calculate the value of limit state function.
- 2) Sort the samples according to the order of the value of limit state function such as z_1, z_2, \dots, z_n in which z_1 is the smallest. The subspace F_{k+1} satisfying $P(F_{k+1}|F_k) = n_s / n_t$ is defined with the following equation for given n_s

$$F_{k+1} = \{\mathbf{x} | z(\mathbf{x}) < C_{k+1}\}, \quad C_{k+1} = \frac{z_{n_s} + z_{n_s+1}}{2} \quad (7)$$

- 3) Generate n_t samples from the samples z_i ($i=1, \dots, n_s$) in the subspace by using MCMC (Gilks *et al*, 1996).
- 4) If the number of samples reaches failure zone becomes large enough, then stop the calculation, otherwise go back to the step 2.

The failure probability can be calculated with the number of samples in failure zone n_f in subset k ,

$$P(z < 0) = \left(\frac{n_s}{n_t}\right)^k \frac{n_f}{n_t} \quad (8)$$

MCMC is a powerful tool to generate samples satisfying an arbitrary density function (see reference for more information). The conditional probability function in the subspace F_k is given by

MCMC is a powerful tool to generate samples satisfying an arbitrary density function (see reference for more information). The conditional probability function in the subspace F_k is given by

$$pdf(\mathbf{x} | F_i) = \frac{pdf(\mathbf{x}) I_{F_i}(\mathbf{x})}{P(F_i)} \quad (9)$$

where $I_{F_i}(\mathbf{x})$ is indicator function that is 1 if \mathbf{x} is inside of subspace F_k , otherwise 0.

A sample \mathbf{x} obeying a certain probability distribution function can be obtained from a sample \mathbf{u} generated from a uniform distribution function if cumulative distribution function $\Phi(\mathbf{x})$ is given as $\mathbf{x} = \Phi^{-1}(\mathbf{u})$. The Eq.(9) can be rewritten as

$$pdf(\mathbf{u} | F_i) = \frac{pdf(\mathbf{u}) I_{F_i}(\mathbf{u})}{P(F_i)} = \frac{I_{(0,1)}(\mathbf{u}) I_{F_i}(\mathbf{u})}{P(F_i)} \quad (10)$$

In our study, proposal distribution is also assumed to be an uniform distribution.

$$q(\mathbf{u}' | \mathbf{u}_k) = \begin{cases} \frac{1}{2a}; & |\mathbf{u}_k - \mathbf{u}'| < a \\ 0; & \text{otherwise} \end{cases} \quad (11)$$

where \mathbf{u}' is a candidate, \mathbf{u}_k is a current sample. Then the acceptance ratio can be simplified as

$$\alpha(\mathbf{u}_k, \mathbf{u}') = \min\{1, I_{(0,1)}(\mathbf{u}') I_{F_i}(\mathbf{u}')\} \quad (12)$$

Eq.(12) contains two kinds of criteria $I_{(0,1)}(\mathbf{u}')$ and $I_{Fk}(\mathbf{u}')$. For $I_{(0,1)}(\mathbf{u}')$, each variable is separately updated and judged. Then judge $I_{Fk}(\mathbf{u}')$ in full uncertain parameters. As a parameter “a” in Eq.(11) has a strong influence on the efficiency of the simulation, several values of “a” are used sequentially in the simulation.

4. FRAGILITY CURVE OBTAINED BY PUSH-OVER ANALYSIS

We apply the proposed methodology to an actual steel frame bridge shown in **Fig. 2** and calculate a fragility curve of this structure in which we consider several uncertainties of the structural parameters including the mass of upper structure, yield stress, thickness of plate and so on. We divide the bridge into 6 parts and consider 6 yield stresses for each part. Limit acceleration (PGA, peak ground acceleration) is used as limit seismic intensity. Though three limit states, bending, shear and deformation, are considered in an actual design, we consider only bending mode for simplicity. We followed the ordinary design procedure of a bridge pier in Japan (Design of Highway Bridge Foundations in Japan, 2003) which is consisted of the following three steps: 1) Perform two-dimensional push over analysis and obtain relation between applied load and bending deformation. 2) Estimate applied load to cause failure based on energy conservation principle and limit stage design point. 3) Limit acceleration is calculated based on the applied load, the predominant period and weight of the bridge.

Based on the energy conservation principle we calculate seismic load to cause the structure failure, however, it has been shown that this principle tends to overrate the maximum response displacement for steel structures in comparison with the result of nonlinear dynamic analysis. Some researchers study this reason and show that it is based on the difficulty to define yield point and damping characteristic of steel structures. Because this overrating brings designed structures in the safer region we use this principle even though there are still controversial opinions. We, however, take this uncertainty into account to calculate the fragility curve.

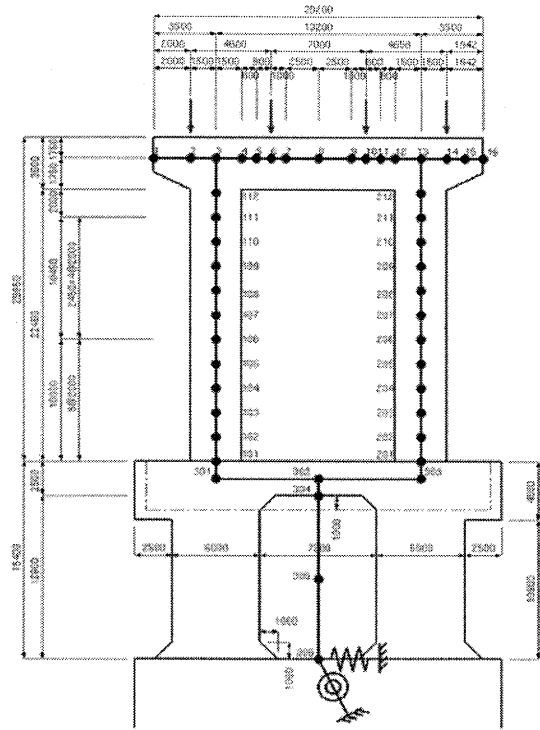


Fig. 2 The model of steel bridge pier

Basic parameters of the Pier Model

Young's Modulus of steel and concrete are 2.0×10^8 [kN/m²] and 2.0×10^7 [kN/m²], respectively. Damping constant of them are 0.03 and 0.02. The caisson foundation is modeled by a mass with rotation and horizontal springs. Mass of upper structure is loaded at node 2, 6, 10, 15 (**Fig. 2**), and they are 21551.18[kN], 915.32[kN], 985.88[kN], 19763.66[kN], respectively. Stress strain relationship of steel is assumed to be expressed by the Bi-linear model and we calculate M - ϕ relation of the box type steel pier element to obtain equivalent bending rigidity of beam element based on the Guide line of anti-seismic reinforcement for existing steel bridges (Hanshin Expressway Public Corporation, 1997). Furthermore we take into the corrosion effect account on the reduction of thickness of steel plate used for bridge pier.

Uncertainties to be considered

(1) Mass of upper structures

From observation data for several bridges, we assume the ratio between observed value and design value is distributed as normal distribution with the mean 1.03 and standard deviation of 0.02.

(2) Strength of component

• Yield stress

We define $M_m = \sigma_y / F_y$. σ_y is observed yield stress of actual structures and F_y is designed value. From 1122 data, we assume M_m is distributed as lognormal distribution with the mean of 1.15 and c.o.v. of 0.11.

• Thickness of steel plate

We define $F_m = S_m / S_n$. S_m is observed cross-section factor of actual structures and S_n is designed value. From data, we assume F_m is distributed as normal distribution with the mean of 1.00 and c.o.v. of 0.05.

(3) Foundation part

Because variation of soil parameters is not easy to evaluate for defining equivalent spring constants of foundation model we assume soil spring factor is distributed as normal distribution with c.o.v. of 0.1.

(4) Energy conservation principle

The energy conservation principle tends to overrate the maximum response displacement for steel structures. From investigation (by Kitahara, 2001), we assume that the ratio between maximum response displacement derived by this principle and that obtained by nonlinear dynamic analysis is 1.42 (mean) and its c.o.v. is 0.329.

(5) Corrosion

10 years have passed since the target bridge was constructed. From observation data, we assume the mean decrement of the thickness of plate caused by corrosion is 0.255mm and its standard deviation is 0.4.

(6) Ultimate strength

Ultimate strength is assumed to be distributed. From results of buckling experiment, we assume ultimate strength is distributed as normal distribution with c.o.v. of 0.05.

Criteria

Because there are many elements in the bridge pier model we define the critical condition (failure) of the pier as one of element's curvatures exceeds the threshold value. At this time, the displacement of top of the pier (node 8 in **Fig. 2**) is defined as the final horizontal displacement and the horizontal

Table 1 Uncertainties considered in the example (CASE1)

Uncertainties		Mean(μ)	Standard Deviation(σ)	C.O.V	Distribution
Mass of upper structure observed value / design value		1.03	0.02	0.019	Normal
Strength of component	Yield stress M_m observed value / design value	1.15	0.1265	0.11	Lognormal
	Thickness of plate F_m observed value / design value	1.00	0.05	0.05	Normal
Ground factor	Soil Spring	$1.0 \times \text{Calc.}$	0.1μ	0.1	Normal

load as final horizontal load to cause failure. Using them, we estimate the applied load to cause failure based on energy conservation principle and we obtain limit acceleration dividing this load by the mass

of superstructure.

Numerical Examples

We calculate several fragility curves by changing number of uncertainties in which two cases are shown below. Uncertainties for CASE1 are summarized in **Table 1**. In this case, we consider 9 uncertainties and assume ultimate strain of $10 \varepsilon_y$ (ε_y is yield strain) as critical condition of pier (Guide line of anti-seismic reinforcement for existing steel bridges, 1997). So the curvature when strain exceeds $10 \varepsilon_y$ is defined as a threshold value. First, we perform the ordinary MCS to obtain the fragility curve with 30,000 samples. Then we estimate the fragility curve by Subset simulation with 100 samples in each subspace. The computation time is less than 1/70 of ordinary MCS. We adopt the parameter $n_i=100$, $n_s=10$, and the ten types of proposal density function using different values of parameter “ a ”. The obtained fragility curves are shown in **Fig. 3**. An accuracy of MCS is represented by c.o.v. δ . When the failure probability P_F is small, the number of samples N_δ required to achieve given δ is expressed by,

$$N_\delta = \frac{1 - P_F}{P_F \delta^2} \approx \frac{1}{P_F \delta^2} \quad (13)$$

As we use 30,000 samples for ordinary MCS, we can estimate $P_F=10^{-3}$ with an accuracy of $\delta=0.2$. In **Fig. 3**, the fragility curve obtained by using Subset Simulation agrees well with the fragility curve obtained by the ordinary MCS up to the level of 10^{-3} . Additionally, the distribution of the generated samples (pdf) is shown in **Fig. 4**. This result shows that the samples are well generated from the tail part of the former subset.

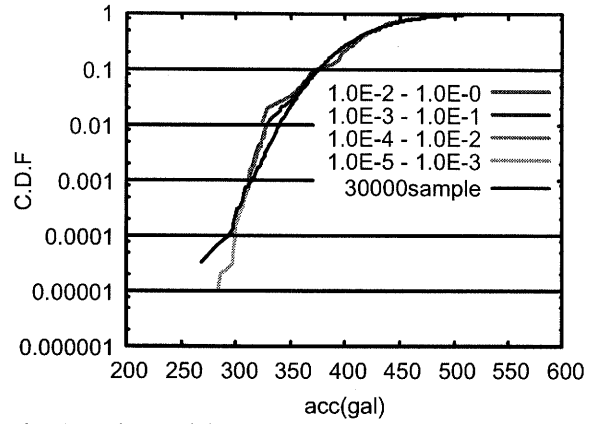


Fig. 3 Estimated fragility curve (cdf)(9 uncertainties)

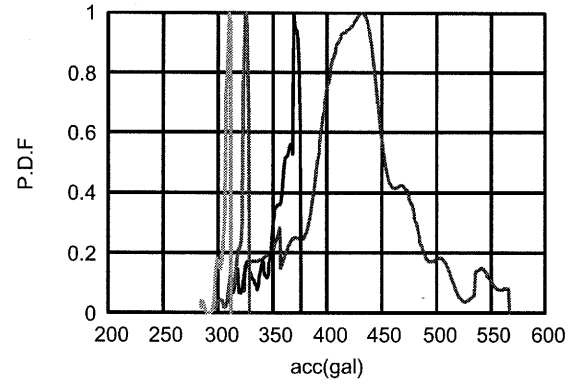


Fig. 4 Distribution of samples

Table 2 Uncertainties considered in the example (CASE2)

Uncertainties		Mean(μ)	Standard Deviation(σ)	C.O.V	Distribution
Mass of upper structure observed value / design value		1.03	0.02	0.019	Normal
Strength of component	Yield stress M_m observed value / design value	1.15	0.1265	0.11	Lognormal
	Thickness of plate F_m observed value / design value	1.00	0.05	0.05	Normal
Ground factor	Soil Spring	$1.0 \times \text{Calc.}$	0.1μ	0.1	Normal
Ultimate strength		M_{u2}, ϕ_{u2}	0.05μ	0.05	Normal
Corrosion thickness		0.225	0.4	1.7	Lognormal
Energy conservation principle		1.42.	0.467	0.329	Normal

In CASE2, we consider 12 uncertainties including the decrement of the thickness of plate caused by corrosion, the error of energy conservation principle, and the ultimate strength as summarized in **Table 2**. And we assume ultimate strain expressed by $(20-25R_f) \varepsilon_y$ (R_f is parameter of width-thickness ratio) as the critical condition of pier (Design of Highway Bridge Foundations in Japan, 2003). In this case, we adopt the parameter $n_f=1000$, $n_s=100$, and the ten types of proposal density function using different values of parameter " α ". The obtained fragility curves are shown in **Fig. 5**. Comparing **Fig. 3** and **4**, we can see that the fragility curve in CASE2 has wider distribution than CASE1 and it is shifted to left hand side which means the bridge pier being damaged by small acceleration if the number of uncertainties increases.

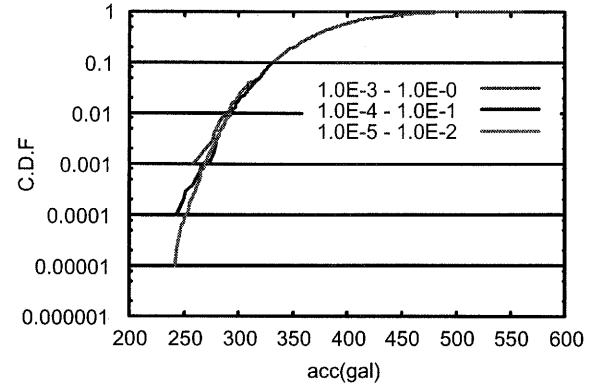


Fig. 5 Estimated fragility curve (cdf)
(12uncertainties)

5. ESTIMATION FRAGILITY CURVE TROUGH DYNAMIC ANALYSIS

In this section we consider structural uncertainties given in **Table 1**. We estimate fragility curves by dynamic analysis using two different input motions, which are shown in **Fig. 6**, Higashi Kobe (NS) and JMA Kobe (NS) records observed during the 1995 Hyogoken Nambu earthquake in Japan. Their Fourier amplitude spectra are modified to be compatible with the design acceleration response spectrum (**Fig. 7**). There is an obvious difference between two fragility curves (**Fig. 8**). This difference is caused by the difference of phase spectrum between two input motions.

In order to investigate effect of phase spectrum uncertainties on structure response, several input motions are simulated using the stochastic model of phase spectrum (Sato *et al.*, 1999). This stochastic model provides the regression equations of mean and standard deviation of group delay time as functions of earthquake magnitude M and epicentral distance Δ . The group delay time is the first order derivative of phase spectrum with respect to the circular frequency.

Using regression coefficients derived by Sato *et al.*, we generate samples of group delay time for earthquakes with magnitude of 8.0 and epicentral distance 10 [km] assuming normal distribution for characteristics of group delay time at each discrete circular frequency. Integrating a sample group delay time, we can obtain a sample phase spectrum and then simulate an input motion compatible with the design acceleration response spectrum. The obtained fragility curves are shown in **Fig. 9**, in which 30 fragility curves are shown with thin line and the mean fragility curve with thick line.

The effect of phase uncertainty on the fragility curve is rather high as can be seen that the width of limit acceleration at the failure probability 10^{-3} is about 160[cm/sec²] even though amplitude spectrum shape is restricted by the design response spectrum. This fact tells us that it is important to consider phase characteristics of input motions for evaluating a fragility curve through dynamic analysis of a structural system.

Fragility curve including phase spectrum uncertainties can be obtained by cumulating many fragility curves. The fragility curve cumulating fragility curves obtained from 30 sample input motions is shown in **Fig. 10**, and distribution can be seen wider than the mean fragility curve.

We calculated the ductility demand response spectra using the sample input motions as shown in **Fig. 11** (for the case of $\mu=2$ and 4). The strength demand spectrum is obtained through nonlinear dynamic response analyses of a single degree of freedom system. The strength demand spectrum expresses the relationship between the yield seismic coefficient and elastic natural period (T) of

SDOF. The yield seismic coefficient of the SDOF is controlled until the SDOF response reaches the target ductility. In this study, the hysteretic model used for the analyses is a bi-linear model. The second stiffness is selected as 20% of the first, and 5% damping coefficient assigned. Although we used the same elastic response spectrum (the design acceleration response spectrum) to simulate sample input motions, variation of the strength demand spectrum can be seen at each T in **Fig. 11**. The difference among fragility curves in **Fig. 9** is attributed to this variation.

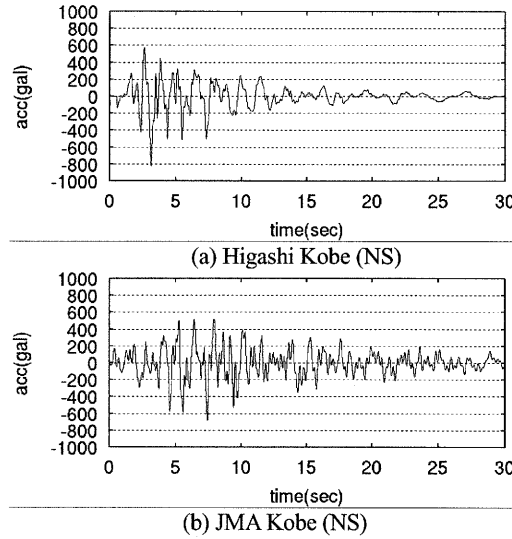


Fig.6 Time histories of acceleration

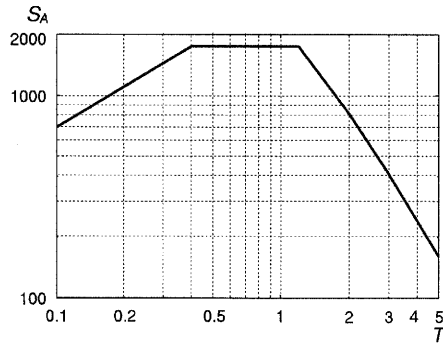


Fig.7 Design response spectrum

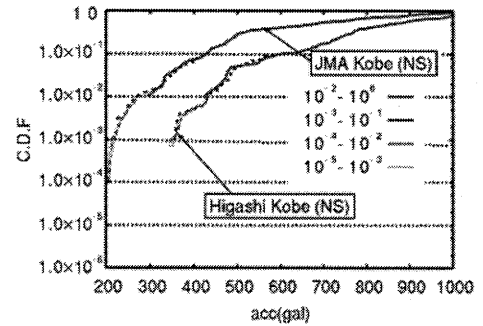


Fig.8 Estimated fragility curves

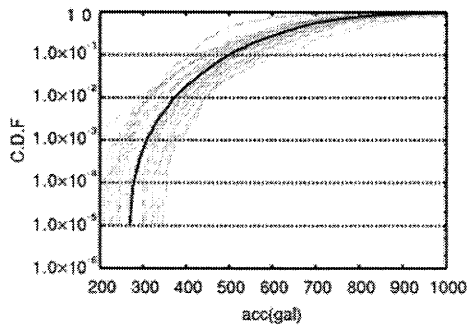


Fig.9 Estimated fragility curves
by sample input motions

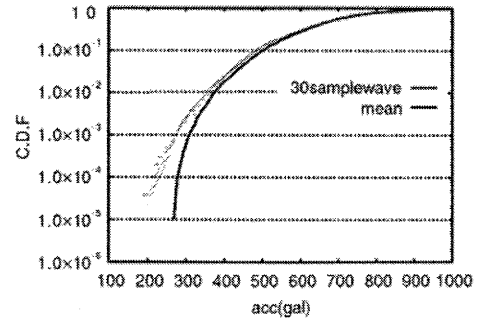


Fig.10 Fragility curve including
phase spectrum uncertainties

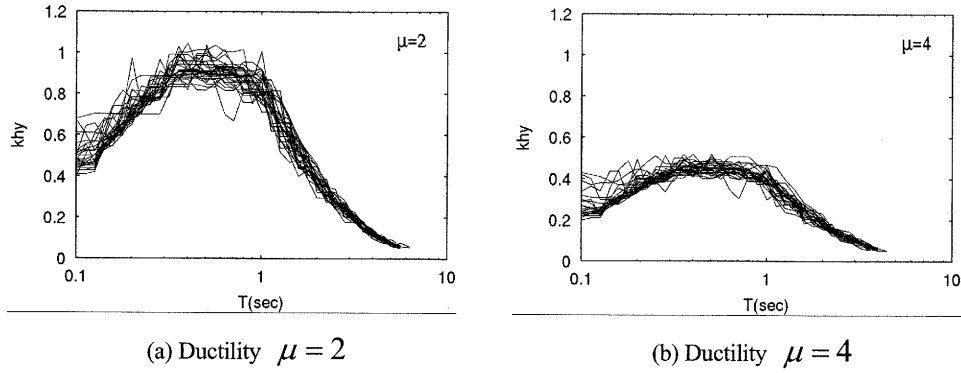


Fig.11 Strength demand spectra obtained by using sample inputs

6. DESIGN EARTHQUAKE MOTION CONSIDERING NONLINEAR BEHAVIOUR OF STRUCTURE SYSTEM

Design earthquake motions often are defined by response spectra. As described above, design response spectrum compatible earthquake motion, however, is not unique and strongly affected by the phase spectrum uncertainties. We could not obtain the same fragility curve and strength demand spectrum using sample input motions even though their response spectra satisfy the same response spectrum.

In this section we develop a method to simulate an input motion, which is compatible with defined response spectrum and strength demand spectrum, as the design earthquake motion. Therefore, there are 2 target spectra that the design earthquake motion should satisfy. One of them is “design response spectrum”. We can obtain this spectrum as a function of magnitude M and epicentral distance Δ according to attenuation law. The other is “design strength demand spectrum”. We can define this based on strength demand spectra obtained using many sample input motions. These sample input motions are modeled as functions of M and Δ . One way to defined the design strength demand spectrum is to choose the strength demand spectrum with non-exceedance probability of 90% as shown in **Fig. 12** (for example $M=7.0$, $\Delta=30[\text{km}]$, $\mu=4$).

The sum of square errors between the target spectra (design elastic response spectrum and strength demand spectrum) and spectra calculated from sample motions is defined as an objective function. First, samples of group delay time are generated according to M and Δ , and phase spectra can be obtain by integrating these samples of group delay time. Second we calculate sample input motions by inverse Fourier transform then calculate the sum of square errors. Using the concept of Subset Simulation method, we search for better Fourier amplitude and phase spectrum in subspace.

Now we consider from 0 to 5 subspaces. Subset 0 means total space. The optimum spectra in subspace 0 are shown in **Fig. 13** (a). Error is 0.0244. In subspace 5, final subspace, obtained spectra are shown **Fig. 13** (b) with the error of 0.0169. Using final Fourier amplitude and phase spectra in the final subspace we can defined the design input motion which satisfy the target elastic response spectrum and the strength demand spectrum (**Fig. 14**).

In this method, we use the design response spectrum defined as a function of M and Δ , and the design strength demand spectrum which is also defined as a function of M and Δ , through the model of phase spectrum. We can, therefore, define the design earthquake motion for each combination of M and Δ .

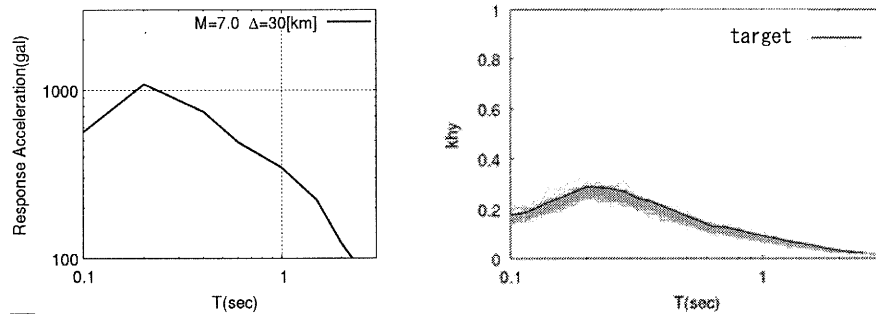


Fig.12:Target spectra (left: design response spectrum, right: design strength demand spectrum)

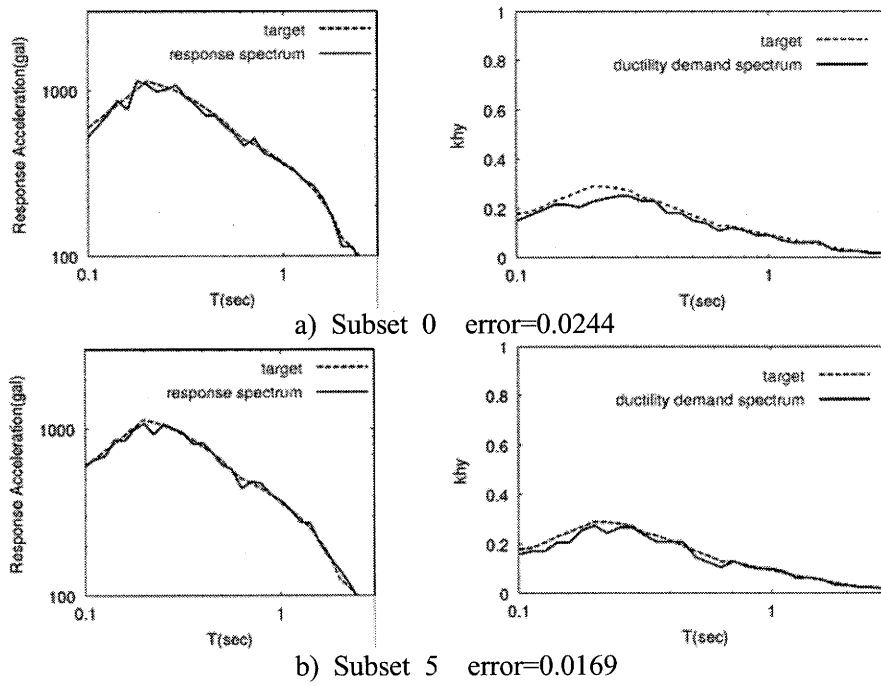


Fig.13:Response spectrum and strength demand spectrum

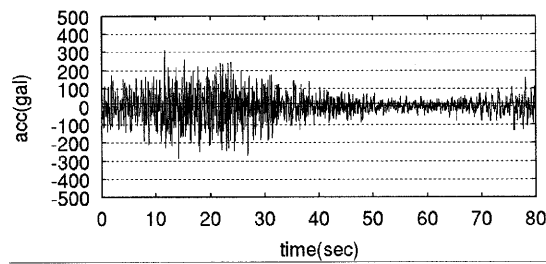


Fig.14:The design earthquake motion

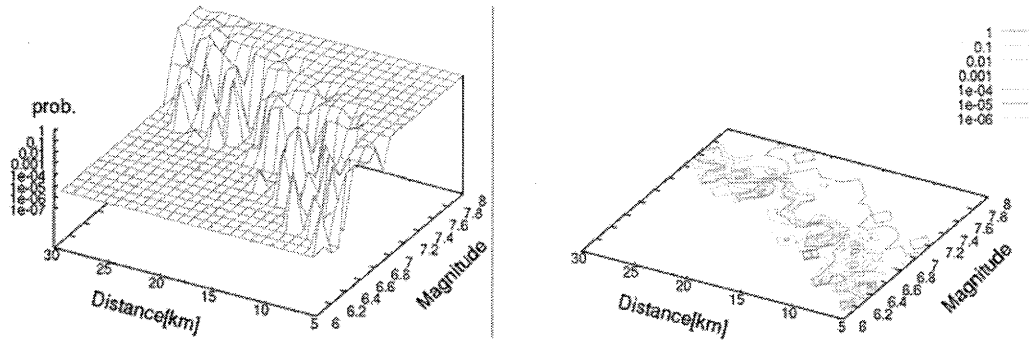


Fig.15: Failure probability surface

Table 3: Uncertainties and Parameters

		Mean(μ)	C.O.V	Distribution
Uncertainties	Mass	1500	0.02	Normal
	Stiffness	250000	0.05	Normal
	Yield point	0.02	0.03	Normal
Ductility $\mu = 4$		4.0	-	-
K_2/K_1		0.2	-	-

Using this design earthquake motion, we calculate failure probability of structure for each combination of M and Δ , then get failure probability surface which has 2 axes M and Δ . We estimate failure probability surface of SDOF model with a bi-linear hysteretic characteristic. The second stiffness is 20% of the first, and 5% damping coefficient assigned. Uncertainties and parameters are shown in **Table 3**. And obtained failure probability surface is shown in **Fig. 15**. If we know the M and Δ of an objective seismic source, we can get directly the failure probability of the structure from this surface.

7. CONCLUDING REMARK

An efficient method based on MCS was proposed to estimate a fragility curve. The concept of Subset simulation was adopted because the tail part of the fragility curve becomes important. Since efficiency of MCMC plays an important role in the Subset simulation several method were proposed to improve the efficiency by using such as hit and run algorithm. We applied proposed method to actual bridge piers considering several uncertainties of the structure. The efficiency of this method was demonstrated by numerical examples. We also investigated the effect of phase uncertainties of earthquake motion on a fragility curve using sample input motion then modeled a fragility curve including phase uncertainties. Finally we propose a method to simulate design earthquake motions which satisfy defined response spectrum and strength demand spectrum by controlling Fopurier amaplitude and phase sptetra..

Acknowledgements:

The authors acknowledge support from Japan Society for the Promotion of Science for project Number 16360230. The support has made possible to develop the model of phase spectra of earthquake motions.

References

- Au, S-K and Beck, J. L. (2002), "Application of Subset Simulation to Seismic Risk Analysis", *15th ASCE Engineering Mechanics*
- Gilks, W.R., Richardson, S., Spiegelhalter, D.J. (1996), Markov chain Monte Carlo in practice, Chapman & Hall
- Design of Highway Bridge Foundations in Japan, Foundation Engineering Research Team, Structures Research Group, Public Works Research Institute, 2003
- Guide line of anti-seismic reinforcement for existing steel bridges, Hanshin Expressway Public Corporation, 1997.
- Takeshi Kitahara (2001), Aseismic design method considering periodic and phase characteristics of earthquake motions, doctoral dissertation of Nagoya University
- Tadanobu Sato, Yoshitaka Muroto and Akihiko Nishimura (1999), "Modeling of Phase Spectrum to Simulate Design Earthquake Motion", *Proceedings of Optimizing Post-Earthquake Lifeline System Reliability*, TECLEE, ASCE, No.16, pp.804-813, 1999.8

STRONG MOTION RECORDS OBSERVED IN THE 2004 NIIGATA-KEN-CHUETSU EARTHQUAKE

S. Midorikawa¹⁾ and H. Miura²⁾

1) Professor, Department of Built Environment, Tokyo Institute of Technology, Japan

*2) Post-Doctoral Research Fellow, Center for Urban Earthquake Engineering, Tokyo Institute of Technology, Japan
 smidorik@enveng.titech.ac.jp, hmiura@enveng.titech.ac.jp*

Abstract: The 2004 Niigata-Ken-Chuetsu earthquake produced many strong motion records including in near-field. At several sites, the observed accelerations and velocities exceed 1g and 100cm/s, respectively. The source directivity and hanging wall effects are manifested in the near-field records. Strong nonlinear soil response was observed at a soft soil site. In Tokyo which is 200km away from the epicenter, long-period ground motion excited by the basin structure was observed.

1. INTRODUCTION

On October 23, 2004, a major earthquake ($M_J 6.8$, $M_W 6.6$) struck Niigata Prefecture. The earthquake was named the 2004 Niigata-Ken-Chuetsu earthquake by Japan Meteorological Agency. Forty people were killed, about 4,600 were injured, and about 14,000 houses were severely or moderately damaged. Niigata Prefectural Office estimated the monetary loss at US\$30 billion which is one third of that for the 1995 Kobe earthquake. Owing to the dense strong motion networks constructed after the Kobe earthquake, the earthquake produced many strong motion records including in near-field. Analyses of the records will give additional knowledge on the characteristics of near-field ground motions. This paper describes the characteristics of strong motion records observed in the earthquake.

2. EARTHQUAKE AND OBSERVED RECORDS

The earthquake is due to reverse-faulting on a fault striking the northeast and dipping down to the northwest (Yamanaka, 2004). The moment magnitude is 6.6, and the rupture area is approximately 20km in length and 10km in width. No clear surface rupture was observed, indicating that this event is caused by a buried fault. Figure 1 shows the intensity distribution with surface projection of the fault plane. The intensity 7 which is the highest grade in the JMA scale was observed at Kawaguchi town located above the fault plane. The intensity 6- or greater was observed at about fifteen municipalities including Ojiya and Nagaoka cities.

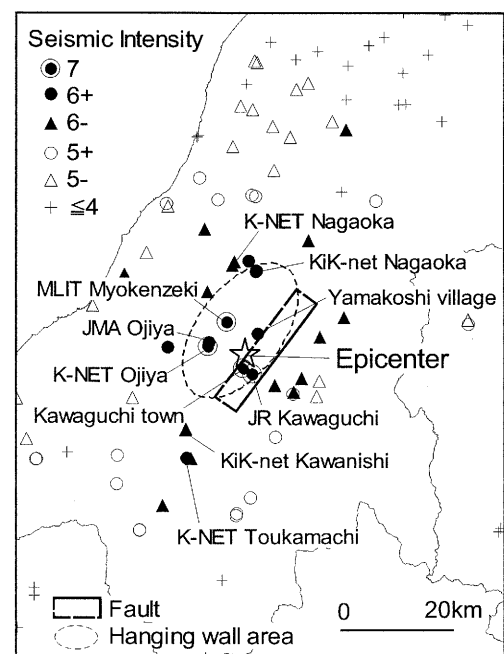
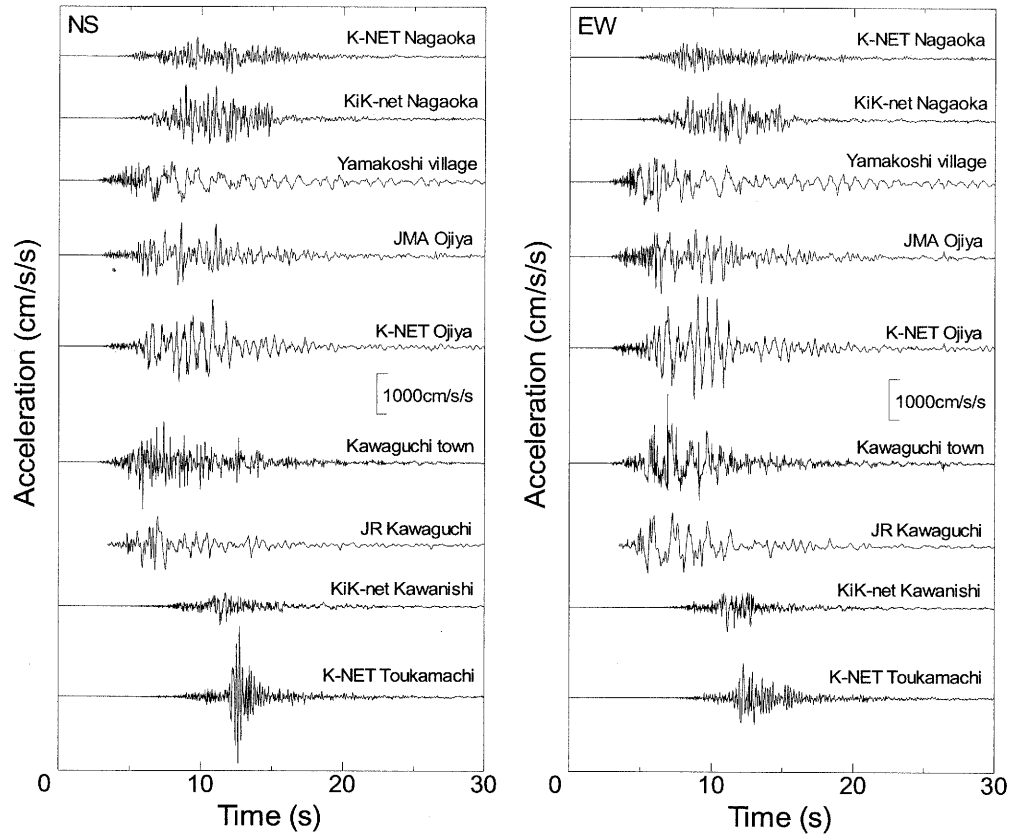
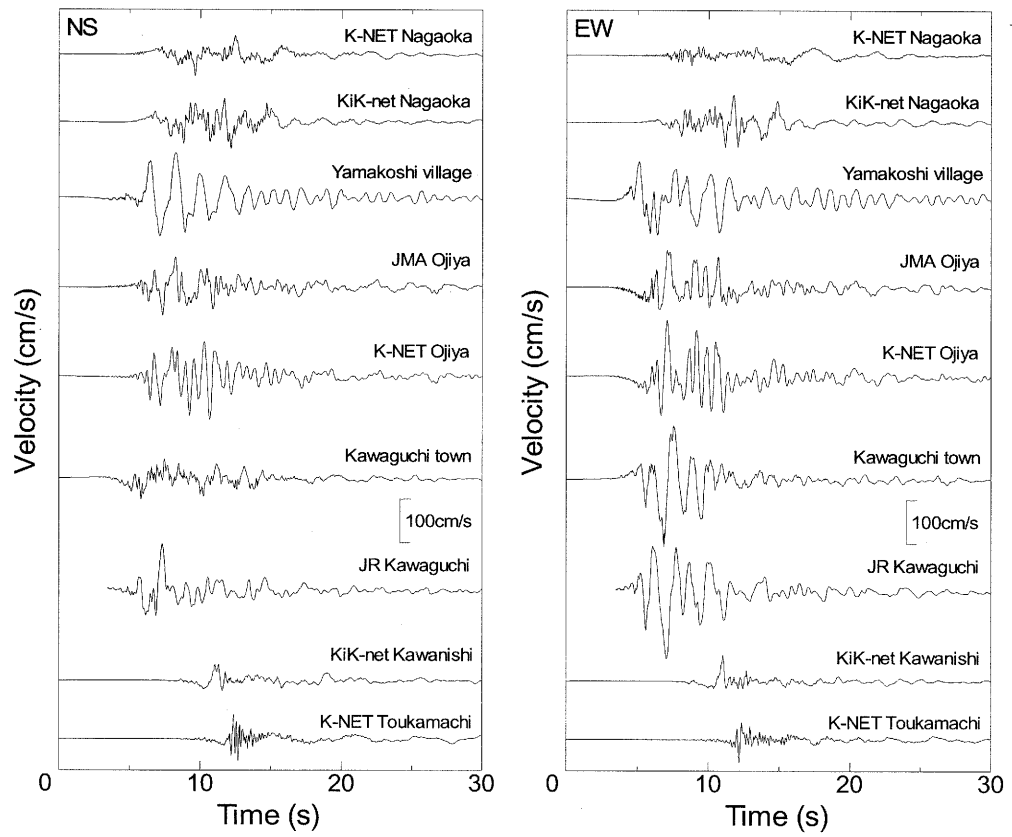


Figure 1 Intensity Distribution



(a) Acceleration Time Histories



(b) Velocity Time Histories

Figures 2 Paste-ups of Near-field Records

Figures 2 show the paste-ups of the acceleration and velocity time histories of the records. Large peak ground accelerations higher than 1g were observed at several sites such as K-net Ojiya, K-net Toukamachi, and Kawaguchi town. Also peak ground velocities are higher than 100cm/s at several sites. The duration of strong shaking is less than 10 seconds. The K-net Ojiya and JMA Ojiya sites are adjacent to each other, and the distance is about 800m. The peak ground acceleration and velocity, however, are significantly larger at K-net Ojiya than at JMA Ojiya. Figure 3 shows the velocity response spectra. The spectrum at K-net Ojiya has a strong peak at period of 0.7 second, while the spectrum at JMA Ojiya is rather flat with period. This suggests strong local site effects at K-net Ojiya.

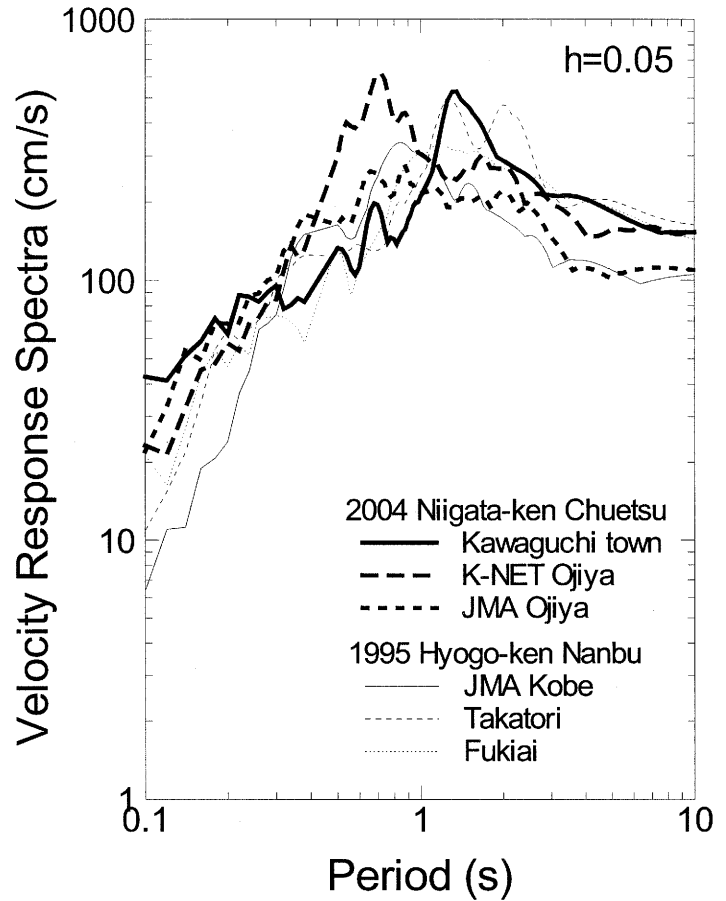


Figure 3 Velocity Response Spectra

In the figure, the spectrum at Kawaguchi town is also shown. The spectrum has a strong peak at period of 1.2 second, which is almost the same as that observed in the disastrous belt zone such as Takatori during the 1995 Kobe earthquake. This is probably due to a directivity pulse. Figure 4 shows the particle orbits of ground velocity at K-net Ojiya and JR Kawaguchi. The ground motions are strongly polarized to the fault normal direction. This polarization was observed in most of the records in near-field.

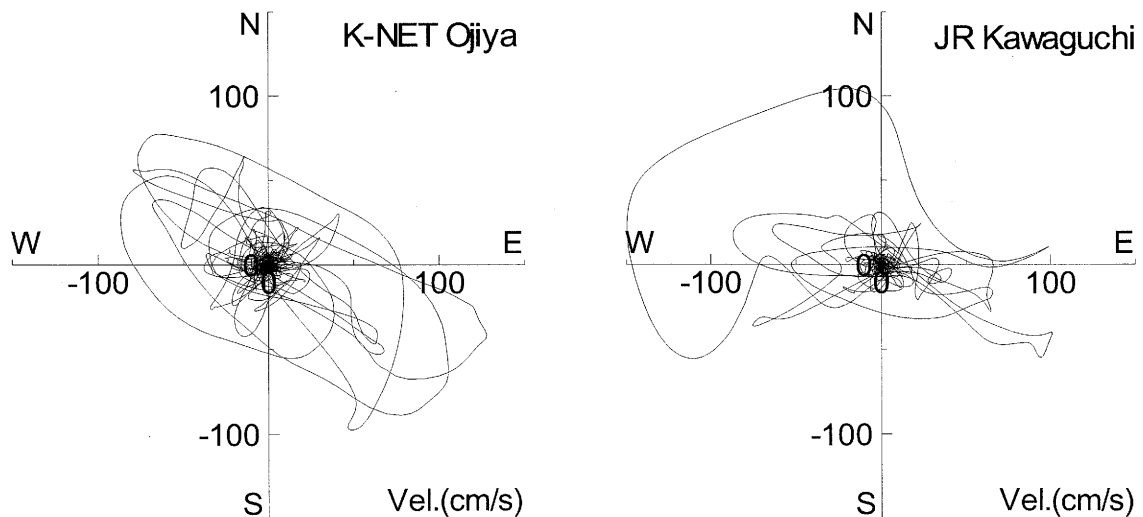


Figure 4 Particle Orbit of Ground Velocity

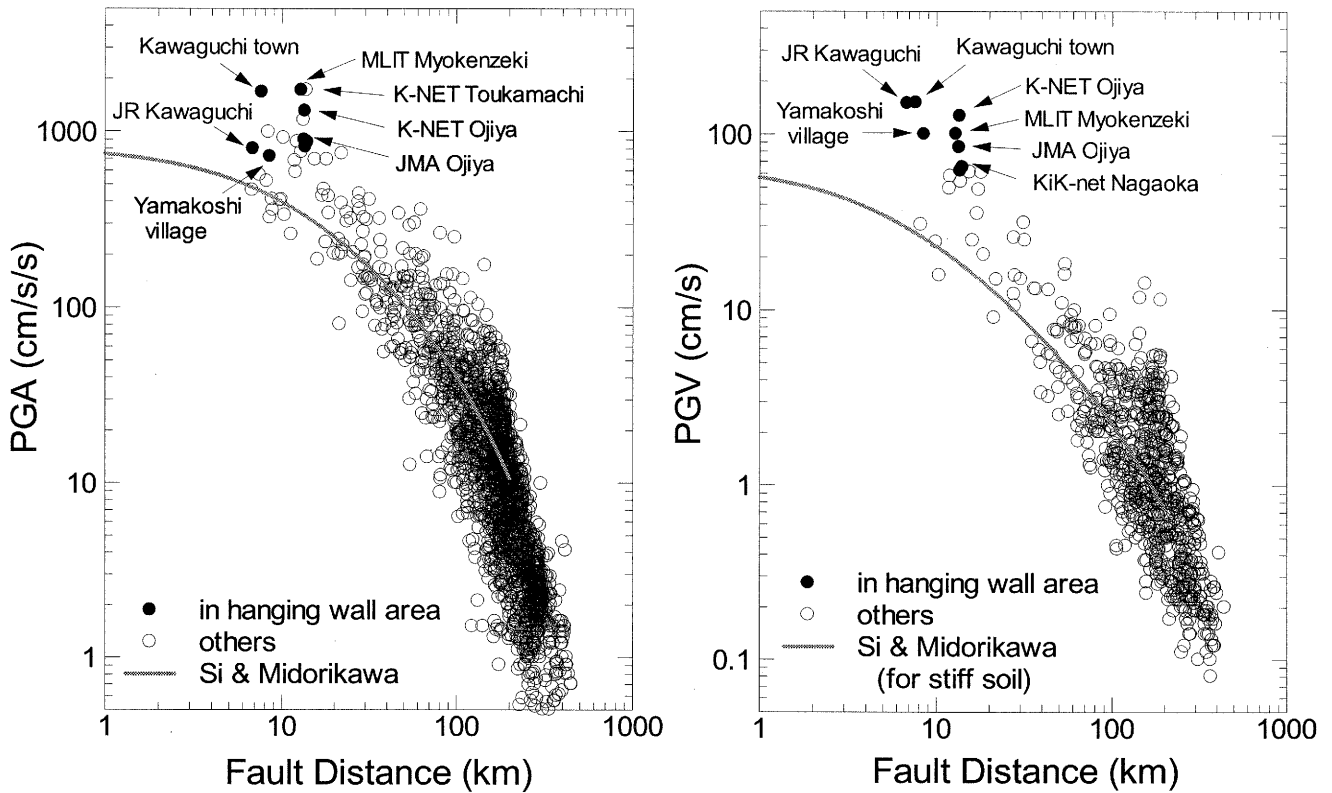


Figure 5 Attenuation of Peak Ground Acceleration and Velocity

Figure 5 show the attenuations of peak horizontal acceleration and velocity. The solid lines in the figures indicate the attenuation curves from the empirical relationships derived from Japanese records (Si and Midoriakwa, 2000). In general, the observations tend to be larger than the curves, which may suggest the effects of buried faulting (Somerville, 2004). Higher amplitudes were observed at the sites located in the hanging wall area, indicated by solid circles. Hanging wall effects were manifested more clearly in the velocities than in the accelerations. The effects seem about 1.5 and 2 times for the acceleration and velocity, respectively. The value for the acceleration is almost the same with the result by Abrahamson and Somerville (1996).

Long period ground motion was observed in Tokyo which is approximately 200km away from the epicenter, as shown in Fig.6. The predominant period is about 6 seconds, and the duration is 2 minutes or more. Super high-rise buildings in Tokyo were shaken and the elevators were stopped. Some of the elevators were damaged by vibration of the governor rope. The long period motion was caused by surface waves excited in the Kanto basin. Generation of larger long period motion in Tokyo is anticipated during a large subduction earthquake such as the Tokai earthquake.

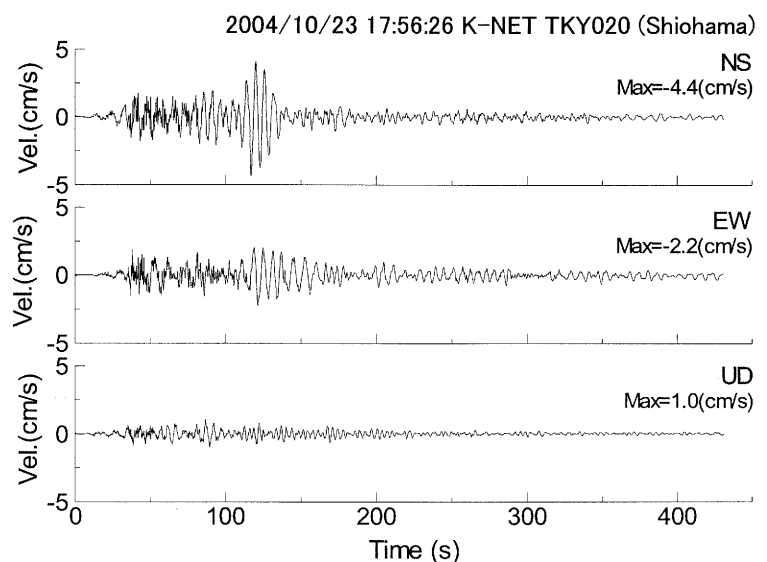


Figure 6 Long-period Ground Motion Observed in Tokyo

3. SITE CHARACTERISTICS OF STRONG MOTION SITES

To examine the site characteristics at the strong motion sites, microtremors were measured at the sites where the observed intensity was 6 or more. Figure 7 shows locations of microtremor measurement sites with surface geology. The velocity seismometer whose response is constant in periods shorter than 2 seconds is used in the measurement. The horizontal to vertical spectral ratio (H/V ratio) is computed for each record to evaluate the local site effect.

Figure 8 show the H/V ratios at the sites. The H/V ratios are different site by site, suggesting variation of local site effects. For example, the K-net Ojiya site has the peak of the H/V ratio at about 0.3 second, while the peak period is about 0.1 second at the JMA Ojiya site. This can explain that the larger ground motion was observed at K-net Ojiya. At Kawaguchi town, the H/V ratio is small and constant with period, indicating no significant site amplification at the site. This suggests that the highest intensity 7 observed at Kawaguchi town would not be due to site effects but due to source effects. At the other sites in the hanging wall area, such as KiK-net Nagaoka, MLIT Myokenzeki, and JR Kawaguchi, the H/V ratios are small at periods longer than 0.4 second. This reinforces the existence of hanging wall effects mentioned earlier.

Figure 9 shows the spectra of the main shock, its aftershocks and the events before the main shock at K-net Ojiya. For smaller records, the predominant periods are around 0.3 second, which is the same with that for the microtremor. For the larger aftershocks the

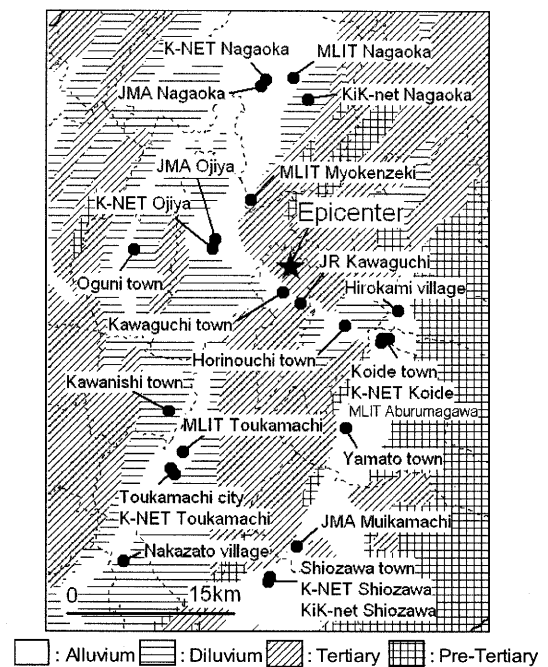


Figure 7 Location of Sites

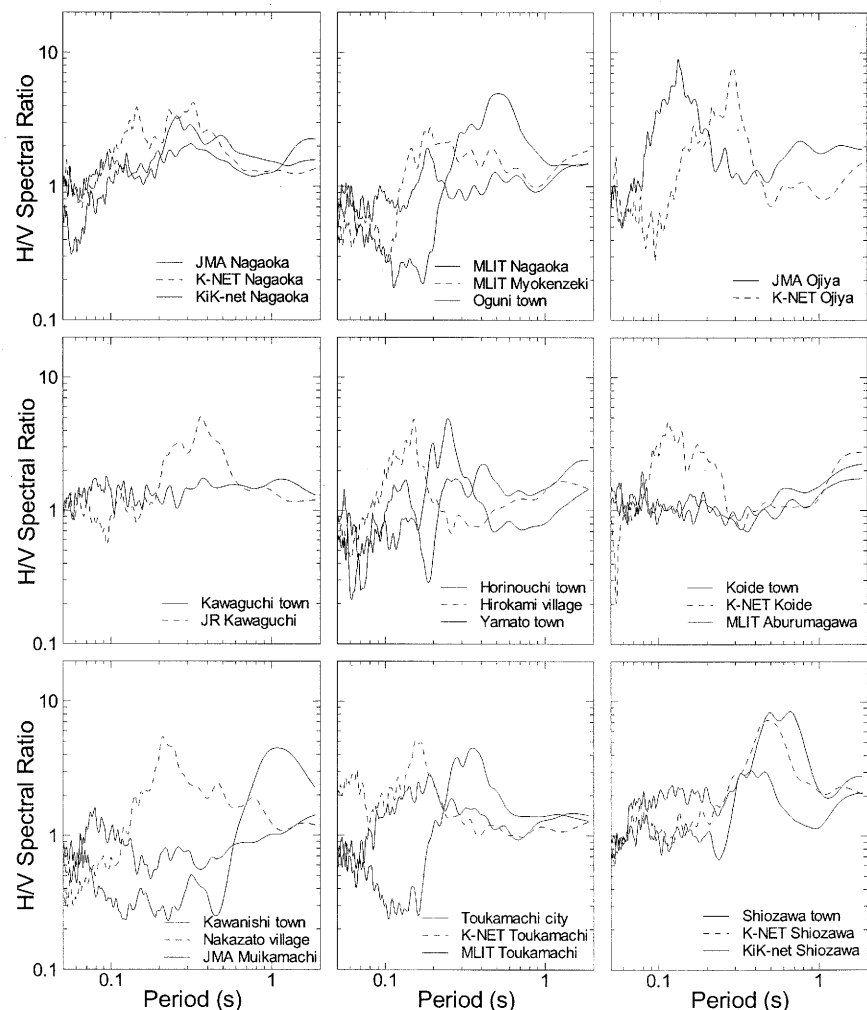


Figure 8 H/V Spectral Ratios of Microtremors at Strong-Motion

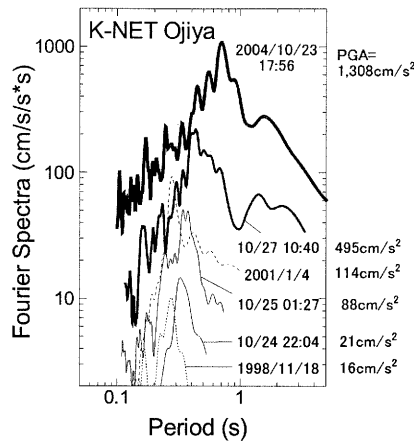


Figure 9 Spectra at K-net Ojiya

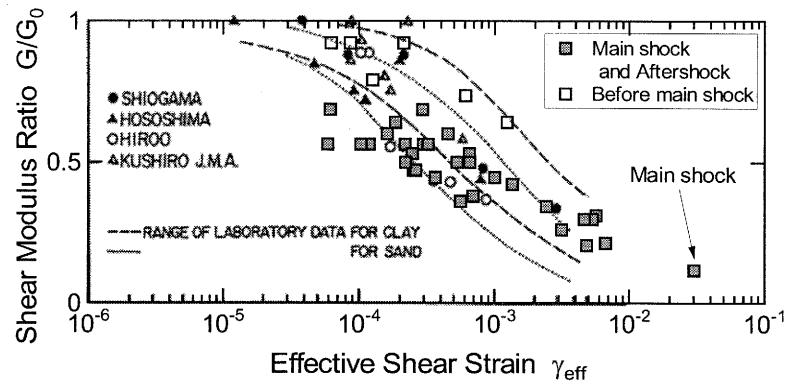


Figure 10 Relationship between Shear Modulus Ratio and Effective Shear Strain at K-NET Ojiya

period is about 0.4 to 0.5 second, and 0.7 second for the main shock. The change of the period is considered to be the effect of nonlinear soil response. At the K-net Ojiya site, stiff gravel layers are overlaid by soft soil deposits with thickness of 3 m. If the period change is due to nonlinear behavior of the soft deposits, the shear modulus ratio and effective shear strain of the deposits can be roughly estimated from the period and velocity time history (Tokimatsu et al., 1989). Figure 10 shows the relationship between shear modulus ratio and effective shear strain estimated from the records of the main shock and smaller events. During the main shock, the shear modulus ratio and effective shear strain are estimated 0.1 and 3×10^{-2} , respectively. The relationship estimated from the records is consistent with the laboratory data.

4. CONCLUDING REMARKS

The 2004 Niigata-Ken-Chuetsu earthquake produced many strong motion records including in near-field, owing to the dense strong motion networks constructed after the Kobe earthquake. At several sites, the observed accelerations and velocities exceed 1g and 100cm/s, respectively. The source directivity and hanging wall effects are manifested in the near-field records. Strong nonlinear soil response was observed at a soft soil site. Long-period ground motion excited by the basin structure was observed in Tokyo which is 200km away from the epicenter.

Acknowledgements:

The strong motion records used in this study are provided by National Research Institute of Earth Science and Disaster Prevention, Japan Meteorological Agency, Niigata Prefecture, Ministry of Land, Infrastructure and Transport, and East Japan Railway Company.

References:

- Abrahamson N.A. and Somerville, P.G. (1996), "Effects of the Hanging Wall and Footwall on Ground Motions Recorded during the Northridge Earthquake," *Bulletin of the Seismological Society of America*, **86**(1B), S93-S99.
- Si, H. and Midorikawa, S. (2000), "Attenuation Relationships of Peak Ground Acceleration and Velocity Considering Effects of Fault Type and Site Condition," *Proceedings of the Twelfth World Conference on Earthquake Engineering*, 532-1-532-6.
- Somerville, P. (2004), "Characterizing Earthquake Rupture Models for the Prediction of Strong Ground Motion," *Proceedings of a Symposium in Honor of Kojiro Irikura "Strong Ground Motion Prediction: Present Status and Future Perspectives*, 19-24.
- Tokimatsu, K., Midorikawa, S. and Yoshimi, Y. (1989), "Dynamic Soil Properties Obtained from Strong Motion Records," *Proceedings of the Twelfth International Conference on Soil Mechanics and Foundation Engineering*, 2015-2018.
- Yamanaka, Y. (2004), "04/10/23 Near the West Coast of Honshu Japan," *EIC Seismological Note No.154*, http://www.eri.u-tokyo.ac.jp/sanchu/Seismo_Note/2004/EIC154e.html.

STRONG MOTION CHARACTERISTICS AND STRUCTURAL DAMAGE POTENTIAL

H. Kawase¹⁾

*1) Professor, Faculty of Human-Environment Studies, Kyushu University, Japan
kawase@arch.kyushu-u.ac.jp*

Abstract: Based on the reproduced strong motions in Kobe during the 1995 Hyogo-Ken Nanbu earthquake (Matsushima and Kawase, 2000), we successfully simulated building damage ratios in Kobe and delineate what kind of strong motion parameters are important and how to judge the damage potential of ground motions to structures. Our approach is different from previous ones, because we construct nonlinear structural models with statistically distributed base-shear coefficients (Nagato and Kawase, 2004). We construct models for 3, 6, 9, and 12 storied RC buildings, 3 to 5 storied steel buildings, and 2 storied wooden houses. Our study shows that only a strong ground motion with both sufficiently large PGA and PGV can yield devastating damage to these ordinary structures. In recent years we have accumulated a lot of strong motion data with various characteristics. It is especially interesting to see the damage potential of strong motions with high PGA and PGV observed during 2003 Tokachi-Oki earthquake of M8.0. We report here the simulated damage ratios of wooden houses and low-rise RC buildings for the earthquake and discuss the relationship of strong motion characteristics and damage potential to buildings.

1. INTRODUCTION

Because of the devastating damage caused by the Hyogo-ken Nanbu earthquake of 1995, it is crucial to understand what was the real cause of damage in order to prevent similar earthquake disaster in future. We found that the observed strong motions in the near-source region are characterized by a couple of distinctive pulses whose peak ground velocity (PGVs) should exceed 150 cm/sec in a narrow belt of the damage concentration in Kobe (Kawase, 1996 Matsushima et al. 1998, Kawase et al. 2000a). To have such velocity pulses with high amplitude both the source effect and the site effect are equally important. As for the source it turns out that the forward rupture directivity creates a clear pulse-like shape of ground motions in the near-source region because of the constructive summation of motion in the forward direction of the rupture (e.g., Somerville 2000). Such a velocity pulse in the near-source ground motions can be called as “the directivity pulse”. The directivity itself is a well-known phenomenon in seismology, however, it is not considered to be a primary cause of the near-source damage for historical earthquakes in the past. Thus the impact of the directivity pulse has not been considered yet in the current building codes in the world, except for California.

The most important fact on the directivity pulse is that the natural period (i.e., twice of the pulse width) of the directivity pulse is controlled by the size of a distinctive asperity, L (Kawase et al. 2000b). If the slip distribution is very smooth in space, then the directivity pulse has a characteristic period related to the whole size of the fault surface. We note that we should use here the directivity velocity $(1/v-1/\beta)^{-1}=3\sim 4\beta$ as a reference speed, where v is the rupture velocity and β the S-wave velocity. Since the predominant periods of the directivity pulses in Northridge and Kobe were in the range of 1 to 2 seconds, which means 0.5 to 1 second in terms of the pulse width, the size of the

asperities should be the order of several kilometers. The validity of such distinctive asperities as a source model of the Hyogo-ken Nanbu earthquake is proved by Matsushima et al. (1998), Kawase et al. (2000a), and Matsushima and Kawase (2002) who successfully reproduced the observed ground motions in Kobe by using a multiple asperity model and a three-dimensional basin structure. We should note here that the 3-D basin edge structure in Kobe is very efficient to amplify the directivity pulses of 1 second due to the so-called “edge effect” (Kawase 1996) and so the PGVs on the basin surface would have amplitudes three to four times of those on the bedrock.

To reproduce observed strong motions is one thing, but, what is more important is to reproduce the observed structural damage from the viewpoint of seismic risk estimation for future events. To this end we need to establish a methodology how to translate strong motion parameters such as PGV into the damage index such as a damage ratio of buildings. Previous attempts have been directed to finding out a simple function between them based on the observed data, that is to say, the vulnerability function. It is useful as long as a stock of buildings in the target area is the same as in the observed area, which is quite unlikely and difficult to prove. Also it is useful only when we can neglect the effects of waveforms on the damage impact to structures. Since any structural damage is the result of nonlinear response of structures, it must depend on the waveforms of ground motions, not just on PGV or other strength indexes. It is much more useful to find a set of theoretical models of actual structures that can reproduce observed damage ratios. Therefore, we have established a set of building models to evaluate the structural damage potential that can reproduce the damage ratios in Nada and Higashinada-Ward, Kobe, observed during the Hyogo-ken Nanbu earthquake (Kawase and Nagato 2000, Nagato and Kawase 2004). In this paper we apply this method to the observed strong motions in the epicentral area of the Tokachi-oki earthquake of 2003 for low- and mid-rise RC buildings and wooden houses to see their damage potential.

2. METHOD OF ANALYSIS

2.1 Brief explanation of established models

We have constructed numerical building models with nonlinear parameters that can reproduce the damage observed in Kobe during the Hyogo-ken Nanbu earthquake. Since we successfully reproduced strong ground motions by using a distinctive asperity model (Matsushima and Kawase 2002) and we have detailed statistics of the building damage survey conducted for Kobe (AIJ, 1998), we can tune up parameters so as to reproduce observed building damage in Kobe. Details of procedures can be found in Nagato and Kawase (2004).

Here is a brief explanation of the procedure. First we construct basic building models based on the current building design. We assume rigid floors so we use a 1 column multi-degrees-of freedom system. Fig.1 shows nonlinear characteristics of such basic models for reinforced concrete (RC) buildings. We use degrading trilinear models for RC buildings. We also need to introduce probabilistic distribution of yield strength to estimate damage probability for a given strong motion. We assume a log-normal relationship proposed by Shibata (1980). As for wooden houses we use combined characteristics of a degrading trilinear model and a slip model to mimic slip phenomenon at the connections of beams and columns. Since we have no statistical survey on strength distribution for wooden houses in Japan, we assume 12 different shear strengths based on the detailed survey for 31 wooden houses in Kobe. Assumed relative strengths of the first and second stories and their existing ratios are summarized in Fig.2.

Once we assume initial models for different numbers of stories (3, 6, 9, and 12) and for different ages of construction (before and after 1982) for RC buildings, then we can calibrate these models to the observed ratios of building damage (here “damage” means either “collapsed” or “heavily damaged”). In Figure 3 we show the target damage ratios for RC buildings with different categories. After the initial calculation we found that the initial models for RC buildings are too weak to

reproduce the actual damage ratios in Kobe. So we increase the average yield strengths for different building categories. Fig. 4 shows final multiplication factors for RC buildings. It turns out that the average strengths of low-rise RC buildings are 2 to 4 times larger than those assumed in the ordinary design. As for wooden houses we found that the appropriate ratio of strength is 1.95 times. However, these factors are close to 1 for low-rise steel buildings, which is a direct consequence of high damage ratios of steel buildings in Kobe. The advantage to use our prediction models for building damage prediction is that we can automatically reflect the effects of waveforms and predominant periods of ground motions to the building damage prediction. For example, very high PGV records observed in Taiwan during 1999 Chi-Chi earthquake (Shin et al. 2000) did not produce so heavy damage to ordinary buildings in the observed areas and our model successfully predict such observed fact (Kawase and Nagato 2000).

2.2 Observed Ground Motions

Here we explain the basic characteristics of observed ground motions used in this paper. In Tables 1 and 2 we summarize strong motion data obtained by K-NET and KiK-net of NIED (Kinoshita, 1998, Aoi et al., 2002) during the 2003 Tokachi-oki earthquake. We select strong motion records with peak ground acceleration (PGA) more than 400 Gals or peak ground velocity (PGV) more than 30 cm/s. In total we use data at 34 sites in southeastern Hokkaido. We use two components as independent data for PGA or PGV related analysis so that total numbers of waves will be 68. Tables 1 and 2 also show JMA seismic intensity as well as the filtered PGA, A0, for JMA seismic intensity calculation. JMA intensity can be calculated by Kawasumi's formula:

$$I_{JMA} = 2 \log (A0) + 0.7 \quad (1)$$

For detailed description of JMA intensity and A0 see Karim and Yamazaki (2002), for example.

The site conditions of these sites vary significantly from hard rock to soft sediments. Since we want to see the damage potential of strong motions to ordinary structures, we do not investigate here the effects of surface geology in any detail. Just for reference we show the averaged S-wave velocity (Vs) for top ten meters in these tables since 10m Vs is the best representative value for site amplification (Kawase and Matsuo, 2004). We also list the equivalent period of ground motions based on the following formula:

$$T = 2\pi \text{ PGV/PGA}$$

most of which lie in the range of 0.5 s to 1.5 s.

Figure 5 show an example of observed waveforms at HKD086 and Figure 6 show their velocity response spectra (NS and EW components). We can see high (~200 cm/s) peak amplitude at around 0.8 second for 5% damping. At other sites peak periods are varying from site to site but lie in the range between 0.5 to 2 seconds. Peak amplitudes of velocity response spectra is ranging from 100 cm/s to 200 cm/s for 5% damping.

3. RESULTS

Based on the proposed models for damage prediction and observed strong motions described above we conduct numerical calculations for these observed data to obtain expected damage ratios. The damage ratios here is the total sum of the existing ratios of buildings whose maximum story drift angle exceeds 1/30 radian for RC buildings or 1/10 radian for wooden houses.

Figure 7 shows total damage ratio of each category (for 12 stories RC building we use only one category since the estimated strength of new buildings was smaller than that of old buildings due to too small numbers of damaged buildings) for all the 34 earthquakes. In this case NS and EW components are used as combined input to one building. From this figure it is apparent that the averaged damage ratios in the region close to the epicenter are not so high; at most 10 %. However, this number is the averaged ratios for all the 34 sites, which means that we implicitly assume that these

observed records would be representative ones for strong motions in the epicentral region of a magnitude 8 class subduction-zone earthquake. Actual damage ratios are strongly dependent on the waveforms as shown in Figures 8 and 9, where we plot each damage ratio for each site. These figures show that HKD086 is strongest in terms of the building damage potential. The next strongest record is TKCH07 whose peak velocity response of 5% damping is around 150 cm/s at 1 second. Thus these two examples support the idea that the most dangerous waves for ordinary buildings are those with high amplitude in the intermediate (~1 second) period range.

For simple damage prediction it would be better to have the so-called vulnerability function, which relates the damage ratios to a single strength index of ground motion. In the past we have been using PGA or PGV as a simple yet effective single strength index for damage evaluation. However, we can investigate any kind of strength indexes if we use our damage prediction models. Masuda et al. (2002) tried to find a better index by using Nagato and Kawase's building models and found that JMA intensity and $\text{PGA} \cdot \text{PGV}$ will be a better index for most of the cases of RC buildings. Here we follow their method of analysis and see the correlation of strength index of ground motion with the predicted damage ratios. Because calculated damage ratios are relatively low for RC building and because studies on RC buildings have already been conducted by Masuda et al. thoroughly, we focus here our attention to wooden houses.

Figure 10 shows relationships of calculated damage ratios for wooden houses in terms of PGA, PGV, filtered PGA, A0, used for JMA intensity, and $\text{PGA} \cdot \text{PGV}$. Calculated values for K-NET input and KiK-net input are shown by different symbols. As we can see correlation with PGA is quite poor so apparently PGA is not a recommended index. Please note that natural frequencies of Japanese wooden houses are ranging from 2.5 Hz to 10 Hz, mostly more than 5 Hz in their elastic regime. This poor correlation strongly suggests that the predominant frequency of elastic (linear) regime does not play any major role during strong shaking close to collapse. Compared to PGA, PGV does much better job to represent heavy damage on wooden houses. When we perform regression analysis by assuming log-normal distribution, we find vulnerability functions as shown also in Figure 10 by blue curves. The correlation with data is best (0.826) if we use A0 as a strength index. $\text{PGA} \cdot \text{PGV}$ is not as good as A0 and PGV but much better than PGA only. The reason why $\text{PGA} \cdot \text{PGV}$ is no better than PGV would be low equivalent predominant frequency in the nonlinear regime. Since our wooden house model use slip function as well as trilinear nonlinearity, equivalent frequency in the nonlinear regime is relatively low compared to ordinary low-rise RC buildings. Thus simply PGV may be enough to predict heavy damage for wooden houses.

Two lower panels in Figure 10 have broken lines, which correspond to the vulnerability functions of wooden houses determined by Masuda and Kawase (2004). When we compared them with current regression curves, we found that their curves yield only one half of the damage ratios. This suggests that the damage potential of the 2003 Tokachi-oki earthquake is significantly higher than those of ground motions for moderate-sized earthquakes (as Masuda and others used in their analysis). It is easy to say that this would be due to long duration of strong motions characteristic to big earthquakes. However, nonlinear behavior, and hence heavy damage will emerge as a transient phenomena so that the effect of long duration could not be so strong. We need further investigation on the damage potential of strong motions and their relation to strong motion characteristics including duration of motion.

4. CONCLUSIONS

By using Nagato and Kawase's set of building models that was calibrated to reproduce damage ratios observed in Kobe during the Hyogo-ken Nanbu earthquake of 1995, we evaluate damage potential of strong motion records observed by K-NET and KiK-net strong motion networks of NIED during the recent large subduction-zone earthquake, namely the Tokachi-Oki earthquake of 2003. We

have confirmed that relatively small amount of damage is estimated in the epicentral region of southeastern Hokkaido. We also confirmed that strong motions with high potential to induce heavy damage to ordinary low- and mid-rise RC buildings and wooden houses are those with sufficient power in the intermediate (~1 second) period range. Among different indexes tested for simple damage estimation of wooden houses, we found filtered PGA, A0, for JMA intensity would be the best choice. PGV is the second best probably because of long period nature of wooden houses if they behave nonlinearly. The damage potential of ground motions observed during the 2003 Tokachi-oki earthquake seems much higher than previously used strong motions. We need further investigation to find the source of this difference. We also check the validity of our damage prediction models at HKD086 site since estimated damage at this site seems too high compared to the actual damage. We may need to introduce a regional correction factor for better prediction in future.

Acknowledgements:

The author acknowledges kind invitation from Prof. Wada of Tokyo Institute of Technology to attend the Symposium. This study was partially supported by the Special Coordination Funds of the Ministry of Education, Culture, Sports, Science and Technology, Japan (P.I.: Prof. Kojiro Irikura of Kyoto University).

References:

- Architectural Institute of Japan, (1998), "Report on the Hanshin-Awaji Earthquake Disaster", Building Series, Vol.1, Structural damage to reinforced concrete building, (in Japanese with English abstract).
- Aoi, S., K. Obara, S. Hori, K. Kasahara, and Y. Okada (2000), "New Strong Motion Observation Network: KiK-net", *Eos Trans. AGU*, 81(48), Fall Meeting, Suppl., Abstract S71A-05.
- Karim K.R. and F. Yamazaki, (2002), "Correlation of JMA Instrumental Seismic Intensity with Strong Motion Parameters", *Earthquake Engng Struct. Dyn.* Vol.31, 1191-1212.
- Kawase, H., (1996), "The Cause of the Damage Belt in Kobe: "The Basin-Edge Effect," Constructive Interference of the Direct S-wave with the Basin-Induced Diffracted/Rayleigh Waves", *Seismo. Res. Lett.*, 67, 25-34.
- Kawase, H., S. Matsushima, R.W. Graves, and P.G. Somerville, (2000a), "Strong Motion Simulation of Hyogo-ken Nanbu (Kobe) Earthquake Considering both the Heterogeneous Rupture Process and the 3-D Basin Structure", *Proc. of 12th W. Conf. Earthq. Eng.*, Auckland, New Zealand, No.990.
- Kawase, H., S. Ito, and H. Kuhara, (2000b), "Strong Motion Prediction for Fukuoka City based on Distinctive Asperities and Statistical Green's Functions", *Proc. 6th Int. Conf. on Seismic Zonation*, CD-ROM, Palm Springs, California, EERI.
- Kawase, H., and K. Nagato, (2000), "Structural Damage Impact of Strong Motions Evaluated by the Nonlinear Analyses of a Set of Building Models", *Proc. 6th Int. Conf. on Seismic Zonation*, CD-ROM, Palm Springs, California, EERI.
- Kawase, H. and A. Masuda, (2004), "Damage Prediction of Yatsushiro City and its Vicinity due to a Hypothetical Hinagu Fault Earthquake", *J. Struct. Constr. Eng.*, AIJ, No.581, 39-46.
- Kawase, H and Matsuo, (2004), "Relationship of S-wave Velocity Structures and Site Effects Separated from the Observed Strong Motion Data of K-NET, KiK-net, and JMA Network", *J. of Japan Assoc. Earthq. Eng.*, Vol.4, No.4, 126-145.
- Kinoshita, S., (1998), "Kyoshin Net (K-NET)", *Seismological Research Letters*, 69, 309-332.
- Masuda, A., K. Nagato and H. Kawase, (2002), "Study on Construction of Vulnerability Functions by Earthquake Response Analysis for Reinforced Concrete Buildings", *J. Struct. Constr. Eng.*, AIJ, No.558, 101-107.
- Matsushima, S., H. Kawase, T. Sato, R.W. Graves, and P.G. Somerville, (1998), "3D Simulation of Aftershocks of the Hyogo-ken Nanbu Earthquake of 1995", *The Effect of Surface Geology on Seismic Motion*, K. Irikura et al. (Eds.), Balkema, Rotterdam, Vol.2, 1129-1136.
- Matsushima, S. and H. Kawase, (2000), "Strong Motion Simulation in Kobe during the Hyogo-Ken Nanbu Earthquake of 1995 Based on a Three-Dimensional Basin Structure", *J. Struct. Constr. Eng.*, AIJ, No.534, 33-40 (in Japanese with English abstract).
- Shibata, A., (1980), "Prediction of the Probability of Earthquake Damage to Reinforced Concrete Building Groups in a City", *Proc. of 7th W. Conf. Earthq. Eng.*, Vol.4, 395-402.
- Shin, T.C., K.W. Kuo, W.H.K. Lee, T.L. Teng, and Y.B. Tsai, (2000), "A Preliminary Report on the 1999 Chi-Chi (Taiwan) Earthquake", *Seismo. Res. Lett.*, 71, No.1, 23-29.
- Somerville, P.G., (2000), "New Developments in Seismic Hazard Estimation", *Proc. Int. Conf. on Seismic Zonation*, CD-ROM, Palm Springs, California, EERI.

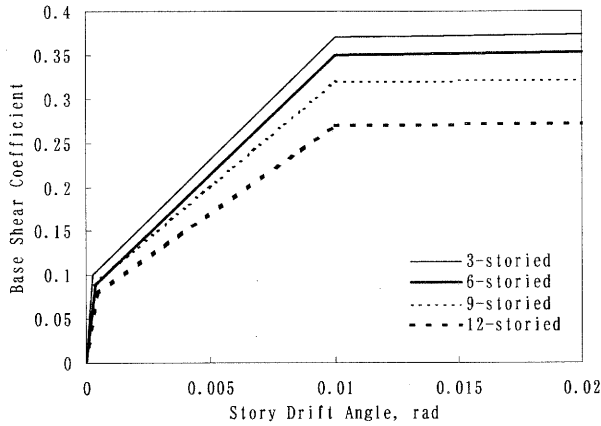


Figure 1 Nonlinear relationships at the basement of standard models, that is, the story drift angle versus the base shear coefficient.

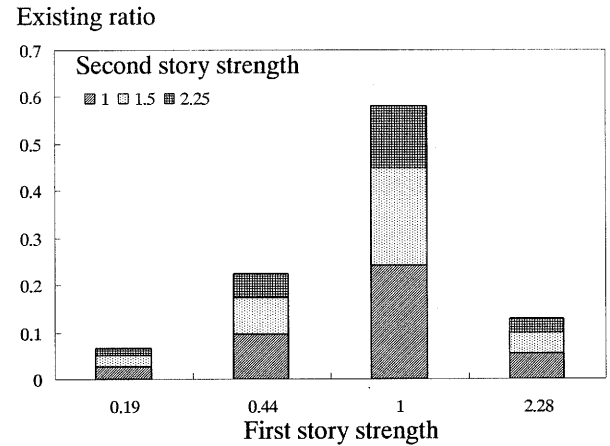


Figure 2 Existing ratios of wooden houses for 12 categories with different relative strengths for the first and second stories.

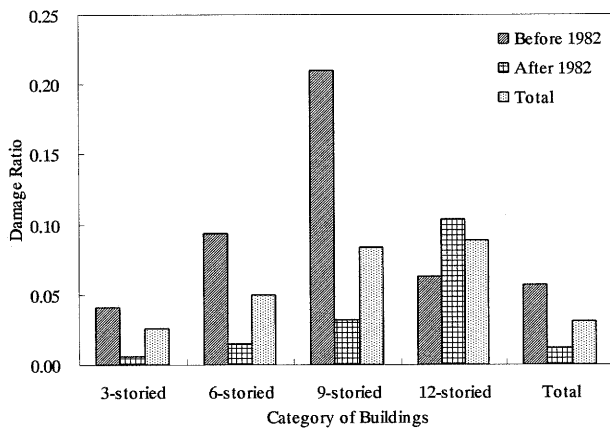


Figure 3 Observed damage ratios of RC buildings in Nada and Higashinada-Ward, separately for floor numbers (3, 6, 9, and 12) and the construction age (before and after the large code modification in 1981).

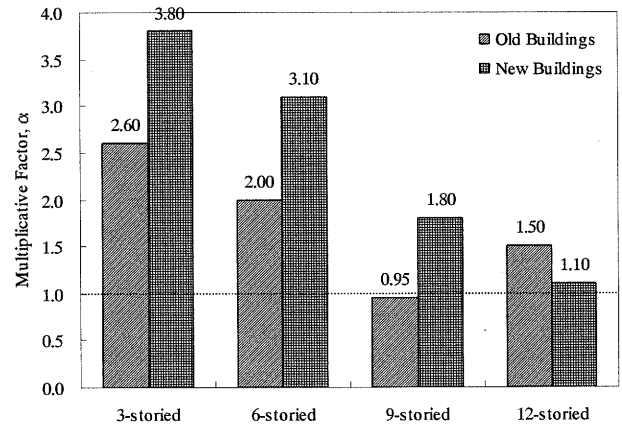


Figure 4 Multiplicative factors necessary to apply to the base shear coefficient of the standard model in order to reproduce observed damage ratios of RC buildings in Kobe (Fig.3), estimated separately for story numbers (3, 6, 9, and 12) and construction age (before and after the large code modification in 1981).

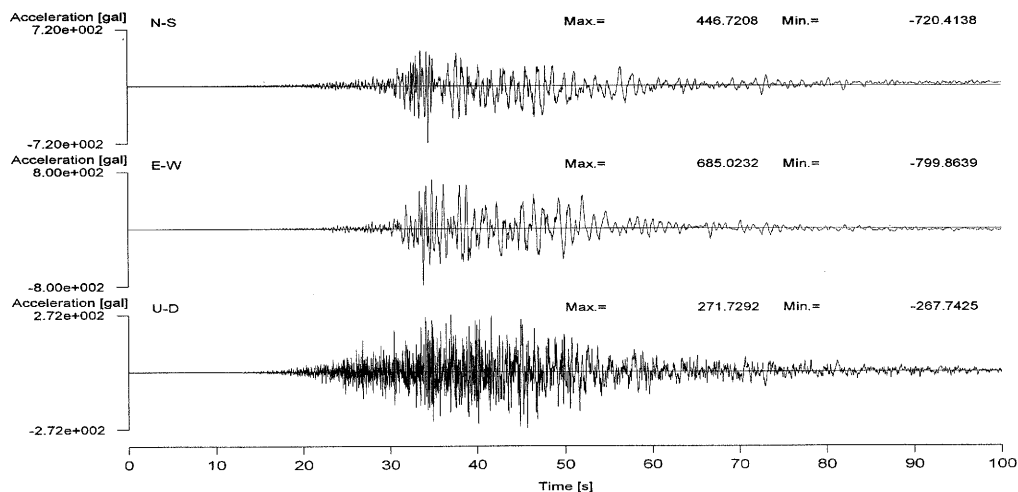


Figure 5 An example of observed three component strong motions (HKD086)

Table 1 Observed K-NET data of 2003 Tokachi-oki earthquake used for the analysis

	Site code	Epicentral Distance (km)	JMA Intensity	A0 (Gal)	PGA (Gal)	PGV (cm/s)	10m Average Vs.(m/s)	Equiv. Period (s)
1	HKD066	226	5.91	404.0	491.2	51.87	111	0.663
2	HKD067	210	5.39	220.9	334.0	42.92	208	0.808
3	HKD068	190	5.38	218.3	302.7	36.67	191	0.761
4	HKD070	204	5.68	308.4	475.3	36.79	135	0.486
5	HKD075	168	5.47	242.5	507.2	28.43	249	0.352
6	HKD076	155	5.38	218.9	216.4	38.71	133	1.124
7	HKD077	136	5.61	283.9	406.9	42.62	155	0.658
8	HKD078	156	5.33	207.5	401.5	36.34	178	0.569
9	HKD084	148	5.71	318.9	353.8	49.25	298	0.875
10	HKD085	131	5.49	249.6	277.3	55.54	150	1.259
11	HKD086	120	6.35	668.7	796.8	119.80	117	0.945
12	HKD090	154	5.39	222.3	468.9	35.24	484	0.472
13	HKD091	119	5.86	382.1	391.0	67.98	60	1.092
14	HKD092	138	5.95	422.5	609.0	57.05	197	0.589
15	HKD098	103	5.95	422.3	366.4	74.62	400	1.280
16	HKD100	84	6.06	480.0	970.2	44.74	121	0.290
17	HKD106	154	5.31	201.8	186.0	34.55	188	1.167
18	HKD110	102	5.37	216.0	216.0	57.25	170	1.666
19	HKD126	198	5.48	245.4	189.4	46.14	111	1.530

Table 2 Observed KiK-NET data of 2003 Tokachi-oki earthquake used for the analysis

	Site	Epicentral Distance (km)	JMA Intensity	A0	PGA	PGV	10m Average Vs.(m/s)	Equiv. Period (s)
1	HDKH04	187	5.37	217.36	215.70	58.22	200	1.696
2	HDKH06	156	5.45	236.57	210.00	47.87	280	1.432
3	HDKH07	104	5.27	191.91	199.20	45.95	390	1.449
4	IBUH03	206	5.92	405.45	375.88	89.56	84	1.497
5	KSRH02	148	5.78	347.73	405.02	50.47	130	0.783
6	KSRH03	184	5.71	319.75	806.04	31.35	194	0.244
7	KSRH07	152	5.43	232.46	500.06	38.30	124	0.481
8	KSRH09	134	5.85	373.93	391.06	85.50	142	1.374
9	KSRH10	180	5.85	377.56	580.62	39.11	166	0.423
10	NMRH02	223	5.45	238.46	514.01	26.75	236	0.327
11	NMRH04	199	5.44	233.20	437.89	26.81	136	0.385
12	NMRH05	188	5.44	233.47	391.29	38.57	166	0.619
13	TKCH05	154	5.50	249.88	406.21	27.95	256	0.432
14	TKCH07	123	5.99	439.30	404.18	93.95	104	1.460
15	TKCH08	109	5.62	287.61	500.72	38.38	340	0.482

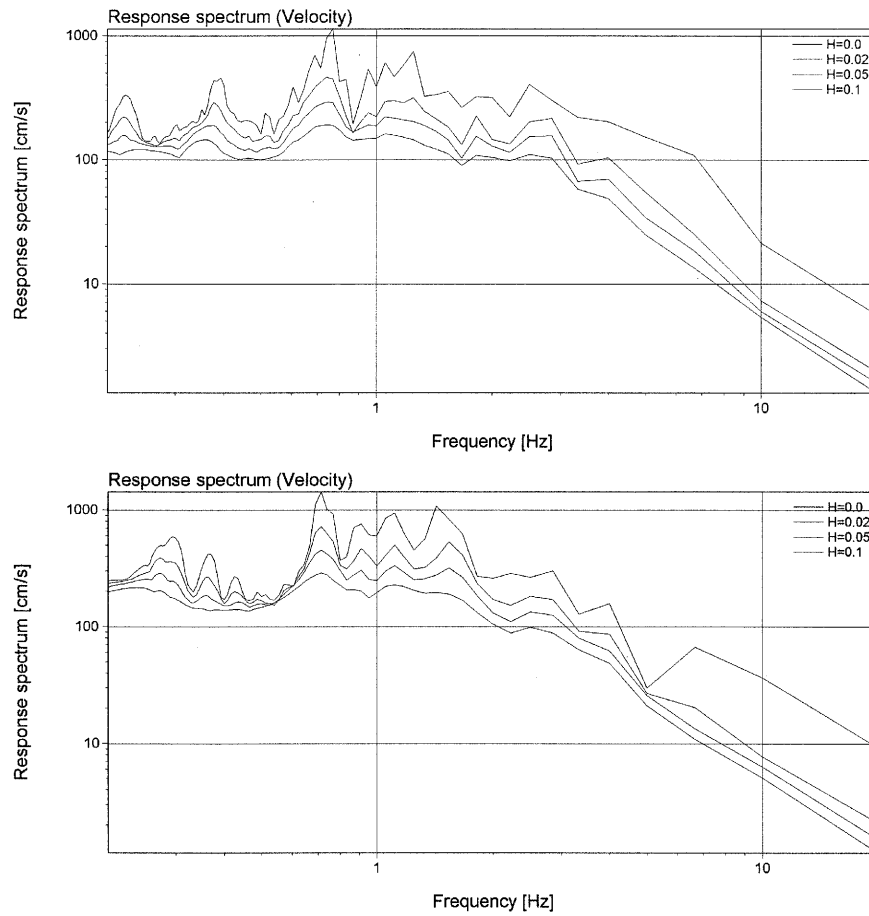


Figure 6 Velocity response spectra of observed ground motions (NS and EW components at HKD086)

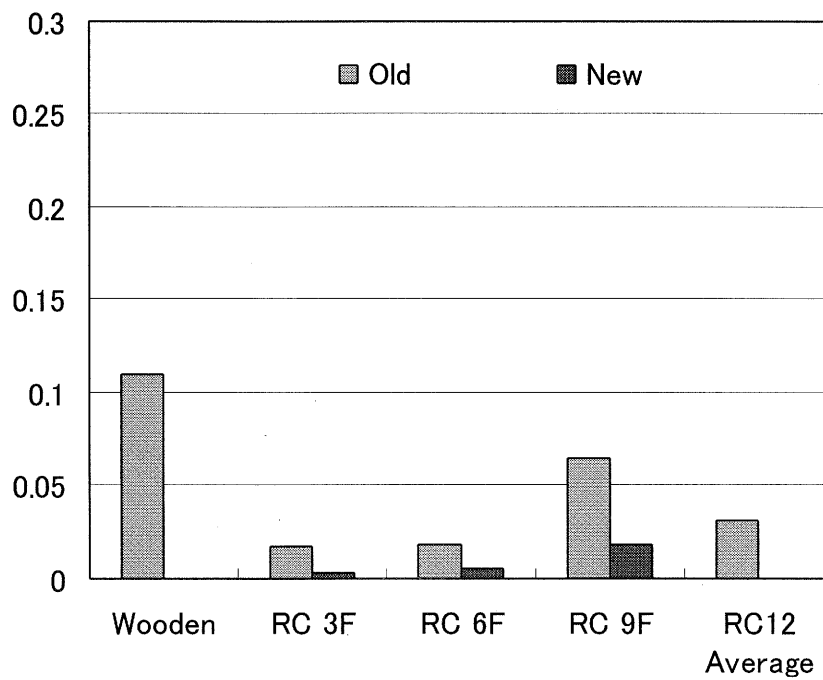


Figure 7 Averaged damage ratios of buildings with different categories for all the records used.

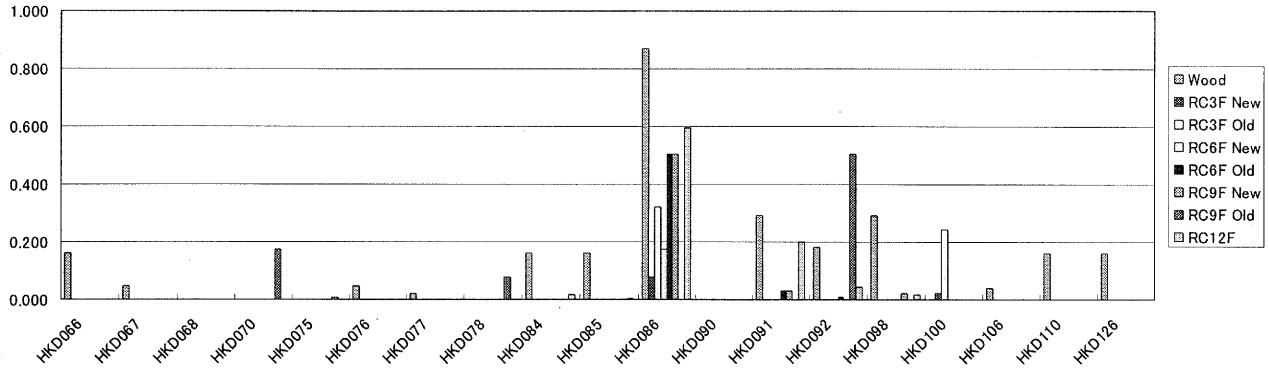


Figure 8 Damage ratios of buildings with different categories for each K-NET record used.

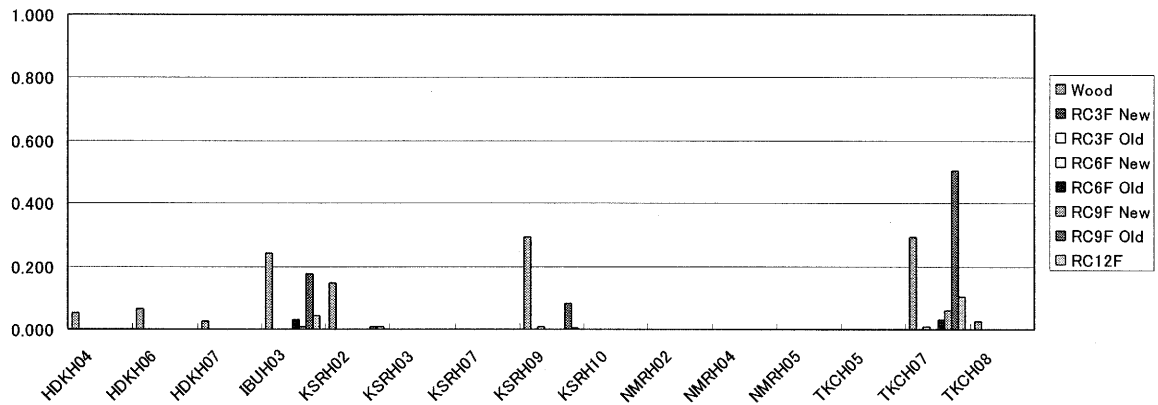


Figure 9 Damage ratios of buildings with different categories for each KiK-NET record used.

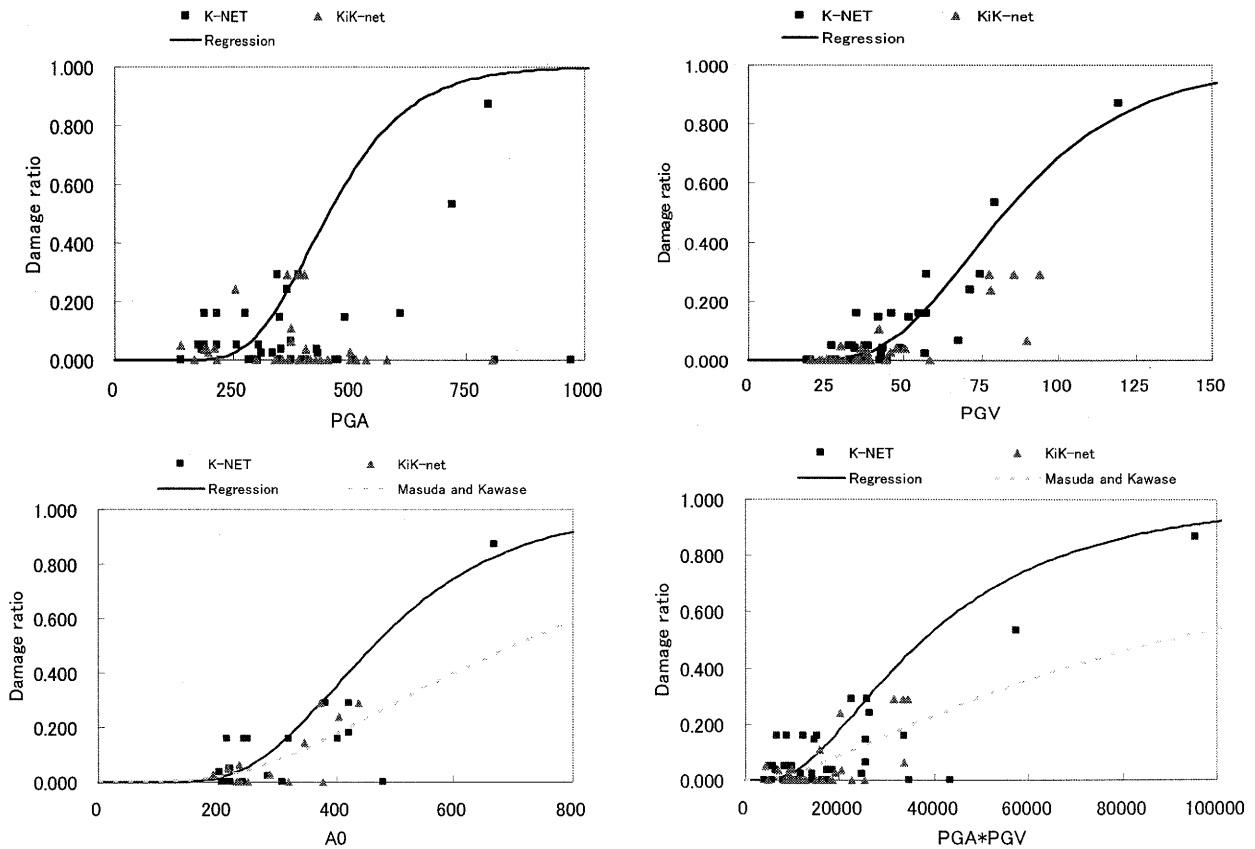


Figure 10 Damage ratios of wooden houses as a function of four strong motion strength indexes.

EFFECTIVENESS OF DIAPHRAGM WALL IN REDUCING THE POTENTIAL OF SOIL LIQUEFACTION INDUCED BY EARTHQUAKES

H.T. Chen¹⁾, and W.H. Chen²⁾

1) Associate Professor, Department of Civil Engineering, National Central University, Taiwan

*2) Former Graduate Student, Department of Civil Engineering, National Central University, Taiwan
chenht@cc.ncu.edu.tw*

Abstract: In this paper, a 3D finite element model based on nonlinear effective stress method is applied to investigating the effectiveness of grid-type diaphragm wall in reducing the potential of soil liquefaction induced by earthquakes. When a grid-type diaphragm wall is adopted as the countermeasure for liquefaction of ground, its effectiveness increases as the confining area becomes smaller. Furthermore, the duration of earthquake motion affects the results significantly, and it is recommended that the full duration be used in the analysis of soil liquefaction problem. The main function of diaphragm wall used as a countermeasure for soil liquefaction is the reduction of settlement, not the reduction of pore water pressure build-up.

1. INTRODUCTION

Ever since the 1969 Niigata Earthquake and Alaska Earthquake, tremendous efforts have been devoted to the investigation of soil liquefaction. On one hand, the experimental studies performed in the laboratory and in the field have provides the insights into the mechanism of soil liquefaction and on the other hand, the evolution of computer technology makes the numerical modeling of soil liquefaction feasible, stimulating the development of different procedures to study the soil liquefaction problems numerically.

Based on the comprehension of mechanism of soil liquefaction, several countermeasures against soil liquefaction have been developed, which can be categorized as (1) method of increasing soil density, (2) method of lowering the underground water table or increasing effective stress, (3) method of compaction, (4) method of accelerating the dissipation of pore water pressure and (5) method of limiting shear deformation of soil. For the method of limiting shear deformation of soil, it requires the installation of steel pile wall or construction of diaphragm wall in the soil stratum to limit the shear deformation to hinder the development of soil liquefaction. This method does not alter the properties of in-site soil and can be used for existing structures built on liquefiable ground.

Fukutake and Ohtsuki (1994) compared the effectiveness of diaphragm walls of parallel type and grid type in reducing the soil liquefaction using 3D effective stress finite element method. They found that the grid-type diaphragm wall is more effective and the effectual region is within 1.5 times the wall thickness measured from the inner face of wall. Sato and Matsuda (2000) investigated the effectiveness of grid-type diaphragm wall in reducing the liquefaction potential of soil by shaking table test and 2D effective stress finite element method. They found that the effectiveness decreases with increasing distance from the wall, and since this countermeasure does not alter the properties of soil, to prove their effectiveness one can not use the in-situ or soil element test, but has

to resort to numerical analysis as a supplement to the design process. Tanaka, Murata, Kita and Okamoto (2000) used the 2D effective stress finite element method to study the effectiveness of sheet-pile wall in reducing the liquefaction of embankment. They also performed the shaking table test to examine the effectiveness of sheet-pile wall in reducing the liquefaction for the cases such as oil tank, underground structure and pile foundation.

In this paper we employ 3D effective stress finite element method to investigate the effect of the confining area of wall and duration of earthquake on the effectiveness of grid-type diaphragm wall in reducing the liquefaction potential of soil.

2. METHOD OF ANALYSIS

In this section the method of analysis used in this study is briefly described and interested reader may consult the work by Jou (1997) for detailed formulation. The 3D effective stress finite element analytical procedure employed in this study is derived using the Biot theory for porous media. After some processes, the so-called U-W form equation of motion is obtained as follows:

$$\begin{bmatrix} M_{uu} & M_{uw} \\ M_{wu} & M_{ww} \end{bmatrix} \begin{Bmatrix} \ddot{U} \\ \ddot{W} \end{Bmatrix} + \begin{bmatrix} C_{uu} & 0 \\ 0 & C_{ww} \end{bmatrix} \begin{Bmatrix} \dot{U} \\ \dot{W} \end{Bmatrix} + \begin{bmatrix} K_{uu} & K_{uw} \\ K_{wu} & K_{ww} \end{bmatrix} \begin{Bmatrix} U \\ W \end{Bmatrix} = - \begin{bmatrix} M_{uu} & 0 \\ 0 & 0 \end{bmatrix} \{J\} \ddot{U}_g \quad (1)$$

where U_i is the displacement of soil particle and W_i the displacement of water relative to soil particle. The submatrix C_{uu} is a Rayleigh damping matrix to account for the damping mechanism other than the nonlinearity of soil. The vector $\{J\}$ is made up of 1 and 0 to account for the desired direction of input motion. \ddot{U}_g is the input motion specified at the bedrock of soil stratum.

The nonlinear behavior of soil is modeled using the Cap model with Mohr-Coulomb type failure line. To be consistent with the nonlinear model, the pore pressure model adopted is the one proposed by Pacheco (1989), which is also based the Cap model. In Pacheco's model a sub-yielding surface is introduced to simulate the nonlinearity upon loading-unloading process and a calibration function is employed to transform the total stress path to effective stress path. The pore pressure generated is due to both confining stress and shear stress. To simulate the lateral extent of soil stratum to infinity, the viscous boundary for porous medium proposed by Akiyoshi (1994) is adopted. Finally, the nonlinear time domain solution is performed using initial stiffness method and the numerical integration scheme is the Newmark β method with time step of 0.001 seconds.

3. RESULTS AND DISCUSSIONS

3.1 Finite Element Models and Input Motions

Shown in Figure 1 is the hypothetical model for free field adopted in this study. It is a soil stratum of 10m deep underlain by rigid bedrock. The upper layer of 6m thick is considered as a liquefiable layer, underlain by a nonliquefiable layer of 4m thick. In the analysis the stratum is further subdivided into 6 layers with the first layer of 1m thick, the second and third layers of 1.5m thick each and the fourth to sixth layer of 2m thick each. The soil stratum assumed to be fully saturated is discretized into 8-node block elements. The damping ratio for the Rayleigh damping is 2% for the first two modes. The permeability of soil is taken as 10^{-5} m/sec. Tables 1 and 2 show the other parametric values used in this study.

Figure 2 depicts the model with diaphragm wall consisting of only one cell of grid-type wall. The shaded portion is the diaphragm wall which has thickness of 0.5m and an embedment depth of 10m. The shear-wave velocity, Poisson ratio and mass density of wall are 793m/sec, 0.17 and

2.3t/m³, respectively. The wall is assumed to be impervious and behaves elastically during the earthquake. Both soil stratum and wall are also discretized into 8-node block finite elements as that for the free-field case. The elements in the soil columns denoted as a, b and c will be used for the discussion of pore pressure development and the nodes A, B and C will be used for the discussion of settlement.

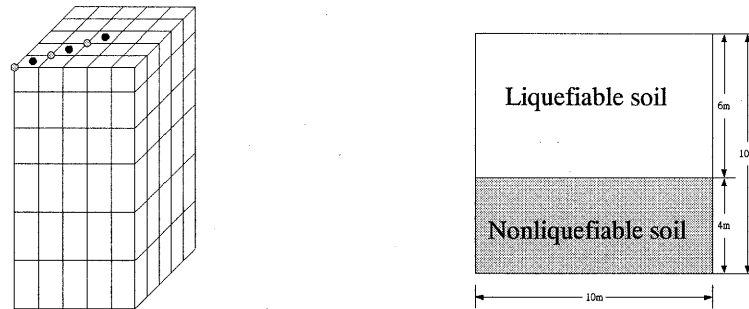


Figure 1 Finite Element Model for Free Field

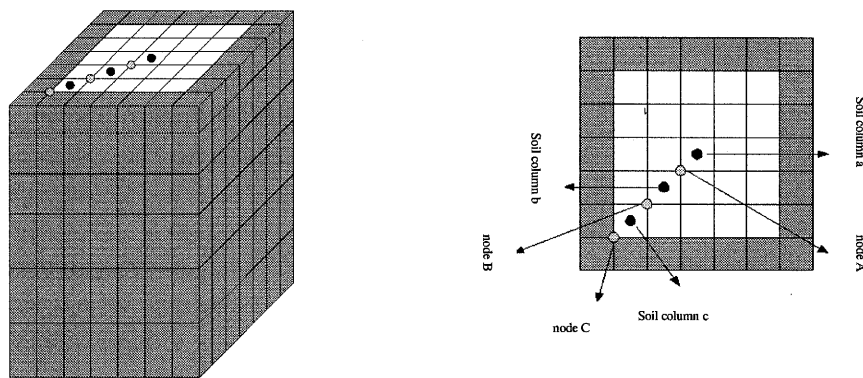


Figure 2 Finite Element Model for One Cell of Grid-Type Diaphragm Wall

Table 1 Parametric Values for Soil Stratum

Parameter	Nonliquefiable layer	Liquefiable layer
Shear-wave velocity(m/sec)	154	117
Poisson ratio	0.33	0.33
Mass Density(t/m ³)	1.9	1.9
Porosity	0.45	0.45
Coefficient of Static Earth pressure	0.74	0.45

Table 2 Parametric Values for Pore Pressure Model

Parameter	Nonliquefiable layer	Liquefiable layer
Cohesion (KN/m ²)	0	0
Angle of friction (°)	35	28
D1	5	5
D2	0.5	0.5
D3	0.6	1.0
R	5	5
W	0.25	0.25
D (1/KN)	0.75x10 ⁻⁵	0.75x10 ⁻⁵

Shown in figure 3 are the three components of normalized motion recorded at Dadu station during the 1999 JiJi Earthquake. This station is near the Taichung Harbor where severe liquefaction occurs. The ground motion of NS direction is normalized first so that the peak value is 0.1g and the same normalization factor is then used to normalize the ground motions of the other two directions.

The duration of motion is taken as 40 seconds over which the motion is significant.

In the following discussion the effectiveness of grid-type diaphragm wall in reducing the liquefaction potential of soil is evaluated using the surface settlement and the maximum pore pressure ratio which is the ratio of maximum pore water pressure developed during the earthquake to the initial effective stress.

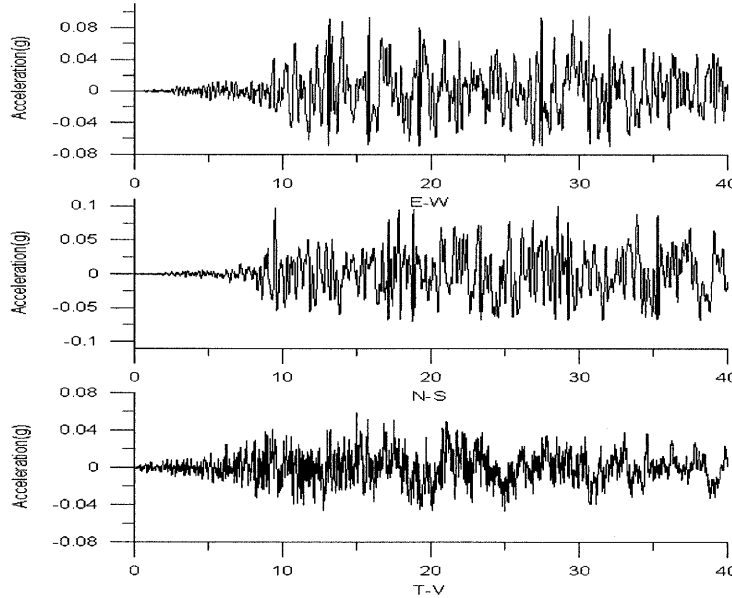


Figure 3 Normalized Earthquake Motion of JiJi Earthquake at Dadu Station

3.2 Discussions

In investigating the effect of confining area on the effectiveness of grid-type diaphragm wall in reducing the liquefaction potential of soil, five models are considered, which are 5m x 5m x 10m (MD-1), 7m x 7m x 10m (MD-2), 9m x 9m x 10m (MD-3), 11m x 11m x 10m (MD-4) and 13m x 13m x 10m (MD-5).

From the previous studies, it is known that the closer to the wall, the less the pore water pressure is generated. Therefore, in the following discussions we use the results obtained for the elements in soil column a which are farthest from the wall. Table 3 shows the maximum pore water ratio for elements in soil column a. It can be seen that as the confining area increases, the efficiency deteriorates and the results for MD-4 and MD-5 are very similar. The maximum pore water pressure ratios of last two layers are less than 1 as expected. The fourth layer of MD-1 and MD-2 have the maximum pore water pressure ratio less 1, while for the other cases the maximum pore water pressure ratios are all larger than 1, indicating that the pore water pressure development is not effectively refrained. In fact, as compared with the results of the free field case, the use of grid-type diaphragm wall cause the upper three layers to have higher maximum pore water pressure ratio.

Shown in Figure 4 are the time histories for the pore water pressure development of top element of each soil column. At early stage, the use of grid-type wall can indeed slow the development of pore water pressure; however, at certain instant of earthquake motion, significant amount of pore water pressure which is very close to that generated in free field is generated. After that instant, the pore water pressure developed in MD-1 and MD-2 starts to dissipate, while that for the other models remains also constant. It should be mentioned that in the previous studies, only a short duration of motion was considered, and the observation of the pore water pressure development being refrained at this stage, as also displayed in this study, led to the conclusion that the use of grid-type diaphragm wall can refrain the development of pore water pressure. However, from our result, it indicates that the use of grid-type wall apparently can not prevent the development of pore water pressure as expected, but it does have the function to cause a delay in time to reach the maximum pore water pressure.

Table 3 Maximum Pore Water Pressure Ratio for Soil Column a

	MD-1 (5m*5m)	MD-2 (7m*7m)	MD-3 (9m*9m)	MD-4 (11m*11m)	MD-5 (13m*13m)	FREE FIELD
Layer 1	1.38	1.17	1.16	1.09	1.12	1.09
Layer 2	1.06	1.15	1.11	1.08	1.05	1.04
Layer 3	1.25	1.13	1.14	1.13	1.13	1.10
Layer 4	0.77	0.95	1.07	1.08	1.09	1.08
Layer 5	0.63	0.76	0.92	0.93	0.96	0.96
Layer 6	0.35	0.28	0.34	0.42	0.41	0.64

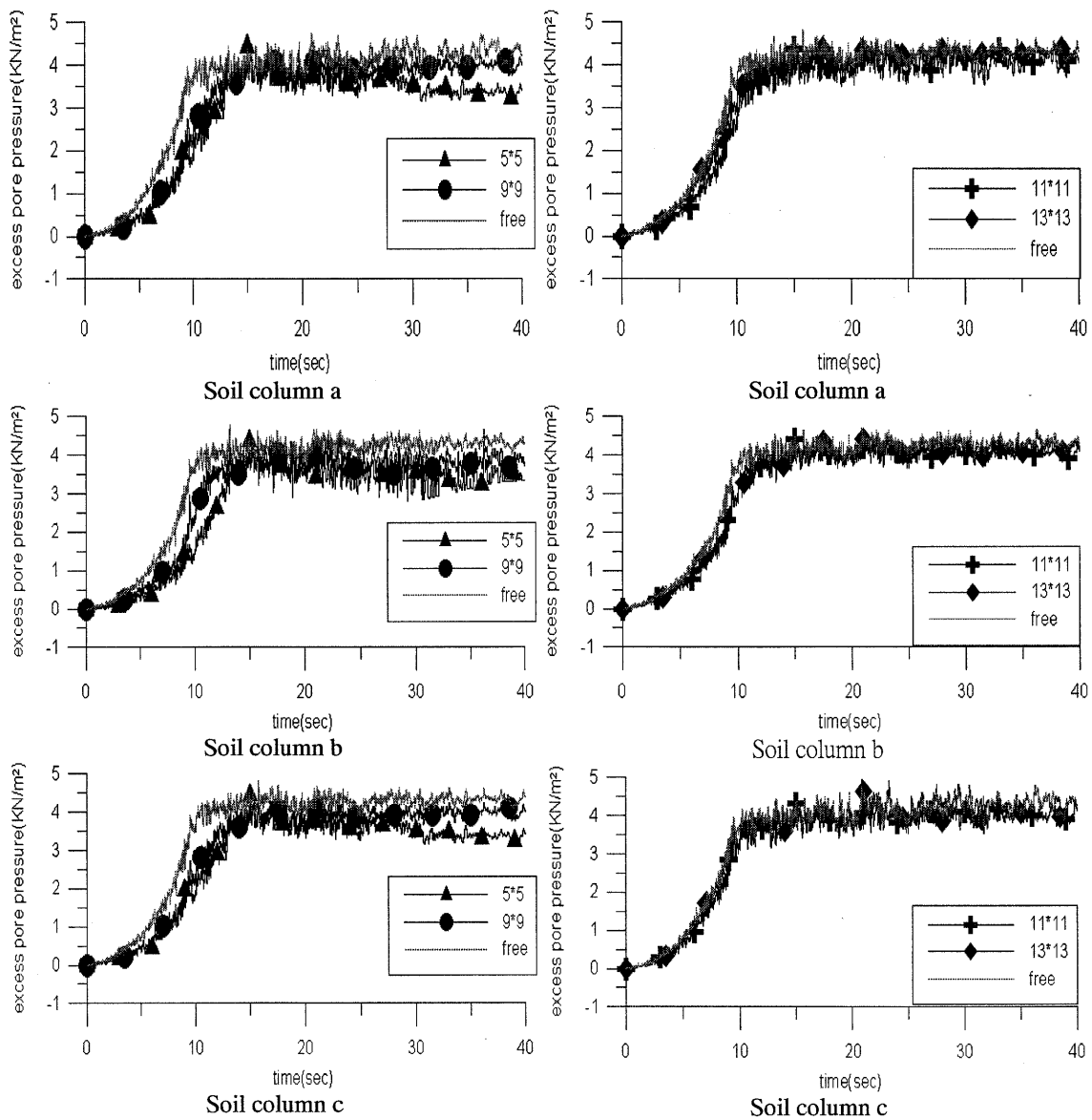


Figure 4 Development of Pore Water Pressure for Top Elements of Each Soil Column

Table 4 shows the maximum settlement at nodes A, B and C for different models. The positive value indicates uplift. We can still see that the settlement increases with increasing distance from the wall for a given confining area. However, the use of the grid-type wall can lead to the reduction of surface settlement. For node A which is the farthest from the wall among all models, we can still observe a significant reduction in the settlement. On the other hand, for a given node, its settlement decreases as the confining area becomes smaller. The reason for node C of MD-1 to have zero settlement is that it is on top of the wall in that model.

Table 4 Settlement of Nodes A, B and C for All Models (Unit: cm)

MODEL \ NODES	A	B	C
MD-1(5m*5m)	-0.34	-0.27	0.0
MD-2(7m*7m)	-0.56	-0.73	0.66
MD-3(9m*9m)	-0.55	1.54	2.60
MD-4(11m*11m)	0.83	2.42	3.77
MD-5(13m*13m)	1.46	3.40	5.35
FREE FIELD	-13.15	-13.02	-12.77

Depicted in Figure 5 are the time histories of settlement of nodes A, B and C for all models. The settlements for all models are almost the same and small until 10 seconds, which corresponds to the onset of liquefaction in the free-field case. After 10 seconds, the settlement of free-field case starts to increase significantly with time, while the other cases with grid-type diaphragm wall still undergo very small amount of settlement or uplift, which also increases with increasing confining area. It can be observed that for the MD-1 the settlements of three nodes are very small, indicating that a 5m x 5m confining area will render best efficiency in reducing the settlements induced by earthquake in the liquefiable ground.

From previous discussion, it is found that the duration of earthquake motion used in the analysis affects the final results. Sato et al. (2000) proposed a linear relation between the settlement and the ratio of confining area to the embedment depth of wall. Figure 6 depicts the results from this study. If we take the duration to be 10 seconds, a linear relation is obtained as well; however, if the duration is taken to be 40 seconds, the linear relation no longer exists. Thus, it clearly demonstrates the importance of duration of motion in the soil liquefaction analysis, and it is recommended that the full duration be used in the analysis of soil liquefaction problem.

4. CONCLUSIONS

In this paper, a 3D finite element model based on nonlinear effective stress method is applied to investigating the effectiveness of grid-type diaphragm wall in reducing the potential of soil liquefaction induced by earthquakes. It is found that when a grid-type diaphragm wall is adopted as the countermeasure for liquefaction of ground, its effectiveness increases as the confining area becomes smaller and in this study the use of 5m x 5m confining area can lead to excellent reduction in the settlement. Furthermore, the duration of earthquake input motion affects the results significantly, and it is recommended that the full duration be used in the analysis of soil liquefaction problem. Finally, the main function of diaphragm wall used as a countermeasure for soil

liquefaction is the reduction of settlement, not the reduction of pore water pressure build-up.

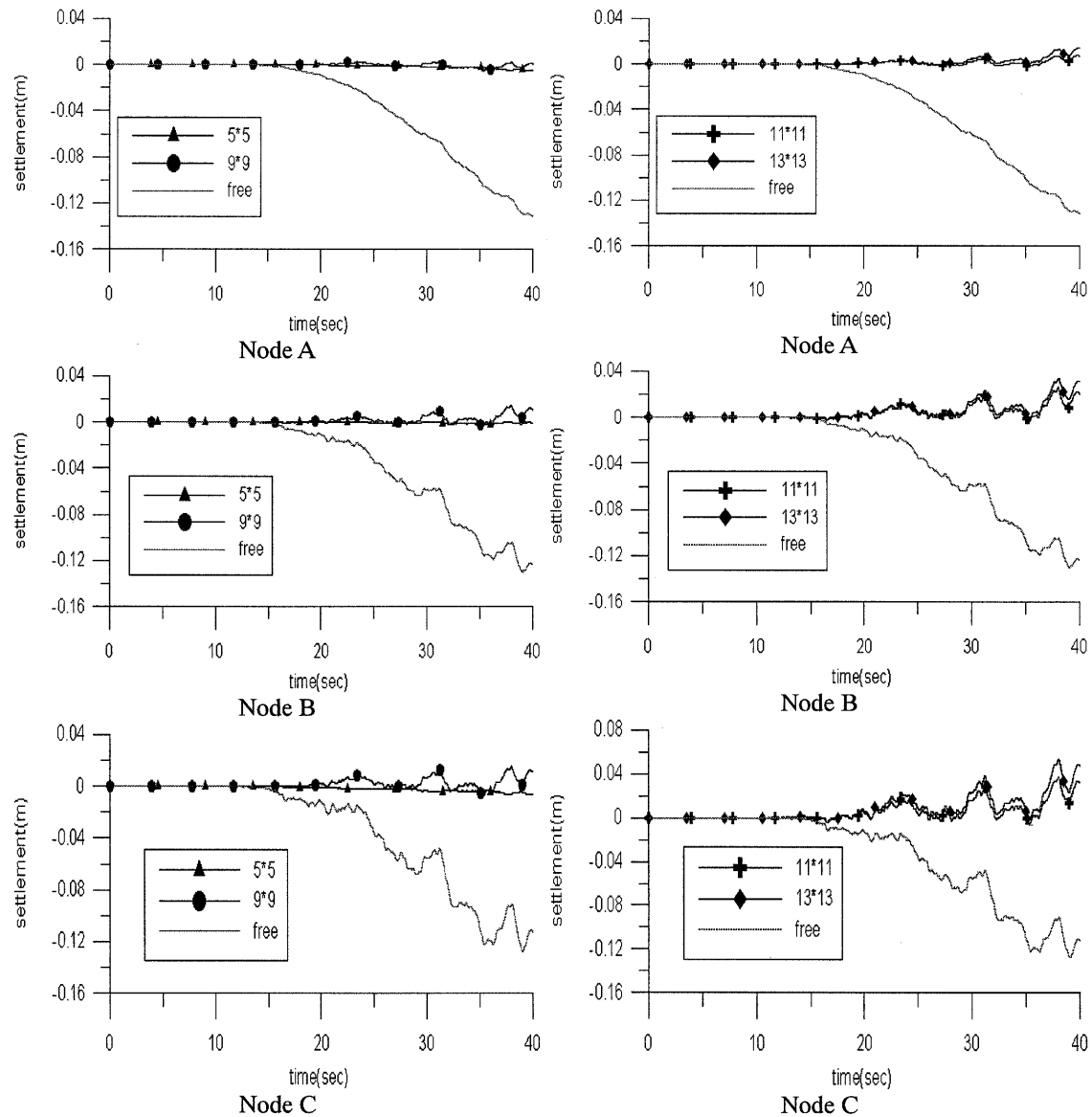


Figure 5 Time Histories of Settlement of Nodes A, B and C for All Models

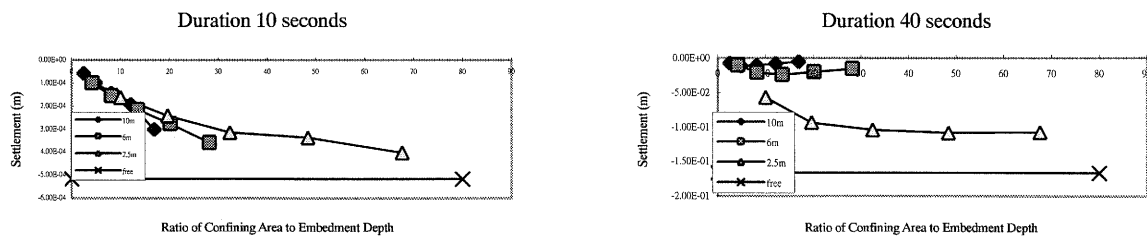


Figure 6 Effect of Duration on Relation Between Settlement and Ratio of Confining Area to Embedment Depth

Acknowledgements:

The results presented are part of a research supported by National Science Council, Taiwan, under the Grant No. NSC89-2211-E-008-095. The authors appreciate such a support to make this study possible.

References:

- Pacheco, M.P., Altschaeffl, A.G., and Chameau, J.L. (1989), "Pore Pressure Prediction in Finite Element Analysis," *International Journal for Numerical and Analytical Methods in Geomechanics*, **13**, 477-491.
- Akiyoshi, T., Fuchida, K. and Fang L. (1994), "Absorbing Boundary Conditions for Dynamic Analysis of Fluid-Saturated Porous Media," *Soil Dynamics and Earthquake Engineering*, **13**, 387-397.
- Fukutake, K. and Ohtsuki, O. (1994), "Prediction of Liquefaction-Preventing Effect of Partially-Improved Soil by Three-Dimensional Liquefaction Analysis," *Ninth Symposium of Earthquake Engineering*, pp.134-140 (1994).
- Jou, J.J. (1997), "Seismic Analysis of Pile Foundation of Bridge considering the Change in Pore Water Pressure," *7th Conference on Current Researches in Geotechnical Engineering in Taiwan*, 319-326.
- Sato, K. and Matsuda, T. (2000), "Effect of the Grid-Shaped Stabilized Ground Improvement to Liquefaction Ground," *Proceedings of 12th World Conference on Earthquake Engineering*, Paper No. 2228.
- Tanaka, H., Murata, H., Kita, H. and Okamoto, M. (2000), "Study on Sheet Pile Wall Method as a Remediation Against Liquefaction.," *Proceedings of 12th World Conference on Earthquake Engineering*, Paper No. 0535.

SAFETY OF FILL DAMS UNDER LEVEL 2 EARTHQUAKE MOTIONS: LESSONS FROM THE 2004 NIIGATA-CHUETSU EARTHQUAKE

T. Ohmachi¹⁾

*1) Professor, Center for Urban Earthquake Engineering,
Tokyo Institute of Technology, Japan
ohmachi@envng.titech.ac.jp*

Abstract: The Niigata-ken Chuetsu earthquake (Mj6.8), Japan, occurred on October 23, 2004. Several fill dams located in and around the near field were more or less damaged by the earthquake. Among them, Asagawara Dam which is 37m high and completed in 1945, suffered longitudinal cracks along the crest and maximum settlement of the crest amounting to 75cm. Yamamoto Dam which is 28m-high, completed in 1954, sustained longitudinal cracks mainly observed on the riprap surface. Shin-yamamoto Dam which is 42.4m high, completed in 1990, suffered maximum settlement of the crest exceeding 80cm and sand liquefaction. Thick sedimentation in front of the drain layer is presumably responsible for the liquefaction. To prevent secondary damage to the downstream areas, reservoir water was safely released from each reservoir shortly after the main shock.

1. INTRODUCTION

The Niigata-ken Chuetsu earthquake (Mj6.8), Japan, occurred at 17:56 (local time) on October 23, 2004. Forty people were killed, and numerous landslides of various types took place on natural slopes and man-made banks. The highest seismic intensity of 7 on the JMA scale was registered at Kawaguchi town. Strong motion accelerometers of K-net registered peak acceleration of 1501gal at Ojiya, and 1750gal at Tokamachi during the main shock. The main shock was followed by many strong aftershocks for weeks. As detailed description about the earthquake and strong motion in near field is available elsewhere (Midorikawa et al 2005), it is omitted in the present paper.

Several fill dams built for hydroelectric power generation or agricultural irrigation were damaged by the earthquake. Due to the end of a harvest season, those dams for irrigation were empty of reservoir water at the time of the main shock, which served to avoid secondary damage to the downstream. While three dams for power generation were impounded with water from the Shinano river, the longest river in Japan. The three dams are Yamamoto Dam and Shin-yamamoto Dam located in Ojiya, 6 and 5km from the epicenter respectively, and Asagawara Dam in Tokamachi, 22km from the epicenter (see Location Map in Appendix). The electric power generated with the water from these dam is used to drive JR trains in the Tokyo metropolitan area. Since

much of the electric power is used during morning and evening rush hours, these dams are always subjected to rapid draw down of the water level twice a day. Although these three dams suffered earthquake damage, there was no secondary damage to the downstream because the storage water was safely released from each reservoir after the damage to the dams was discovered. The owner of the dams (JR East) established a committee to investigate causes and effects of the damage. Although the author has been one of the committee members and given much information to be described in this paper, he is solely responsible for any errors and misunderstanding.

2. CASES OF DAMAGE TO DAMS

2.1 Asagawara Dam (Built in 1945)

This dam is 37m high, and has a crest length of 292m with a standard cross section shown in Figure 1. Longitudinal cracks developed on the entire crest. At the middle cross section, several wide and deep cracks were seen, stepping down to the upstream side as shown in Figure 2. From comparison of the elevation along the crest before and after the earthquake, maximum settlement of the crest was 20cm at the downstream shoulder and 50cm at the center.

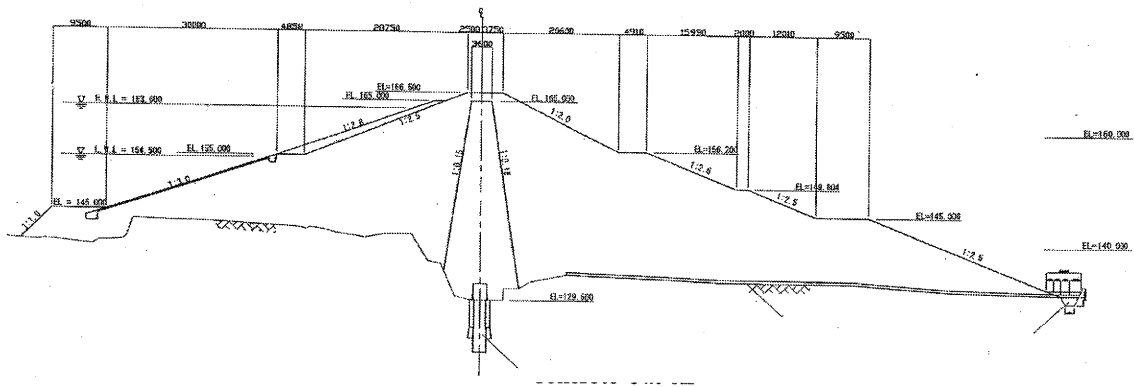


Figure 1 Standard Cross Section of Asagawara Dam

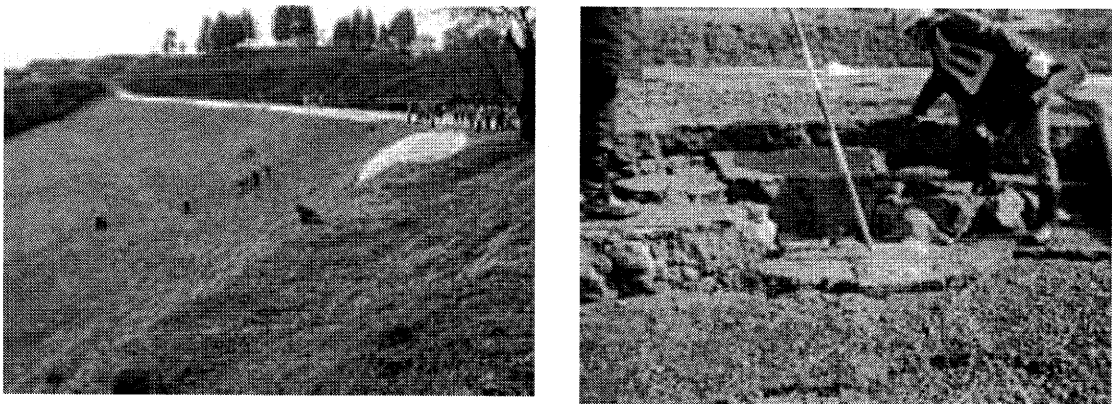


Figure 2 Downstream View (left) and Cracks on the Crest (right) of Asagawara Dam. Trenches excavated at 3 cross sections and 8 borings on the dam body revealed that

the cracks disappeared at around the boundary between the upper shell zone and clay core, and did not penetrate the core zone, as shown in Figure 3. Due to the earthquake-induced settlement together with long-term one, the top of the core was 0.5~1.0m lower than that of an original design. From sampling tests of dam materials and cone penetration tests, the shell zone above the core was rather loose in density in comparison with the rest of the dam body. According to in-situ tests using several pits dug on top of the clay core, the coefficient of permeability and dry density of the core were $0.9 \sim 1.3 \times 10^{-7} \text{cm/s}$ and 1.25g/cm^3 , respectively. Judging from a series of investigation, the clay core was free from the earthquake-induced cracking or sliding.

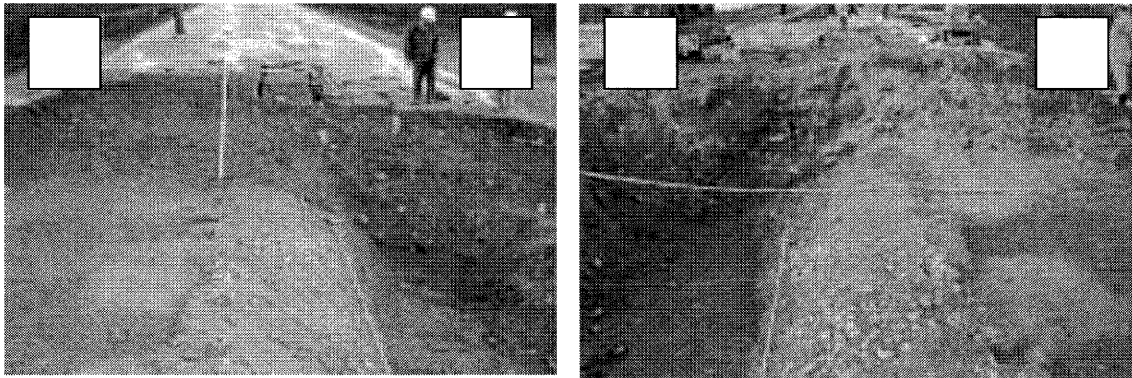


Figure 3 Cracks on Side Walls of a Trench at Asagawara Dam.
(U and D indicate upstream and downstream sides, respectively.)

2.2 Yamamoto Dam (Built in 1954)

This dam is a zoned earth dam with a standard cross section shown in Figure 4. It is 28m high, and has a crest length of 927m. At a first look, there was nothing abnormal all over the crest, but settlement and horizontal displacement along the crest was 10~20cm and 10~12cm in the upstream direction, respectively. On the upstream slope, mainly on the riprap zone, longitudinal cracks as shown in Figure 5 were observed, as well as boiled sand at several places at EL.90~92m.

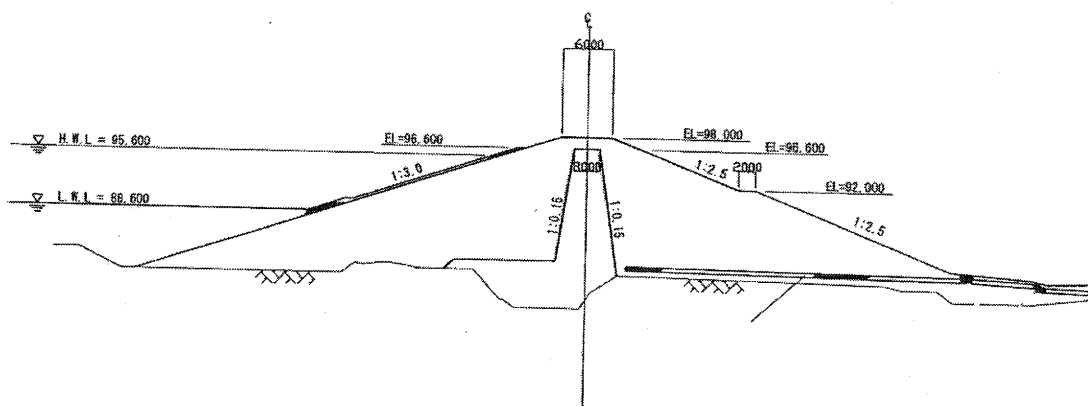


Figure 4 Standard Cross Section of Yamamoto Dam

To investigate the cracks and boiled sand, trench excavation and drilling of bore holes of 86mm or 116mm in diameter were conducted on the dam body. These investigation and tests revealed that the cracks were as shallow as 0.3~0.5m in depth, and boiled sand was originated from shell materials located at around 1m in depth.

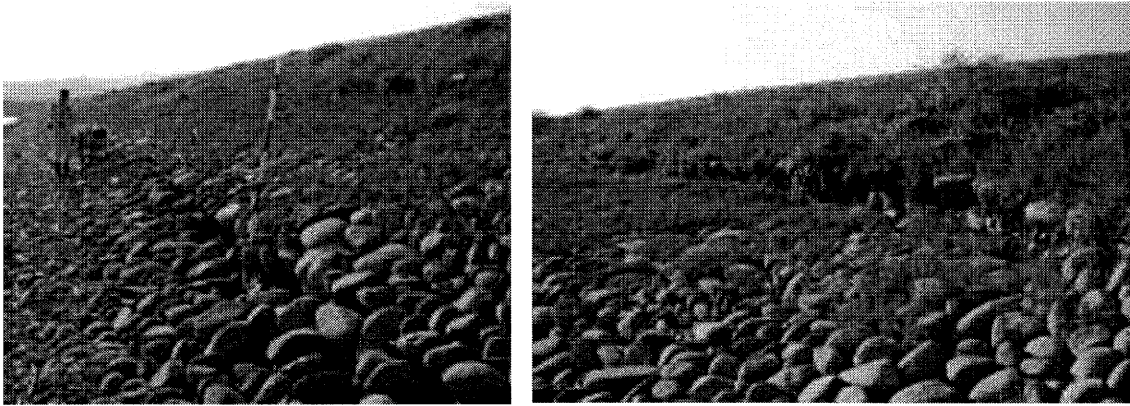


Figure 5 Cracks found on the upstream slope of Yamamoto Dam

2.3 Shin-yamamoto Dam (Built in 1990)

This dam is 42.4m high, and has a crest length of 1,392m with a standard cross section shown in Figure 6. This is a zoned fill dam with a dam axis of a semi-circular shape as shown in Figure 7. Both right and left ends of the dam are plunged into natural slopes. To facilitate the rapid draw down of the water level, there is a horizontal drain layer on the upstream side at the elevation of EL.143.8m~147.3m, which is just above the low water level of EL. 143.8m. The entire crest is covered with asphalt pavement.

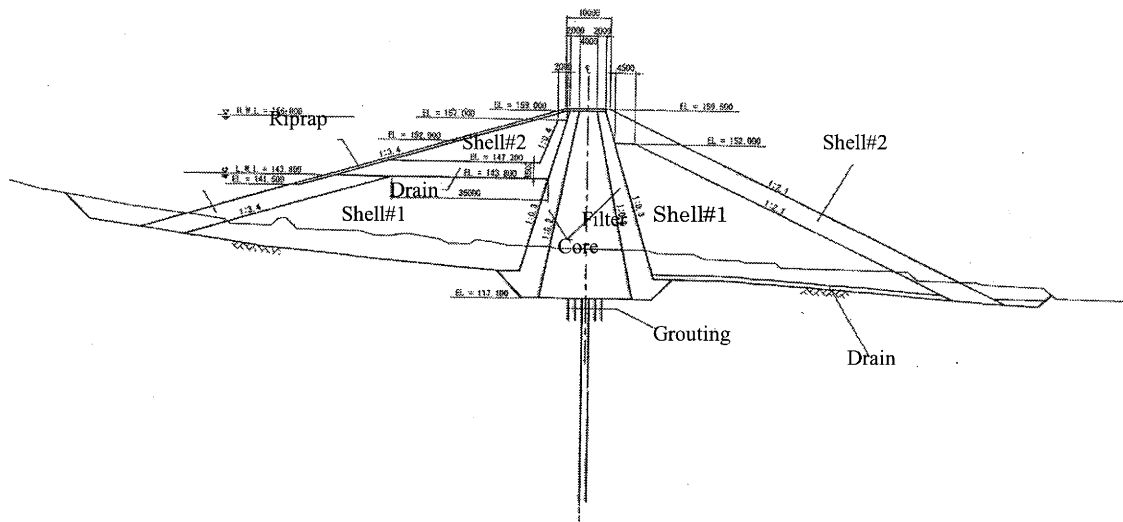
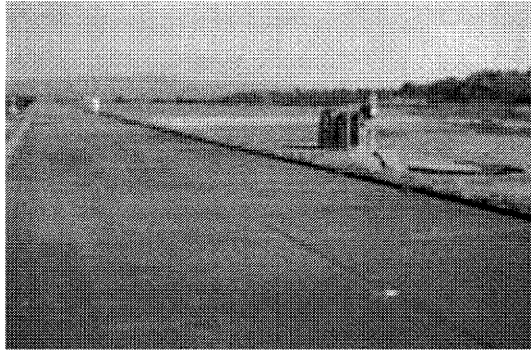


Figure 6 Standard Cross Section of Shin-yamamoto Dam



(a) Right Half Side

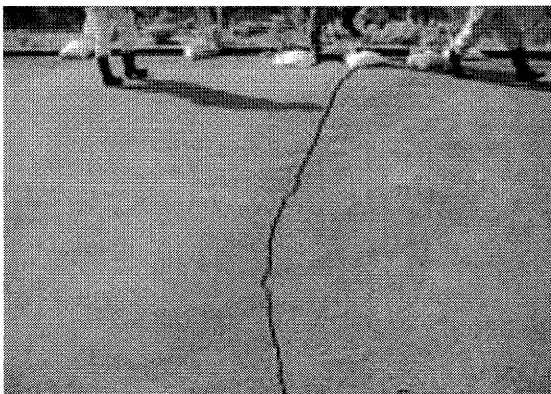


(b) Left Half Side

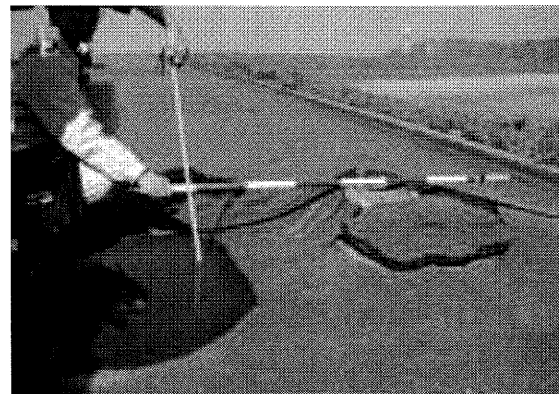
Figure 7 Overview of Shin-yamamoto Dam

Many cracks of asphalt pavement as shown in Figure 8 (a) were seen on the crest. In fear of core's safety, all the asphalt pavement on the crest was removed to trace the cracking under the pavement. It was confirmed that the cracks were limited in the pavement only and did not reach the core.

Settlement of the crest was about 10~40cm on the right half side of the dam where both core and shell zones are founded on rock, while it was about 50~90cm on the left half side where the shelter zone is founded on terrace deposits. The crest was also displaced upstream about 20~40cm on the left half side, while downstream about 3~10cm on the right half side. Due to the large settlement, a top of an H-shaped steel beam which was embedded to protect monitoring cables from bottom to crest in the filter zone was observed protruding about 30cm from the asphalt pavement as shown in Figure 8 (b). According to micro-tremor measurement conducted along the crest in November 2004, the fundamental period of the dam is 0.24s. The period is in a period range of many other existing rockfill dams. This fact implies that Shin-yamamoto dam has an appropriate shear wave velocity as a whole, as a result of adequate compaction during construction.



(a) Crack on the Asphalt Pavement



(b) H-beam's Top indicating Settlement

Figure 8 Cracks and settlement of the crest of Shin-yamamoto Dam

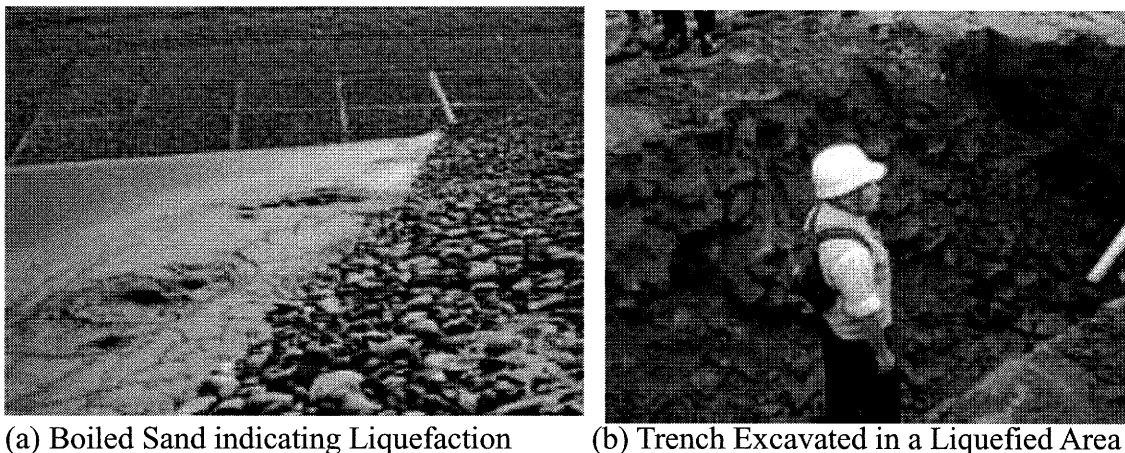


Figure 9 Liquefaction Observed near the Left End of Shin-yamamoto Dam

On the upstream side near the left end, boiled sand was found at several places on the riprap surface at EL. 145~150m and nearby sedimentation as shown in Figure 9 (a). Trenches were excavated to investigate origin of the boiled sand and soil properties such as permeability and grain size distribution in and around the liquefied areas, as shown in Figure 9 (b). The origin of the boiled sand was mostly concentrated in and around the drain layer whose sand content was higher than that at the construction stage. In addition, near the left end of the dam, it is noted that fine sedimentation was thick enough to cover the mouth of the drain layer, as shown in Figure 9 (a). It seems reasonable to think that the thick sedimentation in front of the drain layer caused pore water pressure buildup under the strong shaking followed by the liquefaction.

3. SAFETY OF FILL DAMS UNDER LEVEL 2 MOTIONS

3.1 Requirements for Dam Safety against L2 Motion

Since the 1995 Kobe earthquake, seismic design of civil engineering structures in Japan has been required to consider Level 2 (L2) earthquake motion. The L2 motion addresses input motions of extremely high intensity like that experienced in Kobe city during the 1995 earthquake. The earthquake motion in the near field of the 2004 Niigata-en Chuetsu earthquake is thought to be another example of the L2 motion, and the damage caused by the earthquake gives us good lessons for dam safety under the L2 motion.

In general, for the L2 motion, structures are allowed to undergo plastic deformation as long as collapse and loss of life are prevented. In this context, when it comes to fill dams, such deformation as settlement, horizontal displacement of the crest, cracking, sliding and even liquefaction may be technically allowed as long as serious damage are prevented. The serious damage should include not only direct or structural damage to a dam body and appurtenant structures but also indirect one in consequence of the direct damage like loss of life in the downstream. Hence, regardless of dam type, requirement for dam safety against the L2 motion is stated as (Japan Dam Engineering

Center 2005):

A dam subjected to the L2 motion is required (1) to maintain its capability of water storage during and after the earthquake, and (2) to remain within repairable damage even if it suffers earthquake-induced damage.

When we think about requirements for appurtenant structures such as spillways and outlets, the statement (1) can be paraphrased into the following statement:

A dam subjected to the L2 motion is required (3) not to release uncontrolled outflow discharge from reservoir.

3.2 Discussion

Due to sudden disruption of power generation immediately after the main shock, reservoir water level at the aforementioned three dams increased first and decreased later because it took several hours to start the outflow discharge from each reservoir. Causes and effects of the damage to the dams are still under investigation now, but the damage to each dam is apparently limited and recognized as repairable.

In view of the above statements for the safety requirements, these three dams withstood the L2 motion in the near field of the 2004 earthquake somehow or other, and satisfied the requirements (1)~(3) despite considerable damage to the dam bodies. The basic concept of the requirements is clean-cut and seemingly acceptable not only to dam engineers but also general citizens.

In a sense, the requirements taking into account the downstream safety are considered necessary and minimum conditions for any dams, because we should also pay attention to damage-related costs when we think about the level of the seismic safety of dams. Reportedly in the present cases, the disruption of power generation caused JR East extra expenses of 1 billion Yen (9.7 million USD) a month only to compensate the power loss.

4. CONCLUSIONS

The strong shaking in the near field of the 2004 Niigata-ken Chuetsu earthquake caused considerable damage to fill dams such as Asagawara, Yamamoto and Shin-yamamoto dams. The damage was different from dam to dam, maybe because of the difference in the strong motion intensity, dam configuration, construction practice, and dam materials. Among them, longitudinal cracks, settlement and minor sliding were commonly observed on these dams. In the author's opinion, special attention should be paid to the boiled sand observed at Shin-yamamoto Dam. Since most of the sand was originated from the drain layer covered with fine sedimentation, the thick sedimentation in front of the drain layer was presumably responsible for the liquefaction of the sand. This gives us a new lesson for seismic safety of fill dams, especially for those repeatedly subjected to rapid draw down of reservoir water level.

In addition, some statements in "Guidelines for Seismic Safety Evaluation of Dams under Level 2 Earthquake Motions (Draft)" which has recently been compiled in Japan,

demonstrated their validity through the present cases.

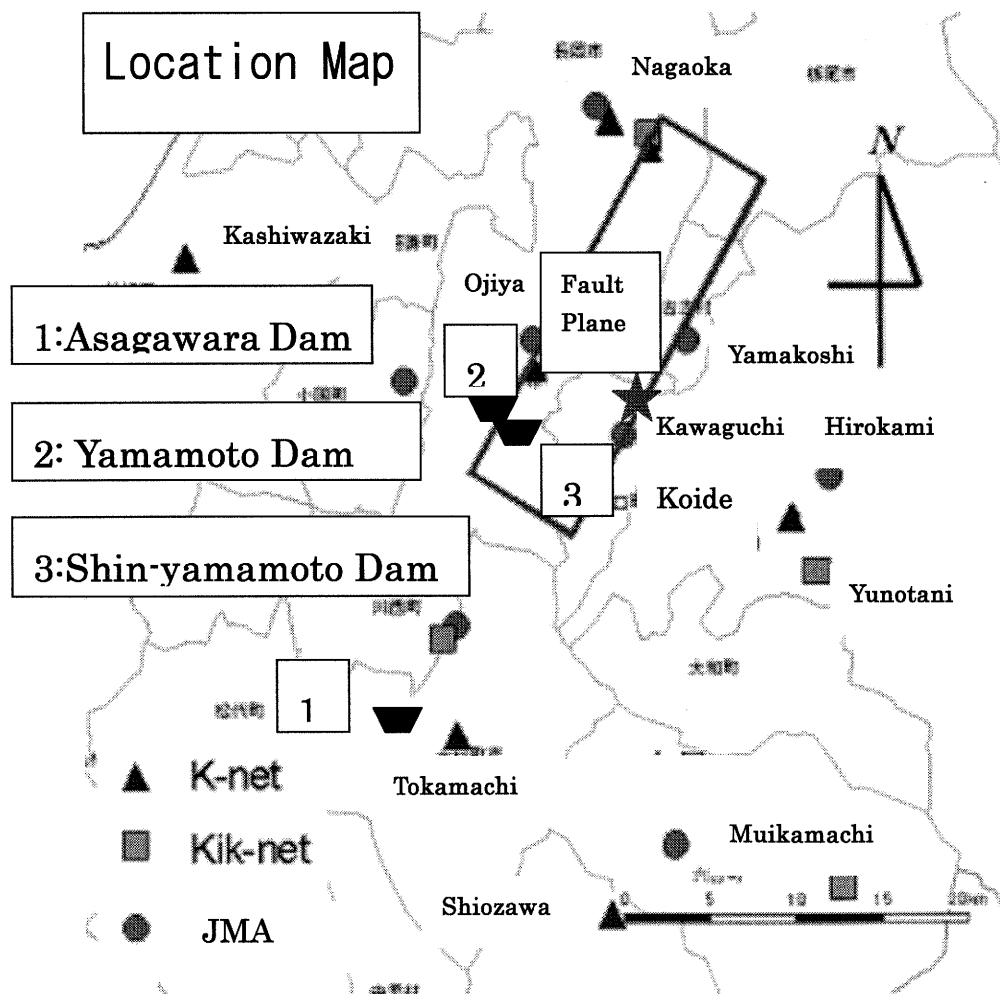
Acknowledgements:

The author acknowledges technical information and support given from JR East in the post earthquake investigation followed by active discussion on the causes and effects of the damage to the dams described in this paper. He also acknowledges information from “Guidelines for Seismic Safety Evaluation of Dams under Level 2 Earthquake Motions (Draft)” which is to be published soon.

References:

Japan Dam Engineering Center: (2005), “Guidelines for Seismic Safety Evaluation of Dams under Level 2 Earthquake Motions (Draft)” (to be published in Japanese)
Midorikawa, S. and Miura, H. (2005), “Strong Motion Records Observed in the 2004 Niigata-ken-chuetsu Earthquake” *Proceedings of the 2nd International Conference on Urban Earthquake Engineering*, (to be presented).

Appendix: Location Map



EXPERIMENTAL EVALUATION OF SEISMIC PERFORMANCE OF SMA BRIDGE RESTRAINER

E. Maragakis¹⁾, M. Saiidi²⁾, R. Johnson³⁾, R. DesRoches⁴⁾, J. Padgett⁵⁾

1) Professor and Chair, Department of Civil and Environmental Engineering, University of Nevada, Reno, USA

2) Professor, Department of Civil and Environmental Engineering, University of Nevada, Reno, USA

3) Graduate Research Assistant, Department of Civil and Environmental Engineering, University of Nevada, Reno, USA

4) Assistant Professor, Department of Civil and Environmental Engineering, GA Institute of Technology, Atlanta, GA, USA

5) Graduate Research Fellow, Department of Civil and Environmental Engineering, GA Institute of Technology, Atlanta, GA, USA

maragaki@ce.unr.edu, saiidi@unr.edu, rjohnson@nevada.unr.edu, reginald.desroches@ce.gatech.edu,

jamie.padgett@ce.gatech.edu

Abstract: Experiments were conducted at the University of Nevada Reno (UNR) Large Scale Structures Laboratory, in cooperation with Georgia Institute of Technology, to determine the effects of shape memory alloy (SMA) cable restrainers on the seismic performance of in-span hinges of a representative multiple-frame concrete box girder bridge subjected to earthquake excitations. These experiments were also used to compare the performance of SMA to steel restrainers as restraining devices to reduce hinge displacement. Data collected from SMA restrainer experiments was compared to information gathered in a previous UNR study on the performance of steel restrainers. The experimental set up consisted of two concrete blocks, simulating adjacent bridge spans, which were mounted on one of the shake tables. The blocks were connected with a bridge hinge retrofitted with SMA restrainers. The SMA restrainers showed promise as restraining devices to limit hinge displacement in bridges and the ability to dissipate energy. Under equivalent loading, the steel restrainers produced relative hinge displacement approximately three to four times that of the SMA restrainers. The hysteretic damping that was seen is the larger ground accelerations show the materials ability to dissipate energy with small residual strain.

1. INTRODUCTION

Bridges in seismic regions are susceptible to collapse due to excessive longitudinal movement at expansion joints and support. Subsequent to the 1971 San Fernando earthquake, California highway bridges include restrainers in their design and those built prior to 1971 have been retrofitted with the installation of cable restrainers. The University of Nevada, Reno (UNR) and others have conducted analytical and experimental studies to determine the performance of these seismic restrainers (Vlassis et al. 2000, Maragakis et al. 2004). A series of tests were conducted at the UNR large scale structures laboratory, in cooperation with Georgia Institute of Technology, to determine the effect of shape memory alloy (SMA) cable restrainers on the seismic performance of in-span hinges of a representative multiple-frame concrete box girder bridge subjected to earthquake excitation (Johnson et al. 2004). The test set-up and parameters for the SMA restrainer tests were the same as those used in

previous steel restrainer tests, also conducted at UNR, to enable comparisons between steel and SMA restrainer performance.

1.1 Shape Memory Alloy

Shape memory alloys are binary alloys, most frequently made by a combination of Nickel and Titanium (NiTi). They change their crystalline arrangement as they are cooled down or heated up, as well as in the presence of a stress field (Reference). These changes are solid-solid transformations between a crystallographically more-ordered parent phase (austenite) and a crystallographically less-ordered phase (martensite). A consequence of this transformation is the superelastic effect (the recovery of large deformation in loading-unloading cycles) and the shape memory effect (the recovery of large deformations by a combination of mechanical and thermal processes (Hodgson 2003)). Figure 1 shows a typical stress-strain relationship of SMA.

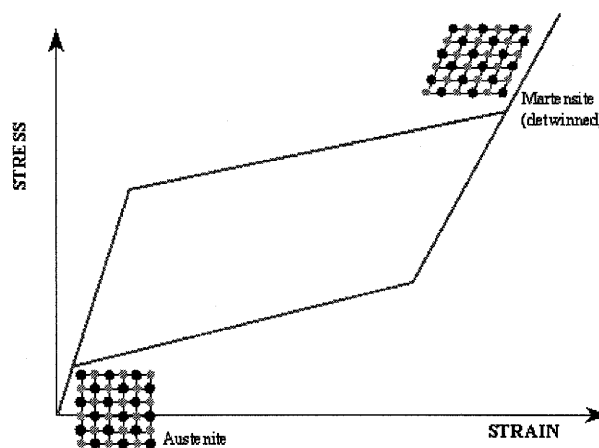


Figure 1 Stress-strain relationship of SMA.

The interest in SMAs in civil engineering applications has been growing over the last 10 years. Research groups throughout the world are finding that SMA-based devices offer advantages in terms of recentering, unlimited fatigue resistance, high durability, and low maintenance (Magonette 2001).

1.2 In-Span Hinge

Much of the bridge failure seen during the San Fernando earthquake of 1971 was a result of excessive longitudinal displacement and un-seating at thermal expansion joints or in-span hinges (Figure 2). Bridge collapse, such as that seen at the Gavin Canyon Bridge (Figure 3), initiated the use



Figure 2 In-span hinge of multi-frame bridge



Figure 3 Bridge collapse at in-span hinge

of seismic bridge restrainers in California. The use of bridge restrainers is growing throughout the United States as a seismic design aid (Saiidi et al. 1993). The two box girder reinforced concrete cells representing adjacent segments of a multi-span bridge used in the SMA restrainer tests is shown in Figure 4.

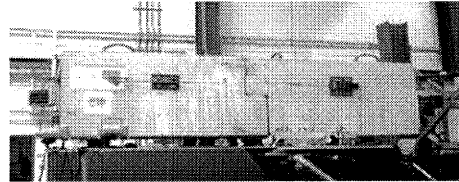


Figure 4 Representative in-span hinge used in SMA cable restrainer shake table tests.

2. TEST SPECIMEN AND EXPERIMENTAL PROCESS

The test specimen, shown in Figure 4 and Figure 5, was designed during previous UNR steel cable restrainer experiments (Vlassis et al. 2000, Maragakis et al. 2004). Dimensions of the specimen were based on superstructure dimensions of representative CALTRANS bridges. The box girder cells used typify the end part of the frames at expansion joints. Block A, shown as the right block in Figure 4 and Figure 5., is the lighter of the concrete cells, with a mass of 0.787 kg, while Block B, the left block in Figure 4, with additional lead added (Figure 6), is the heavier cell with a mass of 1.09 kg.

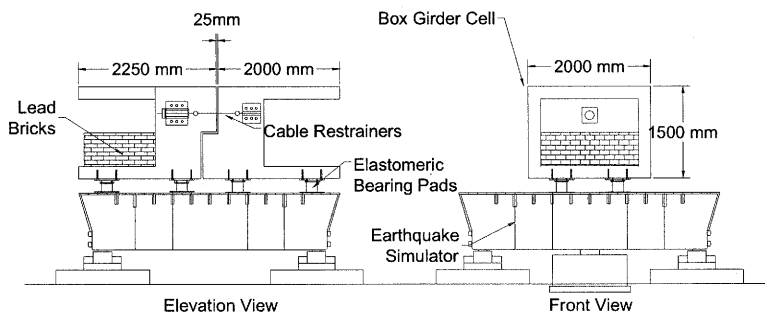


Figure 5 Shake table test set-up

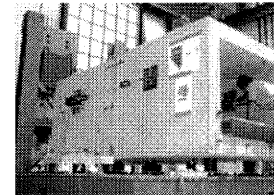


Figure 6 Additional lead in block.



Figure 7 Elastomeric bearing pad.

Elastomeric bearing pads, shown in Figure 7, simulating the substructure stiffness, were attached between the bottom of the box girder cells and the shake table, seating the lighter of the frames over the stiffer pads, with a collective stiffness of 1303 kN/m and the heavier of the frames (the cell supplemented with lead bricks) over the less stiff pads, with a collective stiffness of 683 kN/m. This resulted in a period ratio between blocks of 0.6.

The SMA restrainers are shown in Figure 8. Two sizes of SMA cable restrainers were used in the study. The smaller of the cable restrainers consisted of an 84-wire strand, encased in latex, with a total cross-sectional area of 22.6 mm². The larger of the SMA restrainers consisted of 130 strand cables with a cross-sectional area of 34.8 mm. The SMA restrainers were attached to the frames using steel mountings with a strength of 248 MPa (Figure 9). The wires of the looped end of the SMA cables were spread over a 19 mm diameter steel pin that was part of a yoke system that was welded to one side of

the plates. A piece of leather was placed between the steel pin and cable ends to act as a stress reliever and prevent cutting action on the wires that could lead to early failure. The larger of the plates held the load cell to detect force in the restrainers.

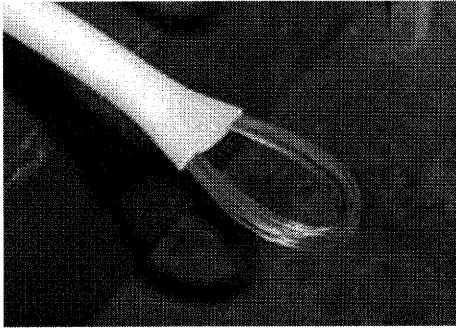


Figure 8 Close-up of SMA Cable Restrainer.

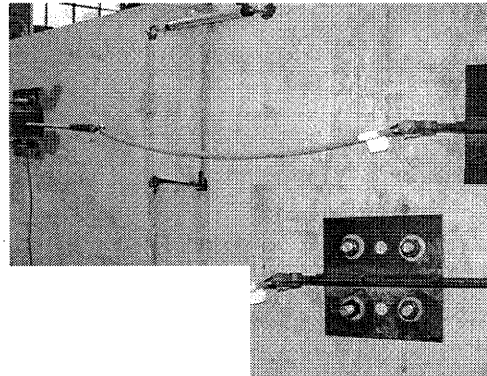


Figure 9 Attachment System

3. PARAMETERS OF STUDY

The parameters of study used in these experiments are the same as those used in comparable steel restrainer studies (Vlassis et al. 2000, Maragakis et al. 2004). The worst-case scenario from the previous UNR experimental studies in which the steel restrainers either had significant displacements or failed also established the parameters of study used in the SMA restrainer experiments. They include:

(a) A frame period ratio of 0.6 between the two adjacent bridge frames was determined to result in large out-of-phase motions. This ratio between the structural periods is taken as the period of the stiffer frame (the frame producing less movement during dynamic motion) over the period of the more flexible frame (the adjacent frame producing more movement).

(b) Restrainer stiffness is another important parameter. Each set consists of steel cable restrainers and “equivalent” SMA cable restrainers that have the same stiffness as the steel restrainers. In the first set each cable system has a stiffness equal to 0.42 kN/mm and in the second, each system has stiffness equal to 0.7 kN/mm. The stiffness of the restrainers was determined based on geometric properties (length and cross-sectional area), material properties (modulus of elasticity), and number of cables used. The 6% strain that was used for the basis of the design stiffness of the restrainers was also used in the calculation of the chord modulus.

(c) Restrainer slack, the amount of displacement necessary to stretch the cables so they start providing tensile forces, was another important parameter during the SMA restrainer shake table tests. Two different values of restrainer slack, 12.7 mm (1/2 in) and 0 mm (0 in) were used. As in the earlier steel restrainer tests, zero slack was used for the restrainer with a stiffness of 0.42 kN/mm, while a slack of 12.7 mm was used for the stiffer (0.7 kN/mm) SMA cables. These combinations of slack and stiffness produced the maximum responses in the case of the steel restrainers.

(d) The earthquake input motion was a synthetic Applied Technology Council ATC32-E motion for soft soils (California Department of Transportation 2001) based on a design spectrum for CALTRANS. It is based on expected magnitude of earthquake (6.5), soil type of the site (E or soft soil), and peak ground acceleration (PGA). Past steel restrainer experiments utilizing various soil types, determined soil type E to be an important factor in producing the large out of phase motion that

resulted in frequent restrainer engagement during shake table testing. Peak ground accelerations between 0.05g and 0.25g with 0.05g increments were selected.

4. EXPERIMENTAL RESULTS

4.1 SMA Restrainers

Binary NiTi SMAs appear to possess the properties desired in seismic resistant design and retrofit of structures. These properties, which include energy dissipation, large elastic strain capacity, hysteretic damping and recentering capabilities, are evident in the tests performed in this study. The stress vs. strain relationship observed under the incrementally increasing input excitation of 0.05g, from 0.15g to 0.25g, for the 84-wire SMA cable is shown in Figure 10.

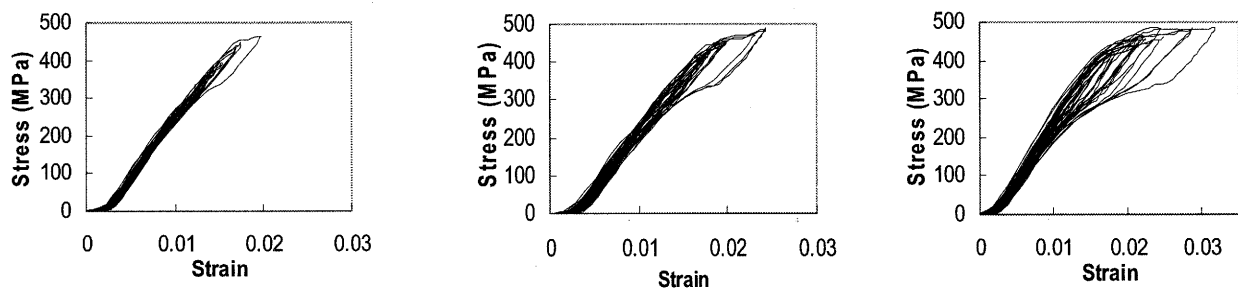


Figure 10 (Left to right) Stress vs. strain relationship for SMA restrainer with increasing

The increasing maximum earthquake acceleration of the runs, shown in Figure 10, shows an opening of the hysteretic loop that is characteristic of the superelastic effect of SMA. The ability of shape memory alloy to recover its shape after undergoing large deformations can be seen in Figure 10. The pseudo elasticity that is apparent in these graphs shows the ability of this material to go through repeated deformation cycles with minimal accumulation of residual strain. The recentering ability of the SMA is most visible at the larger accelerations, presented in the right graph of Figure 10. At the maximum PGA of 0.25g, the stress of the 84-wire cable is approximately 483 MPa and the corresponding strain is approximately 3%. Due to the large displacement of the elastomeric bearings, and the effectiveness of the SMAs in limiting the relative hinge displacement, a strain of 6% in the SMA was not achieved during these tests. The usable strain range of this material is 6-8%. Even at 3% strain, the SMA hysteresis that results from its mechanical ability to recover deformation after stress removal is clearly evident in the typical flag shape loop that is synonymous with SMA superelasticity.

4.2 84-Wire vs. 130-Wire SMA Cable

A comparison, taken during shake table tests, of the relative hinge displacement between blocks and total restrainer force for both the 84-wire and 130-wire SMA cable at a PGA of 0.25g is illustrated in Figure 11.

The initial 12.7 mm restrainer slack for the larger restrainer is seen as the point where the force in the large restrainer begins to increase. The relative hinge displacement, as viewed in Figure 11, is larger for the 130-wire cable, but subtracting the initial 12.7 mm slack gives a restrainer elongation of 32.5 mm for the 130-wire cable vs. a restrainer elongation of 37.2 mm for the smaller 84-wire cable

restrainer. At a PGA of 0.25g, the force in the 84-wire cable is 11 kN while the force in the 130-wire restrainer is almost 19 kN.

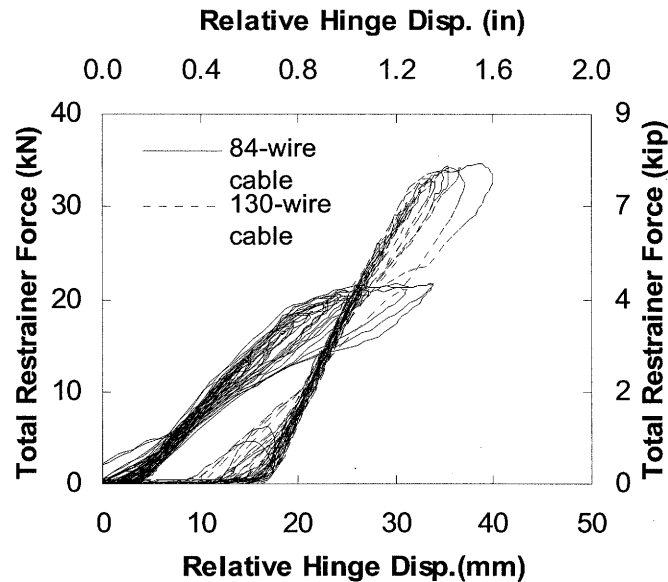


Figure 11 Force vs. displacement relationship of small and large SMA cable restrainers subjected to shake table tests at 0.25g.

4.3 SMA vs. Steel Restrainers

In order to evaluate the performance of the NiTi restrainers in relation to the past research performed on steel restrainers with comparable stiffness, the test parameters and equivalent earthquake motions were necessary. An overlay of earthquake response spectra, shown in Figure 12, of the steel and SMA tests revealed equivalency between the dynamic steel and SMA restrainer tests for a PGA of 0.15g and 0.2g.

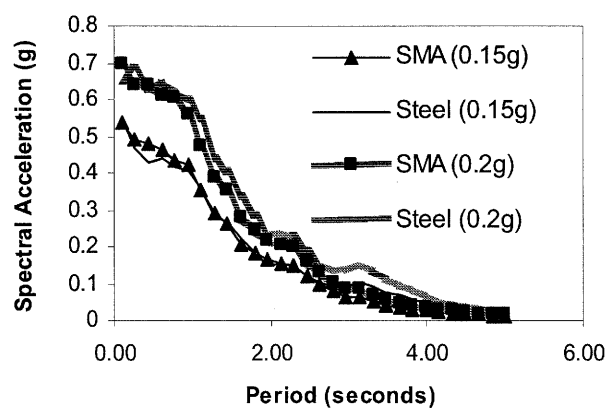


Figure 12 Equivalency of earthquake motion for steel and SMA tests

The acceleration history for Block B (soft frame) from the SMA experiment was compared to the Block B acceleration histories from previous steel restrainer tests. During earthquake tests, two

equivalent cases produced lower acceleration in the blocks with SMA restrainers compared to those being restrained by steel.

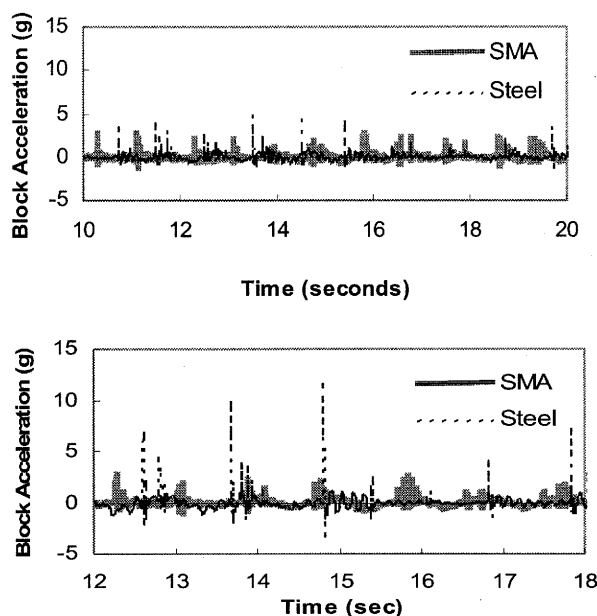


Figure 13 (Top to bottom) Block acceleration histories for equivalent SMA vs. steel restrainer, 0.15g and 0.2g.

In the upper graph of Figure 13, at a block acceleration of 0.15g, the measured acceleration for the SMA vs. steel restrainer shake table tests were 2.7g vs. 6.3g. In the lower graph of Figure 13, at a PGA of 0.2g, the acceleration in the block resulting from earthquake motion in which steel restrained the blocks was more than 3.5 times larger (11.6g vs. 3.2g) than the block acceleration produced in the system in which SMA was the restraining device.

Table 1 shows equivalent cases for the SMA restrainers and past steel restrainer tests. The first column of the table shows the run number. Case 1, 2 and 3 are SMA restrainer shake table runs that are directly equivalent to the previous steel restrainer experiments. These runs were used for comparing behavior of the SMA and steel cable restrainers. Relative displacement between the blocks was generated in output files from the data acquisition system. Increasing displacement was noted with escalating ground accelerations. Data was collected every 0.005 seconds during shake table testing for the 20-second dynamic test for the steel cable restrainer and the 38-second test for the SMA cable restrainer. The data collected during these experiments measuring maximum restrainer force and maximum relative hinge displacement for these three cases is shown in Table 2.

Figure 14 shows a graphical representation of the force-displacement relationships for case 1, 2, and 3. The restrainer force-displacement relationships shown in Figure 14 reveals fairly equivalent steel and SMA restrainer force but larger relative hinge displacement with the steel restrainers. One can observe that the maximum hinge displacement for steel in Case 1 and 2 is nearly double that of the SMA restrainers. In Case 1, the 3-cable steel restrainer has elongated 43 mm (1.7 in) while the equivalent 84-wire SMA restrainer has an elongation of 23 mm (0.91 in). The maximum hinge displacement for the larger 5-cable steel restrainer and 130-wire SMA restrainer in Case 2 is 61 mm (2.39 in) and 32mm (1.26 in) respectively. As viewed in Table 3, Case 1 and 2 are at the equivalent

earthquake motion of a PGA of 0.15g. Figure 10c reveals an extremely large relative hinge displacement in the 5-cable steel restrainer at a PGA of 0.2g. This figure shows that in Case 3, there was a restrainer failure in two of the five cables in the steel restrainer resulting in a maximum restrainer displacement more than three times larger in the steel vs. the SMA restrainer. The displacement of the steel cable restrainer in Case 3 is 120 mm (4.73 in) while that of the SMA cable restrainer is 39 mm (1.53 in). Figure 10c also reveals that while the steel restrainer has failed, the SMA restrainer is just reaching yield beyond which the SMA can undergo large elastic deformation with reversibility.

TABLE 1: Peak Displacements and Maximum Forces for East-Side Restrainer

Run	PGA	SMA Cable size	Slack		Peak Disp		Cable Strain (%)	Max Force		Max Cable Stress	
			(mm)	(in)	(mm)	(in)		(kN)	(kip)	(MPa)	(ksi)
84-1	0.05g	84-wire	0	0	9.5	0.37	0.81	4.6	1.04	206.4	29.9
84-2	0.10g	84-wire	0	0	15.8	0.62	1.35	8.4	1.89	373.1	54.1
84-3 (case1)	0.15g	84-wire	0	0	23.0	0.91	1.97	10.5	2.35	464.9	67.4
84-4	0.20g	84-wire	0	0	28.4	1.12	2.43	11.1	2.49	492.1	71.4
84-5	0.25g	84-wire	0	0	37.2	1.46	3.18	11.0	2.47	487.4	70.7
130-1	0.05g	130-wire	12.7	0.5	21.2	0.83	0.72	4.7	1.05	134.4	19.5
130-2	0.10g	130-wire	12.7	0.5	28.7	1.13	1.37	12.0	2.70	344.6	50.0
130-3 (case 2)	0.15g	130-wire	12.7	0.5	32.1	1.26	1.66	17.5	3.94	503.1	73.0
130-4 (case 3)	0.20g	130-wire	12.7	0.5	38.9	1.53	2.25	18.9	4.24	541.8	78.6
130-5	0.25g	130-wire	12.7	0.5	45.2	1.78	2.78	18.8	4.23	539.6	78.3

TABLE 4: Max Force and Max Displacement for Cases 1, 2 and 3

	Total Force		MaxDisp	
	(kN)	(kip)	(mm)	(in)
Case 1				
Steel	27	5.98	43	1.7
SMA	21	4.62	23	0.91
Case 2				
Steel	30	6.73	61	2.39
SMA	31	7.00	32	1.26
Case 3				
Steel	36	8.14	120	4.73
SMA	35	7.96	39	1.53

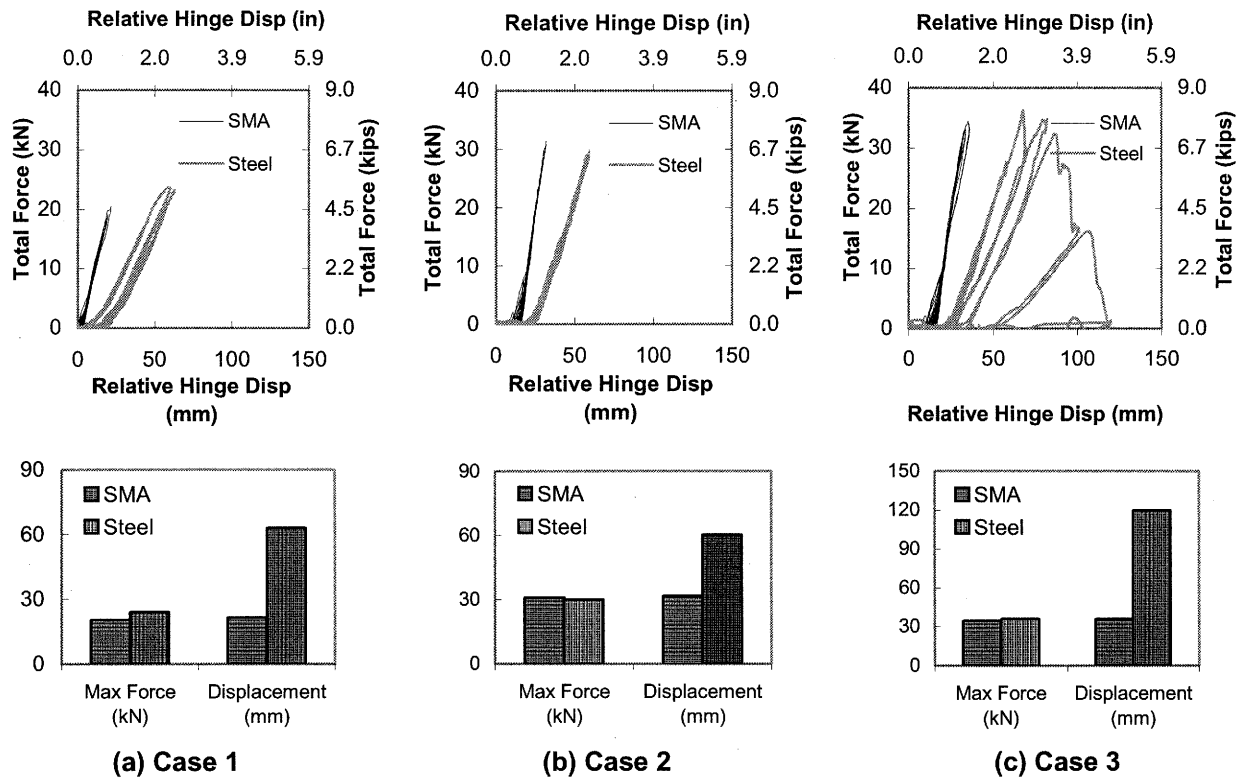


Figure 14 Total restrainer force and relative hinge displacement for case 1(a), case 2(b), and case 3(c).

5. SUMMARY

The objective of this research was to evaluate the seismic performance of shape memory alloy (SMA) as a retrofit or construction material for bridge restrainers and to compare their performance to the seismic performance of steel restrainers. The design of the SMA restrainers was based on data collected from steel restrainer experiments in an identical test set-up that was performed in the large-scale structures laboratory at the University of Nevada, Reno. The tests were performed at incremental increases of ground motion on a shake table. The period ratio of 0.6, which resulted in an out-of-phase motion between the simulated single width box girder cells remained constant throughout the experiments. The tests utilized two identical SMA restrainers, one on either side of the specimen. A 3% strain was realized in the cables under dynamic loading and the SMA cables displayed the hysteretic damping and energy dissipation associated with superelastic shape memory alloys.

6. CONCLUSIONS

1. The SMA restrainers were superior to the steel restrainers in limiting relative hinge displacements. This would reduce the possibility of unseating of frames at the in-span hinge of bridges during seismic activity.
2. In an identical earthquake motion and with restrainer equivalency, the steel restrainer failed while the SMA restrainers just reached their yield level.

3. SMA restrainers produce lower block accelerations during earthquake excitation compared to experiments with equivalent steel restrainers. The energy associated with the phase transformation of SMA from the austenite to martensite phase results in lower energy transfer to the structure.
4. The forces in the SMA and steel restrainers were comparable. This demonstrates that the capacity of SMA restrainers is similar to that of traditional steel bridge restrainers.
5. The SMA cable restrainers had minimal residual strain after repeated cycling. SMA can undergo many cycles of loading with little degradation of properties. This would result in less restrainer replacement than traditional steel restrainers.

Acknowledgments

This study was funded by the California Department of Transportation. The financial support and the technical input from Drs. Saad El-Azazy and Allaoua Kartoum are gratefully acknowledged. Special thanks are due to Sherif Elfass of the Civil Engineering Department for his help and support.

References

- DesRoches, R. and Fenves, G. L. (2000), "Design of Seismic Cable Hinge Restrainers for Bridges," *J. Struct. Eng.*, 126(4), 500-509.
- DesRoches, R. and Delemont, M., (2001), "Seismic Retrofit of Multi-Span Simply Supported Bridges Using Shape Memory Alloy," *Engineering Structures*, Vol. 24, pp. 325-332.
- DesRoches, R. and Smith, B. (2002), "Shape Memory Alloys in Seismic and Retrofit: A Critical Assessment of the Potential Limitations," *Journal of Earthquake Engineering, In Press*, August 2002.
- Hodgson, D. (2003), Personal Communication, Probable Causes of SMA Results.
- Johnson, R., Maragakis, M., Saiidi, M., DesRoches, R., Barbero, L., (2004), "Experimental Evaluation of Seismic Performance of SMA Bridge Restrainers," *Rep. CCEER 04-2*, Center for Civil Engineering Earthquake Research, University of Nevada, Reno, Nev.
- Magonette, G., (2001), "Shape Memory Alloys in Civil Engineering Applications," *Advances in Modeling and Applications*, Ed. Auricchio, R., Faravelli, L., Magonette, G., Torra, V., CIMNI, Barcelona, Spain, pp 269-403.
- Saiidi, M., et al (1993), "Response of Bridge Hinge Restrainers During Earthquakes: Field Performance, Analysis, and Design," *Rep. CCEER 93-6*, Center for Civil Engineering Earthquake Research, University of Nevada, Reno, Nev.
- Maragakis, E. M., Saiidi, M. S., Sanchez-Camargo, F., Elfass, S., (2004), "Seismic Performance of Bridge Restrainers at In-Span Hinges," *Rep. CCEER 04-4*, Center for Civil Engineering Earthquake Research, University of Nevada, Reno, Nev.
- Vlassis, A. G., Maragakis, E. M., and Saiidi, M. S. (2000), "Experimental Evaluation of Seismic Performance of Bridge Restrainers," *Technical Rep. MCEER-00-00123*, Multidisciplinary Center for Earthquake Engineering Research, Buffalo, N.Y.

SEISMIC PERFORMANCE OF UNBONDED COLUMNS AND ISOLATOR BUILT-IN COLUMNS BASED ON CYCLIC LOADING TESTS

K. Kawashima¹⁾ and G. Watanabe²⁾

1) Professor, Department of Civil Engineering, Tokyo Institute of Technology, Japan

2) Research Associate, Department of Civil Engineering, Tokyo Institute of Technology, Japan

kawasima@cv.titech.ac.jp, gappo@cv.titech.ac.jp

Abstract: Enhancement of ductility capacity of RC bridge columns by unbonding main bars at the plastic hinge region is clarified based on a cyclic loading test. It is found that unbonding is effective to enhance the seismic performance. However it is required to use ductile reinforcing bars for this purpose. Effect of setting isolators at the plastic hinge region of RC bridge columns for the enhancement of ductility capacity is also clarified based on a cyclic loading test. This paper presents the test results as well as analytical simulation.

1. INTRODUCTION

Enhancement of the ductility capacity of reinforced concrete piers is essential to improve the seismic performance of bridges under extreme ground excitation. The importance of lateral confinement by ties has been studied by many researchers (Pristley et al 1996). It is known that residual drift is likely to be induced in single columns after an earthquake (MacRae and Kawashima 1997, Kawashima et al 1998), and that it significantly affects the reparability of the columns.

Various attempts have been conducted to enhance the ductility capacity and to reduce residual drift of reinforced concrete columns. Interlocking spiral is effective on enhancing the seismic performance (Tanaka and Park 1993, Fujikura and Kawashima 2000). The interlocking spiral is being implemented to columns with sections over 6 m in Japan (Shito et al 2002). Prestressed concrete members exhibit stable seismic performance under a combined action of shear and flexure. Residual drifts after an extreme earthquake are also mitigated in the prestressed concrete columns (Ikeda 1998). Unbonding longitudinal bars at the plastic hinge is effective to enhance the ductility capacity (Takiguchi et al 1976). The unbonding was applied to bridge columns (Kawashima et al 2001). Isolator built-in column is also effective to enhance the ductility capacity and to mitigate the residual drift (Kawashima and Nagai 2002, Yamagishi and Kawashima 2004).

This paper presents the effect of the unbonding of longitudinal bars and the isolator built-in for the enhancement of ductility capacity of RC bridge columns.

2. UNBONDING OF LONGITUDINAL BARS AT THE PLASTIC HINGE

In single RC bridge columns damage of longitudinal bars progresses at the plastic hinge under an extreme earthquake excitation. The bond between longitudinal bars and the concrete results in concentration of damage at a specific localized region. One of the measures to mitigate such concentration of damage at the plastic hinge is to unbond the longitudinal bars from the concrete (Takiguchi, Okada and Sakai 1976). By appropriately unbonding the longitudinal bars at an interval with length L_{ub} as shown in Figure 1, the deterioration of longitudinal bars is mitigated resulted from reduced strain at the interval L_{ub} . The unbonding of longitudinal

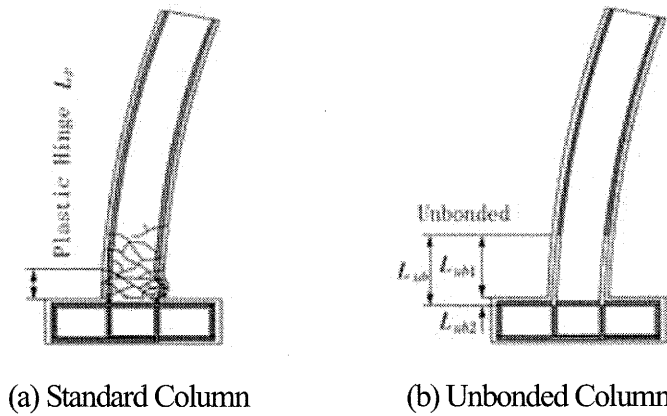


Figure 1 Unbonding of Longitudinal Bars

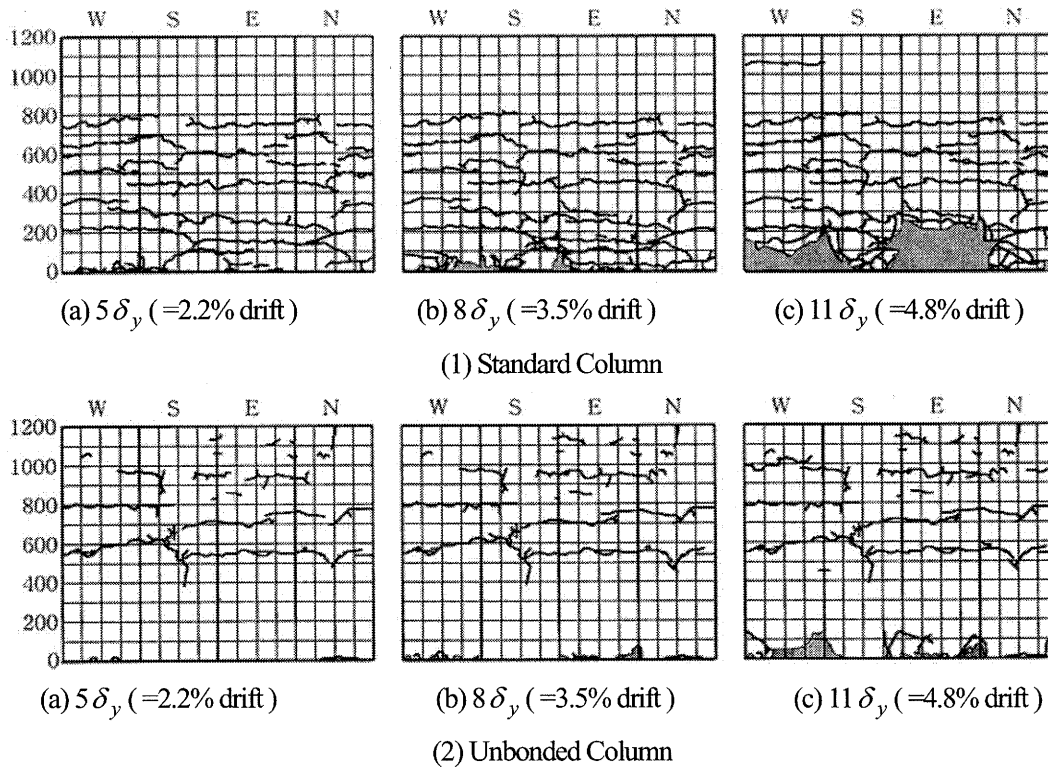


Figure 2 Progress of Damage

bars may be achieved by wrapping them by plastic tubes. Protection may be required for corrosion of the unbonded longitudinal bars.

Figure 2 shows the effect of unbonding the longitudinal bars on a 1.45 m tall single column with a square section of a width D equal to 400 mm (Kawashima et al 2001). Although several tests were conducted, only two cases are presented here. The concrete strength was 24 MPa, the longitudinal reinforcement ratio was 0.95%, and the volumetric tie reinforcement ratio was 0.77%. The longitudinal bars are unbonded at an interval of the column width D . In the standard column, the covering concrete started to significantly spall off at $8\delta_y$, in which δ_y is the yield displacement of the standard column. Since δ_y is equal to 6 mm, 1% drift corresponds to $2.3\delta_y$. The column was loaded 3 times at each loading displacement of $\delta_y, 2\delta_y, 3\delta_y, \dots$, until failure. The same loading hysteresis was used for both the standard and the unbonded columns.

The concrete failed within about 200 mm from the bottom after $11\delta_y$ ($\approx 4.8\%$ drift) in the standard column. In comparison, failure of concrete was much less in the unbonded column than the standard column. The

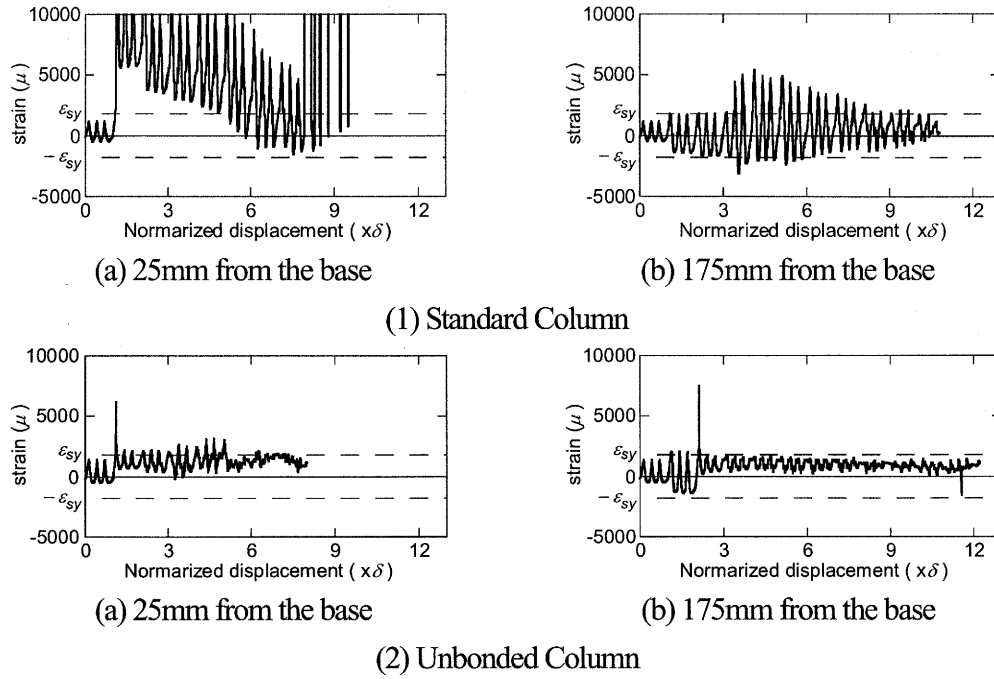


Figure 3 Strain on a Longitudinal Bar

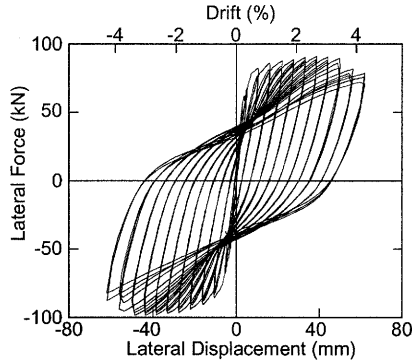
covering concrete failed no higher than 120 mm from the bottom even after $13\delta_y$ ($=5.7\%$ drift). Figure 3 compares the strains on a longitudinal bar at 25 mm and 175 mm from the bottom of the column. The strain at 25 mm builds up over the yield strain at the first load excursion of $2\delta_y$ in the standard column. On the other hand, strain on a longitudinal bar which was unbonded at an interval of D was much smaller than the strain on a longitudinal bar in the standard column. The strains were similar, although not the same, between 25 mm and 175 mm from the bottom in the unbonded column. The strains on the longitudinal bars exceeded $6,000\mu$ at 25 mm and 175 mm from the bottom at the first excursion of $2\delta_y$ and $3\delta_y$ loadings, respectively.

An important feature of the unbonded column is that it responds in a rocking mode. Since the longitudinal bars are unbonded at an interval of L_{ub} , the deformation of longitudinal bars in tension results in the dominant rocking mode of the column. As a result of the small flexural deformation of the column, the flexural failure at the plastic hinge of the column is limited.

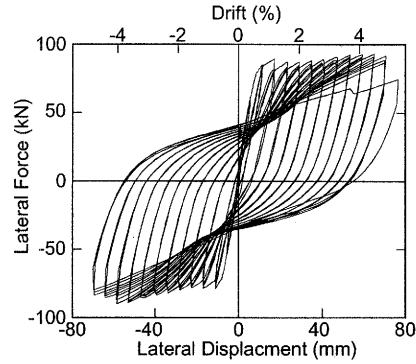
Figure 4 compares the lateral force vs. lateral displacement hysteresis between the standard and unbonded columns. The restoring force of the standard column starts to deteriorate at $9\delta_y$ ($=3.9\%$ drift), while the restoring force is stable until $11\delta_y$ ($=4.8\%$ drift) in the unbonded column.

As a result of the deformation of the unbonded longitudinal bars in the plastic hinge, the initial lateral stiffness is slightly smaller in the unbonded column than the standard column. Figure 5 compares the equivalent lateral stiffness and the accumulated energy dissipation between the unbonded and standard columns. The equivalent lateral stiffness is defined here as the secant stiffness between the maximum and minimum displacements in a hysteresis loop at each loading displacement. Although the equivalent lateral stiffness is slightly smaller in the unbonded column than the standard column at the lateral displacement smaller than 1% drift, the difference of equivalent lateral stiffness between the two columns decreases as the lateral displacement increases. This resulted from larger deterioration in the standard column. The difference of the accumulated energy dissipation between the two columns is negligible.

Based on the studies, it is considered that the unbonding is an effective means to increase the ductility capacity of columns by properly choosing the unbond length L_{ub} .

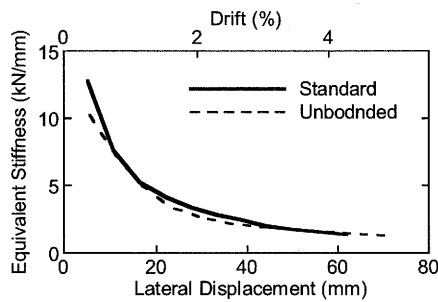


(1) Standard Column

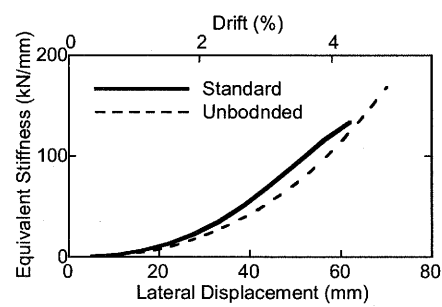


(2) Unbonded Column

Figure 4 Lateral Force vs. Lateral Displacement Hystereses



(1) Equivalent Lateral Stiffness



(b) Accumulated Energy Dissipation

Figure 5 Equivalent Lateral Stiffness and Energy Dissipation

3. ISOLATOR BUILT-IN COLUMNS

(1) Isolator Built-in Column

Since the hysteretic behavior of a reinforced concrete column occurs only at the plastic hinge, it is interesting to replace the concrete in the plastic hinge by an appropriate material that provides enough deformation and energy dissipation so that the flexural deformation in the rest of a column is mitigated. The material has to be appropriately softer than the reinforced concrete in order to reduce the flexural deformation of the column. The material must be stable under repeated seismic loading with large strains, and durable for long term use. It is preferable if energy dissipation is available associated with the deformation of the material.

One material studied is the high damping rubber that is used for standard high damping rubber bearings for seismic isolation. If one sets a high damping laminated rubber unit at the bottom of a column, the column deforms as shown in Figure 6 under a lateral seismic force. The longitudinal bars are continuous through the laminated rubber unit. Prestressed tendons are effective to prevent sudden deterioration of the restoring force and to mitigate residual drift. Shear-keys are required to prevent an excessive lateral displacement of the column relative to the footing when the laminated rubber unit is thick. Since such a column is virtually equivalent to a built-in high damping rubber isolator, it is called here an *isolator built-in column* (Kawashima and Nagai 2002).

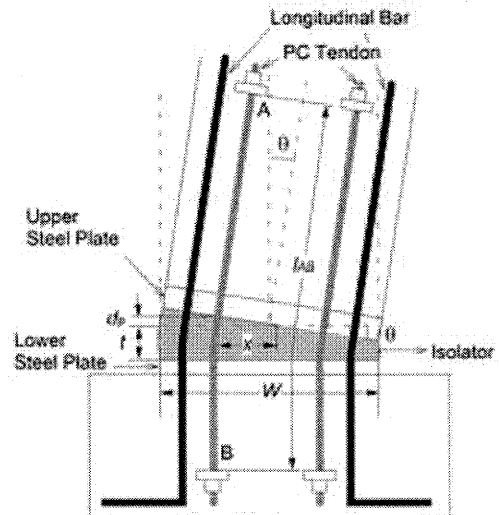


Figure 6 Isolator Built-in Column

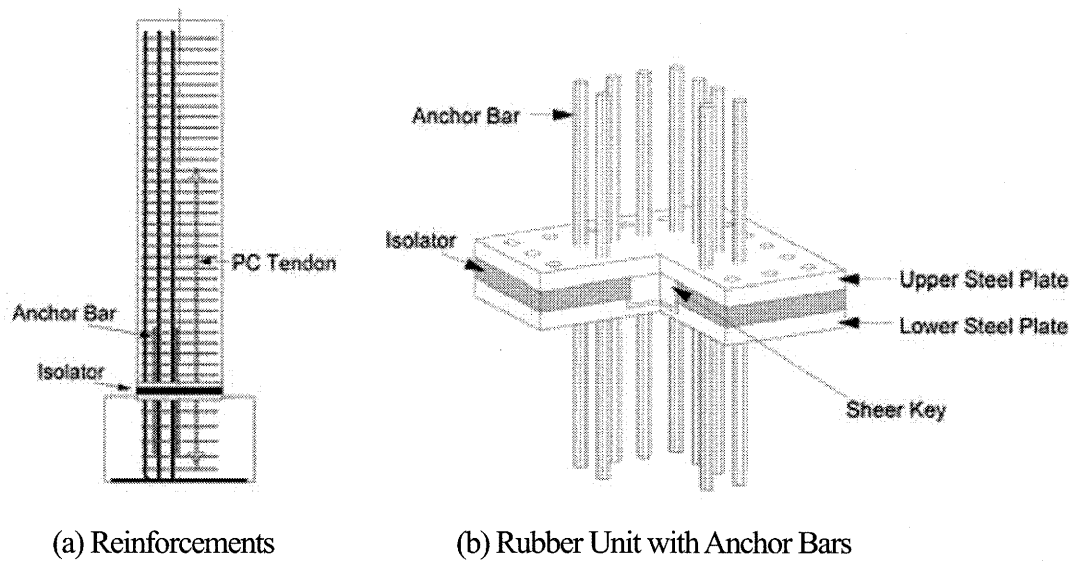


Figure 7 Model Columns

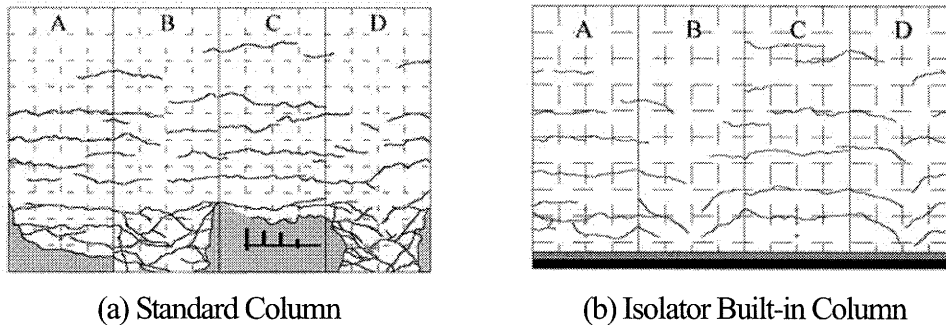


Figure 8 Failure of Columns after 4% Drift (Loaded in AC Direction)

(2) Loading Tests

A series of seismic loading tests was conducted on 11 columns to verify the performance of the isolator built-in columns. Model columns were constructed 1350mm tall (effective height) with a 400mm by 400mm rectangular section as shown in Figure 7. They were designed so that the hysteresees are stable until 4% drift. As a consequence, 30 mm and 60 mm thick damping rubber units were used with an initial shear modulus of 1.2 MPa. The longitudinal reinforcement ratio was 1.58%, and the volumetric tie reinforcement ratio was 0.79%. A shear-key was provided at the center, and four prestressed tendons were provided at the four corners. Four PC tendons with a diameter of 9.2 mm were provided at the corners. Prestress of 20 kN was introduced in each tendon, so that stress of concrete induced by the prestressing force was 0.5MPa. The columns was laterally loaded under displacement control subjected to a constant axial force of 240 KN.

Figure 8 compares the failure of the isolator built-in column and the standard column after 4% drift loadings. Extensive failure of the concrete occurs until 4% drift at the compression fiber in the standard column. The longitudinal bars start to rupture at 5.5% drift, which results in the significant deterioration of restoring force. On the other hand, the failure of concrete is much limited in the isolator built-in column until 4% drift. However the longitudinal bars start to rupture in the rubber unit at 4.5% drift. The use of ductile steel is required to mitigate the rupture of the longitudinal bars.

Figure 9 compares the lateral force vs. lateral displacement relations of the two columns. A remarkable change of the shape of the hysteresis loops is seen. The lateral force is virtually the same at the post-yield zone in the standard column, while it increases as the lateral displacement increases in the isolator built-in column. The extensive deterioration of the restoring force at 4.5% drift results from the rupture of longitudinal bars in the isolator built-in column. An important difference of the isolator built-in column is the smaller initial stiffness, as

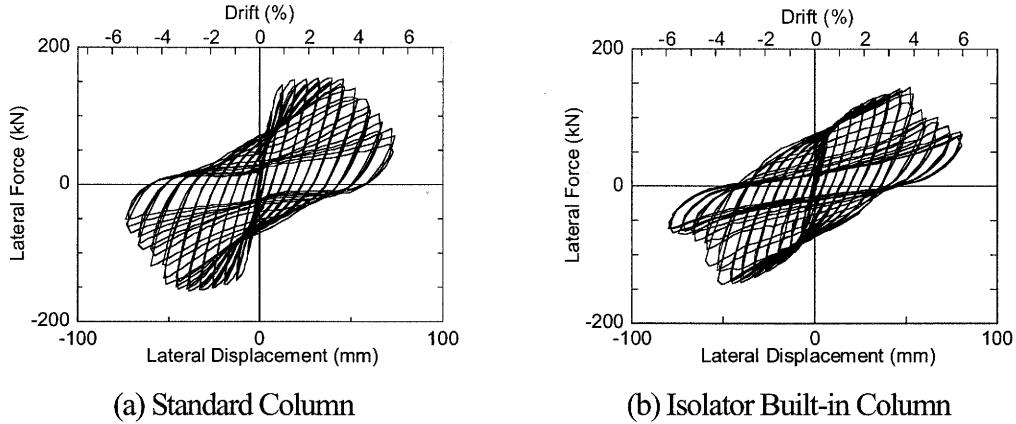


Figure 9 Lateral Force vs. Lateral Displacement Hystereses

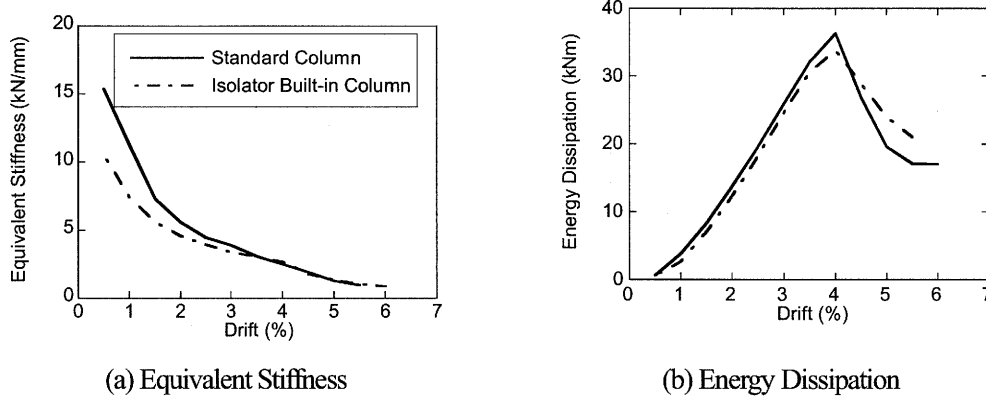


Figure 10 Effect of Isolator on the Equivalent Stiffness and Energy Dissipation

shown in Figure 10 (a), due to the soft deformation of the rubber unit. However, since the stiffness of the standard column deteriorates due to progress of failure, the difference of lateral stiffness between two columns becomes small over 2.5% drift. The energy dissipation per load reversal is nearly the same between the isolator built-in column and the standard column as shown in Figure 10 (b).

(3) Analytical Correlation

The columns were idealized as shown in Figure 11 to correlate the experimental results. The isolator and the column inside the plastic hinge were idealized by fiber elements. A stress and strain relation of concrete including the lateral confinement effect was used (Hoshikuma et al 1997). The column outside the plastic hinge was idealized by a linear beam element with the yield stiffness. Longitudinal rebars were idealized by beam elements with hysteresis behavior (Menegotto and Pint 1973). Unbonding of rebars inside the isolator and PC tendons was included in analysis using idealizations as shown in Figure 11 (2) and (3), respectively.

Figures 12 and 13 show the correlation of hysteresis of the lateral force vs. lateral displacement relation on the standard and isolator built-in columns, respectively. Correlation on the hysteresis of the first excursion at specific loadings are also shown for comparison. It is seen in Figure 12 that the computed hysteresis are virtually the same with the experimental results until deterioration of the restoring force due to rupture of main bars becomes predominant. The computed hysteresis in Figure 13 are also very close to the experimental results, although the computed hysteresis are slightly slender than the experimental results at 3.5% drift.

Figure 14 shows the computed strains of the core concrete and main bars at the extreme fiber and the computed strain of a PC tendon in the isolator built-in column. It is seen that the computed concrete stress is still at the peak stress even at 6% drift. PC tendon remains in elastic range. However main bars are subjected to repeated loadings over 0.7% tension and 1.5% compression. It is noted that compression is larger than tension because isolator is built-in.

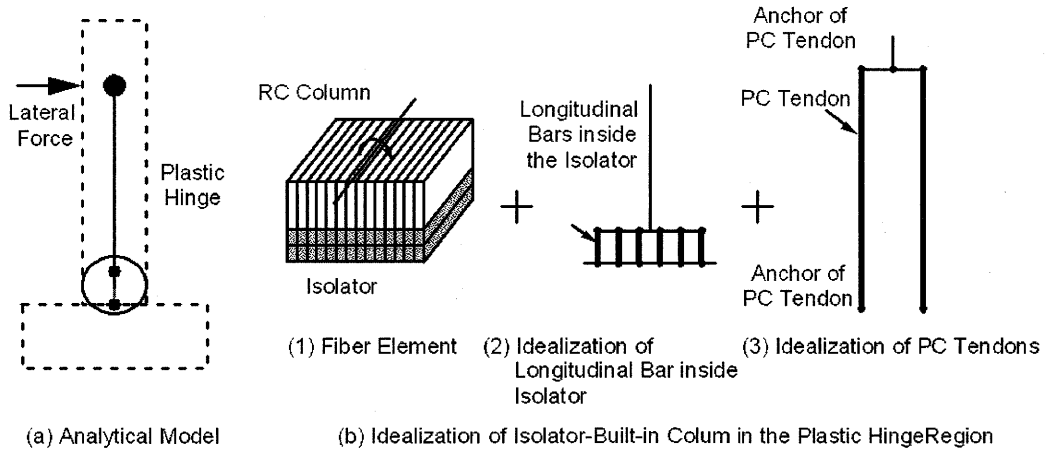


Figure 11 Idealization of Isolator-Built-in Columns

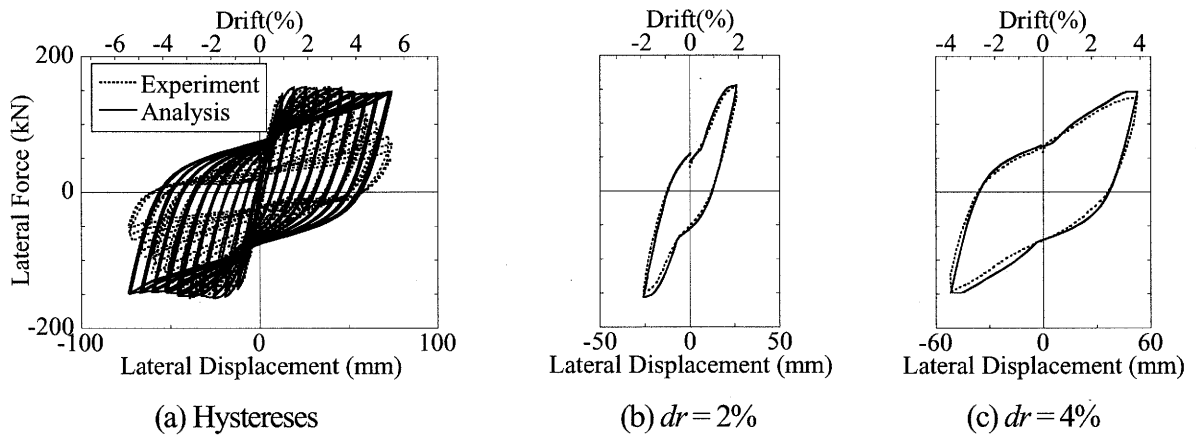


Figure 12 Correlation for the Standard Column

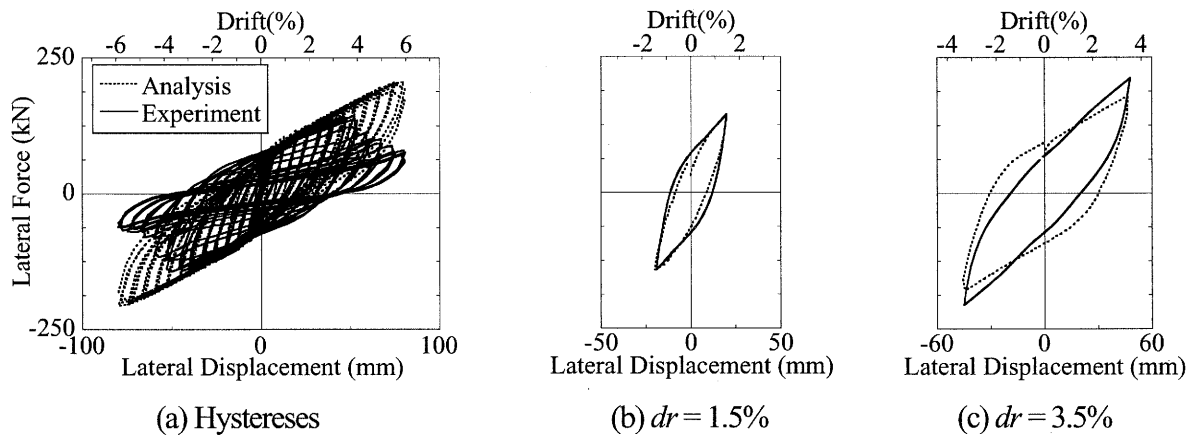


Figure 13 Correlation for the Isolator-Built-in Column

4. CONCLUSIONS

Effectiveness of unbonding main bars at the plastic hinge and the isolator built-in was clarified based on cyclic loading tests and correlation Analysis. Based on the results presented herein, the following conclusions may be deduced:

- 1) Unbonding of main bars at the plastic hinge is effective to enhance the ductility capacity of RC single

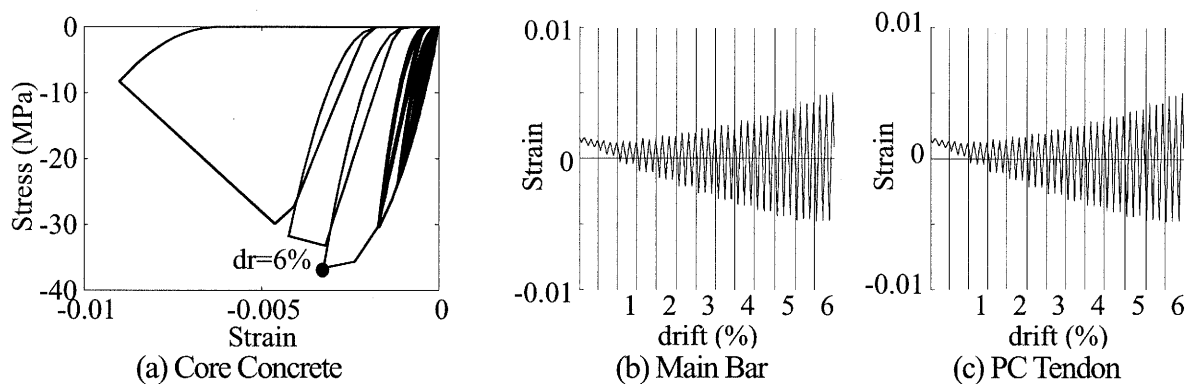


Figure14 Computed Strains of Core Concrete, Main Bar and PC Tendon

columns because the unbonding reduces the strain concentration of main bars and thus mitigates the deterioration of bars. Although the main bars were unbonded at an interval equivalent to the column width in this study, an appropriate unbond length needs further clarification, in particular at full size columns.

2) Isolator built-in columns are also effective to enhance the ductility capacity of single columns. However ductile bars have to be used to prevent rupture inside the isolator because strain of bars here is extremely high.

Acknowledgements

The authors thank Professor Katsuki Takiguchi, Tokyo Institute of Technology for suggesting the effectiveness of unbonding of main bars.

References:

- Fujikura, S., Kawashima, K., Shoji, G., Jiandong, Z. and Takemura, H. (2000), "Effect of the Interlocking Ties and Cross Ties on the Dynamic Strength and Ductility of Rectangular RC Bridge Piers," *Structural and Earthquake Engineering, Proc. JSCE*, No. 640/I-50, 71-88, 2000
- Hoshikuma, J., Kawashima, K., Nagaya, K. and Taylor, A. W. (1997), "Stress-Strain Model for Confined Reinforced Concrete in Bridge Piers," *Journal of Structural Engineering, ASCE*, 123 (5), 624-633.
- Ikedo, S. (1998), "Seismic Behavior of RC Columns and Improvement by Vertical Prestressing," *Proc. 13th FIP Congress on Challenges for Concrete in the Next Millennium*, Vol. 2, 879-884.
- Kawashima, K., MacRae, G.A., Hoshikuma, J. and Nagaya, K. (1998), "Residual Displacement Response Spectrum," *Journal of Structural Engineering, ASCE*, 124(5), 523-530.
- Kawashima, K., Hosoi, K., Shoji, G. and Watanabe, G. (2001), "Effect of Unbonding of Main Reinforcements at Plastic Hinge Region for Enhancing Ductility of RC Bridge columns," *Proc. Structural and Earthquake Engineering, JSCE*, 689/I-57, 45-64
- Kawashima, K. and Nagai, M. (2002), "Development of RC Pier with Rubber Layer in the Plastic Hinge Region," *Proc. Structural and Earthquake Engineering, JSCE*, 703/I-59, 113-128.
- MacRae, G.A. and Kawashima, K. (1997), "Post-Earthquake Residual Displacement of Bilinear Oscillators," *Earthquake engineering and Structural Dynamics*, 26, 701-716.
- Menegotto, M. and Pinto, P. E. (1973) "Method of Analysis for Cyclically Loaded RC Plane Frames including Changes in Geometry and No=Elastic Behavior of Elements under Combined Normal Force and Bending," *Proc. IABSE Symposium on Resistance and Ultimate Deformability of Structures Acted by Well Defined Repeated Load*, 15-22.
- Priestley, N.M.J., Seible, F. and Calvi, G.M. (1996), "Seismic Design and Retrofit of Bridges," John Wiley & Sons.
- Shito, K., Igase, Y., Mizugami, Y., Ohasi, G., Miyagi, T. and Kuroiwa, T. (2002), "Seismic Performance of Bridge Columns with Interlocking Spiral/Hoops, First fib Congress, Osaka, Japan
- Takiguchi, K., Okada, K. and Sakai, M. (1976), "Ductility Capacity of Bonded and Unbonded RC Members, *Proc. Architectural Institute of Japan*, 249, 1-11.
- Tanaka, H. and Park, R. (1993), "Seismic Design and Behavior of RC Columns with Interlocking Spirals," *ACI Structural Journal*, pp. 192-203.
- Yamagishi M. and Kawashima, K. (2004), "Development of a Rubber Layer Built-in RC Columns," *Proc. Structural and Earthquake Engineering, JSCE*, 752/I-66, 43-62

EFFECT OF NEAR FIELD GROUND MOTIONS ON FORCE REDUCTION FACTOR AND RESIDUAL DISPLACEMENT OF STRUCTURES

G. Watanabe¹⁾, K. Kijima²⁾ and K. Kawashima³⁾

1) Research Associate, Department of Civil Engineering, Tokyo Institute of Technology, Japan

2) Department of Civil Engineering, Tokyo Institute of Technology, Japan

*3) Professor, Department of Civil Engineering, Tokyo Institute of Technology, Japan
gappo@cv.titech.ac.jp, kijimax@cv.titech.ac.jp, kawasima@cv.titech.ac.jp*

Abstract: In the equivalent static seismic design, the inelastic force demand is determined in terms of the force reduction factor. Near-field ground motions have impulsive accelerations with large amplitudes. They are damaging to structures as was evident in past earthquakes. However, the effect of near field ground motions on the force reduction factor and the residual displacement has not yet been clarified. This paper presents an analysis on the dependency of the force reduction factor and the residual displacement response spectra on ground motion characteristics.

1. INTRODUCTION

After 1994 Northridge and 1995 Kobe earthquake, as the number of records of near-fault ground motions increases, more attention has been paid to mathematical representations of near-fault ground motions (Inoue and Miyatake 1998, Mavroeidis and Papageorgiou 2003, Hisada et al 2003). Near-fault ground motions have impulsive accelerations with long natural periods and large amplitudes. They are extensively damaging to structures as was evident in past earthquakes.

In the ductility design, the inelastic force demand is determined by force reduction factor (R factor). Since careful evaluations of force reduction factors are required, force reduction factors have been empirically determined based on the past earthquakes which were composed of far-field ground motions. The effect of near-fault ground motions on the force reduction factors, however, has not yet been clarified (Newmark et al 1973, Nassar and Krawinkler 1991, Miranda and Bertero 1994, Watanabe and Kawashima 2001).

Under strong excitations, large force reduction factors could result in the residual displacements of structures as well as plastic deformations. The large residual displacements passively cause the severe obstruction to the retrofit of the bridges after earthquakes. The residual displacement was included in the seismic design of Japanese bridges as a design requirement after 1995 Kobe earthquake (MacRae and Kawashima 1997, Kawashima et al 1998).

This paper presents an analysis on the dependency of the force reduction factor and the residual displacement response spectra on ground motion characteristics.

2. FORCE REDUCTION FACTOR AND RESIDUAL DISPLACEMENT

2.1 Definition of Force Reduction Factors

If one idealizes a structure in terms of a single-degree-of-freedom (SDOF) oscillator with an

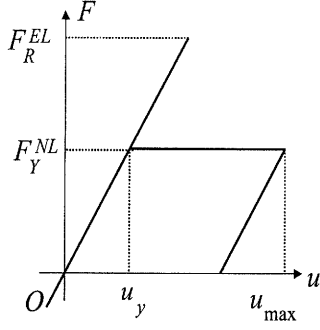


Figure 1 Definition of R factor

elasto-plastic Takeda stiffness degrading hysteretic behavior as shown in Figure 1 (Takeda et al 1970), the force reduction factor R_μ may be defined as

$$R_\mu(T, \mu_T, \xi_{EL}, \xi_{NL}) = \frac{F_R^{EL}(T, \xi_{EL})}{F_Y^{NL}(T, \mu_T, \xi_{NL})} \quad (1)$$

where T : natural period, F_R^{EL} and F_Y^{NL} : maximum restoring force in an oscillator with a linear and a Takeda stiffness degrading hysteresis, respectively, μ_T : target ductility factor, and ξ_{EL} and ξ_{NL} : damping ratio assumed in the evaluation of linear and bilinear responses, respectively. In the present study, it was assumed that $\xi_{EL} = 5\%$ and $\xi_{NL} = 2\%$ (Watanabe and Kawashima 2002). Thus $R_\mu(T, \mu_T, \xi_{EL}, \xi_{NL})$ is represented as $R_\mu(T, \mu_T)$ hereinafter.

Takeda stiffness degrading model was developed as a trilinear hysteresis model. In the present study, however, Takeda degrading stiffness model was used to represent elasto-plastic bilinear hysteresis, by eliminating crack path. The natural period T may be evaluated based on the yield stiffness of columns. Representing u_y the yield displacement where the stiffness changes from the initial stiffness to the post-yield stiffness, a target ductility factor μ_T may be defined based on the yielding displacement u_y as

$$\mu_T = u_{\max T} / u_y \quad (2)$$

where $u_{\max T}$ is a target maximum displacement of an oscillator. The post-yield stiffness is assumed to be 0 in the present study.

2.2 Idealization of Force Reduction Factors and Residual Displacement Ratio

As is discussed later, the scattering of the force reduction factors around the mean values is extensive. The mean values of the force reduction factors are idealized as (Watanabe and Kawashima 2002)

$$R(\mu, T) = (\mu - 1) * \Psi(T) + 1 \quad (3)$$

where,

$$\Psi(T) = \frac{T - a}{ae^{bT}} + 1 \quad (4)$$

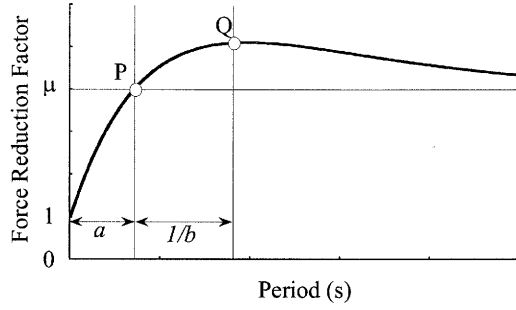


Figure 2 Idealization of force reduction factor with parameters a and b

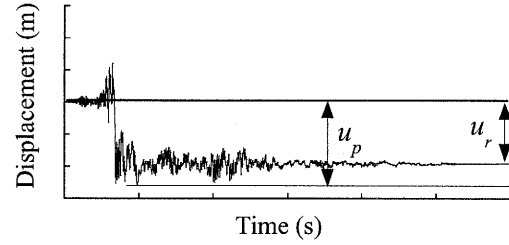


Figure 3 Peak and residual displacements

where parameter a represents the natural period where R factor is equal to μ (point P). Representing Q as the point where R factor takes the maximum value, $1/b$ stands for the period between P and Q , as shown in Figure 2.

Residual displacement which occurs in a structure after an earthquake as shown in Figure 3 is generalized by the residual displacement response spectrum (Kawashima et al 1998). Residual displacement ratio r_r is defined as

$$r_r = u_r / u_p \quad (4)$$

where u_r and u_p are residual displacement and peak displacement, respectively, of SDOF oscillators.

3. FORCE REDUCTION FACTORS AND REDISUDAL DISPLACEMENTS FOR GROUND MOTIONS

3.1 Effect of Near Field Ground Motions on Force Reduction Factors

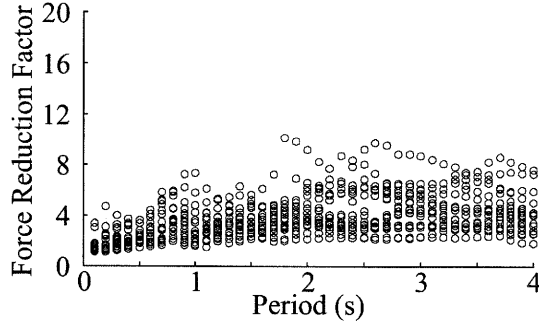
To analyze the effect of near-field ground motions on force reduction factors, 54 components of free-field ground motions were used in the analysis; 20 near-field ground motions, 20 middle-field ground motions, and 14 far-field ground motions. Ground motions recorded within 40km, 40km to 200km and over 200km from the epicenters are defined here as the near-field, middle-field and far-field ground motions, respectively.

Figure 4 shows the effect of three types ground motions on force reduction factors for $\mu_T = 4$ are presented here. It is seen in Figure 4 that scattering of the force reduction factors depending on ground motions is significant. For example at natural period of 1 second, the force reduction factors varies from 1.9 to 10.3 depending on ground motions for near-field ground motions with a target ductility μ_T of 4. It is apparent that such a large scattering of the force reduction factors result in a large change of sizing of a structure in seismic design. Obviously smaller force reduction factors should be assumed in design to provide conservative design. It is observed in Figure 4 that the dependence of force reduction factors on the epicentral distance is significant.

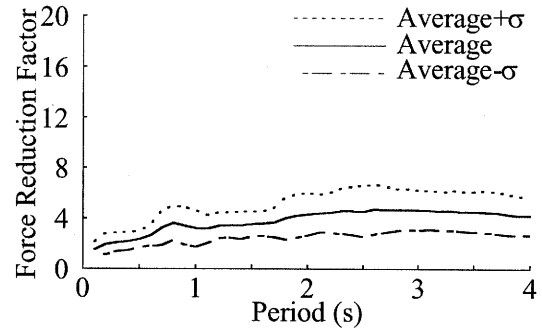
The mean values and standard deviation of force reduction factors at every period are evaluated as shown in Figure 5. Force reduction factors increase as natural periods increase up to certain periods, and decrease beyond those natural periods to approach μ at long natural periods.

Table 1 Parameter a and b in Eq.(2)

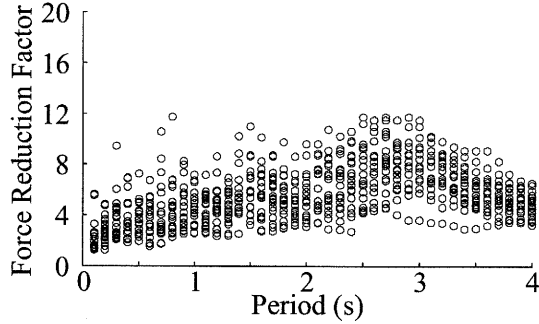
Ground Motions	$\mu=2$		$\mu=4$		$\mu=6$		$\mu=8$	
	a	b	a	b	a	b	a	b
Near	1.549	0.669	1.550	0.547	1.628	0.558	1.689	0.533
Middle	0.834	0.516	0.664	0.475	0.604	0.496	0.572	0.516
Far	0.875	0.500	0.666	0.483	0.578	0.513	0.526	0.550



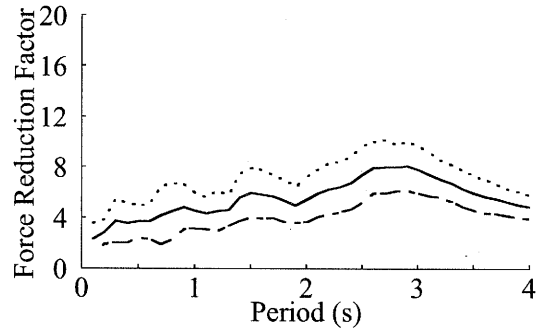
(a) Near-field



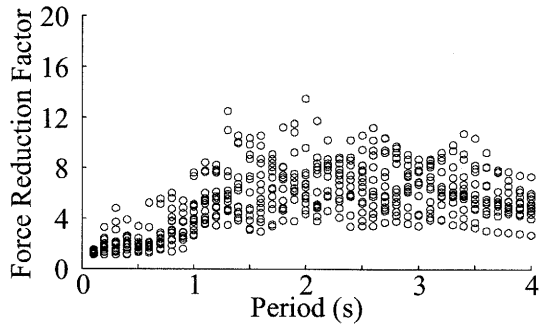
(a) near-field ground motions



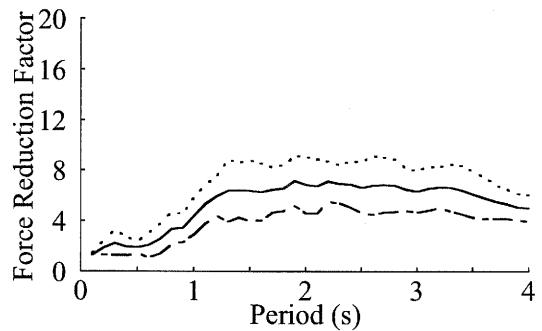
(b) Middle-field



(b) middle-field ground motions



(c) Far-field



(c) far-field ground motions

Figure 4 Force Reduction Factors for 54Components ($\mu_T = 4$)

Figure 5 Mean value and standard deviation of force reduction factors ($\mu_T = 4$)

Table 1 shows the parameters a and b determined by nonlinear fitting for mean R factors of $\mu=2, 3, 4, 5, 6, 7, 8$ and 10 . Figure 6 compares the empirical and computed R factors. It is seen that Eq.(1) provides the general trend of the R factors. Figure 7 shows the difference of near, middle and far-field ground motions on R factors predicted by Equation 3. R factors for near-field ground motion are smaller than those for middle-field and far-field ground motions.

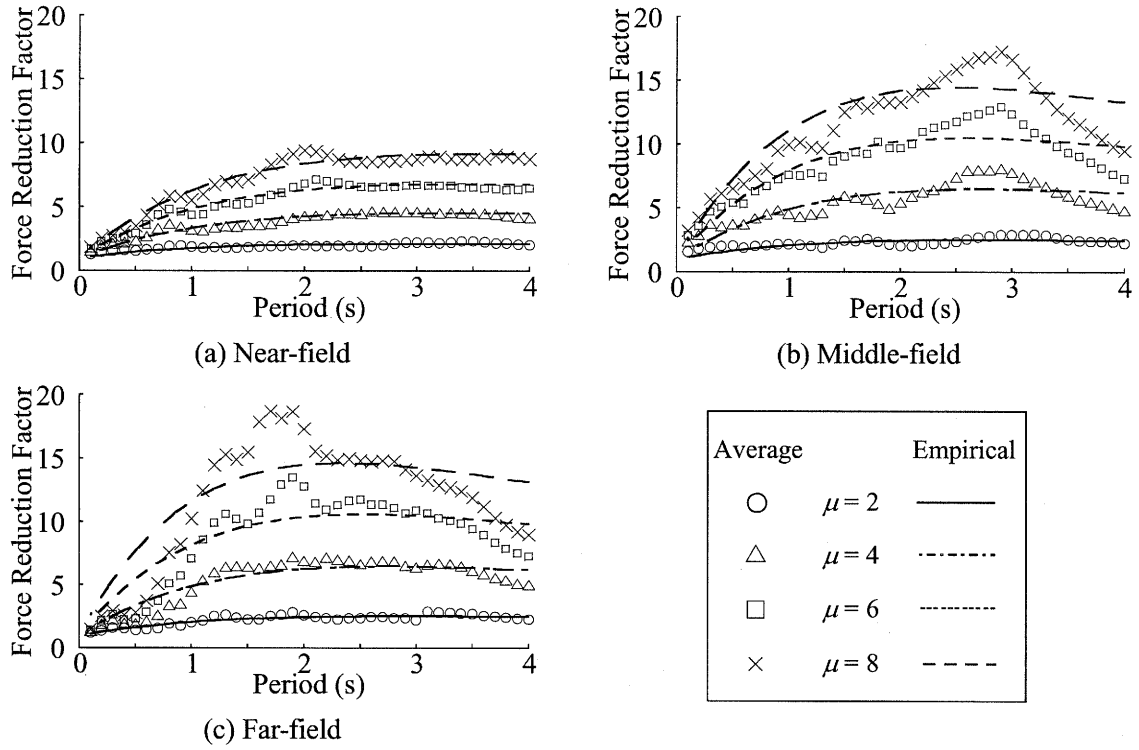


Figure 6 Empirical and mean computed

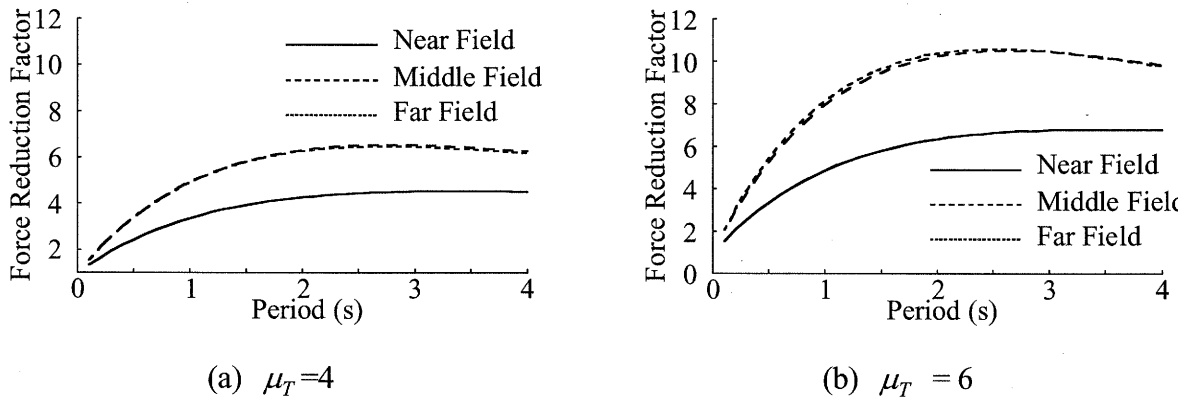
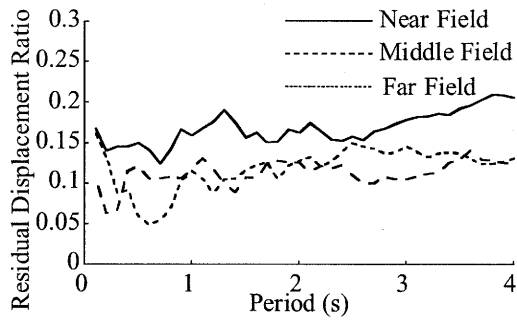


Figure 7 Effect of distance on R factor

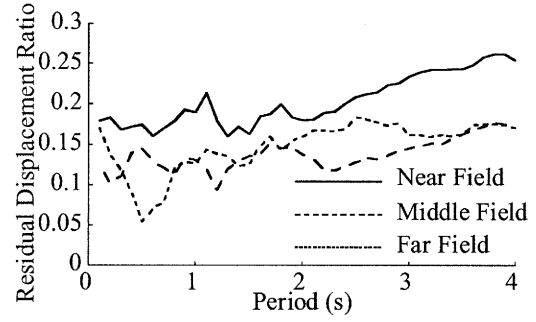
3.2 Effect of Near Field Ground Motions on Residual Displacements

The residual displacement ratios response spectrum were computed for the total 316 components, and they were averaged at every period for near, middle and far-field as shown in Figure 8. It is noted that the residual displacement ratio r_r is larger at the near-field ground motions than middle and far-field ground motions.

Figure 9 shows dependence of residual displacement on R factor for near, middle and far-field. Scatterings of the relations are considerable. It is considered that residual displacements are independent of the force reduction factors.

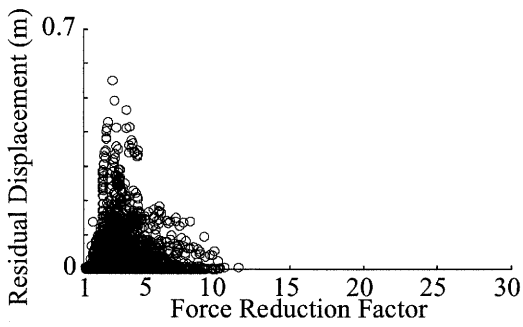


(a) $\mu_T=4$

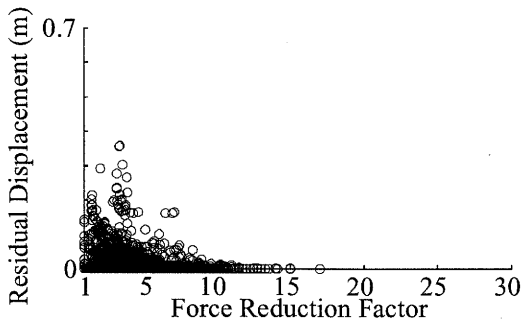
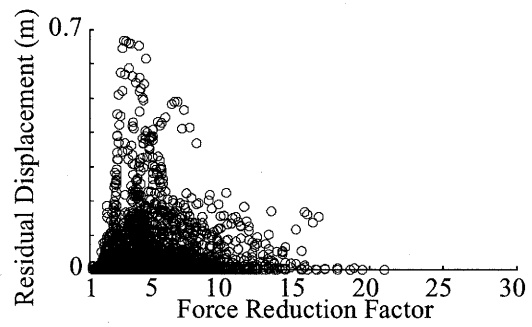


(b) $\mu_T = 6$

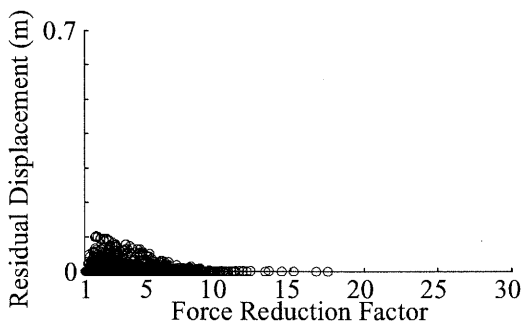
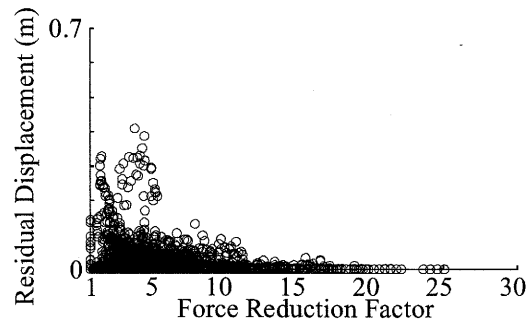
Figure 8 Effect of ground motions on residual displacement ratio response spectra



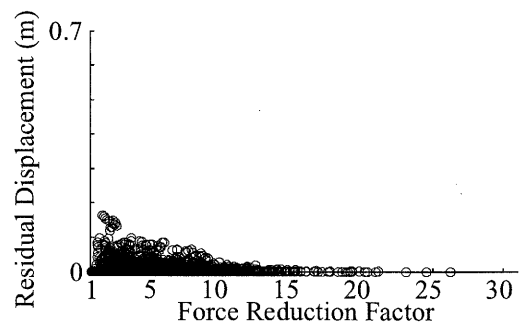
(a) Near-field



(b) Middle-field



(c) Far-field



(1) $\mu_T=4$

(2) $\mu_T = 6$

Figure 9 Dependence of residual displacement on R factor

4. CONCLUSIONS

An analysis was conducted for the force reduction factor based on response of SDOF oscillator using 70 free-field ground motions. Based on the analysis presented herein, the following conclusions may be deduced:

- (1) R factors depend on the types of ground motions. R factors for near-field ground motions are smaller than middle and far-field ground motions. The R factors are similar for middle and far-field ground motions.
- (2) The residual displacement ratios depend on the types of ground motions. The residual displacement ratios are larger for near-field ground motions than middle-field and far-field ground motions.
- (3) There is not an apparent relation between R factors and residual displacements. For the same R factors, residual displacements have large scattering for every ground motions. It seems that residual displacements are independent of R factors.

References:

- Hisada, Y, and Bielak, J. (2003), "A Theoretical Method for Computing Near-Fault Strong Motions in Layered Half-Space Considering Static Offset due to Surface Faulting, with a Physical Interpretation of Fling Step and Rupture Directivity," *Bulletin of the Seismological Society of America*, 93(3), 1154-1168.
- Japan Road association (2002), "Part V Seismic design, Design specifications of highway bridges," Maruzen, Tokyo, Japan.
- Kawashima, K, MacRae, G. A., Hoshikuma, J., and Nagaya, K. (1998), "Residual displacement response spectra," *Journal of Structural Engineering, ASCE*, 124(5), 513-530.
- Mavroeidis, G. P. and Papageorgiou, A. S. (2003), "A Mathematical Representation of Near-Fault Ground Motions," *Bulletin of the Seismological Society of America*, 93(3), 1099-1131.
- Miranda, E. and Bertero, V. (1994). "Evaluation of strength reduction factors for earthquake resistant design," *Earthquake Spectra*, 10(2), 357-379.
- Nassar, A. A. and Krawinkler, H. (1991). "Seismic demands for SDOF and MDOF systems," Report No. 95, The John A. Blume Earthquake Engineering Center, Stanford University, California
- Newmark, N. M. and Hall, W. J. (1973). "Seismic design criteria for nuclear reactor facilities," Report No. 46, Building Practices for Disaster Mitigation, National Bureau of Standards, U.S. Department of Commerce, 209-236.
- Press, W.H., Teukolsky, S.A., Vetterling, W.T. and Flannery, B.P. (1996). "Numerical recipes in Fortran 77," Second Edition, *The Art of Scientific Computing*, Cambridge University Press, 678-683.
- Takeda, T., Sozen, M. A. and Nielsen, N. N. (1970). "Reinforced concrete response to simulated earthquake," *Journal of Structural Engineering*, 96(12), 2557-2573, ASCE
- Inoue, T., and Miyatake, T. (2003), "3D Simulation of Near-Field Ground Motion Based on Dynamic Modeling," *Bulletin of the Seismological Society of America*, 88(6), 1445-1456.
- Watanabe, G., and Kawashima, S. (2001), "Evaluation of Force Reduction Factor in Seismic Design," *Structural Engineering and Earthquake Engineering, Proc. JSCE*, No. 682/I-56, 115-128.
- Watanabe, G and Kawashima, K. (2001), "An Evaluation of the Force Reduction Factor in the Force-Based Seismic Design," 34th Joint Meeting of US-Japan Panel on Wind and Seismic Effects, UJNR, Gaithersburg, MD, USA, NIST Special Publication, 987, 201-218, National Institute of Standards and Technology

SEISMIC RESISTANCE VERIFICATION OF FATIGUE RETROFITTED STEEL BRIDGE BENTS (A CASE STUDY IN THE METROPOLITAN EXPRESSWAY)

C. Miki¹⁾, E. Sasaki²⁾, and T. Shimozato³⁾

1) Professor, Department of Civil Engineering, Tokyo Institute of Technology, Japan

2) Assistant Professor, Department of Civil Engineering, Tokyo Institute of Technology, Japan

3) Chief of Design and Research Division, Metropolitan Expressway Public Corp., Japan

miki@cv.titech.ac.jp, esasaki@cv.titech.ac.jp, shimozato@mex.go.jp

Abstract: Fatigue retrofitting works to actual steel bridge bents in the Tokyo Metropolitan Expressway system were described and the effects of them on the seismic resistance behaviors were discussed and verified through push-over analysis. The target steel bridge bents have circular column to rectangular beam connections. Round brackets were attached by bolt splicing as a temporary support for the fatigue retrofitting by welding. However, the unexpected occurrence of lamellar tearing during the weld repairing changed the role of the round brackets to a permanent retrofit detail. The fatigue cracks were not removed all as planned and just stop-holed for the prevention of further propagation. Therefore, it was important to evaluate the seismic performance considering the effects of the round brackets and the stop-holed fatigue cracks.

1. INTRODUCTION

Recently many fatigue cracks were observed in the beam-to-column connections of actual steel bridge piers in the Tokyo Metropolitan Expressway system (Morikawa et al 2002). The investigations on the causes of the fatigue damage unveiled that the cracks initiated from inherent weld defects at the corners of beam-to-column connections where severe local stress concentration occurred due to shear-lag phenomenon (Miki et al 2002). Such inherent weld defects were contained in the welded joints due to the complicated plate assembling method (Miki et al 2003).

In order to make retrofitting works to the fatigue damaged beam-to-column connections in steel bridge bents, it is essential to remove fatigue cracks and the inherent weld defects referred to “delta zones” and to reduce the local stress concentration at the corners. Until so far, several retrofitting techniques against the fatigue problem such as welding, plate attaching by bolt splicing (Morikawa et al 2002), additional brackets, rib attachment (Tanabe et al 2004) have been proposed and the effects of them on the fatigue performance of the structures were examined by a series of experiments, FEM analysis, and field stress measurements. However, in order to choose a proper retrofitting work for a specific steel bridge bent, it is necessary to consider the structural characteristics and also material properties especially for weld repairing.

This paper describes the fatigue retrofitting procedure and the verification of the seismic performance through push-over analysis for an actual steel bridge bent.

2. DESCRIPTION OF THE STRUCTURE

2.1 Structure and Fatigue Damage

The target steel bridge bents are located at Ikebukuro in the Route 5 in the Tokyo Metropolitan Expressway system. They are two-story structures with circular column to rectangular beam connections as shown in **Figure 1**. The plate assembling method is shown in **Figure 2**. The web plates of rectangular beam penetrate into the circular column and the flange plates of the beam are welded on the wall of the circular column. This plate assembling method caused inherent weld defects at the corners where the peak local stress occurred due to shear lag effect. The fabrication code provides full penetration welds for all of the joints inside of beam-to-column connections. However, the most of welds are partial penetrated or fillet welds. Fatigue cracks initiated and propagated from such inherent defects and root face. Figure 3 shows observed fatigue cracks. One of the fatigue cracks appeared on surface at the corner of beam-to-column connections (Figure 3 (a)). The fatigue cracks initiated from the root of welds between the beam flange and the column wall, which penetrated along the beam flange. Fatigue cracks also initiated from the big cavity between the beam web and the column wall. The other cracks appeared on the welds surface, which initiated from the fillet welds. Actually, the throat thickness of the welds was extremely small, 2-4mm, because of wide gap. This wide gap was filled with small steel pieces.

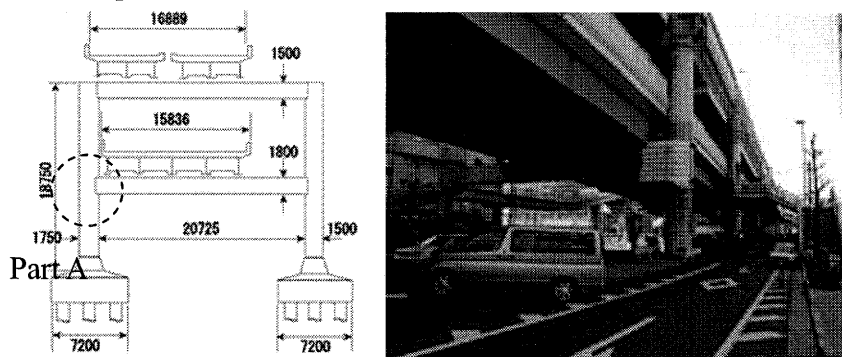


Figure 1 The Target Structure

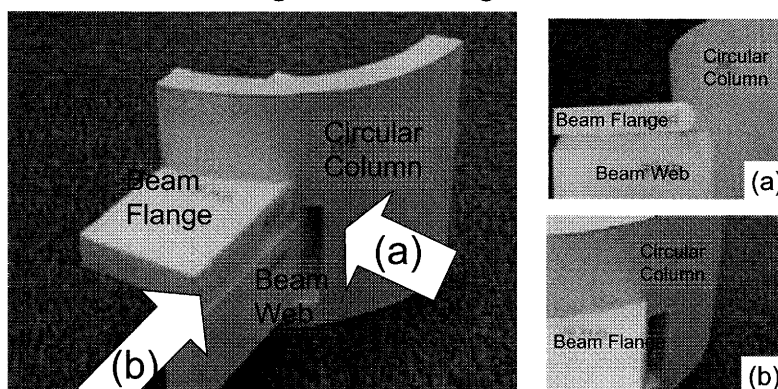


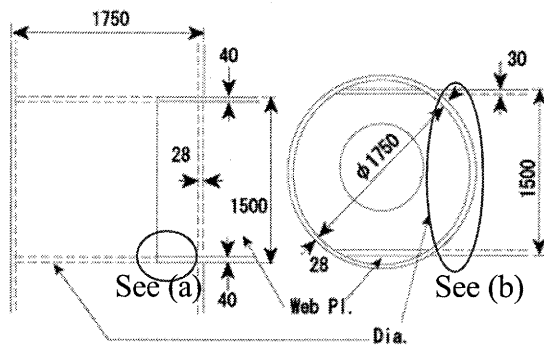
Figure 2 Plate Assembling Method of The Damaged Connections

2.2 Retrofitting Works

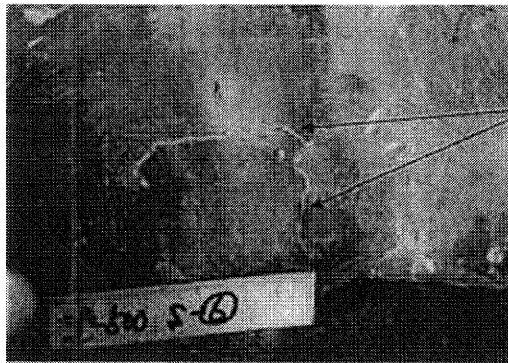
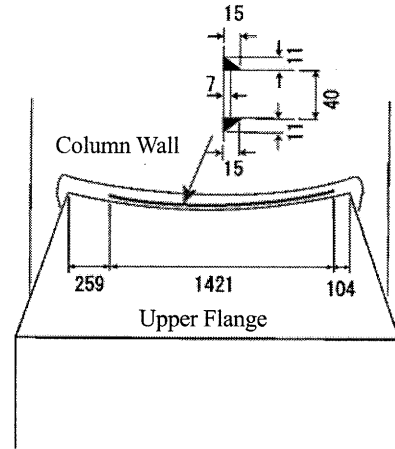
Considering the causes of fatigue cracks, conditions of weld defects, and stress conditions due to live loads, weld repairing was chosen as a proper retrofitting method. The fatigue damaged welded joints would be replaced by full penetrated welding. Round brackets were attached by bolt splicing as a temporary support for the fatigue retrofitting by welding (Figure 4). The results of FEM analysis indicated that the round brackets reduced stresses due to traffic load up to 50%.

2.3 Lamellar Tearing

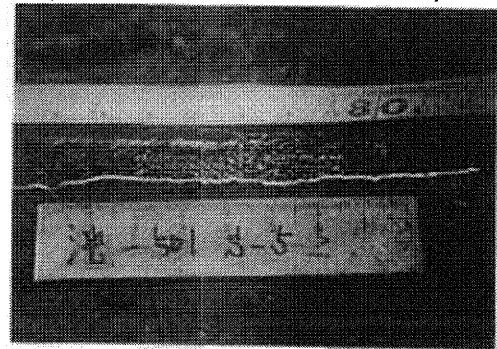
However, during the weld repairing works, cracks were detected inside of the base metal of column flange (Figure 5). There were lamellar tearing cracks. Table 1 shows the material properties of used steel in this structure. The Sulfur inclusion affecting lamellar tearing phenomenon is high, and the



Details of The Connection (Part A in Figure 1)



(a) Fatigue Cracks at the Corner



(b) Fatigue Crack on Beam Flange

Figure 3 Fatigue Damage

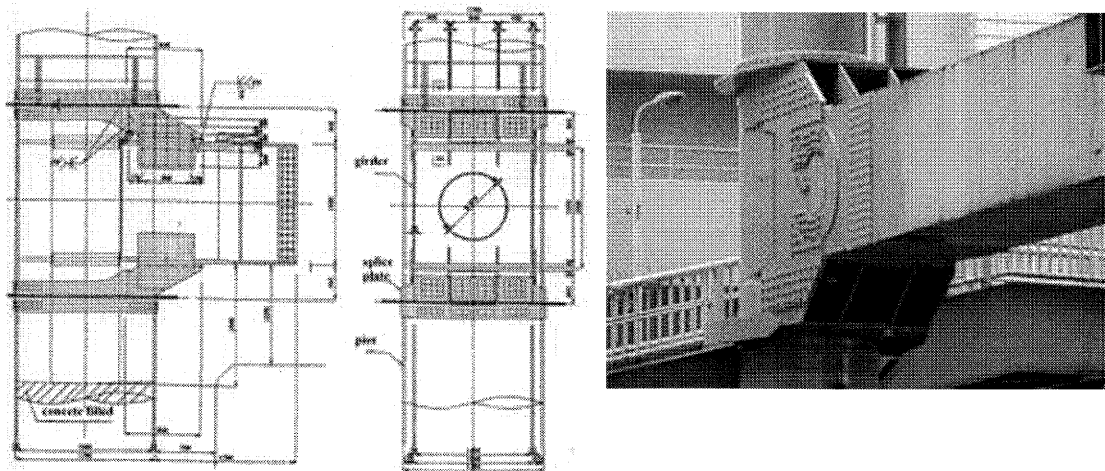


Figure 4 Round Bracket

thickness direction tensile test results show that the ductility in thickness direction, reduction of area (RAZ) is surprisingly low (Miki et al 2004).

The accident forced us to change the retrofitting method. As a result, the round brackets installed as a temporary support changed its role to a permanent retrofitting structure. And the fatigue cracks were not removed all and remaining in the joints by piercing holes for the limitation of crack propagation direction and for the prevention of unstable crack propagation (Figure 6). We expected fatigue cracks propagated into these holes and stopped. Eventually, the upper flange and the column wall would separate. This retrofitting work is expected to be effective enough to prevent fatigue damage, but it gave the structure additional stiffness and weights at the beam-to-column connections and remaining cracks in the joints. Therefore, it is important to evaluate the effects of the retrofitting work on the seismic performance of the whole structure of the bent.

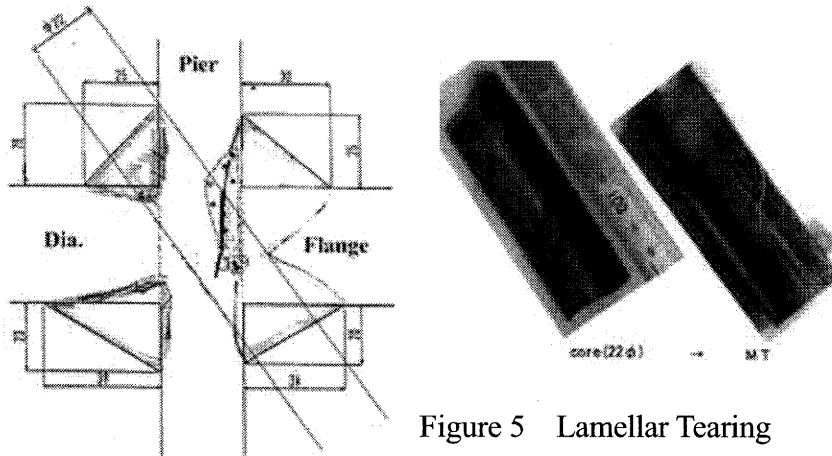


Figure 5 Lamellar Tearing

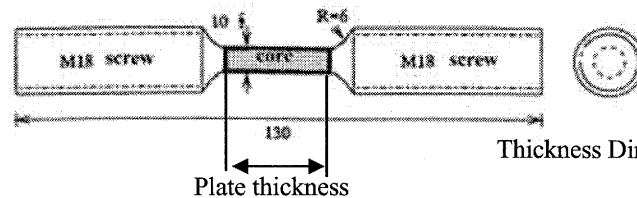
Table 1 Material Properties

(a) Chemical Composition

sample No.	chemical composition(mass %)										parameters	
	C	Si	Mn	P	S	Ni	Cu	Cr	Mo	V	Ceq	Pcm
No.1	0.16	0.29	1.36	0.012	0.012	0.017	0.04	0.018	0.012	0.003	0.406	0.242
No.2	0.17	0.29	1.36	0.012	0.01	0.017	0.04	0.018	0.012	0.003	0.416	0.252
No.3	0.17	0.29	1.35	0.012	0.009	0.016	0.04	0.017	0.012	0.003	0.414	0.251

(b) Thickness Direction (Z-Direction) Tensile Test Results

sample No.	diameter (mm)	0.2% load		tensile stress		elongation (%)	RAZ (%)	break point
		Load(kN)	N/mm2	Load(kN)	N/mm2			
No.1a	9.99	26.81	342	27.89	356	3	0.2	connection
No.1b	9.99	28.34	362	39.78	508	12	8	A
No.1c	9.99	27.57	352	40.13	512	10	12	A
No.2a	10.00	26.49	337	39.41	502	18	20	A
No.2b	10.00	26.39	336	40.16	511	10	19	A
No.2c	9.99	24.92	318	36.84	470	6	10	A



Thickness Direction Tensile Test Specimen

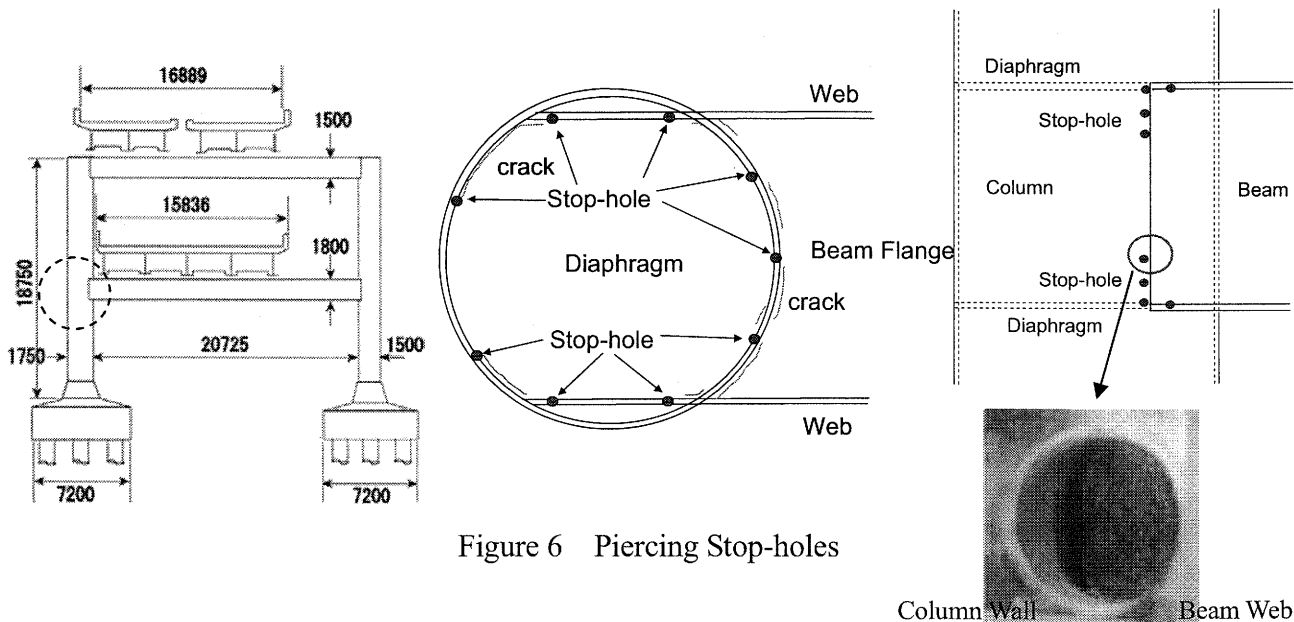


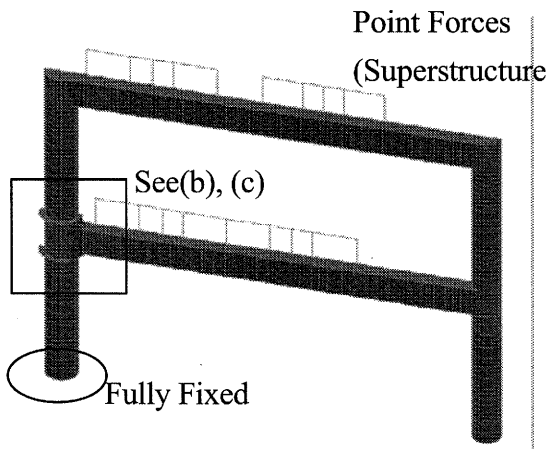
Figure 6 Piercing Stop-holes

3. PUSH-OVER ANALYSIS OF THE STEEL BENT

In order to verify the effects of the fatigue retrofitting methods on the seismic performance of the steel bridge bents, in this study, push-over analysis by FEM was conducted. In this study, two cases are considered. Case 1 is the case of the original structure before retrofitting works. Case 2 is the case that the round brackets are installed into structure. Case 3 is the case that the round brackets are installed, the diaphragm is removed and flange plate and are not connected to the column wall to simulate fatigue cracks with stop-holes.

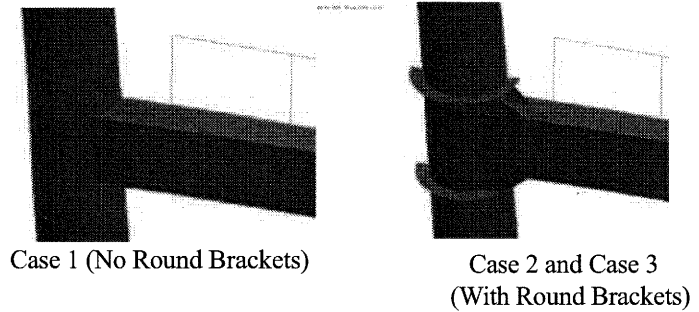
3.1 Analysis Conditions

The finite element model is shown in Figure 7. All the steel plates were modeled with shell elements and the concrete filled in the base of the circular piers was modeled with solid elements. At the base, shell elements and solid elements are connected to simulate composite action. In Case 3, to model the crack in the flange plate, only for the compressive flange, the nodes on the column wall and the nodes in the flange mode together only in the direction of the component axis (Figure 8). The considered material properties are defined as shown in Figure 9. The vertical reaction forces due to the weights of the superstructure are modeled as the point loads on the beam. The horizontal loads for the push-over analysis were applied at the same points as the reaction forces. The base of the columns is fully fixed as boundary condition. The model is half model considering the symmetry in the vertical plane.

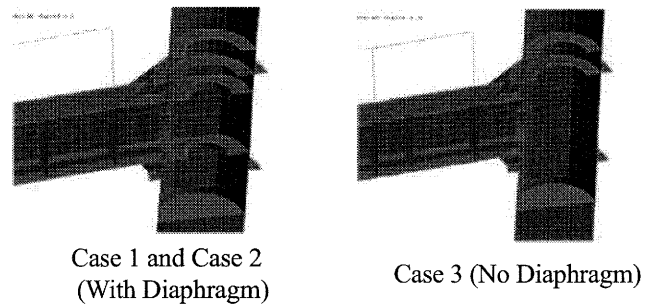


(a) The Whole Structure

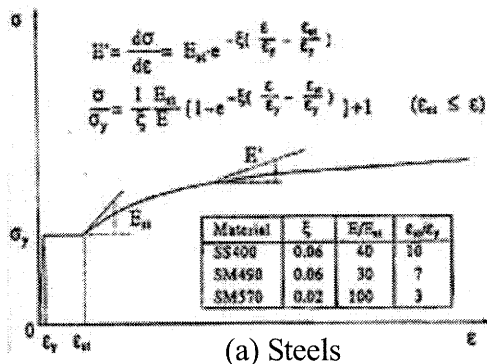
Figure 7 FEM Model



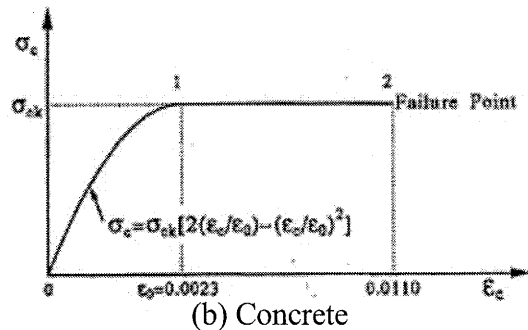
(b) Retrofitting of Beam-to-Column Connections



(c) Simulated Crack in Diaphragm



(a) Steels



(b) Concrete

Figure 8 Material Properties Used in FEM

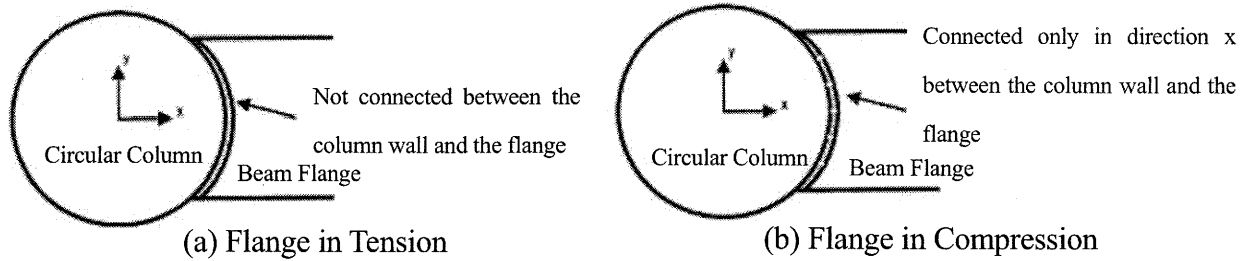


Figure 9 Modeling of the Crack in the Flange

3.2 Results

Figure 10 shows the deformation at ultimate state in the push-over analysis. In Case 1, in the original structure without round brackets, the local buckling occurred in the beam just out of the beam-to-column connection. In the existing steel bridge bents, the beam-to-column connections are relatively rigid because they are designed by considering the local peak stress due to shear lag (Okumura et al. 1968). That causes local buckling during earthquakes just out of the beam-to-column connections (Sasaki et al. 2004).

In both of Case 2 and Case 3, the yielding and the ultimate state were governed by the strength of the base. The analysis results such as the horizontal seismic coefficients at the yielding and at the ultimate state were shown in Table 2. Focusing on the behavior of the retrofitted beam-to-column connections, in both of the cases, the local buckling occurred at the thickness-changing portion just out of the beam-to-column connections as shown in Figure 10. This is the same feature described as that in Case 1, so it can be said that the fatigue retrofitting works did not affect the seismic behavior of the steel bridge bent. The von-Mises stress distribution shown in Figure 11 also illustrates that no damage represented in the fatigue retrofitted beam-to-column connections even in Case 3 with cracks remaining in the beam flanges.

Table 2 also summarized the verification of the horizontal strength and the residual displacement based on the analysis results. As shown in Table 2, in both of the cases, the horizontal strength was exceeded the required horizontal strength proposed in the Japanese Specifications for Highway Bridges and the residual displacement was also within the allowable residual displacement. Therefore, it was concluded that the steel bridge bent with the fatigue retrofitted details in the beam-to-column connections possesses enough seismic performance.

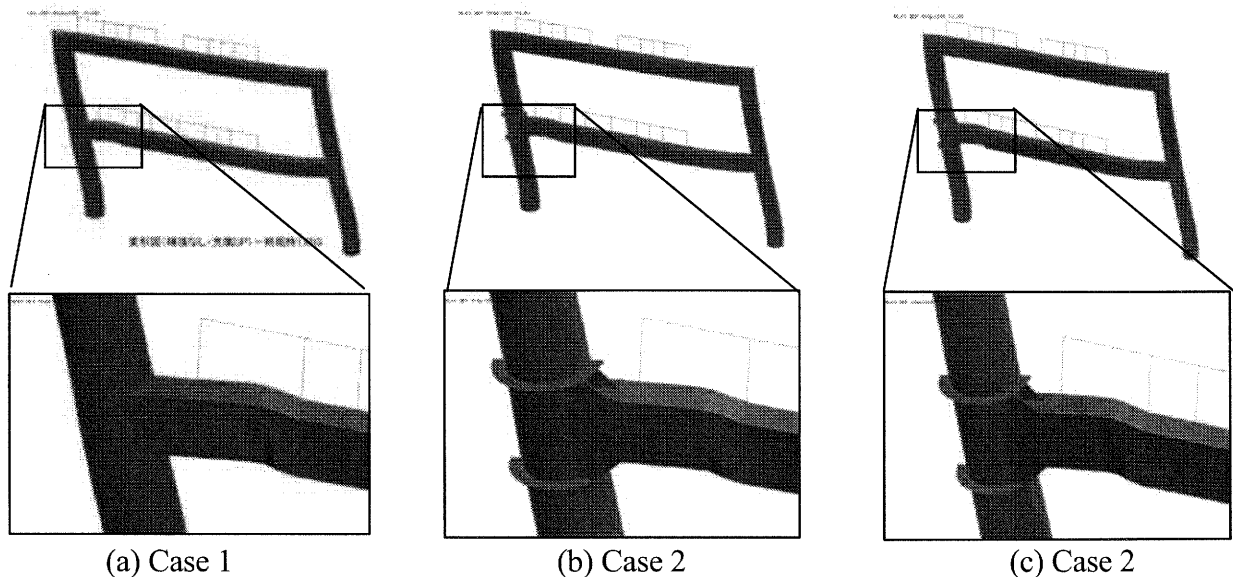


Figure 10 Deformation at Ultimate State

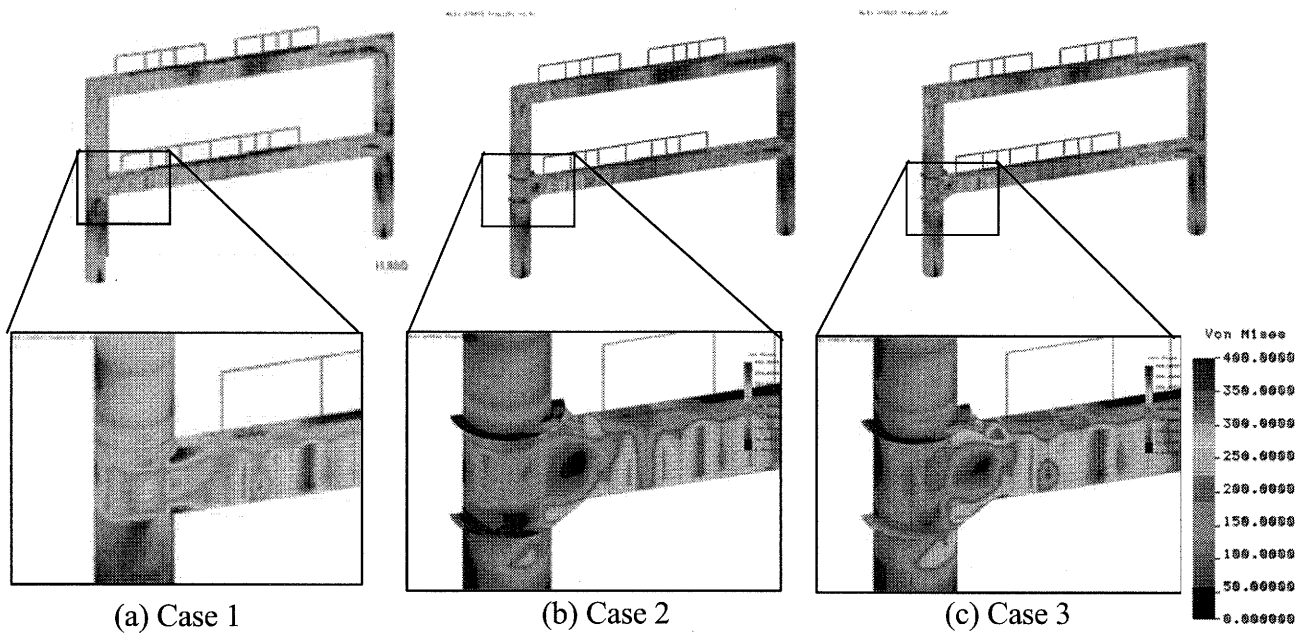


Figure 11 Von Mises Stress Distribution at Ultimate State

Table 2 Summary of Push-Over Analysis Results and Verification of The Seismic Performance

Case		Case 1	Case 2	Case 3
Earthquake Type		Type II	Type II	Type II
Analysis Results	Horizontal Yield Strength (kN)	4153.48	3390.59	3348.21
	Horizontal Yield Displacement (m)	0.086	0.065	0.066
	Seismic Coefficient at Yield	0.98	0.8	0.79
	Horizontal Ultimate Strength (kN)	7840.74	6823.57	7883.13
	Horizontal Displacement at Ultimate State(m)	0.282	0.177	0.287
	Seismic Coefficient at Ultimate State	1.85	1.61	1.86
Verification of Horizontal Strength	Horizontal Strength, Ha(kN)	6611.65	5679.24	6371.49
	Required Horizontal Strength, Khew(kN)	4432.37	4936.04	3827.95
	Results	OK	OK	OK
Verification of Residual Displacement	Residual Horizontal Displacement (m)	0.0354	0.0419	0.0406
	Allowable Horizontal Displacement (m)	0.20455	0.20445	0.20445
	Results	OK	OK	OK

4. DETAILED ANALYSIS OF CONNECTIONS

In order to investigate on the effects of the fatigue retrofitting to the beam-to-column connections, more detailed analysis was conducted by zooming method using the results of the push-over analysis of the whole bent. The round brackets were installed to the actual structure by bolt-splicing. In the process to the ultimate state of the bent, sectional forces to bolts can exceeded the strength of them and lead to fracture. In the detailed analysis, the behavior of a beam-to-column connection in the bent was discussed with considering the possibility of fracture of bolts.

4.1 Analysis Conditions

The cases of Case 2 and Case 3 discussed in Chapter 3 were analyzed in detail on the behavior of a beam-to-column connection. The FEM model for the detailed analysis is shown in Figure 12. The bolts were modeled by beam elements. The tensile and the shear strengths of the bolts are 342.1kN and 197.5kN, respectively. In the analysis, the damage condition of the connection at the horizontal load of the required horizontal strength was investigated. The displacement at the boundary of the detailed model was obtained from the analysis result of the whole bent and applied as the boundary condition. When the sectional force to the bolts reached the strengths of the bolts, elements modeling the bolts were removed and the following analysis was continued without the elements.

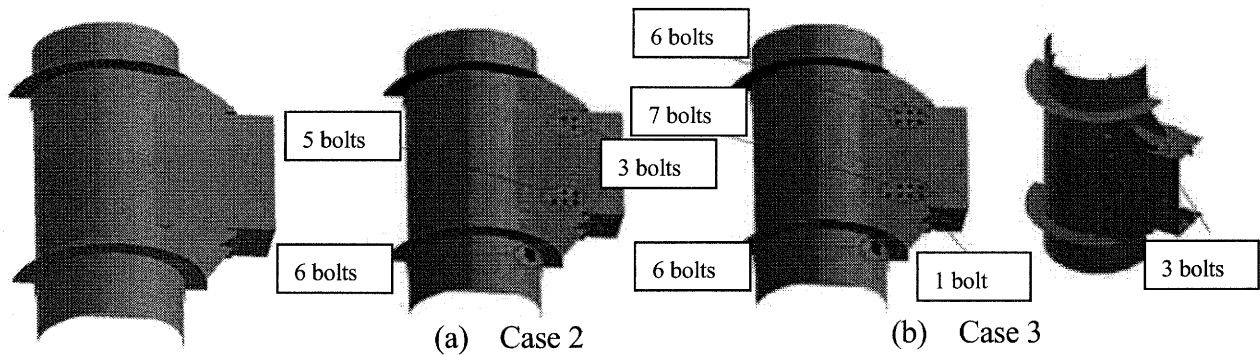


Figure 12 Detailed FEM Model

Figure 13 Location of Fractured Bolts

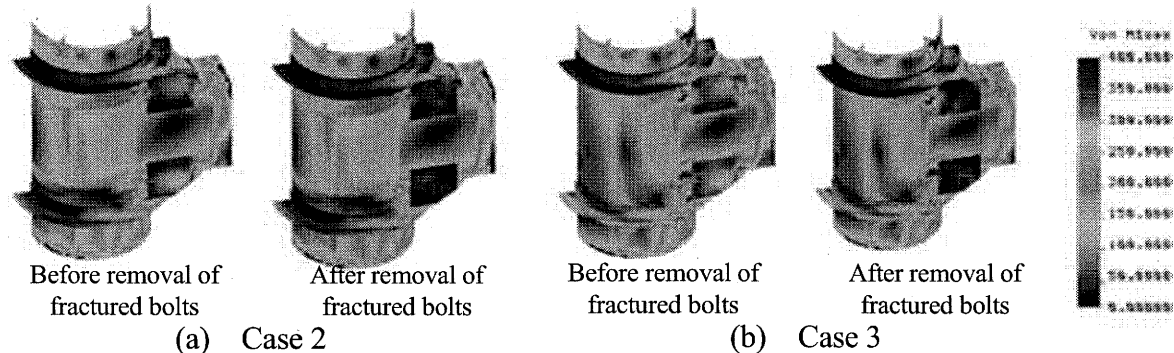


Figure 14 Stress Distribution

4.2 Analysis Results

Figure 13 shows the location of the fractured bolts in both of the cases. The number of the fractured bolts in Case 2 and Case 3 was 14 and 20, respectively. Figure 14 shows the deformation and the von-Mises stress distribution before and after the removal of bolts. The removal of bolts did not change the stress distribution in both of Case 2 and Case 3. Therefore, the effect of the fracture of the bolts on the behavior of the beam-to-column connections is not significant, so it can be said that the fatigue retrofitted connections possesses the required level of strength.

5. CONCLUSIONS

The seismic performance was not affected by the fatigue retrofitting works using round brackets. Furthermore, it was confirmed that even in the case that the flange plate was cut by fatigue cracks, the steel bridge bent still has satisfactory ductility and strength against the seismic loads.

References:

- Morikawa, H., Shimozato, T., Miki, C., Ichikawa, A. (2002), "Study on Fatigue Cracking in Steel Bridge Piers with Box Section and Temporary Repairing", Proc. of JSCE, No.703/I-59, 177-183.
- Miki, C., Ichikawa, A., Sakamoto, T., Tanabe, A., Tokida, H., Shimozato, T. (2002), "Fatigue Performance of Beam-to-Column Connections with Box Sections in Steel Bridge Frame Piers", Proc. of JSCE, No. 710/I-60, 361-371.
- Miki, C., Hirabayashi, Y., Tokida, H., Konishi, T., Yaginuma, Y. (2003), "Beam-Column Connection Details of Steel Pier and Their Fatigue Damage Mode", Proc. of JSCE, No.745/I-65, 105-119.
- Tanabe, A., Miki, C., Ichikawa, A., Sasaki, E., Shimozato, T. (2004), "Fatigue Strength Improvement of Beam-to-Column Connections with Box Section In Steel Bridge Frame Piers", Proc. of JSCE, No.777/I-69, 137-148.
- Miki, C., Tominaga, T., Yaginuma, Y., Shimozato, T. (2004), "A Study on Lamellar Tear Risk of Steel Bridge Piers Retrofit Welding", Proc. of JSCE, No.759/I-67, 69-77.
- Okumura, T., Ishizawa, N. (1968), "The design of knee joints for rigid steel frames with thin walled section", Proc. of JSCE, No.153, 1-18.
- Sasaki, E., Miki, C., Ichikawa, A., Takahashi, K. (2004), "Behavior of Steel Bridge Frame Piers during Earthquakes", Journal of Structural Eng., JSCE, Vol. 50A, 1467-1477.
- Japan Road Association (2001), Specifications for Highway Bridges (JSHB)

ENERGY DISTRIBUTION AND POWER FLOW IN PASSIVELY CONTROLLED STRUCTURES

T. Igusa

Guest Professor, Materials and Structures Laboratory, Tokyo Institute of Technology, Japan
Professor, Department of Civil Engineering, Johns Hopkins University, U.S.A.
tigusa@jhu.edu

Abstract: The response of buildings with passive control systems is examined using energy principles. Two fundamental types of response motion are considered: free-vibration response and response to wide-band stochastic input. The goal is to understand relationships between the power flow between the building floors, the kinetic and potential energy of each floor, and the energy dissipation by the passive control system.

This paper is a preliminary study that serves as a prelude to further research investigations of damping in passively control structures that will be performed jointly by Professor K. Kasai and the author at the Tokyo Institute of Technology.

1. INTRODUCTION

We begin with a brief review of the wave approach to the analysis of relatively tall buildings. We follow a wave approach, which can be traced back to D'Alembert (1747) and has been described for building analysis in textbooks such as Clough and Penzien (1975). Such an approach has been used in various applications such as system identification and damage detection (e.g., Safak, 1998). In this paper, the emphasis is on the analysis and design of passively controlled buildings.

2. WAVE EQUATIONS

2.1 Review

Consider a continuous cantilever shear beam model for a building with equation given by

$$-\rho \frac{\partial^2 w}{\partial t^2} + \frac{\partial}{\partial x} \left(\frac{\kappa \partial w}{\partial x} \right) = 0 \quad (1)$$

where $w(x,t)$ is the absolute displacement at location x and time t . Here $\rho(x)$ is the mass per unit length and $\kappa(x)$ is related to the shear stiffness of the beam at x . Usually, κ is denoted as kAG where A is the cross-section area, G is the shear modulus, and k is used to account for the non-uniform distribution of shear stress over the cross section. For a base motion $w_g(t)$, the boundary conditions for the cantilever beam are $w(0,t) = w_g(t)$ at the base and $\partial w(L,t)/\partial x = 0$ at the top free end.

The simplest way to include material damping is to insert an imaginary component to κ .

$$\kappa^* = \kappa(\sqrt{1-h^2} \pm ih)^2 \quad (2)$$

where h is related to the degree of material damping and the sign of the imaginary term must be examined in Fourier transform space.

We can begin with the D'Alembert (1747) approach to solving the equation of motion. In this approach, the absolute displacement is expressed as

$$w(x, t) = w_U(t - x/c) + w_D(t + x/c) \quad (3)$$

where the subscripts U and D are used to designate waves moving upwards and downwards. Substituting into the equation of motion (1), it can be seen that the wave speed c is given by

$$c = \sqrt{\kappa/\rho} \quad (4)$$

With material damping, we have

$$c^* = c(\sqrt{1-h^2} \pm ih) \quad (5)$$

To satisfy the boundary conditions, we must have

$$w_U(t) + w_D(t) = w_U(t) + w_U(t - 2T_0) = w_g(t) \quad (6)$$

where $T_0 = L/c$ is the time required for a wave to travel from the base of the building to the top.

Taking the FT of (6), we have

$$W_U(\omega) = \frac{1}{1 + \exp(-2i\omega T_0^*)} W_g(\omega) \quad (7a)$$

$$W_D(\omega) = \exp(-2i\omega T_0^*) W_U(\omega) \quad (7b)$$

where

$$T_0^* = T_0(\sqrt{1-h^2} - ih \operatorname{sgn}(\omega)) \quad (7c)$$

Here, the sign of the imaginary term is determined by the fact that the waves must always be decaying as T_0 increases (or as the beam becomes longer); hence the sign of the frequency, denoted as $\operatorname{sgn}(\omega)$ is needed in the above. It is also noted that the sign of the imaginary term in (2) for harmonic loads is also given by $\operatorname{sgn}(\omega)$. In the following, we use the non-dimensional distance $\xi = x/L$ so that $\xi T_0 = x/c$ is the time required for a wave to travel the distance x . Using (6) to combine (7a) and (7b), we obtain:

$$W(\xi, \omega) = \frac{\exp(-2i\omega_D T_0^*)}{1 + \exp(-2i\omega T_0^*)} [\exp(-i\omega \xi T_0^*) + \exp(-i\omega(2 - \xi)T_0^*)] W_g(\omega) \quad (8)$$

We can expand this as an infinite series by using the relation $1/(1+y) = 1 - y + y^2 - \dots$

$$W(\xi, \omega) = \sum_{j=0}^{\infty} (-1)^j [\exp(-i\omega_D T_0^*(\xi + 2j)) + \exp(-i\omega_D T_0^*(-\xi + 2(j+1)))] W_g(\omega) \quad (9)$$

This can be interpreted as a series of waves traveling up or down at time intervals that are slightly less than T_0 . The decay rate $h|\omega|$ increases with frequency ω . If the strain response is of interest, we simply take the spatial derivative.

2.2 Comparison with modal analysis

If equation (1) is analyzed using standard modal analysis (e.g., as shown in Clough and Penzien, 1975) instead of a wave analysis, then the response can be expanded in the following form:

$$W(\xi, \omega) = \sum_{j=0}^{\infty} \frac{2\omega_j}{T_0} \frac{1}{\omega_j^2 - \omega^{*2}} \phi_j(\xi) W_g(\omega) \quad (10)$$

where ω_j and $\phi_j(\xi)$ are the natural frequencies and mode shapes and ω^* is a complex frequency defined as follows:

$$\omega_j = \frac{(2j-1)\pi}{2T_0} \quad (11a)$$

$$\phi_j(\xi) = \sin \frac{(2j-1)\pi}{2} \xi \quad (11b)$$

$$\omega^* = \omega(\sqrt{1-h^2} - ih \operatorname{sgn}(\omega)) \quad (11c)$$

3. WAVE-MODE DECOMPOSITION

Next we examine possible decompositions of the harmonic response which includes both wave and mode components. This is particularly useful when the first mode dominates the response of the building, but the effects of the higher modes must be retained for accuracy. The essential step here is to retain the modal analysis only for the first mode vibration and to use the more concise wave analysis for all remaining higher modes.

3.1 Separation of the first upward and downward waves

The first two terms of (9) correspond to the first upward and downward waves. We write this as

$$W_U^{(1)}(\xi, \omega) + W_D^{(1)}(\xi, \omega) = [\exp(-i\omega T_0^* \xi) + \exp(-i\omega T_0^* (-\xi + 2))] W_g(\omega) \quad (12)$$

The remaining wave correspond to $j > 0$:

$$W_{\text{remaining}}^{(1)}(\xi, \omega) = -\exp(-2i\omega T_0^* \xi) W(\xi, \omega) \quad (13)$$

If these remaining waves are dominated by the fundamental mode, then we have:

$$W_{\text{remaining}}^{(1)}(\xi, \omega) \approx -\exp(-2i\omega T_0^* \xi) W_m^{(1)}(\xi, \omega) \quad (14a)$$

in which

$$W_m^{(1)}(\xi, \omega) = \frac{2\omega_1}{T_0} \frac{1}{\omega_1^2 - \omega^2} \sin\left(\frac{\pi\xi}{2}\right) W_g(\omega) \quad (14b)$$

is the response of the first mode.

3.2 Interpretation of the mode-wave decomposition

In the preceding mode-wave decomposition, we have the first wave propagating upwards from the base, given by $W_U^{(1)}(\xi, \omega)$ and the first reflected wave propagating downwards from the top of the building, given by $W_D^{(1)}(\xi, \omega)$. These two waves carry most of the energy of the initial seismic input. However, there are some remaining waves that continue to propagate upwards and downwards after these two initial waves. It can be seen, from the exponential decay of the wave formulation with higher decay at higher frequencies, as indicated by (8) and (9), that the lower frequency components of the harmonic response will dominate this remaining wave energy. Hence, in (14a) and (14b), we use only the fundamental mode to characterize the remaining waves. It can be shown that for moderately damped buildings, this mode-wave decomposition accurately describes building response to wide-band seismic input.

4. EFFECT OF VARIABLE PARAMETERS ON ENERGY DISTRIBUTION

For design applications, it is of interest to examine how the preceding equations would change when the parameters $\kappa(x)$ and $h(x)$ vary slowly with location x . An energy and power flow approach is useful here. In the following, we consider the case where the damping is sufficiently high such that only the initial upward propagating wave is of interest. Hence, this is applicable to buildings with passive damping control. (For smaller damping, it would be necessary to consider the returning downward propagating wave and any succeeding reflected waves.)

4.1 Energy formulation

Consider a single cycle of a sinusoidal wave at the base, with frequency ω and amplitude A_0 . We are interested in the case where the parameters $\kappa(x)$ and $h(x)$ vary sufficiently slowly with respect to the location x . This criterion is satisfied if these parameters vary slowly as compared with the variability of the sinusoidal waveform. We compare the sinusoidal waveform at two different locations of the beam: $w_0(x, t)$ at a neighborhood of the base at $x_0 = 0$ and $w_1(x, t)$ at a neighborhood of a location x_1 elsewhere. The waveforms would be given by

$$w_k(x, t) = A_k \sin(\omega[t - t_k - x/c_k]) \quad (15)$$

for $k = 0, 1$. The goal is to determine the relationships between the beam parameters κ_k and h_k and the wave speeds and amplitudes, c_k and A_k , where we assume that the beam parameters can be replaced by constants κ_k and h_k when x is in the neighborhood of x_k . We begin with the undamped case, with $h(x) = 0$. It can be shown that the strain and kinetic energy densities per unit length are given by

$$\frac{\partial E_k^{(strain)}(x, t)}{\partial x} = \frac{A_k^2 \omega^2 \kappa_k}{2c_k^2} \cos^2(\omega[t - t_k - x/c_k]) \quad (16a)$$

$$\frac{\partial E_k^{(kinetic)}(x, t)}{\partial x} = \frac{A_k^2 \omega^2 \rho}{2} \sin^2(\omega[t - t_k - x/c_k]) \quad (16b)$$

It can be seen that there are four conversions between strain and kinetic energy per cycle. By

equating the amplitudes of the strain and kinetic energy densities, we get the relation

$$c_k = \sqrt{\kappa_j / \rho} \quad (17)$$

which is a generalization of (4). This simply shows that the wave speed is proportional to the square root of the shear stiffness.

To determine the amplitude relation, it is necessary to consider the total energy, which is simply the energy density integrated in space over one wavelength. The wavelengths are $\lambda_k = 2\pi c_k / \omega$ and the integrals are:

$$E_k^{(strain)} = \int_{x_k}^{x_k + \lambda_k} \frac{\partial E_k^{(strain)}(x, t)}{\partial x} dx = \frac{\pi A_k^2 \omega \kappa_k}{2 c_k} \quad (18a)$$

$$E_k^{(kinetic)} = \int_{x_k}^{x_k + \lambda_k} \frac{\partial E_k^{(kinetic)}(x, t)}{\partial x} dx = \frac{\pi A_k^2 \omega \rho c_k}{2} \quad (18b)$$

Combining the wave speed and total energy relations, (17), (18a), and (18b), we obtain the desired result for the amplitude relation

$$\frac{A_k}{A_0} = \sqrt{\frac{c_0}{c_k}} = \left(\frac{\kappa_0}{\kappa_k} \right)^{1/4} \quad (19)$$

This shows that the amplitude is inversely proportional to the square root of the wave speed and the fourth-root of the shear stiffness.

4.2 Power flow

To obtain the power dissipation density at a single point in space due to damping, then the following key relation is needed. If $z = Z \exp(i\omega t)$ is the strain, then the average power dissipation density per unit length is given by

$$\frac{\partial \Pi}{\partial x} = \frac{\omega}{2\pi} \int_0^{2\pi/\omega} \text{Re}(\kappa^* z) \text{Re}\left(\frac{\partial z}{\partial t}\right) dt = \frac{\kappa h}{2} |Z|^2 \quad (20)$$

We are now ready to combine the energy relations with the power flow equation. The energy conservation relation is

$$E_1^{(strain)} + E_1^{(kinetic)} - [E_0^{(strain)} + E_0^{(kinetic)}] = \int_{x_0}^{x_1} \frac{\partial \Pi(x)}{\partial x} dx \quad (21)$$

Substituting (16a), (19) and (20) into (21) we obtain

$$\pi \omega \left(\frac{A_1^2 \kappa_1}{c_1} - \frac{A_0^2 \kappa_0}{c_0} \right) = \frac{\omega^2}{2} \int_{x_0}^{x_1} \frac{A^2(x) \kappa(x) h(x)}{c^2(x)} dx \quad (22a)$$

which can be rewritten as

$$A_1^2 \sqrt{\kappa_1} - A_0^2 \sqrt{\kappa_0} = \frac{\omega \sqrt{\rho}}{2\pi} \int_{x_0}^{x_1} A^2(x) h(x) dx \quad (22b)$$

Using an auxiliary variable $B(x) = A^2(x) \sqrt{\kappa(x)}$, the preceding can be written in differential form:

$$\frac{dB(x)}{dx} = \frac{\omega}{2\pi} \sqrt{\frac{\rho}{\kappa(x)}} h(x) B(x) \quad (22c)$$

with solution

$$B(x) = \exp \left[\frac{\omega \sqrt{\rho}}{2\pi} \int_0^x \frac{h(s)}{\sqrt{\kappa(s)}} ds \right] B(0) \quad (22c)$$

The final result for the amplitude would be

$$A(x) = \frac{\kappa^{1/4}(0)}{\kappa^{1/4}(x)} \exp \left[\frac{\omega \sqrt{\rho}}{4\pi} \int_0^x h(s) \kappa^{-1/2}(s) ds \right] A(0) \quad (23)$$

This is the basic relation that can be used to provide insight into the appropriate values for the damping $h(x)$ and shear stiffness $\kappa(x)$ for the design of passively controlled buildings.

5. CONCLUSIONS

This paper provides two sets of mathematical relationships for buildings with passive control devices. The first is a combination of wave and mode formulations for building response. The second is the relationships between wave amplitude and spatially variable damping and shear stiffness.

The most important difference between the wave and mode formulations is that the wave formulation is more suited for the analysis of power flow for input that is of relatively short duration, while the mode formulation is more suited for stationary energy distribution for input that is of relatively long duration. In this short paper, it is shown how these two formulations are mathematically related and it is also shown how they can be combined to make best use of each formulation.

The amplitude relationships were derived using an analysis of power flow and energy distribution. With these relationships it is possible to determine the spatial variability of the shear stiffness and damping that provides a desired distribution of shear strain. Hence, these mathematical relationships may be useful in the design of passive control of tall buildings.

Acknowledgements:

The author acknowledges support from Japan Ministry of Education, Culture, Sport, Science, and Technology (MEXT) for the Guest Professorship at the Materials and Structures Laboratory of the Tokyo Institute of Technology.

References:

- J. D'Alembert. (1747), "Memoire sur la cause generale des vents," David Aine, edition Paris.
- Clough, R.W. and Penzien, J. (1975), "Dynamics of Structures," McGraw-Hill.
- Safak, E. (1998), "Propagation of Seismic Waves in Tall Buildings," *Structural Design of Tall Buildings*, 7, 295-306.

EXPERIMENT AND ANALYSIS OF A STEEL FRAME WITH VISCO-ELASTO-PLASTIC DAMPER

K. Kasai ¹⁾, and N. Minato ²⁾

1) Professor, Structural Engineering Research Center, Tokyo Institute of Technology, Japan

2) Graduate Student, Department of Built Environment, Tokyo Institute of Technology, Japan
kasai@serc.titech.ac.jp, minaton@enveng.titech.ac.jp

Abstract: A visco-elasto-plastic (VEP) damper that combines a visco-elastic device and an elasto-plastic device in series is proposed. Experiments of an isolated damper as well as a frame having the damper indicated the performance that is very consistent with the analytical predictions. The VEP damper combines advantages of the two different devices, showing excellent energy dissipation over a wide range of cyclic deformations. The system using the damper shows better performance than those using single kind of the device, thus, it can extend performance limitations of currently used passive control systems.

1. INTRODUCTION

Recent earthquakes in metropolitan areas of Japan (Kobe) and U.S. (Northridge) lead to intensive research effort of the two countries regarding building performance. Conventional structural systems are now found to have difficulty in satisfying the performance required for protecting socio-economic value of the buildings. Use of powerful seismic energy dissipaters could be essential, if both safety and serviceability of the buildings are to be improved significantly. Pursuant to this, we conducted various studies related to the use of energy dissipaters such as visco-elastic (VE), viscous (VS), and elasto-plastic (EP) dampers (e.g., Kasai and Watanabe 1997, Kasai et al. 1998, Fu and Kasai 1998).

The VE damper (Fig.1a) uses polymer, and it dissipates energy through molecular motion of the material. This damper, due to its linear characteristics, adds consistent amount of damping and stiffness to a structure regardless of the earthquake type and intensity. However, increased earthquake intensity leads to proportionally increased acceleration and inertia force of the structure, which can cause failure of the connection and supporting member of the VE damper. Temperature-dependency of the material is another concern, when using the VE damper (Kasai et al. 1993, 2001, 2002b).

The EP damper (Fig.1b) utilizes yield mechanism of ductile steel (i.e., steel damper) or slip mechanism at interface of two metal surfaces (i.e., friction damper). Under the earthquake of large intensity, the EP damper dissipates energy without significantly increasing its force, and thus excessive loading against the connection and supporting member can be avoided. However, under the more

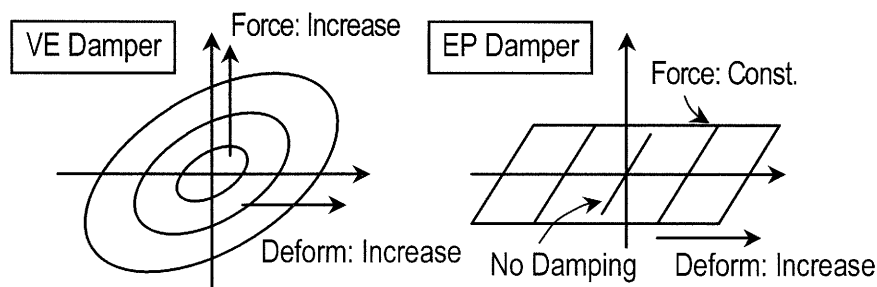


Figure 1 Hysteresis Loops: (a) VE Damper and (b) EP Damper

frequent and smaller earthquakes, the damper behaves elastically without dissipating energy, and may cause relatively large acceleration and consequent failure of the nonstructural component. If yielding or slipping force is lowered to overcome this problem, the performance against larger quake will be sacrificed, and in a case of the steel damper low-cycle fatigue may occur. The EP damper also develops residual plastic deformation and stress, which may cause various problems regarding the post-earthquake operation (Kasai et al. 1998a).

2. VEP DAMPER

The above problems clearly impose limitations to passive control effectiveness of the VE and EP dampers. In general, these limitations are also applicable to a linear velocity-dependent damper type and a nonlinear deformation-dependent damper type, respectively. It is difficult to enhance the performance of each damper due to its inherent energy dissipation mechanism.

Accordingly, as a method to gain enhanced passive control effectiveness, we consider the development of a mixed damper, which combines the VE part and the EP part in series (Fig. 2). From now on, this damper will be called the Visco-Elasto-Plastic (VEP) damper. Our current analytical and experimental studies have indicated that the VEP damper can eliminate the demerits and yet maintain the merits of each of VE and EP dampers. This is briefly explained below:

- (1) Under a small earthquake, the EP part is elastic. While it does not dissipate energy, the VE part does, making the VEP damper effective (advantage over the EP damper).
- (2) Under a large earthquake, the EP part either yields or slips, preventing increase of the force of the VEP damper as well as accelerations of the system (advantage over the VE damper).
- (3) Under a large earthquake, the EP part deformation confines VE part deformation to a certain range, leading to the reliable/economical design of the VEP damper (advantage over the VE damper).
- (4) Due to the combined action of the EP and VE parts, temperature-dependency of the VE part is reduced considerably (advantage over the VE damper).
- (5) Residual deformation of the EP part is absorbed by the VE part having low static stiffness, resulting in negligible residual force of the VEP damper (advantage over the EP damper).

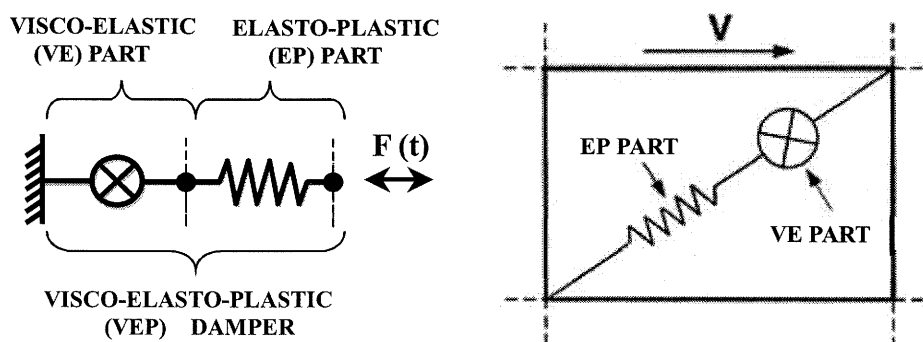


Figure 2 Schematic Illustrations of (a) VEP damper, and (b) Passive Control System

3. EXPERIMENT AND ANALYSIS OF VEP DAMPEER

We have conducted dynamic testing of a full-size VEP damper in order to examine its feasibility (Fig. 3). For the VE part, we use the acrylic material called ISD 111, produced by Sumitomo 3M Company, Japan (e.g., see Kasai et al. 2001). For the EP part, we consider a friction device

consisting of the vehicle brake pads and steel plates with slotted holes (e.g., see Sasani and Popov 1997). The details of the VEP damper are shown in Fig. 4 and 5.

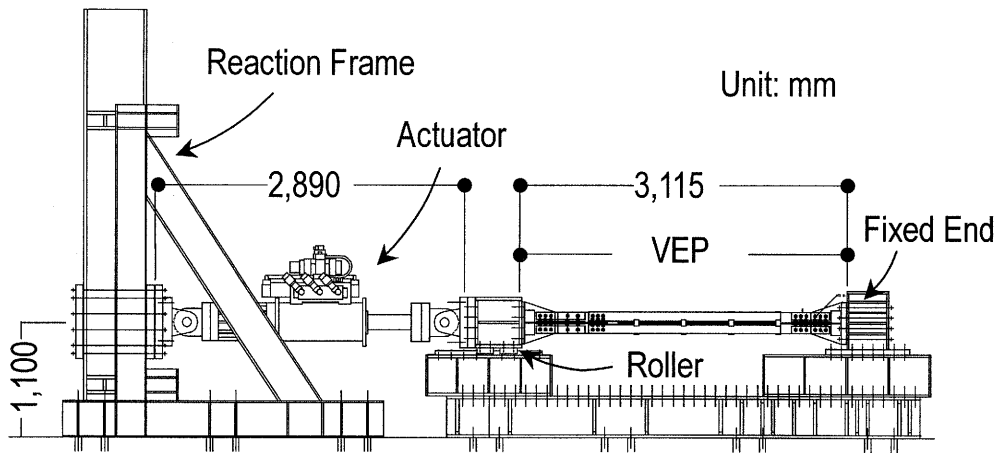


Figure 3 Test Set-Up

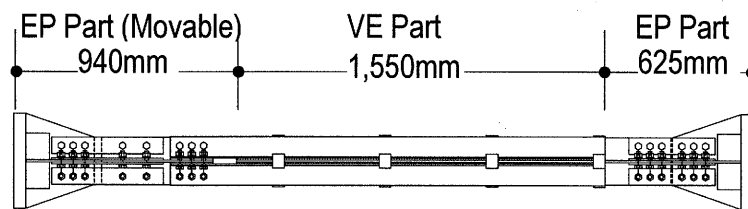


Figure 4 VEP Damper Specimen

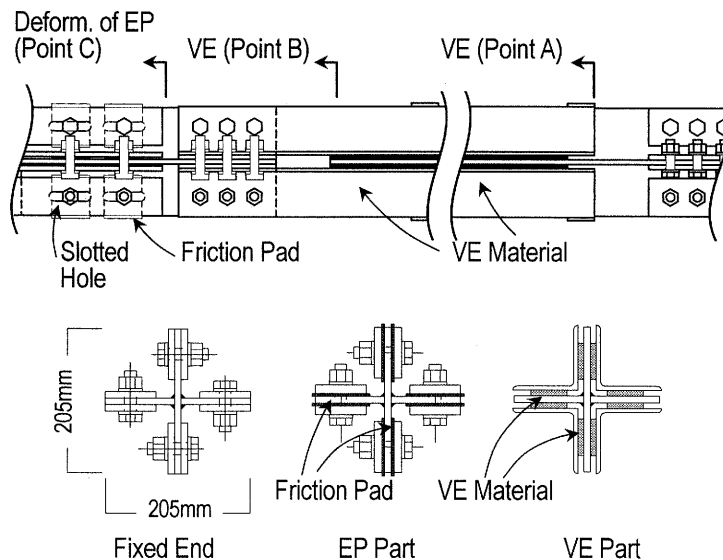


Figure 5 Details of VEP Damper

Fig. 6 compares the results of cyclic loading tests and analyses. The sinusoidal deformation of 1Hz frequency is applied to the VEP damper. Five different magnitudes of the peak deformation ranging from 8 mm to 40 mm are considered. Analysis uses Kasai's (1993, 1998, 2001) visco-elastic constitutive rule consisting of fractional time-derivatives of the stress and strain for the VE part, and a

bilinear constitutive rule for the EP part. The responses of the VEP damper, VE part, and EP part are shown, respectively. Analysis correlates extremely well with the experiments.

Under the small deformation imposed, the EP part is elastic, and the VE part as well as VEP damper exhibit typical elliptical hysteresis loops. Under the larger deformations, the EP part slips and maintain a constant force, which is advantageous for the design of the damper connections and supporting members. In the tests applying VEP peak deformation of 16 mm or more, the deformation of the VE part is limited to about 16 mm and the rest of the deformation taken by the EP part. This indicates that the thickness of the VE material can be designed with high confidence, since it must be large enough not cause excessive shear strain and consequent tearing failure of the material. Fig. 7 also shows the case of random loading. Good agreement between the experiment and analysis is obtained even under the random loading case.

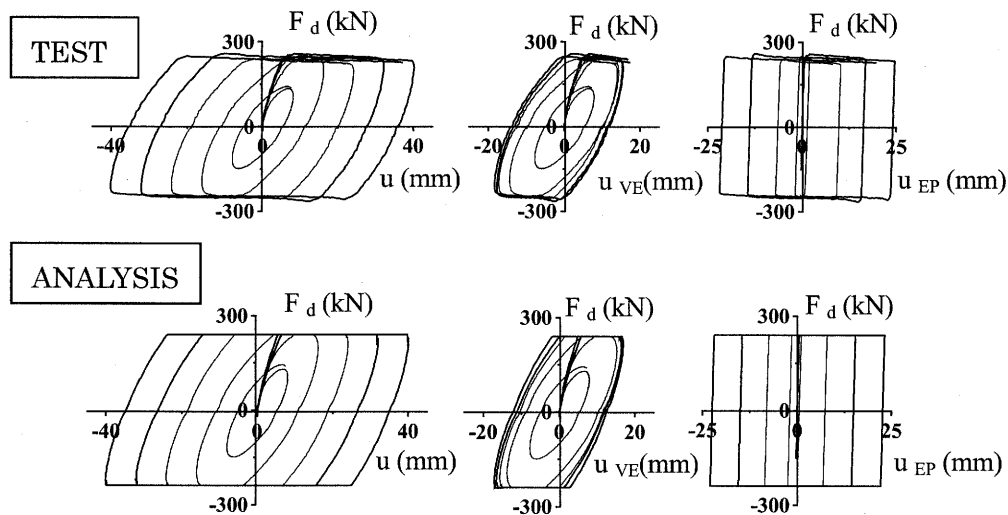


Figure 6 Sinusoidal Deformation Test: Comparison between Experiment and Analysis (VEP Damper, VE Part, and EP Part, in the order from left to right)

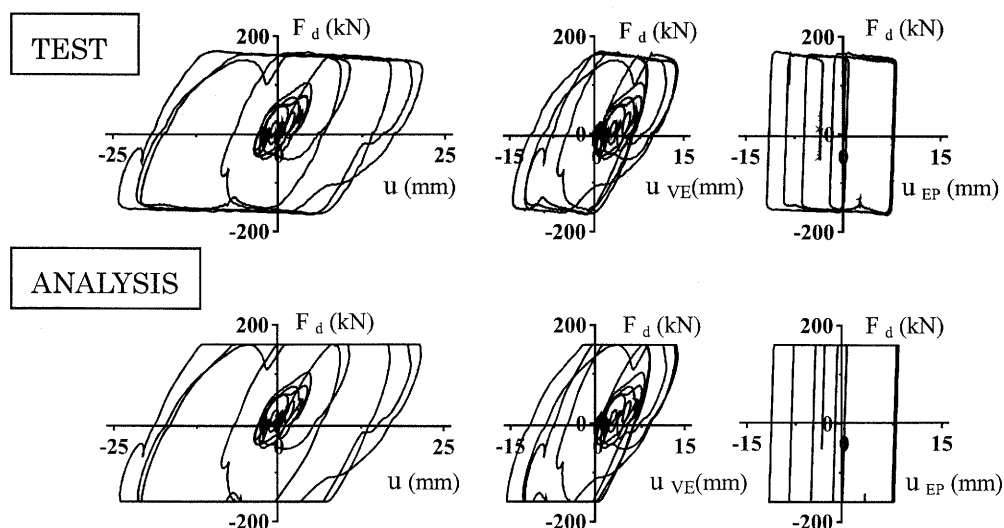


Figure 7 Random Deformation Test: Comparison between Experiment and Analysis (VEP Damper, VE Part, and EP Part, in the order from left to right)

4. EXPERIMENT OF FRAME WITH VEP DAMPER

We have also conducted dynamic testing of a 0.4-scale steel frame with the VEP damper (Fig. 8). One of the objectives of this experiment is to examine how properly the damper works when it is inserted into the frame. Fig. 9 shows the responses of the system and damper, respectively. They confirm proper functioning of the VEP damper: Under a small drift, the system acts as a structure with a VE damper only, as evidenced by the elliptical hysteresis loop of the system and damper, respectively. On the other hand, under a larger drift the system is approximately changed into a structure with an EP damper. The observations are in conformity with those described earlier for the VEP damper, and the system has functioned as expected.

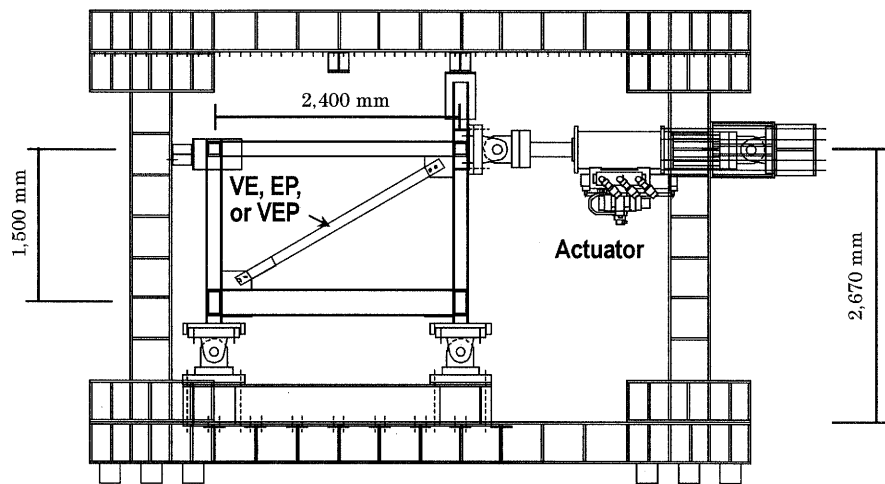


Figure 8 Experimental Set-Up for Steel Frame with VEP Damper

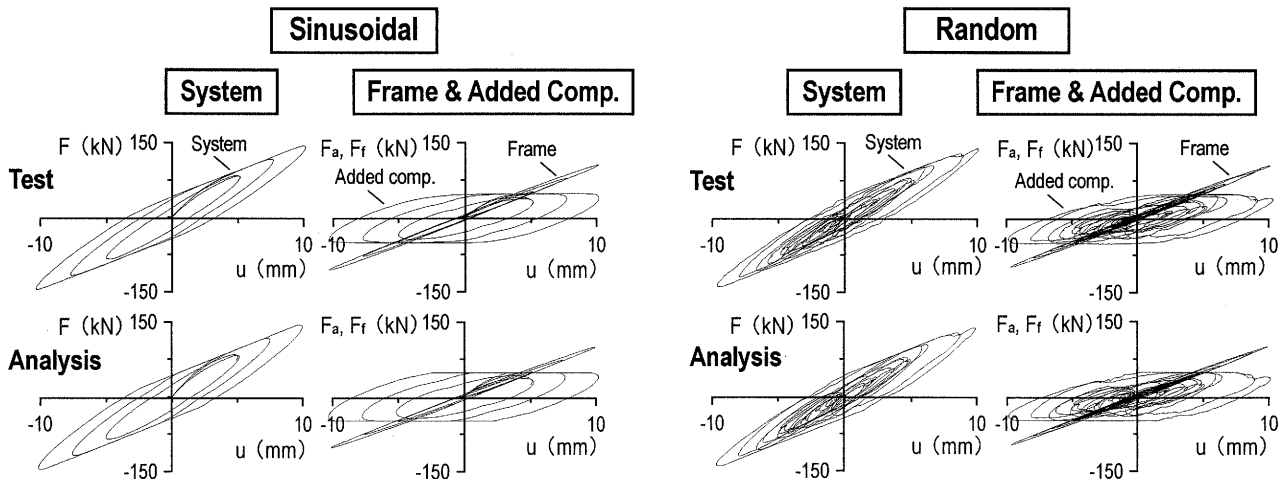


Figure 9 Sinusoidal and Random Deformation Test: Comparison between Experiment and Analysis (VEP System, Frame, and Added component, in the order from left to right)

5. PROTOTYPE DESIGN AND EARTHQUAKE RESPONSE ANALYSES

The above results indicate that the experimental results are consistent with the analytical results, and that there is no appreciable changes of the VEP damper performance when inserted into a frame.

Based on this, we have conducted various time history analyses of a prototype 12-story steel frame

with the VEP dampers, herein called as the VEP system. In addition, the VE system (frame with VE dampers only) and the EP system (frame with EP dampers only) are also analyzed to compare with the VEP system. Analytical models are shown in Fig. 10.

Fig. 11 shows the response of the three systems under the 1995 JMA Kobe record whose peak velocity is scaled to 50 cm/s. The VEP system indicates elliptical hysteresis in a small amplitude range, and elato-perfectly-plastic hysteresis in a large amplitude range.

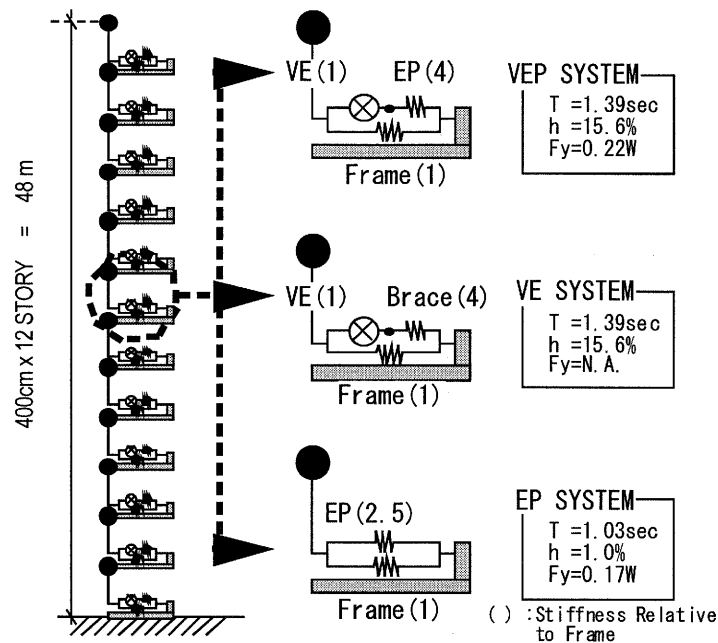


Figure 10 Three Prototype Systems of 12-Story Height

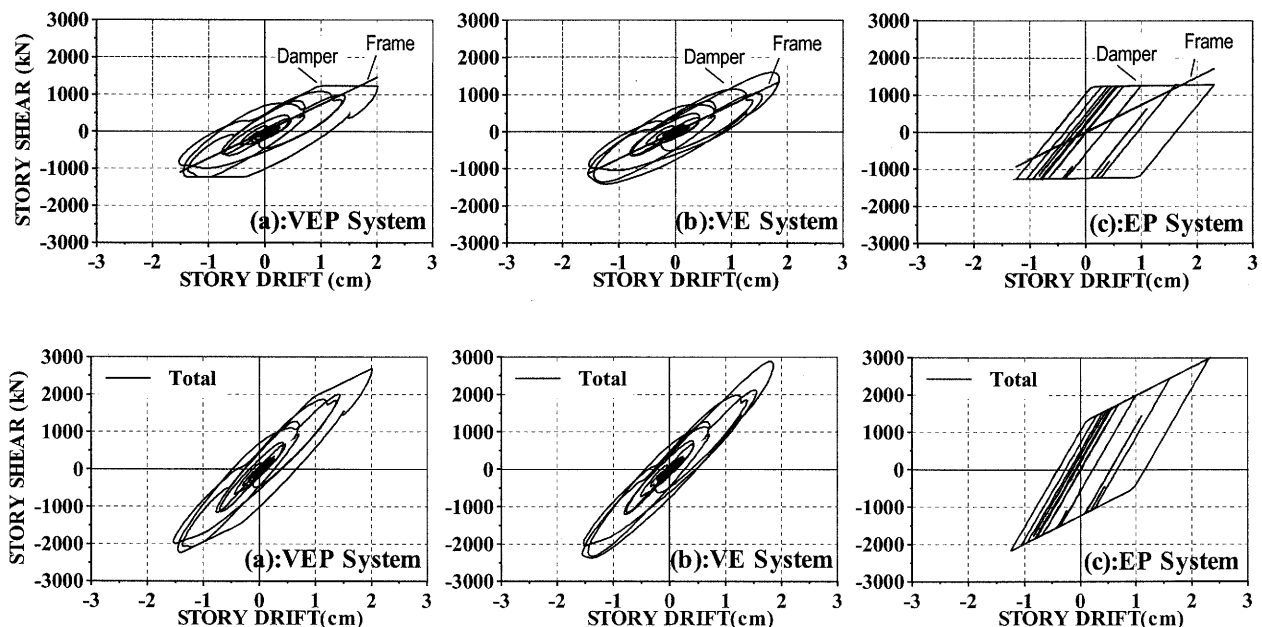


Figure 11 Responses at 1st Story Level of 3 Systems

Fig. 12 plots the peak base shear force and largest peak story drift for each of the three 12-story systems, under the JMA Kobe earthquakes of various scales ranging from 10 cm/s to 75 cm/s. Also, Fig. 13 shows the story shear distributions as well as story drift distributions of the three systems under the Level-1 (10 cm/s), Level-2 (50 cm/s), and Level-3 (75 cm/s) input. The three systems are designed to show similar peak responses under the Level-2 input. This could be confirmed from both Figs. 12 and 13.

Under Level-1 input, the VE system and the VEP system show good control of both the base shear and story drift, because each system generates damping. In contrast, the EP system shows large shear force (and accelerations, although not shown) and displacements, since no damping is generated from the EP damper under this small excitation.

Under Level-3 input, the EP system and VEP system show good control of the base and story shears by virtue of the slip mechanism that limits the damper force. Whereas, the VE system shows larger shear force, since it increases proportionally with the input magnitude.

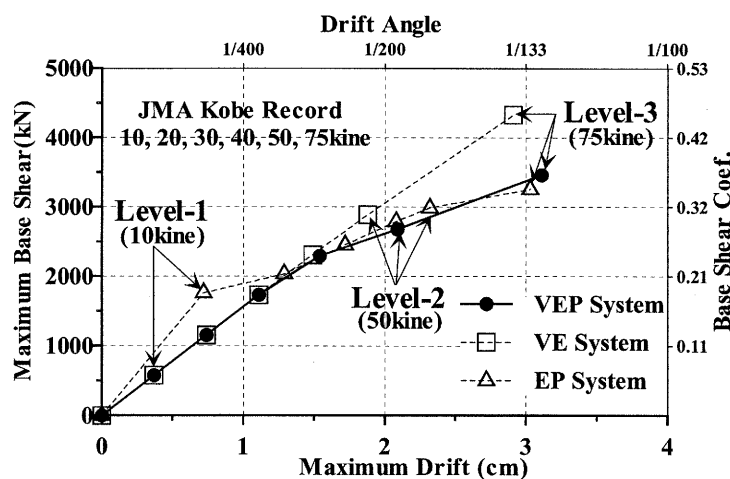


Figure 12 Base Shear Forces and Story Drifts of 3 Systems under Various Seismic Intensities

Overall, the VEP system reduces all the three response quantities of the displacement, story shear, and acceleration. The EP system and VE system show performance problems under a small/medium earthquake and a very large earthquake, respectively. It is also interesting to note that the base shear of the VEP system is always the smallest of those of both VE system and EP system under the wide range of seismic input considered (Fig. 12 and 13 Right).

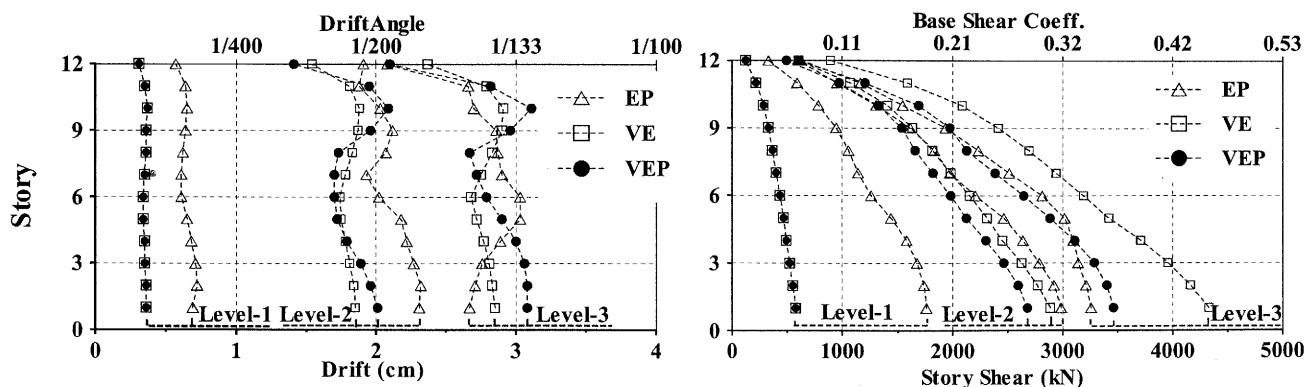


Figure 13 Drift and Shear Distributions of 3 Systems under Levels-1, 2, and 3 Inputs.

6. CONCLUSIONS

The following conclusions are given:

- (1) In the proposed visco-elasto-plastic (VEP) damper, regardless the type of excitation, not only the force but also the VE part deformation appears to be bounded, which provides confidence in deformation-based design of the VE part. This bound can be predicted by our theory to be reported elsewhere.
- (2) Experiments of an isolated VEP damper as well as a frame having the damper indicated the performance that is very consistent with the analytical predictions. Accordingly, extensive analytical work is on-going at Tokyo Institute of Technology in order to evaluate the performance of various building structures using the damper.
- (3) VEP damper combines advantages of VE device and EP device, showing excellent energy dissipation over a wide range of cyclic deformations. The VEP system shows better performance than VE and EP systems, thus, it extends performance limitations of currently used passive control systems.

Although not explained in this paper due to the page limitations, the writers have developed hand-calculation methods to predict equivalent stiffness and energy dissipation of the damper as well as equivalent period and damping ratio of the system. Future, the writers have developed an efficient design method for the VEP system. For the details, see the papers by Kasai et al. (2002a, 2005).

Acknowledgement:

This research is a part of the US-Japan Cooperative Research in Urban Earthquake Disaster Mitigation, sponsored by Monbu-Kagaku-sho and The National Science Foundation. The financial support is gratefully acknowledged. The writers also express their sincere gratitude to Prof. Kazuhiko Kawashima, a research group leader on Smart Structures for Improved Seismic Performance in Urban Regions, for his tremendous effort of research coordination and guidance.

References:

- Sasani, M. and Popov, E.P., (1997) "Experimental and Analytical Studies on the seismic Behavior of Lightweight Concrete Panels with Friction Energy Dissipators", EERC Report No.97/17, University of California, Berkeley, December
- Kasai, K., Fu, Y., and Watanabe, A. (1998a) "Two Types of Passive Control System for Seismic Damage Mitigation", *Journal of Structural Engineering*, ASCE, Vol. 124, No. 5, May
- Fu, Y., and Kasai, K. (1998b) "Comparative Study of Frames Using Viscoelastic and Viscous Dampers", *Journal of Structural Engineering*, ASCE, Vol. 124, No. 5, May
- Kasai, K., and Watanabe, A. (1997) "Performance of Passive Control Systems", Panel Discussion Paper, Panel Discussion- Comparison of Traditional Structure, Base Isolated Structure, and Passively Controlled Structures, AIJ Annual Conference, Funabashi, JAPAN (In Japanese).
- Kasai, K., Munshi, J.A., Lai, M.L. and Maison, B.F. (1993) "Viscoelastic Damper Hysteretic Model: Theory, Experiment and Application". ATC-17-1, Vol.2, 521-532, Applied Technology Council, San Francisco, CA, March.
- Kasai, K., et al. (2001) "Constitutive Rule for Viscoelastic Materials Considering Temperature, Frequency, and Strain Sensitivities, Part 1", *Journal of Structural and Construction Engineering (Transactions of AIJ)*, No. 543, 77-86, May, (In Japanese).
- Kasai, K., Teramooto, M., and Watanabe, Y. (2002a) "Behavior of a Passive Control Damper Combining Visco-Elastic and Elasto-Plastic Dampers in Series", *Journal of Structural and Construction Engineering (Transactions of AIJ)*, No. 556, 51-58, June. (In Japanese).
- Kasai, K., and Tokoro, K. (2002b) "Constitutive Rule for Viscoelastic Materials Considering Temperature, Frequency, and Strain Sensitivities, Part 2", *Journal of Structural and Construction Engineering (Transactions of AIJ)*, No. 561, 51-53, Nov. (In Japanese).
- Kasai, K., Watanabe, Y., and Nao, M. (2005), "Study on Dynamic Behavior of a Passive Control System with Visco-Elasto-Plastic Damper", *Journal of Structural and Construction Engineering (Transactions of AIJ)*, No. 588, pp. 87-94, Feb. (in Japanese)

SHAKING TABLE TEST OF PASSIVELY CONTROLLED LIGHT-GAGE STEEL FRAMES

Y. Ooki¹⁾, K. Kasai²⁾, A. Wada²⁾, M. Midorikawa³⁾,
S. Yokoyama⁴⁾, and K. Iwasaki⁵⁾

1) *Research Assoc., Structural Engineering Research Center, Tokyo Institute of Technology, Japan*

2) *Professor, Structural Engineering Research Center, Tokyo Institute of Technology, Japan*

3) *Research Coordinator of Building Technology, Building Research Institute, Japan*

4) *Assistant Manager, Technology R&D Institute, Sekisui House Ltd., Japan*

5) *Graduate Student, Dept. of Built Environment, Tokyo Institute of Technology, Japan*

ooki@serc.titech.ac.jp, kasai@serc.titech.ac.jp, wada@serc.titech.ac.jp, midori@kenken.go.jp,

yokoyan@gz.sekisuihouse.co.jp, iwasakik@enveng.titech.ac.jp

Abstract: Passive control of prefabricated light-gage steel house is discussed in this paper, and the effectiveness is validated through the shaking table tests. For effective response reduction, the structural characteristics, such as the frame stiffness, damping factor, and damper yield force are expected to be given according to the assumed earthquake intensity. The simple response evaluation method of the viscoelastic system and the elasto-plastic system is adopted, and the design procedure of the system is explained.

In order to realize the required performance, the small-sized viscoelastic damper and the friction damper are developed, and applied to light-gage steel frames. The performance of frames with dampers is compared with that of conventional frame through the shaking table tests. The shear forces and displacements of passively controlled frames were significantly reduced, and it is also verified that the damage of the frames is quite small.

1. INTRODUCTION

Prefabricated light-gage steel frame structure is one of the structural types which has relatively high seismic performance in Japan, and recently, new technical development such as the application of the seismic isolated system has been achieved. On the other hand, however, since the development of passive control for light-gage steel houses has not excessively done, there is not much room for choice of design in order to improve the seismic performance. In this paper, a passive control system for light-gage steel house is proposed for mitigating the damage under the severe earthquakes. A light-gage steel house has significantly short period as compared with the tall buildings. However, there are few researches which examine the damping effect for those systems with short period.

1.1 Intensity of Assumed Earthquake

Since the light-gage steel houses have short period, the response of the structure exists in the domain of constant acceleration response of the design spectrum. That is, since the acceleration response is constant, the displacement response is proportional to the square of the period. Such a characteristics differs from those of the high-rise and medium-rise building, and it is needed to examine the response reduction considering this difference.

Fig. 1 shows the design spectrum based on the Japanese Building Code. The structure assumed to be a two-story house on the medium soil, and the spectrum shows 1.3 g from 0.16 sec to 0.86 sec. Spectrum of JMA Kobe (NS, 1995) and Taft (EW, 1952) are also shown, which are normalized to 0.6 g of peak ground acceleration, and the average of the spectrum of these earthquakes from 0.16 sec to 0.6 sec are about 2.0 g. Here, 1.3 g acceleration response is assumed as Level 2, and 2.0 g from normalized earthquakes can be regarded as Level 3. The light-gage steel structures with passive dampers are designed against the Level 3 earthquake.

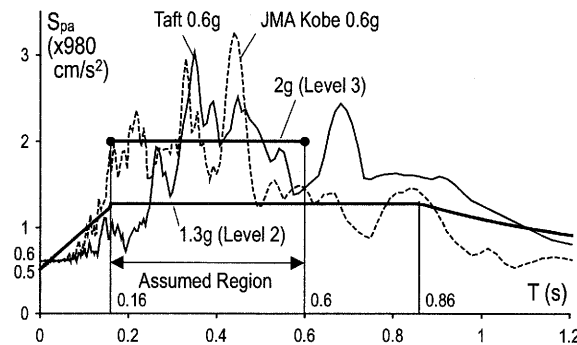


Figure 1 Response Spectrum

1.2 Prediction of Maximum Response of System with Short Period

The design aims at suppressing the story drift to 1/100 rad. and reducing acceleration as much as possible even under Level 3 earthquake. In the design procedure, the two-story light-gage steel house is assumed as SDOF model, considering the lateral stiffness of 1st story and mass ranging from the half height of 1st story to the top. However, the effect of the external and internal non-structural member is not taken into account.

The maximum response of the frame with viscoelastic dampers is evaluated using the equivalent period and damping factor. Fig. 2 shows relationship between pseudo acceleration spectrum S_{pa} and displacement spectrum S_d of the frame with viscoelastic dampers. The slope of straight portion in the figure indicates the square of the equivalent circular frequency of the system. The factor D_h , which shows the response reduction ratio when the damping factor changes from h_0 (initial damping) to h_{eq} (equivalent damping), is given as $D_h = \sqrt{(1 + 25h_0)/(1 + 25h_{eq})}$.

In Fig. 2, two types of system, $\omega_{eq}^2 = 542$ and 322 (rad.²/s²), are shown and $h_{eq} = 0.08$ and 0.26 are required respectively in order to suppress the story drift to 1/100 rad. As mentioned before, since the maximum displacement is proportional to the square of the equivalent period T_{eq} , the difference of the period has large influence on maximum displacement, and h_{eq} to provide the same maximum displacement differs considerably. For the frame with viscoelastic dampers, the equivalent period should not be short excessively and high damping should be applied to reduce not only the displacement, but also the acceleration as small as possible.

In Fig. 3, two types of system with initial elastic period $T_0 = 0.16$ and 0.21 sec are shown. Yield forces of these system are set to $0.49W$, $0.70W$ (W = weight), respectively, against the given target of the story drift (= 1/100 rad.). From the curves shown in the figure (Kasai, Ito and Watanabe, 2003), response reduction of the acceleration and displacement of elasto-plastic system can be evaluated based on the elastic period. Low yield force of the system can suppress the acceleration response while satisfying the given displacement limit. However, when the yield force is too low, it is necessary to evaluate carefully since the displacement response is sensitive to yield force.

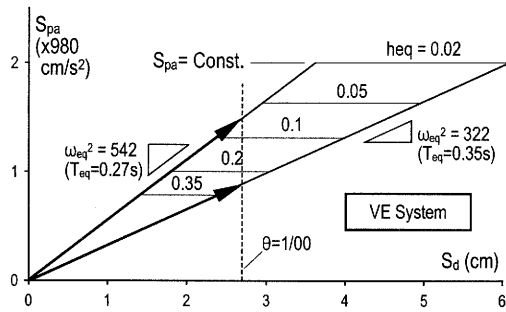


Figure 2 S_{pa} vs. S_d of Viscoelastic System

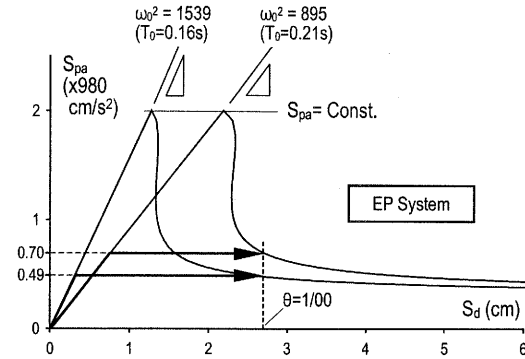


Figure 3 S_{pa} vs. S_d of Elasto-Plastic System

2. DESIGN OF LIGHT-GAGE STEEL FRAMES WITH DAMPERS

2.1 Effect of Stiffness of Major Members

The conventional light-gage steel frame can resist against the lateral force by the tension brace of 16 mm diameter steel bar. Fig. 4 shows the relationship between shear force and relative story displacement of the frame. When the compression force of the brace becomes zero, the lateral stiffness of the system is slightly changed. Tension brace yields at 21 kN, and after that, hysteresis loop shows nonlinear characteristic. This causes the decrease of the stiffness and energy dissipation, and is obstacle to the reduction of seismic response. Therefore, by applying the damper, these issues are avoided.

However, only by attaching the damper, the performance will not be improved because original frame is so flexible that connections and columns deform too much and effective damper deformation becomes relatively small. Fig. 6 is the relationship between shear force and relative story displacement obtained by analysis of viscoelastic system and elasto-plastic system (Fig. 5). Thin line indicates the original frame with dampers and bold line shows the improved frame with dampers, that is, the stiffness of the member except for the damper is doubled. The damper deformations are increased and the stiffness and energy absorption of the system are enhanced by this improvement. It is recognized that the deformation of connections and columns should be considered for enhancing the performance.

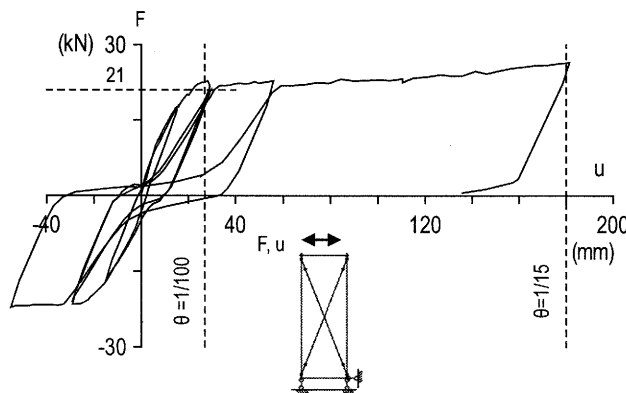


Figure 4 Shear Force vs. Relative Story Disp. of Conventional Light-Gage Steel Frame

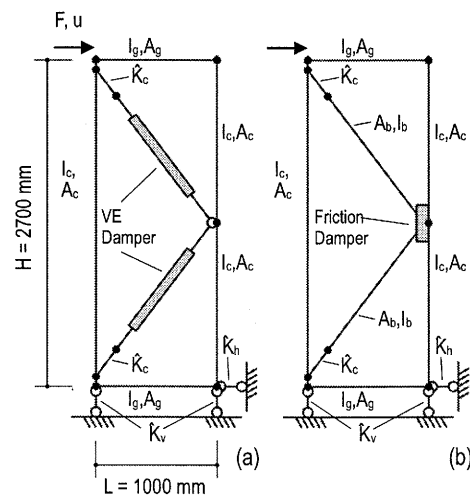


Figure 5 Numerical Model of Frame with (a) VE Damper, (b) EP (Friction) Damper

Table 1 Property of Major Members

		VE System		EP System	
		Case A	Case B	Case A	Case B
Column	Ac (cm ²)	9.4	Double	9.4	Double
	Ic (cm ⁴)	49.6		49.6	
Beam	Ag (cm ²)	2.9		2.9	
	Ig (cm ⁴)	3.3		3.3	
Brace	Ab (cm ²)	---	---	3.5	
	Ib (cm ⁴)	---	---	7.0	
Base	K _v (kN/cm)	716.1	Double	716.1	
Joint	K _c (kN/cm)	887.3		2278.0	
	K _h (kN/cm)	206.7		206.7	
Damper		K _d ' = 42.5 (kN/cm) C _d = 2.3 (kN*s/cm)		F _d y = 60.0 (kN)	

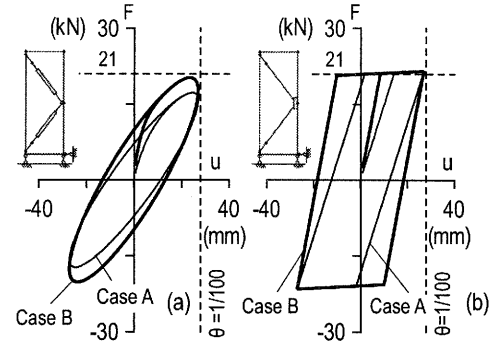


Figure 6 Result of Numerical Analysis Using Models Shown in Figure 5

2.2 Details of Proposed Frames

Fig. 7 shows the light-gage steel frames examined in shaking table test. The dimension is 2.7 m by 1 m. (a) is conventional frame with steel braces. (b) and (c) are the frame with viscoelastic damper and the frame with friction damper, respectively. As mentioned before, original frame is so flexible that connections and columns deform too much. To avoid this, stiffness of the column and connection is increased by making the steel members thicker, by welding the steel plate at the brace joint, and by piling up a thick washer plate to the base plate of column base.

Yield force of conventional frame is about 21 kN, and the frames with dampers are designed so that they have similar strength. The details shown here are designed to avoid great change of the member size since those matters often requires remodeling of the manufacturing system.

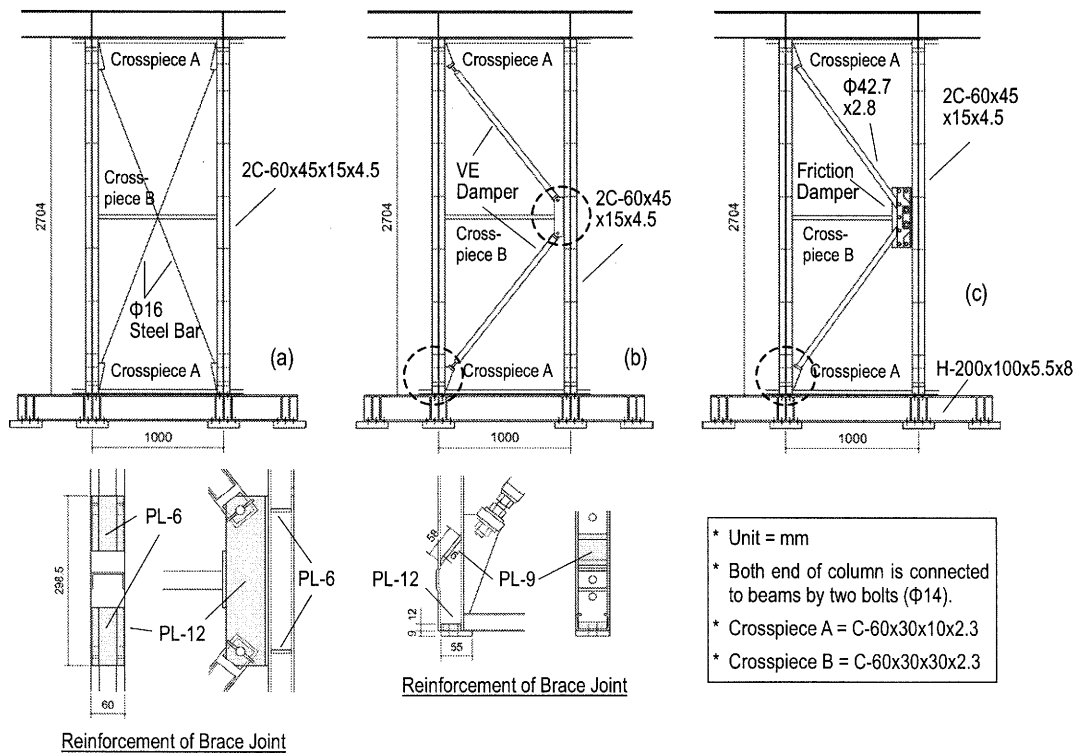


Figure 7 (a) Frame with Steel Braces, (b) Frame with Viscoelastic Dampers, and (c) Frame with Friction Damper

2.3 Details of Applied Dampers

Fig. 8 shows the details of viscoelastic damper. Since the viscoelastic material is settled between the inner and outer steel tube, the damper becomes compact. Viscoelastic material used here shows an elliptic stress-strain relationship under small strain, and it changes to a bi-linear hysteresis as the strain increases. By this characteristic, the damper force under large deformation is mitigated.

Large initial stiffness of the elasto-plastic system can contribute to the reduction of maximum displacement (Sec. 1.2). The initial stiffness of friction damper is significantly large, and this characteristic is suitable to our purpose. The details of friction damper are shown in Fig. 9. This damper is applied the brake pad used in automobiles, and the dimensions of the pad is only 50 mm by 50 mm. These pads are tightened with two high-tension bolts, and the pre-tension force is controlled by the bolt gauge.

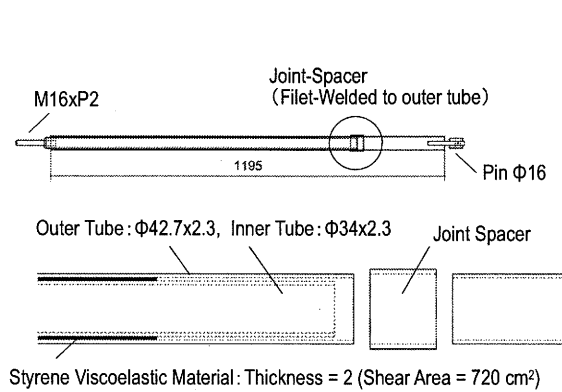


Figure 8 Viscoelastic Damper

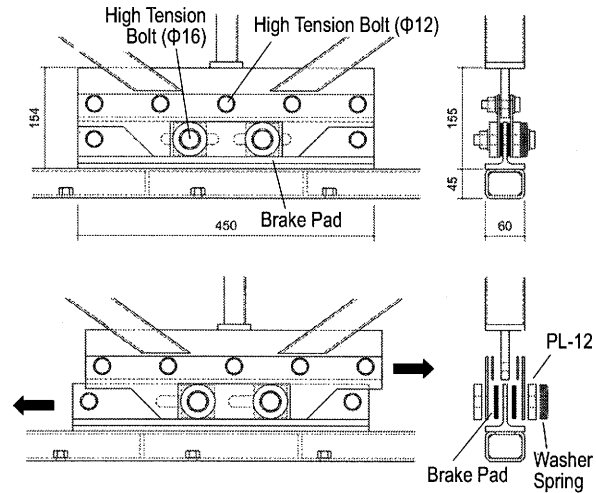


Figure 9 Friction Damper

2.4 Required Damper Size

Conventional light-gage steel frame cannot resist against the lateral force without the brace. This indicates that the system can be evaluated using simplified model which consists of two kinds of springs representing the damper and other major member shown in Fig. 10.

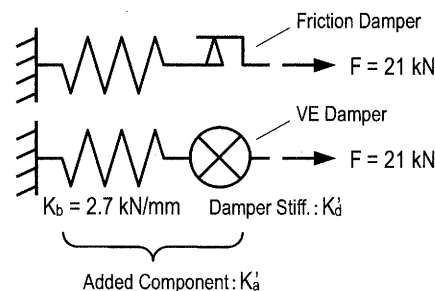


Figure 10 Simplified Models Representing Light-Gage Steel Frames with Dampers

Typical natural frequency is supposed 3.1 Hz (Ooki, Kasai, and et al., 2004) in this study, and how to decide the shear area of viscoelastic material under ambient temperature 20 °C is explained. The target performance is set as shear force at story drift 1/200 rad. (relative story displacement = 13.7 mm) = 21.3 kN. Equivalent stiffness K'_d at this point is evaluated as follows (Kasai and Kibayashi, 2003):

$$\text{Stiffness of Added Component: } K'_a = \frac{\{(1+\eta_d^2)K'_d + K_b\}K'_dK_b}{(K'_d + K_b)^2 + (\eta_d K'_d)^2} \quad (1)$$

$$\text{Target: } K'_a = F/(H/200) = 1.56 \text{ kN/mm}$$

where η_d = loss factor of VE damper, K'_d = damper stiffness (two dampers in series are considered), K_b = stiffness of member in series (2.70 kN/mm). When supposing $\eta_d = 0.9$ and substituting it to Eq. (1), $K'_d = 2.62$ kN/mm is obtained. Then damper deformation u_d in Fig. 10 is obtained as $u_d = F/K'_d = 8.0$ mm. The deformation parallel to the movable direction of the damper $\hat{u}_d = 5.0$ mm since the cosine of the angle between the brace and horizontal line is 0.62.

If the thickness of viscoelastic material is given as $d = 2.0$ mm, the shear angle of the material applied to one damper $\gamma_d = (\hat{u}_d/2)/d = 2.5/2 = 1.25$. From our research on viscoelastic material (Kasai, Ooki, and et al., 2002), storage modulus G' and loss factor of the damper can be evaluated, using frequency (3.1Hz), ambient temperature (20 °C), and shear angle of the material γ_d , as $G' = 30.0 \times 10^{-5}$ kN/mm² and $\eta_d = 0.84$. Obtained η_d is almost same with supposed one, and in such a case, loss factor of added component is 0.32 and equivalent damping ratio is evaluated as 0.16 (Kasai and Ookuma, 2001). Finally, required shear area of viscoelastic material used for one damper is obtained:

$$A_s = 2d K'_d / G' / (0.62)^2 = 90878 \text{ mm}^2 \quad (2)$$

However, for the damper shown in Fig. 8, it is difficult to hold the shear area shown above because of the limit of length and diameter of the steel pipe, therefore 80000 mm² is adopted.

On the other hand, as for the friction damper, it is needed to be consistent with $F = 21$ kN (Fig. 10) and yield force of controlled frame F_y . By transforming F to movable direction of friction damper, required damper force F_d is obtained:

$$F_d = F \times H/L = 21 \times 2.7 = 56.7 \approx 60 \text{ kN} \quad (3)$$

3. SHAKING TABLE TEST OF PASSIVELY DAMPED SYSTEM

3.1 Specimens and Applied Excitations

By combining the three kinds of light-gage frames, five kinds of specimens are tested. That is, frame with two sets of conventional braces, viscoelastic dampers, friction dampers, frame with brace and viscoelastic damper, and brace and friction damper (Fig. 11). Test scheme is shown in Table 2, and the natural period and the damping factor are evaluated using the white noise before and after the each loading in order to examine the damage of the specimens.

Fig. 12 shows the overview of the specimen on the shaking table. The specimen has three planes parallel to the earthquake direction, and the brace/damper are applied to the center plane.

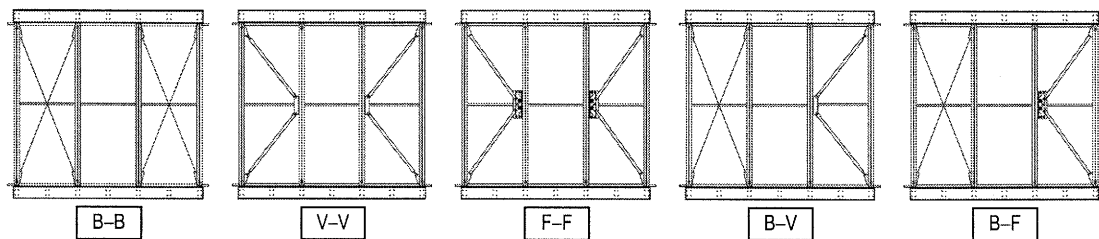


Figure 11 Combinations of Frames

Outer planes on both sides consist of the beams and slender columns, and they can hardly resist to the lateral force. And the weights on the specimen are distributed so that the axial force of the column is similar to that in the actual houses. Total weight is 65 kN.

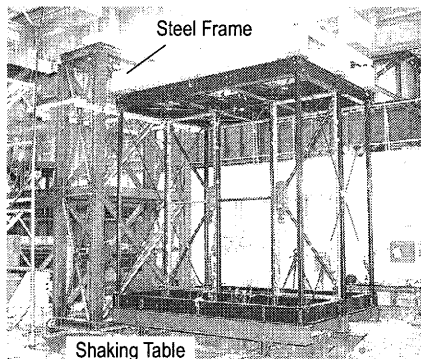


Figure 12 Specimen on Shaking Table

Table 2 Applied Earthquakes

No.	Earthquake	PGA (cm/s ²)
1	White Noise w1	
2	Hachinohe (NS, 1968)	200
3	White Noise w2	
4	Taft (EW, 1952)	200
5	White Noise w3	
6	JMA Kobe (NS, 1995)	200
7	White Noise w4	
8	JMA Kobe (NS, 1995)	600
9	White Noise w5	
10	JMA Kobe (NS, 1995)	200
11	White Noise w6	
12	Taft (EW, 1952)	600
13	White Noise w7	

* Peak Ground Acc. of White Noise = 100 cm/s²

3.2 Test Results

Fig. 13 shows the maximum relative story displacement and base shear of the specimens. As for specimen F-F, response under Level 3 earthquake is considerably small and almost equal to 1/100 rad. Total amount of viscoelastic material is smaller than that is expected (Sec. 2.4), therefore the responses of specimen V-V and B-V are slightly large as compared to specimen F-F or B-F. The maximum base shear through the test is not so different among all of specimens because the increase of the shear force is mitigated by the changing of the stiffness of the damper or the yielding of the braces.

Fig. 14 shows the natural frequency and damping factor of specimen. These are calculated from the transfer function obtained from test results under white noise waves. The specimen which consists of two sets of damper frames doesn't change the frequency, and this indicates that these specimens are hardly damaged under Level 3 earthquakes. The frame with viscoelastic

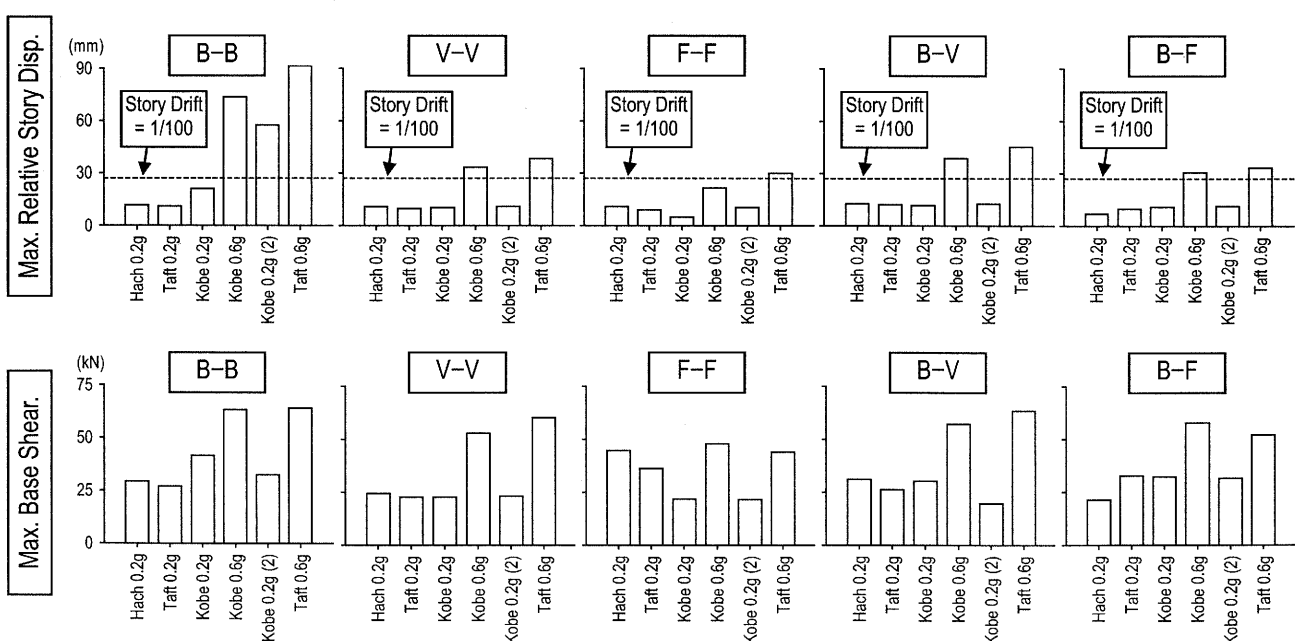


Figure 13 Maximum Responses (Relative Story Displacement and Base Shear)

damper shows about damping ratio of 13 %, and frame with friction damper shows about 2 % because the damper doesn't work under small deformation caused by white noise. The reduction of stiffness can be supposed by the changing of the natural frequency, and the stiffness of conventional frame becomes 1/10 as compared with initial condition. In the case of the specimen B-V and B-F, in which the brace and the damper are combined, reduction of stiffness is about half.

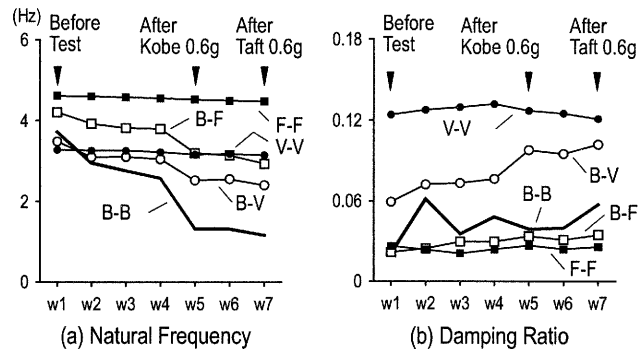


Figure 14 Natural Frequencies and Damping Ratios Obtained from Transfer Function under White Noise Excitations

4. CONCLUSIONS

A passive control technology was applied to prefabricated light-gage steel frame and the effectiveness was verified by the shaking table test. The results are concluded as follows:

- 1) Using the response spectrum, the design policy of the passively controlled frame was shown. For the viscoelastic system, high damping was rather required for the response reduction. On the other hand, the high stiffness caused good control to the elasto-plastic system.
- 2) Lateral stiffness and energy dissipation capability were improved not only by applying the dampers, but also by increasing the stiffness of major members. Without this improvement, the contributions of major members to the story drift were too large and the performance of the passively controlled frame was spoiled.
- 3) Two kinds of compact dampers were developed. These small size dampers are needed so that the application of the passive dampers did not affect the manufacturing system of the pre-fabricated light-gage steel frames.
- 4) Five specimens were tested by shaking table. Conventional frame showed the story drift of 1/30 rad. under Level 3 earthquake, while the frame with dampers showed 1/2 to 1/3 responses. The specimens with two sets of damper frames were hardly damaged under Level 3 earthquakes.

References:

- Kasai, K. and Ookuma, K. (2001), "Kelvin-Type Formulation and Its Accuracy for Practical Modeling of Linear Viscoelastic Dampers Part 1: One-Mass System Having Damper and Elastic/Inelastic Frame", *Journal of Struct. Constr. Engng. of AIJ*, (550), 71-78 (in Japanese)
- Kasai, K., Ooki, Y., Amemiya, K., and Kimura, K. (2002), "Nonlinear Model of Isobutylene Viscoelastic Materials Considering Temperature, Frequency, and Strain Sensitivities", *Proc. of 3rd Symposium on Passively Controlled Structures, Tokyo Institute of Technology*, 181-194, (in Japanese)
- Kasai, K., Ito, H., and Watanabe, A. (2003), "Peak Response Prediction Rule for A SDOF Elasto-Plastic System Based on Equivalent Linearization Technique", *Journal of Struct. Constr. Engng. of AIJ*, (571), 53-62 (in Japanese)
- Kasai, K. and Kibayashi, M. (2003), "Manual of Design and Construction for Passively Controlled Structures", Japan Society of Seismic Isolation (JSSI), (in Japanese)
- Ooki, Y., Kasai, K., Wada, A., Midorikawa, M., Yokoyama, S., and Iwasaki, K. (2004), "Passive Control of Prefabricated Light-Gage Steel Houses: Dynamic Loading Test, Shaking Table Test, and Analysis", *Proc. of 4th Symposium on Passively Controlled Structures, Tokyo Institute of Technology*, 203-218, (in Japanese)

PROPOSAL REGARDING SEISMIC STRENGTHENING CHARACTERISTICS FOR MORE EFFICIENT EARTHQUAKE DISASTER MITIGATION OF WOODEN HOUSES

Y. Yoshikawa¹⁾, K. Ouchi²⁾, M. Harada³⁾

1) Toyota Auto Body Co., Ltd., Japan

2) Nox Electronics Co., Ltd., Japan

3) Managing Director, Toyota Auto-body Co., Ltd., Japan

yosik123@aqua.ocn.ne.jp, kimihiro.ouchi@exc.tokai-rika.co.jp, MINORU.HARADA@mail.toyota-body.co.jp,

Abstract: This paper proposes a method using strength oriented and passively controlled earthquake resistant structures to enable earthquake disaster mitigation, including that of existing wooden buildings, to progress more efficiently. A two-DOF model was created to represent a building, and the force characteristics were assumed to have nonlinear elasticity. Buckling analysis was performed to formulate the modes of building collapse, and a method of seismic strengthening was determined by analyzing how to stabilize these modes. Returning to the subject of building earthquake response analysis, this paper also describes the restoring force characteristics that are required for seismic strengthening of buildings on an overall and a local basis, after performance evaluations are taken into consideration.

1. Introduction

It has been suggested that not enough progress is currently being made in Japan with regard to earthquake disaster mitigation for houses in need of measures for earthquake resistance. This process, however, takes a considerable amount of time. Performing a seismic diagnosis to investigate the entire structure of a building so that the appropriate strengthening technique can be determined is time consuming and expensive. Furthermore, houses have a myriad of structural features, all of which require individual measures to be carried out. It is currently felt that substantial progress can be made toward earthquake disaster mitigation if two conditions can be achieved for buildings as groups. These are, 1) if demonstrable building strengthening characteristics for seismic performance can be expressed for structures as a whole; and 2) if, for existing wooden houses, methods (including the application of local measures) can be expressed to convert buildings as a whole into buildings that possess a seismic performance. If this is possible, then progress may be made toward a concept of earthquake resistance that treats buildings as groups rather than individually. The analysis performed in order to formulate this method took into consideration the fact that substantial damage is caused as a result of the collapse of roofs and the like. The first step of the analysis was the classification of the modes of collapse deformation for buildings as a whole. These classifications were then used to determine a method to perform seismic strengthening on a comprehensive basis.

2. Method of Analysis

2.1 Methods of earthquake disaster mitigation

Preventing the collapse of houses, which are comprised of various types of structural features, requires exhibition of the necessary seismic strengthening characteristics. A method for more efficient earthquake disaster mitigation of wooden houses is considered on the basis of the current movement toward a performance-based code, and demands for design and strengthening techniques based on seismic performance evaluations. The method employed two-DOF model analysis,

taking a nonlinear restoring force into consideration as the seismic strengthening characteristic that reduces building response acceleration on a multi-step basis. As a result, the following method can be proposed. This method assumes that the earthquake-opposing restoring force characteristics that a building should possess have been determined. If this is the case, seismic performance may be achieved by designing these characteristics into newly constructed buildings or, if local strengthening is being applied to an existing building, by carrying out the strengthening so as to engender these characteristics. Furthermore, this proposal shows that it is possible to carry out local strengthening simply by providing a characteristic whereby stiffness is changed multi-step wise, which is similar to the characteristics that a building as a whole should possess. As a result, earthquake resistance design is feasible using the same method for new buildings and existing buildings.

2.2 Analysis settings

a) Modes of deformation

Fig. 1 shows typical patterns of damage (mainly collapse) suffered by wooden houses in the 1995 Hyogo-ken Nanbu Earthquake. It was reported that the most common form of damage suffered by general houses was the tilting or collapse of portions of the first story, followed by the collapse of the second story or roof (trusses). Traditional style wooden houses that had totally collapsed or that had suffered lateral movement were also observed. When analysis settings were made in the method described below for the deformation and restoring force characteristics of wooden unit frames, the dominant mode of unit frame deformation was assumed to be that of shear deformation. Note that deformation was assumed to be small displacement, and that the lateral movement or the dislocation of pillars, and other forms of rigid body displacement were not taken into consideration.

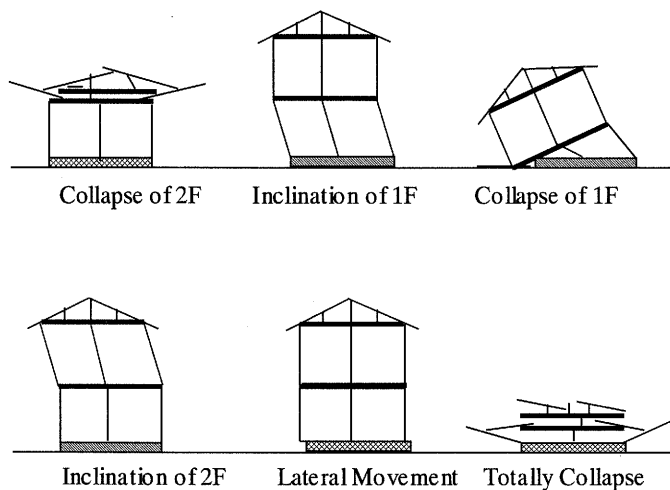


Figure 1 Modes of Deformation

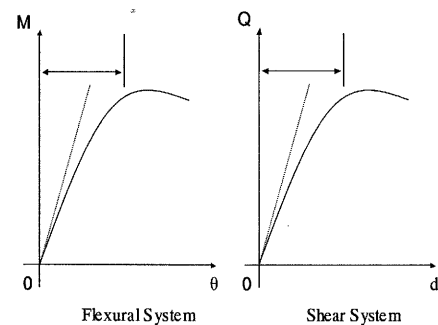


Figure 2 Restoring Force Characteristics

b) Unit frame restoring force characteristics

The unit frame restoring force characteristics were calculated by superimposing the models of the restoring force characteristics for each earthquake-resisting element (unit frames). In this paper, the restoring force characteristics of the earthquake-resisting elements are considered to have the nonlinear elasticity shown in Fig. 2. Here, the lateral displacement of each element within the unit frame was assumed to be uniform, and the axial deformation of the horizontal members (beams) that connect the top of each earthquake-resisting element pillar was assumed either to be zero, or at an ignorable level.

2.3 Analysis flow

The first step in the analysis procedure was the classification of the modes of collapse deformation for buildings as a whole. The process up to the point of collapse was analyzed by treating the issue as a buckling problem under vertical load. For this purpose, a two-DOF model with various types of mass distributions was created to represent a building. The restoring force characteristics of each building layer were assumed to have nonlinear elasticity. The perturbation frequency of the system was also calculated by integrating perturbation theory for nonlinear systems into the analysis.

Next, a horizontal restoring force was imparted in order to determine a method of seismic strengthening capable of preventing collapse deformation, in an attempt to stabilize the building. In other words, stabilization analysis was carried out with regard to a restoring force that applies a horizontal force, instead of one that is strengthening-based. By doing so, it was possible to clarify a method for strengthening buildings on an overall and a local basis, in accordance with the classifications of the modes of collapse.

Subsequently, the seismic strengthening characteristics required for a building as a whole, which take the various performance evaluations for the method of strengthening into consideration, were determined by resolving the earthquake response problem using the similar two-DOF model. Finally, a method of seismic strengthening by means of local strengthening was determined for existing wooden buildings. The summary of analysis flow is shown in Fig. 3.

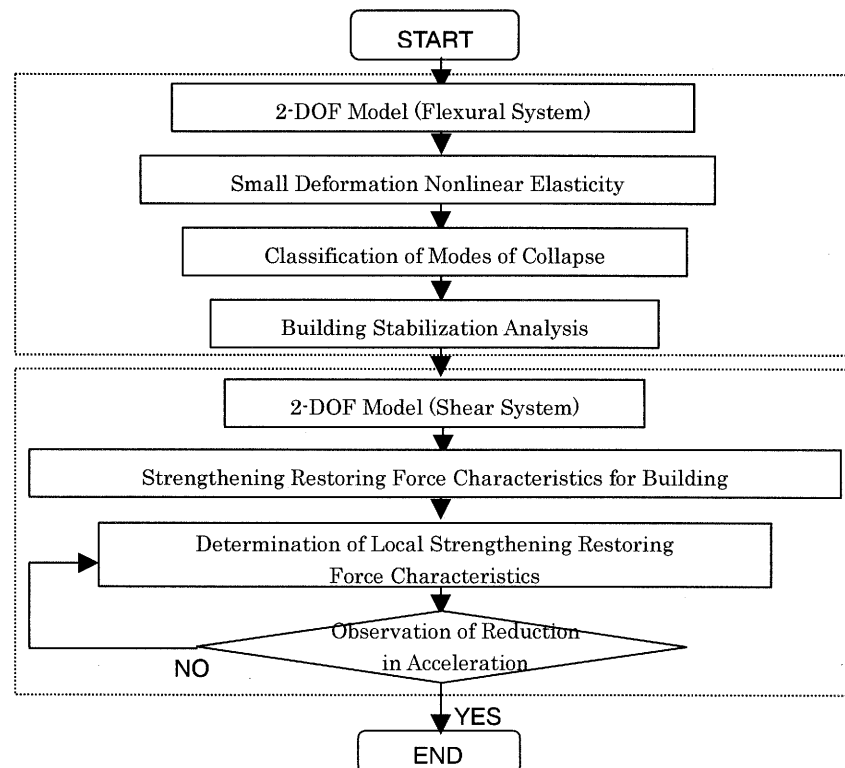


Figure 3 Flow Chart

3. Analytical Model

3.1 Two-DOF model

The two-DOF model of a building as shown in Fig. 4 was applied for the purposes of expressing the modes of collapse deformation and for analysis of methods of strengthening. For the purpose of analysis, this diagram assumes the action of static end loads P_v (vertical load) and P_h (horizontal

load). Furthermore, the hinges that express the restoring moment of the pillars are assumed to have the nonlinear elasticity characteristics as described in Section 2.2 b). The modes of collapse deformation are analyzed below within the range of small deformation.

First, the modes of collapse deformation were analyzed and categorized as a buckling problem of the structure under the action of only the vertical load P_v . Then, stabilization states were examined after the application of the horizontal load P_h as a restoring force against these unstable modes. As shown in Fig. 4, these stability states come down to a question of the external forces acting while being maintained at a constant angle of ϕ times the tangential angle of the end of the system. In other words, when $\phi=0$, only the vertical load P_v acts, while $\phi \neq 0$ is equivalent to the presence of a non-conservative force (follower force), in which the horizontal load P_h also acts.

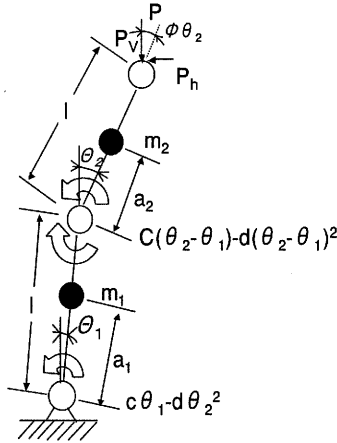


Figure 4 Two-DOF Models

3.2 Basic equations

The hinges in the analytical model shown in Fig. 4, which possess a nonlinear restoring force, are assumed to have the characteristics as shown in Fig. 2. This restoring force is relatable using the following equation, in accordance with the nonlinear elastic potential U , with regard to a small dimensionless relative displacement d .

$$\frac{dU}{dd} = c\delta - dd^2 \quad (c > 0, d > 0) \quad \text{-----(1)}$$

The analytical model shown in Fig. 4, which is comprised of a series of stiff members joined by hinges with the nonlinear elasticity described in equation (1), is a two-DOF model in which the length l of the stiff members has a common value, and m_1 and m_2 are concentrated masses located freely at positions a_1 and a_2 on the respective members. Thus, when the vertical and the horizontal external forces are acting on this system, the following equation of motion can be acquired, taking the small rotation angles θ_1 and θ_2 of each mass point into consideration, and calculating the relative displacement in equation (1) as $d=\theta_i - \theta_{i-1}$ ($i=1, 2; \theta_0=0$) by non-dimensional forms;

$$\left. \begin{aligned} (g_1 l_1^2 + g_2) \ddot{\theta}_1 + g_2 l_2 \ddot{\theta}_2 + (2 - \kappa^2) \theta_1 \\ + (f \kappa^2 - 1) \theta_2 - \beta (2 \theta_1 \theta_2 - \theta_2^2) &= 0 \\ g_2 l_2 \ddot{\theta}_1 + g_2 l_2^2 \ddot{\theta}_2 - \theta_1 + \{1 - (1-f) \kappa^2\} \theta_2 \\ - \beta (\theta_1 - \theta_2)^2 &= 0 \end{aligned} \right\} \quad \text{----- (2)}$$

where κ^2 is the load parameter and β is the nonlinear elasticity parameter. g_1 and g_2 , and l_1 and l_2 denote the mass ratio and position of each concentrated mass respectively. The respective definitions are as follows.

$$\kappa^2 = \frac{Pl}{c}, \quad \beta = \frac{d}{c}; \quad m_1 = g_1 m, \quad m_2 = g_2 m, \quad a_1 = l_1 l, \quad a_2 = l_2 l \text{-----}(3)$$

4. Stability Analysis

4.1 Determination of nonlinear system frequencies

Since basic equation (2) is a nonlinear differential equation system, a solution was determined conventionally by means of fixed components. This, however, could not be applied directly under the stability criterion method, which involves finding the root of the characteristic equation, i.e. the natural frequency. Therefore, the nonlinear system was analyzed in accordance with perturbation theory. By doing so, it was possible to determine a frequency with the characteristics of this nonlinear system once a perturbation approximation solution was calculated using a nonlinear elasticity parameter β as the perturbation parameter. This enabled the behaviour of the system to be analyzed. Hereafter, β is assumed to have a low range value. To carry out the analysis, the linear term (the term where $\beta=0$) of basic equation (2) is transformed by normal coordinates. When diagonalization is performed, the following result is obtained.

$$\left. \begin{aligned} \ddot{\xi}_1 &= -\omega_1^2 \xi_1 + \beta(e_1 \xi_1^2 + e_2 \xi_1 \xi_2 + e_3 \xi_2^2) \\ \ddot{\xi}_2 &= -\omega_2^2 \xi_2 + \beta(e_4 \xi_1^2 + e_5 \xi_1 \xi_2 + e_6 \xi_2^2) \end{aligned} \right\} \text{-----}(4)$$

The form of the solution with respect to basic equation (4) expressed by the normal coordinates (ξ_1, ξ_2) is assumed to be as follows, with β as the perturbation parameter.

$$\xi_1 = A_1 \cos t_1 + \beta \xi_{11} + \beta^2 \xi_{12} + \dots, \quad \xi_2 = A_2 \cos t_2 + \beta \xi_{21} + \beta^2 \xi_{22} + \dots \text{-----}(5)$$

where $t_1 = O_1 t + v_1$, $t_2 = O_2 t + v_2$, in which O_1 and O_2 are natural frequencies to be determined below taking the nonlinear terms into consideration. v_1 and v_2 denote the initial phase.

The solution from equation (5) is substituted into basic equation (4) in order to determine the frequencies O_1 and O_2 , which have nonlinear system characteristics. As a result, the following is obtained for up to the second order term of β . When the various amounts (3) denoting the mass ratio and the position in the model shown in Fig. 4 are as follows,

$m_1 = 2m$, $m_2 = m$, $a_1 = l$, $a_2 = l$, the change in the nonlinear system frequencies O_1^2 and O_2^2 with respect to the vertical load κ^2 is as shown in Fig. 5.

$$\begin{aligned} O_1^2 &= \omega_1^2 - \beta^2 \left\{ \frac{e_2^2 A_2^2}{4\{\omega_1^2 - (O_1 + O_2)^2\}} + \frac{e_3 e_5 A_2^2}{2\{\omega_2^2 - (O_1 + O_2)^2\}} + \frac{e_2^2 A_2^2}{4\{\omega_1^2 - (O_1 - O_2)^2\}} + \frac{e_3 e_5 A_2^2}{2\{\omega_2^2 - (O_1 - O_2)^2\}} \right. \\ &+ \left. \frac{e_1^2 A_1^2}{2\{\omega_1^2 - 4O_1^2\}} + \frac{e_2 e_4 A_2^2}{4\{\omega_2^2 - 4O_1^2\}} + \frac{e_1^2 A_1^2 + e_1 e_3 A_2^2}{\omega_1^2} + \frac{e_2 e_4 A_1^2 + e_2 e_6 A_2^2}{2\omega_2^2} \right\} \text{-----}(6) \end{aligned}$$

$$O_2^2 = \omega_2^2 - \beta^2 \left\{ \frac{e_2 e_4 A_1^2}{2\{\omega_1^2 - (O_1 + O_2)^2\}} + \frac{e_5^2 A_1^2}{4\{\omega_2^2 - (O_1 + O_2)^2\}} + \frac{e_2 e_4 A_1^2}{2\{\omega_1^2 - (O_1 - O_2)^2\}} + \frac{e_5^2 A_1^2}{4\{\omega_2^2 - (O_1 - O_2)^2\}} \right. \\ \left. + \frac{e_3 e_5 A_2^2}{4\{\omega_1^2 - 4O_2^2\}} + \frac{e_6^2 A_2^2}{2\{\omega_2^2 - 4O_2^2\}} + \frac{e_1 e_5 A_1^2 + e_3 e_5 A_2^2}{2\omega_1^2} + \frac{e_4 e_6 A_1^2 + e_6^2 A_2^2}{\omega_2^2} \right\} \quad (7)$$

On the curves for O_1^2 and O_2^2 in the same diagram, the static Euler buckling load value (assumed to be κ_{cr}^2) can be acquired by making the linear frequency $\omega_1^2 \rightarrow 0$. The frequency O_1^2 in the nonlinear system, however, causes substantial differences in behaviour. As shown in Fig. 5, a change was observed in the frequency of the system when $\kappa^2 = \kappa_{cr}^2$, with $\beta = 0.1$. The buckling of the building occurs following the “Transitional” type of collapse mode.

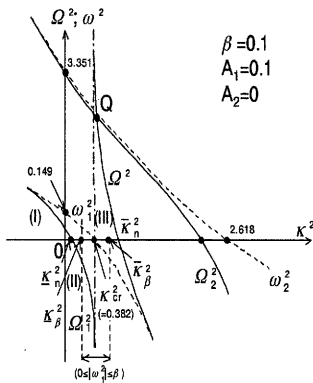


Figure 5(1) Frequency Curves of Nonlinear System

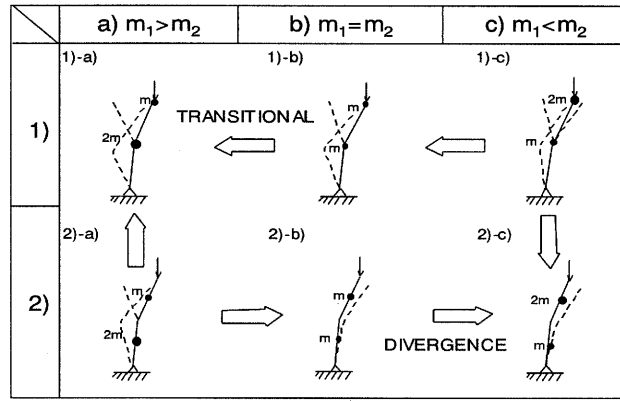


Figure 7 Changes of Instability Modes in Systems

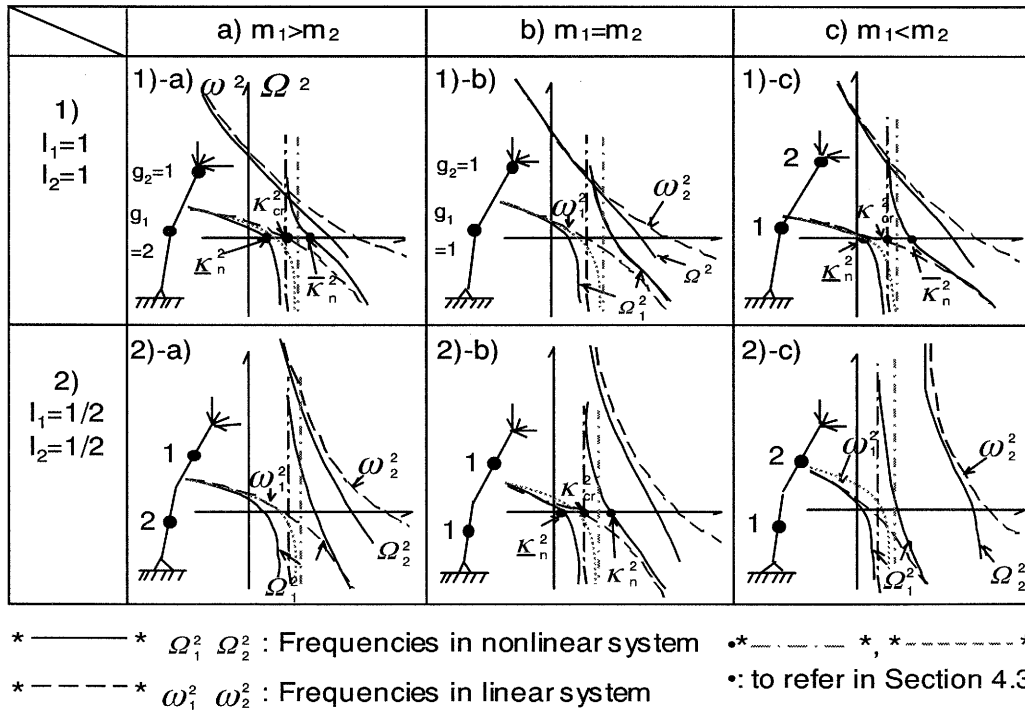


Figure 6(1) Changes of Frequency Curves in Systems

4.2 Buckling analysis: analysis of modes of collapse

The analysis from the previous sections was used to try to express classifications of the modes of collapse deformation for the wooden buildings described in Section 2.2 based on the analytical model. The amounts denoting the various mass ratios and mass positions are expressed as follows;

$$\begin{array}{lll} \text{a) } m_1 > m_2 & \text{b) } m_1 = m_2 & \text{c) } m_1 < m_2 \\ 1) l_1 = 1, l_2 = 1 & 2) l_1 = 0.5, l_2 = 0.5 & \end{array} \quad (8)$$

Figs. 6 shows the changes with respect to the vertical load $\kappa^2 (P_v)$ that has the nonlinear system frequencies O_1^2 and O_2^2 (the same as described above) in each respective case. These are shown in Fig. 7 alongside the form taken by the instability modes. Two classifications are shown, "Divergence" caused by the primary mode of collapse, and "Transition", where a shift to a secondary mode occurs.

These classifications are compatible with the classifications of collapse modes indicated in Fig. 1 of Section 2.1.

4.3 Stabilization analysis: seismic strengthening analysis

In the model described in Fig. 4 of Section 3.1, instability states caused by the vertical load can be stabilized by imparting the horizontal force P_h . In other words, it is possible to describe an increase in the critical value on application of the restoring force for seismic strengthening. This involves adding the horizontal force P_h to basic equation (2) and calculating the frequency, and it can be given in the same form as equations (6) and (7). The colored lines in Fig. 6 show the respective results when $P_h=0.2P_v$, for the case of the mass distribution. In the frequency curves O_1^2 and O_2^2 , the stable region in the Divergence classification caused by the primary mode of collapse was enlarged. With the Transition classification, the shift to the secondary mode occurs. In other words, a method of strengthening using the application of the horizontal force P_h can be considered as a quantitative method for preventing building collapse.

5. Efficient Methods of Seismic Strengthening

5.1 Overall seismic strengthening

5.1.1 Response analysis

The characteristics for strengthening a building as a whole (i.e., the strengthening restoring force characteristics) were determined as restoring force characteristics that reduce the building response acceleration on a multi-step basis in response to the requirements of the various performance evaluations. A model of a two-layer building has been presented as shown in Fig. 4 of Section 3.1 for stability analysis. The model is shown as a shear system for response analysis in Fig. 8 (1). In the model, damping is not taken into consideration, and the first and second layers of the building have been provided with the three types of nonlinear elasticity characteristics as shown in Fig. 8 (2). The equations of motion for each layer when the external forces impart a typically harmonically seismic load (with a ground acceleration of \ddot{u}_g) as displacements u_1 and u_2 of each layer are as follows;

$$\left. \begin{array}{l} g_1 \ddot{u}_1 + (2u_1 - u_2) - \beta(u_2^2 - 2u_1 u_2) = -g_1 \ddot{u}_g \\ g_2 \ddot{u}_2 + (u_1 - u_2) - \beta(u_2 - u_1)^2 = -g_2 \ddot{u}_g \end{array} \right\} \text{-----} (9)$$

where the restoring characteristics of the strengthening members are expressed by the following equation

$$Q = c_b d_i + d_b d_i^3 \quad (d_i = u_i - u_{i-1}) \text{-----(10)}$$

Here, the parameters in the above equation are the same as in equations (2) and (3) in Section 3.2, and the stiffness of each layer is assumed to be equal. The respective definitions are: $\beta = d_b/c_b, g_1 = 2, g_2 = 1, k_1 = k_2 = c_b$.

Fig. 8 shows numerical results calculated at this point for acceleration generated on the second story of the building when a harmonically seismic load is imparted. The stiffness after strengthening in the diagram is rated according to size as $I < II < III$. It was found that the greater the stiffness of the nonlinear spring characteristic (when the nonlinear elasticity shown in Fig. 8(2) for 3 types β 's, respectively), the lower the peak values for response acceleration with respect to the same harmonic forces as shown in Fig. 8(3).

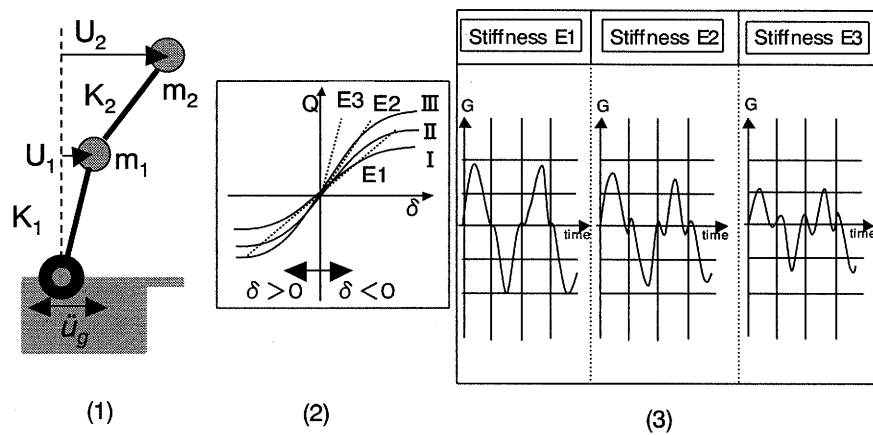


Figure 8 Response Analysis: (1) 2-DOF Model (2) Q-d (3) Result of Analysis

5.1.2 New strengthening proposal

The results calculated for response in Fig. 8 (3) show that the seismic force and acceleration after strengthening decrease in sequence with the initial stiffness values I, II and III (denoted respectively as E1, E2 and E3). The diagram also shows that the peak values decrease if, after strengthening, initial stiffness changes from $I \Rightarrow II \Rightarrow III$ multi-step wise in accordance with the performance requirements. It is therefore possible to propose the following strengthening characteristics that incorporate this multi-step change in stiffness (see Fig. 9(2)), and perform elastic restoration and hysteresis damping (see Fig. 9 (3)). That is, the proposal incorporates the following characteristics:

- (1) $E1 < E2 < E3$; (2) elastic restoration; and (3) hysteresis damping.

To carry out strengthening to reduce factors such as seismic force, acceleration, and the like to targeted design values, it is therefore sufficient to strengthen the building as a whole to achieve these reduced values by employing characteristics that cause stiffness to change multi-step wise and that also perform hysteresis damping.

LEVEL	Deformation	Criterion
I	$0 \sim \delta_1$	$0 < Q < Q_1$
II	$\delta_1 \sim \delta_2$	$Q_2 < Q < Q_3$
III	$\delta_2 \sim$	$Q_4 < Q$

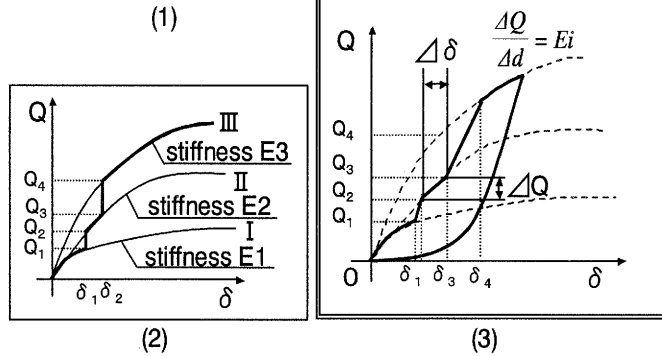


Figure 9 New Proposal: (1)Criterion (2)Multi-step (3)Strengthening characteristics

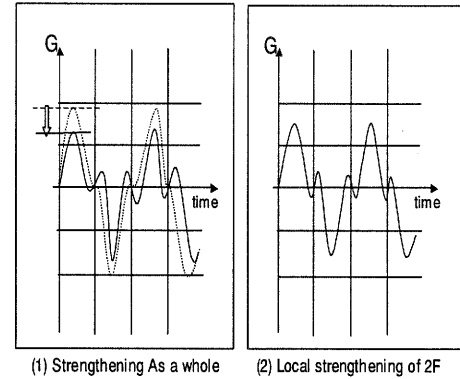


Figure 10 Acceleration reduction : (1) Reduction for a building as a whole (2) Acceleration by local strengthening

5.2 Local strengthening characteristics

In the stabilization analysis performed in Section 4.3, the seismic strengthening effect by means of a horizontal restoring force was described. It is considered possible to provide local strengthening by imparting each layer with a restoring force equivalent to this horizontal restoring force. Fig.10 shows the extent of acceleration reduction for a building as a whole when this kind of local strengthening is performed. This diagram demonstrates the same reduction as when the building as a whole was strengthened to the characteristics shown in Fig. 9(3). As a result, seismic strengthening on a local basis may be performed by application of the same strengthening characteristics as for a building as a whole.

6. Conclusions

This paper has focused on the prevention of building collapse based on modes of roof collapse that are considered likely to occur in the future, in order to propose a method for strengthening buildings that takes performance evaluation requirements into consideration. This method can be summarized as follows.

(1) The method was applied to classifications of collapse deformation modes of actual buildings. It used modes of instability deformation obtained from buckling analysis based on a two-DOF model with various types of mass distribution. This paper also discussed the possibility of stabilization by adding a horizontal restoring force for the purpose of seismic strengthening.

(2) Next, response analysis using the same model was performed in order to determine the strengthening characteristics in response to the requirements of the various performance evaluations. Strengthening characteristics were determined that have elastic restoration and hysteresis damping characteristics, and that incorporate multi-step changes in stiffness.

(3) It was determined that localized strengthening of layers requiring stabilization using the same seismic strengthening characteristics as those for buildings as a whole provided the same reduction in response acceleration as was seen in buildings as a whole.

The next step in this research shall be to discuss actual cases of actual earthquake resistance design that integrate this proposal.

SEISMIC RETROFIT OF TOWER STRUCTURES WITH BUCKLING RESTRAINED BRACES

T. Takeuchi¹⁾

*1) Associate Professor, Dept. of Architecture and Building Eng., Tokyo Institute of Technology, Japan
ttoru@arch.titech.ac.jp*

Abstract: Truss frame generally had to be designed elastically even against large seismic force, because of fragile characteristics led by member buckling. The author has proposed damage tolerant design concept for truss structures using energy dissipation members in critical positions. In this paper, detailed retrofit designs for steel truss communication towers whose critical members are replaced to Buckling Restrained Braces are discussed, and their performances are examined with real-size mock-ups modeling parts of the existing tower.

1. INTRODUCTION

Large earthquake is expected within coming ten years in Tokai area in Japan, and public facilities in this area are required seismic retrofit against near future seismic impact. Microwave communication towers owned by electric companies are placed on the top of buildings in the city and suburb area, communicating the information controlling the power plants serving electric power within the supplying area. Such communication towers are composed of steel truss structures with pipe section members, basically designed against wind forces. However, it is appeared that such structures can collapse with expected large seismic forces, with amplitude caused by the building structures which the towers are placed on. If the members of such tower once collapse with seismic forces, it will be catastrophic for such truss structures have less-ductile characteristics caused by member buckling. Normal reinforcement strengthening the weak members is not necessarily effective, because the other members or connections become critical after reinforcing the weak members, and reinforcing whole members will be required after all. Such whole reinforcement also shortens the own period of the structure, often causes higher seismic input furthermore. In these reasons, normal reinforcement can be time-and-cost consuming.

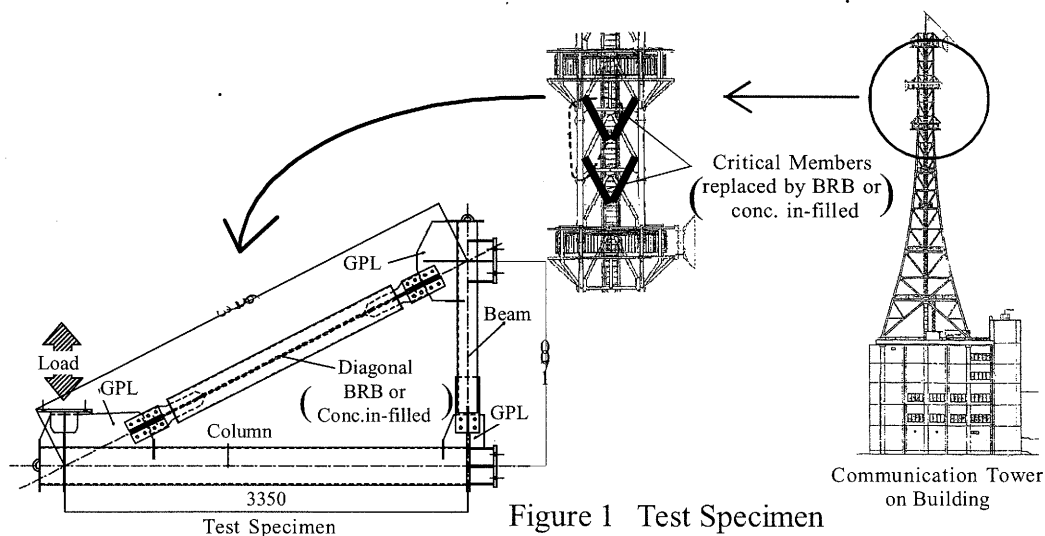


Figure 1 Test Specimen

The author has proposed seismic retrofit method by replacing the critical truss member by buckling restrained braces (BRB), which work as high-performance hysteretic damper, and their effects on tower structures have been confirmed by analyses¹⁾⁻²⁾. In this study, the real size truss frame around the damper are mock-upped, and hysteretic-loading tests was carried out. Their results are compared with normal pipe diagonal members or concrete in-filled members, and energy dissipation capacities of each system are discussed. When structures were reinforced, retrofit work for connection need to be minimum and simple. In this study, two types of connections are tested, and their out-of-plane stability are also compared and discussed. Application layout of BRB for communication towers and mock-up for the test specimen are shown in Figure 1.

2. EXPERIMENTAL METHOD

The test configuration is shown in Figure 2, and the list of the test specimens is shown in Table 1. The specimens are divided into Series 1 and Series 2 by their design strength, and each series consists of four types of retrofit design. In Type-TO, all truss members have normal pipe sections modeling members before retrofit. In Type-TC, concrete is in-filled within the diagonal member to strengthen member strength. In Type-TA and TB, diagonals are replaced by BRB whose yield strength are meeting with the buckling strength of original pipe diagonals. They are distinguished by connection type. One is welding additional stiffener plates on Gusset-plates (Type-TB), another uses angle instead of splice plate (Type-TA). Type-TB needs site-welding works at high positions. On the other hand, Type-TA can use gusset plate as existing, while its out of plane rigidity is smaller than Type-TB. The details of BRB are shown in Figure 3, and joint configurations for Type-TB and TA are shown in Figure 4.

Loading program is shown in Figure 5. Basic loading history is consists of increasing cyclic loading up to 1/25 story drift. Near field loading history for TA-1' and TA-2' assumed an earthquake directly above its epicenter is modeled up to 1/20 from 1/50 story drift.

3. RESULTS & DISCUSSION

3.1. Hysteretic Characteristics under Loading History

The test results are shown in Figure 5 through 8, respectively. In each figure, (a) are load-displacement relationship of truss structure, (b) are axial force-deformation of diagonal members, and (c) show the failure modes.

For Type TO-1, story drift up to 1/100 is followed by slip of connection bolts, then the diagonal pipe started buckling at 1st 1/50 cycle in compression, elbow buckling was created at

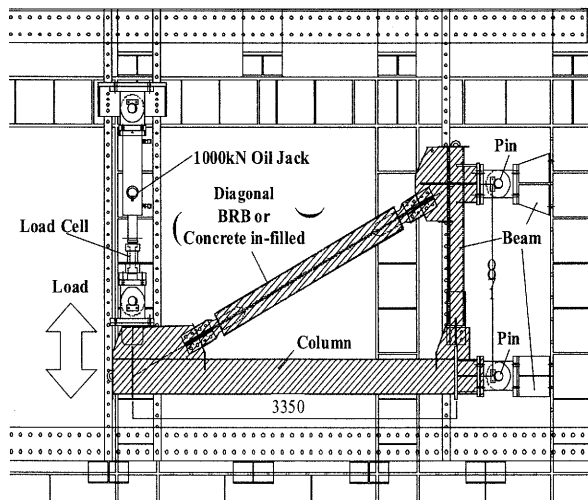


Figure 2 Test Configuration

Table 1 Test Specimens

	Brace	Bolt	Type	Loading History
TA-1	BRB-16x92 ($P_y=300\text{kN}$)	4M-20	Angle Joint	Basic
TA-1'			Angle Joint	Near-Field
TB-1	pipe $\phi 165.2 \times 4.5$	4M-20	Welding rib	Basic
TC-1			Concrete in-filled	
TO-1	BRB-16x58 ($P_y=190\text{kN}$)	2M-20	Ordinary	Near-Field
TA-2			Angle Joint	
TA-2'				

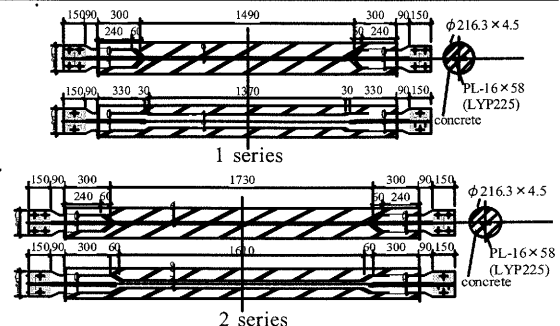


Figure 3 Details of BRB

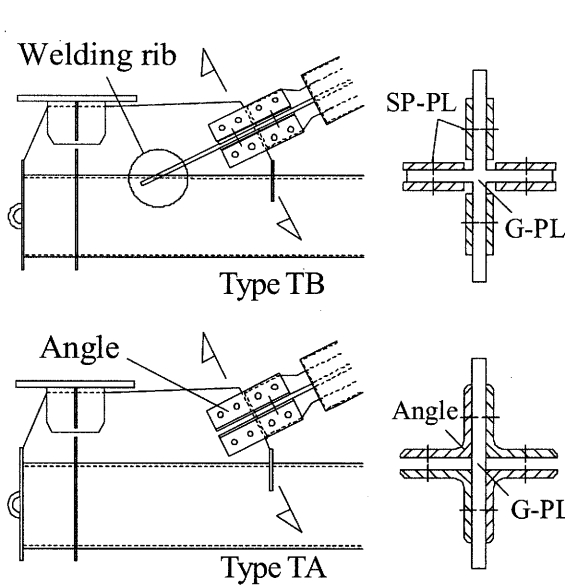


Figure 4 Joint Configurations

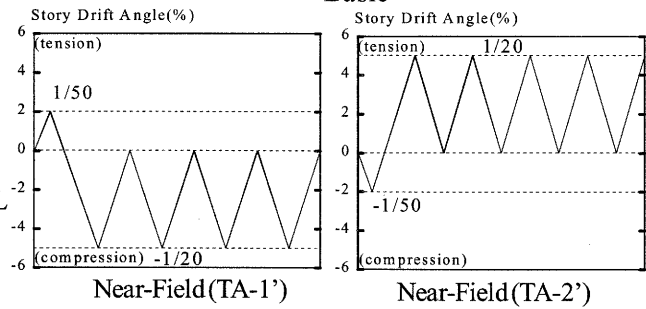
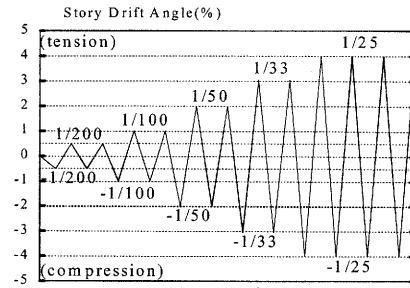


Figure 5 Loading Program

2nd 1/50 cycle in compression, and torn off at 1st 1/25 cycle in tension. The maximum axial force to start buckling was about 820kN.

For Type TC-1, the gusset plate at diagonal-to-beam connection started to deform in out-of-plane direction at 1st 1/50 cycle in compression, and was buckled at 1st 1/33 cycle in compression before brace was buckled. From these result, it is found that strengthen diagonal member only will cause collapse in other parts as connections.

For Type TA and TB used BRB, braces and connections was not buckled and they show quite stable and symmetrical hysteretic loop up to 1/25 story drift. Each specimens dissipated enough energy until core plate fracture (For Type TB-1, at 3rd 1/25 cycle in tension, For Type TA-1, at 4th 1/25 cycle in tension, For Type TA-2, at 4th 1/25 cycle in tension.).

For Type TA-1 and 2 with angle joint, out-of-plane deformation did not increased and shows stable deformation capacity as same as Type-TB. Connection and main frame did not damaged until BRB showed enough plastic deformation capacity and connection failures were avoided compared with TO-1 or TC-1.

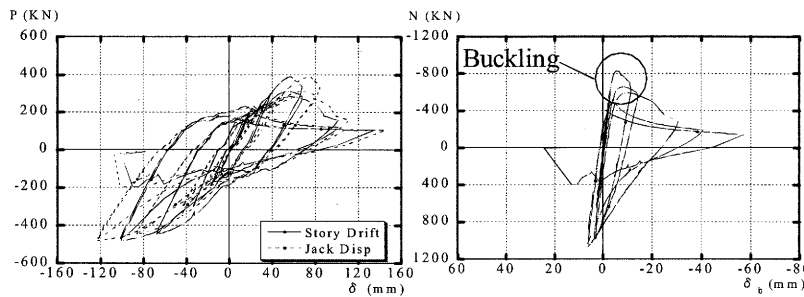


Figure 5(a) Type TO-1

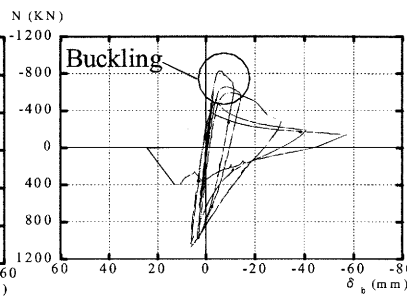


Figure 5(b) Type TO-1



Figure 5(c) Diagonal Buckling

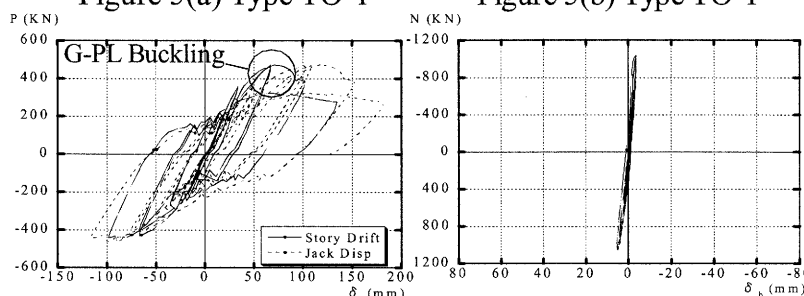


Figure 6(a) Type TC-1

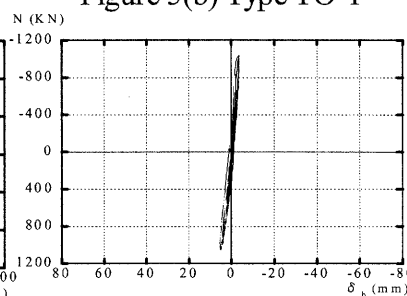


Figure 6(b) Type TC-1

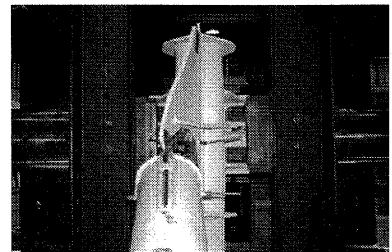


Figure 6(c) G-PL Buckling

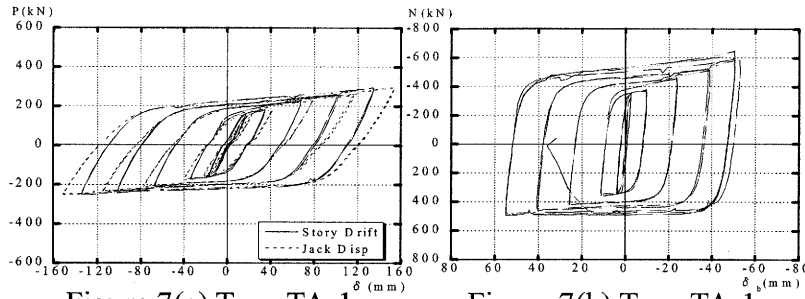


Figure 7(a) Type TA-1

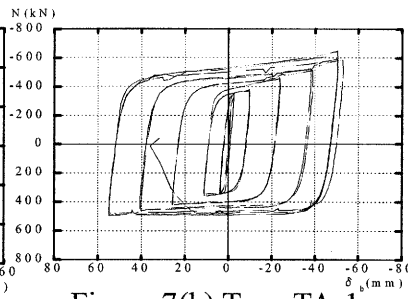


Figure 7(b) Type TA-1

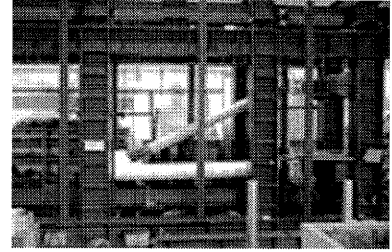


Figure 7(c) Test End (TA-1)

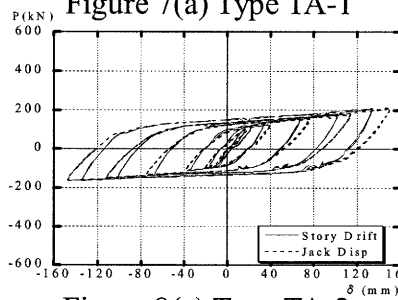


Figure 8(a) Type TA-2

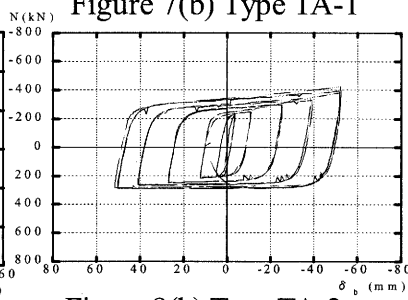


Figure 8(b) Type TA-2

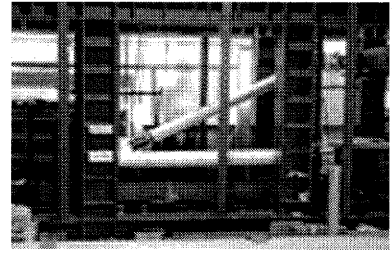


Figure 8(c) Test End (TA-2)

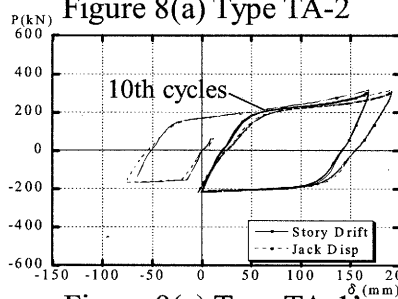


Figure 9(a) Type TA-1'

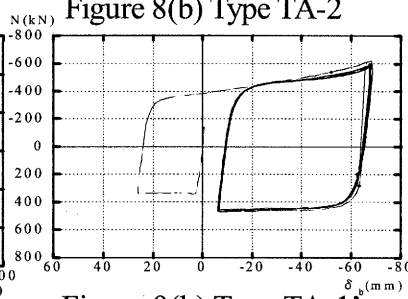


Figure 9(b) Type TA-1'

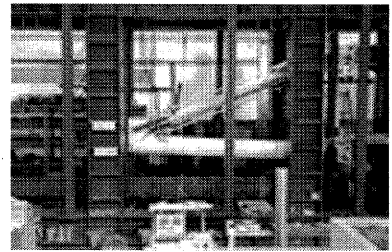


Figure 9(c) TA-1' 1/20 (comp.)

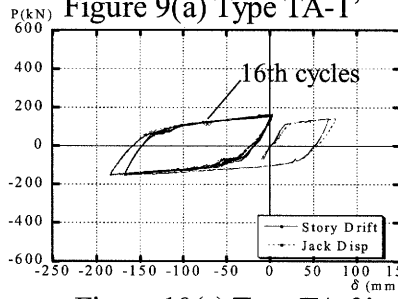


Figure 10(a) Type TA-2'

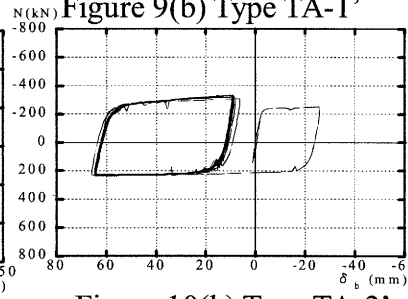


Figure 10(b) Type TA-2'

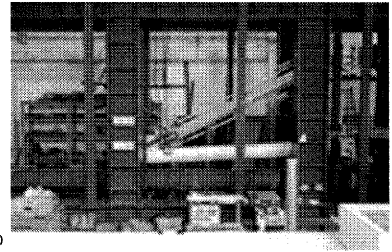


Figure 10(c) TA-2' 1/20 (tens.)

3.2. Hysteretic Characteristics under Near-Field Loading History

The test results under near-field loading programs on BRB are shown in Figure 9 through 10. In each figure, the contents in (a)(b)(c) are the same as Figure 5-8.

For Type TA-1' and TA-2', In spite of more severe story drift, none of deformation, buckling at brace and connections were occurred. Both types showed stable hysteresis loop, with 10th cycles for TA-1' and with 16th cycles for TA-2'. As though maximum story displacement increase, the number of hysteresis loops increase until core plate fracture, which indicates cumulative deformation capacity relies its amplitude than maximum displacement.

3.3. Behavior of Connections

Figure 11 shows strain in gusset-plates. For Type TO-1, after brace buckling in compression, gusset-plate went into plastic before the brace reaches to the maximum strength. In Type TC-1, gusset-plate buckled out-of-plane direction, and plastic strain was largely developed. In Type TB-1, strain of gusset-plate is kept in elastic range as brace strength is limited. In Type TA-1, strain of gusset-plate was larger than TB-1 since stiffener plates is not added still in almost elastic range. In Type TA-2, the same result was obtained as Type TA-1.

Table 2 shows the displacement of bolt hole with connections after the test. In Type TO-1 and Type TC-1, bolt holes were deformed by bearing because brace strength is higher than joint.

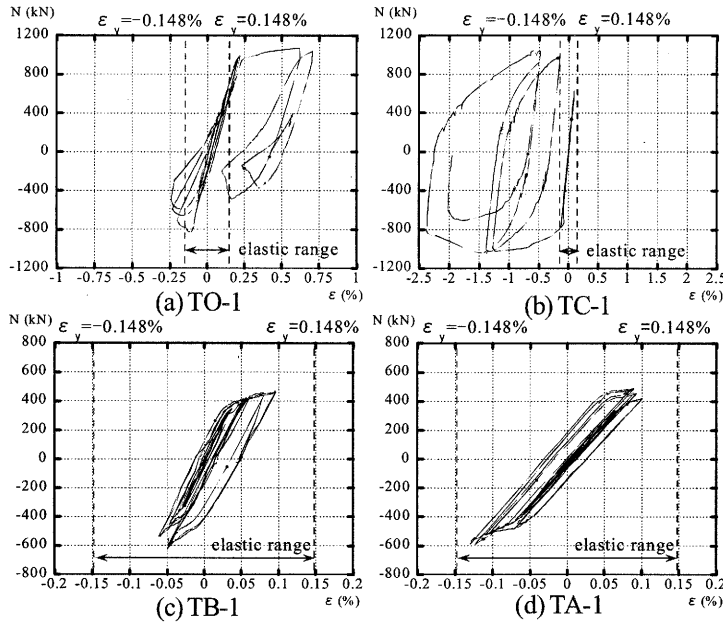


Figure 11. Strain of Gusset-Plates

Table 2. Deformation of Bolt Holes

TO-1	TC-1	TA-1	TA-2
dx	dx	dx	dx
dy	dy	dy	dy
1 26.6 22.1	1 27.8 23.1	1 22.0 22.0	1 23.1 22.2
2 26.2 22.4	2 26.6 22.2	2 22.3 21.9	2 23.0 22.0
3 27.8 22.4	3 28.1 22.4	3 22.0 22.0	
4 26.8 22.9	4 26.4 22.2	4 22.1 22.1	
5 26.1 22.1	5 28.3 22.8	5 22.2 22.1	5 24.8 22.0
6 25.7 22.1	6 28.9 22.3	6 22.4 22.4	6 23.9 22.0
7 27.8 22.5	7 27.8 22.8	7 22.2 22.1	
8 27.0 22.8	8 27.7 22.1	8 22.2 22.4	
9 22.1 22.1	9 22.0 22.0	9 22.5 22.1	9 22.0 22.1
10 22.2 22.2	10 22.0 22.1	10 22.3 22.3	10 22.2 22.0
11 22.1 22.0	11 22.0 22.0	11 22.4 21.9	11 22.0 21.9
12 22.4 22.0	12 22.1 21.9	12 22.3 22.0	12 22.5 22.0

(mm)

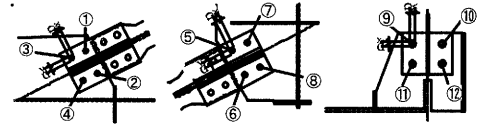


Table 3. Material Properties

	Gauge	E ($\times 10^5 \text{ N/mm}^2$)	σ_y (N/mm^2)	σ_u (N/mm^2)	ϵ_u (%)
Brace-1	STK490	2.05	459	554	32
Brace-2	STK490	2.11	397	466	28
Column-1	STK490	2.02	455	525	37
Column-2	STK490	2.04	418	533	41
Beam-2	STK490	2.05	495	556	32
BRB core	LYP225	2.07	215	306	41

Especially hall deformation in TC-1 is remarkable. In Type TA-1, deformation of bolt hole was not observed because brace strength was limited. Some deformation was observed in TA-2. Table 3 shows result of material tests. Generally yield strength of tube is much higher than allowable stress of 325N/mm. Relatively joint strength tend to be smaller than brace itself.

3.4. Behavior of BRB Ends

For the sake of securing energy dissipation capacity of BRC, it is necessary to avoid out-of-plane buckling including connection plates. When the length of BRB ends with stiffener ribs is short, restriction is feeble and rotation occurs easily. Then 3 hinges are created in the brace member and it buckles in out-of-plane direction.

Figure 12 shows flexural behavior model of BRB end and Figure 13 shows horizontal rotation angle and axial displacement. In these tests, BRC ends of 300mm are adopted length to avoid creating hinges. As in Figure 12 considering displacement progress, BRB ends deform compressing unbond material. In case of ignoring the deformation of restrained tubes, rotational angle ($1/75$) is expected with unbond material thickness. In these tests, it is found that all test pieces rotate until to maximum $1/50$ with amplitude. These difference are caused by the deformation of restrainer tube, but still rotation in out-of-plane direction was limited. In conclusion, it is found that these details have enough strength and stiffness to avoid buckling.

3.5. Cumulative Strain and Energy

Table 4 and Figure 14 shows cumulative strain capacity of each specimen and Table 5 and Figure 15 shows dissipated energy until fracture. The cumulative equivalent strain capacity in BRB diagonal was about 6 times and the dissipated energy in BRB diagonal was about 5 times of

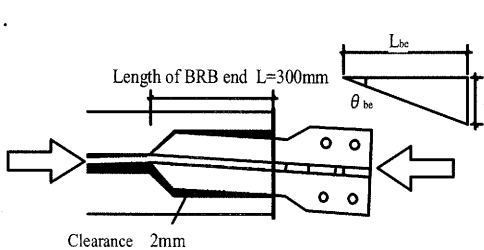


Figure 12 Flexural Behavior of BRB Ends

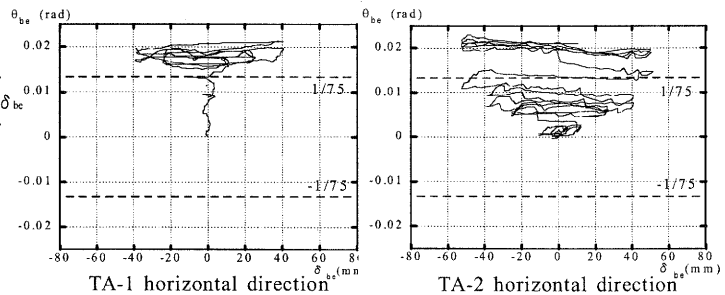


Figure 13 Horizontal Rotation Angle of BRB Ends

Table 4 Cumulative strain capacity

Test Piece	Cum. Strain Capacity $\Sigma \Delta \epsilon $ (%)			Ratio (tens/comp)	Ave. of Strain $\epsilon_{t,ave}$ (%)
	tension	compression	total		
TB-1	44.13	42.87	87.00	1.03	4.216
TA-1	50.40	50.22	100.62	1.00	4.354
TA-1'	51.93	49.11	101.04	1.06	4.090
TA-2	42.30	43.46	85.77	0.97	3.621
TA-2'	58.92	61.09	120.01	0.96	3.549
TO-1	7.43	8.96	16.39	0.83	
TO-1(pre-buckling)	0.83	0.94	1.76	0.89	
TC-1	2.19	1.68	3.87	1.31	

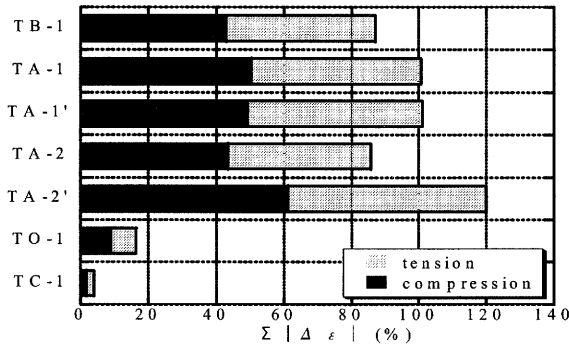


Figure 14 Cumulative strain capacity

Table 5 Dissipated Energy

Test Piece	Dissipated Energy Σw_p (N·m)			Ratio (tens/comp)
	tension	compression	total	
TB-1	215051	228010	443061	0.94
TA-1	286507	272928	559434	1.05
TA-1'	290810	273885	564694	1.06
TA-2	163507	182298	345805	0.90
TA-2'	188754	259118	447871	0.73
TO-1	46612	51405	98016	0.91
TO-1(pre-buckling)	90	1196	1286	0.08

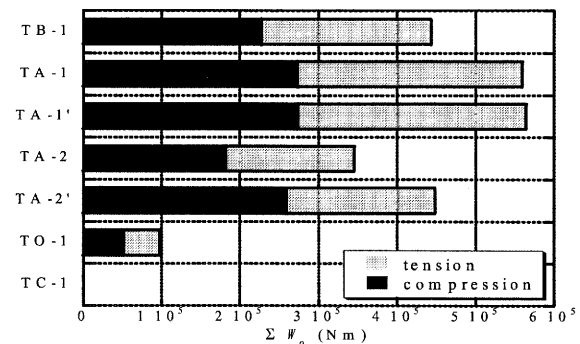


Figure 15 Dissipated Energy

normal pipe (Type TO-1). Estimating until brace was buckled, BRB has capacity of 10 times of Type TO-1. For the present normal pipe, dissipated energy capacity is quite limited and possibility of brace fracture is high. Replacing braces into BRB, yield strength is kept in the limit. Damage to the other members and connections are avoided. In Type TA-1' and TA-2' under near-field loading history, they show the similar displacement capacity as basic loading history. In above, BRB showed stable capacity in all types of loadings.

4. CONCLUSIONS

In these studies, applying hysteretic damper for communication towers are investigated by cyclic loading tests with real size mock-ups. By these studies, the following points became clear.

- 1) Replacement of diagonals into BRB is considered to have excellent performance. The system showed the most stable hysteretic loops, displacement capacity and dissipated energy capacity up to 1/20 story drift. Also it is found that angle joint is valid for keeping enough stiffness to avoid out-of-plane buckling.

- 2) Replacement of diagonal into Concrete in-filled tube improves the buckling strength of brace itself, however it might cause collapse in other parts as connections. Therefore reinforcing only members is not necessarily effective.

Acknowledgement

This study is supported by Chubu Electric Power Co., Inc. and Nippon Steel Corp., cooperated with Prof. T.Ogawa of Tokyo Institute of Technology and Prof. S.Kato of Toyoashi Univ. of Technology.

References

- Takeuchi, T., Suzuki, K.,(2003), "Performance-based Design of High-rise Truss Structures Using Hysteretic Dampers", *STESSA 2003 Napel*, 2003.6
- Kato, S., Nakazawa, S., Sugiyama, T., Matsui, N., and Yoshida, T.,(2003), "on an Efficient Method to Improve the Earthquake Resistant Capacity of steel Tele-communication Towers", *IASS-APCS 2003 Taipei*, 2003.10
- Takeuchi, T., Yamada, S., Kitagawa, M., Suzuki, K., Wada, A.,(2004), "Stability of Buckling-Restrained Braces Affected by the Out-of-Plane Stiffness of the Joint Element", *J. Struct. and Constr. Eng., A.I.J.*, No. 575, pp. 121-128
- Uchiyama, T., Takeuchi, T., Suzuki, K., Ookouchi, Y., Ogawa, T. and Kato, S.(2004), "Seismic Refinement for Communication Towers", *Proceedings Annual Meeting of A.I.J.* Kanto, 2004.3
- Takeuchi, T., "Passive Vibration-Control Concept For Truss Frame Structures", *Proceedings for the First International Conference on Urban Earthquake Engineering*, Tokyo Institute of technology, pp.133-140, 2004.3

BEHAVIOR OF REINFORCED CONCRETE WALLS WITH DIAGONAL WEB REINFORCEMENT SUBJECTED TO CYCLIC LATERAL LOADING

S. Shaingchin¹⁾, P. Lukkunaprasit²⁾, C. Sittipunt³⁾, and S.L. Wood⁴⁾

1) Graduate student, Dept. of Civil Engineering, Chulalongkorn University, Bangkok, Thailand

2) Professor, Dept. of Civil Engineering, Chulalongkorn University, Bangkok, Thailand

3) Assistant professor, Dept. of Civil Engineering, Chulalongkorn University, Bangkok, Thailand

4) Professor, Dept. of Civil Engineering, The University of Texas at Austin, Texas, USA

Somboon.Sh@student.netserv.chula.ac.th, lpanitan@chula.ac.th, fcecst@eng.chula.ac.th, swood@mail.utexas.edu

Abstract: Five reinforced concrete (RC) structural wall specimens were tested subjected to cyclic loading in order to study the influence of diagonal web reinforcement. The parameters varied in each specimen included the amount and orientation of web reinforcement. The wall with conventional web reinforcement failed due to web crushing with an abrupt drop in load capacity, whereas the walls reinforced with diagonal web reinforcement failed in a more ductile mode. Test results clearly indicate that the walls with diagonal web reinforcement have higher ductility than the one with conventional web reinforcement at the same amount of web reinforcement. The specimens with diagonal web reinforcement exhibit less pinching in the hysteresis loop than the wall with conventional reinforcement. Consequently, the energy dissipation capacity of the former is superior to that of the latter. Finite element analyzes reveal that diagonal web reinforcement helps reduce the principal compressive stress in the concrete strut, thereby deferring web crushing with enhanced performance.

1. INTRODUCTION

Observations of RC buildings after earthquake events indicate that the buildings with wall or frame-wall systems are effective in resisting earthquake forces and they sustain less damage than buildings that rely solely on frames for lateral resistance (Fintel 1974, 1991). One of the basic requirements in performance-based design is controlling damage in the structure during an earthquake. To achieve this, the structure should be able to dissipate energy reliably during an earthquake and brittle modes of failure should be avoided. The inelastic behavior of RC structural walls subjected to cyclic loads has received considerable attention in an attempt to improve the seismic performance of structural walls. The results of recent studies by Sittipunt et al. (2001) and Mansour et al. (2001) indicate that walls with diagonal web reinforcement have greater energy dissipation than walls with conventional web reinforcement. Furthermore, it was postulated that web crushing could be avoided by using diagonal web reinforcement. However, the real mechanism leading to such an improved behavior is yet to be investigated, which is the main objective of this study.

2. TEST SPECIMENS

The dimensions and reinforcement details of the test specimens are shown in Fig.1 and 2, respectively. The specimens had a barbell-shaped cross section with a web thickness of 130 mm and 250 x 250 mm boundary columns. The overall length of the cross section was 1500 mm. On the top of the specimen a 250 mm wide by 250 mm deep load transfer beam was cast monolithically with the wall.

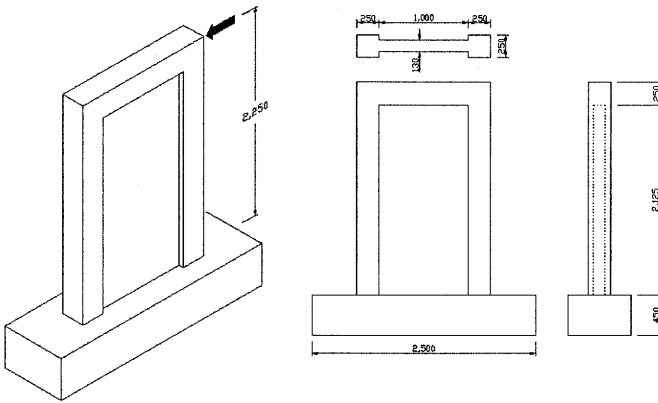


Figure 1 Dimensions of Specimens (unit in mm)

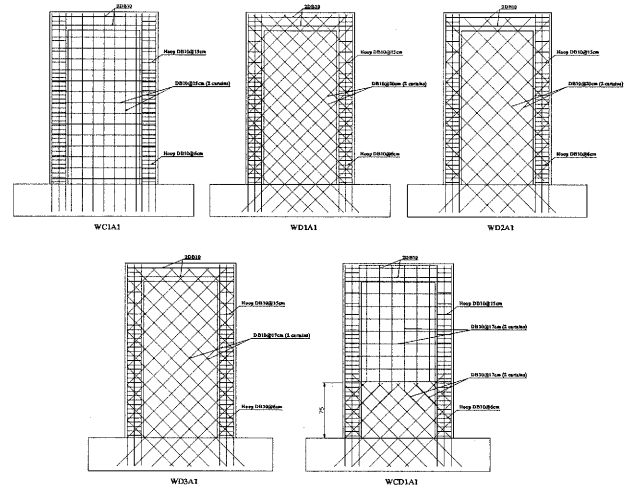


Figure 2 Reinforcement Details

The reinforcement details and material properties of the specimens are listed in Table 1. The longitudinal and transverse reinforcements in the boundary elements were the same in all specimens. The selected longitudinal reinforcement in each boundary element was eight 16 mm deformed bars (reinforcement ratio, $\rho_b = 2.57\%$). The transverse reinforcement was designed according to ACI provision for seismic design (ACI committee 318, 2002). The columns were confined with 10 mm deformed bar at 60 mm (reinforcement ratio, $\rho_t = 2.37\%$) over the first 1500 mm from the base of specimen and at 150 mm ($\rho_t=0.95\%$) over the remaining height of specimen. The shear web reinforcement of specimen WC1A1 was arranged in the horizontal and vertical directions. It was selected such that the nominal shear strength was higher than the flexural strength. The selected web reinforcement was two curtains of 10 mm deformed bars at 150 mm (ratio of web reinforcement area to gross concrete area, $\rho_h = \rho_v = 0.8\%$) for both horizontal and vertical directions. To study the influence of web reinforcement orientation and amount of reinforcement, specimens WD1A1, WD2A1 and WD3A1 were reinforced with 0.8%, 0.6% and 0.7% web reinforcement, respectively, arranged in diagonal directions at 45 degrees.

Since it is not convenient in practice to arrange reinforcement in diagonal directions, therefore, it is proposed to compromise by providing diagonal web reinforcement over one-third of the wall height above the base and with conventional web reinforcement over the remaining height of wall as in specimen WCD1A1. The amount of diagonal and conventional web reinforcement in this specimen was 0.7%. The combination of diagonal and conventional web reinforcement helped considerably in reducing the time in laying the reinforcement.

All specimens were loaded with an axial load of 0.07 of the axial load capacity based on concrete ultimate strength f'_c and gross cross sectional area A_g .

Table 1 Reinforcement Details and Material Properties

Specimens	f_c' (MPa)	Longitudinal steel	$f_{y,b}$ (MPa)	Web reinforcement*	$f_{y,w}$ (MPa)
WC1A1	27.3	$\rho_b = 2.57\%$ (8DB16)	574.9	$\rho_h = \rho_v = 0.0080$ (DB10 at 15 cm)	451.3
WD1A1	40.3	2.57%	574.9	$\rho_d^{**} = 0.0080$ (DB10 at 15 cm)	451.3
WD2A1	33.7	2.57%	574.9	$\rho_d^{**} = 0.0060$ (DB10 at 20 cm)	451.3
WD3A1	32.9	2.57%	595.7	$\rho_d^{**} = 0.0070$ (DB10 at 17 cm)	505.9
WCD1A1	33.9	2.57%	595.7	$\rho_h = \rho_v = \rho_d = 0.0070$ (DB10 at 17 cm)	505.9

* Reinforcement is in 2 curtains, ** Diagonal reinforcement

3. TEST SETUP AND PROCEDURE

The vertical uniform load was simulated by means of a three-point force system with the forces distributed to the cross-section through the top cap beam. Three hydraulic jacks, all connected to the same pump to maintain the same constant axial force, were used to apply the axial loads at the loading points. The lateral force was applied to the specimen by a calibrated actuator attached to the reaction wall. The specimen was also braced laterally in order to prevent out-of-plane distortion.

All specimens were subjected to a cyclic displacement history. The cyclic lateral displacement history consisted of several stages and each stage consisted of three loading cycles. During the first stage, the specimen was pushed (pulled) under load-control until first cracking in concrete occurred. In subsequent stages, the specimen was loaded under displacement-control to the integer multiples of the observed yield displacement until failure. In each stage the wall was repeatedly loaded in three cycles. During testing, lateral displacements, shear deformation, lateral loads and strains in reinforcements were recorded by means of LVDT's, load cells and strain gages, whose signals were input to a computerized data acquisition system.

4. TEST RESULTS

4.1 Load Displacement Response

Figure 3 shows the relationship between the lateral load and the lateral displacement of the wall specimens. Clearly, the hysteresis loops of wall specimens with diagonal web reinforcement exhibited less pinching than the wall specimen with conventional web reinforcement.

The total lateral displacement can be decomposed into the flexural, shear, and sliding components. For the specimens with diagonal web reinforcement, the flexural displacement comprised around 70-80 percent of the total displacement at ductility level of 4 while that of the specimen WC1A1, reinforced with conventional reinforcement, was around 45 percent of total displacement at the same ductility. For all specimens, the shear deformation gradually decreased while the sliding displacement gradually increased with an increase in the ductility level. It is important to observe that the specimens reinforced with diagonal web reinforcement had smaller shear displacement and sliding displacement components than the specimen reinforced with conventional web reinforcement by about 30% and 50%, respectively, at ductility level 4. An

increase in the amount of diagonal web reinforcement reduced the shear deformation and sliding displacement.

It should be noted that due to the large discrepancy in the concrete strengths of specimens WC1A1 and WD1A1, the reduction in shear component may be somewhat larger than reality if the concrete strengths of those specimens were equal. A finite element investigation was therefore conducted for specimens possessing the same concrete properties, the results of which will be discussed in a later section.

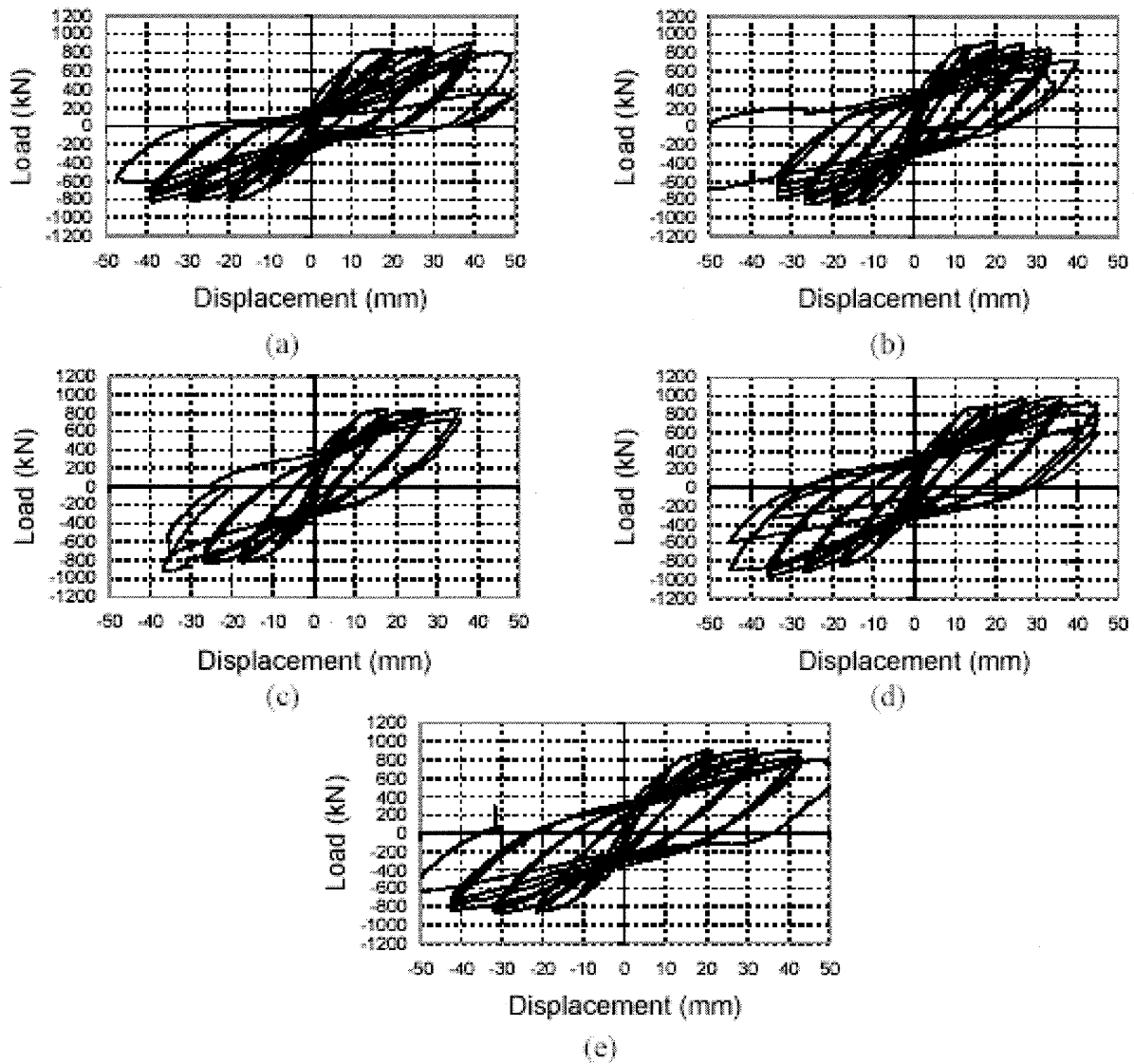


Figure 3 Hysteresis Loops
(a) WC1A1 (b) WD1A1 (c) WD2A1 (d) WD3A1 (e) WCD1A1

4.2 Ductility and Failure Modes

It is not economical to design structures to remain elastic during a major earthquake and it may even be impossible in the case of a large earthquake. Ductility allows the structures to respond beyond the elastic limit without collapse, provided that sufficient lateral strength could be maintained. The displacement ductility factor is defined as the ratio of the maximum lateral displacement to the lateral displacement at first yielding of reinforcing bars, with 80% of the peak lateral load sustained at the maximum displacement. In order for a given structural element to develop a larger ductility ratio, special reinforcement details in critical regions are needed. For structural walls, special confinement of the boundary elements can help to increase the displacement ductility. Shear modes of failure may limit the deformation of walls and must be controlled to ensure ductility. In this experiment, boundary elements of all specimens were highly confined following the ACI provision (ACI committee 318, 2002).

All specimens, except specimen WD1A1, had ductility capacity of 4 while specimen WD1A1 developed a ductility factor of 5. Although the specimen WC1A1 could sustain a ductility factor of 4 as specimen WD3A1, the lateral load of the former dropped suddenly after failure whereas a more gradual decrease in load capacity at failure was observed in the specimen with diagonal web reinforcement.

The specimen WC1A1 reinforced with 0.8% conventional web reinforcement failed due to web crushing. The specimens WD1A1 and WD3A1 reinforced with 0.8 and 0.7% diagonal web reinforcement, respectively, failed in flexural mode but the specimen WD2A1 reinforced with 0.6% diagonal web reinforcement failed due to buckling of web reinforcement. Failure modes of the specimens are shown in Fig. 4 and are summarized in Table 2.

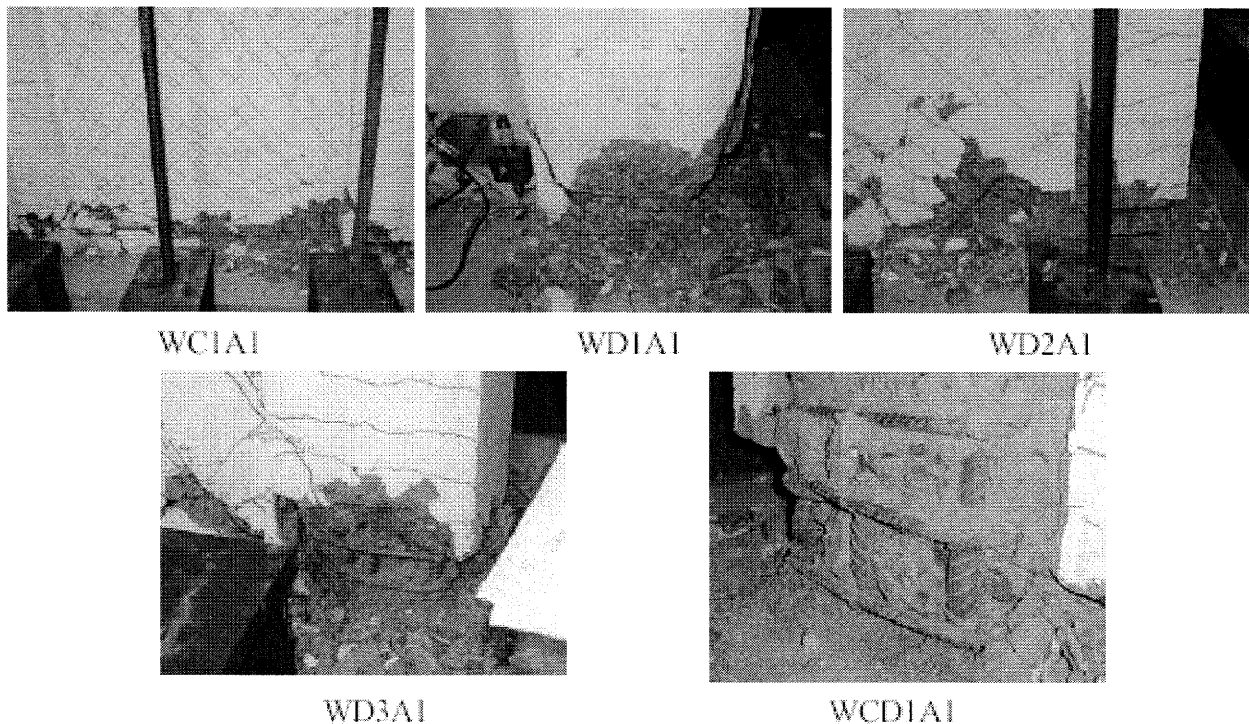


Figure 4 Failure Modes of Wall Specimens

4.3 Lateral Load Capacity

The lateral load capacities $V_{u,f}$ and $V_{u,w}$ as predicted by ACI Code (ACI committee 318, 2002) based on flexural and web shear crushing failure modes are tabulated in Table 2. Since the strain hardening in reinforcing steel is neglected in the analysis, the flexural strengths ($V_{u,f}$) are less than the peak test loads by 5-16%. The web shear crushing, $V_{u,w}$ shown in Eq. (1), is seen to be underestimated by as much as 20%.

$$V_{n,w} \leq \frac{2}{3} \sqrt{f'_c} A_{cv} \quad (\text{unit in MPa}) \quad (1)$$

Table 2 First Yield Response and Failure Mode

Specimen	First yield displacement	Peak load	$V_{u,f}$	$V_{n,w}/$ Peak load	Ductility factor	Mode of failure*
WC1A1	9.7 mm	870 kN	800 kN	0.78	4	WC
WD1A1	6.7 mm	890 kN	840 kN	0.93	5	BL
WD2A1	8.8 mm	880 kN	785 kN	0.86	4	BW
WD3A1	8.9 mm	980 kN	823 kN	0.76	4	BL
WCD1A1	10.7 mm	890 kN	830 kN	0.85	4	FL

*WC: Web crushing, BL: Buckling of longitudinal bars, BW: Buckling of web bars, FL: Fracture of longitudinal bars

4.4 Energy Dissipation

Figure 5 shows the cumulative energy dissipation as a function of the drift ratio. The following can be observed:

- Specimen with diagonal web reinforcement had a higher energy dissipation capacity than the specimen with conventional web reinforcement (WC1A1) by 23% or more at the drift ratio of 1.5%.
- The energy dissipation capacity of the specimen with mixed web reinforcement types (WCD1A1) is only slightly less than that of with diagonal reinforcement (by about 6%). Thus, the mixed mode of web reinforcement is quite promising in practice.

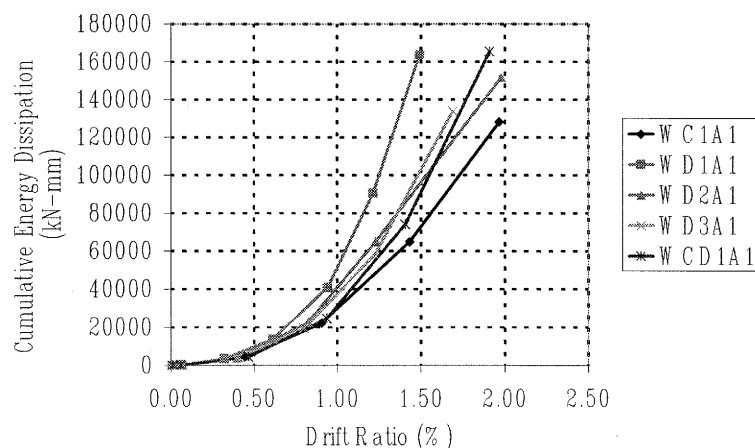


Figure 5 Energy Dissipation

5. FINITE ELEMENT ANALYSIS

The test results seem to indicate that web crushing, which creates a more brittle mode of failure, is prevented when the web reinforcement is oriented in the diagonal directions. Unfortunately, due to the large discrepancy in the concrete strengths of the test specimens, it is not possible to make a definite conclusion of the hypothesis. To gain insight into the effect of diagonal reinforcement, finite element monotonic static analyzes were performed for specimens WC1A1 and WD1A1, using the same material properties as specimen WC1A1. In this study, concrete was modeled with smear rotating cracks and reinforcing bars were modeled as truss elements connected between nodes of concrete elements as shown in Fig. 6. Concrete in compression was modeled with Hognestad model for unconfined web concrete elements and with Saatcioglu model (1992) for confined concrete elements in columns. Tension model in concrete proposed by Belarbi et al. (1994) was used in this study. For the reinforcing steel, the average stress-strain curve of steel reinforcement embedded in concrete suggested by Belarbi et al. (1994) was adopted. Buckling of reinforcing bars was not considered. Analyses were conducted using the finite element program, FINITE (Lopez et al.). Analyses were terminated when the principal compressive strain in web concrete reached the crushing strain of 0.003, after which numerical convergence was not achieved.

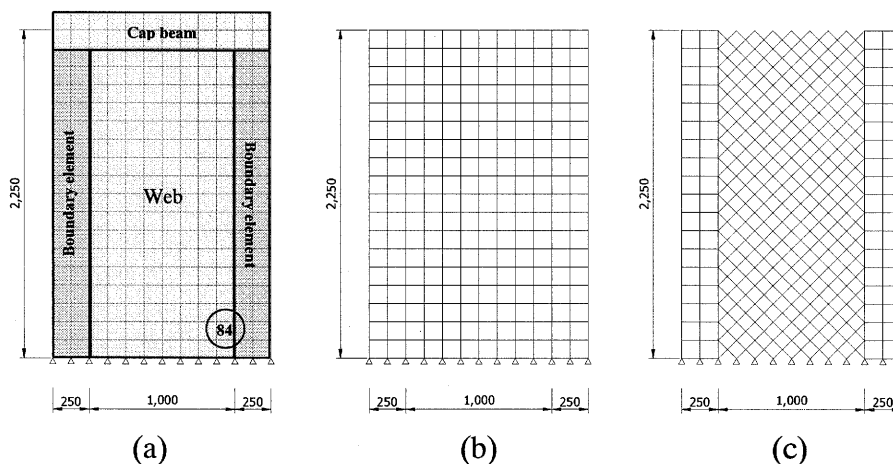


Figure 6 Finite Element Modeling: (a) Concrete Elements (b) Steel Elements of WC1A1
(c) Steel Elements of WD1A1

5.1 Finite Element Analysis Results

Figure 7 depicts the results from finite element analyzes. The lateral load-displacement curves in Fig. 7a indicate that the web concrete in the conventionally reinforced wall reaches the crushing strain at a drift of about 80% of the wall with diagonal reinforcement. Thus, ductility is enhanced by about 20% with the use of diagonal reinforcement. The principal compressive stresses in the most severely stressed element (element 84 indicated in Fig.6) are compared in Fig. 7b for the two walls. It is observed that at the same loading close to peak load, the compressive stress in the wall with diagonal reinforcement is reduced by about 20% compared with the case of conventional reinforcement. The shear strain in the same element, plotted in Fig. 7c, reveals that diagonal web reinforcement contributes to resisting part of the external shear, and consequently helps reduce the shear strain in concrete by about 25%.

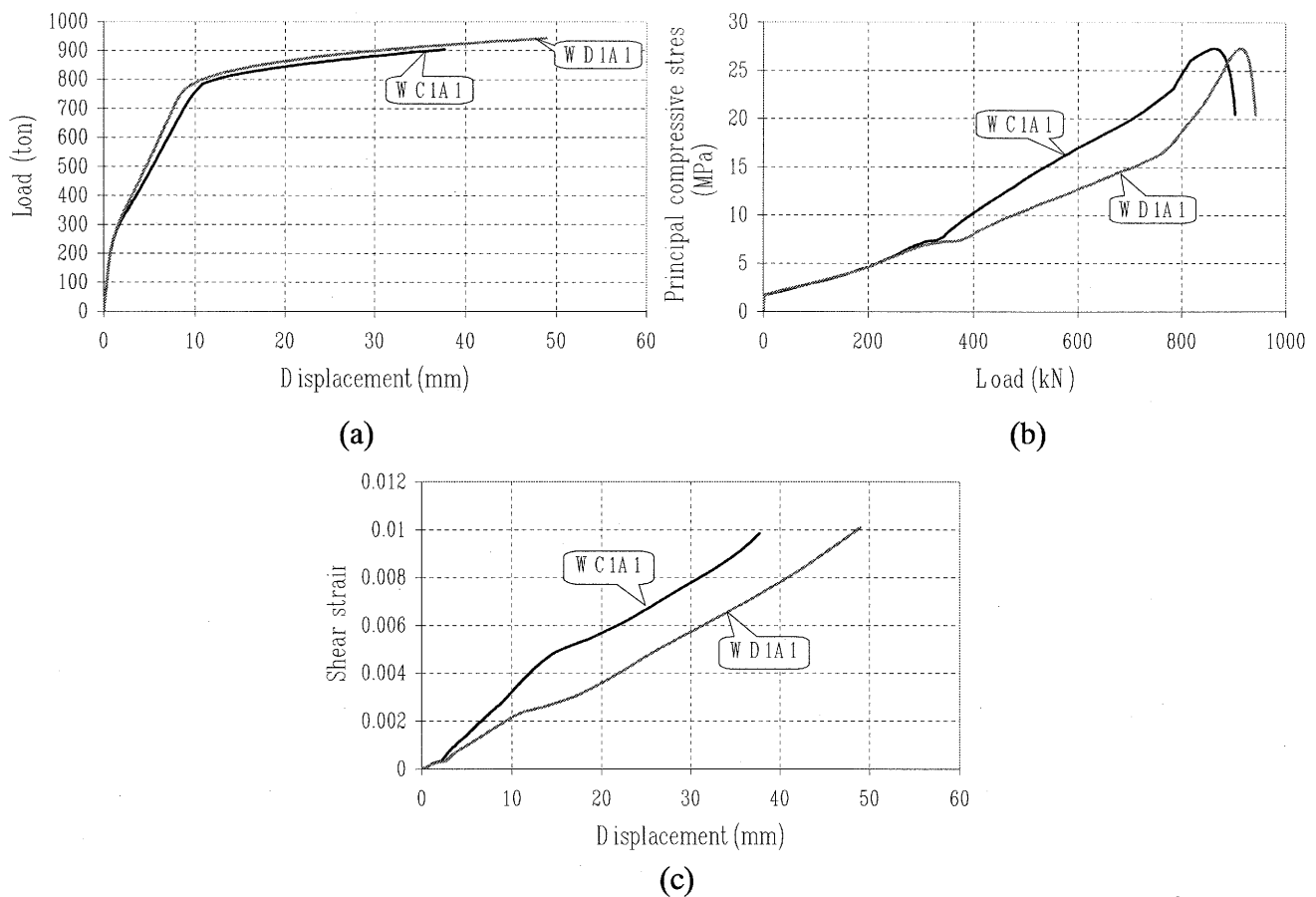


Figure 7 Finite Element Analysis Results:

- (a) Lateral Load-Displacement, (b) Lateral Load-Principal Compressive Stress of Element 84
(c) Lateral Displacement-Shear strain of element 84

6. CONCLUSIONS

Based on the experimental and analytical results, walls with diagonal web reinforcement exhibit better performance than the one with conventional web reinforcement. The following conclusions can be drawn for the specimens tested:

1. The shapes of hysteresis loops of walls with diagonal web reinforcement exhibit less pinching than the wall with conventional reinforcement. Therefore, the energy dissipation capacity of walls with diagonal web reinforcement is superior to that with conventional web reinforcement.
2. Diagonal web reinforcement reduces the shear and sliding displacement components by about 25% and 50%, respectively, at ductility level 4.
3. The effect of diagonal reinforcement is to reduce the shear strain in the web concrete (by about 20%) leading to a reduction in the peak compressive stress in the compression strut. As a consequence, web crushing in the walls with diagonal reinforcement is deferred with the improvement of ductility by about 20% compared with the case of conventional reinforcement.
4. Although the brittle web crushing failure mode is alleviated with the use of diagonal reinforcement, the diagonal bars, subjected to high compressive stress, tend to buckle, resulting in spalling of the concrete cover with subsequent loss of load capacity. Hence, cross ties preventing buckling of diagonal web reinforcements are needed for improved performance.

5. The energy dissipation capacity of the specimen with mixed web reinforcement types (WCD1A1) is only slightly less than that with diagonal reinforcement (by about 6%). Thus, the mixed mode of web reinforcement is quite promising in practice.
6. The web shear crushing strength as predicted by ACI Code (2002) can be under-estimated by as much as 20%.

Acknowledgements:

The authors gratefully acknowledge the Thailand Research Fund for a Senior Research Scholar Grant to the senior author and the Royal Golden Jubilee Ph.D. Program scholarship to the junior author.

References:

- ACI Committee 318 (2002), "Building Code Requirements for Structural Concrete (ACI318-02) and Commentary (318R-02)," *American Concrete Institute*, Farmington Hills, Michigan.
- Belarbi, A., Hsu, T.T.C. (1994), "Constitutive Laws of Concrete in Tension and Reinforcing Bars Stiffened by Concrete," *ACI Structural Journal*, **91**(4), 465-474.
- Fintel, M. (1974), "Ductile Shear Walls in Earthquake Resistant Multistory Buildings," *ACI Journal*, June, 296-305.
- Fintel, M. (1991), "Shearwalls - An Answer for Seismic Resistance?," *Concrete International*, **13**(7), 48-53.
- Lopez, L.A., Dodds, R.H., Rehak, D.R., and Schmidt, R.J., "Polo-Finite: A Structural Mechanics System for Linear and Nonlinear, Static, and Dynamic Analysis," University of Illinois, Urbana.
- Mansour, M., Lee, J.-Y., and Hsu, T. T. C. (2001), "Cyclic Stress-Strain Curves of Concrete and Steel Bars in Membrane Elements," *Journal of Structural Engineering*, American Society of Civil Engineers, **127**(12), 1402-1411.
- Saatcioglu, M., Razvi, S.R. (1992), "Strength and Ductility of confined concrete," *Journal of Structural Engineering*, American Society of Civil Engineers, **118**(6), 1590-1607.
- Sittipunt, C., Wood, S.L., Lukkunaprasit, P., and Pattararattanakul, P. (2001), "Cyclic Behavior of Reinforced Concrete Structural Walls with Diagonal Web Reinforcement," *ACI Structural Journal*, **98**(4), 554-562.

EFFECT OF ACTIVE CONFINEMENT ON SHEAR CRACK BEHAVIORS FOR R/C COLUMNS PRESTRESSED Laterally

Y. Shinohara¹⁾, K. Miyano²⁾, M. Inagaki³⁾ and H. Watanabe⁴⁾

1) Associate Professor, Structural Engineering Research Center, Tokyo Institute of Technology, Japan

2) Kajima Corporation, Japan

3) Graduate Student, Structural Engineering Research Center, Tokyo Institute of Technology, Japan

4) Assistant Professor, Department of Architecture, Nagasaki Institute of Applied Science, Japan
yshinoha@serc.titech.ac.jp, miyanok@kajima.com, minagaki@serc.titech.ac.jp, hwatanab@arch.nias.ac.jp

Abstract: Experiments and 3-D FEM analyses were performed on reinforced concrete columns laterally prestressed by the shear reinforcements to study the influence of the active confinement upon shear strengths and crack behaviors. The relation between the width of shear crack and the strain of reinforcement has been proven by measuring every crack over reinforcements and gluing three strain gauges on reinforcements. With increasing lateral pressure, shear crack strength and ultimate shear strength have increased proportionally, shear crack patterns have changed appreciably, and shear crack widths have decreased drastically. The FEM analyses using smeared crack model cannot evaluate a localized crack accurately but can provide valuable information about the total damage in the overall depth of a specimen.

1. INTRODUCTION

The prestress in concrete structures is generally aimed at controlling the flexural cracks by the arrangement of tendons in an axial direction of the member. On the other hand, in order to delay initiating a shear crack and to reduce its width, not to control a flexural crack, experimental studies have been conducted on the reinforced concrete (RC) columns laterally prestressed by the shear reinforcements with high strength (Watanabe et al. 2004). The results of the flexure-shear tests have indicated that the shear crack strength is increased and the width of a crack, especially its residual opening is remarkably reduced by introducing the lateral prestress. This reduction of the width has improved not only durability but also earthquake resistance since the ability to transmit shear force across a rough crack increases dramatically by reducing its width. The three dimensional finite element (FEM) analyses were also performed on RC columns mentioned above to investigate the mechanics of the lateral confinement using the equivalent confining pressure and the degree of damage in compressive zone as the gauges to evaluate active confinement and compressive-shear failure quantitatively (Shinohara et al. 2004). These studies have revealed that an increase in the resistance against shear failure as well as shear cracking with increasing prestress in the shear reinforcements could be explained by the triaxial state of stress in the core concrete.

The primary purpose of this study is to investigate how the lateral prestress in RC columns would affect the shear crack behaviors on the basis of the triaxial state of stress in the analysis, to clear the relationship between the width of a shear crack and the strain of a shear reinforcement and to see the extent to which the FEM analysis with a smeared crack model can evaluate the actual shear crack behavior and the shear strength.

2. OUTLINE OF TEST AND ANALYSIS

2.1 Test Specimens and Analysis Models

The details of the test specimen and the finite element model are shown in Fig.1. The specifications of the specimens are summarized in Table 1. The flexure-shear tests have been performed on two columns which are laterally prestressed (LPRC) and not prestressed (RC). The test specimens have a square cross section of 340 mm x 340 mm and a height of 900 mm. The specimens were designed to cause a shear failure before the longitudinal reinforcements yield by Architectural Institute of Japan (1999). For that reason, a high strength steel bar (D22 in Fig.1, $\sigma_y=1196 \text{ N/mm}^2$) was used as the longitudinal reinforcements. Moreover, an additional reinforcement (D13 in Fig.1) was arranged to keep a bond splitting failure off. The lateral prestress was introduced into concrete as follows: 1) the high strength transverse hoops (U6.4 in Fig.1, $\sigma_y=1459 \text{ N/mm}^2$) were pretensioned to about 40% of the yield stress using the rigid steel molds and special jigs shown in Fig.1, 2) concrete was placed into the molds and cured until the strength of concrete increased adequately, 3) the core concrete was laterally prestressed by removing the steel molds. The product of the ratio and the stress of the pretensioned transverse reinforcements is defined as average lateral prestress $\sigma_L (=p_w \sigma_{wp})$ to indicate the intensity of lateral prestress. The mix proportion of concrete used in the test specimens is given in Table 2. The coarse aggregate is semi-rounded sea gravel with a maximum grain size of 25 mm. Concrete was placed in the vertical direction. The mechanical properties of concrete and reinforcements are shown in Fig. 2 and 3 together with their idealizations in analyses.

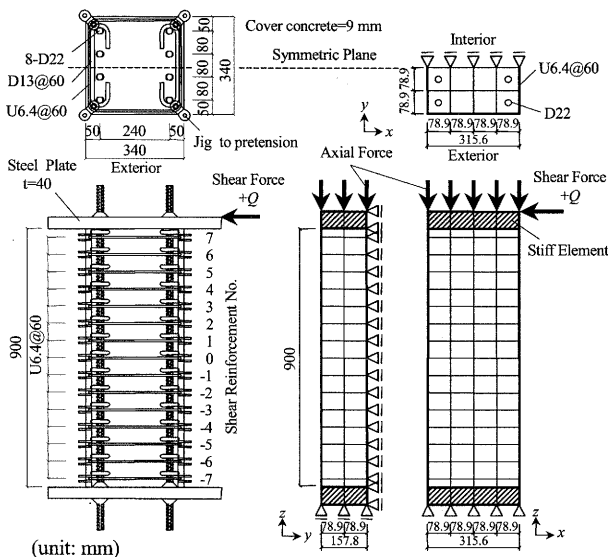
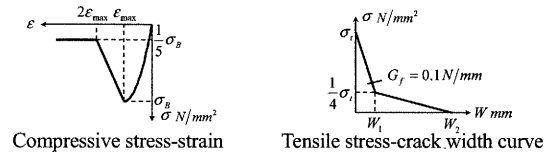


Fig. 1 Details of test specimen and finite element model



Test series	σ_B N/mm ²	ϵ_{max}	E_c N/mm ²	σ_t N/mm ²	W_1 mm	W_2 mm	ν
RC	50.8	-0.002	3.51E+4	2.9	0.031	0.15	0.2
LPRC	46.5	-0.002	3.45E+4	2.9	0.031	0.15	0.2

ν : Poisson's ratio

Fig. 2 Mechanical properties and analytical models for concrete

Type	σ_y (N/mm ²)	σ_{max} (N/mm ²)	E_s (N/mm ²)
D22	1196	1281	1.92E+5
U6.4	1459	1499	2.04E+5
D13	344	488	1.92E+5

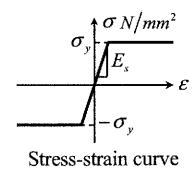


Fig. 3 Mechanical properties and analytical model for reinforcement

Table 1 List of test specimens

Test Designation	$b=D$ (mm)	M/QD	p_w (%)	σ_0/σ_B	σ_{wp} (N/mm ²)	σ_L (N/mm ²)
RC	340	1.3	0.29	0.30	0	0.0
LPRC					536	1.6

b & D =width & depth of column, M/QD =shear span-depth ratio, p_w =ratio of transverse hoop, σ_0 =axial stress of column, σ_B =compressive strength of concrete, σ_{wp} =introduced prestress in transverse hoop, σ_L =lateral prestress ($=p_w \sigma_{wp}$)

Table 2 Mix proportion

Proportion, by weight				Admixture	Slump
Cement	Sand	Coarse Aggregate	Water		
1	2.04	2.53	0.50	Super plasticizer	21 cm

2.2 Loading and Measuring Methods in Tests

The loading apparatus is shown in Fig.4. The vertical force on the test specimen was supplied by the 2 MN hydraulic jack, and the ratio of axial load to axial strength was kept constant at 0.3 during a test. The horizontal force was supplied by two hydraulic jacks with the capacity of 500 kN, and controlled in displacement. The cyclic horizontal load was applied in the way to produce an

antisymmetric moment in a column. The horizontal load was turned back when the deflection angle of member, R reached $\pm 1/400$, $\pm 1/200$, $\pm 1/100$, $\pm 1/67$ and $\pm 1/50$, until after the peak load.

The widths of every shear crack over shear reinforcements were measured using two digital microscopes with a resolution of 0.01 mm every cycle three times in loading and two times in unloading. The crack width used in this paper is defined as a distance normal to the direction of a crack, as illustrated in Fig. 5. Three strain gauges were glued on each leg of all transverse hoops, and their locations and designations are shown in Fig.5.

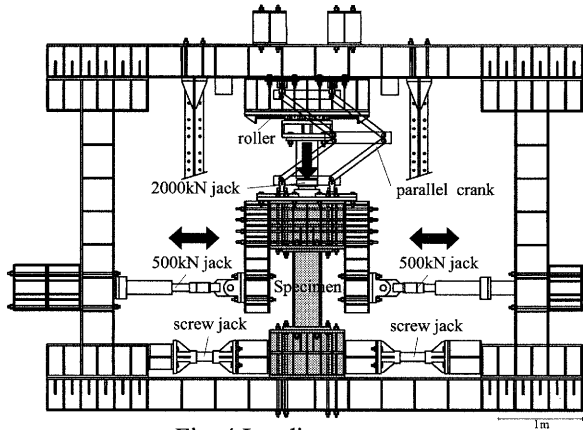


Fig. 4 Loading apparatus

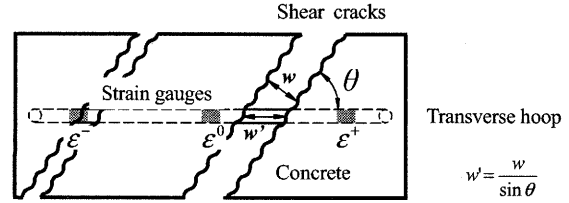


Fig. 5 Definition of crack width and designations of strain gauges

2.3 Idealizations in Analysis

The finite element mesh and boundary conditions are shown in Fig.1. Due to the symmetry, only one half of the column was analyzed. The stiff elements were attached at the top and bottom of a column to idealize steel stubs. The top nodes were constrained to move uniformly in the vertical direction and not to allow the upper stiff elements to rotate, so that a column deformed in an antisymmetric mode. Concrete was modeled by a twenty-node isoparametric solid brick element, and longitudinal reinforcements were embedded in concrete elements to add stiffness to them. The shear reinforcements were modeled by a two-node numerically integrated truss element because the effect of bending was negligible. The bond-slip between concrete and reinforcements was not considered in this analysis because an additional reinforcement was installed to avoid a bond splitting failure. The prescribed prestress was introduced into the shear reinforcements, and then the axial load was applied in load control with ten steps up to the axial load ratio of 0.3, finally the shear load was applied in displacement control with a step of 0.01 mm. The maximum-tensile-stress criterion of Rankine was adopted as a failure criterion in the tension zone of concrete. According to this criterion, a crack arises when the maximum principal stress exceeds the tensile strength, regardless of the normal or shearing stresses that occur on other planes. Smeared cracking and bi-linear tension softening shown in Fig.2 are adopted in this analysis. The shear stiffness of cracked concrete is generally dependent on the crack width. This phenomenon is taken into account by decreasing the shear stiffness with an increase of the normal crack strain. Drucker-Prager criterion was used for a failure criterion in the compressive zone of concrete. The formulation is given by

$$f(I_1, J_2) = \alpha I_1 + \sqrt{J_2} - k = 0 \quad (1)$$

$$\alpha = \frac{2 \sin \phi}{\sqrt{3}(3 - \sin \phi)} \quad (2)$$

$$k = \frac{6 \cos \phi}{\sqrt{3}(3 - \sin \phi)} c \quad (3)$$

$$I_1 = \sigma_1 + \sigma_2 + \sigma_3 \quad (4)$$

$$J_2 = [(\sigma_1 - \sigma_2)^2 + (\sigma_2 - \sigma_3)^2 + (\sigma_3 - \sigma_1)^2] / 6 \quad (5)$$

where ϕ is the internal-friction angle, c is the cohesion; σ_1 , σ_2 and σ_3 are the principal stresses (see

Chen 1982). The internal-friction angle of Drucker-Prager was determined based on experimental results performed on concrete cylinders with different strengths and hoops to study the effect of lateral confinement by Takamori et al. (1996). According to their test results, the strength of concrete confined by lateral reinforcements similar to our specimen increases to $(\sigma_B + 2.0\sigma)$, where σ_B is the compressive strength of plain concrete and σ is the averaged lateral confining stress. An increasing rate to σ of 2.0 is under half 4.1 proposed by Richart (1928) due to the partial confinement by hoops. From this equation, a set of principal stresses that corresponds to the strength of concrete in a triaxial state of stress with confining pressure is determined as: $\sigma_1 = \sigma_2 = -\sigma$, $\sigma_3 = -(\sigma_B + 2.0\sigma)$. The minus refers to compression. By substituting this state of principal stresses into Eq. (1)

$$f(I_1, J_2) = (1 - \sqrt{3}\alpha)\sigma_B + (1 - 4\sqrt{3}\alpha)\sigma - \sqrt{3}k = 0 \quad (6)$$

Because Takamori's tests (1996) showed a constant coefficient of 2.0 for any value of the averaged confining stress, Eq. (6) must be valid regardless of σ , as well. Therefore, the multiplication factor of second term in Eq. (6) must be zero:

$$(1 - 4\sqrt{3}\alpha) = 0 \Rightarrow \alpha = 1/4\sqrt{3} \quad (7)$$

By substituting Eq. (7) into Eq. (2), the internal-friction angle of 20° is estimated to be suitable for triaxial state of stress confined laterally by reinforcements.

3. RELATION BETWEEN SHEAR STRENGTH AND LATERAL CONFINEMENT

3.1 Shear Load-Deflection Angle R Curves

The shear load Q -deflection angle R curves obtained from the tests are shown in Fig.6, compared with the results of analysis. For the typical crack behavior observed during tests, flexural cracks appeared first, and they extended into flexural shear cracks near the both end of the specimen, and finally shear cracks occurred with increasing shear load. The maximum shear loads for RC and LPRC column are 617 kN when $R=1/100$ and 762 kN when $R=1/67$ respectively. The shear loads for both RC and LPRC were gradually reduced without any reinforcement's yielding by crushing concrete in the compressive zone at the top and bottom ends. The shear crack strength and ultimate shear strength obtained from experiments and FEM analyses are compared in Table 3 together with the calculation results taking account of the lateral prestress by Watanabe (2004). The shear crack strength of analyses is defined as the shear load which causes a strain in shear reinforcements to increase rapidly. As can be seen from Fig. 6, FEM analyses show a higher stiffness than experiments because of the stress locking by the use of smeared crack model and the additional damage by cyclic loadings. However, FEM analyses can predict with a fair degree of precision the difference between the shear strengths of RC and LPRC columns. The relations between shear crack stress $\tau_{sc} (= \exp Q_{sc} / bD)$ and lateral prestress, and between ultimate shear stress $\tau_{su} (= \exp Q_{su} / bD)$ and lateral prestress are plotted in Fig.7 together

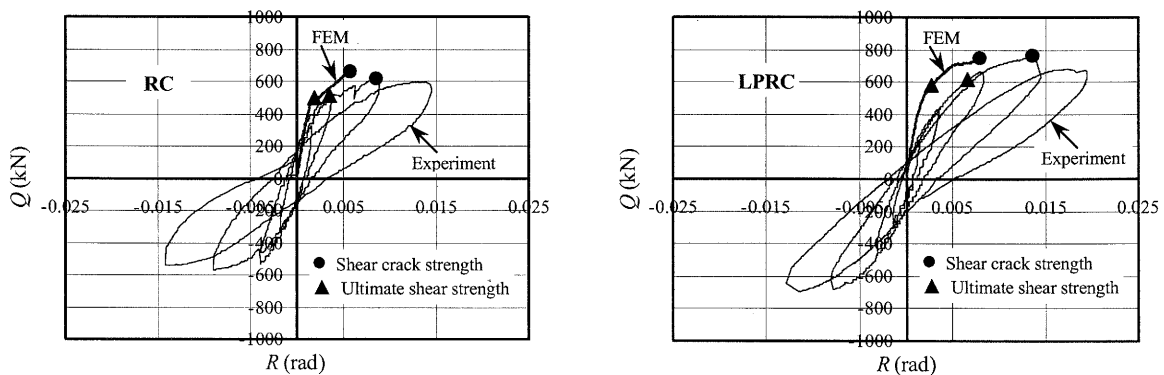


Fig. 6 Comparisons between analytical and experimental Q-R curves for RC (left) and LPRC (right) specimens

with Watanabe's data (2004) marked by solid-white ($\sigma_B=35 \text{ N/mm}^2$). The difference in strength of concrete was adjusted by dividing them by the characteristic strength to determine their failure modes. It can be seen from Fig.7 that the shear crack strength and ultimate shear strength have increased proportionally with increasing lateral pressure. Furthermore, Fig.8 shows a comparison of the shear strengths obtained from experiment and analysis. The predictions of FEM analysis are consistent with all existing experimental data for the shear crack strength and the ultimate shear strength.

Table 3 Shear crack strength and ultimate shear strength

Test Designation	$exp Q_{sc}$ (kN)	$exp Q_{su}$ (kN)	$FEM Q_{sc}$ (kN)	$FEM Q_{su}$ (kN)	$cal Q_{sc}$ (kN)	$cal Q_{su}$ (kN)
RC	515	617	495	655	496	648
LPRC	611	762	577	747	606	725

$exp Q_{sc}$ =shear crack strength by experiment, $exp Q_{su}$ =ultimate shear strength by experiment
 $FEM Q_{sc}$ =shear crack strength by FEM, $FEM Q_{su}$ =ultimate shear strength by FEM
 $cal Q_{sc}$ =shear crack strength by Watanabe, $cal Q_{su}$ =ultimate shear strength by Watanabe

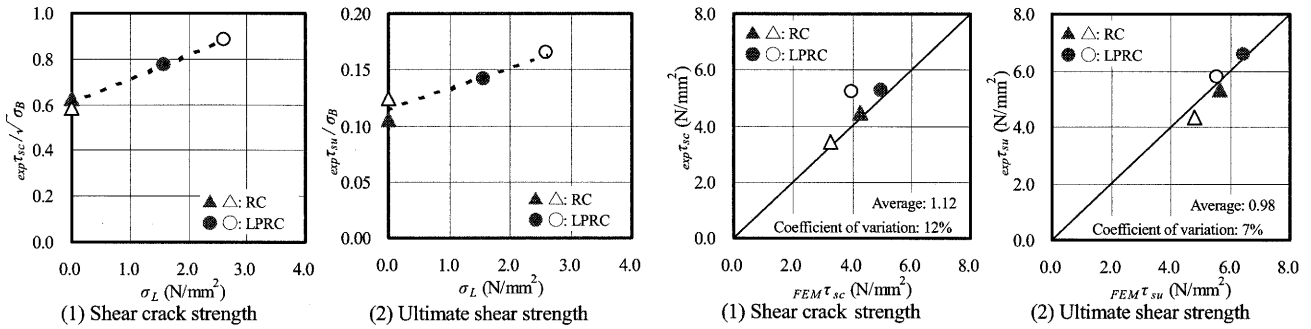


Fig. 7 Increase of strength with increasing lateral prestress σ_L

Fig. 8 Comparison of strength from experiment and analysis

3.2 Triaxial State of Stress by FEM Analysis

Fig.9 shows the distributions of the minor principal stress in the center of RC and LPRC specimens. For RC specimen, the compressive strut formed by a large compressive stress was revealed at the shear load of 550 kN, thereafter, the width of the strut reduced slightly and localized in a diagonal direction at the maximum load. For LPRC specimen, on the other hand, the compressive strut appeared at the shear load roughly similar to the maximum load of RC and the width of the strut increased gradually up to the maximum load. This difference is probably due to the crack patterns of RC and LPRC specimens described in Section 4. The degree of damage for compressive failures and the equivalent confining pressure were introduced as the gauges to evaluate the effect of active confinement on the stress state in the core concrete quantitatively, as shown in Fig.10. The degree of damage for compressive failures is defined using the deviated part of the stress state in principal stress space. Fig.11 shows the degree of damage for compressive failures in the surface of RC and LPRC specimens at the same shear load as Fig.9. It can be seen from Fig.9 and Fig.11 that the distributions of the degree of damage correspond roughly with those of the minor principal stress. This degree of damage for LPRC is lowered compared with RC specimen because of the active confinement. The red parts dotted with a white dot at the top and bottom ends represent the post-peak softening zone of concrete, so that the failure mode of analysis is quite similar to that of experiment. The softening of concrete for RC specimen occurred when the shear load is about 600 kN, and the softening zone was limited to the small area. This softening for LPRC specimen, on the contrary, occurred at the shear load of 700 kN, and the softening zone was gradually expanded up to the maximum load. The equivalent confining pressure is defined as the lateral pressure when converting the stress state on a random stress-path into that on the stress-path according to the triaxial compressive test with a constant lateral pressure, as shown in Fig.10. Consequently, the equivalent confining pressure increases with increasing hydraulic component and decreasing deviated component of the stress state in principal stress space. The ratio of the equivalent confining pressure to the strength of concrete is shown in Fig.12 to compare RC with LPRC at maximum shear loads. Although the very small passive confining was induced in RC specimen by applying the axial load (Shinohara et al. 2004), it was

vanished with an increase in the shear load by 400 kN. It can be seen from Fig.9 and Fig.12 that with further increasing shear load, the equivalent confining pressure increase in the same area where the compressive stress grew larger and localized. As for LPRC specimen, the active confinement that is over ten times higher than the passive confinement was produced after applying the axial load, and it covered wider parts of the specimen than RC specimen until the maximum shear load.

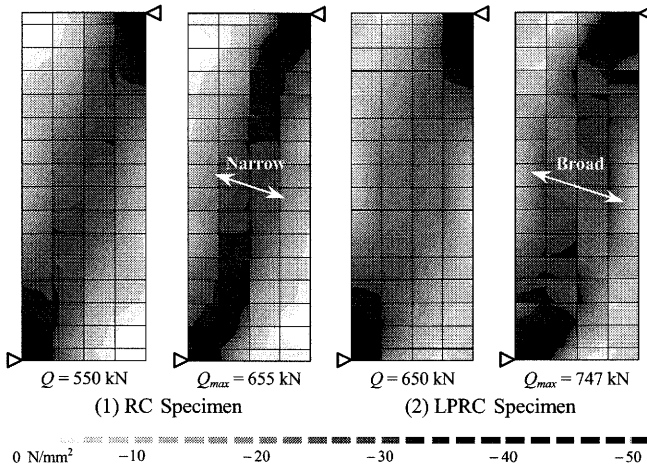


Fig. 9 Compression strut based on minor principal stress

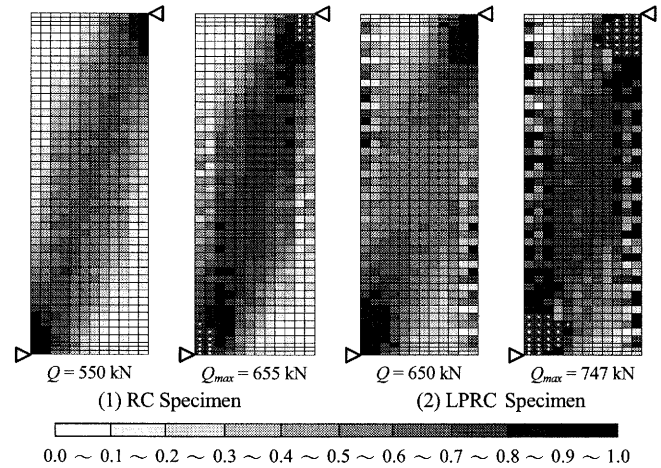


Fig. 11 Comparison of damage in compression zone

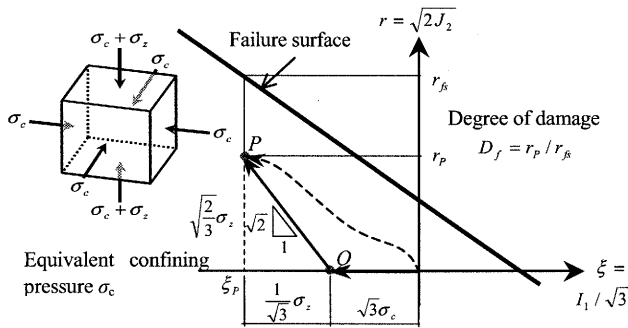


Fig. 10 The degree of damage and equivalent confining pressure for triaxial state of stress in meridian plane of Drucker-Prager criterion

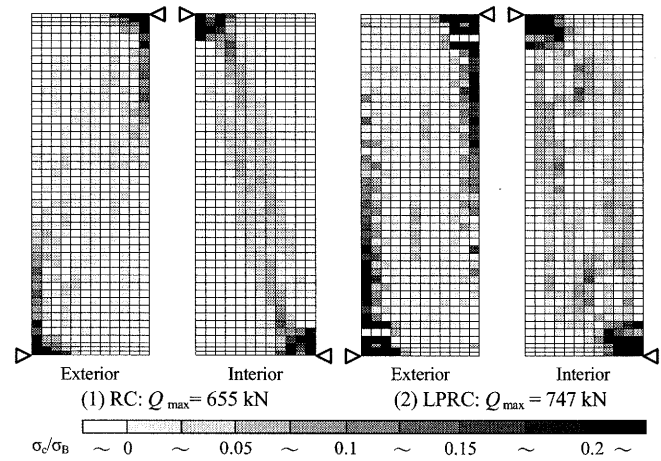


Fig. 12 Equivalent confining pressure at maximum shear load

4. SHEAR CRACK BEHAVIOR AND STRAIN IN SHEAR REINFORCEMENT

4.1 Relation between Shear Crack Patterns and Strains in Shear Reinforcement

Fig.13 shows the contours of the crack strain obtained by analyses and the diagrams of shear cracks observed by experiments. The crack patterns in front and back of specimens were basically similar (Miyano et al. 2004). The lateral confinement in LPRC specimen restrained greatly shear cracks from propagating at the shear load similar to the peak load of RC specimen, and the final crack pattern of LPRC differed drastically from that of RC. The shear cracks developed scatteringly in the upper and lower side of LPRC specimen, whereas they developed intensively in the center of RC specimen. The spacing and width of scattered cracks in LPRC specimen are smaller than those of localized cracks in RC specimen. This small crack spacing developed in LPRC specimen is probably due to the increase in bond strength (Braam 1990) and to the tensile stress generated by introducing lateral prestress. Because the ability to transmit shear force across a rough crack is exponentially reduced with increasing crack width (Shinohara et al. 1999), the scattered crack with a smaller width can reduce to a certain degree a decrease in shear stiffness of a column.

Fig.14 shows the distribution of strains in shear reinforcements at the maximum shear loads obtained from experiments and analyses. As can be seen from Figs. 13 and 14, an increment of strains in the shear reinforcement is roughly consistent with the width of shear cracks. In the case of RC experiment, because the shear cracks localized and deviated to the right around middle height, the corresponding strain ε^+ was highest and the three strains of gauges glued on each reinforcement differed by a maximum of 2700μ . In the case of LPRC experiment, on the other hand, because the shear cracks did not localized and were scattered over the depth of the column, the differences among three strains in each reinforcement were within 800μ . The strain distributions by analysis for RC specimen are antisymmetric to half height and do not fully correspond with those by experiment because of localized shear cracks, whereas the analytical result for LPRC shows a good agreement with the experimental result including the shape of the vertical distribution showing higher strains in the upper and lower side due to the distributed shear cracks in there. The relationship between the width of shear cracks and the elongation of shear reinforcements is shown in Fig.15 where the total crack widths over a reinforcement observed by microscope, $\Sigma_{exp} w'$ (see Fig.5) are plotted as the abscissa and the elongations of the corresponding reinforcement calculated using the strains, $\Sigma_{cal} w$ as the ordinate. The elongation, $\Sigma_{cal} w$ in Fig15 (1) is calculated using only one strain at center and $\Sigma_{cal} w$ in Fig.15 (2) using all three strains. If shear cracks are scattered over shear reinforcements such as LPRC specimen, the total crack widths, $\Sigma_{exp} w'$ can be estimated fairly accurately by one strain of the reinforcement. In the case of localized shear cracks such as RC specimen, a better estimate of $\Sigma_{exp} w'$ can be obtained by integrating the strain distribution of three gauges.

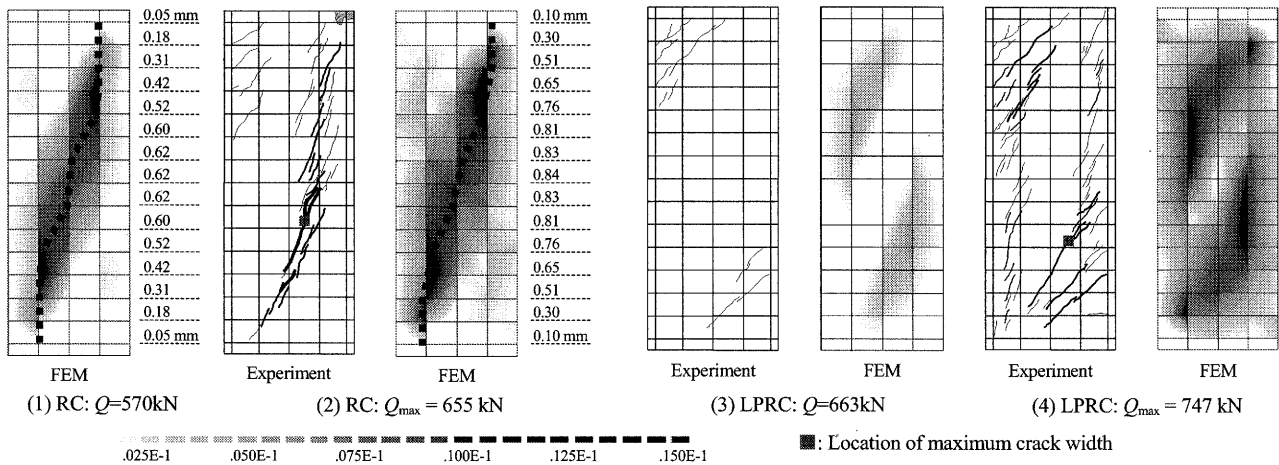


Fig. 13 Comparisons between crack pattern from experiment and crack strain from FEM

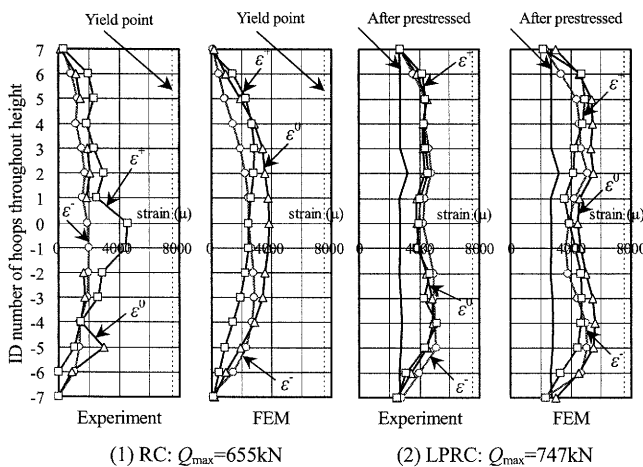


Fig. 14 Comparisons between strain distribution of hoop from experiment and analysis

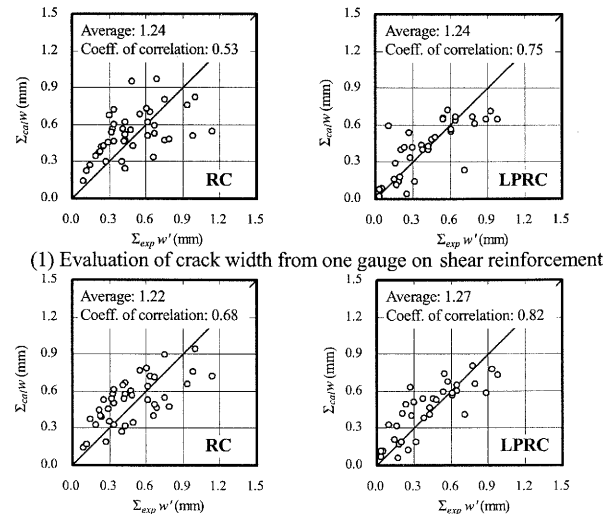


Fig. 15 Relations between shear crack width and strain of hoop

4.2 Estimations of Shear Damage by FEM Analysis

To investigate how accurate the FEM analysis with a smeared crack model can evaluate the extent of actual shear crack damage, the total crack width by FEM analysis, $\Sigma_{FEM}w$, which is estimated from the nodal displacements at both ends of a shear reinforcement by neglecting the strains of concrete, is shown in Fig.16 together with $\Sigma_{exp}w$ by microscopes and $\Sigma_{cal}w$ by strains. Although $\Sigma_{exp}w$ is observed on the surface of concrete while $\Sigma_{cal}w$ and $\Sigma_{FEM}w$ are estimated by a reinforcement, these three crack widths exhibit broadly similar behavior due to the small cover concrete of 9 mm. The difference between the crack width behaviors of RC and LPRC specimen is basically consistent with that of shear crack behaviors in Fig.13 and strain behaviors of reinforcements in Fig.14 since the total crack width faithfully reflects their behaviors. Especially, the experimental and analytical crack width, $\Sigma_{cal}w$ and $\Sigma_{FEM}w$ are similar and closely related to the apparent Poisson's ratio including cracks. The comparison among three crack widths indicates that most of the apparent Poisson's ratio is due to the shear cracks. In addition, the FEM analyses using smeared crack model cannot accurately evaluate a localized crack but can provide valuable information about the total damage in the overall depth of a specimen.

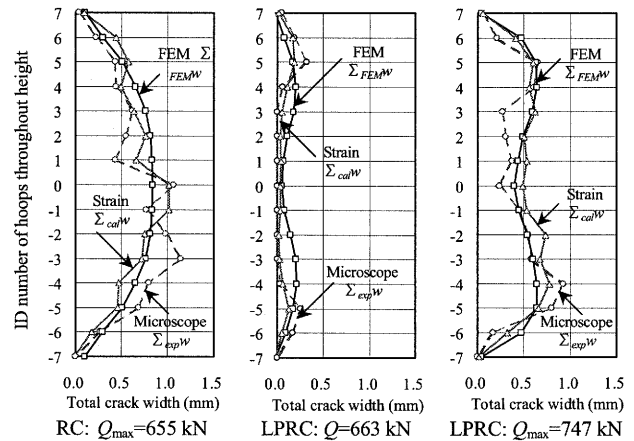


Fig. 16 Total crack width obtained from microscope, strain of shear reinforcement and FEM analysis

5. CONCLUSIONS

- 1) The shear crack strength and ultimate shear strength have increased proportionally with increasing lateral pressure.
- 2) The FEM analyses have revealed that an increase in resistance against shear failure as well as shear cracking with increasing lateral prestress could be explained by the triaxial state of stress.
- 3) The shear crack patterns have changed appreciably, and the spacing and width of cracks have decreased drastically by introducing lateral prestress into a RC column.
- 4) The close relationship between the width of shear cracks and the distributed strain in reinforcements has been proven both by experiments and by FEM analyses.
- 5) The FEM analyses using smeared crack model cannot evaluate a localized crack accurately but can provide valuable information about the total damage in the overall depth of a column.

References:

- Watanabe, H., Katori, K., Shinohara, Y. and Hayashi, S. (2004), "Shear crack control by lateral prestress on reinforced concrete column and evaluation of shear strength", *J. of Struct. and Const. Eng.*, AIJ, No.577, pp.109-116
- Shinohara, Y., Miyano, K., Watanabe, H. and Hayashi, S. (2004), "Active confining effect and failure mechanism for RC columns prestressed laterally", *Journal of Structural and Construction Engineering*, AIJ, No.578, pp.115-121
- Architectural Institute of Japan (1999), "Design Guidelines for Earthquake Resistant Reinforced Concrete Buildings Based on Inelastic Displacement Concept"
- Takamori, N., Benny Benni Assa, Nishiyama, M. and Watanabe, F. (1996), "Idealization of Stress-Strain Relationship of Confined Concrete", *Proceedings of the Japan Concrete Institute*, Vol.18, No.2, pp.395-400
- Richart, F.E., Brandtzaeg, A. and Brown, R. L. (1928), "A Study of the Failure of Concrete under Combined Compressive Stresses", Univ. of Illinois, Engineering Experiment Station, Bulletin, No.185
- Chen, W. F. (1982), "Plasticity in Reinforced Concrete", McGraw-Hill Book Company
- Miyano, K., Shinohara, Y., Watanabe, H. and Hayashi, S. (2004), "Effect of Lateral Prestress on Control of Shear Crack Width in R/C Columns", *Proceedings of the Japan Concrete Institute*, Vol.26, No.2, pp.223-228
- Shinohara, Y. and Kaneko, M. (1999), "Compressive shear behavior in fracture process zone of concrete", *Journal of Structural and Construction Engineering*, AIJ, No.525, pp.1-6
- Braam, C. R. (1990), "Control of Crack Width in Deep Reinforced Concrete Beams", *HERON*, Vol. 35, No. 4

SEISMIC PERFORMANCE OF STEEL REINFORCED CONCRETE MEMBERS USING LIGHT-WEIGHT AGGREGATE CONCRETE

H.L. Hsu¹⁾, H.C. Chen²⁾, and J.Z. Chen²⁾

1) Professor, Dept. of Civil Engineering, National Central University, Taiwan

2) M.S. Dept. of Civil Engineering, National Central University, Taiwan

t3200178@ncu.edu.tw

Abstract: Steel reinforced concrete (SRC) has been widely used in building constructions. In order to perform well in an earthquake, the SRC design must possess sufficient strength and high ductility. To further improve the seismic-resistant efficiency of such design, reduction in member weight so that member ductility can be maintained and a higher strength/mass ratio can be accomplished is essential. For this purpose, application of light-weight aggregate concrete becomes a promising solution, because member weight can be significantly reduced. This study is focused on the experimental evaluation of seismic performance of SRC members using light-weight aggregate concrete. Specimens with various sectional placements were tested under combined bending and axial loads. Test results showed that the energy dissipation capacity of light-weight aggregate concrete SRC members with adequate confinements stayed at the equivalent level as that of normal-weight concrete SRC, which justified the applicability of light-weight aggregate concrete SRC to the seismic-resistant design.

1. INTRODUCTION

Steel reinforced concrete (SRC) members possess high strength and significant ductility, thus are effective structural forms for earthquake resistant purposes. Current information on the behavior of SRC members composed of structural steel and traditional normal weight concrete can be found in several design codes, such as AIJ(1991), ACI(2002), LRFD(2001), etc. In general, the reinforced concrete contributes the major portion of the member weight. Although the reinforced concrete can help prevent the local buckling of the encased steel and enhance the structural stiffness, the higher structural weight due to comprising concrete might limit the application of the design when seismic design efficiency is considered. In this regard, a minimization approach to reduce the weight of the SRC members so that the design efficiency can be improved is essential. To accomplish this goal, an attempt to employ lighter concrete material, such as light weight aggregate concrete (LWAC), for SRC designs is made in this study.

In general, LWAC possesses higher brittleness and less concrete-steel bond than the normal weight concrete (Wang et al. 1978, Khaloo et al. 1999, Ahmad and Barker 1991). These characteristics are particularly important if the material is used for SRC designs, because the SRC member performance is significantly affected by the composite behavior between the concrete and structural steel. In order to apply the LWAC to the SRC seismic design, the member strength and ductility under dynamic loading must be validated so that the applicability can be justified. This study is focused on the experimental evaluation of seismic performance of LWAC SRC members by a series of combined loading tests.

2. EXPERIMENTAL PROGRAM

Ten specimens with various steel-concrete compositions and various confinement conditions were fabricated for testing. They included two normal weight concrete SRC members and eight LWAC SRC members. Two types of structural steels were used for member fabrications: JIS SS400 H125x125x6.5x9 and H150x150x7x10. Compressive strengths of the normal and light weight aggregate concretes were 34 and 37.2 Mpa, respectively. Specific weight for the LWAC was 1.8. Half of the specimens were confined with traditional stirrups, and the others were confined with stirrups and additional tie bars, named bi-lateral confinement hereafter. The longitudinal and transverse reinforcements of the reinforced concrete were composed of #5 and #3 deformed bars. The length of the members' confining zones was 650 mm. The stirrup spacings within and outside the confining zones were 100 mm and 150 mm, respectively. Specimen details are shown in Figure 1.

All specimens were tested under combined axial and cyclic lateral loads. The magnitude of the axial load was set to a prescribed fraction of the members' compressive strength (P_n), which was determined by the following expression:

$$P_n = 0.85A_c f'_c + A_s f_y + A_r f_{yr} \quad (1)$$

in which, A_c , A_s , A_r are the cross-sectional areas of the concrete, steel, and longitudinal bars, respectively; and f'_c , f_y , f_{yr} are the concrete compressive strength, yield strength of steel and longitudinal bars, respectively. Axial load magnitude for the normal weight concrete SRC was $0.2 P_n$. Results from these tests were used for comparison purposes. Axial load magnitudes used for the LWAC SRC members were $0.2 P_n$ and $0.35 P_n$, respectively. The purposes for these load combinations were to investigate whether performance differences existed when different concrete materials and various load levels were adopted. Specimen labels and the corresponding load combinations are listed in Table 1. Axial load was applied by a hydraulic jack and the cyclic lateral load was generated by a servo-controlled hydraulic actuator through a series of prescribed displacement commands. The test set-up is shown in Figure 2.

3. OBSERVATIONS

When members were subjected to combined axial and lateral loads, the flexural cracks were first observed at the members' confining zones. Drifts at which flexural occurred for both normal and light weight concrete SRC members were all less than 1%. Among them, the LWAC members exhibited cracks slightly earlier than the normal weight ones. This can be attributed to the higher brittleness of the LWAC. Cover concrete spalled following the occurrence of longitudinal bar buckling at drift ratio approximately equaled to 6%. In general, the normal and light weight concrete SRC members exhibited similar failure patterns, however, they differed in the length of the damaged regions, as shown in Figure 3. It can be found from the figure that the length of crushed concrete was larger in members composed of LWAC. It is also observed that the extent of damage of the core concrete was reduced when the bi-lateral confinement was adopted.

4. COMPARISONS OF TEST RESULTS

The typical load-displacement relationships for the test specimens are shown in Figure 4. In order to define the seismic performance of the LWAC SRC members, the members' ductility, μ_E , was evaluated by their energy dissipation capabilities as follows:

$$\mu_E = \frac{\sum E_{80}}{\sum E_y} \quad (2)$$

in which SE_y is the elastic strain energy and SE_{80} is the cumulative energy dissipation at the ultimate stage, determined by the value when the member strength dropped to 80% of its maximum strength. These values were further normalized with the ductility of the normal weight concrete SRC members, so that their performance level could be defined.

Table 1 and Figure 5 show the normalized ductility of the test members. It can be found from the comparisons that, when member weight was ignored, the LWAC SRC members with smaller steel ratios, i.e. 2.474% in this study, would develop less ductility than the normal weight ones. However, when adequate steel ratio was used, i.e. 3.277% in this study, the LWAC SRC members did possess equivalent seismic resistance as those of the normal weight ones. It is also found in this figure that for members subjected to higher degree of axial load, i.e. LTBC35, member ductility can still be maintained as long as effective confinement was presented. These phenomena first validated that the application of LWAC to the SRC design was promising when adequate sectional detailing was adopted.

Applicability of LWAC to SRC design can be further validated by considering the member weight of the LWAC. As shown in Figure 6, when normalized member ductility is scaled by the member weight, defined as the normalized unit-weight ductility, the ductility of member with smaller steel ratio can reach a value close to the normal weight member. Furthermore, the ductility of LWAC SRC members with sufficient steel ratio and effective bi-lateral confinements were also significantly enhanced. These comparisons concluded the feasible application of LWAC to SRC designs.

5. CONCLUSIONS

This paper presents the combined loading test information of a series of SRC members using various confinements and concrete with different compositions. Test results showed that the failure patterns of the LWAC SRC members were similar to those of the normal weight ones. Test results also demonstrated that the energy dissipation capacity of LWAC SRC members with adequate confinements stayed at the equivalent level as that of normal-weight concrete SRC, which justified the applicability of LWAC SRC to the seismic-resistant designs.

Acknowledgements:

This study was partially supported by the National Science Council of the Republic of China under Grant No. NSC 93-2211-E-008-021, which is gratefully acknowledged.

References:

- ACI (2002), "Building Code Requirements for Reinforced Concrete (ACI 318-02)," American Concrete Institute, Detroit.
- AISC(2001) , "Load and Resistance Factor Design Specification for Structural Steel Design," American Institute of Steel Construction, Chicago, Illinois.

AIJ(1991), "Standards for Structural Calculation of Steel Reinforced Concrete Structures," Architectural Institute of Japan.

Khaloo .A.R. .EI-Dash .K.M. .and Ahmad .S.H. (1999), "Model for Lightweight Concrete Columns Confined by Either Single Hoops or Interlocking Double Spirals," *ACI Structural Journal*, Dec., 883-890.

Ahmad .S.H. .and Barker .R.(1991), "Flexural Behavior of Reinforced High-Strength Lightweight Concrete Beams," *ACI Structural Journal*, Feb., 69-77.

Wang .P. T. .Shah .S.P. .and Naaman .A. E. (1978), "Stress-Strain Curves of Normal and Lightweight Concrete in Compression," *ACI Structural Journal*, Nov., 603-611.

Table 1 Loading Combinations and Normalized Ductility for Test Specimens

Specimen	Concrete used	Confinements	Steel ratio (%)	Axial load (Pn)	SE_y (kN-m)	SE_{80} (kN-m)	μ_E (SE_{80}/SE_y)	Normalized ductility
NSAC20	Normal	Stirrups	2.474	0.20	1.53	46.6	30.46	1
LSAC20	LWAC	Stirrups	2.474	0.20	2.18	46.94	21.53	0.71
LTAC20	LWAC	Bi-lateral	2.474	0.20	2.41	60.92	25.28	0.83
LSAC35	LWAC	Stirrups	2.474	0.35	2.20	32.72	14.87	0.49
LTAC35	LWAC	Bi-lateral	2.474	0.35	2.87	44.76	15.60	0.51
NSBC20	Normal	Stirrups	3.277	0.20	1.92	61.76	32.17	1
LSBC20	LWAC	Stirrups	3.277	0.20	2.63	86.82	33.01	1.03
LTBC20	LWAC	Bi-lateral	3.277	0.20	3.11	144.27	46.39	1.44
LSBC35	LWAC	Stirrups	3.277	0.35	2.60	52.56	20.22	0.63
LTBC35	LWAC	Bi-lateral	3.277	0.35	3.50	113.15	32.33	1

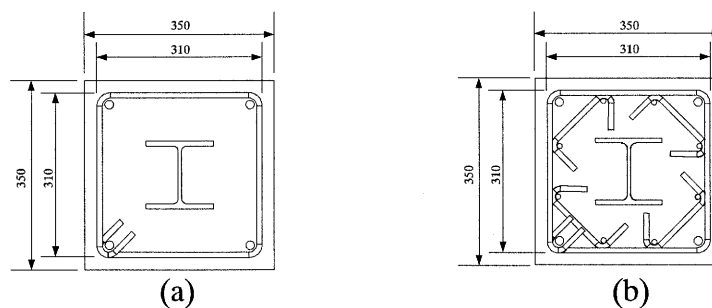


Figure 1 Specimen Details: (a) Confined by Stirrups, (b) Bi-Lateral Confinements

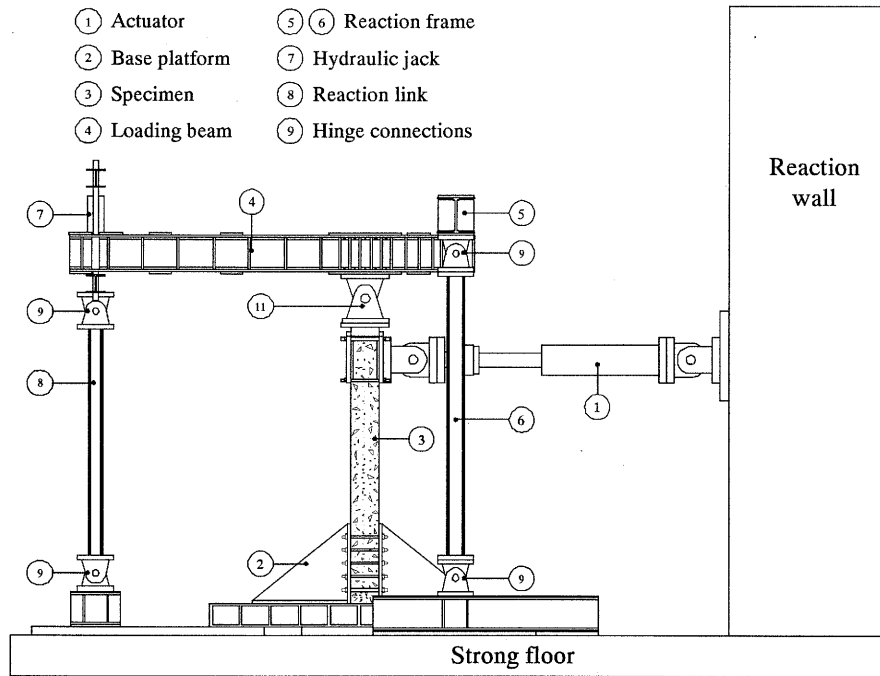
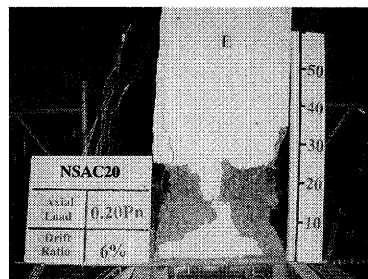
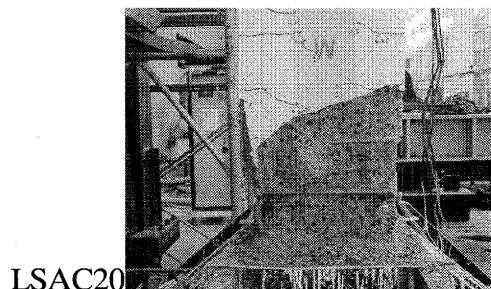


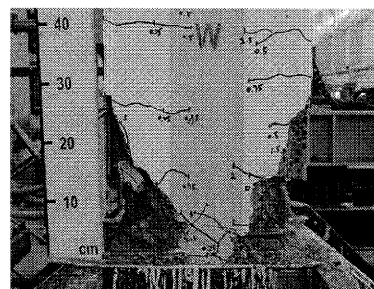
Figure 2 Test Set-up



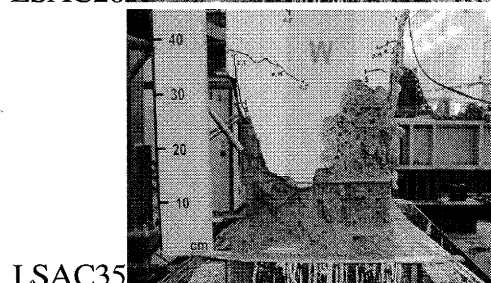
NSAC20



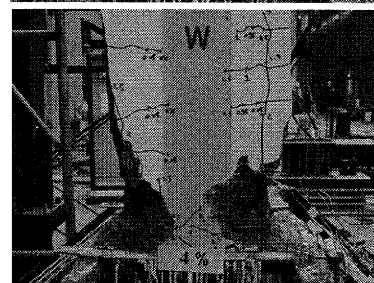
LSAC20



LTAC20

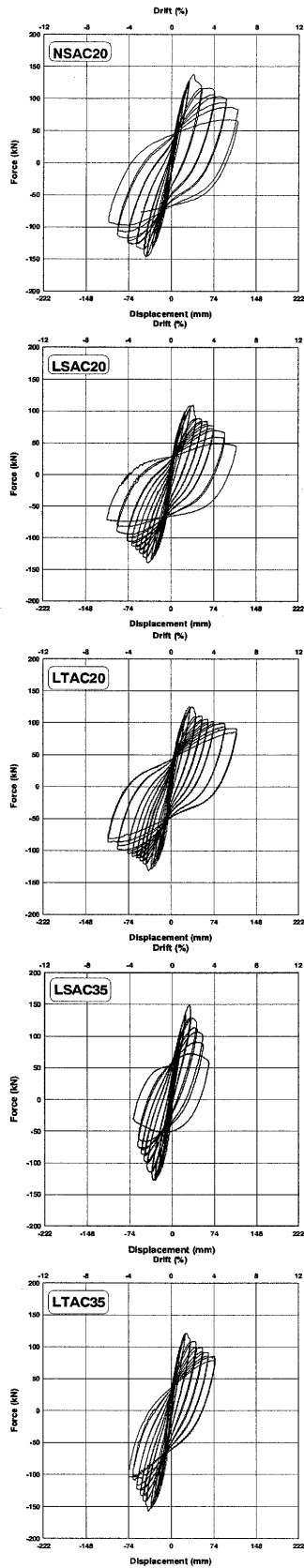


LSAC35

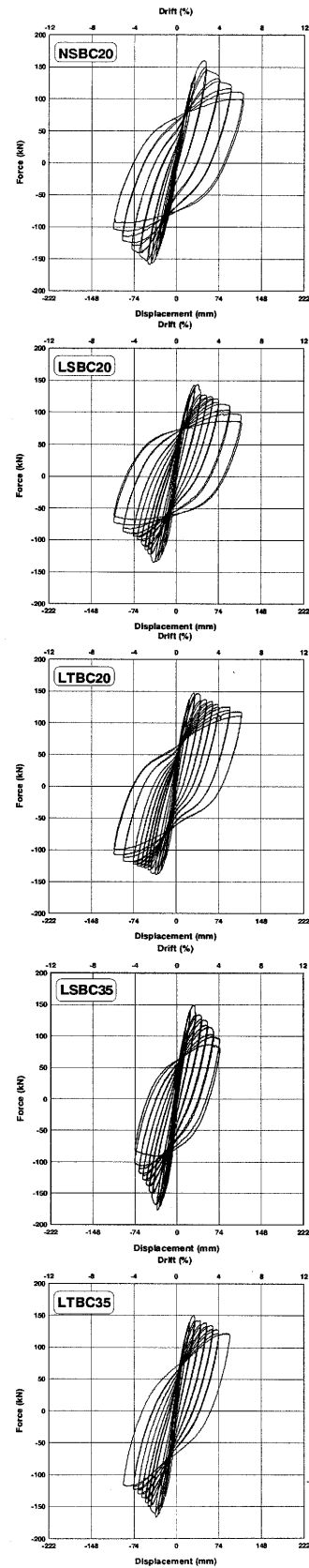


LTAC35

Figure 3 Typical Failure Patterns of Test Specimens



(a)



(b)

Figure 4 Load-Displacement Relationships:
 (a) Specimens with Smaller Steel Ratio,
 (b) Specimens with Larger Steel Ratio

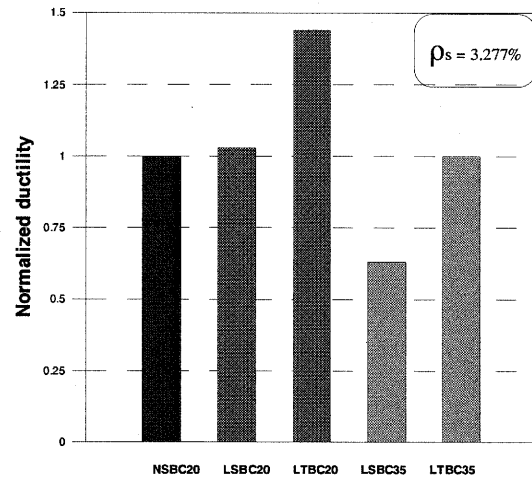
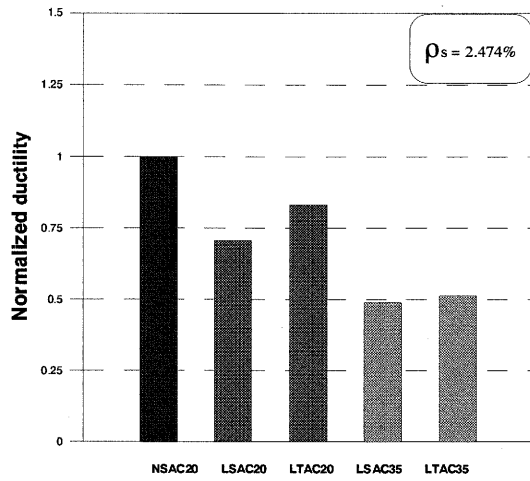


Figure 5 Normalized Ductility of the Test Specimens

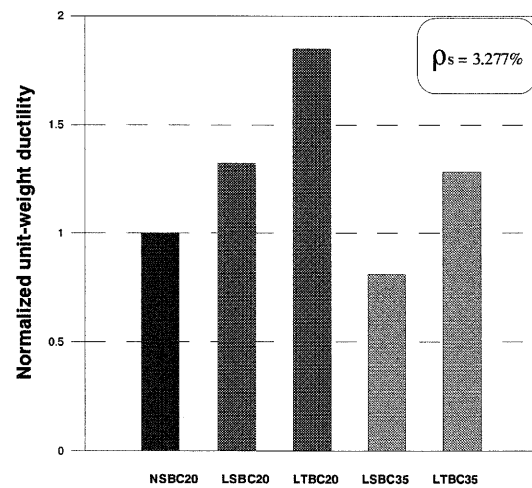
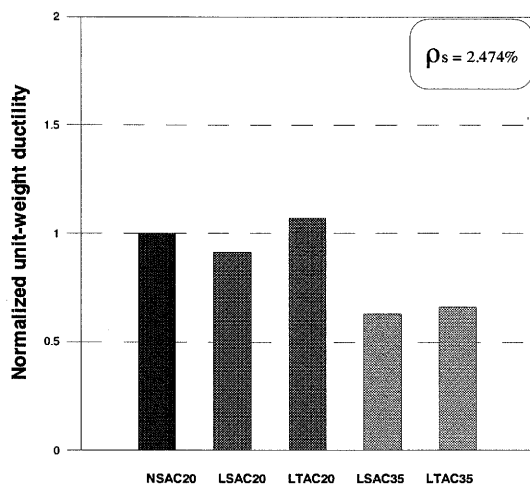


Figure 6 Normalized Unit-Weight Ductility of the Test Specimens

DIFFERENCE BETWEEN STATIC TEST RESULTS AND REAL RESTORING FORCE CHARACTERISTICS

K. Nishimura¹⁾, K. Takiguchi²⁾, and K. Masaki³⁾

1) Assistant Professor, Dept. of Architecture and Building Engineering, Tokyo Institute of Technology, Japan

2) Professor, Dept. of Mechanical and Environmental Informatics, Tokyo Institute of Technology, Japan

*3) Graduate Student, Dept. of Mechanical and Environmental Informatics, Tokyo Institute of Technology, Japan
knishimu@tm.mei.titech.ac.jp, ktakiguc@tm.mei.titech.ac.jp, kmasaki@tm.mei.titech.ac.jp*

Abstract: A static loading test is effective method to understand restoring force characteristics of structural members. Test results are usually regarded as the characteristics of the members, but the test results include friction of experimental apparatus and measuring error. This problem is very serious because hysteresis loops obtained from test results are expected to dissipate energy input of real earthquake. Purpose of this study is to consider estimation of static test results based on test results of three steel pipe specimens subjected to three-directional cyclic loading. As results, in this investigation, the test results had more than 3% of equivalent damping factor, and differences of axial load and of amplitude of cyclic displacement didn't influence equivalent damping ratio on one-directional cyclic loading in elastic range.

1. INTRODUCTION

A static loading test is effective method to understand restoring force characteristics of structural members. Test results are usually regarded as the characteristics of the members, but the test results include friction of experimental apparatus and measuring error. This problem is very serious because hysteresis loops obtained from test results are expected to dissipate energy input of real earthquake. Purpose of this study is to consider estimation of static test results based on test results of three steel pipe specimens subjected to three-directional cyclic loading. Steel is one of the most predictable materials of restoring force characteristics, and pipe must show isotropic behaviors under bi-axial bending. Three steel pipe column specimens were prepared for the test. The specimens have 101.6mm outside diameter, 5.7mm thickness, and 600mm clear span. The specimens were subjected to three-directional loading in elastic range those were axial load and two-directional anti-symmetric bending. The experimental apparatus used in this investigate have been developed for large displacement to obtain elasto-plastic behaviors of members. If friction of experimental apparatus and measuring error are a little enough, test results show linear behaviors in the elastic range. Influence of error included in the test results was investigated from the test results.

2. EXPERIMENTAL PROGRAM

2.1 Specimens

Three identical steel pipe column specimens were prepared for the test those were named SP-1, SP-2, and SP-3. As shown in Figure 1, the specimens have 101.6mm outside diameter, 5.7mm

thickness, and 600mm clear span. Sixteen strain gages were pasted on sections near the head and the base of column. Table 1 shows material properties of steel those were obtained from material test.

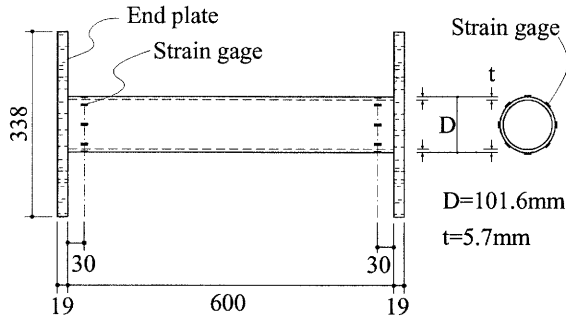


Figure 1 Detail of Specimens

Table 1 Material Properties of Steel

Yield strength [N/mm ²]	320
Yong's modulus [kN/mm ²]	210
Poisson's ratio	0.30

2.2 Loading Plans

Figure 2 shows loading setup. The specimens were subjected to two directional anti-symmetric lateral cyclic loadings and varying axial force by the experimental apparatus, which developed by the authors (Nishimura and Takiguchi, 2005) that allows tri-axial translation and restricts tri-axial rotation of the head of specimens. This apparatus been developed for large displacement to obtain elasto-plastic behaviors of columns. Therefore measuring error included in test result must be larger than that of an apparatus aimed to one directional lateral loading test and range of small displacement.

Figure 3 shows loading plans of the three specimens. Displacements and forces are expressed on rectangular coordinate, and compressive axial displacement and force are taken as positive, as shown in Figure 4. SP-1 was loaded in cross-shaped path and square path with a constant axial ratio of 0.2. SP-2 was loaded rectangular path with a constant axial ratio of 0.2. SP-3 was subjected to square loading and one directional lateral loading with different axial force ratio of 0.1, 0.2, and 0.3.

As shown in Figure 3, The SP-1 was subjected to one-directional cyclic loadings, which were numbered 1 to 12, and then square loading path, which was from 13 to 19, was repeated twice. The SP-2 was subjected to rectangular loading, which was from 1 to 14, twice on square of inside and once on square of outside. The SP-3 was subjected to one-directional cyclic loadings with different constant axial force ratios of 0.1, 0.2, and 0.3, and then square-loading path was acted under a constant axial load by 0.3 in axial force ratio.

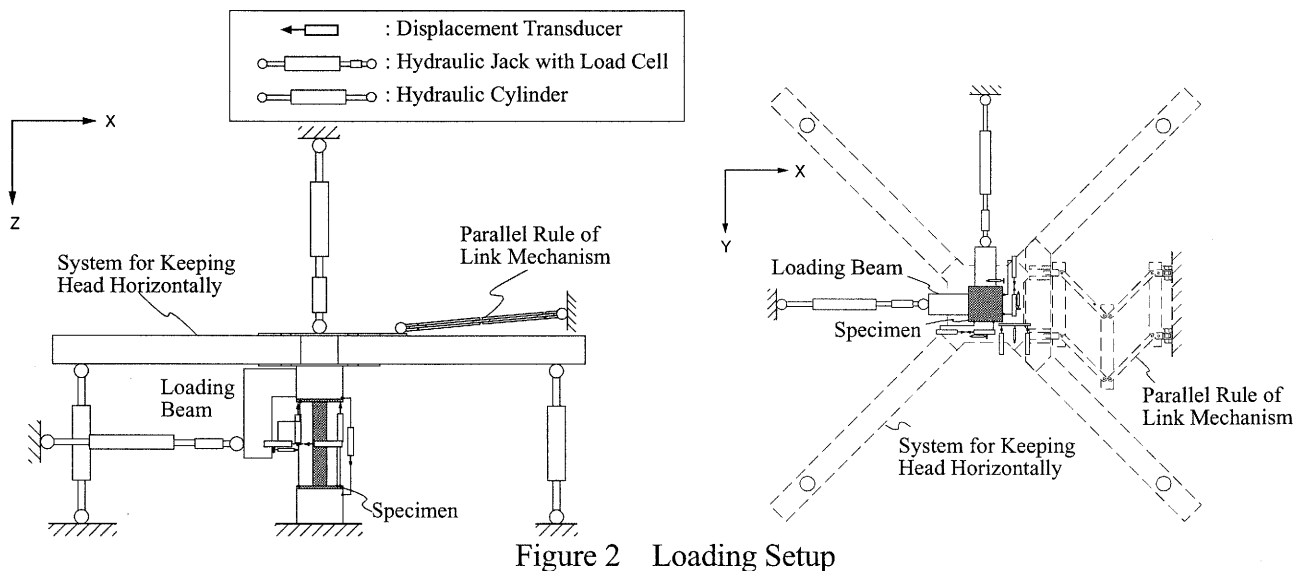


Figure 2 Loading Setup

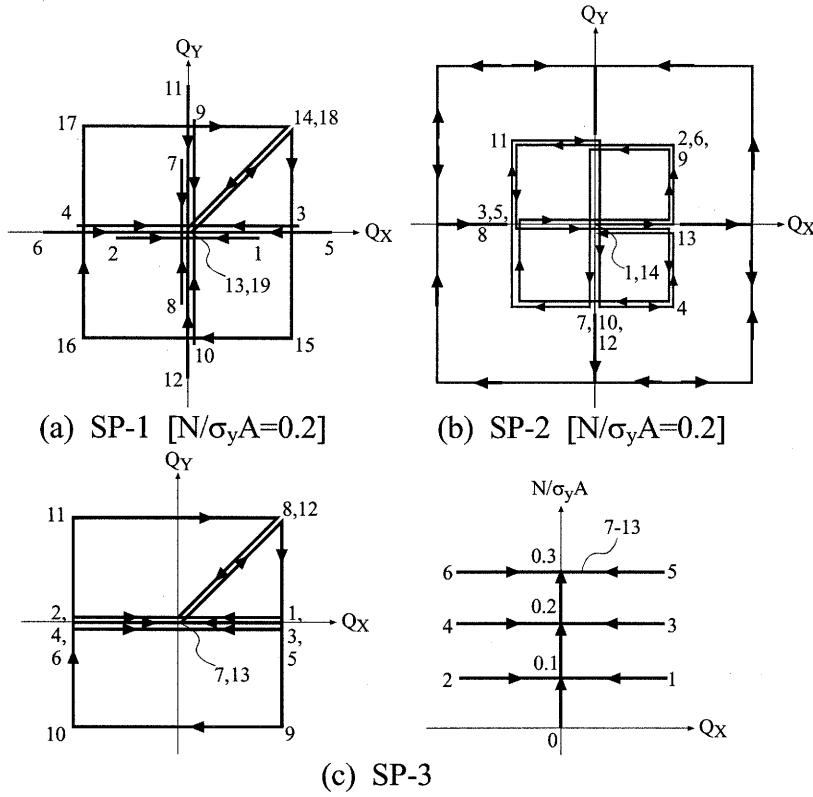


Figure 3 Loading Plan of Each Specimens

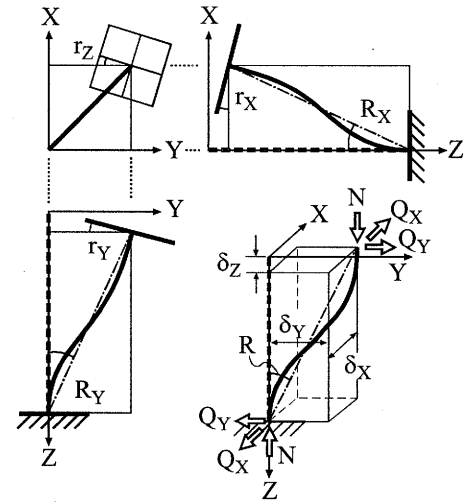


Figure 4 Coordinate of Force and Deformation

3. TEST RESULTS

Figure 5, 6, and 7 show the test results. As shown in these figures, Q_X - R_X and Q_Y - R_Y relationship curves weren't linear and quadrilaterals shown in R_X - R_Y relationships aren't precise squares.

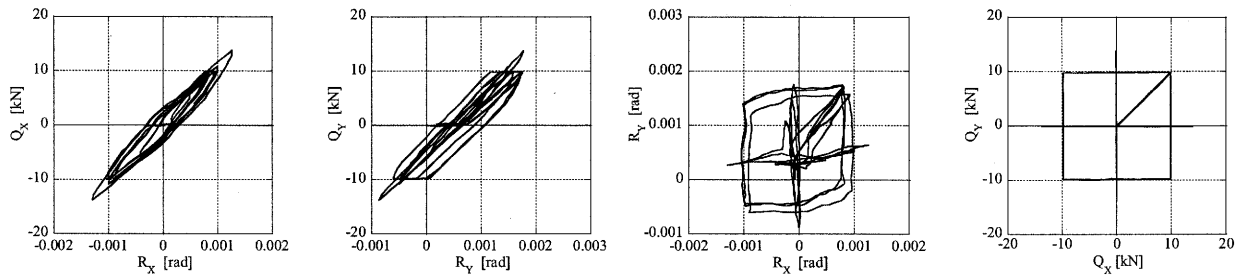


Figure 5 Test Result of SP-1

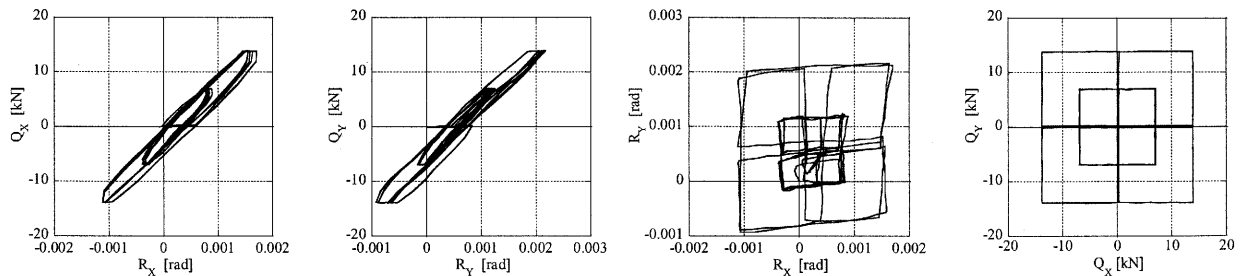


Figure 6 Test Result of SP-2

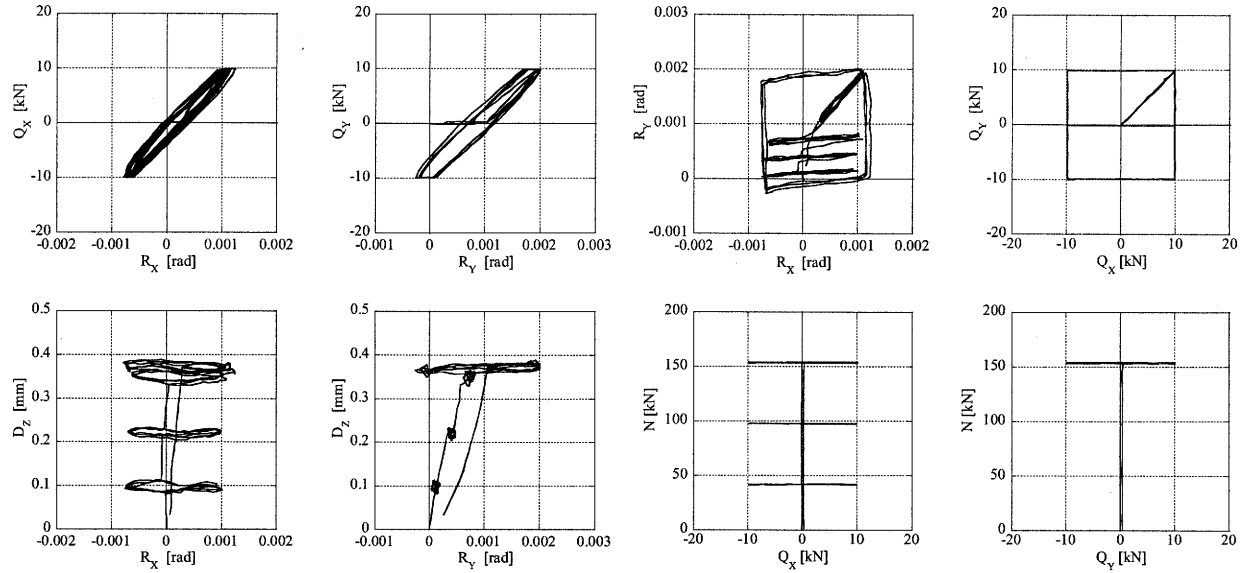


Figure 7 Test Result of SP-3

4. CONSIDERATION

4.1 Equivalent Damping Ratio

Equivalent damping ratios of every cycle at one-directional lateral cyclic loading stages were calculated. SP-1 had one-directional lateral cyclic loading stages on X-direction and Y-direction with different displacement amplitudes under a constant axial load. SP-3 had one-directional lateral cyclic loading stages on X-direction with constant axial ratios of 0.1, 0.2, and 0.3. Figure 8 shows equivalent damping ratios and displacement amplitudes relationships. Circle and square marks express the results of SP-1, and diamond and triangle marks express the results of SP-3. As shown in this figure, the equivalent damping ratios in this investigation were more than 3%.

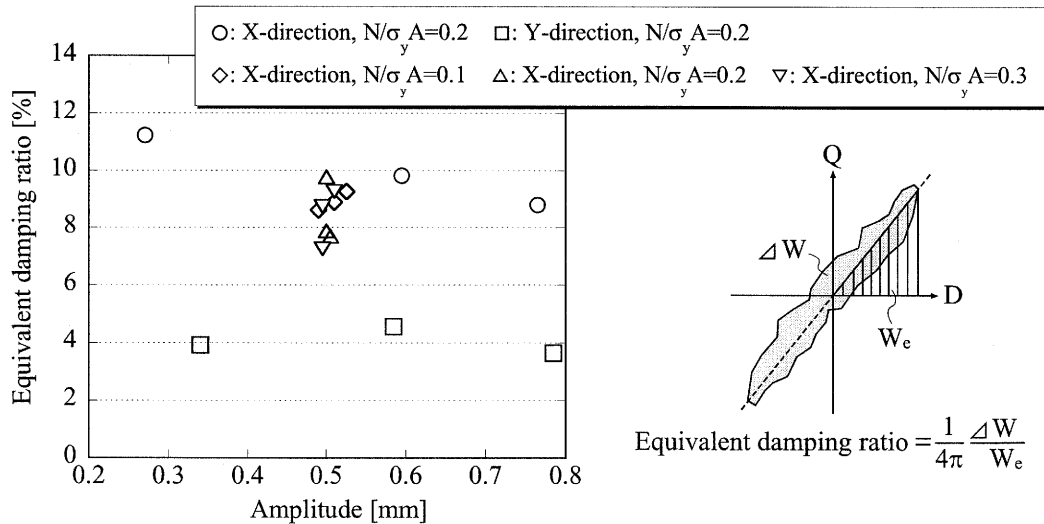


Figure 8 Equivalent Damping Ratios and Displacement Amplitudes Relationship

As shown in Figure 8, differences of axial load and of amplitude of cyclic displacement didn't influence equivalent damping ratio. The equivalent damping ratio of 0.27mm amplitude on X-direction with axial load ratio of 0.2 was larger than others. The reason for this is that loading

direction wasn't agree with center of the column specimens, which could be seen on R_X - R_Y relationship curves in Figure 4 that leaned against X-axis. It seems reasonable to suppose that this difference between loading direction and center of the specimens made the equivalent damping ratio relatively larger as amplitude of displacement was smaller.

4.2 Bending Moment and Curvature Relationship

Figure 9 shows the test results of bending moment and curvature relationships at sections where the strain gages were pasted on. The bending moment at the section is assumed as a value given by multiplying shear load and length between the section and center of the column together. The curvature is average of curvatures at the sections of upper side and lower side of the column, which were calculated from strain of the test results.

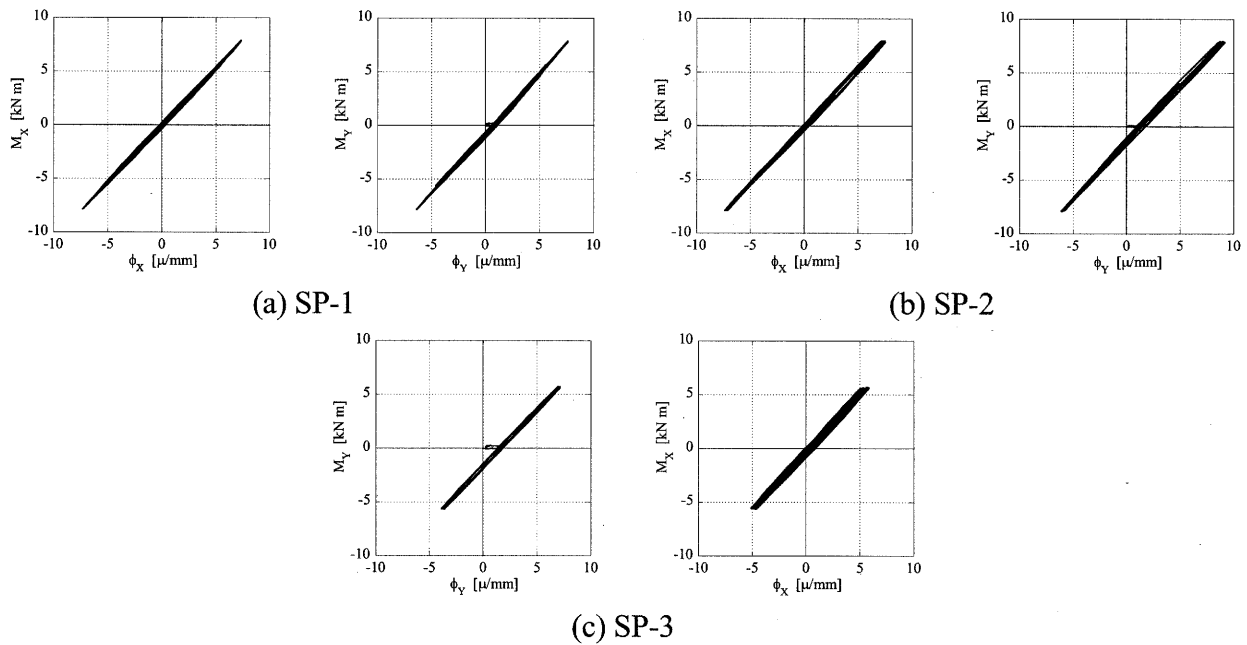


Figure 9 Bending Moment and Curvature Relationships

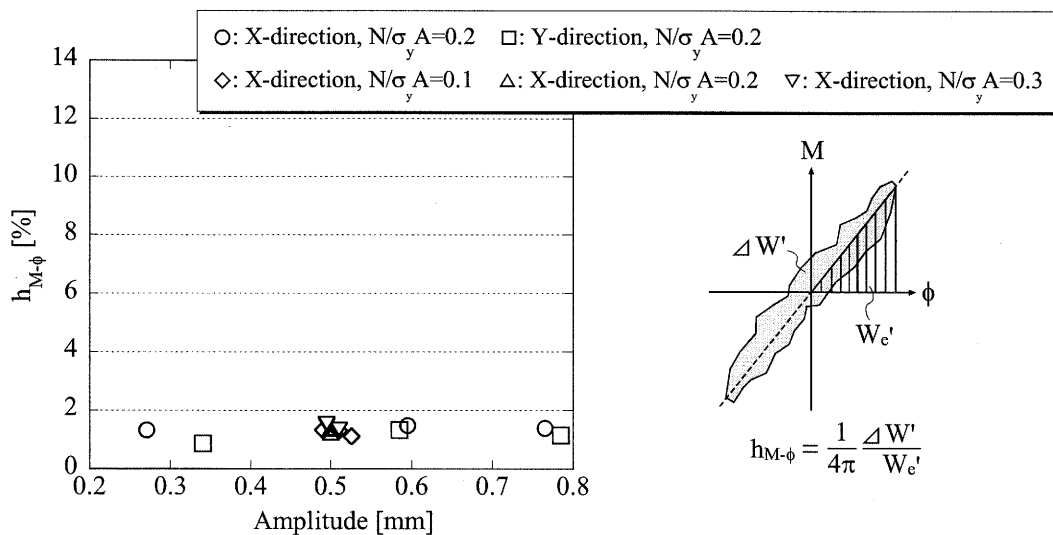


Figure 10 $h_{M-\phi}$ and Displacement Amplitudes Relationship

As shown in Figure 10, ratios of areas of M - ϕ relationships were calculated in the same way as equivalent damping ratios. Circle and square marks express the results of SP-1, and diamond and

triangle marks express the results of SP-3. As shown in this figure, $h_{M-\phi}$ is smaller than equivalent damping ratio shown in Figure 8. One of the main causes of these differences must be measuring error, because displacement of head of column was measured through measuring jigs.

4.3 Effect of Two-directional Loading

Figure 11 shows ratio of residual displacement in case of no lateral loads and maximum displacement. Circle marks express the results of SP-1, and diamond marks express the results of SP-2. If this ratio can be regarded as an index of measuring error, it can be said that two-directional loading and amplitude of cyclic displacement don't influence measuring errors.

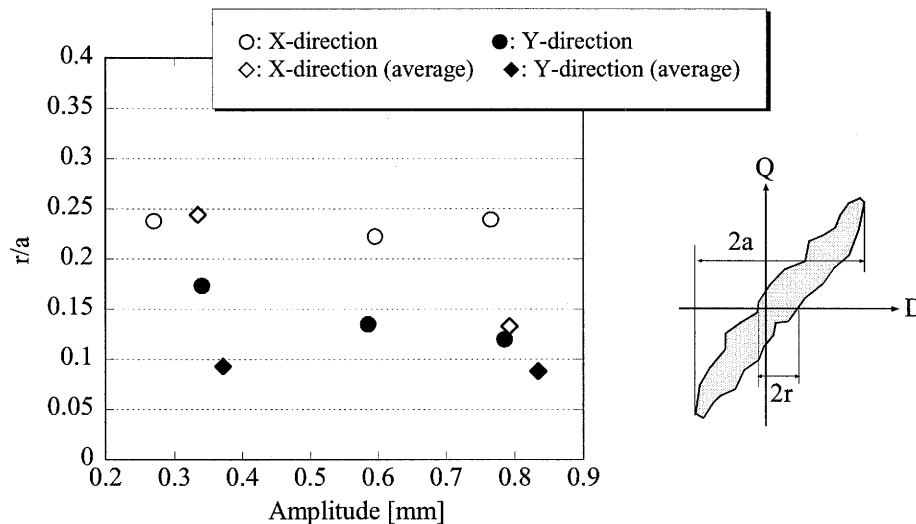


Figure 11 r/a and Displacement Amplitudes Relationship

5. CONCLUSIONS

Three identical steel pipe column specimens were prepared, and three-directional loading test of the columns were carried out to consider estimation of static test results. The base of the columns was fixed, and the specimens were subjected to two directional anti-symmetric bending and a constant axial load. As results, the following were founded.

1. The test results had more than 3% of equivalent damping factor under one-directional cyclic loading in elastic range.
2. Differences of axial load and of amplitude of cyclic displacement didn't influence equivalent damping ratio on one-directional cyclic loading in elastic range.
3. Two-directional loading and amplitude of cyclic displacement didn't influence ratio of residual displacement and maximum displacement of cycle.

References:

- Chopra, A.K. (2000), "Dynamics of Structures: Theory and Applications to Earthquake Engineering (2nd Edition)" Prentice-Hall Inc.
- Nishimura, K. and Takiguchi, K. (2005), "Experimental Study on Tri-axial Nonlinear Restoring Force Characteristics of R/C Columns Yielded in Flexure," *Journal of Structural and Construction Engineering*, AIJ, **587**, 173-180.

COLUMN-TO-BEAM STRENGTH RATIO EFFECT ON SEISMIC BEHAVIOR OF REINFORCED CONCRETE BUILDINGS

A. Jalali¹⁾, and A. Mostashari²⁾

1) Assistant Professor, Civil Engineering Department., University of Tabriz, Iran

*2) Graduate Student, Civil Engineering Department., University of Tabriz, Iran
jalali@tabrizu.ac.ir*

Abstract: Reinforced concrete (RC) buildings are vastly used in seismic prone areas in variety of building applications. During strong ground motions, such buildings have been subjected to soft-story or column side sway failure mechanisms. These mechanisms are characterized by the development of plastic hinges at all columns or joints of a story, leaving the structure without significant reserve strength capacity and possibly without significant reserve deformation capacity. Previous research efforts have shown that the column-to-beam flexural strength ratio at the joints in RC frame buildings plays an important role in determining the building's response to earthquake loading, including whether or not a soft story mechanism will form.

Three basic reinforced concrete (RC) moment frame buildings, one three-story, the other six-story, and the last one nine story were considered as study buildings. For each basic building, multiple models were created, each with a different column-to-beam strength ratio. Six strength ratios were evaluated, ranging from 0.8 to 2.4. The strength ratio was varied by increasing the column strength in two separate ways: (1) adding reinforcement without changing the gross dimensions; and (2) increasing the gross dimensions and holding the reinforcement ratio constant. This gave six sets of models: (1) three-story, constant column-to-beam stiffness ratio; (2) three-story, varied column-to-beam stiffness ratio; (3) six-story, constant column-to-beam stiffness ratio; (4) six-story, varied column-to-beam stiffness ratio; (5) nine-story, constant column-to-beam stiffness ratio; (6) and nine-story, varied column-to-beam stiffness ratio.

Nonlinear time history analyses of all of the model buildings were conducted under three suites of earthquakes (having 50%, 10%, and 2% probabilities of exceedence in 50 years by IDARC computer program. By conducting 540 analyses and evaluation of story drifts, local and global damage indexes, and number and sequence of plastic hinges formation, it was concluded that the column to beam strength ratio of two insures the most desirable performance of the buildings and prevents the soft story mechanism from being developed. Also it was shown that increasing the column to beam strength ratio lead to considerable decrease in overall damages in buildings, and developing considerable number of plastic hinges before formation of mechanism in building.

1. INTRODUCTION

Reinforced concrete frames are used in modern buildings all over the world. In the past earthquakes, some of RC frames have developed soft story mechanism in response to strong ground shaking. Soft story mechanism involves developing plastic hinges at all columns or joints of a story, and results in an unstable building which is not able to carry further lateral load. Several studies have shown that the column to beam strength ratio at the joints of RC buildings is an important factor in the probability of formation of soft story under earthquakes. ACI 318-71 (1971) requires that, the sum of the moment strengths of the columns at the design axial load should be greater than the sum of the moment strengths

of the beams at beam-column connections in order to ensure the plastic hinges will form in beams rather than columns. In ACI-ASCE 352-85 (1985) the minimum column to beam strength ratio of 1.4 was recommended. ACI-ASCE 352-91 (1991) in response to very extensive research work, recommended that, the sum of the nominal column flexural strengths exceed the sum of the nominal beam flexural strengths by at least 40%. ACI 318-99 (1999) requires that the sum of nominal column flexural strengths exceed the sum of the nominal beam flexural strengths by at least 20% at beam-column connections. According to ACI 318-2002 (2002) sum of nominal column flexural strengths must be 1.2 times greater than the sum of the nominal beam flexural strengths. In an extensive research work by Dooley and Bracci (2001) they have also reached at ratio 2.0. Some building codes such as Mexico and New Zealand require much larger minimum strength ratio about 2.0. In current study we have extended the previous studies by using the performance based earthquake engineering concepts in order to examine the column to beam strength ratio and find out the suitable ratio in the context of PBEE.

2. BUILDING DESCRIPTION

Three RC frames have been considered in this investigation. The frames have three bays, with three, six, and nine stories respectively. The plan, elevation and beam cross section for nine storey frame has been shown in Figure 1. All of the buildings have been designed according to Iranian code which is mostly same as UBC97, and ACI 318-99. In order to evaluate the effect of strength ratio on seismic behavior different ratios have been considered. Different ratios are possible by changing all of the parameters affecting the flexural strength of beams and columns such as f'_c , f_y , overall dimensions of cross sections, and reinforcement percentage. In current study a simple approach has been adopted. By maintaining f'_c , and f_y the same for all of the beams and columns we have varied strength ratio in two ways, first by using different percentage of reinforcement for columns and keeping its dimensions constant, which we call it constant column to beam stiffness; and second by using a constant percentage of reinforcement while changing the column dimensions, which is called varied column to beam stiffness in this study. It should be reminded that in constant column to beam stiffness case the stiffness of column remains constant, because the overall dimensions of column do not change, while in varied column to beam stiffness case the reinforcement percentage remains almost the same and stiffness changes because of variation in cross sectional dimensions. Based on the approach outlined the two categories of frames have been used in this study. Three, six, and nine story buildings with constant stiffness ratio of column to beam, and three, six, and nine story buildings with varied stiffness ratio of column to beam. Dimensions and reinforcement percentage of the columns for the case of varied column to beam stiffness ratio of the nine storey building has been shown in Table 1. Required flexural strength of columns for both constant and varied stiffness has been selected based on flexural strength of beams connected to columns in joints and according to Eq. (1).

$$(M_n)_{col,required} = 1/2 * (Strength\ Ratio) * [(M_n^+)_{beam} + (M_n^-)_{beam}] \quad (1)$$

Table 2 shows the required flexural strength of columns for all of frames and all of the strength ratios considered.

3. GROUND MOTIONS, AND REPRESENTATION OF RESULTS

In performance based engineering earthquake shaking demands are expressed in terms of ground motion response spectra, discrete parameters that define these spectra, or suites of ground motion time

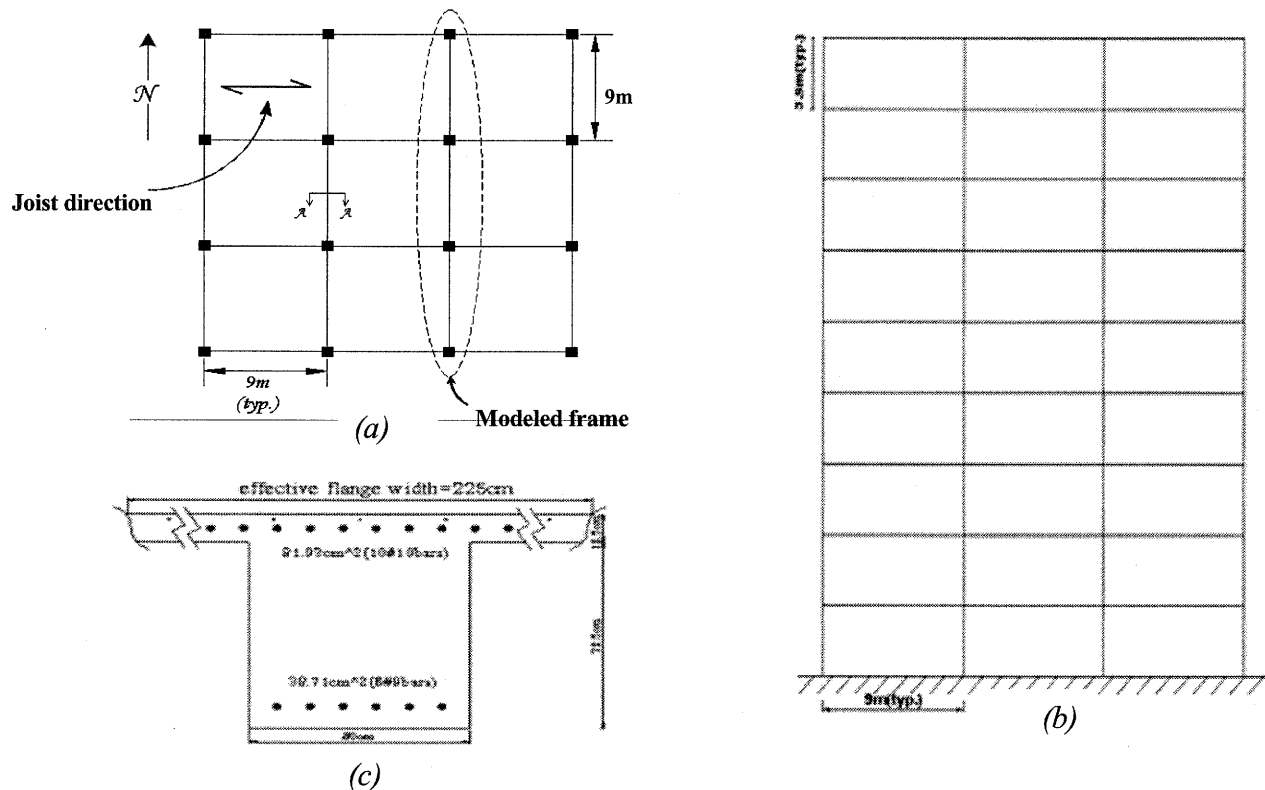


Figure 1. Details for nine story frame, (a) plan; (b) elevation; (c) beam cross section

Table 1. Dimensions and reinforcement percentage of the columns for the case of varied column to beam stiffness ratio of the nine storey frame

Strength Ratio	$M_{n,required}$	Column Size (cm*cm).	Possible Reinforcement	P (%)
	(kN-m)			
0.8	1468	74×74	114	2.08
1.0	1835	80×80	131	2.04
1.2	2202	84×84	150	2.12
1.6	2936	93×93	177	2.04
2.0	3670	100×100	204	2.04
2.4	4404	106×106	228	2.02

Table 2 Required flexural strength of columns for all of frames

3-story Building		6-story Building		9-story Building	
Strength Ratio	$(M_n)_{col,required}$	Strength Ratio	$(M_n)_{col,required}$	Strength Ratio	$(M_n)_{col,required}$
	(kN-m)		(kN-m)		(kN-m)
0.8	718	0.8	1090	0.8	1468
1.0	898	1.0	1362	1.0	1835
1.2	1078	1.2	1634	1.2	2205
1.6	1437	1.6	2179	1.6	2936
2.0	1796	2.0	2724	2.0	3670
2.4	2155	2.4	3269	2.4	4464

histories, depending on the analysis procedure selected. Earthquake demands are function of the location of the building with respect to causative faults, the regional and site-specific geologic characteristics, and the ground motion hazard level(s) required in the code. Hazard levels may be defined on either a probabilistic or deterministic basis. Probabilistic hazards are defined in terms of the probability that more severe demands will be experienced (probability of exceedance) in a 50-year period. Deterministic demands are defined within a level of confidence in terms of a specific magnitude event on a particular fault, which is most appropriate for buildings located within a few miles of a major active fault. Probabilistic hazard levels frequently used and their corresponding mean return periods (the average number of years between events of similar severity) are as follows:

Earthquake Having Probability of Exceedance	Mean Return Period (years)
50%/50 year	72
20%/50 year	225
10%/50 year	474
2%/50 year	2,475

These mean return periods are typically rounded to 75, 225, 500, and 2,500 years, respectively.

The suit of ground motions used in this study is selected from the records developed for Los Angeles area with certain return period for SAC Joint Venture Phase 2 Steel Project (Woodward Clyde Federal Services, 1997). Each set of ground motions has probability of exceedence of 50%, 10%, 2% in 50 year, respectively, and consisted of five records. Table 3 shows the ground motions having probability of exceedence 2% in 50 year.

We have used six sets of models: (1) three-story, constant column-to-beam stiffness ratio; (2) three-story, varied column-to-beam stiffness ratio; (3) six-story, constant column-to-beam stiffness ratio; (4) six-story, varied column-to-beam stiffness ratio; (5) nine-story, constant column-to-beam stiffness ratio; (6) and nine-story, varied column-to-beam stiffness ratio. Six strength ratios have been evaluated, ranging from 0.8 to 2.4. The combination of the six models with six different strength ratios resulted in 36 building models, which were analyzed under five seismic excitations with probability of exceedance of 2%,10%, and 50% in 50 years. In the process we have done 540 nonlinear time history analyses by running IDARC-2D. Only part of the results will be shown in the following section.

Table 3. Ground motions having probability of exceedence 2% in 50 year

SAC Name	Record	Earthquake Magnitude	Distance (km)	Scale Factor	Number of Points	DT (sec)	Duration (sec)	PGA (cm/sec²)
LA23	1989 Loma Prieta	7	3.5	0.82	2500	0.01	24.99	409.95
AL24	1989 Loma Prieta	7	3.5	0.82	2500	0.01	24.99	463.76
AL25	1994 Northridge	6.7	7.5	1.29	2990	0.005	14.945	851.62
LA27	1994 Northridge	6.7	6.4	1.61	3000	0.02	59.98	908.70
LA30	1974 Tabas	7.4	1.2	1.08	2500	0.02	49.98	972.58

3.1 Story drifts and overall structural damages

Response of the structures under the selected earthquake intensities has been measured by the story drifts and overall structural damage index. IDARC determines the index based on the damage occurred in the beams and columns. The earthquake having the probability of exceedance of 2% in 50 years, is a rare and very intense excitation, and will be used as a controlling excitation in order to obtain a suitable strength ratio. After establishing a suitable ratio which prevents collapse, and limits the drifts to acceptable amounts, the same ratio will be used with less intensive earthquakes to check other performance levels of buildings. Table 4 shows the number of instabilities occurs in the structures under the earthquake with return period of 2475 years. It clearly shows that at the ratio of two all of the structures do not experience any instability. Figures 2-7 show the inter story drifts for three, six, and nine story frames in two case of constant and varied column to beam stiffness ratio, for strength ratio of two. Inter story drift are maximum for stories 2- 3, stories 2-4, and stories 2-5 for three, six, and nine story buildings, respectively. As can be seen inter story drifts for varied column to beam stiffness are less than constant column to beam stiffness ratio. Also shown in Tables 5, and 6 is overall structural damage index for strength ratio of 1.2, recommended by ACI, and 2. As the Tables show for ratio of 1.2 there are a lot of instabilities in buildings, while for the ratio of 2 all of the buildings remain stable. We have examined the same response parameters for earthquakes having return period of 474, and 72 years. The trend has been found in complete agreement with the above mentioned results for earthquake with return period of 2475. Finally we have compared maximum story drift ratio for different performance levels. Table 7 shows that the results are in good agreement with the story drift ratio suggested by different references Saito,Kanda, and Kanai (1998).

Table 4. Instabilities occurred in the structures under the earthquake with return period of 2475 years

Strength Ratio	3 story CCBSR	3 story VCBSR	6 story CCBSR	6 story VCBSR	9 story CCBSR	9 story VCBSR
0.8	4	4	2	2	2	3
1.0	4	3	1	1	3	2
1.2	3	2	2	1	2	1
1.6	3	1	1	1	1	1
2.0	-	-	-	-	-	-
2.4	-	-	-	-	-	-

CCBSR:constant column to beam stiffness ratio; VCBSR:varied column to beam stiffness ratio

Table 5 Overall structural damage index for strength ratio of 1.2

EQ	3story CCBSR	3 story VCBSR	6 story CCBSR	6 story VCBSR	9 story CCBSR	9 story VCBSR
La23	0.135	0.128	0.096	0.096	0.075	0.083
La24	Collapse	0.344	Collapse	Collapse	Collapse	Collapse
La25	Collapse	Collapse	0.213	0.212	0.176	0.178
La27	Collapse	Collapse	Collapse	0.307	Collapse	0.331
La30	0.237	0.243	0.208	0.204	0.203	0.19

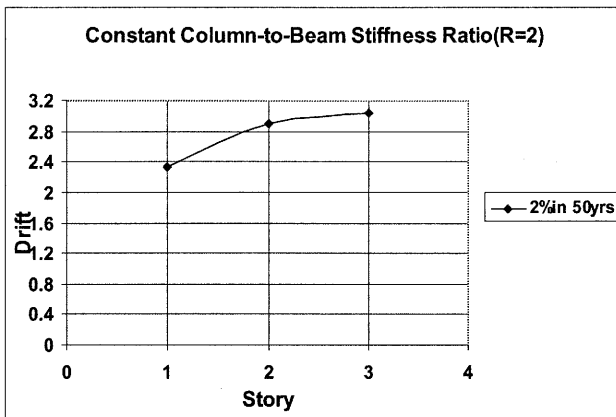


Figure 2 Story drifts for three story frame

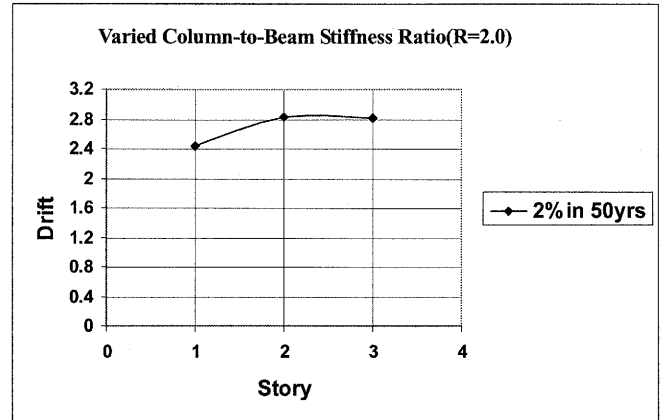


Figure 3 Story drifts for three story frame

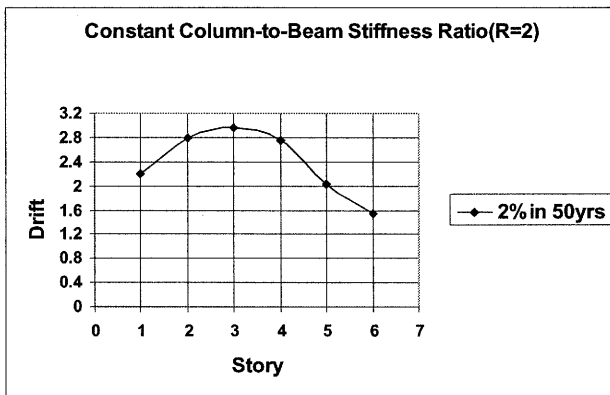


Figure 4 Story drifts for six story frame

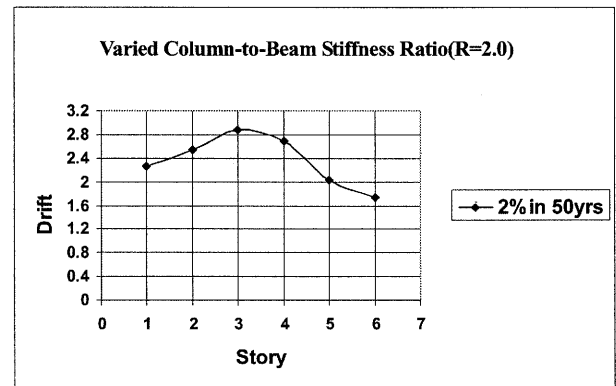


Figure 5 Story drifts for six story frame

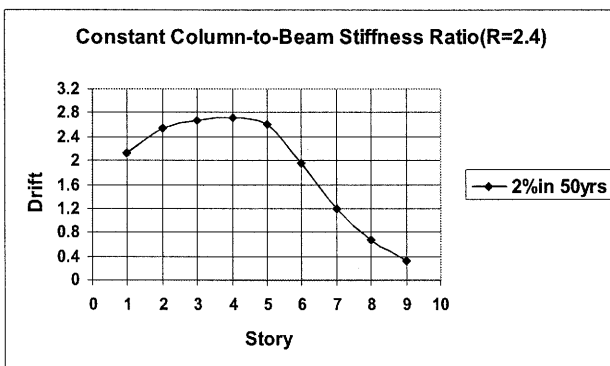


Figure 6 Story drifts for three story frame

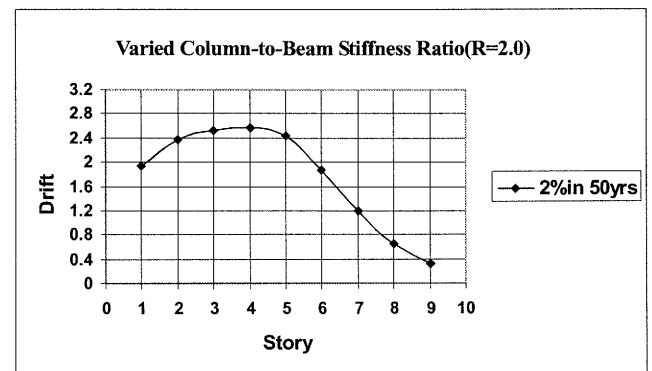


Figure 7 Story drifts for three story frame

Table 6 Overall structural damage index for strength ratio of 2

EQ	3story CCBSR	3 story VCBSR	6 story CCBSR	6 story VCBSR	9 story CCBSR	9 story VCBSR
La23	0.114	0.142	0.115	0.101	0.093	0.089
La24	0.231	0.208	0.275	0.247	0.245	0.224
La25	0.294	0.272	0.220	0.208	0.182	0.177
La27	0.259	0.256	0.220	0.207	0.263	0.241
La30	0.168	0.126	0.158	0.155	0.155	0.152

Table 7 Maximum story drift ratio for different performance level

Limit State	Performance of building	Deformation Criteria, Tokyo site	Deformation Criteria, Osaka site	Deformation Criteria Fema 273	Deformation Criteria ATC 40	Current study
Immediate Occupancy	Concrete crack	5.00E-03	4.00E-03	1.00E-02	1.01E-2	4E- 03
Life Safety	Failure of Structural element	2.00E-02	1.7E-03	2.00E-02	2.60E-2	1E- 02
Structural Stability	Collapse of building	3.33E-02	3.33E-02	4.00E-02	$0.33 \frac{V_i}{P_i}$	3E- 02

3. CONCLUSIONS

1. With increasing column to beam strength ratio, the number of instabilities in the structure under maximum design earthquake, which has 2% probability of exceedance in 50 years, decrease, and at ratio of two in both cases of constant and varied column to beam stiffness, under all of the seismic excitations the structures remain stable.
2. By increasing the strength ratio the probability of formation of plastic hinges on columns decreases, which results in lowering the probability of developing of soft-story.
3. The strength ratio is more effective in the case of varied column to beam stiffness than the constant column to beam stiffness ratio; that is the rate of decrease in column drift by increasing the strength ratio in the first case is more than the latter case.
4. In all cases damage index decreases by increasing the strength ratio, and plastic hinges develop in the beams first.
5. Overall structural damage decreases by increasing strength ratio. The amount of decrease is more in the case of varied column to beam stiffness ratio.

References:

- ACI 318-71 (1971). Building Code Requirements for reinforced Concrete, American Concrete Institute, Farmington Hills, Michigan
- ACI 318-83 (1983). Building Code Requirements for reinforced Concrete, American Concrete Institute, Farmington Hills, Michigan
- ACI 318-99 (1999). Building Code Requirements for reinforced Concrete, American Concrete Institute, Farmington Hills, Michigan.
- ACI 2002 American Concrete Institute, "Building Code Requirements for Structural Concrete," ACI, P.O. Box 9094, Farmington Hills, MI.
- ACI-ASCE 352-85 (1985). "Recommendations for Design of Beam-Column Joints in Monolithic Reinforced Concrete Structures," ACI Journal, 82(3), 266-283.
- Dooley, K. and Bracci, J. (2001). "Effect of Column-to-Beam Strength Ratio on Earthquake Resistance of RC Moment Frames Using Probabilistic Performance-Based Design Methodologies," Center for Building Design and Construction, Technical Report 01-02, Texas A&M University, 249 pages.
- IDARC 2D Version 6.0, July 2004, Reinhorn A. M.; University at Buffalo 231 Ketter Hall, SUNY/Buffalo Buffalo, NY 14260 USA.
- Saito, T., Kanda, J. and Kanai, N. (1998) "Seismic reliability estimate of building structures designed according to the current Japanese design code", Proceedings of the Structural Engineers World Congress (SEWC 98).
- Woodward-Clyde Federal Services (1997). "Develop Suites of Time Histories," SAC Joint Venture Steel Project Phase 2, Draft Report, Richmond, California.

INFLUENCE OF JOINT CONCRETE INTERFACIAL SLIP ON THE SEISMIC RESPONSE OF NON-DUCTILE FRAMES UPGRADED WITH RC JACKETING

Y.C. Wang¹⁾, W.H. Ho²⁾, R.T. Ko²⁾, and T.F. Ya²⁾

1)Associate Professor, Department of Civil Engineering, National Central University, Taiwan

2)Former ME Students, Department of Civil Engineering, National Central University, Taiwan
wangyc@cc.ncu.edu.tw

Abstract: Simulated seismic load tests on reinforced concrete one-way interior beam-column joints with substandard reinforcing details typical of low-rise buildings constructed in Taiwan are described. These substandard reinforcing details of the beam-column joints are mainly lower concrete strength and lack of transverse reinforcement. RC jacketing offers a versatility for retrofitting those deficient buildings. The improvement in performance of the joints rehabilitated with RC jacketing, without dowel anchors into the concrete-to-concrete interface for preventing premature bond failure, is demonstrated. The experimental investigation toward the effect of the interfacial bond slip is discussed in the paper. Results showed the slip observed in newly casting concrete joint is unlikely to influence the overall seismic performance of the jacketed sub-assemblages if being strengthened to ensure the strong-column and weak-beam mode.

1. INTRODUCTION

The study motivation came from a premature debonding normally occurred in the interface of composite materials such as FRP or steel plates newly attached to as-built RC columns or beams for flexural/ shear strengthening (Wang 2003, Wang and Chen 2003). What we called “premature” could be defined that the debonding failure of such composite plates appeared in an earlier load prior to member strength and/or in an unexpected elastic or post-yield range before ductility demand. To prevent premature debonding failure caused by the composite-to-concrete interface, dowel anchors installed into the interface between two different materials are normally required to prevent the premature debonding. Similar care is taken to substandard concrete frames strengthened with the concrete jacket as the way engineers adopt.

Although the dowel installation into the concrete-to-concrete interface is likely to prevent the interfacial bond slip, it consumes extra labor cost and construction duration in practice. In Taiwan, dowel anchors are normally required prior to the application of RC jacketing. This is due to a conservative consideration as previously mentioned. However, how much of the new-to-old concrete interfacial slip, especially in the joint core, will influence the overall seismic performance of the jacketed frames is more concerned in the study.

A recent study carried out by the authors (Wang and Lee 2004) was an investigation onto the seismic behavior of non-ductile RC beam-column joints retrofitted with RC jacketing. The paper only involved a part of results to deal with the effect of the new-to-old concrete interfacial bond slip in the joint core. Seven tested joint sub-assemblages were chosen for discussion.

2. TEST PROGRAM

2.1 Details of the Test Units

Two series of beam-column joint sub-assemblages, series-Ko and series-Ho, were presented in the paper. Table 1 and Figure 1 depict the details of test units and material properties. All units including retrofitted units were cast in the horizontal plane. The thickness of 100 mm of RC jacketing was taken into account.

Table 1 Details of Tested Beam-Column Joint Sub-assemblages

Test series		Ko				Ho		
Unit		Ko-JI1 As-built	Ko-JI2 Retrofit	Ko-JIR1 Retrofit	Ko-JIR2 Retrofit	Ho-JI1 As-built	Ho-JIR1 Retrofit	Ho-JIR2 Retrofit
Applied axial load, $f_c'A_g$		0.14	None	None	0.14	None		
Concrete casting time(s)		1	1	2	2	1	2	2
Column	h_c , mm	300	500	500	500	400	600	600
	b_c , mm	300	500	500	500	400	600	600
	Rebar (as-built)	6-D25	6-D25	6-D25	6-D25	8-D25	8-D25	8-D25
	Rebar (retrofit)	--	4-D25	4-D25	4-D25	4-D25	4-D25	4-D25
Jacket Thickness (mm)		--	100	100	100	--	100	100
Beam	h_b , mm	500	500	500	500	400	400	400
	b_b , mm	300	300	300	300	300	300	300
	Rebar	4-D25up 4-D25low	4-D25 4-D25	4-D25 4-D25	4-D25 4-D25	4-D19up 4-D19low	4-D19 4-D19	4-D19 4-D19
f_c' , MPa	As-built	32	32	32	32	27	27	27
	Retrofit	--	32	25	25	--	24	49
	Average ⁽²⁾	--	32	28	28	--	25	38
f_y , MPa		533 (D25), 554(D10)				541(D25), 514(D19), 471(D10)		

(1) The jacketed unit cast concrete in a time is to simulate perfect bond condition of the new-to-old concrete interface.

(2) Averaged concrete strength adopted from root square of Eq. (1).

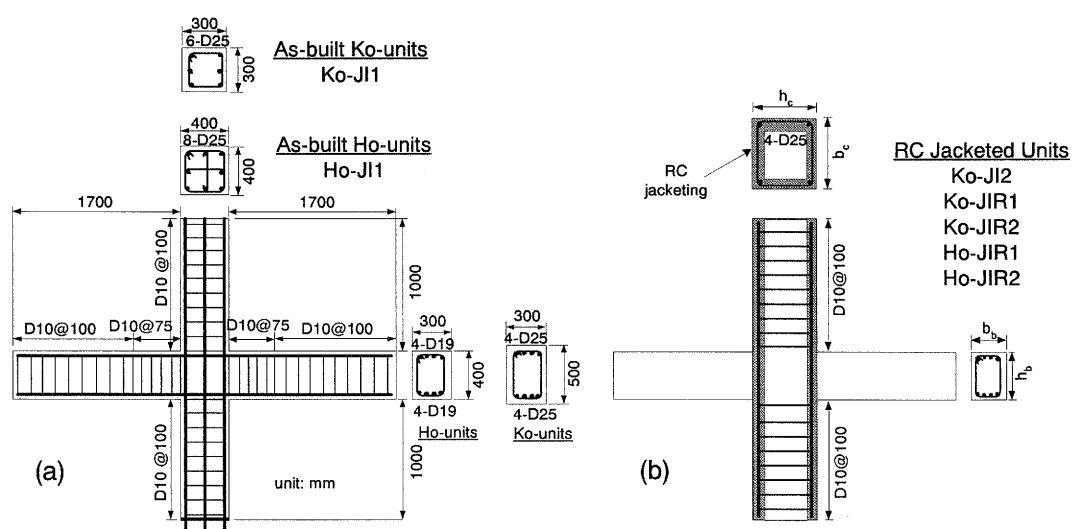


Figure 1 Details of Tested Beam-Column Joints: (a) As-built Units, and (b) RC Jacketed Units.

When estimating joint shear strength of the jacketed units, a consistent concrete strength in the joint cores was adopted by means of a root-mean rule (Alcocer and Jirsa 1993), stipulated in Eq. (1).

$$A_j \sqrt{f'_{c,j}} = A_1 \sqrt{f'_{c,1}} + A_2 \sqrt{f'_{c,2}} \quad (1)$$

where A_j is overall joint core area in the case of jacketed units. $f'_{c,j}$ is the weighted average concrete strength. A_1 is the gross area of existing column. $f'_{c,1}$ is the concrete strength in existing column at joint. A_2 is the area of column jacket included in the joint core, equaling to $A_j - A_1$. $f'_{c,2}$ is the concrete strength in jacketed column at joint.

Series-Ko units were designed to joint shear failure mode whereas series-Ho units were designed to beam-end flexural hinging mode. The purpose of Ko-units was to examine the effect of new-to-old concrete interfacial slip on joint shear strengths. Ko-units except Ko-JI2 were retrofitted by RC jacketing without installing dowel anchors into concrete interface. Those retrofitted units needed to cast concrete for two times. However, unit Ko-JI2 with the part of RC jacket cast concrete in a time to simulate the jacketed concrete with a perfectly interfacial bond condition. The bond slip effect on joint shear strength could be observed by means of comparing two units, Ko-JI2 and Ko-JIR1. Meanwhile, units Ko-JI1 and Ko-JIR2 were subjected to a constantly axial column load to inspect the influence of vertical load on the behavior of the beam-column joints.

Series-Ho units were selected to verify the seismic performance of the non-ductile concrete beam-column joints retrofitted with concrete jacketing. The joint shear failure of the prototype unit Ho-JI1 was expected to occur due to the substandard details in joint with low concrete strength and without transverse reinforcement. Then, the non-ductile frame was rehabilitated with RC jacketing to ensure a strong-column and weak-beam failure mode as represented in units Ho-JIR1 & 2. The new-to-old concrete interface was treated without dowel anchors similar to units Ko-JIR1 & 2. Note that the design of jacketed columns of longitudinal and transverse reinforcement were adopted according to ACI 318-02 (ACI 2002), except to check jacketed joint area. The joint shear strengths for all units, Ko-series and Ho-series, were examined by joint shear degradation model (Park 1997). That is the capacity of joint shear strength v_{jh} of Eq. (2) is taken into account.

$$v_{jh} = k \sqrt{f'_c} \sqrt{1 + \frac{N^*}{A_g k \sqrt{f'_c}}} \leq 1.5 \sqrt{f'_c} \quad (\text{MPa}) \quad (2)$$

Where, for interior joint, $k=1.0$. N^* is the axial compressive load acting on the column. A_g is gross area of column. f'_c is probable compressive cylinder strength of concrete, taking average from Eq. (1) if having two different joint concrete strengths.

2.2 Test Set-up

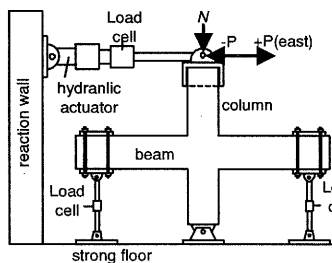


Figure 2 Test Set-up and Loading Sequence.

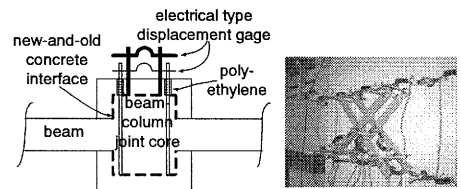


Figure 3 Measurement of Joint Shear Strain.

Figure 2 shows the test set-up and test sequence. During testing, load controlled cycles were initially imposed to the units to find the secant stiffness and horizontal displacement at 75% of the estimated flexural capacity of the beam in each direction of loading. Displacement controlled cycles

were then applied to the units when loaded beyond the elastic range. These cycles were controlled in terms of the displacement ductility, μ , which is defined as the ratio of the applied horizontal displacement Δ to the displacement at first yield of beams Δ_y . The displacement at first yield is defined as 4/3 times the horizontal displacement observed in the load-controlled cycles to 75% of flexural strength capacity of beams. Horizontal displacements were measured at the point of application of loading. Figure 3 displays a diagram of joint shear strain measurement. The joint shear strains were developed by two diagonal gage strains attained during testing.

3. EXPERIMENTAL RESULTS

3.1 General Behavior

The column shear versus lateral displacement and the failure mode at the end of testing are represented in Figure 4. Due to two different series, the results are described in the following two parts.

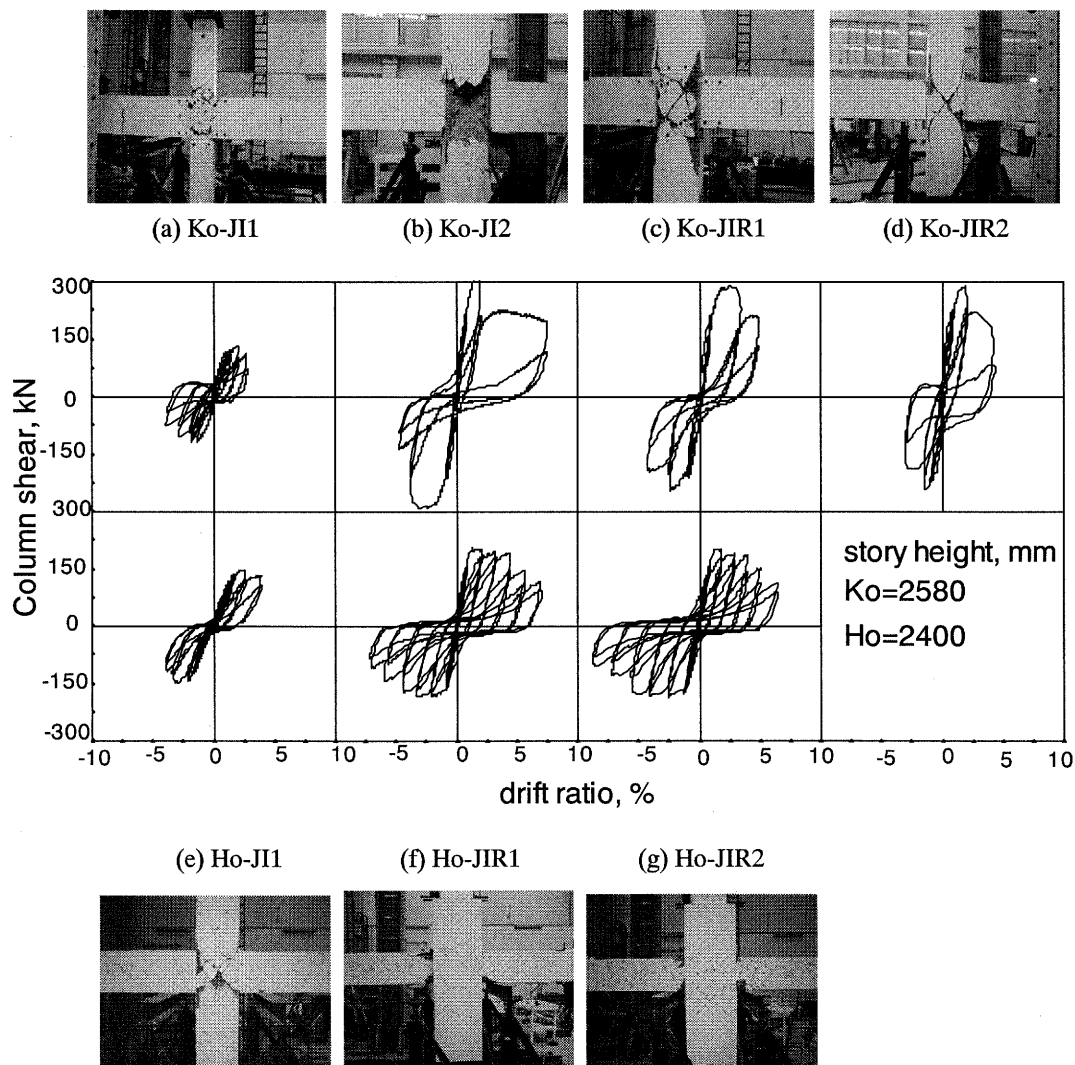


Figure 4 Hysteresis Loop and Failure Mode at the End of Test.

Series-Ko Units

The series units were designed to joint shear failure as expected, see Figures 4 (a) to (d). In Ko-JI1 with $0.14f'_cA_g$ constantly axial load, story column shear starts degrading when maximum column

shear of 134 kN reached at 2% drift ratio. Thus in the following drift ratio, shear pinching was developed due to occurrence of joint shear failure. In Ko-JI2 without axial load, maximum column shear of 321 kN was attained and maintained until 3% drift ratio to the negative cycle, when afterwards shear pinching began. Note that Ko-JI2 cast concrete in a time to simulate the retrofitted frame with perfect bond in the interface between new and old concrete joint. It means no interfacial bond slip occurred during joint shear degradation. Ko-JIR1 has similar details to Ko-JI2 except concrete casting times (see Table 1). The maximum column shear of 290 kN, lower than Ko-JI2, was attained at about 3% drift ratio. In Ko-JIR2 with axial load of $0.14f'_cA_g$, a similar maximum column shear of 289 kN to Ko-JIR1 was obtained but an earlier shear degradation was generated after about 2% of drift ratio. The difference of tendency in shear degradation between Ko-JIR1 (3% drift ratio) and Ko-JIR2 (2% drift ratio) probably resorted to the effects of interfacial bond slip or/and axially compressive load.

Series-Ho Units

The series was designed to confirm the seismic performance of non-ductile beam-column joints rehabilitated with RC jacketing. Jacketing scheme was similar to Series-Ko that no dowel anchors were provided to the new-to-old concrete interface. It can be seen in Figures (e) to (g) that as-built unit Ho-JI1 was loaded to joint shear failure whereas jacketed units Ho-JIR1 and Ho-JIR2 were damaged to flexural hinging occurred at the ends of beams. That is, the RC jacketing scheme proposed by the study can improve non-ductile frame with joint shear failure to ductile one that code requirement of strong-column and weak-beam mode is ensured. The difference between Ho-JIR1 and Ho-JIR2 is jacket concrete strength, see Table 1, with normal and higher concrete strength, respectively. Both retrofitted units repealed a similar seismic behavior as beam-end flexural hinging developed. It is worth mentioning that original jacket thickness 70 mm was evaluated according to imposed joint shear force when beam hinging mode with steel post-yielding of $1.2 f_y$ was desired. 100 mm in lieu of 70 mm thick jacket was then adopted due to the construction problem.

3.2 Effect of Concrete Interfacial Slip on Joint

Table 2 Results of Imposed Column and Joint Shear

	Ko-JI1 As-built	Ko-JI2 Retrofit	Ko-JIR1 Retrofit	Ko-JIR2 Retrofit	Ho-JI1 As-built	Ho-JIR1 Retrofit	Ho-JIR2 Retrofit	Limit by Park ¹⁹⁹⁷
Failure mode	Joint shear	Joint shear	Joint shear	Joint shear	Joint shear	Beam flexure	Beam flexure	
f'_c (MPa)	32	32	28	28	26	25	38	
Column shear V_{col} (kN)	134	321	290	289	148	200	200	
Column shear stress v_{col} (MPa)	1.5	1.3	1.2	1.2	0.93	0.56	0.56	
v_{col}/v_{fc}'	0.27	0.23	0.23	0.23	0.18	0.11	0.09	0.29
Joint shear V_{jh} (kN)	759	1383	1277	1425	893	1145	1166	
Joint shear stress v_{jh} (MPa)	8.4	5.53	5.28	5.88	5.58	3.18	4.74	
$v_{jh}/v_{fc}'^{(1)}$	-- 1.5	1.0 --	1.0 --	-- 1.11	1.09 --	0.64 --	0.77 --	1.0 1.33

⁽¹⁾ The value presented in lower level means the column subjected to $0.14f'_cA_g$ axial compressive load. Otherwise for no axial compressive load, the value was marked in upper level.

Imposed maximum column and joint shear were reduced from raw data as presented in Table 2. Figure 5 displays two sequences of joint shear strain measured in as-built old concrete and newly casting concrete joint, respectively. In the section, special care will be taken to joint shear behavior.

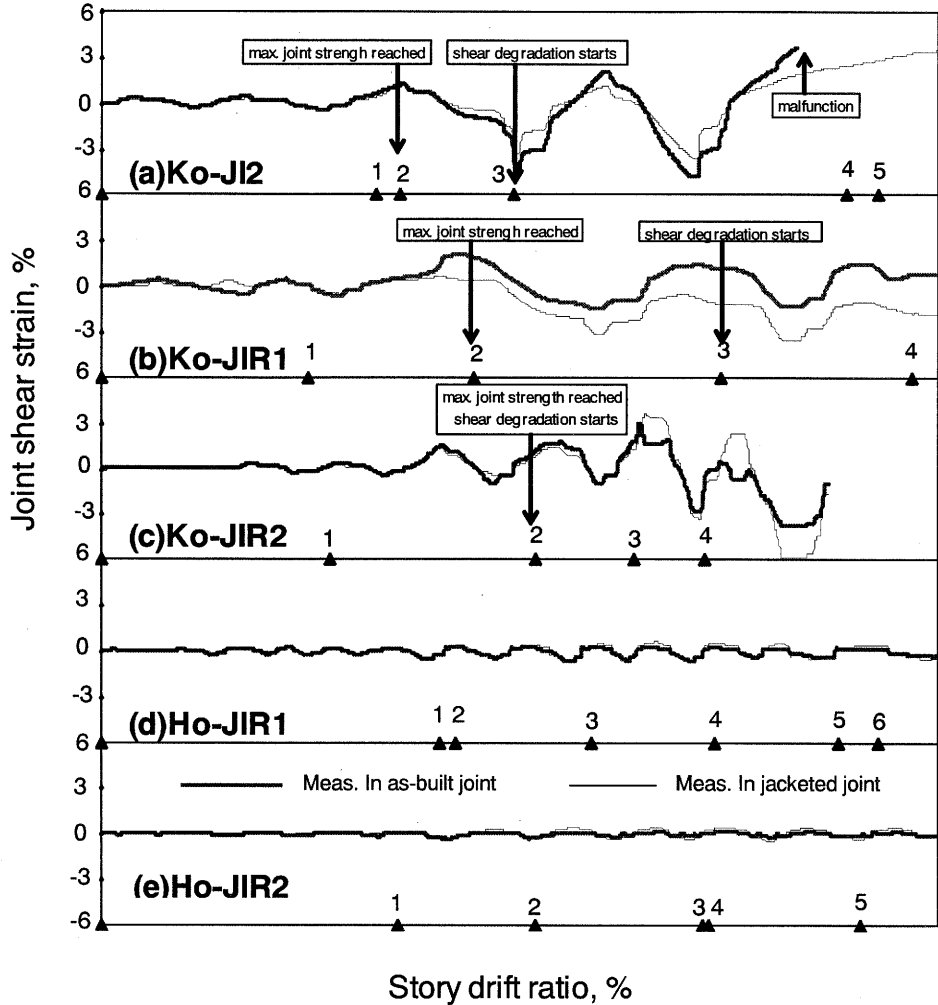


Figure 5 Measured Joint Shear Strain in As-built and Newly Jacketed Concrete Joints

In order to waive the effect of concrete strength, the imposed joint shear stresses were normalized by the ratio of $\sqrt{f'_c}$, referring shear degradation model proposed by Park (1997) as stipulated in Eq. (2), to represent the joint shear strength. Comparing the units without applying axial load and with shear failure mode, i.e. Ko-JI2, Ko-JIR1, and Ho-JI1, Park's model (1997) of $1.0\sqrt{f'_c}$ of interior joint shear capacity agreed test results very well as depicted in Table 2.

In Figure 5, Ko-JIR1 showed an obviously relative concrete slip in joint core but it had same joint shear strength with Ko-JI2. It repealed that the shear strength of the jacketed joint was able to be sustained by means of the interlocking of concrete-to-concrete interface, which is similar to the aggregate interlocking mechanism in diagonal shear cracks (Park and Paulay 1975). Both units Ko-JI2 and Ko-JIR1 had similar tendency of shear degradation that the maximum joint shear strength was lasted from 2% to 3% of drift ratio. Therefore, it was concluded that the interfacial slip of concrete jacket did not influence the overall seismic performance of the retrofitted frame.

For the jacketed units, Ho-JIR1 and Ho-JIR2, with the failure mode of beam-end hinging as depicted in Figure 5 (d) and (e), the smaller joint shear stresses (see Table 2) than the stresses imposed

to series-Ko units lead to consistent reaction of joint shear strains measured in new and old concrete joint. The slip is sure not be created in such jacketed frames if ductile behavior is confirmed.

The effect of axially compressive load on jacketed joint can be seen in the comparison between Ko-JIR1 and Ko-JIR2, as shown in Table 2 and Figures 5 (b) and (c). The relatively interfacial slip for Ko-JIR2 is much smaller and the joint shear strength is higher. That is, axial load with the load level of $0.14f_c A_g$ can hamper the jacketed concrete slip generated in joint core and improve the ability of joint shear resistance. However, one bad effect was found that the tendency of shear degradation was developed at 2% drift ratio when the maximum shear strength reached. Also, this phenomenon is similar to as-built unit Ko-JI1, which has the same axial load level with Ko-JIR2.

4. CONCLUSIONS

The project of non-ductile beam-column joints rehabilitated with RC jacketing is still underway to find an adequate consideration of the retrofit scheme for engineering purpose. The concrete jacket without installing dowel anchors to as-built column and joint, as a view of lowering labor work, was proposed in the study. Some brief conclusions are:

1. RC jacketing applied to columns can effectively improve the frame with substandard joint details to a ductile behavior.
2. The interfacial bond slip observed in newly casting concrete joint is unlikely to influence the overall seismic performance of beam-column joints retrofitted with the RC jacketing.
3. The effect of axially compressive load on hampering the slip of the jacketed concrete in joint and increasing the joint shear strength is positively confirmed. However, the joint shear degradation might occur earlier.
4. Further tests on as-built and/or concrete jacketed beam-column joints, subjected to different axial load levels, without or with little shear reinforcement, needed to calibrate the assessment model of joint shear degradation.

Acknowledgements:

The financial assistance provided by Taiwan National Science Council, Project No. NSC-92-2211-E-008-039, is gratefully acknowledged. The National Central University of Taiwan is also thanked for supporting the traveling budget.

References:

- Wang, Y.C. (2003), "Analytical and Experimental Study on Seismic Performance of RC T-beams with Design Deficiency in Steel Bar Curtailment," *Engineering Structures*, **25**, 215-227.
- Wang, Y.C. and Chen, C.H. (2003), "Analytical Study on Reinforced Concrete Beams Strengthened for Flexure and Shear with Composite Plates," *Composite Structures*, **59**, 137-148.
- Wang, Y.C. and Lee, M.G. (2004), "Rehabilitation of Nonductile Beam-Column Joint Using Concrete Jacketing," *Proceedings of 13th World Conference on Earthquake Engineering*, Paper No. 3159.
- Alcocer, S.M. and Jirsa, J.O. (1993), "Strength of Reinforced Concrete Frame Connections Rehabilitated by Jacketing," *ACI Structural Journal*, **90**(3), 251-261.
- ACI Committee 318 (2002), "Building Code Requirements for Structure Concrete (ACI 318-02) and Commentary (ACI 318R-02)," *American Concrete Institute*.
- Park, R. (1997), "A Static Force-Based Procedure for the Seismic Assessment of Existing Reinforced Concrete Moment Resisting Frames," *Bulletin of the New Zealand National Society for Earthquake Engineering*, **30**(3), 213-226.
- Park, R. and Paulay, T. (1975), "Reinforced Concrete Structures, Chapter 7," John Wiley & Sons Inc.

LATTICE MODEL ANALYSIS CONSIDERING CYCLIC STRESS-STRAIN RELATIONSHIPS OF CONCRETE

J. Niwa¹⁾, N. Suzuki²⁾, and T. Miki³⁾

1) Professor, Department of Civil Engineering, Tokyo Institute of Technology, Japan

2) Master Course Student, Department of Civil Engineering, Tokyo Institute of Technology, Japan

3) Post-graduate Student, Department of Civil Engineering, Tokyo Institute of Technology, Japan
jniwa@cv.titech.ac.jp, nsuzuki@cv.titech.ac.jp, tmiki@ucsd.edu

Abstract: Static analysis using 2D lattice model considering cyclic stress-strain relationships of concrete is performed on the shear failure of RC columns. The lattice model can predict the shear carrying capacity of RC columns accurately. Analytical target is 1/3-scale model of a RC column, tested by Xiao, Seible et al. (1993) at the University of California, San Diego. Analytical study for the shear resisting mechanism is carried out by separating flexural and shear deformations and by noting the stress-strain relationships of each component in the lattice model. It is found out that the updated lattice model can predict on the energy-absorption performance at inelastic region highly accurately. In addition, it is revealed that the shear failure in the analysis will happen when the compressive softening behavior of concrete occurs.

1. INTRODUCTION

Kobe earthquake on January 1995 in Japan caused destructive damage to various structures, including reinforced concrete (RC) structures. The observations following this earthquake showed that the main causes of severe collapses were due to the shear failure and the insufficient ductility of structures. Therefore, we reconfirmed the importance of high energy-absorption performance at inelastic region after the longitudinal reinforcement yields. In the design of RC bridge piers, the analytical study for seismic response of RC structures subjected to earthquake motion is necessary. Because of these reasons, in recent years, several significant progresses of the analytical technique for concrete structures have been achieved. In addition, the rapid development of computer technology brought to the reduction of the time required for the analysis and the high accuracy to incorporate more realistic material constitutive model.

To clarify the resisting mechanism for RC members, the lattice model is used in this study. The lattice model discretizes a RC member into truss elements. The lattice model is an objective and simple procedure, which can be used to explain the shear resisting mechanism for RC members. Appropriate stress-strain relationship considering nonlinearity is incorporated into each member of the lattice model. In order to suitably describe the performance of energy-performance, it is important to deal with nonlinearity of unloading and reloading paths. However, the conventional analysis is insufficient on the field of unloading and reloading paths of concrete. The aim of this study is to incorporate the updated stress-strain relationship of concrete into the analysis.

To carry out the shear analysis and to clarify the shear resisting mechanism for RC columns, 1/3-scale model of RC column tested by Xiao, Seible et al. (1993) at the University of California, San Diego was selected as analytical target.

2. ANALYTICAL MODEL

2.1 Outlines of Lattice Model

The lattice model consists of members of concrete and reinforcement, as demonstrated in Figure 1. The column subjected to the load from left hand side is shown. In a RC column, the concrete is modeled into flexural compression members, flexural tension members, diagonal compression members, diagonal tension members, horizontal members and two arch members. The longitudinal and transverse reinforcements are modeled into vertical and horizontal members, respectively. The diagonal members are regularly arranged with the inclined angles of 45 and 135 degrees with respect to the longitudinal axis of the column. The arch members connecting the nodes at the opposite diagonal corners between the loading point and the bottom of the column are arranged according to the direction of the internal compressive stress flow.

Figure 2 illustrates a schematic diagram of cross section of a RC column. The concrete is divided into the truss part and the arch part. When the value of t is defined as a ratio of the width of arch part to the width of cross section, the widths of the arch part and the truss part are given as $b \times t$ and $b \times (1-t)$, respectively where t is in the range from 0 to 1. The value of t is determined based on the theorem of the minimization of the total potential energy for the lattice model with the initial elastic stiffness. The total potential energy is obtained from the difference between the summations of the strain energy in each element and the external work. The pre-analysis using the lattice model is carried out to the total potential energy.

2.2 Material Constitutive Models

(1) Steel Model

The envelope curve for the stress-strain relationship of reinforcing bars is modeled as bi-linear in which the tangential stiffness after yielding is $0.01 E_s$, where E_s denotes Young's modulus. After yielding, the stiffness of reinforcing bars decreases when the stress state changes from tension to compression, while the similar behavior is observed when the stress state changes from compression to tension. In the analysis, by using Fukuura's model (1997), this phenomenon, so-called Bauschinger effect, is considered by the numerical model of reinforcing bars. In addition, in order to evaluate the buckling behavior of longitudinal reinforcing bars, the buckling model proposed by Dhakal (2000) is adopted.

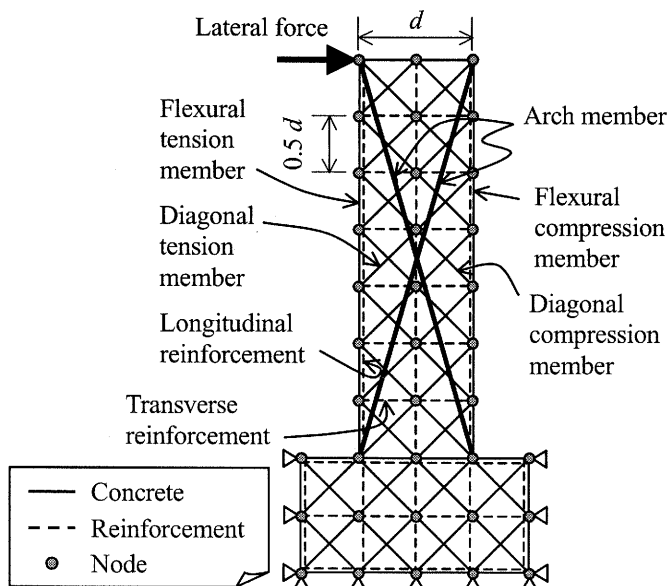


Figure 1 Outlines of 2D lattice model

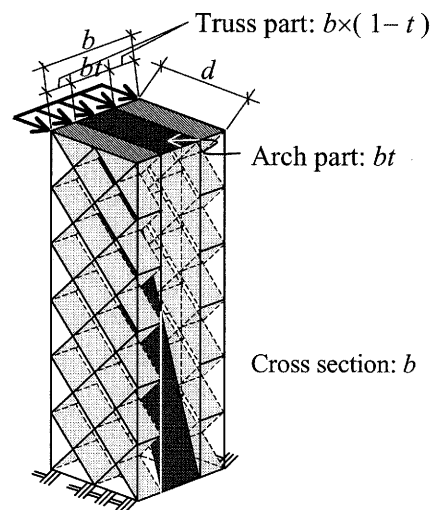


Figure 2 Cross section of RC column modeled by 2D lattice

(2) Envelope Curve of Concrete

In order to consider the effect of lateral confinement of concrete due to suitable arrangement of transverse reinforcement, the stress-strain relationship of confined concrete proposed by Mander et al. (1988) is applied to the diagonal compression members and the arch members in the lattice model. For cracked concrete, the compressive softening behavior of concrete proposed by Vecchio and Collins (1986) is considered. The ability of cracked concrete to resist compressive stress decreases as the transverse tensile strain increases. For the flexural compression members, the stress-strain relationship represented by the parabolic curve is used.

For the flexural tension members of concrete, which are provided near reinforcing bars, the tension-stiffening model (Okamura and Maekawa 1991) is applied considering the bond effect between the concrete and reinforcing bars. On the other hand, for the diagonal tension members, 1/4 tension softening model (Rokugo et al. 1989) is applied.

(3) Conventional and Updated Cyclic Stress-Strain Relationships of Concrete

Figure 3 demonstrates conventional cyclic stress-strain relationships. In the unloading path of compression, the stress was assumed to decrease with the initial stiffness, E_c . The reloading curve was assumed to follow the same path as the unloading one, that is, the decrease in the stiffness due to reversed cyclic loading was not taken into account for simplicity. In the tensile model of concrete, the unloading path was assumed to fall directly to the origin and the reloading path was assumed to follow the unloading path.

To improve the cyclic behavior of concrete under both compression and tension, the cyclic stress-strain relationships proposed by Naganuma et al. (2000) are used in the lattice model. Figure 4 shows the updated cyclic stress-strain relationships. The compressive model can evaluate the decrease in the stiffness of concrete during unloading and reloading paths as the maximum compressive strain increases.

The detailed scheme about the unloading and reloading hysteresis of internal curves is abstractly illustrated in Figure 5. In the

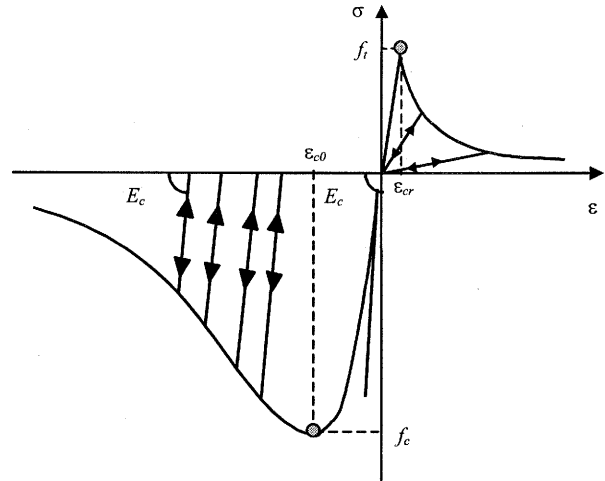


Figure 3 Conventional concrete model

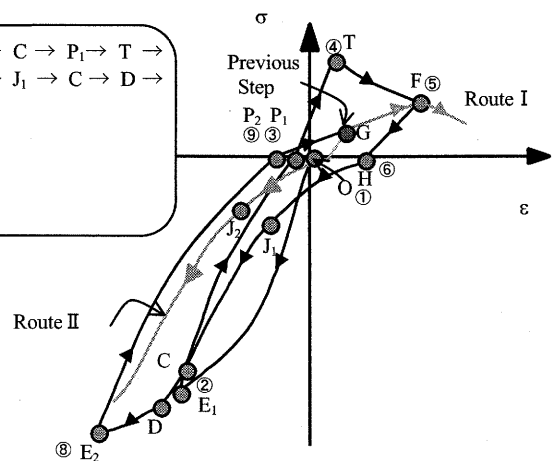
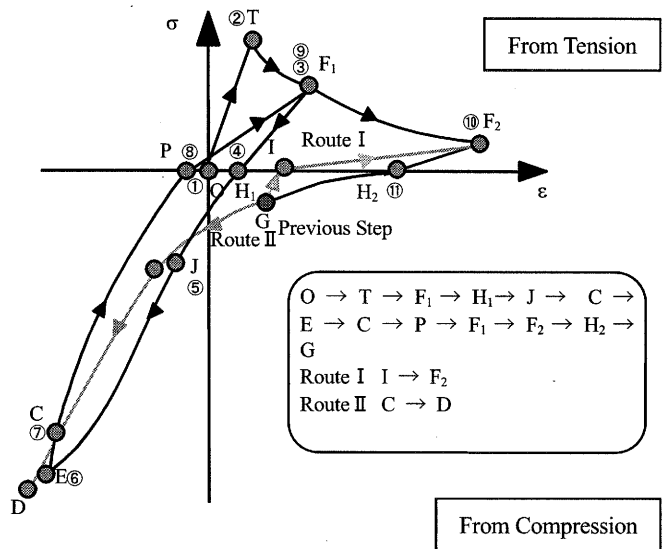


Figure 4 Updated concrete model

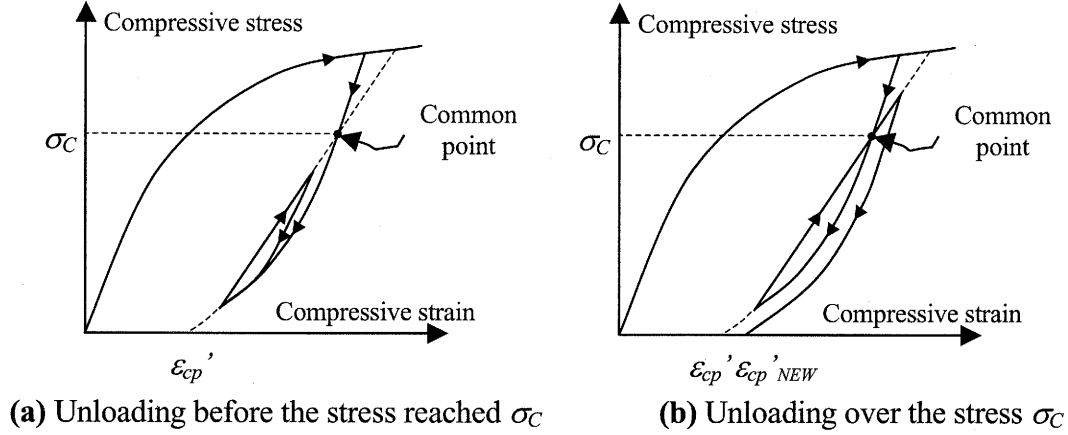


Figure 5 Detailed rules for internal loops of updated compressive model

unloading and reloading hysteresis, the path is reset when the strain exceeds the point of stress σ_C (Common point, Figure 5) and the plastic strain of concrete in compression, ε_{cp}' is calculated again. On the other hand, during the internal state where the strain does not exceed the point of stress σ_C , the unloading path is assumed to proceed to the state of plastic strain calculated in the previous calculation step.

For the tensile model of concrete, the unloading path is assumed to fall according to the stiffness as represented by the following equation.

$$E_{tmax} = 1.5 \frac{\varepsilon_{cr}}{\varepsilon_{tmax}} E_{t0} \quad (1)$$

where E_{tmax} is the stiffness in the tensile stress-tensile strain relationship of concrete immediately after the transition from loading to unloading. In addition, ε_{cr} and E_{t0} are the strain corresponding to the tensile strength of concrete and the initial stiffness in the tensile stress-tensile strain curve of concrete.

In the loading process from tension to compression, the closure of cracks is generated due to the loss of the load. On closing of cracks, the compressive stress is transmitted to the concrete across the crack surface. Hence the two crack surfaces make contact with each other even though the strain of the concrete becomes zero. The stress-strain model for the contact of crack surfaces is represented by the following logarithm function.

$$\sigma = (\log_e(\varepsilon + a) + b) \cdot c \quad (2)$$

where a , b , and c are constants. These constants are determined from the condition that the curve passes through the points at the plastic strain in tension and at the stress represented by Equation (3).

$$\sigma_J = - \left(1.0 + 0.02 \left(\frac{\varepsilon_{tmax} - \varepsilon_{cr}}{\varepsilon_{cr}} \right) \right) \cdot f_t \quad (3)$$

where, ε_{tmax} is the maximum tensile strain of concrete during loading hysteresis. Similarly, ε_{cr} is the strain corresponding to the tensile strength of concrete, f_t .

3. EXPERIMENTAL SETUP AND THE LATTICE MODEL

3.1 Experimental Setup

A series of 1/3-scale models of RC bridge columns were tested by Xiao et al. (1993) at the University of California, San Diego. The tested columns of target analysis had different strengths of longitudinal and transverse reinforcements and the shear span to effective depth ratio. Because of these conditions, all columns had relatively low shear carrying capacity. We focused on the column R-3.

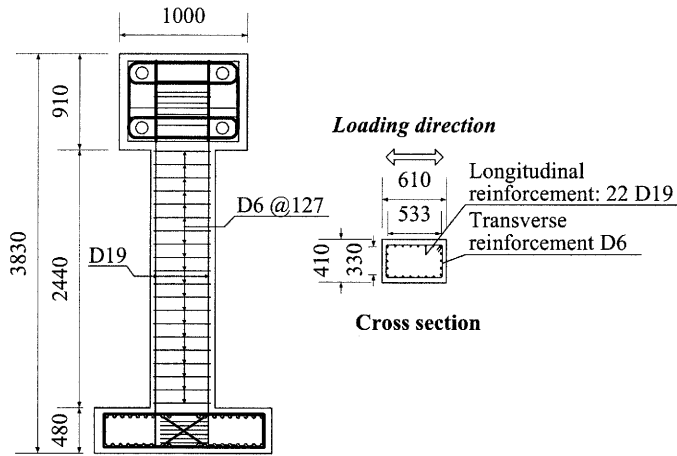


Figure 6 Details of R-3

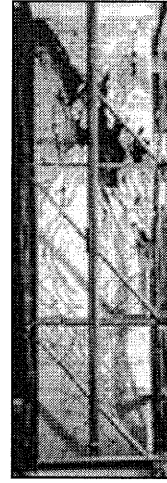


Figure 7 Crack patterns of R-3

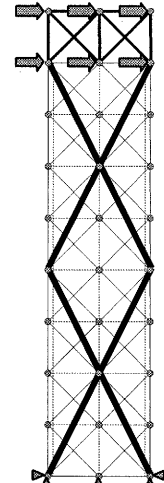


Figure 8 2D lattice model

Figure 6 shows the column R-3. The cross section of the column was 610 mm width and 410 mm depth. The column was 2440 mm height. All reinforcing bars had minimum concrete covering of 25 mm. The longitudinal reinforcement had the yield strength of 469 N/mm^2 . The yield strength of transverse reinforcement was 324 N/mm^2 . The compressive strength of concrete was 34.1 N/mm^2 .

During the loading test, the footing of the column was fixed laterally against slip and rotation. The lateral cyclic displacement is applied to the top of the column while the double bending prevents the rotation. The amplitude of the lateral displacement was increased step wisely during the test. Throughout the test, a constant axial compressive load of 507 kN was applied at the top of the column to simulate the weight of a superstructure. Since the column R-3 had stronger longitudinal reinforcement and weaker transverse reinforcement, pronounced shear failure happened. Figure 7 shows the crack patterns of R-3 at its final loading stage. The major diagonal shear cracks were formed near the top and bottom of the column.

3.2 Configuration of Lattice Model

The 2D static lattice model and the boundary conditions used in the analysis are illustrated in Figure 8. Since the columns subjected to lateral cyclic loads at its top in the condition of preventing the rotation, the arch members are installed according to a moment distribution as illustrated in Figure 8. A constant axial compressive load is applied throughout the analysis in order to simulate the vertical load in the experiment. The lateral load is applied through controlled displacements in the horizontal direction. In order to prevent the rotation during additional lateral load, the elastic elements are utilized as a loading stub in the analysis. This loading condition prevents the rotation at the top of the column while allowing free vertical displacement.

4. ANALYTICAL RESULTS AND DISCUSSIONS

4.1 Load-Displacement Relationship

The nonlinear analysis by 2D static lattice model is carried out. Figure 9 shows the load-displacement relationships of the column R-3 obtained from the experiment and the lattice model analysis. In the experiment, the column R-3 was found to fail in a brittle shear failure at the displacement ductility 1.5, followed by the severely pinched response. It is also clear from Figure 9 that the failure is attributed to shear in the analytical results. That is, the lattice model analysis is able to capture the brittle shear failure of RC members. On the other hand, residual displacement in the analytical load-displacement relationship with updated model of concrete is found to be smaller than that with conventional model. The reason is that the updated model considers the decrease in the

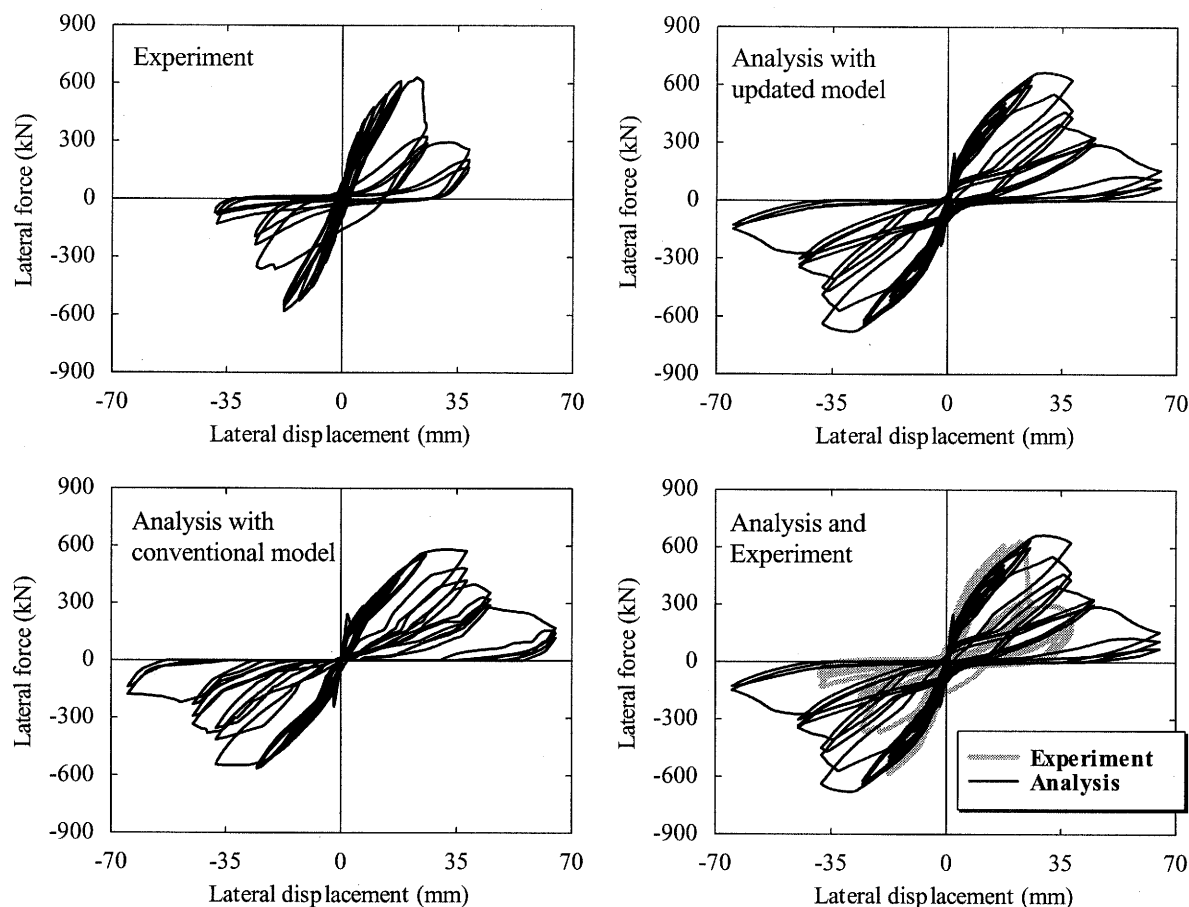


Figure 9 Load-displacement relationships

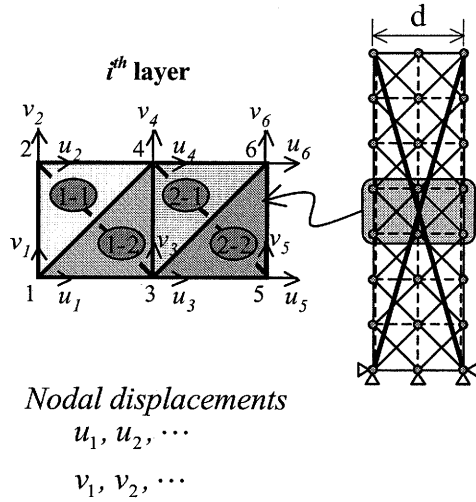
stiffness on the compression model. Hence, residual compressive strain in the analytical stress-strain relationships of each component with updated model is less than that of conventional model.

4.2 Flexural and Shear Deformations

To understand the behavior of the shear-dominated RC column, the total horizontal displacement at the top of the column is separated into flexural and shear components. In the experiment, this can be obtained by separated displacements from the three portions of horizontal, vertical and diagonal measurements throughout the column height as illustrated in Figure 7. In the analysis, the scheme to separate the deformation into flexural and shear components performed by Ueda et al. (2002) is applied. In this study, the horizontal displacements of each layer in the 2D lattice model are calculated as schematically shown in Figure 10. The shear deformation at the top of the column can be obtained by the integration throughout the column height. On the other hand, the flexural deformation at the top of the column is calculated by subtracting the shear deformation from the total horizontal deformation. The experimental and analytical results of the flexural and shear deformations of the column R-3 are illustrated in Figure 11. It is found that the analytical results show the same tendency with the experimental result. That is, in the analysis, the shear deformation preceding the shear failure is found to increase more rapidly than the flexural deformation. From this analytical observation, we can come to the conclusion that this failure was the shear failure.

4.3 Shear Resisting Mechanism

In order to discuss the shear-resisting mechanism of the column that showed the shear failure, we note the stress-strain relationships of each component in the lattice model. To express the decrease in the shear carrying capacity in connection with the development of the diagonal crack, the compression



1. Calculation of shear strain of each element

$$\gamma_{xy}^{1-1i} = \frac{u_1 - u_2}{0.5d} + \frac{v_4 - v_2}{0.5d} \gamma_{xy}^{2-1i} = \frac{u_3 - u_4}{0.5d} + \frac{v_6 - v_4}{0.5d}$$

$$\gamma_{xy}^{1-2i} = \frac{u_3 - u_4}{0.5d} + \frac{v_3 - v_1}{0.5d} \gamma_{xy}^{2-2i} = \frac{u_5 - u_6}{0.5d} + \frac{v_5 - v_3}{0.5d}$$

2. Calculation of shear deformations in each element

$$\delta_s^{1i} = \frac{1}{2} (\gamma_{xy}^{1-1i} + \gamma_{xy}^{1-2i}) \cdot 0.5d \delta_s^{2i} = \frac{1}{2} (\gamma_{xy}^{2-1i} + \gamma_{xy}^{2-2i}) \cdot 0.5d$$

3. Averaged shear deformation in a layer

$$\delta_s^i = \frac{1}{2} (\delta_s^{1i} + \delta_s^{2i})$$

4. Shear deformation at the top of the column

$$\delta_s = \sum_{i=1}^n \delta_s^i$$

Figure 10 Decomposition method of shear deformation from nodal displacement

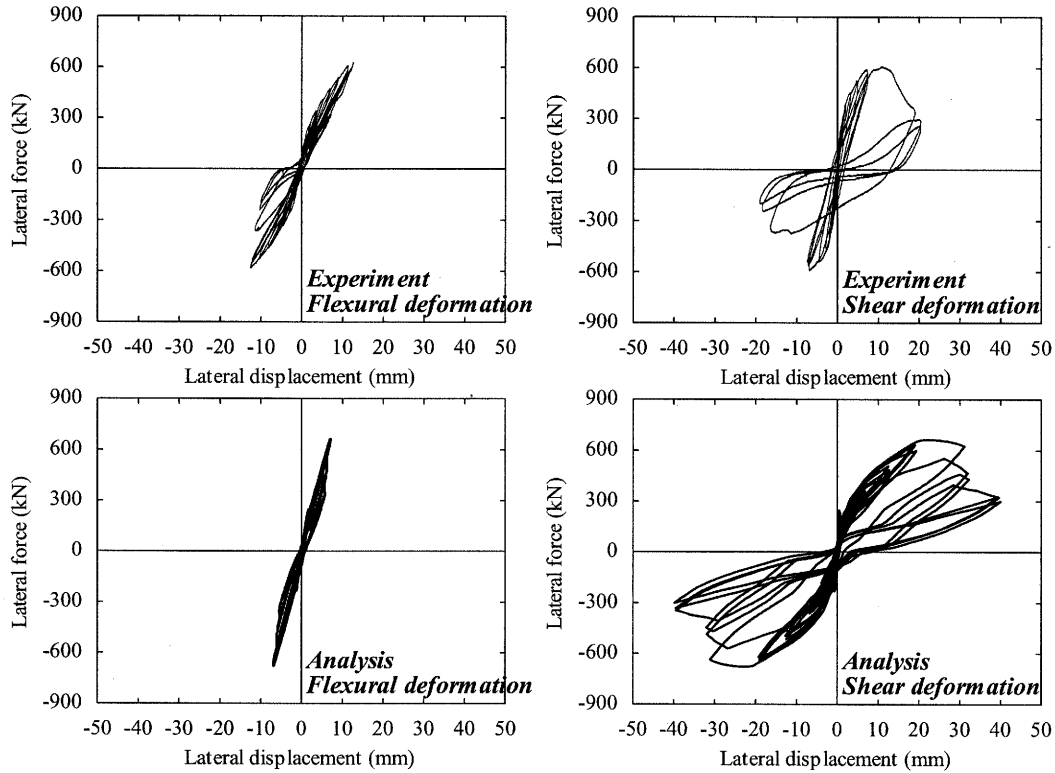


Figure 11 Component of flexural and shear deformations

softening behavior was considered in the diagonal compression members and arch members. Figure 12 illustrates the stress-strain relationship of each concrete member of the column R-3. As shown in the case of the lateral displacement at 38 mm (peak load, Figure 9), the arch member and the diagonal compression member exhibit the peak stress. On the other hand, the flexural member does not exhibit the peak stress. It is found that at the lateral displacement at 65 mm (post peak, Figure 9), the arch member and the diagonal compression member show compression softening behavior in connection with the increase in the tension strain in the diagonal tension member. Then, the flexural member shows pre-peak stress. Through these analytical results, it is found that the rapid compression softening behavior of the arch member and the diagonal compression member damaged by shear force,

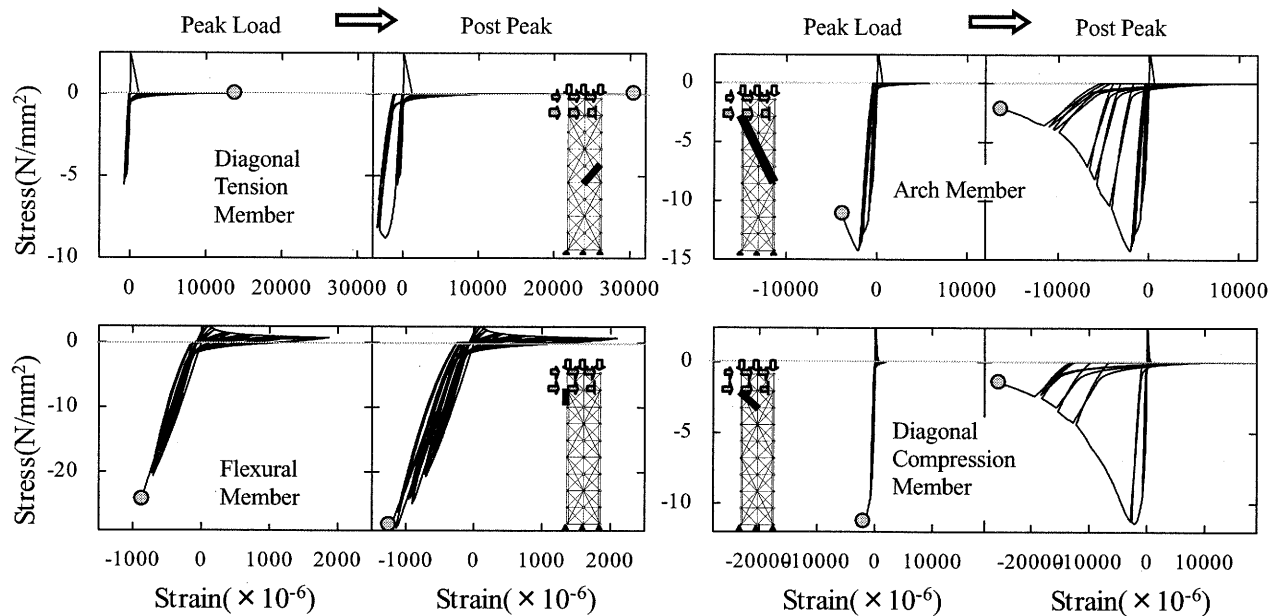


Figure 12 Stress-strain relationship in each concrete member

lead to the brittle shear failure.

5. CONCLUSIONS

The lattice model analysis is carried out to simulate the behavior of the shear-dominated RC column tested by Xiao, Seible et al. (1993). In the analysis, the updated stress-strain relationship of concrete is incorporated. The conclusions of this study can be drawn out as follows:

- (1) Considering the realistic cyclic behavior of concrete under both compression and tension, the prediction of residual displacement is improved.
- (2) The shear deformation preceding the shear failure is found to increase more rapidly than the flexural deformation.
- (3) The shear failure in the analysis is predicted to happen when the compressive softening behavior of concrete occurs.

References:

- Dhakal, R. P. (2000), "Enhanced Fiber Model in Highly Inelastic Range and Seismic Performance Assessment of Reinforced Concrete." PhD Thesis, The University of Tokyo.
- Fukuura, N., and Maekawa, K. (1997), "Computational Model of Reinforcing Bar under Reversed Cyclic Loading for RC Nonlinear Analysis." *Journal of Materials, Concrete Structures and Pavement*, JSCE, **564**(35), 291-295. (in Japanese)
- Mander, J. B., Priestly, K. J. N., and Park, R. (1988), "Theoretical Stress-strain Model for Confined Concrete," *Journal of Structural Engineering*, ASCE, **114**(8), 1804-1826.
- Naganuma, K. and Ohkubo, M. (2000): "An Analytical Model for Reinforced Concrete Panels under Cyclic Stresses." *Journal of Structural and Construction Engineering*, AIJ, **536**, 135-142. (in Japanese)
- Niwa, J., Choi, I.C., and Tanabe, T. (1995), "Analytical Study for Shear Resisting Mechanism Using Lattice Model." *Concrete Library International*, JSCE, **26**, 95-109.
- Okamura, H. and Maekawa, K. (1991), "Nonlinear Analysis and Constitutive Models of Reinforced Concrete," Gihodo-Shuppan.
- Rokugo, K., Iwasa, M., Suzuki, T., and Koyanagi, W. (1989), "Testing Method to Determine Tensile Strain Softening Curve and Fracture Energy of Concrete," *Fracture Toughness and Fracture Energy*, Balkema, 153-163.
- Ueda, T., Sato, Y., Ito, T., and Nishizono, K. (2002): "Shear Deformation of Reinforced Concrete Beam." *Journal of Materials, Concrete Structures and Pavements*, JSCE, **711**(56), 202-215.
- Vecchio, F. J. and Collins, M. P. (1986), "The Modified Compression-Field Theory for Reinforced Concrete Elements Subjected to Shear." *ACI Journal*, **83**(2), 219-231.
- Xiao, Y., Priestly, M. J. N., and Seible, F. (1993), "Steel Jacket Retrofit for Enhancing Shear Strength of Short Rectangular Columns", Report No. SSRP-92/07, Department of Applied Mechanics and Engineering Sciences, University of California, San Diego.

TSUNAMI DAMAGE IN SRI LANKA DUE TO THE SUMATRA EARTHQUAKE OF DECEMBER 26, 2004— PRELIMINARY RECONNAISSANCE

Anil C. Wijeyewickrema¹⁾, Shusaku Inoue²⁾, and Toru Sekiguchi³⁾

1) Associate Professor, Department of Civil Engineering, Tokyo Institute of Technology, Japan

2) Research Associate, Department of Built Environment, Tokyo Institute of Technology, Japan

*3) Doctoral Student, Department of Architecture and Building Engineering, Tokyo Institute of Technology, Japan
anil@cv.titech.ac.jp, shusaku@enveng.titech.ac.jp, tsekiguc@mail.arch.titech.ac.jp*

Abstract: This paper describes the field visit to Sri Lanka to inspect the effects of the tsunami which resulted from the Sumatra earthquake of December 26, 2004. The team from Tokyo Institute of Technology was the first international team of scientists to visit Sri Lanka to gather data about the effects of the tsunami. It is expected that the data reported in this paper will be useful for researchers to calibrate their tsunami simulation models.

1. INTRODUCTION

The essential details of the Sumatra earthquake are as follows: Magnitude: 9.0; Time: December 26, 2004 at 00:58:53 (Coordinated Universal Time); Local time at epicenter: December 26, 2004 at 7:58:53 AM; Location: 3.3° N 9.9° E; depth: 33 km; Region: off the West coast of Northern Sumatra. This is the fourth largest earthquake in the world since 1900 and is the largest since the 1964 Prince William Sound, Alaska earthquake. The tsunami generated by the Sumatra earthquake resulted in more casualties than any previous tsunami (USGS, 2004). Due to the earthquake and tsunami around 200,000 people lost their lives in Indonesia. The other countries that reported a large number of casualties due to the tsunami were Sri Lanka – around 30,000, India – around 11,000 and Thailand – around 6,000. The location of the epicenter and surrounding countries are shown in Fig. 1.

2. PREPARATIONS AND PLANNING BEFORE ARRIVING IN SRI LANKA

The Sumatra earthquake occurred on December 26, 2004 which was a Sunday. In the evening of December 27 (Mon), Prof. Tatsuo Ohmachi, COE Program Leader Center for Urban Earthquake Engineering (CUEE) suggested that a team from Tokyo Institute of Technology make a trip to Sri Lanka to gather data from the affected areas. On the same day Prof. Kohji Tokimatsu, COE Program Sub-Leader agreed that such a trip should be carried out and it was decided that the team members would be the three authors of this paper, Anil C. Wijeyewickrema (ACW), Shusaku Inoue (SI), and Toru Sekiguchi (TS).

The next day Dec 28 (Tue) the team members had a meeting to and it was agreed that ACW would see about the arrangements in Sri Lanka and that SI would see about the airline tickets and that the team would leave for Sri Lanka on Dec. 29 (Wed). E-mails were sent and calls were also made to academics in Sri Lanka known to ACW, to find out whether any of them could also assist with the data

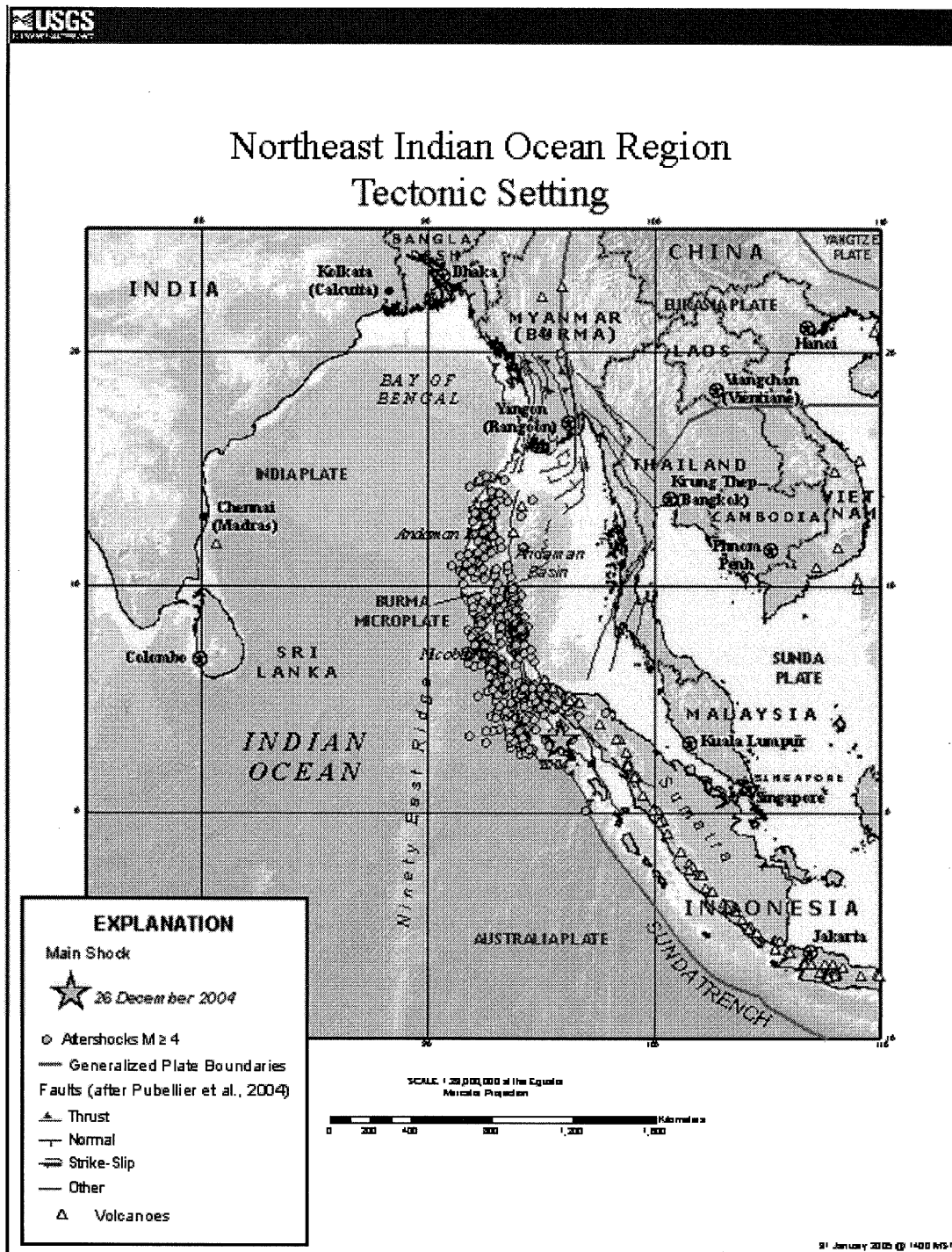


Fig. 1. Epicenter of Sumatra earthquake and surrounding countries (USGS, 2004).

gathering and local arrangements. Attempts to make hotel reservations through the internet and calling Sri Lanka were not successful as all major hotels were already fully occupied. This was because in addition to December being the peak tourist season in Sri Lanka, many foreigners from

international organizations were arriving or had arrived to assist in relief operations, and tourists already in Sri Lanka whose vacation plans were disrupted were coming to Colombo from the tsunami affected areas. Finally ACW was able to make reservations in a small tourist inn in Mount Lavinia through a friend who knew the owner. The next task was to get some academics from University of Moratuwa (UM) which is one of the best Engineering Universities in Sri Lanka to agree to join the field visit. Although e-mails were sent to Dr. U. G. A. Puswewala and Dr. Priyantha Gunaratna of UM, attempts to reach them by phone were not successful. Fortunately, ACW was able to get in touch by phone with a graduate student Mr. Manoj Madurapperuma from UM who had applied to Tokyo Tech to continue his graduate studies. Mr. Manoj was requested to organize a van capable of carrying a minimum of six persons with a driver.

Not knowing exactly what the ground situation was like in the affected areas it was decided to take face-masks and rubber gloves to Sri Lanka. At Narita Airport a few face-masks were purchased but rubber gloves were not available. Since the flight to Colombo was via Singapore a box of rubber gloves were purchased at the Singapore airport.

3. ARRIVAL IN SRI LANKA AND PREPARING FOR THE TRIP

We left Narita at 11:30 on Dec 29 (Wed), arrived in Singapore at 1800, left Singapore at 2240 and arrived in Sri Lanka at 0020 on Dec 30 (Thu). We checked in to the 'Tropic Inn' in Mount Lavinia which is just South of Colombo around 0200.

In the morning of Dec 30 (Thu) a meeting was held at University of Moratuwa (UM) which is located South of Mount Lavinia and about 20-30 minutes by van. Those participating in the meeting were Prof. Samantha Hettiarachi, Prof. Priyan Dias, Dr. U. G. A. Puswewala, Dr. Priyantha Gunaratna and Mr. Manoj Madurapperuma from UM and the three team members from Japan. The discussion centered on which parts of Sri Lanka would be accessible by road and which parts could be covered within the time available. The areas that were badly affected by the tsunami were the SW, S, SE, E and NE parts of Sri Lanka. Some sections of the main highway from Colombo to the South (called Galle Road as it goes through that town) had been closed by the government because of damage caused to the highway by the tsunami. But now most of this highway was open and only a few detours were expected. It was decided that the team would leave Colombo on Dec. 31 (Fri) and go South hopefully upto Yala National park in the SE. Dr. Priyantha Gunaratna and Mr. Manoj Madurapperuma agreed to join the field visit.

Dr. Priyantha also agreed to arrange for accommodation at University of Ruhuna on Dec. 31 (Fri). Due to inadequate information about the availability of food and drinking water in the tsunami affected areas it was decided that all necessary supplies including food and drinking water would be purchased in Colombo and taken in the van.

4. FIELD VISIT ROUTE

The field visit commenced on Dec 31 (Fri) in the morning and we headed South from Mount Lavinia along the main Colombo-Hambantota highway. The main cities that were visited to gather data are indicated in Fig. 2. A section of the highway close to Seenigama where a train was swept off the train tracks by the tsunami was closed, and a detour had to be made to arrive in Hikkaduwa, and then we went North to Seenigama to inspect the train wreckage. On Dec 31 (Fri) night we stayed at the faculty guest house of the University of Ruhuna which is located in Hapugala, East of Galle town.

The next day the field visit continued from Galle upto Hambantota where the field visit ended, since the highway goes away from the coast at Hambantota. The van and the members of the field visit are shown in Fig. 3.

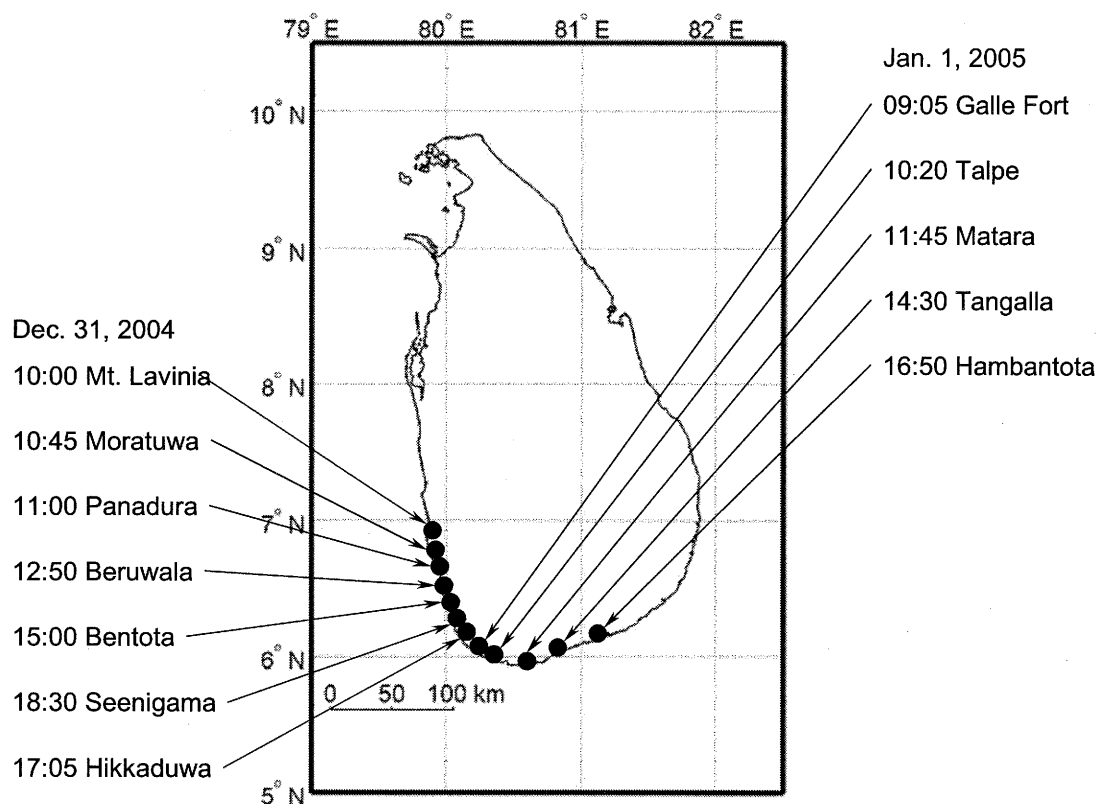


Fig. 2. Field visit route.



Fig. 3. Field visit team members: (from left to right) Rohana (driver), Manoj Madurapperuma, Shusaku Inoue, Priyantha Gunaratna and Anil C. Wijeyewickrema. In the inset is Toru Sekiguchi.

5. SUMMARY OF THE TSUNAMI DAMAGE

The damage due to the tsunami is shown in Figs. 4-14. In general, the damage caused by the tsunami was most severe in regions between Galle and Hambantota and extended several hundred meters from the coast. However it was observed that the damage caused was not uniform with some areas having only, minor damage. Most of the houses that were damaged were masonry houses. But in some instances the more recently constructed houses seemed to have sustained less damage. Damage to houses have been mainly due to the tsunami wave pressure but some houses have been damaged due to boats, trees and vehicles that were swept away by the tsunami.

The Colombo-Matara rail tracks run mostly along the coast. Damage to train tracks were observed in many places. The only train that was swept away was stopped between stations when the tsunami struck and around 1,000 people are estimated to have lost their lives due to this incident (see Fig. 9).

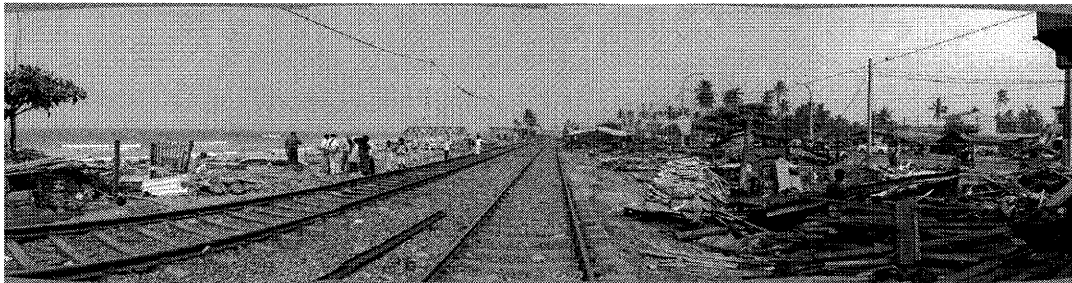


Fig. 4. South Moratuwa: Tsunami came from the left, houses on both sides of the rail tracks were destroyed.



Fig. 5. Beruwala Fishery Harbor: Many boats in the harbor had been damaged.



Fig. 6. South Bentota: Coastal region is covered by palms and bushes, not much damage could be observed.



Fig. 7. North Ambalangoda: Electric poles lean to the right, rail tracks had been damaged.



Fig. 8. Hikkaduwa: Boat was swept into the hotel, outside wall of the hotel was broken, but the hotel was not destroyed.



Fig. 9. Seenigama: Though this area is inland about 200m from the coastal line, express train was washed away by tsunami and about 1,000 people lost their lives.

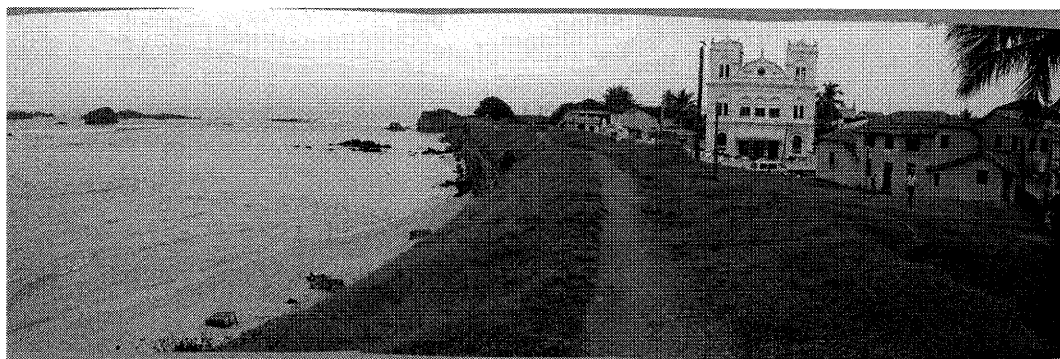


Fig. 10. Galle Fort: Galle Fort is a peninsula in the center of Galle city which was one of the most damaged cities. The interior of Galle Fort was safe from the tsunami due to the 5-6 m high walls of the Fort.



Fig. 11. Talpe: An inland area away from the sea. The overturned lorry on the left was swept away from the right where another lorry can be seen.

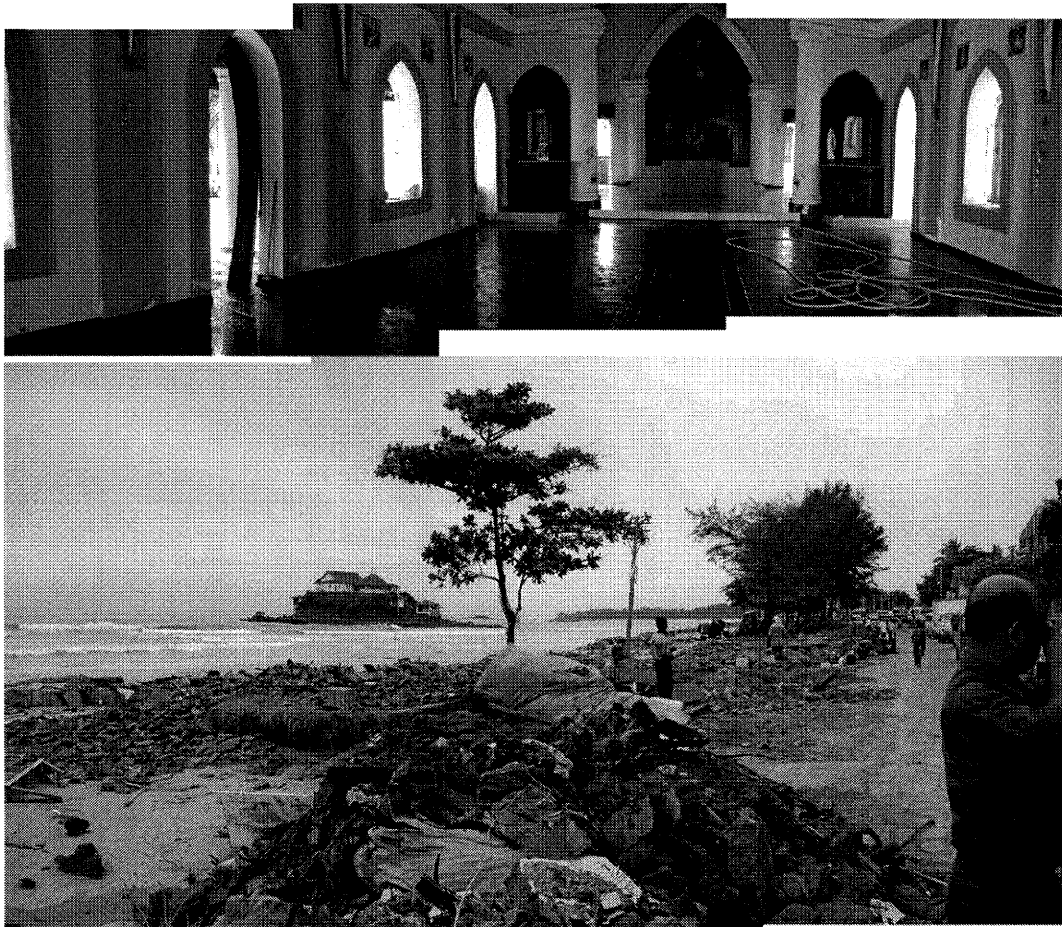


Fig. 12. Matara: (Top) Inside of St. Mary's church which is located near the coast, the water level reached up to the feet of the crucifix. (Bottom) Coastal area outside the church, the bottom of the island was shaved by the tsunami.

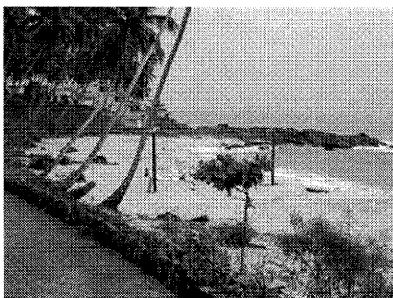


Fig. 13. Tangalla: Normal view on left, waves due to tsunami on right (photo on right courtesy of Tangalla guest house).



Fig.14. Hambantota: Masonry houses located within a few hundred meters from the coast were completely destroyed, a few more recently constructed houses had less damage.

6. EYEWITNESS AND ARRIVAL TIME OF TSUNAMI

In this investigation one of the main objectives was to interview people who had witnessed the tsunami and record their observations before they forget details such as arrival times. The arrival times obtained from this field trip are shown in Fig. 15, together with some data from Chapman (2004). The eyewitness accounts of arrival times are not necessarily accurate as some witnesses did not have watches and some witnesses did not see all the waves. It is most likely that there were one or two waves before the biggest wave. Each wave period was about 30 minutes. Before the biggest wave arrived the water receded for several hundred meters in some locations and the wave height of the biggest wave is estimated to have been 5-6 meters.

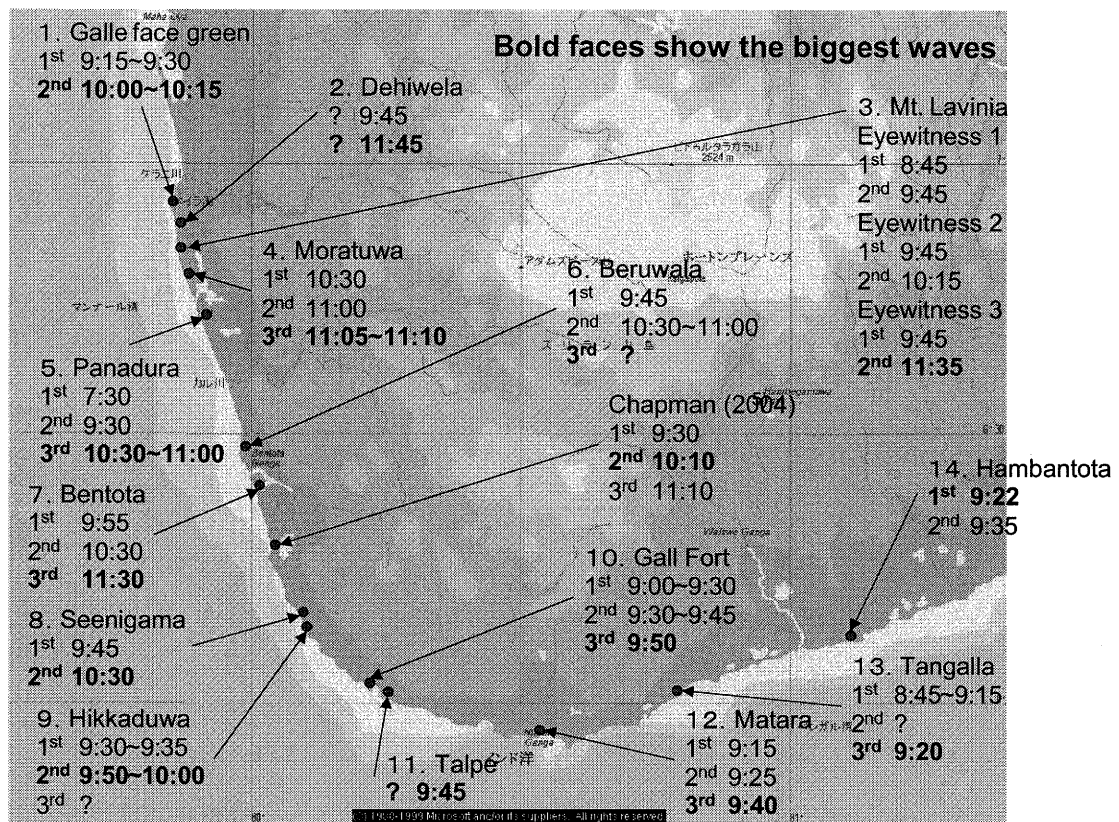


Fig. 15. Tsunami arrival time from eyewitness accounts. In this figure, date from Chapman (2004) is also included.

7. CONCLUDING REMARKS

Difficulties encountered during data gathering:

When questioned about wave arrival times, different villagers would give different wave arrival times as many persons do not use watches. Obviously more accurate wave arrival times could be obtained from tidal wave gauges and efforts are being made to get such records from the appropriate government organizations, if available. Some villagers were requesting financial assistance to purchase food etc. Such requests were politely declined by explaining that the team mission was scientific and not a relief operation, as otherwise crowds would rapidly gather for handouts and it would be impossible to gather data. Some villagers who had lost family members and or dwelling places were too traumatized to give useful answers.

The team rested on Jan. 02 (Sun) for the most part but visited the Galle Face Green in Colombo and interviewed people who had witnessed the tsunami wave phenomena. On Jan. 03 (Mon) various newspaper offices were visited to purchase back issues of newspapers such as Daily News, Sunday Observer, Sunday Times and Sunday Leader, giving information about the tsunami. On the same day detailed maps of the coastal areas that were investigated were purchased from the Survey Department of Sri Lanka. On the last day Jan. 04 (Tue), a meeting was held at University of Moratuwa to share the information that was collected by the team and a meeting was held in the Colombo Port with Prof. Fumihiko Imamura (Tohoku University) and another team from Japan who had recently arrived in Sri

Lanka to investigate the tsunami. We left Colombo at 0135 on Jan. 05 (Wed) arrived in Singapore at 0725 and left Singapore at 0940 and arrived in Narita at 1705 on the same day.

The team from Tokyo Institute of Technology was the first international team of scientists to visit Sri Lanka to gather data about the effects of the tsunami. Other international scientific teams that arrived afterwards were from the USA led by Prof. Philip Liu (Cornell University) and Prof. Harindra Fernando (Arizona State University) and from Japan led by Prof. Yoshiaki Kawata (Kyoto University) and Prof. Fumihiko Imamura (Tohoku University).

As the first field visit reported in this paper was limited to the SW and South Sri Lanka, a second field trip from March 10-18, 2005 is planned to visit NE, East and SE parts of Sri Lanka, including Trincomalee, Batticaloa and Yala to get inundation data using GPS equipment.

Acknowledgements:

Financial support from the Center for Urban Earthquake Engineering (CUEE), Tokyo Institute of Technology, to undertake this visit to Sri Lanka is gratefully acknowledged. The advice and support of Prof. Tatsuo Ohmachi, COE Program Leader of CUEE and Prof. Kohji Tokimatsu, COE Program Sub-Leader of CUEE, is gratefully acknowledged. This field visit was successfully completed due to the kind cooperation of Dr. Priyantha Gunaratna and Mr. Manoj Madurapperuma of University of Moratuwa, who joined the field trip.

References:

- Chapman, C. (2004), "The Asian Tsunami in Sri Lanka: A Personal Experience", EOS, Vol. 86, No. 2, 13-14.
USGS (2004), "Magnitude 9.0 - SUMATRA-ANDAMAN ISLANDS EARTHQUAKE,
<<http://earthquake.usgs.gov/eqinthenews/2004/usslav/>>

OVERTURNING OF BUILDINGS IN ADAPAZARI, DURING THE 1999 KOCAELI EARTHQUAKE

G.Gazetas ¹⁾, I. Anastasopoulos ²⁾, N. Gerolymos ³⁾

¹⁾ Professor, School of Civil Engineering, National Technical University of Athens

²⁾ Doctoral Candidate, School of Civil Engineering, National Technical University of Athens

³⁾ Postdoctoral Associate, School of Civil Engineering, National Technical University of Athens
gazetas@ath.forthnet.gr

ABSTRACT : The behaviour of foundations and buildings in Adapazari during the 17-8-99 Izmit (Kocaeli) Earthquake is outlined. Settlement, tilting, and complete overturning of numerous buildings during this devastating earthquake are attributed to the interplay between the yielding/liquefying soil and the rocking/uplifting foundation, under large inertial overturning moments generated by the slender buildings. The overturning of Terveler building is studied in detail. It is shown that even such a slender building, with $H/B \approx 2$, when it stands alone, despite the repeated cyclic mobilization of the bearing capacity of the supporting soil, survives the earthquake essentially with only a minor tilt. Significant uncontrollable tilting leading to overturning occurs only when two buildings stand back-to-back and the ensuing bearing capacity mobilization is unavoidably one-sided.

1. INTRODUCTION – THE ADAPAZARI FAILURES

Among the numerous failures observed in the Izmit (Kocaeli) earthquake of 17 August 1999, of particular technical interest were the building–foundation failures in Adapazari: foundation settlement, permanent tilting, and complete overturning of numerous buildings, which otherwise retained their structural integrity, captured the attention of the world geotechnical and earthquake community. Liquefaction of shallow silty soil layers was evident in the ground surface, but not in abundance.

Detailed scrutiny of the Adapazari failures showed that significant tilting and toppling were observed only in relatively slender buildings (with aspect ratio: $H/B > 2$), provided they were laterally free from other buildings on one of their sides. Wider and/or contiguous buildings suffered small if any rotation. Our observations are summarized in the graph of Fig. 1, which plots the angle of permanent tilting as a unique function of the slenderness ratio H/B . Although this diagram is not of general applicability (it refers mainly to the district of Tigcilar), it does suggest that for the prevailing soil conditions and type of seismic shaking, most buildings with $H/B > 1.8$ overturned, whereas buildings with $H/B < 0.8$ essentially only settled vertically, with no visible tilting. (Note that several other researchers [Yasuda et al 2001, Yoshida et al 2001] have attempted to correlate building rotation to a number of other problem parameters, but with rather limited success.)

2. THE TOPPLING OF TERVELER BUILDING

To introduce the issues arising from the Adapazari failures, we outline the case of one of the buildings (named Terveler), which overturned onto the neighboring building (named Yagcioglu). Terveler was back-in-back with another building, which also overturned in the opposite direction (see Fig. 2). Soil profiles based on three SPT and three CPT tests, performed in front of each building of interest, reveal

the presence of a number of alternating sandy-silt and silty-sand layers, from the surface down to a depth of at least 15 m with values of point resistance $q_c \approx (0.4 - 5.0)$ MPa (Gazetas 2001). Seismo-cone measurements revealed wave velocities V_s less than 60 m/s for depths down to 15 m, indicative of extremely soft soil layers (EERI 2001, Bray et al 2001, Erken 2001).

Ground acceleration was not recorded in Tigcilar. Using in 1-D wave propagation analysis, the EW component of the Sakarya accelerogram (recorded on soft rock outcrop, in the hilly outskirts of the city) leads to acceleration values between $0.18\text{ g} - 0.28\text{ g}$, with several significant cycles of motion, with dominant period in excess of 2 seconds. Even such relatively small levels of acceleration would have liquefied at least the upper-most loose sandy silt layers of a total thickness 1–2 m, and would have produced excess pore-water pressures in the lower layers. The small amount of water expelled by such a small-thickness layer, covered by 2 m of fill, barely reached the surface; hence the scarcity of sand boils. But the effect on foundation stability is predicted to have had been significant.

Building geometry and rotation was the only culprit for the different behaviour of the Terveler and Yagcioglu buildings. Indeed, Terveler had a base width $B \approx 7\text{ m}$ and aspect ratio $H/B = 2.1$, while the Yagcioglu had $B = 12\text{ m}$ ratio $H/B = 1.1$. The only problem of the latter was the post-seismic consolidation of the liquefied layers and the ensuing small settlement.

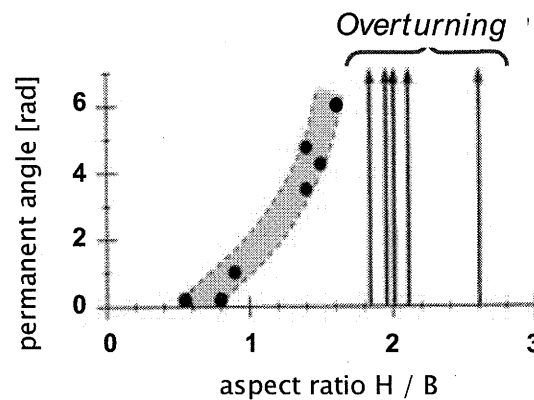


Figure 1 The angle of permanent tilting as a unique function of the slenderness ratio H/B .



Figure 2 The Terveler building (left) and its “back-to-back” neighbouring building (right), both of which toppled in the earthquake, in opposite directions

3. OVERTURNING OF RIGID STRUCTURE ON YIELDING SOIL

A most interesting extension of the rocking of foundations on deformable base is when the supporting soil is soft and weak, and may itself undergo significant deformation and bearing-capacity type failure as the structure is rocking and uplifting. The problem is becoming of increasing engineering interest in the realm of the very strong shaking observed in recent earthquakes and prescribed in modern-day seismic codes. The failures in Adapazari serve as an ideal example of this problem. Our tentative analysis of its response comprises two consecutive steps (see Gazetas et al 2003):

(a) pseudo-static computation of the critical acceleration a_c applied at the effective center of mass of the building that would produce bearing-capacity failure of the foundation soil for the given (static) vertical load from the super-structure

(b) dynamic computation of the rocking response of the structure in the time domain, subjected to the acceleration time-history computed from the Sakarya rock-outcrop record with wave propagation filtering through the soil.

A set of typical results is summarized in Fig. 3. Elasto-plastic finite-element analysis with Mohr-Coulomb plasticity gives the so-called $M-Q$ Interaction Diagram, i.e., the combination of M and Q values that lead to bearing-capacity failure. The scatter reflects uncertainties in soil parameters. The intersection of the limiting $M-Q$ curve with the likely loading paths $M = Q h_c = (1/2) Q H$ or $M = (2/3) Q H$ gives the limiting shear force, whence the critical acceleration is obtained

$$a_c \approx 0.16 \text{ g}$$

To visualize the result of the second step of analysis we merely present Fig. 4. As the reader may expect even a long-period excitation with the expected acceleration levels could not have toppled this building. Referring to Ishiyama (1982, 1984), Makris & Roussos (2000), and Apostolou et al (2005), we can state that for a rigid block to overturn whether it is founded on a rigid base, on a deformable elastic soil, or on a yielding soil, the imposed base acceleration levels must exceed by far (usually at least by a factor of 2 or 3) the pseudo-statically required critical acceleration a_c . An acceleration $a_{max} \approx 0.20-0.25 \text{ g}$ would not have toppled a structure with $a_c = 0.16 \text{ g}$.

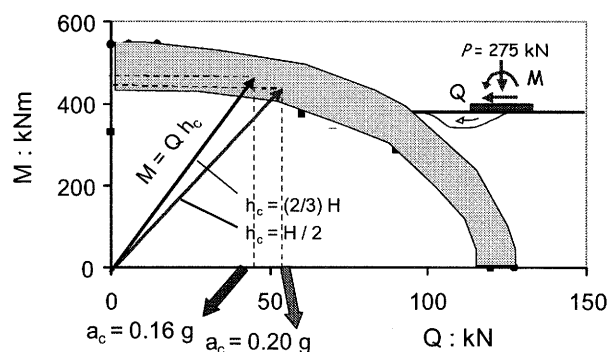


Figure 3 Moment – Shear force interaction diagram for the Terveler building as computed with finite element analysis

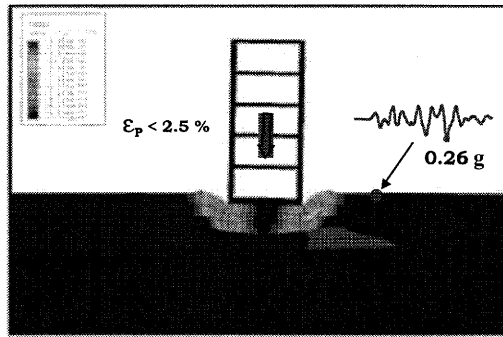


Figure 4 The Terveler Building displaced after the last time increment of the finite element analysis, exhibiting appreciable settlement, but only a minor permanent rotation

Indeed, a preliminary analysis verifies this expectation. The result in Fig. 4 of a finite-element elastoplastic Mohr-Coulomb dynamic analysis, in the form of a snapshot at the time of the largest rotation of the building, shows that despite the development of a severe plastic deformation (max $\epsilon_p \approx 2.5\%$) under the foundation edges, only a limited permanent rotation occurs. Such deformation is indicative of a partial mobilization of the maximum soil resistance (bearing-capacity failure mechanism). Under pseudo-static conditions, development of this rotational mechanism on either side of the foundation would have led to toppling of the structure. Dynamically, each “side” of the rotational mechanism deforms plastically for a short duration, giving a limited inelastic rotation which is partially cancelled by the ensuing deformation on the opposite side. Hence, survival is possible.

How do we then explain this and other overturning failures in Adapazari? What may be different from what we have assumed in the above preliminary analysis? Here is a list of potentially contributing factors:

(a) Ground shaking could have been more severe than that computed from the Sakarya record with the help of one-dimensional wave propagation analysis (which led to a ≤ 0.25 g). Three possible reasons:

- A strong “forward-directivity” effect in the “fault-normal” NS component of motion, (which was not recorded due to malfunctioning in the Sakarya station) could have led to a more deleterious base ground shaking than the utilized EW component;
- The soil characteristics especially at relatively large depths may be different from those assumed in our analysis, playing a more detrimental role; and
- 2D and 3D “valley” effects arising from the recently discovered [Komarawa et al (2002)] rapid fluctuations of the alluvia depth to bedrock across the city may have produced wave focusing and diffraction effects, further aggravating the ground shaking to which the building was subjected.

However, none of these three factors seems capable of easily explaining the toppling of the building.

(b) The presence of the neighbouring (back-to-back) building could have worsened the performance of Terveler in a number of ways:

- The apparently out-of-phase motion of the two buildings may have produced impact forces, aggravating the tendency for outward rotation of each building. This hypothesis can be completely dismissed on the basis of abundant field evidence which includes the lack of even a mere scratch on the back sides of the two buildings.
- Mobilization of bearing capacity mechanism in the soil can only happen under the external side of each foundation, “thanks” to the confining pressure of the neighboring building. When the building

rotates in the outward direction and this soil yielding mechanism is momentarily mobilized, a permanent rotation develops. Reversal of this rotation of the structure can not proceed beyond the point of “impact” at the base the two buildings. Thus no full reversal of the permanent soil rotation occurs, and the plastic strains continue to accumulate with each exceedance of the critical acceleration in the outward direction — until the weight of the building “Takes over” and leads to overturning (Fig. 5).

Substantial evidence exists in support of the latter mechanism. The velocity of overturning, for example, is computed to be very low — in fact, when the building is at the critical angle, $\theta_c = \arctan B/H$, at which overturning is imminent, the natural period of the system tends to infinity (Psycharis & Jennings 1983), which means that its velocity becomes vanishingly small. In the field, evidence of a low velocity impact of the overturning Terveler onto the Yagcioglu building (and in several other cases as well) is overwhelming :

- the failed building was structurally and architecturally unscratched
- there were no fatalities (on either building)
- the “injuries” of Yagcioglu building revealed after demolition of Terveler were unbelievably minor
- in other overturned buildings, where no support were provided by a neighbour, the rotation continued slowly many hours after the earthquake — evidence of toppling cushioned by the reaction of the same soil that had initiated the failure in the first place.

4. CONCLUSION

The overturning of numerous buildings in Adapazari can be attributed mainly to the following factors/phenomena:

- (a) The nature of the soil profile, especially its top 4 meters below the foundation base: very soft and/or liquefiable silty/sandy soils, with very high water table.
- (b) The directivity and fling affected seismic excitation, which produced strong high–period shaking at the base of the building, despite the “filtering” effect by the extremely soft soil profile.
- (c) The presence of an equally–tall contiguous building only on one side; this neighbour did not “allow” exceedance of bearing capacity in its direction that (under cyclic conditions) would have reversed the inelastic rotation occurring in the opposite direction, and would thus have saved the building from overturning.

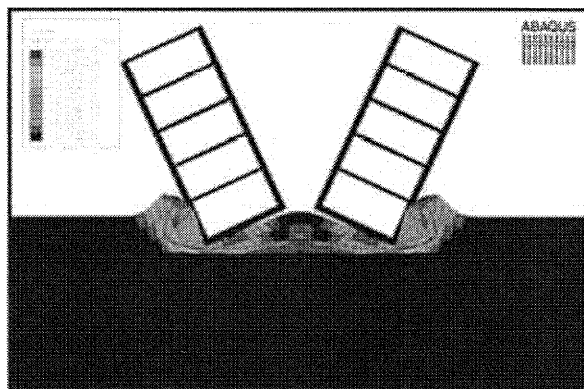


Figure 5 The permanent rotation exhibited by the two neighbouring buildings subjected to the Sakarya record (at rock outcrop) would have been sufficient to initiate a slow complete overturning driven by gravity

References:

- [1] Apostolou M., Gazetas G., and Garini E.,[2005] “Seismic Response of Simple Structures with Foundation Uplift”. *Soil Dynamics and Earthquake Engineering* (in press).
- [2] Bray J.D. et al [2001] “Ground Failure in Adapazari, Turkey”. In *Lessons Learned form Recent Strong Earthquakes*, A.M. Ansal, editor, pp.19 – 28
- [3] EERI. [2001] “1999 Kocaeli, Turkey”. Earthquake Reconnaissance Report, *Special Issue of Earthquake Spectra*
- [4] Erken A. [2001] “The Role of Geotechnical Factors on Observed Damage in Adapazari during 1999 Earthquake”. In *Lessons Learned form Recent Strong Earthquakes*, A.M. Ansal, editor, pp. 29 – 32
- [5] Gazetas G. [2001] “Foundation Failures in Adapazari during the 17-8-99 Izmit (Kocaeli) Earthquake”. *Proc. 4th National Greek Conf. on Geotechnical Engineering*, Athens, Vol. 3, (in Greek).
- [6] Gazetas G., Apostolou M., Anastasopoulos J. [2003] “Seismic Uplifting of Foundations on Soft Soil, with Examples from Adapazari (Izmit 1999 Earthquake)”. *Foundations–Innovations, Observations, and Design Practice*, Thomas Telford, London, pp. 37–30.
- [7] Ishiyama Y. (1984) “Criteria for Overturning of Rigid Bodies by Sinusoidal and Earthquake Excitations”. *Proceedings of the 8th World Conference on Earthquake Engineering*, pp.198–206.
- [8] Ishiyama Y. (1982) “ Motions of Rigid Bodies and Criteria for Overturning by Earthquake Excitations”. *Earthquake Engineering and Structural Dynamics*, Vol. 10, No.5, pp. 175–190.
- [9] Japan Society of Civil Engineers. [1999] “The 1999 Kocaeli Earthquake, Turkey – Investigation into the damage to civil engineering structures”. *Report of Earthquake Engineering Committee*.
- [10] Komarawa M., Morikawa H., Nakamura K., Akamatsu J, Nishimura K., Sawada S., Erken A., Onalp [2002] “A. Bedrock Structure in Adapazari, Turkey—a Possible Cause of Severe Damage by the 1999 Kocaeli Earthquake”. *Soil Dynamics and Earthquake Engineering*, Vol. 22, No 9-12
- [11] Makris M & Roussos Y. (2000) “ Rocking Response of Rigid Blocks under Near–Source Ground Motions”. *Geotechnique* 50, No. 3, 243–262.
- [12] Psycharis J.N. & Jennings P.C. (1983) “Rocking of Slender Bodies Allowed to Uplift”. *Earthquake Engineering and Structural Dynamic*, Vol 11 pp. 57–76.
- [13] Yasuda S., Yoshida N., Irisawa T. [2001] “Settlement of Buildings due to Liquefaction during the 1999 Kocaeli Earthquake”. *Lessons Learned form Recent Strong Earthquakes*, A.M. Ansal, editor, pp.77 – 82
- [14] Yoshida N., Tokimatsu K., Yasuda S., Kokusho T., & Okimura T. [2001] “Geotechnical Aspects of Damage in Adapazari City during 1999 Kocaeli, Turkey Earthquake”. *Soils and Foundations*, Vol. 41, pp.25-45

INVESTIGATION ON BUILDING DAMAGES CAUSED BY GROUND FAILURE AND THEIR REHABILITATION IN YUANLIN AFTER THE TAIWAN CHI-CHI EARTHQUAKE

C. J. Lee ¹⁾, T. K. Hsiung ²⁾, H. Y. Wen ²⁾, and C. M. Shia ²⁾

1) Associate Professor, Dept. of Civil Engineering, National Central University, Taiwan

2) Graduate Students, Dept. of Civil Engineering, National Central University, Taiwan

cjleeciv@cc.ncu.edu.tw, s3264003@cc.ncu.edu.tw, u3260445@cc.ncu.edu.tw, s932208@cc.ncu.edu.tw

Abstract: The extent of liquefied areas and the associated ground damages in Yuanlin township were investigated and analyzed after the Chi-Chi earthquake. The investigations on the rehabilitation of damaged building and their remedial expenses were performed as well. The contours of liquefaction potential index and the post-earthquake settlements were first established, and then using the data from both the field reconnaissance and making a survey of the means of damaged building remediation with the questionnaire. Finally a GIS was developed to integrate the results of the liquefaction analysis and the means of the rehabilitation of the damaged buildings. A comparison of the results from the liquefaction analysis and the settlement calculations with the means of rehabilitation and the expenses was performed. A new boundary curve on the relation of the thickness of liquefied and un-liquefiable layers is proposed to assess whether the building will be damaged due to ground failure. The outcome in the study can provide the valuable information for the earthquake scenario simulation and the rapid damage assessment of liquefaction at the sites having the geological conditions in Taiwan similar to the current study areas.

1. INTRODUCTION

The 1999 Taiwan Chi-Chi earthquake ($M_w=7.6$) triggered numerous ground failures in the form of liquefaction, ground softening, and lateral spreading in inland alluvial areas. After the Chi-Chi earthquake, the extent of liquefied areas and the associated ground damages in central part of Taiwan have been investigated and analyzed by many experts. Figure 1 shows the counties that were affected by liquefaction. In particular, Yuanlin township, Nanto township, and Wufeng township suffered severe liquefaction damages. However, the investigations on the remediation of damaged buildings and their remedial expenses after the earthquake were still not available. In the paper, Yuanlin area is the focus of the investigation reported here. The contours of liquefaction potential index and the post-earthquake settlements were first established, and then using the data from both the field reconnaissance and the surveys of the local residents on the means of remediation of their own damaged buildings with the questionnaire. Finally a Geographic Information System was developed to integrate the results of the liquefaction analysis and of the remediation measures of damaged buildings. A new boundary curve on the relation of the thickness of liquefied and un-liquefiable layers is proposed to assess whether the building will be damaged due to ground failure.

2. DOCUMENTATION OF FIELD DATA AND LIQUEFACTION POTENTIAL ANALYSIS

The town of Yuanlin (population about 116,000; area about 40 km²) is approximately 15 km from

the Chelungpu fault rupture, it suffered the severe liquefaction damages. Many buildings in the town settled and tilted due to ground liquefaction. According to the geotechnical study of the area by MAA (1999), soil conditions generally consist of Holocene alluvium to depths of 50-60m, which overlie older sedimentary deposits. Ground water levels are relatively shallow, generally occurring at depths 0.5 m to 3 m. Ground motion records from Station TCU110 in Yuanlin as shown in Figure 2 indicated a peak acceleration of 0.2 g. This Station is located in an area where no ground failure was observed. Figure 3 shows a typical soil profile from west to east. The soils in the second layer were classified as loose silty fine sand and would be considered potentially susceptible liquefaction, especially Boreholes BH29, BH30, and BH44 have the thicker second layer and are all situated at the severe subsidence and liquefied area in the southeast of town.

The logs of the SPT borings of 57 holes and of the CPT soundings of 38 points as shown in Figure 2 were prepared in a uniform format as a geological investigation database linked with GIS. The data included the boring No., coordinates of borehole location, SPT-N values, depth, grain size distribution, PL, LL, PI, soil classification, water content for SPT boring and q_c and f_s for CPT soundings. A program of liquefaction assessment and settlement calculation programming with Visual Basic language were used in performing the liquefaction potential analysis efficiently. First of all, this program is capable of checking the accuracy of input data automatically. Various options of the

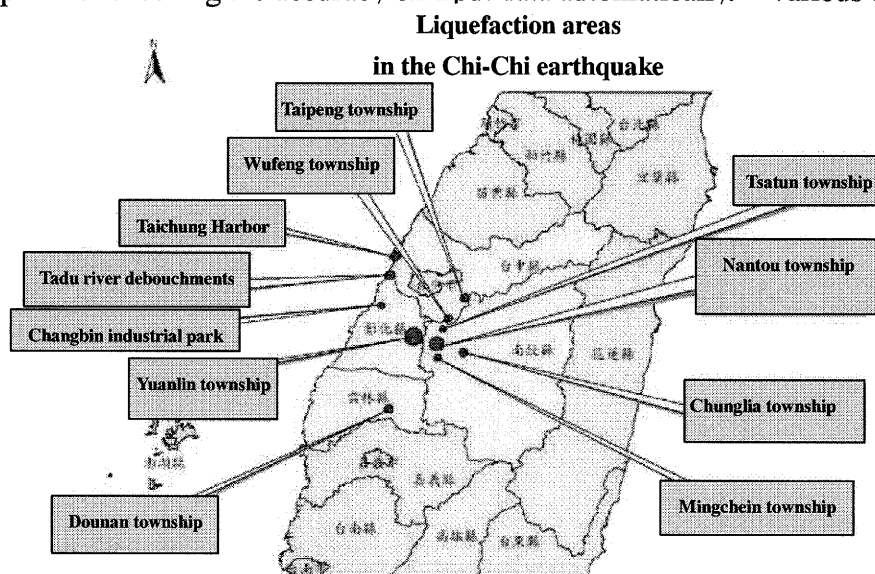


Figure 1 Liquefaction areas in the Chi-Chi earthquake

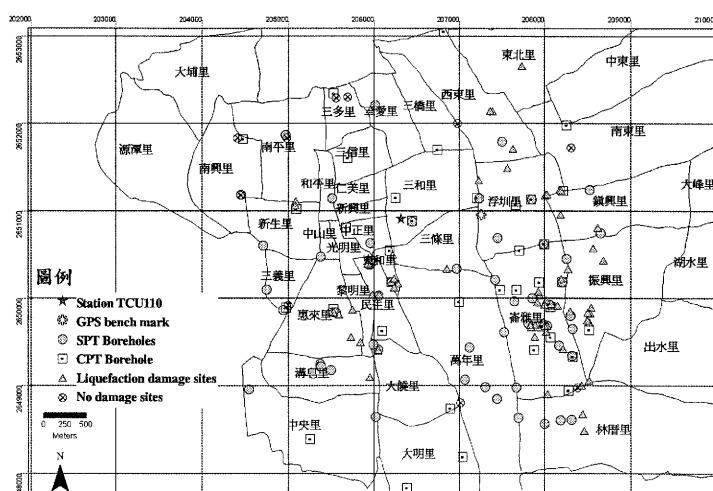


Figure 2 Map of Yuanlin showing locations of surveyed liquefaction damaged and non-damaged sites and locations of SPT and CPT boreholes

method of liquefaction potential analysis are available. The simplified methods based on SPT-N value include the simplified Seed's liquefaction potential analysis [abbreviated to Seed's method] (Youd 2001), New Japanese Road Association Method (Japan Road Association 1996), Tokimatsu and Yoshimi Method [T&Y method] (Tokimatsu and Yoshimi 1983) in the first part of the program. The simplified methods based on CPT include the R&W method (Robertson and Wride 1998) and the Olsen method (Olsen 1997) in the second part of the program. In addition, the liquefaction potential index, L_p (Iwasaki et al. 1982) and the settlement after liquefaction can be calculated as well. In the paper, only the results derived from the Seed's method are reported.

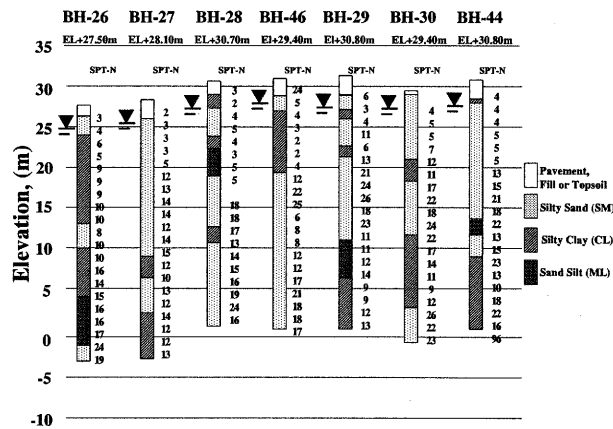


Figure 3 Typical soil profiles from west to east in Yaulin

3. FIELD SURVEYS ON DAMAGE PATTERN OF BUILDINGS, MEANS OF BUILDING REHABILITATION, AND THEIR EXPENSES

The detailed damage data, the means of rehabilitation, and their expenses on the damaged buildings after the earthquake were collected by making the survey of local residents in Yuanlin township in the study. A questionnaire sheet was designed to obtain the information of building needed by sending students visiting the owner of the damaged building or of undamaged building. The selected visiting sites included: (1) the damaged sites due to ground failure or where the buildings had undergone severe settlement and tilting and both were reported by the NCEER reconnaissance team or by local news reporters or the other official reports after the earthquake; (2) the sites neighboring on the locations where CPT or SPT were conducted; (3) the regions where the soils were considered potentially susceptible to liquefaction on the basis of the simplified methods or the calculated settlements were larger but no damages were reported. There were effective samplings of 93 (including damaged sites of 83 and undamaged sites of 10).

The contents of the questionnaire sheet are divided into four parts: (1) basic parameters of building: GPS positioning of damaged building, building type and what the buildings were made of, foundation type and depth, number of stories, the building size (length and width), age of building, buildings near rivers/irrigation canals/ditches or not; (2) degree and extent of ground failure around the damaged building including sand boiling or ejection of water, lateral spreading, the total ground subsidence and the differential settlements between the ground and the buildings, tilting of building, and extent of the ground failure and subsidence in the surrounding region, any manhole floating up, the road re-paved and the river or ditch dredged by officers or not after the earthquake; (3) type and degree of failure on the building including the ground floor, beams and columns, and the lifelines broken or not; (4) the means of rehabilitation or soil improvement or soil modification used and their total remedial expenses if buildings were damaged. The survey items described above were aim at justifying that the building damages were mainly resulted from the ground failure and how many expenses needed to rehabilitate

the function of building to an acceptable level for the general public. All the spatial data including the subsurface profiles, the basic parameters of building, the means of rehabilitation and their costs, and the surveyed damage patterns of building, the results of liquefaction analysis were integrated with the local map through a GIS system and then to manipulate the several spatial analyses for giving a better understanding of the scenario during and after the earthquake.

4. ANALYTICAL AND INVESTIGATION RESULTS AND DISCUSSIONS

4.1 Assessment of liquefaction potential and seismic settlement

The Seed's SPT simplified method was first used to perform the liquefaction potential analysis in the study. Figures 4 and 5 show the contours of the calculated liquefaction potential index (P_L) defined by Iwasaki et al. (1982) and of the calculated seismic settlement (Ishihara and Yoshimine, 1992) to quantified the severity of possible liquefaction at any site. In these two figures, once one calculated point using the Seed's SPT simplified method manifested the occurrence of susceptible to liquefaction ($FS < 1$), the locations of this borehole were indicated by hollow circles in the figures 4 and 5. Most of the boreholes were manifested susceptible to liquefaction, as observed from these two figures. The darker shade regions have the larger values of P_L (Ranges of P_L , 0-5, 5-10, and 10-13) and the bigger calculated seismic subsidence (Ranges of settlements, 0-10, 10-20, 20-30, and 30-40.77 cm), respectively. The measured settlement at the GIS bench mark located at the roof of the building of land administration in Yuanlin township after the earthquake is 17 cm, while the calculated settlement from the soil profile of the nearest borehole is about 8 cm. No damage related to the ground failure was observed in the building of land administration.

Detailed surface reconnaissance of ground failure on the buildings in Yuanlin township was performed in the study. The major observed damages were that roads were deformed and the damaged buildings experienced significant settlement or tilting in the severe damaged regions as shown within the confines of the dotted lines in these two figures. However, the severe damaged regions are not consistent with the regions having the highest calculated P_L and the largest calculated settlements, as observed from Figures 4 and 5.

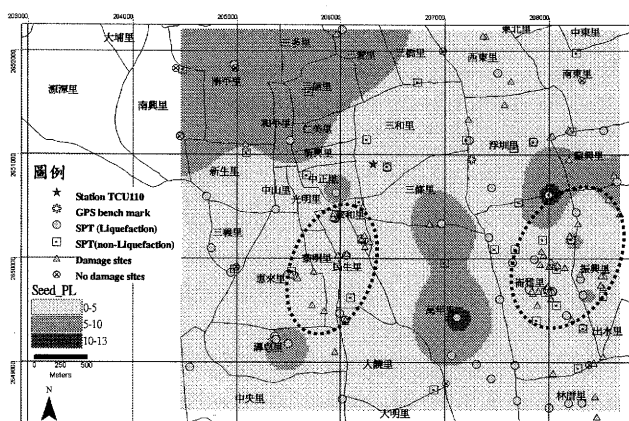


Figure 4 contour lines of liquefaction potential index (P_L)

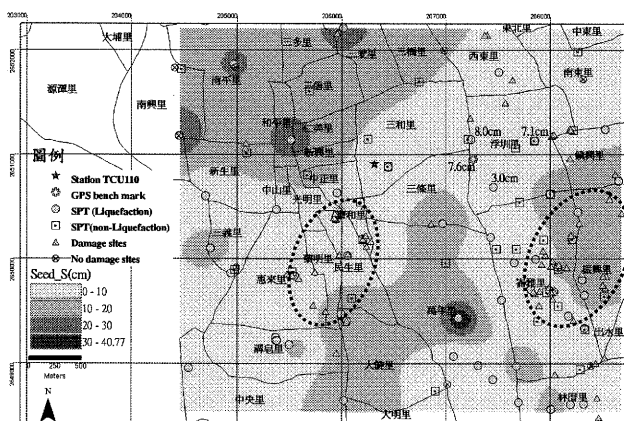


Figure 5 contour lines of the calculated seismic

4.2 Correlating Building damages with thickness of liquefied and of un-liquefiable layers

For engineering practice, assessing whether soil liquefaction to cause the damages of building or not is the essence of performing the liquefaction potential analysis on a site. As described in the previous section, no good correlations between the building damages and the values of P_L or the calculated settlement were found in the study area. Ishihara (1985) presumed that the occurrence of liquefaction at some depth within a soil profile is not necessarily related to damaging a building founded on or near the ground surface. Only when the development of liquefaction is sufficiently

extensive and shallow enough in proximity to the building, the damages of building will occur. Therefore, Ishihara proposed the relationships between the thickness of un-liquefiable layer, H_1 , and the thickness of underlying liquefied layer, H_2 . The method of the determination of H_1 and H_2 proposed in the study is shown in Figure 6. The liquefaction potential analysis was first performed to calculate the FS s along the depths using the developed program for all the collected boreholes. Any layer with the calculated FS less than 1 was judged as a liquefied layer and greater than 1 as a un-liquefiable layer. The depth of the ground water table is taken as the thickness of un-liquefiable layer, H_1 (in the case of Figure 6-a). If the layers near the surface with $FS > 1$, the thickness of these layers is also chosen to be H_1 (in the cases of Figure 6-b and 6-c). The sand stratum with $FS < 1$ is taken as a liquefied layer. The thickness of such a layer is chosen to be H_2 . For the alternative strata including un-liquefiable layer and liquefied layer, summing the thickness of layers that were identified to be susceptible to liquefaction ($FS < 1$) up is chosen to be equal to H_2 (in the case of Figure 6-d).

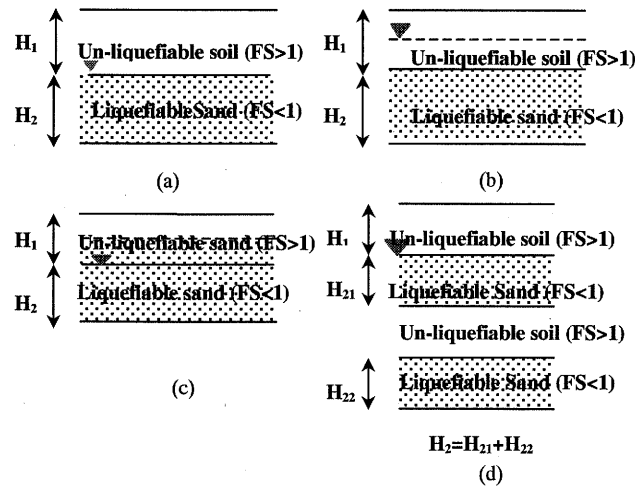


Figure 6 Definitions of the surface un-liquefiable layer and the underlying liquefied layer

Figures 7 and 8 demonstrate the spatial distributions of the thickness of un-liquefiable layer and of the thickness of the underlying liquefied layer, respectively, in the study area. In the zones with the darker shade both the un-liquefiable layer and the underlying liquefied layer are thicker, whereas in the zones with the lighter shade the un-liquefiable layer and the liquefied layer are thinner. The triangle symbols indicate the sites where the damaged buildings were manifest. We can see the most of the damaged buildings concentrated in the zones where the depths of un-liquefiable layer was less than 4 m and the underlying liquefied layer was thicker, as observed from Figures 7 and 8.

The pairs of H_1 and H_2 are compiled and plotted in the abscissa and ordinate as shown in Figure 9 for the sites of known liquefaction-induced building damage (indicated with solid symbols) and the sites without building damage (indicated with hollow symbols) give a new boundary curve differ from Ishihara already proposed at the shaking of 200 gal for justifying the surface manifestation of liquefaction-induced damages. It may be seen in Figure 9 that the data points with known liquefaction-induced damage fall mostly in the zone on the left of the boundary curve. The new boundary curve moves left and downward. It can be concluded that a building founded on the place where the underlying liquefied layer close to the ground surface is more vulnerable to damage during ground liquefaction.

4.3 Results on the damaged and rehabilitation investigation

The building performance on sustaining the liquefaction-induced ground failure is a very complex interaction among many variables, including building type and its foundation type, ground motion, and the soil conditions as described in the last section. The types of building and the geological conditions in Yuanlin township are typical of Taiwan's midsize cities, especially in the central and southern parts of Taiwan. The next bigger earthquake may hit these areas unpredictably and cause

heavy casualties again. The results of the damaged buildings on their rehabilitations' investigations and remedial expenses in the study can provide the important information for local residents and the government officers in charge of the task of hazard prevention when they estimating the possible property loss in the near future earthquake attack.

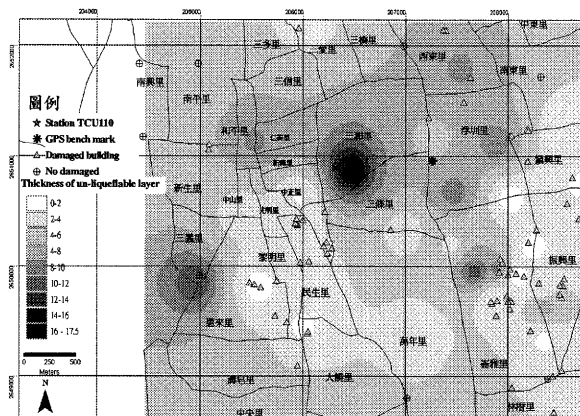


Figure 7 Contour lines of the thickness of the un-liquefiable layer

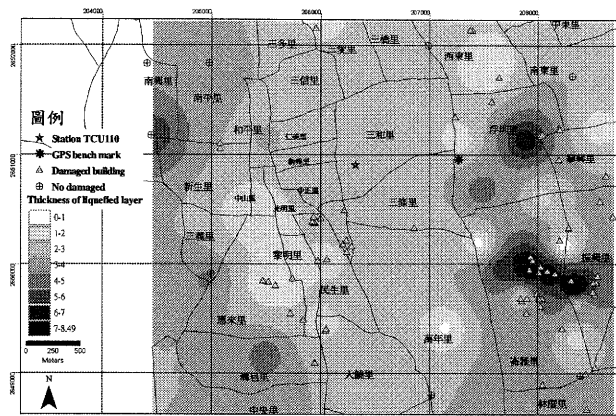


Figure 8 Contour lines of the thickness of the liquefied layer

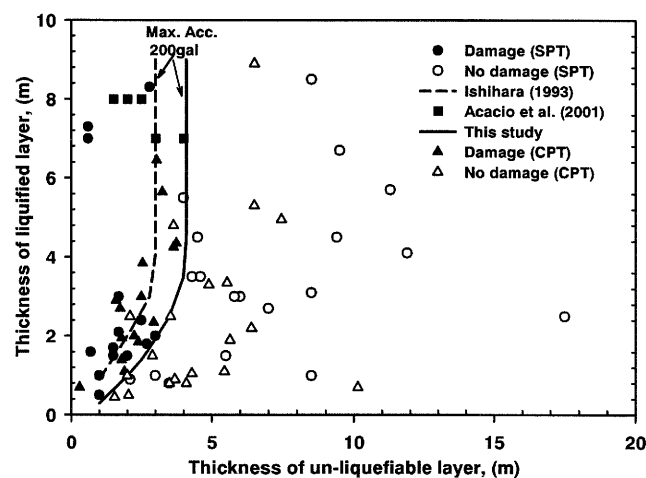


Figure 9 Boundary curve for the manifestation of liquefaction-induced building damages in the shaking of 200 gal

There are effective samples of 93 (including damaged sites of 83 and undamaged sites of 10). Each sample represented a typical damage site not just only a damaged building. Most of buildings that were visited in the study can be roughly categorized into four types: (1) Mud brick residences (MBR): they are single-story un-reinforced masonry buildings and over 30 years old. (2) Small factories with un-reinforced brick masonry wall and covered with sheet iron (SFSI): Most of them are single-story. These two types of buildings were not designed by Engineers. (3) Reinforced Masonry Brick Construction (RMBC): They have non-ductile reinforced concrete frames and reinforced concrete slabs with un-reinforced brick masonry infill. They are 2-4 stories high and very common in Taiwan's midsize cities. (4) Reinforced concrete buildings of apartment and condominium (RC): They are 6-12 stories high.

Figure 10 shows the distribution of the types of damaged building. The buildings with the expenses to retrofit the damages were about 74% of the damaged buildings. The right small pie chart in Figure 10 displays the percentages of the types of the damaged buildings without expenses in an overall estimate. In general, the buildings of MBR, SFSI, and RMBC were easiest to be damaged during the liquefaction event, accounting for 67% of the damaged cases, because the depths of

foundation were very shallow (about 0.5 -1m depth) and the ground floor slabs were only paved with a poor grade concrete. Figure 11 shows the distribution of the foundation types of damaged building. All the buildings of MBR, SFSI, and RMBC were founded on the shallow spread footings. They were very susceptible to differential settlements. The soil liquefied in shallower layers caused settlements and even partial bearing failure to the spread footings. In addition, floor slab fracture due to settlements at walls and columns was the most frequent failure types occurred in these buildings. For the buildings supported with a strap foundation, the damages cases greatly decreased although the buildings still experienced large settlement. No damage observed inside buildings but outside ground floor suffered considerable damages. The use of different foundation types beneath a single building, those that were cataloged as “Others” in Figure 11, (one building with a basement in the one part and the shallow spread footings in the other part, one building supported by a short pile foundation and the spread footing, 3% of the damages buildings) led to large differential settlements. Figure 12 shows the stories of the damaged buildings. The buildings with no basement and 1- to 5-stories high were the most vulnerable to damages during the liquefaction event, accounting for 92.6% of the damaged cases, because most of these buildings were MBR, SFSI, and RMBC. Figure 13 shows the distribution of the means of rehabilitation that the local residents used to make a recovery from the earthquake. The means of rehabilitation were related to the degree of damage, i.e., ground floor and lifeline retrofits (68%), grouting to strengthen the tilting building (16%), Jacking building up using a conventional moving house method (6%), stabilization of foundation soil with grouting (6%), and demolition (4%). Figure 14 demonstrates the expenses needed to rehabilitate the damaged building with various remedial means. The expenses to retrofit the ground floor and lifelines took no more than 500,000 NT\$. The expenses to strengthen the tilting buildings were related the number of stories. The higher the building the more expenses were needed (100,000 3-stories to 600,000 (NT\$) 7-stories). The expenses to soil modification on foundation were from 50,000 to 230,000 NT\$. The expenses to jack building up took about 600,000 – 1,600,000 NT\$ depending on the cases.

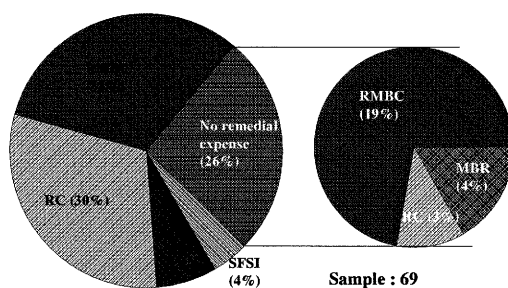


Figure 10 Percentages of various types of damaged building

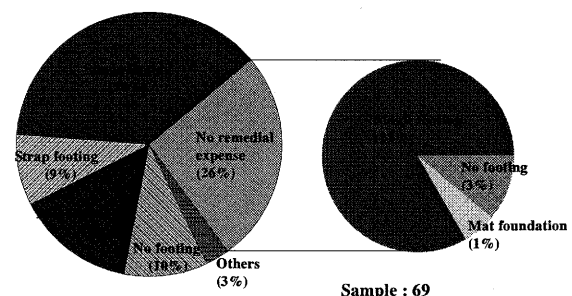


Figure 11 Percentages of various foundation types of damaged building

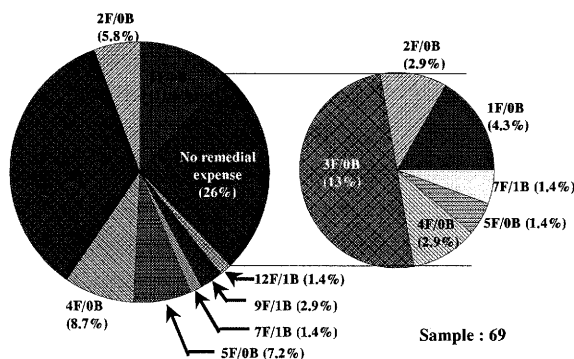


Figure 12 Percentages of the stories of damaged buildings

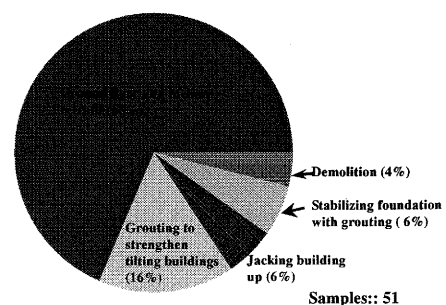


Figure 13 Percentages of the means of rehabilitation on damaged buildings

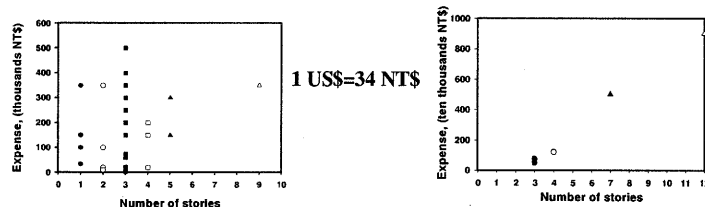


Figure 14-a retrofits of ground floor and lifeline

Figure 14-b grouting to strengthen the tilting building

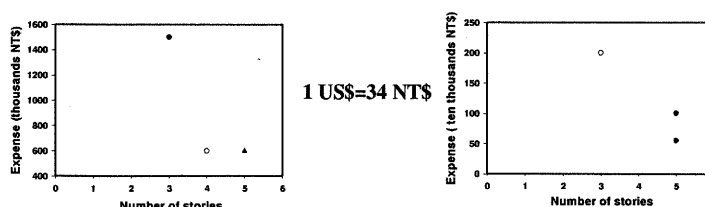


Figure 14-c Jacking buildings up

Figure 14-d stabilization of foundation soil with grouting

5. CONCLUSIONS

The extent of liquefied area and the associated ground damages in Yuanlin township were investigated. The investigations on the rehabilitation of damaged buildings and their expenses with the questionnaire were performed. The buildings without basement and founded on the spread footings were the most vulnerable to damages during the liquefaction event. The spread footings connected with reinforced concrete straps can greatly reduce the liquefaction damages. The higher the building height is the larger seismic settlement the building will experience, especially no building stands surroundings and the building easily tilts to the building short direction. A new boundary curve on the relation of the thickness of liquefied and un-liquefiable layers is proposed to assess whether the building will be damaged due to ground failure. The outcome in the study can provide the valuable information for the earthquake scenario simulation and the rapid damage assessment of liquefaction at the sites having the geological conditions in Taiwan similar to the current study areas.

References:

- Acacio, A. A., Kobayashi, Y., Towhata, I., Bautista, R. T., and Ishihara, K. (2001), "Subsidence of Building Foundation Resting Liquefied Subsoil: Case Studies and Assessment," *Soils and Foundations*, **41**(6), 111-128
- Ishihara, K. and Yoshimine, M., (1992) "Evaluation of Settlements in Sand Deposits Following Liquefaction During Earthquakes," *Soils and Foundations*, **32**(1), 173-188.
- Ishihara, K., Acacio, A.A., and Towhata, I. (1993), "Liquefaction-induced ground damage in Dagupan city in the July 16, 1990 Luzon earthquake, *Soils and Foundations*, **33**(1), 133-154.
- Iwasaki, T., Arakawa, T. and Tokita, K.I., (1982) "Simplified Procedures for Assessing Soil Liquefaction During Earthquake," *Proceedings of the conference on soil dynamics and earthquake engineering*, **Vol. II**, 925-935.
- Japan Road Association (1996) "Specifications for Highway Bridges—Part V: Seismic Design," Tokyo, Japan.
- MAA. (2000), "Soil Liquefaction Assessment and Remediation Study, Phase I (Yuanlin, Dachun and Shetou)," Summary report, Taipei, Taiwan: Moh and Associates (MAA) Inc. (In Chinese)
- Olsen, R.S. (1997), "Cyclic Liquefaction Based on the Cone Penetration Test", *Proc., NCEER Workshop on Evaluation of liquefaction Resistance of Soil*, NCEER, State University of New York at Buffalo, 225-276.
- Robertson, P.K. and Wride, C.E. (1998), "Evaluation cyclic liquefaction potential using cone penetration test", *Canadian Geotechnical Journal*, **35**(3), 442-459.
- Tokimatsu, K. and Yoshimi, Y. (1983), "Empirical Correlation of Soil Liquefaction Based on SPT-N Value and Fines Content", *Soils and Foundations*, **23**(4), 56-74.
- Youd, T.L. and Idriss, I.M. (2001), "Liquefaction Resistance of Soils: Summary Report from the 1996 NCEER and 1998 NCEER/NSF Workshops on Evaluation of Liquefaction of Soils", *Journal of Geotechnical and Geoenvironmental Engineering*, ASCE, **127**(4), 297-313.

EFFECTS OF INERTIAL AND KINEMATIC INTERACTION ON SEISMIC BEHAVIOR OF PILE FOUNDATIONS BASED ON LARGE SHAKING TABLE TESTS

K. Tokimatsu¹⁾ and H. Suzuki²⁾

1) Professor, Dept. of Architecture and Building Engineering, Tokyo Institute of Technology, Japan

*2) Graduate student, Dept. of Architecture and Building Engineering, Tokyo Institute of Technology, Japan
kohji@o.cc.titech.ac.jp, hsuzuki@arch.titech.ac.jp*

Abstract: Effects of inertial and kinematic interaction on pile stresses are studied based on large shaking table tests on pile-structure models in dry and liquefiable sand deposits. The test results show that the combination of inertial and kinematic forces on bending moment, shear force and axial force varies depending on such factors as the relation of natural period of a superstructure and ground, the presence of foundation embedment, and pile stiffness. A pseudo-static analysis is presented into which these findings are incorporated and its effectiveness is examined by simulating pile stresses in large shaking table tests. It is assumed that the pile stress is equal to the sum of the two stresses caused by the inertial and kinematic effects if the natural period of the superstructure is shorter than that of the ground or the square root of the sum of the squares of the two if the natural period of the superstructure is longer than that of the ground. The estimated pile stresses are in good agreement with the observed ones regardless of the occurrence of soil liquefaction, the presence of foundation embedment and pile stiffness.

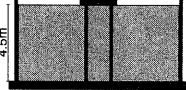


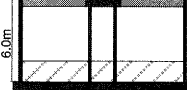

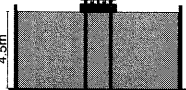
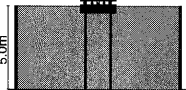



1. INTRODUCTION

Field investigation and subsequent analyses after recent catastrophic earthquakes confirmed that kinematic effects arising from the ground movement as well as inertial effects from superstructure had significant impact on the damage to pile foundations (e.g., BTL Committee, 1998). It is therefore important that both inertial and kinematic interaction effects be taken into account in seismic design of pile foundations. Many studies have been made to examine soil-pile-structure interaction during earthquakes based on physical model tests as well as theoretical and numerical analyses (e.g., Mitsuji et al., 1993, Nishimura et al., 1997, 1998). Little is known, however, concerning the degree of contribution of the two effects particularly in liquefiable soil.

The objective of this paper is to examine the combined effects of inertial and kinematic forces on pile foundations in both dry and liquefiable sand deposits, based on large shaking table tests, and to examine how these effects are taken into account in the pseudo-static analysis such as Beam-on-Winkler-springs method.

2. LARGE SHAKING TABLE TEST

To investigate effects of dynamic soil-pile-structure interaction on pile stresses during earthquakes qualitatively, several series of shaking table tests were conducted on nearly full-scale soil-pile-structure systems using the shaking table facility at the National Research Institute for Earth

		without embedment	with embedment			without embedment	with embedment	
without superstructure	Model layout			without superstructure	Model layout			
	Test ID & T_b	DAN	DBN		Test ID & T_b	SAN	SBN	SBNR
with superstructure	Model layout			with superstructure	Model layout			
	Test ID & T_b	DAS (0.06s, $T_b < T_g$) DAL (0.7s, $T_b < T_g$)	DBS (0.06s, $T_b > T_g$) DBL (0.7s, $T_b > T_g$)		Test ID & T_b	SAS (0.2s, $T_b < T_g < T_{gL}$) SAL (0.8s, $T_g < T_b < T_{gL}$)	SBS (0.2s, $T_b < T_g < T_{gL}$) SBL (0.8s, $T_g < T_b < T_{gL}$)	SBSR (0.2s, $T_b < T_g < T_{gL}$) SBLR (0.8s, $T_g < T_b < T_{gL}$)
		Flexible pile: D=165.2mm, t=3.7mm				Flexible pile: D=165.2mm, t=3.7mm		Stiff pile: D=318.5mm, t=6.0mm
		T_b : Natural period of superstructure T_g : Natural period of ground (≈ 0.16 s)				T_b : Natural period of superstructure T_g : Natural period of non-liquefied ground (≈ 0.3 s) T_{gL} : Natural period of liquefied ground (> 1.0 s)		

(a) Test models with dry sand

(b) Test models with liquefiable saturated sand

Fig. 1 Soil-pile-structure models

Science and Disaster Prevention (Tamura et al., 2000, 2002, Tokimatsu et al., 2002, 2003, 2005). Fig. 1 illustrates fifteen soil-pile-structure models tested. A 2x2 pile group was used throughout the tests. A model ID consisting of three or four alphabets specifies the test conditions. The first one indicates soil condition (D: dry sand and S: saturated sand), the second one the presence of foundation embedment (A: No and B: Yes), and the third one the presence of a superstructure and its natural period (T_b) relative to those of non-liquefied and liquefied ground (T_g and T_{gL}) (N: without a superstructure, S: with a superstructure having $T_b < T_g < T_{gL}$ and L: with a superstructure having $T_g < T_b < T_{gL}$). The fourth one, if exist, indicates that piles are stiff, having a diameter of 318.5 mm with a 6.0 mm wall thickness; otherwise, they are flexible, having a diameter of 165.2 mm with a 3.7 mm wall thickness.

The dry sand deposit prepared in the laminar box consisted of a homogeneous layer of 4.0 or 4.5 m. The liquefiable saturated sand deposit consisted of three layers including a top dry sand layer 0.5 m thick (if a foundation was embedded), a liquefiable saturated sand layer 3 to 4 m thick and an underlying dense sand or gravel layer about 1.5 m thick. Prior to each shaking table test, cone penetration tests were conducted to estimate density distribution of the deposit with depth.

The tips of the flexible piles were connected with pin joints and those of the stiff piles were fixed to the base of the laminar shear box. The heads of all the piles were fixed to a foundation of a weight of 20.6 kN. The foundation was able to carry a superstructure of 139kN, if needed.

The soil-pile-structure systems were densely instrumented with accelerometers, displacement transducers, strain gauges and, if saturated, pore water pressure transducers. The observed axial and bending strains in piles give the axial force, N , and bending moment, M , and the differentiation of bending moment with depth gives the shear force, Q . The double integration of accelerations of the ground and pile with respect to time yields their displacements. The total inertial force from the superstructure and the foundation, F , is given from their accelerations and weights.

Either artificial accelerogram called Rinkai or accelerogram recorded during the 1940 El Centro Earthquake was used as an input motion to the shaking table. In total, thirty-one tests were conducted on soil-pile-structure models with Rinkai and El Centro, a maximum acceleration of which was scaled to a value in between 1.2 and 3.1 m/s^2 .

3. PILE STRESSES IN DRY SAND

Figs. 2 to 5 show time histories of the inertial force from the superstructure and foundation, the

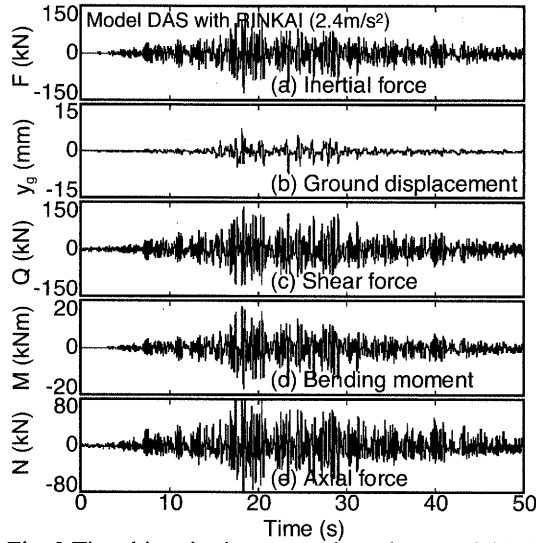


Fig. 2 Time histories in test conducted on model DAS

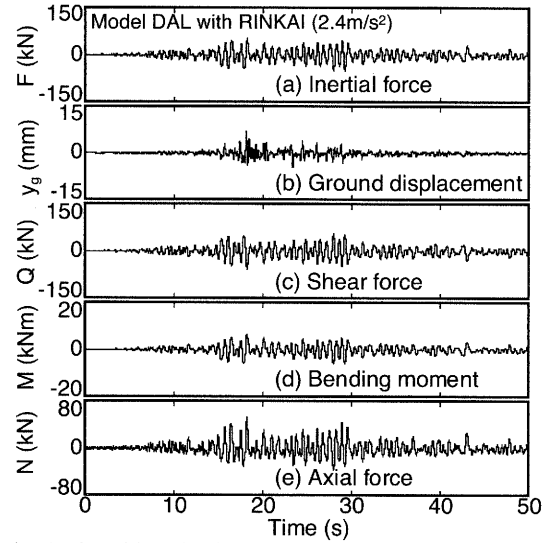


Fig. 3 Time histories in test conducted on model DAL

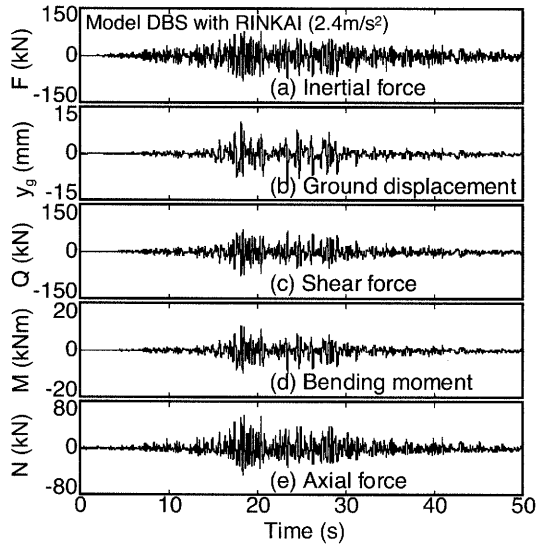


Fig. 4 Time histories in test conducted on model DBS

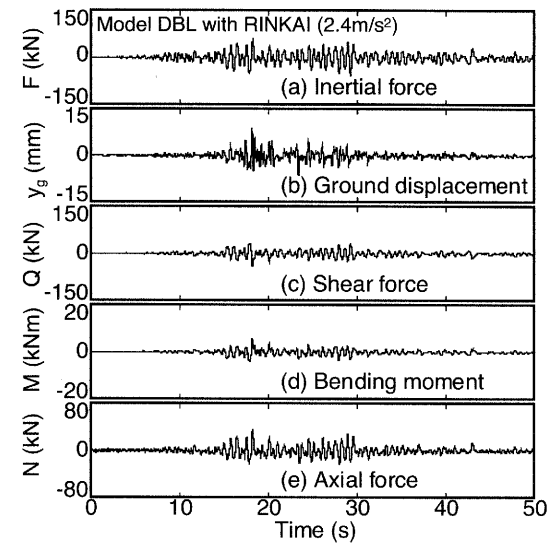


Fig. 5 Time histories in test conducted on model DBL

ground surface displacement and the bending moment, shear force and axial force at the pile head for four tests with a dry sand deposit (Fig. 1(a)) with Rinkai having a maximum acceleration of $2.8\text{--}3.0\text{ m/s}^2$. Although the ground surface displacements of the four tests are similar with each other (Figs. 2 to 5(b)), the pile stresses, including bending moment, shear force and axial force, as well as the inertial forces are quite different from test to test. The pile stresses in the tests with a short-period superstructure without foundation embedment (Fig. 2(c)(d)(e)) are the largest among all, probably due to the largest inertial force. This confirms that the inertial force is the major cause of the stresses in piles. Among the remaining three tests (Figs. 3 to 5) having almost the same inertial forces, the pile stresses in test DBL are significantly smaller than those in tests DBS and DAL. This suggests that factors other than the magnitude of inertial force might have affected the pile stress as well.

To investigate the effects of the inertial force on pile stresses, Fig. 6 shows the relations of the maximum inertial force with the maximum pile stresses at the pile head in all the tests with dry sand. An increase in the pile stresses with respect to the inertial force for test models with a superstructure is more significant in foundation without embedment (tests models DAS and DAL) than in foundation with embedment (tests models DBS and DBL). It is interesting to note that the shear force in the tests with foundation embedment is smaller than the inertial force from the superstructure and the foundation, while that in the tests without foundation embedment is as large as the inertial force (Fig. 6(a)). This suggests that the presence of foundation embedment does have a significant effect on

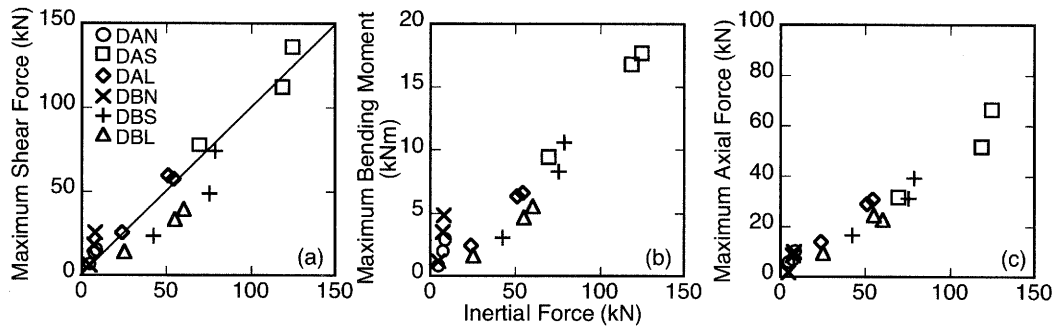


Fig. 6 Relation of maximum pile stresses with inertial force in dry sand

reducing shear forces transmitted from the superstructure to the piles. In addition, the pile stresses become larger in tests with a short-period superstructure than in tests with a long-period superstructure. This is because the inertial force and ground displacement are in phase in tests with a short-period superstructure but out of phase in tests with a long-period superstructure (Tokimatsu et al., 2005).

4. PILE STRESSES IN LIQUEFIED SAND

Figs. 7 to 10 show time histories of the inertial force from the superstructure and foundation, the ground surface displacement and the bending moment, shear force and axial force at the pile head for four tests with a liquefiable saturated sand deposit (Fig. 1(b)) with Rinkai having a maximum acceleration of $2.4\text{--}2.8\text{ m/s}^2$. The pore water pressure ratio reaches 1.0 in 10–20 s, indicating that soil liquefaction develops. After soil liquefaction, the ground surface displacement increases. The inertial forces in tests with flexible piles decrease with increasing ground surface displacement (Figs. 7 and 9(a)), while the inertial force in the test with stiff piles does not show any sign of decrease (Fig. 10(a)). The pile stresses in all the four tests become larger after liquefaction than before liquefaction. It is interesting to note that stresses in piles of an embedded foundation without a superstructure (Fig. 7) after liquefaction is similar to those in the tests with a superstructure after liquefaction (Figs. 8 and 9), despite their different inertial forces. These findings indicate that factors other than the inertial force might have affected pile stresses in liquefied soil.

To investigate how the inertial force is transmitted to piles, Fig. 11 shows the relations of the maximum inertial force with the maximum bending moment, the shear force and the axial force at the pile head in all the tests with liquefiable saturated sand. The pile stresses tend to be larger in the tests with foundation embedment (model IDs starting with SB) than in tests without foundation embedment (model IDs starting with SA). This suggests that the presence of foundation embedment does have a significant and yet opposite effect on pile stresses before and after liquefaction in such a way that it reduces the shear force transmitted to piles before liquefaction but increases it after liquefaction. In addition, the pile stresses in the test with stiff piles (models SBNR, SBSR and SBLR) are much larger than those in other tests, suggesting that pile rigidity might have significant effects on pile stresses.

A comparison between Figs. 6 and 11 indicates that increases in shear force, bending moment, and axial force with respect to inertial force are larger in liquefied sand (Fig. 11) than in dry sand (Fig. 6). Fig. 12 illustrates why the significant increase in pile stresses occur in liquefied ground. In dry or non-liquefied sand, the soil near the ground surface can resist most of the inertial force from the superstructure, reducing shear force transmitting to the piles and limiting the equilibrium of horizontal force almost in the area above the pile cap. Thus, the axial force in piles depends on base moment induced by the inertial force. In liquefied sand, in contrast, the non-liquefied crust overlying liquefied layer and liquefied upper soil layer becomes unable to resist most of the inertial force or even push the foundation to increase the shear force in piles. This extends the equilibrium of horizontal force towards the lower or below the liquefied layer that can only resist the shear force from the

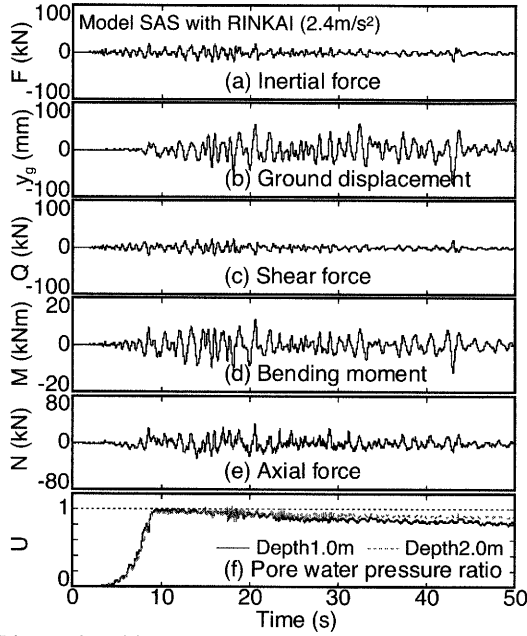


Fig. 7 Time histories in test conducted on model SAS

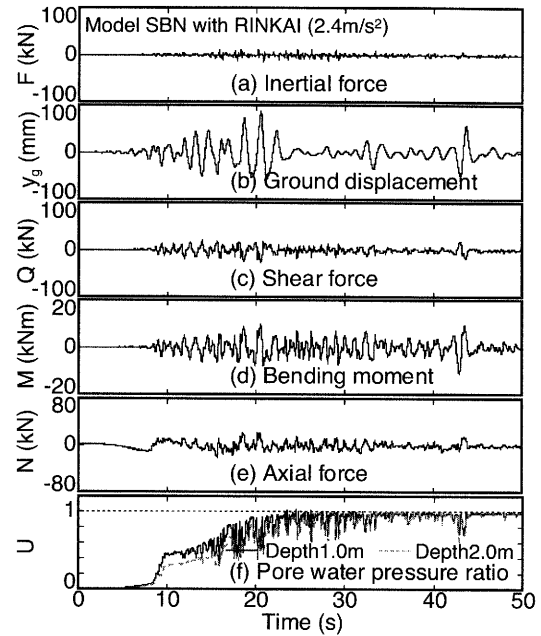


Fig. 8 Time histories in test conducted on model SBN

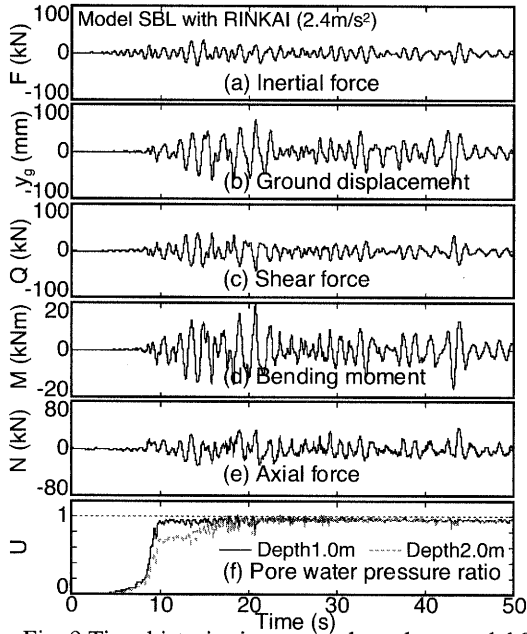


Fig. 9 Time histories in test conducted on model SBL

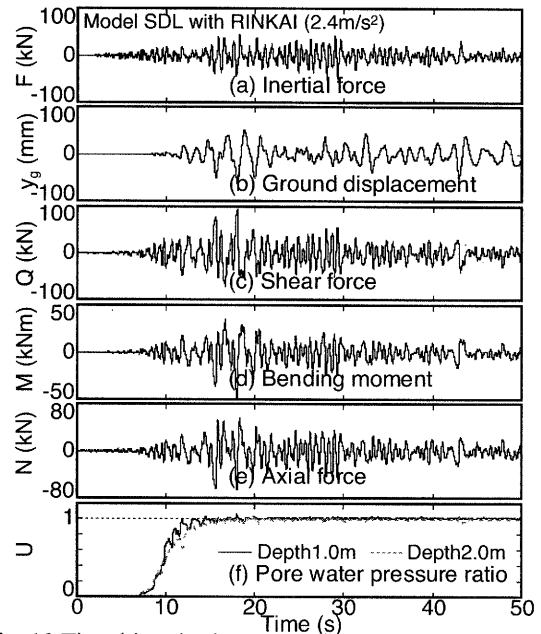


Fig. 10 Time histories in test conducted on model SDL

inertial force and ground displacement. Thus, the axial force in piles depends on an overturning moment of which center located towards the lower part or near the bottom of the liquefied layer. This may result in an increase in overturning moment and thus an increase in fluctuating axial force. This suggests that the change in kinematic effects due to soil liquefaction could have significant effects not only on bending moments and shear forces but also on axial forces in piles

5. ESTIMATION OF PILE STRESSES BASED ON PSEUDO-STATIC ANALYSIS

Pseudo-static analysis considering inertial and kinematic interaction

A pseudo-static analysis based on Beam-on-Winkler-springs method is conducted to examine its effectiveness in estimating pile stresses in the large shaking table tests. Simplified pseudo-static design methods using p-y curves for pile foundations are based on the following equation

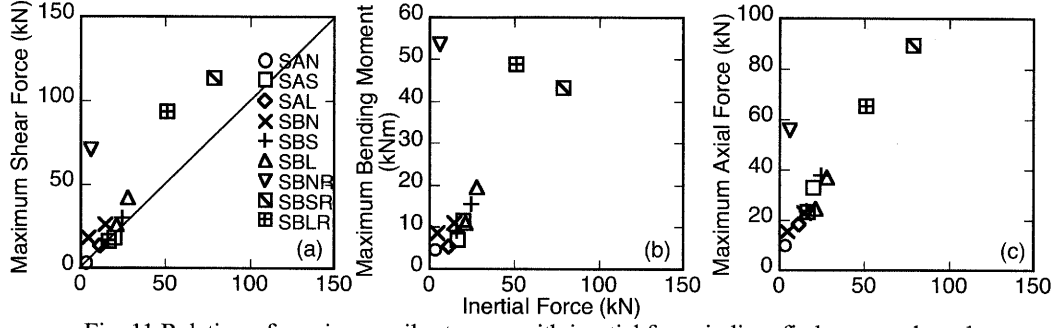


Fig. 11 Relation of maximum pile stresses with inertial force in liquefied saturated sand

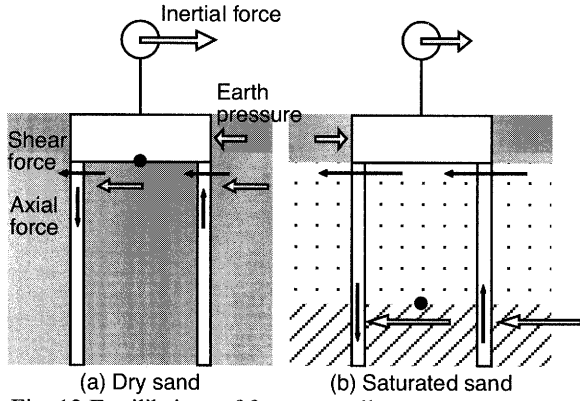


Fig. 12 Equilibrium of forces on pile-structure systems

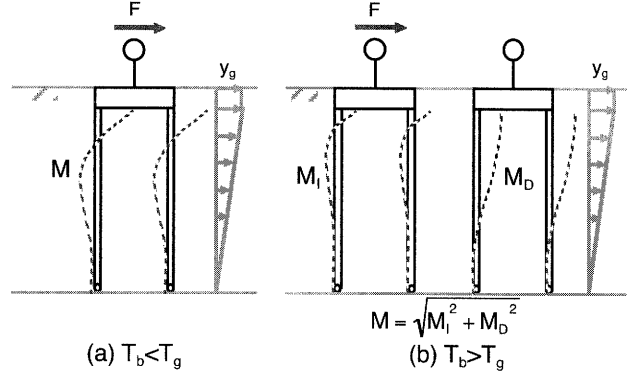


Fig. 13 Combination of inertial force and ground displacement (Tokimatsu et al., 2005)

(Architectural Institute of Japan, 1988, 2001, Nishimura, 1978):

$$EI \frac{d^4 y}{dz^4} = -k_h B_p (y - y_g) \quad (1)$$

in which z is the depth, y and y_g are the pile and ground displacements, EI is the flexural rigidity, k_h is the coefficient of horizontal subgrade reaction, and B is the pile diameter.

In estimation of pile stress from Eq. (1), not only the maximum values of inertial and kinematic forces but also the combination of the two is important, as schematically shown in Fig. 13. When the natural period of the superstructure (T_b) is shorter than that of the ground (T_g), the pile stress may be estimated, provided that both inertial and kinematic forces are in phase and act on the pile at the same time (Fig. 13(a)). When $T_b > T_g$, the pile stress may be given by the square root of the sum of the squares of the two values estimated, provided that the inertial and kinematic forces are out of phase and act on the pile separately (Fig. 13(b)).

In the analysis, the total earth pressure, P_E , acting on the embedded part of a foundation is given by the difference in passive-side and active-side earth pressures acting on the foundation as the following equation (Tamura et al., 2002, Tokimatsu et al., 2003):

$$P_E = P_{Ep} - P_{Ea} = \frac{1}{2} \gamma H^2 B (K_{Ep} - K_{Ea}) \quad (2)$$

in which γ is a unit weight of soil, H and B are the height and width of foundation and K_{Ea} and K_{Ep} are the coefficients of earth pressures on the active and passive sides. Zhang et al. (1998) introduced the earth pressure coefficients, K_{Ea} and K_{Ep} , which can be expressed by a function of relative displacement between the foundation and the ground. Thus, the total earth pressure for any relative displacement can be determined from Eq. (2). The coefficient of subgrade reaction, k_h , in Eq. (1) is given by (Architectural Institute of Japan, 1988, 2001, Tokimatsu et al., 2002):

$$k_h = k_{hl} \frac{2\beta}{1 + |y_r/y_l|} \quad (3)$$

$$k_{hl} = 80 E_0 B_0^{-0.75} \quad (4)$$

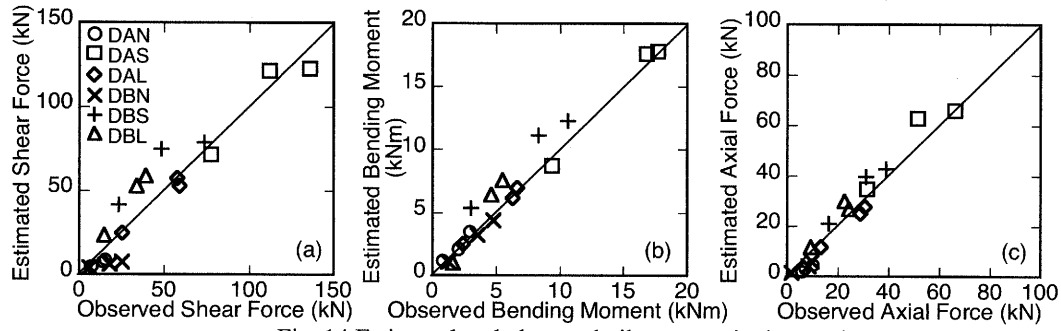


Fig. 14 Estimated and observed pile stresses in dry sand

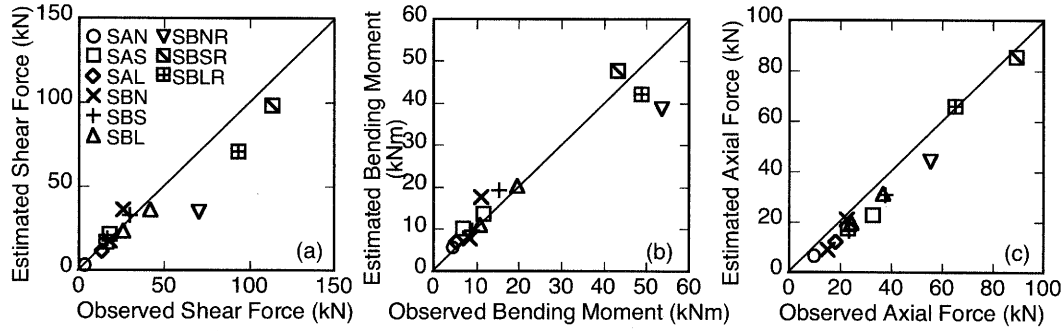


Fig. 15 Estimated and observed pile stresses in liquefied saturated sand

$$E_0 = 0.7N \quad (5)$$

in which k_{h1} is the reference value of k_h defined as Eqs. (4) and (5), β is the scaling factor for liquefied soil, y_r is the relative displacement between pile and soil, $y_r (= y - y_g)$, y_1 is the reference value of y_r , E_0 (MN/m^2) is the Young's modulus of soil, N is the SPT N-value, and B_0 is the pile diameter in cm.

Estimation of pile stresses in shaking table tests based on pseudo-static analysis

To demonstrate the effectiveness of the pseudo-static analysis described in the previous section, the maximum bending moment, shear force and axial force in the thirty-one tests were computed. It was assumed that the inertial force is equal to the observed maximum and the ground displacement above the base of the foundation is equal to the observed maximum at the ground surface and decreases linearly to zero at the base of the laminar box for dry sand or at the bottom of the liquefied layer for saturated sand. The N-values to be used in Eq. (5) were estimated from the CPT-values measured prior to the shaking table test (Yamada et al., 1992). It was also assumed that β is 0.1 for the liquefied sand and 1.0 for the non-liquefied sand and gravel and y_1 in Eq. (3) is 1.0 % of pile diameter.

Figs. 14 and 15 compare the observed and computed maximum bending moment, shear force and axial force in piles in all the tests. The computed pile stresses agree reasonably well with the observed values, indicating that the pseudo-static analysis together with the consideration of the effects of ground displacement is promising for estimating pile stress.

6. CONCLUSIONS

The effects of inertial and kinematic interaction on pile stresses have been studied based on large shaking table tests on pile-structure models in dry and liquefiable saturated sand deposits. A pseudo-static analysis taking into account the inertial and kinematic interaction effects has been conducted for estimating pile stress in the tests. The results and analysis have shown the following:

- 1) In dry or non-liquefied sand, the soil near the ground surface can resist most of the inertial force from the superstructure, reducing shear force transmitting to the piles and limiting the equilibrium

of horizontal force almost in the area above the pile cap. Thus, the axial force in piles depends on base moment induced by the inertial force.

- 2) In liquefied sand, the non-liquefied crust overlying liquefied layer and liquefied upper soil layer becomes unable to resist most of the inertial force or even push the foundation to increase the shear force in piles. The axial force in piles cannot be estimated from the equilibrium above the bottom of the foundation but from the equilibrium including the bottom of the liquefied layer.
- 3) In the pseudo-static analysis on soil-pile-structure systems, when the natural period of the superstructure (T_b) is shorter than that of the ground (T_g), the pile stresses can be estimated, provided that the inertial force and the ground displacement are applied on the pile at the same time. When $T_b > T_g$, the pile stresses can be estimated by the square root of the sum of the squares of the two values estimated, provided that the inertial force and the ground displacement are applied on the pile separately.
- 4) The maximum pile stresses estimated from the proposed pseudo-static analysis are in good agreement with the observed values regardless of the natural period of a superstructure, pile stiffness, the presence of foundation embedment and the occurrence of soil liquefaction.

Acknowledgments:

The study described herein was made possible through two research projects related to soil-pile-structure interaction using the large shaking table at the NIED, including Special Project for Earthquake Disaster Mitigation in Urban Areas, supported by the Ministry of Education, Culture, Sports, Science and Technology (MEXT). The authors express their sincere thanks to the above organization.

References:

- Architectural Institute of Japan (1988, 2001), *Recommendations for design of building foundations*, (in Japanese).
- BTL Committee (1998), *Research Report on liquefaction and lateral spreading in the Hyogoken-Nambu earthquake* (in Japanese).
- Mitsuji, K., Yokoi, Y. and Sugimoto, Y. (1993), Evaluation of horizontal load of piles based on results of dynamic analysis (Part 2 Proposal of horizontal load), *Proc. of Twenty-eighth Japan National Conference on Geotechnical Engineering*, **2**, 1847-1848 (in Japanese).
- Nishimura, A. (1978), Design of structures considering ground displacement, *Kisoko* **6** (7), 48-56 (in Japanese).
- Nishimura, A., Murono, Y., and Nagatsuma, S. (1997), Experimental studies on the seismic design method for pile foundations in the soft ground (Part 1)-(Part 3), *Proc. of Thirty-second Japan National Conference on Geotechnical Engineering*, **1**, 961-966 (in Japanese).
- Nishimura, A., Murono, Y., and Nagatsuma, S. (1998), Seismic response characteristics of pile foundation in soft ground and its application to seismic design, *Proc. of Thirty-third Japan National Conference on Geotechnical Engineering*, **1**, 1079-1080 (in Japanese).
- Tamura, S., Tsuchiya, T., Suzuki, Y., Fujii, S., Saeki, E. and Tokimatsu, K. (2000), Shaking table tests of pile foundation on liquefied soil using large-scale laminar box (Part 1 Outline of test), *Proc. of Thirty-fifth Japan National Conference on Geotechnical Engineering*, **2**, 1907-1908 (in Japanese).
- Tamura, S., Tokimatsu, K., Miyazaki, M., Yahata, K. and Tsuchiya, T. (2002), Seismic earth pressure action on embedded footing based on liquefaction test using large scale shear box, *Journal of Structural and Construction Engineering*, AIJ, **554**, 95-100 (in Japanese).
- Tokimatsu, K., Suzuki, H. and Saeki, S. (2002), Modeling of horizontal subgrade reaction of pile during liquefaction based on large shaking table, *Journal of Structural and Construction Engineering*, AIJ, **559**, 135-141 (in Japanese).
- Tokimatsu, K., Tamura, S., Miyazaki, M. and Yoshizawa, M. (2003), Evaluation of seismic earth pressure acting on embedded footing based on liquefaction test using large scale shear box, *Journal of Structural and Construction Engineering*, AIJ, **570**, 101-106 (in Japanese).
- Tokimatsu, K., Suzuki, H. and Sato, M. (2005), Effects of dynamic soil-pile-structure interaction on pile stresses, *Journal of Structural and Construction Engineering*, AIJ, **587**, 125-132.
- Zhang, J.-M., Shamoto, Y. and Tokimatsu, K. (1998), Evaluation of earth pressure under any lateral displacement, *Soils and Foundations*, JGS, **38** (2), 143-163.
- Yamada, K., Kamao, S., Yoshino, H. and Masuda, Y. (1992), Correlation between N-value and cone index, *Tsuchi-to-Kiso*, JGS, **40** (8), 5-10 (in Japanese).

Ground Motion Responses in the Taipei Urban Area

Kuo-Liang Wen¹⁾, Tao-Ming Chang²⁾, and Che-Min Lin¹⁾

1) Institute of Geophysics, National Central University, Taiwan

2) Department of Information Management, Hsing-Wu College, Taiwan

wenkl@earth.ncu.edu.tw,

Abstract: Taipei basin is a triangle-shaped alluvium structure. The ground surface of the Taipei basin is almost flat and tilting gently to the northwest. The total area of the Taipei basin is about 240 square kilometers with an altitude below 20 meters. Taipei urban area had been suffered damages during earthquakes. For example the 1909 Taipei earthquake, 1986 Hualien earthquake (May 20 and Nov. 15), 1999 Chi-Chi earthquake, and March 31, 2001 earthquake, all these earthquakes are far away from the Taipei basin, but Taipei urban area had damages occurred. By the way, even some earthquakes did not have damage in the epicenter area.

A dense strong motion observation network provides an opportunity to realize the basin effects in the Taipei urban area. The Taiwan Strong Motion Instrumentation Program (TSMIP) executed by the Seismological Observation Center of the Central Weather Bureau, Taiwan, ROC since 1991. About 100 free field stations are already in operation in Taipei area, and 43 stations are within the Taipei basin. The station interval is about 2 km, on average. Another research plan, conducted by the Central Geological Survey, Ministry of Economic Affairs since August 1991, proposed the installation of down-hole accelerometer arrays in the Taipei Basin one site per year to analyze the variation of seismic waves propagated from basement to ground surface. In February 2002, the CGS finished the research project and removed it to Institute of Earth Sciences, Academia Sinica. After few months rearranging and planning, four additional downhole sites were under consideration.

The vertical and horizontal peak ground accelerations at different depths with respect to those at ground surface are compared. The results of V_p and V_s for the ground layer from surface to different depths are calculated. The interval Q values are calculated from the records at the WK site. The ground responses are simulated through the theoretical one-dimensional modeling, based on the interval Q and its velocity structure. The results of the site responses in the Taipei basin had been studied by Kuo *et al.* (1995) and Wen *et al.* (1995a, 1998). The average spectral ratio contours at some specific frequencies are selected to compare with the geological and velocity structures under the Taipei basin. Microtremor surveys at each TSMIP site in the Taipei basin are conducted and the 2D and 3D numerical simulations also done for this basin to compare the results with that from the TSMIP earthquake records. With all the observations still ongoing and the down-hole arrays expanding to different sites, hopefully, the characteristics of the ground motions of the Taipei Basin during an earthquake may be better understood. Accordingly, the seismic resistant design code of the Taipei urban area can be improved. This, in turn, will help mitigate the possible damage in any future earthquakes.

1. INTRODUCTION

Amplification of strong ground motion by alluvial deposits during an earthquake has been documented on a lot of occasions and caused damage in recent large earthquakes, for example, 1985 Michoacan earthquake, 1989 Loma Prieta earthquake, 1994 Northridge earthquake, and 1995 Kobe earthquake. Many studies (Boore *et al.*, 1993, 1994; Anderson *et al.*, 1996) shown that the top alluvium layer will play an important role for site amplification effects. Therefore, site effects

study is very important for mitigating damage during an earthquake. Many methods have been used to characterize the site amplification. The best approach is through direct observation of seismic ground motion, although such observations are limited to high seismic areas and by high cost. A dense strong motion observation network provides an opportunity to realize the basin effects in the Taipei basin. The preliminary results of the site responses in the Taipei basin had been studied by Kuo *et al.* (1995) and Wen *et al.* (1995a). In this study, we collect more data and systematically analyze the TSMIP earthquake records for realizing the basin responses by using the spectral ratio method. The average spectral ratio contours at some specific frequencies are selected to compare with the geological and velocity structures under the Taipei basin. Microtremor surveys at each TSMIP site in the Taipei basin are conducted and the 3D numerical simulation also done for this basin to compare the results with that from the TSMIP earthquake records. A research plan, conducted by the Central Geological Survey (CGS), Ministry of Economic Affairs since August 1991, proposed the installation of downhole accelerometer arrays in the Taipei Basin one site per year to analyze the variation of seismic waves propagated from basement to ground surface. In February 2002, the CGS finished the research project and removed it to Institute of Earth Sciences, Academia Sinica. After few months rearranging and planning, four additional downhole sites were under consideration. The vertical and horizontal peak ground accelerations at different depths with respect to those at ground surface are compared. The results of V_p and V_s for the ground layer from surface to different depths are calculated. The interval Q values are calculated from the records at the WK site. The ground responses are simulated through the theoretical one-dimensional modeling, based on the interval Q and its under ground structure.

2. GEOLOGY OF THE TAIPEI BASIN

The Taipei basin is a triangle-shaped alluvium structure, with Shanchia, Kuantu, and Nankang at the southwestern, northwestern, and eastern corners (Fig. 1). The ground surface of the Taipei basin is almost flat and tilting gently to the northwest. The total area of the Taipei basin is about 240 square kilometers with an altitude below 20 meters. The Keelung River flows through it in an east-west direction, the Dahang Creek from the south through the basin center and then northwest to the ocean, and the Chingmei Creek from the southeast merge in the Dahang Creek at around the basin center. Because the basin is filled with the unconsolidated sediments, the subsurface geology of the Taipei basin can only be established by the information obtained from boring, electrical, and seismic prospecting (Wang *et al.*, 1978; Wang and Lin, 1987). Recently, the basement structure in the Taipei basin area had been modified through the work of deep boring by the Central Geological Survey (Fei and Lai, 1994) and dense reflection seismic survey by the National Central University (Wang *et al.*, 1994a, 1994b; Hsieh *et al.*, 1994).

The geological structure inside the basin is the Quaternary layers above the Tertiary base rock. The stratigraphic formations of the Quaternary layers are, in descending order, surface soil, the Sungshan Formation, the Chingmei Formation, and the Hsinchuang Formation. The Sungshan Formation is composed mainly of alternating beds of silty clay and silty sand, and covers almost the whole Taipei basin. The Chingmei Formation is a fan-shaped body of conglomerate deposits. The Hsinchuang Formation consists of bluish grey, clayey sand with some conglomerate beds (Wang and Lin, 1987). Recently, Teng *et al.* (1994) separated the Hsinchuang Formation into Wuku and Panchiao Formations. Wen *et al.* (1995b) calculated the V_p and V_s from surface to the depth of 350 meters through the travel time analysis of seismic waves by using the Wuku down-hole records in the western part of Taipei basin. The average P- and S-wave velocity structures of the Taipei basin from the reflection seismic survey in the whole Taipei basin area done by Wang *et al.* (1996).

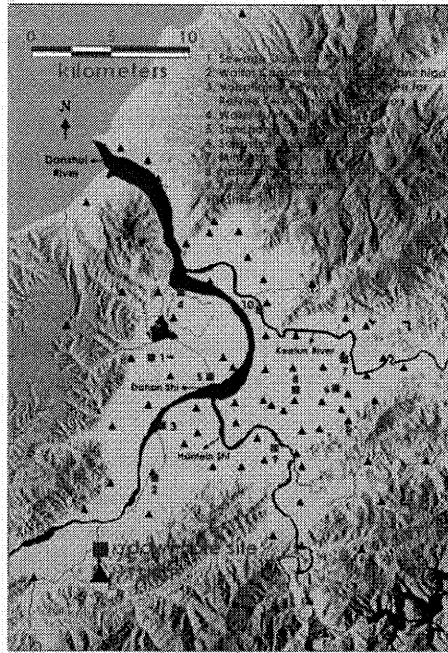


Figure 1. Locations of the strong motion stations in the Taipei urban area. Black triangles indicate the stations of TSMIP network. The red squares indicate the down-hole array sites.

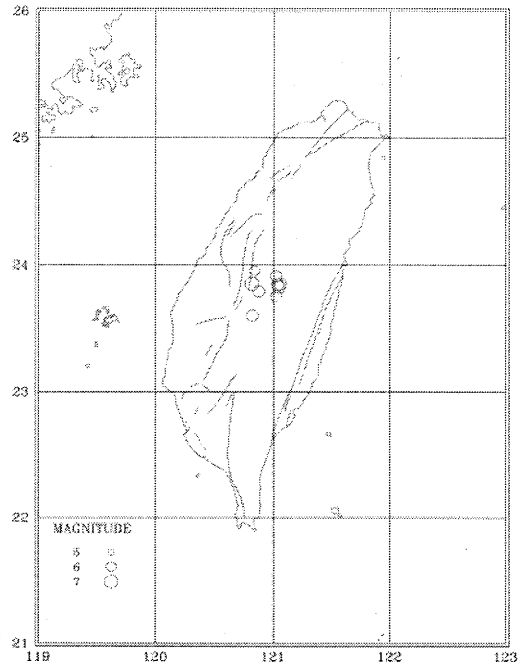


Figure 2. Locations of the epicenters of the Chi-Chi earthquake and its aftershocks used in this studies.

3. TSMIP NETWORK AND EARTHQUAKE DATA

The Taiwan Strong Motion Instrumentation Program (TSMIP, Shin, 1993; Kuo *et al.*, 1995) executed by the Seismological Observation Center of the Central Weather Bureau, Taiwan, ROC since 1991. The main purpose of this program is to study the characteristics of the ground motion in different geological conditions, and the response of different types of man-made structures. All results can be used to improve the design spectrum and building codes of current use. The program installed more than 600 digital free field strong motion instruments and 400*3 digital channels of strong motion monitoring systems (building arrays) in nine metropolitan areas. About 100 free field stations are already in operation in Taipei area, and 43 stations are within the Taipei basin. The station interval is about 2 km, on average. The distribution of stations is shown in Fig. 1 of black triangle symbols. Each station includes one strong motion instrument and a recording room. Strong motion instrument is a force-balance accelerometer. The recorder has 16 bits' resolution, can record the ground motion within $\pm 2g$, and has pre-event and post-event memory. Each strong ground motion station has the same design. A small fiberglass house covered on a concrete plate. All stations have AC power. When the power system shutdown by earthquake or other problem, the DC powers of the recording system still can operate about 4 days.

Before the Chi-Chi Earthquake, many earthquakes had been recorded by this network since its installation. By the end of 1995, there are 23 events that triggered more than ten stations (Wen and Peng, 1998). All events were at least 30 km away from Taipei basin. The magnitude range is from 4.6 to 6.6 on the local magnitude scale, hypocenter depths cover from 3 to 116 km, and most of the peak ground accelerations (PGA) within the basin are all lower than 50 gal except five events. The characteristics of the ground motions are analyzed in the frequency domain by the spectral ratio method to understand the site effects in the Taipei basin area.

The Chi-Chi Earthquake and its 8 aftershocks which magnitude is over 6.0 were recorded by

the TSMIP network which is located in the Taipei basin since September 20 to 22, 1999 (Wen *et al.*, 2000). Fig. 2 shows the location of the 9 events. In the Fig. 2 we can find that, Chi-Chi earthquake and its aftershocks are all located at the south-western direction of Taipei basin and the Taipei basin is located more than 100 km away from the epicenters of these earthquake. In this study, 9 earthquakes will be used to make spectral ratio to understand the site response in the Taipei basin during the Chi-Chi earthquake and its aftershocks.

4. DOWNHOLE ARRAYS AND EARTHQUAKE DATA

The instrument installations were finished in the site of Sewage Disposal Plant of Wuku Industry Area (WK), Panchiao Water Conservancy Bureau (BS), Panchiao Committee for Retired Servicemen (TF), Water Pump Station in Luchou (LC), and Chungshin Bridge (HS), Sungshan cigarette factory (SS), Mingchuan park (MP), National Taipei Univ. of Science and Tech. (TU), Yeongho (YH), and Shilin (SL). The red squares in Fig. 1 represent the site positions. Each site includes one free-surface accelerometer and several down-hole sensors. The down-hole array observation system includes accelerometers, GPS timing system, and a digital recording system. Products of the Kinemetrics Inc., the FBA23 and the FBA23DH accelerometers are used for the surface station and for down-hole sites, respectively. With the full scale of $\pm 2g$ (FBA23) and $\pm 1g$ (FBA23DH), and the natural frequency is 50 Hz. The sampling rate is 200 pts/sec.

Many earthquakes already recorded by these downhole arrays. Their magnitudes range from 2.7 to 7.0. Most earthquakes were far away from the down-hole array, causing the peak ground accelerations recorded at ground surface to be lower than 70 gals in each of these events.

5. SITE EFFECT ANALYSIS

5.1 Surface TSMIP network

Before the Chi-Chi Earthquake, many earthquakes had been recorded by this network since its installation. By the end of 1995, there are 23 events that triggered more than ten stations (Wen and Peng, 1998). All events were at least 30 km away from Taipei basin. The magnitude range is from 4.6 to 6.6 on the local magnitude scale, hypocenter depths cover from 3 to 116 km, and most of the peak ground accelerations (PGA) within the basin are all lower than 50 gal except five events.

In order to understand the soil amplification effects in the frequency domain, the spectral ratios of the soft soil stations were calculated with respect to the rock site that is near the south-western edge of the basin. The spectral ratios are calculated as follows (Beresnev and Wen, 1996) : (1) a window containing the shear wave is identified; (2) the window is tapered at both ends (at 5% of the length) using a cosine function; (3) the Fourier amplitude spectrum is calculated; (4) the spectrum is smoothed 1 times using a 3-point running Hanning average; (5) two smoothed spectra are divided; (6) the root-mean-square (RMS) spectral ratio is then calculated from the two horizontal ratios of EW and NS components.

For the purpose of the earthquake resistant design, earthquake engineers must consider the site response at a specific period. For example, the structure period of a ten-floor building is at about 1 second. If the input ground motion is dominate at 1 Hz, then the building will has a resonant effect. Which may easily causes big damage to this building. Therefore, in this study, we select 7 periods (4, 3, 2, 1.5, 1, 0.5, and 0.3 sec) to plot out the contour map for understanding the frequency responses in the Taipei basin. Fig. 3 shows an example of the mean spectral ratio contour for the period of 2 sec. From these contours, it is obvious that the waves at different frequencies have different amplification patterns in the Taipei basin. For the low frequency responses (period from 4 to 1.5 seconds) in the Taipei basin, the contours show that main amplification effects occurred at

the western part of the Taipei basin and the Sungshan area. Nevertheless, the response at the higher frequency band of larger than 1 Hz shows different amplification effects. The high contour areas occur near the basin edges at the north, east, and south basin boundaries. The responses in western part of the Taipei basin and the Sungshan area do not show strong amplification effect anymore. The basement structure may explain the high spectral ratio area occurred at the western part of the Taipei basin, which is the deepest area of the Taipei area. But it can not explain the contour high area at the Sungshan area of the low frequency responses. The top alluvium layer in the Taipei basin seems play an important role for site amplifications as mentioned by Anderson et al. (1996). The two deepest areas of the soft Sungshan Formation (Fig. 4) can correlate with the two high spectral ratio areas at the lower frequency bands. More research works are needed to clarify the role of this top alluvium layer of the Sungshan Formation.

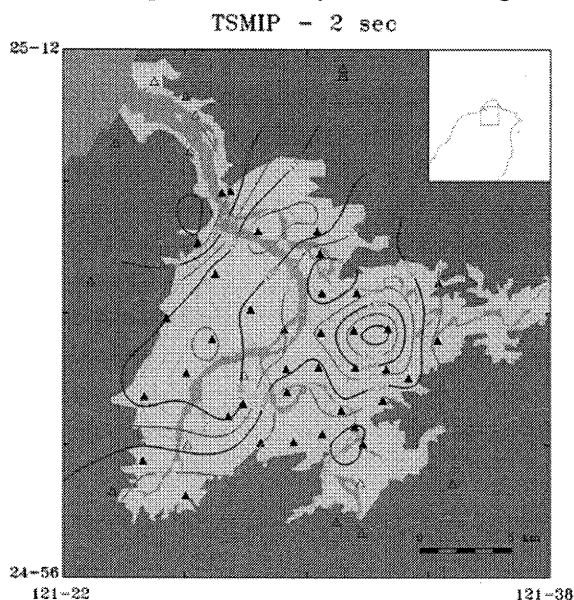


Figure 3. Contours of the mean spectral ratio at 2 sec in the Taipei basin from the TSMIP records.

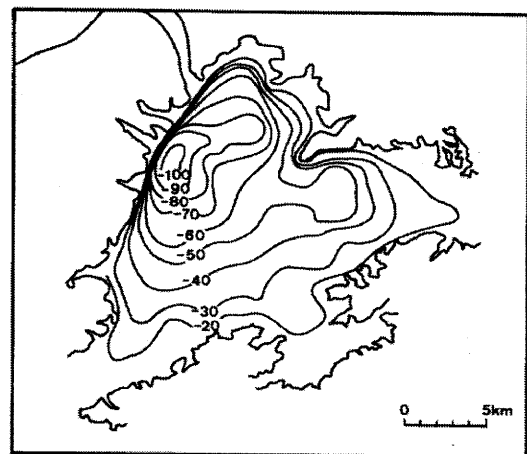


Figure 4. Taipei basin Sungshan formation Bottom.

5.2 Microtremor survey

Kagami et al. (1982; 1986) proposed that the ratio of the horizontal components of the velocity spectra at the sediment site to those at the rock site (Kagami's ratio) can be used as a measure of microseism ground motion amplification. This proposition assumes a common source and similar paths for sediment and bedrock sites. Nakamura (1989) proposed a hypothesis that microtremor site effects can be determined by simply evaluating spectral ratio of horizontal versus vertical components of motion observed at the same site (Nakamura's ratio).

Measurements are done at each TSMIP station in the Taipei basin. During the measurement, one system was continually operated in the station TAP016 which near the edge of the basin. Then, both methods can be used in the analysis. From these spectral ratios, the values at each frequency can be selected at each site and drew the contours to show the basin effects at this frequency.

The results from the Kagami's ratio show very consistent with those from the earthquake records in the frequency band of lower than 1 Hz. The responses in the basin center at periods of 0.5 sec show very high value. It will affects the contour pattern, but over all the eastern part still shows a contour high in the area near station 22. The variations of the Kagami's ratio from the microtremor survey more or less can be compared with that from the earthquake records. So, the comparison still has a good result. The results from the Nakamura's ratio not only in the low frequency band but also in the higher frequency band are very consistent with the results from the earthquake records. Fig. 5 is an example of the result at 2 sec. The responses in the north, east, and

south edges are all show a contour high in the frequency band higher than 1 Hz. The amplification factor in the higher frequency band only can be a factor of 2.5. It is lower than that from the Kagami's ratio which is more consist with the factor from the earthquake record.

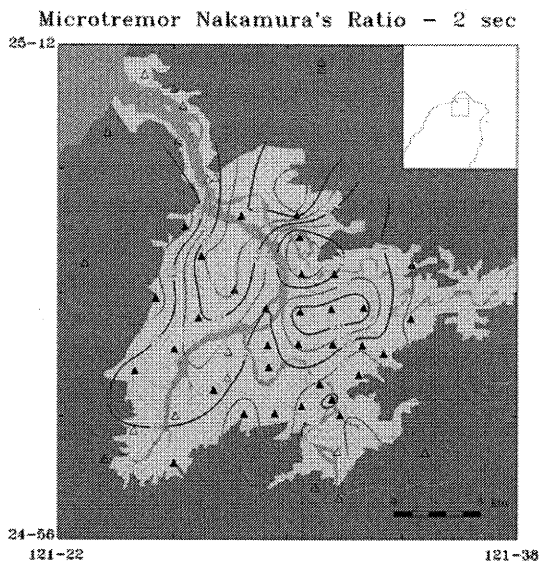


Figure 5. Contours of the mean Nakamura's ratio at 2 sec in the Taipei basin.

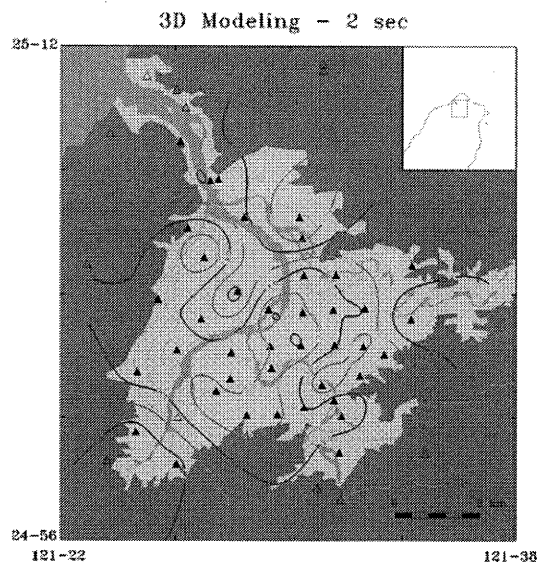


Figure 6. Contours of the mean spectral ratio at 2 sec in the Taipei basin from the 3D simulation.

5.3 NUMERICAL MODELING

Theoretical model of the Taipei basin is assumed to be a single dipping layer embedded within a half-space. The 3D model is based upon the geological structure. Based on the 3D basin model, we use indirect boundary integral equation method to calculate the transfer function between TAP016 rock site and other observation points in the frequency range from 0 to 3 Hz with 1/40.96 (0.0244) Hz interval. After we get the transfer function at each observation point atop the basin, we can plot out the same contour of the transfer function at different frequency.

The result at 0.5 sec is the same as previous observation measurements that the contour high areas are around the basin edge, in the south, southeast and northwest edges of the basin. The result at 2 sec (Fig. 6) also shows a contour high at the western part as that of the observation measurements. But the eastern part of the Taipei basin near the south of the Sunghsan airport does not has a contour high as those showed in the observation measurements. This implied that the low frequency response at this area is not the result of the basin structure. Most come from the soft Sunghsan alluvium layer.

5.4 DOWNHOLE ARRAYS ANALYSIS

To study the soil layer response, it is necessary to know the velocity structure first. The velocities of the Sungshan and Chingmei Formations are the most important for engineers in the Taipei area. From the data recorded by these down-hole arrays, the arrival times of the P- and S-waves at each station can be picked out. Based on the distance between two stations and the difference in travel times, the average velocity within this two-station pair can be calculated. The spectral ratio method also used for double check. The P- and S-wave velocity profiles at the WK, BS, TF, LC, and SS sites are obtained. The results for BS and TF sites are only for reference, because the data still not enough. Fig. 7 shows the P- and S-wave velocity profiles at the WK site. The velocity structures at these sites can be compared with the geological profiles.

Most engineers judge the ground motion level by the peak ground acceleration (PGA). The variation of the PGA with respect to depth can be analyzed through the records of the downhole array. Because the deepest holes at some sites are not drilled to the basement, the station at free surface is used as a reference point to study the variation of the PGA with respect to depth. Using

linear regression analysis, the attenuation curve of the normalized PGA with respect to depth at the WK, BS, and TF sites are calculated. Fig. 8 shows the result of the WK site. On the basis of the geological profile, the ground motion amplification is mainly occurred on the top soil layer (Sungshan Formation).

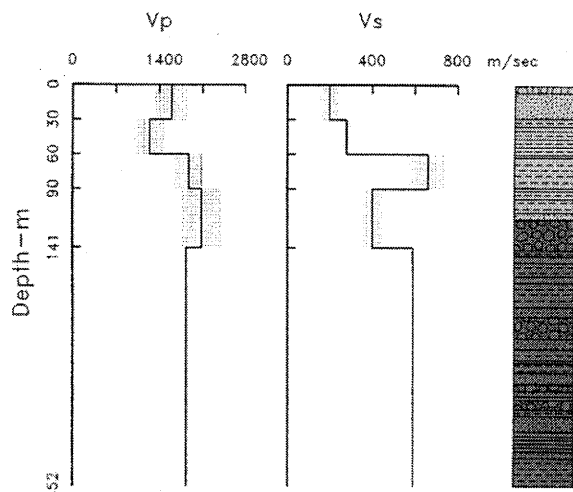


Figure 7. V_p and V_s profiles at the WK site. The shaded areas represent ± 1 standard deviation of the average.

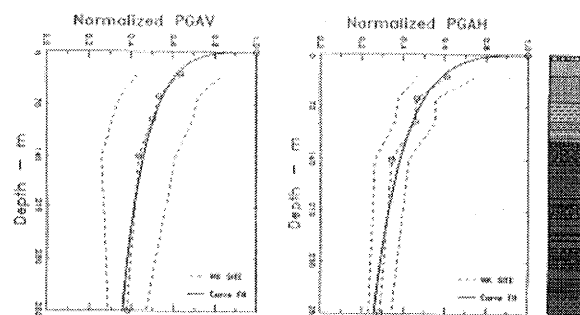


Figure 8. Variations of the normalized PGA with respect to depth at the WK site. The dashed area represents ± 1 standard deviation around the average (open circles).

Many studies have suggested that seismic waves recorded at ground surface are modified by attenuation of high frequencies and/or dominated by a narrow band of frequencies amplified through reverberation near the ground surface. Very low Q values near the surface are found by comparing the surface ground motions with downhole motions. In these studies, the down going waves were not considered in their analysis. Downhole arrays in the Taipei basin provide an opportunity to study the near surface Q in soft Quaternary soil layer. The down-going wave reflected from the free-surface was considered in this study.

The spectral ratio method is used to calculate the attenuation of shear wave. Based on the density and velocity data, the shear wave amplification factor from depths of 90 m to ground surface is about 2.4. After the correction of the amplification factor and free-surface effect, the corrected records can be used to calculate the Q value of Sungshan Formation. Ten-second records after the arrival of S wave is used and the window length is 0.05 seconds. From the spectral ratio at each frequency, the average Q can be calculated. Averaging the results of 16 events, the mean and one standard deviation are calculated. The frequency dependence of interval Q can be calculated by the least-square fit of the different station pairs. The results are as follows:

$$\begin{aligned} 0\text{m}-30\text{m}: & \quad Q(f) = 3.6 f^{0.96} \\ 30\text{m}-60\text{m}: & \quad Q(f) = 7.2 f^{0.99} \\ 60\text{m}-90\text{m}: & \quad Q(f) = 10.2 f^{1.17} \\ 90\text{m}-141\text{m}: & \quad Q(f) = 40.7 f^{1.24} \end{aligned}$$

Horizontal layer model was used to do the waveform simulation through the Haskell method (Haskell, 1953; 1960) for realizing the reliability of the results of $Q(f)$. Based on the shear wave velocity model, the transfer function between the stations at ground surface and that at different depths were calculated. Then, the observation records at ground surface were used to simulate the records at different depths. Before convolve with the transfer function, the shear wave record at the ground surface was rotated to the transverse and radial directions. A bandpass filter was utilized in the input signal from 0.4 to 10 Hz. Fig. 9 shows the results of February 4, 1994 event and Fig. 10 shows the results of the June 5, 1994 event. The simulated and observed waveforms are very consistent; include phase arrival time, and up- and down-going waves. These simulation results show that the velocity structure and the frequency dependent Q obtained in this study are

suitable for use.

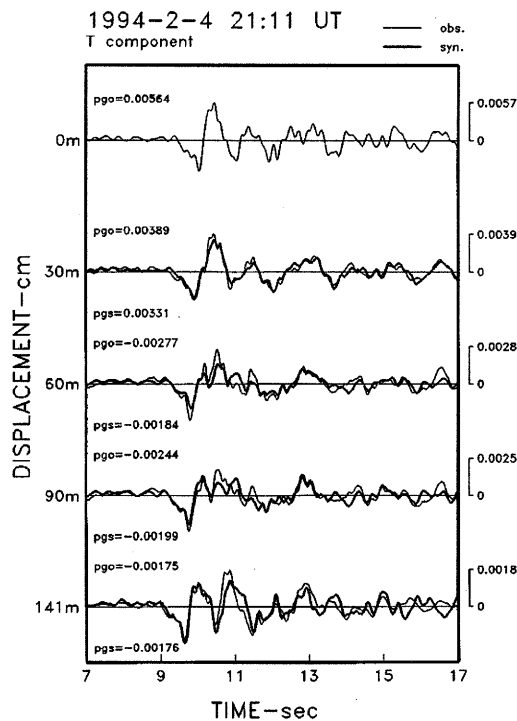


Figure 9. Synthetic displacement seismograms at the WK site of tangential component for Feb. 4, 1994 earthquake.

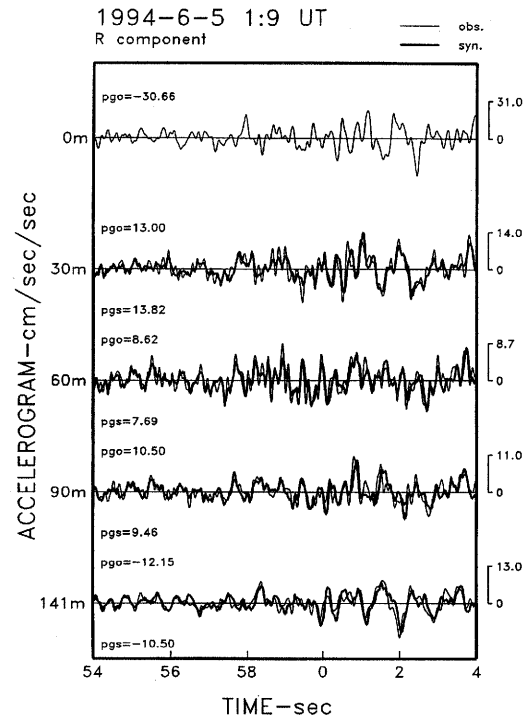


Figure 10. Synthetic acceleration seismograms at the WK site of radial components for June 5, 1994 earthquake.

6. THE DAMAGE DISTRIBUTION OF THE CHI-CHI EARTHQUAKE IN THE TAIPEI BASIN

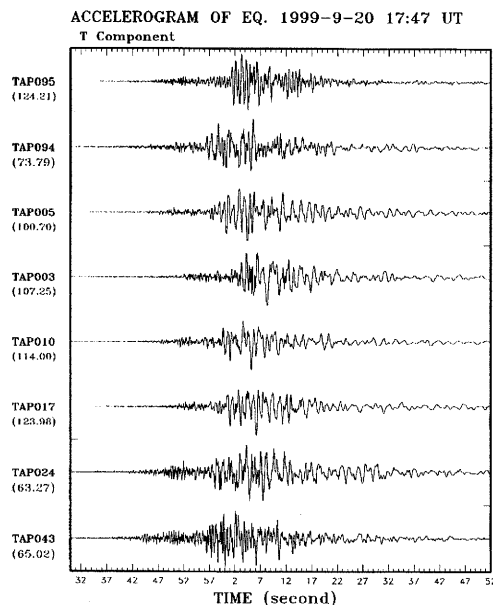


Figure 11. EW component accelerograms recorded in the Taipei basin area. The stations from bottom to top are located from south to the north direction. Unit in gals.

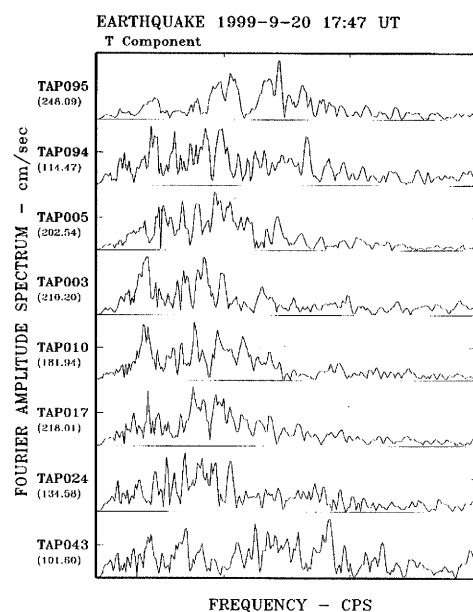


Figure 12. Fourier amplitude spectra of the EW component accelerograms recorded in the Taipei basin.

Taipei basin is located in the north of the epicenter of the Chi-Chi earthquake and the closed

distance to the fault rupture is more than 100 km away. Fig. 11 plots the waveforms from south to north in the western part of the basin. They indicate that the seismic waves from the south to the north edge of the basin show the amplification effects. If we consider the frequency response (Fig. 12), the ground motions change from high frequency to low frequency, as the basin becomes deeper. Toward the north edge, the response turns to higher frequency again. The edge effects (Kawase, 1996) seem also play an important role for this event.

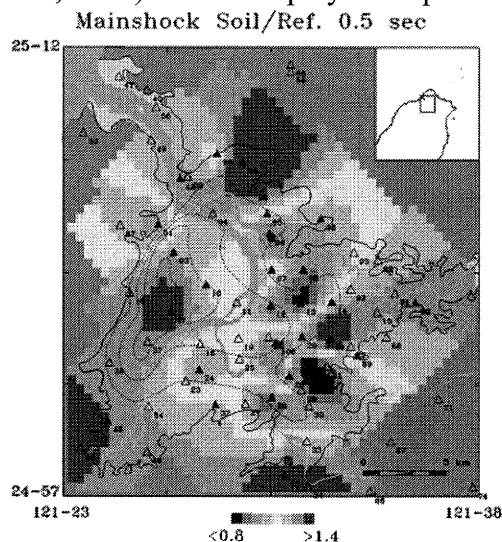


Figure 13. The spectral ratio contour of Chi-Chi earthquake at 0.5 sec in the Taipei basin from the TSMIP records. The black triangles are stations that used in this analysis.

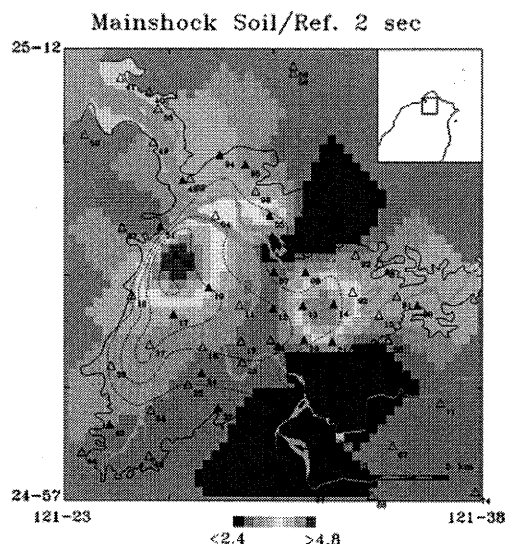


Figure 14. The spectral ratio contour of Chi-Chi earthquake at 2 sec in the Taipei basin from the TSMIP records. The black triangles are stations that used in this analysis.

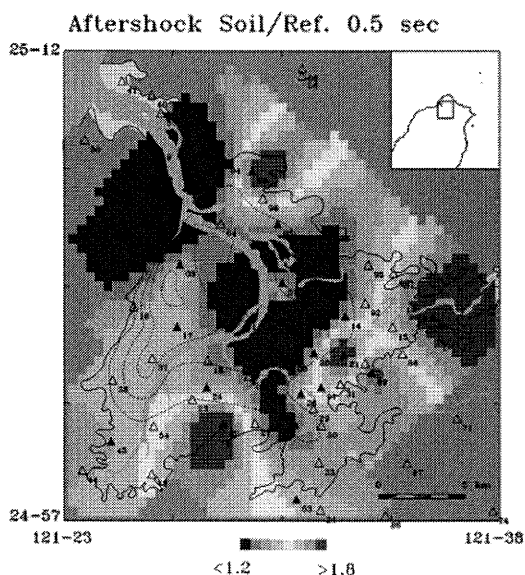


Figure 15. The mean spectral ratio contour of Chi-Chi earthquake aftershocks at 0.5 sec in the Taipei basin from the TSMIP records. The black triangles are stations that used in this analysis.

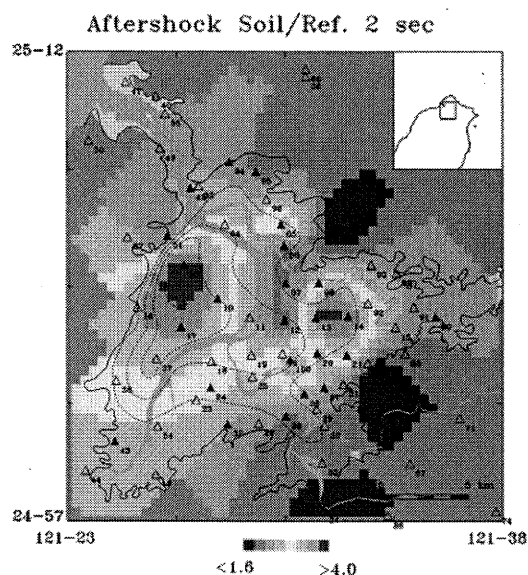


Figure 16. The mean spectral ratio contour of Chi-Chi earthquake aftershocks at 2 sec in the Taipei basin from the TSMIP records. The black triangles are stations that used in this analysis.

Although Taipei basin is located more than 100 km away from the epicenter of Chi-Chi earthquake, there are also three tall buildings collapsing and some low-rise structures damaging during the earthquake. As the spectral ratio method we used above, we chose the Chi-Chi earthquake and its aftershocks records to analyze the site effect of Taipei basin. Figure 13 and Figure 14 show the examples of spectral ratio contour of Chi-Chi earthquake for period of 0.5 sec

and 2 sec. Figure 15 and Figure 16 show the examples of mean spectral ratio contour of the Chi-Chi aftershocks for period of 0.5 sec and 2 sec. These patterns of spectral ratio contour are very consistent with above results. The damages distribution of the Chi-Chi earthquake can compare with the site response in the Taipei basin. The three tall buildings are located in the high response areas of the lower frequency. The low-rise buildings are located near the basin edges where had higher response in the higher frequency band. This phenomenon also shown in the Hualien earthquake of November 15, 1986.

7. DISCUSSIONS

Strong motion observations in the Taipei Basin include a dense surface strong motion observation network and several down-hole accelerometer arrays. The dense strong ground motion observation network began to operate in the Taipei Basin area as part of the TSMIP Program. It is operated by the Seismology Center, Central Weather Bureau. One hundred free-field accelerometers have been installed in the Taipei metropolitan area. Many earthquakes recorded by this network to the end of July 1997, but only 16 earthquakes triggered more than 30 stations. From the analysis of earthquake records of the dense Taipei strong motion observation network, the results of the microtremor measurements, and the results from theoretical 3D modeling all indicate the low frequency response consist with the geological structure. A research plan was conducted by the Central Geological Survey, Ministry of Economic Affairs since August 1991. This project proposed the installation of down-hole accelerometer arrays in the Taipei Basin one site per year to analyze the variation of seismic waves propagated from basement to ground surface. The vertical and horizontal peak ground accelerations at different depths with respect to those at ground surface are compared. The results of V_p and V_s for the ground layer from surface to different depths are calculated. The interval Q values are calculated from the records at the WK site. The ground responses are simulated through the theoretical one-dimensional modeling, based on the interval Q and it's under ground structure. The results were good enough to prove the accuracy of Q(f) value obtained in this study.

With all the observations just beginning and the downhole array expanding to different sites, hopefully, the characteristics of the ground motions of the Taipei Basin during an earthquake may still be better understood. Accordingly, the seismic resistant design code of the Taipei area can be improved. This, in turn, will help mitigate the possible damage in any future earthquakes.

Acknowledgments

This work has been supported by the Central Geological Survey, the Seismological Observation Center of Central Weather Bureau, and the National Science Council, ROC.

References

- Anderson, J.G., Lee, Y., Zeng, Y., and Day, S. (1996), "Control of strong motion by the upper 30 meters," *Bull. Seism. Soc. Am.*, **86**(6), 1749-1759.
- Beresnev, I.A. and Wen, K.L., (1996), "The accuracy of soil response estimates using soil-to-rock spectral ratios," *Bull. Seism. Soc. Am.*, **86**(2), 519-523.
- Boore, D.M., Joyner, W.B., and Fumal, T.E., (1993), "Estimation of response spectra and peak accelerations from western United States earthquakes: an interim report," U.S. Geol. Surv. Open-File Rep. 93-509, 72pp.
- Boore, D.M., Joyner, W.B., and Fumal, T.E., (1994), "Estimation of response spectra and peak accelerations from western United States earthquakes: an interim report, Part 2," U.S. Geol. Surv. Open-File Rep. 94-127, 40pp.
- Fei, L.Y. and Lai, T.C., (1994), "The preliminary result of an integrated survey of subsurface geology and engineering environment of the Taipei basin," *Proc. of the Joint Symposium on Taiwan Quaternary (5) and on Investigation of Subsurface Geology/Engineering Environment of Taipei Basin*, 121-128.
- Haskell, N.A., (1953), "The dispersion of surface waves on multilayered media," *Bull. Seism. Soc. Am.*, **43**, 17-34.

- Haskell, N.A., (1960), "Crustal reflection of plane SH waves," *J. Geophys. Res.*, **65**, 4147-50.
- Hsieh, C.H., Lin, C.M., and Hsieh, S.H., (1994), "Seismic and well logging surveys in Taipei basin," *Proc. of the Joint Symposium on Taiwan Quaternary (5) and on Investigation of Subsurface Geology/Engineering Environment of Taipei Basin*, 185-191.
- Kagami, H., Duke, C.M., Liang, G.C., and Ohta, Y., (1982), "Observation of 1- to 5-second microtremors and their application to earthquake engineering, Part II: Evaluation of site effect upon seismic wave amplification due to extremely deep soil deposits," *Bull. Seism. Soc. Am.*, **72**(3), 987-998.
- Kagami, H., Okada, S., Shiono, K., Oner, M., Dravinski, M., and Mal, A.K., (1986), "Observation of 1- to 5-second microtremors and their application to earthquake engineering, Part III: A two dimensional study of site effects in the San Fernando Valley," *Bull. Seism. Soc. Am.*, **76**(6), 1801-1812.
- Kawase, H., (1996), "The cause of the damage belt in Kobe: the basin-edge effect, constructive interference of the direct S-wave with the basin-induced diffracted/Rayleigh waves," *Seism. Res. Lett.*, **67**(5), 25-34.
- Kuo, K.W., Shin, T.C., and Wen, K.L., (1995), "Taiwan strong motion instrumentation program (TSMIP) and preliminary analysis of site effects in Taipei basin from strong motion data," in *Urban Disaster Mitigation: The Role of Engineering and Technology*, Edited by F. Y. Cheng and M.-S. Sheu, Elsevier Science Ltd., 47-62.
- Nakamura, Y., (1989), "A method for dynamic characteristics estimation of subsurface using microtremor on the ground surface," *Quarterly Report of Railway Tech. Res. Inst.*, **30**(1), 25-33.
- Shin, T.C., (1993), "Progress summary of the Taiwan Strong Motion Instrumentation Program," *Symposium on Taiwan Strong Motion Instrumentation Program*, 1-10.
- Teng, L.S., Wang, S.C., Chang, C.B., Hsu, C., Yuan, P.B., and Chen, P.Y., (1994), "Quaternary strata frame of the Taipei basin," *Proc. of the Joint Symposium on Taiwan Quaternary (5) and on Investigation of Subsurface Geology-Engineering Environment of Taipei Basin*, 129-135.
- Wang Lee, C.M., Cheng, Y.M., and Wang, Y., (1978), "Geology of the Taipei basin (in Chinese)," *Taiwan Mining*, **30**(4), 350-380.
- Wang Lee, C.M. and Lin, T.P., (1987), "The geology and land subsidence of the Taipei basin," *Memoir Geol. Soc. China*, **9**, 447-464.
- Wang, C.Y., Hsiao, W.C., and Sun, C.T., (1994a), "Reflection seismic stratigraphy in the Taipei basin (I) - Northwestern Taipei," *J. Geol. Soc. China*, **37**(1), 69-95.
- Wang, C.Y., Tsai, Y.L., Ger, M.L., and Chang, H.C., (1994b), "Investigation of Tertiary basement in Taipei basin using shallow reflection seismics," *Proc. of the Joint Symposium on Taiwan Quaternary (5) and on Investigation of Subsurface Geology-Engineering Environment of Taipei Basin*, 169-175.
- Wang, C.Y., Lee, Y.H., and Chang, H.C., (1996), "P- and S-wave velocity structures of the Taipei basin," *Symposium on Taiwan strong motion instrumentation program (II)*, Central Weather Bureau, 171-177.
- Wen, K.L., Peng, H.Y., Liu, L.F., and Shin, T.C., (1995a), "Basin effects analysis from a dense strong motion observation network," *Earthq. Eng. Struct. Dyn.*, **24**(8), 1069-1083.
- Wen, K.L., Fei, L.Y., Peng, H.Y., and Liu, C.C., (1995b), "Site effect analysis from the records of the Wuku downhole array," *Ter. Atm. Oce.*, **6**(2), 285-298.
- Wen, K.L. and Peng, H.Y., (1998), "Site effect analysis in the Taipei basin: results from TSMIP network data," *Ter. Atm. Oce.*, **9**(4), 691-704.
- Wen, K.L., Peng, H.Y., Chang, C.L., and Liu, L.F., (2000), "Site response in the Taipei basin from the 1999 Chi-Chi, Taiwan earthquake sequence," *Proceedings of international workshop on annual commemoration of Chi-Chi earthquake*, **1**, 305-316.

ESTIMATION OF 3D S-WAVE VELOCITY MODEL OF THE KANTO BASIN, JAPAN, FOR PREDICTION OF LONG-PERIOD STRONG GROUND MOTION

H. Yamanaka¹⁾, N. Komaba²⁾, and N. Yamada³⁾

1) Associate Professor, Dept of Environmental Sci. and Tech., Tokyo Institute of Technology, Japan

2) Graduate Student, Dept of Environmental Sci. and Tech., Tokyo Institute of Technology, Japan

*3) Post-doctoral Researcher, Disaster Prevention Research Institute, Kyoto University, Japan
yamanaka@depe.titech.ac.jp, komaban@depe.titech.ac.jp, yamada@egmdpri01.dpri.kyoto-u.ac.jp*

Abstract: We conducted microtremor array explorations of deep sedimentary layers of the Kanto basin, Japan, in order to estimate strong ground motion. 1D S-wave profiles for the sediments are deduced from inversions of Rayleigh wave phase velocities obtained from array records of long-period microtremors. Phase velocities obtained in previous explorations are also inverted to S-wave profiles using the same assumptions in the inversion. We constructed a 3D S-wave velocity model from the inverted profiles at more than 200 sites.

1. INTRODUCTION

Estimation of long-period strong ground motion is one of the important subjects in earthquake engineering for seismic design of large man-made structures. Since the 1985 Mexico earthquake, many studies were devoted to understand long-period strong motion observed at sites in the valley of the Mexico City. Recently, the importance of long-period motion was again recognized during the Tokachi-oki earthquake, when huge oil tanks were damaged by fire caused by sloshing of crude oil. Although several numerical studies could simulate long-period ground motion considering effects of deep sedimentary layers (e.g., Olson et al. 1996, Sato et al. 1999), quantitative reproduction of observed motion contains still difficult problems. This is mainly due to lack of our knowledge of physical parameters in subsurface structure at a target site. It is significantly crucial in three-dimensional numerical simulations of long-period ground motion in large basins. S-wave velocity distribution from the surface to basement which corresponds to the top of the Crust of the Earth is prepared in such a 3D simulation of long-period strong ground motion. S-wave structural data are usually derived from geophysical explorations. Among many geophysical explorations, it is recognized that the microtremor array technique is the most powerful and economic technique to know an S-wave velocity profile of a deep basin (e.g., Horike, 1985). In the method, Rayleigh wave phase velocity in the long-period range up to several seconds is derived from array observation of ambient noises for estimating an S-wave profile. Since the wave type and the period range used in the microtremor array exploration is the same as those in strong motion estimation. This can be regarded as one of the advantages of the methods over the other geophysical exploration techniques.

In this study, we conducted microtremor array explorations in the Kanto basin, Japan to estimate 1D S-wave velocity profiles of deep sedimentary layers over the basement with an S-wave velocity of about 3km/s. Combining with phase velocities in previous explorations, a new 3D S-wave velocity model of the deep basin is constructed.

2. MICROTRREMOR EXPLORATION

2.1 Method

Figure 1 shows the procedure of acquisition and processing of microtremor data in the microtremor array exploration. First we installed vertical seismometers in an array, and measured vertical microtremors simultaneously. Then, a frequency-wavenumber spectral analysis was applied to array data of microtremors. Once frequency-wavenumber (f-k) spectra have been obtained for various period ranges, we could estimate phase velocity at each period from a wavenumber for the maximum spectral peak of each f-k spectrum. Repeating these procedures for every f-k spectra, we obtained a phase velocity dispersion curve that corresponds to Rayleigh wave phase velocity.

Next, we invert Rayleigh wave phase velocity obtained from microtremor array data to a 1D S-wave velocity profile by an inversion method. Several inversion algorithms have been already developed in seismological community to know crustal and/or mantle structures using linearized least square approaches. In this study, we applied an inversion method based on genetic algorithms by Yamanaka and Ishida (1996). Unknown parameters in the inversion are S-wave velocity and thickness for each layer. P-wave velocity is derived using an empirical relation with S-wave velocity, and density is fixed in the inversion. An S-wave profile is estimated so as to fit observed phase velocity with calculated phase velocity for fundamental Rayleigh wave.

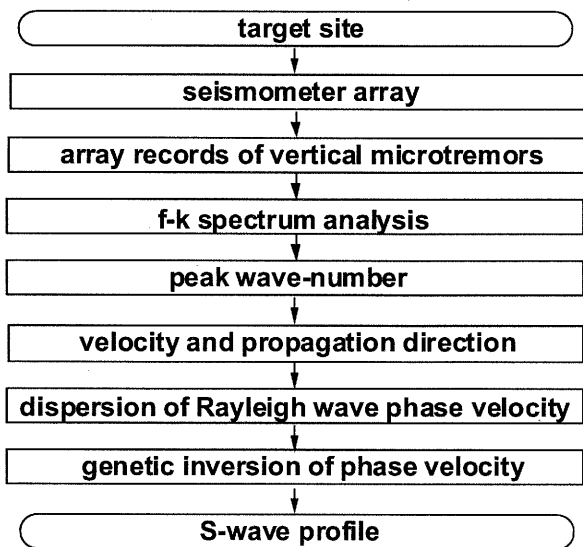


Figure 1 Flow of acquisition and processing microtremor data in microtremor array exploration. previous work and present study

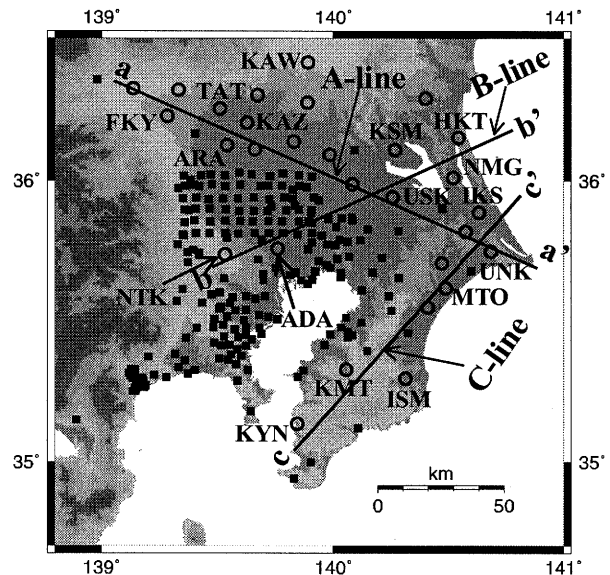


Figure 2 Map of locations of microtremor array explorations in Kanto basin, Japan. The solid and open circles indicate sites for the surveys in previous work and present study

2.2 Measurements

We observed microtremors in temporary arrays at 29 sites as shown in Figure 2. Since many microtremor explorations were conducted in the southwestern and central parts of the basin (Matsuoka et al., 1996; Yamanaka et al., 2000), we tried to make measurements in northern and eastern parts in this study. At each site, 2 arrays with different array sizes were deployed by installing 7 seismometers with station spacing of 0.3 to 3 km. An example of configuration of stations in these arrays is shown in

Figure 3. At each station, we installed an accelerometer or a velocity seismometer, an amplifier, and a digital recorder with a clock signal. Output signals from the amplifier were digitized every 0.01 sec. Recording was started with a timer and continued for 30 to 90 minutes in one array configuration. Figure 4 shows vertical microtremor records at USK and their spectra. We can see coherent waves in the records. Spectral amplitudes at the seven sites are also identical in wide period range. From the f-k spectral analysis we estimated Rayleigh wave phase velocity at each site. The Rayleigh wave phase velocities observed in this study are shown in Figure 5. The phase velocities are different at periods longer than one second indicating strong variation of subsurface structure.

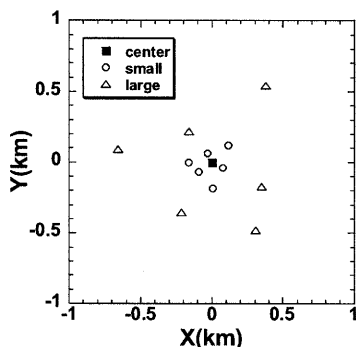


Figure 3 Example of arrays at USK

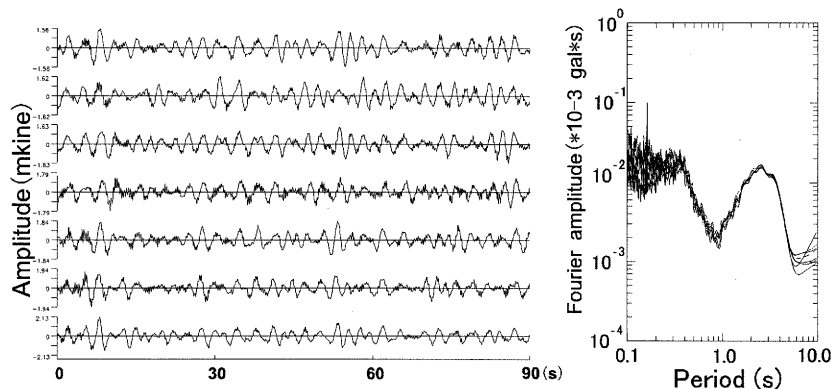


Figure 4 Example of array records and their spectra at USK

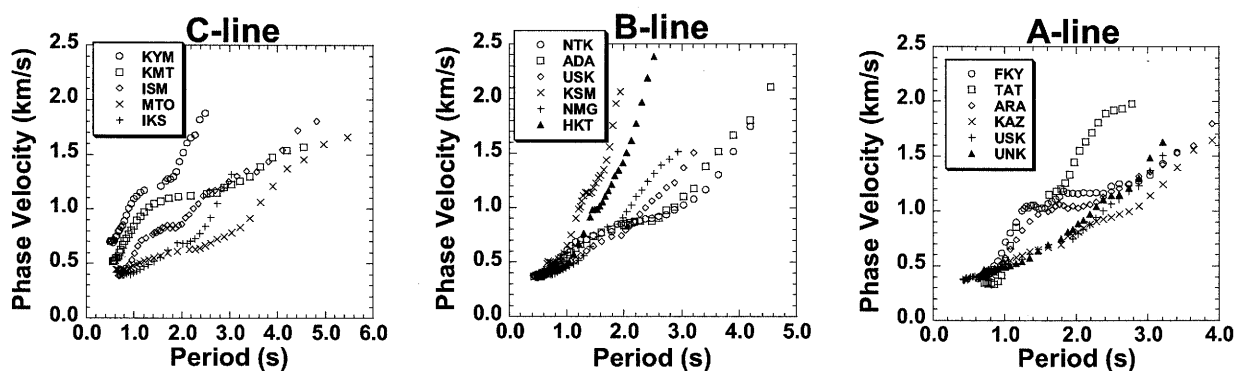


Figure 5 Comparison between Phase Velocities obtained in microtremor array explorations

2.3 Inversion of 1D S-wave profile

The phase velocity estimated at each site is inverted to an S-wave velocity profile by the genetic inversions. In the inversion of all the phase velocities, we assumed a 4-layers model, because there are 4 major geological formations in the area. They are, namely, Quaternary layer, two Tertiary layers and basement. A 1D S-wave profile is determined with the genetic inversion of phase velocity. Figure 6 shows the inverted S-wave profile and the comparison between the observed and theoretical phase velocities at USK. The theoretical phase velocity well explains the observed one.

All the phase velocities obtained in this study were inverted to 1D S-wave profiles. The profiles along the three lines in Figure 2 are displayed in Figure 7. S-wave velocity profiles along the A-line and C-line indicates a typical basin shape, which is characterized by deepest sediments at ARA and KMT. The Vs-profile at northeastern end of the B-line has the minimum depth to the basement near the Tsukuba Mountain which is covered with granite.

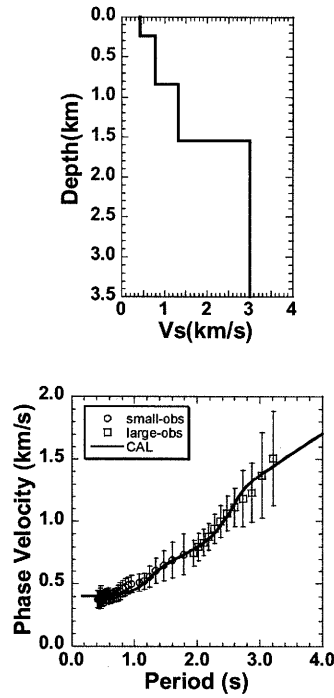


Figure 6 Inverted S-wave profile and comparison of observed and calculated phase velocities at USK.

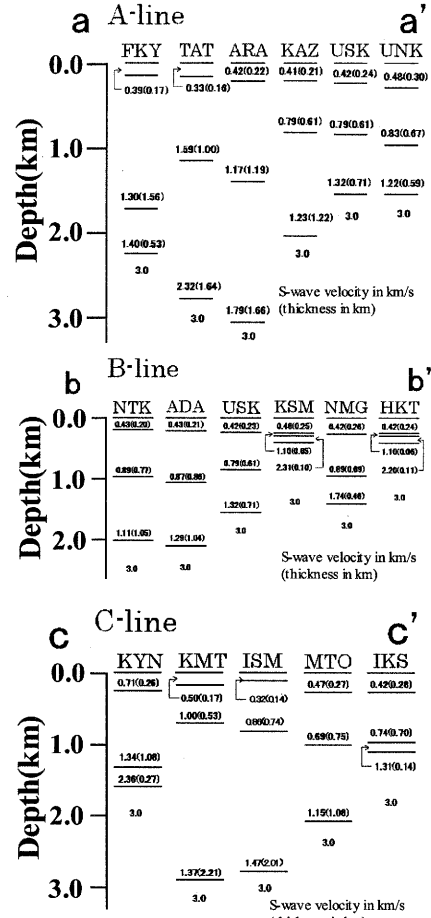


Figure 7 S-wave profiles inverted from phase velocities.

3. CONSTRUCTION OF 3D S-WAVE VELOCITY MODEL

3.1 Data

Microtremor explorations were conducted in the Kanto plain by several researchers (e.g., Kanno, 2000, Matsuoka et al, 2002; Yamanaka et al, 2000) and local governments, such as Tokyo Metropolitan Government, Kanagawa and Chiba prefectures, and Yokohama and Kawasaki cities. In particular, number of the explorations has been increased rapidly since 2000, because the Japanese government supports financially local governments to promote geophysical explorations including microtremor array explorations in order to provide basic information on deep basin structure.

We collected Rayleigh wave phase velocity data from the previous microtremor array explorations in order to construct a 3D S-wave velocity model only from Rayleigh wave phase velocity. The locations of sites in the microtremor array explorations where the phase velocity was collected are shown in Figure 2. Totally we could get the phase velocities at the 232 sites in the area, including the sites discussed above. Since period range and interval of the phase velocities collected are not the same, we interpolate the phase velocity at the same period interval. Figure 8 shows the average and the standard deviation of the Rayleigh wave phase velocity. The phase velocity was obtained in a period range from 0.6 to 5 seconds at many sites. The data are not enough at periods of more than 5 seconds. Probably, this is due to reduction of power of microtremors in the period range. The standard deviation is large in a period range from 1 to 5 seconds, suggesting the wide variation of the phase velocity.

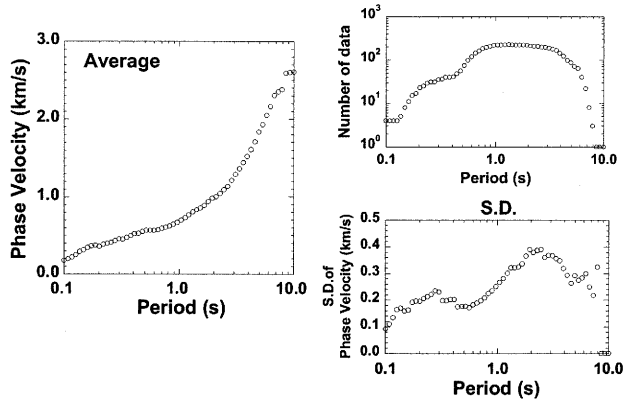


Figure 8 Averaged Rayleigh wave phase velocity in Kanto basin with their standard deviation. Number of phase velocity data at each period is also shown

3.2 3D maps

The phase velocities obtained in the previous explorations were inverted to 1D S-wave profiles using inversion methods or forward modeling. However, assumptions and constraint conditions in the inversions of the phase velocity are significantly different in each exploration. This makes it difficult to unify the results of all the explorations for a 3D model. Therefore, we again invert the collected phase velocities with the same assumptions that we used in the genetic inversion explained above. A four-layer model is assumed in the inversions of the phase velocities at all the sites. Thickness of each layer and the S-wave velocity of the top layer are selected as unknown parameters and the other parameters are given in advance. The S-wave velocities assumed are 1.0, 1.5 and 3.0 km/s, considering the results of our inversions shown above.

Figure 9 shows the depth maps to the interfaces of the four-layer models obtained from the inversions. We assumed existence of no sedimentary layers in the mountain area in drawing the maps. The basement depth is the deepest at the eastern part of the basin. The depths to the other 2 interfaces are also deep in that area of the basin.

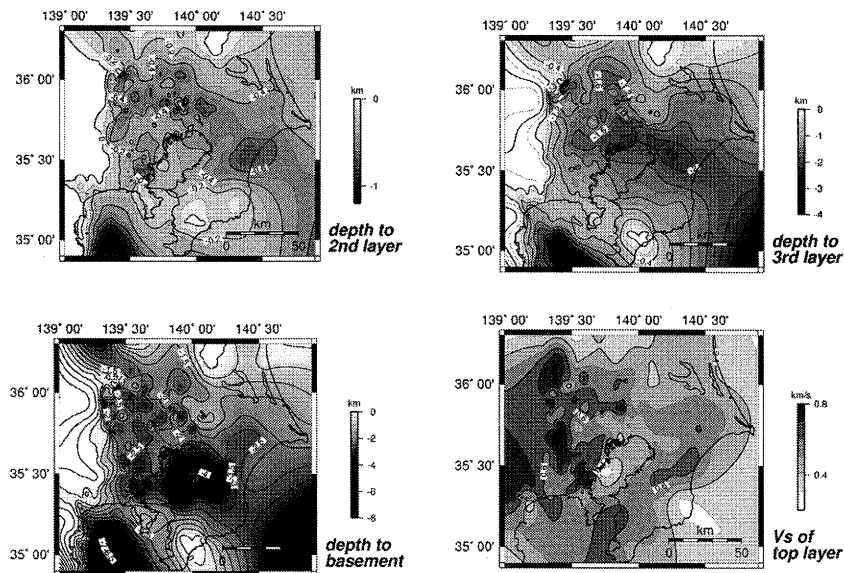


Figure 9 3D map for depths to the 2nd, 3rd layers and basement. Distribution of S-wave velocity for the top layer is also shown (lower left).

4. CONCLUSIONS

In this study, the microtremor array technique was applied to know deep S-wave profiles in the northern and eastern parts of the Kanto basin, Japan. The phase velocities of Rayleigh waves were newly estimated at 29 sites by the frequency wavenumber spectral analysis of array records of vertical microtremors at periods from 0.5 to 5 sec. Genetic inversion were, then, applied to the phase velocities to deduce 1D S-wave profiles of sedimentary layers down to a depth of the basement with an S-wave velocity of 3 km/s. A new 3D S-wave velocity model of the Kanto basin was constructed combining the existing phase velocity data with our observed data. We are now trying to simulate long-period earthquake motion in the basin by considering 3D basin structure similar to previous our work (Yamada and Yamanaka, 2000). Performance of the new model will be tested with comparison of observed ground motion with synthetic motion from a 3D calculation in the future work.

Acknowledgements:

A part of the phase velocity data were provided from Tokyo Metropolitan Government, Kanagawa, Chiba and Saitama prefectures, Yokohama and Kawasaki cities. We also thank Nippon Geophysical Prospecting, Tokyo Soil research for providing phase velocity data. This study supported by Special Project for Earthquake Disaster Mitigation in Urban Areas of the Ministry of Education, Science and Culture, Japan.

References:

- Horike, M. (1985). Inversion of phase velocity of long-period microtremors to the S-wave velocity structure down to the basement in urbanized area, *Jour. Phys. Earth*, 33, 59-96.
- Kanno, T. (2000). A study on design input motion considering deep subsurface structure, PhD thesis, Univ. of Tokyo, 1-164 (in Japanese).
- Matsuoka, T and Shiraishi H. (2002). Application of an exploration method using microtremor array observation for high resolution survey of deep geological structure in the Kanto plains, *Butsuri-Tansa*, 55, 127-143 (in Japanese).
- Matsuoka, T., Umezawa, N., and Makishima, H. (1996), "Experimental studies on the applicability of the spatial autocorrelation method for estimation of geological structures using microtremors", *BUTSURI-TANSA (Geophysical Exploration)*, 49, pp26-41 (in Japanese).
- Olson, K.B, and Archuleta, R.J. (1996), "Three-dimensional simulation of earthquakes on the Los Angeles fault system", *Bull. Seis. Soc. Am.*, 86, pp575-596.
- Sato, T, Graves, R.W. and Somerville, P.G. (1999), "Three-dimensional finite-difference simulations of long-period strong motions in the Tokyo Metropolitan area using the 1990 Odawara earthquake (Mj 5.1) and the Great 1923 Kanto earthquake (Ms 8.2) in Japan", *Bull. Seis. Soc. Am.*, 89, pp579-607
- Yamanaka H. and Ishida H. (1996). Application of genetic algorithms to an inversion of surface-wave dispersion data, *Bull. Seis. Soc. Am.*, 86, 436-444.
- Yamanaka, H. et al (2000) Exploration of basin structure by microtremor array technique for estimation of long-period ground motion. 12th World Conf. Earthq. Eng. CDROM, No.1484
- Yamada, N. and Yamanaka, H. (2000), "Three-dimensional finite difference simulation of long-period seismic wave propagation in the Kanto plain, Japan", submitted to 12WCEE, New Zealand.

ANALYTICAL INVESTIGATION INTO BAM EARTHQUAKE OF 26 DEC 2003 - IRAN

E.Ghanbari¹⁾

*1)Azad Islamic University of Tabriz Civil Eng. Dep.
ebghanbari@yahoo.com*

Abstract: The town of Bam with geographical coordinates of about 59° in eastern length and 28-29° latitude lies east south of Iran. Its distance to the border of Pakistan is about 370 km and to Tehran is about 6°, 51' and 11" and its height from high seas is 1050 m.

Bam devastating earthquake with the magnitude of 6.5 degree on the scale of Richter which occurred on December 26 2003 caused killing of about 28000 people, wounding of 25000 persons. It made the rest 90 percent of residents in the town and its suburbs homeless, collapsing and devastating 85-90 percent of urban buildings and structures.

The region of Bam is located between two large tectonic Lut depression at the north and Jazmourian depression at the south.

Two main tectonic elements of Lut block and the zone of flysch extends to out of central Lut and includes the main part of eastern state of Iran.

The block of Lut which Bam town resides in its western edge is an extended part with northern extension surrounded with different unstable faults which faults are often at the raw of seismic faults.

Lut block extends to the more than 800 km from Jazmourian depression at the south to the region of Gonabad in Khorasan at the north. The average width of it in the central part and south is about 200-250 Km. Its western border is performed by an extended and main fault called Nayband. If we study the movement and action of Nyband fault, it is observed that it has experienced the segmentation of strike - slip fault, and faulting series of 1978-2004 is one of the most obvious type of segmentation which is observable on the ground and any segment of it has been activated at one time and this activity has been accomplished from north to the south, i.e. from Tabas city towards the country of Nayband (Nayband seismic fault is nominated through the same country) and from Nayband towards Shahdad and from there towards Bam.

1. INTRODUCTION

Earthquakes occur in narrow belt. Major earthquakes resulting from slip along a fault plane are commonly measured by a Richter Magnitude.(Figure 1) shows the distribution of large and moderate sized earthquakes that occurred between 1900-2000 in IRAN.

IRAN is situated within the Alpine – Himalayan seismic belt and is characterized by high level of seismic activity. The central part of Iran particularly Kerman province and south the Khorasan is characterized by a moderate to high level of seismicity and several complex seismotectonic environments. According to a tectonic hypothesis. The movement of African Plate towards the Touran Plate , pushing the Arabian plateau and southwest of Asia, leads to the creation of faults and rupture on the earth crust in the zone including Iran.

Central part of Iran especially the region of Tabas to Bam city has a high density of Neogene - Quaternary faults and frequent destructive earthquakes which reactive some existing faults at the surface.

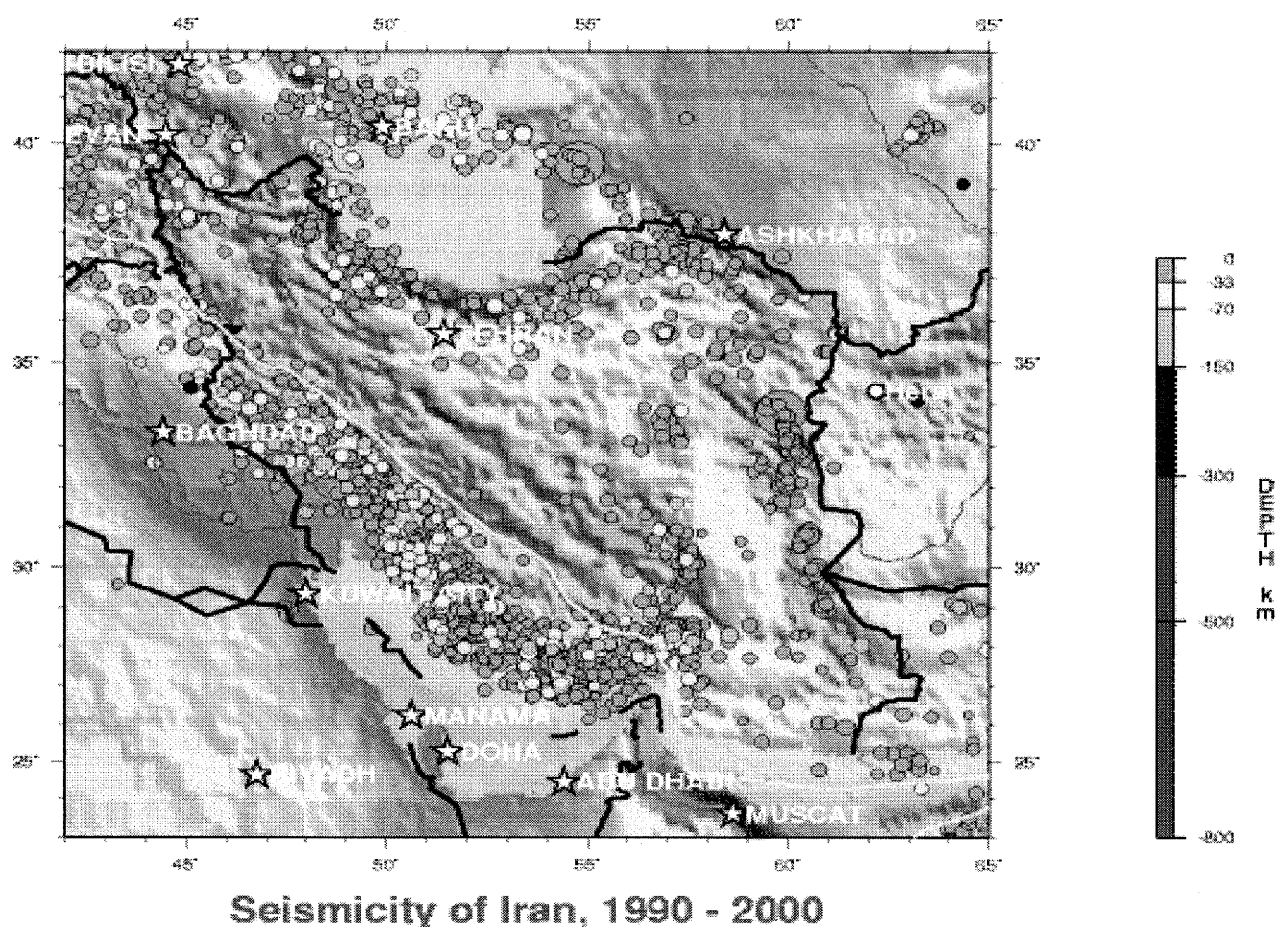


Figure 1 Distribution of large and moderate sized earthquakes that occurred between 1900-2000 in IRAN.

The region of Bam is located between two large tectonic Lut Depression at the north and Jazmourian depression at the south.

Two main tectonic elements of Lut block and the zone of flysch extends to out of central Lut and includes the main part of eastern state Lut and includes the main part of eastern state of IRAN. The Block of Lut which Bam town resides in the western edge is an extended part with northern extension surrounded with different unstable faults which faults are often at the raw seismic faults.

Lut block extends to the more than 800 Km from Jazmourian depression at the south to the region of Gonabad in Khorasan at the north. The average width of it in the central part and south is about 200-250 Km.

Its western border is performed by an extended and main fault called Nayband – Bam fault. If we study the movement and action of Nayband – Bam fault, it is observed that it has experienced the segmentation of strik – slip fault, and faulting series of 1978-2004 is one of the most obvious type of segmentation which is observable on the ground and any segment of it has been activated at one time and this activity has been accomplished from north to the south. I.e from Tabas city towards the country of Nayband (Nayband seismic fault is nominated through the same country) and from Nayband towards Shahdad and from there towards Bam town.

Paleoseismicity and Newseismicity of the southeast of IRAN

Unit the last few years, seismicity in IRAN was mainly characterized through two kinds of data: 1. Historical data, and 2. Instrumental data. For the last three decades, however, In such areas with strong and moderate seismicity and present – day deformation, this period of observation is

certainly representative of long – term activity. It has therefore been necessary to implement new studies in order to define and analysis seismic events older than the historical period, I, e. paleoearthquakes. Paleoseismicity is the study of these ancient earthquakes using the traces they have left in geological terrain (surface ruptures or paleoliquefaction – in this paper we deal with surface ruptures only).

Large parts of Iran are seismically very active. In highly seismic zones, paleoseismicity has been used for many years to fill in the gaps in our knowledge of active structures (i, e Cabrera Nunez, 1988, or the summary articles by Vittori et al 1991 and Weldon 1991).

In the past few years such studies have been carried out in various areas in Iran following major earthquakes, in order to determine whether similar events had already occurred. Under these conditions, the parallel study of recent seismic events and of paleoseismic trenches enables of severe earthquakes on the structure being studied and trough comparison, to attempt to quantify these events. Studies of surface ruptures observed during recent earthquakes have evidenced very rapid variations of the value of displacement along the active fault: variation in vertical displacement during the Bam earthquake, depending on the topography; the Bam fault has created a major topographic dislocation in the eastern Bam plain towards Baravat. (Figure 2).

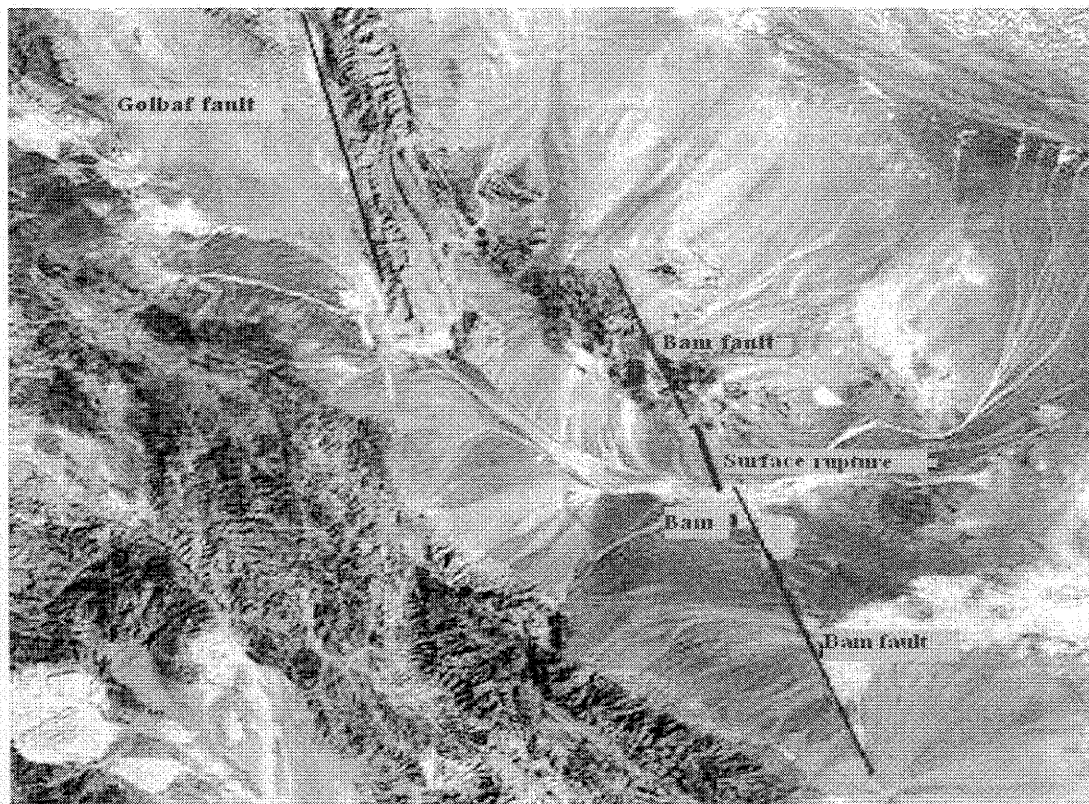


Figure 2 Satellite map of the area –Bam and Golbaf faults are indicated.

This fault scarp, shows the vertical displacement of about 10 to 20 meters in different places (M. Zare and H. Hamzehloo 2004), Regarding seismotectonics maps of IRAN and active faults and seismic areas in the north, northwest, east, and especially east and central of Iran has located Iran among the most instable of world's country. More than 8 destructive earthquakes, listed below, have been reported during a 50 - year period in the history of southeast and central part of Iran.

- 1- The Dasht – Bayaz earthquake 31 August 1968 $M_s = 7.2$.
- 2- The Tabas Earthquake is September 1978 $M_b = 7.7$.
- 3- The Qainat earthquake 13 November 1979, $M_b = 6.6$.
- 4- The Qainat (Kowlivillage) 26 November 1979, $M_b = 7.1$

5- The Golbaf earthquake 11 June 1981, Ms= 6.6

6- The Sirch earthquake of 28 July 1981, Ms = 7.

7- The North Golbaf earthquake (Fandogha) of 14 march 1998, Mw = 6.6

8- The Bam earthquake, 26 December 2003, Ms = 6.5

The trends of main faults (including the Bam fault) in Bam region and a rounded approximately are north - south and NW – SE, which are intersected by a fault in the western Lut block. The NW - SE faults (Kuhbanan and Ravar faults) and the north south faults (Nayband, Chahar – Farsakh, Anduhjerd, Gowk, Sarvestan and Bam faults) define the border of north – south structures in the Lut area, with the NW – SE structures. The Gowk fault system is recognizable for its surface ruptures during the 1981, 1989 and 1998 earthquake as well as a hot spring system.

Table1 Earthquakes greater than 6.25 Richter (Magnitude) occurred in Iran (area) between 1900-2004.

No	Date	Time (GMT)	Longitude	Latitude	Magnitude Mb	Focal depth Km	Place of occurrence	Damages and loses.
1	23 January 1909	02h48m18s	49°E	33°-5 N	7.4	25 Km	Dorud (Silakhor) (Zogross.SW.Iran)	5000-6000 people killed
2	12 Feb 1953	08h15m29s	54°5 E	35°N	6.25	12-18 Km	Torud (NE Great salt Kavir)	920 People were killed.
3	16Feb 1941	16h38m59s	58°7 E	33°3 N	6.25	12.18 Km	Eastern Central Iran	600 people were killed – destroyed 2500 houses
4	1Sep1962	19h20m38.75	49°9 E	35°6 N	7.25	20 Km	Buyin - Zahra SW of Tehran	12225 Killed, 2776 Injured damaged beyond repair 21,310 houses (294 villages)
5	31August 1968	10h47m, 37.4s	58°-60° E	34°N	7.2	15 Km	Dashlbayaz east.khorassan) province.	Killed more 10000 people damaged about 12000 houses.
6	April 1972	02h06m,52.9s	52°.79E	28°.43N	6.9	15-18 (shallow focal)	Qir (central Part of the Zagross active folded belt)	5000 people killed 1300, Injured 5000 houses destroyed
7	6 May 1930	22h34m, 27s	44°, 66°E	38°.22 N	7.2, 7.4	20-25 Km	Salmas Azerbaijan area	2514 killed 60 villages destroyed
8	1Jul 1995	-	-	-	7.3	20-25	Sangchal.	-
9	12Dec1995	-	-	-	7.2	20-25	Farsinaj	1130 Killed 200 villages destroyed
10	15 Aug 1956	-	-	-	6.7	20 Km	Nahavand (Firouzabad)	191 Killed 110 villages destroyed
11	20 Mars 1967	-	-	-	7		Bandar Abbass Khorgo	128 Killed.
12	15 Sep 1978	-	-	-	7.7	15-20	Tabas (Khorassan) North. Depression Lut	19600 Killed 16 villages destroyed.

Table1 Earthquakes greater than 6.25 Richter (Magnitude) occurred in Iran (area) between 1900-2004.

No	Date	Time (GMT)	Longitude	Latitude	Magnitude Mb	Focal depth Km	Place of occurrence	Damages and loses.
13	13 Nov 1979	-	-	-	6.6	15-20	Qainat	250 Killed.
14	26 Nov. 1979	-	-	-	7.1	15-20	Qainat (Kowli village)	130 Killed 150 Villages destroyed.
15	10 Jun 1981	-	-	-	6.7	15-20	Golbaf (Kerman province)	1.28 Killed destroyed the villages
16	27 Jul 1981	-	-	-	7.3	15-20	Sirj-Kerman	1300 Killed destroyed the villages
17	20 Jun 1990	-	-	-	7.4	20-25	Manjil – Roudbar (Zanjan – Guilan)	35000-40000 Killed The number villages and towns destroyed
18	26Dec 2003	05.26h	58°.01E	29°.01 N	6.5	10-12Km	Bam (Kerman)	28000-30000 Killed 25000 Persons wounding destroyed the number villages collapsing and devastating 85-90 percent of urban buildings

The major active faults and their relationship with the seismic hazard assessment of the southeastern in Iran.

Over the last three decades methods for assessing seismic hazards in engineering and other practical applications have continuously evolved. Because of the uncertain nature of the supporting seismic data and the changing needs of the community - such as the use of probabilistic risk analysis and risk - based regulations the predominantly deterministic approach of the early days is slowly being replaced the early days is slowly being replaced by probabilistic techniques.

Probabilistic techniques are highly data – Intensive and call for integrated multidisciplinary approaches to make maximum use of the available data.

The purpose of this presentation is to describe some of the limitations and identify the issues of importance in the assessment of seismic hazards in the southeastern and central Iran.

In this latter case, extensive Plio – Quaternary geology in investigations were performed which resulted in a better understanding of the potential occurrence of large earthquakes in the Tabas, Shahdad To Bam depression particularly southeastern areas of Iran.

A series of faulting events has happened during 1854- 2003 for example: The 27 may 1897 earthquake with magnitude $M = 5.7$ which affected a larger area, caused damage in the Kerman city. In 17 January 1864 the Chatrood earthquake ($M = 6.0$) occurred in the region. In April 1854 the Horjand earthquake ($M = 5.8$, $I = VIII$) occurred in northeast of Kerman. This catalogue shows that the earthquake had a same trend as Lakarkuh fault. Sirch earthquake is the largest event recorded instrumentally in the Kerman province (M. Mostafazadeh and other 2004) the large earthquakes in

1981 were associated with a total 64 km of fresh movements along northern end of Golbaf (gowk) fault and 10 Km in the segment of Lakarkuh fault. (Table 1)

A maximum vertical displacement of 10 Cm were observed east of Golbaf, whereas after the second shock displacement of 14 cm vertical and 20 cm. horizontal (Dextral) were measured near Chahar – Farsang and poshteh along the Lakarkuh fault system. (M.Mostafazadeh and other 2004).

Finally we can remind the last earthquake in bam city 26 Dec 2003 which occurrence trend to Bam fault.

Bam city is located in the seismic hazard zone of Iran. Many earthquakes have been recorded around Bam area, which was explained, but Bam city itself had no report of great historical before Dec 26 2003 earthquake. (Figure 3). Shows the historical and instrumental seismicity of the region According to the seismicity map, most of the major earthquakes occurred in the northwest region of Bam.

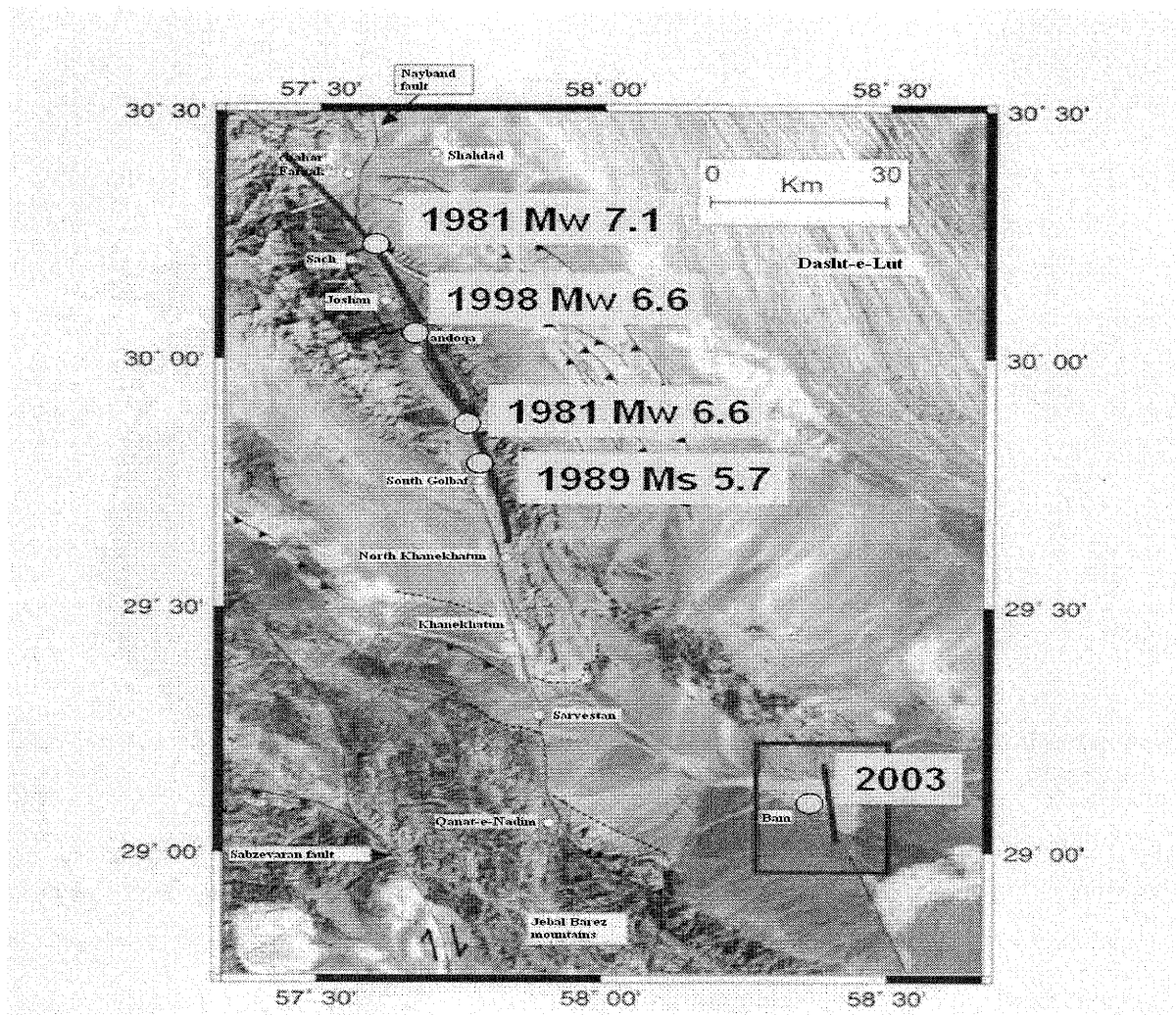


Figure 3 Recent major earthquakes in the region.
Main shock and aftershocks of the 26 December 2003 event

Average recurrence interval large earthquake in this region is estimated to be between 50-60 years.

More than 50-60 destructive earthquakes have beendescribed in the last & 1000-1200 years in the history of southeastern and central part of Iran.

2. CONCLUSIONS

Central part of Iran especially the region of Tabas to Bam region has a high density of Neogene - Quaternary fault and frequent destructive earthquakes which reactive some existing faults at the surface.

Its western border is performed by an extended and main fault called Nayaband – Bam fault. If we study the movement and action of Nayaband – Bam fault, it is observed that it has experienced the segmentation of strike - slip fault, and faulting series of long periods, is one of the most obvious type of segmentation which is observable on the ground and any segment of it has been activated at one time and this activity has been accomplished from north to the south, i.e. from Tabas city.

No surface - rupturing historic earthquake have been recorded on the Bam fault during the long period of the 2000 years of record keeping there.

However numerous trenches have been excavated across the fault and prehistoric earthquakes have been identified.

References:

- Ambrasey, N. N., Moinfar, A., (1973). The seismicity of Iran – the Silakhor (Lurestan) earthquake of 23 January 1909. *Ann di Geofis.*, 26 (4) p. 659-678.
- Ambraseys, N. N., Tchalenko, J. S. (1969). The Dasht- E – Bazaz (Iran) earthquake of August 31, 1968 a filed report, *Bull, seism. Soc. Am*; 59 (5). P. (75) – 1972.
- Ambraseys, N. N; (1974). Historical seismicity of north – Central Iran. In materials for the study of seismotectonics of Iran; North – Center Iran. *Geol surv. Iran. Rep* 29, p. 47-95.
- Ambraseys, N, N; A., Tchalenko, J. S., (1972). Ghir earthquake of 10 April 1972. UNESCO, SN 2789/RMO, RD / SCE. Paris 102 pp.
- Berberian, M., (1976). Contribution to the seismotectonics of Iran (part II). Geological Survey of Iran. Report No 39 516 pp.
- Bertrand Grellet, David Carbon and Philippe Combes (1995). Paleoseismicity studies in France main results. *Earthquake Hazard Assessment in Interplate regions*. Ouest editions, pp 25-33.
- Cabrera, Nunez J. (1988) Neotectonique et sismotectoniques dans La cordillere andine au niveau du changement de Geometrie de la subduction: La region de Cuzco (Perou), thesis, Docteur ES sciences of L'Univeriste de Paris – Sud, 275 pp.
- Ghanbari, E, Afshin, H, Hosseini, D (2004). Analytical investigation into Bam earthquake of Dec 2003- Iran. *Earthquake engine ring research center, Sahand university of technology. (EERC)* 112 pp.
- Ghanbari, E. (2004) The brittle faults and paleoseismicity and Newseismicity in the Azerbaijan Iran. “Colloque
- Ghanbari, E (2004) the analysis of earthquake risk and the periodicity of shakes along the Tabriz fault, inter conf on geotechnical Engineering, Geo-Beyrouth pp 883-886.
- Ghanbari, E (2004). Seismic Hazards of the Azerbaijan area and in the south Caspian sea. 13th world conference on earthquake engineering August 5-1st 6th Vancouver, British. Columbia, Canada.
- Gubbins, D (1990). *Seismology and plate tectonics*. Cambridge University press. Pp 339.
- Nadim, F; Dahle, A and Gudmestad, O. T. (1991) consistent treatment of Uncertainties in Earthquake Hazard evaluation. *Proceedings of the first international conference on seismology and earthquake engineering Vol (I)*. International institute of earthquake engineering and seismology (IIIES) pp 267.276.
- Vittori, E., S.S labini, and L. Serva (1991). “Paleoseismology: Review of the state of the art” *tectonophysics*, No 193, pp. 9-32.
- Welon, R. J. (1991). “Active tectonic studies in the united states, 1987-1990” *Reviews of Geophysics, supplement*, U.S.Nat, Report to INT. Union of Geodesy and Geoph 1987-1990, pp 890-906.
- Zare, M, and Hamzeloo, H (2004). A study of the strong ground motions of 26 December 2003 Bam earthquake *journal of Seismology and Earthquake Engineering. IIIES*. pp 33-56.

AN ESTIMATION OF SITE EFFECTS DURING THE 2004 NIIGATAKEN CHUETSU EARTHQUAKE BASED ON MICROTREMOR MEASUREMENTS

K. Motoki¹⁾, H. Yamanaka²⁾, K. Seo³⁾, N. Yamada⁴⁾, and S. Fukumoto⁵⁾

1) Research Associate, Dept. of Built Environment, Tokyo Institute of Technology, Japan

2) Associate Professor, Dept. of Environmental Science and Technology, Tokyo Institute of Technology, Japan

3) Professor, Dept. of Built Environment, Tokyo Institute of Technology, Japan

4) Research Fellow, Disaster Prevention of Research Institute, Kyoto University, Japan

5) Manager, Engineering Quarter of Tokyo Soil Research Co. Ltd., Japan

kmoto@enveng.titech.ac.jp, yamanaka@depe.titech.ac.jp, seo@enveng.titech.ac.jp,

yamada@egmdpri01.dpri.kyoto-u.ac.jp, fukumoto@tokyosoil.co.jp

Abstract: We performed mobile microtremor measurements to estimate site effects during the 2004 Niigataken Chuetsu earthquake around the center of Ojiya city and Kawaguchi town where are ones of the most damaged areas. We arranged measurement points around the strong motion stations and to cover over the center of Ojiya city and several residential areas in Kawaguchi town and Shidojima Town. Near Shinano River, the periods are shorter than 0.2 seconds or no significant peak in H/V spectral ratio, and in the western part of Ojiya basin, the periods are estimated longer than 0.4 seconds. Around K-NET station, the periods highly varied spatially, therefore it is said that the earthquake motion observed by K-NET were caused by the local site condition. In Kawaguchi, conspicuous peaks in H/V spectral ratio were recognized in severely damaged areas, and on the contrary, such peaks could not be found in relatively slightly damaged area. The result of microtremor measurements is effectively consistent with the distribution of the damage, and said that the effects of surface geology are related to the damage.

1. INTRODUCTION

The 2004 Niigataken Chuetsu earthquake with an Mj of 6.8 caused disastrous damage in buildings and civil engineering structures, for example, more than 2800 of wooden houses were completely collapsed (Fire and Disaster Management Agency 2005). The damage was the most devastating after the 1995 Hyogoken Nanbu earthquake and raised a formidability of an inland earthquake again. They widely appeared near the source region, concentrating in several isolated areas (Active Fault Research Center 2004). Even though this earthquake took place in the mountain area where residential clusters are rather sparse, the difference of the damage intensities due to their places emerged considerably. This phenomena implies that the characteristics of the strong motion projected the complication of the topography in mountain area. Earthquake motions were successfully recorded near the source region at 2 stations in Ojiya, at 1 station in Kawaguchi. These records are evaluated quite high in seismic intensity comparing to previous records, and the motion observed at K-NET Ojiya station was the highest of all records observed ever, especially in the shorter period range (Aoi et. al. 2004). Despite JMA Ojiya station is 1km distant from K-NET Ojiya station, JMA record show a difference in amplitude from the other. Furthermore, the damage looks slight for the seismic intensity at K-NET Ojiya and only a small number of data also makes it difficult to figure out strong motion characteristics spatially. In this study, we performed mobile

microtremor measurements to estimate site effects during the 2004 Niigataken Chuetsu earthquake around the center of Ojiya and Kawaguchi where are ones of the most damaged areas.

2. MICROTREMOR MEASUREMENTS

Microtremor Measurements were performed on 160 points (see in Figure 1) which were arranged to connect densely between the earthquake motion observatories of JMA Ojiya and K-NET Ojiya and to cover over the center of Ojiya city and some residential areas in Kawaguchi and Horinouchi. Tamugiyama, Budokubo, Kawaguchi and Wanazu in Kawaguchi town and Shindojima in Horinouchi town are ones of the most damaged areas where a lot of completely collapsed houses could be discerned. In particular, we found the damage in Tamugiyama and Budokubo is the most severe through this investigation. In Ojiya city, although some of collapsed buildings were seen the downtown area, we found the western part of the Ojiya basin is higher in the intensity of the damage than the downtown area. Most of the measurement points were placed on Alluvial deposits which have been formed by the erosion of Shinano River. They were conducted from October 27th to December 8th, 2004, before snow accumulation to avoid uncertain influences of snow to microtremors. We used velocity meter and accelerometer which are all useful in the period range from 0.05 to 5 seconds and measured microtremors for more than 5 minutes. We regarded high amplitude parts in time domain as noise and removed them and the rests were divided by a unit of 20.48 seconds and were picked up as samples. Then, we used FFT and smoothed spectra with a logarithmic window suggested by Konno (1995) and we calculated ensemble averages of

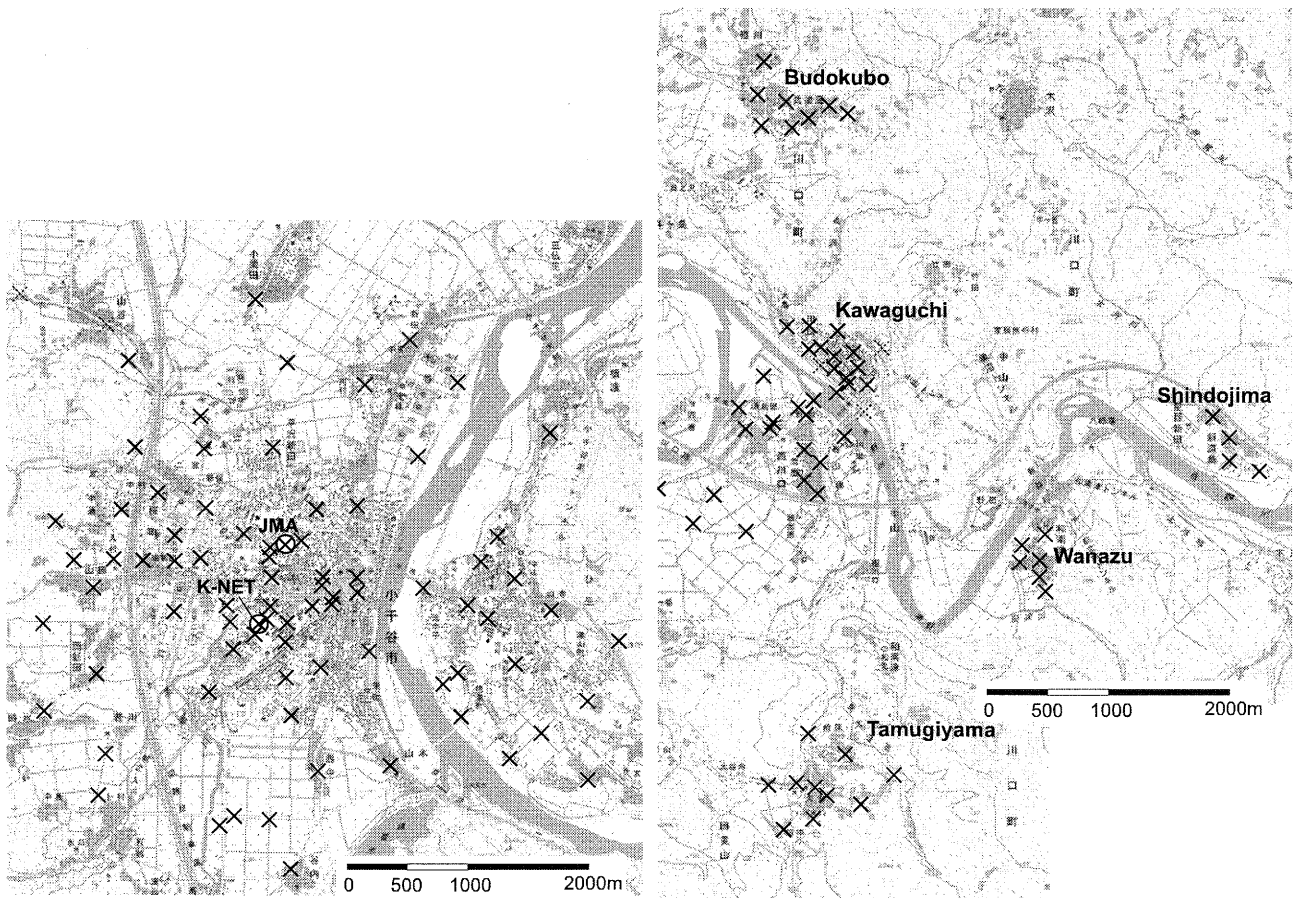


Figure 1 The distribution map of measurement points. Left figure shows around the center of Ojiya, and right figure shows around Kawaguchi town. Crosses indicate measurement points for microtremors and circles indicate strong motion stations.

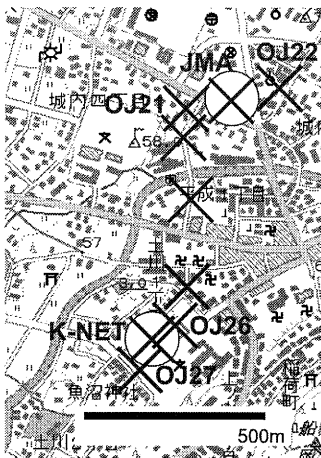


Figure 2 Closed up Fig. 1 around strong motion stations

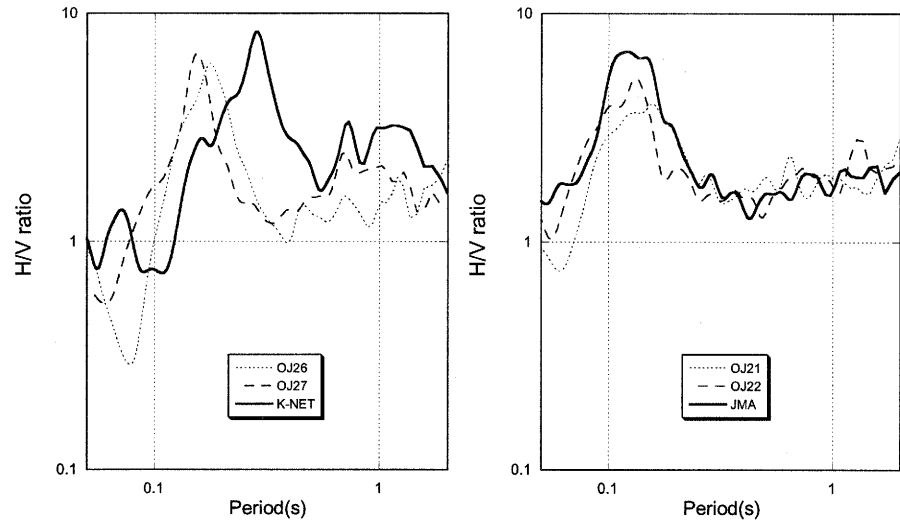


Figure 3 H/V spectral ratio of microtremors around K-NET Ojiya (left) and JMA Ojiya (right)

them of which the number is more than 3 per data at a point. We take advantage of horizontal to vertical amplitude ratio (H/V ratio) to estimate effects of surface geology during the 2004 Niigataken Chuetsu earthquake. A horizontal component was calculated with RMS of NS and EW components. The previous researches (e.g. Tokimatsu et. al. 1994, Konno and Ohmachi 1995 and Kawase and Tsuzuki 2005) said that H/V ratio is useful and consistent with its underground structure and the characteristics of earthquake motions. It is well known that H/V ratio demonstrate microtremors are mostly composed of the fundamental mode of Rayleigh wave, especially on a site which has a high contrast velocity profile. We took such characteristics of microtremors into consideration from both of amplitudes and periods of H/V ratio.

3. RESULTS AND DISCUSSIONS

We measured microtremors on 9 points on and around K-NET Ojiya and JMA Ojiya stations as shown in Figure 2 enlarged from Figure 1. Figure 3 (left) shows H/V ratios of microtremors around JMA and Figure 3 (right) shows ones around K-NET. The shapes of H/V ratios are similar around JMA, but we can recognize the difference in the peak periods in H/V ratios around K-NET. Midorikawa et. al. (2004) also pointed out that such characteristics vary drastically around K-NET and the velocity profiles on its borehole couldn't explain the period of about 0.3 second. This variation suggests that the underground structure of surface geology might be complicated and its own local site effect might be included in the strong motion recorded at K-NET. Lower amplitude due to the variation than K-NET earthquake motion were possibly raised as the reason why houses around K-NET were slightly damaged for the intensity of the record. H/V ratios are similar around JMA as mentioned above, and they are similar to ones measured around the center of Ojiya as well.

We plotted the peak periods in H/V ratio with the radius of the circles and drew contours of the period in Figure 4. Crosses in Figure 4 indicate stations at which a significant peak in H/V ratio could not be caught. In case an underground structure does not have the clear boundary at which the impedance suddenly changed, the shape of the H/V ratio will be vague (Tokimatsu et. al. 1994). It can be easily recognized that the periods are relatively short less than 0.2 second or no peak near Shinano River and the periods in western part are much longer than other in Ojiya basin. The longest period is around 0.7 second, which is longer than twice the period of K-NET. The nonlinear behavior were observed during this earthquake at K-NET station. Midorikawa et. al. (2004)

said the period were extended from 0.3 to 0.7 second. Figure 4 was based on microtremors and reflected the elastic characteristics of surface geology. Therefore, the predominant period during the main shock can be guessed longer than the periods in Figure 4. In Kawaguchi town, we could catch the peak in H/V ratio in the severely damaged area except for Kawaguchi. On the contrary, there is no peak in H/V ratio on other areas. Severely damaged area could be estimated to be located on soft soils. Pseudo response spectra of strong motions were shown in Figure 5. The motions recorded in Ojiya city has high amplitude in shorter period range than 1 second but the longer period range than 1 second predominated in Kawaguchi. These difference expresses Kawaguchi record has some effects not only surface geology. In that case, it is difficult to estimate site effect based on microtremors, however, Only an adding component of amplification in the short period range due to surface geology can be estimated.

Figure 6 shows the distribution of the peak value in H/V ratio. It is difficult to relate amplitude of H/V ratio to amplification factor during earthquakes directly (Konno and Ohmachi 1995, Kawase and Tsuzuki 2004). However, Konno and Ohmachi (1995) said that H/V peak value can be used for a calculation of site amplification when using a logarithmic window to smooth spectra. A composition ratio of Love wave is necessary to convert a peak amplitude to an amplification factor. In this paper, because of difficulty of the estimation, we treated a peak amplitude of H/V ratio as a relative site amplification factor. We can recognized that higher peak appeared in the western part of Ojiya basin similar to the distribution of the peak periods. From both of the peak amplitudes and periods, it can be considered that soft soil accumulated deeply in the western part as back marsh of Shinano River and these distributions really are consistent with damage. Such tendency can be also seen with an aftershock motion reported by Yamanaka et. al. (2004). In Kawaguchi, the distribution of the peak values were very similar result to the period as well as the result in Ojiya. The results

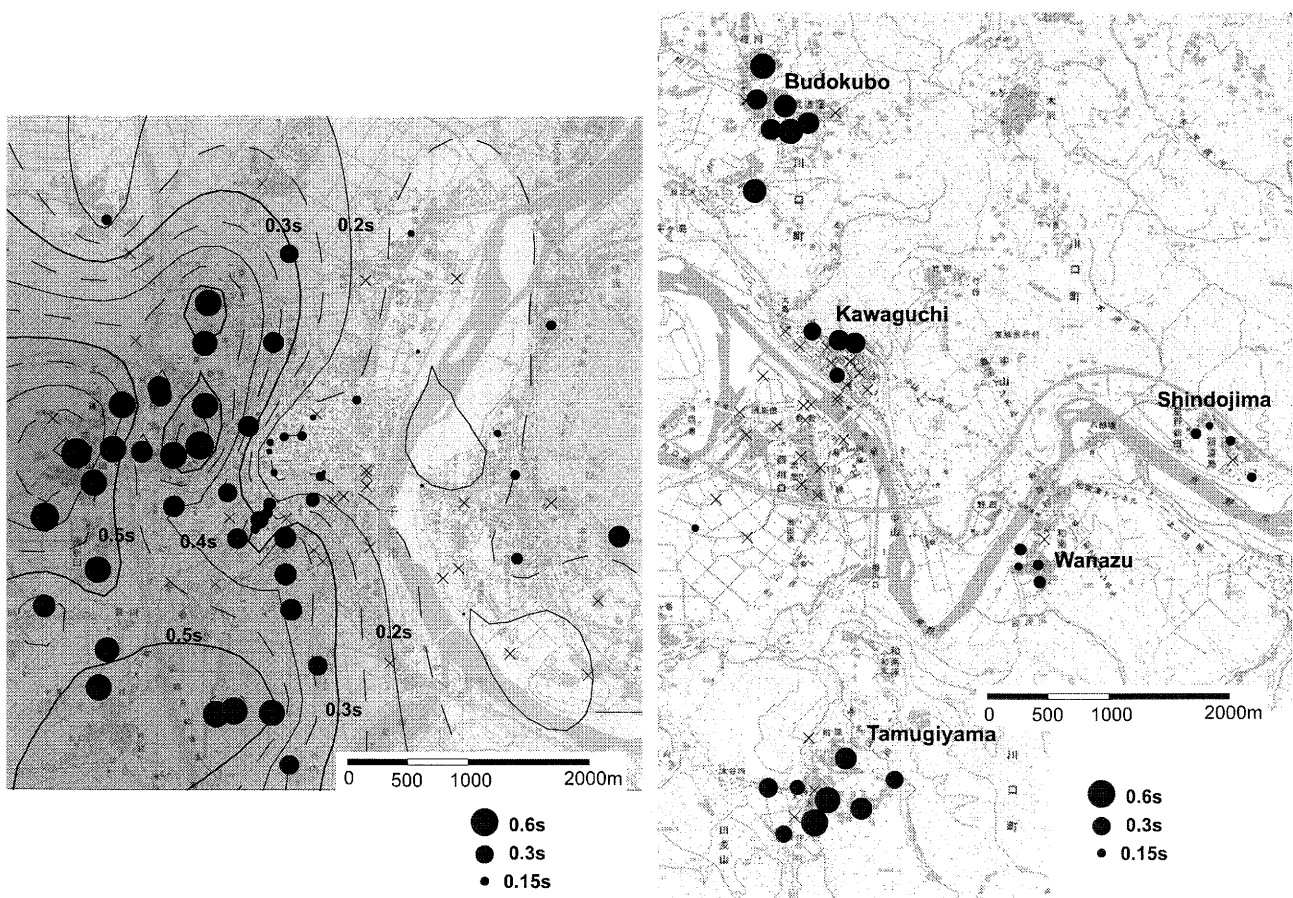


Figure 4 The distribution maps of peak periods of H/V ratio. Left figure shows around Ojiya city, and right figure shows around Kawaguchi town.

might not directly relate to site effects due to nonlinear effects and uncertain effects as mentioned above, but they correspond to damage distribution, and we are considering microtremors can be useful for a qualitative estimation during this earthquake. For a quantitative estimation, microtremors should be used as supporting data to extend the characteristics of underground structures at reference sites and earthquake motions.

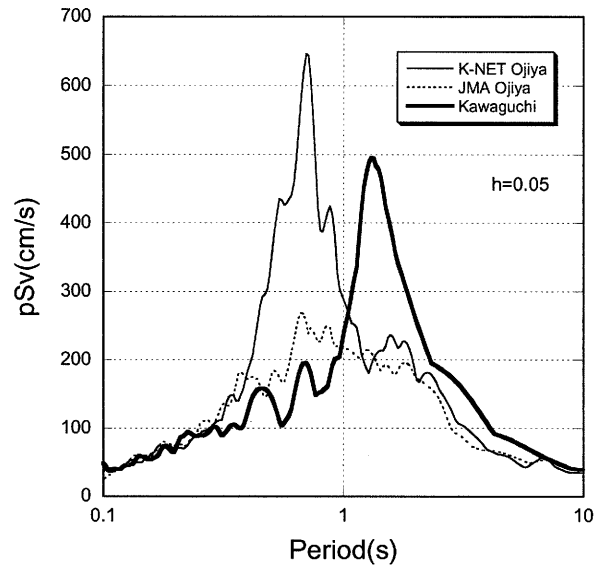


Figure 5 Pseudo response velocity spectra of strong motions during main shock. These are calculated with 5 % damping.

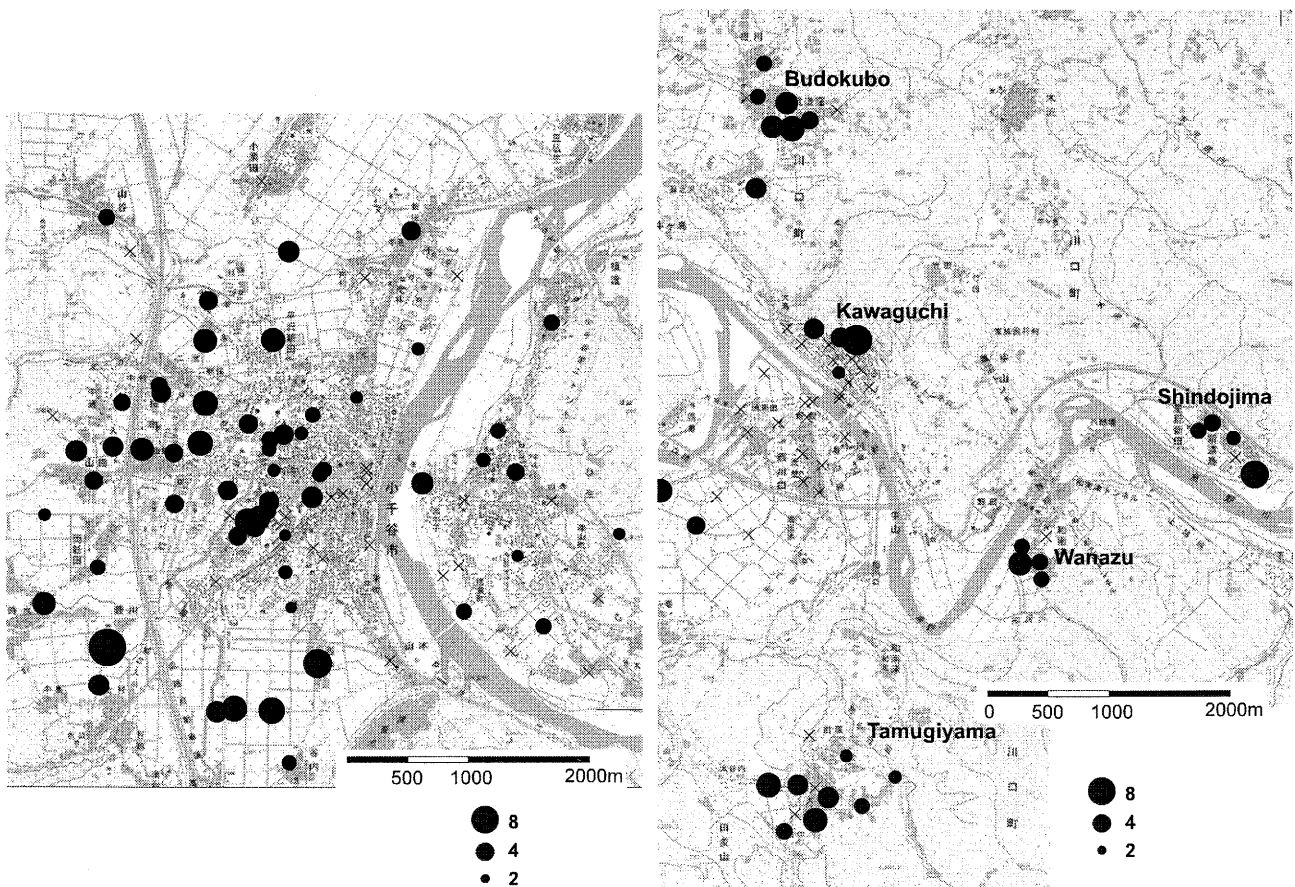


Figure 6 The distribution maps of peak amplitudes of H/V ratio. Left figure shows around Ojiya city, and right figure shows around Kawaguchi town.

4. CONCLUSIONS

We performed microtremor measurements focusing on the damaged area during the 2004 Niigataken Chuetsu earthquake in order to estimate site effects. From a variation of microtremors, K-NET site should be affected by its own local geology. JMA site has similar microtremors to the downtown area of Ojiya. The periods evaluated by microtremors are shorter than 0.2 second near Shinano River and the western part of Ojiya basin has longer periods and high site amplification. The peak periods and peak amplitudes of H/V ratio were correspond to damage intensity in both of Ojiya city and Kawaguchi town. A further direction of this study will be to provide more useful and reliable estimation combining with microtremor array measurements and aftershock observations.

Acknowledgements:

The strong motion data used in this study are provided by the K-NET of the National Research Institute of Earth Science and Disaster Prevention, and by Japan Meteorological Agency. This study was supported by the 21st COE Program "Evolution of Urban Earthquake Engineering" of the Ministry of Education, Culture, Sports, Science and Technology (MEXT) and the Grant-in-Aid for Special Purposes (16800054) titled "Urgent research on the Mid Niigata Prefecture Earthquake in 2004" of the MEXT.

Reference:

- Active Fault Reseach Center (2004), "Reconnaissance Report of Oct. 23, 2004, Mid-Niigata Earthquake", http://staff.aist.go.jp/yoshimi.m/damages_hp/index.html (in Japanese)
- Aoi, S., Morikawa, N., Honda, R., Sekiguchi, H., Kunugi, T. and Fujiwara, H. (2004), "Large Ground-Motion Observed during 2004 Niigataken-Chuetsu Earthquake", Summary on Reconnaissance Report of the 2004 Niigataken-Chuetsu Earhtquake, JAEE, 19-26 (in Japanese)
- Fire and Disaster Management Agency (2005), "The 64th Report of the 2004 Niigataken Chuetsu Earthquake", <http://www.fdma.go.jp/data/010500121630278280.pdf> (in Japanese)
- Kawase, H. and Tsuzuki, H. (2004), "Site Amplification Factors at K-NET Stations, Ground Structures, and H/V Ratios of Microtremors", Summaries of Technical Papers of Annual Meeting, AIJ, B-2, 671-672 (in Japanese)
- Konno, K. and Ohmachi, T. (1995), "A Smoothing Function Suitable for Estimating of Amplification Factor of the Surface Ground from Microtremor and Its Application", Journal of Structural Mechanics and Earthquake Engineering, JSCE, 525(I-33), 247-259 (in Japanese)
- Midorikawa, S., Miura, H. and Akiba, S. (2004), "The characteristics of strong motions during the 2004 Niigataken Chuetsu Earthquake", Research Reports on Earthquake Engineering, 92, 1-10 (in Japanese)
- Tokimatsu, K., Nakajo, Y. and Tamura, S. (1994), "Horizontal-to-Vertical Amplitude ratio of Short Period Microtremors and Its Relation to Site Characteristics", Journal of Structural and Construction Engineering, AIJ, 457, 11-18 (in Japanese)
- Yamanaka, H., Motoki, K., Fukumoto, S., Takahashi., H., Yamada, N. and Asano, K. (2004), "Estimation of Local Site Effects in the Ojiya City Using Aftershock Records of the 2004 Chuetsu Earthquake and Microtremors", Earth Planet Space, submitted

A BASIC STUDY ON ESTIMATION OF THE PHASE VELOCITIES OF MICROTREMORS USING TIME-FREQUENCY ANALYSIS

H. Morikawa¹⁾ and S. Udagawa²⁾

1) Associate Professor, Department of Built Environment, Tokyo Institute of Technology, Japan

2) Graduate Student, Department of Built Environment, Tokyo Institute of Technology, Japan

morika@enveng.titech.ac.jp, udagawas@enveng.titech.ac.jp

Abstract: The microtremors will provide useful information to estimate the ground velocity structure. For this purpose, many methods have been proposed, and almost methods of them assume that the microtremors are stationary processes. We, however, are afraid that the sources of microtremors might not be always stationary. Thus, to obtain more accurate estimations of phase velocities, we consider the non-stationarity of the microtremors and propose a method to find the stationary portions of microtremor data and to estimate the phase velocities directly by using the Hilbert-Huang transform (HHT) which is a method for the time-frequency analyses. Furthermore, the numerical simulations are carried out in order to examine the stability and applicability of the proposed method.

1. INTRODUCTION

The microtremors will provide useful information to estimate the ground velocity structure. For this purpose, we can apply the frequency-wave number (F-K) spectrum method or spatial auto-correlation (SPAC) method to obtain the phase velocities as the basic analyses. While these methods assume that the microtremors are stationary processes, the sources of them, which is, for example, sea waves, artificial causes such as automobiles and factories etc., are not always stationary. Thus, to obtain more accurate estimations of phase velocities, it must be effective to consider the non-stationarity of the microtremors. We will propose a method to find the stationary portions of microtremor data and estimate the phase velocities directly by using the Hilbert-Huang transform (HHT) which is a method for the time-frequency analyses. As the first step of this study, the possibility and applicability of the proposed method are demonstrated using some simple numerical examples.

2. HILBERT-HUANG TRANSFORM

To determine the non-stationarity and estimate the phase velocity of microtremors, we will apply the Hilbert-Huang transform (HHT) proposed by Huang et al. (1998). Before describing the method to estimate the phase velocity, the outline of HHT is summarized.

HHT is a one of methods for time-frequency analysis and Huang et al. have provided the various applications to analyze time histories, that is sea waves, earthquake ground motions, and so on (Long et al. 1995, Huang et al. 1996, 1999, 2001). This method can provide better

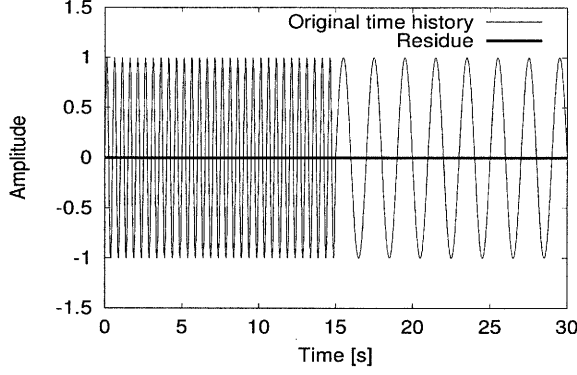


Figure 1 An original signal (Eq.(7)).

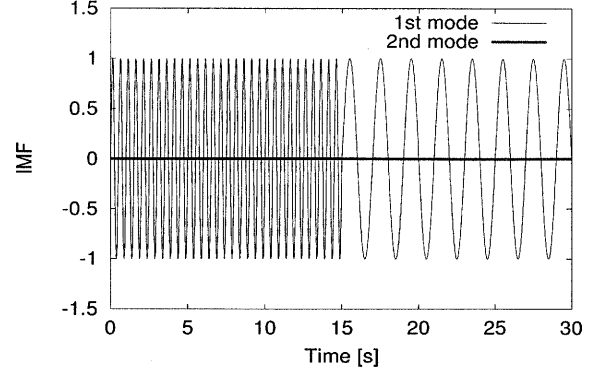


Figure 2 IMFs decomposed from the given signal.

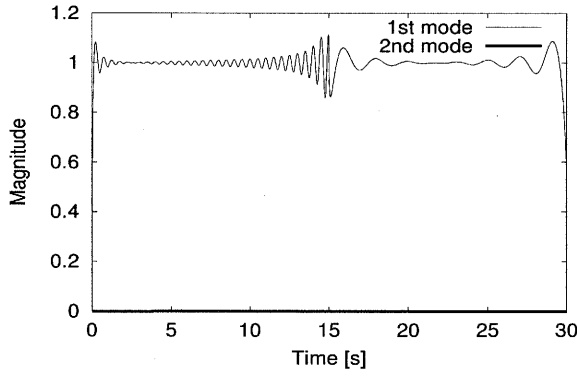


Figure 3 Amplitudes, $A_k(t)$.

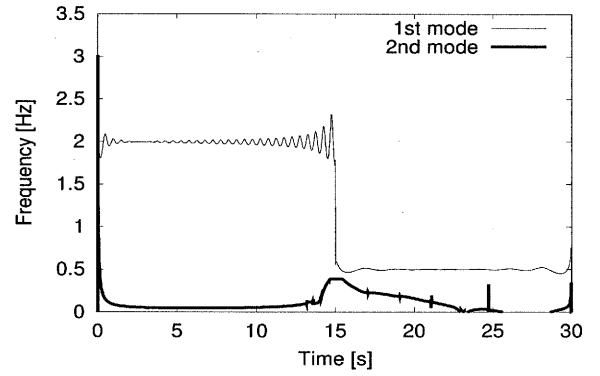


Figure 4 Instantaneous frequencies, $\omega_k(t)$.

resolution in time and frequency than the conventional methods for time-frequency analysis such as wavelet analysis (for example, Daubechies 1992), Wigner distribution (for example, Cohen 1995), etc.

Let us consider a complex time signal, $s(t)$ which are represented by

$$\begin{aligned} s(t) &= s_r(t) + js_i(t) \\ &= A(t)e^{j\phi(t)}, \end{aligned} \quad (1)$$

where $j = \sqrt{-1}$, $s_r(t)$, $s_i(t)$, $A(t)$, and $\phi(t) \in \mathbb{R}$, and

$$A(t) = \sqrt{s_r^2(t) + s_i^2(t)} \quad (2)$$

$$\phi(t) = \tan^{-1} \left(\frac{s_r(t)}{s_i(t)} \right), \quad (3)$$

in which $A(t)$ and $\phi(t)$ are amplitude and phase angle, respectively. The instantaneous frequency $\omega(t)$, which represents the frequency at time t , is defined as the follows (Cohen 1995):

$$\begin{aligned} \omega(t) &= \frac{d\phi(t)}{dt} \\ &= \frac{s_r(t)s_i'(t) - s_r'(t)s_i(t)}{A^2(t)}. \end{aligned} \quad (4)$$

In a case where $s(t)$ is a real signal, that is $s(t) = s_r(t)$, the instantaneous frequency obtained by Eq.(4) is zero at whole the values of t . To avoid this and get physically appropriate

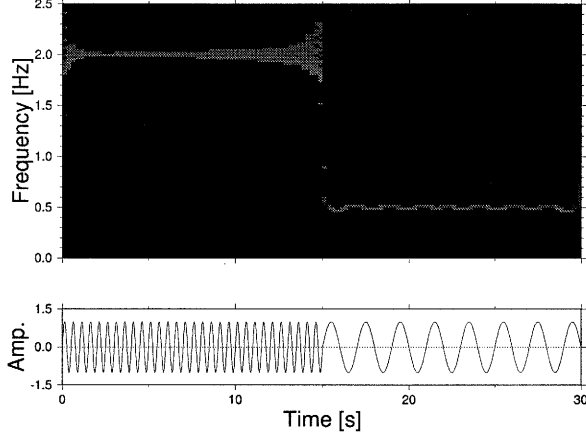


Figure 5 The time-frequency distribution of the signal Eq.(7). The lower pannel shows the original signal which is same as Fig. 1.

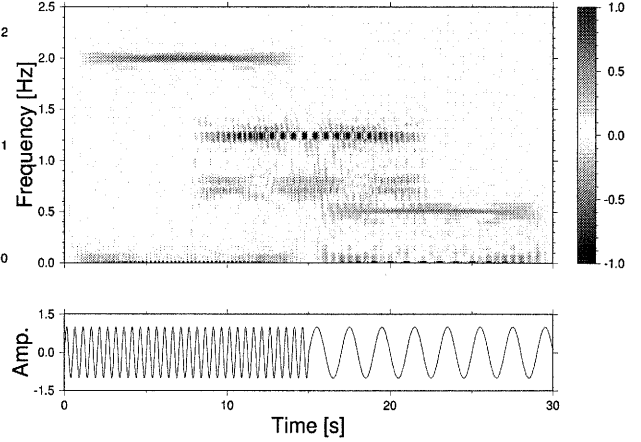


Figure 6 Wigner distribution of Eq.(7).

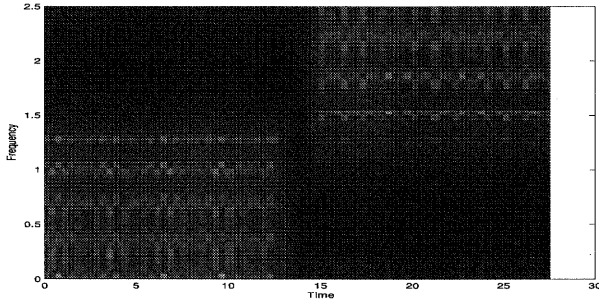


Figure 7 Spectrogram of Eq.(7). (length of time window: 2.048 s)

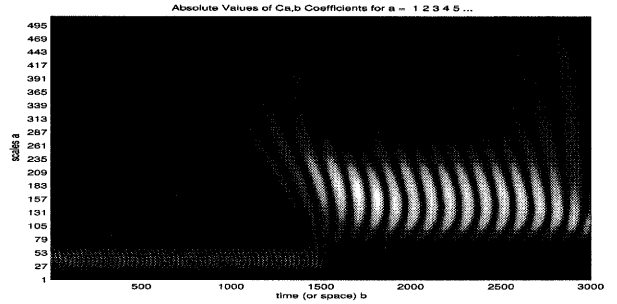


Figure 8 Wavelet transform of Eq.(7). (mother wavelet: Daubechies)

instantaneous frequencies, we have to give reasonably the imaginary part for the real signal $s_r(t)$. The imaginary part $s_i(t)$ can be set freely, though we will introduce a constraint: that is, the value of spectrum is zero for negative frequencies. Then, the imaginary part corresponding to $s_r(t)$ can be uniquely determined as the Hilbert transform of $s_r(t)$ (Cohen 1995);

$$s(t) = s_r(t) + \frac{j}{\pi} \int \frac{s_r(t')}{t - t'} dt'. \quad (5)$$

The complex signal composed by Eq.(5) is called “analytical signal” and we will deal with the analytical signal, hereafter.

According to Huang et al. (1998), to obtain the appropriate instantaneous frequencies, which should be reasonable with the physical meaning, the real signal is required to be locally symmetrical with respect to the axis of $s(t) = 0$. Thus, they proposed a procedure to calculate the intrinsic mode function (IMF) which local averages in time are zero.

In a case where a signal consists of some harmonic waves with various frequencies, the instantaneous frequencies cannot represent the appropriate frequency. This properties are presented as “paradoxes of instantaneous frequency” by Cohen (1995). Thus, to escape this problem, Huang et al. (1998) have proposed a method to decompose the the signal into some harmonic waves at each time. They call this technique “empirical mode decomposition (EMD).”

A real signal can be decomposed into some IMFs using EMD. Since the obtained IMFs are still real, Eq.(5) is applied to each IMF for obtaining the complex signals. For each analytical signal derived from IMF, the amplitudes $A_k(t)$ and instantaneous frequencies $\omega_k(t)$ are calculated by Eqs.(2) and (4), respectively, where $k = 1, 2, \dots, n$ denotes the number of IMFs.

Thus, a signal can be represented as

$$\begin{aligned} s(t) &= \sum_{k=1}^n s_k(t) = \sum_{k=1}^n A_k(t) e^{j\phi_k(t)} \\ \omega_k(t) &= \frac{d\phi_k(t)}{dt}. \end{aligned} \quad (6)$$

From this, the time-frequency distribution $U(t, \omega)$ can be defined as the value of $A_k(t)$ at $(t, \omega_k(t))$ ($k = 1, 2, \dots, n$).

To demonstrate the resolution of HHT, a simple example is shown. We analyze the following function:

$$x(t) = \begin{cases} \sin(2\pi t/2) & (\text{if } 0 \leq t \leq 15) \\ \sin(2\pi t/0.5) & (\text{if } 15 \leq t \leq 30). \end{cases} \quad (7)$$

The shape of Eq.(7) is shown in Fig. 1. Using EMD, two IMFs are decomposed from the original signal as shown in Fig. 2. The second mode of IMF, however, is obtained caused by the numerical error, because the amplitude for second mode is tiny (Fig. 3). Fig. 4 shows the instantaneous frequencies for each mode of IMF. From these results, the time-frequency distribution, $U(t, \omega(t))$ can be represented as Fig. 5.

To compare the differences among some methods for time-frequency analysis, we will show the results for same signal Eq.(7) in Figs. 6 to 8. From these figures, it is observed that HHT can provide the good resolution for time and frequency.

3. METHOD

3.1 Stationary Case

We consider that the microtremors are observed simultaneously at two sites with distance D . At first, it is assumed that the observed data are stationary. Since IMFs are obtained through the procedure of HHT, we will represent k -th IMF at site ℓ ($\ell = 1, 2$) as

$$s_{\ell k}(t) = A_{\ell k}(t) \exp[j\phi_{\ell k}(t)]. \quad (8)$$

Then, the instantaneous frequencies are derived as

$$\omega_{\ell k}(t) = \frac{d\phi_{\ell k}(t)}{dt}. \quad (9)$$

In a case where a harmonic component of microtremors propagates from site 1 to site 2, we may find an IMF $s_{2\hat{k}}(t)$ at site 2 which corresponds to $s_{1k}(t)$ at site 1. If the data of microtremors are stationary, the following relationships should be satisfied:

$$k = \hat{k} \quad (10)$$

$$A_{1k}(t) = A_{2k}(t) \equiv \tilde{A} \quad (\text{const.}) \quad (11)$$

$$\omega_{1k}(t) = \omega_{2k}(t) \equiv \tilde{\omega} \quad (\text{const.}) \quad (12)$$

$$|\phi_{1k}(t) - \phi_{2k}(t)| \equiv \tilde{\Delta}_\phi. \quad (\text{const.}) \quad (13)$$

From this, the apparent phase velocity, $c(\omega)$, between two sites 1 and 2 is derived from

$$c(\tilde{\omega}) = \frac{D \cdot \tilde{\omega}}{\tilde{\Delta}_\phi}. \quad (14)$$

The above conditions are not strictly satisfied for the numerical calculations, because of the numerical errors. Thus, the equation to estimate the apparent phase velocity is replaced by

$$c(\bar{\omega}(t)) = \frac{D}{2} \cdot \frac{\omega_{1k}(t) + \omega_{2k}(t)}{|\phi_{1k}(t) - \phi_{2k}(t)|}, \quad (15)$$

where $\omega_{1k}(t) \approx \omega_{2k}(t)$ and

$$\bar{\omega}(t) = \frac{\omega_{1k}(t) + \omega_{2k}(t)}{2}. \quad (16)$$

In this equation, the instantaneous frequencies $\tilde{\omega}$ of Eq.(14) are replaced by $\bar{\omega}(t)$ which is the average of instantaneous frequencies at two sites. The phase velocity should be constant analytically, but Eq.(15) suggests that it depends on time and may fluctuate over the time.

3.2 Non-Stationary Case

In a case where the data of microtremor are non-stationary, we have to pick up the stationary portion before estimating the phase velocities. It is assumed that the time-frequency distribution $U_\ell(t, \omega)$ at site ℓ ($\ell = 1, 2$) takes same values mutually in stationary portions: that is, the stationary space S are defined as

$$S = \{(t, \omega) \in \mathbb{R}^2; U_2(t, \omega)/U_1(t, \omega) \approx 1\}, \quad (17)$$

where we use “ \approx ” instead of “ $=$,” considering the numerical errors for the calculations. It is noted that the mode number of IMFs, k , are generally different between the sites 1 and 2, because the processes of the decomposition by EMD are different. Thus, the apparent phase velocities are estimated for stationary space S using the following equation:

$$c(\bar{\omega}(t)) = \frac{D}{2} \cdot \frac{\omega_{1k}(t) + \omega_{2\hat{k}}(t)}{|\phi_{1k}(t) - \phi_{2\hat{k}}(t)|}, \quad (18)$$

where $\{\omega_{1k}(t|t \in S) \approx \omega_{2\hat{k}}(t|t \in S)\} \in S$ and

$$\bar{\omega}(t) = \frac{\omega_{1k}(t) + \omega_{2\hat{k}}(t)}{2}. \quad (19)$$

To obtain the phase velocity, $c(\bar{\omega}(t))$, we have to search appropriate pairs of IMFs, $s_{1k}(t)$ and $s_{2\hat{k}}(t)$ on the stationary space, S , by trail and error.

In the following numerical examples, we consider the following range of $U_2(t, \omega)/U_1(t, \omega)$ to be stationary:

$$\frac{1}{2} < \frac{U_2(t, \omega)}{U_1(t, \omega)} < 2. \quad (20)$$

4. NUMERICAL EXAMPLES

4.1 Stationary Case

To verify the propriety of the method proposed in the previous section, some simple numerical calculations are carried out. For the stationary case, the data of microtremors are simulated as the time series which consists of three harmonic waves with the properties as shown in Table 1. The sample waves at sites 1 and 2 are shown in Fig. 9. In this simulation, the distance between sites 1 and 2 is 100m.

Table 1 Specifications for a sample of microtremors. (stationary case)

Frequency [Hz]	0.5	1.0	2.0
Phase velocity [m/s]	1000	500	333

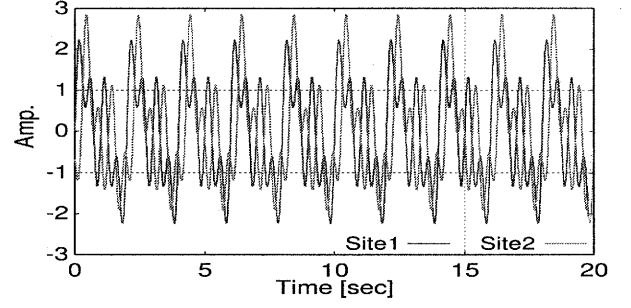


Figure 9 Sample data of microtremors observed simultaneously at sites 1 and 2. It is assumed that the time histories are stationary.

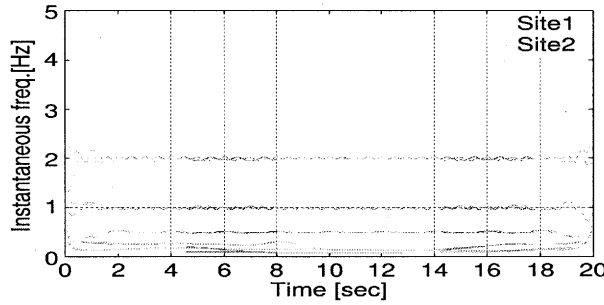


Figure 10 Instantaneous frequency of Fig. 9.

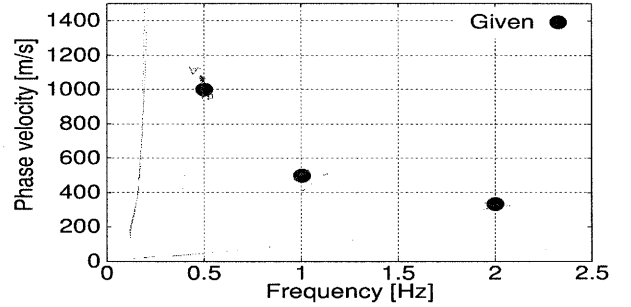


Figure 11 The apparent phase velocities estimated by using the technique of HHT. (stationary case)

Following the procedure of HHT mentioned in the previous sections, the instantaneous frequencies are calculated as shown in Fig. 10. Although three harmonic waves are contained in the sample waves, four or five IMFs are detected. However, the insignificant IMFs have small amplitude and are negligible as discussed for Fig. 3. It is observed that the instantaneous frequencies are accurately estimated at 0.5, 1.0, and 2.0 Hz.

Using the above results, the apparent phase velocities are estimated by Eq.(15). Fig. 11 shows the estimated phase velocities, $c(\bar{\omega}(t))$. In this figure, the given values shown in Table 1 are also plotted. It is observed that $c(\bar{\omega}(t))$ fluctuates around the given values because of the numerical errors. The almost all estimated values, however, are concentrated into the given value and the center of the cluster composed by the estimated values corresponds the given value. From these remarks, one may say that the proposed method can provide the good estimators for the phase velocities.

However, we may find some problems to resolve. The estimated values are scattered much more at 0.5 Hz than 1.0 and 2.0 Hz. This scatter is caused by the less of resolution for discrete time. Thus, we have to use higher sampling frequency to observe the waves in low frequency range. Since this is well-known property for the conventional methods to estimate the phase velocities such as SPAC and F-K method, etc., we can manage this problem.

The other problem is the errors in low frequency range and low phase velocities. It is considered that these errors are occurred by some numerical errors in the procedure for the calculations. We cannot divide into the signal and this type of noise in this time, unfortunately. Thus, some appropriate method should be developed to reduce the noises. We are understanding that this problem must be important to apply the proposed method to the actual microtremor data, though we will leave this problem for the future developments.

Table 2 Specifications for a sample of microtremors. (non-stationary case)

	0.5 [Hz]	1 [Hz]	1.5 [Hz]	2 [Hz]	3 [Hz]
	4000 [m/s]	1600 [m/s]	1000 [m/s]	600 [m/s]	400 [m/s]
0 to 5 [s]	✓	✓		✓	
5 to 10 [s]	✓	✓			
10 to 15 [s]	✓		✓		✓
15 to 20 [s]	✓		✓		

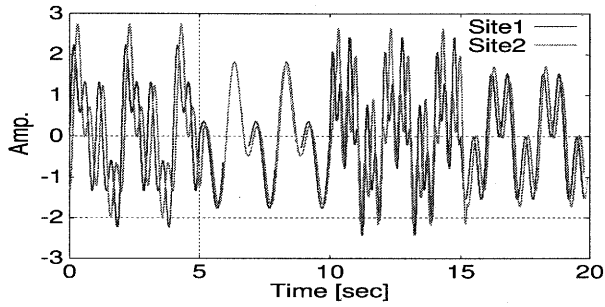


Figure 12 Sample data of microtremors observed simultaneously at sites 1 and 2. It is assumed that the time histories are non-stationary.

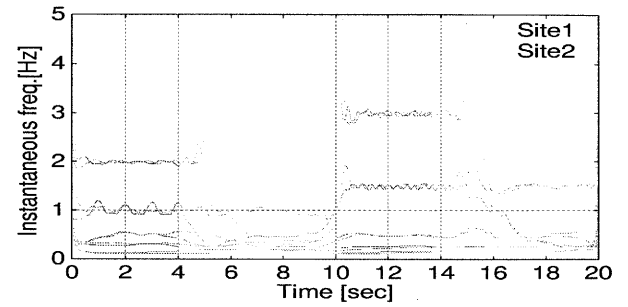


Figure 13 Instantaneous frequency of Fig. 12.

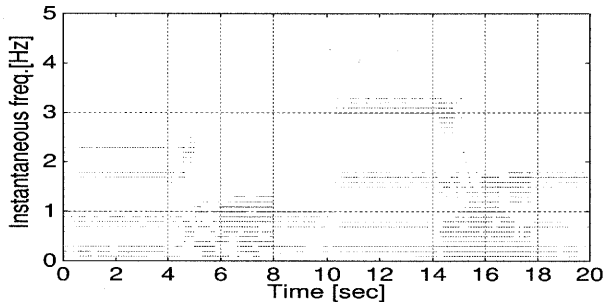


Figure 14 Stationary portions picked up from the time-frequency distributions at site 1 and 2.

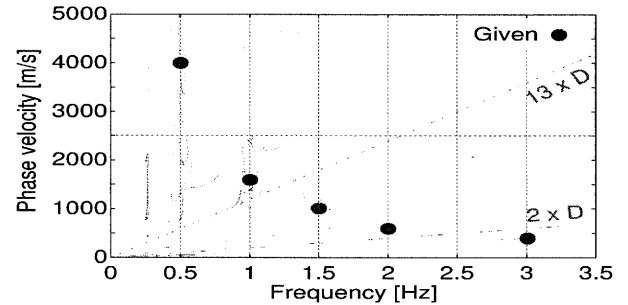


Figure 15 The apparent phase velocities estimated by using the technique of HHT. (non-stationary case)

4.2 Non-Stationary Case

In a case where a non-stationary time series are observed at two sites as shown in Fig. 12, which properties are listed in Table 2. In this sample, the frequencies of harmonic waves depend on time to represent the non-stationary time series. The various harmonic waves appear at the time windows which are marked by “✓” in the table.

The instantaneous frequencies of the time series at site 1 and 2 are shown in Fig. 13. It is observed that the non-stationary properties are detected well, comparing the obtained instantaneous frequency with Table 2. Following the procedure to choose the stationary space S , the stationary portions are picked up as the colored area of Fig. 14. Although the colored area should coincide with the given values listed in Table 2, the resolutions of the low frequency range are not good. This properties are relate partially to the procedure of HHT: namely, the harmonic waves are detected from higher frequency range.

On the basis of the picked up stationary portions and the instantaneous frequency at the corresponding time, the apparent phase velocities are estimated. The results of the estimation are shown in Fig. 15. In this figure, the estimated phase velocities are compared with the given ones of Table 2. It is observed that the estimated values agree with the given phase velocities

except for in the frequency range of less than 1 Hz, in which the sampling frequency of the waves is not enough to resolve the time differences between two sites. The dashed lines in this figure denotes the positions corresponding to the wave length with twice and 13 times of the distance between two sites. From some other numerical examples, it is found empirically that the good estimators of phase velocities are obtained between these two dashed lines.

5. CONCLUSIONS

We proposed a method to estimate the phase velocities using the one of time-frequency methods, that is Hilbert-Huang transform (HHT). A simple numerical example is shown to understand the properties of HHT. Then, the proposed method is applied to a dataset of artificial time series which properties are known. The numerical simulations for both stationary and non-stationary cases are carried out, and we have verified the stability and resolution of the proposed method through the numerical simulations.

On the other hand, some problems to resolve are revealed: the limitation of the resolution of discrete time, the reductions of noise which is infected during the numerical calculations, and so on.

To settle these problems are left for the future developments of the proposed method. Furthermore, we will apply the method to the actual data of microtremors and examine the validity and usability of the method.

References:

- Cohen, L. 1995. *Time-Frequency analysis*. New Jersey: Prentice Hall PTR.
- Daubechies, I. 1992. *Ten Lectures on Wavelets*. Philadelphia: Society for Industrial and Applied Mathematics.
- Huang, N.E., Long, S.R. & Shin, Z. 1996. The mechanism for frequency downshift in nonlinear wave evolution. *Advances in Applied Mechanics*. Vol. 32: 59-121.
- Huang, N.E., Shen, Z., Long, S.R., Wu, M.C., Shin, H.H., Zheng, Q., Yen, N.-C., Tung, C.C. & Liu., H.H. 1998. The empirical mode decomposition and the Hilbert spectrum for nonlinear and non-stationary time series analysis. *Proc. of the Royal Society of London*. Vol. 454: 903-995.
- Huang, N.E., Shen, Z., & Long, S.R. 1999. A new view of nonlinear water waves: the Hilbert spectrum. *Annu. Rev. Fluid Mech.* Vol. 31: 417-457.
- Huang, N.E., Chen, C.C., Huang, K., Salvino, L.W., Long, S.R., & Fan, K.L.. 2001. A new spectral representation of earthquake data: Hilbert spectral analysis of station TCU129, Chi-Chi, Taiwan, 21 September 1999. *Bulletin of Seismological Society of America*. Vol. 91, 1310-1338.
- Long, S.R., Huang, N.E., Tung, C.C., Wu, M.L., Lin, R.Q., Mollo-Christensen, E., & Yuan, Y. 1995. The Hilbert techniques: an alternate approach for non-steady time series analysis. *IEEE Geoscience Remote Sensing Soc. Letter*. Vol. 3: 6-11.

RECENT ACTIVITIES IN UNESCO RELATED WITH URBAN DISASTER MITIGATION

B. Rouhban¹⁾

1) Chief, Section for Disaster Reduction, National Sciences Sector, UNESCO

Abstract: The United Nations Educational, Scientific and Cultural Organization (UNESCO) is a specialized Agency which promotes sustainable development through activities in education, science, culture and communication. The purposes of UNESCO in the field of natural disasters are to promote a better scientific understanding of natural hazards and of their intensity, to help set up reliable observatory and early warning networks and systems, to encourage the establishment of rational land use plans, to promote the adoption of suitable building design, to contribute to the protection of educational buildings and cultural monuments, to strengthen environmental protection for the prevention of natural disasters, to enhance preparedness and public awareness through information and education, and to foster post-disaster scientific and technical investigation. The protection of urban areas is among the preoccupations of UNESCO's programs.

1. VULNERABILITY OF CITIES

Over half the six thousand million or so inhabitants of the earth are living in urban areas. In developing countries, more than two thousand million people live in the towns. Another thousand million live in the urban areas of the industrialized countries. Of the sixty cities with over five million inhabitants, close to forty-seven are located in the developing countries. This phenomenon, unprecedented in scale and linked to population growth and movements, has important implications for the environment and for the well-being of populations, and poses serious social as well as economic problems for the majority of countries. Above all it is increasing the exposure of the populations and of the physical and built environment to natural and anthropogenic hazards.

The trends in urban populations are accompanied by a radical upheaval in the very structure of the cities. The inability to control simultaneously land-use and the communication networks leads to a progressive exacerbation of cities vulnerabilities. Decried by some as places characterized by pollution, time-wasting difficulties, segregation, loneliness and insecurity, towns nevertheless remain, broadly speaking, the hub of cultural life, medical services, industrial production, public administration, education, research and information. They ought to be protected and preserved.

To date, planning has in most cases scarcely taken account of the complexity of the relationship between the town and the vulnerability to hazards; this is without doubt one of the major shortcomings. As they develop, towns come to neglect fundamental aspects of disaster risk reduction. A better understanding of the hazards and development of risk management measures should make it possible to reduce the vulnerability ensuring the well-being of the populations concerned and encourage the maintaining of a normal life in the town.

2. UNESCO'S MISSION

UNESCO, the United Nations Educational, Scientific and Cultural Organization, is engaged, since 1960, in the assessment and mitigation of risks arising from natural hazards of geological origin (earthquakes, tsunamis, volcanic eruptions and landslides), and contributes to the study of hazards of hydrometeorological origin (storms, floods, prolonged droughts, desertification and avalanches). The social and educational programmes also address the preparedness to/ and alleviations of consequences of/ disasters of technological origin.

The purposes of UNESCO in the field of natural disasters are to promote a better scientific understanding of the distribution in time and space of natural hazards and of their intensity, to help set up reliable observatory and early warning networks and systems, to encourage the establishment of rational land use plans, to promote the adoption of suitable building design, to contribute to the protection of educational buildings and cultural monuments, to strengthen environmental protection for the prevention of natural disasters, to enhance preparedness and public awareness through information and education, and to foster post-disaster scientific and technical investigation.

The action of UNESCO is placed in the framework of the International Strategy for Disaster Reduction. It will be intensified in the follow-up to the United Nations World Conference on Disaster Reduction (WCDR) which took place in Kobe, Hyogo, Japan from 18 to 22 January 2005. The Hyogo Framework for Action 2005-2015 which was adopted at the Conference gave priority to the intersectoral Thematic Cluster "Knowledge, Innovation and Education - building a culture of resilient communities", a cluster in which UNESCO acted as a lead agency.

Disaster reduction forms indeed an integral part of UNESCO's overall response to recent major United Nations Conferences including the Johannesburg World Summit on Sustainable Development held in 2002, the Small Islands Developing States Mauritius Meeting and the WCDR. UNESCO is an active member of the United Nations Inter-Agency Task Force on Disaster Reduction and a close partner to the UN/ISDR Secretariat and to other organizations and entities involved in the ISDR.

3. UNESCO'S PROGRAMMES

The scientific and technical work of UNESCO in disaster reduction is essentially promoted by its natural hazards programme, by its intergovernmental scientific programmes such as the International Geoscience Programme (IGCP), the International Hydrological Programme (IHP), the Man and Biosphere (MAB) Programme, the programmes of UNESCO's Intergovernmental Oceanographic Commission (IOC), the Management of Social Transformation (MOST) Programme and the activities on the applications of remote sensing and space technologies. Through these undertakings, UNESCO also contributes to the three global observing systems, the Global Ocean Observing System (GOOS), the global Climate Observing System (GCOS) and the Global Terrestrial Observing System (GTOS). These are joint initiatives of UNESCO, IOC, Food and Agriculture Organization (FAO), World Meteorological Organization (WMO), United Nations Environment Programme (UNEP) and the International Council of Scientific Unions (ICSU).

The Organization's activities in the Education Sector encourage the integration of disaster prevention into the school educational programmes. Information and communication programmes support public awareness and information related to disaster prevention and preparedness. The Culture Sector contributes to the protection and preservation of cultural monuments and sites including the World Heritage Sites.

4. EARTHQUAKE HAZARDS

Regarding earthquake risk, UNESCO encourages the establishment of international, regional and national centres, systems and networks for the exchange and analysis of earthquake data and training;

the identification of seismically active zones and the quantitative assessment of earthquake hazard in those zones; field studies of the effects of large earthquakes; exchange of experience among scientists and engineers, and the training of qualified personnel. Among the achievements is the promotion for the establishment of the International Institute of Seismology and Earthquake Engineering, Japan, the Institute of Earthquake Engineering and Engineering Seismology, Skopje, the International Seismological Centre, Newbury, United Kingdom, the Regional Seismological Centre for South America (CERESIS), Lima, the Earthquake Engineering Centre in Algiers, the International Institute of Earthquake Engineering and Seismology, Tehran. Regional initiatives include the regional seismological networks in Southeast Asia, the Balkan Region, the Programme for Assessment and Mitigation of Earthquake Risk in the Arab Region (PAMERAR) and the recent UNESCO/USGS programme on Reducing Earthquake losses in the Eastern Mediterranean Region (RELEMR) and Reducing Earthquake losses in the South Asia Region (RELSA). These projects help bringing together seismologists, geologists and engineers from neighbouring countries to define seismic risk on a regional basis and in terms directly applicable to earthquake-resistant design and construction, and to implement actions towards the reduction of this risk. In this context, specific study groups and projects relate to topics such as induced seismicity, strong ground motion, earthquake prediction, experimental sites for earthquake prediction, global seismic data bank, earthquake engineering, etc.

As an illustration of UNESCO's recent activities, a project entitled "Reduction of natural disasters in Asia, the Caribbean and Latin America" has yielded good practices. In partnership with the UN/ISDR, this project was carried out as a cross-cutting effort encompassing several sectors. The project has focused on four earthquake-prone cities. The overall purposes were to promote the development and application of wise disaster reduction practices by improving preventive action and disaster preparedness through community empowerment and elaboration, dissemination and application of prevention tools and information. To achieve its goal, the initiative worked in close collaboration with local authorities, experts, and institutions of selected cities in Asia and Latin America to a) evaluate the cities' existing development plans and determine their potential impact on the level of urban earthquake risk, b) utilize the cities' growth tendencies (demographic, economic) to estimate future earthquake risk if urban growth continues with the current characteristics, and c) identify feasible, effective mitigation options for each participating city and perform cost-benefit analyzes to determine the most efficient risk reduction activities for each particular city. The cities selected for the project were Antofagasta (Chile), Kathmandu (Nepal), and Tijuana (Mexico). In addition, the project has initiated links with the city of Dehradun (India). The UNESCO offices in Kathmandu, New Delhi, San José (Costa Rica), Mexico and Santiago (Chile) and the UN/ISDR office in San José have facilitated the project activities.

The project placed the participation of local communities at the centre of disaster reduction initiatives by promoting the empowerment and capacity-building of local government staff and stakeholders. This vocation was accomplished. The initiative produced urban planning mitigation options tailored to the particular needs and implementation capacity of each city. These options are being incorporated into the cities' development plans. Additionally, the project increased local capacity by installing risk assessment tools in the computer systems of the local governments and training city official and local experts on the use and application of those tools to urban planning. Also, the project increased public awareness through the active participation of city institutions and representatives of the various sectors of the community throughout the project and a collaborative interaction with the local mass media. In the course of the project, the professionals and officials of the participating cities presented their work to the international community and exchanged experiences and best practices.

5. VOLCANIC HAZARDS

Facing volcanic hazards, particular attention is given to techniques for detecting and monitoring the

phenomena preceding violent eruptions, and to problems of communication between scientists, civil defence services, and the general public. General guidelines are issued on volcanic-hazards zonation, and on volcanic emergency management. UNESCO has promoted a study on an International Mobile Early-Warning System for Volcanic Eruptions (IMEWS), on the basic premise that an improved international system of rapid response and mutual assistance is needed to better cope with volcanic crises. The study has permitted the revision of existing volcano-monitoring facilities and the identification of 100 high risk volcanoes in the world.

6. TSUNAMIS

The tsunami disaster in the Indian Ocean has led the international community to recognise that tsunamis can occur at any time and almost anywhere, causing death and destruction both locally and across oceans thousands of miles away. The establishment of a global tsunami warning system is now on the international agenda. UNESCO became, in 1965, the organization through which international co-operation in tsunami warning was formally initiated. In that year, the IOC of UNESCO set up an International Tsunami Information Centre (ITIC), now located in Honolulu, which works closely with the Tsunami Warning System in the Pacific operated by the United States. Connected to this field is the International Co-ordination Group for the Tsunami Warning System in the Pacific (ITSU) which today numbers twenty-six member countries. ITSU meetings provide an opportunity for the Member States to examine together means for tsunami preparedness and risk mitigation. UNESCO is now calling for the establishment of early warning systems not only in the Indian Ocean but also in the Caribbean and the Mediterranean and for their reinforcement in the SW Pacific. Indeed, the Organization is actively promoting the setting up of a global early warning system for tsunamis that would provide an integrated international framework for establishing regional systems and responsible national centres and facilities.

7. HYDROLOGICAL HAZARDS

Under the International Hydrological Programme (IHP) which develops in several phases, considerable attention is given to hydrological hazards. The hydrological processes of these phenomena, including river floods, and flood risk assessment, are studied as well as the management and prevention aspects regarding the design of engineering works for flood control. Basis are laid down for the development of a decision-support system for urban water disaster mitigation

At the WCDR, the International Flood Initiative was launched as a global effort involving UNESCO, the World Meteorological Organization (WMO), the United Nations University, the UN-ISDR and the International Association of Hydrological Sciences. The mission of this initiative is to promote an integrated approach to flood management in order to maximize the long-term net benefits of floods and minimize the loss of life, hardship, goods and other assets that result from floods. This new initiative is set to integrate the scientific, operational, formal and public educational aspects of flood management, including the social response and communication dimensions of flooding and related disaster preparedness. The headquarters for the new project will be based at a planned Centre for Water Hazard and Risk Management to be hosted by the Public Works Research Institute in Tsukuba, Japan.

8. LANDSLIDE HAZARDS

Various studies have been conducted by UNESCO on the cause and prevention of landslides, in

particular the publication of guidelines on landslides hazards zonation. Projects in this area resulted in significant multi-national landslide research and mitigation. Recently UNESCO has promoted jointly with other organizations the establishment of the International Consortium on Landslides and the launching of the International Programme on Landslides which both represent timely and promising initiatives geared to cooperative research and capacity building for landslide risk mitigation. The research Centre on Landslides within the Disaster Prevention Research Institute at Kyoto University constitutes the operational focus of the ICL and IPL. As a result of these endeavours, a UNITWIN Programme on Landslide Risk Mitigation for Society and the Environment has been set up at Kyoto University. UNITWIN programme is a UNESCO programme denoting the University twinning and networking for the transfer and sharing of knowledge and the promotion of academic solidarity across the world.

9. OTHER HAZARDS

Studies on droughts and desertification are undertaken in the framework of IHP and the Man and Biosphere (MAB) Programme which started in 1971. The arid land studies including drought and desertification problems are given an important place in MAB activities, with significant input to the Convention to Combat Desertification. These studies are undertaken in the framework of integrated pilot projects aimed at better understanding the functioning of arid and semi-arid ecosystems and at devising optimal land-use systems in drought-prone areas thus contributing to the combat against desertification in these areas. Such projects were developed in particular in Africa (Sahelian countries, Kenya, Lesotho and Tunisia). A large number of scientific publications and guidelines tailored to decision-makers and the general public have emanated from these projects, including poster and audio-visual series.

10. EDUCATIONAL BUILDINGS AND CULTURAL MONUMENTS

UNESCO helps Member States to deal with the problems that sudden natural hazards present for school buildings. Emphasis is laid on practical advice on how to build schools that will be relatively safe if a natural disaster occurs. This is mainly done through the holding of national/sub-regional training seminars and the publication and dissemination of guidelines on the construction of disaster-resistant educational buildings. In addition, all school construction projects benefiting from UNESCO technical collaboration are examined from the point of view of their vulnerability to natural hazards and the necessary changes are made in the projects. The programme has also fielded a significant number of reconnaissance missions to countries that have experienced disasters, assessing the damage to educational buildings and recommending rehabilitation measures. Immediate actions are also proposed to minimize discontinuity in educational programmes. The emphasis of the programme is now on the development of schools that can be used as a place of community refuge during, and as a relief centre after, a disaster. Recently some pilot studies have also included the introduction of disaster-preparedness in the curricula covering social and behavioral aspects. In addition, prototype schools (pilot projects) with emphasis on disaster resistance have been developed in certain countries to serve as models for large scale projects.

Sites, monuments and other works of art are liable to be affected by natural disasters. UNESCO participates in the operations undertaken to safeguard such property against disasters and issues guidelines for the protection of cultural monuments. Within the framework of risk preparedness and emergency response for the safeguard of cultural properties and museums in relation to disasters, a computer assisted multimedia system for reporting, recording, and communicating information and data is being produced together with a set of plans criteria and policies.

11. EDUCATION AND INFORMATION

Activities on education and information in the field of disaster preparedness and prevention are carried out involving the Natural Sciences, the Education and the Communication and Information Sectors. Basis are laid down for developing guidelines on crisis and risk management for the use by special target groups, in particular policy-makers and community leaders. Studies are elaborated on the role of mass communication media in disaster situation.

An international on Education for Disaster Reduction has been launched at the WCDR. This initiative has a dual goal: (i) the integration of education and sensitization of disaster reduction into the educational programs of schoolchildren at the primary and secondary level; (ii) ensuring that schools and educational buildings are safe during the occurrence of disasters. This project shall substantially contribute to the United Nations' Decade of Education for Sustainable Development (2005-2015).

12. POST-DISASTER INVESTIGATIONS

In the aftermath of natural disasters, and at the request of Member States affected, UNESCO's intervention is aimed at investigating and introducing transitional actions to draw lessons from the event, to propose and, sometimes, execute measures for reducing the impacts of the disaster as well as losses from any future event, and for developing human resources as a catalyst for recovery and national self-reliance. The purpose is also to fill the gap between emergency relief operations and the long-term recovery and rehabilitation action.

It was on the initiative of UNESCO that first post-natural disaster reconnaissance missions started to operate from 1962 onwards in areas stricken by earthquakes, volcanic eruptions, landslides, floods and cyclones. In instances, these missions have resulted in the implementation by UNESCO of international meetings, of projects related to hazard-zonation prior to reconstruction, to future risk mitigation, and to rehabilitation or reconstruction of educational and cultural buildings.

13. CONCLUSIONS

UNESCO mandate covers a broad spectrum of disciplines and concerns involved in disaster prevention, making the Organization a crossroads of disciplines involved in disaster reduction. As such, UNESCO provides a unique intellectual setting linking, within a single organization, the natural sciences with education, culture, communication and the social sciences, thereby integrating many of the ingredients for disaster studies.

UNESCO action is carried out through networking and strengthening of regional and international co-ordination systems, direct partnership with Member States, field implementation of operational projects, reconnaissance and advisory missions, preservation and dissemination of data, seminars and training courses. Constant co-operation is maintained with competent international and non-governmental bodies.

METHODOLOGY TO STUDY THE SEISMIC RISK TO BUILDINGS IN A MODERN HIGH RISE CITY IN A REGION OF MODERATE SEISMICITY

J. W. Pappin¹⁾, M. W. Free²⁾, and D. G. Vesey³⁾

1) Director, Ove Arup and Partners Hong Kong Ltd, Hong Kong

2) Associate, Ove Arup and Partners, London UK

3) Director, Ove Arup and Partners Hong Kong Ltd, Hong Kong

jack.pappin@arup.com, matthew.free@arup.com, david.vesey@arup.com

Abstract: This paper reports on the methods that can be used to determine the level of seismic risk to buildings in a modern high rise city in a region of moderate seismicity and to explore cost effective methods of reducing risk. Initially the level of seismic hazard and site response effects needs to be quantified. Typical building types are then identified and their response to seismic ground motion established by various types of analysis ranging from simple elastic response spectral methods to non-linear dynamic time-history analysis. The HAZUS methodology is used as a basis for the work but it is realized that the high proportion of high-rise reinforced concrete buildings up to about 60 stories cannot be adequately characterized using the default HAZUS building capacity and fragility curves. A Geographical Information System grid analysis is then proposed to determine the damage risk to the whole building stock in terms of amount of building damage, the damage cost and casualties. Finally, cost benefit analyses can be used to determine whether the introduction of a moderate level of seismic design with some detailing rules would be cost effective.

1. INTRODUCTION

In many modern cities in regions of moderate seismicity many people live and work in high-rise buildings. Often the relevant codes of practice for building design do not require any seismic considerations. The combination of the extremely densely populated urban environment, the economic significance of the region and the potential vulnerability of the building stock to earthquakes warrant further investigation of the seismic risk to these buildings.

This paper describes the methodology that can be used to determine the level of seismic risk to buildings in such a city as a result of potential future seismic ground motion. It goes on to describe extending the methodology to determine whether the introduction of a moderate level of seismic design with some detailing rules would be cost effective.

2. SEISMIC HAZARD AND SITE RESPONSE EFFECTS

The seismic hazard needs to be quantified in terms of uniform hazard response spectra having a 50%, 10% and 2% chance of being exceeded in 50 years for bedrock sites using the standard procedure suggested by Cornell (1968). The basis of the input and the typical type of results are described in Free et al. (2004). Site response effects can then be allowed for by reviewing existing borehole logs and classifying them using the NEHRP site classification system (FEMA 1997). In this system the stiffness of the upper 30m of soil or rock is considered and classified into Site Class A for hard rock to Site Class E for soft soil. The paper by Pappin et al. (2004) describes the application of

such a classification procedure in some detail and Figure 1 shows an extract of the resulting Site Class zoning map that was produced. It can be seen that only Site Classes B, C, D and E were applicable to that particular location.

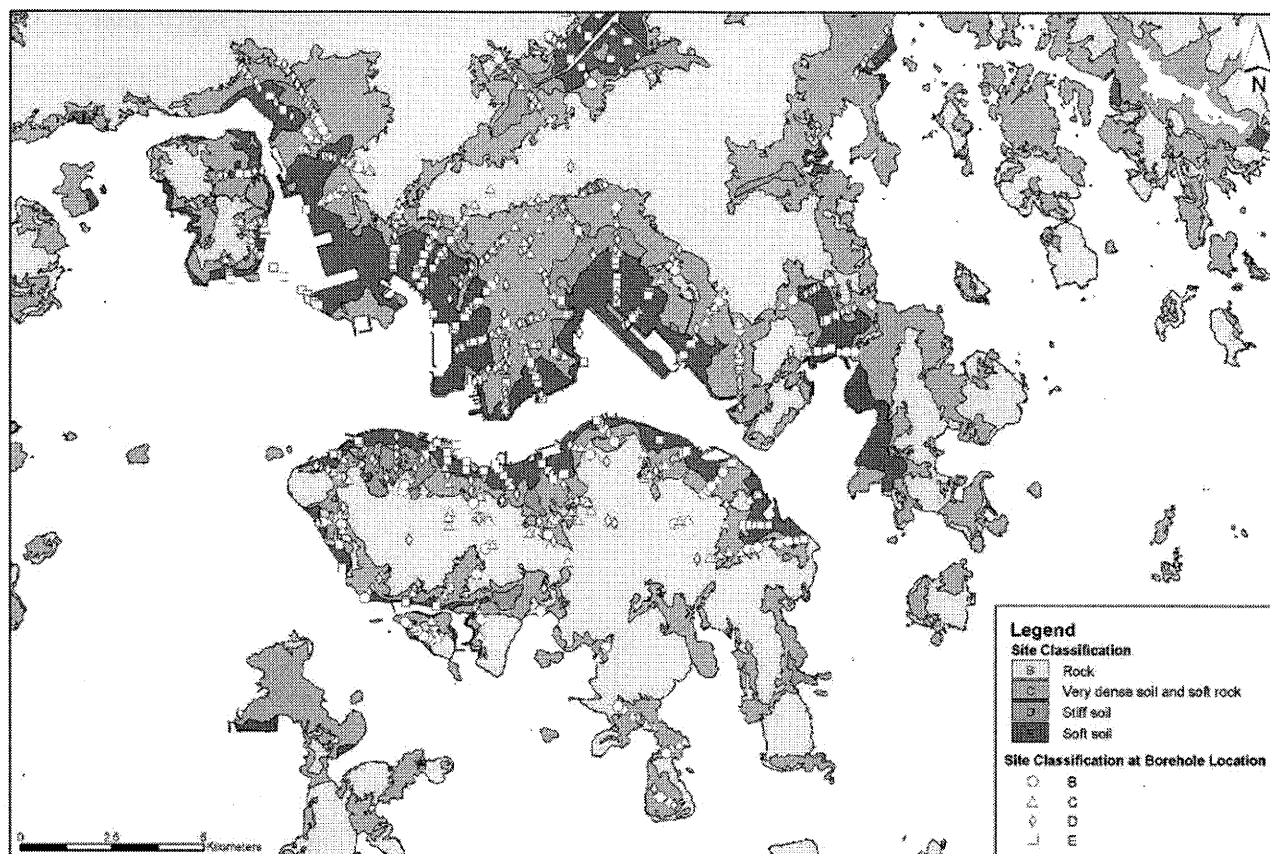


Figure 1: Extract of a Site Class Zoning Map (Pappin et al., 2004)

Having classified the boreholes a representative selection of each Soil Class should be subjected to one dimensional site response calculations and response spectral amplification factors determined as a function of period for a range of bedrock outcrop ground motion corresponding to the 50%, 10% and 2% probabilities of being exceeded in 50 years. For all ground motion levels both the median amplification and standard deviations of the amplification factors need to be determined as a function of period. Pappin et al. (2004) report that for a certain period each of these factors could be expressed as a function of the bedrock response spectral value at that period. While the median spectral amplification factors were dependent on the Site Class it was found that the standard deviations could be expressed as a function of the median spectral amplification factor and were independent of Site Class.

Figure 2 shows an example of calculated horizontal uniform hazard response for ground motion levels having a 50% and 2% probability of being exceeded in 50 years. The bedrock outcrop response spectra are shown as solid black lines and the ground surface response spectra for Site Classes B to E are shown as lines with symbols. For each Site Class the median values are shown as solid lines and the median plus two standard deviations are shown as dashed lines. For reference the bedrock spectra have peak horizontal ground accelerations of about 5%g and 35%g for the 50% and 2% in 50 year probability values respectively. The 5% damped peak response spectral acceleration values occur at a period of about 0.1 seconds and are about double these values (see Free et al., 2004).

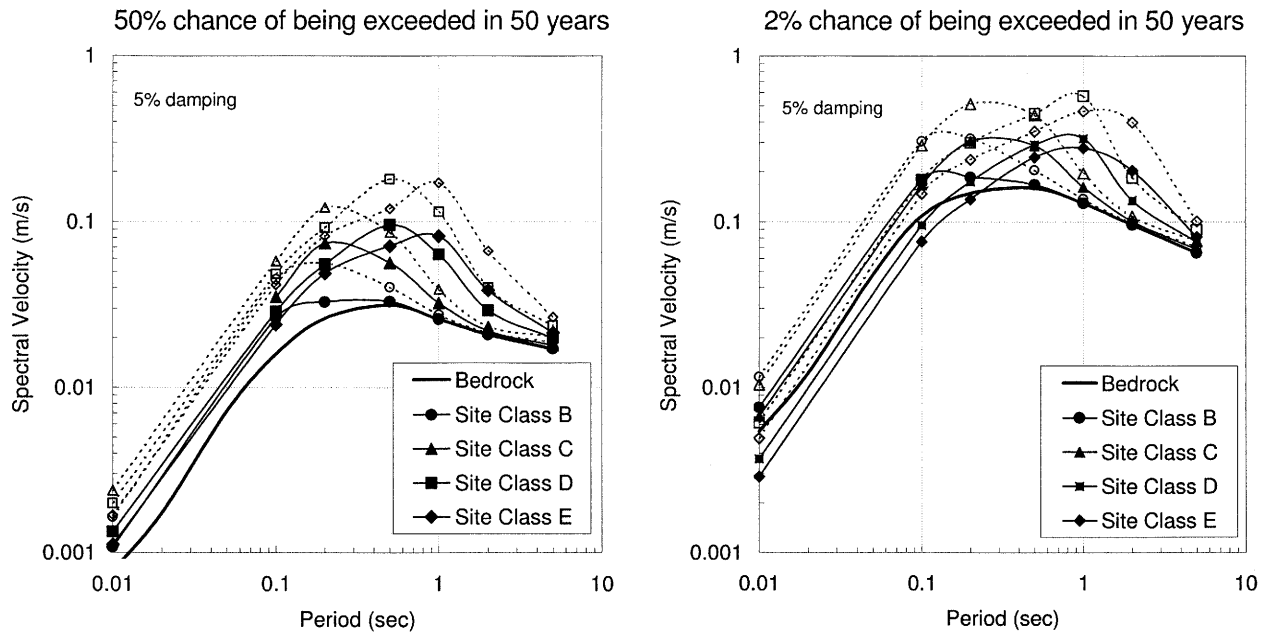


Figure 2: Horizontal velocity uniform hazard response spectra for various Site Classes
(Pappin et al., 2004)

3. RESPONSE OF BUILDINGS TO SEISMIC GROUND MOTION

The methodology suggested to determine the response of buildings to seismic ground motion is based on the HAZUS recommendations, FEMA (2003). This methodology includes default values to characterize the response of a range of building structural types up to a height of about stories. Where these HAZUS building categories are applicable, modifications to the HAZUS default values may still be necessary to account for the wind loads that buildings are designed to resist. In addition the building stock in many modern cities comprises many buildings with 15 to 60 stories and additional building categories need to be introduced to cater for these.

3.1 Inventory of the Building Stock

As a first step an inventory of buildings needs to be compiled, ideally in a Geographical Information System (GIS) database. The inventory needs to record the building footprint, total floor area, the number of stories, the building usage and the number of occupants in day and night time. It is inevitable that the data will not be complete and some rules will be need to be derived, based on building usage, to derive structural type and occupancy rate. The building monetary value also needs to be estimated in terms reconstruction cost.

Generally the modern building stock is dominated by reinforced concrete buildings with some unreinforced masonry buildings in the older low rise buildings. It is suggested that the building heights be divided into 5 ranges as follows

- 1 to 2 stories and 3 stories, generally referred to as Low-rise (L) buildings,
- 4 to 7 stories, referred to as Mid-rise (M) buildings,
- 8 to 15 stories, referred to Intermediate high-rise (I) buildings,
- 16 to 30 stories, referred to as High-rise (H) buildings and
- 31 to 60 stories, referred to as Very high-rise (V) buildings.

A suggested breakdown of building structural systems is as follows:

Unreinforced Masonry Bearing Walls (URM): These buildings include structural elements that vary depending on the building's age and, to a lesser extent, its geographic location. For older buildings built before say 1900, the majority of floor construction may well comprise wood sheathing supported by wood framing whereas in newer buildings, the floors may be cast-in-place concrete supported by the unreinforced masonry walls and/or concrete interior framing. The perimeter walls, and possibly some interior walls, are often unreinforced masonry and may or may not be anchored to the diaphragms. Ties between the walls and diaphragms are more common for the bearing walls than for walls that are parallel to the floor framing. Roof ties usually are less common and more erratically spaced than those at the floor levels.

Reinforced Concrete Moment Resisting Frames (CF): These buildings have a reinforced concrete frame and develop their stiffness by full or partial moment connection of these frames. Many buildings are likely to have a reinforced concrete core that transfers a significant part of the lateral loading to the ground.

Concrete Frame Buildings with Infill Walls (CFIW): These buildings have a reinforced concrete frame and develop their stiffness by full or partial moment connection of these frames, as for CF buildings, but with infill walls. In these buildings, the shear strength of the columns, after cracking of the infill, may limit the semi-ductile behavior of the system. In older buildings the infill will typically be unreinforced masonry. In newer buildings concrete infill with a single layer of steel mesh reinforcement is typically used. These walls are not designed to take any of the lateral load however.

Concrete Shear Walls (CSW): The vertical components of the lateral-force-resisting system in these buildings are concrete shear walls that are usually bearing walls. In older buildings, the walls often are quite extensive and the wall stresses are low but reinforcing is light. In newer buildings, the shear walls are often limited in extent, leading to concerns about boundary members and overturning forces.

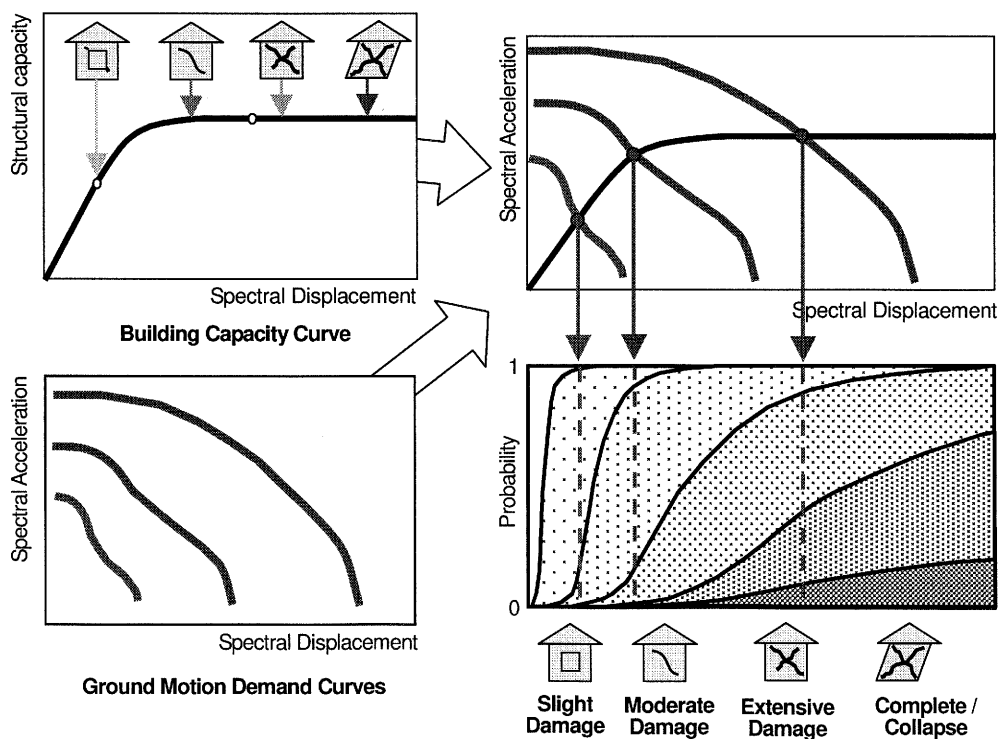


Figure 3: HAZUS Methodology

3.2 The HAZUS Building Response Methodology

It is proposed that the HAZUS methodology (FEMA, 2003) is used as the basis for determining the seismic response of the building stock. The methodology is summarized in Figure 3. Default values for building response are only directly applicable to buildings up to about 15 stories high. Calibrating the HAZUS method for the building categories in a particular location and extending the method to cover buildings above 15 stories is discussed later. In HAZUS, the general building stock represents typical buildings of a building type designed to either High-Code, Moderate-Code, or Low-Code seismic standards, or not seismically designed (referred to as Pre-Code buildings). For the application of the method to buildings to many cities in regions of moderate seismicity, only the Low-Code and Pre-Code building types are likely to be appropriate.

Building Damage States

In HAZUS the building damage is predicted in terms of one of four ranges of damage or “damage states”: Slight, Moderate, Extensive, and Complete. For example, the Slight Damage state extends from the threshold of Slight Damage up to the threshold of Moderate Damage. General descriptions of these damage states are provided for the model building types with reference to observable damage incurred by structural building components. Damage predictions resulting from this physical damage estimation method are expressed in terms of the probability of a building being in any of these four damage states. As an example the description of Slight, Moderate, Extensive, and Complete Structural Damage is provided here for reinforced concrete frame buildings (CF).

Slight Damage: Flexural or shear type hairline cracks in some beams and columns within or near joints.

Moderate Damage: Most beams and columns exhibit hairline cracks. In ductile frames some of the frame elements have reached yield capacity indicated by larger flexural cracks ($>4\text{mm}$) and some concrete spalling. Non-ductile frames may exhibit larger shear cracks and spalling.

Extensive Damage: Some of the frame elements have reached their ultimate capacity, indicated in ductile frames by larger flexural cracks, spalled concrete and buckled main reinforcement. Non-ductile frame elements may have suffered shear failures or bond failures at reinforcement splices, or broken ties or buckled main reinforcement in columns which may result in partial collapse.

Complete Damage: Structure has collapsed or is in imminent danger of collapse due to brittle failure of non-ductile frame elements or loss of frame stability. About 13% (low-rise), 10% (mid-rise) or 5% (intermediate high-rise) of the buildings with Complete Damage are expected to have collapsed.

Building Capacity Curves

Except for a few brittle systems and acceleration-sensitive elements, building damage is primarily a function of building distortion or drift, rather than force. In the inelastic range of building response, increasingly larger damage would result from increased building drift although lateral force would remain constant or decrease. Hence, successful prediction of earthquake damage to buildings requires reasonably accurate estimation of building drift response in the inelastic range. While linear elastic analysis methods can be used to estimate drift they will under-predict the building drift as the buildings respond in-elastically to earthquake ground shaking of interest for damage prediction. Building capacity curves, used with the demand spectrum as recommended by the HAZUS methodology, provide a simple and reasonably accurate means of predicting inelastic building displacement response for damage estimation purposes.

A building capacity curve, also known as a pushover curve, is a plot of a building's lateral load resistance as a function of a characteristic lateral displacement or drift, i.e. a force-deflection plot. It is derived from a plot of static-equivalent base shear versus a measure of the building displacement or drift, for example at roof level. In order to facilitate direct comparison with earthquake demand (i.e. overlaying the capacity curve with a demand spectrum), the force (base shear) axis is converted to spectral acceleration and the drift axis is converted to spectral displacement. Such a plot provides an estimate of the building's “true” deflection (drift response) for any given earthquake demand spectrum.

The parameters used by HAZUS to define the capacity curve are shown in Figure 4. Three control points, that define the building capacity curve, are as follows:

- *Design Point* (D_D, A_D): representing the expected nominal strength for the building. In the HAZUS default parameters wind design is not considered in the estimation of design capacity.
- *Yield Point* (D_Y, A_Y): representing the true lateral strength of the building considering redundancies in design, conservatism in code design calculation methods and true (not nominal) strength of materials.
- *Ultimate Point* (D_U, A_U): representing the maximum strength of the building when the global structural system has reached a fully plastic state. Ultimate capacity implicitly accounts for loss of strength due to shear failure of brittle elements. Typically, buildings are assumed to be capable of deforming beyond their ultimate point without loss of stability, but their structural system provides no additional resistance to lateral earthquake force.

Up to the Yield Point, the building capacity curve is assumed to be linear with stiffness based on an estimate of the true period (T) of the building. As this point represents the condition where the building is beginning to yield and experience permanent damage the true period is typically longer than the measured small deformation period of the building. For concrete frame buildings HAZUS recommends that the true period be assumed as 1.33 times larger than the code specified period. For concrete shear wall buildings and concrete frame buildings with infill walls this ratio is about 1.5 and for unreinforced masonry the ratio increases to about 2. From the Yield Point to the Ultimate Point, the capacity curve changes in slope from an essentially elastic state to a fully plastic state. The capacity curve is assumed to remain plastic past the Ultimate Point. As shown in Figure 4 the control points are defined by the following parameters:

C_s	design strength coefficient (fraction of building's weight),
α_1	fraction of building weight effective in pushover mode,
γ	"over-strength" factor relating "true" yield strength to design strength,
λ	"over-strength" factor relating ultimate strength to yield strength, and
μ	"ductility" factor relating ultimate displacement to λ times the yield displacement over-strength.
T	Building period (seconds)

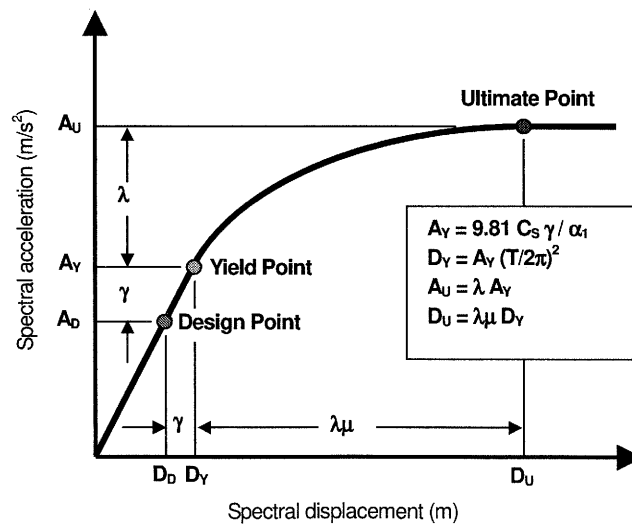


Figure 4: HAZUS Capacity Curve Definition

In HAZUS the design strength coefficient, C_s , is approximately based, on the lateral-force design requirements of current seismic codes. Its value is a function of the seismic zone location, the site soil

condition, type of lateral-force-resisting system and building period. Figure 5 shows the HAZUS capacity curves for buildings with no seismic design provisions for the range of buildings discussed previously. The three diagonal dashed lines show how the building period varies as a function of the spectral acceleration and displacement. As expected the building period is constant before the yield point is reached.

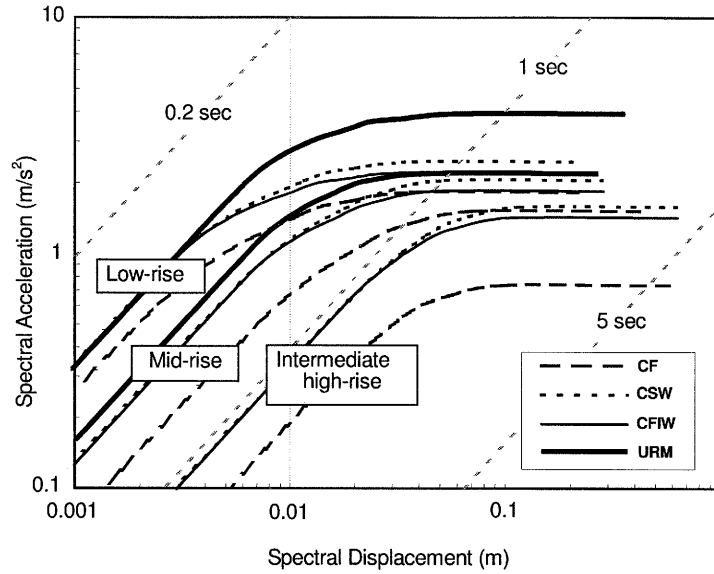


Figure 5: HAZUS Curves for Pre-Code Buildings

Building Structure Fragility Curves

The probability of being in, or exceeding, a given damage state is modeled as a cumulative lognormal distribution. The lower part of Figure 6 shows an example set of fragility curves for a Pre-Code low-rise Concrete Frame building determined using the default HAZUS values. Median values of structural component fragility are based on building drift ratios that describe the threshold of damage states. Damage-state drift ratios are converted to spectral displacement using;

$$\bar{S}_{d,Sds} = \delta_{R,Sds} \cdot \alpha_2 \cdot h$$

where: $\delta_{R,Sds}$ is the drift ratio at the threshold of structural damage state, ds,
 α_2 is the fraction of the building (roof) height at the location of pushover mode displacement, = 0.75 for low-rise to 0.6 for high-rise buildings.
 h is the typical roof height, of the building type.

A lognormal standard deviation is used to describe the total variability for structural damage state. In HAZUS it is often taken to include the variability of the ground motion as well as that of the building stock and also allows for variability of the capacity curve. A value of 0.5 for the natural log is used in Figure 6 and, as discussed later, is a reasonable value for use with uniform hazard spectra that already contain specific allowance for the known variability of the input ground motion.

To illustrate how the capacity curve, the fragility curve and the demand curve interact the upper part of Figure 6 shows the default HAZUS capacity curve and a set of three demand spectra. These are for illustration only and approximately correspond to the demand spectra that envelope those shown in Figure 2. For each intersection point a line is drawn down to the fragility curves in the lower diagram.

The damage predicted to arise from the 10% in 50 year ground motion, for example, is about 30% of the building stock will experience Slight Damage, 50% Moderate Damage and 5% Extensive Damage.

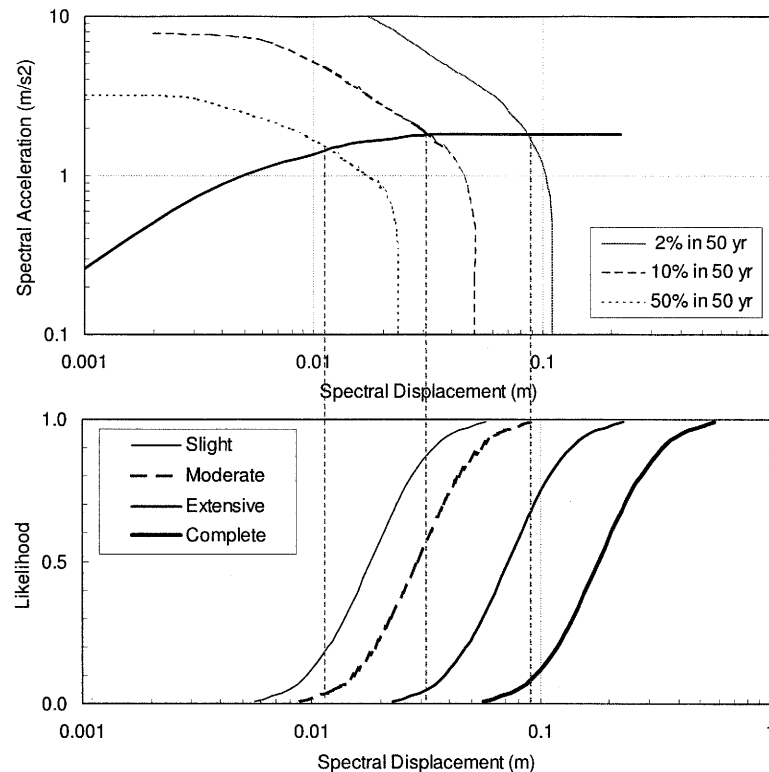


Figure 6: Example for Low-rise Concrete Frame (CF) Buildings using the default HAZUS values for Pre-Code buildings

It should be noted that HAZUS gives a method to reduce the demand spectra for additional damping that the building will experience as it reaches the ultimate capacity point. For the low ductility buildings that often exist in regions of moderate seismicity however this effect is not likely to be that significant however and a structural damping of 5% will often be adequate.

3.3 Structural Analysis Methods

Various analysis methods can be used as follows:

Linear Elastic Dynamic Analysis

For this analysis method the building design seismic forces, the distribution of these forces over the height of the building, and the corresponding internal forces and displacements are determined using a linear-elastic, dynamic analysis. These time-history analyses involve a step-by-step analysis of the mathematical model of a building using digital earthquake time-histories. The forcing function for the analysis can be an acceleration time-history that has a response spectrum similar to the 2% in 50 year ground motion as shown for example in Figure 2. For a building that does not yield the linear elastic time-history analyses accurately predict element stresses and displacements. If the building response is anticipated to yield and be beyond the elastic region, the predicted displacements will be too small and the predicted internal forces will exceed those that would be obtained in the yielding building. For small levels of non-linearity the predicted displacements will still be quite close to the correct result but the internal forces may be too large.

Non-linear Dynamic Time-History Analysis

Modeling the full non-linear behavior of certain building components is required to understand failure mechanisms. The program *Oasys* LS-DYNA or equivalent can be used to perform non-linear time-history analyses. The static dead and live loads are applied to a mathematical model of the building and the stresses within the structural element are determined. An earthquake time-history is then applied to the base of the model and a dynamic analysis carried out. LS-DYNA can model geometric non-linearity, material non-linearity and inelastic behavior and higher mode effects. In addition, it is capable of capturing local instability in the structure and assessing the “Yielding Surface” defining the relationship between the two axes of bending and the axial force. This is important for corner columns common to two intersecting frames.

Pseudo Static Pushover Analysis

A pushover analysis is used to determine the capacity of a structure to resist lateral seismic forces. A mathematical model of the building is first subjected to the static gravity loads to determine the stresses within the structural elements and then the model is pushed horizontally with increasing static lateral load until it is unable to support any additional loading. The amount of force the building is able to sustain is plotted versus the relative displacement at the roof level. The resulting pushover curve is a plot of the base shear versus drift and is equivalent to the capacity curve used by the HAZUS methodology. The pushover analysis procedure is defined and detailed in ATC 40, FEMA-273, FEMA-274 and FEMA-356. To be consistent ACI 318 should be used to estimate member strengths and the HAZUS guidelines (FEMA, 2000), used to derive the capacity curves. The pushover curves should be calculated for each direction of response and the flexibility of all elements and components, including infill walls that contribute significantly to the building response incorporated into the analyses. The pushover models are usually three-dimensional in order to capture any torsional behavior of the response.

Base Shear Analysis

This is the simplest form of analysis and forms the basis of most seismic codes of practice. It comprises using the fundamental period of the building with an acceleration response spectrum to give an estimate the maximum base shear as a ratio of the building weight that the building will experience under the action of the design seismic event. The fundamental periods of the buildings can be estimated using the conventional code formula adjusted as recommended by HAZUS. If a time-history analysis was carried out the building period from that analyses can be used.

An interesting product of the base shear analysis, when compared with the base shear resulting from the linear time-history analyses, is a measure of the significance of higher mode responses of the building. In the HAZUS methodology the modal parameter α_1 describes the amount of the building mass that is likely to participate in the fundamental mode pushover analysis. If the building response is dominated by this mode, with only small input from higher modes, it would be expected that the base shear resulting from the time-history dynamic analyses would be similar to that predicted by the simplified base shear analysis method multiplied by the α_1 value given by HAZUS.

For buildings with longer periods however higher mode effects may become significant and it can be observed that the base shear predicted by the linear dynamic time-history analysis is significantly greater than that implied by the response of the structure to the first mode only. This can especially be the case for ground motions whose response spectra have low values at higher periods such as those indicated in Figure 2. In the building damage assessments of high-rise buildings this effect from higher mode effects must be taken into account. This adjustment can be achieved by using a base shear factor η that relates the calculated peak base shear to that predicted by the first mode response only. The α_1 factor is replaced by the base shear factor η . For low-rise and mid-rise buildings it is set equal to the appropriate HAZUS α_1 factor, but for higher buildings it may become significantly larger than unity.

Design Wind Load

The wind forces that the buildings have been designed for can be used to derive the minimum lateral yield capacities of the buildings. To derive the expected building design capacity it is necessary

to allow for any material factors that are inherent in the structural codes and also to allow for the expected difference between the expected material strength and the characteristic strength likely to be used in the original calculations. The resulting yield capacity is used to derive a yield capacity coefficient by dividing this expected yield capacity by the seismic weight of the building. The coefficient, referred to here as C_{SY} , is the same as $C_S * \gamma$ in the HAZUS methodology.

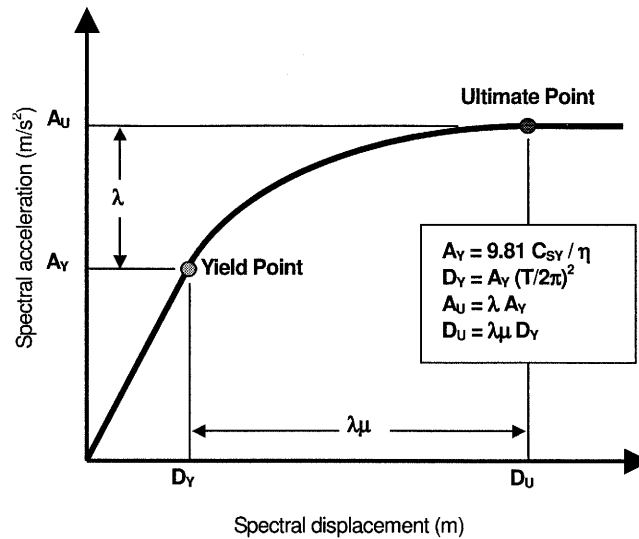


Figure 7: Definition of Capacity Curve

3.4 Derivation of the Building Capacity Curves

Figure 7 shows how the building capacity curves are defined using the C_{SY} and the η coefficients suggested above and the over-strength, λ , and ductility, μ , coefficients already defined by the HAZUS methodology. Comparison with Figure 4 shows that the definition is very similar to that used by the HAZUS methodology and for suitable building classes, could be directly defined using the HAZUS coefficients. For low-rise to intermediate high-rise buildings it is necessary to calibrate and possibly modify the default HAZUS coefficients to ensure they are appropriate to the buildings being characterized. For high-rise and very high-rise buildings not covered by the default HAZUS values additional coefficients need to be generated.

For building categories that correspond to the HAZUS default classifications, comprising low-rise to intermediate high-rise buildings up to about 15 stories, the following procedure is recommended:

- For a selection of buildings the capacity curves can be derived from a non-linear pushover analysis.
- For most buildings an estimate of the lateral shear capacity can be derived from the wind loads as a check on the HAZUS values. The design wind loads are assumed to give a lower bound indication of the capacity of the building. Wind loads depend on the height, plan area and shape of the building and can be substantially different in each direction. For the buildings the wind load is determined and used to assess the minimum expected lateral yield capacity as explained previously. By combining the expected yield capacity with an estimate of the building period a capacity curve can be generated using the default HAZUS over strength and ductility coefficients.

For high-rise buildings that do not correspond to a HAZUS classification the following procedure is recommended:

- Carry out linear elastic dynamic time-history analyses.
- If the time-history calculation shows that the main building structure does not experience yield no further analysis is required. If significant yield is predicted however, non-linear time-history analyses or pushover analyses are required. It must be emphasised that the pushover method, in a similar way to the HAZUS procedure, assumes the first mode response is generally sufficient to represent the behaviour

of the building. Therefore non-linear time-history dynamic analyses are necessary to confidently predict the response of high-rise buildings to extreme ground motions.

- For high-rise buildings wind loads can be very significant and can be used to derive the expected yield capacity of the building. As for lower rise buildings this needs to be combined with an estimate of the building period to derive the building capacity curve. Other coefficients need to be assessed by suitable extrapolation from the lower-rise buildings.

3.5 Derivation of Building Fragility Curves

As illustrated in Figure 6 Fragility Curves are functions that describe the probability of the buildings within each category reaching, or exceeding, the various damage states for a given building response. This family of curves has inherent properties that can be assessed from earthquake damage data. In a seismic risk study carried out previously for the UK Government (Arup, 1993), the prime building type was unreinforced masonry. Damage data had been obtained from a wide variety of damage surveys as reported in Coburn and Spence (2002) and these are shown in Figure 8. Each damage survey location is represented by a series of points vertically above each other at a single location on the horizontal Intensity scale. It can be seen that the various levels of damage are interrelated. For example if 50% of the buildings have experienced Heavy Damage or more (at an Intensity ψ value of 10) it is observed that about 25% have experienced at least Partial Destruction and about 80% at least Moderate Damage. All buildings have experienced at least Slight Damage. Given the interrelation of curves vertically however means that the width (or lateral spread) of the curves and their relative horizontal position are mutually dependent. The family of curves needs therefore to be viewed as a whole and the horizontal axis chosen to best fit the observed levels of damage.

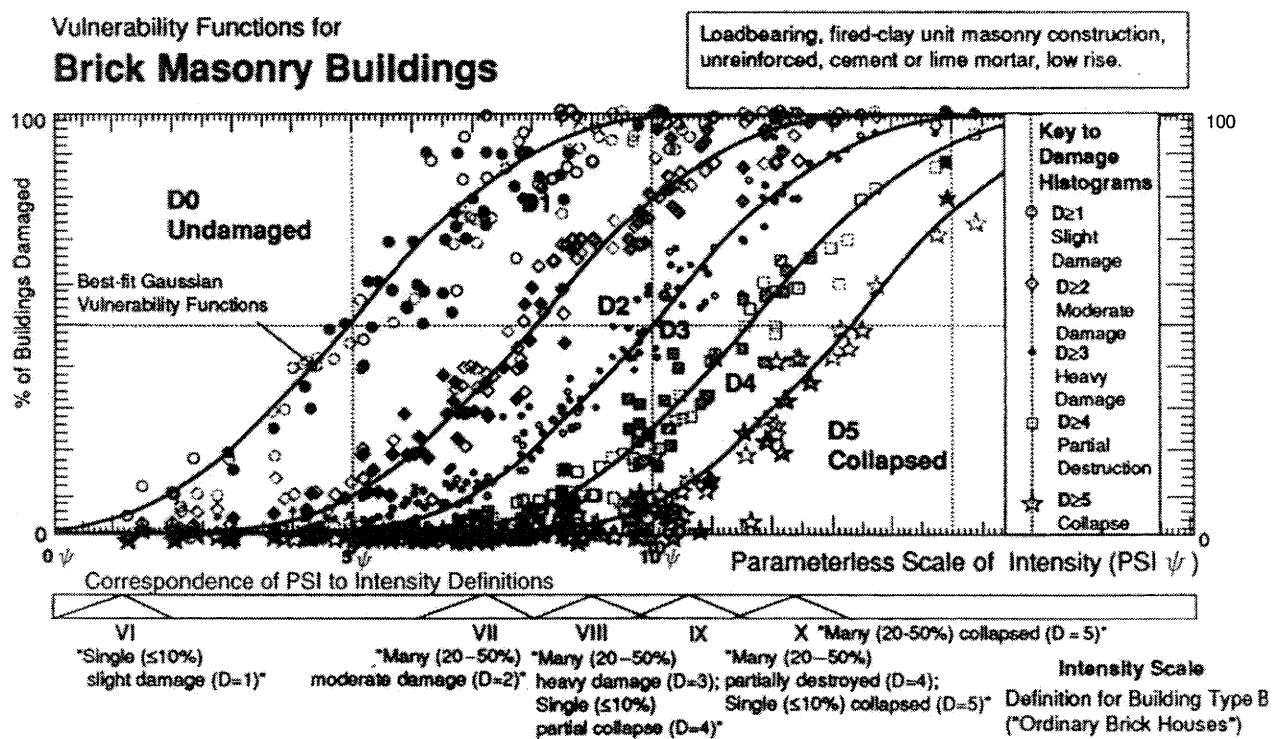


Figure 8: Observed Fragility Curves for Ordinary Brick Buildings (Coburn and Spence, 2002)

The shape of the fragility curves should reflect the variability of buildings within the same category. For a particular category of buildings where all buildings are very similar it would be expected that the variability should be very low. In general damage surveys are a reasonable guide for

deriving the inherent variability of buildings and the variance derived using these methods should be adhered to unless there is a clear reason to deviate. The variability of the natural logarithm of 0.47 to 0.5 specified in HAZUS for Low-Code and Pre-Code buildings is a reasonable starting point. A value of 0.5 accords well with that shown for unreinforced masonry as shown in Figure 8 and is recommended. As noted previously Figure 6 is based on a value of 0.5.

As described above HAZUS presents median values of the fragility curves defining each damage state. For buildings where pushover analysis is carried out a check on the HAZUS values can be made. This can be done following the HAZUS methodology, FEMA (2000), which defines two sets of criteria for each damage state. The criteria are shown in Table 1 and refer to the percentage of elements that have reached various points on their non-linear response curve. Figure 9 shows the schematic response curve where Point B is yield and point C is the ultimate capacity. Criteria Set 1 in Table 1 refers to the fraction of components that have reached the ultimate capacity (Point C) and Criteria Set 2 the fraction of components that have reached yield.

Table 1: General Guidance for Relating Component (or Element) Deformation to the Average Inter-story Drift Ratios of Structural Damage State Medians (FEMA, 2000)

Damage State	Component (Criteria Set No. 1) ¹			Component (Criteria Set No. 2) ¹		
	Fraction ²	Limit ³	Factor ⁴	Fraction ²	Limit ³	Factor ⁴
Slight	> 0%	C	1.0	50%	B	1.0
Moderate	≥ 5%	C	1.0	50%	B	1.5
Extensive	≥ 25%	C	1.0	50%	B	4.5
Complete	≥ 50%	E	1.0 - 1.5 ⁵	50%	B	12

1. The average inter-storey drift ratio of structural damage state is lesser of the two drift ratios defined by Criteria Sets No.1 and No.2 respectively.
2. Fraction defined as the replacement value of components at the limit divided by the total replacement value of the structural system.
3. Limit defined by the control points of Figure 9 and the acceptance criteria of NEHRP Guidelines.
4. Factor applied to average inter-storey drift of structure at deformation (or deformation ratio) limit to calculate average inter-storey draft ratio of structural damage state median.
5. Complete factor is largest value in the range for which the structural system is stable.

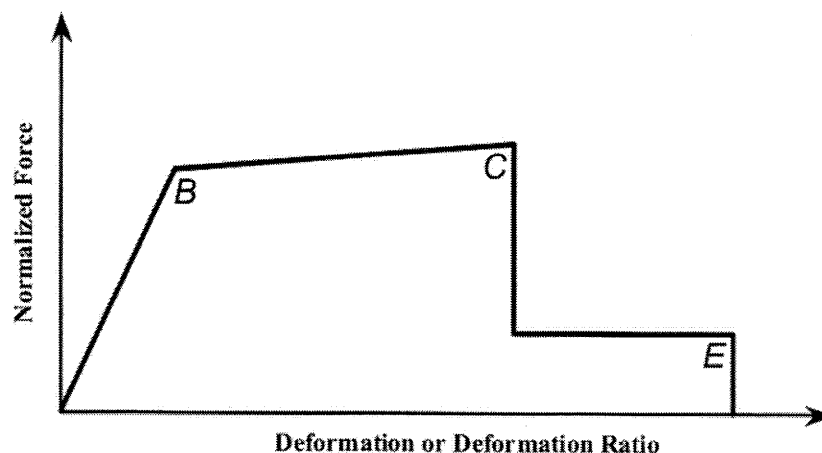


Figure 9: Idealized force deformation curve, FEMA (2000)

The fraction of components is weighted to the replacement value of the components and if any one group of components can lead to the building collapse (e.g. the columns on the ground floor) they will

represent the full replacement value. The Criteria Set that gives rise to the lowest drift is the controlling case.

Figure 10 shows a schematic diagram for relating the pushover curves to the Damage State median values. The Slight Damage point is seen to be near to the first significant yield point and the Extensive Damage point slightly beyond the highest capacity point calculated by the pushover analysis. For buildings that do not correspond to a HAZUS classification (i.e. high-rise buildings) linear time-history analyses can be used to determine the median value for the threshold of Slight Damage by assuming this occurs at a displacement a little greater than that required to cause the first yield of any part of the primary structure. For Moderate, Extensive and Complete Damage the threshold displacements can be assumed to occur at multiples of the yield value respectively. HAZUS generally recommends ratios of 1.5, 4.5 and 12 as implied in Table 1.

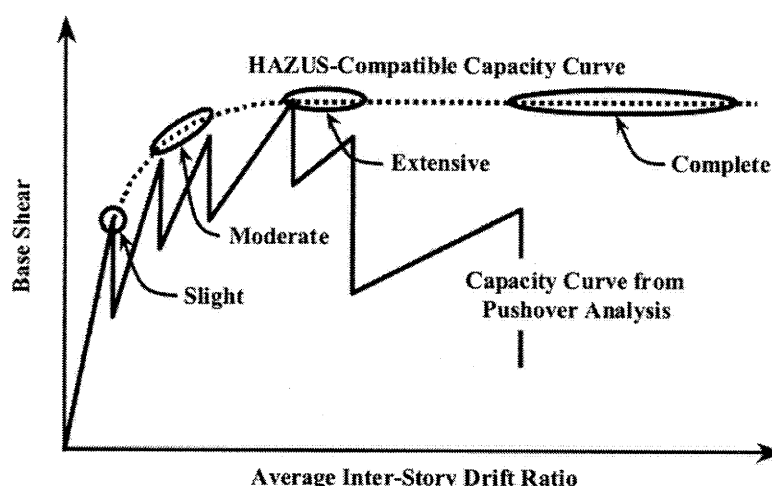


Figure 10: Example Damage state medians from “Saw tooth” Pushover curve, FEMA (2000)

Allowances can also be made for the effects of pounding where existing buildings are built touching each other and for high rise shear wall buildings that are built on transfer plates that are only supported by a column frame system.

4. CALCULATION OF SEISMIC RISK

To determine the risk to buildings from seismic ground motion a series of calculations must be carried out to determine the level of damage to all the buildings in the city. In this risk calculation the uniform hazard bedrock spectra having probabilities of being exceeded of 2%, 10% and 50% in a 50 year period, are imposed on the building stock. The resulting damage is evaluated in terms of square meters of floor area to experience Slight, Moderate, Extensive and Complete Damage. The resulting overall cost and number of casualties are also calculated. By integrating the results over the different probabilities of being exceeded the overall annual cost to buildings as a whole can be estimated. It must be emphasized that these calculations are not to predict the effects of a single earthquake but rather the aggregated effect of all the future possible earthquake events.

To reduce the number of calculations to a manageable number a square grid, of the order of 100m x 100m, can be used and the GIS building database used to assign each building to a grid square by virtue of the central point of the building footprint. The building information within each grid square can then be summed to give the total floor area of each building type and height range. The population within each grid square is derived in the same way.

4.1 Input Ground Motions

The ground motion is defined in terms of demand spectra, which are the response spectra as shown in Figure 2 but re-plotted as spectral acceleration against spectral displacement. The ground motion spectrum at a particular site is that expected to occur at the base of the building structure and must take into account any site response effects and any other local site effects. From a Site Class zoning map (see Figure 1 for example) a GIS analysis can be used to assign a Site Class to each of the grid squares. To allow for variability of the site response effects, the median site response amplification factor together with the median plus and median minus one and two standard deviations need to be considered as shown in Figure 11. These ground motion spectra correspond to those shown for a Site Class D in Figure 2.

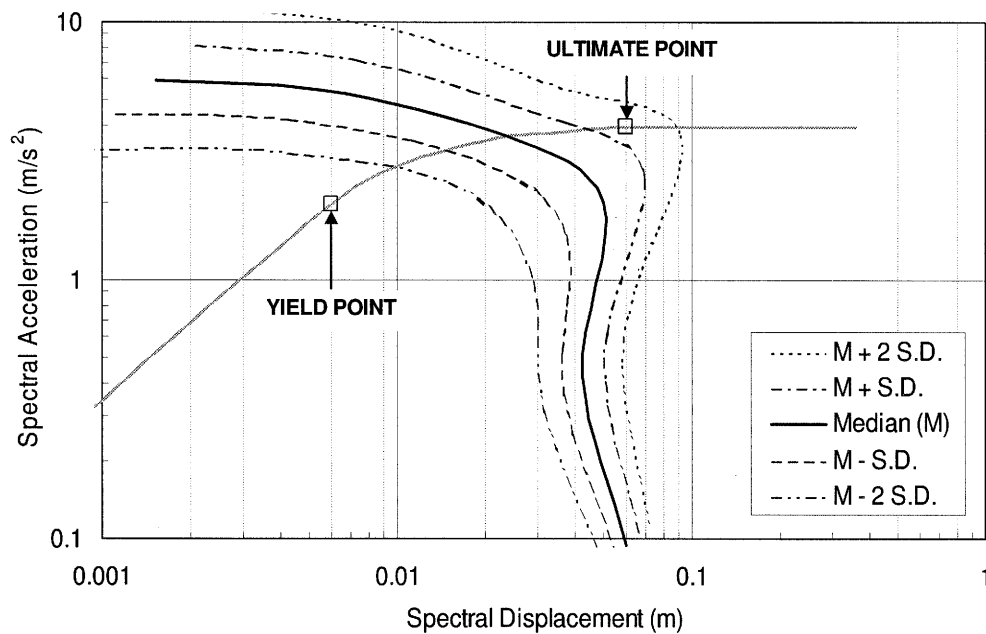


Figure 11: Example for the Determination of Spectral Displacement for a HAZUS Default Pre-Code Low rise Unreinforced Masonry Building when Subjected to the 2% in 50 year Uniform Hazard Ground Motion for Site Class D shown in Figure 2

It can be seen that applying the procedure illustrated in Figure 6 the fraction of the building stock to experience Slight, Moderate, Extensive and Complete Damage can be determined for each of these 5 ground motions. An overall result is then derived by using a weighted sum of these values with a weighting of 0.4 used for the median value, 0.25 for the median plus and median minus one standard deviation and 0.05 for the median plus and median minus two standard deviation values. Allowances can also be made for the effects of liquefaction and steeply sloping ground.

4.2 Cost Calculation

To determine the cost due to seismic ground motion a Cost Ratio is applied to each Damage State in accordance with the HAZUS recommendations (FEMA, 2003). The Cost Ratios are 2%, 10%, 50% and 100% for Slight Damage, Moderate Damage, Extensive Damage and Complete Damage respectively. The overall damage Cost Ratio is a fraction of the replacement value of the building. The damage cost in each grid square is derived by multiplying the value of each building by its respective overall damage Cost Ratio and summing these for all buildings within that grid square.

While this procedure is valid for the building structure, non-structural elements of the buildings can also be assessed. HAZUS divides non-structural components into those that are drift-sensitive and those that are acceleration-sensitive. The relative construction value of the building structure,

drift-sensitive non-structural components and acceleration-sensitive non-structural components needs to be considered.

For buildings in the Low-Code or Pre-Code category the HAZUS default parameters show that the damage to drift-sensitive non-structural components is always less than that experienced by the building structure. Considering the likely effects of repairs to the building structure to the non-structural components it was recommended that the damage Cost Ratio to non-structural components will never be less than the damage Cost Ratio to the building structure. It follows that the damage Cost Ratio to drift-sensitive non-structural components should always be the same as that derived for the building structure.

The damage Cost Ratio to acceleration-sensitive non-structural components is a function of the peak floor accelerations experienced by the structure and can vary quite significantly in comparison to the damage Cost Ratio to the building structure. Figure 12 shows an example calculation of damage Cost Ratio for low rise unreinforced masonry buildings defined using the default HAZUS coefficients. It can be seen that for the 10% in 50 year ground motion the damage Cost Ratios to both the building structure and the acceleration-sensitive non-structural components are similar. For the more frequent ground motion with a probability of being exceeded of 50% in 50 years however, the damage Cost Ratio to the non-structural components is greater than that to the building structure and must be considered directly in the overall cost calculation.

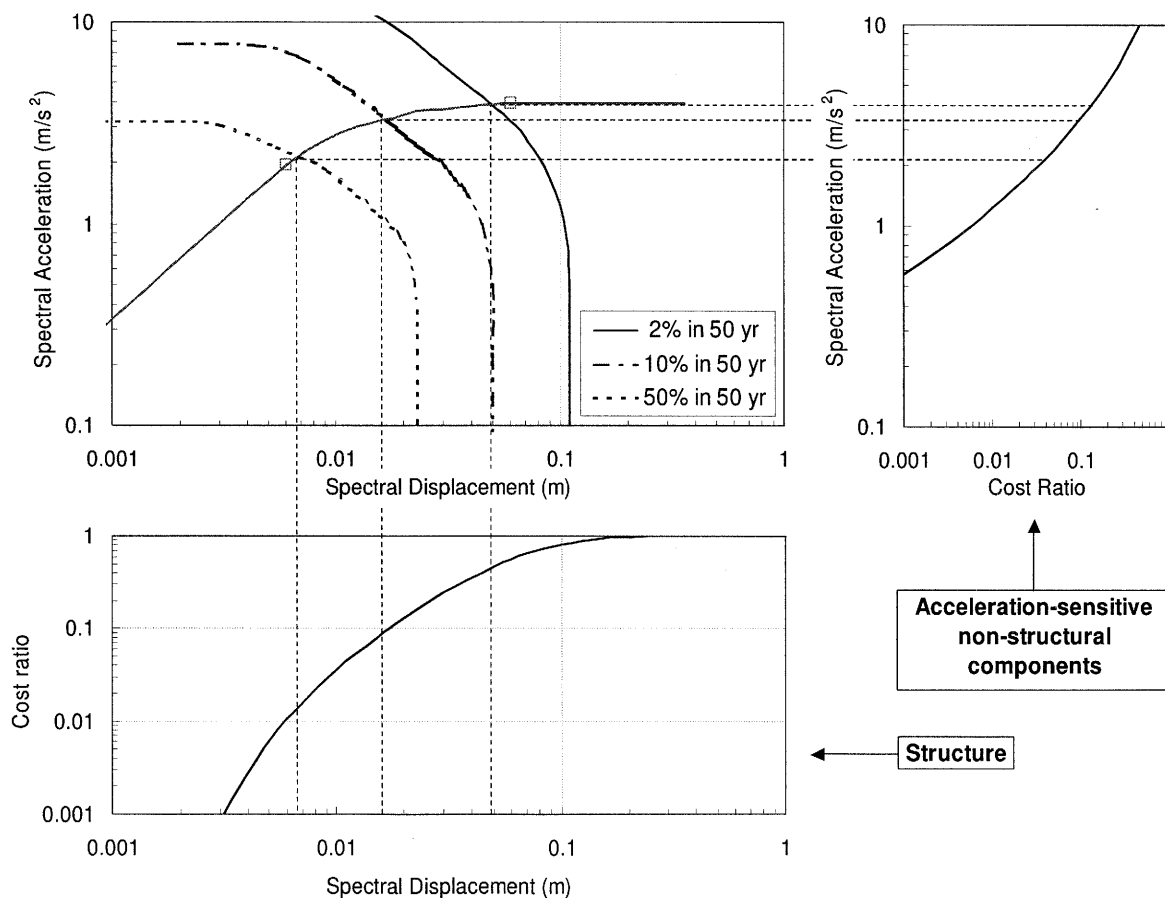


Figure 12: Damage Cost Ratios for the Structure and Non-structural Elements of a HAZUS Default Low-rise Unreinforced Masonry Building Subjected to three Levels of Ground Motion

It must be noted that for low-rise and mid-rise buildings the peak floor accelerations will correspond very well to the spectral acceleration of the fundamental mode of the building. For higher

buildings however where higher mode effects become significant the time-history analyses are likely to show that the calculated peak floor accelerations significantly exceed that implied by the spectral acceleration at the fundamental period of the building. Allowances, based on the results of the linear dynamic time history analyses, are likely to be required to determine the peak floor acceleration for high rise buildings.

4.3 Estimating Casualties

It is recommended that the HAZUS methodology be used as a basis to assess casualties arising from seismic ground motion. In this methodology four different Severity levels are assessed with Severity 1 being a minor injury, Severity 2 a serious injury requiring hospitalisation, Severity 3 a life threatening condition requiring intensive care and Severity 4 being instantly killed. The assessment of the quantity of casualties is derived as a percentage of the number of people in the building at the time of the earthquake and the level of damage sustained by the building.

Table 2: HAZUS Recommended Probabilities of Casualties as a Function of Building Damage State (from FEMA, 2003)

Injury Level	Building Damage State				
	Slight	Moderate	Extensive	Complete	Collapse
Severity 1	0.05	0.25	1	5	40
Severity 2	0	0.03	0.1	1	20
Severity 3	0	0	0.001	0.01	5
Severity 4	0	0	0.001	0.01	10

The probabilities of injury severity level is recommended by HAZUS to be a function of the building Damage State and their recommended values for reinforced concrete frame and shear wall buildings are shown in Table 2. It can be seen that the probabilities of all injury severity levels are very dependent on the amount of building damage, particularly Collapse. It is noteworthy that there is a very low likelihood of critical injuries and death, Severities 3 and 4, except where there is Building Collapse.

HAZUS recommends that the amount of Building Collapse is fraction of the buildings to experience Complete Damage. The number of casualties can be calculated for an earthquake ground motion occurring during day time (3:00pm) when the working population can be assumed to be at their place of work and at night time (3:00am) when everyone can be assumed to be at their residence.

4.4 Estimating Annual Damage Cost

To determine the annual damage cost the predicted damage cost for each of the three ground motion levels (2%, 10% and 50% probabilities of being exceeded in a 50 year period) must be integrated over time. To do this calculation it is necessary to use the annual frequency that the ground motion is being exceeded rather than the probability of being exceeded within any given time period. The 2%, 10% and 50% probabilities in 50 years correspond to annual frequencies of being exceeded of 0.0004, 0.0021 and 0.014. A smooth curve is fitted to these damage cost values and the curve then divided into small increments and the annual frequency of each increment determined. The annual frequency of each increment is determined by calculating the difference in the annual frequencies of being exceeded at each successive increment. The annual damage cost of each increment is then derived by multiplying the average damage cost for that increment by the annual frequency of that increment. The overall annual damage cost is the sum of the annual damage costs from all of these

increments. It must be emphasized that the overall annual damage cost is the average over a very long period of time (several thousands of years) and is usually significantly influenced by the effects of very rare and quite large seismic events.

5. COST BENEFIT ANALYSES

Cost benefit analyses can be carried out to determine the economic benefit of introducing various code rules. The procedure basically comprises considering a range of buildings, and then, for each, determining what additional construction cost would be implied by the introduction of the code rules and determining the reduction in damage cost over the useful lifetime of the building. Only reinforced concrete frame buildings and reinforced concrete shear wall buildings will usually need to be considered as it is apparent that if a code is introduced unreinforced masonry buildings and buildings with unreinforced infill walls are not likely to be permitted.

When determining the additional cost the additional material cost of both reinforcement and concrete must be considered. Seismic design forces for the buildings can be derived from the soil surface spectra shown in Figure 2 using the procedure suggested by IBC 2003. The additional material cost of the detailing rules conforming to Intermediate Moment Frames as required by IBC 2003 must also be included. If a column size is required to increase the loss of floor area can also be assigned a cost. There will also be a cost due to additional construction time and design effort.

To determine the benefit from the estimated reduction in damage cost, the median values of the fragility functions can be adjusted as recommended by HAZUS. This amounts to changing from Pre-code Seismic Design values to those for Moderate-Code Seismic Design values. Figure 13 shows these values for the height ranges covered by the default HAZUS values. The risk calculations described above can then be repeated so that for each building type the annual damage cost for each Site Class is determined and compared to the original value. The benefit is then derived by multiplying the reduction in annual damage cost by the useful life of the building, often assumed to be 50 years.

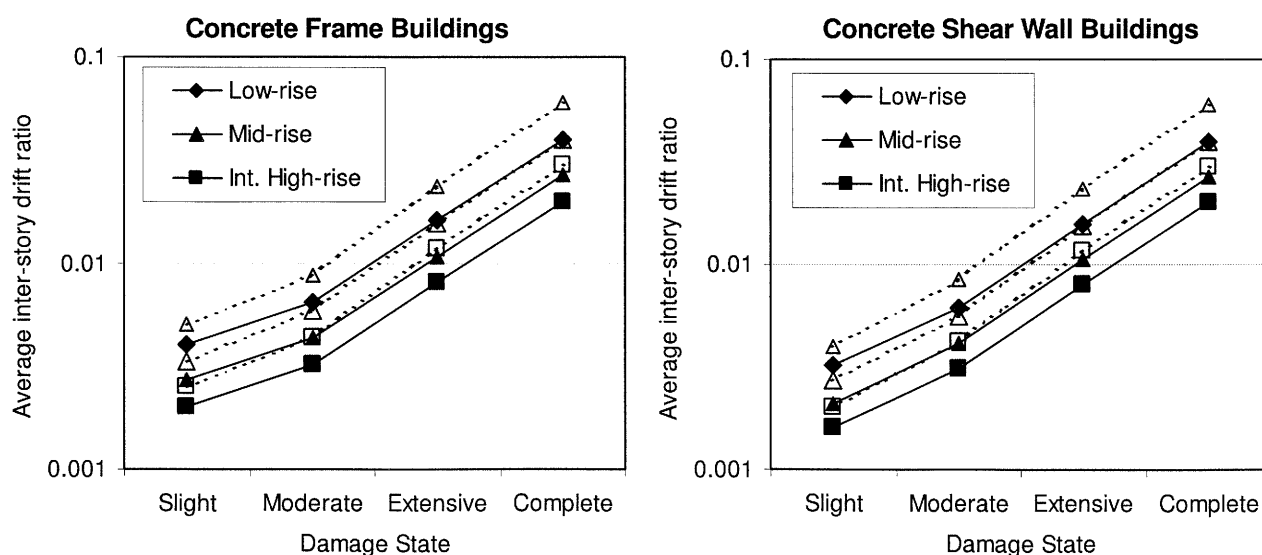


Figure 13: Default Median Values of HAZUS Fragility Functions for Concrete Buildings; Solid Lines are for Pre-Code Seismic Design and Dashed Lines for Moderate Code Seismic Design

6. CONCLUSIONS

The paper has presented a methodology for determining the seismic risk to buildings in a modern high-rise city in a region of moderate seismicity.

The input ground motions are determined for probabilities of being exceeded of 50%, 10% and 2% in 50 years using conventional seismic hazard calculation methods. The ground conditions need to be classified using the NEHRP recommendations and a Site Class zoning map produced. A methodology has then been presented for determining the amplification functions and their variability.

Ideally a GIS based building database is established to identify representative building types to enable a sensible classification system to be established. A method is presented for determining the building response to seismic ground motion that is largely based on the HAZUS methodology as described in FEMA (2003) and methods for calibrating this methodology to a new region and extrapolating it to high rise building types are discussed.

By combining the ground surface seismic motions with the building capacity curves and fragility functions the amount of building damage experienced by each building type on each soil Site Class is determined. A GIS analysis can then be carried out by laying a grid over the region to enable the total floor area of building damage to be determined for each level of seismic ground motion. At the same time the total damage cost and the number of casualties are estimated. A method for determining the annual damage cost from seismic loading (averaged over a very long time period) is presented.

Finally a method to carry out a cost benefit analysis of introducing seismic design rules is discussed. The additional cost of applying a set of design rules is quantified in terms of additional construction materials. The benefit is derived by first deriving revised fragility functions assuming the buildings have been designed, detailed and constructed in accordance with the seismic design rules. The annual damage cost that would be expected if these rules were in place can then be determined. The benefit is the reduced annual damage cost applied over the service life of the building.

References:

- ACI 318-02 (2002), "Building Code Requirements for Structural Concrete", Reported by ACI Committee 318, *American Concrete Institute*, USA.
- Arup (1993), "Earthquake Hazard and Risk in the UK", The Department of the Environment. *HMSO*, UK.
- ATC 40 (1996), "Seismic Evaluation and Retrofit of Concrete Buildings." *Advanced Technology Council*, California, USA.
- Coburn, A. and Spence, R. (2002), "Earthquake protection," 2nd Edition, *John Wiley and Sons Ltd*.
- Cornell, C.A. (1968), "Engineering seismic risk analysis", *Bulletin of the Seismological Society of America*, **58**, 1583-1606.
- FEMA (2000), "Earthquake Loss Estimation Methodology, HAZUS 99 Service Release 2 (SR2) Advanced Engineering Building Module, Technical and User's Manual." *Federal Emergency Management Agency*, Washington, D.C., USA.
- FEMA (2003), "Multi Hazard Loss Estimation Methodology, Earthquake Model, HAZUS MH Technical Manual", *Federal Emergency Management Agency*, Washington, D.C., USA.
- FEMA-273 (1997), "1997 NEHRP Recommended Provisions for Seismic Regulations for New Buildings", *Federal Emergency Management Agency*, Washington D.C., USA.
- FEMA-274 (1997) "NEHRP Commentary on the Guidelines for the Seismic Rehabilitation of Buildings." Prepared for: Building Seismic Safety Council, Washington, D.C., *Applied Technology Council*, California, USA.
- FEMA-356 (2000), "Pre-standard and Commentary for the Seismic Rehabilitation of Buildings." *Federal Emergency Management Agency*, Washington, D.C., USA.
- Free, M.W., Pappin, J.W. and Koo, R. (2004), "Seismic hazard assessment in a moderate seismicity region, Hong Kong", *Proceedings of the 13th World Conference on Earthquake Engineering*, Paper No. 1659, Vancouver, Canada.
- International Code Council (2003). "International Building Code IBC-2003", *ICC*, USA.
- Pappin, J.W., Free, M.W., Bird, J. and Koo, R. (2004), "Evaluation of site effects in a moderate seismicity region, Hong Kong", *Proceedings of the 13th World Conference on Earthquake Engineering*, Paper No. 1662, Vancouver, Canada.

RESEARCH ACTIVITIES ON EARTHQUAKE DISASTER MITIGATION IN ARMENIA

K. Seo¹⁾, S. Sasano¹⁾, and K. Motoki²⁾

1) Professor, Department of Built Environment, Tokyo Institute of Technology, Japan

2) Research Associate, Department of Built Environment, Tokyo Institute of Technology, Japan

seo@enveng.titech.ac.jp, ssasano@enveng.titech.ac.jp,

kmoto@enveng.titech.ac.jp

Abstract: When we visited Armenia in September 2003 for a field survey of Armenian traditional churches and monasteries, we also visited Armenian researchers in the field of seismology and earthquake engineering. Then the contents of this paper would be related with the 1988 Spitak earthquake and with the research activities they have made after the earthquake. After all it turned out that the potential of research activities in seismology looked very high. On the other hand, the remaining problem might be the vulnerable condition of recent reinforced-concrete building structures. Although collapsed building structures have been demolished in the damaged area and new buildings after the 1988 earthquake could be improved already, the further difficulty still remains most of all in the capital region of Yerevan. With respect to traditional masonry structures including old churches and monasteries, they looked much better than recent RC buildings. The most significant advantage for traditional churches was that they were built in good site condition without exception. Therefore we are sure that the maintenance of such traditional heritages could be possible with the minimum efforts in structural enforcement. The harder problem might be in modern cities with vulnerable structures where huge amount of people are living now.

1. INTRODUCTION

An opportunity to visit Armenia was given in September 2003. We made a field survey for Armenian traditional churches and monasteries from the historical and architectural point of view. At that time we need to evaluate site conditions around the churches and to estimate the degree of damage for individual structures. For this reason, our interest was to visit as many as seismologists and earthquake engineers in the country. Their suggestion must be very useful if we want to keep such traditional heritages in safe condition from future earthquake disasters. Probably the experience of the 1988 Spitak earthquake should be very important.

2. SEISMOLOGICAL AND EARTHQUAKE ENGINEERING ACTIVITIES IN ARMENIA

2.1 Armenian Association of Seismology and Physics of the Earth (AASPE)

Before we visited Armenia, Prof. Balassanian, President of AASPE, had been in Tokyo for the 2003 IUGG meeting. While we are in Yerevan, a brief meeting was set with him for discussing about research topics, and we exchanged an agreement draft for our future research cooperation. He arranged a trip to visit Prof. Nazaretyan in Gyumri for us. Actually it was one of our most important subjects to be there, as Gyumri (It was called as Leninakan during the Soviet period) had suffered the severest damage during the 1988 Spitak earthquake.

2.2 Northern Department in Gyumri, National Survey for Seismic Protection (NSSP)

Mr. Sos Margaryan, a researching staff of Prof. Balassanian, kindly took us to Gyumri. He has

been a trainee in the 2000/2001 seismology course, prepared by Building Research Institute (BRI) and JICA every year for young researchers from earthquake countries. Then we visited Prof. Nazaretyan, Director of NSSP Gyumri, to know what happened in Gyumri during and after the 1988 Spitak earthquake. The important aspects could be observed as follows.

(a) Damage due to the 1988 earthquake in Gyumri

Seismic intensity in MSK scale was estimated as X in Spitak, IX in Gyumri (Leninakan at that time), and VIII in Vanazor (Kirovakan at that time) and Stepanavan, respectively. The amount of deaths in Gyumri counted about 17 thousands among 230 thousands in population, while the present population in Gyumri is about 140 thousands. Destroyed buildings counted as 167, and 80% of them were totally collapsed. The significant damage appeared in the taller buildings with 5 floors through 9 floors, and they were precast frame-panel structures. The lower buildings and masonry houses did not suffered such sever damage. The reason of failures was regarded that welding skill was not enough, and that the building code was ignored in some cases.

Prof. Nazaretyan guided us to Freedom Square, the central area of Gyumri, to tell a very interesting story. There are two churches facing to the square. St. Astvatsatsin Church on the Square's north side (Photo.1) did not suffer any damage during the 1988 earthquake. On the contrary All Savior's Church on the south side (Photo.2) suffered very heavy damage, and it is on the process to be repaired up to now. According to Prof. Nazaretyan, the soil condition might be quite different even in such close distance. It is certain that Kumayri River runs across the square in the north-south direction.

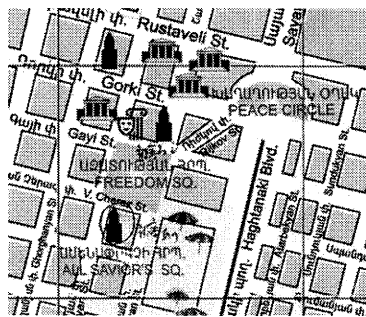


Fig.1 Freedom Square in Gyumri

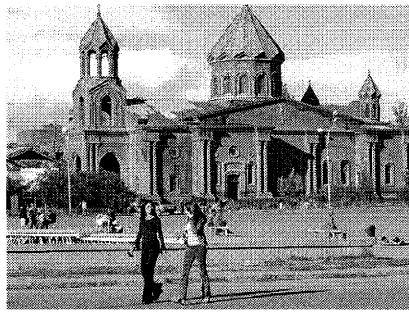


Photo.1 St. Astvatsatsin Church undamaged

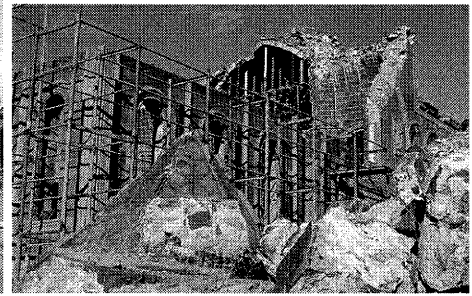
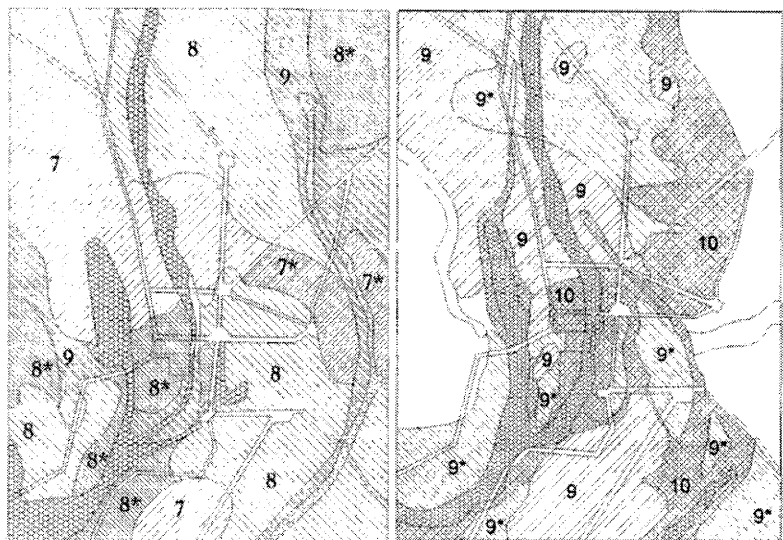


Photo.2 All Savior's Church heavily damaged

(b) Engineering aspects before and after the 1988 earthquake in Gyumri

It was our greatest surprise knowing that a seismic microzoning map (expected MSK intensity distribution map for future earthquakes) had been prepared for Gyumri city in 1978 (Balassanian, Chief editor, 2002). According to Prof. Nazaretyan, Profs. Nazarov, A.G. and Medvedev, S.V. contributed very well to do this work since 1965. A database including soil classification with water level, shear wave velocity of the uppermost 10 meters in surface layers, measured micro-tremors and observed seismic motions was taken into account for the mapping. The map has been improved in 1990 by means of reevaluation after the 1988 earthquake. These two maps can be compared each other in Fig.2. Then it could be pointed out that the 1988 earthquake brought



Նկար 2.11 Գյումրի քաղաքի տարածքի սեյսմիկ միկրոշրջանացման քարտեզները կազմված տարբեր ժամանակներում.

ա) 1978թ., երբ քաղաքի ելակետային վտանգը գնահատված էր 8 բալ;

բ) 1990թ., երբ քաղաքի ելակետային վտանգը գնահատվեց 9 բալ:

Fig.2 Seismic microzoning maps made in 1978 (left) and in 1990 (right).

much harder damage in Gyumri than that had been estimated before the earthquake.

Just after the 1988 earthquake, there were four types of consideration about new buildings those should be reconstructed. 1) Monolithic concrete structures with 4 or 5 floors, 2) large panel structures also with 4 or 5 floors, 3) stone masonry structures using tuff (volcanic) material, and 4) base isolated structures were recommended. But new constructions of private buildings and houses were not permitted in the period from 1992 through 1995.



Photo.3 Large panel structure under construction, but nobody is found around the site. (outer Gyumri)

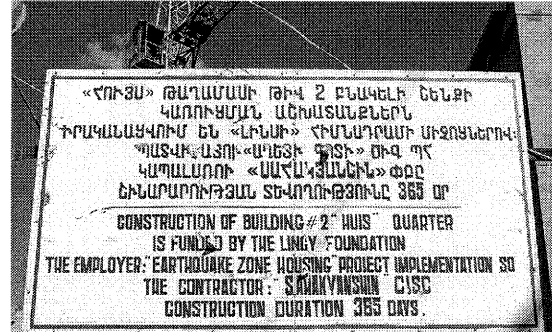


Photo.4 A new construction site in Gyumri. The panel indicates as Earthquake Zone Housing Project.



Photo.5 Typical infilled RC frame structure for residence in Ani district, new town in Gyumri.

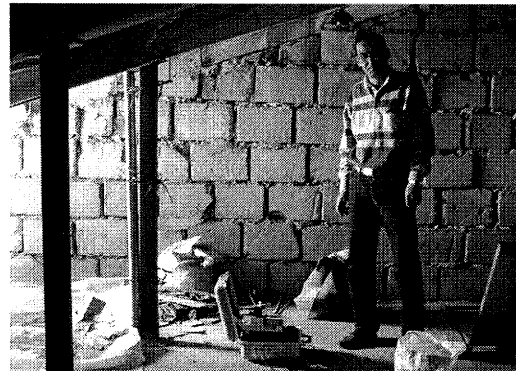


Photo.6 Roof floor of the structure in Photo.7 to see infilled wall. (with Mr. Sos Margaryan)

2.3 National Survey for Seismic Protection (NSSP) in Yerevan

We have met with Mr. Hamlet Mirzoyan, Security Officer Assistant of United Nations in Yerevan, by chance because his office located just in the neighbor of our hotel. He kindly offered guiding us to National Survey for Seismic Protection (NSSP) in Yerevan. It was actually the research institute related to earthquake engineering, engineering seismology and seismic hazard assessment. Among them, research activities by Dr. Khlghatyan were the closest with our occasional interest. At that time he was engaged in developing new technologies to upgrade earthquake resistance of existing buildings. Base isolation technology has been applied for retrofitting. He provided some of pictures showing such works. It was so good for us knowing that his section has been trying the maintenance of traditional churches by means of structural analyses and actual enforcements.

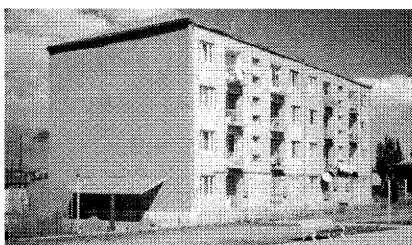


Photo.7 Base isolated building in Spitak

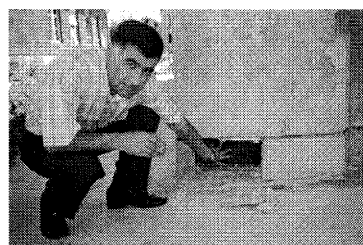


Photo.8 Dr. Khlghatyan showing base isolation element

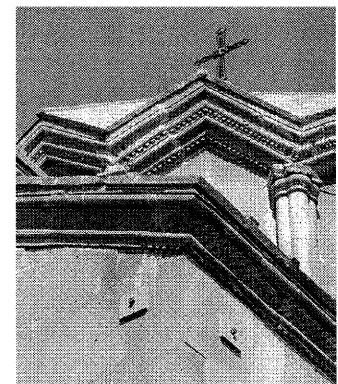


Photo.9 Structural enforcement in Marmashen Church

3. LESSONS LEARNED FROM THE 1988 SPITAK EARTHQUAKE

With respect to the 1988 Spitak earthquake, Japanese investigation team has been dispatched twice after the earthquake. Their activities were reported in detail (JICA, 1990). According to this report, they pointed out quite vulnerable condition of building structures most of all in framed precast reinforced concrete (RPC) construction. On the other hand, wall-type precast reinforced concrete (WPC) structures did not suffer severe damage. Dr. Hiroyoshi Kobayashi, Professor Emeritus of Tokyo Institute of Technology, was in the second investigation team. He measured microtremors on the ground surface and on the top of some of buildings to evaluate site condition of damaged city areas and dynamic behavior of buildings. After such field surveys by himself, he pointed out the possibility of resonance effects between predominant period of ground and natural periods of building structures on the damage distribution. And he recommended that seismic microzoning should be taken into account in the city planning and reconstruction process after the earthquake. Now we are confusing a little bit about two kinds of meaning of seismic microzoning, one by Dr. Kobayashi and the other considered in Armenia that we introduced above. Probably we need additional surveys to get an agreement between them.

Our sympathy appears in existing buildings around Yerevan capital district. It is sure that several improvements could be taken in the reconstruction process after the 1988 earthquake as Prof. Nazaretyan and Dr. Khlghatyan suggested before. But around the Yerevan district, the older buildings constructed before the earthquake remained without any damage. It was mealy because of far distance from the source region. Therefore we are really afraid that the vulnerable condition of the capital region might have serious problem in case of the closer earthquake in the future. We can recognize such examples of vulnerable structures in the following pictures. The only uncertain point about under construction sites was that we could not find any working people in most of the cases. Therefore we are not sure whether they are actually under construction or they stop the construction.

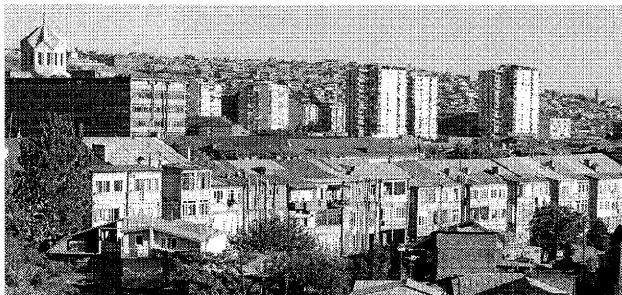


Photo.10 A scene of Yerevan (toward the south)



Photo.11 A scene of Yerevan (a scene from Hotel Erebuni)

Fortunately very firm soil condition in the central Yerevan will provide an advantage in spite of vulnerable building structures. But in the process of the further developments toward the southwestern direction, we should be very careful about the effects of surface geology on strong earthquake motion as an additional subject.

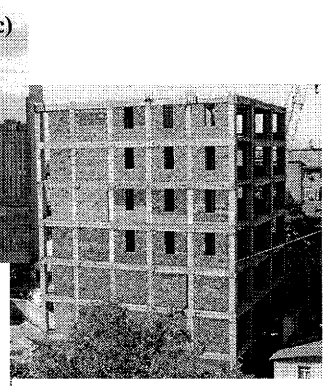
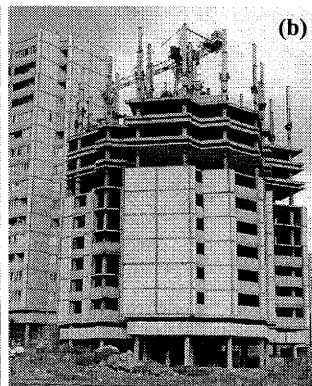


Photo.12(a-c) Tall buildings with lift-slab method are still under construction in Yerevan. There is no wall on the ground level, and outer walls in upper floors are non-seismic.

Photo.13 Infilled PC frame structure in Yerevan

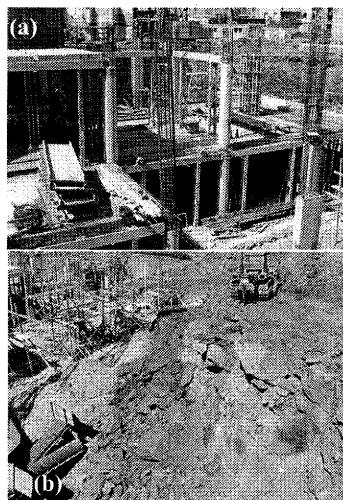
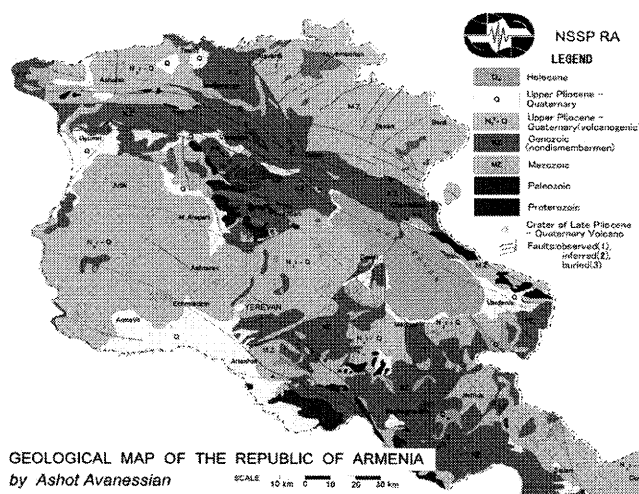


Photo.15(a,b) Construction site in Central Yerevan with cast-in-place RC (a) and its soil condition (b).



4. FIELD SURVEYS FOR TRADITIONAL ARMENIAN CHURCHES

- 274 -

recent framed precast reinforced concrete (RPC) structures. The only problem was inevitable weathering effects through a thousand years or more. Very careful maintenance should be required in necessary frequencies. It does not look so difficult if the economic condition permits to do it. Finally the most typical pictures will be presented below in Photo.22. Because we are very sure that nobody can imagine about inside beauty from the outside. Who can help this situation now?

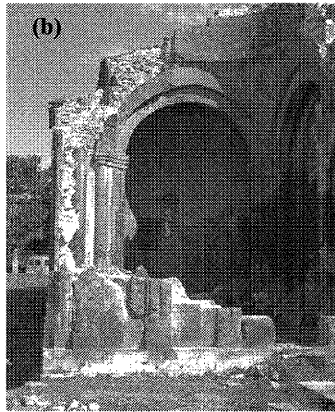


Photo.19(a,b) Marmashen Church near Gyumri heavily damaged by the 1988 earthquake. Enforcement can be seen on the top of wall tiles.

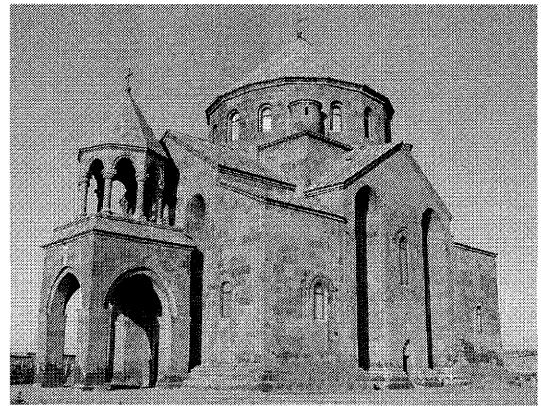


Photo.20 Beautiful Hripsime Church with balcony near Ejmiatsin. It is still being used up to now.

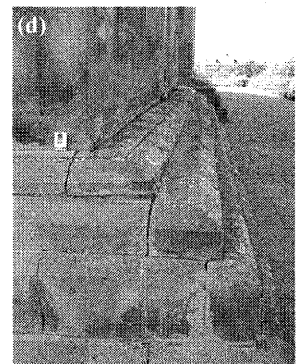
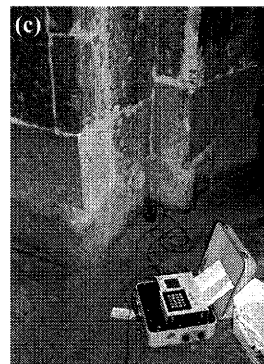


Photo.21(a-d) Hripsime Church in detail. A ladder to balcony (a). Wall cracks repaired with white mortar (b). Equipments measuring ambient motions at the base floor (c). Skirting stone blocks as there is no foundation (d).

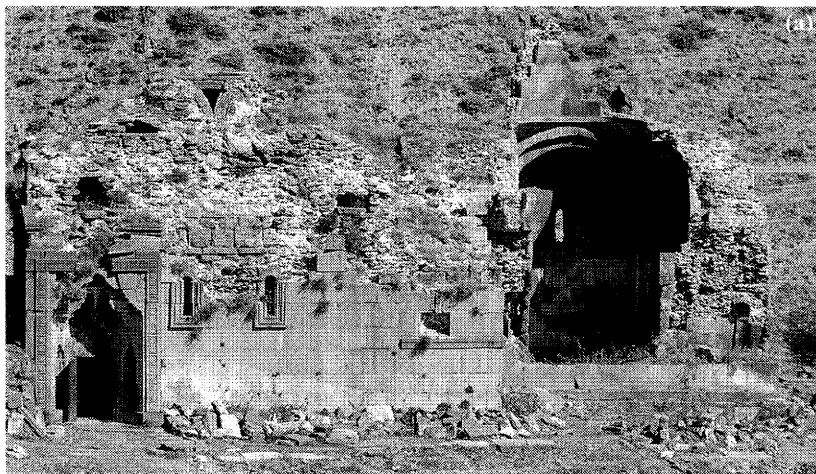


Photo.22(a,b) Neghuchivank between Yerevan and Sevan Lake. It shows the highest contrast between almost collapsing outside view and very beautiful inside view. Repairing works should be urgently required to keep such an important cultural heritage in safe from natural disasters.

5. CONCLUDING REMARKS

When we have visited Armenia in September 2003 for a field survey of Armenian traditional churches and monasteries, we also made a brief effort to visit Armenian researchers in the field of seismology and earthquake engineering. Thanks to this opportunity, we could learn many things not only about our research aspects but also about cultural background in Armenia. Surely our highest interest was about the 1988 Spitak earthquake and about the research activities they have made after the earthquake. Through the interviews to concerning members, it was made clear that the potential of research activities in seismology looked very high. On the other hand, the remaining problem might be the vulnerable condition of recent reinforced-concrete building structures. Although collapsed building structures have been demolished in the damaged area and new buildings after the 1988 earthquake could be improved already, the further difficulty still remains most of all in the capital region of Yerevan. With respect to traditional masonry structures including old churches and monasteries, they looked much better than recent RC buildings. The most significant advantage for traditional churches was that they were built in good site condition without exception. Therefore we are sure that the maintenance of such traditional heritages could be possible with the minimum efforts in structural enforcement. The harder problem might be in modern cities with vulnerable structures where huge amount of people are living now.

ACKNOWLEDGEMENTS

Our research activities in Armenia, that had been made in September 2003, was supported by many related institutions and their members in deed. In addition to several members we have introduced already in our report, we will appreciate the following members for their supports. Minister Tamara Poghosyan, Ministry of Culture, Youth Affairs, showed her interest about our research and offered her cooperation in the future. President Gurjan, the Agency for Cultural Affairs, kindly provided enough information for our field investigation and enough hospitality during our stay in Armenia. Mr. Leonid always supported us with language translation. He also tried his efforts teaching us Armenian culture as the background. Thanks to his effort, we could understand a little bit how Armenian people were able to keep their own language and culture during the long term occupation by Soviet from 1920 to 1991. According to his saying, the Armenian Church played an important role to organize all Armenians, including domestic three millions and another eight millions staying abroad. We would like to express our respect for their greatest cultural activities.

On November 23, 2004, very sad news was brought from Armenia that Prof. Serguei Balassanian passed away because of sudden automobile accident. We pray his soul may rest in peace.

REFERENCES

- Cisternas, A. et al.: The Spitak (Armenia) Earthquake of 7 December 1988: Field Observations, Seismology and Tectonics, *Nature*, Vol.339, No.6227, pp.675-679, 1989
- Armenia Earthquake Reconnaissance Report, *Special Supplement of Earthquake Spectra*, 1989
- Japan International Cooperation Agency (JICA): Report of Japan Disaster Relief Team on Earthquake at Spitak, Armenia, USSR, 1990
- Balassanian, S. et al.: Retrospective Analysis of the Spitak Earthquake, *Annali di Geofisica*, Vol.38, No.3-4, pp.345-372, 1995
- Balassanian, S. et al.: The New Seismic Zonation Map for the Territory of Armenia, *Natural Hazards*, Vol.15, pp.231-249, 1997
- Balassanian, S. et al.: Seismic Hazard Assessment for the Caucasus Test Area, *Annali di Geofisica*, Vol.42, No.6, pp.1139-1151, 1999
- Balassanian, S. et al.: Seismic Hazard Assessment in Armenia, *Natural Hazards*, Vol.18, pp.227-236, 1999
- Martirosyan, A. et al.: Computation of Probabilistic Seismic Hazard for the GHSAP Test Area 'Caucasus', *Natural Hazards*, Vol.20, pp.1-20, 1999
- Balassanian, S. et al.: Seismic Risk Assessment for the Territory of Armenia and Strategy of its Mitigation, *Natural Hazards*, Vol.20, pp.43-55, 1999
- Margaryan, S.: Country Report on Seismic Observation and Seismic Hazard Assessment in Armenia, Country Report for the Group Training Course in Seismology and Earthquake Engineering 2000/2001, Japan International Cooperation Agency, 2001
- Balassanian, S. (Chief editor): The Seismic Protection and its Organization (Training Manual), 2002 (in Armenian)

DEVELOPMENT OF AN INTEGRATED GIS AND SPACE TECHNOLOGY APPLICATIONS FOR SEISMIC RISK MANAGEMENT AND MITIGATION IN URBAN PLANNING IN HIGH SEISMIC ZONES

Biswajit Sarma¹⁾ and Jayanta Pathak²⁾

1) Senior Lecturer, Department of Civil Engg., Jorhat Engg. College, JORHAT-785001, Assam, India

*2) Assistant Professor, Department of Civil Engg., Jorhat Engg. College, JORHAT-785001, Assam, India
iambiswajit@yahoo.com , jayanta_pathak@rediffmail.com*

Abstract: Urban planning in disaster prone areas especially in areas of high seismic activities is a difficult task. In India, rapid urbanization is resulted due to the unprecedented population growth coupled with unplanned developmental activities. The North Eastern region of India is recognized as being highly seismic and two world's most severe earthquakes of June 1897 and August 1950 have occurred in the region, which has affected the city of Guwahati in the past. The earthquake risk assessment and mitigation is a multidisciplinary task and requires collateral approach and collection of huge amount of data in different fields, its integration and interpretation. Soil Liquifaction susceptibility, ground rupture and failure of slopes are the earthquake induced destabilization processes, which are the main factors responsible for seismic disasters. It has been realized that there is a strong need of application of space technology to create a global digital database containing urban sprawl information, available land for urban growth, the rate of land development and land use change, information regarding bedrock profile, liquefaction potential information etc. for standardization of Disaster Mitigation and Management Planning. In this study, an integrated GIS and Remote Sensing based methodology is developed and successfully tested by taking the city of Guwahati as a typical case. This database comprises of general principle of risk analysis, integration of seismic hazard/vulnerability data, equivalent damage ration (EDR) and index for people living in structures susceptible to damage, damage to different lifeline structures, retrofitting procedures etc. Finally, a Remote Sensing and GIS based Information and Decision Support System for earthquake risk management and mitigation planning is designed to provide facilities to the planning authorities to take strategic decisions and to set guidelines regarding the new constructions and vulnerability assessment of the existing structures. The three dimensional simulated sub surface ground conditions with the facilities to get cross sectional views in any specified direction with geotechnical details are the major highlights in this Information System.

1. INTRODUCTION

The cities are like trees; both of them grow under natural limits. These limits affect in the formulation of a city's master plan (*Mahrour, et al, 2002*). In India, rapid urbanization is resulted due to the unprecedented population growth coupled with unplanned developmental activities. This urbanization, which lacks in infrastructure facilities, has posed serious implications on the resource base of the region. The urbanization takes place either in radial direction around a well-established city or linearly along the highways (Guwahati Path finder, 2000). The city of Guwahati in India provides a

typical case of haphazard and unplanned urbanization.

Keeping these perspectives in view, attempt has been made to provide opportunities to realize a strategic assessment to determine the current status of land use, land suitability information, identification of the patterns of change during the past years, assessment of the impact of infrastructure development in terms of zoning regulations, transportation facilities, public utilities, drainage system, population, industry, tourism etc to meet the challenges in Planning and Management of Guwahati City using integrated remote sensing and GIS technology.

The data elements (Landuse / landcover, infrastructure, drainage etc.), which have both static and dynamic components, pose a formidable challenge for proper maintenance and operations in different sectors concerns. Due to development of automation in technological processes applied to data gathering, integration and processing of topographic details and their customized presentation, analysis and interpretation the challenges can be met with the help Desktop GIS system. While Geographic Information System (GIS) involves in integration of spatially referenced data in a problem-solving environment. GIS-based Decision Support System (DSS) is an interactive computer-based systems that help decision makers utilize data and models to solve unstructured problems. Combining both the ideas, in the present times such powerful software technology has been developed that allows virtually unlimited amounts of information to be linked to a geographic location. Coupled with a digital map, GIS records, stores, and analyzes information about the features that make up the earth's surface, thus allowing a user to see regions, countries, neighborhoods, and the people who live in them with unprecedented clarity (Betty, et al, 1998).

In this study an integrated remote sensing and GIS based methodology is developed and successfully tested by generating an up to date digital database. Finally a Decision Support System is designed for the city development authorities.

1.1 Objectives

The main objectives of this study area with respect to its problems are:

- 1) To identify the urban sprawl by using remote sensing data
- 2) To identify the available land for urban growth or satellite township
- 3) To monitor the rate of land development and land use change
- 4) To highlight areas which are close to reach saturation and require immediate attention from the concerned authorities
- 5) To know the growth pressure with land use and zoning regulations into perspective from available data
- 6) To identify areas which exhibit high rate of development and are faced with the problem of over densification and suffering from stagnation due to lack of adequate infrastructure.
- 7) To determine the depth of bed rock profile from the borehole data with N values.
- 8) To assist the decision makers in laying the foundation for the growth of the Guwahati Metropolitan area
- 9) To develop a Web based interactive Decision Support System (DSS) for immediate and ready extraction of plot wise detailed information.

2. THE STUDY AREA: IT'S PROBLEMS

The city of Guwahati, located at latitude $26^{\circ}10'45''$ N & longitude $91^{\circ}45'0''$ E in the district of Kamrup District is considered as the gateway to the seven northeastern states known as Assam,

Arunachal Pradesh, Meghalaya, Manipur, Nagaland, Mizoram and Tripura of India. The city spreads about 10 km in north south direction and 27 km in east west direction. Naturally the city plays a vital role in the socio-economic development of the entire region. The first aspect of the city that strikes a visitor is the natural beauty of the place. It is ringed around on three sides by a chain of hills stretches to the horizon. The northern side is bounded by awesome Brahmaputra river.

Major problem with the study area can be identifies as are (i) Rapid Growth of Population within the three decades till date and (ii) Unplanned growth of the city both horizontally in all direction and vertically so also.

There is a rapid growth of population in the city from 292029 to 1067400 within a period of 30 years from 1971 to 2001 (Census of India, 1991 and 2001). The rapid increase in population of the city coupled with its importance in terms of being the center of social, commercial, educational, political and industrial activities made the city to be the important center of the entire north eastern region of India. This has resulted in rapid expansion of constructed areas at a very fast pace almost beyond the control of the authorities entrusted with planning and development actions and regulation of the city works. Secondly, due to the unplanned growth of the city both in horizontal and vertical directions, there is a need for proper planning for the careful handling of this alarming situation.

3. DATA USED

There are three different datasets are used in this study. They are (i) Satellite data in digital format, (ii) Analog data in the form of maps and (iii) field data collected from various sources. The data sets used in the present study with their specific purposes are listed in table 1.

Table 1 List of data used in the present study.

Name of Map	Data Base	Year	Scale
Proposed Land Use	DRG: TPO/GMP/83 – 84/ 01 dated 20/05/83	1983	1:30000
Master Plan for Guwahati	DRG/: GUO/TP/GMP/R/01 dated 10/05/79 Revised on 07/05/79	1992	1:20000
Land Use	SPOT – 1 HRV 2PLA MLA PATH – D 238, ROW – 298; 78 N/12 NE, 78 N/16 SE, 78 N/12 NW, 78 N/16 SW Acquisition date: 18/10/90; SOI 78 N/12, 78 N/16	1990	1:50000
Population	Ward map GMC, Census 1991 Survey of India, 78 N/12, 78 N/16	1991	1:50000
Drainage and Flood Prone	SPOT MLA P-238, P-298; Acquisition date:18/10/90 Landsat TM P-137, P-042 Acquisition date:10/06/88; Survey of India, 78 N/12, 78 N/16	1990	1:50000
Urban Sprawl	SPOT MLA P-238, P-298; Acquisition date:18/10/90 Landsat TM P-137, P-042 Acquisition date:10/06/88; Survey of India, 78 N/12, 78 N/16	1990	1:50000
Land Suitability	SPOT MLA P-238, P-298 Landsat TM P-137, P-042 Survey of India, 78 N/12, 78 N/16	1991	1:50000

To support image classification and thematic information collection, several field trips have been realized to the study area. Information on land cover and land use has been collected by using a video recorder and Konica LandMaster GPS camera. The GPS camera with a built-in GPS chip provides information such as date and time, geographical co-ordinates and bearing captured on the film media together with image. This information combination represents an excellent tool for accurate data registration and enhances the efficiency of the in-house work.

4. METHODOLOGY

The methodology adopted in the study can be described in the following steps.

- a) The map of Guwahati City and its surrounding areas is digitized. The Cadastral data comprises of the characteristics of the drainage network, road and railway network and infrastructure facilities in the city.
- b) The satellite data were processed and classified using supervised classification method to prepare the land use/land cover map. The spatial and temporal changes in growth pattern are recognized from the digital data.
- c) Plot-wise urban land use map is prepared and attributes were assigned for every plot with full ownership and built-up information.
- d) A Decision Support System has been created to acquire information regarding every plot with its all attributes.
- e) The entire database is converted into a web supported format and is customized to provide query facilities for immediate and ready extraction of information through Web

The entire database has been developed by using data from diverse sources. The pattern of urban sprawl is identified and modeled using remotely sensed data. This helped in identifying the linear and radial pattern of growth and its rate. The analyses involved were land cover, land use, spatial and temporal changes and urbanization growth pattern recognition. The cadastral data comprises of the characteristics of land use / land cover, drainage network, roads and railway network and the administrative boundaries of 1991 from the toposheets provided by the Survey of India. The remote sensing data was classified for land use, based on themes - built up, transportation (road and rail network), water bodies (rivers, streams, etc.), agriculture and barren (uncultivable and waste land). For the change detection, temporal data between 1972 and 2002 (e.g. SPOT-1, Landsat TM, IRS-LISS-III and PAN) were used. This helped to identify the patterns of the change with respect to time.

5. RESULTS AND DISCUSSION

The entire database has been created using ArcView 3.2 GIS Software. The SPOT – I Satellite data and LANDSAT TM Digital Data are utilized for land use and land cover mapping. The different land use classes identified from these images are shown in table 2.

It is evident from the urban sprawl map that the city of Guwahati is rapidly increasing in the recent years and the growth is found mainly in south, south east direction of the original city (Figure 1). The infrastructure facilities are also growing in the city with its gradual expansion. Figure 2 shows the road network and the available infrastructure facilities found in the city. Figure 3 shows the land suitability map prepared using satellite data, which can provide a clear guidance to the city planners for

proper planning of the city in terms of proposed construction.

Table 2 Different landuse classes identified from Guwahati city area from satellite data.

Level I	Level II	Level III	Code
Urban land Use	RESIDENTIAL	Medium	1
		Low	2
	Industrial	Heavy	3
		Medium	4
		Light	5
	Commercial	Commercial	6
	Transportation	Bus terminus	8
		Railway yards	9
		Air port	10
	Public & Semi-public	Educational institution	11
		Cantonment/army camp	12
		Other/ hospital	13
	Recreational	Stadium/ playground	14
		Parks/gardens	15
Mixed built up	Mixed built up	Mixed built up	16
Agriculture	Agriculture	Agriculture	17
Forest	Dense mixed forest	Dense mixed forest	18
	Open mixed forest	Open mixed forest	19
Wasteland	Water logged area	Water logged area	20
	Marshy/ swamps	Marshy / swamps	21
	Scrubland	Scrubland	22
	Grassland	Grassland	23
Water bodies	River /stream	River /stream	24
	Riverine sand	Riverine sand	25
	Tank /Lake	Tank /Lake	26
Others	Brick kiln	Brick kiln	27
	Excavation	Excavation	28

IRS-1D-LISS-III data merged with IRS-1D-PAN data are used to generate plot wise urban landuse map (Figure 4) of the Guwahati city and attributes regarding ownership as well as built up information with complete geotechnical details were provided. This is very helpful for the controlling authorities to extract all the relevant information immediately. The Decision Support System thus produced helps the development authorities to set up the required guidelines for further development of the city.

The entire database has been converted to a web-supported format, which makes it more accessible, and faster information system for a large number of users. Moreover it is customized to offer multiple query facilities, which enable any individual to extract any information regarding any area, plot or individual plot owner (Figure 5).

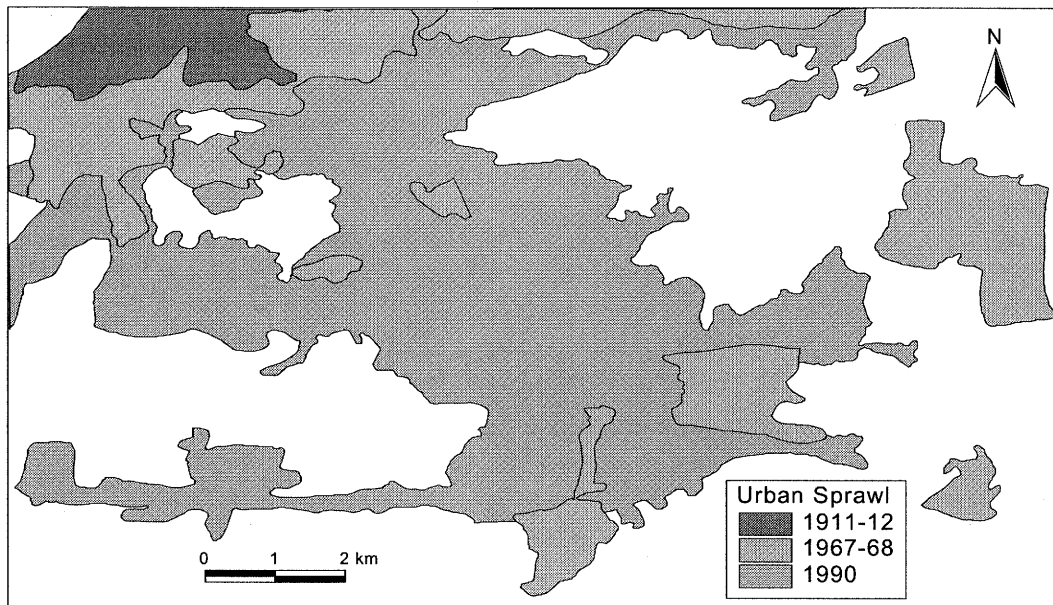


Figure 1 Urban Sprawl map of Guwahati City.

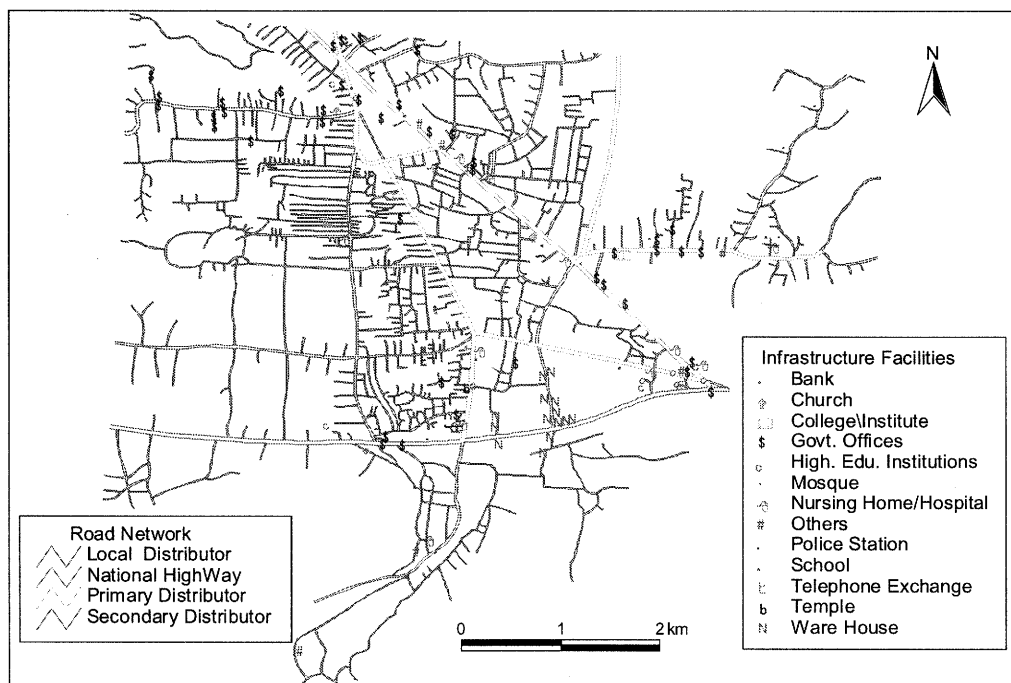


Figure 2 Road network and infrastructure facility map of Guwahati City.

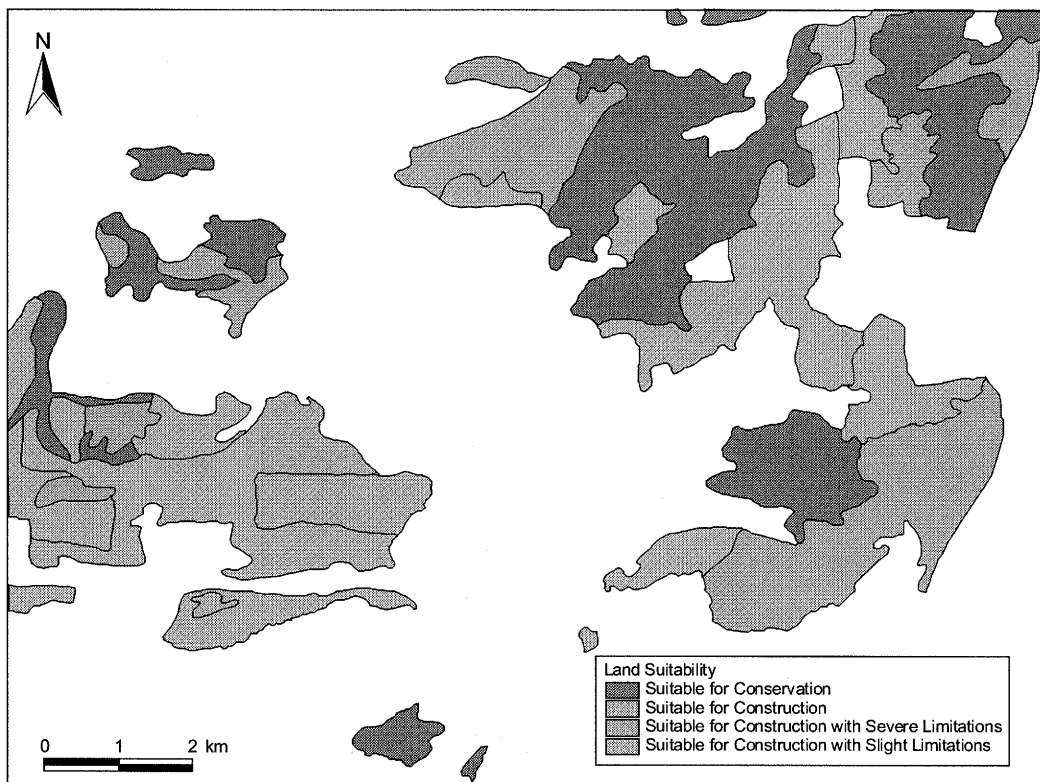


Figure 3 Land suitability map of Guwahati City.



Figure 4 Plot wise land information map of Guwahati City.



Figure 5 GIS based plot wise Decision Support System (DSS) for Guwahati City.

6. CONCLUSIONS

The following conclusions can be made from the above study:

- 1) The Integrated remote sensing and GIS methodology is found to be very useful in monitoring the urban growth of a thickly populated and rapidly increasing city like Guwahati in India.
- 2) The GIS based Decision Support System provides important tools for the developers and planners to extract information of the infrastructure facilities.
- 3) The geotechnical properties have been determined from the borehole data with N values.
- 4) The liquefaction potential at any site can be easily determined from the geotechnical properties.
- 5) The web based plot wise information system provides the facility for ready and immediate extraction of information regarding land ownership, built up history and geotechnical characteristics.
- 6) The multi query facility provided in the Web based Decision Support System allows any individual to gather information regarding land holding.
- 7) This DSS sets a meaningful relationship, which addresses zoning and its link to the existing urban density distribution, the demand of building permits, the rate of urban growth, and the index of saturation.

This Decision Support System can be utilized in much larger cities anywhere in the world with the addition of more information and desired modifications.

References:

- M S Mahrous, Prof Eng M Kyselka, Dr P Spiea, 2002, "Application of GIS to describe historical Urban Development of Kharga City, Egypt", *GIS @ Development*, June 2002, Vol. 6, Issue 6, pp 18-21.
- Guwahati Path Finder, 2000, Published by Society for Research and Communication, Guwahati, Assam.
- Statistical Hand Book, Assam, 2001, Directorate of Economics and Statistics, Government of Assam, Guwahati.
- Michael Batty, Martin Dodge, Bin Jiang, and Andy Smith, 1998, *GIS and Urban Design*. Centre for Advanced Spatial Analysis, London.
- Census of India 1991, Part III-B Series, Economic Tables (B-4(S)), Directorate of Census, Assam

CORRELATION BETWEEN HORIZONTAL AND VERTICAL COMPONENTS OF NEAR-FIELD STRONG MOTIONS

K. Shirai¹⁾ and T. Ohmachi²⁾

1) Doctoral Student, Department of Built Environment, Tokyo Institute of Technology, Japan

2) Professor, Department of Built Environment, Tokyo Institute of Technology, Japan

kshirai@enveng.titech.ac.jp, ohmachi@enveng.titech.ac.jp

Abstract: When earthquake records are treated as a causal time function, they are decomposed into the Minimum-Phase-Shift (MPS for short) and All-Pass (AP) functions that are often used in the signal analysis. This decomposition is called factorization of a causal time function. In this paper, correlation between horizontal and vertical components of near-field strong motions is discussed by means of the factorization. As a result, MPS spectral ratios and phase differences between horizontal and vertical components are dependent on each other in terms of Hilbert transforms. As for AP, phase differences between fault normal and fault parallel components are found by about π from AP time histories.

1. INTRODUCTION

In earthquake resistant design of civil engineering structures, a vertical component of input ground motion has rarely been taken into account. However, regarded earthquake response of critical structures such as large dams, long span bridges and nuclear power facilities, the vertical component sometimes plays an important role and should be considered in earthquake resistant design. Since the vertical and horizontal ground motions from earthquake events have some common features such as source and path, it seems to be natural to think that there should be some close relationship between horizontal and vertical components. In this study, correlation between both components of near-field strong motion observed during the 2000 Tottori western earthquake is discussed using the concept of signal analysis.

2. FACTORIZATION OF EARTHQUAKE RECORDS (Izumi et al. 1988, Katukura et al. 1990)

A time function is causal if it equals zero for negative time:

$$x(t) = 0 \quad \text{for} \quad t < 0 \quad (1)$$

A causal time function can be decomposed into two functions. One is the Minimum-Phase-Shift function (MPS for short) and another is the All-Pass function (AP). A causal time function $x(t)$ is written by convolution MPS $x_M(t)$ and AP $x_A(t)$ as follows Eq.(2)

$$x(t) = x_M(t) * x_A(t) \quad (2)$$

Where the subscripts M and A denote MPS and AP, respectively. The decomposition is often introduced as factorization of a causal time function in signal analysis (Papoulis, A.1977). $x_M(t)$ and $x_A(t)$ satisfy

$$x_M(t) = 0 \quad \text{for} \quad t < 0 \quad (3)$$

$$x_A(t) = 0 \quad \text{for} \quad t < 0 \quad (4)$$

In the meantime, Fourier transforms $F(\omega)$ is defined by

$$x(t) \Leftrightarrow F(\omega) = |F(\omega)| e^{i\phi(\omega)} \quad (5)$$

Where ω is circular frequency, the absolute $|F(\omega)|$ Fourier amplitude and $\phi(\omega)$ its phase.

When the Fourier transform is applied to Eq.(2), Eq.(6) will be obtained below:

$$F(\omega) = F_M(\omega) F_A(\omega) \quad (6)$$

MPS and AP have the Fourier amplitude and phase respectively as follows:

$$F_M(\omega) = |F_M(\omega)| e^{i\phi_M(\omega)} \quad (7)$$

$$F_A(\omega) = |F_A(\omega)| e^{i\phi_A(\omega)} \quad (8)$$

Here, the Fourier amplitude of AP is unity:

$$|F_A(\omega)| = 1 \quad (9)$$

The Fourier transform $F(\omega)$ of $x(t)$ shall be written by means of MPS and AP:

$$F(\omega) = |F_M(\omega)| e^{i(\phi_M(\omega) + \phi_A(\omega))} \quad (10)$$

Therefore the Fourier amplitude $|F(\omega)|$ is equals to $|F_M(\omega)|$ and the Fourier phase of $x(t)$ is the sum of MPS and AP phases.

$$|F(\omega)| = |F_M(\omega)| \quad (11)$$

$$\phi(\omega) = \phi_M(\omega) + \phi_A(\omega) \quad (12)$$

The Fourier amplitude and phase of MPS satisfy the equations:

$$\phi_M(\omega) = \frac{1}{\pi} \int_{-\infty}^{\infty} \frac{\log |F_M(y)|}{\omega - y} dy \quad (13)$$

$$\log |F_M(\omega)| = -\frac{1}{\pi} \int_{-\infty}^{\infty} \frac{\phi_M(y)}{\omega - y} dy \quad (14)$$

Eq.(13) and Eq.(14) are known as the Hilbert transforms (Papoulis, A. 1962) .

3. MPS AND AP IN THE FREQUENCY DOMAIN

3.1 Earthquake Data Used in Examples

Near-field strong motion observed at the K-net (Kyoshin network, NIED) stations during the 2000 Tottori western earthquake Japan whose JMA-magnitude is 7.3 the source depth about 11km and strike from true north 150° clockwise used to discuss in the present paper. The epicenter and the K-net stations are represented in Figure1 and Distances from epicenter to each station is in Table 1. Every station is within less than 50km from the epicenter.

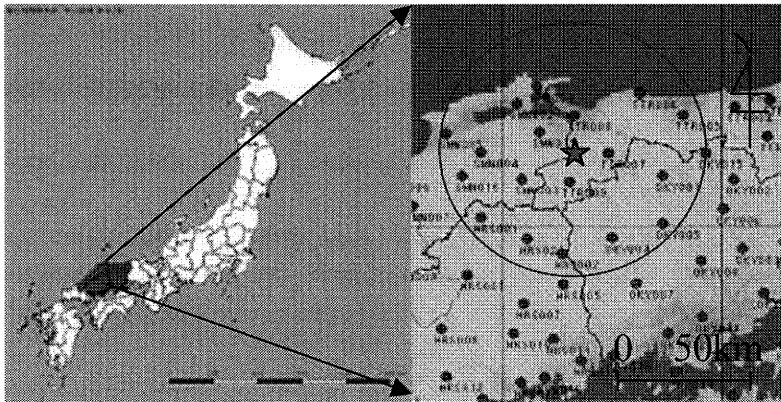


Figure 1 K-net stations and the epicenter during the 2000 Tottori western earthquake ($M_J 7.3$ Oct.6th).

Table 1 K-net Station locations and distance from epicenter.

No.	Station code	Latitude	Longitude	Distance(km)
①	TTR009	35.1681N	133.3143E	12
②	TTR007	35.2794N	133.4902E	13
③	TTR008	35.4227N	133.3327E	16
④	SMN015	35.3613N	133.1730E	19
⑤	SMN003	35.1763N	133.0955E	25
⑥	SMN001	35.5341N	133.1638E	33
⑦	SMN002	35.4683N	133.0708E	33
⑧	TTR006	35.5075N	133.6330E	37
⑨	OKY004	34.9547N	133.5044E	38
⑩	SMN004	35.2850N	133.9030E	40
⑪	HRS021	34.9497N	133.1197E	42
⑫	HRS002	34.8919N	133.2781E	43
⑬	OKY005	35.0060N	133.7344E	46
⑭	TTR005	35.4258N	133.8280E	47
⑮	SMN016	35.1925N	133.8172E	49
⑯	HRS001	35.0305N	132.9044E	49

3.2 MPS and AP in the Frequency Domain

Horizontal (Fault normal and parallel) and vertical components accelerations at the K-net station TTR009 for example that is the nearest and about 12 kilometers away from epicenter are shown in Figure 2, the Fourier amplitude and phase of MPS in Figure 3 and those of AP in Figure 4. The Fourier amplitude of AP is omitted because the amplitude defined by Eq. (9) is unity all over frequency. The Fourier amplitudes of MPS are equals to those of the earthquake records.

From Figure 3, horizontal components of the Fourier amplitude are twice or three times as large as vertical one as the Fourier amplitudes is associated with the time histories in Figure 2. When the Fourier amplitude of three components of MPS in Figure 3 (a) show steep fall, those phases of MPS shown in Figure 3 (b) rise up in the same frequency.

As for the Fourier phases of AP in Figure 4, they vary in inverse proportion to the frequency up to 1Hz and each component of AP appears to be random in the higher frequency range.

The Fourier amplitude ratios of MPS between horizontal and vertical components (H/V ratios) and their phase differences (H-V MPS differences) are shown in Figure 5. H-V MPS differences tend to show exponential increase in the frequency when the H/V ratios become trough. The H/V ratios shall be characterized by H-V MPS differences in the terms of the Hilbert transforms Eq. (13), (14).

Figure 6 shows the Fourier phase differences of AP between horizontal and vertical components (H-V AP differences). From Figure 6, two H-V AP differences, Normal-Vertical (N-V) and Parallel-Vertical (P-V), represent peak and valley shapes in the same frequency but the disparity between N-V and P-V are about π . This indicates that there is a difference of about π between normal and parallel components in their phase difference.

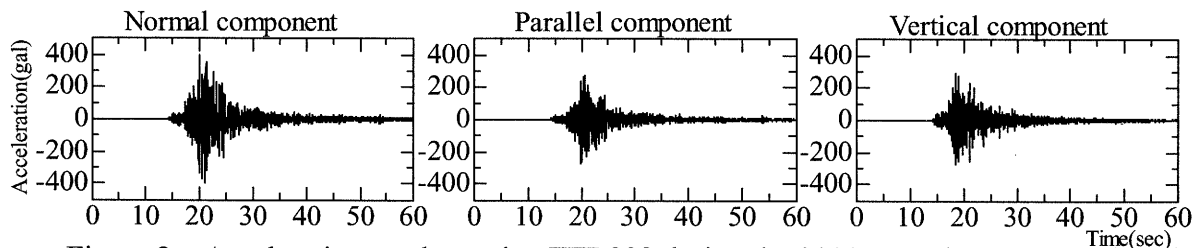


Figure 2 Accelerations at the station TTR009 during the 2000 Tottori western earthquake

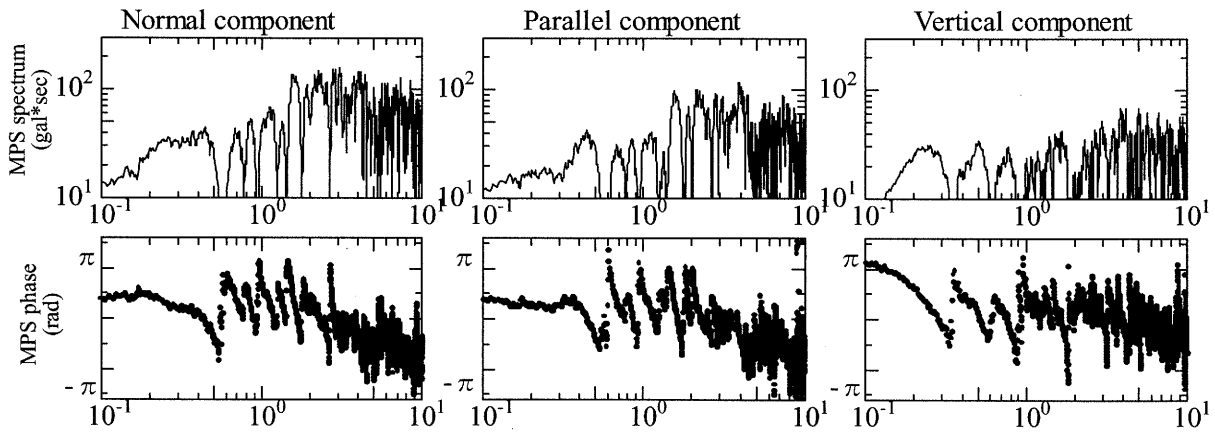


Figure 3 MPS Fourier amplitude (upper) and phase of earthquake record shown in Figure.2

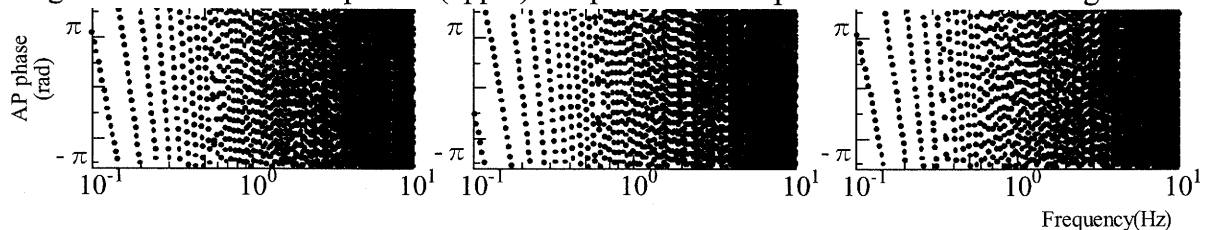


Figure 4 AP Fourier phase spectra of earthquake record shown in Figure.2

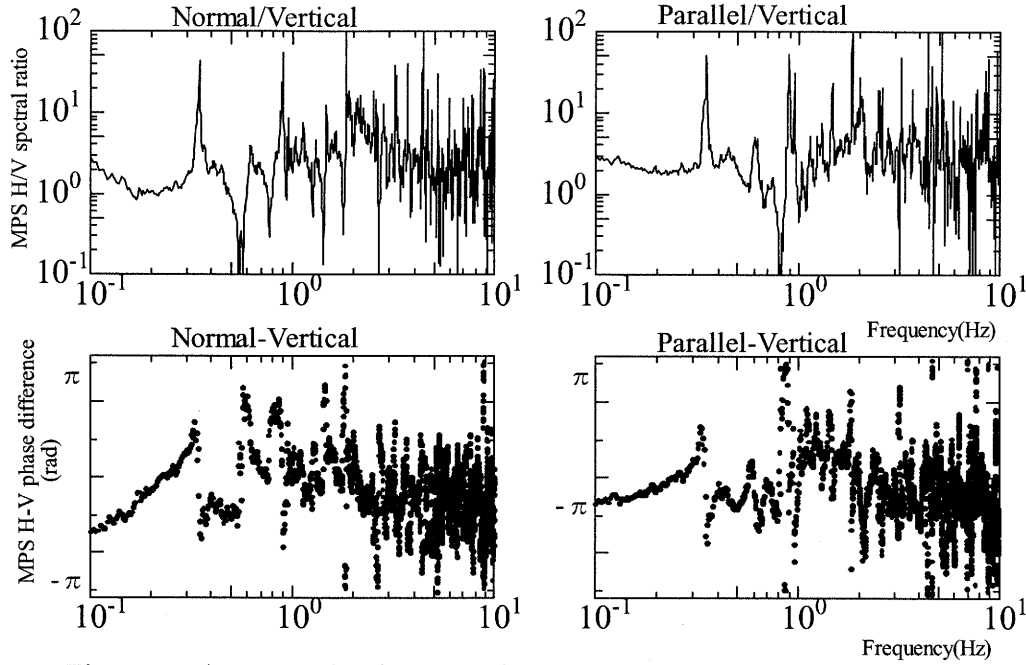


Figure 5 H/V spectral ratios (upper) and H-V MPS phase differences

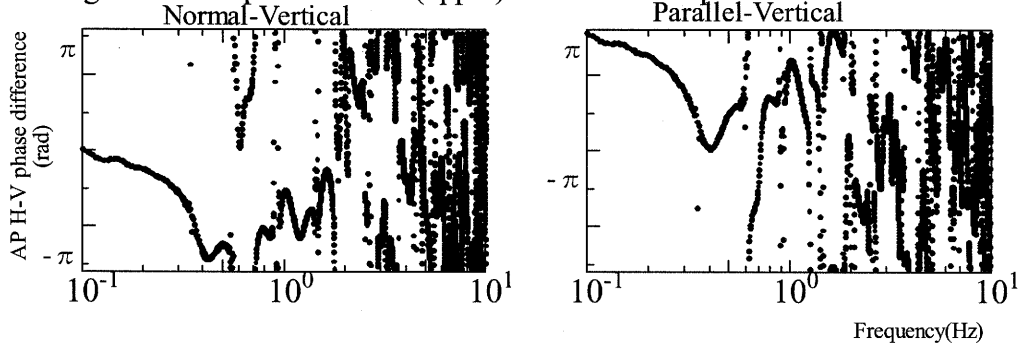


Figure 6 H-V AP phase differences between horizontal and vertical components

3.3 Time Histories of MPS and AP

MPS and AP time histories of three components in acceleration at the TTR009 station are shown in Figure 7. MPS shows the peak amplitude at about zero second and the amplitude of horizontal components is twice or three times as large as that of a vertical component. As for AP, the peak ground accelerations of both components are approximately from 10 to 15 cm/s^2 . This is the fact that the Fourier amplitude of AP is defined as Eq.(9) and the Equation expresses that AP is dependent on the only the Fourier phase excluding the phase characteristics of MPS.

To see AP time histories in more detail, AP velocities are shown in Figure 8. From Figure 8, each component comes to the peak velocity about 1 cm/s . Normal and parallel components of the envelopes are symmetrical with respect to the time axis each other. This has already been pointed in previous section 3.2 that there is a phase difference between normal and parallel components in AP. A vertical envelope is different from horizontal ones because AP has been pointed out that AP includes the information of the path seismic waves have passed from the source (Izumi, et al.1990, Sato, et al. 1999) and vertical motion shall dominantly consist of primary wave meanwhile horizontal motion shear wave.

4. PEAK GROUND ACCELERATION OF BOTH COMPONENTS

Figure 9 shows distributions of horizontal and vertical peak ground acceleration (PGA) and the time

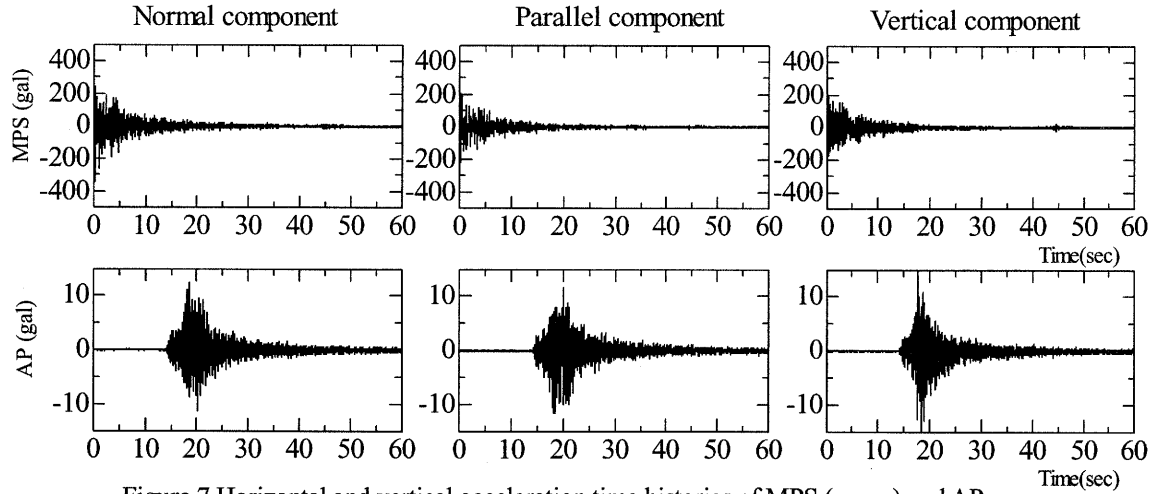


Figure.7 Horizontal and vertical acceleration time histories of MPS (upper) and AP

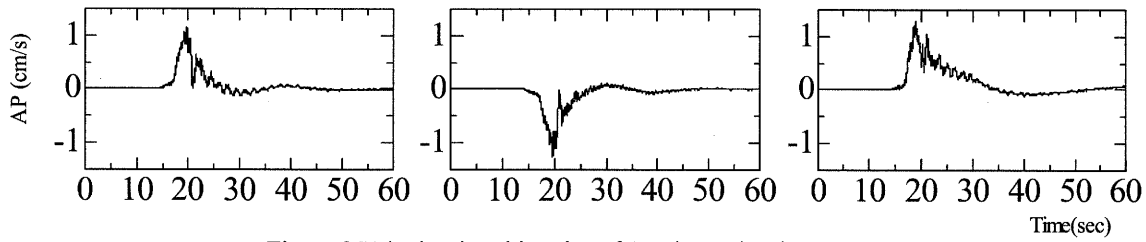


Figure.8 Velocity time histories of AP shown in Figure.7

at PGA in each component using all records in Table 1. Figure 9 (a) is observation records, (b) MPS and (c) AP. From Figure 9 (a) and (b), PGA ratio between horizontal and vertical components is among one and one-third but in MPS that is among two and half. Comparing Normal-Vertical and Parallel-Vertical components, the former is larger than the latter. The time at PGA in horizontal and vertical MPS is roughly zero second.

Figure 9 (c) expresses that PGA in horizontal and vertical AP is distributed from 10 to 20 cm/s^2 and they appear at from 16 to 26 seconds. However, horizontal components are likely to arrive later than vertical one. This is due to a factor that horizontal components shall be mainly made up with Shear wave and vertical one primary wave above mentioned in previous section.3.3.

5. CONCLUSIONS

Based on the concept of the factorization taking causality into consideration in signal analysis, relationship between horizontal and vertical components of earthquake ground motion has been formulated using MPS and AP in the present paper. We have applied the factorization to the 2000 Tottori western earthquake and found new findings as follows.

Firstly, the Fourier amplitudes of earthquake records equal to those of MPS and the H/V ratios are seemed to have relevant to H-V MPS differences by the Hilbert transforms.

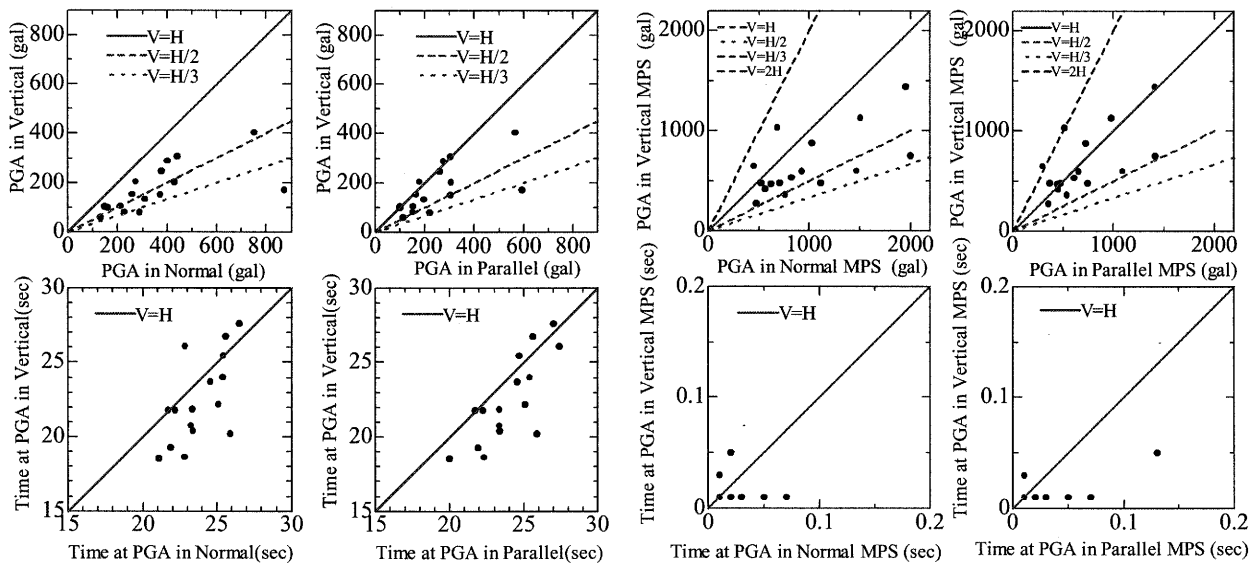
Next, earthquake records are expressed by the convolution MPS and AP in time domain. The time histories of MPS show the peak amplitudes at about zero second and horizontal amplitudes are larger than vertical one. Regarding AP, both of PGA is approximately from 10 to 20 cm/s^2 . Peak ground velocities of AP are about 1 cm/s but the envelope of vertical component is apparently different from horizontal ones.

Finally, horizontal and vertical PGA and the time in earthquake records, MPS and AP are plotted. PGA ratios between horizontal and vertical components in earthquake records are distributed among one and one-third but those in MPS become from two to half. The time at PGA in both components of MPS is nearly zero second. As for AP, horizontal and vertical components show the maximum

amplitudes from 10cm/s^2 to 20cm/s^2 and that appear at from 16 to 26 second but horizontal components are likely to arrive later than vertical one. This will be due to a factor that horizontal components are mainly made up with shear wave and vertical one primary wave.

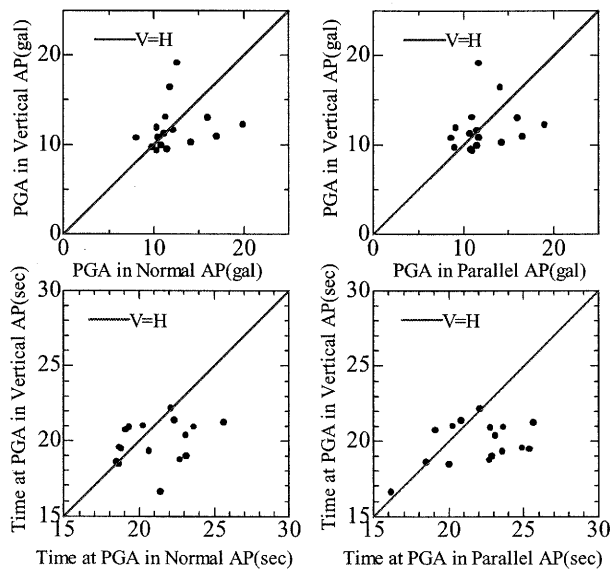
References:

- Papoulis, A. (1967). "Signal Analysis", McGraw-Hill.
- Izumi, M., Katukura, H. and Ohno, S. (1988) "A Study on Deconvolution on Seismic Waves", *Transactions of AIJ*, No.390, pp27-33.
- Katukura, H., Ohno, S. and Izumi, M. (1989), "Symmetrical FFT Technique and Its Applications to Earthquake Engineering", *Earthquake Engineering and Structural Dynamics*, Vol.18, pp717-725.
- K-net (Kyoshin Network), National research Institute for Earth science Disaster prevention (NIED) homepage, <http://k-net.bosai.go.jp/>
- Izumi, M., Kurita, S., Endo, Y., Tobita, J. and Hanzawa, T. (1990), "Study on causality of transfer functions and components of causal transfer functions in systems of seismic wave propagation in soil", *Transactions of AIJ*, No.412, pp31-41.
- Sato, T., Muroto, Y. and Nisimura, A. (1999), "Modeling of phase characteristics of strong earthquake motion", *Proceedings of JSCE*, No.612/I-46, pp201-213.



(a) Horizontal and vertical PGA in the records and the time

(b) Horizontal and vertical PGA in MPS and the time



(c) Horizontal and vertical PGA in AP and the time

Figure 9 Horizontal and vertical components of PGA in earthquake records (a), MPS (b) and AP (c).

SLOPE FAILURE POTENTIAL MAPPING IN URBAN AREA USING HIGH-RESOLUTION DIGITAL ELEVATION MODEL

H. Miura¹⁾ and S. Midorikawa²⁾

1) Post-Doctoral Research Fellow, Center for Urban Earthquake Engineering, Tokyo Institute of Technology, Japan

2) Professor, Center for Urban Earthquake Engineering, Tokyo Institute of Technology, Japan

hmiura@enveng.titech.ac.jp, smidorik@enveng.titech.ac.jp

Abstract: Risk of slope failure in an urban area is increasing because development of urbanized areas has been expanded to hillside areas. It is important to evaluate the potential of the slope failure in the large urban area in order for efficient earthquake disaster mitigation planning. Remotely sensed data is useful to grasp the characteristics of the slopes in the large area. However, the scale of the slope in the densely built-up area is not enough large to identify from the existing remotely sensed data. In this study, a methodology for detection of steep slopes from high-resolution DEM is proposed. The DEM whose resolution is 1m observed in Yokohama city area is used in this study. The computed gradient, the slope height, and the slope area are utilized in the method. The slopes whose gradients and heights show more than 30 degrees and 5 meters are detected in the analysis. The result of the detections shows good agreement with the slope failure susceptibility map and the ground survey.

1. INTRODUCTION

Risk of slope failure in an urban area has been increasing because development of urbanized areas has been expanded to hillside areas. In order for efficient disaster mitigation planning, it is necessary to evaluate the potential of the slope failure. In Japan, mapping of slope failure susceptible areas has been conducted by the local government. However, the detailed ground surveys are required for the mapping. It is important to develop a methodology for the mapping of slope failure susceptibility without great cost and labors.

Digital elevation model (DEM) is useful to evaluate the characteristics of the slope in the large area. The DEM and the geomorphological map have been employed for the mapping of the slope failure potentials (Mora and Vahrson 1994, Matsuoka and Midorikawa 1995, Technical Committee for Earthquake Geotechnical Engineering 1999). They developed methods for zoning on earthquake-induced or rain-induced slope failure susceptibility considering the terrain relief and the geological conditions. However, it is difficult to identify the small-scale slopes in an urban area because the resolutions of the data are larger than 500m.

Recently, high-resolution DEM constructed from airborne scanner laser data has been available (e.g., Wehr and Lohr 1999). Since the resolution of the data is 1m or less, it has become possible to consider carrying out a survey for small-scale slopes in an urban area. In this study, a methodology for mapping of steep slopes by using high-resolution DEM and GIS data is proposed. The applicability of the method is examined compared with the existing slope failure susceptibility map and the ground survey.

2. STUDY AREA AND DATA SOURCES

The study area is a part of Yokohama city, Japan, where the high-resolution DEM and the complete GIS data are available. Figures 1 show the DEM with the resolution of 1m and the GIS building inventory data used in this study. The study area covers the central part of Yokohama city. The solid regions in Figs. 1 show the slope failure susceptible areas defined by the local government (Kanagawa Prefectural Government 2004).

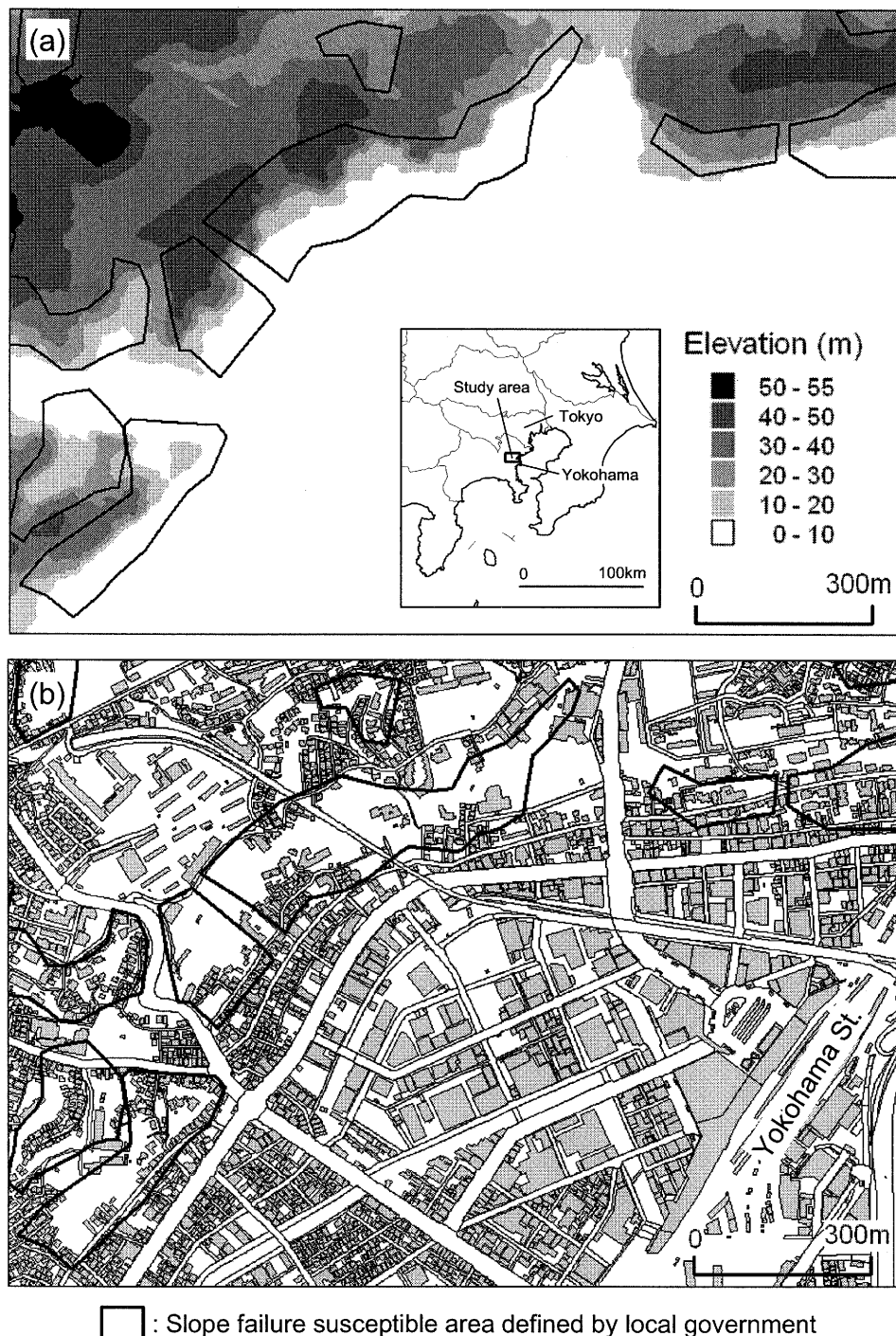


Fig. 1 (a) High-resolution Digital Elevation Model (DEM) and (b) GIS building inventory data used in this study

Figure 2 shows the illustration of a slope and the surroundings. The criteria for the slope failure susceptible areas defined by the local government are as follows;

1. The gradient of the slope (ϕ) is more than 30 degrees.
2. The height of the slope (H) is more than 5 meters.
3. More than five houses or more than one public building (city office, school, hospital, etc.) are situated within the distance H or $2H$ to the slope.

The coverage for the third criterion is also shown by the arrows in Fig. 2. While the coverage for the top of the slope is the distance H , that for the bottom of the slope is the distance $2H$. In this study, slopes that satisfy the criteria mentioned above are detected from the high-resolution DEM.

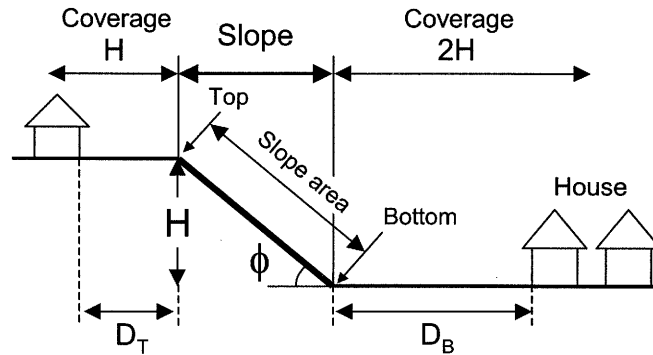


Fig. 2 Illustration of slope with the coverage

3. METHODOLOGY FOR DETECTION OF STEEP SLOPES

Figure 3 shows the flowchart of the method for detecting the steep slopes from the DEM. First, the gradient and the flow direction are computed for each mesh. The gradient of the mesh (G) is computed by the following equation (e.g., Dunn and Hickey (1998));

$$G = \tan^{-1}(\max((Z_0 - Z_i)/L)) \quad (i=1-8) \quad (1)$$

Here, L means the mesh size that is equal to 1m in this study. Z_0 and Z_i indicate the elevation of the mesh and that of the neighboring mesh, respectively. The eight neighboring meshes are used in the computation. The flow direction represents the direction to the neighboring mesh that shows larger difference of the elevation than the other neighboring meshes.

After the computation, the mesh whose gradient shows larger than the threshold value (G_{S_Th}) is selected as a starting point to chase the steep slope. The meshes are chased and connected along the flow directions. The chase is continued until the gradient of the chased mesh is lower than the threshold value (G_{E_Th}).

Since the first criterion for the slope failure susceptible areas is that the gradient of the slope should be 30 degrees, G_{S_Th} is determined to be 30 degrees. Building damage caused by slope failure around the bottom of the slope would be larger than that around the top of the slope. Since it is necessary to detect the bottom of the slope completely, G_{E_Th} is determined to be 20 degrees.

Then, the slope height (H) is computed from the difference of the elevations between the starting mesh and that of the ending mesh. The slope whose height is lower than the threshold value (H_{Th}) is eliminated in the analysis. Referring the second criterion for the slope failure susceptible areas, H_{Th} is determined to be 5m.

The distance from the slope to a building is considered by using GIS building inventory data. As shown in Fig. 2, D_T and D_B are defined as the closest distance to a building from the top of the slope and that from the bottom of the slope, respectively. Referring the third criterion, the slope whose D_T and D_B are larger than H and $2H$ respectively is eliminated in the analysis.

The slope area is calculated by counting the areas of the detected slopes. Since small slopes do not produce damages to structures, the slopes whose areas are smaller than the threshold value (S_{Th}) are eliminated. Finally, the slopes that satisfy those criteria are detected as the steep slopes.

It is difficult to determine S_{Th} because the description for the slope area is not included in the criteria. Then, the appropriate threshold value for the slope area is discussed in the following steps.

4. RESULT OF ANALYSIS

The proposed method is applied to the data shown in Figs. 1. Figures 4 show the distributions of the gradients computed from the DEM and that of the slope heights. The steep slopes whose gradient are larger than 30 degrees and heights are more than 15m are distributed in the northwest and the southwest part of the study area. The maximum of the computed gradient and that of the slope height are 80 degrees and 33m, respectively.

Figure 5 (a) shows the close-up of the elevation indicated by the broken region in Figs. 4 with the GIS building inventory data. Figures 5 (b) show the profile of the elevation and the computed gradient along the line A-B. While the solid circles indicate the meshes whose gradients are larger than 30 degrees, the gray circle indicate the mesh whose gradient is larger than 20 degrees at the bottom of the slope. In the method, the solid and gray meshes are detected as the steep slope. Figure 5 (c) shows the ground photograph in the area. White lines in the photo represent the top lines and the bottom lines of the slopes. The ground survey reveals that the gradient of the slope is larger than 30 degrees and the height is more than 5m. This indicates that the area detected by the proposed method agree with the slope failure susceptible area.

Figure 6 shows the distribution of the steep slopes detected by the method. All the detected slopes including small slopes are shown in the figure. Darker area in the figure represents larger slope area. About 170 slopes are detected in the analysis. The broken regions in the figure indicate the slope failure susceptible areas. The result shows that the slopes in the susceptible areas are well detected by the proposed method. Most of the detected slopes in the susceptible areas are larger than $1,000\text{m}^2$. However, as shown by the circles in Fig. 6, some of the detected slopes whose areas are larger than $1,000\text{m}^2$ are not defined as the slope failure susceptible areas.

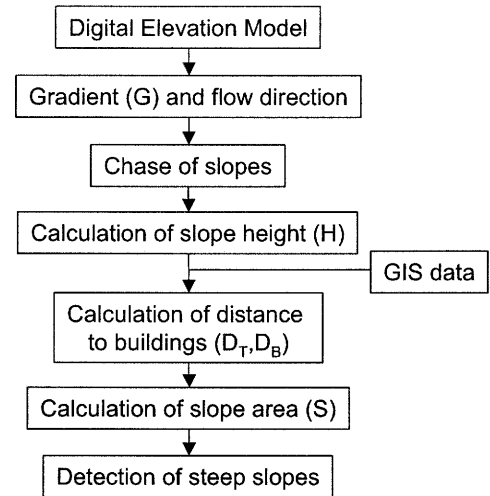


Fig. 3 Flowchart for detection of steep slopes

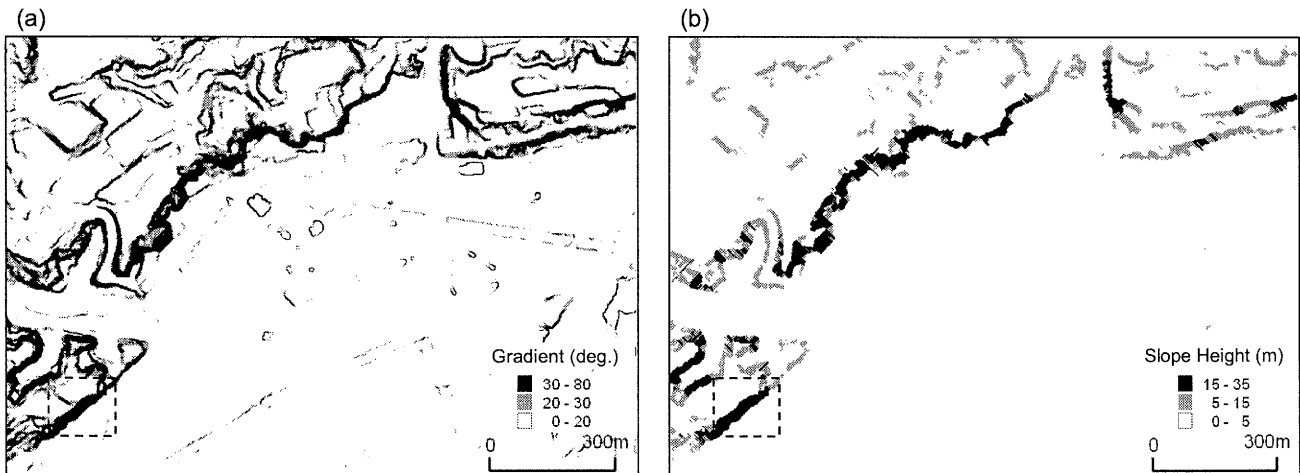


Fig. 4 (a) Distribution of gradient; (b) Distribution of slope height

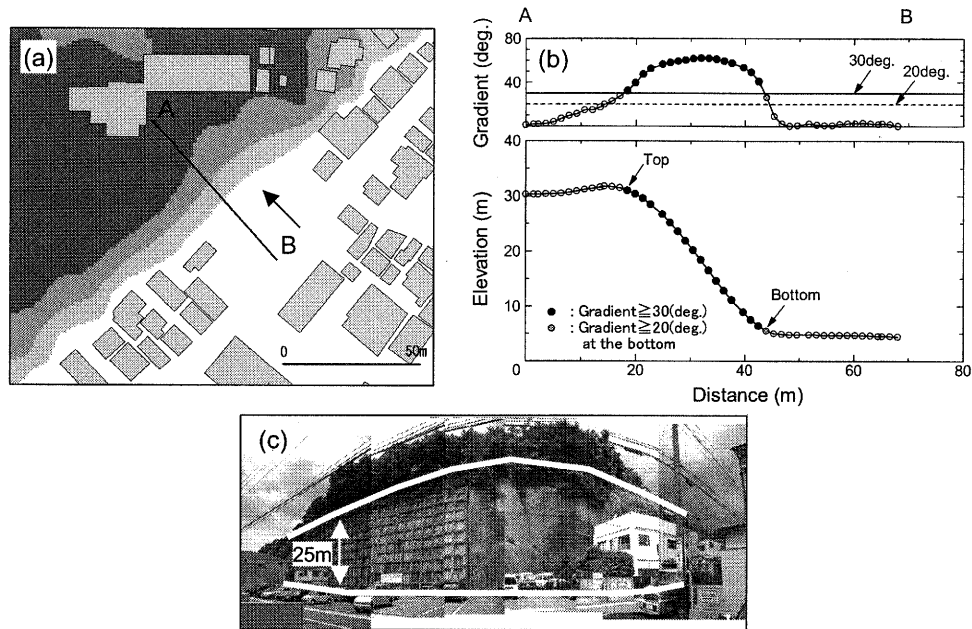


Fig. 5 (a) Close-up of the DEM indicated by broken region in Figs. 4 with GIS building inventory data. The arrow indicates the shooting direction of the photograph; (b) Profiles of the elevation and the computed gradient along the line A-B; (c) Ground photograph in the area.

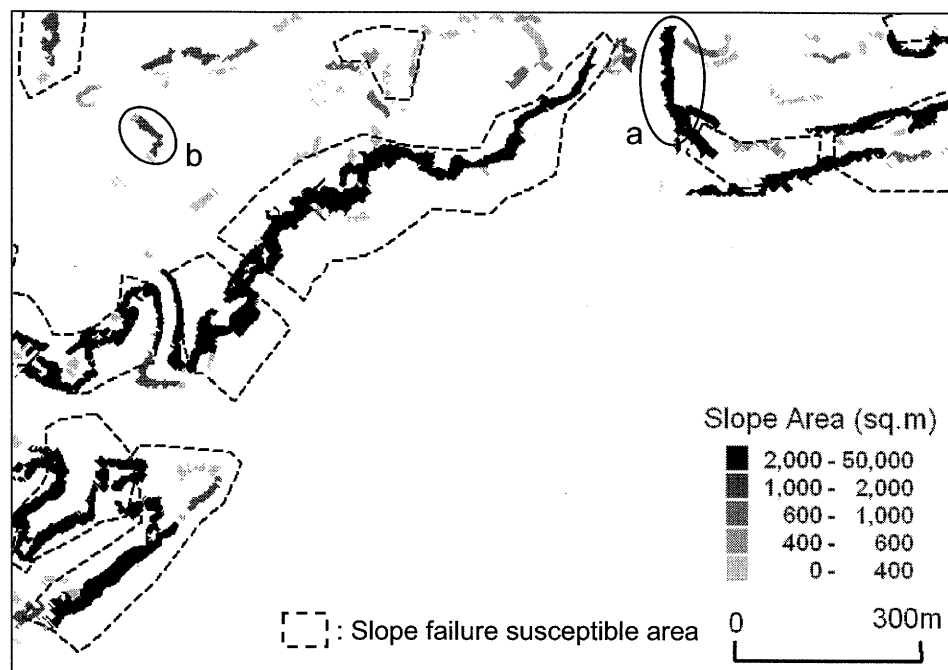


Fig. 6 Distribution of detected steep slopes with the slope areas.
Close-ups of the areas indicated by solid circles are shown in Fig. 7.

Figures 7 show the close-ups of the slopes indicated by the circles in Fig. 6 with the GIS building inventory data and the ground photographs. The arrow and the broken circle indicate the shooting direction of the photograph and the coverage area of the slope, respectively. Although the heights of the slopes are larger than 5m, the numbers of the buildings in the slope areas are less than five as shown in Fig. 7 (a-1) and (b-1). Therefore, the slopes are not defined as the slope failure susceptible areas. However, many households are located in the slope areas because the adjacent buildings are apartment houses or commercial buildings. Since the detected slopes would produce the damage to the inhabitants in the buildings, they should be defined as the slope failure susceptible areas. These indicate that the proposed method is useful to detect the risk of slope failure in an urban area.

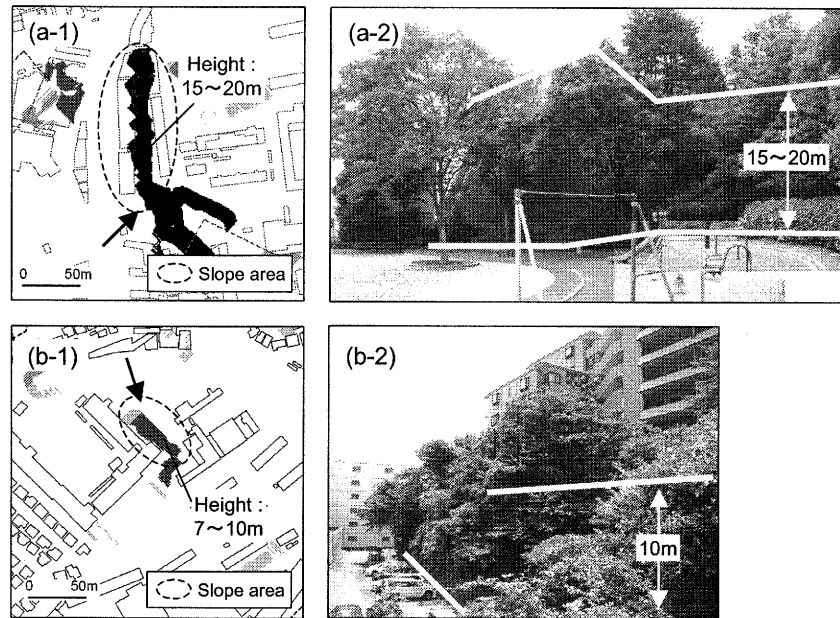


Fig. 7 Close-ups of the detected slopes and the ground photographs.
(a-1, 2) and (b-1, 2) correspond with the region “a” and “b” in Fig. 6, respectively.

5. CONCLUSION

In this study, a methodology to detect steep slopes from the high-resolution DEM is introduced. The criteria for the slope failure susceptible areas are considered in the analysis. The gradient, the slope height, and the distance from a slope to a building are utilized for the detection. The slopes whose gradients are more than 30 degrees and heights are more than 5m are detected as the steep slopes. The proposed method is applied to the data in a part of Yokohama city, Japan. The ground survey is conducted to examine the applicability of the method. The result of the analysis shows that the steep slopes in the slope failure susceptible areas are well detected, indicating that the proposed method is useful to detect the risk of slope failure in the urban area.

Acknowledgements:

The authors acknowledge Aero Asahi Co., Ltd. for providing the high-resolution digital elevation model in Yokohama.

References:

- Dunn, M. and Hickey, R. (1998), “The Effect of Slope Algorithms on Slope Estimates within a GIS”, *Cartography*, Vol.27, No.1, 9-15.
- Kanagawa Prefectural Government (2004), “*Slope Failure Susceptibility Map in Kanagawa Prefecture*”, <http://www.pref.kanagawa.jp/osirase/sabo/bousai/dosha/dosha.html> (in Japanese).
- Matsuoka, M. and Midorikawa, S. (1995), “Earthquake-Induced Slope Failure Potential Mapping Using The Digital National Land Information”, *Journal of Structural and Construction Engineering, AIJ*, No.474, 59-66 (in Japanese).
- Mora, S. and Vahrson, W. (1994), “Macrozonation Methodology for Landslide Hazard Determination”, *Bulletin of International Association of Engineering Geologists*, Vol.31, No.1, 49-58.
- Technical Committee for Earthquake Geotechnical Engineering, Tc4; ISSMGE (1999), “*Manual for Zoning on Seismic Geotechnical Hazards (Revised Version)*”, The Japanese Geotechnical Society, 209pp.
- Wehr, A. and Lohr, U. (1999), “Airborne Laser Scanning –An Introduction and Overview”, *ISPRS Journal of Photogrammetry & Remote Sensing*, No.54, 68-82.

PALEOSEISMICITY AND NEWSEISMICITY STUDIES IN AZERBAIJAN AREA AND THE NECESSITY OF MICROSEISMIC ZONATION IN TABRIZ CITY AND OTHER SEISMIC REGIONS OF AZERBAIJAN

E. Ghanbari¹⁾

*1) Azad Islamic University of Tabriz Civil Eng. Dep.
ebghanbari@yahoo.com*

Abstract: Azerbaijan is the site of convergent plate collisions along the Alpine – Himalayan Active Mountain Belt. Brittle faults in the Azerbaijan belong mostly to Cenozoic of younger in age Quaternary. The data presented demonstrate clearly that geological structures are commonly repeated at all scales from outcrop to regional. In order to forecast earthquake activity we need to determine the past history of faults. A fault that is active is likely to move again. The great earthquakes of 6 May 1930 at 22 h 34 m. 24s (GMT) with $M = 7.3$ (Salmas Earthquake) and Tabriz Earthquake in 4 January 1780 with $M = 7.7$ and Zanjan – Roudbar Earthquake on 21 June 1990 at minutes after midnight of the local time a magnitude 7.4 earthquake struck about 320 km NE of Tabriz, causing about 40 to 50 thousand people killed. 60000 injured and 50000 to 60000 Homeless these earthquakes have ruptured the progressively from east to west. The probability of large Earthquake occurrence in the north Tabriz fault (NTF) and the central part of Tabriz to Khoy-Salmas fault. Average recurrence interval is estimated to be 250-300 years, More than 60-80 destructive Earthquakes have been described in the 1000-1200 years in the history of Azerbaijan, Therefore, as there is large and dangerous Earthquake periods in Tabriz microseismic zonation is Necessary in Tabriz and other seismic regions of Azerbaijan to include in Future construction planning of the country and it will be effective in macro – economic and industrial planning the country.

1. INTRODUCTION

The fight against damage, destruction, loss of property and life from earthquakes continues. Efforts for prediction of earthquakes for over the last 100 years have not enable researchers to effectively predict the location, time and size, so as to save loss of life and property. Even if the prediction of individual large earthquakes was possible, it would be of questionable utility. The Azerbaijan and of the south Caspian Sea basin belongs to the Alpine- Himalayan system, an area high geological complication and large- scale active deformation (McKenzie 1983).

This paper is concerned with the active tectonics and structure of the Azerbaijan and South Caspian basin and its role in the collision between Arabian and Eurasian plates.

This studies can be effective in seismic- microzonation for industrial and economical aims and planning in the area. On a map of earthquake epicenters (fig 1).

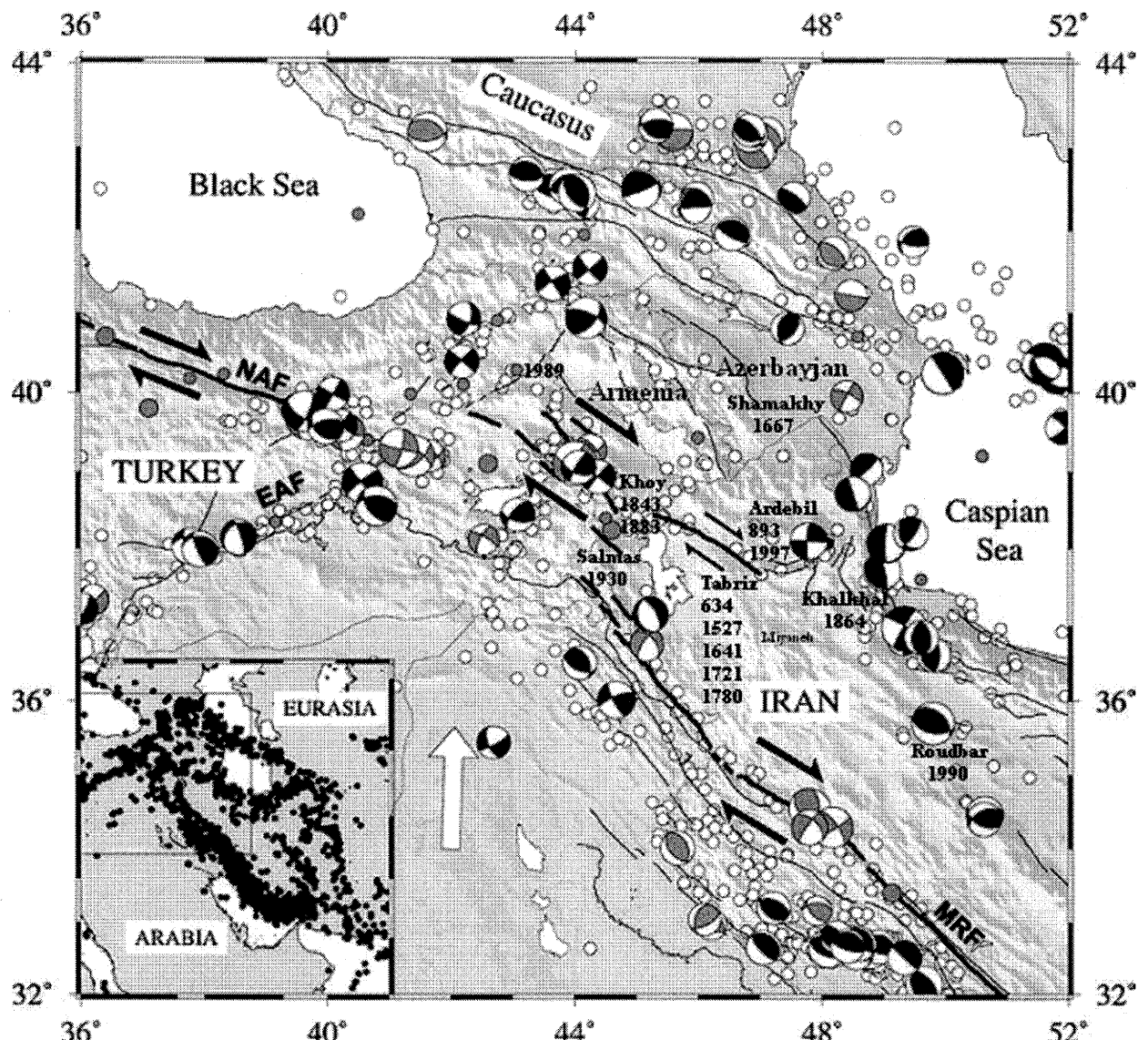


Figure 1 Summary seismotectonic map of NW Iran, eastern Turkey and the Caucasus (Jackson and Mckenzie 1984)

The Azerbaijan and southern Caspian basin stands out as a seismic block about $300 \times 300 \text{ km}^2$ (Jackson, j and others 2002) surrounded by belts of intense earthquake activity.

Other similar a seismic blocks occur in the same region, such as the Dasht-Lut, Central Iran, south of Ourmiah- lake in Azerbaijan and NW, historical studies show that the seismically within all of these blocks has bee low for at least 1000 years (Ambraseys, N.N and Melville 1982). The amplification is that these a seismic blocks are effectively rigid, and that the $30\text{-}35 \text{ mm yr}^{-1}$ of N-S shortening between Arabian and Eurasian plats, is absorbed in the active earthquake belts that surround them (Jackson and McKenzie 1984).

Tabriz city in Azerbaijan is in a seismically active region and hence it is important to understand the existing earthquake hazard to the city on a scientific basis.

A general review of the seismic status of Tabriz, high lighting the importance of seismic microzonation.

Tabriz and its surroundings as the felt region of severe earthquakes.

- seismotectonics events and the major active faults in Azerbaijan and south Caspian basin.

Iran, as one of the world's most earthquake-prone countries, has been exposed to many devastating earthquakes in the past long years. Earthquakes occur when any of the 12 or 13 plate collide at their boundaries.

A 13th plate was created by the breakup of the Indo-Australian plate was documented in 1995.

The paleoseismics and newseismics is due to compression between the Arabian and or Tour a plates in the area.

The Iranian plateau accommodates the 35 (mm/yr) convergence rate between the Eurasian and Arabian plates by strike-slip and reverse faults with, relatively low slip rates in a zone 1000 km across. (Berberian, M and Yeats, 2002). GPS measurements suggest right-lateral displacements in Azerbaijan and south Caspian basin. The right-lateral deformation occurring between south Kura basin and the Central Iranian block could be distributed along NW-SE Iranian and Nakhjvan – Armenian fault systems.

Paleoseismologic studies (Philip et al., 2001) suggest low velocities and long-recurrence time interval (2.24 ± 0.96 mm/yr, 3000-4000 years).

along Nakhjvan-Armenian faults.

The recurrence time interval on the north Tabriz fault (NTF) are shorter ~250 year Berberian and Yeats (1999) with large events up to $M=7.7$ if we assume that about 5mm/yr of right-lateral displacement occurs along the (NTF) with a recurrence time interval of 250 years.

The average displacement is about 1.25m for each event.

Using empirical relationship among moment magnitude and maximum displacement the magnitude is ≈ 7 . (Wells and Coppersmith 1994)

The series of faulting events during 1780-1999 (Tabriz earthquake 4 January 1980, $M_s=7.7$, Salmas earthquake 6 May 1930 $M_s=7.5$, $M_b=7.0$, and Manjil earthquake 21 June 1990) is one of the most striking observed examples of fault segmentation on land. The Tabriz to Salmas faults have produced more than two large earthquakes have ruptured the fault progressively from east to west (Ghanbari, E 2001) the probability of large earthquake occurrence in the (NTF) and the central part of the Tabriz to Salmas fault.

Finally agrees with the magnitudes proposed by Berberian and Yeats (1999) for the historical events along the (NTF). Therefore, most of the right-lateral displacements could be located on the (NTF) and other faults in the NW Iran and south Caspian basin.

NTF bundle could be the eastward prolongation of the north Anatolian fault (NAF) in Turkey.

Background information on the historical earthquakes in Tabriz and its relationship with NTF.

Seismicity in Azerbaijan especially in Tabriz city is moderate and high.

Reliable historical records of earthquakes in Azerbaijan based on macro seismic observations, cover a period of 1200 years. The historical record of small, felt earthquakes with no damage to constructions is complete for the period 1780.

The map of historical seismicity of Azerbaijan (Fig2) displays regions and zones of differing seismic activity a similar pattern of seismically active and less active regions shows up both in the distribution of stronger earthquakes and in the distribution of weak local events.

North-west to south-east Azerbaijan trending zones of higher seismic activity are located in NW of Iran and in the western Caspian basin.

paleoseismic investigation performed a long the (NTF) scarp, which is part of a NE-NW oriented fault system along the Moro - Mishow - Dag mountains, show clear evidence of repeated normal faulting events. The fault trace is approximately $N115^\circ E$ and is dip vertical (Berberian, M and Arshadi, S. 1976). Over its central part, between Sofian town and north of Tabriz (Baghmesha). The north Tabriz fault (NTF) forms a well-marked boundary between the rocks of the Miocene upper red formation of Tabriz border folds and Pliocene-Quaternary alluvial deposits.

Of the Tabriz piedmont zone, up thrusting the Miocene rocks against the alluvial deposits, especially west of Tazekand and Khaje-Marjan villages and NE of Tabriz airport.

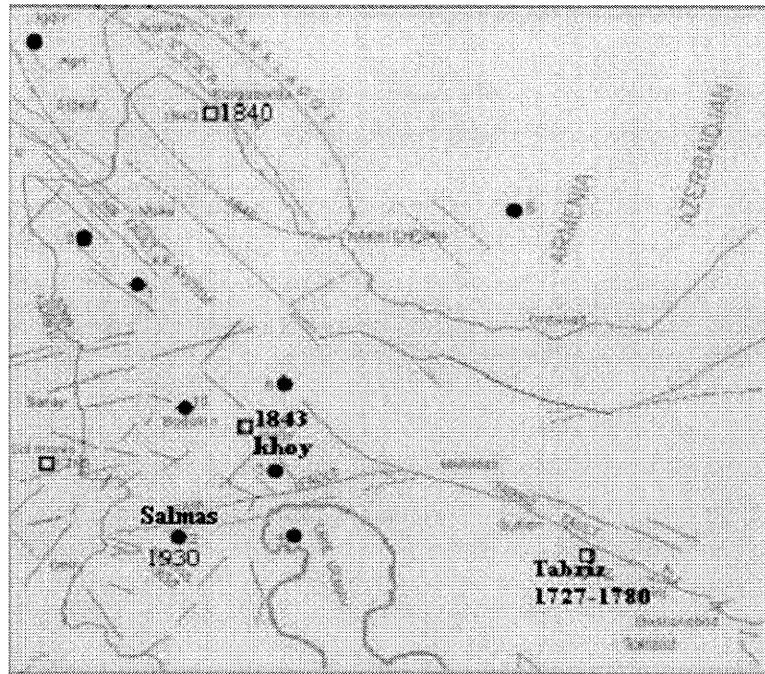


Figure 2 Distribution of historical large earthquakes of NW IRAN (Azerbaijan)

2. HISTORICAL DEVASTATING EARTHQUAKES IN TABRIZ CITY

The (NTF) is a geological fault which has been reactivated during movements. In recent times parts of it have been reactivated, and the rest also has high seismicity.

Study of the seismic history of Tabriz based on available data shows that the region has been seismically active since 634 A.D., although there are several recorded shocks for which there is no macroseismic information, however these earthquakes were strong enough to be reported by the early chroniclers (Ambraseys, N,N and Berberian,M 1976).

The destruction of Tabriz by several catastrophic earthquakes during historical times needs critical study to establish whether they were associated with the (NTF), one of the most likely cases of ground deformation which could be due to earthquake faulting is mentioned by Brydges (1834) is this description of the region just north of Basminj town.

According to Eprikian (1903), five major destructive earthquakes are remembered as having occurred in Tabriz, four which took place in 634, 1441, 1522, and 1780.

During the first two (634, 1441) earthquakes the city was completely destroyed, and during the latter two (1522, 1780) suffered 70,000 and 40,000 casualties, respectively (M. Berberian 1973).

During these destructive earthquakes the most famous historical building of Tabriz collapsed.

Finally nowadays in (NTF) piedmont of Tabriz a number of small and large towns have been built such as " Bagmesha, Eram, Rushdieh... that all are parallel to (NTF) of Tabriz north freeway, with length of 15 km. extending from SE to NW of Tabriz end is to airport. In any probability of earthquake this part of Tabriz will have considerable damage because of its location.

3. CONCLUSIONS

Iran is one among the countries which are most vulnerable to a variety of natural disasters. Perhaps, due to their relatively higher frequency, hazards due to floods, droughts and earthquakes hazard are managed in a more professional manner.

A spate of earthquakes in the recent past, causing extensive damage, has heightened sensitivity of engineers and planners to the looming seismic risk in densely populated Azerbaijan cities. Tabriz city is in a seismically active region and hence it is important to understand the existing earthquake hazard to the city on a scientific basis considering the studies performed on the period of historical earthquakes and comparison with the return period of earthquakes larger than $M=7$. That have been occurred during last three decades in (NTF), the occurrence period of dangerous earthquakes are about 250 to 260 years.

This requires the seismic microzonation is of Tabriz and other cities with earthquake potential in Azerbaijan and the regions of Caspian basin and NW of Iran.

References :

- Ambraseys, N. and Jackson, J. (1990) "Seismicity and associated strain of central Greece between 1890 and 1988" *Geophys.j int* . 101, 663-708.
- Ambraseys, N, and Melvill, C. (1982), *A History of Persian earthquakes* (Cambridge University press).
- Ambraseys, N., and Moinfar, A., (1973) the seismicity of Iran- the Silakhor (Lurestan) earthquake of 23 January 1909. *Ann digeofis*; 26 (4) p. 659-678.
- Ambraseys, N,N and Tchalenko, j. S; (1969). The Dasth- E- bayaz (Iran) earthquake of August 31, 1968 a field report. *Bull, seism. soc. Am*; 59 (5). P(75-1972).
- Ambraseys, N (1974). Historical seismicity of north- central Iran. In materials for the study of seismotectonics of Iran; north- center Iran. *Geol surv. Iran rep* 29 p- 47-95.
- Berberian, M; (1974) macroseismic data of the earthquakes in Iran during 1971, 1972, 1973 and 1974. *Geol. Surv. Iran int. rep*.
- Berberian, M; Arshadi, S (1975). On the evidence of the youngest activity of the north Tabriz fault (NTF) and the seismicity of Tabriz city. *Geol. Surv. Iran. Inter. Report*.
- Berberian, M; and Yeats, R. S; (1999) patterns of historical earthquake rupture in the Iranian plateau. *Bull. Seism. Soc. Am* 18, 120-139.
- Berberian, M; and Yeats, R. S; (2001) Contributions of archeological data to studies of earthquake history in the Iranian plateau ,*J. Struct. Geol.* 23-563-584.
- Brydges, H. J; (1834). *Account of the transactions of H.M.S mission to the court of Persia*.
- Eprikian, H; (1903) *Bnashkarik patkerazard bararan* (illustrated dictionary of names and places; in Armenian) Venice.
- Jackson, J. A and McKenzie, D. P; (1984). Active tectonics of the alpine- Himalayan belt between western Turkey and Pakistan *Geophysics. J. R astr. Soc*; 77, 185- 264.
- Jackson, J. A and others (2002) Active tectonics of the south Caspian basin. *Geophy. J. int.* 148. P 214-245.
- McKenzie, D. and Jackson, J. A; (1983) The relationship between strain rates. Crustal thickening, paleomagnetism, finite strain and fault movements, within a deforming zone earth planet. *Sa: Lett. Gs*, 182-202. and correction *ibid* 700444.
- McKenzie, D; (1972) Active tectonics on the Mediterranean region. *Geophy. J. R. astr. Soc*; 30 109-185.
- Wells, P., and Coppersmith, K. J; (1994). New empirical relationship among magnitude, rupture without, rupture area, and surface displacement, *Bull. Seismol. Soc. Am*; 84 (4), 974-1002.
- Philip, H; A. Avagyan, A. S Karakhanian , J. F. Ritz, and S. Rebai (2001) estimating slip rates and recurrence intervals for strong earthquakes along inter continental fault; example of the pambak- Seven- Sunic fault (Armenia), *tectonophysics*, 161, 1-21.
- Stocklin, J; (1968). Structural history and tectonics of Iran: A review, *Am. Ass. Petrel . Geol. Bull.*, 52, 1229-1258.
- Ghanbari, E. (1998) Seism tectonic events along the along the Tabriz and Anatolian fault 11th European conference on earthquake engineering Paris- France.
- Ghanbari, E; (1999) Siesmoactive faults systems, and assessing earthquake hazards in the north and NW of Iran. Ninth international conference on soil dynamics and earthquake engineering sdee 99. Bergen, Norway August- 9-12, 1999.
- Ghanbari, E (2000) Seismic zonation of Azerbaijan area in relation to the behavior of active faults.
- Ghanbari, E (2004) The analysis of earthquake risk and the periodicity of shakes along the Tabriz fault. *Inter. Conf. On earthquake. Engineering, geo- Beyrouth* pp. 883-886.
- Ghanbari, E; Afshin. H; Hosseini; D. (2004) Analytical investigation into Bam earthquake of 26 dec 2003 – Iran. *Earthquake engineering research Center, Sahand university of technology (EERC)* 112p.

TWO DIMENSIONAL MODELING OF PILES SUBJECTED TO LIQUEFIED GROUND

J.R. Dungca¹⁾, J. Kuwano²⁾, and A. Takahashi³⁾

1) Doctoral Student, Department of Civil Engineering, Tokyo Institute of Technology, Japan

2) Professor, Dept. of Civil Engineering, Tokyo Institute of Technology, Japan

3) Public Works and Research Institute, Japan

jrdungca@cv.titech.ac.jp, jkuwano@cv.titech.ac.jp, aki-taka@pwri.go.jp

Abstract: This paper presents the numerical analysis of the lateral resistance of a pile and double piles subjected to liquefaction-induced lateral flow. The main objective of this analysis is to study the behavior of the pile and the surrounding liquefied soil when a large relative displacement between the pile and the soil is induced. The pile cross-section in an arbitrary depth below the ground was modeled similar to the experimental model done in Takahashi et al. (2002). Results show different behaviors of the pore water pressures surrounding the pile which affects the lateral resistance of the pile.

1. INTRODUCTION

Past experiences from major earthquakes show that the pile foundations are susceptible to liquefaction-induced lateral spreading. Many studies have already been done to study the behavior of the laterally spreading liquefied ground surrounding the pile as well as the lateral resistance of piles. Some of these are the works of Tokimatsu (1999), Abdoun and Dobry (2002), Finn and Fujita (2002), Abdoun et al. (2003), and Suzuki and Tokimatsu (2004)

This paper shows the numerical analysis of the experimental model presented in the paper of Takahashi et al. (2002). In this experimental model, the pile was modeled as a buried cylinder that corresponds to the sectional model of the pile at a certain depth in the subsoil. In order to create a realistic stress condition in the model ground, the model was prepared in a sealed container and the overburden pressure was applied to the ground surface by a rubber pressure bag. Figure 2 shows the schematic diagram of the experimental setup.

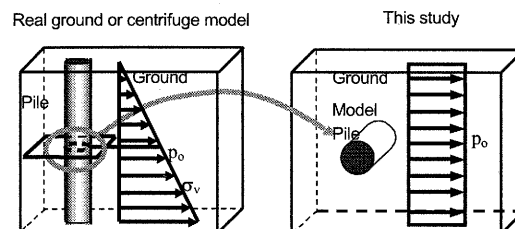


Figure 1 Schematic Diagram of the Experimental Model, Takahashi (2002)

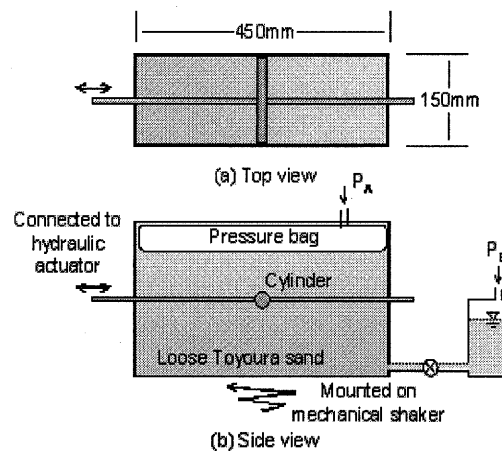


Figure 2 Schematic Drawing of the Model Container, Takahashi (2002)

This experimental model enabled the authors to observe the behavior of the liquefied ground as well as the pile before during and after an earthquake event. It is attempted in this paper to simulate the similar condition in the experiment using the finite element program created by Takahashi (2002b).

2. ANALYSIS PROCEDURES

2.1 Finite Analysis Program

To verify the results gathered in the experimental modeling, a finite element analysis program has been developed by Takahashi (2002). This program is designed to analyze soil-structure interaction, especially dynamic events. The finite element program solves the governing equations for dynamic behavior of saturated porous media by Biot (1956),(1956b),(1962) (for details of mathematical formulations, integration scheme along time, sensitivities of parameters for soil model used in this program, refer to Takahashi(2002b). This program can calculate initial stress state by self-weight analysis, calculate first eigen value of the system by modal analysis, evaluate dynamic responses of soils and structures, evaluate soil-structure interactions in static events, and pick up relevant data from output file.

Geomaterial parameters used in the analysis is based on the extended subloading surface model proposed by Hashiguchi (1996)(1998) since the loading criterion is simple and the model has the capability to describe realistic strain accumulation behavior during a cyclic loading though many material parameters are needed. Details of the constitutive model are described in Takahashi (2002b). The pile was modeled as linear elastic element with Young's modulus of 1.0×10^9 N/m², Poisson's ratio of 0.33, and density of 2.69Mg/m³). The rubber pressure bag on top of the model ground that will provide overburden pressure was also modeled as linear elastic element with Young's modulus of 1.0 N/m², Poisson's ratio of 0.33, and density of 500 Mg/m³).

The size of the element was 10mm x 10mm. Fluid flow velocities were set to zero at all the boundaries except at the surface of the ground. In order to take into account the fact that the horizontal movement of the soil was not allowed at the side boundaries of the model container, the horizontal displacements of the nodes at the side boundaries are fixed. The applied earthquake motion was similar to the wave utilized in the shaking table test.

In this analysis, two stages of calculations had been undertaken. Dynamic response analysis was first undertaken to simulate the condition of the model ground during a seismic event and when the model ground reached the point of liquefaction, shaking is terminated and the second stage of calculation, which is the static analysis followed immediately. In the static response analysis, pile

loading is induced to simulate the movement of the prototype pile immediately after the liquefaction. Takahashi (2002b)

2.2 Analysis Conditions

Table 1 shows the summary of the analysis conditions considered for this study. Single pile and double piles with center-to-center spacing of three times (3D) and four times (4D) the diameter of the pile were analyzed. A loading rate of 10mm/sec was considered. Maximum displacement of the pile was set to 5 millimeters.

Table 1. Summary of the Analysis Conditions

No. of Piles	Diameter of the Pile (mm)	Center-to-center Spacing of Piles	Pile Loading Rate (mm/sec)	Maximum Pile Displacement (mm)
Single	20		10	5
Double	20	3 x Diameter of pile	10	5
Double	20	4 x Diameter of Pile	10	5

Finite element meshes for the three (3) test conditions were shown in Figure 2. There are 945 joints and 880 elements used in this analysis. Pile element meshes are located at the center marked by gray shades in Figure 3.

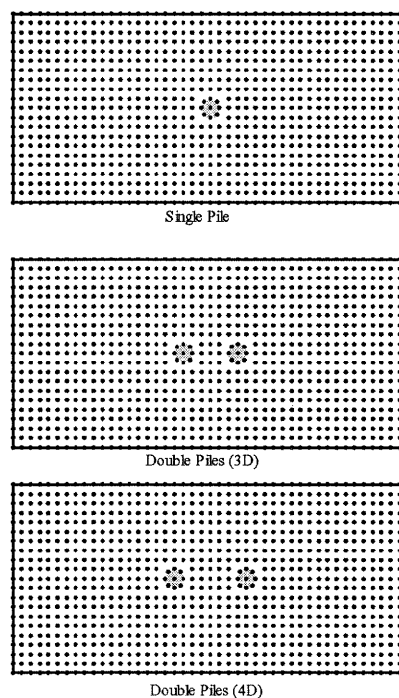


Figure 3 Finite Element Mesh

Cyclic pile loading rate of 10mm/sec used in the analysis is shown in Figure 4.

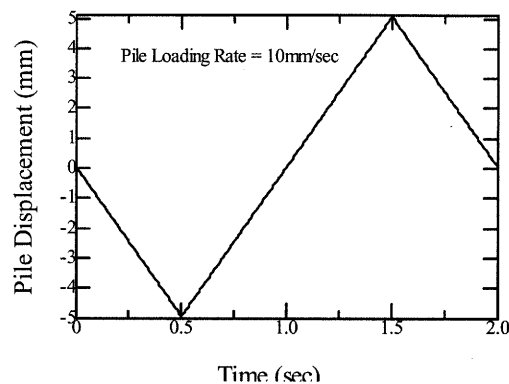


Figure 4 Pile Loading Diagram

3. RESULTS AND DISCUSSIONS

3.1 First Stage Calculation – Dynamic Response Analysis

To simulate the condition of the model ground during a seismic event, dynamic response analysis (first stage calculation) was undertaken. Figure 5 shows the input acceleration in the first stage calculation. Maximum acceleration of 5g was applied to the dynamic response analysis (first stage calculation). Pore water pressure was normalized by dividing the amount of the initial overburden pressure of 49 kPa. It can be observed from the figure that liquefaction occurred around 0.2 sec after the start of the shaking.

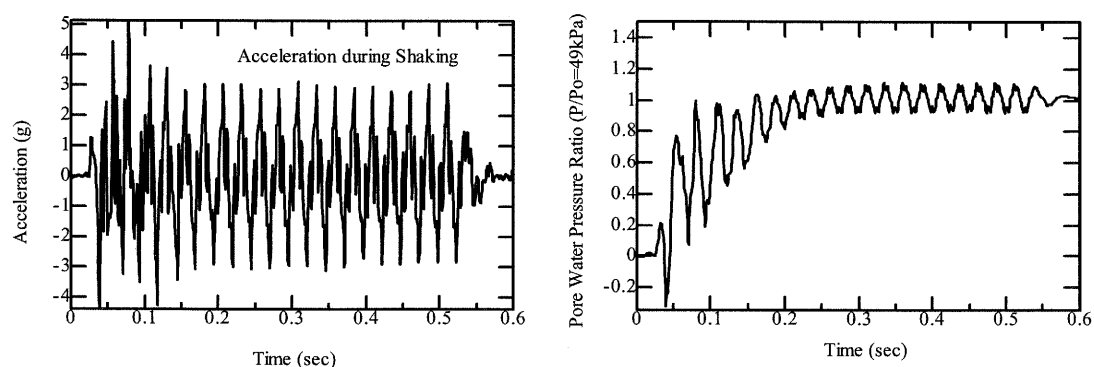


Figure 5 Input Acceleration and Pore Water Pressure in the First Stage Calculation

3.2 Second Stage Calculation

Second stage calculation or the static response analysis was undertaken immediately after the first stage calculation. In the static response analysis, pile loading (Figure 4) was induced to simulate the movement of the prototype pile immediately after the liquefaction. The changes in the pore water pressures, normal stresses and shear stresses of the soil surrounding the pile were observed and presented individually as follows:

3.2.1 Pore Water Pressure

Pore water pressure of the soil surrounding the pile(s) shown in Figure 6 were normalized by dividing the pore water pressure values by the initial overburden pressure of 49 kPa. To easily observe the changes in the pore water pressure around the pile, five (5) element meshes on each side of the pile were chosen as represented by the rainbow colors in the legend on the right of Figure 6. Visible colors in the graph represent the pore water pressures on the extension side and broken lines represent the pore pressure on the compression side. When the pile is approaching its maximum displacement of 5 mm (at time, $t=1.5\text{sec}$) it can be observed that the pore water pressure on the extension side reduces considerably as the pile moves to its maximum displacement while the pore water pressure on the compression side is almost unchanged.

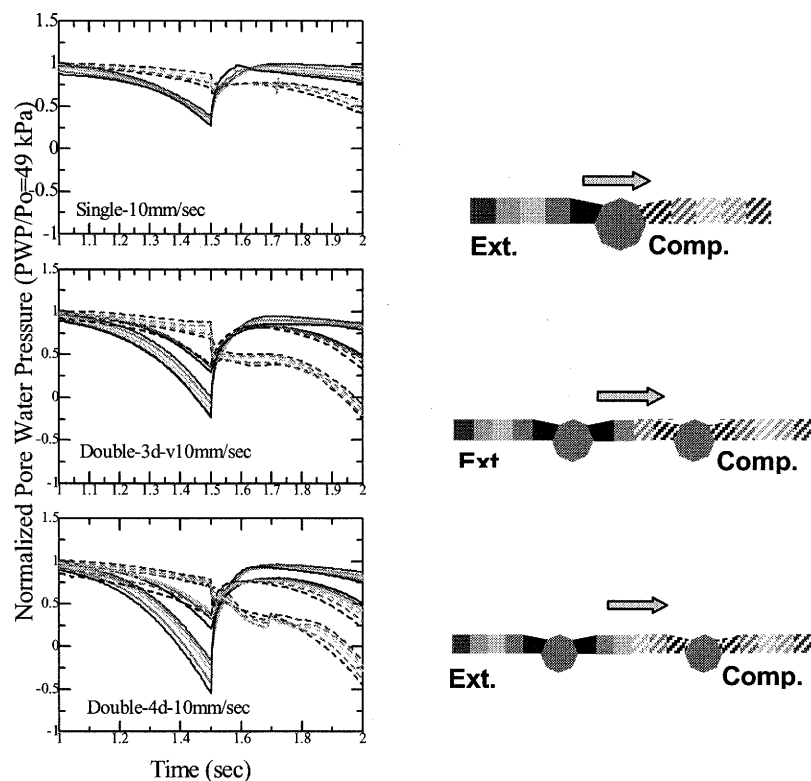


Figure 6 Pore Water Pressure History

3.2.2 Normal and Shear Stress

Like the pore water pressure graphs, the graphs of the normal stress histories and shear stress histories shown in Figure 7 and Figure 8, respectively, were normalized by dividing their values by the initial overburden pressure of 49 kPa. The legend of the graphs in these figures are the same as in Figure 6.

As the pile moves to its maximum displacement it can be observed the built-up of normal stresses and shear stresses both in the extension and compression sides of the piles. It is believed that the combination of the normal stress and the shear stress in the extension side is the cause of the large decrease of the pore water pressure on that side. However, the opposite effects of the combination of the normal stress and shear stress in the compression side might be the reason why the change in the pore water pressure is almost unchanged.

Almost zero normal and shear stresses were observed in the meshes between the piles in the

double pile conditions. The extension stress produced by the leading pile (right pile) and the compression stress brought by the trailing piles (left pile) are believed to be cancelled out, thus, produced almost zero normal and shear stresses. This is probably the reason why the reduction in the pore water pressure in between the pile is smaller than that on the extension side. If the piles are far from each other (4D spacing case), there is a slight evidence of increase in compression and extension stresses at the points close to the piles.

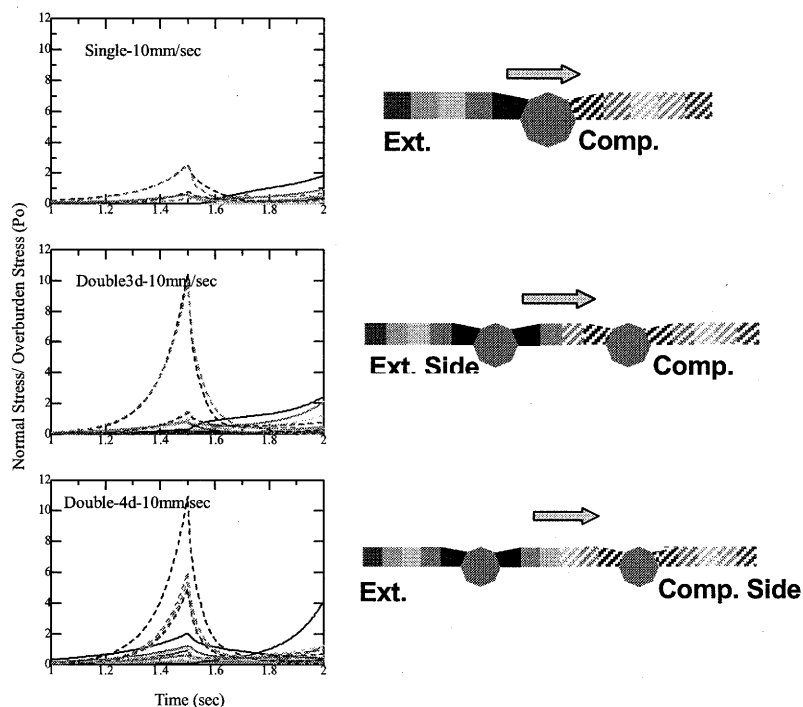


Figure 7 Normal Stress Time Histories

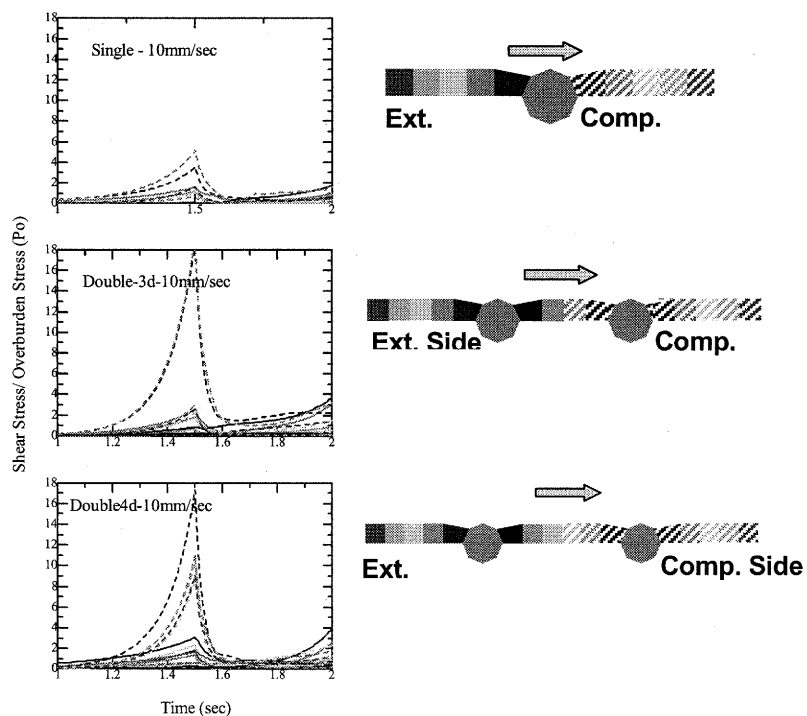


Figure 8 Shear Stress Time Histories

3.2.3 Pile Horizontal Stress

Due to the difference in the stress states in the extension and compression side mentioned above, the pile horizontal stresses in the leading (broken line in Figure 9) and trailing piles (visible line in Figure 9) were also affected. The horizontal stresses in the leading piles are 2-3 times larger than the trailing piles for different pile spacing considered as shown in Figure 9.

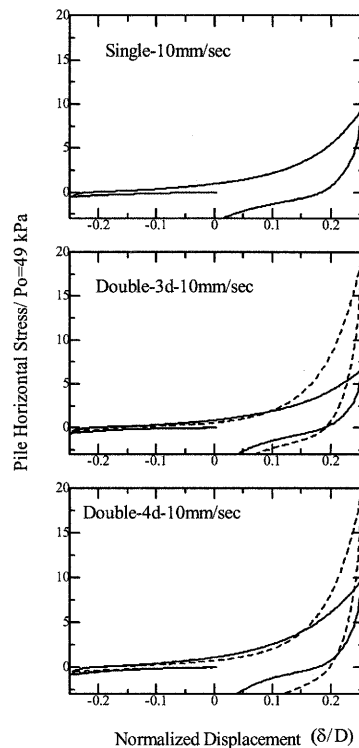


Figure 9 Normalized Horizontal Stress of the Pile against the Normalized Displacement of the Pile

4. CONCLUSIONS

The pore water pressure on the extension side reduces considerably as the pile moves to its maximum displacement while the pore water pressure on the compression side is almost unchanged or increases slightly.

The combination of the normal stress and the shear stress in the extension side is believed to be the cause of the large decrease of the pore water pressure on that side. However, the opposite effects of the combination of the normal stress and shear stress in the compression side might be the reason why the change in the pore water pressure is almost unchanged.

Due to the difference in the stress states in the extension and compression side of the pile(s), the pile horizontal stresses in the leading and trailing piles were also affected. The horizontal stresses in the leading piles are 2-3 times larger than the trailing piles for different pile spacing considered

References:

- Abdoun T, Dobry R., O'Rourke, T. Goh S. (2003), "Pile Response to Lateral Spreads: Centrifuge Modeling," *Journal of Geotechnical and Geoenvironmental Engineering*, American Society of Civil Engineers, **129**(10), 869-878.
Abdoun T and Dobry R.. (2002), "Evaluation of Pile Foundation Response to Lateral Spreading," *Soil Dynamics and*

- Earthquake Engineering*, **22** (2002) 1051-1058.
- Biot, M.A. "Theory of Propagation of Elastic Waves in Fluid-Saturated Porous Solid, Part I – Low Frequency Range." *Journal of the Acoustical Society of America*; 28(2):168-178, 1956.
- Biot, M.A. "Theory of Propagation of Elastic Waves in Fluid-Saturated Porous Solid, Part II – High Frequency Range." *Journal of the Acoustical Society of America*; 28(2):179-191, 1956.
- Biot, M.A. "Mechanics of Deformation and Acoustic Propagation in Porous Media." *Journal of Applied Physics*; 33(4):1482-1498, 1962.
- Finn W.D.L and Fujita N. (2002), "Simplified Piles in Liquefiable soil," *Soil Dynamics and Earthquake Engineering*, **22** (2002) 731-742.
- Hasiguchi K., Ueno M., and Chen Z. P. "Elasto-Plastic Constitutive Equation of Soils Based on the Concepts of Subloading Surface and Rotational Hardening." *Journal of Geotechnical Engineering, JSCE*; III-36 (547): 127-144, 1996. (In Japanese).
- Hasiguchi K., Chen Z. P. "Elasto-Plastic Constitutive Equation of Soils with the Subloading Surface and Rotational Hardening." *International Journal for Numerical and Analytical Methods in Geomechanics*; 22: 197-277, 1998.
- Suzuki H. and Tokimatsu K. (2004), "Pore Water Pressure Response Around Pile and its Effects on P-Y Relation During Liquefaction," *Proceedings of the First International on Urban Earthquake Engineering*, 493-499.
- Takahashi A., Kuwano J., Arai Y., Yano A. (2002), "Lateral resistance of Buried Cylinder in Liquefied Sand," *Physical Modelling in Geotechnics: ICPMG '02* Phillips, Guo & Popescu (eds.). 477-482
- Takahashi A. (2002b), "Soil-Pile Interaction in Liquefaction-Induced Lateral Spreading of Soils," *Tokyo Institute of Technology Dissertation*.
- Tokimatsu K. (1999), "Performance of Pile Foundations in Laterally Spreading Soils," *Earthquake Geotechnical engineering*, Seco e Pinto (eds). 1999 Balkema, Rotterdam, ISBN 90 5809 1163 957-964

ESTIMATION OF EFFECTS OF PORE WATER PRESSURE RESPONSE ON P-Y BEHAVIOR OF PILE GROUP IN LIQUEFIED GROUND

H. Suzuki¹⁾ and K. Tokimatsu²⁾

1) Graduate student, Dept. of Architecture and Building Engineering, Tokyo Institute of Technology, Japan

2) Professor, Dept. of Architecture and Building Engineering, Tokyo Institute of Technology, Japan

hsuzuki@arch.titech.ac.jp, kohji@o.cc.titech.ac.jp

Abstract: Effects of pore water pressure response on subgrade reaction of a closely spaced pile group are examined through large shaking table tests conducted on liquefiable soil-pile-structure systems. Once liquefaction occurs in dense sand, the pore water pressure on the extension side of each pile decreases with increasing relative displacement between soil and pile, probably due to the combined effect of extension stress and soil dilation induced by shear stress developed on that side. The pore water pressure on the compression side of each pile, in contrast, maintains almost constant probably due to the adverse effect of compression stress and dilation induced by shear stress developed on that side. In addition, similar compression and extension stress states occur on both sides of the pile group. As a result, the pore water pressure reduction around a pile is more significant on the extension side of the pile group than on the compression side of the pile group. In spite of the difference in pore water pressure change around each pile, the subgrade reactions of piles are almost the same within the pile group. This is because the horizontal subgrade reaction of each pile is induced by the difference in pore water pressures on both sides of the pile and this difference in pore water pressures is almost the same within the pile group.

1. INTRODUCTION

Field investigation after recent catastrophic earthquakes indicated that kinematic effects played a significant role on pile damage where large ground movements occurred (e.g., Kansai Branch of Architecture Institute of Japan, 1996; BTL Committee, 1998). In order to clarify the kinematic effect on piles, not only the earth pressure acting on embedded foundations but also the p-y behavior, defined as the relation of subgrade reaction of pile with relative displacement between the pile and soil, has been studied using physical model tests. Many studies have shown that the p-y behavior of a pile group in non-liquefied sand varies depending on its location (e.g., Rollins et al., 1998; Suzuki & Adachi, 2003). The p-y behavior of a pile group in liquefied sand is, however, still uncertain.

The objective of this paper is to investigate pore water pressure response around piles through large shaking table tests conducted on a liquefiable soil-pile-structure system with a 3x3 pile group and to estimate the horizontal subgrade reaction of each pile within the pile group. In the shaking table tests, many pore water pressure transducers were installed on and/or around piles in addition to many strain gauges, giving stress states in soil around the pile group.

2. LARGE SHAKING TABLE TEST

To investigate effects of pore water pressure response on subgrade reaction of a pile group, large shaking table tests were conducted on soil-pile-structure systems using the shaking table facility at the National Research Institute for Earth Science and Disaster Prevention in Japan. The soil-pile-structure systems were constructed in a laminar shear box with dimensions of 5.6 m x 12.0 m x 3.5 m on the shaking table. Fig. 1 shows the soil-pile-structure systems used in the tests.

The soil profile prepared in the laminar shear box consisted of three layers including a top dry sand layer 0.5 m thick, a liquefiable saturated sand layer 3.5 m thick and an underlying dense sand layer about 1.5 m thick. The sand used was Kasumigaura Sand ($e_{\max} = 0.961$, $e_{\min} = 0.570$, $D_{50} = 0.31$ mm, $F_c = 5.4$ %). Prior to each shaking table test, geophysical test and mechanical cone penetration test were conducted to characterize the soil profile. The geophysical test showed that the liquefiable sand layer was under nearly saturated condition with a P-wave velocity close to 1,500 m/s (Tamura et al., 2002) and a S-wave velocity of about 100 m/s. The cone penetration test results indicated that the density of soil increased with depth.

Each pile used in the tests had a diameter of 165.2 mm with a 3.7 mm wall thickness and thus a flexural rigidity of 1.26 MNm^2 . The length of the piles was 5.0 m. The piles were set up with a horizontal space of four-pile diameters center to center (Fig. 1(b)). The tips of piles were fixed to the base of the laminar shear box and their heads were fixed to a foundation of 16.7 kN. The foundation carried a superstructure of 176 kN.

The soil-pile-structure systems were densely instrumented with accelerometers, displacement transducers, strain gauges and pore pressure transducers, as shown in Fig. 1(a). In particular, to clarify stress states in soil around piles, many pore water pressure transducers were densely installed not only in the ground away from the pile but also on both sides of the piles at 1.5 and 2.5 m depth below the pile head (Fig. 1(b)).

In the shaking table test, an artificial ground motion called Rinkai having a maximum acceleration scaled to 2.0 m/s^2 was used as an input motion. The pore water pressure response and its effects on p-y behavior at 2.5 m depth are discussed in this paper. The relative density at 2.5 m was about 70 %, which was estimated by the relation between CPT resistance and SPT N-value proposed by Yamada et al. (1992) in addition to the relation between SPT N-value and relative density (e. g., Meyerhof, 1957).

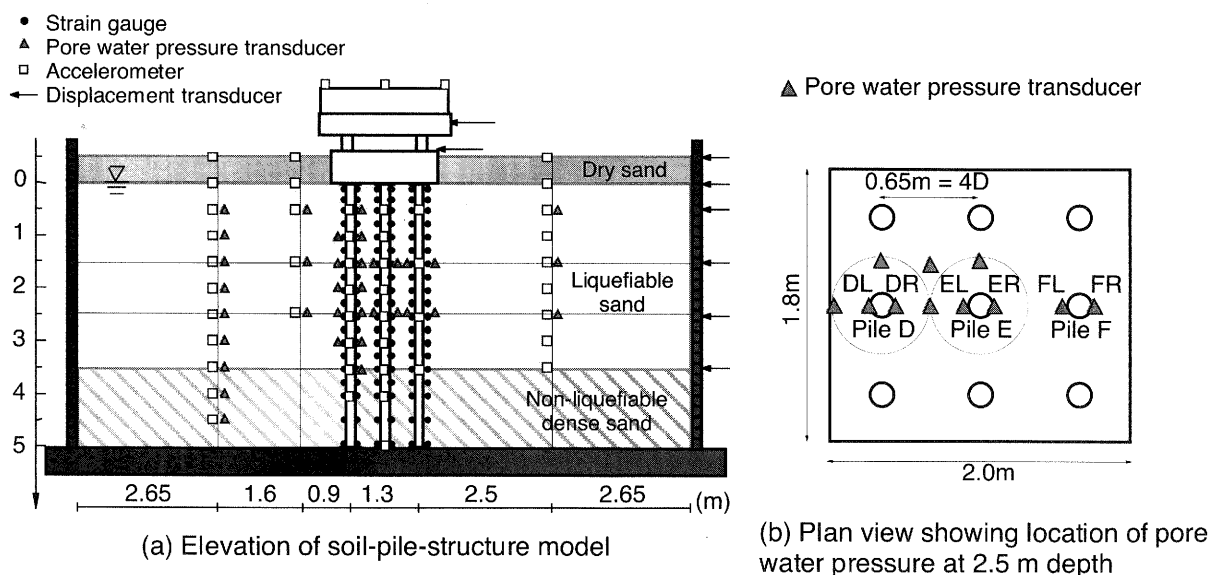


Fig. 1 Soil-pile-structure system

3. EFFECTS OF PORE WATER PRESSURE RESPONSE ON P-Y BEHAVIOR

Fig. 2 shows time histories of the displacements of pile E and the ground 2.5 m away from the foundation, the relative displacement of the two, horizontal subgrade reactions of three piles (piles D, E and F) and excess pore water pressure measured on both sides of the three piles at 2.5 m depth together with those of the input motion. Note that pile D was located in the left/outside row of the 3x3 pile group, pile E in the middle/inside row and pile F in the right/outside row (Fig. 1(b)). Displacements of pile and soil as well as the relative value of the two were calculated by double integration of observed accelerations with time. Subgrade reaction of each pile was calculated by double differentiation of observed bending moment of the pile with depth. The displacements of piles D, E and F are almost the same, and thus the pile displacement and the relative displacement shown in Fig. 2(b)(c) are those for pile E only.

Fig. 2 shows that soil liquefaction develop in 10-20 s, at which all the excess pore water pressures reach about 30 kPa. All the excess pore water pressures show significant changes after liquefaction, the trends of which are different from place to place. The pore water pressure reduction is particularly significant on the left side of the left pile (pile D) and the right side of the right pile (pile F) (Fig. 2(d)(l)). This indicates that the pore water pressure reduction is more significant in the soil outside the pile group than inside the pile group. Despite the difference in pore water pressure change depending on the location of the piles, in contrast, the subgrade reactions of the piles are almost the same within pile group.

To estimate the difference in pore water pressures in soil around the three piles, Fig. 3 shows the relations of the relative displacement between pile and ground with the excess pore water pressures measured on both sides of each pile at 2.5 m depth. The positive relative displacement in the figure indicates that the pile pushes the soil on the right and the negative relative displacement indicates that the pile pushes the soil on the left.

Once soil liquefaction develops, the pore

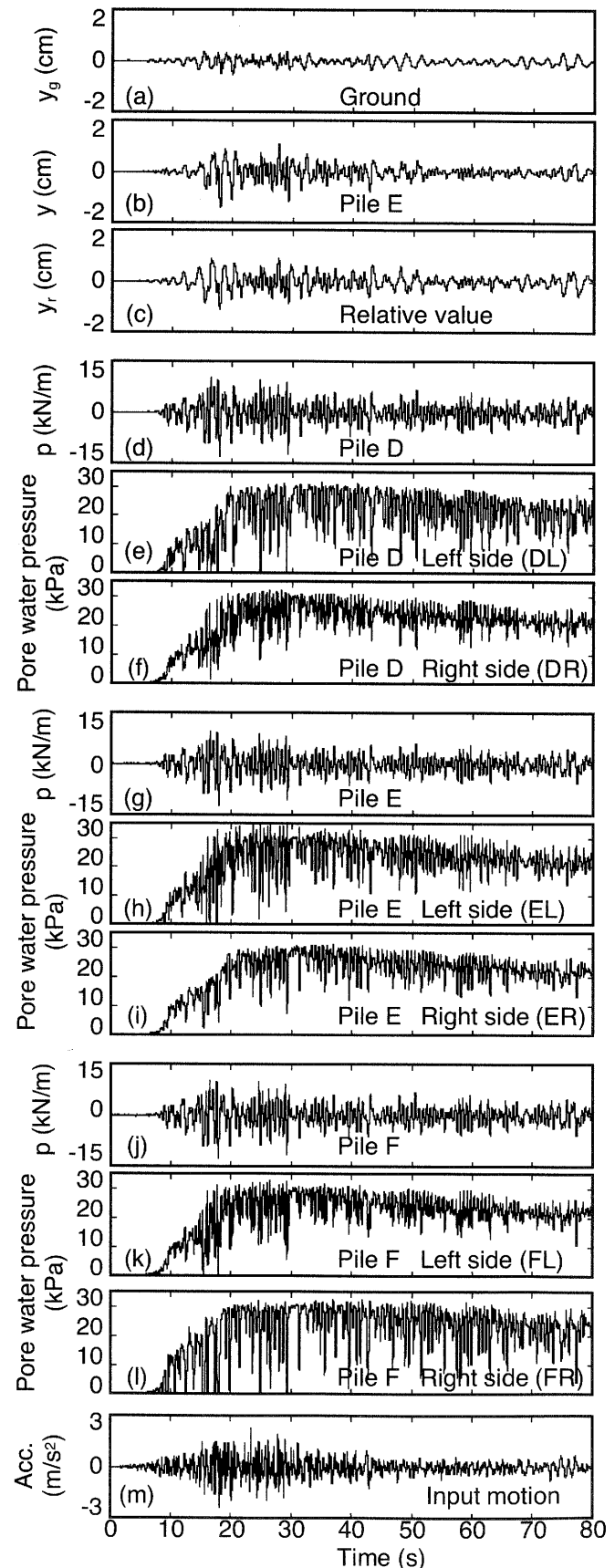


Fig. 2 Time histories of test results

water pressures of all the piles tend to decrease significantly with increasing relative displacement; however, the manner and degree of pore water pressure reduction around a pile vary depending on its location within the pile group. When the pile in the middle/inside row of the pile group (Pile E) pushes the soil on the right (i.e., positive relative displacement develops), the pore water pressure on the back/left side (EL) decreases significantly, while that on the front/right side (ER) maintains almost constant. When the pile pushes the soil on the left (i.e., negative relative displacement develops), the pore water pressures on both sides are reversed, i.e., the pore water pressure on the back/right side (ER) decreases significantly, while that on the front/left side (EL) maintains almost constant.

This trend in pore water pressure responses on both sides of a pile relates to the previous study (Tokimatsu & Suzuki, 2004) in which the stress states around a pile have been described as shown in Fig. 4. The relative displacement between pile and soil cyclically creates not only compression and extension stresses on the right and left sides of the pile but also shear stresses on both sides. On the extension side, the reduction in pore water pressure becomes pronounced probably due to the combined effects of extension stress and shear stress, as both stresses decrease pore water pressure. On the compression side, in contrast, the reduction in pore water pressure becomes small probably due to the adverse effects of compression stress and shear stress, as the former tends to increase pore water pressure. As a result, the pile is pulled by the soil on the extension side where reduction in pore pressure occurs. Such mechanism of subgrade reaction development in liquefied soil is completely different from that in dry sand where horizontal subgrade reaction is induced by the increase in soil pressure on the compression side of the pile.

When the pile in the left/outside row of the pile group (pile D) pushes the soil on the left (i.e., negative relative displacement develops) or the pile in the right/outside row (pile F) pushes the soil on the right (i.e., positive relative displacement develops), the pore water pressure on the rear side (DL and FR) decreases significantly, while that on the front side (DR and FL) maintains almost constant. The trends in pore water pressures on both sides of the piles are similar to those observed in the middle/inside row of the pile group (pile E) as well as those shown in Fig. 4. In contrast, when the pile in the left/outside row of the pile group (pile D) pushes the soil on the right (positive displacement) or the pile in the right/outside row (pile F) pushes the soil on the left (negative displacement), the pore water pressures on both sides of the piles decrease significantly. The trend is different from that observed in the middle/inside row (pile E).

Abovementioned trend also indicates that the pore water pressure reduction around a pile with respect to relative displacement depends on its location within the pile group. With increasing relative displacement, the pore water pressure decreases on the extension side of all the pile as well as the compression side of the rear pile (i.e., the right side of pile D (DR) with positive displacement and the left side of pile F (FL) with negative displacement). In particular, the pore water pressure

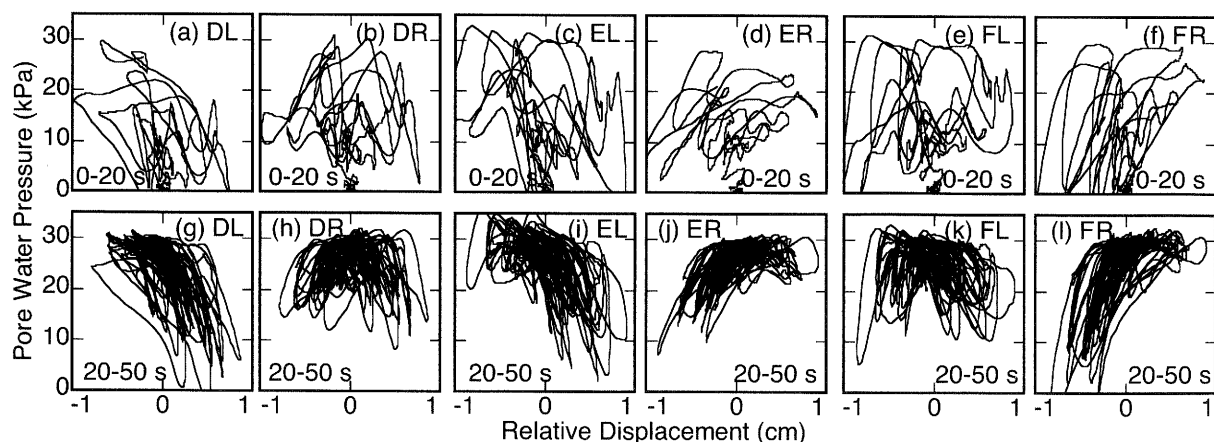


Fig. 3 Relation of pore water pressure with relative displacement between pile and soil

reduction on the extension side of the rear pile is significant (i.e., the left side of pile D (DL) with positive displacement and the right side of pile F (FR) with negative displacement). These trends further indicate that the pore water pressure reduction around the rear pile is most significant among others.

Fig. 5 illustrates a schematic figure indicating how the pore water pressure changes around the piles are different from each other, depending on their locations. With increasing relative displacement between soil and pile, the compression and extension stresses develop on the front and rear sides of each pile (Fig. 5(a)). If piles are closely spaced within a pile group, the piles tend to move together with the ground nearby. As a result, the compression and extension stresses develop also on the front and rear sides of the pile group (Fig. 5(b)). This is probably one of the major reasons why the pore water pressure is more significant on the rear side than on the front side of the pile group.

To investigate the effects of pore water pressure reduction around the piles on the subgrade reaction development of the pile group, Fig. 6 compares the difference in the two pore water pressures on both sides of three piles with the p-y behavior at 2.5 m depth. Despite the difference in pore water pressure around each pile, the differences in the two pore water pressures are almost the same within

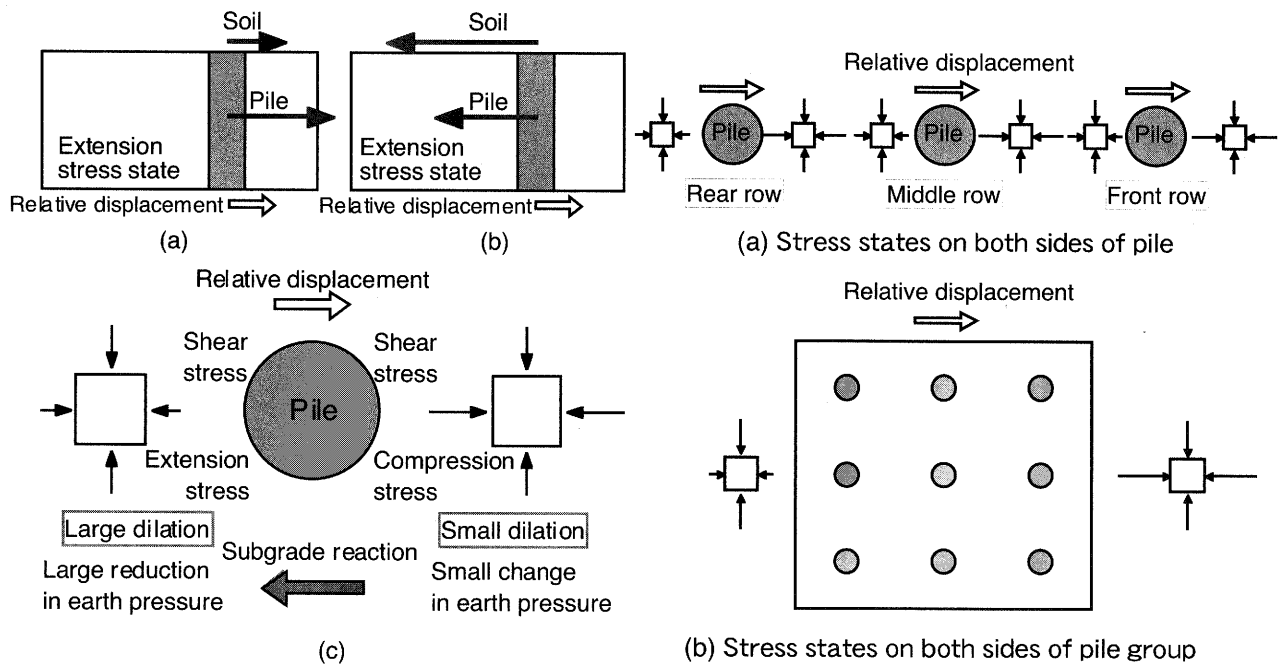


Fig. 4 Stress states around pile
(Tokimatsu & Suzuki, 2004)

Fig. 5 Stress state around pile group

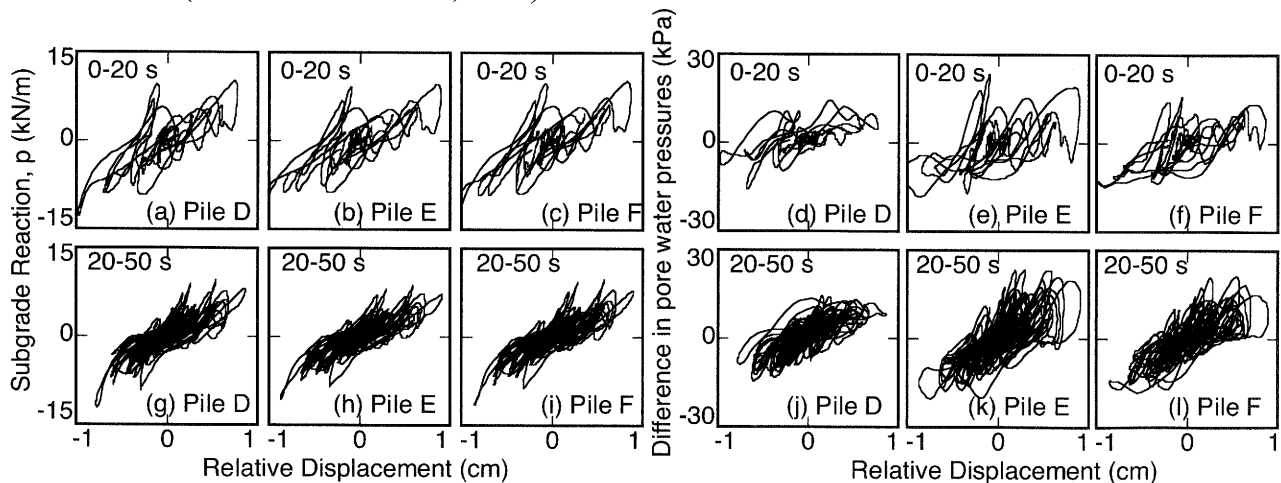


Fig. 6 Relation of subgrade reaction and difference in pore water pressures with relative displacement

the pile group (Fig. 6(a)-(c)(g)-(i)). This is probably one of the major reasons why the subgrade reactions of piles become almost the same within the pile group (Fig. 6(d)-(f)(j)-(l)).

4. CONCLUSIONS

The pore water pressure response around piles and its effects on p-y behavior of a pile group in liquefied ground have been investigated thorough the large shaking table tests conducted on soil-pile-structure systems. The test results and discussions have led to the following conclusions:

- 1) With increasing relative displacement, the compression and extension stress states develop cyclically on front and rear sides of a pile, in addition to the shear stress on both sides. In dense sand, the pore water pressure on the extension side of the pile decreases significantly due to the combined effect of the extension stress and the shear stress, while that on the compression side maintains almost constant due to the adverse effects of the compression stress and the shear stress. An increase in horizontal subgrade reaction in dense sand is caused by the difference in stress states on both sides of the pile. This means that the pile is pulled by the soil where the extension stress state develops. Such mechanism of p-y behavior in liquefied soil is completely different from that in dry sand where horizontal subgrade reaction is induced by the increase in soil pressure on the compression side of the pile.
- 2) If piles are closely spaced within a pile group in dense sand, compression and extension stress states occur in soil on both sides of the pile group as well as on both sides of each pile. As a result, the pore water pressure reduction around a pile is more significant on the extension side of the pile group than on the compression side of the pile group. The subgrade reactions of piles in dense sand are almost the same within the pile group, in spite of the difference in pore water pressures changes among the piles. This is because the differences in pore water pressures between the front and rear sides of the piles are almost the same within the pile group.

Acknowledgments:

The study described herein was made possible through the Special Project for Earthquake Disaster Mitigation in Urban Areas, supported by the Ministry of Education, Culture, Sports, Science and Technology (MEXT). The authors express their sincere thanks to the above organization.

References:

- BTL Committee (1998), *Research Report on liquefaction and lateral spreading in the Hyogoken-Nambu earthquake* (in Japanese).
- Kansai Branch of Architecture Institute of Japan (1996), *Report on case histories of damage to building foundations in Hyogoken-Nambu earthquake*, Committee on Damage to Building Foundations (in Japanese).
- Meyerhof, G. G. (1957), Discussions, *Proc. of 4th International Conference on Soil Mechanics and Foundation Engineering*, **3**, 110.
- Rollins, K. M., Kris, T. P. and Thomas, J. W. (1998), "Lateral load behavior of full-scale pile group in clay", *Journal of Geotechnical and Geoenvironmental Engineering*, ASCE, **124** (16), 468-478.
- Suzuki, Y. and Adachi, N. (2003), "Relation between subgrade reaction and displacement of model pile group based on horizontal loading tests", *Journal of Structural and Construction Engineering*, AIJ, **570**, 115-122 (in Japanese).
- Tamura, S., Tokimatsu, K., Abe, A. and Sato, M. (2002), "Effects of air bubbles on B-value and P-value velocity of partly saturated sand", *Soils and Foundations*, JGS, **42** (1), 121-129.
- Tokimatsu, K., and Suzuki, H. (2004), "Pore water pressure response around pile and its effects on p-y behavior during soil liquefaction", *Soils and Foundations*, JGS, **44** (6), 101-110.
- Yamada, K., Kamao, S., Yoshino, H. and Masuda, Y. (1992), Correlation between N-value and cone index, *Tsuchi-to-Kiso*, JGS, **40** (8), 5-10 (in Japanese).

P-DELTA EFFECT OF PILES FOUNDED ON Laterally SPREADING AND LIQUEFIABLE SOILS

S. Bhattacharya¹⁾, K. Tokimatsu²⁾

1) *Fellow, Centre for Urban Earthquake Engineering, Tokyo Institute of Technology, Japan. Currently Fugro Limited (U.K)*

2) *Professor, Dept of Architectural and Building Engineering, Tokyo Institute of Technology, Japan*

S.Bhattacharya.00@cantab.net, kohji@o.cc.arch.titech.ac.jp

Abstract: In laterally spreading soils, during seismic liquefaction, large lateral loads are induced in a pile due to the permanent ground displacements. In addition – earthquakes also induce lateral loads on a pile due to inertial action of the superstructure. These lateral loads may cause a pile to collapse by bending failure. On the other hand, if the axial load acting on a pile is high enough, a pile-supported structure may fail if the surrounding soil liquefies in an earthquake. The mechanism of failure in this case is buckling instability. These two established facts hint that load-deformation effect, commonly known as P-delta effect should be considered in pile design. For design of piles in seismic liquefaction areas, most codes of practice focus only on bending strength and omit considerations necessary to avoid buckling in the event of soil liquefaction. This paper provides a simplified approach to account for P-delta effect.

1. INTRODUCTION

Collapse of pile-supported structures is still observed in liquefiable soils after most major earthquakes such as 1995 Kobe earthquake (JAPAN), 1999 Kocheli earthquake (TURKEY), 2001 Bhuj earthquake (INDIA). The failure not only occurred in laterally spreading grounds but also was observed in level grounds; see for example Tokimatsu et al (1997). The failure was often accompanied by settlement and tilting of the super structure rendering it useless after the earthquake. Following the earthquake of 1995 Kobe earthquake, many research has been done to find the failure pattern of the piles, Yoshida and Hamada (1990), BTL Committee (2000). Piles were excavated or pulled out from the subsoil, borehole cameras were used to take photographs, and pile integrity tests were carried out. These studies hinted the location of the cracks, damage patterns for the piles under investigation. Of particular interest is the formation of plastic hinges in the piles. This indicates that the stress in the pile during liquefaction exceeded the yield stress of the material of the pile.

The failure of piled foundations can be classified into two groups:

(a) Structural failure of the pile whereby the load carrying capacity of the foundation drops. The fundamental failure mechanisms that can cause plastic hinge formation in a pile are shear failure, bending failure and buckling failure. The above three forms of failure are often known as LIMIT STATE OF COLLAPSE. It must be mentioned that each of these types of failure can cause a complete collapse of the foundations.

(b) Failure by excessive settlement rendering it useless. Often the settlement of piled foundations exceeds the acceptable limits of the structure, which is essentially SERVICEABILITY LIMIT STATE. In this type of failure, the piles may not fail structurally.

The current method of pile design such as Eurocode 8, JRA (1996), Indian Code (IS 2911, IS 1893) is based on a bending mechanism where lateral loads due to inertia or slope movement induces bending failure on the pile. Recent research such as Bhattacharya et al. (2004) has shown that if piles are too slender they require lateral support from the surrounding soil if they are to avoid buckling instability. During earthquake-induced liquefaction, the soil surrounding the pile loses effective confining stress and can no longer offer sufficient support to the pile. A slender pile may then buckle sideways in the direction of least elastic bending stiffness pushing aside the initially liquefied soil, and eventually rupturing under the increased bending moment and shear force. Lateral loading due to slope movement, inertia or out-of-straightness increases lateral deflections, which in turn induces plasticity in the pile and reduces the buckling load, promoting more rapid collapse. These lateral loads are, however, secondary to the basic requirements that piles in liquefiable soil must be checked against Euler's buckling. This theory has been formulated based on a study of fourteen case histories of pile foundation performance and verified using dynamic centrifuge tests. Analytical studies also support this theory of pile failure, see for example Kimura and Tokimatsu (2004), Bhattacharya and Bolton (2004). In other words, part of the pile in liquefiable soil needs to be treated as an unsupported structural column. In contrast, the piles in liquefiable soils are erroneously designed as beams.

Structurally, most piles are designed to carry the bending moments due to the lateral loads. The semi-empirical P-y concept is normally used to design piles. However, this approach cannot be applied if buckling under axial loading is a possibility for the member under consideration. These considerations would lead to the fact that, if part of the pile loses lateral support during its design period, the pile should be treated as unsupported column in that region. The structural design of the pile in the unsupported zone should conform to a column carrying lateral loads. The current design codes however do not consider this issue. The aim of this paper is thus to discuss the effect of lateral load on buckling due to the axial load acting on the pile. In other words, the inclusion of P-delta effect for fully embedded piles in liquefiable soils.

2. PREDOMINANT LOADS ACTING ON A PILED FOUNDATIONS DURING AN EARTHQUAKE AND THE FUNDAMENTAL FAILURE MECHANISMS

During earthquakes, the predominant loads acting on a pile are:

1. Axial load (P) that acts at all times on a pile. The axial load may increase due to inertial effect of the superstructure and kinematic effects due to soil movement.
2. Inertia loads due to the superstructure which is oscillating in nature
3. Loads due to ground movement commonly known as kinematic effects. This load can be of two types, such as transient (during shaking due to the dynamic effects) and residual (after the shaking ceased due to lateral spreading).

Piles failed by forming plastic hinges. This implies that there was a structural failure in the pile. The fundamental failure mechanisms for a structural concrete or steel section are

1. Shear failure in the pile due to the lateral loads such as inertia or kinematic loads or a combination of the above. This is particularly damaging to hollow circular concrete piles (non-ductile) with a low shear capacity.
2. Bending failure due to the combined effect of lateral and axial loads i.e. formation of a collapse mechanism as shown schematically in Figure 1.
3. Buckling failure in slender piles due to the effect of axial load and the loss of surrounding

confining pressure provided by the soil owing to liquefaction, see Bhattacharya (2003), Bhattacharya and Bolton (2004), Bhattacharya et al (2004). Buckling is sensitive to imperfections such lateral loads, out-of-line straightness. This would imply that in presence of lateral loads, a pile would buckle at a load much lower than the Euler's Critical Load. A typical configuration is shown in Figure 2.

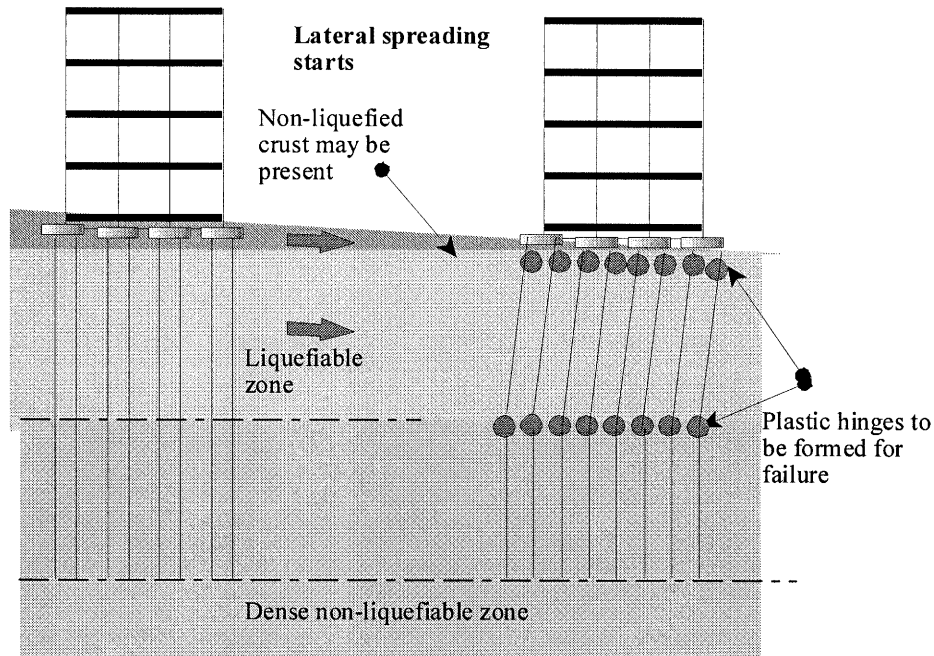


Figure 1: Mechanism of failure by lateral spreading

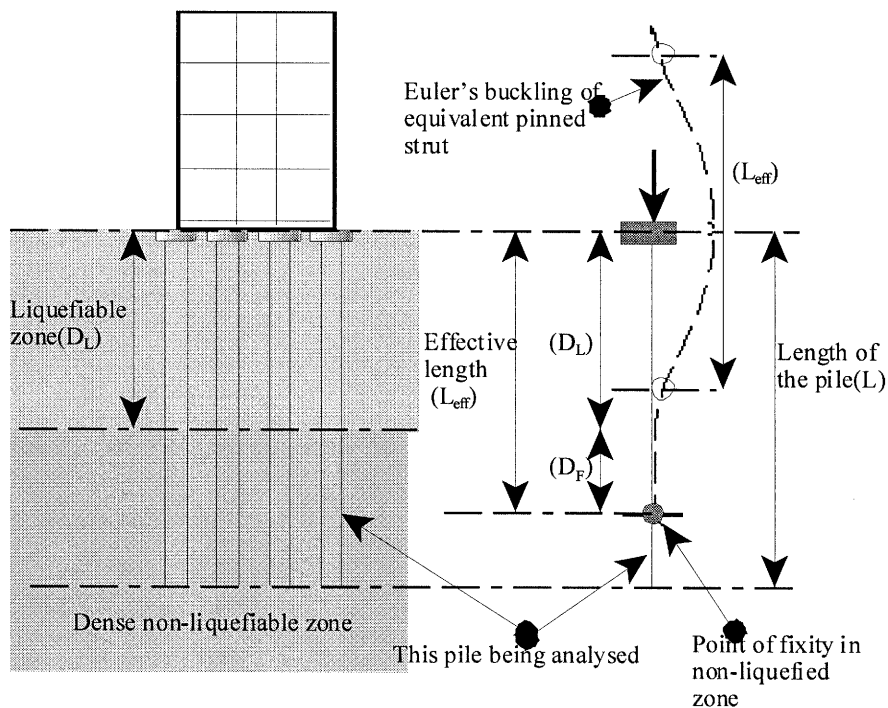


Figure 2: Mechanism of failure by buckling

3. ROLE OF LATERAL LOAD ON BUCKLING

A pile can be best described as a beam-column i.e. a column section carrying lateral loads. A general equation can be described as follows.

$$EI \frac{d^4 y}{dx^4} + \left[P_0 - \int_0^x f(x) dx \right] \frac{d^2 y}{dx^2} - f(x) \frac{dy}{dx} + k(x) \cdot y = 0 \quad (1) \text{ where}$$

EI = Flexural rigidity of the pile;

P_0 = External axial compressive force applied at the top of the pile i.e. $x = 0$

$f(x)$ is the friction per unit length

$k(x)$ is the modulus of subgrade reaction.

The above equation suggests that if part of the soil surrounding the pile loses its effective stress, then $f(x) = 0$ and $k(x)$ will be near zero, and the equation reduces to Euler's buckling equation. The theoretical buckling load can be estimated by equation 2.

$$P_{cr} = \frac{\pi^2 EI}{L_{eff}^2} \quad (2) \text{ where}$$

L_{eff} = Effective length of the pile in the unsupported zone. This depends of the boundary condition of the pile below and above the support loss zone, see Bhattacharya et al (2004).

Rankine (1866) recognized that the failure load of structural columns predicted by equation 2 is more than the actual failure load (P_F) i.e. equation 2 is unconservative. This is because buckling is very sensitive to imperfections in the pile and lateral loads. The collapse also involves an interaction between elastic and plastic modes of failure. Lateral loads and geometrical imperfections both lead to the creation of bending moments in addition to axial loads. Bending moments have to be accompanied by stress resultants that diminish the cross-sectional area available for carrying the axial load, so the failure load P_F is less than the plastic squash load (P_P) given by $A \cdot \sigma_y$ (A =area of the pile section, σ_y is the yield stress of the material). Equally, the growth of zones of plastic bending reduces the effective elastic modulus of the section, thereby reducing the critical load for buckling, so that $P_F < P_{cr}$. Furthermore these processes feed on each other, as explained in Horne and Merchant (1965). As the elastic critical load is approached, all bending effects are magnified. If lateral loads in the absence of axial load would create a maximum lateral displacement δ_0 in the critical mode-shape of buckling, then the displacement δ under the same lateral loads but with a co-existing axial load P is given by:

$$\left(\frac{\delta}{\delta_0} \right) = \frac{1}{1 - \left(\frac{P}{P_{cr}} \right)} \quad (3)$$

The same magnification factor applies to any initial out-of-line straightness of the pile in the mode shape of potential buckling. Correspondingly, all curvatures are similarly magnified and so are the bending strains induced in the column by its lateral loads or eccentricities. The progression towards plastic bending failure is accelerated as axial loads approach the elastic critical load (P_{cr}). Not only do axial loads induce extra bending moments ($P-\Delta$ effects), but the full plastic bending resistance cannot be mobilized due to the fact that part of the pile section is required to carry the axial loads. Equation 3 indicates that for a column carrying an axial load of half its Euler load, that lateral displacements and therefore bending moments would be $1/(1-0.5)$ or 100% bigger than those calculated ignoring axial load effects. This is important if

significant lateral loads must also be carried. Equation 3 is sketched in Figure 3. The figure shows as the (P/P_{cr}) ratio approaches 1, the amplification of lateral deflections tends to infinity.

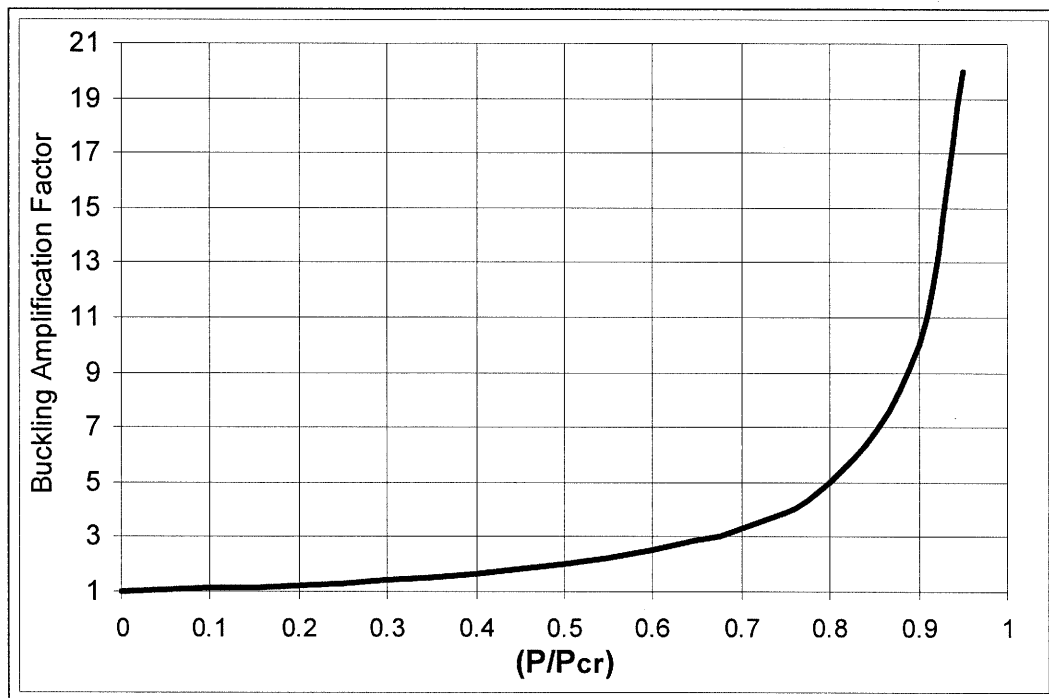


Figure 3: Amplification of lateral deflections due to axial load

4. ESSENTIAL CHECKS THAT A SAFE DESIGN PROCEDURE SHOULD ENSURE

A safe design procedure should ensure that the piles have enough strength and stiffness to sustain the following:

- (1) A collapse mechanism should not form in the piles under the combined action of lateral loads imposed upon by the earthquake and the axial load. Figure 1 shows such a mechanism. At any section of the pile, bending moment should not exceed allowable moment of the pile section. The shear stress load at any section of the pile should not exceed the allowable shear capacity.
- (2) A pile should have sufficient embedment in the non-liquefiable hard layer below the liquefiable layer to achieve fixity to carry moments induced by the lateral loads. If proper fixity is not achieved, the piled structure may slide due to the kinematic loads. The fixity depth is shown by D_F in Figure 2. Typical calculations carried out using the method proposed by Davisson and Robertson (1965) shows that the point of fixity lies between 3 to 6 times the diameters of the pile in the non-liquefiable hard layer. Details can be seen in Bhattacharya (2003).
- (3) Axial load acting on the pile during full liquefaction without buckling and becoming unstable. It has to sustain the axial load and vibrate back and forth, i.e. must be in stable equilibrium when the surrounding soil has almost zero stiffness owing to liquefaction. As mentioned earlier, lateral loading due to ground movement, inertia, or out-of-straightness, will increase lateral deflections which in turn can cause plastic hinges to form, reducing the buckling load, and promoting more rapid collapse. These lateral load effects are, however, secondary to the basic requirements that piles in liquefiable soils must be checked against Euler's buckling. This implies that there is a requirement of a minimum diameter of pile depending on the likely liquefiable depth.
- (4) The settlement in the foundation due to the loss of soil support should be within the acceptable limit. The settlement should also not induce end-bearing failure in the pile.

Bhattacharya and Tokimatsu (2004) proposed essential criteria for design of piles in liquefiable soils. They are stated below:

- (1) During the entire earthquake, the pile should be in stable equilibrium, the amplitude of vibration should be such that no section of the pile should have an ultimate limiting strain for the material. For example in the case of concrete piles, the ultimate strain in the pile should not exceed 0.003. At this strain, visible cracks appear in concrete leading to deterioration of bending stiffness. This criterion automatically ensures that no plastic hinge will form and no cracks will open up. Steel tubular piles are ductile i.e. they can withstand large amount of inelastic strain before yield and thus can be a good choice.
- (2) The settlement of the piled foundation should be within acceptable limits for the structures. However, the settlement should be limited to a maximum of 10% of the pile diameter to avoid base failure (end-bearing failure) based on Fleming et al (1992).

5. SIMPLIFIED METHOD TO CONSIDER P-DELTA EFFECT

Lateral spreading loads and inertia loads may act in two different planes depending on the topography of the site and orientation of the superstructure, see for example Figure 4. Thus the pile not only has axial stress but also may have bending stresses in two axes. The pile represents a most general form of a “beam-column” (column carrying lateral loads) element with bi-axial bending. If the section of the pile is a “*long column*”, analysis would become extremely complex and explicit closed-form solution does not exist. The solution of such a problem demand an understanding of the way in which the various structural actions interact with each other i.e. how the axial load influences the amplification of lateral deflection produced by the lateral loads. Section 3, equation 3 and Figure 3 discuss the most likely form of influence for a pile which is borrowed from structural engineering. Piles are more slender than structural columns, is more likely to have more imperfections than columns due to the driving stresses.

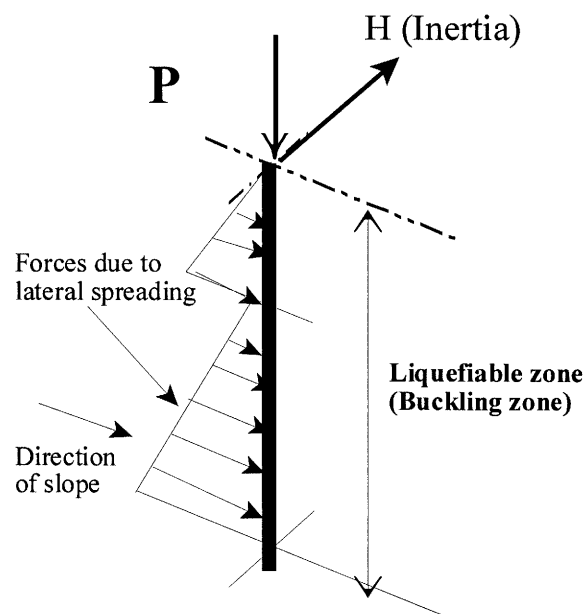


Figure 4: Generalized loading for a pile.

In the simplest cases i.e. when the section is “*short column*”, i.e. length to diameter ratio less than 12; superposition principle can be applied i.e. direct summation of the load effects. In other cases, i.e. for long columns, careful consideration of the complicated interactions needs to be accounted for. Designing such type of member needs a three-dimensional interaction diagram where the axes are:

Axial (P), major-axis moment (M_x) and minor-axis moment (M_y). The analysis becomes far more complicated in presence of dynamic loads. A simplified approach to avoid the above complicated non-linear process and to account for P-delta effect is designing piles as “short column” i.e. for concrete section - length to least lateral dimension less than 15 (British Code 8110) or a slenderness ratio (effective length to minimum radius of gyration) less than 50.

Figure 5 shows the study of 14 reported case histories of pile foundation during earthquakes, after Bhattacharya et al (2004). Six of the piled foundations survived while others suffered severe damage. Essentially, it is assumed that the pile is unsupported in the liquefiable zone. For each of the case histories, the L_{eff} of the pile in the liquefiable region is plotted against the minimum radius of gyration (r_{min}) of the pile. r_{min} is introduced to represent piles of any shape (square, tubular, circular) and is given by $\sqrt{I/A}$ where I is the second moment of area; and A is the cross sectional area of the pile section. For a solid circular section; r_{min} is 0.25 times the diameter of the pile and for a hollow circular section r_{min} is 0.35 times the outside diameter of the pile. L_{eff} is dependent on the thickness of the liquefiable zone, depth of embedment and the fixity at the pile head.

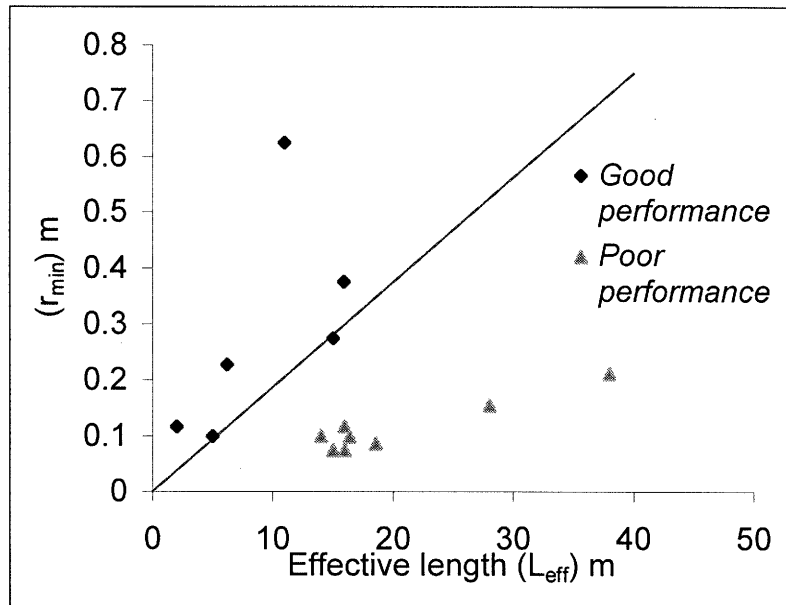


Figure 5: Study of 14 case histories, after Bhattacharya et al (2004)

In the figure, a line representing a slenderness ratio of 50 could differentiate the good performance piles from the poor performance. Thus the study shows that piles should be designed as short column, i.e. large diameter piles are better. Figure 6 shows a typical graph showing the minimum diameter of pile necessary to avoid buckling (and carrying out non-linear analysis) depending on the thickness of liquefiable soil. The slenderness ratio is kept around 50. The main assumptions are that the piles are solid concrete section having E (Young's modulus) of 22.5×10^3 MPa and for steel E of 210 GPa. The piles are not in a single row and at least in 2×2 matrix form. The thickness of the steel pile is based on API code (American Petroleum Code) i.e. the minimum thickness is $6.35 \text{ mm} + (\text{diameter of the pile}/100)$ based on stress analysis due to pile driving.

6. CONCLUSIONS

For design of piles in seismic liquefaction areas, most of the codes of practice focus on bending strength and do not mention the bending stiffness required to avoid buckling in the event of soil liquefaction. The current design codes needs to address buckling of piles due to the loss of soil support

owing to liquefaction. Analytical studies and case histories shows that to avoid buckling instability of piles, it is necessary to keep the slenderness ratio of the piles in the liquefiable zone below 50; i.e. length to diameter ratio of about 15. Simplified design chart to avoid buckling of solid concrete and steel tubular piles passing through liquefiable soils have been proposed in the paper. A pile must also be sufficiently embedded in the non-liquefiable hard layer below the liquefiable soil to ensure fixity and avoid sliding. The settlement of the structure due to loss of shaft resistance of the pile in the liquefiable soils should be within acceptable limits.

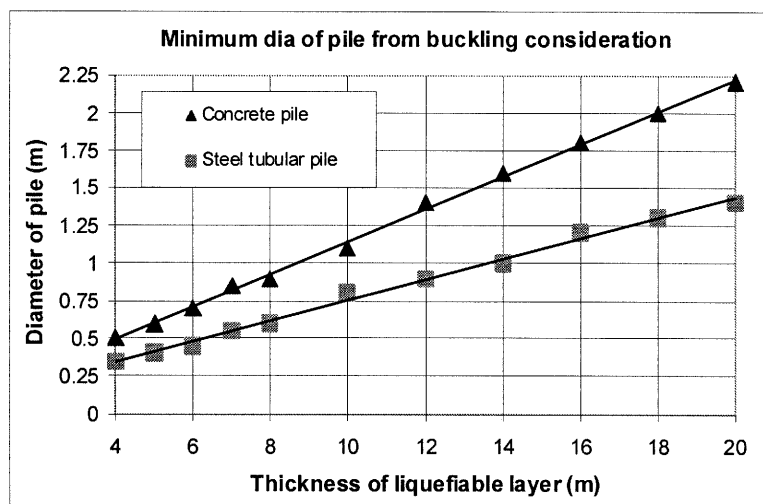


Figure 6: Minimum diameter of pile from buckling considerations

Acknowledgements:

The second author acknowledges the support from the Center for Urban Earthquake Engineering (CUEE) in Tokyo Institute of Technology for providing the 21st Century Centre of Excellence Fellowship for carrying out the research.

References:

- Bhattacharya, S (2003): Pile Instability during earthquake liquefaction, PhD thesis, University of Cambridge (U.K).
- Bhattacharya, S and Bolton, M.D (2004): "A fundamental omission in seismic pile design leading to collapse", *Proceedings of the 11th International Conference on soil dynamics and earthquake engineering*, Berkeley, 7 - 9th Jan 2004, pp 820-827.
- Bhattacharya, S., Madabhushi, S.P.G., and Bolton, M.D. (2004): "An alternative mechanism of pile failure in liquefiable deposits during earthquakes", *Geotechnique* 54, April issue, No.3.
- Bhattacharya and Tokimatsu (2004): Essential criteria for design of piled foundation in liquefiable soils, *Proceedings of the 39th Japan National Symposium for geotechnical engineering*, 7th to 9th July 2004, Niigata (Japan).
- BTL Committee (2000). Study on liquefaction and lateral spreading in the 1995 Hyogoken-Nambu earthquake, Building Research Report No. 138. Building Research Institute, Ministry of Construction, Japan (in Japanese).
- Davissson, M.T. and Robinson, K.E (1965): "Bending and buckling of partially embedded pile, *Proc. 6th Int. Conf of Soil Mechanics and Foundation Engineering*, Canada, Volume 2, pp- 243-246.
- Eurocode 8 (1998). Code of Practice for earthquake resistant design.
- Fleming, W.G.K., Weltman, A.J., Randolph, M.F., and Elson, W.K (1992), *Piling Engineering*, Surrey University Press, John Wiley and Sons. NY.
- Horne and Merchant (1965): *The stability of frames*, Pergamon.
- J.R.A (1996): Japanese Road Association Code, Highway bridge specification, Part 5.
- Kimura, Y and Tokimatsu, K. (2004) Buckling load of slender piles in liquefied soil; *Proc. 39th Japan National Conference on geotechnical engineering*, Niigata, pp 1579-1580.
- Rankine (1866). Useful Rules and Tables, London
- Tokimatsu, K., Oh-oka Hiroshi, Satake, K., Shamoto Y. and Asaka, Y (1997): "Failure and deformation modes of piles due to liquefaction-induced lateral spreading in the 1995 Hyogoken-Nambu earthquake", *Journal Struct. Eng. AIJ (Japan)*, No-495, pp 95-100.
- Yoshida, N and Hamada, M. (1990): Damage to foundation piles and deformation pattern of ground due to liquefaction-induced permanent ground deformations. *Proceedings 3rd Japan-US workshop on Earthquake Resistant Design of Lifeline Facilities and Countermeasures for Soil Liquefaction*, San Francisco, pp 147-161.

TO HELP SCHOOLTEACHERS TAKE APPROPRIATE ACTION IN THE EVENT OF EARTHQUAKE DISASTER

K. Hashimoto¹⁾, T. Ohmachi²⁾, and S. Inoue³⁾

1) Doctoral Student, Department of Built Environment, Tokyo Institute of Technology, Japan

2) Professor, Department of Built Environment, Tokyo Institute of Technology, Japan

3) Assistant, Department of Built Environment, Tokyo Institute of Technology, Japan

khashimo@enveng.titech.ac.jp, ohmachi@enveng.titech.ac.jp, shusaku@enveng.titech.ac.jp

Abstract: In an earthquake disaster schoolteachers should play many important roles such as escape guiding of schoolchildren, confirming the student's safety, caring the mental health of schoolchildren and assisting the evacuation shelter management activities. The purpose of this study is to grasp and model the whole activities of schoolteachers after an earthquake for better emergency response. They are identified as nine types of works; First reaction, Establishment of the management office, Collecting information, Education Planning, Other operations, Recovery of facilities and equipment, Healthcare, Assistance for managing the evacuation shelter and Communication with other organization. The communication activity is modeled individually because this work has many overlap with other activities. The assistance activity of the evacuation shelter management is independent of other schoolteachers' activities so that individual model of the evacuation shelter management activities is created.

1. INTRODUCTION

In the event of an earthquake disaster schoolteachers have to do many activities such as escape guiding of schoolchildren, confirming the student's safety, preparing emergency education, restoring facilities, caring the mental health of schoolchildren and assisting the evacuation shelter management activities if the shelter is open on school property. To fulfill these activities, schoolteachers have to respond appropriately to many emergencies. To grasp and model the emergency responses are most necessary to take appropriate actions. Tahara (2004) also advocates that to grasp and model the emergency responses are very helpful to municipalities. Nevertheless, many schoolteachers do not understand the whole activities in the emergency because they can obtain only the disproportionate or confusing information. It is feared that they do their activities without grasping the whole tasks and some activities are one step behind when a disaster attacks them. This research will discuss about some materials concerned with schoolteachers' activities and propose the model of schoolteachers' activities classified by the works to grasp the whole activities easily and take appropriate actions.

2. SOURCE MATERIALS ASSOCIATED WITH SCHOOLTEACHERS' ACTIVITIES

2.1 Reports Developed by the Ministry of Education, Culture, Sports, Science and Technology

Soon after the 2004 Niigata-ken Chuetsu Earthquake happened, the ministry of education, culture, sports, science and technology released the reports about the present conditions of schools; the response of the minister to schools, the disaster damage of schools, the number of temporary closed

school and the number of schools used as the evacuation shelter. According to the reports from October 26 to November 11 in 2004, the maximum 256 schools out of 451 schools were closed on October 28. Afterwards, the number of closed schools was declined gradually and all schools except for one high school were open on November 9. In addition, the number of schools used as the evacuation shelter has been larger than that of the closed schools since November 4. This result reveals that students and refugees used one facility together for a period. When the school faces this situation, the school activities have to be limited because the refugees use a part of the school facility and playground as shown in figure 1. For example schoolchildren have to play in the limited area of playground because the playground are used as the car parking space and the space to build the temporary house.

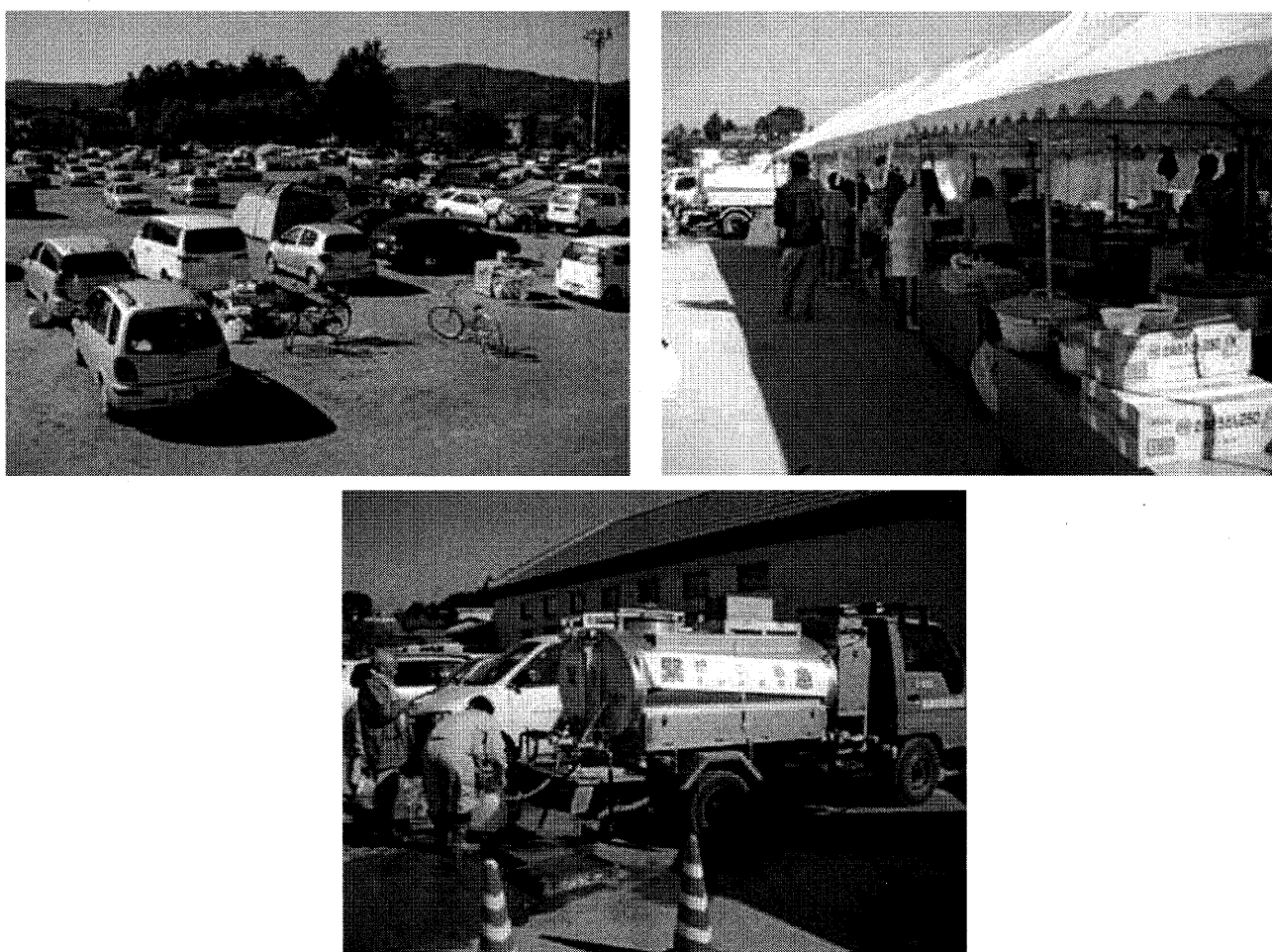


Figure 1 The situations of the evacuation shelter in Ojiya elementary

2.2 Reports about the 1995 Hyogo-ken Nanbu Earthquake

Many reports about the 1995 Hyogo-ken Nanbu earthquake were published. They show the real trouble, the real schoolteachers' activities and the important reminders with time. For example, Kobe city board of education (1996) shows that the safety of only 20 % students could be confirmed on the day when the 1995 Hyogo-ken Nanbu earthquake happened and two weeks later finally the safety of most students could be confirmed. These reports reveal the particulars about the individual activities, but it is difficult to grasp the big figure. After this earthquake Hyogo prefecture board of education (1998) published the project report creating the model area about the disaster education. This report

shows the emergency manual for Hokutan town elementary school and junior high school. It is determined in detail about the first reaction when an earthquake happened. The activities for restoring are itemized based on their experiences, but they are not systematized.

2.3 The Ward Official Activity Manual

The Taito ward official activity manual (1997) clarifies the activities of the ward officers after an earthquake. This manual includes the activities for the education board and for managing the evacuation shelter. The activities of the education board are accomplished in close collaboration with schoolteachers. This manual reveals the informative matter caught from the reports of the schoolteachers, so that the schoolteachers' activities can be expected by it. However it should be careful when considering the schoolteachers' activities, because they have to cooperate with other organizations as well as the board of education. In addition, this manual classifies the activities in unit associations, and some activities overlap in several associations.

3. MODEL OF SCHOOLTEACHERS' ACTIVITIES

3.1 The Whole Model of Schoolteachers' Activities

The above source materials show only parts of schoolteachers' activities. It is difficult to grasp their activity from them. To know the whole activities of schoolteachers, the individual activities are abstracted from these sources. The individual activities are discussed in detail below:

1. *Escape Guiding of School Children*: When the large scale of an earthquake occurs, schoolteachers have to lead and evacuate schoolchildren to safer place for protecting them.
2. *Contact with student's guardians*: Schoolteachers protect schoolchildren until their guardians pick up them. For determining the measure to hand schoolchildren over to their guardians, schoolteachers contact with their guardians.
3. *Safety Check and Rescue*: At the same time as leading schoolchildren, some schoolteachers should safety-check gas and fire, battle the fires, search for missing people and rescue the injured.
4. *First Aid*: In the event of injury schoolteachers should give the injured first aid or hurry the injured to the hospital.
5. *Mobilization of Schoolteachers*: If schoolteachers are not in school in the event of earthquake disaster, they should gather at school for responding to any emergencies.
6. *Setting of Home Base*: The management office should be set up in the safety place to control all activities in the emergency.
7. *Request and Acceptance of Support*: In the emergency the school needs more people to accomplish their activities than usual. If the school does not have enough hands, they should request and accept backups.
8. *Confirmation of the Human Safety*: The safety of schoolchildren, schoolteachers and their family and the environment conditions surrounding their life should be confirmed.
9. *Confirmation of the Disaster Damage*: The disaster damage in and outside school should be confirmed such as the damage of buildings, lifelines, school equipments, school roads, schoolbooks and critical documents.
10. *Temporary School Assembly*: In the emergencies schoolteachers should explain to schoolchildren about their actual conditions and the plan for their future. For explaining them the temporary school assembly is held.
11. *Emergency Education*: In the emergency there are in sufficient facilities, equipments and staffs. Schoolteachers should secure the spot for educating, replenish the textbook, fill a shortage of teachers and make the temporary time schedule and the temporary class.

12. *Long-term Planning*: The disaster causes the delay of educating and the count of the absences. It is difficult to solve them for the short-term. Schoolteacher should prepare the long-term planning to solve them.
13. *Procedure for Filing a Change of Address*: In the emergency some schoolchildren lose their house or cannot live there. They should move to some other place and may procedure for changing addresses and schools.
14. *Procedure for Filing a Subsidy*: The government gives some subsidies to the schools and people that are damaged by the disaster. To get these subsidies schoolteachers should procedure for filing them.
15. *Night Watch*: In the emergency many people go in and out the school. To manage the school facilities some schoolteachers have to stay for twenty-four hours including night.
16. *Records of Emergency Activities*: Records of emergency activities is one of the important affairs to improve their future work.
17. *Emergency Medical Care*: The injured have to be provided medical care in school or be hurried to the hospital if they cannot be treated in school.
18. *Mental and Physical Healthcare*: After the disaster some schoolchildren, their guardians and teachers get severe physical and mental problems. They need to care for emotional and spiritual needs.
19. *Hygienic Management*: In the emergency the people and the facilities are not usual conditions. To keep the good health of people schoolteachers need to carry out through hygienic practices.
20. *Cleaning*: Many equipments and documents are scattered about on the floor caused by earthquake. To use the facilities again schoolteachers have to clean the school.
21. *Space Use Planning and Control*: Some activities need the spaces where the gas and water can be used, but the numbers of such rooms are limited in school. Space use planning and control are necessary.
22. *First-Aid Treatment of the facilities*: It takes a long time to recovery the facilities completely. Some facilities have to be used before complete recovering. Schoolteachers give the first aid to these facilities.
23. *Recovery of the Facilities*: The facilities have to be recovered completely for living in much the same way as before.
24. *Communication with Other Organizations*: The above affairs cannot be achieved without the corporations between schoolteachers and many other organizations. There are many overlaps between the communication activities and the other activities. The following section will describe further details about these corporations.
25. *Assistance for Managing the Evacuation Shelter*: If the evacuation shelter is open on school property, schoolteachers assist the activities for managing the evacuation shelter. The evacuation shelter management activities are independent of other schoolteachers' works and consist of many kinds of works. The independent section will describe further details about the whole activities of managing the evacuation shelter. Schoolteachers do only parts of these activities.

These individual activities can be classified by the kind of works to grasp quickly the big picture. They are identified as nine types of works; First reaction, Establishment of the management office, Collecting information, Education Planning, Other operations, Recovery of facilities and equipment, Healthcare, Assistance for managing the evacuation shelter and Communication with other organization. The relations between these assortments and activities can be seen in figure 2. This figure is expected to help to grasp the whole activities of schoolteachers before beginning their own activities.

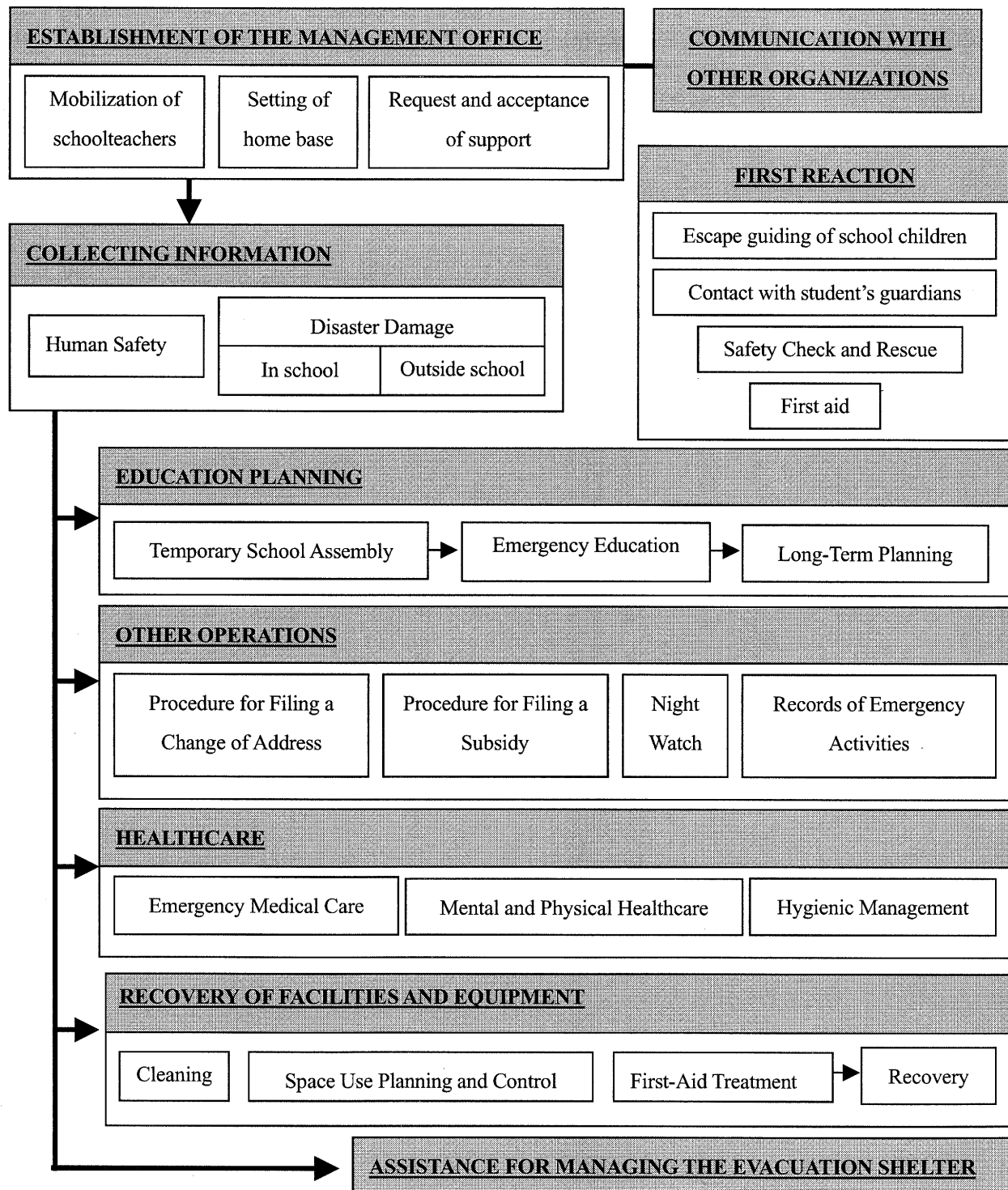


Figure 2 The whole model of schoolteachers' activities

3.2 The Model of the Communications with Other Organizations

To accomplish schoolteachers' activities the corporations with many organizations are necessary. For example, the injured have to be hurried to the hospital if they cannot be treated in school. However, there are little documents described about the complete information substances to be exchanged with other organization. In this study the relations between the school and other organizations are estimated

from the schoolteachers' activities shown in the preceding section. Figure 3 shows the relations between the school and some organizations such as the board of education, the evacuation shelter that is open on school property, the disaster countermeasure office, schoolchildren, student's guardians, other schools, mass media, hospitals, school lunch services, construction company and public health center. However there are still many unclear contents. It is not clear to communicate with some agencies concerned with school's activities directly or through the board of education. The information substances to be exchanged are also hardly revealed. Only the parts of the information substances to be exchanged between the school and the board of education and between the evacuation shelter and the disaster countermeasure office can be seen from the ward official activity manual, but the time to exchange the information and each information substances are not clear. To understand the complete communication activities the cooperating organizations, the information substances and the time to exchange such information should be revealed.

Above all, three communications are considered to be particularly important. The communications with the school should be considered with a focus on these three connections.

1. *Instruction of the Board of Education*: In the emergency the board of education instructs schools to conduct the report about student safety, the disaster damage, the shortage of student supplies, emergency education plan and recovery of school facilities. If schoolteachers do not have their own activity manual, they may act according to the instruction of the board of education. The instruction substances of the board of education have a great influence on the schoolteachers' activities.
2. *Educating Schoolchildren*: The most important work of schoolteachers is educating schoolchildren. In the emergency schoolteachers should explain to schoolchildren about their actual conditions, the important reminders in the emergency and the plan for their future. Schoolchildren who damage the physical and mental health have to be treated carefully for a prolonged period. The delay of educating and the count of the absences have to be restored by the long-term planning.
3. *Each Other's Request between the School and the Evacuation Shelter*: If the evacuation is open on school property, one facility have to be used by two organizations. Spaces and lifelines used by teachers and students are restricted, and schoolteachers have to make students stop fussing.

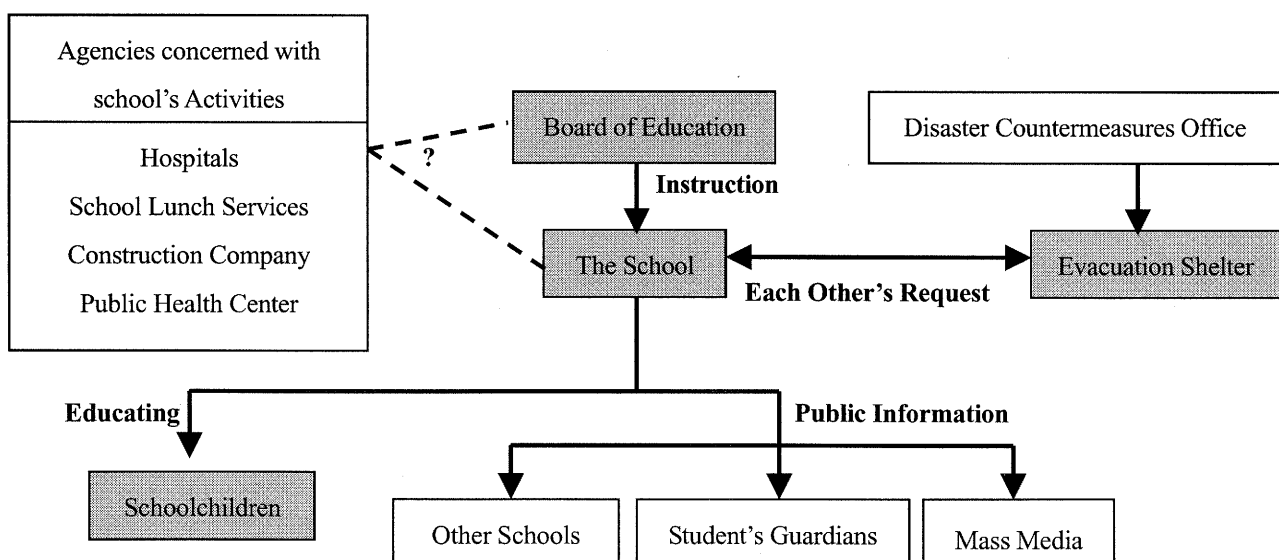


Figure 3 The Model of the Communications with Other Organizations

3.3 The Model of the Managing Activities in the Evacuation Shelters

Some schools, wards and municipals created the evacuation shelter management manual. However in these manuals the activities are classified in unit associations, and some activities overlap in several associations. To grasp quickly the big picture, the classification by works is expected. The management activities are identified as seven types of works; Opening of evacuation shelter, Setting of the evacuation life management office, Managing of home base, Life environmental consideration, Communication with refugees, Feeding service and supplies, Healthcare,

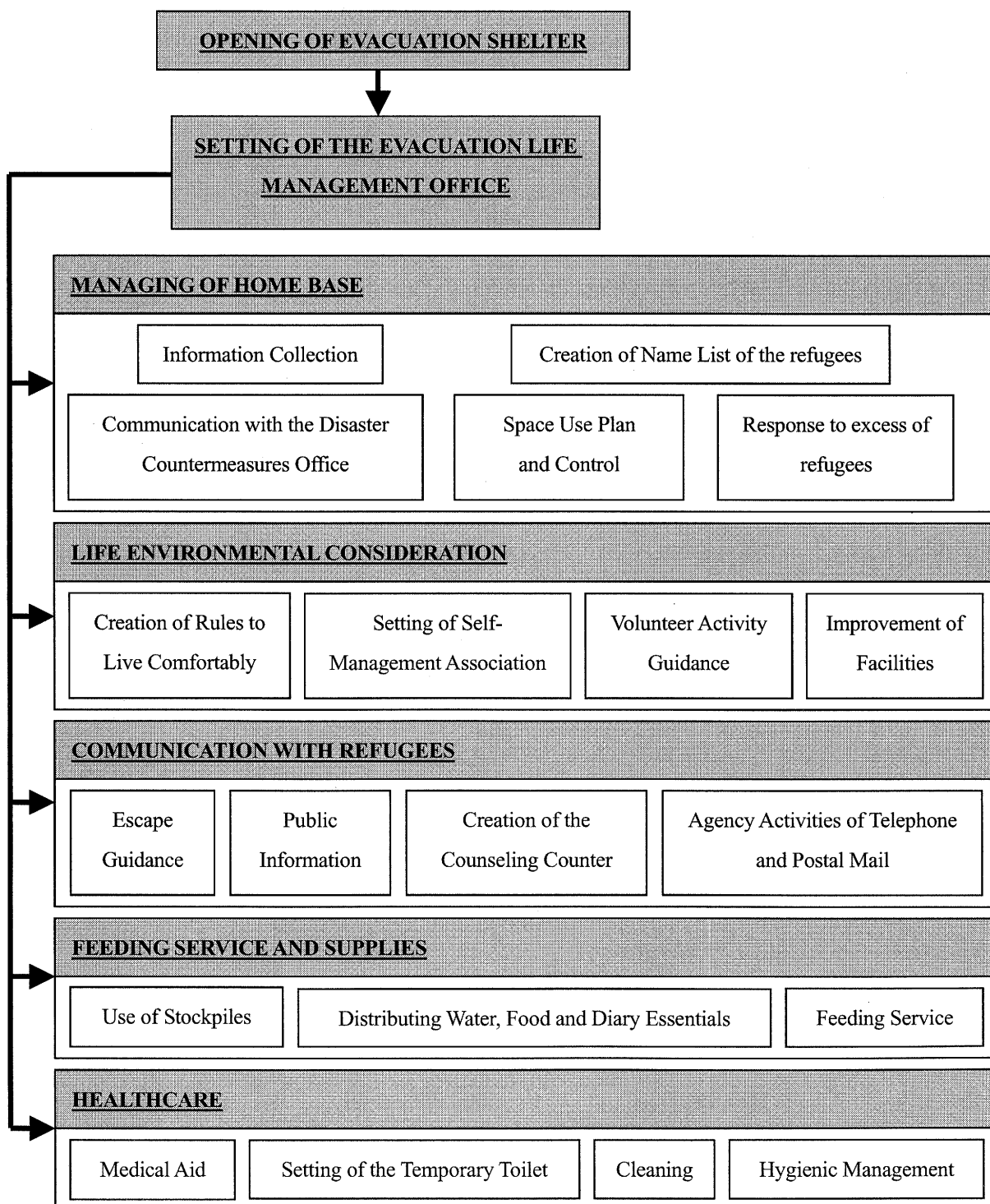


Figure 4 The Model of the Managing Activities in the Evacuation Shelters

Communication with refugees, Feeding service and supplies and Healthcare. The relations between these assortments and activities can be seen in figure 4. Schoolteachers assist parts of these works. These activities are considered to divide from the educational activities, so that it is easy to grasp the whole activities of schoolteachers.

4. CONCLUSIONS

The whole model of schoolteachers' activities, the individual model of the communications with other organizations and the independent model of the evacuation shelter management activities were proposed. These models will be helpful to grasp the whole activities and take appropriate actions. However some detail contents of these models are not clear such as the information substances to be exchanged between the school and other organizations, the time to do each activity and the method to accomplish each activity. These unknown contents will be cleared up in our future work.

References:

- Tahara, M. (2004), "A study on municipalities' emergency responses conducted at the 2000 Tottoriken-Seibu earthquake and their modeling," *Doctoral thesis in Tokyo Institute of Technology*
- The Ministry of Education, Culture, Sports, Science and Technology (2004), "about the extent of the damage caused by the 2004 Mid Niigata Prefecture Earthquake," http://www.mext.go.jp/b_menu/houdou/16/10/04102901.htm
- Kobe city board of education (1996), "The great Hanshin earthquake: Steps toward recovery and creation of education in Kobe," Kobe city sports education public corporation
- Physical education and health division in Hyogo prefecture board of education (1998), "The project report creating the model area about the disaster education," 8-25.
- Taito ward in Tokyo (1997), "The Taito ward official activity manual"

QUESTIONNAIRE SURVEY ON DRIVERS' REACTION IN THE 2003 SANRIKU-MINAMI EARTHQUAKE

Y. Maruyama¹⁾ and F. Yamazaki²⁾

1) *Postdoctoral Research Fellow, Center for Urban Earthquake Engineering, Tokyo Institute of Technology, Japan*

2) *Professor, Dept. of Urban Environment Systems, Chiba University, Japan*

maruyama@cv.titech.ac.jp, yamazaki@tu.chiba-u.ac.jp

Abstract: The relationship between the seismic intensity and the reactions of expressways drivers were investigated based on the questionnaire survey conducted by Japan Highway Public Corporation (JH) after the Sanriku-Minami earthquake, which occurred on May 26, 2003. The distribution of seismic intensity was estimated using 132 earthquake records at K-NET stations and 52 records at JH stations. Kriging technique was employed to obtain the spatial distribution of seismic intensities. The results of the questionnaire survey were evaluated with respect to the estimated seismic intensity along the expressways. Only 40 % of drivers were aware of the earthquake in the areas where the Japan Meteorological Agency (JMA) seismic intensity is smaller than 4.0. On the contrary, more than 80 % of drivers recognized the earthquake in the areas where the JMA seismic intensity is larger than 4.5. The abnormal vibration of the vehicle was indicated as the reason why the drivers recognized the earthquake. Hence, the seismic motion is considered to affect safe and stable driving.

1. INTRODUCTION

The number of automobiles in Japan is increasing year by year, and it is larger than 77 million including motorcycles (Japan Automobile Federation, 2004). It is supposed that many people are driving just when a large earthquake occurs. As the demand for highway traffic increases, safety requirements for highways significantly increase even at the time of an earthquake (Yamazaki, 2001). Therefore, it is important to realize the response characteristics of automobile drivers during an earthquake.

Kawashima *et al.* (1989) have conducted the questionnaire survey for the drivers who were driving during earthquakes. The survey revealed that some drivers mistakenly interpreted the earthquake as a tire blowout, and they could not control the steering wheel properly due to abnormal vibration. The presented authors have conducted the driving simulator experiments to reveal the drivers' response characteristics when they are subjected to strong shaking (Maruyama and Yamazaki, 2004). Based on the results, the drivers protrude their running lane. Hence, they might be involved in an accident because of strong shaking.

Japan Highway Public Corporation (JH) has conducted the questionnaire survey to investigate drivers' behaviors during an earthquake, which occurred on May 26, 2003. In order to reveal the relationships between seismic intensity and drivers' reactions, the results of the questionnaire survey conducted by JH are compared with the seismic indices, which are estimated based on Kriging technique (Cressie, 1993) using 184 ground motion records.

2. ESTIMATION OF THE DISTRIBUTION OF SEISMIC INDICES BASED ON KRIGING TECHNIQUE

Kriging technique, a method of stochastic interpolation, is employed to estimate the spatial distribution of ground motion indices from recorded values. In Kriging technique, observed values are realized at the observation points. Between the observation points, stochastic interpolation consisting of the trend (mean) and random components gives an estimation of the spatial distribution (Yamazaki *et al.*, 2000; Shabestari *et al.*, 2004). In this study, 132 ground motion records at K-NET seismic observation stations, which were deployed by National Research Institute for Earth Science and Disaster Prevention, and 52 ground motions recorded at JH seismic observation stations (Maruyama *et al.*, 2000) are used for the estimation of the spatial distribution of the peak ground acceleration (PGA) and the JMA seismic intensity (I).

Since the earthquake motion on the ground surface is affected by amplification characteristics of subsurface layers, the interpolation should be carried out at the (outcrop) base. The amplification ratios estimated from attenuation relationships (Shabestari and Yamazaki, 2000) are used for the seismic indices of K-NET records, and those estimated from the digital national land information of Japan (Yamazaki *et al.*, 1999) are used for JH records. Then, the recorded seismic indices at the ground surface (PGA_{si} and I_{si}) are converted to those at the base by Eq. (1) and (2).

$$PGA_{bi} = PGA_{si} / ARA_i \quad (1)$$

$$I_{bi} = I_{si} - ARI_i \quad (2)$$

where PGA_{bi} and I_{bi} are the PGA and JMA seismic intensity at the base, respectively. ARA_i and ARI_i are the amplification ratios for PGA and JMA seismic intensity, respectively.

Based on the seismic indices at the base, the attenuation relations are constructed. These attenuation relations are used as the trend component of Kriging. The relations obtained in this study are

$$\log_{10} PGA = 4.768 - \log_{10} r - 0.0050r \quad (3)$$

$$I = 9.014 - 1.89 \log_{10} r - 0.0085r \quad (4)$$

where r is the shortest distance (km) to the fault rupture. Figure 1 shows the attenuation relationships of PGA and JMA seismic intensity at the base.

In the Kriging technique, a spatial auto-correlation function should be assigned. An exponential function is employed in this study. The correlation distance, which controls the influence of observed data, is assumed as 5.0 km (Shabestari *et al.*, 2004). Kriging technique is employed for the residuals between the converted observed values at the base and the trend component. Simple Kriging is carried out assuming the residual distributions as a zero-mean Gaussian stochastic field. Adding the trend component to the obtained random component, the strong motion indices at the base are estimated. Multiplying the amplification factors to the obtained values at the base, the spatial distribution at the ground surface is finally obtained (Eq. (1) and (2)). The validity of this estimation method is discussed by Shabestari *et al.* (2004).

3. RELATIONSHIP BETWEEN SEISMIC INTENSITY AND REACTIONS OF DRIVERS

3.1 Distribution of Seismic Intensity along the Expressway

Figure 2 shows the estimated spatial distribution of JMA seismic intensity. To reveal the relationship between the seismic indices and the reactions of expressway drivers, the distribution of

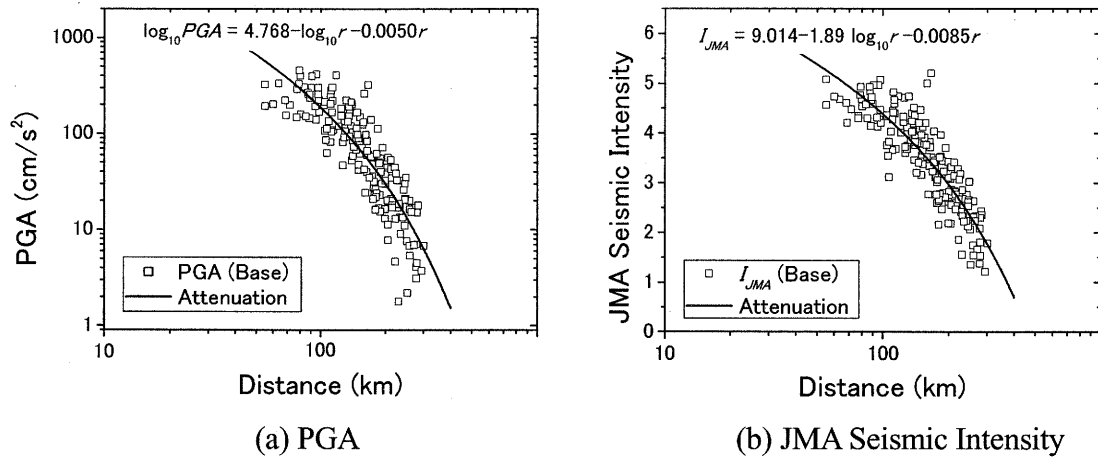


Figure 1 Attenuation Relationships of PGA and JMA Seismic Intensity at the Base in the 2003 Sanriku-Minami Earthquake

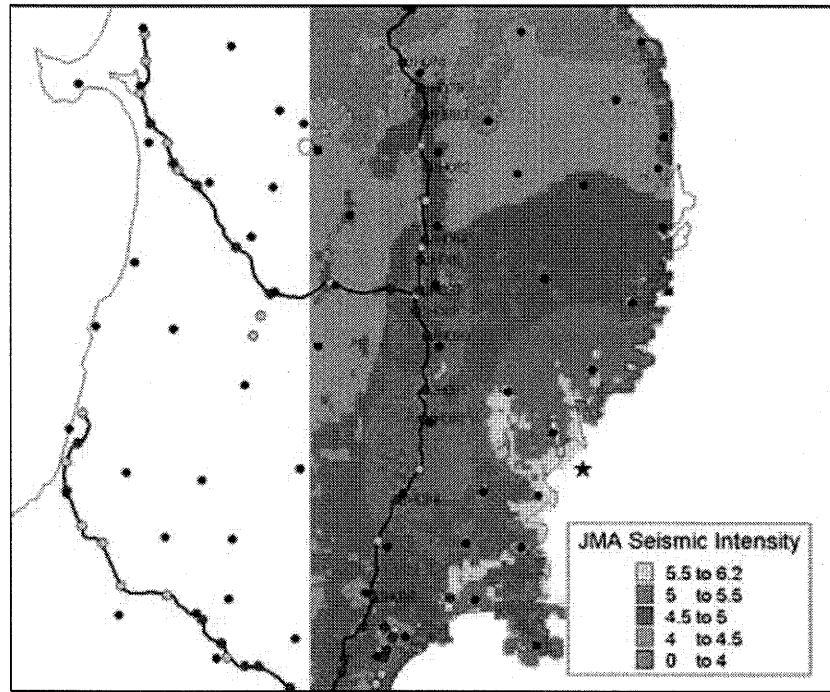


Figure 2 Estimated Distribution of JMA Seismic Intensity on Ground Surface

seismic intensity along the expressway is necessary. The estimated seismic indices along the expressways are extracted as shown in Fig. 3. It should be noted that the spatial distribution is estimated in the entire Tohoku district, however, in Fig. 2 and Fig. 3, only a part of the obtained results is illustrated.

According to the questionnaire survey conducted by JH, the expressway section (between the adjacent interchanges) where the responders were driving during the earthquake can be identified. The seismic indices between the adjacent interchanges are calculated as the weighted average by Eq. (5).

$$\bar{X} = \sum x_i r_i / \sum r_i \quad (5)$$

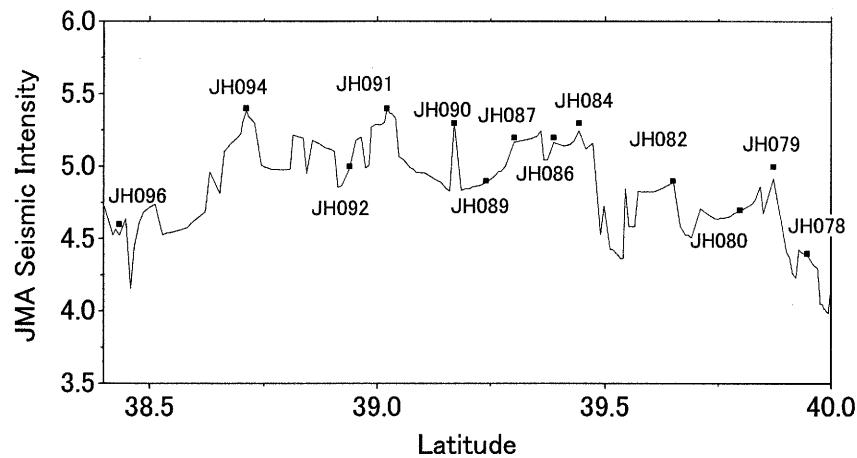


Figure 3 Estimated Distribution of JMA Seismic Intensity along the Expressway

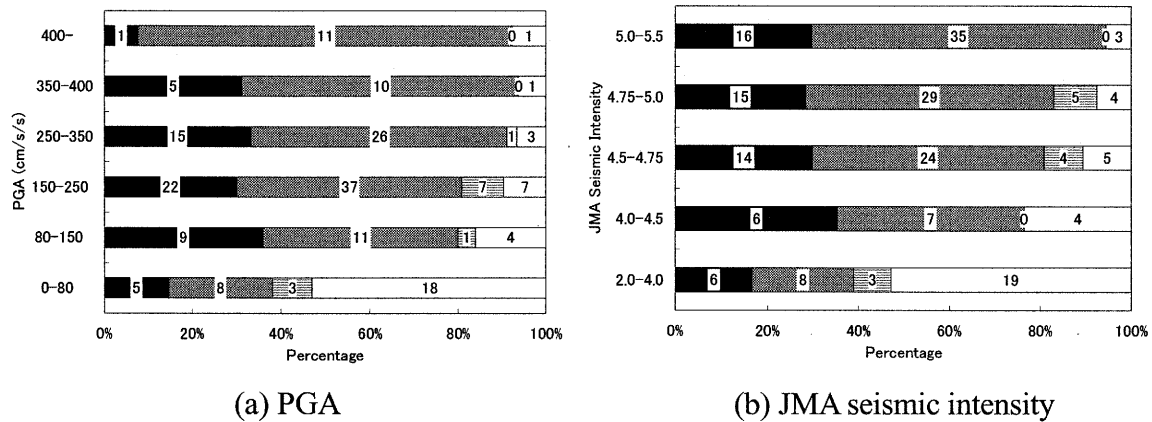


Figure 4 Drivers' Degree of Recognition of Earthquake Occurrence

where x_i is the estimated seismic index at a point on the expressway, and r_i is the representative length of x_i . \bar{X} is the weighted average of the estimated seismic index.

3.2 Questionnaire Survey on Drivers' Reactions during Earthquake

JH has conducted the questionnaire survey for drivers in the 2003 Sanriku-Minami earthquake. In total, 206 answers were collected (ratio of respondents is 1 %). In the survey, the age of the responder, driver's license issued period, type of the vehicle, the driving section of the expressway when the earthquake occurred and so forth were requested to answer.

3.3 Relationship between Seismic Intensity and Drivers' Response

Figure 4 shows the relationship between the estimated PGA and the driver's degree of recognition of earthquake occurrence, and the relationship between the estimated JMA seismic intensity and the degree of recognition. As PGA and JMA seismic intensity become larger, more drivers recognized the earthquake occurrence. Only 40 % of drivers were aware of the earthquake in the areas where the JMA

seismic intensity is smaller than 4.0. On the contrary, more than 80 % of drivers recognized the earthquake in the areas where the JMA seismic intensity is larger than or equal to 4.5.

Figure 5 shows the relationship between the type of the vehicle and the degree of earthquake recognition. Note that the results of the drivers in the area where the JMA seismic intensity is larger than or equal to 4.5 are shown in Fig. 6. As the size of the vehicle becomes larger, less drivers recognized the earthquake occurrence. It is considered that the seismic motion affects the moving stability severely for a large-sized vehicle because the center of gravity is higher. However, the result was found to be opposite. Generally speaking, the vibration of an ordinary moving vehicle is large for large-sized vehicles, and hence, less drivers may feel the seismically induced vibrations. To draw a solid conclusion, more investigations are necessary in this viewpoint.

Figure 6 shows the reason why the driver recognized the earthquake occurrence with respect to the JMA seismic intensity. More than half of the respondents indicate the abnormal vibration of the vehicle as the reason for recognition. About 20 % of drivers felt the earthquake because the surrounding facilities, such as electric boards, and houses along the expressway were oscillating. The clear trend of the reason of recognition with respect to the JMA seismic intensity is not seen in the figure.

Figure 7 shows the relationship between the JMA seismic intensity and the behaviors of drivers after recognizing the earthquake. About 40 % of drivers in the area where the JMA seismic intensity is smaller than 4.0 kept on driving as usual even though they recognized the earthquake occurrence. As the JMA seismic intensity becomes larger, less drivers kept on going. Only 10 % of drivers kept on driving if the JMA seismic intensity was larger than or equal to 4.75. When the JMA seismic intensity is in the range of 4.5-4.75, 20% of drivers stopped the vehicle in the road shoulder. As the JMA seismic intensity becomes larger, that proportion becomes larger. As a whole, more than 50 % of drivers reduced the vehicle speed gradually, and some drivers stopped in the road shoulder when the JMA seismic intensity exceeds 4.0. It should be noted that three drivers stopped in their running lane after they recognized the earthquake.

4. CONCLUSIONS

In this study, the relationship between the seismic intensity and the reactions of expressway drivers were investigated based on the questionnaire survey conducted by Japan Highway Public Corporation

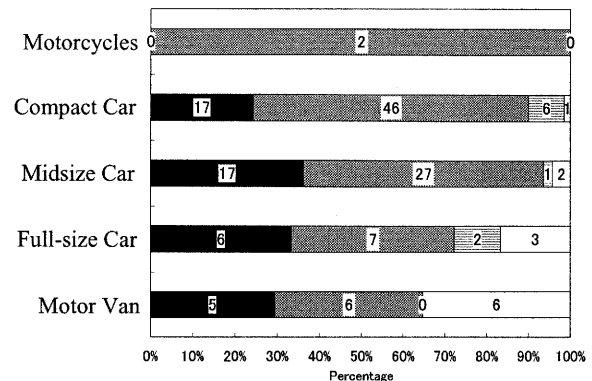


Figure 5 Relationship between the Type of the Vehicle and the Degree of Recognition of the Earthquake in the Area where the JMA Seismic Intensity is Larger than 4.5 (The Legend of the Figure is the Same as Fig. 4)

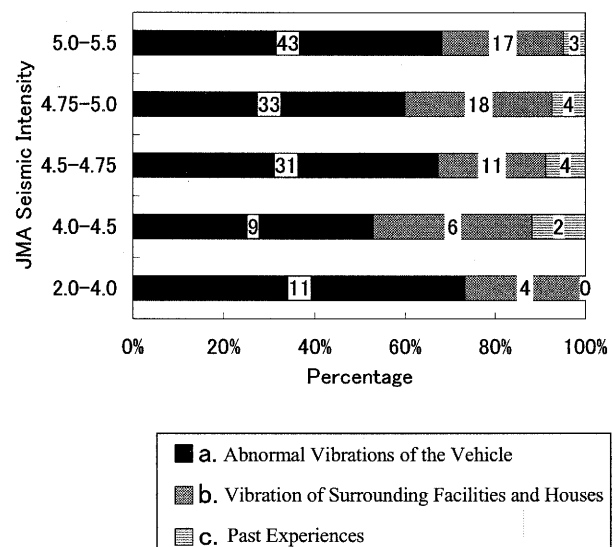


Figure 6 Reason of Recognition of Earthquake Occurrence

(JH) after the 2003 Sanriku-Minami earthquake.

The spatial distribution of seismic intensity was estimated using the seismic records at 132 K-NET stations and 52 JH stations which were deployed along the expressways. The results of the questionnaire survey were evaluated with respect to the estimated peak ground acceleration and the Japan Meteorological Agency (JMA) seismic intensity. Only 40 % of drivers were aware of the earthquake in the areas where the JMA seismic intensity is smaller than 4.0. On the contrary, more than 80 % of drivers recognized the earthquake in the areas where the JMA seismic intensity is larger than 4.0.

The abnormal vibration of the vehicle was indicated as the main reason for the recognition of the earthquake occurrence. This finding suggests that the strong ground motion will affect safe and stable driving. In this regard, it is important to reveal the effects of seismic motion to moving vehicles quantitatively. When the JMA seismic intensity is larger than or equal to 4.5, 20 % of drivers stopped in the road shoulder because they strongly felt the earthquake. If the traffic is heavy at the time of strong shaking, there may be difficulties in stopping safely in the road shoulder.

In this questionnaire survey, the relationship between the type of the vehicle and the effects of seismic motion is not so clear. The driving condition during an earthquake should be also considered for a further investigation. To draw a solid conclusion, it is necessary to accumulate this kind of questionnaire surveys.

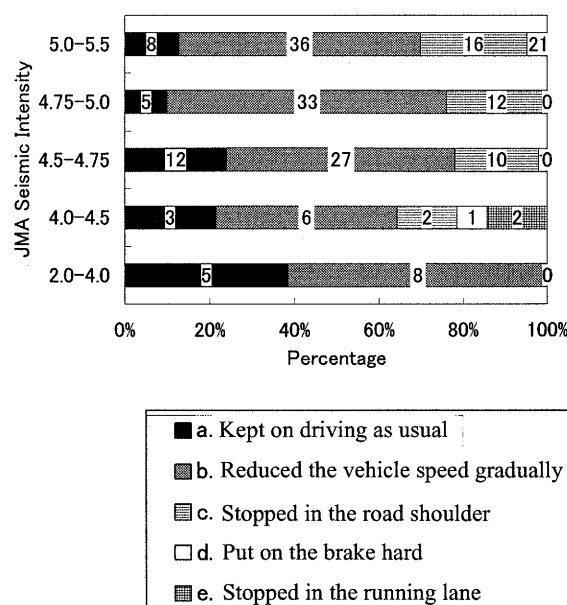


Figure 7 Relationship between the JMA seismic intensity and the responses of drivers after the recognition of earthquake

Acknowledgements:

The authors appreciate Japan Highway Public Corporation for providing the data of the questionnaire survey.

References:

- Cressie, N. (1993), "Statistics for Spatial Data," Wiley.
- Japan Automobile Federation. (2004), "http://www.jaf.or.jp/data/carnum.htm" (in Japanese).
- Kawashima, K., Sugita, H. and Kanoh, T. (1989), "Effect of Earthquake on Driving of Vehicle based on Questionnaire Survey," *Structural Eng./Earthquake Eng.*, Japan Society of Civil Engineers, **6**, 405-412.
- Maruyama, Y., Yamazaki, F. and Hamada, T. (2000), "Microtremor Measurements for the Estimation of Seismic Motion along the Expressways," *Proceedings of 6th International Conference on Seismic Zonation*, **2**, 1361-1366.
- Maruyama, Y. and Yamazaki, F. (2004), "Fundamental Study on the Response Characteristics of Drivers during an Earthquake based on Driving Simulator Experiments," *Earthquake Engineering and Structural Dynamics*, **33**, 775-792.
- Shabestari, K.T. and Yamazaki, F. (2000) "Attenuation Relation of Response Spectra in Japan Considering Site-Specific Term," *Proceedings of 12th World Conference on Earthquake Engineering*, CD-ROM, 8p.
- Shabestari K.T., Yamazaki, F., Saita, J. and Matsuoka, M. (2004), "Estimation of the Spatial Distribution of Ground Motion Parameters for Two Recent Earthquakes in Japan," *Journal of Tectonophysics*, **390**(1-4), 193-204.
- Yamazaki, F., Wakamatsu, K., Onishi, J. and Yamauchi, H. (1999) "Relationship between Geomorphological Classification and Soil Amplification Ratio Based on JMA Strong Motion Records," *Bulletin of ERS*, Institute of Industrial Science, University of Tokyo, **32**, 17-33.
- Yamazaki, F., Motomura, H. and Hamada, T. (2000), "Damage Assessment of Expressway Networks in Japan based on Seismic Monitoring," *Proceedings of 12th World Conference on Earthquake Engineering*, CD-ROM, 8p.
- Yamazaki, F. (2001), "Seismic Monitoring and Early Damage Assessment Systems in Japan," *Progress in Structural Engineering and Materials*, **3**, 66-75.

PERCEPTION OF EARTHQUAKE HAZARD BY URBAN CHILDREN

M. Katayama¹⁾, R. Ohno²⁾, M. Soeda³⁾, and S. Nara⁴⁾

1) *Research Fellow, Center for Urban Earthquake Engineering, Tokyo Institute of Technology, Japan*

2) *Professor, Department of Built Environment, Tokyo Institute of Technology, Japan*

3) *Assistant Professor, Department of Built Environment, Tokyo Institute of Technology, Japan*

4) *Master Student, Department of Built Environment, Tokyo Institute of Technology, Japan*

katamegu@enveng.titech.ac.jp, rohno@n.cc.titech.ac.jp, msoeda@n.cc.titech.ac.jp, snara@enveng.titech.ac.jp

Abstract: The purpose of this study is to investigate how children perceive earthquake hazard, especially focusing on the influence of their image toward earthquakes, knowledge of activities that can reduce the damages. The survey was conducted with primary school children and their parents. As results following influential factors are revealed. Age: Children tend to perceive risks and damages of earthquake hazards more serious than adults, however they are more optimistic about confidence in own behavior during earthquake and satisfied with their parents' preparedness at their home. Girls pay more attention to the physical damage while adult females concern more about the sufferers' post-disaster living conditions. Gender: Girls have lesser confidence in own behavior during earthquake, and evaluate their parents' preparedness lower than boys. Housing structure: People living in wooden houses anticipate the damage severer than those in other types of houses. Area of living: Adults in Akashi city anticipate the probability of a great earthquake occurrence lower than those in Yokohama city, and this may suggest that an earthquake experience has an effect to pay less attention to its occurrence. Communication at home: Children who do not talk with their parents about disaster prevention seem to feel helpless and have passive attitude to the earthquake hazard.

1. INTRODUCTION

Since Japan suffers so many kinds of natural disasters frequently, it can be said that Japanese people livings side-by-side with these risks. Among them, a high probability of earthquake occurrence has been pointed out recently by the governmental expert committee, which will bring a great damage. Each resident is therefore required to know more about the risk and to take effective prevention countermeasures.

Considering how people establish their attitudes toward hazards, they first acquire fragmental information about the past calamity through stories of personal experiences of sufferers and visual images obtained by the mass media. They farther acquire technical knowledge, and then they begin to perceive the risk properly and take effective countermeasures. With regards to the perception of such risks, adults can manage various information and lead to a comprehensive judgment and they to proper activities. However, children who have inferior information gathering capabilities and comprehension cannot be expected to make such judgments or take actions. Kiser(1993) shows that one prediction of a quake that did not happen produced mild but widespread stress disorders in children. This result suggests that children can not cope with uncertainty and anticipation properly and are easily influenced by the media.

Most of studies on children's psychological response to the disasters deal with the shocks after experiencing a catastrophe. Recent studies in Japan mainly focus on post-traumatic stress disorder (PTSD) after experiencing the Great Hanshin-Awaji Earthquake occurred in 1995. On the other hand, little has been studied on the perception of earthquake hazard by children who have never experienced. Masuda et al (1988) survey consciousness of earthquake preparedness of junior high school students

in some region in Japan and suggest a method to evaluate the effects of earthquake education. In big cities, many children commute alone to distant schools by public transport. Considering the possibility that they might experience a disaster when they are alone, it is important to know about the perception of earthquake hazard by children and give them the knowledge to cope with the situation accordingly.

The purpose of this study is to investigate how children perceive earthquake hazard, especially focusing on the influence of their image toward earthquakes, knowledge of activities that can reduce the damages. The perception of the children's parents and communications about disaster prevention at their home are also investigated.

2. RESEARCH METHOD

This research aims to clarify the children's perception of the earthquake hazard. Gifford (2002) shows that attitudes toward environmental hazards are rooted in such antecedent factors as individual differences (gender, age, education, and personality), past experience with disasters, proximity to the potential disaster site, and exposure to media report. In this study, we classified these factors into three categories (individual factors, environmental factors, and information) and made a basic research framework shown in Fig. 1. In this model, disaster preventing countermeasures is also hypothesized to relate with the perception of earthquake hazard. A questionnaire was designed to investigate the influence of these factors on how people perceive earthquake hazard.

In order to explore the geographical differences, a survey was conducted at the primary schools in Yokohama city and Akashi city. Yokohama city is included in the area where earthquake has been pointed out with a high probability recently. Akashi city, next to Kobe city, experienced the Great Hanshin Awaji Earthquake in 1995. The surveys for the children (fourth and sixth grades) were conducted by researchers and class teachers at their class rooms. As for the parents, the questionnaires were taken to home by children and collected after they were filled in. The outline of the survey is shown in Table 1.

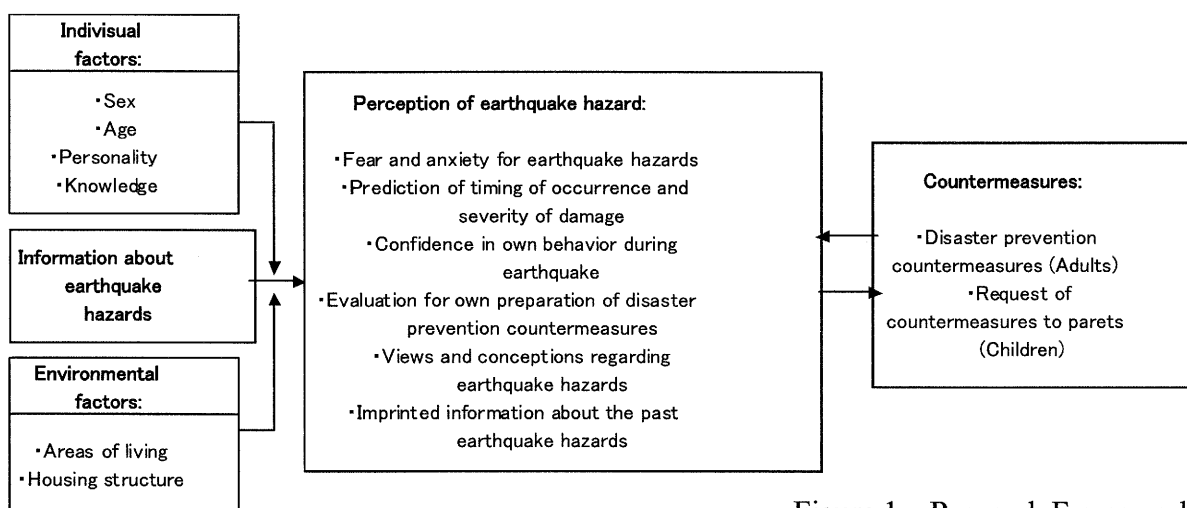


Figure 1 Research Framework

Table 1 Outline of the survey

Area	Respondents			Housing structure	
	Number of children		Number of parents	Wooden	Other types
	4th grade	6th grade			
Yokohama city	146 (Boy:61/Girl:85)	126 (Boy:68/Girl:58)	197 (Mother:142)	43%	57%
Akashi city	76 (Boy:32/Girl:44)	71 (Boy:33/Girl:38)	127 (Mother:103)	38%	62%
Total	419 (Boy:194/Girl:225)		324 (Mother:245)		

3. COMPARISON OF EARTHQUAKE FEAR WITH OTHER DISASTERS

3.1 Disaster fear ranking

In order to know the fear level of earthquakes, it was compared with that of other disasters (war, traffic accident, fire and flood). The fear of earthquakes was expected to rank high as it is difficult to prevent or predict the occurrence, however, both adults and children chose war as the most fearful event, accounting for more than 80%, and earthquakes remained as second (Fig. 2).

3.2 Reasons for the fear

It was revealed that the reasons for the fear were different according to the kind of disaster and respondents' age (Fig. 3). More than 40% among adults who chose war as the most fearful answered that "because it is unlikely that I can prevent its occurrence", showing "helpless" (lack of sense of control). More than 70% of the children, on the other hand, chose "because I or my family may die if it happens", showing their concern about physical damage. However, among adults and children who chose earthquake as the most fearful, half of them in each group chose the reason "because it is unlikely to be able to predict the occurrence". This means that "the unpredictability of the timing of occurrence" is the reason to fear earthquakes, regardless of the age of the respondents.

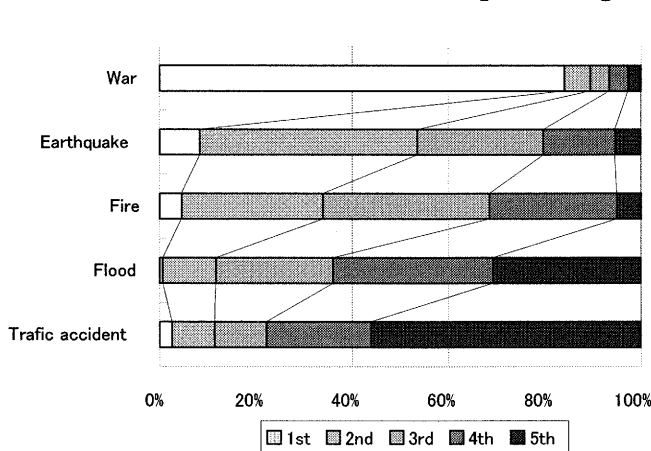


Figure 2 Disaster fear ranking

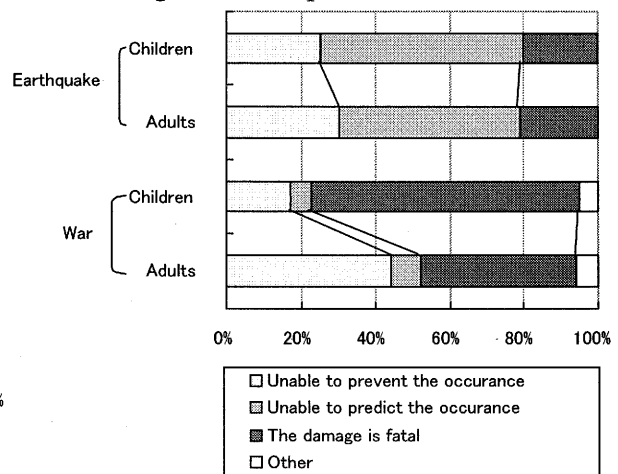


Figure 3 Reasons of the fear

4. IMPRINTED INFORMATION OF THE RECENT EARTHQUAKE DISASTER

What aspect of earthquake disasters imprints children was investigated. Adults and children were expected to receive different aspect of disaster such as physical damage, loss of human life and sufferers' post-disaster living conditions. The contents of news related with Chuetsu Earthquake which happened two months prior to this survey were used. Respondents were asked to choose the most imprinted aspect among items shown in the bottom of Figure 4. The result, shown in the top of the figure, revealed that the influence of age is seen among adult females and

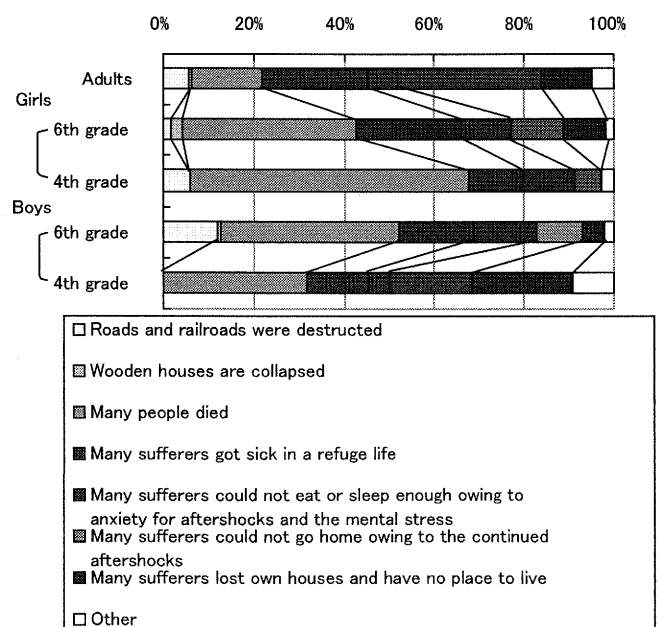


Figure 4 The most imprinted aspect of the news related with Chuetsu Earthquake

schoolgirls, showing the tendency to pay attention to the sufferers' living condition over physical damage as the age of the respondent becomes higher.

5. SOME INFLUENTIAL FACTORS OF PERCEPTION OF EARTHQUAKE HAZARD

5.1 Prediction of timing of occurrence

Concerning the prediction of the timing of occurrence, respondents were asked "When in the future do you think an earthquake of more than M7 will attack your area". As a result children expect the earthquake to occur in the relatively near future than adults (Fig. 5). Comparing the adults' response, those in Akashi city anticipate the probability lower than those in Yokohama city, with 20% more adults in Akashi city anticipate "It will not happen in my lifetime". Since Akashi city had less damage than neighboring Kobe city, it seems that the earthquake experience does not necessarily raise the concern of its risk but in fact it has an opposite effect to pay less attention to it.

5.2 Prediction of the severity of damage

As for the severity of damage, respondents were asked "in case a big earthquake of more than M7 happens in the late afternoon on a weekday while you are at home, how do you estimate the damage". Concerning the damage to the respondent himself/herself, children anticipate the damage severer than adults, and likewise those living in wooden houses anticipate it severer than those in other types of houses (Fig. 6). This tendency remains the same for the damage to the family members and their own house. Regarding the anxiety for family dispersion, more children answered that they would be able to meet their family soon after the earthquake.

5.3 Confidence in own behavior during earthquake

Regarding the level of confidence in own behavior during an earthquake, more children than adults answered that they are "confident" or "confident to some extent" (Fig. 7). A tendency was also observed that more schoolboys than schoolgirls answered they were "confident".

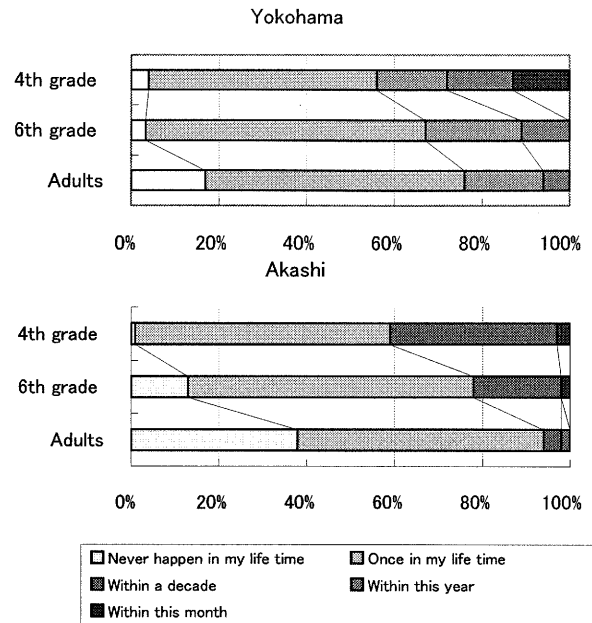


Figure 5 Prediction of timing of occurrence

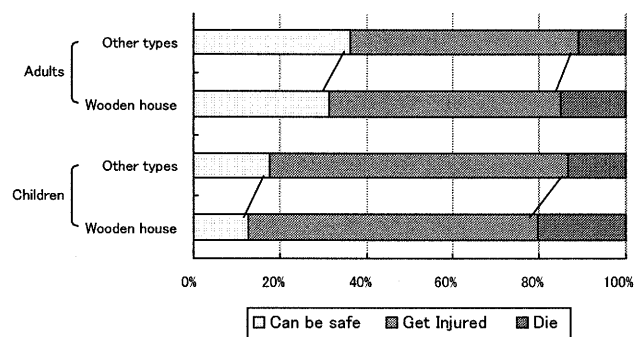


Figure 6 Prediction of own damage

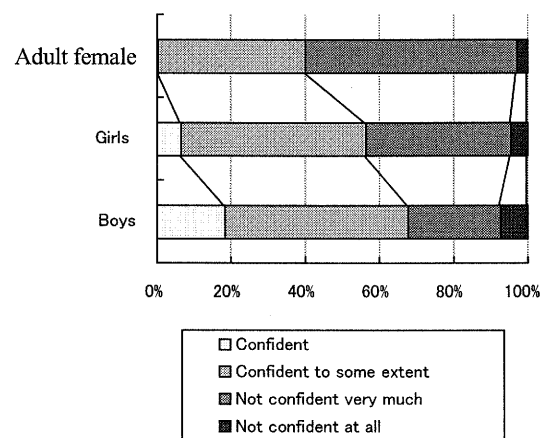


Figure 7 Confidence in own behavior during earthquake

It was often said that the more knowledge about countermeasure actions the person possesses, the more confidence that person has. However, this is not confirmed in the present survey. As for the true and false of the knowledge concerning countermeasures, no differences were observed without regard to the age, sex or the area of residency (Table 2). The items which are least acquired correctly were “to turn off fire of heaters and cookers before the tremor ends”, “to take refuge in a high-rise building nearby”, and “to get out from underground space as soon as possible”.

5.4 Preparedness for the earthquake disaster and its self-evaluation

It was observed that the person who takes more disaster countermeasures tends to evaluate own preparation higher. As shown in Table 3, among the measures taken relatively often are “to keep water and food in stock” and “to discuss the measures to be taken among the family”, both recording around 50%. The measure with the lowest execution rate is “to have the house examined by a specialist against earthquake resistance”, which accounted for 13%.

As for the evaluation of disaster countermeasures taken at own home, more adults than children gave negative answers that it is “insufficient” or “rather insufficient” (Fig. 8). This tendency is supposed to refer that the social responsibility makes them evaluate own actions severer. Moreover it is also seen between the genders of the children: schoolgirls tend to be more negative than schoolboys.

5.5 Views and conceptions regarding earthquake hazard

For the views and conceptions regarding earthquake disaster, respondents were asked the following four items. Q1: “I do not want an earthquake to occur at all because it is so frightful.” Q2: “As long as there is no serious damage, it would be fun to have earthquakes occasionally.” Q3: “There is no need to worry about earthquakes if sufficient preparations have been made.” Q4: “As earthquakes are natural phenomena, they can not be helped if an earthquake causes major damage once in a while.” Respondents were asked to choose one of four grades ranging from “I agree” to “I do not agree” according to their views. The item

Table 2 Knowledge about countermeasure actions

Type of knowledge	Questions	Ratio of correct answer
Countermeasure actions at the moment of an earthquake	1 To go out of a house immediately	86%
	2 To get under a desk immediately	88%
	3 To turn off fire of heaters and cookers before the tremor ends	23%
	4 To crouch down close to a wall or fence when in outside	94%
	5 To take refuge in a high-rise building nearby	18%
	6 To get out as soon as possible if I am in underground	23%
Aftershock and secondary disasters	7 Once an earthquake shakes greatly, it may happen continuously in the same place	92%
	8 To take refuge to a high place when your are near the seashore because tsunami	95%
Actions that become troublesome to other people	9 To go to a nearby evacuation center by a car when you take refuge	88%
	10 To confirm the safety of your family member by a cellular phone	28%

Table 3 Disaster prevention countermeasures taken at home

Disaster prevention countermeasures	Ratio that adults have been taking	Ratio of recognition by children
1 To keep water and food in stock	54%	45%
2 To fix furniture in order for they to do not move or fall down	41%	30%
3 To take the house check by a specialist against earthquake resistance (Item for adults)	13%	
4 To make a contract of earthquake insurance (Item for adults)	20%	
5 To discuss the measures to be taken among the family	50%	32%
6 To check a nearest evacuation center and a place to meet among family	48%	30%

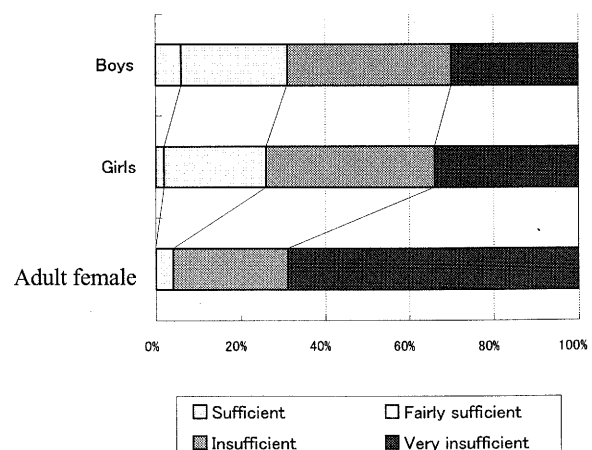


Figure 8 Self-evaluation for disaster prevention countermeasures

Q1 and Q2 relate to how seriously they perceive earthquake hazards, and the item Q3 and Q4 relate to how they believe the effectiveness of disaster prevention countermeasures.

As for Q1, 80% of both adults and children agree with it. For Q2 20% of children agree with it, while no adult agrees. This means that children tend to play down earthquake disasters. Figure 9 shows the results of Q3 and Q4. As for Q3, children tend to worry about earthquakes even when sufficient preparations are made and think the major damage is unavoidable. On the other hand adults worry as well, however they think the major damage is avoidable.

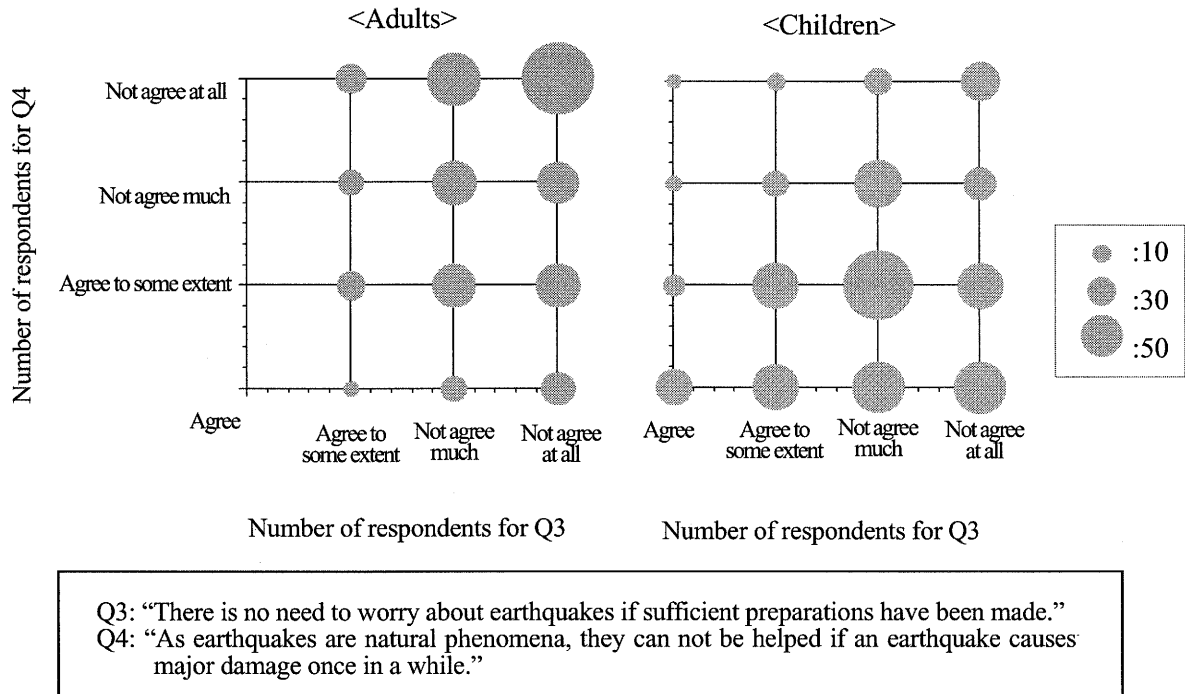


Figure 9 Children and parents' views regarding effectiveness of countermeasures for earthquake hazard

6. CHILDREN'S VIEWS OF EARTHQUAKES AND COMMUNICATION WITH PARENTS

Those who answered Q3 negatively and Q4 positively (their answers are plotted in the right bottom corner in the Fig. 9) as "I worry even when sufficient preparations are made, and think that major damage is unavoidable as earthquakes are a natural phenomena" are defined in this paper as a "Helpless type". They feel resigned and helpless about taking disaster countermeasures while feeling worried about the occurrence of earthquakes.

Focusing on children who belong to "Helpless type", we examined how these children recognize the countermeasures taken at their home. Table 4 shows the number of these children and other children who do not recognize the countermeasures taken at their home. Some countermeasures are not recognized by these children even if their parents have been taking.

Moreover we examined about the communication between children and their parents. Table 5 shows the number of children who did not get affirmative responses from their parents when they asked to take countermeasures. As a result significantly more children belong to "Helpless type" did not get the parents' responses. This refers the communication concerning disaster countermeasures between parents and children may be insufficient, and this may explain why these children have less sense of protection from earthquake disasters. They may think the countermeasures are helpless against earthquakes.

Table 4 Children's recognition about the countermeasures taken by parents at home

	To keep water and foods in stock		To fix furniture		To discuss the necessarily measures among the family		To check an evacuation center and a place to meet with family	
	Helpless type	Others	Helpless type	Others	Helpless type	Others	Helpless type	Others
Number of children	36	232	36	232	36	232	36	232
Number of children without recognition	12	43	6	66	19	77	11	57
Ratio	33%	19%	17%	28%	53%	33%	31%	25%
Significance level	*						*	

*: $p < 0.05$

Table 5 Parents' response to their children's request of taking countermeasures

	To request parents to take countermeasures	
	Helpless type	Others
Number of children	36	232
Number of children who could not get their parents' response	12	32
Ratio	33%	14%
Significance level	*	

*: $p < 0.05$

7. CONCLUSIONS

In this study, we investigated the characteristics of children's perception of the earthquake hazard, and examined influential factors as well as activities for disaster prevention countermeasures.

Children tend to perceive risks higher than adults in both probable period of a great earthquake occurrence and the damage seriousness. However they are more optimistic than adults about confidence in own behavior during earthquake and satisfied with their parents' preparedness at their home. Moreover although they recognize the efficiency of countermeasures a little more than adults, they show a passive attitude to the unavoidable damage than adults. The influence of age on how to receive mass media information was seen among adult females and schoolgirls. As their age becomes higher they pay more attention to the sufferers' post-disaster living conditions over physical damages.

With regard to the influence of gender, schoolgirls than schoolboys have lesser confidence in countermeasure actions under an earthquake, and evaluate their parents' preparedness of countermeasures more negatively.

As for the influence of environmental factors such as the housing structure and the area of living following results were revealed. People living in wooden houses anticipate damages severer than those in other types of houses. Adults in Akashi city anticipate the probability of a great earthquake lower than those in Yokohama city, and this may suggest that the earthquake experience has an effect to pay

less attention to its occurrence.

The communication about disaster mitigation measures and prevention activities at their home influences the children's perception of earthquake hazard. The children who do not communicate with their parents about disaster prevention at their home seem to feel helpless and have passive attitude to the earthquake disaster.

References:

- Kiser, L., Heston, J., Hickerson, S., Millsap, P., Nunn, W. and Pruitt, D. (1993), "Anticipatory Stress in Children and Adolescents", *American Journal of Psychiatry*, 150, 87-92
- Masuda H., Midorikawa, S., Miki C. and Ohmachi, T. (1988), "Formative Process of Consciousness of Earthquake Preparedness and Evaluation of Effects of Earthquake Education", *Journal of the Society of Civil Engineers*, 398, 359-365.
- Gifford R. (2002), "Environmental psychology: Principles and Practice -third edition", chapter 13; nature, Optimal Books, 391.

FUNDAMENTAL STUDY ON ESTABLISHMENT OF EVALUATION METHOD FOR SEISMIC RESISTANCE OF FLOOR FINISHING SYSTEM

Y. Yokoyama¹⁾, and T. Yokoi²⁾

1) *Assoc. Prof., Dep. of Architecture and Building Eng., Tokyo Institute of Technology, Japan*

2) *21st Century COE Researcher, Graduate School, Tokyo Institute of Technology, Japan*

tyokoi@mail.arch.titech.ac.jp

Abstract: Various floor construction methods are developed and supplied, and sometimes non-structural materials are constructed on floor groundwork. At an earthquake, there is a possibility that safety is ruined by breakage of non-structural materials or a tumble of furniture, even if a structure is not ruined. So, it is necessary to consider groundwork surface, interlayers, upper finish materials, furniture, etc. to be additionally a floor finishing system, and to evaluate seismic resistance as the whole. The final purpose of this research is to set an appropriate evaluation method of a seismic resistance of a floor finishing system, that make it possible to develop and improve more safety floor finishing systems reasonably. This thesis is an interim report described to results of studies about a input wave using for vibration test of seismic resistance evaluation, and about qualities of a floor groundwork surface which are one of experimental conditions.

1. INTRODUCTION

A floor is the most important part of a building, because it is always touched by humans, furniture, etc., and influences safety, habitability, comfort, etc. greatly. For seismic safety, requested performance items take up various topics besides resistance of structural breakage, such as resistance of breakage of non-structural materials, prevention of a tumble of furniture, etc.

On the other hand, various floor construction methods are developed and supplied. As shown some examples in Figure 1, non-structural materials (interlayers and upper finishing materials) are constructed on floor groundwork. Then, the kind of furniture is also various, and some of them are fixed directly on groundwork or interlayers.

At an earthquake, there is a possibility that safety is ruined by breakage of non-structural materials or a tumble of furniture, even if a structure is not broken. It is a large problem related to life or death, so it is necessary to examine seismic resistance from such a viewpoint and to manage countermeasures urgently.

There are some examples of situations that non-structural materials of floors are damaged at earthquakes. Picture 1 shows a situation that a weak groundwork surface was destroyed and an interlayer came off from groundwork. And, picture 2 shows a situation that steel panels of a interlayer, where a bookshelf was fixed on, was greatly bent. In other words, not only interlayers and upper finishing materials, various factors (such as groundwork surface, furniture, etc.) are also influence seismic safety greatly. Therefore, it is necessary to consider a groundwork surface, an interlayer, an upper finish material, furniture, etc. to be a floor finishing system additionally, and to evaluate seismic resistance as the whole. However, the investigation in the past that

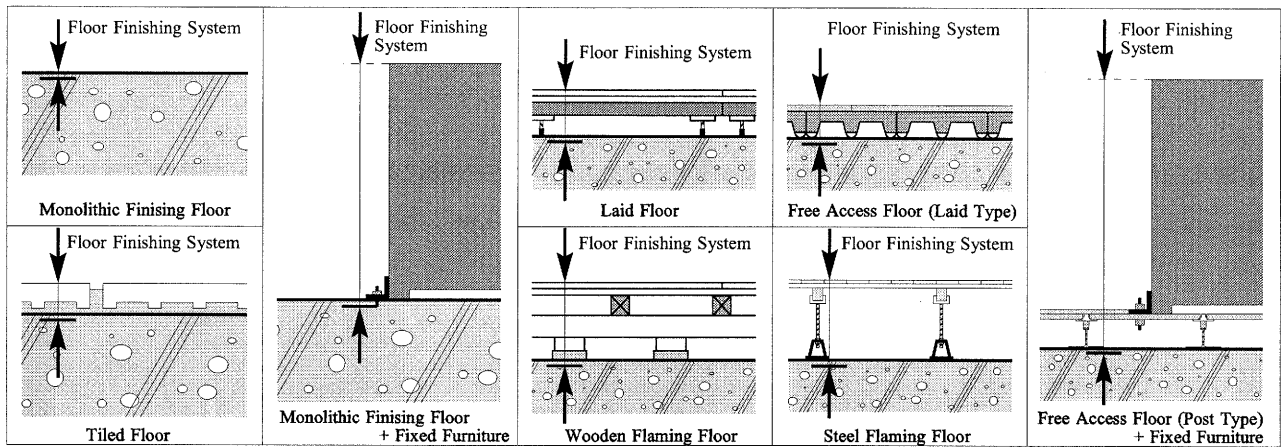
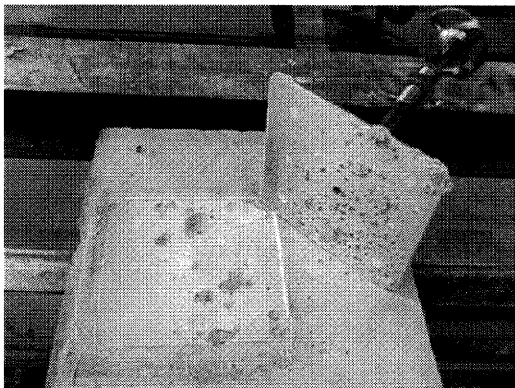
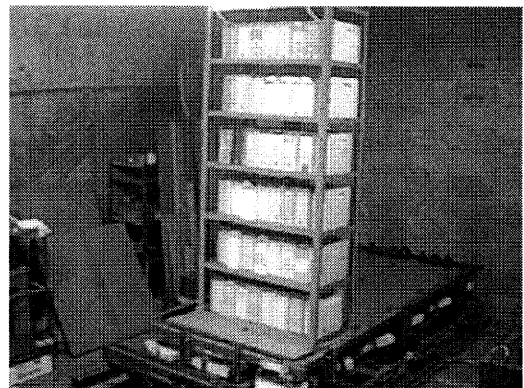


Figure 1 Typical Examples of Floor Finishing System



Picture 1 Destroyed Weak Groundwork Surface and Come Off Interlayer from Groundwork



Picture 2 Bent Steel Panels of Interlayer due to Bookshelf Fixed on Interlayer

examines seismic resistance considering a groundwork surface, an interlayer, an upper finishing material, furniture, etc. to be a floor finishing system is not found. The final purpose of this investigation is to set an appropriate evaluation method of a seismic resistance of a floor finishing system, that make it possible to develop and improve more safety floor finishing systems reasonably.

As shown in the above-mentioned, a seismic resistance of a floor finishing system is influenced complexly by strength of an interlayer and an upper finishing material, a detail of its joint, a quality of a groundwork surface, furniture, etc. And it is difficult to predict behavior of a floor finishing system at an earthquake by using analyzing methods or static experimental methods. Therefore, to evaluate seismic resistance of the floor finishing system, it is avoided to take out a part, to simplify or to standardize without appropriate foundation. And it is tried to establish the evaluation method with a dynamic vibration test that is done under the same situation as an actual floor.

This thesis is an interim report described to results of studies about the input wave using for vibration test of seismic resistance evaluation, and about a quality of a floor groundwork surface which is one of experimental situations.

2. MANNER OF EVALUATION

Approach of this evaluation method is described in procedural manner as follows; At first, the object floor finishing system is constructed to the same situation as an actual floor on a vibration table. Next, the vibration test is done, and the state of the system is measured. Finally, the relation between the state of the system and strength of the input wave is examined and

seismic resistance is evaluated. This manner of the evaluation on seismic resistance of a floor finishing system is shown in Figure 2 by a flowchart.

For establishment of the evaluating method along this manner, it is necessary to set an input wave for a vibration test, to set situations that influences seismic resistance (about a quality of the groundwork surface, furniture, etc.), to set the way of grading the state of the system, etc., as shown in Figure 2 too

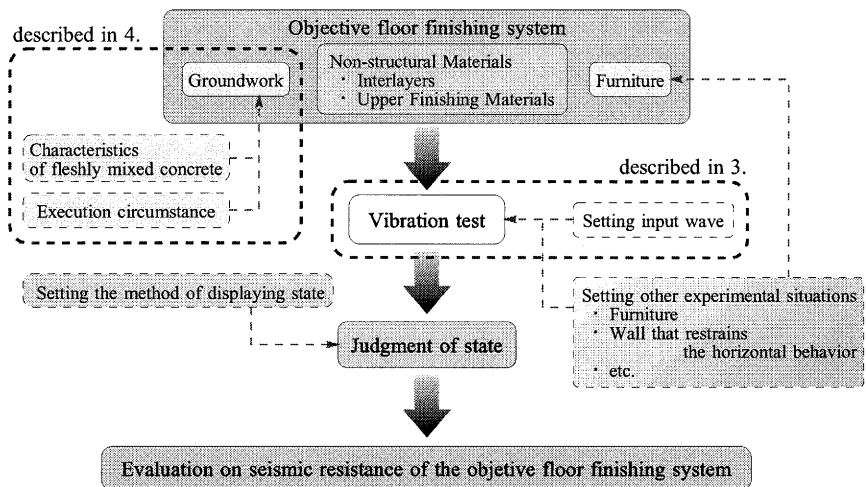


Figure 2 Manner of Evaluation on Seismic Resistance and Items of Experimental Situations to be Set in Advance

3. SETTING OF INPUT WAVE USING FOR VIBRATION TEST

The setting of the input wave using for the vibration test of seismic resistance evaluation has been tried so far in this study. At present, vibration tests using specific real seismic waves are sometimes carried as a method of evaluating seismic resistance. However, it is thought that the vibration test using real seismic wave admits of improvement, because a vibration table that can input real seismic waves lacks handiness (it needs comparatively large-scale, expensive equipments), and using a specific wave lacks generality. Therefore, first of all, it is examined that the wave simplified a part of real seismic waves is able to be applied as an input wave for the seismic resistance evaluation.

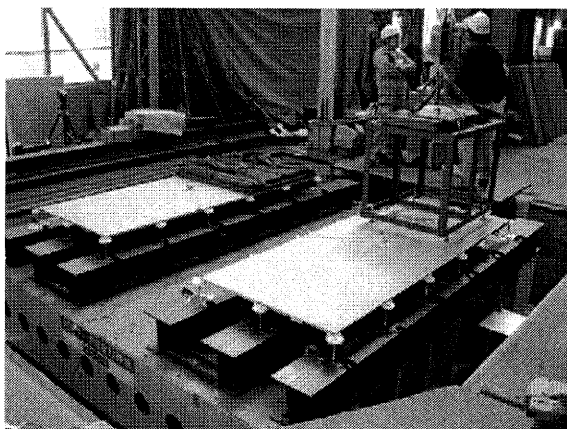
3.1. Manner of Study

The free access floor (FA) was used as a specimen for the examination. First of all, the behavior of specimen inputted real seismic waves was observed. Next, as abstracted parts impacting the behavior of specimen by real seismic waves, input waves are obtained. And then, simple vibration table is made to reproduce input waves. Finally, it is configured that an input wave for evaluating the seismic resistance of FA, substituted for real seismic waves.

3.2. Observation of Behavior of Specimen Inputted Real Seismic Waves

The specimen FA was constructed as on the existing oil pressure type vibration table. Then the real seismic wave in one horizontal direction was inputted to specimen, and the behavior of specimen was observed. The specimen is shown in Picture 3. The specimen FA was an independent post type (type of putting the corner of the panel of four a post), that seemed to be typical to examine seismic resistance. The number of panels was 2×5 , and a heavy weight that imitated furniture was set in 2×2 parts at the edge. Posts were fixed directly to the vibration table without the groundwork, and the weight was not fixed to the panel. It was because exclusion of factors other than the input wave differences was necessary. Additionally, horizontal strength was intentionally reduced more than the usual by thinning posts to compare the input wave differences easily.

Input waves used for the examination are shown in Table 1. There were 5 kinds of the real seismic wave that imitate a response of a lower level in a building. And there were also 3 kinds of the sine wave that imitate a response of a middle or higher level.



Picture 3 Specimen FA

Table 1 Input Waves

Lower Level in Building	Middle or Higher Level in Building
Real Seismic Wave	Sine Wave
El centro (NS)	
Taft (EW)	0.5 Hz
Hachinohe (EW)	1 Hz
Hanshin (NS)	2 Hz
Miyagi Cost (EW)	

specimen after the vibration test was observed and judged by 3 stages as "Safety", "Damaged" and "Destroyed" from a viewpoint of inclination of the post or space between panels.

Figure 3 shows the relation between the state of the specimen and the maximum value of the acceleration amplitude measured on the vibration table. The following etc. are considered from this figure.

- As the maximum acceleration grows, the specimen is damaged and finally destroyed.
- The maximum acceleration that the breakage began or the specimen was destroyed varies according to input waves.

Incidentally, the resonance of the specimen was hardly generated.

3.3. Setting of Input Wave

The behavior of the specimen inputted real seismic waves was observed again in detail with the video. As a result, it seemed that the state of the specimen is influenced predominantly on the largest amplitude part of acceleration in a real seismic wave. Then, this part decided to be substituted in the sine wave. The outline of this Simple Input Wave is shown in Figure 4. To reduce impact at the beginning (ending) of the vibration test, the frequency was set to increase (decrease) in the straight line before and behind the sine wave.

Incidentally, handy and cheap Simple Vibration Table (Figure 5) that is able to construct the floor finishing

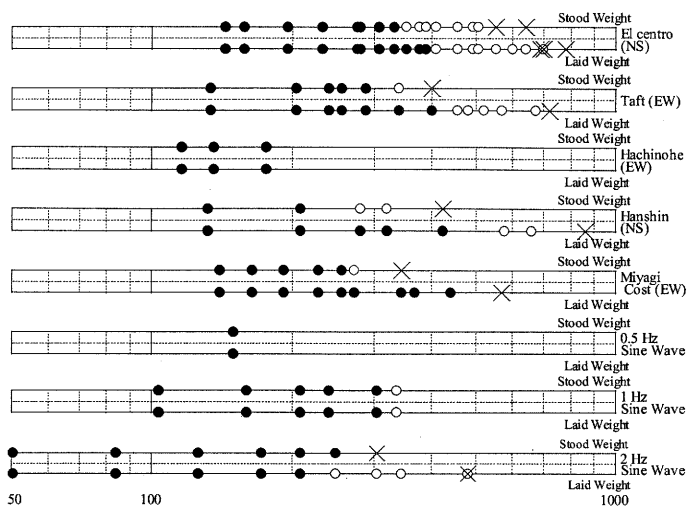


Figure 3 Relation between State of Specimen and Maximum Value of Acceleration Amplitude

The vibration test began from the maximum acceleration about 50-150 gal every 8 kinds of input waves. Afterwards, the amplitude was gradually increased at every test, and it went until the specimen finally was destroyed or until it reaches the peak magnitude on the ability of the vibration table. And the state of the

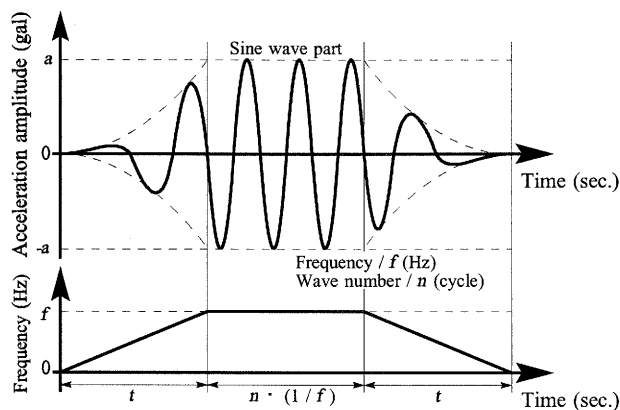


Figure 4 Outline of Simple Input Wave

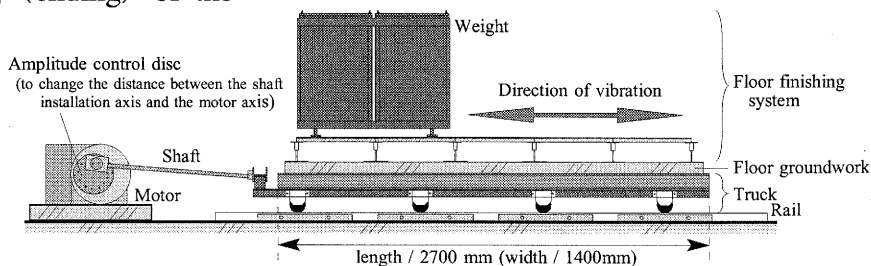


Figure 5 Outline of Simple Vibration Table

system and to input Simple Input Wave into system was made.

3.4. Observation of Behavior of Free Access Floor Inputted Simple Input Waves

Relations between the specimen behavior and the amplitude, the frequency, the Wave number, etc. of Simple Input Wave were examined through vibration tests using the Simple Vibration Table. The specimen was the same as 3.2.

Based on the frequency of a real seismic wave etc., the frequency of the input wave was set to be 3 kinds, 1, 2 and 3 Hz. And the wave number was set to be 3 kinds, 1, 2 and 3 cycles. Comparatively few wave numbers was enough because the resonance of the specimen is hardly generated. The vibration test was done by using the 9 kinds of Simple Input Waves combined these frequency and the wave number according to the same procedure as 3.2.

Figure 6 shows the relation between the state of the specimen and the maximum value of the acceleration amplitude measured on the vibration table. The following etc. are considered from this figure.

- Frequency; The acceleration amplitude of the 2 Hz wave when the specimen is damaged or destroyed is smaller than that of the 1 Hz wave. And that of 3 Hz wave is also smaller than that of 2 Hz.
- Wave number; There is no great difference by the wave number. Then it is thought the result by waves of more than 4 cycles are also not so different from the result by the wave of 3 cycles.

3.5. Setting Input Wave for Seismic Resistance Evaluation

The following etc. are considered from the comparison between Figure 3 and Figure 6.

- Among real seismic waves etc., Wave of Miyagi Cost (EW) and sine wave of 2 Hz damage or destroy the specimen at the comparatively small value of maximum acceleration.
- Among Simple Input Waves, the Wave of 2 Hz damage or destroy the specimen at the similar value of maximum acceleration of Wave of Miyagi Cost (EW) and sine wave of 2 Hz

In conclusion, the Simple Input Wave of 2 Hz / 3 cycles is set as the input wave for the seismic resistance evaluation.

At present, this input wave can be applied only to FA. A further examination is being done to set the input wave that can be applied to the seismic resistance evaluation by various floor finishing systems now. A further examination is being done to set the input wave that can be applied to the seismic resistance evaluation by various floor finishing systems.

4. STUDY ABOUT QUALITY OF FLOOR GROUNDWORK SURFACE

The setting of experimental conditions concerning the quality on the groundwork surface has been tried, too. A characteristic of a freshly mixed concrete and an execution effort when constructing floor groundwork greatly influence a quality of the surface. Therefore, in setting a test situation about a quality of a groundwork surface, it is necessary to consider an actual grade

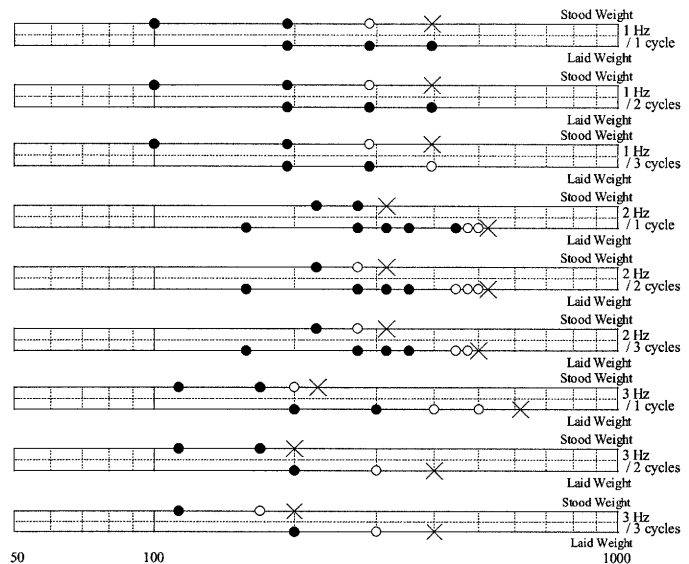


Figure 6 Relation between State of Specimen and Maximum Value of Acceleration Amplitude

of a surface realized by the construction method in an actual site, in addition to demand grade from mechanism of floor finishing system. Then, first of all, the relations between quality of a groundwork surface, characteristics of freshly mixed concrete, and execution circumstances were examined quantitatively.

4.1. Manner of Study

First of all, several kind of freshly mixed concrete was constructed to the form imitated the floor groundwork. At this time, construction was done under some kinds of execution circumstances concerned with execution efforts of actual sites. Next, the quality of specimen surfaces were measured. Finally, relations between quality of surfaces, characteristics of freshly mixed concrete, and execution circumstance were shown.

From a viewpoint of seismic resistance of the floor finishing system, flatness, strength of the surface layer, and the amount of moisture are considered as very important items for quality of floor background surface. This thesis describes the result of the study about surface strength.

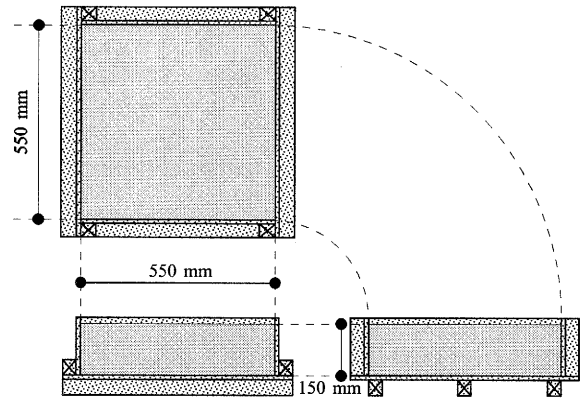


Figure 7 Outline of Specimen

4.2. Experiment to Construct Floor Groundwork

4.2.1 Outline

(1) Specimen

The outline of the specimen is shown in Figure 7. The specimen was set to imitate a part of a general structural slab, and its thickness was set to be 150 mm. Then, the size of the specimen was made 550 mm square in consideration of the convenience of the management of the temperature and humidity at the curing. Incidentally, reinforcing bar was not arranged to the specimen, because it was thought that reinforcing bar doesn't influence surface strength so much.

(2) Execution Circumstance

The execution circumstance concretely provided for tools used for each work, time spent on work, method of curing, etc. 3 kinds of execution circumstances were set as shown in Table 2. These were set based on the result of the field investigation about the execution effort (construction speed, number of workers, area one worker takes charge, procedure, tools used for each work, method of curing, etc.) on an actual site. Meanings of each condition of I - III are as follows.

I (Poor condition) ; Condition that workers think "In the experience or in hearing, it is the worst condition."

Table 2 Execution Circumstance

	I (Poor condition)	II (General condition)	III (Ideal condition)
Rough Leveling Compaction	Vibrator	Shovel, Hoe, Straightedge with handlebar, Vibrator	Shovel, Hoe, Straightedge with handlebar, Vibrator
	Rough Leveling / 4 sec. Compaction / 4 sec.	Rough Leveling / 11 sec. Compaction / 11 sec.	Rough Leveling / 44 sec. Compaction / 44 sec.
Leveling	Hoe	Hoe, Straightedge with handlebar, Straightedge, Wooden trowel, Metal trowel	Hoe, Straightedge with handlebar, Straightedge, Wooden trowel, Metal trowel
	4 sec.	22 sec.	65 sec.
Trowelling	Wooden trowel	Wooden trowel	Wooden trowel
	6 sec. / 1 time	11 sec. / 1 time	11 sec. / 2 times
	Metal trowel	Metal trowel	Metal trowel
	6 sec. / 1 time	7 sec. / 2 times	7 sec. / 2 times
Wet curing	none	none	3 days / Wet mat

II (General condition); Condition that workers think "This degree of condition is general recently."

III (Ideal condition) ; Condition that workers think "It is enough to construct the floor groundwork with good surface quality."

(3) Freshly Mixed Concrete

4 kinds of freshly mixed concretes shown in Table 3 were used.

The nominal strength of every concrete was 27 N/mm². The harnesses of these concretes were varied by changing the amount of water chiefly.

(4) Worker

Students of Tokyo Institute of Technology did "Rough Leveling" and "Compaction", and the special skilled worker who specialize in floor concrete finishing did "Leveling" and "Trowelling".

4.2.2 Passage and Result

The experiment was carried under 12 kinds of conditions (combined 4 kinds of the freshly mixed concretes and 3 kinds of the execution circumstances) as described by 4.2.1.

At the same time, slumps of the freshly mixed concrete were measured. The slump is an index indicating the stiffness of the freshly mixed concrete. And it is also an index indicating the amount of water which influences surface strength greatly.

4.3. Measurement of Surface Strength of Specimen

After the specimens had been cured for 28 days in the laboratory of 20 °C in temperature and 60% in humidity according to the condition shown in Table 2, surface strength was measured. Concretely, the surface of the specimen was scratched with the Scratch Tester of Japan Society for Finishing Technology that installed the needle of pressurizing power 1.0 kgf (9.8 N), and those scratch widths were measured by using the crack scale. Here, the speed of scratching was adjusted to about 2 cm/sec., and about 10 cm in length was scratched along a ruler. Each specimen was measured several times, and the average value was requested. However, because of the roughness of the surface, the scratch width of the specimen, constructed under execution circumstance I and by using concrete which slump was 7.8 cm, was not able to be measured appropriately.

4.4. Index about Surface Strength

Figure 8 shows relations between the scratch widths, the slumps of the freshly mixed concrete and the execution circumstance. In figure, the vertical line is drawn so that a small value is plotted upper. The dotted line in figure is a curve that shows correspondence.

The following etc. are considered from this figure.

- Regardless of the value of the slump, the good of bad of the execution circumstance is clearly reflected in the grade of the scratch width. In other words, the scratch width of execution circumstance III is more narrow than that of II, and the scratch width of I is the broadest.
- In execution circumstance III, though the rate of water and the cement of the freshly mixed concrete is fixed, the scratch width

Table 3 Outline of Freshly Mixed Concrete

Type	Nominal Strength (N/mm ²)	Slump (cm)	Mixture Proportion					
			W / C (%)	Water (kg/m ³)	Cement (kg/m ³)	Fine Agg. (kg/m ³)	Coarse Agg. (kg/m ³)	Admixture (kg/m ³)
Normal	27	7.8	55.0	165	300	837	1001	0.900
		16.8		172	313	824	985	0.940
		20.1		183	323	803	961	1.000
		24.8		195	355	780	933	1.060

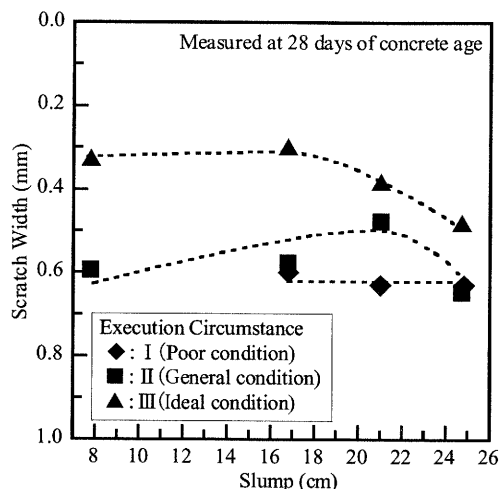


Figure 8 Relations between Scratch Widths, Slumps of Freshly Mixed Concrete and Execution Circumstance

insufficient for a stiff concrete to make its surface strong through the finishing work. As a proof, in execution circumstance III, surface strength of a stiff concrete is hardly decreased because an enough execution circumstance is secured.

- In execution circumstance I, the clear trend is not seen between the scratch width and the slump. It is because the execution circumstance is so insufficient that the difference of the stiffness of the freshly mixed concrete is hardly reflected in surface strength.

In conclusion, Figure 8 shows the appearance concretely and quantitatively that the characteristic of the freshly mixed concrete and the execution circumstance are reflected in the surface strength. When the characteristic of freshly mixed concrete and the execution circumstance are set at planning construction, the surface strength of the completed floor groundwork can be expected from this figure. Oppositely, the characteristic of freshly mixed concrete and the execution circumstance can be selected reasonably according to the demand degree of surface strength.

Incidentally, the relations between flatness of floor groundwork surface, finishability of freshly mixed concrete and execution circumstances etc. have been examined. Then, also relation between surface strength and bonding strength among interlayer and floor groundwork (for floor finishing systems bonded to interlayers or floor groundwork), jumping up of interlayers originated in in-flatness of floor groundwork surface (for floor finishing systems laid on floor groundwork), etc. will be investigated. And finally, experimental situations about the quality of floor groundwork surface for evaluating of the seismic resistance of the floor finishing system will be set appropriately.

5. CONCLUSION

This investigation is on the way to establish the appropriate evaluation method of the seismic resistance of the floor finishing system. This thesis described about the input wave using for vibration test and about the quality of a floor groundwork surface.

References;

- Yokoyama, Y., Katagi, U., Yokoi, T. and Ono, H. (2005), "Configuration of Input Wave for Evaluating Seismic Resistance on Free access Floor", *Journal of Structural and Construction Engineering*, A.I.J., reviewing
- Yokoyama, Y., Katagi, U., Yokoi, T. (2004), "Example of quality index on surface layer of concrete ground work", *Journal of Structural and Construction Engineering*, A.I.J., No. 586, 15-23

AN EXPERIMENTAL STUDY ON THE PERFORMANCE OF RC COLUMNS SUBJECTED TO CYCLIC FLEXURAL-TORSIONAL LOADING

P. Tirasit¹⁾, K. Kawashima²⁾, and G. Watanabe³⁾

1) Graduate Student, Department of Civil Engineering, Tokyo Institute of Technology, Japan

2) Professor, Department of Civil Engineering, Tokyo Institute of Technology, Japan

*3) Research Associate, Department of Civil Engineering, Tokyo Institute of Technology, Japan
paiboon@cv.titech.ac.jp, kawasima@cv.titech.ac.jp, gappo@cv.titech.ac.jp*

Abstract: During an earthquake, torsion possibly occurs in the piers of some special bridges, such as C-bent column bridges, skewed bridges and curved bridges, and influences their behaviors. An experimental study was conducted in order to investigate the performance of reinforced concrete columns under cyclically applied bending and torsional loading. Ten column specimens with the same structural properties were tested under various loading conditions; cyclic torsion, cyclic uniaxial bending and combined cyclic torsion and cyclic uniaxial bending with and without the effect of a constant axial compression force. Several combinations of cyclic bending and cyclic torsion expressed in the form of the rotation-drift ratio (θ/Δ) were applied in order to observe the behavior and the interaction between torsional and flexural capacities of columns.

1. INTRODUCTION

Presently, many cities have to face the problems about the space limitation for the transportation systems. One probable solution is to construct the bridges with special configurations. The examples of these bridges are C-bent column bridges, skewed bridges and curved bridges. During an earthquake, torsion may occur in C-bent columns due to the eccentricity of inertia force transferred from the superstructure. In skewed bridges, collision between bridge deck and abutment may cause the inplane rotation of superstructure and consequently induced the torsion in the piers. Furthermore, since the responses of curved bridges in the transverse and longitudinal directions are coupled, the piers are subsequently subjected to the multi-directional deformation with torsion. The combination of seismic torsion and other internal forces can result in the complex flexural and shear failure of these bridge piers.

Hsu and Wang (2000) and Hsu and Liang (2003) conducted the experimental studies on the effect of combined cyclic bending and constant torsion on the performance of composite columns with various steel sections. They revealed that the flexural capacity and ductility of composite columns reduced when the constant torsion was simultaneously applied. Kawashima et al. (2003) and Nagata et al. (2004) conducted a cyclic bilateral loading test and a hybrid loading test on the reinforced concrete C-bent columns, respectively. They showed that C-bent columns suffered extensive damage on the eccentric compression side and the residual displacement occurred accumulatively in this direction. This resulted from the eccentricity of vertical load coupled with the bending moment and torsion from the eccentric lateral force.

However, naturally the seismic torsion does not constantly occur during an earthquake. The knowledge of the interaction between bending moment and torsion is still limited as well. Moreover,

the reliable torsional hysteresis model has not been yet available and the behavior of reinforced concrete column subjected to combined cyclic bending and torsion has not been well clarified.

This paper presents a cyclic loading test of 10 reinforced concrete columns to investigate the effect of combined cyclic bending and torsion on the column behavior. The experimental results about the progress of column failure and the hysteresees are discussed.

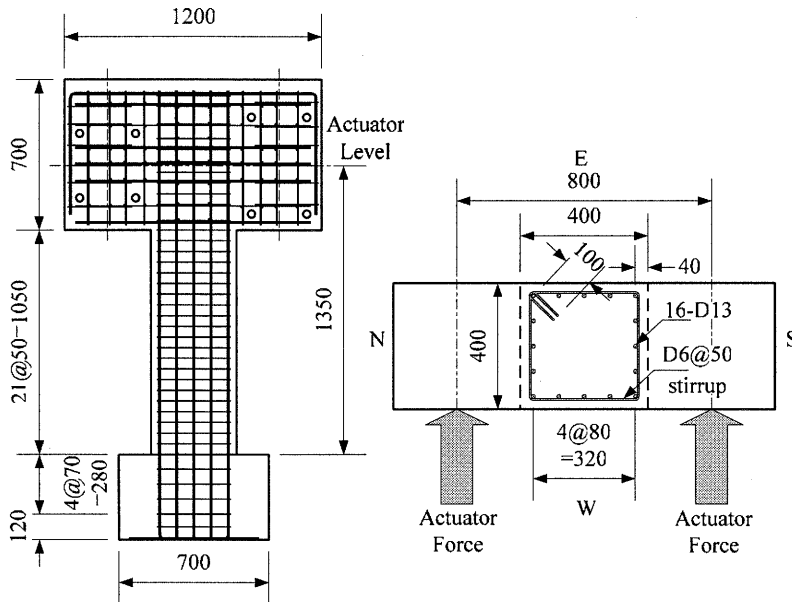


Figure 1 Specimen Configuration

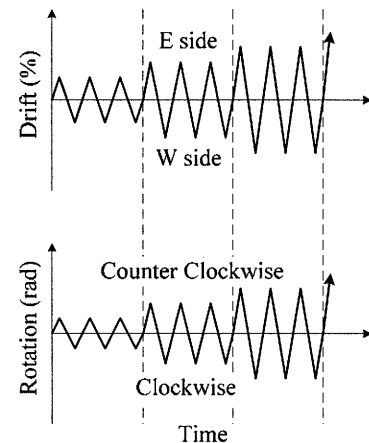


Figure 2 Loading Pattern

Table 1 Experimental Cases

Specimen	f'_c (MPa)	Loading Scheme	θ/Δ
P1	31.28	T	∞
P2	28.30	T	∞
P3	25.61	T+P	∞
P4	28.60	M+P	0
P5	32.16	T+M+P	0.5
P6	32.39	T+M+P	1
P7	25.34	T+M+P	1
P8	32.54	T+M+P	2
P9	32.79	T+M+P	2
P10	33.08	T+M+P	4

T: Cyclic torsion

M: Cyclic uniaxial bending

P: 160kN constant axial compressive force

MPa. Sixteen 13mm diameter deformed bars with 295 MPa nominal strength (SD295A) were employed as the longitudinal reinforcement. The same grade 6mm deformed bars were provided as the tie reinforcement at every 50 mm interval. The longitudinal reinforcement ratio and the tie volumetric ratio were 1.27% and 0.79%, respectively. The design concrete compressive strength was 30 MPa. Table 1 shows the actual concrete strength of each column.

2.2 Loadings

Cyclic load test was conducted by using the dynamic testing facility in Tokyo Institute of Technology. Table 1 presents the loading conditions of all columns. A constant 160 kN compression was applied to the specimens to produce the 1 MPa axial stress in the plastic hinge region, except columns P1 and P2. The test was conducted under lateral displacement and rotation being

2. EXPERIMENTAL SETUP

2.1 Specimen Properties

Ten reinforced concrete columns with the structural properties as shown in Figure 1 were constructed. The columns had a 400mmx400mm square cross section and they were 1750 mm tall with a 1350 mm effective height. All columns were designed in accordance with the Japanese 1996 Design Specification of Highway Bridges. Type I (middle-field) and Type II (near-filed) ground motions with the moderate soil condition were assumed. The axial compression stress at the plastic hinge zone of the column due to the superstructure dead weight was assumed to be 1

controlled. Cyclic torsion, and combined cyclic uniaxial bending moment and cyclic torsion were generated by controlling two horizontal actuators as shown in Figure 1. The effect of axial force on the torsional hysteresis was inspected on columns P1, P2 and P3. Column P4 was tested under cyclic uniaxial bending. Columns P5 to P10 were tested under several combinations of cyclic bending and cyclic torsion which were defined by a ratio of rotation, θ (radian), and lateral drift, Δ , (θ/Δ) as shown in Table 1. The lateral drift and rotation were simultaneously applied 3 cycles at every loading step as shown in Figure 2.

However, it is noted that columns P1, P6 and P8 were not in the good condition. The segregation of concrete occurred in columns P1 and P6 because of the insufficient vibrating during construction and the accidental loading from one of horizontal actuators caused some initial cracks in column P8. Due to the space limitation, the results of columns P1, P6 and P8 are not presented here.

3. PERFORMANCE OF COLUMNS

3.1 Columns under Cyclic Torsional loading

Figure 3 shows the damage of columns P2 and P3, which were under cyclic torsion without and with an axial load respectively, at 0.09 rad rotation. Diagonal cracks were first observed at 0.005 rad rotation in both columns and the checker board crack patterns were formed. The covering concrete of both columns P2 and P3 deformed outward as the rotation increased and they suffered extensive damage around their mid height. However, the angles of cracks referring to the column cross section were about 45 degrees in column P2 while those were larger in column P3. This results from the effect of the 1 MPa axial force. No buckling occurred in column P2 while longitudinal bars slightly buckled outward in column P3.

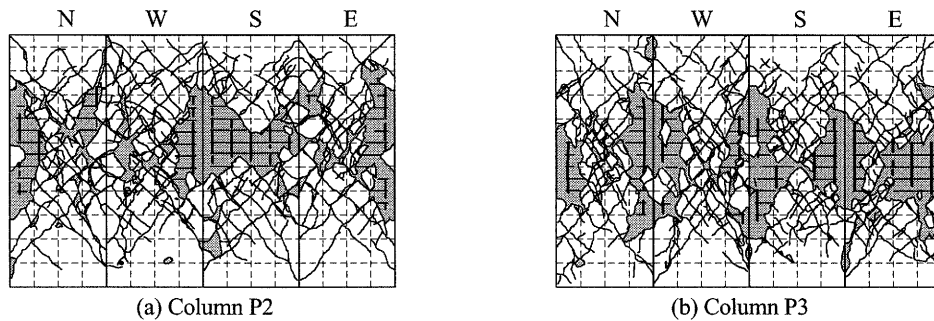


Figure 3 Damage of Columns P2 (Cyclic torsion) and P3 (Cyclic torsion with Axial Force) at 0.09 rad Rotation

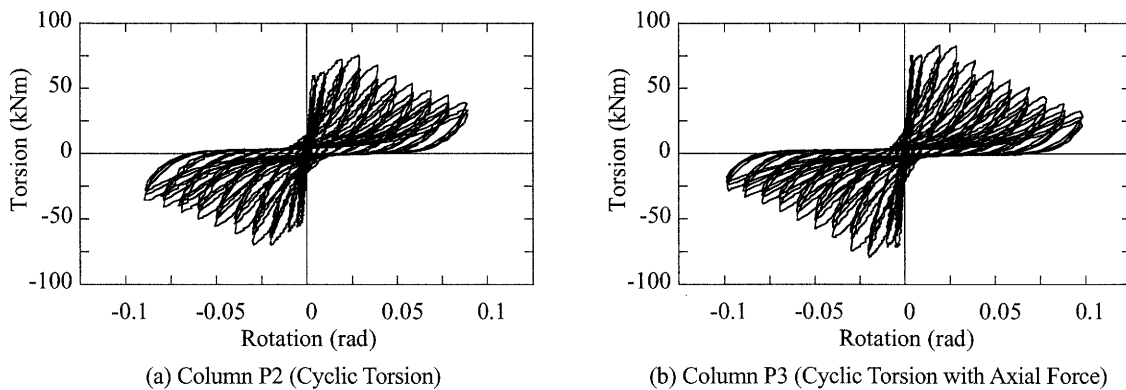


Figure 4 Torsional Hystereses of Columns under Cyclic Torsional Loading

The torsional hystereses of columns P2 and P3 were compared in Figure 4. In the torsional hysteresis of column P2, the torsional stiffness remarkably decreased after cracking at 0.005 rad rotation. The torsional strength reached 75.7 kNm at 0.03 rad rotation and then gradually

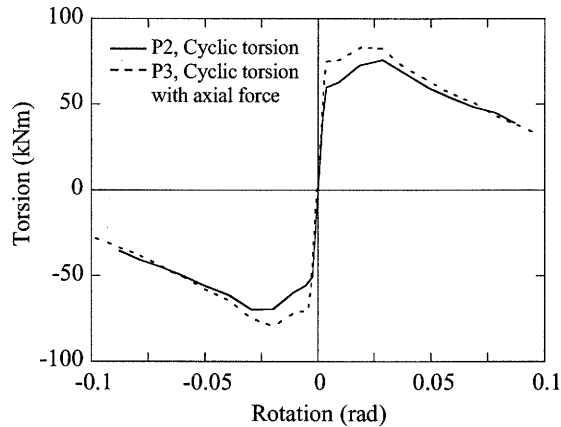


Figure 5 Comparison of Envelopes of Torsional Hystereses of Columns P2 (Cyclic torsion) and P3 (Cyclic Torsion with Axial Force)

deteriorated due to the progress of damage at the middle of column. The torsional capacity of column P2 decreased to 78.8% of its strength at 0.05 rad rotation. In column P3 under cyclic torsion with axial force, the torsional stiffness significantly deteriorated after cracking at 0.005 rad rotation. Column P3 reached its strength of 83.4 kNm at 0.02 rad rotation. This torsional strength was 10.2% larger and occurred earlier than that of column P2. The torsional capacity of column P3 reduced to 76.3% of its strength at 0.05 rad rotation. Nevertheless, the effect of axial force became less significant as the rotation increased, based on the comparison of envelopes of columns P2 and P3 shown in Figure 5.

3.2 Column under Cyclic Uniaxial Bending

The damage at the end of testing of column P4 subjected to cyclic uniaxial bending with axial force is shown in Figure 6(a). The damage occurred in the plastic hinge zone due to the compression failure of covering concrete and the buckling of the longitudinal reinforcement.

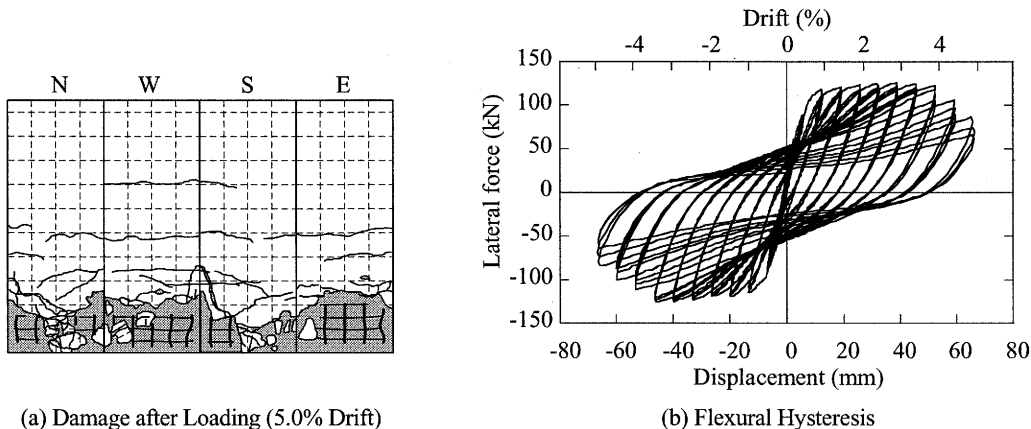


Figure 6 Damage after Loading and Flexural Hysteretic of Column P4 (Cyclic Uniaxial Bending with Axial Force)

Figure 6(b) presents the flexural hysteresis of column P4. The hysteresis reached its maximum capacity of 125.7 kN at 3.0% drift and was stable until 4.0% drift. After that the flexural capacity began to deteriorate due to the compression failure of covering concrete and the buckling of longitudinal reinforcement. The column lost the confinement and its restoring force was 31.3% smaller than its strength at 5.0% drift.

3.3 Columns under Combined Cyclic Uniaxial Bending-Torsional Loading

Several rotation-drift ratios (θ/Δ) were investigated to clarify the interaction between bending moment and torsion. Figure 7 shows the damage after the tests of columns P5, P7, P9 and P10 under different combinations of cyclic bending-torsional loading. The N surfaces of all columns suffered less significant damage compared to the S surfaces. The reason is the N surfaces experienced smaller displacements than the S surfaces during the tests (refer to Figures 1 and 2). Moreover, the angle of cracks on the column surfaces tended to increase as the rotation-drift ratio increased. The more complex flexural and shear failure occurred and the damage was likely to happen outside the plastic hinge region as the rotation-drift ratio increased. For the column P5 under 0.5 rotation-drift ratio, its

damage pattern was close to that of column P4 subjected to cyclic uniaxial bending. On the other hand, the damage pattern of column P10 under 4 rotation-drift ratio was similar to that of column P3 subjected to cyclic torsion with axial force.

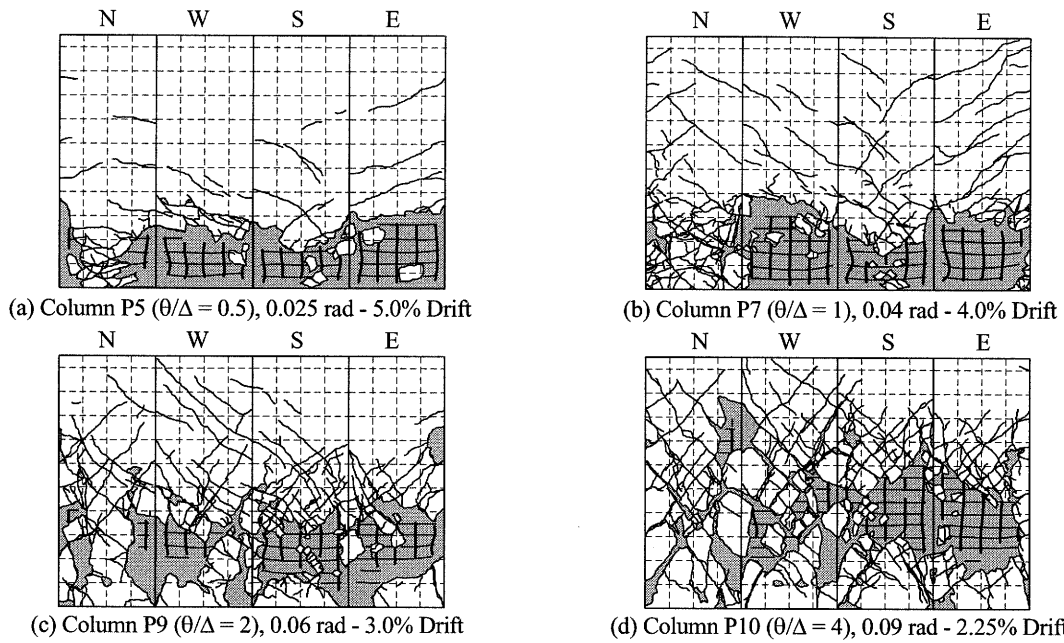


Figure 7 Comparison of Damage in Columns P5, P7, P9 and P10 (Combined Cyclic Uniaxial Bending-Torsional Loading) after the Tests

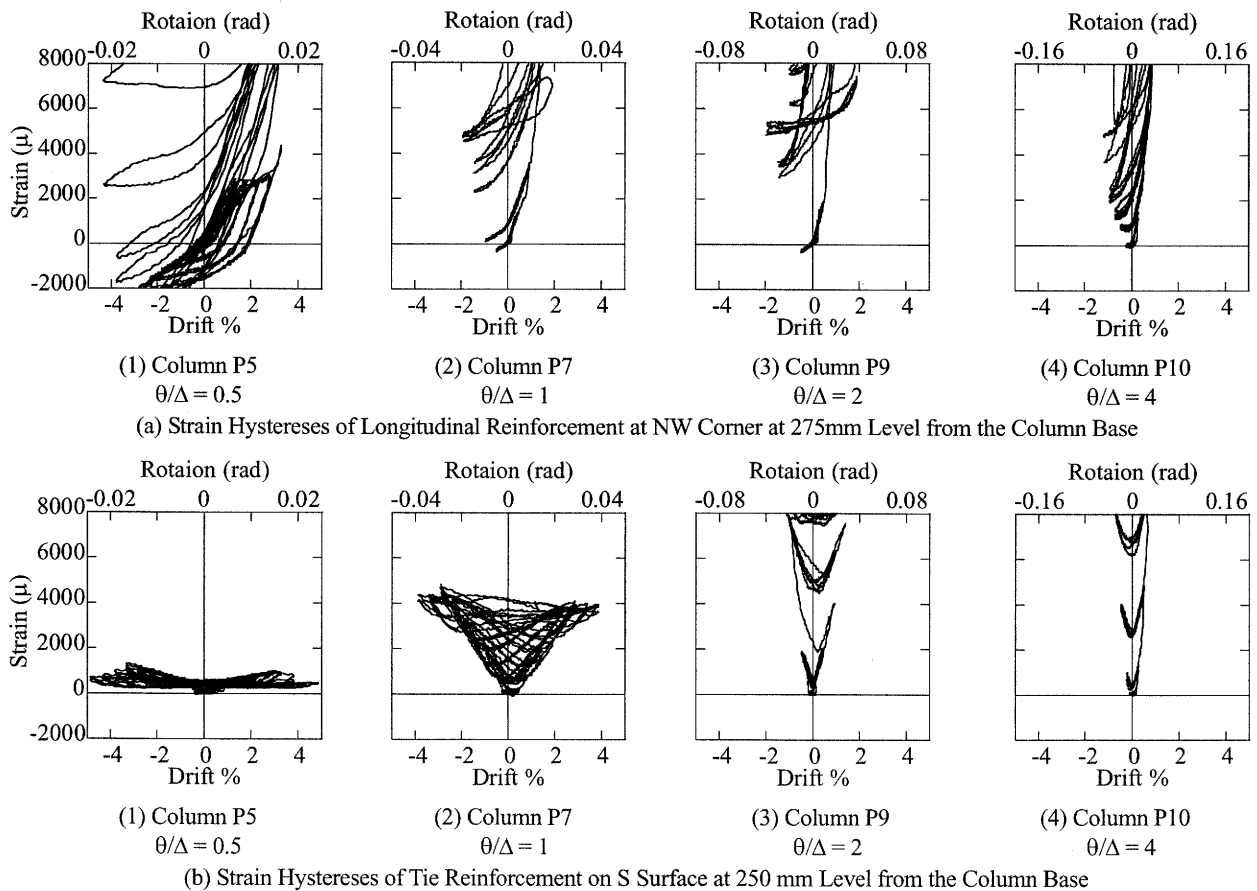


Figure 8 Comparison of Strain Hystereses of Longitudinal and Tie Reinforcement of Columns under Combined Cyclic Uniaxial Bending-Torsional Loading

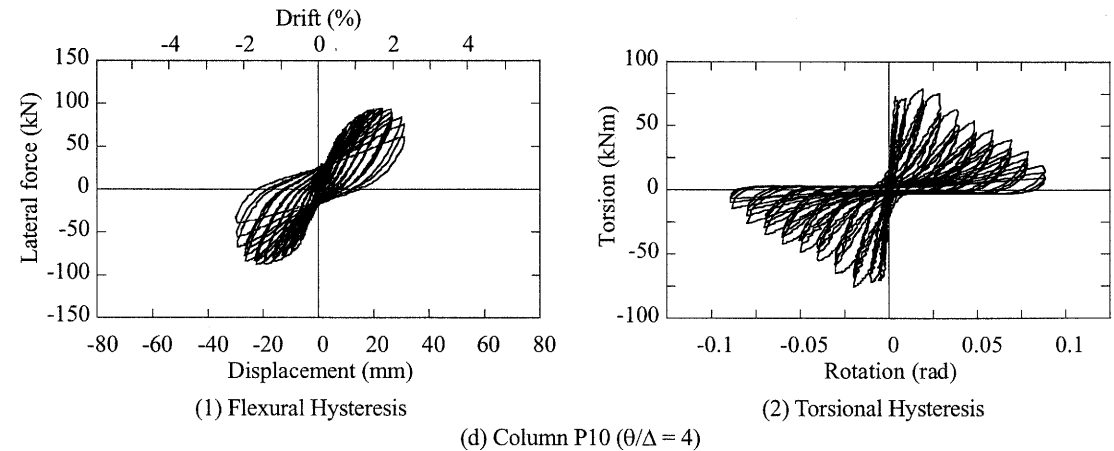
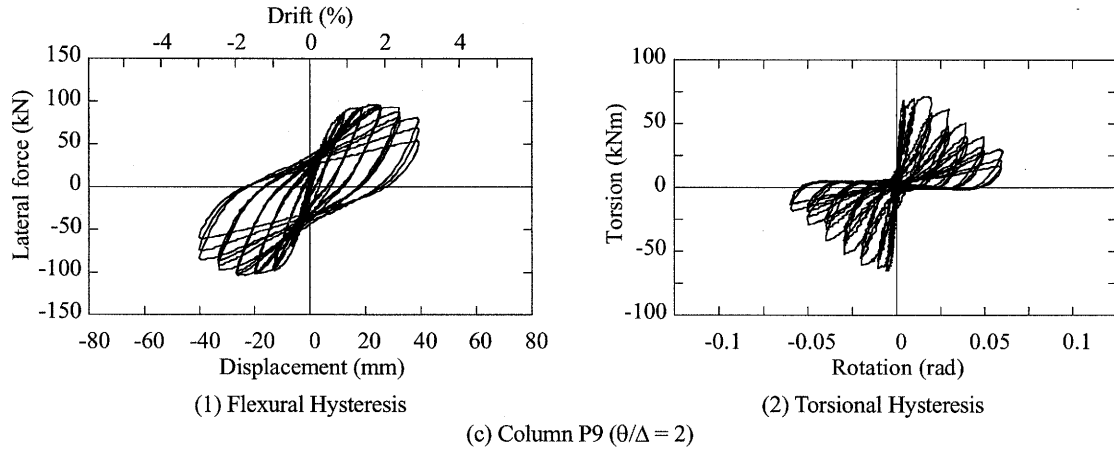
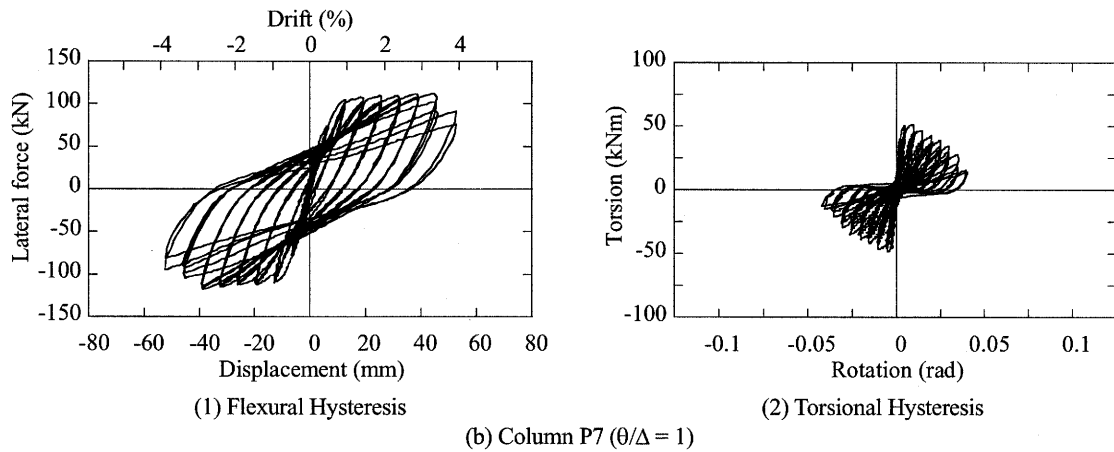
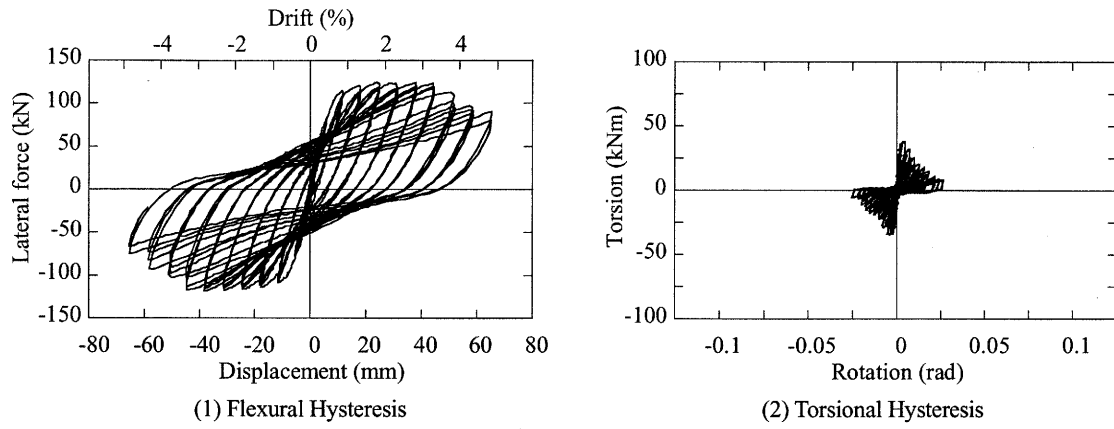


Figure 9 Flexural and Torsional Hystereses of Columns under Combined Cyclic Uniaxial Bending-Torsional Loading

The comparison of strain hystereses of longitudinal reinforcement at NW corner at 275mm level from the bottom of columns P5, P7, P9 and P10 is presented in Figure 8(a). This 275mm level is outside the plastic hinge zone of the column. It indicates that the strain of the longitudinal reinforcement increased as the rotation-drift ratio increased. This is because the damage of the columns was likely to occur above the plastic hinge region. This phenomenon can also be obviously seen in the comparison of strain hystereses of tie reinforcement on S surface at 250mm level from the column base shown in Figure 8(b).

The flexural and torsional hystereses of columns P5, P7, P9 and P10 are shown in Figure 9. It can be seen clearly that the maximum lateral force and the flexural ductility of columns decreased as the rotation-drift ratio increased. On the other hand, the torsional strength and the torsional ductility of columns increased as the rotation-drift ratio increased. The flexural and torsional strengths, and the ultimate displacement and rotation are respectively presented in Tables 2 and 3 in the next section.

4. INFLUENCE OF COMBINED CYCLIC UNIAXIAL BENDING-TORSIONAL LOADING

Figure 10 shows the comparison of envelopes of flexural and torsional hystereses of the columns. In Figure 10(a), the envelope of flexural hysteresis of column P5 under 0.5 rotation-drift ratio is very close to that of column P4 under cyclic uniaxial bending. This is because the influence of applied cyclic torsion in column P5 was limited. The deterioration of flexural stiffness increases as the rotation-drift ratio increases. In addition, the reduction of the rotation-drift ratio results in more extensive deterioration of the secondary torsional stiffness as shown in Figure 10(b). The torsional envelope of column becomes close to that of column under cyclic torsion with axial force as the rotation-drift ratio increases.

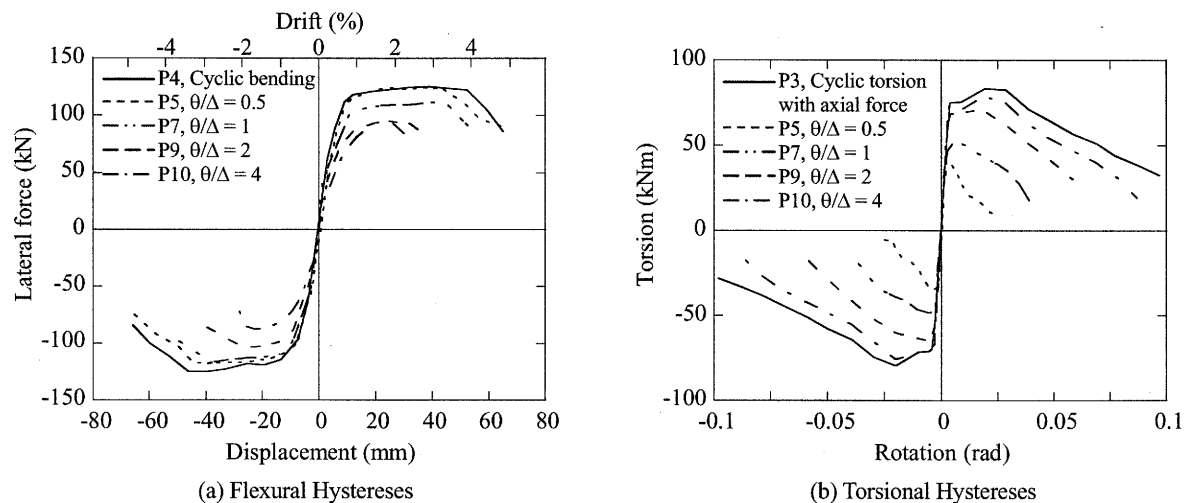


Figure 10 Comparison of Envelopes of Flexural and Torsional Hystereses of Columns

Table 2 Maximum Lateral Force and Torsion

Specimen	θ/Δ	Maximum Lateral Force (kN)			Maximum Torsion (kNm)		
		Positive	Negative	Average	Positive	Negative	Average
P1	∞	-	-	-	70.9	64.9	67.9 (83.3%)
P2	∞	-	-	-	75.7	70.0	72.9 (89.3%)
P3	∞	-	-	-	83.4	79.7	81.6 (100.0%)
P4	0	125.7	125.4	125.6 (100.0%)	-	-	-
P5	0.5	124.2	118.5	121.4 (96.7%)	38.4	34.7	36.6 (44.8%)
P6	1	103.4	108.9	106.2 (84.5%)	47.1	46.7	46.9 (57.5%)
P7	1	111.5	117.9	114.7 (91.4%)	50.8	48.4	49.6 (60.8%)
P8	2	99.9	98.1	99.0 (78.9%)	72.9	65.5	69.2 (84.9%)
P9	2	95.9	103.8	99.9 (79.5%)	71.0	64.9	68.0 (83.3%)
P10	4	94.5	87.9	91.2 (72.6%)	79.0	75.6	77.3 (94.8%)

Table 3 Ultimate Displacement and Rotation

Specimen	θ/Δ	Ultimate Displacement (% Drift)			Ultimate Rotation (rad)		
		Positive	Negative	Average	Positive	Negative	Average
P1	∞	-	-	-	0.05	0.05	0.05 (100.0%)
P2	∞	-	-	-	0.05	0.05	0.05 (100.0%)
P3	∞	-	-	-	0.05	0.05	0.05 (100.0%)
P4	0	5.0	4.5	4.75 (100.0%)	-	-	-
P5	0.5	4.5	4.5	4.5 (94.7%)	0.01	0.01	0.01 (20.0%)
P6	1	3.5	3.5	3.5 (73.7%)	0.02	0.015	0.0175 (35.0%)
P7	1	4.0	4.0	4.0 (84.2%)	0.025	0.025	0.025 (50.0%)
P8	2	3.0	3.0	3.0 (63.2%)	0.04	0.04	0.04 (80.0%)
P9	2	3.0	3.0	3.0 (63.2%)	0.04	0.04	0.04 (80.0%)
P10	4	2.25	2.25	2.25 (47.4%)	0.04	0.04	0.04 (80.0%)

Tables 2 and 3 summarize the maximum lateral force and torsion, and the ultimate displacement and rotation of the columns, respectively. The ultimate displacement and rotation are defined here as the displacement and rotation where the lateral force and torsion deteriorate to less than 80% of their maximum capacity, respectively. The columns under cyclic torsion with a constant axial load (P3) and under cyclic uniaxial bending with a constant axial force (P4) are used as the benchmarks. It is apparent that the flexural strength and the ultimate displacement decrease as the rotation-drift ratio increases. In contrast, the torsional strength and the ultimate rotation reduce as the rotation-drift ratio decreases. At the large rotation-drift ratio, $\theta/\Delta=4$, the flexural strength and the ultimate displacement are 27.4% and 52.6% smaller than those of column under cyclic uniaxial bending, respectively.

5. CONCLUSIONS

To investigate the effect of combined cyclic bending and torsion on the performance of reinforced concrete columns, a series of cyclic loading tests was conducted. Based on the experimental results presented herein, the conclusions may be deduced as follows:

- 1) Axial compression force increases the torsional strength and the angles of cracks referring to the column cross section. However, the effect of axial force becomes less significant as the rotation increases.
- 2) Damage of column tends to shift upward from the plastic hinge zone as the rotation-drift ratio increases. The length and location of plastic hinge region, therefore, have to be carefully evaluated for the column under the combined bending moment and torsion.
- 3) The flexural capacity and the ultimate displacement of column reduce as the torsion increases. On the other hand, the increase of bending moment results in the deterioration of the torsional capacity and the ultimate rotation. Thus, it is essential to take this interaction into the consideration in seismic design of column subjected to the combined flexural and torsional load.

Acknowledgements:

The authors express their sincere appreciation to Messrs. Fukuda, T., Nagai, T., Wang, Y., Ogimoto, H., Kijima, K., Nagata, S. and Maruyama, Y. for their extensive support in constructing the columns and executing the experiment.

References:

- Hsu, H.-L. and Wang, C.-L. (2000), "Flexural-Torsional Behavior of Steel Reinforced Concrete Members Subjected to Repeated Loading," *Earthquake Engineering and Structural Dynamics*, **29**, 667-682.
- Hsu, H.-L. and Liang, L.-L. (2003), "Performance of Hollow Composite Members Subjected to Cyclic Eccentric Loading," *Earthquake Engineering and Structural Dynamics*, **32**, 433-461.
- Kawashima, K., Watanabe, G., Hatada, S. and Hayakawa, R. (2003), "Seismic Performance of C-bent Columns Based on A Cyclic Loading Test," *Journal of Structural Mechanics and Earthquake Engineering*, **745**(I-65), 171-189. (In Japanese)
- Nagata, S., Kawashima, K. and Watanabe, G. (2004), "Seismic Performance of Reinforced Concrete C-bent Columns Based on A Hybrid Loading Test," *Proceedings of the 1st International Conference on Urban Earthquake Engineering*, Tokyo Institute of Technology, Tokyo, Japan, 409-416.
- Japan Road Association (1996), "Specifications for Highway Bridges - Part V Seismic Design," Maruzen, Tokyo.

AN EXPERIMENTAL STUDY ON BEHAVIOR OF NON-BOND RC COLUMNS SUBJECTED TO THREE-AXIAL COMPULSORY FORCE

HH. Nguyen¹⁾, K. Takiguchi²⁾, and K. Nishimura³⁾

1) Doctor Candidate, Dept. of Mechanical and Environmental Informatics, Tokyo Institute of Technology, Japan

2) Professor, Dept. of Mechanical and Environmental Informatics, Tokyo Institute of Technology, Japan

3) Assistant Professor, Dept. of Architecture and Building Engineering, Tokyo Institute of Technology, Japan
huyhoang76@tm.mei.titech.ac.jp, ktakiguc@tm.mei.titech.ac.jp, knishimu@tm.mei.titech.ac.jp

Abstract: This research deals with three-axial behavior of non-bond RC columns subjected to multi-axial compulsory force. Four identical non-bond RC column specimens were prepared for experiment. Each of them had 150x150 mm square section and clear height of 600 mm. A layer of paraffin wax was used to cover around reinforcement bar in order to remove the bond between concrete and reinforcement bar. All of the specimens were tested under multi-axial compulsory force by hydraulic jacks with axial force ratio of 0.02 and 0.2. Obtained results revealed several significant understanding on slipping behavior of non-bond RC columns. Moreover, experimental data, which is necessary for modeling restoring force characteristic of RC structures, was also collected.

1. INTRODUCTION

In order to evaluate seismic safety in building design, an estimation of multi-dimensional non-linear restoring force characteristic of building structure subjected to earthquake excitation is highly essential. Restoring force characteristic of building structure can be divided into two types: Flexural type can be seen in restoring force characteristic of rigid frame and shear type is familiar with that of bearing wall structure. Considering restoring force characteristic of a RC column experiment subjected to one-directional lateral force, there appeared slipping behavior on the hysteresis loop in the latter state, when the bond between concrete and reinforcement became extremely weak. In case of RC bearing wall experiment, the evidence of slipping behavior was investigated on the hysteresis loop from initial state, when the bond between concrete and reinforcement is very strong, to the last state, when the bond is greatly decreased. This slipping behavior takes characteristics of slipping type, which was well considered in one-axial behavior in "Earthquake-Resistant Limit-State Design for Buildings" of H. Akiyama (H. Akiyama, 1985).

In order to idealize this slipping behavior in experiment, the use of experiment on RC member without bond between reinforcement and concrete seems to be suitable. An experiment of non-concrete-reinforcement bond RC columns (non-bond RC columns) subjected to one lateral force was carried out in the past research of K. Takiguchi (K. Takiguchi, et al 1976, K. Takiguchi, 1977). However, experimental study focused on two and three-axial slipping behavior of non-bond RC columns is still limited. Therefore, the research concerning in such kind of this field is becoming necessary more than ever.

In this study, four identical non-bond RC column specimens were prepared for experiment. Each of them had 150x150 mm square section and clear height of 600 mm. A paraffin wax was used to cover around reinforcement bar in order to remove the bond between concrete and reinforcement.

All of the specimens were tested under one vertical and two lateral cyclic loads by hydraulic jacks in the range of 0.02 to 0.2 axial force ratio. This research firstly aims to understand slipping behavior of non-bond RC structure, on that base modeling of restoring force characteristics of RC structure, which is one of macro modeling (Takizawa and Aoyama 1976) will be carried out.

2. EXPERIMENTAL PROGRAM

2.1 Specimens

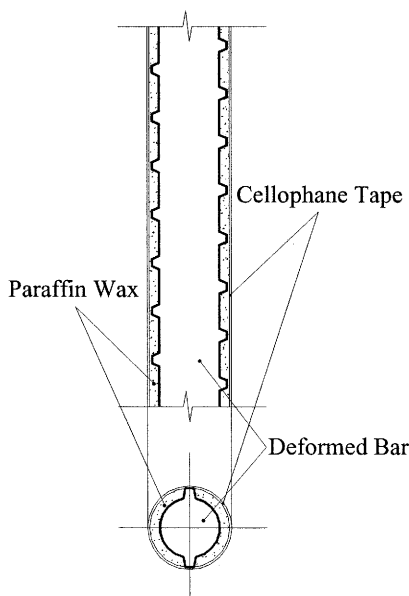
In all, four reinforce concrete column specimens were prepared for the test. Table 1 shows dimensions of specimens and mechanical properties of concrete and reinforcements. Details of specimen were shown in Figure 1.b. Eight deformed bar D10 (diameter= 10 mm) and round bar R4 (diameter=4 mm) hoops spaced at 15 cm were used for longitudinal bars and shear reinforcements, respectively. The height and the cross section of original column were 600 mm and 120x120 mm. A layer of paraffin wax was used to cover around reinforcement bar in order to remove the bond between concrete and reinforcement as shown in Figure 1.a. All of the specimens were tested under multi- axial compulsory force by hydraulic jacks with constant axial force ratio of 0.02 and 0.2.

Table 1. Dimension of Specimens and Mechanical Properties of Concrete

Name of Specimen	Section bxD (mm)	Length of Clear span (mm)	Reinforcements			Concrete			Axial Force ratio (%)
			Main Reinf. Pg(%)	Shear Reinf. Pw(%)	Yield strength (N/mm ²)	Age at Column Test (days)	Compressive Strength σ_B (N/mm ²)	Splitting Tensile Strength σ_T (N/mm ²)	
CBS-NB-1	150x150	600	8-D10 2.54	4 ϕ @25 0.67	371(D10) 452(4 ϕ)	45-46	32.1	2.81	20
CBS-NB-2						49-52	31.9	2.63	1.8
CBS-NB-3						58-60	32.1	2.60	1.8
CBS-NB-4						63-66	33.0	2.60	1.8

Curing: in air

(a). Non- Bond Deformed Bar



(b). Specimen

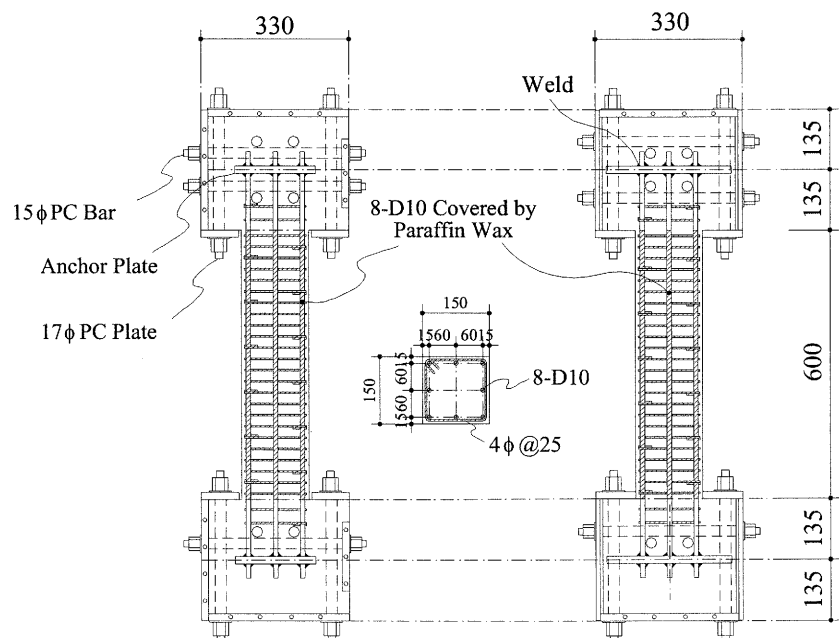


Figure 1. Detail of Specimen and Bond Rejected Method

2.2 Apparatus and Loading Program

Figure 2 shows loading and displacement measuring system. The tested column was fixed horizontally on the base. The head of the column was allowed to move in three axes. A parallel rule of link mechanism was used to restrict rotation that causes torsion of the column (Takiguchi et al. 1979). In addition, to ensure parallelism between the head and bottom of the column specimen, a parallel keeping system, which consisted of eight hydraulic cylinders connected to a cross beams system were employed to keep horizontal equilibrium as shown in Figure 2. As shown in Figure 3, the loading system with eight hydraulic cylinders allows vertical translation and keeps horizontal. The specimen columns were subjected to lateral loading by two hydraulic jacks of 200 kN capacity through L-shaped loading beam. This L-shaped loading beam connected to hydraulic jack at the mid-height of the column. The specimen CBS-NB-1 was subjected to cyclic one-directional lateral under a constant axial force ratio of 0.2, while the specimens CBS-NB-2 to CBS-NB-4 were subjected to lateral compulsory force under a constant axial force ratio of 0.02. Load cells on the hydraulics jacks were used to measure compulsory force of these three jacks.

Five displacement transducers were used to measure tri-axial rotation of specimen's head as shown in Figure 2. The displacement transducer No.1 to No.3 examines the lean of the specimen's head, while No.4 and No.5 checks the column head's rotation. Displacements of tested column in vertical, horizontal direction were measured and recorded by measuring instruments. The measuring instrument connects measuring position through ball bearing of self-align rod-ends. Figure.4 show detail of loading history.

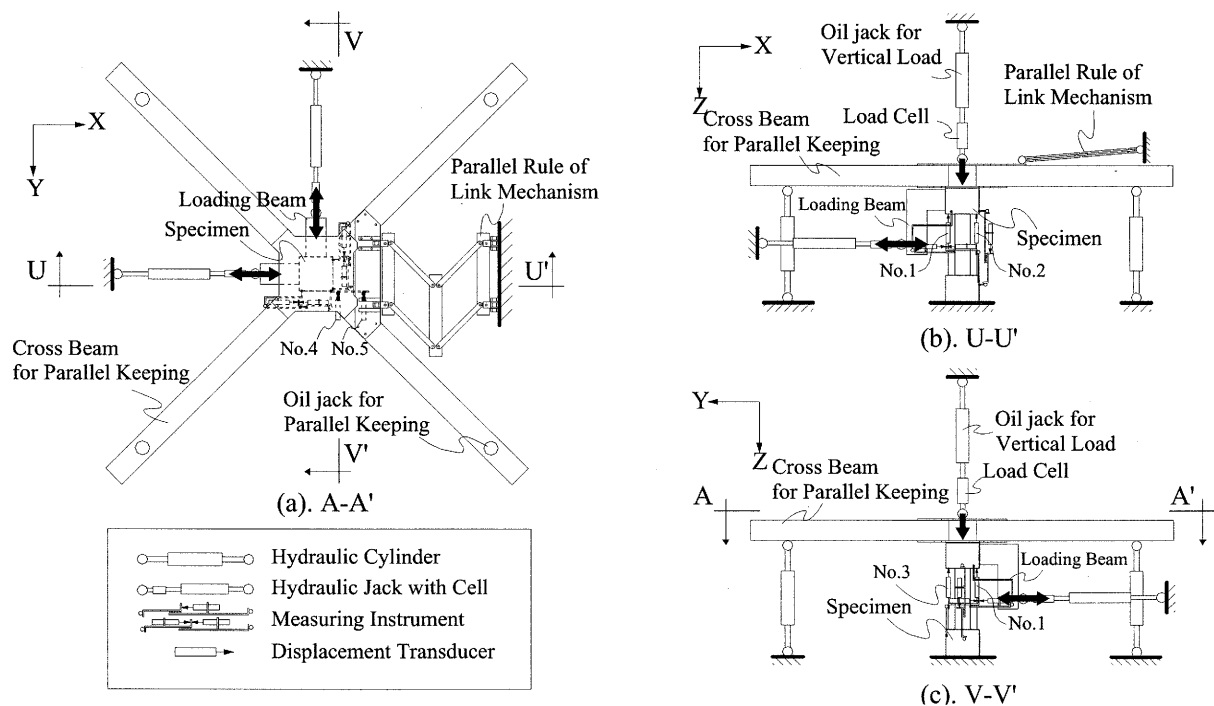


Figure 2. Loading and Measuring System

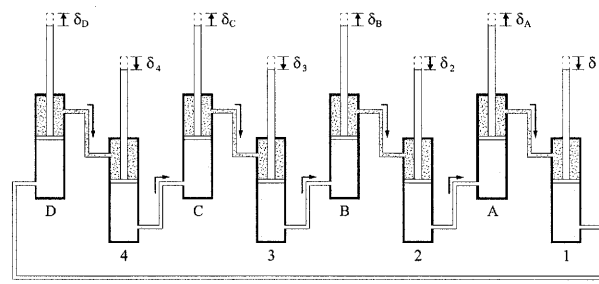


Figure 3. System of Horizontal Balance Keeping Cylinder

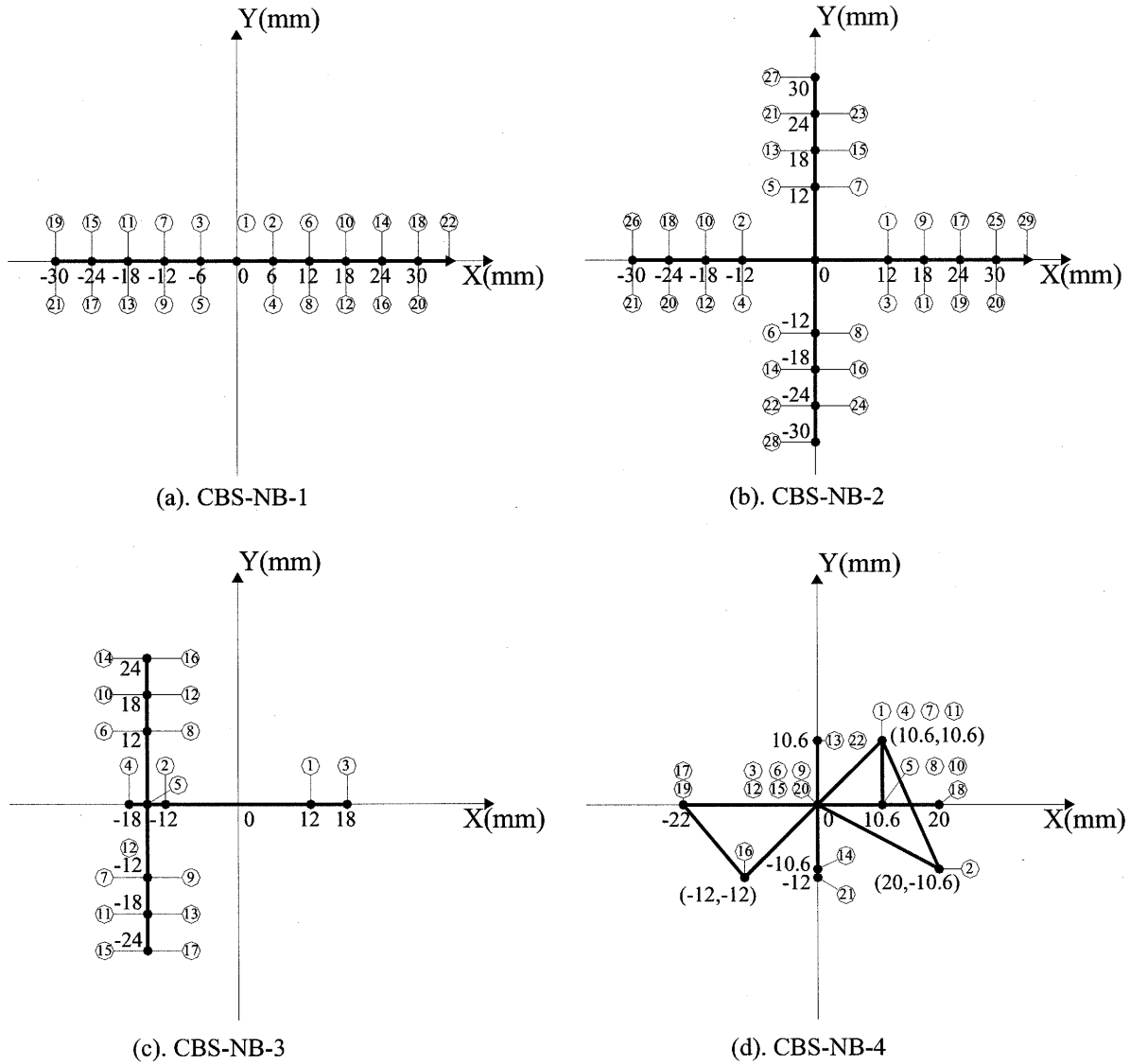


Figure 4. Loading History

3. TEST RESULTS AND CONSIDERATION

3.1 The bond of reinforcement bar

The strain of reinforcement bar was measured at position of head, mid height and bottom of experimental columns. There is no considerable difference in the value of transformation in each position. Similar result was obtained in all experiment columns. As a result, it can be said that the bond of the main reinforcement bar will be taken in the actual experiment.

When the member bears the shearing force, all the reinforcement transforms into tension side. The tension force always acts on the main reinforcement bar. From this remark point, it can be said that in the non-bond RC columns, concrete bears compression force, reinforcement bar bears tension force to resist external force.

3.2 Slipping behavior

Figure 5 to 8 show test results of four specimens CBS-NB-1 to CBS-NB-4. Q_x , Q_y , N express shearing force, compression force in X direction, Y direction and Z direction, respectively. δ_x , δ_y , δ_z express deformation in X, Y, and Z direction, respectively.

Considering the hysteresis loop of CBS-NB-1 with axial force ratio of 0.2 as shown in Figure 9.a, there is no appearance of slipping behavior when the value of lateral deformation reaches gradually to 12 mm. In case of CBS-NB-2 with axial force ratio of 0.02, slipping behavior appeared when the value of lateral deformation reaches to 12 mm. From this remark, it can be said that the value of axial force ratio affects to slipping behavior in non-bond RC column.

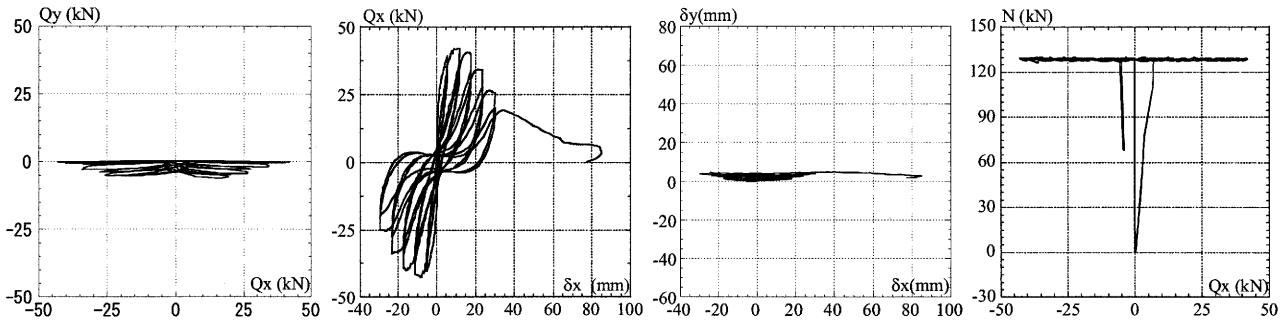


Figure 5. CBS-NB-1

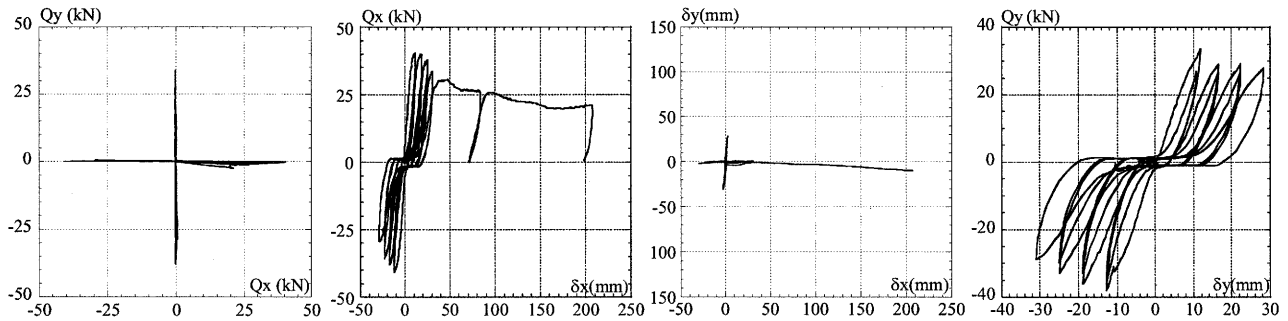


Figure 6. CBS-NB-2

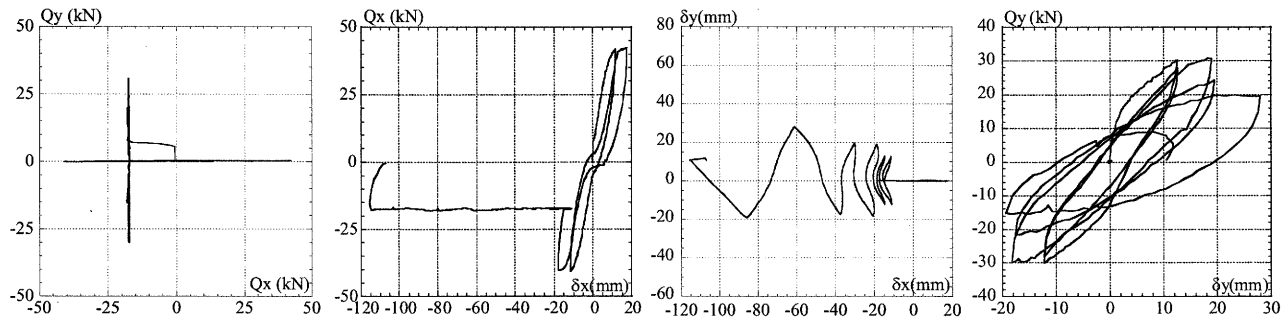


Figure 7. CBS-NB-3

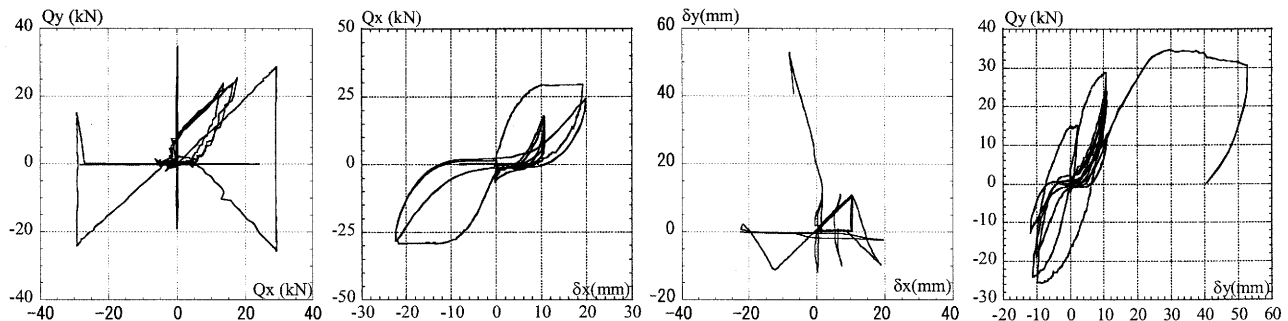


Figure 8. CBS-NB-4

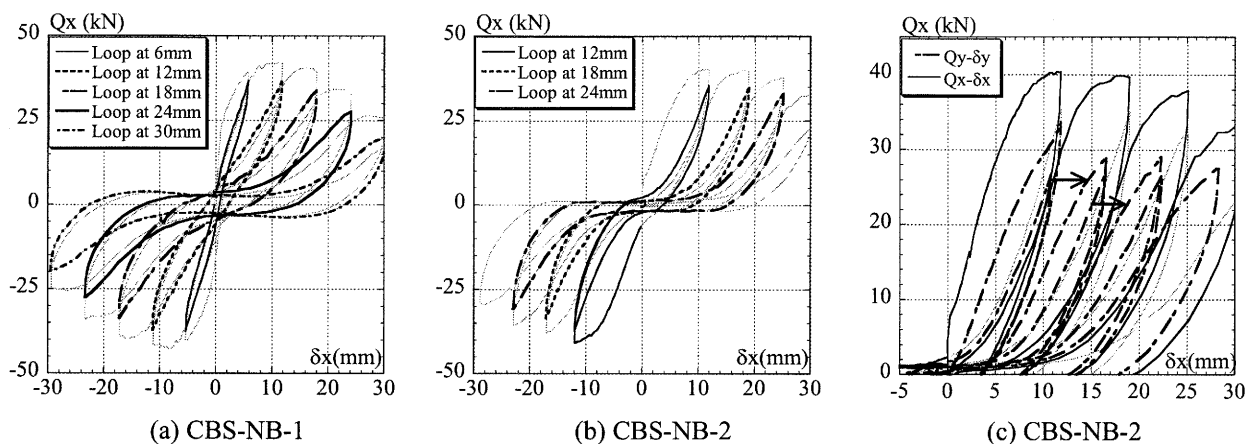


Figure 9. Hysteresis Loops

Slipping behavior, however, appeared in CBS-NB-1 when the value of lateral deformation reaches to 24mm as shown in Figure 9.a. At that time, the value of compression force acts on reinforcement bar approximately 87.3 kN, while the axial force of CBS-NB-1 is around 128.5 kN. The compression force that concrete bears was decreased, while compression force acts on reinforcement bar increased and take about 70% the value of axial force. It can be said that, when the damage of concrete strongly increases, the compression force that concrete bears decreases, and member shows slipping behavior.

Slipping behavior appeared in the hysteresis loop of CBS-NB-3 force in X direction as shown in Figure 7. Applying a constant lateral force to X direction and cyclic force to Y direction at the same time, there was no slipping behavior appears in Y direction. It is obvious that there existed a compression force acts on concrete along X direction to resist slipping behavior in Y direction.

From the above mentioned, for the non-bond RC member subjected to lateral cyclic force with a constant axial force ratio 0.02, because the compression force that concrete bears is small, therefore the member cannot resist bending-shearing force and slipping behavior appears. In case of a constant axial force ratio 0.2, because the compression force acts on concrete large, so the slipping behavior is not easily appeared until member has a large lateral transformation.

3.3 Effect of loading history to orthogonal direction.

Figure 9.b, c shows relationship of $Q_x-\delta_x$ and $Q_y-\delta_y$ of CBS-NB-2. As can be seen, lateral rigidity of member in Y direction is smaller than that of X direction. Moreover, when the deformation becomes large, the area of slipping behavior is expended. It is possible that, because of cyclic force in X direction, the damage of concrete in Y direction increase, therefore lateral rigidity of member in Y direction decreased, and area of slipping behavior in Y direction was expanded.

3.4 Force-displacement Relationship

Figure 8 shows experimental result of CBS-NB-4. Loading history of CBS-NB-4 was shown in Figure 4.d. From the stage 1 to stage 3, specimen column was subjected to two-directional lateral force with axial ratio force 0.02. The yielding state appeared in both X and Y direction in this stage. From the stage 3 to stage 12, lateral deformation move in non-yielding area. Considering lateral displacement and hysteresis loop of CBS-NB-4 in this stage, it can be said that the member shows similar behavior regardless route of displacement.

From stage 12 to stage 13, transformation increases toward Y direction at a low load, the direction of compulsory force and that of transformation were different. The direction of transformation directed toward to severe damage area side in X direction. It is possible that, because the transformation was given to a positive side of X direction, therefore, the damage of concrete at the bottom of specimen column along positive side of X direction is larger than that of negative side

of X direction. When applying an external force in Y direction, because of the large damage of concrete in positive side of the X direction, direction of transformation directed toward the X direction side.

4. CONCLUSIONS

This paper describes an experimental study on behavior of non-bond RC columns subjected to multi-axial compulsory force. Four identical non-bond RC column specimens were prepared for experiments. Each of them had 150x150 mm square section and clear height of 600 mm. A paraffin wax layer was used to cover around reinforcement bar in order to remove the bond between concrete and reinforcement. All of the specimens were tested under multi-axial compulsory forces by hydraulic jacks with constant axial force ratio of 0.02 and 0.2. The main findings were obtained as follows:

- In the experiments of non-bond RC columns subjected to one-directional lateral cyclic force with constant axial force ratio of 0.02, the compression force acts on concrete is small. The value of shearing force does not change much while that of deformation has fluctuation enclosed with appearance of slipping behavior. However, applying a constant lateral force to a certain direction of specimen column and lateral cyclic force to orthogonal direction at the same time, there was no slipping behavior appears in orthogonal direction. Obviously, there already existed a compression force acts on concrete to resist slipping behavior along orthogonal direction. In case of experimental column subjected to lateral one- directional cyclic force with constant axial force ratio of 0.2, because the compression force acts on concrete was large, therefore slipping behavior was not clearly investigated. However, there appeared evidence of slipping behavior in the latter states, when the lateral deformation became large and compression force that concrete bears decreased. It can be said that the value of compression force that acts on concrete affected to occurrence of slipping behavior in non-bond RC columns.
- Considering restoring force characteristic of non-bond RC member subjected to lateral one-directional cyclic force in turn of two lateral directions, because of the effect of loading history in one axis, the lateral rigidity of non-bond RC member along orthogonal axis is decreased. Moreover, the area of slipping behavior along orthogonal axis was expended.
- In the condition of non-bond RC member subjected to two-directional lateral force with axial force ratio of 0.02 experienced yielding state, when lateral displacement moves in non-yielding area, the members show similar behavior regardless of the route of given displacement.
- Considering the route of lateral transformation of non-bond RC member subjected to two-directional lateral, when appearing an area of damage in the concrete section, direction of deformation is not same with that of force increment but directed toward to severe damage area.

References:

- Akiyama, H. (1985). *Earthquake-Resistant Limit-State Design for Buildings*. University of Tokyo Press, Tokyo, Japan.
- Takiguchi, K., Kokusho, S., K., Ishida, A., and Kimura, M. (1979), "Study on the Restoring Force Characteristics of Reinforced Concrete Columns to Bi- Directional Displacements, Part 1 Development and Examination of Loading Apparatus for Testing Reinforced Concrete Columns Subjected to Bi- Directional Horizontal Force and Axial Force," *Journal Structural and Construction Engineering*, Architectural Institute of Japan, 286,29-35,(in Japanese).
- Takiguchi, K., (1977), "Deforming Characteristics of RC Members with and Without Bond. II," *Transaction of the Architectural Institute of Japan*, Architectural Institute of Japan, 262,53-59(in Japanese).
- Takiguchi, K., Okada, K., Sakai, M. (1976), "Deforming Characteristics of RC Members with and without Bond," *Transaction of the Architectural Institute of Japan*, Architectural Institute of Japan, 249,1-10(in Japanese).
- Takizawa, H., and Aoyama, H. (1976). Biaxial effects in modeling earthquake response of R/C structures. *Earthquake Engineering and Structural Dynamics*, Vol.4, 523-552.

FIBER ELEMENT ANALYSIS OF REINFORCED CONCRETE C-BENT COLUMNS

S. Nagata¹⁾, K. Kawashima²⁾, and G. Watanabe³⁾

1) Graduate Student, Department of Civil Engineering, Tokyo Institute of Technology, Japan

2) Professor, Department of Civil Engineering, Tokyo Institute of Technology, Japan

3) Research Associate, Department of Civil Engineering, Tokyo Institute of Technology, Japan
nseiji@cv.titech.ac.jp, kawashima@cv.titech.ac.jp, gappo@cv.titech.ac.jp

Abstract: This paper presents a series of fiber element analysis to reproduce experimental behavior of RC C-bent columns under cyclic and seismic excitations. In the fiber element analysis, the plastic hinge region of column was idealized by a fiber element to compute flexural hysteresees. A torsional behavior is represented by a rotational spring, assuming that the torsional and the flexural hysteresees are independent. The analysis provides a good numerical simulation in the longitudinal direction, while it does not correlate well in the longitudinal direction.

1. INTRODUCTION

In urban areas, some special bridges such as C-bent columns have been constructed due to limitation of the utilized space. C-bent columns are subjected to an eccentric dead load of the superstructure. A side of the eccentricity and the other side of the eccentricity are subjected to compression and tension, respectively, due to the dead load of the superstructure. They are called hereinafter the eccentric compression side and the eccentric tension side, respectively.

According to experimental studies on RC C-bent Columns, it was found that the eccentricity of the columns resulted in a large residual displacement in eccentric compression side under a strong excitation (Kawashima and Unjoh 1994, Tsuchiya et al. 1999, Kawashima et al. 2003, Nagata and Kawashima et al. 2004). The damage of the columns and the residual displacement under the bilateral excitation are more extensive than those under the unilateral excitation. In analytical studies, Tsuchiya et al revealed that the fiber element analysis correlates with good accuracy the experimental hysteresees and the progress of the residual displacement under unilateral cyclic loading in longitudinal direction (Tsuchiya et al. 1999).

In this study, to reproduce the experimental response of RC C-bent columns under the bilateral cyclic and seismic excitation, a fiber element analysis was conducted.

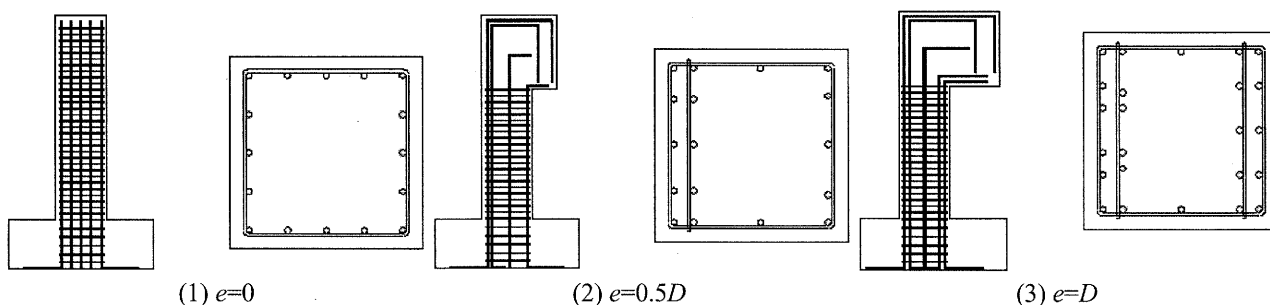


Figure 1 Model Columns

Table 1 Test Specimens

(1) Cyclic Loading Test			
Eccentricity e	0	$0.5D$	D
Longitudinal reinforcement ratio (%)	1.27	1.35	1.9
Tie reinforcement ratio (%)	0.79	0.99	1.19
Longitudinal reinforcement strength (MPa)	486		
Tie reinforcement strength (MPa)	492		
Concrete Strength (MPa)	31.3	27.1	25.5
(2) Hybrid Loading Test			
Eccentricity e	0	$0.5D$	D
Longitudinal reinforcement ratio (%)	1.27	1.35	1.9
Tie reinforcement ratio (%)	0.79	0.99	1.19
Longitudinal reinforcement strength (MPa)	481		
Tie reinforcement strength (MPa)	486		
Concrete Strength (MPa)	31.2	29.1	28.6

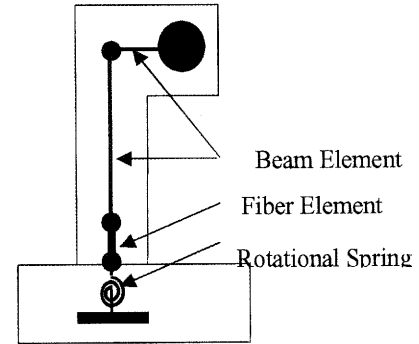


Figure 2 Fiber Model

2. TEST SPECIMENS AND ANALYTICAL MODEL

2.1 Test Specimens

Model columns without an eccentricity and with the eccentricities of $0.5D$ and D (D : width of the columns) were used in the cyclic and hybrid loading tests as shown in Table 1 and Figure 1. They were designed in accordance with the current Japanese seismic design codes assuming that they are “small prototype” columns. They have a 400 mm \times 400mm square cross section with an effective height from the bottom to the loading point of 1350mm.

The cyclic and hybrid loading tests were conducted using the dynamic testing facility with a vertical and two lateral actuators in the Tokyo Institute of Technology. Since the lateral actuators in the longitudinal direction as well as the actuator in the vertical direction was set apart from the column center with an eccentricity, it is noted that a torsion occurred in the columns as a result of the eccentricity in the both cyclic and hybrid loading tests.

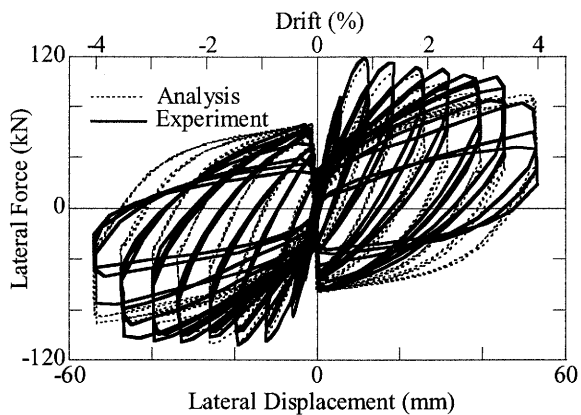
In the Cyclic loading test, under a constant vertical load of 160 kN, which induced a stress 1 MPa at the plastic hinge of the column, a rectangular orbit was used. Amplitude of the lateral displacement was stepwisely increased from 0.5% drift until failure with an increment of 0.5% drift. Three cyclic loading were conducted at each step.

In the hybrid loading test, the columns were subjected to a bilateral excitation under a constant vertical load of 160 kN. The ground acceleration recorded at JMA Kobe Observatory during the 1995 Kobe earthquake was used as an input motion by scaling down its intensity to 30% of the original. NS and EW components were used in the longitudinal and transverse directions, respectively.

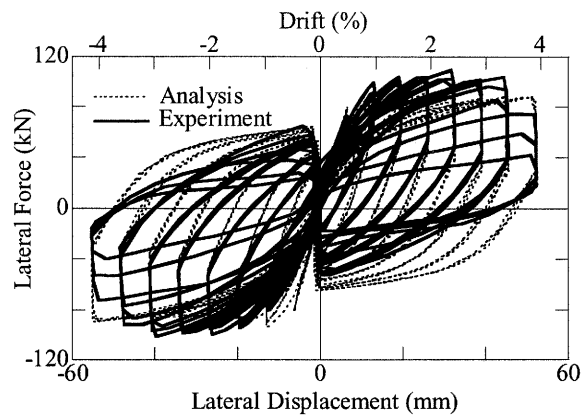
2.2 Analytical Model

To simulate the experimental behavior of the columns, the column was modeled as shown Figure 2. The plastic hinge zone was idealized by a fiber element. The effect of deformation of longitudinal bars in the footing was represented by a rotational spring at the bottom of the columns. The stress vs. strain relation of confined concrete was assumed based on a model by Hoshikuma and Kawashima et al (Hoshikuma and Kawashima et al. 1997). Unloading and reloading hysteresees were idealized based on a model by Sakai and Kawashima (Sakai and Kawashima 2000). The modified Menegotto-Pinto model (Menegotto and Pinto 1973, Sakai and Kawashima 2003) was used to idealize the stress vs. strain relation of the reinforcements.

A torsional behavior is idealized by a linear rotational spring using the gross section stiffness. Although torsion and bending interact each other in the experiment (Otsuka et al. 2003, Tirasit and Kawashima 2005), the flexural and torsional behaviors are assumed to be independent in this analysis.

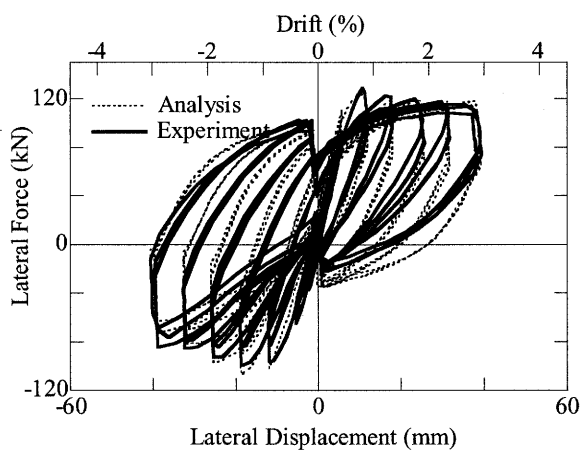


(a) Transverse Direction

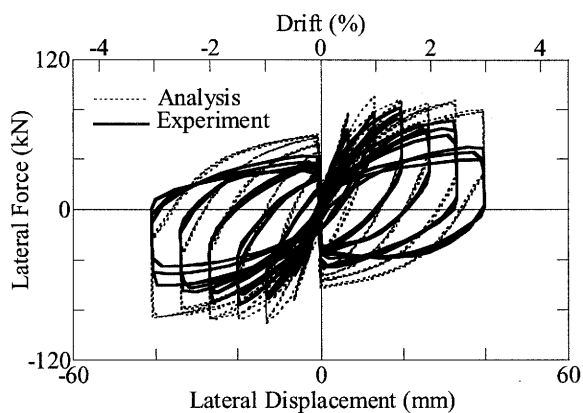


(b) Longitudinal Direction

(1) $e=0$

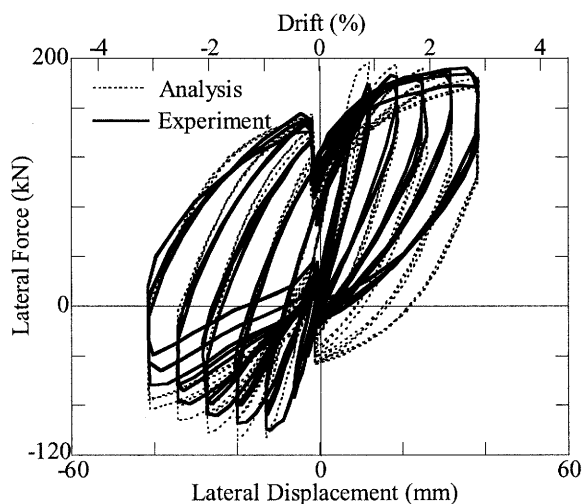


(a) Transverse Direction

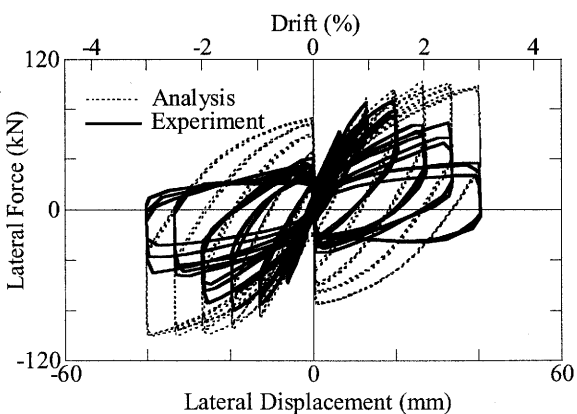


(b) Longitudinal Direction

(2) $e=0.5D$



(a) Transverse Direction



(b) Longitudinal Direction

(3) $e=D$

Figure 3 Comparison of Lateral Force vs. Lateral Displacement Hystereses between Experiment and Analysis

3. ANALYSIS FOR THE CYCLIC LOADING TEST

3.1 Experimental Behavior under the Cyclic Loading

Figure 3 shows the lateral force and lateral displacement hysteresses of the column without an eccentricity and the columns with eccentricities of $0.5D$ and D under the cyclic loadings. The computed hysteresses which will be discussed later are also presented here. The restoring force in the transverse direction reaches the maximum strength of 120 kN at 1 % drift, and it deteriorates significantly at 2nd and 3rd excursions in 3.5 % drift. This is because not only concrete but also reinforcements suffered significant damage at all surfaces of the column in the 3.5 % drift loading. On the other hand, the restoring force in the longitudinal direction reaches the maximum strength of 109 kN at 2.5 % drift. A sudden deterioration of the restoring force occurs at 3.5 % drift.

In the column with eccentricities of $0.5D$ and D , the restoring force in the eccentric compression side (negative side in the transverse direction) is lower than that in the eccentric tension side (positive side in the transverse direction), due to effect of the eccentric dead load. The maximum strength in the eccentric compression side was 99 kN and 100 kN, while that in the eccentric tension side was 127 kN and 192 kN, respectively, in the columns with the eccentricities of $0.5D$ and D , respectively. It is obvious that difference of the restoring force between the eccentric compression and tension sides increases as the eccentricity increases. On the other hand, in the longitudinal direction, the restoring force reaches the maximum strength of 81 kN and 87 at 1.5 % drift, and it deteriorates from 2 % drift loading in the column with eccentricities of $0.5D$ and D , respectively.

Failure modes of the columns are not shown here because of the space limitation. The compression failure of concrete was earlier and more extensive in the eccentric compression side than the other sides in the columns with eccentricities of $0.5D$ and D , while damage level was almost same at all surfaces in the column without an eccentricity.

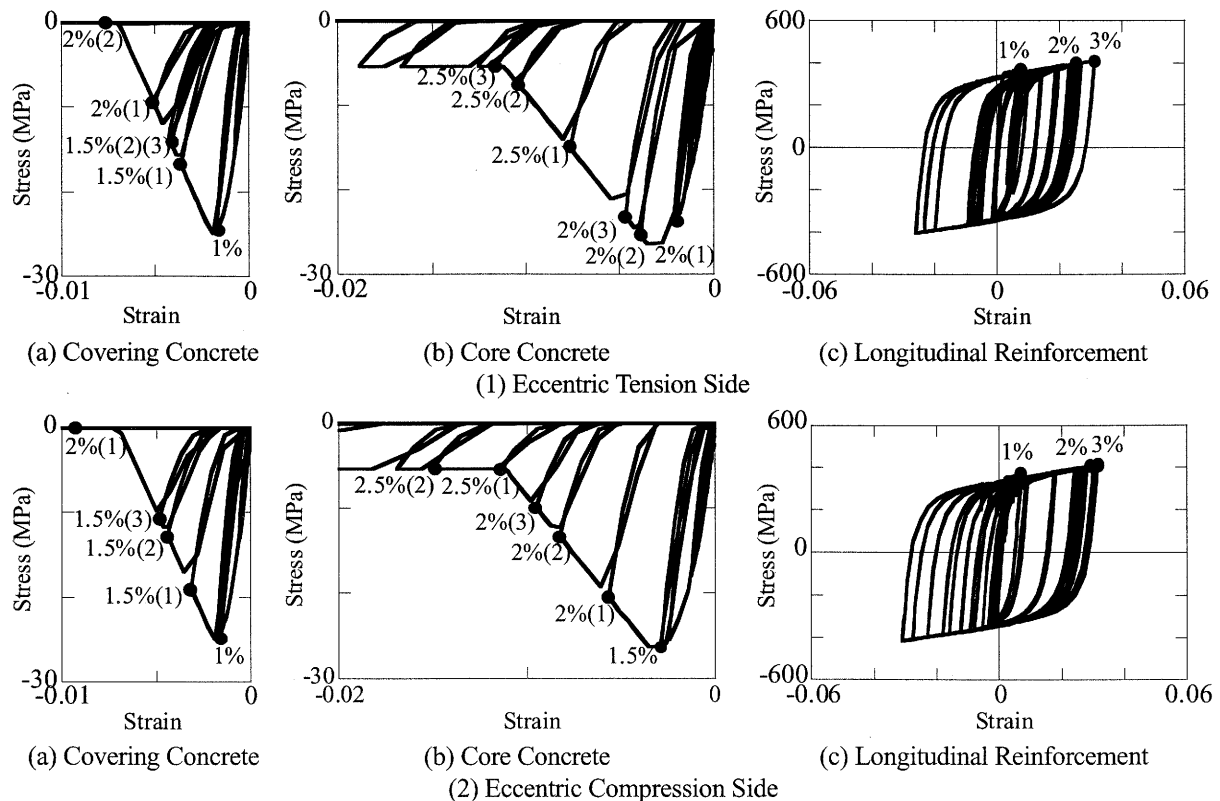


Figure 4 Computed Stress vs. Strain Hysteresses of a Column with an Eccentricity of D subjected to Cyclic Loading (numbers of parentheses represent the number of loading excursions)

3.2 Analytical Correlations on the Cyclic Loading Test

The analytical hysteresis of the column without an eccentricity are close to the experimental results until 3.5 % drift, the restoring force in both the transverse and longitudinal directions as shown in Figure 3. Since the effect of local buckling and rupture of main reinforcements is not include in the analysis, the hysteresis after 3.5 % drift are not accurately predicted.

On the other hand, in the column with eccentricities of $0.5D$ and D , the fiber element analysis provides a good numerical simulation in the transverse direction, while it does not correlate well in the longitudinal direction. The computed restoring force in the longitudinal direction became larger than the experimental results after 2 % drift. This is probably because the effect of interaction between torsion and bending is not included in the analysis.

Figure 4 shows the computed stress vs. strain hysteresses of the covering and core concrete, and longitudinal bar at the eccentric tension and compression sides. Progress of the strain of the covering and core concrete is earlier at the eccentric compression side than tension side.

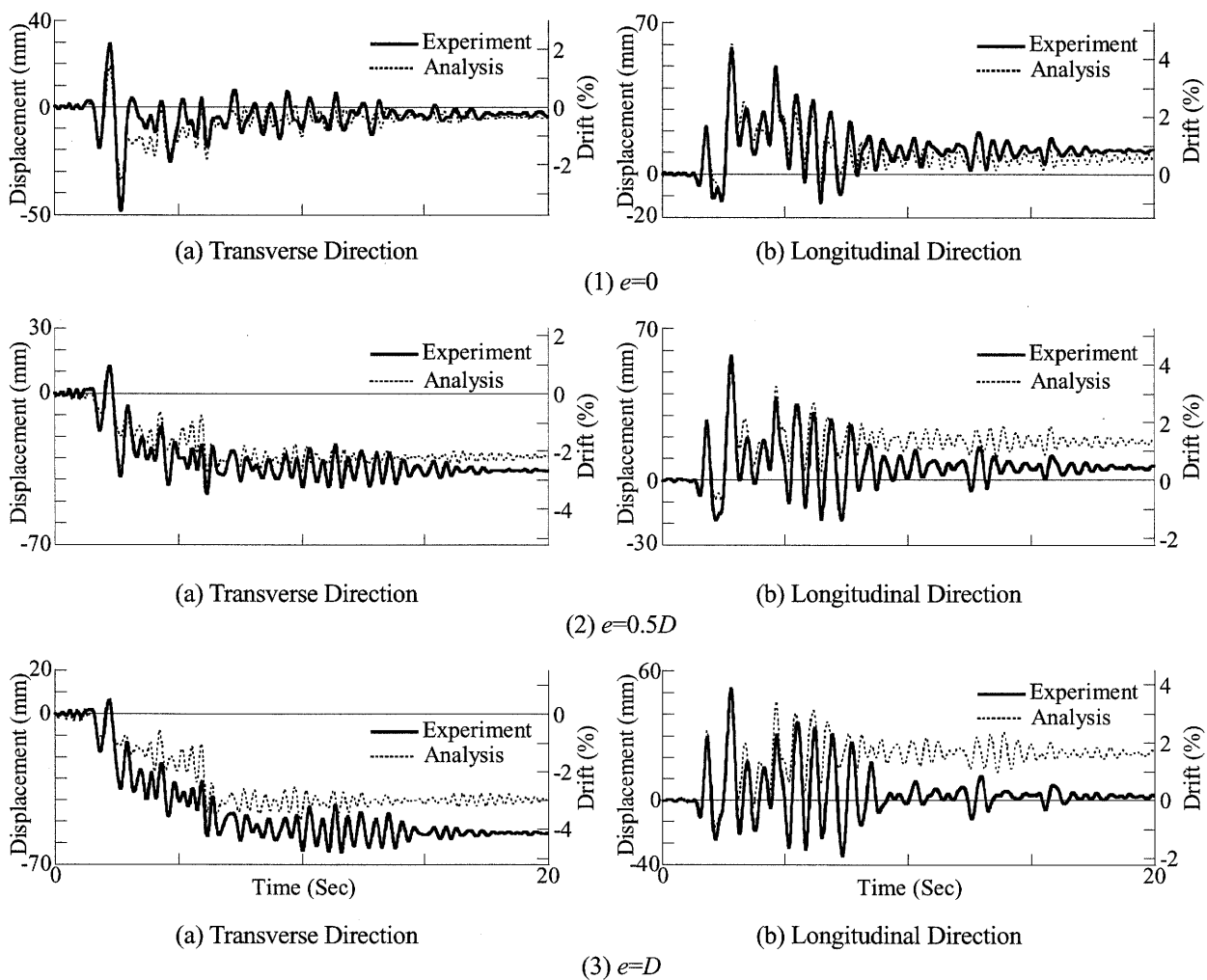


Figure 5 Comparison of Displacement Response between Experiment and Analysis

4. ANALYSIS FOR THE HYBRID LOADING TEST

4.1 Experimental Response under Hybrid Loading

Figure 5 and 6 show the displacement responses and the lateral force vs. lateral displacement hysteresses of the columns without an eccentricity and with eccentricities of $0.5D$ and D under the ground motion excitation. The computed responses which will be described later are also presented

here. In the columns without an eccentricity, the maximum displacement was -3.6 % and 4.3 % drift, and residual displacement was -0.2 % and 0.8 % drift in the transverse and longitudinal direction, respectively. Residual drift was not significant in the both directions. The strength of the column was -124 kN and 117 kN in the transverse and longitudinal directions, respectively. Significant deteriorations of the restoring force did not occur. After the excitation, flexural cracks occurred at all surfaces of the column. However, longitudinal and ties bars suffered no visible damage.

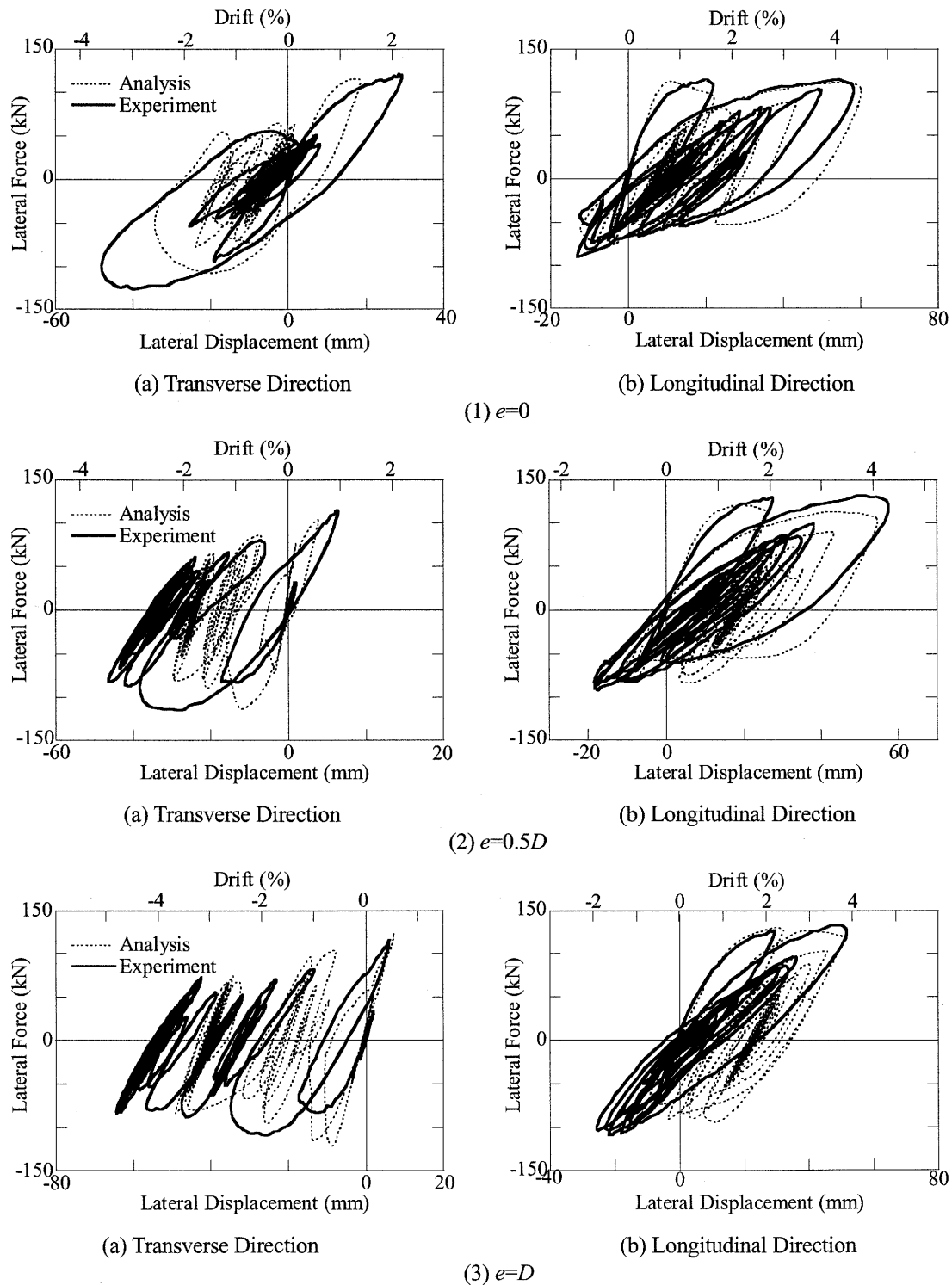


Figure 6 Comparison of Lateral Force vs. Lateral Displacement Hystereses between Experiment and Analysis

On the other hand, the maximum displacement in the transverse direction was -3.6 % and 4.6 % drift in the column with eccentricities of $0.5D$ and D , respectively. A remarkable feature of the C-bent columns is progress of a large residual displacement in the eccentric compression side (negative side in the transverse direction). The residual displacement was 2.7 % and 4.1 % drift in the column with eccentricities of $0.5D$ and D , respectively. The residual displacement in the eccentric compression side increases as the eccentricity increases. In the longitudinal direction, the maximum displacement was 4.2 % and 3.9 % drift in the column with eccentricities of $0.5D$ and D , respectively. Residual displacement in the longitudinal direction was not significant in the both columns.

The strength in the transverse direction was -116 kN and -117 kN in the columns with the eccentricities of $0.5D$ and D respectively. The strength in the longitudinal direction was 129.8 kN and 133.6 kN in the columns and with the eccentricities of $0.5D$ and D , respectively. Significant deteriorations of the restoring force did not occur in the both columns.

After the tests, spalling off of the covering concrete as well as flexural cracks occurred at the surface in compression side in the columns with eccentricities of $0.5D$ and D . The damage becomes extensive as eccentricity increases. Longitudinal bars suffered no visible damage in the columns.

4.2 Analytical Correlations on the Hybrid Loading Test

The analytical response and hysteresees of the column without an eccentricity are close to the experimental results in both the transverse and longitudinal directions as shown in Figure 5 and 6.

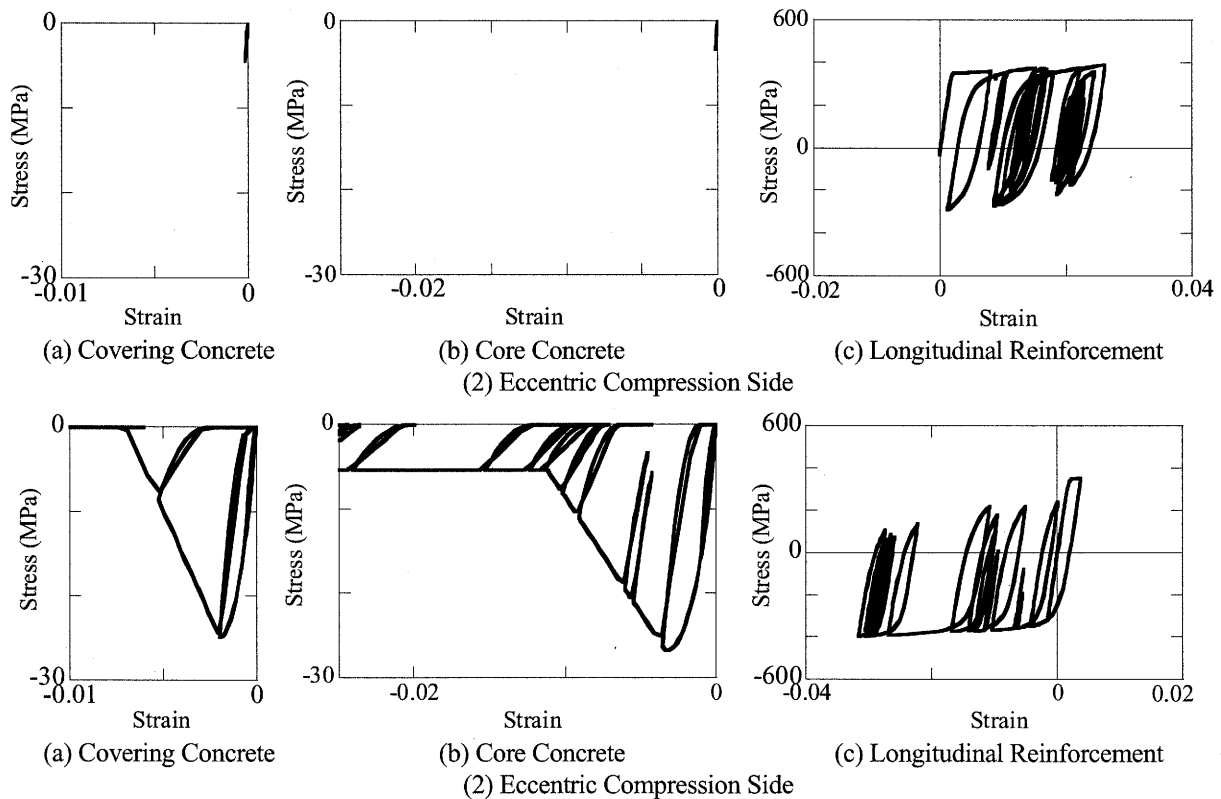


Figure 7 Computed Stress vs. Strain Hysteresees of a Column with an Eccentricity of D subjected to Seismic Excitation

On the other hand, in the columns with eccentricities of $0.5D$ and D , the analysis correlates the accumulation of residual displacement in the eccentric compression side. However, the analysis underestimates the residual displacement. The residual displacement computed by the fiber model is 0.6 % and 1.1 % drift smaller than the experimental results, in the columns with the eccentricities of $0.5D$ and D , respectively. In the longitudinal direction, although the agreement of the analysis and experiment during the peak response is good, the residual drift which became predominant after the

peak response is 0.6 % and 1.1 % drift larger in the analysis than the experiment, in the columns with the eccentricities of $0.5D$ and D , respectively. Prediction on the residual displacement requires further improvements.

Figure 7 shows the computed stress vs. strain relations of covering and core concrete, and axial bars at the eccentric tension and compression sides in the column with eccentricity of D . Because the covering and core concrete at the eccentric tension side is subjected to tension, stress was limited during the entire duration of the excitations, while stress of the covering and core concrete was extensive at the eccentric compression side. In the hysteresses of reinforcement, extensive stress in tension and compression developed in the eccentric tension and compression sides, respectively.

5. CONCLUSIONS

To reproduce the experimental response of RC C-bent columns under the bilateral cyclic and seismic excitation, a fiber element analysis was conducted. The following conclusions may be derived from the results presented herein.

- (1) From the analysis on the cyclic loading, the fiber model provides a good numerical simulation in the transverse direction, while it does not correlate well in the longitudinal direction. The computed restoring force in the longitudinal direction became larger than the test results after 2 % drift.
- (2) From the analysis on the hybrid loading tests, the analysis correlates the accumulation of residual drift in the eccentric compression side. However, the analysis underestimates the residual drift. In the longitudinal direction, although the agreement of the analysis and experiment during the peak response is good, the residual drift is larger in the analysis than the experiment.

Acknowledgements:

The authors express their sincere appreciation to Messrs Hayakawa, R. and Fukuda, T., Tokyo Institute of Technology for conducting the fiber element analysis.

References:

- Kawashima, K. and Unjoh, S. (1994), "Seismic Response of Reinforced Concrete Bridge Piers subjected to Eccentric Loading," *Proc. of 9th Japan Earthquake Engineering Symposium*, 1477-1482, Tokyo, Japan.
- Tsuchiya, T., Ogasawara, M., Tsuno, K., Ichikawa, E. and Maekawa, K. (1999), "Multi-axis Flexure Behavior and Nonlinear Analysis of RC Columns subjected to Eccentric Axial Forces," *J. of Materials, Concrete Structure, Pavements*, JSCE, No. 634/V-45, 131-143.
- Kawashima, K., Watanabe, G., Hatada, S. and Hayakawa, R. (2003), "Seismic Performance of C-bent Columns based on a Cyclic Loading Test," *J. of Structural Mechanics and Earthquake Engineering*, JSCE, No. 745/I-65, 171-189.
- Nagata, S., Kawashima, K. and Watanabe, G. (2004), "Seismic Performance of RC C-bent Columns based on a Hybrid Loading Test," *Proc. of 1st International Conference on Urban Earthquake Engineering*, 409-416, Tokyo, Japan.
- Hoshikuma, J., Kawashima, K., Nagaya, K., and Taylor, A., W. (1997), "Stress-Strain Model for Confined Reinforced Concrete in Bridge Piers," *J. of Structural Engineering*, ASCE, 123(5), 624-633.
- Sakai, J. and Kawashima, K. (2000), "An Unloading and Reloading Stress-Strain Model for Concrete confined by Tie Reinforcements," *Proc. of 12th World Conference of Earthquake Engineering*, 1432 (CD-ROM), Auckland, New Zealand.
- Menegotto, M. and Pinto, P.E. (1973), "Method of Analysis for Cyclically Loaded R.C. Plane Frames including Changes in Geometry and Non-Elastic Behavior of Elements under Combined Normal Force and Bending," *Proc. of IABSE Symposium on Resistance and Ultimate Deformability of Structures Acted on by Well Defined Repeated Loads*, 15-22.
- Sakai, J. and Kawashima, K. (2003), "Modification of the Giuffre, Menegotto and Pint Model for Unloading and Reloading Paths with Small Strain Variations," *J. of Structural Mechanics and Earthquake Engineering*, JSCE, No. 738/I-64, 159-169.
- Otsuka, H., Takeshita, E., Wang, Y., Yabuki, W., Tsunomoto, M. and Yoshimura, T. (2003), "Study on the Seismic Performance of Reinforced Concrete Columns subjected to Torsional Moment, Bending Moment and Axial Force," *J. of Earthquake Engineering*, JSCE, Vol.27, 67 (CD-ROM), Osaka, Japan.
- Tirasit, P., Kawashima, K. and Watanabe, G. (2005), "Seismic Performance of RC Columns under Cyclic Bending-Torsional Loading," *Proc. of the 8th Symposium on Ductility Design Method for Bridges*, 325-332, Tokyo, Japan.

SIMPLIFIED TRUSS MODEL FOR SHEAR CARRYING CAPACITY ANALYSIS OF NON-RECTANGULAR CROSS SECTIONAL PC SLENDER BEAMS

M. Lertsamattiyakul¹⁾, J. Niwa²⁾, S. Tamura³⁾, and Y. Hamada³⁾

1) Graduate student, Department of Civil Engineering, Tokyo Institute of Technology, Japan

2) Professor, Department of Civil Engineering, Tokyo Institute of Technology, Japan

3) Research Engineer, Research and Development Center, DPS Bridge Works Co., Ltd., Japan
96b31110@cv.titech.ac.jp, jniwa@cv.titech.ac.jp, s_tamura@dps.co.jp, y_hamada@dps.co.jp

Abstract: In this study, the simplified truss model with a small number of degrees of freedom has been proposed for evaluating the shear carrying capacity of prestressed concrete (PC) slender beams with non-rectangular cross section. The shear compression failure in PC slender beams without transverse reinforcement is confirmed based on the parametric study using FEM analysis. The changes of critical stress flow due to the variations of influential parameters are investigated and incorporated to the modeling. By utilizing the equivalent elastic analysis, the shear carrying capacity can be simply calculated with high accuracy in prediction comparing with the experimental data.

1. INTRODUCTION

Without doubt, the prestressed concrete (PC) members, presently, become the important structures because of their high shear resistance and reduction of dead load to the substructures. When the earthquake occurred, it is necessary to confirm that the shear failure of PC superstructures does not take place before the development of hinge in the columns. Therefore, the analytical methods should yield not only the comprehensive failure mechanism, but also the accurate prediction of shear carrying capacity of PC members. Different from the reinforced concrete (RC) beams, even PC slender beams where shear span to effective depth ratio, a/d , is greater than or equal to 2.5, it is usually observed that, they fail in the shear compression mode of failure. That is, after the diagonal cracks occurred, the beams yield the resistance due to the arch action until the crushing of concrete occurred.

For the current methods in evaluating the shear carrying capacity of PC slender beams, the decompression moment method recommended by JSCE (JSCE 2002) is given. Without the consideration of stress distribution, the scatter and quite conservative predicted results are usually observed. Moreover, M_{cr} method (Ito et al. 1994) is the method considering the resistance at the flexural cracking as the extra to the shear resistance due to the contribution of compression. It was indicated that no comprehensive explanation is given about how the resistance at the flexural cracking remains until the ultimate stage can be obtained.

In this research, the parametric study using the finite element method (FEM) has been performed to investigate the failure mechanism of PC slender beams influenced by the variations of many parameters. The tendencies of change of stress flows obtained from the analytical results are summarized and applied to propose the analytical model, named *the simplified truss model*. In order to verify its applicability, the proposed model is used to evaluate the shear carrying capacity of non-rectangular cross sectional PC slender beams. The analytical targets in this study are PC slender beams with I- and T-shaped cross section without transverse reinforcement.

2. PARAMETRIC STUDY

2.1 Finite Element Analysis

In order to examine the failure mechanism of PC slender beams with non-rectangular cross section, finite element analysis has been conducted. A PC slender beam with I-shaped cross section is applied as the representative of beams with non-rectangular cross section. A half of beam is modeled with an 8-node quadrilateral isoparametric plane stress element in a two dimensional (2D) configuration as shown in Figure 1. Even though there is the discontinuity between flange and web in non-rectangular cross sectional PC beams, 2D model is considered to be applicable to predict their failure mechanism. In this analysis, the smeared crack model is used as the crack model to concrete elements. As the constitutive models under compressive and tensile stress states, Thorenfeldt's model (Thorenfeldt et al. 1987) and Hordijk's model (Hordijk 1991) are applied, respectively. The yield conditions of Drucker-Prager and Rankine are correspondingly used as the failure criterions for compression and tension. The bilinear elasto-plastic model of steel is employed for the longitudinal reinforcement. Details of geometric properties of model are mentioned in the figure. Here, b_f and b_w stand for widths of flange and web, respectively. And r_l and r_s represent the width of loading plate and support, respectively.

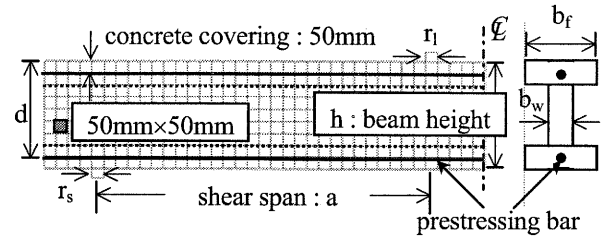


Figure 1 FEM of PC slender beam with non-rectangular (I shaped) cross section

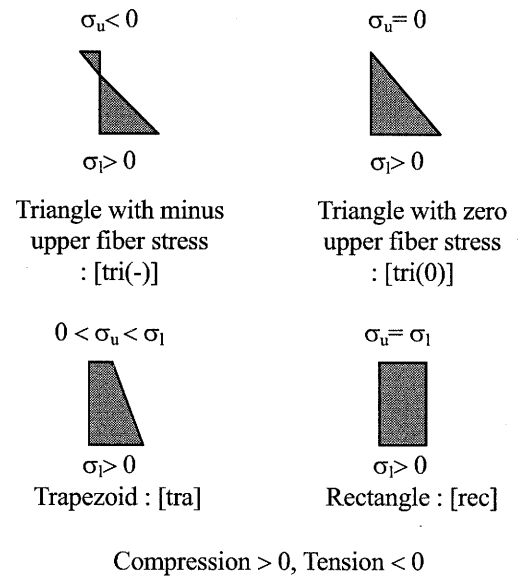


Figure 2 Types of stress distribution due to the prestressing forces

2.2 Influential Parameters

The parameters, which are considered to effect to shear failure mechanism, are varied as follows. The prestressing force, P , in upper and lower prestressing bars are proportionally adjusted to produce 4 types of stress distribution as shown in Figure 2. These 4 types of stress distribution are triangle with minus (tension) upper fiber stress [tri(-)], triangle with zero upper fiber stress [tri(0)], trapezoid [tra], and rectangle [rec]. The upper and lower fiber stresses are expressed in terms of σ_u and σ_l , respectively. They are correspondingly varied in the ranges of $-2 \sim 5$ and $1 \sim 15$ MPa. In this study, the prestressing levels under compression and tension are expressed in terms of plus and minus values, respectively. The value of σ_u is set not to generate the cracks at the upper portion of the beams ($\leq f_t$: tensile strength of concrete). Whereas, the values of σ_l is set based on the permissible stress ($= 15$ MPa) in Specification of Highway Bridges (Japan Road Association 2002). Different to PC beams with rectangular cross section, the effect of flange to the failure mechanism cannot be neglected. Thus, the ratios of widths of flange and web, b_f/b_w , are varied from 2.0 to 4.0. The values of the shear span to effective depth ratio, a/d , the effective depth, d , and the compressive strength of concrete, f_c' , are also considered as the parameters influence the shear behavior. The values of a/d are changed from 2.5 to 4.5 with the variation of d from 300 to 600 mm. The compressive strength varying from 30 to 80 MPa is employed. The width of web, b_w , is changed to be 50 or 150 mm. Prestressing bars of $\phi 36$ (cross sectional area: $A_{sp} = 1018 \text{ mm}^2$) is applied to upper and lower bars for all cases (longitudinal reinforcement ratio: $\rho_w = 1.7 \sim 5.1\%$ and yield strength: $f_{py} = 930$ MPa).

2.3 Tendency of Failure Mechanism

From all cases of analytical results, it is observed that, after the diagonal crack occurred ($\varepsilon_1 \leq -0.0001$), the beams still provided the compressive resistance. They failed by the crushing of concrete ($\varepsilon_2 \geq 0.002$) in the web portion or the intersection region between flange and web. This kind of failure is called shear compressive mode of failure. In order to apply the analytical results to propose the model, the tendency of slope of critical stress flow is investigated. Similar to the process done in the previous study (Lertsamattiyakul et al. 2004), the trend of slope of critical stress flow can be assessed based on the consideration of the principal stress, σ_2 , at each Gauss's point at 90% of shear carrying capacity ($90\%V_{max}$). Figure 3 demonstrates the marked location of the maximum absolute values of σ_2 of each horizontal level, σ_{2i-max} , between the upper and lower bars. By considering the location of σ_{2i-max} as the co-ordination in X-Y axes, (x_i, y_i) , the correlation coefficient is calculated from the equation as shown in the figure. This parameter expresses the agreement between the estimated equation and the selected data. A part of Gauss's points, which gives a high value of correlation coefficient (≥ 0.95), is chosen. The concentrated stress flow is assessed as the estimated expression of chosen Gauss's points. In order to adopt these results to the modeling, the concentrated stress flow is evaluated in terms of m , where $m = \cot\theta$ and θ is an angle of the estimated slope of the concentrated stress flow.

Figure 4 shows the contour figures of principal stress σ_2 at $90\%V_{max}$ of PC beams under [tri(0)]. The values of σ_1 are changed from 3 to 12 MPa as the examples. It is found that, with the increase in value of σ_1 , the inclination of concentrated stress flow becomes steeper, that is, m decreases. When the value of σ_1 becomes comparatively large, the concentration of steep stress flow becomes weak, while the stress curvedly transferring to the support becomes critical. In the case like this, the evaluated slope of concentrated stress flow becomes different from the other case that is value of m decreases with the increase in value of σ_1 . In order to conclude the same tendency of value of m , the steep stress flow is used and the evaluation of m for the case like this is determined in the horizontal range of d from the loading point.

In Figure 5, the difference in types of stress distribution (different value of σ_u) is shown. Similar to the change in values of σ_1 , with the increase in value of σ_u , the slope of concentrated stress flow becomes steeper. With the greater value of σ_u , the stress flow curvedly transferring to the support becomes stronger. It can be said that the effect due to σ_u cannot be as the difference of critical stress flow. The value of m decreases with the increase in the value of σ_u . As the example, the relationships between m and σ_1 with σ_u varying with the values of b_f/b_w are summarized and approximated in Figure 6. The parameter σ_m is set to express the main effect of σ_1 with the additional

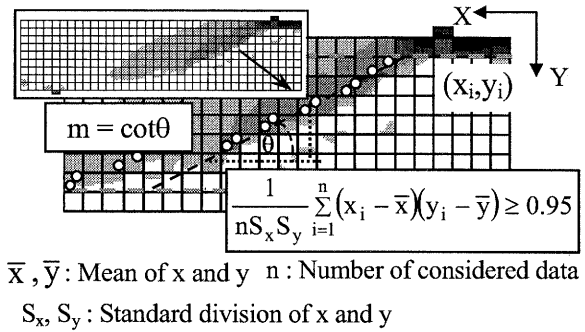


Figure 3 Evaluation of slope of concentrated stress flow in terms of m

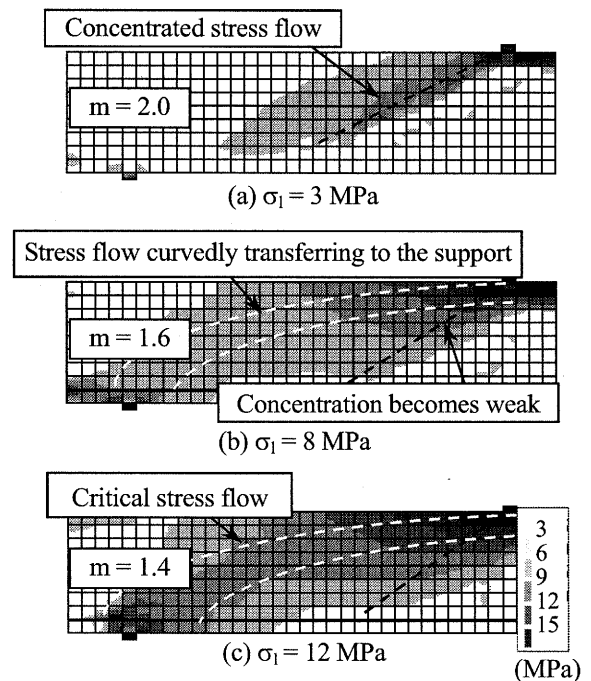


Figure 4 Contour figures of σ_2 at $90\%V_{max}$ (variation of σ_1 : $\sigma_u = 0$ MPa, $a/d = 3.5$, $d = 400$ mm, $b_f/b_w = 2.0$, $b_w = 150$ mm and $f'_c = 40$ MPa)

effect of σ_u . The relationships between m and the other influential parameters, a/d , d , b_f/b_w and f_c' are also summarized. It is noted that the values of m turn to be larger with the increase in values of a/d and f_c' , while the value of d has a slight effect on the value of m . The value of b_f/b_w is inversely proportional to value of m . Without discontinuity for cases of beam with rectangular cross section ($b_f/b_w = 1.0$), all relationships between m and influential parameters can be approximated incorporating the values of b_f/b_w . The expression for predicting the slope of the steep stress flow in terms of m can be summarized as Eq. 1. This equation can also be employed for PC beams with rectangular cross section by substituting b_f/b_w with 1.0. The proposal of simplified truss model will be discussed by using this equation as follows.

$$m = 2.55(\sigma_m)^{\frac{3}{5}(\frac{b_f}{b_w})^{-1}} \left(\frac{a}{d}\right)^{\frac{1}{5}} \left(\frac{b_f}{b_w}\right)^{-\frac{1}{5}} \left(\frac{b_f}{b_w}\right)^{\frac{3}{5}} \left(\frac{f_c'}{100}\right)^{\frac{3}{5}} \quad (1)$$

$$\text{where } \sigma_m = \left(1 + 0.2 \frac{\sigma_u}{\sigma_u + \sigma_l}\right) \sigma_l$$

3. THE SIMPLIFIED TRUSS MODEL

In this study, the simplified truss model is proposed for evaluating the shear carrying capacity of PC slender beams with non-rectangular (I- and T-shaped) cross sections. As depicted in Figure 7, the simplified truss model consists of 7 nodes and 11 elements. The model is subjected by the shear force, V , and prestressing forces, P_1 and P_2 . In modeling, 2 struts, members [3] and [4], are simply modeled with the same horizontal interval in the level of flexural tension members ($= k$, where k is a constant). The thicknesses of transverse tension members [5] and [6] are correspondingly set to be the distance from the loading point to the middle point between 2 transverse tension members ($= 1.5k$) and the left distance to the middle point of the support ($= a-1.5k$). The cross sectional area of flexural compression member is set to be $t_f b_f$, where t_f is the thickness of upper flange. The total cross sectional area of longitudinal bars, A_{ps} , is used as the cross sectional area of flexural tension members. The thickness of strut, w , which is considered to be

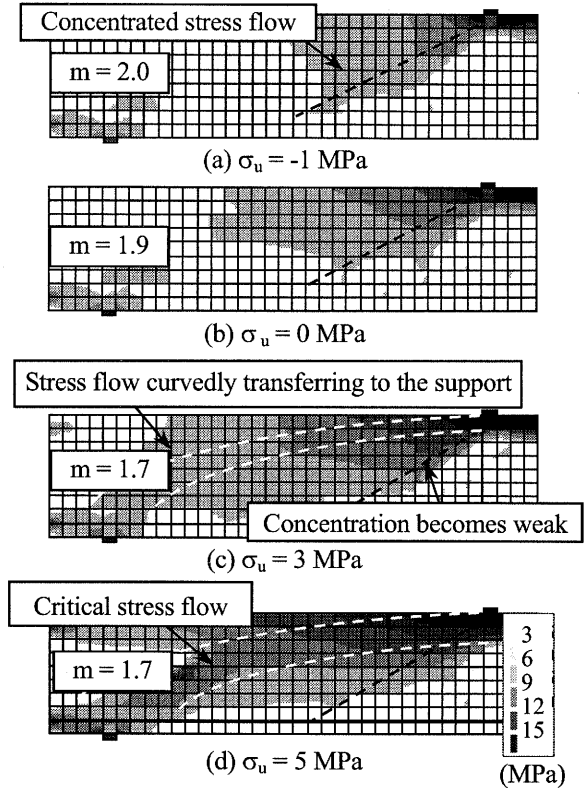


Figure 5 Contour figures of σ_2 at 90% V_{\max} (variation of σ_u : $\sigma_l = 5$ MPa, $a/d = 3.5$, $d = 400$ mm, $b_f/b_w = 2.0$, $b_w = 150$ mm and $f_c' = 40$ MPa)

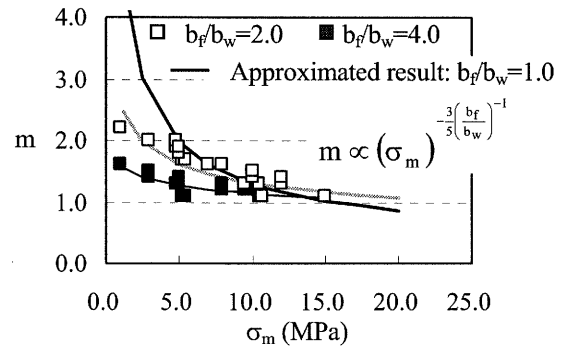


Figure 6 Relationship of m and σ_m (effect of σ_l and σ_u : $a/d = 3.5$, $d = 400$ mm and $f_c' = 40$ MPa)

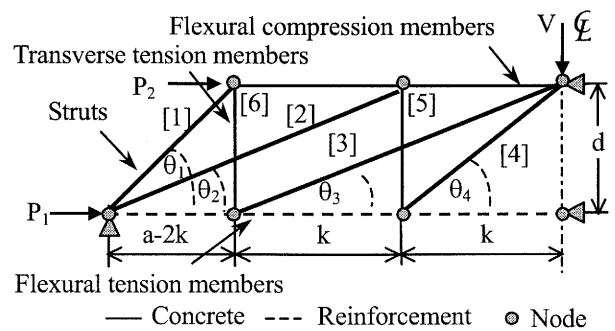


Figure 7 Simplified truss model for a PC beam without transverse reinforcement

important in shear analysis, is investigated in following section.

3.1 Thickness of Strut, w

The value of w is determined from the FEM analytical results identical to the procedure done for case of PC beams with rectangular cross section (Lertsamattiyakul et al. 2004). The way of determination is explained briefly. At $90\%V_{max}$, the stresses in the vertical (Y) direction at each Gauss's points in each horizontal level, σ_{yi} , are considered. The ranges of $0.2d$ inner side of a beam from the upper and lower prestressing bars are investigated. From the distributions of stress σ_{yi} in the vicinity areas to the loading plate and support, the horizontal thickness of stress flow t are assessed. The horizontal thickness of stress flow is determined as the horizontal width of the distribution, t_i , where the ratio of σ_{yi} and the maximum values in that horizontal level, σ_{yi-max} , is equal to 0.3. The obtained horizontal thickness in the vicinity area of a loading point, t_l , and a support, t_s , with the variations of influential parameters are shown as the examples in Figure 8. White and black marks represent the values of t_l and t_s , respectively. It is found that the value of t can be approximated in terms of width of the loading plate, r_l , or support, r_s , the effective depth, d , and the value of b_f/b_w . By substituting b_f/b_w with 1.0, there is no continuity in function of t_l between cases of PC beams with rectangular (Lertsamattiyakul et al. 2004) and non-rectangular. In fact, there should be no discontinuity of values of shear carrying capacity with the change of b_f/b_w . Hence, the value of t_l should be a continuous function that is $(r_l+0.1d)(b_f/b_w)^{1/5}$. The value of t_s are estimated as $2(r_s+0.1d)(b_f/b_w)^{1/5}$. In the proposed model, the members [1] - [2], and members [3] - [4] are considered to be affected by support and loading plates, respectively. The cross sectional area of each strut can be assumed as the values of t_l or t_s multiplied with b_w and its inclination.

3.2 Division of Modeling

By considering the value of m relating with the possible location of the critical strut, the simplified truss model is divided into 2 models as demonstrated in Figure 9. In *Model 1* ($m > 1.0$, Figure 9(a)), the distance md is used as the horizontal distance from the loading point to the ended node of member [3]. When $m \geq 2.0$, the effect of a loading plate is considered to be weak. The cross sectional areas of all struts are summarized in Table 1. The upper bound value of m is set to be $0.9a/d$ in modeling. PC beams with prestressing stress up to medium level are considered to match with this model.

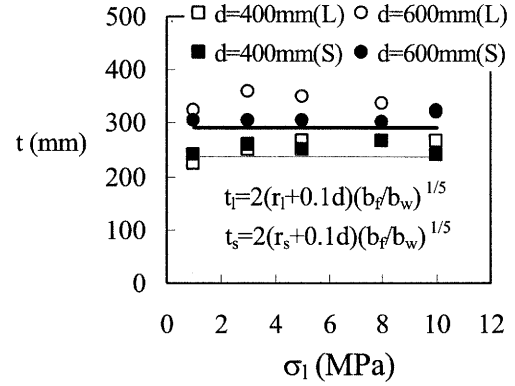


Figure 8 Examples of measured t (variation of σ_1 : $d = 400$ & 600 mm, $b_f/b_w = 4.0$, $\sigma_u = 0$ MPa, $a/d = 3.5$, $r = 50$ mm,)

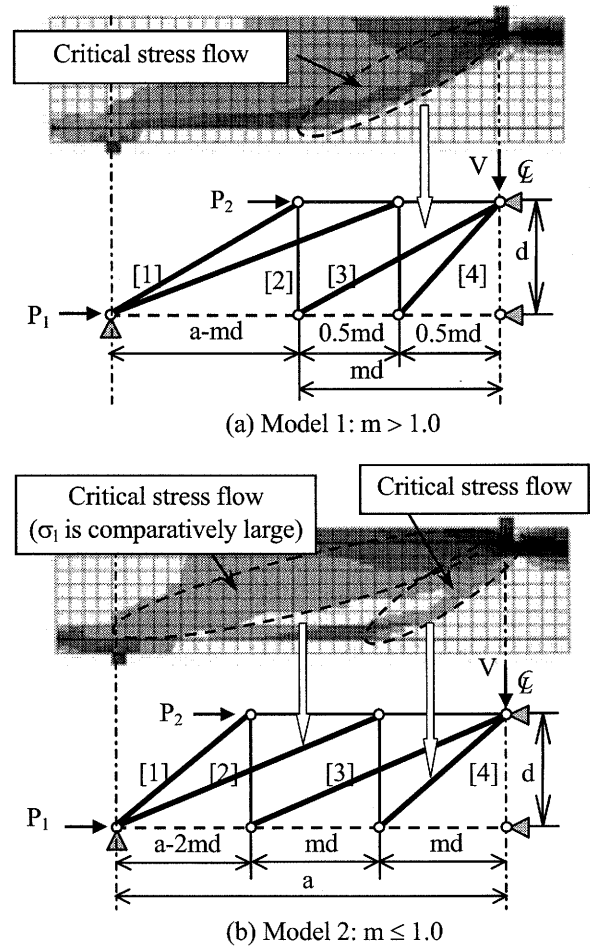


Figure 9 Division of the simplified truss model

Table 1 Cross sectional area of strut and transverse tension members (A_i ; $i = 1-6$)

	A_1 & A_4	A_2 *	A_3	A_5	A_6
Model 1 $m > 1.0$	$A_1 = 2(r_s + 0.1d) \left(\frac{b_f}{b_w} \right)^{\frac{1}{5}} b_w \sin \theta_1$	$2(r_s + 0.1d) \left(\frac{b_f}{b_w} \right)^{\frac{1}{5}} b_w \sin \theta_2$	$(r_1 + 0.1d)b_w \sin \theta_3$	$0.75mdb_w$	$(a - 0.75md)b_w$
Model 1 $m \geq 2.0$			$(a - md)b_w \sin \theta_3$ #		
Model 2 $m \leq 1.0$	$A_4 = (r_1 + 0.1d) \left(\frac{b_f}{b_w} \right)^{\frac{1}{5}} b_w \sin \theta_4$	$mdb_w \sin \theta_2$	$(a - 2md)b_w \sin \theta_3$ #	$1.5mdb_w$	$(a - 1.5md)b_w$

For I-shaped cross section *: $A_2 \geq (a - md)b_w$ and for Model 1 where $\cot \theta_2 < 3.5$, $A_2 \geq 0.5(a - 0.5md)b_w$
 #: $A_3 \leq db_w \sin \theta_3$

In Model 2 ($m \leq 1.0$, Figure 9 (b)), the distance md is adopted as the horizontal distance from the loading point to the ended node of member [4]. Due to the small effect of bearing plates on the size of members [2] and [3], which are expressing the stress flow curvedly transferring to the support, the cross sectional areas are assumed independently from values of t as tabulated in Table 1. This model is considered to suitable for PC beams with comparatively high prestressing stress level.

3.3 Evaluation of Shear Carrying Capacity

The process of evaluation is summarized in Figure 10. In order to simply calculate the shear carrying capacity of PC beams, the equivalent elastic analysis is applied. That is, after modeling by using the value of m , each member force, F_i , caused by the externally applied shear force, V , can be determined by employing the theorem of minimum strain energy. The stiffness of concrete at the ultimate stage as the secant modulus is applied. On the other hand, the resistance of each strut, R_i , can be calculated from f'_c incorporating the concrete softening parameter, η , the cross sectional area, A_i , and the inclination of each member. For simplicity, the practical expression of η is equated with a slight variation from 0.6 to 0.4 in the range of f'_c of 30 to 100 MPa as in Eq. 2.

$$\eta = -0.3 \left(\frac{f'_c}{100} \right) + 0.7 \quad (2)$$

The shear carrying capacity is determined when one of struts becomes critical that is value of F_i/R_i become greatest and equal to 1.0. The components for calculating the shear carrying capacity are expressed in details in the previous study (Lertsamattiyakul et al. 2004).

4. CALCULATED RESULTS AND DISCUSSION

The outlines of the specimens and comparisons between the experimental and calculated results in order to confirm the applicability of the simplified truss model are tabulated in Table 2. By checking the reliability of the test data by using FEM (the experimental results, which are within the range of \pm

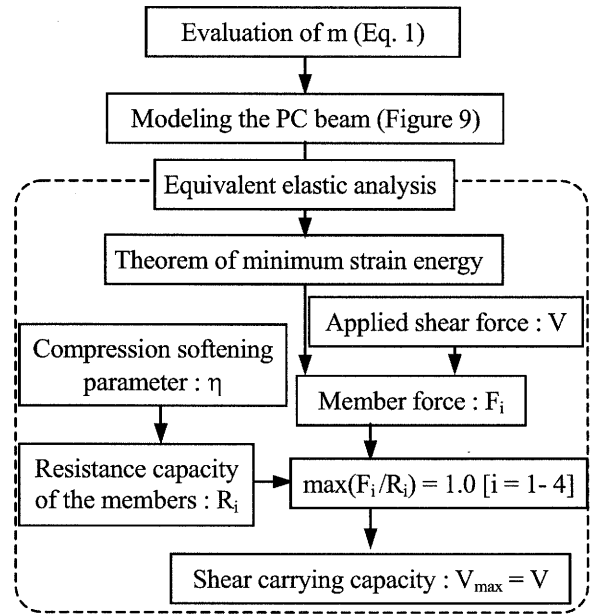


Figure 10 Process in calculating the shear carrying capacity

Table 2 Outline of experimental data and calculated results

Researcher	No.	Specimen	a/d	d (mm)	b _w (mm)	b _f /b _w	f _c (MPa)	σ _u (MPa)	σ ₁ (MPa)	m	V _{exp.} (kN)	V _{cal.} (kN)	V _{exp./} V _{cal.}	Fail
Arthur (1965) (I)	1	A17	4.6	201	51	3.0	38.6	1	9	1.6	32	35	0.91	1
	2	A19	4.6	201	51	3.0	38.6	1	9	1.6	31	34	0.91	1
	3	A22	4.6	201	51	3.0	39.7	1	9	1.7	32	36	0.89	1
	4	B9	3.4	272	51	3.0	40.8	1	10	1.3	38	63	0.60	1
	5	D2	3.9	272	64	2.4	45.2	0	10	1.7	50	68	0.74	3
Elzanaty (1986) (I)	6	CW1	2.9	382	51	4.0	76.6	-3	25	1.3	138	151	0.91	3
	7	CW2	3.8	382	51	4.0	76.6	-3	25	1.6	125	128	0.98	3
	8	CW3	5.0	382	51	4.0	76.6	-3	25	2.0	117	91	1.29	4
	9	CW4	3.8	368	51	4.0	78.6	-3	25	1.6	127	131	0.97	3
	10	CW5	3.8	408	51	4.0	77.9	-3	25	1.6	124	127	0.98	3
	11	CW6	3.8	385	51	4.0	77.6	-2	18	1.7	112	112	1.00	3
	12	CW7	3.8	382	51	4.0	77.9	-2	19	1.7	106	115	0.92	3
	13	CW8	3.8	382	51	4.0	41.4	-2	19	1.2	90	89	1.01	1
	14	CW9	3.8	382	51	4.0	61.0	-2	18	1.5	101	118	0.86	3
Hick (1958) (I)	15	1	3.2	179	38	4.7	37.9	0	14	1.0	32	40	0.80	4
	16	6	5.6	179	38	4.7	37.9	0	14	1.4	29	26	1.12	1
	17	11B	3.9	179	38	4.7	47.6	0	14	1.3	31	33	0.94	2
	18	12	6.2	179	38	4.7	47.6	0	14	1.8	28	27	1.04	1
	19	13B	3.9	179	38	4.7	32.4	0	14	1.0	26	32	0.81	4
	20	15B	3.9	179	38	4.7	43.4	0	14	1.2	34	30	1.13	2
Kar (1969) (I)	21	16	6.2	179	38	4.7	43.4	0	14	1.7	25	25	1.00	1
	22	I-21	3.7	230	50	3.0	35.2	-1	9	1.3	49	48	1.02	1
	23	D-2	3.5	215	50	2.5	35.0	0	7	1.4	43	54	0.80	1
	24	D-5	3.5	215	50	2.5	30.8	0	8	1.2	44	46	0.96	1
	25	D-7	4.0	215	50	2.5	34.5	0	10	1.4	47	45	1.04	1
	26	D-8	4.7	230	50	2.5	34.8	-1	11	1.6	42	43	0.98	1
Sethuna- -rayanan (1965) (I)	27	1	2.8	179	38	4.7	34.5	0	14	0.8	55	53	1.04	4
	28	2	4.3	179	38	4.7	34.5	0	14	1.1	35	32	1.09	1
	29	3	4.6	167	38	4.7	30.5	1	13	1.1	30	26	1.15	1
	30	5	2.5	155	38	4.7	29.9	2	14	0.7	57	54	1.06	3
	31	6	4.9	155	38	4.7	29.9	2	14	1.1	27	23	1.17	2
	32	8	4.3	182	38	3.3	30.7	1	14	1.2	34	30	1.13	1
	33	9	4.2	180	38	4.0	31.6	0	15	1.1	32	31	1.03	1
	34	12	4.3	179	62	2.9	33.9	0	13	1.3	49	44	1.11	1
	35	13B	4.3	179	51	3.5	32.2	0	13	1.2	41	38	1.08	1
	36	14	2.8	179	51	3.5	32.2	0	13	0.9	61	54	1.13	4
	37	15B	4.3	179	38	4.7	29.0	0	14	1.0	32	27	1.19	4
	38	17B	4.3	179	38	4.7	34.5	0	8	1.2	31	27	1.15	1
Sato (1987)(T)	39	3-4	3.3	330	150	3.0	41.7	-3	14	1.2	162	165	0.98	2
	40	3-7	3.3	330	150	3.0	42.3	-5	23	1.1	167	158	1.06	2
													AVE.	1.00
													C.V.	0.13

20% of analytical results, are selected), 40 cases of I- and T- shaped cross sectional PC beams from 6 references are collected (Arthur 1965, Elzanaty et al. 1986, Hick 1958, Kar 1969, Sethunarayanan 1965, Sato et al. 1987). All specimens failed in the shear compression mode of failure. The data consist of wide ranges of geometric properties, that is, the values of a/d vary in the range of 2.5 to 6.2 and the values of d change around 150 to 400 mm. The test data have the ratio of widths of flange and web, b_f/b_w , in the range of 2.5 to 4.7. The values of σ_1 vary from 7.0 to 25.0 MPa including 3 types of stress distribution (except [rec]). The compressive strength of concrete is up to 79 MPa. Since the width of bearing plates was not mentioned, from the observation of pictures of test set up, 50mm is applied as the possible value of width of bearing plates to the data in the studies of Arthur (1965), Hick (1958) and Sethunarayanan (1965). And 100mm is used as the value of width of

bearing plates to the data in the research of Kar (1969). In case that the roller loading was applied, the value of width of the bearing plate is set to be 50 mm in calculation. In Table 2, the number of critical strut mentioned in Figure 7 is declared for each case. It is evident that the calculated results show the good agreement with the experimental results, in many conditions of concrete properties, geometric properties, level of prestressing and type of stress distribution. In Figure 11, the calculated shear carrying capacity by the simplified truss model (*Proposed*) and M_{cr} method (M_{cr}) (Ito et al. 1994) are expressed and compared with the test results. It is apparent that, in the wide range of σ_1 , the proposed model yields the better accuracy and reliability in prediction with an average value (AVE.) of 1.00 and a coefficient of variation (C.V.) of 0.13, while M_{cr} method provides the results which AVE.= 0.85 and C.V. = 0.20.

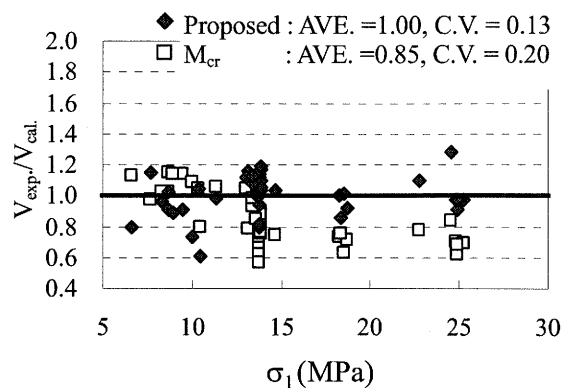


Figure 11 Comparison in shear carrying capacity between the proposed model and M_{cr} method

5. CONCLUSION

The simplified truss model is applicable for evaluating the shear carrying capacity of PC slender beams without transverse reinforcement where their cross sections are I- and T-shapes. Based on the experimental results with wide ranges of influential parameters, the superior accuracy in prediction compared with the current method, is confirmed. By applying the equivalent elastic analysis, the shear carrying capacity can be simply calculated. Moreover, the objective results in terms of critical strut can be checked from this way of calculation. The shear compression mode of failure is expressed as the failure of predicted critical strut. By incorporating the ratio of widths of flange to web, b_f/b_w , to the value of m and thickness of struts, the proposed model can also be utilized to PC slender beams with rectangular cross section without discontinuity in application.

References:

- Japan Society of Civil Engineers (JSCE) (2002), "Standard Specification for Concrete Structures," *Structural Performance Verification*.
- Ito, T., Yamaguchi, T. and Ikeda, S. (1994), "Flexural Shear Behavior of Precast Segmental PC Beam," *Proceedings of the JCI*, **16**(2), 967-972.
- Thorenfeldt, E., Tomaszewicz, A. and Jensen, J.J. (1987), "Mechanical properties of high-strength concrete and applications in design," *Symposium Proceedings, Utilization of High-Strength Concrete*, Norway.
- Hordijk, D.A. (1991), "Local Approach to Fatigue of Concrete," *PhD thesis*, Delft University of Technology.
- Japan Road Association (2002), "Specification for Highway Bridges (Earthquake-resistant design)".
- Lertsamattiyakul, M., Niwa, J., Tamura, S. and Hamada, Y. (2004), "Simplified Truss Model for Prestressed Concrete Slender Beams," *Journal of Materials, Concrete Structures and Pavements*, JSCE, **767**(64), 313-325.
- Arthur, P.D. (1965), "The Strength of Pre-tensioned I beams with Unreinforced Webs," *Magazine of Concrete Research*, **17**(53), 199-210.
- Elzanaty, A.H., Nilson, A.H. and Slate, F.O. (1986), "Shear Capacity of Prestressed Concrete Beams Using High Strength Concrete," *Journal of ACI*, **83**(3), 359-368.
- Hick, A.B. (1958), "The Influence of Shear Span And Concrete Strength upon The Shear Resistance of A Pre-tensioned Prestressed Concrete beam," *Magazine of Concrete Research*, **10**(30), 115-122.
- Kar, J.N. (1969), "Shear Strength of Prestressed Concrete Beams Without Web Reinforcement," *Magazine of Concrete Research*, **21**(68), 159-170.
- Sethunarayanan, R. (1965), "Ultimate Strength of Pre-tensioned I beams in Combined Bending And Shear," *Magazine of Concrete Research*, **12**(35), 83-90.
- Sato, T., Ishibashi, T., Yamashita, H. and Takada, S. (1987), "Shear Strength and Modes of Failure of Prestressed Concrete Beams," *Proceedings of the JCI*, **9**(2), 323-328.

RESEARCH ON WEIGHT REDUCTION OF COMPOSITE PC BEAMS USING VARIOUS UFC WEB MEMBERS

H. Murata¹⁾, J. Niwa²⁾, E. Chigira³⁾, and T. Kawaguchi⁴⁾

1) Doctoral student, Department of Civil Engineering, Tokyo Institute of Technology, Japan

2) Professor, Department of Civil Engineering, Tokyo Institute of Technology, Japan

3) Undergraduate student, Department of Civil Engineering, Tokyo Institute of Technology, Japan

4) Research & Development Department, Taiheiyo Cement Corporation, Japan

hmurata@cv.titech.ac.jp, jniwa@cv.titech.ac.jp, e-chigi@cv.titech.ac.jp, tetsuo_kawaguchi@taiheiyo-cement.co.jp

Abstract: In the improvement of seismic performance of a bridge structure, the weight reduction of a girder is one of the significant factors. Recently, composite prestressed concrete (PC) bridge girders, of which web member is made by various materials, have been developed. In this study, composite PC structural members using Ultra High Strength Fiber Reinforced Concrete (UFC) as a web member are examined. UFC has high compressive strength around 200MPa, high ductility, and high workability. Due to its predominant mechanical properties, variously shaped UFC member is applied to the web member of composite PC bridge girders. So, the self-weight of girders can be extremely reduced compared with normal PC girders. The aim of this research is to investigate the mechanical properties of composite PC members using UFC truss and evaluate the effect of weight reduction. Then, composite PC beams are designed and experiments are carried out. In addition, the level of weight reduction of a web member is examined.

1. INTRODUCTION

For the improvement of seismic performance of bridge structures, the weight reduction of girders is one of the effective factors. A composite prestressed concrete (PC) girder, of which web member is made of different material from a flange member, has been developed. Because of high strength of the web member, its cross sectional area can be reduced. As a result of volume reduction, the total weight of a bridge girder is also reduced.

Ultra High Strength Fiber Reinforced Concrete (UFC) (Rechard et al. 1994) has been developed since 1994. This material provides high compressive strength around 200MPa with high ductility because of the existence of steel fiber reinforcement. Moreover, due to high workability, variously shaped member can be made.

In this study, a composite PC girder utilizing UFC as web members is focused as shown in Figure 1. In case that UFC is used for web members, advantages are as follows: the complexity in the construction can be solved because web members are precast; the total cost of construction can be reduced; the self-weight of girders can be extremely reduced compared with normal PC girders. Then, in order to clarify the mechanical properties of this composite PC structural member with variously shaped web members, composite PC beams utilizing UFC as precast web members were constructed, and the loading test was carried out. The parameter to be considered in this study was the shape of UFC web members, which is triangular panel, quadrangular panel, and Howe truss.

Finally, in point of weight of web members, the composite PC beams were compared with normal PC beams, which provide the same load carrying capacity, in order to discuss the reduction in weight.

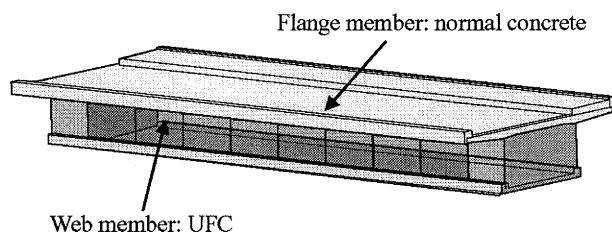


Figure 1 Composite PC girder using UFC

Table 1 Specimen names

Specimen name	Shape of web members	Thickness of web members
TR	Triangular panel	40mm
QU	Quadrangular panel	
HT	Howe truss	

Table 2 Mix proportion of UFC [kg/m^3]

Water	Premix	Steel fiber	Superplasticizer
180	2254	157	22

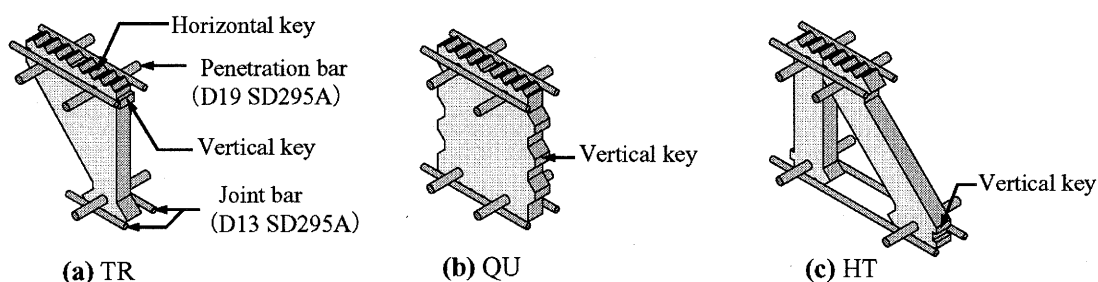


Figure 2 Joint methods

2. EXPERIMENTS

2.1 Experimental procedures

In this study, 3 specimens of composite PC beams using UFC as web members were prepared: named as TR, QU and HT as listed in Table 1. The parameter which was considered in this study was the shape of web members: triangular panel, quadrangular panel and Howe truss. The thickness of web members is 40mm in all cases. Figure 2 illustrates joint methods of each specimen, which are the reinforcing bars with horizontal and vertical keys joint as shown in the work of Kawaguchi et al. (2003) and Sivaleepunth et al. (2004).

The test of simply supported composite PC beams under two points load was performed to compare the mechanical properties depending on the shape of web members. The vertical force, P , was applied monotonically to the specimen through two loading points. In order to reduce the friction at the supports, friction-reducing pads, i.e., two Teflon sheets sandwiching the grease, were inserted between the specimen and the support plates.

In web members of composite PC beams, UFC was introduced because of its superior strength (compressive strength = 200MPa). It results in the significant weight reduction and provides nearly limitless freedom of structural member shape. The mix proportion of UFC is shown in Table 2. The mixing time of UFC is about 12-14 minutes. There was no segregation and sinking of steel fiber from the matrix due to its high viscosity. After casting, the formwork was covered by plastic sheet and put into the chamber, in which the temperature was controlled at 20°C for 48 hours. After the formwork was removed, the specimens were cured again in air with 100% humidity at 90°C for 48 hours.

The outlines of experiments and properties of specimens were summarized in Figure 3. For all specimens, the shear span was set to be 1500mm, effective depth was 350mm and shear span to effective depth ratio was 4.29. In all specimens, four PC bars ($\phi 13$ SBPR1080/1230, yield strength $f_y = 1249\text{MPa}$) were arranged to both upper and lower flanges (two bars per each flange). The longitudinal reinforcement ratio was set to be 1.86%. For all the specimens, the stirrup (D10 SD295A, $f_y = 349\text{MPa}$) was used as the shear reinforcement in both upper and lower flanges. The

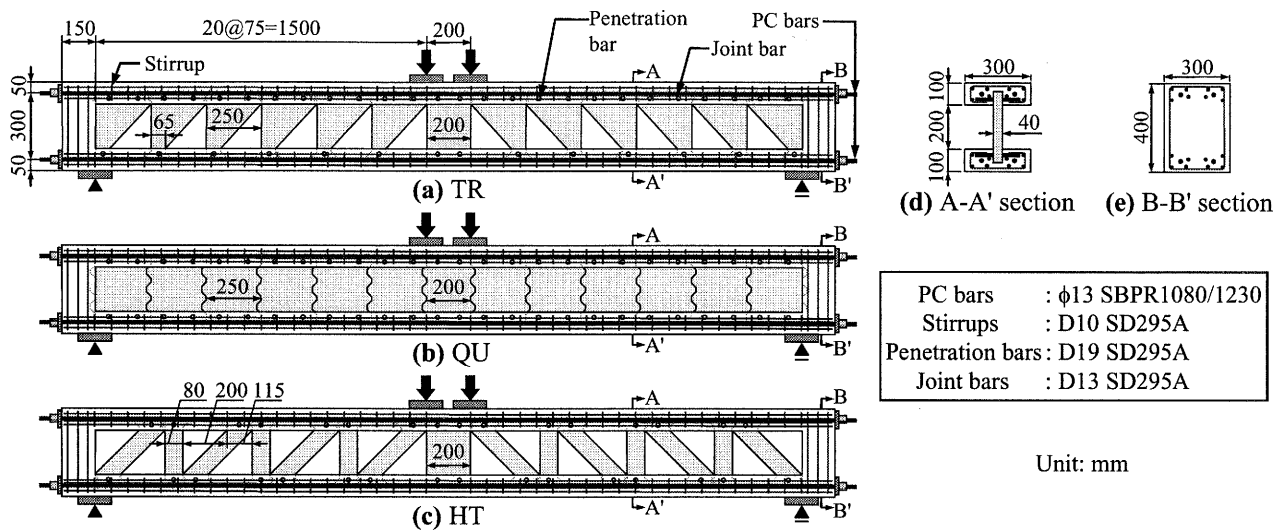


Figure 3 Experimental outlines

Table 3 Mix proportion of concrete

G_{max} [mm]	W/C [%]	s/a [%]	Unit weight [kg/m ³]					
			Water	Cement	Fine aggregate	Coarse aggregate	Super-plasticizer	Defoaming agent
15	30.0	53.2	170	567	857	766	7.93	5.67

Note G_{max} : maximum size of coarse aggregate, W/C: water-cement ratio, s/a: sand aggregate ratio

shear reinforcement ratio for flanges was 0.63%.

Table 3 tabulates the mix proportion of concrete used in the flange. Before casting of concrete into the flange, precast UFC web members were arranged and connected with each other by using epoxy glue. After casting the flange part, the specimens were cured for 7 days. Then, the prestressing force was introduced to both upper and lower flanges in order to generate 3MPa and 5MPa in compression as the upper and lower fiber stresses, respectively. For all the specimens, grouting of cement paste was performed. After that, specimens were cured for another 7 days, thus curing period of concrete in the flange was totally 14 days before loading test.

2.2 Results and discussions

As the first step, the comparison of joints A and B was made. Table 4 tabulates the results of experiments. From the experimental results of TR and HT, the first peak loads, P_a (not the maximum loading capacities), were 117kN and 112kN, respectively. Figure 4 illustrates the load-deflection curve of beams. In TR and HT, from the beginning, the curves rose up to the first peak load, P_a . After that the loads dropped until it reached the stable condition, and then the loads gradually increased again. After the deflections of beams reached 17mm, the behavior of TR and HT was

Table 4 Loading capacity of composite PC beams and material strength

Specimen	Load capacity [kN]	Concrete in Flange			UFC in Web		
		Compressive strength [MPa]	Tensile strength [MPa]	Young's modulus [GPa]	Compressive strength [MPa]	Tensile strength [MPa]	Young's Modulus [GPa]
TR	131	59.3	3.5	28.7	204	9.7	53
QU	301	74.1	3.8	31.7			
HT	132	82.5	4.4	34.1			

almost same. On the other hand, in QU, the load kept on rising until a PC bar in the lower flange yielded without the decrease in load. It can be noted that QU has the highest stiffness and the highest load carrying capacity. In all cases, it should be noted that composite PC beams using UFC web members have very high ductility.

Figure 5 illustrates the crack patterns of specimens. First cracking loads of TR, QU and HT were 86.2kN, 90.7kN and 80.3kN, respectively.

In TR and HT, first crack occurred in a UFC member. However, in QU, the first crack arose in the lower flange. Figure 6 shows the prominent crack in the UFC web member of each specimen. In TR, a crack was propagated in the vertical edge of UFC triangular panel on the right side and the failure was asymmetric. When the crack width increased about 10mm, the load became the value of P_a . After that, cracks occurred in the upper fibre of a upper flange in right side and the inner angle in the lower right corner of concrete frame (see Figure 5(a)).

In QU, after cracks were propagated in the lower flange, spaces of 2-3mm between UFC quadrangular panels arose as shown in Figure 6(b). After that, although diagonal cracks occurred in UFC quadrangular panels on both side (see Figure 5(b)), the specimen failed in flexure mode because of the yield of PC bars.

In HT, crack was propagated in the vertical truss. When the crack width increased about 5mm, the sliding between the upper flange and UFC truss occurred as shown in Figure 6(c). It can be explained that this sliding caused the decrease in load at the point of P_a in Figure 4. After that, cracks

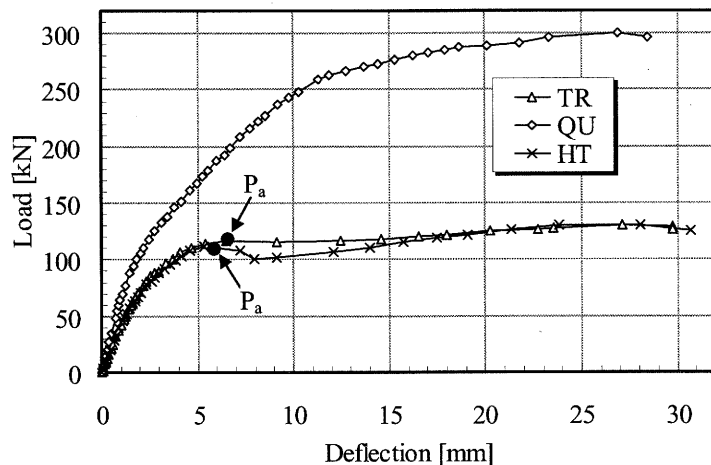


Figure 4 Load-deflection curve

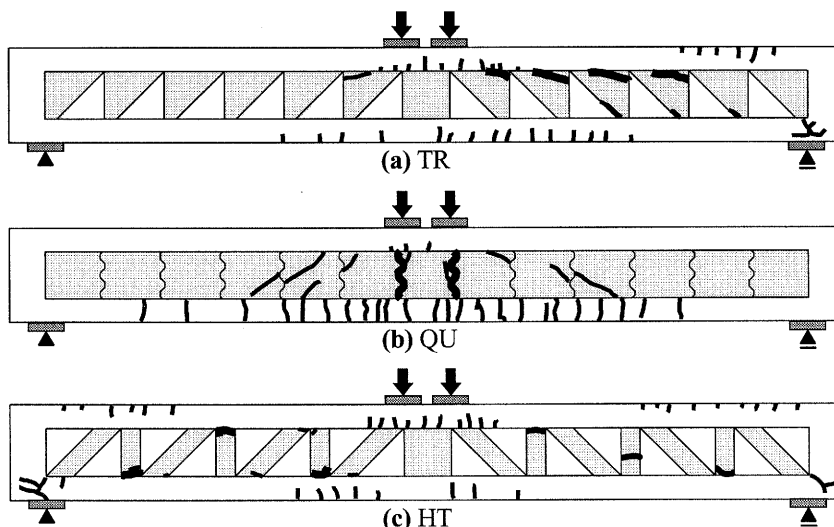
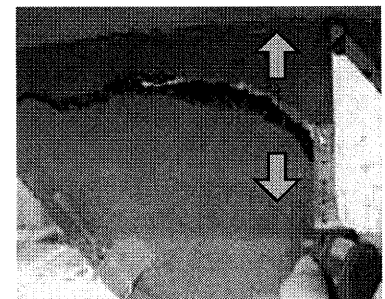
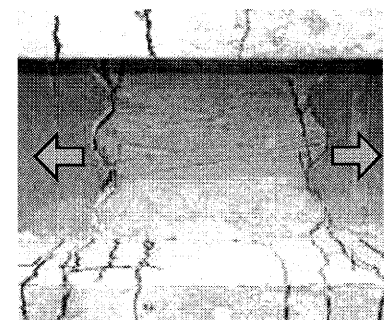


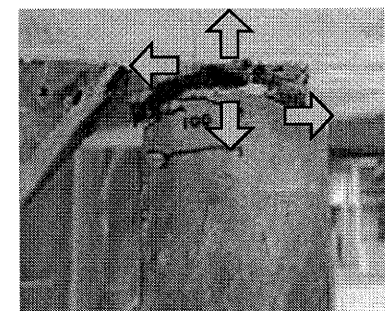
Figure 5 Crack patterns



(a) TR



(b) QU



(c) HT

Figure 6 Cracks of the UFC member

occurred in the upper fibre of upper flange member in both side and the inner angle in the lower corner of concrete frame (see Figure 5(c)).

Thus, it can be understood that the shape of UFC web members significantly influence the failure mode of composite PC beams. Moreover, because the specimens TR and HT showed the same loading capacities, it can be noted that the load carrying capacity depends on the flange member if the web member is highly damaged.

3. COMPARISON WITH NORMAL PC BEAMS

3.1 Design of normal PC beams

I-shaped PC beams which have the same load carrying capacity as all composite PC beams were designed in order to examine the level of weight reduction of a web member. The characteristics of I-shaped PC beams are the same as in the composite PC beams as tabulated in Table 5 and the outlines of I-shaped PC beams are shown in Figure 7. The shear reinforcement ratio of I-shaped PC beams was set to be 0.30%. Prestressing force was 150kN just the same as composite PC beams.

The shear carrying capacity, V_u , of I-shaped PC beams can be obtained from the following Eqs. (1), (2) and (3) (JSCE code 2002).

$$V_u = V_c + V_s \quad (1)$$

$$V_s = \frac{A_w f_{wy} j d (\sin \alpha + \cos \alpha)}{s} \quad (2)$$

$$V_c = 0.2(f_c')^{1/3} \left(\frac{1000}{d} \right)^{1/4} (100 p_w)^{1/3} b_w d \left(1 + \frac{2M_0}{M_u} \right) \quad (3)$$

where, A_w : cross sectional area of stirrup [mm^2], f_{wy} : yield strength of stirrup [MPa], j : 1/1.15, d : effective depth [mm], α : inclined angle of stirrup to axis of beam ($= 90^\circ$), s : spacing of stirrup [mm], f_c' : compressive strength of concrete [MPa], p_w : longitudinal reinforcement ratio ($= A_s / (b_w \cdot d)$), b_w : web thickness of RC beam [mm], M_0 : decompression moment [$\text{N} \cdot \text{m}$] and M_u : ultimate moment [$\text{N} \cdot \text{m}$].

Table 5 Characteristics of I-shaped PC beam and its materials

Compressive strength	f_c' [MPa]	60
Shear span	a [mm]	1500
Effective depth	d [mm]	350
Cross sectional area of longitudinal reinforcement *1	A_s [mm^2]	1058
Cross sectional area of stirrup	A_w [mm^2]	142.6
Yield strength of stirrup	f_{wy} [MPa]	295

*1 Including PC bars (cross sectional area = 265.4 mm^2)

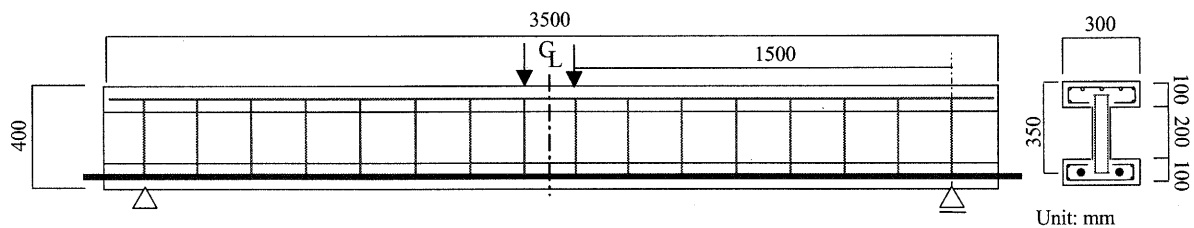


Figure 7 Outline of I-shaped PC beam

Table 6 Comparison of results

Specimen	Maximum Load [kN]	Web thickness of I-shaped PC beams b_w [mm]	Web weight of I-shaped PC beams A [kg]	Web weight of composite PC beams B [kg]	Rate of weight reduction (A-B)/A [%]
TR	131	56.3	90.1	41.8	53.6
QU	301	172.8	276.5	64.0	76.9
HT	132	56.8	90.9	32.0	64.8

By setting the value of $2V_u$ to be corresponding to the maximum loads of composite PC beams, b_w (web thickness of I-shaped PC beams) was determined. From the densities of PC and UFC of 2.5t/m^3 , the weights of a web member of I-shaped PC beams and composite PC beams were compared.

3.2 Comparison of weight

Table 6 shows the results of I-shaped beams with the same load capacity as composite PC beams. It was found that the weight of a web member can be reduced to about 54-77%. Especially, quadrangular panel type can extremely reduce the weight of a web member. It means that the composite PC girder can make the large contribution to the weight reduction of a web member.

This implies that the self weight of a web member of the composite PC girder using UFC is significantly reduced compared with normal PC girders.

4. CONCLUSIONS

The study of mechanical properties of composite PC beams using UFC as variously shaped web members was carried out. In addition, by the experiment, the level of weight reduction of a web member by using UFC was investigated in comparison with normal PC beams.

The conclusions of this study are as follows:

- 1) From the experimental results, it is turned out that the shape of UFC web members significantly influence the failure mode of composite PC beams.
- 2) Based on experimental results of triangular panel and Howe truss types, it is known that the load carrying capacity depends on the flange member if a web member is enormously damaged.
- 3) By comparing composite PC beams with I-shaped PC beams having the same resistance, the weight of a web member can be reduced 54-77% when using the UFC. Especially, quadrangular panel type can extremely reduced the weight of a web member.
- 4) The seismic performance of composite PC bridge structures using UFC as a web member can be enormously improved.

Acknowledgments:

Sincere gratitude is expressed to Oriental Construction Co., Ltd. for their cooperation.

References:

- Richard, P. and Cheyrezy, M. H. (1994), "Reactive Powder Concretes with High Ductility and 200-800 MPa Compressive Strength.", *ACI Spring Convention*, SP144-24, 507-517.
- Kawaguchi, T., Kakei, T., Katagiri, M. and Niwa, J. (2003), "Experimental Research on Mechanical Properties of Composite PC Members Using UHSFRCC.", *Proceedings of the JCI*, **25**(2), 1987-1992. (in Japanese)
- Sivaleepunth, S., Murata, H., Niwa, J. and, Kawaguchi, T. (2004), "Experimental Study on Composite PC Beams by Applying UFC Truss as Web Member.", *Proceeding of the JCI*, **26**(2), 1801-1806.
- JSCE (JSCE CODE) (2002), "Structural Performance Verification, Standard Specification for Concrete Structures." (in Japanese)

DAMAGE PROCESS AND COLLAPSE CAPACITY OF RC FRAME STRUCTURE: -FROM THE VIEWPOINT OF MECHANISM CONTROL-

T. Nagae¹⁾, S. Hayashi²⁾, L. F. Ibarra³⁾, and H. Krawinkler⁴⁾

1) Postdoctoral Fellow, Structural Engineering Research Center, Tokyo Institute of Technology, Japan

2) Professor, Structural Engineering Research Center, Tokyo Institute of Technology, Japan

3) Senior Research Engineer, Southwest Research Institute, USA

4) Professor, Department of Civil and Environmental Engineering, Stanford University, USA
nagae@serc.titech.ac.jp, hayashi@serc.titech.ac.jp, libarra@swri.org, krawinkler@stanford.edu

Abstract: The quantitative representation of the performance of building is not straightforward. At present, the mechanisms formed by strong columns and weak beams (i.e. complete mechanisms) are strongly recommended as a design concept for multistory frame structures. However, from the viewpoint of reparability, it is generally difficult to repair all hinges in beams, in the case of complete mechanism. In addition, costs of downtime can be high because all of stories of the building become targets of repairing. This research came up with a concept of mechanism control that intends to concentrate damages to the lower part of the frame structure and keep the rest of the structure (higher part) intact. The type of mechanism can be controlled by appropriately reinforcing the members in the upper part. However it is obvious that the extreme case, i.e. soft-first-story building can produce a very poor collapse capacity. Thus, for this design, it becomes very important to show the balance between the reparability and the safety against collapse. In this report at the first stage, damage processes up to collapses are presented from results of incremental dynamic analyses for reinforced concrete frame structures with different size of partial mechanisms. The response assessment for the structure is performed through probabilistic approaches, and eventually the probability of collapse is computed and compared.

1. INTRODUCTION

At present, as a design concept for multistory frame structures, the mechanisms formed by strong columns and weak beams (i.e. complete mechanisms) are strongly recommended (AIJ 1990, Paulay 1986, et al.), because the energy dissipation occurs in plastic hinges at both ends of many beams during a major seismic event. However, it is not easy to demonstrate quantitatively the advantages for the performance of the building, such as safety against collapse, even if the complete mechanism is guaranteed during an event. From the viewpoint of reparability, it is generally difficult to repair all hinges in beams in the case of complete mechanisms. In addition, costs in terms of downtime can be high because all of stories of the building become targets of repair.

It can be thought that the types of mechanism of a structure during earthquakes can be controlled by strength ratios of the upper part to the lower part, i.e. by appropriately

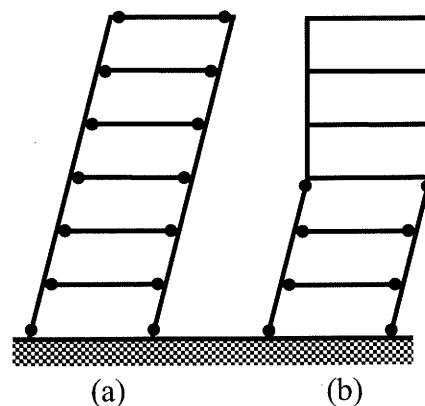


Figure 1 (a) Complete mechanism
(b) Partial mechanism

strengthening the members in the upper part. As shown in Figure 1, if a mechanism is located in a limited area, the rest of building remains intact. Thus, it is expected that repair work is reduced and also losses in terms of downtime can be reduced.

This concept also has benefits in the construction process. Although residential reinforced concrete (RC) buildings tend to have walls surrounding openings, such as wind walls and spandrel walls, it is inevitable to separate all the walls from the main frame using slits in order to attain the complete mechanisms. This type of site work makes the process of construction inefficient. However, in the areas where no plastic hinging occurs, the slits are not necessary anymore. Conversely, using the strength provided by the walls becomes very important for the design based on the mechanism control. That is to say, the type of mechanism can be thought as an option for performance based design, which should follow diverse demands from stakeholders or residents. However, it is clear that a relatively localized partial mechanism means the decrease in the number of members consuming energy. Thus, for a building designed based on mechanism control, it becomes more important to demonstrate adequate performances in terms of the damage process and the collapse capacity.

This paper demonstrates procedures to evaluate performance of RC frame structures with partial mechanism and considers the effects of the size of partial mechanism on the seismic performance. In regard to a procedure to evaluate performance of structures, a couple of studies systematically evaluated responses of buildings and highlighted the collapse capacities (Ibarra and Krawinkler 2004, Zareian and Krawinkler 2004). These studies computed collapse capacity by increasing the intensity measures related to hazard of a site, (i.e. incremental dynamic analysis, Vamvatsikos and Cornell, 2002) until the responses of the structure can be judged to have reached collapse, and statistically computed global collapse capacities to treat large scatter of output data.

2. APPROACH FOR ESTIMATING PERFORMANCE OF STRUCTURE

2.1 Model of Analysis

In this study, twelve-story RC moment-resisting frames are considered (Figure 2). The partial

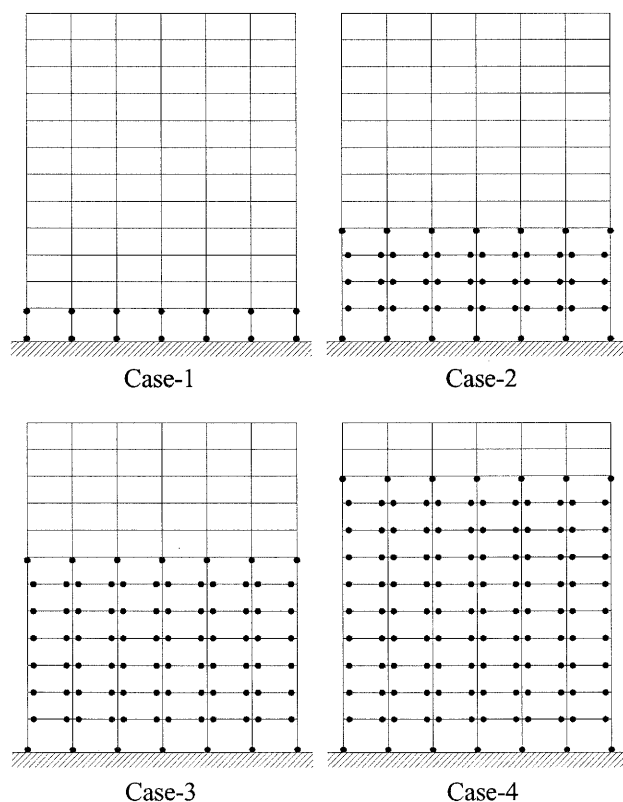


Figure 2 Considered partial mechanisms

mechanism extent of the structure can be controlled by strength ratios of the upper part to the lower part in the structure. The design concept to control the partial mechanism extent is depicted in Figure 3. Thus, one interior frame of the structure is idealized by a two-dimensional frame model, of which upper parts are assumed to be reinforced appropriately. For Case-1, the partial mechanism is located in

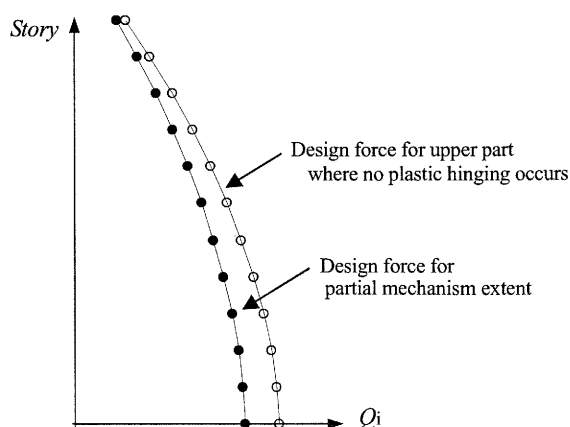


Figure 3 Concept of story shear force Q_i for mechanism control design

only the first story, and for Case-2, Case-3 and Case-4, the mechanisms extended from the first to fourth, the first to seventh and the first to tenth story, respectively.

The original structure was designed in accordance with Design Guideline Based on Ultimate Strength Concept (AIJ, 1990), which intends a complete mechanism. That is to say, the yield strength of beam ends was decided to be larger than the moments from a static analysis assuming elastic members for the combination of a horizontal load, a dead load and a live load. The strength of columns was decided to be stronger than the connecting beams.

In this study, it assumed that the areas where no plastic hinging occurs (Figure 2) are additionally and appropriately designed in terms reinforcing and the members in the partial mechanism extents have the same configurations as those given by the guideline's design. The beams and the top ends and the bottom ends of columns in the partial mechanism extents are modeled as inelastic members. The tops of columns in the partial mechanism extents are weakened in terms of the yield strengths because the guideline does not intend to let them yield. All members in the upper areas and the columns in the partial mechanism extents, where no plastic hinging occurs, are modeled by elastic members.

Flexural deformations of the line elements are concentrated to the ends and modeled using rotational springs. The initial stiffness of the spring K_1 is calculated using the Young modulus of concrete, the moment of inertia of gross section and the clear span. The hysteretic characteristics of the rotational spring in the partial mechanism extent are modeled by revising the Takeda Model (1970) to represent the strength deterioration after the peak strength (Figure 4). The cracking moment and the yield moment are calculated by fiber section analyses. Rotations corresponding to the yield moments are calculated by the Sugano's equation (1973). The rotation at the peak moment θ_1 and the rotation at zero moment θ_0 are assumed 0.03rad and 0.10rad respectively.

That is to say, the members are assumed to be ductile based on the guideline's lateral reinforcing. To simplify the problem, the same pair of θ_1 and θ_0 is used for all of members. The stiffness after yield is defined as K_1 times 0.001. The first-mode period T_1 of the structure from an eigen-value analysis is 0.813 sec. The structure is damped by 5 % coefficient for the first mode, but the damping force of each member is changed in proportion to the instantaneous stiffness of the member. The P - D effects are considered using a geometric stiffness formulation.

Figure 5 shows results of inelastic pushover analyses based on the horizontal load distribution given by the guideline's design. The pushover analyses do not incorporate either strength deterioration or P - D effects. The relationships between shear force ratio C_1 and inter-story drift ratio R_1 of the first story are very close in Case-2, Case-3 and Case-4. This means that the members of the partial mechanism extents reach yielding at the level of stress decided by the guideline's design. Case-1, which the columns of the first story hinge at the two ends, is made as close as possible to other cases by adjusting the amount of main reinforcement.

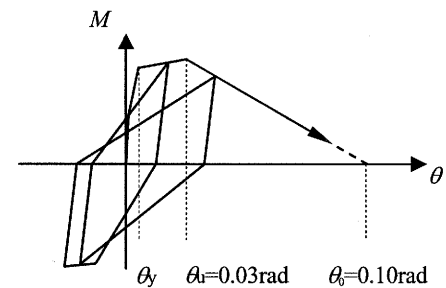


Figure 4 Model of rotational spring

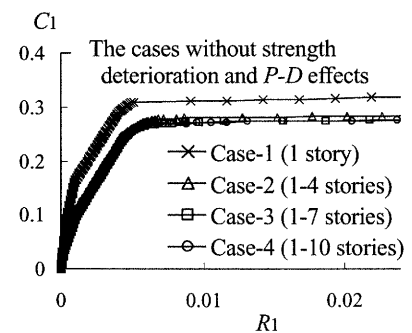


Figure 5 Pushover analyses

2.2 Ground Motion and Hazard

A set of 40 ground motions (Medina 2003) is used for the incremental dynamic analyses. The ground motions were recorded in various earthquakes in California. The sites are categorized as Type-D site of NEHRP ($183\text{m/sec} < V_s < 366\text{m/sec}$ or $15 < N < 50$, where V_s is shear wave velocity, N is N value of SPT test). The earthquake magnitudes are from 6.5 to 7.0, and the source-to-site distance ranges from 13 to 40 km. The selected intensity measure, IM, is the 5% linear elastic spectral acceleration at the first period of the structure, $S_a(T_1)$ (EERI 1989). For the site, this study assumes

Van Nuys, which is located in Southern California and categorized as soil Type-D. The results of hazard analyses by PEER studies are available for Van Nuys. The use of $S_a(T_1)$ as IM implies that all the ground motions are scaled to a common $S_a(T_1)$ at the elastic period of the SDOF system. Thus, the frequency content of the ground motion cannot be considered explicitly. The large dispersion in spectral accelerations due to the different frequency content of the selected ground motions is illustrated in Figure 6, in which the ground motions are scaled to have the same spectral acceleration at $T_1=0.813$ sec. The dispersion increases with period, and response predictions may exhibit significant scatter depending on the extent of inelasticity, which leads to period elongation

2.3 Incremental Dynamic Analysis (IDA) and Collapse Capacity

Figure 7 shows the concept of incremental dynamic analysis and collapse capacity. The left side of the figure represents the hazard curve for $S_a(T_1)$ and the right side represents the maximum inter-story drift ratio in all stories, IDR_{max} , which is computed for increments of $S_a(T_1)$. Eventually, the system becomes unstable because of the large deformation that does not permit a further increase of $S_a(T_1)$. The $S_a(T_1)$ at the last stage is defined as the collapse capacity $S_{a,collapse}$. Note that IDR_{max} decreases several times as $S_a(T_1)$ increases. This return phenomenon occurs because during dynamic responses the pattern such as timing of yielding changes, or because the relationship between the positive value and the negative value in the time history changes in terms of the maximum.

2.4 Statistics of Results from IDA

Figure 8 shows the results of the incremental dynamic analyses for the set of 40 ground motions. The vertical axis is the intensity measure IM of the ground motion (i.e. $S_a(T_1)$) and the horizontal axis is the engineering demand parameter, EDP (in this case, the maximum inter-story drift ratio in all stories, IDR_{max}). In Figure 8, the individual IDA are represented by gray lines, whereas the 50th and 84th curves are indicated with black lines

For these dispersed data, EDP-direction statistics and IM-direction statistics can be conducted. For vulnerability curves (EDP given $S_a(T_1)$) EDP-direction statistics is used, and for collapse statistics (probability of collapse given $S_a(T_1)$) IM-direction statistics is used.

(1) Collapse Fragility Curve and Probability of Collapse

The collapse fragility curves $F_c(x)$ are obtained by IM-direction statistics for collapse capacity data. Thus, the fragility curve can be expressed by

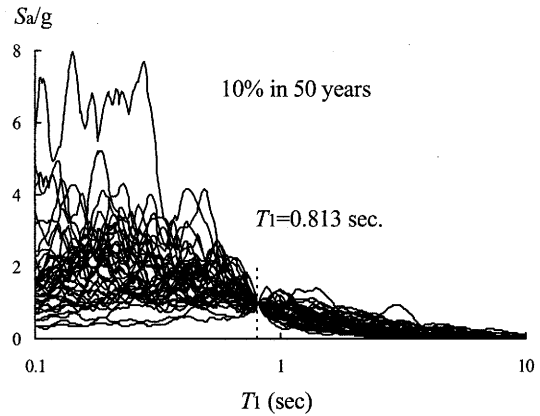


Figure 6 Scaled acceleration spectra

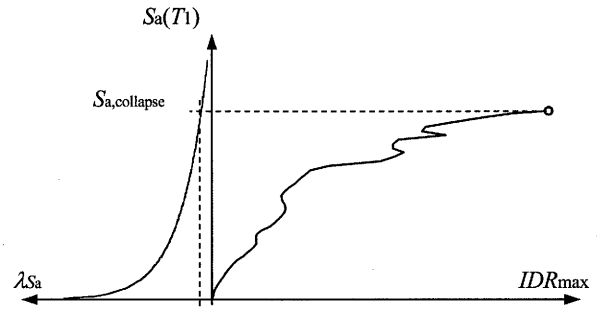


Figure 7 Collapse capacity $S_{a,collapse}$

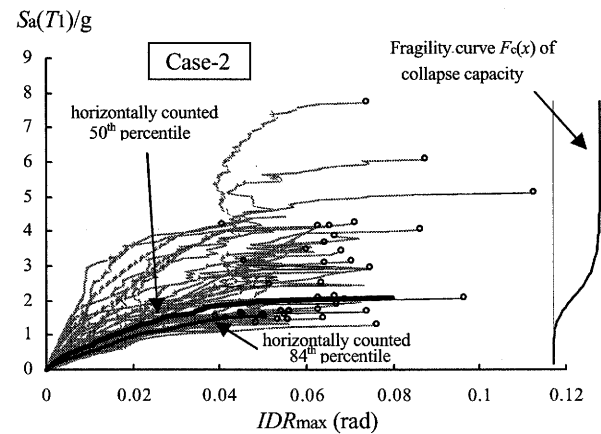


Figure 8 Set of results from IDA

$$F_c(x) = P[S_{a, \text{collapse}} \leq x] \quad (1)$$

$F_c(x)$ can be defined as the probability that $S_{a, \text{collapse}}$ is less than or equal to x .

If the collapse fragility curve $F_c(x)$ for a given system has been determined, probabilistic collapse assessment can be carried out according to the following equation:

$$\lambda_{\text{collapse}} = \int_0^{\infty} F_c(x) d\lambda_{S_a}(x) \quad (2)$$

where $\lambda_{\text{collapse}}$ is mean annual frequency of collapse, $\lambda_{S_a}(x)$ is mean annual frequency of S_a exceeding x .

The fragility curve, $F_c(x)$, can be obtained by fitting a lognormal distribution to the collapse capacity data for the 40 ground motion. The lognormal distribution is a logical selection for several reasons: (a) most of the individual collapse capacity data has a skewed distribution with a longer tail for upper values, (b) collapse capacity values are always positive and, (c) previous studies have associated the distribution of spectral acceleration and the response of a nonlinear structure (in terms of EDP) to lognormal distributions (Shome and Cornell, 1999).

In general, the mean and the standard deviation of the natural logarithm of sample are used to define the entirely moderate shape. The result represents very close fitting around median but also represents errors in both sides of around the median. In this case, because $F_c(x)$ is combined with the differentiated $\lambda_{S_a}(x)$ (i.e. $d\lambda_{S_a}(x)$, annual frequency of S_a of x) as expressed in Eq.(2), it is reasonable to fit the portion less than median, which is combined with relatively large $d\lambda_{S_a}(x)$. In this study, the median of the natural logarithm of the data, $\text{Ln}(S_{a, \text{collapse}})^{50\%}$ and the equivalent dispersion δ_{eq} of the sample are used as parameters, where $\text{Ln}(S_{a, \text{collapse}})^{50\%}$ corresponds to the natural logarithm of the median $S_{a, \text{collapse}}^{50\%}$. By adopting the difference between $\text{Ln}(S_{a, \text{collapse}})^{50\%}$ and $\text{Ln}(S_{a, \text{collapse}})^{16\%}$ as δ_{eq} , δ_{eq} and $F_c(x)$, which focus on the portion less than median, can be calculated by

$$\delta_{eq} = \ln \left(\frac{S_{a, \text{collapse}}^{50\%}}{S_{a, \text{collapse}}^{16\%}} \right) \quad (3)$$

$$F_c(x) = \Phi \left(\frac{\text{Ln}(x) - \text{Ln}(S_{a, \text{collapse}}^{50\%})}{\delta_{eq}} \right) \quad (4)$$

where Φ is the cumulative normal distribution function.

(2) Vulnerability Curve for EDP

For the vulnerability curve, which means the EDP given $S_a(T_1)$, the “counted” EDP-direction statistics is adopted because of the incompleteness of the dataset after one or more ground motions produce collapse. For a set of 40 ground motions, the average of the 20th and 21st sorted value is taken as the median (50th percentile) and the 34th sorted value is taken as the 84th percentile. The median EDP curve at different intensity levels terminates when 50% of ground motions have led to collapse of the frame. In Figure 8, the percentile curves are also shown. The ends of the median EDP curve and the 84th percentile EDP curve are corresponding to the median $S_{a, \text{collapse}}^{50\%}$ and the 16 percentile $S_{a, \text{collapse}}^{16\%}$ that are produced by IM-direction statistics for the collapse capacity data, respectively.

Estimating statistically the EDP curves is useful for several purposes. It can be used to assess performances at a given hazard level, for example the relevant design basis calling for “the 84th percentile demand” etc., ranging from EDP based damage control to collapse.

3. RESULTS OF IDA

3.1 Vulnerability Curve for EDP

For all hinges in the mechanism extents, Figure 9 (1) shows the median (50th percentile) curves of the sum of hysteretic energy dissipation E_{sum} and Figure 9 (2) shows the median curves of the sum of the maximum plastic rotations $p\theta_{max,sum}$ (the maximum rotation θ_{max} minus the yielding rotation θ_y). The figures show that E_{sum} and $p\theta_{max,sum}$ are, respectively, going almost the same trace regardless of the size of the partial mechanism. This tendency suggests that the building consume the same amount of energy during a seismic event regardless of the mechanism type, and then $p\theta_{max,sum}$ has a certain relationship with E_{sum} at a given hazard level. However, collapse occurs at different $S_a(T_1)$ values. Although Case-2 deviates from Case-3 and Case-4 at the late stage, most of the plastic hinges of Case-2 are in the negative slope region of the skeleton curve at that stage.

Figure 9 (3) shows the median IDR_{max} curves for the four cases. It is shown that, at a given hazard level, IDR_{max} of Case-1, which produces first-story mechanism, is the largest, and IDR_{max} decreases as the mechanism extent becomes larger. However, the differences tend to become small for Cases 3 and 4.

The average of the maximum plastic rotations $p\theta_{max,ave}$ can be expressed as $p\theta_{max,sum}/n$, where n is the number of the hinges. As shown in Figure 9 (2), $p\theta_{max,sum}$ is almost the same regardless of the size of the partial mechanism. Thus, it can be concluded that $p\theta_{max,ave}$ in the case of different extents of partial mechanisms is inversely proportional to n , and then the tendency of IDR_{max} with different extents of mechanisms can be explained. That is to say, as the partial mechanisms are enlarged by three stories, the effect of the extent of partial mechanism on IDR_{max} decreases gradually.

An additional important observation can be made from Figure 10, which shows the distribution of the maximum inter-story drift ratio in each story IDR_i over the 12 stories. In Case-4 with the 10-story partial mechanism, the IDR_i values in the lower area are very close to those of Case-3, not only because the increase in the number of plastic hinges is small but also because the hinges in the upper area of the partial mechanism do not dissipate much energy. This phenomenon suggests that the energy dissipation concentrates in the lower area and is not being shared equally across the mechanism as the number of stories becomes large.

3.2 Collapse Fragility Curve and Probability of Collapse

The collapse fragility curves are obtained from Eq.(4) by IM-direction statistics for collapse

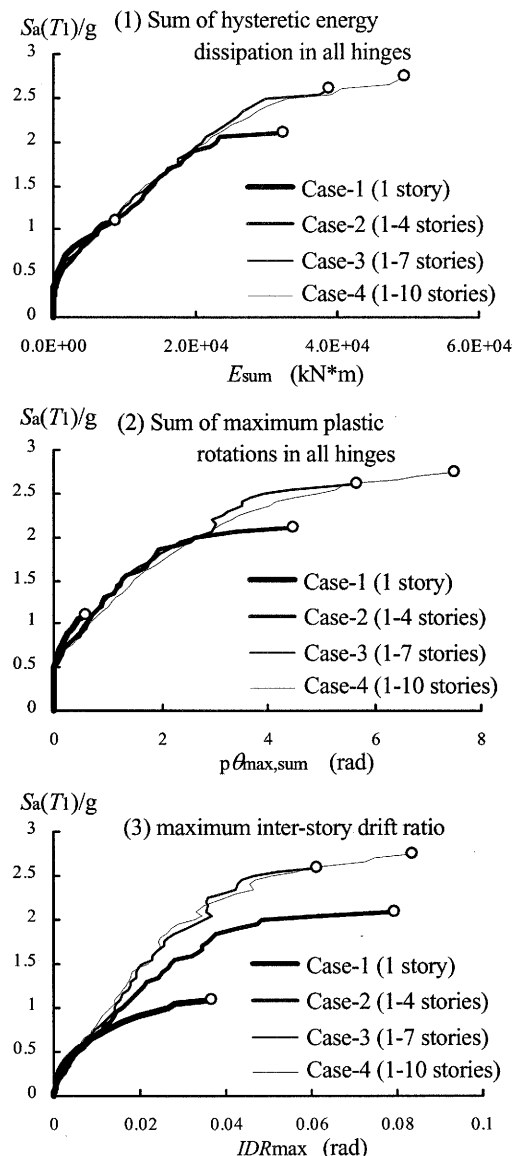


Figure 9 Median EDP curves

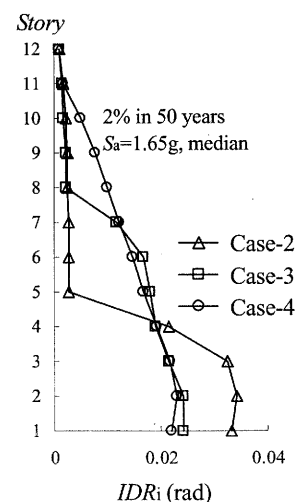


Figure 10 IDR_i distributions

capacity data. Figure 11 shows the fragility curves of the four cases. At a given hazard level, i.e. $S_a(T_1)$, the probability of collapse becomes smaller as the partial mechanism extent becomes larger. However, the differences tend to become small, too, as the partial mechanism takes over a significant area of the structure (Cases 3 and 4).

The fragility curves can be combined with the spectral acceleration hazard curves to provide mean annual frequencies of collapse $\lambda_{\text{collapse}}$, as shown in Eq.(2). The spectral acceleration hazard curves in Figure 12 are obtained using results of hazard analyses for Van Nuys (Somerville and Cornell 2002). Thus, the mean annual frequency of collapse, $\lambda_{\text{collapse}}$ in each case can be obtained by these conditions and numerical integration.

Assuming a Poisson process, the probability of collapse in t years is given by

$$P(\text{collapse} | t) = 1 - \exp(-\lambda_{\text{collapse}} \cdot t) \quad (5)$$

Figure 13 shows the probabilities of collapse in 1 year and 50 years for each case, where, for $t=1$, the probability is the annual hazard. For Case-1 with first-story mechanism, the probabilities in 1 year and 50 years are conspicuously high compared to other cases. For Case-2 with four-story mechanism, the risk of collapse is mitigated drastically. On the other hand, the collapse probability decreases only slightly as the extent of the partial mechanism grows beyond four stories. It can be explained by tendency of the collapse fragility curves combined with the site hazard curve.

4. CONCLUSIONS

In this study, twelve-story reinforced concrete frame structures were considered based on the mechanism control that intends to keep the upper parts of the buildings intact after earthquakes. The structure was originally designed by the ultimate strength concept and the procedures given by AIJ's guidelines (1990). For the analyses, assuming the additional strengthening for the upper part of this structure, and using elastic members in the area, the partial mechanism was forced. From the results of these analyses, the following observations can be made.

(1) EDP-direction statistics

In this study, three EDP are considered as follows:

The sum of the hysteretic energy dissipations of all hinges E_{sum} and the sum of the maximum plastic rotations of all hinges $\theta_{\text{max,sum}}$ at a given hazard level tend to be the same regardless of the size of the partial mechanism, respectively.

On the other hand, the maximum inter-story drift over all stories IDR_{max} decreases as the

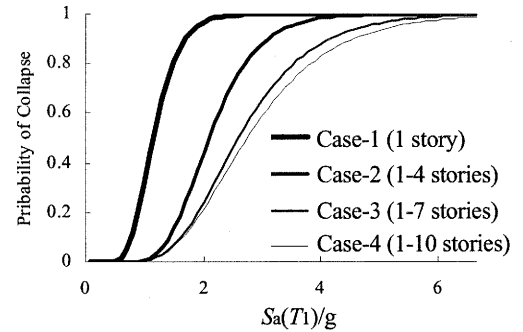


Figure 11 Collapse fragility curves

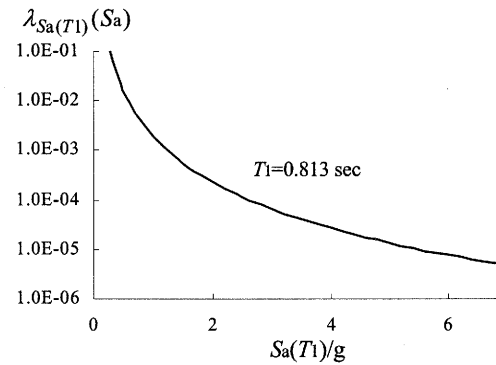


Figure 12 Hazard curve at Van Nuys

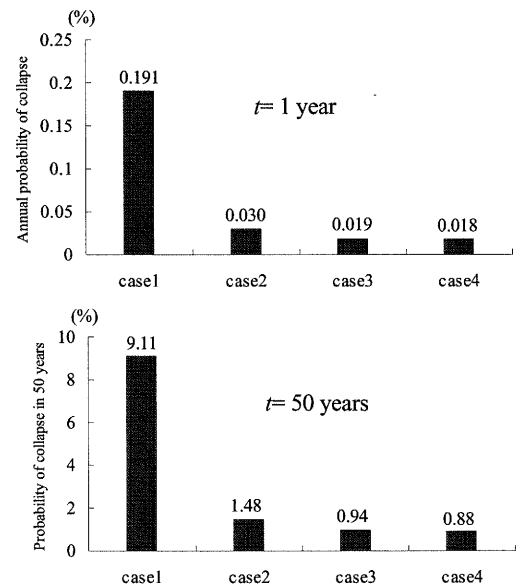


Figure 13 Probabilities of collapse

mechanism extent becomes large. However, simultaneously, the differences tend to become small. The average of maximum plastic rotation $\rho_{\theta_{\max, \text{ave}}}$ is inversely proportional to the number of hinges n . In addition, in the case with the 10-story partial mechanism, the maximum inter-story drift in individual stories IDR_i becomes relatively large in the lower area of the partial mechanism. Thus, IDR_{\max} of the case with the 10-story partial mechanism becomes very close to that of the case with the 7-story partial mechanism at a given hazard level, not only because the increase in the number of plastic hinges is small but also because the hinges in the upper area of the partial mechanism do not dissipate much energy.

(2) IM-direction statistics

A method was illustrated that evaluates the probability of collapse in t years by using the spectral acceleration hazard curve and the collapse fragility curve. The probabilities of the cases with different extents of partial mechanisms were compared.

As a result, it was shown that the probability of collapse is reduced as the mechanism extent becomes large. However, the collapse probability decreases only slightly as the extent of the partial mechanism grows beyond four stories.

Design based on mechanism control could become an option for performance based design, which should satisfy diverse demands from stakeholders and residents. Reducing the number of stories involved in the mechanism can produce benefits in terms of the repair process from earthquakes and even the construction process (see item 1). In this research, it is suggested that involving a certain number of stories in the mechanism is very important, but the impact on improving the seismic performance reaches a ceiling as discussed above. In the near future, performance based design procedures are expected to be developed that consider the balance between the seismic performance and the benefits from mechanism control.

Acknowledgements:

The authors acknowledge suggestions of Farzin Zareian, Paul Cordova, Jorge Ruiz-Garcia, Hassameddin Aslani and Jack Baker at Stanford University.

References:

- AIJ (1990), "Design Guidelines for Earthquake Resistant Reinforced Concrete Buildings Based on Ultimate Strength Concept".
- Paulay, T. (1986), "A Critique of the special Provisions for Seismic Design of the Building Code Requirements for Reinforced Concrete (ACI 318-83)", TECHNICAL PAPER, *ACI Journal*, pp.274-283, March-April.
- Ibarra, L. F., and Krawinkler, H., (2004), "Global Collapse of Deteriorating MDOF Systems", *13th WCEE*, Paper No. 116.
- Farzin Z., Ibarra, L.F., and Krawinkler, H. (2004), "Seismic Demands and Capacities of Single-Story and Low-Rise Multi-Story Woodframe Structures", *13th WCEE*, Paper No. 2144.
- Vamvatsikos, D., and Cornell, C.A. (2002), "Incremental Dynamic Analysis", *Earthquake Engineering and Structural Dynamics*, 31, 3, 491-514.
- Takeda, T., Sozen, M. A., and Nielsen, N. N. (1970), "Reinforced Concrete Response to Simulated Earthquakes", *Journal of the Structure Division*, ASCE, ST12, pp. 2557-2573.
- Sugano, S. (1973), "Study on Hysteretic Behavior of Members of Reinforced Concrete Members", *Concrete Journal* (in Japanese), Vol.11, No.2.
- Medina, R. (2003), "Seismic Demands for Nondeteriorating Frame Structures and Their Dependence on Ground Motions", Ph. D. thesis, Stanford University.
- Federal Emergency Management Agency "Prestandard and Commentary for the Seismic Rehabilitation of Buildings (FEMA356/November2000)".
- EERI Committee on Seismic Risk (1989), "The basics Risk Analysis", *Earthquake Spectra*, 5 (4), 675-702.
- Shome, N., and Cornell, C.A. (1998), "Earthquakes, Records, and Nonlinear Responses", *Earthquake Spectra*, 14 (3), 469-500.
- Somerville P., Cornell, C.A. (2002), "Ground Motion time histories for the Van Nuys Building, *PEER Methodology Testbeds Project*, URS Corporation, Pasadena, CA.

EXPERIMENTAL STUDY ON HYSTERESIS BEHAVIORS OF STRUCTURAL STEEL DURING MULTI-AXIAL LOADINGS

K.S. Chung¹⁾, Y. Matsumoto²⁾, and S. Yamada³⁾

1) Graduate Student, Interdisciplinary Graduate School of Science and Eng., Tokyo Institute of Technology, Japan

2) Research Associate, Dept. of Architecture, Yokohama National University, Japan

3) Associate Professor, Department of Civil Engineering, Tokyo Institute of Technology, Japan

chung@serc.titech.ac.jp, yuka@arc.ynu.ac.jp, knaniwa@serc.titech.ac.jp

Abstract: The stress-strain relationship including the plastic deformation phase is essential information for structural design of buildings. However, lack of empirical data prevents the development of analysis model for multi-axial stress state.

The aim of this study is investigating the hysteresis behavior of structural steel subjected to multi-axial loading. For this purpose, the loading equipment and cylindrical specimens were manufactured. The loading equipment provided various loading paths, such as uni-axial loading, simultaneous loading of axial force and torsion. Uniform multi-axial stresses were generated in the cross-section of cylindrical specimens. The hysteresis loop in terms of effective stress-effective strain was divided into the skeleton curve, the bauschinger part and the elastic unloading part, and the properties were examined.

1. INTRODUCTION

For the ultimate seismic design of steel structures, it is important to estimate the hysteresis behavior and ultimate capacity of the members, which are subjected to complex cyclic loads under severe earthquakes. The stress-strain relationship of material is essential information for this phase.

Among the subjects related to the material properties, stress-strain relationship under multi-axial stress is a complicated problem. The isotropic hardening model and kinematic hardening model is generally used because of its simplicity, but the applicability is limited. Some researches proposed improved models, such as two-surface (Dafalias and Popov, 1976) and multi-surface model (Iwan, 1967). On the other hand, it is more desirable that simplified analysis model is established for practical use. However, the lack of empirical data prevents further research.

With this background, a series of experimental study was planned and the multi-axial loading equipment was designed. In this loading system, a cylindrical specimen is subjected to both axial force and torsion, and a uniform multi-axial stress is generated in the cross-section. The loading equipment provides various loading paths, such as cyclic axial loading, cyclic torsion loading, alternate or simultaneous loading of axial force and torsion.

The final goal of this project is proposing the hysteresis model of structural steel that is applicable to both uni-axial stress and multi-axial stress. In this paper, the experimental method and results are reported, and the hysteresis properties under multi-axial stress are compared with those under uni-axial stress.

2. EXPERIMENTAL PROCEDURE

2.1 Specimens and Material Properties

Two different structural steels, SS400 and SM490A, were examined in this study. The material properties obtained by coupon tests are shown in Figure 1. The measured yield stress of 'SM490A', which was obtained as SM490A in market, doesn't satisfy the requirement for SM490A.

The specimen has cylindrical shape as shown in Figure 2. The axial force generates uniform axial stress and the torsion on its longitudinal axis generates uniform shear stress in the cross-section area. The outer diameter and inner diameter of section area are 14mm and 11mm, respectively. The tube wall is thick enough to prevent the local buckling.

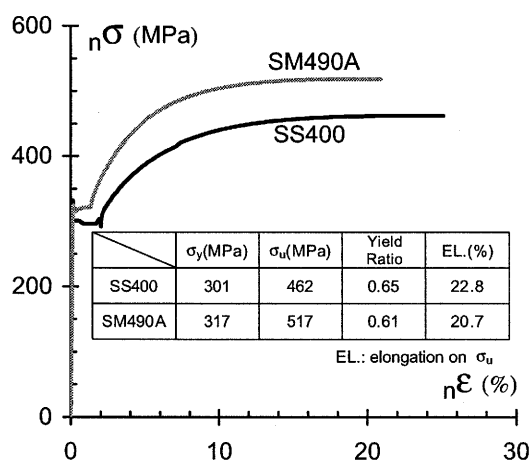


Figure 1 Nominal stress vs. strain curve in monotonic tensile test.

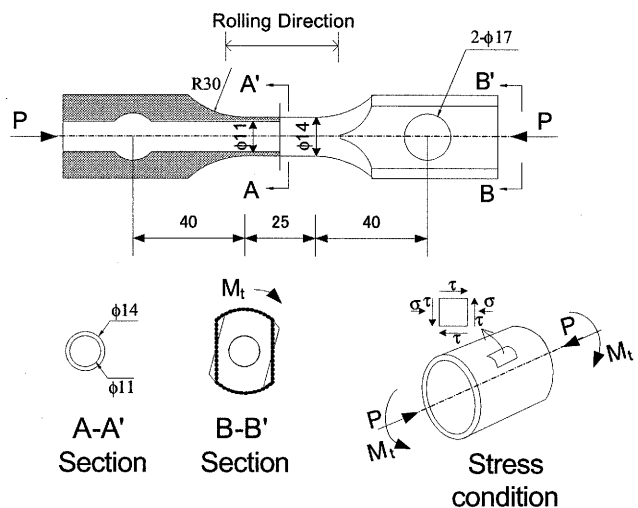


Figure 2 Details of specimen and stress condition in cross section (Unit:mm).

2.2 Experimental Setup

Test setup is shown in Figure 3. The loading equipment is composed of a reaction frame, an oil jack, a universal joint, a loading disk and a load cell. One end of the specimen was fixed to the reaction frame through the load cell, and the other end was fixed to the loading disk, which could rotate on its axis and slide in longitudinal direction of the setup. The loading disk was connected to the oil jack through the universal joint. The specimens were subjected to the axial force by the oil jack and the torsion by the rotation of the loading disk. The loading equipment provided various loading paths, such as cyclic axial loading, cyclic torsion loading, alternate or simultaneous loading of axial force and torsion.

The load cell in Figure 3 provided the axial load and the twisting moment separately. The axial and shear strain were measured by rectangular rosette strain gages and torque strain gages attached on the outer surface of the specimen.

Tests were performed at room temperature. The loading speed was quasi-static.

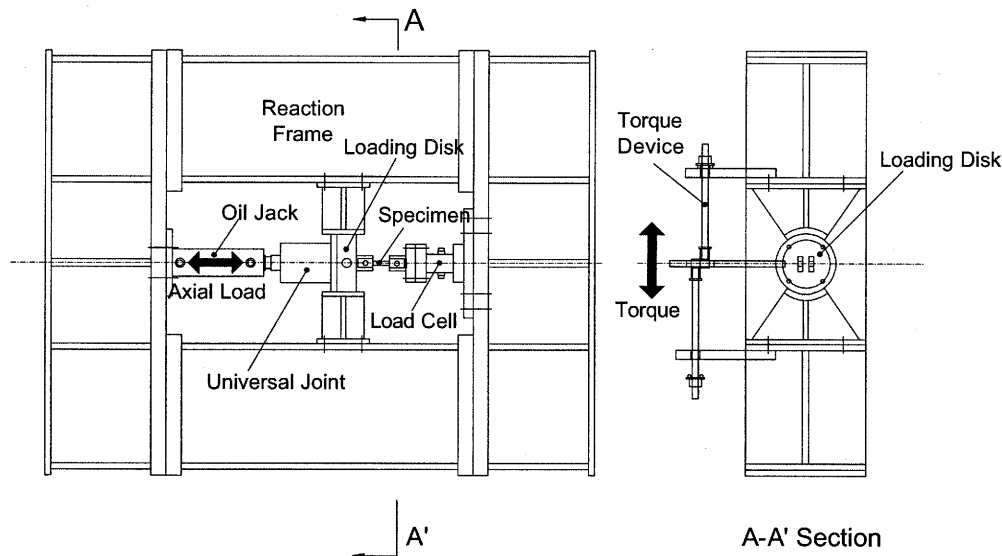


Figure 3 Test setup

2.3 Parameters

This study includes two series of experiments; uni-axial stress series and multi-axial stress series. The experimental parameters for all specimens are listed in Table 1.

1. Uni-axial Stress Series

The specimen was exclusively subjected to axial stress or shear stress. The monotonic tensile loading and four types of cyclic loading were applied as loading protocol. The types of loading protocol are shown in Figure 4. For the type 1, 2 and 3, the loading was controlled by applying specified strain amplitude. For the type 4, the stress in one direction was controlled not to exceed the peak of previous step.

2. Multi-axial Stress Series

The loading process of this series is as follows. First, axial stress or shear stress was applied and held during the whole loading process. The target stress or strain is called 'initial stress' or 'initial strain' in this paper. The direction of axial initial stress is tensile. Second, the other type of stress was applied by the same loading protocol as the uni-axial stress series. The 'Stress type' in Table 1 means the latter.

The specimen's name is composed of abbreviations as follows.

<u>SS</u>	<u>-A</u>	<u>-100</u>	<u>-0</u>
material	stress type	initial stress/strain	loading protocol type
SS: SS400	A: axial	(omitted for uni-axial)	(0: monotonic tension)
SM: SM490A	S: shear		

Table 1 Specimen list and parameters

Specimen	Material	Initial Stress/Strain	Stress Type	Loading Protocol
SS-A-0	SS400	0	Axial	Monotonic
SS-A-1	SS400	0	Axial	Cyclic: Type1
SS-A-3	SS400	0	Axial	Cyclic: Type3
SS-S-0	SS400	0	Shear	Monotonic

SS-S-1	SS400	0	Shear	Cyclic:Type1
SS-S-2	SS400	0	Shear	Cyclic:Type2
SS-S-3	SS400	0	Shear	Cyclic:Type3
SS-S-4	SS400	0	Shear	Cyclic:Type4
SM-A-0	SM490A	0	Axial	Monotonic
SM-A-1	SM490A	0	Axial	Cyclic:Type1
SM-A-3	SM490A	0	Axial	Cyclic:Type3
SM-A-4	SM490A	0	Axial	Cyclic:Type4
SM-S-0	SM490A	0	Shear	Monotonic
SM-S-1	SM490A	0	Shear	Cyclic:Type1
SM-S-2	SM490A	0	Shear	Cyclic:Type2
SM-S-3	SM490A	0	Shear	Cyclic:Type3
SM-S-4	SM490A	0	Shear	Cyclic:Type4
SS-SA-50-0	SS400	$\tau = 50\text{MPa}$	Axial	Monotonic
SS-SA-50-3	SS400	$\tau = 50\text{MPa}$	Axial	Cyclic:Type3
SS-SA-100-0	SS400	$\tau = 100\text{MPa}$	Axial	Monotonic
SS-SA-100-1	SS400	$\tau = 100\text{MPa}$	Axial	Cyclic:Type1
SS-SA-1-0	SS400	$\gamma = 1\%$	Axial	Monotonic
SS-SA-3-0	SS400	$\gamma = 3\%$	Axial	Monotonic
SS-AS-150-0	SS400	$\sigma = 150\text{MPa}$	Shear	Monotonic
SS-AS-150-1	SS400	$\sigma = 150\text{MPa}$	Shear	Cyclic:Type1
SS-AS-100-1	SS400	$\sigma = 100\text{MPa}$	Shear	Cyclic:Type1
SS-AS-200-1	SS400	$\sigma = 200\text{MPa}$	Shear	Cyclic:Type1
SM-SA-50-0	SM490A	$\tau = 50\text{MPa}$	Axial	Monotonic
SM-SA-50-3	SM490A	$\tau = 50\text{MPa}$	Axial	Cyclic:Type3
SM-SA-100-0	SM490A	$\tau = 100\text{MPa}$	Axial	Monotonic
SM-SA-100-1	SM490A	$\tau = 100\text{MPa}$	Axial	Cyclic:Type1
SM-SA-1-0	SM490A	$\gamma = 1\%$	Axial	Monotonic
SM-SA-3-0	SM490A	$\gamma = 3\%$	Axial	Monotonic
SM-AS-150-0	SM490A	$\sigma = 150\text{MPa}$	Shear	Monotonic
SM-AS-150-1	SM490A	$\sigma = 150\text{MPa}$	Shear	Cyclic:Type1
SM-AS-100-1	SM490A	$\sigma = 100\text{MPa}$	Shear	Cyclic:Type1
SM-AS-200-1	SM490A	$\sigma = 200\text{MPa}$	Shear	Cyclic:Type1

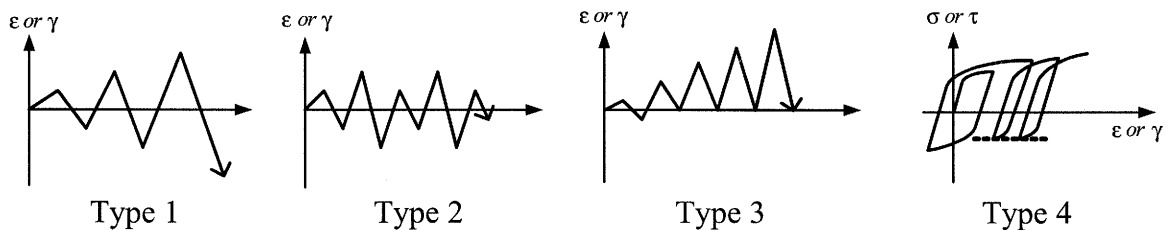


Figure 4 Loading protocol

2.4 Definition of stress and strain

The uniform stress distribution is assumed on the cross section. The nominal axial stress and nominal shear stress are calculated as follows.

$$\sigma = P / A \quad (1)$$

$$\tau = M_t / (2 \cdot t \cdot A') \quad (2)$$

Where, P and M_t are the axial force and twisting moment, respectively. A , t , and A' are the

cross-section area, the tube thickness, and the area of average radius, respectively.

The nominal axial strain ${}_n\varepsilon$ and shear strain $\tilde{\alpha}$ were measured by strain gages. The true axial stress and true axial strain are obtained as follows, based on the assumption of plastic incompressibility.

$${}_t\sigma = (1 + {}_n\varepsilon) {}_n\sigma \quad (3)$$

$${}_t\varepsilon = \ln(1 + {}_n\varepsilon) \quad (4)$$

In order to compare the hysteresis loops under different stress types, the stress-strain relationship is evaluated in terms of effective stress ${}_{eq}\sigma$ -effective strain ${}_{eq}\varepsilon$. These are defined as follows.

$${}_{eq}\sigma = \sqrt{{}_t\sigma^2 + 3\tau^2} \quad (5)$$

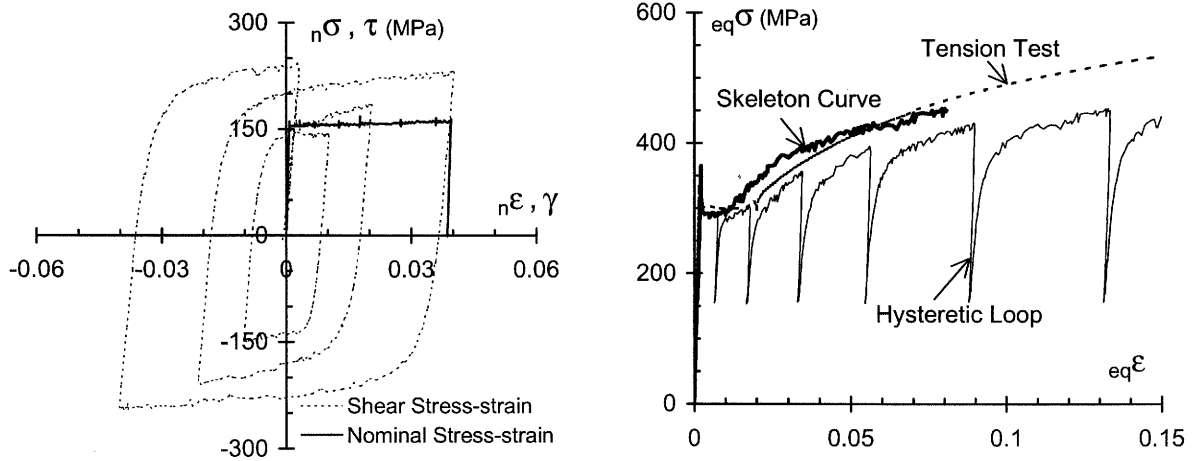
$${}_{eq}\varepsilon_p = \sum_i \sqrt{{}_t\varepsilon_{p,i}^2 + \gamma_{p,i}^2 / 3} \quad (6)$$

where ${}_t\varepsilon_{p,i}$ and ${}_t\gamma_{p,i}$ are axial plastic strain increment and shear plastic strain increment, respectively.

3. EXPERIMENTAL RESULTS AND DATA ANALYSIS

3.1 Outline of Hysteresis Loop

The ${}_n\sigma$ - ${}_n\varepsilon$ curve and $\tilde{\alpha}$ - $\tilde{\gamma}$ curve of SS-AS-150-1 are shown in Figure 5(a). The initial stress, ${}_n\sigma=150\text{MPa}$, is less than σ_y , but the ${}_n\sigma$ - ${}_n\varepsilon$ curve shows plastic strain induced by the shear stress loading. The hysteresis loop in effective stress-effective strain is shown in Figure 5(b). This figure also shows the skeleton curve defined in section 3.2 and the stress-strain curve of tensile test.



(a) Stress vs. strain response under multi-axial stress

(b) Effective stress vs. strain

Figure 5 Hysteresis loop under multi-axial cyclic loading(SS-AS-150-1)

3.2 Analysis of Hysteresis Behavior

In order to analyze the hysteresis behavior of structural steel, previous researches proposed the decomposition method (Kato and Akiyama, 1969). The skeleton curve is obtained by extracting segments from hysteresis loop when the load exceeds the maximum value of preceding loading history. The residual curve is divided into the baushinger part and the elastic unloading part. The hysteresis

model under uni-axial stress was proposed (Akiyama and Takahashi, 1995; Yamada et al., 2002), and this model is based on the following empirical knowledge.

1. The shape of skeleton curve is similar to the stress-strain curve under monotonic loading.
2. The softening due to bauschinger effect is observed in bauschinger part, and the stiffness reduction depends on the accumulative plastic strain in the preceding loading history.

This study is aimed at investigating the applicability of the previous model's concept to multi-axial stress. Therefore, the skeleton curve and bauschinger part were extracted from the effective stress-effective strain curve as shown in Figure 6, and the properties were examined. The experimental observations are reported in the following section.

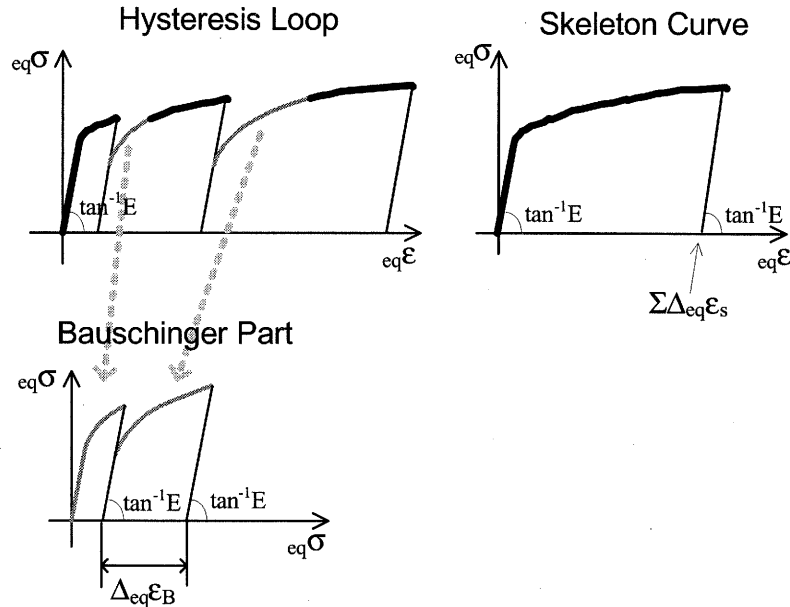


Figure 6 Decomposition method for Hysteresis Loop

(1) Skeleton Curve

The skeleton curves of each material are compared with the monotonic tensile curve in Figure 7. The skeleton curves are similar to the monotonic tensile curve regardless of stress type, loading protocol and material. Thus, the skeleton curve is predicted by the material coupon test.

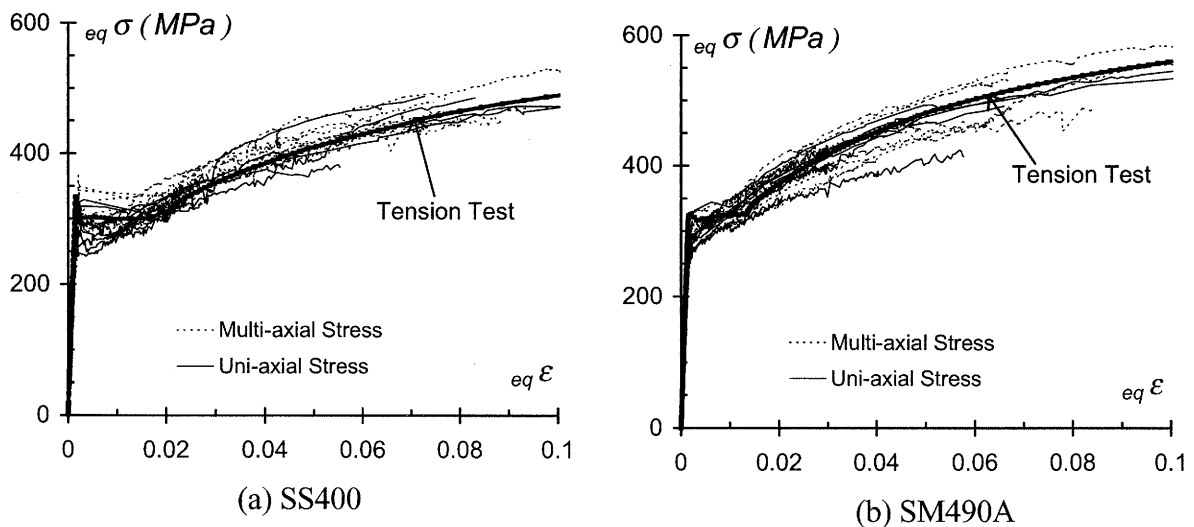


Figure 7 Comparison of skeleton curve and tension test.

(2) Bauschinger Part

As mentioned before, the previous researches reported that the stiffness reduction in bauschinger part depended on the accumulative plastic strain in the preceding loading history. The similar tendency was observed in this study. In order to investigate it quantitatively, the index $\Delta_{eq}\epsilon_B$, $\Sigma_{eq}\epsilon_s$ and α_B are defined as shown in Figure 6 and 8, and the correlations are examined.

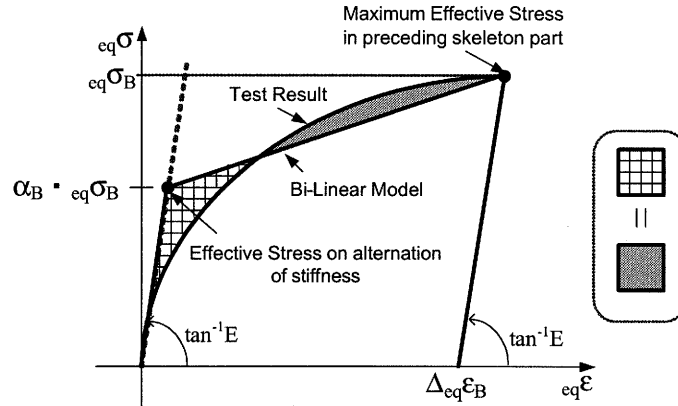


Figure 8 Modeling of bauschinger part.

The $\Delta_{eq}\epsilon_B$, which is effective plastic strain increment in each segment of bauschinger part, reflects the stiffness reduction. The $\Sigma_{eq}\epsilon_s$ is accumulative effective plastic strain in the preceding skeleton curve. The relation between $\Delta_{eq}\epsilon_B$ and $\Sigma_{eq}\epsilon_s$ is shown in Figure 9. In case of uni-axial stress, the $\Delta_{eq}\epsilon_B$ is proportional to the $\Sigma_{eq}\epsilon_s$, and the coefficient is approximately 2/3 regardless of stress type and material. In case of multi-axial stress, the $\Delta_{eq}\epsilon_B$ is proportional to the $\Sigma_{eq}\epsilon_s$. The coefficient slightly depends on the initial stress, and it tends to be lower when the initial stress increases.

In this study, each segment of bauschinger part is modeled as bi-linear, which is equivalent to the original segment in the energy dissipation. The initial stiffness of bi-linear model is equal to the elastic modulus. The α_B is obtained as the ratio of elastic limit stress to $eq\sigma_B$, which is maximum effective stress in preceding skeleton part (see Figure 8). The relation between α_B and $\Delta_{eq}\epsilon_B$ is shown in Figure 10. In the hysteresis model of previous research, α_B is set at 2/3 regardless of $\Delta_{eq}\epsilon_B$ (Yamada et al., 2002). The plotted data in Figure 10 are scattering when the $\Delta_{eq}\epsilon_B$ are relatively small, but it is allowable to consider that α_B is approximately 2/3 in case of uni-axial stress condition. The α_B is unrelated to $\Delta_{eq}\epsilon_B$ in case of multi-axial stress, and it slightly rises with high initial stress.

In summary, the lower $\Delta_{eq}\epsilon_B$ and higher α_B mean that the softening due to bauschinger effect is less remarkable than those under uni-axial stress.

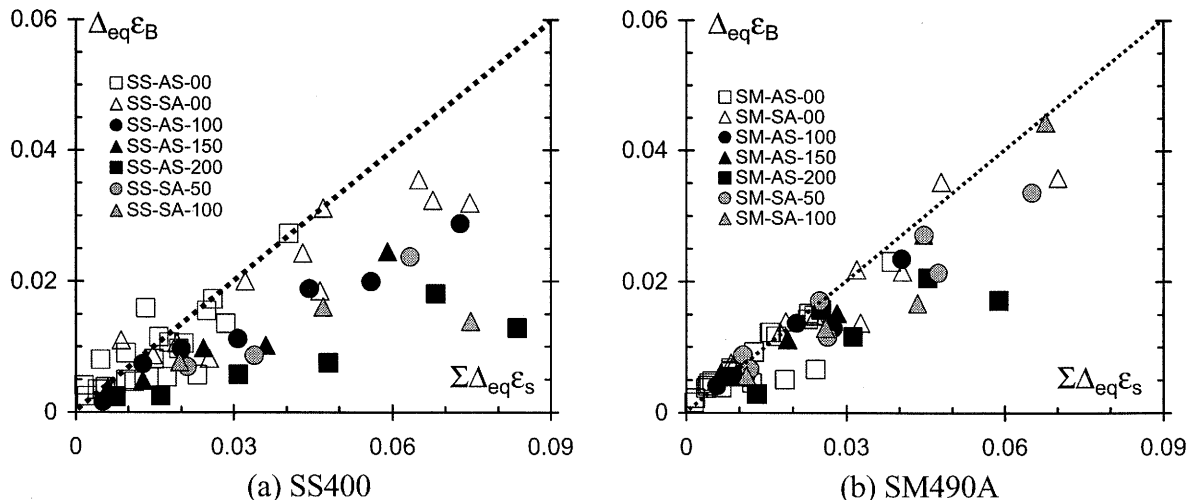


Figure 9 $\Delta_{eq}\epsilon_B$ versus $\Sigma\Delta_{eq}\epsilon_s$ relations

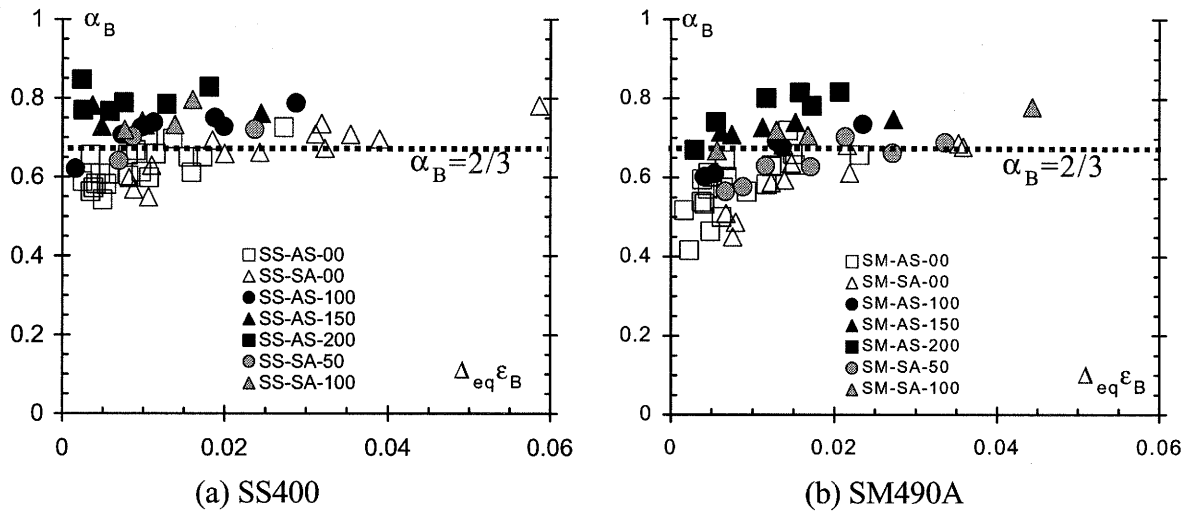


Figure 10 α_B versus $\Delta_{eq}\epsilon_B$ relations

4. CONCLUSIONS

The multi-axial loading experiments were performed in order to investigate the hysteresis behavior of structural steel subjected to multi-axial stress. The skeleton curve and bauschinger part were extracted from the hysteresis loop in term of effective stress-effective strain, and the properties of each part were examined. The skeleton curve was similar to the monotonic tensile curve regardless of stress type, loading protocol and material. The shape of bauschinger part depended on the accumulative effective plastic strain in the preceding skeleton curve, and the softening due to bauschinger effect was less remarkable than those under uni-axial stress.

It is conceivable from the results that the concept of previous hysteresis model is applicable for multi-axial stress. However, further research is required to establish the inclusive hysteresis model.

References:

- W. F. Chen and D. J. Han (1988), "Plasticity for Structural Engineers," Springer-Verlag.
- Y. F. Dafalias and E. P. Popov (1976), "Plastic Internal Variables Formalism of Cyclic Plasticity," *Journal of Applied Mechanics*, ASME, **124**(5), 645-651.
- W. D. Iwan (1967), "On a Class of Models for the Yielding Behavior of Continuous and Composite Systems," *Journal of Applied Mechanics*, ASME, **124**(5), 612-617.
- B. Kato and H. Akiyama (1969), "Inelastic bar subjected to trust and cyclic bending," *Journal of the structural division, Proc. of ASCE*, Vol.95, No.ST1, pp.33-56
- H. Akiyama and M. Takahashi (1995), "Influence of Bauschinger Effect on Seismic Resistance of Steel Structures," *Journal Structural Construction Engineering*, AIJ, **418**(5), 49-57.(In Japanese)
- S. Yamada, T. Imaeda and K. Okada (2002), "Simple Hysteresis Model of Structural Steel Considering the Bauschinger Effect," *Journal Structural Construction Engineering*, AIJ, **559**(5), 225-223.(In Japanese)
- K. S. Chung, Y. Matsumoto and S. Yamada (2004), "Study on the Constitutive Relation of Structural Steel under Multi-axial Stress Part 1. uniaxial cyclic loading history," *Proceedings of the CTBUH 2004 Seoul Conference*, Vol.1, 539-544.

A STUDY ON BOLTED CONNECTIONS USING CONCRETE SLAB AS THE LATERAL FORCE TRANSFER

S. Kishiki¹⁾, S. Yamada²⁾, T. Takeuchi³⁾, K. Suzuki⁴⁾, E. Saeki⁵⁾, and A. Wada⁶⁾

1) Graduate Student, Structural Engineering Research Center, Tokyo Institute of Technology, Japan

2) Associate Professor, Structural Engineering Research Center, Tokyo Institute of Technology, Japan

3) Associate Professor, Department of Architecture and Building Engineering, Tokyo Institute of Technology, Japan

4) Building Construction Division, Nippon Steel Corporation, Japan

5) Building Construction Division, Nippon Steel Corporation, Japan

6) Professor, Structural Engineering Research Center, Tokyo Institute of Technology, Japan

kishiki@serc.titech.ac.jp, naniwa@serc.titech.ac.jp, ttoru@arch.titech.ac.jp, wada@serc.titech.ac.jp

Abstract: As the result of studies after the Kobe earthquake, welding practices have been improved by using higher material toughness and geometrical modification of the weld access hole. However, it is notable that the quality of welds is not easy to control in practices as long as the structural fabrication relies on workmanship. Recently, the new structures system using the high strength bolts instead of welding is proposed in Japan. Naturally, the bolted connections are being applied to the Damage-Controlled-Structures. However, at the beam-end connections, there is a problem that cannot disregard the loss of the lateral force transfer caused by local out-of-plane deformation of column skin plates.

In this study, a cyclic loading test on a steel frame with the buckling-restrained braces was carried out. In the frame, beams connected to columns by high strength bolts. A feature of the test is to propose the new connection details, which use concrete slabs as the transfer of the lateral force of dampers. From the result of the cyclic test, it became clear that concrete slabs could be used as the structural member transferring the lateral forces of dampers.

1. INTRODUCTION

In the Northridge and Kobe Earthquakes, some buildings lost structural functions, although many buildings avoided collapse as to save human life. The loss caused the stop of social and industrial activities, and severe economic loss. At the stage of seismic design, it is important to consider restoring structures soon after an earthquake. Consequently, most of high-rise buildings are designed following the Damage-Controlled-Structure (Wada et al., 1992). On the other hand, in the two earthquakes mentioned above, beam flange fracture occurred at the welded beam-end connections in steel structures. It indicates that the quality of welds is not easy to control in practices as long as the structural fabrication relies on workmanship. Recently, the new steel structures using high strength bolts instead of welding are proposed in Japan (Suita et al., 2003; Kishiki et al., 2004). However, a local out-of-plane deformation of column skin plates and connection elements (T-stub and angles), is not able to be ignored when the bolted connections are applied to the Damage-Controlled-Structures in order to avoid beam flange fractures. In other words, the loss of lateral force transfers of dampers caused by the local out-of-plane deformation at the bolted connections. This study tried to improve the issue by using a concrete slab as a lateral force transfer.

2. TEST PLAN

2.1 Test Specimen and Test Setup

The test specimen was the 1/2 scale model of medium-rise steel structures. It was one-story and one-span plane-frame. It had the height of 2000mm story, and a length of 3000mm span. The test specimen consisted of beams, columns, beam-end connections, the buckling-restrained braces, and concrete slabs. Main features of this specimen were that beams were connected to columns by high strength bolts, and reinforcing bars of transferring the lateral force of dampers were installed into the concrete slabs. The detail of beam-ends connections and concrete slabs will be described later

The test specimen and test setup are shown in Fig.1. Both upper-end and bottom-end of columns were connected to pin supports. The bottom pin supports were connected to reaction devices, and the upper pin supports were connected to a loading beam. And an actuator was mounted to the loading beam.

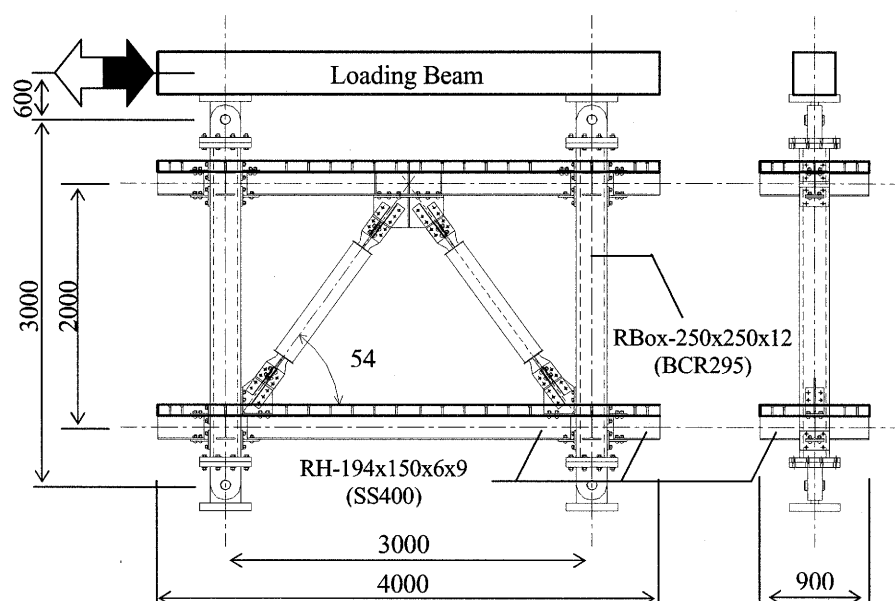


Figure 1 Test Specimen and Test Setup

2.2 Beam and Column

All beams were made of section (depth x width x web thickness x flange thickness) of 194x150x6x9. Steel grades JIS SS400 were chosen for flange and web. The columns were made of cold-formed square-tubes, and had section (width x width thickness) of 250x250x12. As shown in Table 1, mechanical properties were obtained from tensile coupon tests according to JIS-1A.

Table 1 Tension Coupon Data

Sampled Plate & Thickness		Grade	Yield Strength [N/mm ²]	Ultimate Strength [N/mm ²]	Elongation [%]
the Buckling-Restrained Brae	t = 16	LYP225	219	293	24
Column (Rbox-250x250x12)	t = 12	BCR295	388*	464	13
Beam (RH-194x150x6x9)	Web(t = 6)	SS400	382	484	16
	Flange(t = 9)	SS400	316	456	20

* 0.2 % offset strength

2.3 Beam-End Connections (Pin Connections)

The beams were connected to the columns by high strength bolts with T-stubs and gusset-plate parts, connection elements. At the bottom flange of each, specific T-stubs were installed. The specific T-stubs have two slotted holes. The T-stubs were connected to beams through the slotted hole. A feature of the connections is that the high strength bolts are loosely tightened. Consequently, although the beam-end connections can resist shear force, cannot resist bending moment. In other words, it has to be treated as a pin connection.

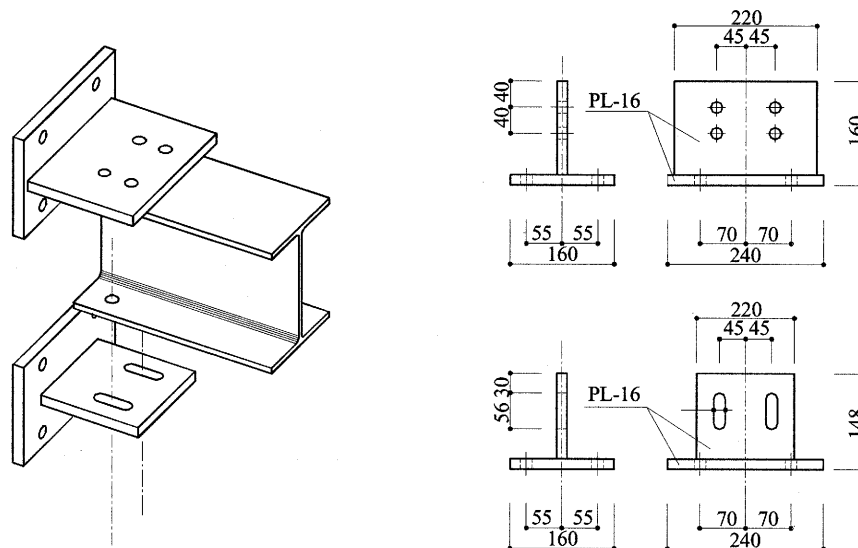


Figure 2 Beam-End Connections (Pin Connections)

2.4 Buckling-Restrained Braces and Gusset-Plate Parts

A buckling-restrained brace consists of a steel core members enclosed in concrete-filled square steel tube. The core member is coated with a non-bonding material, so that no axial force works on the concrete and the steel tube. This brace shows stable hysteresis if the yielding load working on the core member is smaller than the buckling load of the steel tube. And the core member made of Low Yield Point steel (LYP). Mechanical properties of the LYP steel were shown in Table 1. Note that Young's modulus and Poisson's ratio of the LYP steel are identical to those of conventional structural steel.

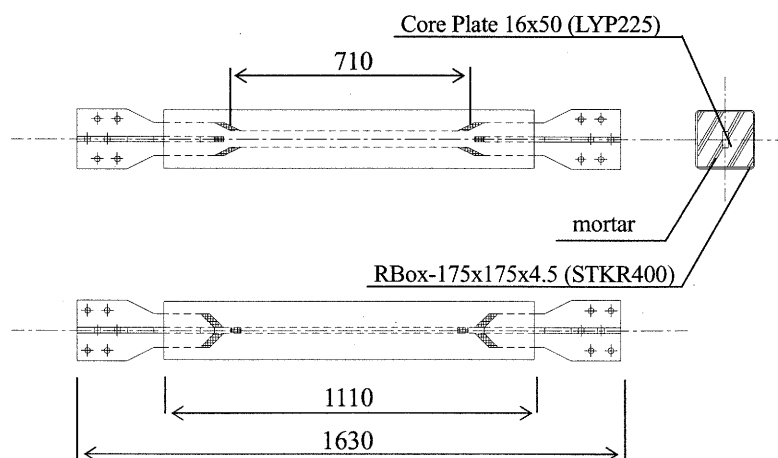


Figure 3 Buckling-Restrained Brace

2.6 Loading Program

Quasi-static cyclic loading test was carried out following the loading program shown in Fig.6. The loading program was based on the story drift angles, which were 1/200, 1/100, 1/50, and 1/33 radian. The relative story displacement was calculated as a difference of the displacement in upper and bottom beams (as shown point A and B in Fig.1). And the story drift angle could be found out by dividing the relative story displacement by the height of the story.

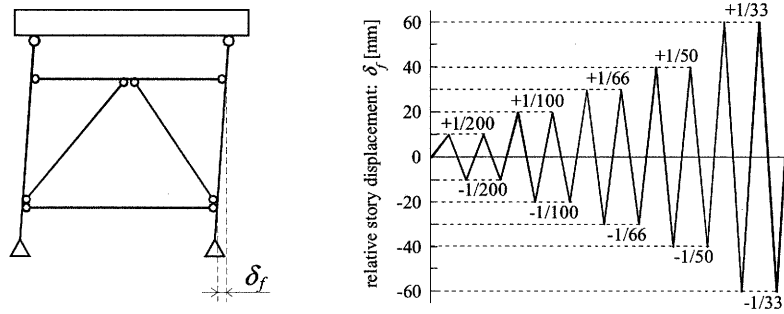


Figure 6 Definition of relative story displacement (δ_f) and Loading Program

2.7 Measurement

The cracks of concrete slabs were observed and written down, in order to grasp the lateral-force transfer mechanism of concrete slabs.

3. TEST RESULT AND CONSIDERATION

3.1 Test Condition

The specimen frame has a condition different from a partial frame in an actual building, where a lateral force is received from an earthquake. Especially, columns in the specimen frame receive a lateral force opposite to an earthquake. Consequently, in this study, lateral force and rotation of the columns are removed, and behavior of the frame is discussed. And lateral forces of the buckling restrained braces are led by equilibrium condition of forces in the specimen frame. Equations shown in (1) and (2) give lateral forces to the buckling restrained respectively.

$$\alpha_L = \frac{(cN_L + cN_R) + Q \cdot \tan \theta_{(R)}}{Q \cdot (\tan \theta_{(L)} + \tan \theta_{(R)})} \quad (1)$$

$$\alpha_R = 1.0 - \alpha_L \quad (2)$$

3.2 Behavior of the Buckling-Restrained Braces

Plots of shear force versus story drift angle for the specimen frame, in which effects of columns are removed, is shown in Fig. 7. And plots of lateral forces to bear responsibility versus axial deformation of the buckling-restrained braces, which are led from equation (1) and (2), also are shown in Fig. 6. The specimen frame showed a stable behavior by yielding of buckling-restrained braces. From 1/50 radians of the loading program in this test, compression strength is larger than tension strength. And fracture of the buckling-restrained brace in right side occurred beyond the first displacement of 1/33 radians. Therefore, the fracture caused strength degradation of the specimen frame.

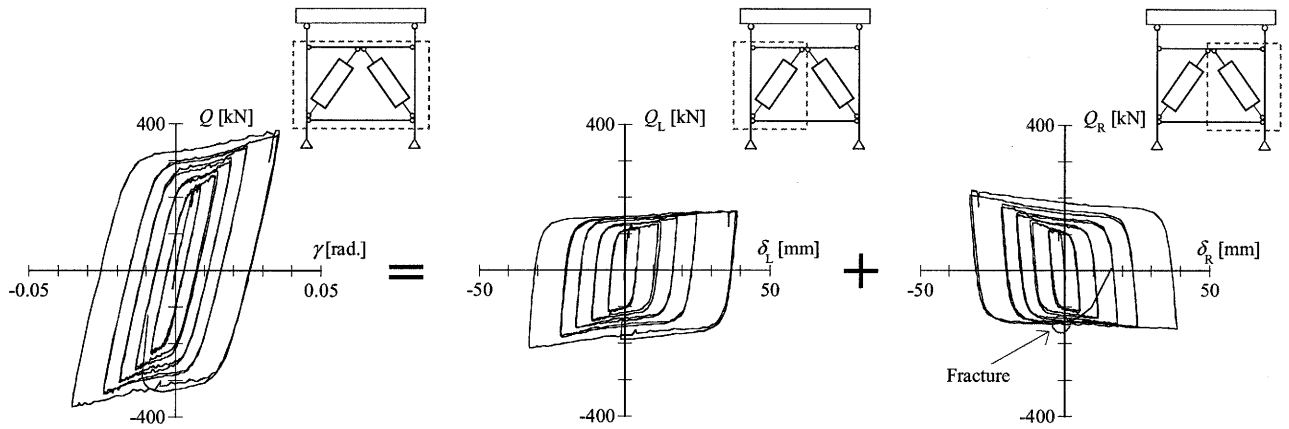


Figure 7 Behavior of Specimen Frame and Buckling-Restrained Braces

3.3 Behavior of Beam-End Connections

The center of rotation and rotation angle of the beam-end connections in the specimen frame are shown in Fig.8. At the beam-end connections of second floor, the center of rotation was located at the top flange during the cyclic loadings. On the other hand, in the case of positive moment at the beam-end connections of first floor, the center of rotation was located at the surface of concrete slab. And in the case of negative moment, it was located at the top flange. Each center of rotation was kept during the cyclic loadings. And rotation angles at the beam-end connections are similar to story drift angle, indicating that the beam-end connections work on as pin connection. However, at the beam-end connection of the second floor, rotation angles move to a positive rotation beyond the displacement of 1/50 radians. It is because the lateral forces of the right and left buckling-restrained brace do not balance. Increase in brace compression strength, followed by cyclic loadings in high strain, caused an unbalance of a right and left strength. Therefore, the rotation angles at the beam-end connection of the second floor were move to a positive rotation, with second floor beam pushed up.

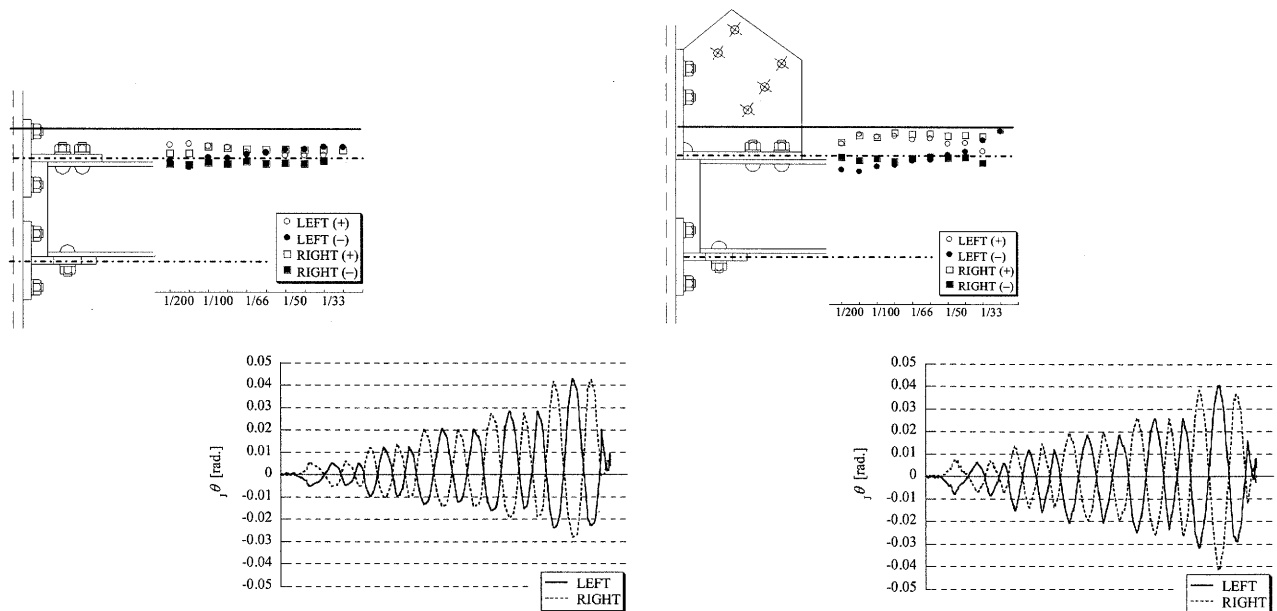


Figure 8 Behavior of Beam-End Connections (Center of Rotation and Rotation Angle)

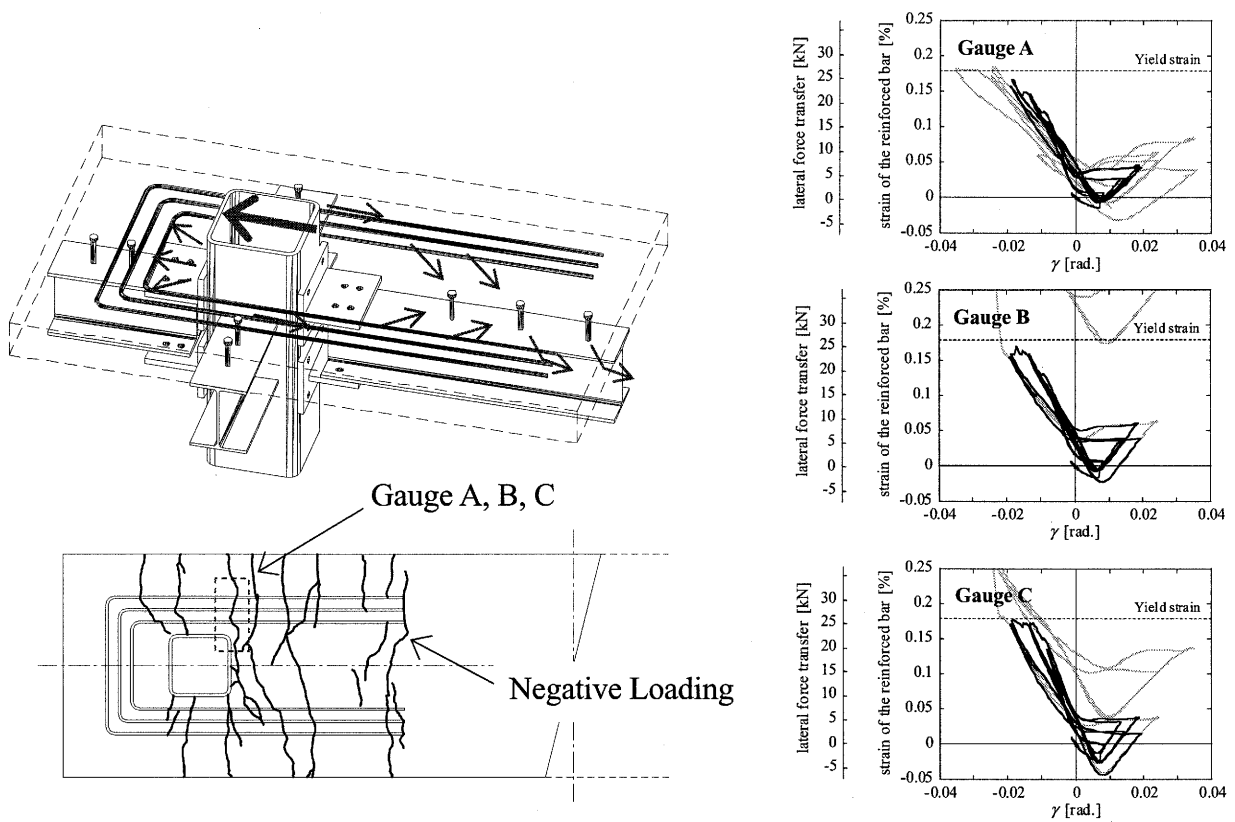


Figure 8 Damage to Concrete Slab and Behavior of Reinforcing Bars (Second Floor)

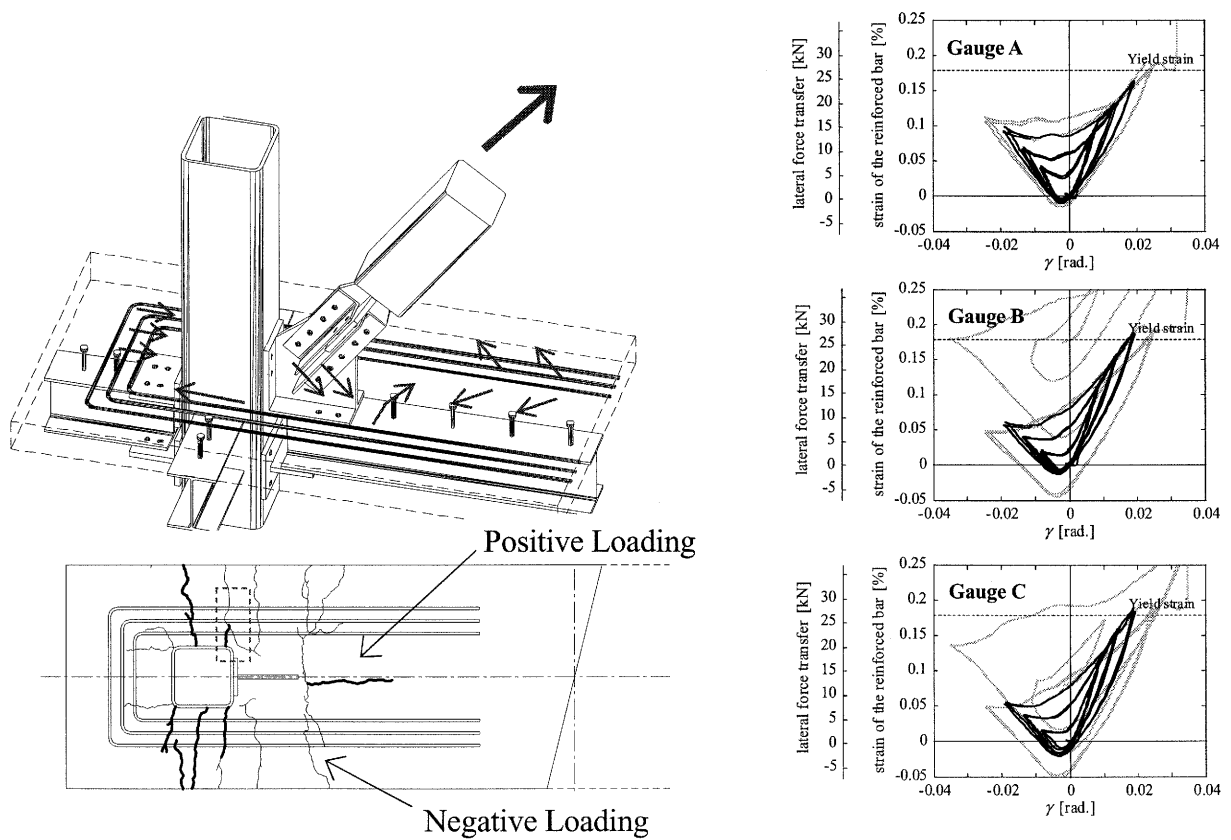


Figure 9 Damage to Concrete Slab and Behavior of Reinforcing Bars (First Floor)

3.4 Damage to Concrete Slabs and Behavior of Concrete Slab

The lateral force transfer mechanism in concrete slab and reinforcing bar, damage to concrete slab in $1/50$ radians, and distribution of lateral forces at the reinforcing bar are shown in Fig. 8 and Fig. 9. Cracks of concrete slabs appeared at the assumed direction of a loading. In the other words, at the second floor, cracks were caused by negative loading, and at the first floor, cracks were caused by positive loading. And distribution of lateral forces at the reinforcing bar indicated that the reinforcing bars were able to transfer a roughly 120kN (20kN per one reinforcing bar). This result is the same as the lateral force transfer assumed at the design stage. From the test results, it is clear that, instead of bolted connection elements, concrete slab with specific reinforcing bars installed is able to transfer the lateral forces of the buckling-restrained braces.

4. CONCLUSION

This study described that the $1/2$ scale specimen frame, that had the buckling-restrained braces and the bolted connections with T-stubs. Test results are summarized as follows:

- 1) The beam-end connections, with specific T-stubs at the bottom flange, showed a behavior as a pin connection. However, because of the strength unbalance caused by cyclic loadings in a high strain, the beam above the buckling-restrained braces was pushed up easily.
- 2) From the value of gauges provide on the U-shaped reinforcing bars, it is clear that, instead of bolted connection elements, concrete slab with specific reinforcing bars installed is able to transfer lateral forces of the buckling-restrained braces.

Acknowledgements:

The test in this paper was supported by Building Construction Division, and conducted in the Steel Structure Research and Development Center of Nippon Steel Corporation. The authors wish to thank Mr. Ichiro Takeuchi, Dr. Ryoichi Kanno, and Mr. Nobutaka Shimizu. The first author is as a research assistant (RA) of the Center of Urban Earthquake Engineering (CUEE) in Tokyo Institute of Technology, awarded by the 21st Century Center of Excellence (COE) program.

References:

- Wada, A., Connor, J. J., Kawai, H., Iwata, M., and Watanabe, A. (1992), "Damage Tolerant Structure" , *5th U.S.-Japan Workshop on the Improvement of Building Structural Design and Construction Practice*
- Suita, K., Inoue, K., Takeuchi, I., Uno, N. (2003), "Mechanical Behavior of Bolted Beam-to-Column Connections with Buckling-Restrained Knee Brace Dampers" , *Journal of Structural and Construction Engineering (Transactions of AIJ)*
- Kishiki, S., Yamada, S., Takeuchi, T., Suzuki, K., Okada, K., Wada, A. (2004), "New Ductile Steel Frames Limiting Damage to Connection Elements at the Bottom Flange of Beam-Ends Part 1 Static tests of beam-to-column connections with weak-web-split-tee" , *Journal of Structural and Construction Engineering (Transactions of AIJ)*
- Kishiki, S., Yamada, S., Takeuchi, T., Suzuki, K., Saeki, E., Wada, A. (2004), "New Ductile Steel Frames Limiting Damage to Connection Elements at the Bottom Flange of Beam-Ends Part 2 Cyclic loading tests of frames with a concrete slab" , *Journal of Structural and Construction Engineering (Transactions of AIJ)*

SEISMIC PERFORMANCE OF LINK-TO-COLUMN CONNECTIONS IN STEEL ECCENTRICALLY BRACED FRAMES

T. Okazaki¹⁾ and M.D. Engelhardt²⁾

1) Postdoctoral Research Fellow, Structural Engineering Research Center, Tokyo Institute of Technology, Japan

2) Professor, Dept. of Civil Engineering, University of Texas at Austin, Texas, U.S.A.

tokazaki@serc.titech.ac.jp, mde@mail.utexas.edu

Abstract: A total of twelve large-scale link-column specimens were tested to study the cyclic loading performance of link-to-column connections in eccentrically braced frames. Four different link-to-column connection types with varying configuration and welding details were tested. Each of the four connection types was tested with three different link lengths to consider a wide range of force and deformation environments at the link-to-column connection. The specimens representing the pre-Northridge practice failed after developing only half of the inelastic link rotation required in US building codes. Additional connection types were tested that implemented improved welding practices, as well as specimens that implements design and detailing modifications. The experimental program and key test results are presented.

1. INTRODUCTION

Eccentrically Braced Frames (EBFs) are a seismic load resisting system in which inelastic action is restricted primarily to ductile links. Some of the common types of EBFs are arranged to have one end of the link connected to a column. In such EBFs, the integrity of the link-to-column connection is essential to the ductile performance and safety of the EBF.

Besides the use of a welded web connection, EBF link-to-column connections have been designed, detailed, and constructed in a manner very similar to the welded flange-bolted web beam-to-column connection detail widely used in moment resisting frames prior to the Northridge Earthquake. Therefore, many of the features responsible for the poor performance of moment frame connections during the 1994 Northridge Earthquake are also likely present in link-to-column connections in currently existing EBFs. While extensive research in recent years has resulted in substantial changes in the design and construction of moment frame connections (FEMA 2000; AISC 2002), less attention has been given to EBF link-to-column connections. Further, because the force and deformation environment at EBF link-to-column connections is significantly different, and in some cases more severe than at moment frame connections, many of the newly developed moment frame connection details may not be applicable to EBF link-to-column connections. For example, the large moment gradient along the relatively short length of the link makes the reduced beam section difficult if not impossible to implement for link-to-column connections. Although the *2002 AISC Seismic Provisions* (AISC 2002) require qualifying cyclic test results for EBF link-to-column connections, very limited test data are currently available. A recent study conducted by Tsai et al. (2000) adds to the concerns for the safety of these connections.

An experimental investigation was conducted to examine the cyclic performance of EBF link-to-column connections. Twelve large-scale link-column specimens were constructed from ASTM A992 rolled steel shapes, and tested using the qualifying cyclic test procedure specified in the *2002*

AISC Seismic Provisions. To the knowledge of the authors, the tests conducted in this program are the first series of experiments specifically aimed at studying the seismic performance of large-scale EBF link-to-column connections constructed using realistic detailing and welding according to the US practices. This paper provides an overview of this experimental program, and discusses details of the specimens and some key test results.

2. EXPERIMENTAL PROGRAM

2.1 Test Setup

The test setup shown in Figure 1 was devised to reproduce the force and deformation environment at a link-to-column connection in an EBF. The loading ram supplied quasi-static vertical motion to the bottom of the column, and thus imposed cyclic shear deformation on the link. As illustrated in Figure 2, the forces developed in the link of an EBF under lateral load were reproduced in the specimen.

2.2 Test Specimens

A total of twelve link-column specimens were tested in this program. All specimens were constructed from W18x40 links and W12x120 columns, both of ASTM A992 steel. The sizes of the link and column sections as well as the column height of 2.44-m were selected to represent full or near full-scale dimensions in actual EBFs. The column was provided with continuity plates, but with no doubler plate. Table 1 summarizes the measured mechanical properties of the test sections for coupon samples taken from the edges of the flanges, and from mid-depth of the web.

The primary test parameters for this investigation were the connection type and the link length. The specifications of each specimen, including the primary features of the link-to-column connection, link length, and link stiffener spacing, are summarized in Table 2. The link stiffeners were detailed per the *2002 AISC Seismic Provisions*. The specimen names represent the two test parameters: the first two letters (PN/MW/FF/NA) represent the connection type, while the third letter (S/I/M) represents the link length.

Three link lengths were chosen to represent the different link length categories defined in the *2002 AISC Seismic Provisions*. Shear dominates the inelastic behavior of links shorter than $1.6M_p/V_p$, whereas flexure dominates for links longer than $2.6M_p/V_p$. Links of intermediate length are affected significantly by both shear and flexure. The provisions also require links to develop different levels of inelastic rotation depending on their length. Therefore, depending on the link length, very different

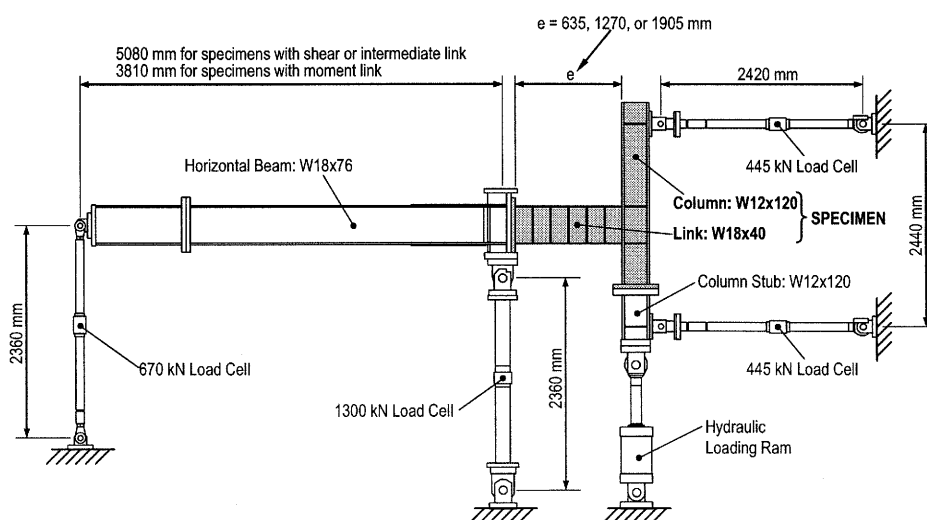


Figure 1 Test Setup

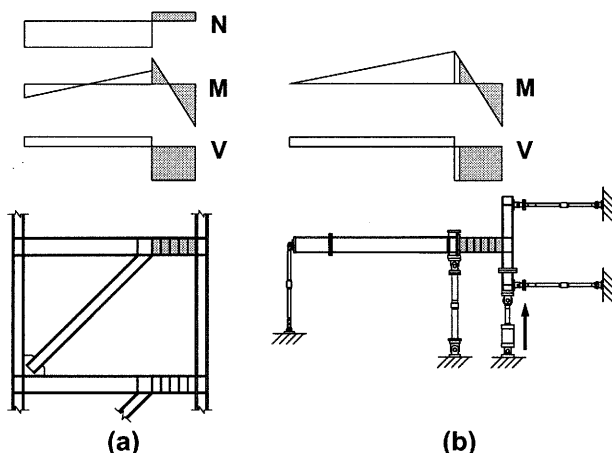


Figure 2 Force Distribution in (a) Typical EBF link and Beam, and in (b) Test Setup

Table 1 Test Section Properties

Section		F_y (MPa)	F_u (MPa)	Elong. (%)
W18x40	Flange	352	499	34
	Web	393	527	31
W12x120	Flange	323	455	29
	Web	353	485	33

Table 2 Test Specimens

Specimen	Connection Feature	e (mm)	$e/(M_p/V_p)$	Intermediate Stiffeners
PNS	Weld metal with no notch toughness requirement; backing bars and weld tabs left in place.	635	1.11	4@127mm
PNI		1270	2.22	5@191mm
PNM		1905	3.34	229mm from each end
MWS	Weld metal with specified notch toughness; modified welding details; modified weld access hole configuration.	635	1.11	4@127mm
MWI		1270	2.22	5@191mm
MWM		1905	3.34	229mm from each end
FFS	Extended free flange length; shear tab welded to link web; modified welding details as in MW-specimens.	635	1.11	3@127mm
FFI		1270	2.22	4@184mm
FFM		1905	3.34	229mm from each end
NAS	No weld access hole; continuous placing of bottom flange groove weld; modified welding details as in MW-specimens.	635	1.11	4@127mm
NAI		1270	2.22	5@191mm
NAM		1905	3.34	229mm from each end

force and deformation environment can be realized at the link-to-column connection. In this paper, links with length of $e = 1.1M_p/V_p$ are referred to as S-links (shear links); links of $e = 2.2M_p/V_p$ are referred to as I-links (intermediate links); and links of $e = 3.3M_p/V_p$ are referred to as M-links (moment links). The link length parameter, $e/(M_p/V_p)$, described herein was evaluated based on the measured section dimensions and the measured yield strength values.

Link-column specimens with the three link lengths described above were tested with four different connection types, designated as the PN, MW, FF, and NA-types. Details of the four connection types are discussed below.

2.3 Connection Types

The PN (pre-Northridge) connection was designed to represent the pre-Northridge practice in detailing and construction for link-to-column connections. A self-shielded flux core arc welding (SS-FCAW) process with an E70T-4 electrode was used for the complete joint penetration (CJP) groove welds connecting the link flanges to the column flange. The backing bars and weld tabs were left in place after completion of the link flange groove welds.

The main feature of the MW (modified welding) connection was the modification in the link flange groove welds following recommendations of FEMA-350 (2000). Among the modifications were: the use of an E70T-6 electrode, which has a designated notch toughness requirement; removal of the backing bar followed by the placement of a supplemental reinforcement fillet weld at the bottom flange groove weld; fillet welding the top flange backing bar to the column flange; removal of

weld tabs at both top and bottom link flanges; and the use of weld access hole configuration recommended by FEMA-350 (2000). These modifications were also adopted in the FF- and NA-connections.

The NA (no weld access hole) connection was designed based on the no weld access hole detail recently developed in Japan. Literature (e.g. Suita et al. 1999) reports excellent performance of moment frame connections with these details, and suggests that fracture initiating at the toe of the weld access hole could be precluded by eliminating the weld access holes. Since Engelhardt and Popov (1992) observed fracture of the link flange typically initiating at the toe of the weld access hole, it was expected that elimination of the weld access holes is also beneficial to EBF link-to-column connections. The CJP groove welds at both the top and bottom link flanges were placed continuously without interruption by the web, thereby reducing the likelihood of weld defects in the bottom flange groove weld (Engelhardt et al. 1993; 1997).

Figure 3 Connection FFS

The cyclic loading protocol specified in Appendix S of the *2002 AISC Seismic Provisions* for testing of link-to-column connections was used for all twelve tests. This loading protocol requires applying increasing levels of cyclic link rotation angle, γ , which was computed as the displacement of one end of the link relative to the other, divided by the link length. The *Provisions* specify link-to-column connections in EBFs to be evaluated based on inelastic link rotation. The inelastic rotation, γ_p , was evaluated by removing the contributions of elastic response from the link rotation, γ . The S-, I-, and M-links, as defined in this paper, are required to develop an inelastic rotation of 0.08, 0.043, and 0.02 rad, respectively, according to the *2002 AISC Seismic Provisions*. In this paper, the

inelastic rotation capacity, γ_p , is defined as the maximum inelastic link rotation amplitude sustained for at least one full cycle of loading prior to loss of strength of the specimen. Loss of strength is defined as either the link shear force or bending moment measured at the column face dropping to below 80-percent of their respective maximum values measured during the test.

Table 3 summarizes test results, listing the γ_p required in the 2002 AISC Seismic Provisions along with the measured γ_p , maximum link shear force, V_{max} , and maximum moment in the link at the column face, M_{max} . Both positive and negative values are reported for V_{max} and M_{max} . Also listed is a brief description of the controlling failure mode for each specimen.

4. DISCUSSION OF TEST RESULTS

As shown in Table 3, all specimens except Specimen NAS failed by fracture at the link-to-column connection. Only one specimen, FFI, sustained the link rotation required in the 2002 AISC Seismic Provisions. Fracture at the link-to-column connection typically caused abrupt and rapid loss of strength, as illustrated in the hysteretic response of Specimen FFI shown in Figure 4. Gradual strength degradation as observed in many moment frame connections prequalified in FEMA-350 (2000) was

Table 3 Test Results

Specimen	Req'd	Measured			Observed Failure Mode
	γ_p (rad)	γ_p (rad)	V_{max} (kN)	M_{max} (kN-m)	
PNS	0.08	0.041	+1025/-999	+365/-353	Fracture of top and bottom link flanges near groove weld
PNI	0.043	0.018	+748/-807	+484/-498	Fracture of link top flange near groove weld
PNM	0.02	0.008	+621/-540	+505/-525	Fracture of top and bottom link flanges near groove weld
MWS	0.08	0.050	+1043/-1051	+368/-348	Fracture of top and bottom link flanges near groove weld
MWI	0.043	0.018	+768/-765	+447/-474	Fracture of link top flange near groove weld
MWM	0.02	0.007	+581/-576	+524/-513	Fracture of top and bottom link flanges near groove weld
FFS	0.08	0.060	+1088/-1093	+396/-390	Fracture of link web around shear tab
FFI	0.043	0.046	+899/-889	+580/-548	Fracture of link top flange near groove weld, and fracture in shear tab/web groove weld
FFM	0.02	0.017	+651/-597	+567/-568	Fracture of top and bottom link flanges near groove weld, and fracture in shear tab/link web groove weld
NAS	0.08	0.070	+1127/-1100	+399/-387	Fracture of link web at stiffeners welds
NAI	0.043	0.027	+826/-862	+530/-509	Fracture of link top flange near groove weld
NAM	0.02	0.017	+597/-600	+557/-531	Fracture of link top flange near groove weld

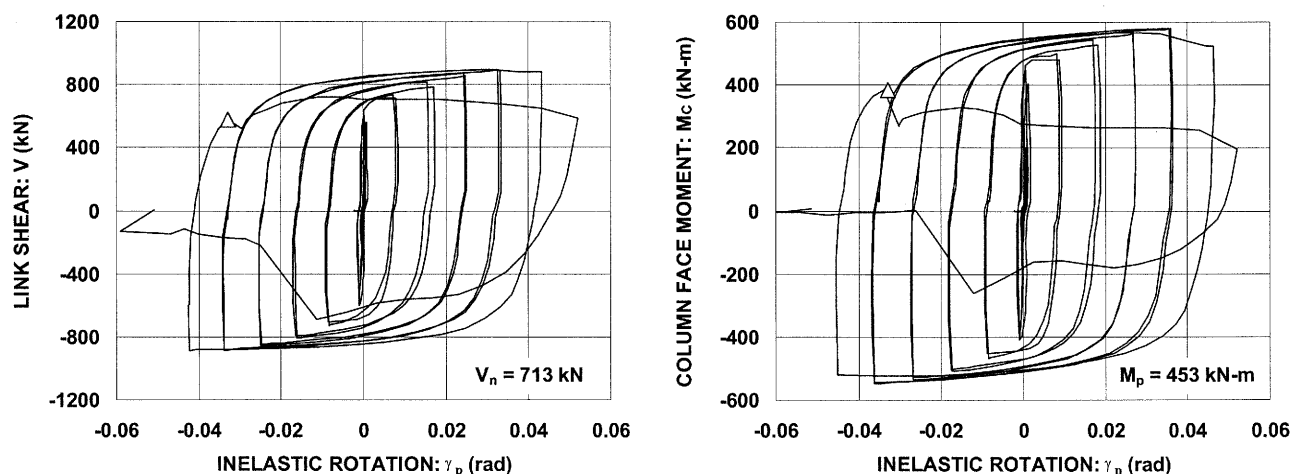


Figure 4 Hysteretic Response of Specimen FFI

not seen in any of the specimens. The excellent buckling control provided by the link stiffeners may have left fracture at the link-to-column connection as the dominating failure mode of the specimens.

4.1 Connection Type

As described earlier, four different connection types were examined in this experimental program. Table 3 suggests that the connection details had a significant effect on the inelastic link rotation achieved by the specimens.

The PN-connection was designed to represent pre-Northridge practices in the detailing and construction of EBF link-to-column connections. The three PN-specimens achieved no more than half of their required inelastic link rotations, and failed due to fracture of the link flange near the groove weld. Fracture initiating at the root of the bottom flange groove weld, as observed in a large number of pre-Northridge moment frame connections (e.g. Engelhardt et al. 1993), did not occur in any of the PN-specimens. The absence of this particular failure mode may be attributed to the relatively high CVN value of the E70T-4 weld metal, and to the difference in the force and deformation environment between link-to-column connections and moment frame connections.

The MW-connection featured the use of a weld filler metal with specified notch toughness and modification in welding details. Similar to the PN-connections, the MW-specimens failed due to fracture of the link flanges near the groove welds. The marginally improved inelastic rotation capacity of the MW-specimens over the PN-specimens suggests that, although the modifications in welding are beneficial, this alone is not sufficient to improve the connection performance to the required level.

The FF-connections were configured to draw the shear force away from the link flanges, and thereby reduce the stress and strain demand near the link flange groove welds. The FF-specimens were successful in preventing or delaying the occurrence of link flange fracture, and sustained significantly greater link rotations compared to the corresponding PN- and MW-specimens with identical link length. Nonetheless, Specimens FFS and FFM failed to meet their link rotation requirements. Specimen FFI failed immediately upon exceeding its link rotation requirement, as shown in **Figure 4**.

The restraint provided by the shear tab welded to the link web had a significant effect on link behavior in the FF-specimens. A direct effect was that yielding was precluded from the segment of the link web welded to the shear tab, as shown in **Figure 5** for Specimen FFS, and thus, inelastic rotation was amplified within an effectively shortened link.

Specimen FFS failed at an inelastic link rotation 25-percent below the required level due to fracture of the link web along the toe of the fillet weld connecting the shear tab to the link web, as shown in **Figure 5**. It is believed that the magnification in link rotation combined with the large restraint imposed on the link web material between the shear tab and the link flange generated severe cyclic inelastic strain demands near the right-angled corner of the shear tab, and induced fracture at this location. After noting the disadvantage of rectangular shear tabs, the subsequently tested specimens, FFI and FFM, were provided with tapered shear tabs. The failure mode of Specimen FFS was not seen in the other two FF-specimens.

In Specimen FFI, fractures were observed at the top and bottom edges of the shear tab and link web simultaneously with fractures in the link flange. In Specimen FFM, development of fractures in the shear tab and link web clearly preceded fracture initiation in the link flange. It appeared that the

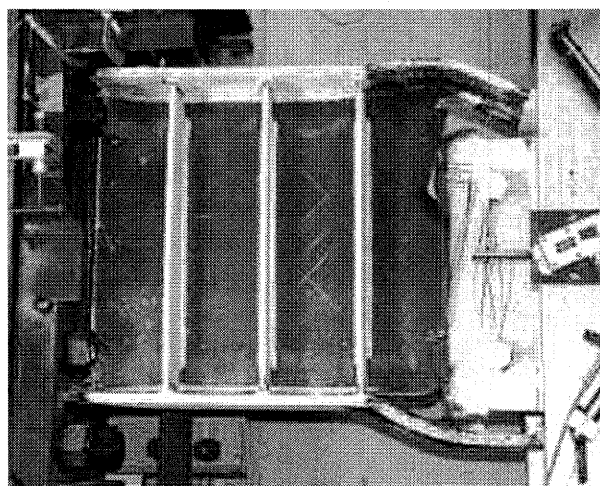


Figure 5 Specimen FFS After Testing

progression of fractures in the shear tab and link web caused redistribution of bending and shear stress from the link web and shear tab to the link flange, and thereby, accelerated fracture of the link flange. Therefore, the FF-connections were very sensitive to fracture initiating at the top and bottom edges of the link web and shear tab near the welds connecting to the column flange.

The NA-connection featured elimination of the weld access hole and a fabrication procedure that enabled continuous placement of the CJP groove weld at the link bottom flange. The NA-specimens sustained significantly greater link rotations compared to the corresponding PN- and MW-specimens with identical link length. Specimen NAS achieved an inelastic link rotation of 0.071 rad, short of the required 0.08 rad, before losing strength due to fracture of the link web. Although crack openings were noted along the toe of the groove welds, it appeared that the link-to-column connection maintained its strength when the test was terminated, and that Specimen NAS exhausted the inherent inelastic rotation capacity of the S-link. Specimens NAI and NAM failed prematurely due to fracture of the link flanges. Fracture of the link flange initiating at the outer edge of the flange appeared to be the dominant failure mode of the NA-connection regardless of the link length.

4.2 Link Length

Links of $e = 1.1, 2.2,$ and $3.3M_p/V_p$ were designated as S-, I-, and M-links, respectively, in this research program. The three link lengths were selected to study the performance of link-to-column connections subjected to a wide range of different possible force and deformation environments.

Table 3 indicates that the inelastic link rotation achieved by the link-to-column connections depended significantly on the link length. Table 3 also indicates that the forces at the link-to-column connection differed significantly depending on the link length. Meanwhile, the link-to-column connection was required to accommodate different levels of link rotation in accordance with the link length. The very significant difference in force and deformation environment had a large influence on the performance of the link-to-column connections.

Despite their very short length, S-link specimens yielded in the link flanges in the region near the column face in the, with the exception of Specimen FFS. Shear yielding in the link web led to a significant reduction in the flexural capacity of the link web, and consequently caused significant bending stress in the link flanges. Specimens PNS and MWS failed by fracture of the link flange near the groove weld. Crack openings were noted in Specimen NAS, along the toe of the link flange groove welds. Therefore, with the exception of Specimen FFS, failure of S-link specimens was controlled by fracture of the link flange. The inelastic link rotation capacity of Specimens PNS, MWS, FFS, and NAS were 51-, 63-, 75-, and 88-percent, respectively, of the required 0.08 rad. However, the link rotation of Specimen NAS was limited by the link itself, and not by the link-to-column connection.

All four M-link specimens failed due to fracture of the link flange near the groove weld, and failed to meet the link rotation requirement. Specimens PNM and MWM achieved 40-percent of the required inelastic link rotation of 0.02 rad, while Specimens FFM and NAM achieved 80-percent of 0.02 rad. Engelhardt and Popov (1992) observed that moment links typically exhibit severe local flange buckling and lateral torsional buckling prior to fracture at the link ends. However, such behavior was not observed in the M-link specimens. Therefore, it appears that the four M-link specimens failed well before the link developed its inherent inelastic rotation capacity.

The I-link specimens failed due to fracture of the link flange near the groove weld, similar to the M-link specimens. Specimens PNI and MWI both achieved 42-percent of the required inelastic link rotation of 0.043 rad, while Specimens FFI and NAI achieved 108- and 63-percent, respectively, of 0.043 rad. However, Specimen FFI exceeded the link rotation requirement with only a small margin, since it failed immediately after completing the first loading cycle with an inelastic link rotation beyond 0.043 rad.

The current test results suggest that Premature failure due to link flange fracture can occur not only in connections of a long link ($e > 1.6M_p/V_p$) to a column, as noted previously by Engelhardt and Popov (1992), but is also likely in connections with a short shear link, such as a link of $e = 1.1M_p/V_p$.

4.3 Fracture of Link Flange

Of the twelve specimens tested in this program, ten specimens failed due to fracture of the link flange near the groove weld. Specimen NAS failed due to fracture of the link web away from the link ends, but was developing a fracture in the link flange during the test. The failure of Specimen FFS resulted from its unique connection configuration. Therefore, with the exception of Specimen FFS, link flange fracture was the dominant failure observed in the link-to-column connection.

The PN-, MW-, and FF-specimens were fabricated with the link web interrupting the placement of the CJP groove weld in the link bottom flange. This practice might be expected to increase the likelihood of weld defects at the point of interruption, and make the bottom flange more susceptible to fracture initiating at this location. Nonetheless, the specimens in this program fractured more frequently in the top flange than in the bottom flange. Therefore, the interruption of the bottom flange groove welds did not appear to be a decisive factor in these tests.

5. CONCLUSIONS

This paper summarized an experimental program to investigate the cyclic loading performance of EBF link-to-column connections constructed using realistic detailing and welding according to the US practices. Link-column specimens with four different connection types and three different link lengths, ranging from short shear yielding links to long flexural yielding links were tested.

The results of this test program showed poor performance of link-to-column connections designed and fabricated using pre-Northridge practices. Consequently, existing EBFs constructed prior to the Northridge Earthquake may be prone to premature failure at the link-to-column connections under severe earthquake loading. The test results also showed that a significant improvement in connection performance can be achieved through modifications in welding practices combined with modifications in connection design and detailing. Nonetheless, even though the connections with improved welding, design and detailing features developed improved levels of link inelastic rotation prior to failure, these connections still did not provide the levels of inelastic rotation required by the *2002 AISC Seismic Provisions*. Consequently, further research is needed to identify satisfactory link-to-column connection details. Until such details are identified, it is recommended that EBF arrangements with links attached to columns be avoided.

References:

- American Institute of Steel Construction, Inc. (AISC). (2002). Seismic provisions for structural steel buildings. Standard ANSI/AISC 341-02, AISC, Chicago, IL.
- Choi, J., Stojadinovic, B., and Goel, S.C. (2000). "Development of free flange moment connection." Report No. UMCEE 00-15, Department of Civil and Environmental Engineering, The University of Michigan, Ann Arbor, MI.
- Engelhardt, M.D. and Popov, E.P. (1992). "Experimental performance of long links in eccentrically braced frames." J. Struct. Engrg., ASCE, 118(11), 3067-3088.
- Engelhardt, M.D. and Husain, A.S. (1993). "Cyclic loading performance of welded flange-bolted web connections." J. Struct. Engrg., ASCE, 119(12), 3537-3550.
- Engelhardt, M.D. and Sabol, T.A. (1997). "Seismic-resistant steel moment connections: developments since the 1994 Northridge earthquake." Construct. Res. Comm. Ltd., ISSN, 1365-0556, 68-77.
- FEMA-350. Recommended seismic design criteria for new steel moment-frame buildings. (2000). Federal Emergency Management Agency, Washington, D.C.
- Suita, K., Tamura, T., Morita, S., Nakashima, N., and Engelhardt, M. (1999). "Plastic rotation capacity of steel beam-to-column connections using a reduced beam section and no weld access hole design—Full scale tests for improved steel beam-to-column subassemblages—Part 1." Journal of Struct. Constr. Eng., Architectural Institute of Japan, 526, 177-184. (in Japanese).
- Tsai, K.C., Engelhardt, M.D. and Nakashima, M. (2000). "Cyclic performance of link-to-box column connections in steel eccentrically braced frames." The First International Conference on Structural Stability and Dynamics, Taipei, Taiwan.

Nonlinear Dynamic Behaviour of Structures Due to Near-Field Ground Motions

M. Tehranizadeh¹, M.S. Rahim Labafzadeh²

1) Prof. Civil Engineering Department, Amir Kabir University of Technology, Tehran, Iran
2) PhD. candidate, International Institute of Earthquake Engineering and Seismology, Tehran, Iran
tehz@govir.ir, mosral@yahoo.com

Abstract: Occurrence of large earthquake close to cities located near faults is inevitable. The resulting ground shaking affected by directivity focusing at near-field regions, contain distinct pulses in acceleration, velocity, and displacement histories, and subject building to these large, rapid pulses. This paper aims at 1) comparing the nonlinear dynamic response of buildings due to near-field and far-field ground motions, and also 2) studying the relationship between the dynamic response characteristics of those buildings, and the parameters of near-fault ground motion (such as PGV/PGA, PGD/PGV ratios, spectral velocity, duration of strong motion, ground input energy, and duration and amplitude of pulses). To gain these two objectives, a 3-D steel building in 5, 13 stories which were designed according to the Iran Building Code, were Selected in this study. All near-field ground motions, recorded at Iran, with Chi Chi and Landers earthquake, which display pulse-like waveform, with 3 far-field ground motions, were utilized as input ground motions to analyze the near-field and far-field nonlinear dynamic behavior of the sample buildings. Based on nonlinear analysis, the values of story displacement, inter-story drift, story acceleration and velocity, base shear and base moment for near-field motions are more than far-field. Studying on the parameters of near-field ground motions indicates that in near-field regions, in comparison with far-field regions the demands of structures have larger values.

Keywords: *near-field, far-field, pulse-like, ground motion, nonlinear behaviour, 3-D steel building*

1. INTRODUCTION

Strong ground motions from close to large magnitude earthquakes are the most sever earthquake loading that structures undergo. (Ambraseys et al., 2003) Based on Loma Prieta Earthquake, Mohras divided the records into three groups: near-field (distance less than 20 km), mid-field (distance between 20 and 50 km) and far-field (Distance greater than 50 km). (Naeim, 2001)

Occurrence of large earthquake close to cities located near fault is inevitable. A challenging research topic in engineering seismology and earthquake engineering is the characterization of near-fault seismic motions and their effects on the performance of special structures. The physical understanding, modeling and simulation of near-fault ground motions and also the characteristics of the structure itself that control its behavior under near-source dynamic excitations are the two fold important aspects of near-fault seismic motions. (Mavroeidis, 2002)

The station No.2 (CO2) record obtained from the 1966 Park Field, California earthquake was the first recorded time history in near-field. Housner and Trifunac (1967) first observed pulses in this record. Since then, the occurrence of recorded major events has verified the existence of these pulses in near-fault regions, as well as their destructive potential when the causative fault is in vicinity of large metropolitan areas. Bertro et al. (1978) were the first engineers to recognize the problem and analyze its effects on flexible structures.

After Northridge and Kobe earthquakes a lot of modern structures were damaged or collapsed in

these areas which were designed due to their developed building codes.(US-Japan Workshop, 1998)

Occurrence of such events made researchers decide to inspect carefully about these two earthquakes. After a lot of researches it was found that most of damages were related to near-fault earthquakes especial characteristics. This was the starting point to pay more attention to near-fault earthquakes. The near-fault earthquakes have special characteristics which distinguished them from far-field earthquakes.

Near-field records have higher acceleration and more narrow frequency content at higher frequency values regard to far-field records. (Combescure et. al, 1998)

Earthquakes records especially when they are affected by forward directivity have pulses with long periods and high amplitude which are observed at the beginning of the earthquake. (Mavroeidis et. al, 2002, Someeville, 2000) Forward directivity occurs when the fault rupture propagates toward a site with rupture velocity approximately equal to the shear wave velocity. Mavroeidis and Papageorgiou (2002) said beside the directivity effect in which the intense directivity pulse is oriented in the normal direction due to the radiation pattern of the shear dislocation on the fault plane, the fling effect which is related to the permanent tectonic deformation of the ground at a specific site due to earthquake, is another factor of appearance of these pulses. The fling effect appears in the form of step displacement and one -sided velocity pulse in the strike-parallel direction for strike-slip faults (e.g. station SKR and YPT from the 1999 Izmit, Turkey earthquake) or in the strike-normal direction for dip-slip faults (e.g., stations TCU052 and TCU068 from the 1999 Chi-Chi, Taiwan earthquake).In that research they distinguished that period of these pulses increases with earthquake magnitude and the amplitude of the pulses appears to be a function of earthquake magnitude and distance of the station to the causative fault.

Because of the existence of these significant pulses in the near-field earthquakes, their records change from the broad band mode to pulse -like. (US-Japan Workshop, 1998)This means that in the Fourier spectrum of records instead of being the maximum amplitude in a wide range of frequencies, it has maximum values in a much narrow range of frequencies or in a specific frequency.The existence of these special pulses changes the response of structure from Mode-Like in which one or some of the modes are determinant in response, to wave-like. In this case the response of structure is determinant by the integration of the effects of propagated waves through the structure. (Iwan, 1995)The radiation pattern of shear dislocation on the fault causes these large pulses to be oriented in the direction perpendicular to the fault, causing the strike-normal peak velocity to be longer than the strike-parallel peak velocity. (Somerville, 2000)

At the beginning of the earthquake, High input energy generated by these pulses changes the nonlinear behavior of structure in a short period of time, so the energy of earthquake is absorbed in the first generated hinges instead of expanding the nonlinear behavior and plastic hinges over the height of the structure. This absorbed energy causes large inter-story drift which is not seen in the current patterns, such as using the first mode shape as a structural response. (Decanini et. al, 2000)

Also these strong pulses push the peak of the response spectrum to the shorter periods, so flexible structures behave in a stiff manner, and this increased base shear controls structural designing instead of velocity or displacement. Therefore the structure vibrates in a stiff manner and doesn't have enough time for move deformation in order to dissipate the energy and reduces apparent flexibility. (Malhotra, 1999)

The earthquakes which in their time histories of velocity and displacements are significant large pulses have higher PGV/PGA and lower PGD/PGV than other records. (Chopra et. al, 2001) Higher PGV/PGA ratio, widen the acceleration-sensitive region in elastic response spectrums and lower PGD/PGV ratio, widen the displacement-sensitive region. (Malhotra, 1999) In another word the near-field elastic spectrum has sharper peak. The implemented investigation on uniform shear beam by Malhotra (1999) and on simple steel frame by Alavi and Krawlinker (2000) shows that these significant pulses increases base shear and ductility demand and reduces contribution of higher modes and effectiveness of supplemental damping.

In order to study the effect of forward directivity on structure's responses, Tagawa and MacRae (2002) Stated that the site position relative to the fault could be represented in the form of, S , the length of the fault measured along the strike from the epicenter, L , the total rupture length, and, θ the horizontal angle between the fault plane and the site measured from the epicenter. (Tagawa et. al, 2002, MacRae et. al, 2001) When θ is small a significant portion of the seismic energy is channeled in the direction of rupture propagation. (Naeim, 2001) These researchers indicated if rupture direction tends more toward the site, θ is smaller or for a limited specified range of r_{rup} the value of S increases, and inelastic displacement amplification factor ($C_\mu = \frac{\Delta_{inelastic}}{\Delta_{elastic}}$) will increase, so in near-field regions which forward directivity is relevant, C_μ has larger value in comparison with far-field regions. (Tagawa et. al, 2002) In the research conducted by Baez and Miranda (2000) it is specified that C_μ for near-field excitation is larger than far-field's.

Andisheh (2003) indicated that the damages related to the distance from the earthquake source inversely, so in near-field regions, the structures are damaged more than far-field. In his research he showed that the duration of strong ground motion in horizontal direction relates inversely to the distance from site to seismic source.

In the research conducted by B.Aagaard, J.Hall and T.Heaton (2000), near-field ground motion time histories were simulated. They found that near-field ground motion strongly sensitive to the material properties, and fault depth, moderately sensitive to the hypocenter location, rupture speed, and maximum slip rate, and relatively insensitive to the distribution of final slip. Also comparing the result with the shape of the near-source factor (N_V) from 1997 uniform Building code shows that there is not enough correlation between this factor and maximum displacements and velocities.

In spite of unique characteristics of near-field earthquakes, the behavior of structures in these regions is affected seriously by these types of earthquakes. This paper aims at two goals, first comparing the nonlinear dynamic response of buildings due to near-field and far-field ground motions, and second studying the relationship between the dynamic response characteristic of those buildings and parameters of near-fault ground motion (such as PGV/PGA, PGD/PGV ratios, spectral velocity, duration of strong motion, ground energy, duration and amplitude of pulses).

2. THE NATURE OF NEAR-FIELD EARTHQUAKE USED IN THIS RESEARCH

In this research it is attempted to use the near-field earthquakes of Iran and the world. So the earthquakes were selected according to the definition of near-field which is said by Mohras. (Naeim, 2001) The selected earthquakes were applied to the structure as a three component. The data base of Iranian near-field earthquakes is prepared from Iran Building and Housing Research Center (BHRC). In order to complete the information of Iranian earthquake data base, Landers and Chi Chi earthquakes are used. They are derived from PEER internet web site. (PEER, 2004) All the details are presented in table No.1.

Table 1 Characteristics of near-field records used in the research

Earthquake	Year	Station	Dir.	PGA cm/sec ²	PGV cm/sec	PGD cm	Dist. km	Soil Type*	Ms	T _d sec	PGV/PGA	PGD/PGV
Ghaen	1976	1	H1	132.435	10.595	3.012	10	I	6.4	19.57	0.080	0.284
			H2	187.371	7.426	2.099				19.51	0.040	0.283
Naghan	1977	1	H1	716.130	61.509	12.361	5	I	6.1	20.99	0.086	0.201
			H2	459.108	54.053	12.165				16.71	0.118	0.225
Tabas	1978	9101	H1	819.930	97.781	39.922	3	III	7.4	32.84	0.119	0.378
			H2	835.577	121.379	94.580				32.84	0.145	0.779
Golbaf	1981	1	H1	209.934	22.759	5.964	13	III	7.0	59.33	0.108	0.262
			H2	258.003	14.126	5.876				59.19	0.055	0.416
Meimand	1994	NM	H1	408.096	17.560	1.991	17	II	6.1	27.17	0.043	0.113
			H2	433.412	19.130	2.540				27.12	0.043	0.133
Bam	2003	GB1	H1	623.444	59.675	20.773	<1	II	6.8	66.555	0.096	0.348
			H2	778.275	123.69	34.480				66.555	0.159	0.174
Landers	1992	24 Lucerne	H1	769.890	31.873	16.415	1.1	I	7.4	48.125	0.041	0.515
			H2	707.070	97.603	70.311				48.125	0.138	0.720
Chi Chi	1999	TCU068	H1	453.222	263.10	430.00	1.09	III	7.6	90.00	0.580	1.634
			H2	555.246	176.60	324.11				90.00	0.318	1.836

*The classification is due to Iranian Code

In order to compare the behavior of structures in the near-field and far-field according to IBC2000 (IBC,2000) three far-field earthquakes which their epicentral distances are more than 50 km are used. They are also derived from PEER site. The characteristics of these earthquakes are shown in table No.2 All the records are scaled due to IBC 2000 Method.

Table 2 Characteristics of far-field records used in the research

Earthquake	Year	Station	Dir.	PGA cm/sec ²	PGV cm/sec	PGD cm	Dist. km	Soil Type*	Ms	T _d sec	PGV/PGA	PGD/PGV
Tabas	1978	Ferdous 71	H1	85.347	5.7	4.61	94.40	I	7.4	40.00	0.066	0.812
			H2	105.948	8.6	9.69				40.00	0.081	1.127
Landers	1992	12026 Indiana	H1	102.024	9.6	5.05	55.70	III	7.4	60.00	0.094	0.527
			H2	106.929	15.2	9.69				60.00	0.141	0.640
Chi Chi	1999	CHY004	H1	97.119	20.00	17.51	50.89	IV	7.6	150.0	0.206	0.875
			H2	98.100	15.80	15.41				150.0	0.161	0.978

*The classification is due to Iranian code

The figures No.1 and No.2 show the time history of acceleration, velocity and displacement for some of the near-field and far field earthquakes which were used. The directivity effect causes single pulses with long periods in the near-field earthquakes' records. By investigation of existing records it is understood that in the earthquakes which in their velocity and displacement records, large rapid pulses are seen, the PGV/PGA is higher and the PGD/PGV ratio is lower. The table No.3 shows the ratio of peaks ground motions.

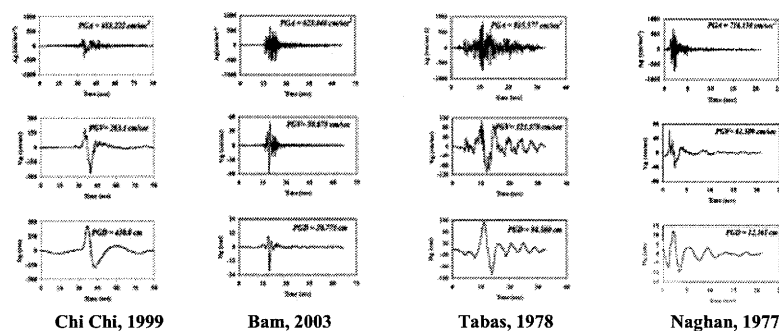


Figure 1 Time history of records for some of the near-field earthquakes

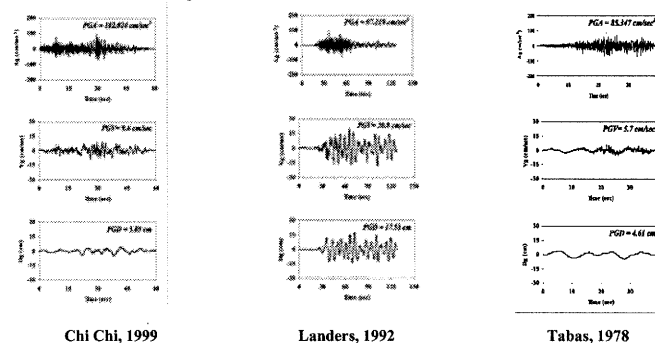


Figure 2 Time history of records for the far-field earthquakes

To compute the duration of strong ground motion Page et al. and Bolt approach is used. (Naeim, 2001) Less distance to the source of earthquake, causes longer duration and increases input energy. To remain the structure safe it must have the capacity to dissipate the ground energy. Input energy is defined as $E_i = \int_{t_a}^{t_b} m \dot{u}^2 dt$ where t_a and t_b are the starting time and end time of strong ground motion respectively, m is the unit mass and \dot{u} is the ground velocity in the considered direction i . There is no unique method to define the duration of the pulse. The simplest way is to determine the pulse duration using the zero crossings of the pulse wave form. A more complicated way is the employment of an equivalent pulse width based on energy consideration (signal spectrum) and basic concepts from the signal processing theory. An alternative approach is the utilization of the peak value of the velocity response spectrum to indirectly define the pulse period. (Mavroeidis, 2002) The peak ground velocity is considered as the amplitude of the pulse. Another selected

parameter for near-field is spectral velocity (S_V) which is higher for sample structures in near-field than far-field. It is found that near the seismic source usually the duration of strong ground motion and respectively the released energy are greater than in far-field.

As it is shown in figure No.3 the Fourier amplitude spectrum of near-field in a very small range of frequency or in another word in a specific period has its maximum value. Another characteristic of near-field earthquakes in comparison with the far-field motions is that, its response spectrum usually has greater amounts than the design spectrum introduced by Iran Code. The figure No.4 shows the response spectrum prepared from some of the earthquakes separately and the comparison of near-field and far-field response spectra, which will prove this subject.

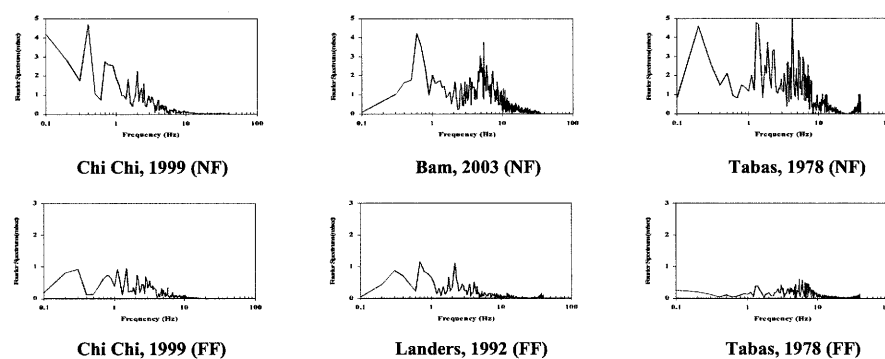


Figure 3 Fourier Amplitude Spectrum for near-field and far-field earthquakes

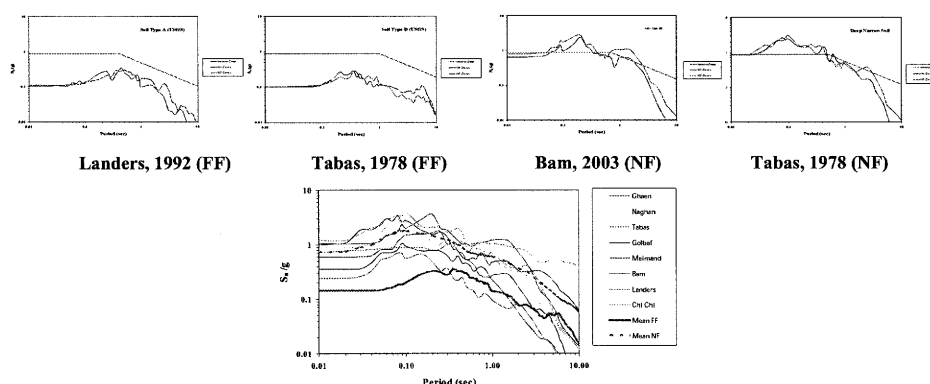


Figure 4 Response Spectra for the near-field (NF) and far-field (FF) earthquakes

3. MODELING AND ANALYZING OF STRUCTURES DUE TO NEAR-FIELD GROUND MOTIONS

The structures used in this research are steel ones with 5, 13 stories which their plans are shown in figure No. 5. The spans are 6 m length and the height of each story is 3 m. The structure has braces in the lateral span of four exterior frames. Dead loads are 500 kg/m^2 for each story and 400 kg/m^2 for roof and live loads are 200 kg/m^2 and 150 kg/m^2 respectively for each story and roof. Sample structures are designed due to Iran Building code for high seismic activity regions and soil type II. (Iranian Code, 1999) In order to make models for nonlinear behavior of structures, tri-linear model was used for hinges. The characteristics of these hinges are selected due to FEMA 273. (FEMA, 1997) Their general behaviors are shown in figure No.6 were used. The nominal strength of each element is calculated due to AISC-LRFD code. (AISC, 1994) The damping of structure is assumed as classical damping (proportional to mass and stiffness), and the damping ratio is applied proportional to period of structure. Damping Ratio in linear case at $T_A = 0.33T_1$ and $T_B = T_1$ and for nonlinear case at $T_A = 0.33\sqrt{\mu} T_1$ and $T_B = \sqrt{\mu} T_1$ is 5%. (RAM International, 2000) T_1 is period of first mode, μ is ductility and here it is equal to 3.

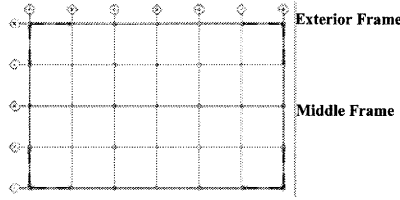


Figure 5 Plan of sample structures

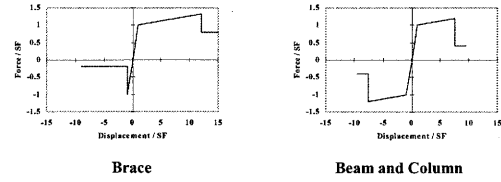


Figure 6 Hinges general behavior

4. EFFECTS OF VARIOUS PARAMETERS OF NEAR-FIELD ON SELECTED MODELS

After designing the structures, nonlinear and linear dynamic analysis are done through direct integration method for selected near-field and far field earthquakes. Relative story velocity and absolute story acceleration, story drift, story displacement in horizontal directions, base shear, and base moment are considered as the response of structures. In order to study the effects of near-field and far-field earthquakes on structures, the characteristics of these motions such as PGV/PGA, PGD/PGV, E_i , T_s , T/T_p and V_p (PGV) are selected and the variation of the response of structures due to the changes of these characteristics are shown in future figures. Distribution of selected parameters over the height of structure for near-field earthquake and the average of far-field motions are shown in figures No.7 and No.8. By comparing the results of near-field and far-field nonlinear analysis, significant differences can be seen obviously. The Sensitivity of the response of structures to selected earthquake characteristics can be effective for explaining the behavior of earthquakes. In figures No.9 the variation of base shear and base moment, maximum displacement, maximum story relative velocity and maximum absolute acceleration, maximum story drift due to different characteristics of selected earthquakes are shown. (Rahim Labafzadeh, 2004)

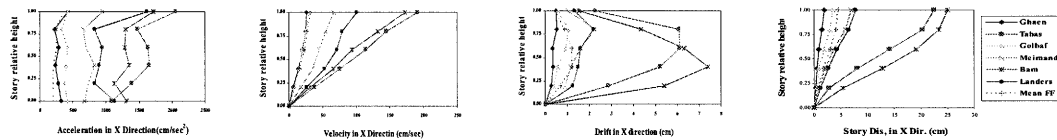


Figure 7 Distribution of response parameters over the height of 5-story structure

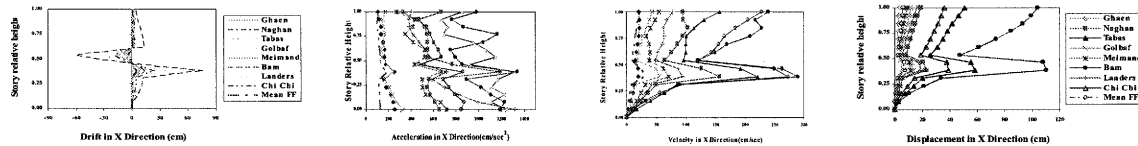
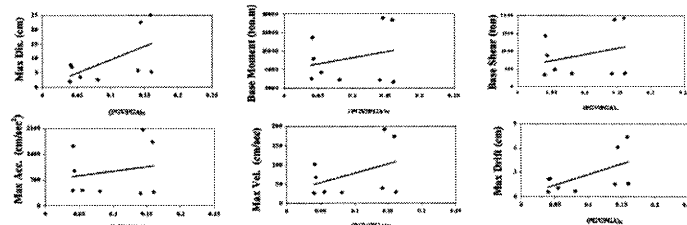
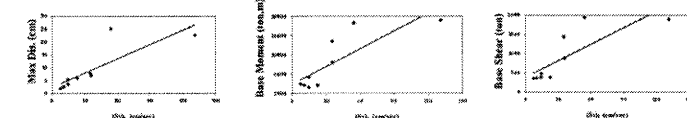
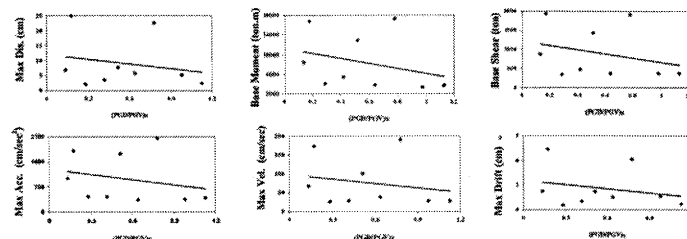


Figure 8 Distribution of response parameters over the height of 13-story

PGV/PGA



PGD/PGV



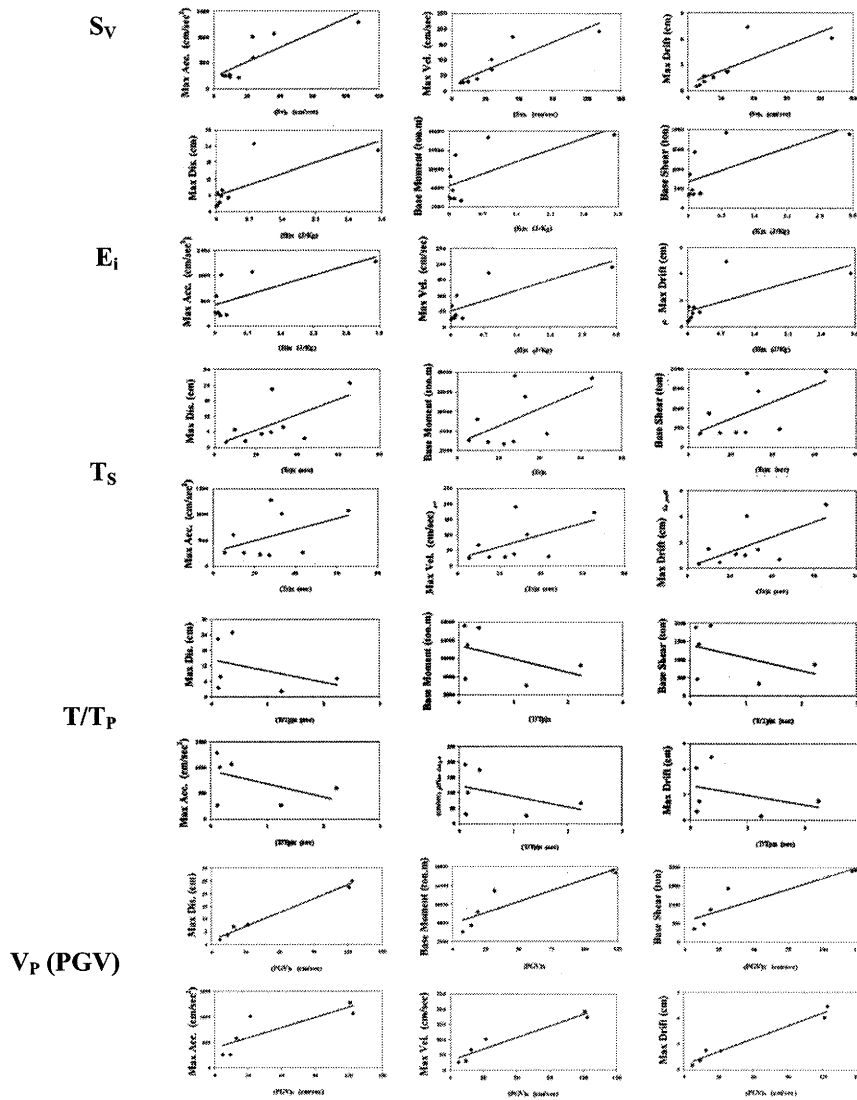


Figure 9 Variation of various response parameters versus earthquake parameters

5. CONCLUSION

The nonlinear dynamic response of 5 and 13 story steel structures due to 8 near-field earthquakes are compared with the response of 3 records of far-field earthquakes. The near-field excitations have greater PGV/PGA, S_v , E_i , T_s and less PGD/PGV than the far-field one. When a structure is exposed to near-field motions, the demands of structure will increase. The distribution of the parameters of structural response such as story displacement, story drift, relative velocity and absolute acceleration of stories over the height of structure show that these parameters will have greater amounts in near-field. In this distribution it was distinguished that the responses due to some of the near-field earthquakes are close to the average responses due to far-field earthquakes. So it can be deduced that the criterion which is introduced for near-field earthquake by Mohraz is an unreal criteria and is not general. Therefore one of the criteria for identifying the near-field earthquakes could be the site-to-source distance but it isn't the only criterion, so beside that we must use velocity and displacement time histories, response spectrum and Fourier amplitude spectrum. By studying the effects of the near-field effective parameters on structural responses, it was distinguished that greater values of PGV/PGA, S_v , E_i , and T_s or less PGD/PGV cause increase

in the responses of the structures. So with regard to the characteristics of near-field earthquakes, it can be concluded that the response of structures in near-field regions is extremely greater than far-field one. Also, in those near-field earthquakes which have pulses with greater, amplitude (greater PGV) or greater duration of the pulse (less T/T_p) the response of the structure increases more. So with respect to these conclusions, in order to reduce the response of structure for those that are close to the seismic sources, the structures must have more ductility.

References

- Agard, B., Hall J., Heaton T.H. (2000), Sensitivity of Near-Source Ground Motion, *12th WCEE*, Auckland, New Zealand, No. 0722.
- AISC (1994), *Manual of Steel Construction, Load and Resistance Factor Design (LRFD)*, 2nd Edition, American Institute of Steel Construction, Chicago, Illinois.
- Alavi, B., Krawinkler, H. (2000), Consideration of Near-Field Ground Motion Effects in Seismic Design, *12th WCEE*, New Zealand, No. 2665.
- Ambraseys, N.N., Douglas, J. (2003), Near-Field Horizontal and Vertical Earthquake Ground Motions, *Soil Dynamics and Earthquake Engineering*, 23, 1-18.
- Andishe, K. (2003), *The Structural Design Criteria In Near-Field Regions*, Master's thesis, Science and Industry University, Tehran, Iran.
- Baez, J., Miranda, E. (2000), Amplification Factors to Estimate Displacement Demands for the Design of Structures in Near-Field, *12th WCEE*, Auckland, New Zealand, No. 1561.
- Bertero, V. V., Mahin, S. A., Herrera, R. A. (1978), A seismic design implication of near-field San Fernando earthquake records, *Earthquake Engineering and Structural Dynamics*, 6, 31-42.
- Combesure, D., Queval, J.C., Sollogoub, P., Bonnici, D., Labbe, P. (1998), Effect of Near-Field Earthquake on a R/C Bearing Wall Structure Experimental and Numerical Studies, *11th ECEE*, Balkema, Brookfield.
- Chopra, A.K., Chintanapakdee, C. (2001), Comparing Response of SDOF Systems to Near-Fault and Far-Fault Earthquake Motions in the Context of Spectral Regions, *Earthquake Eng. Struct. Dyn.*, 30, 1769-1789.
- Decanini, L., Mollaioli, F., Saragoni, R. (2000), Energy and Displacement Demands Imposed by Near-Source Ground Motion *12th WCEE*, Auckland, New Zealand, No. 1136.
- FEMA (1997), *NEHRP Guidelines for the Seismic Rehabilitation of Buildings*, Report No. FEMA 273, Washington, D.C.
- Housner, G. W., Trifunac, M. D. (1967), Analysis of accelerograms – Park field earthquake, *Bulletin of the Seismological Society of America*, 57, 1193-1220.
- International Building Code (2000), ICBO Publisher.
- Iranian Code of Practice for Seismic Resistance Design of Buildings (1999), Standard No.2800, 2nd Edition, Building and Housing Research Center.
- Iwan, W.D. (1995), Near-Field Consideration in Specification of Seismic Design Motions for Structures, *10th ECEE*, Balkema, Rotterdam, PP. 257-267.
- MacRae, G.A., Morrow, D.V., Roeder, C.W. (2001), Near-Fault Ground Motion Effects on Simple Structures, *Journal of Structural Engineering*, September, 996-1004.
- Malhotra, P.K. (1999), Response of Buildings to Near-Field Pulse Like Ground Motion, *Earthquake Engineering and Structural Dynamics*, 28, 1309-1326.
- Mavroeidis, G.P., Papageorgiou, A.S. (2002), Near-Source Strong Ground Motion: Characteristics and Design Issues, *7th US NCEE*, Boston, Massachusetts, No. 0240.
- Naeim, F. (2001), *The Seismic Design Handbook*, 2nd edition, Kluwer Academic Publishers.
- Pacific Earthquake Engineering Research Center (2004), PEER Strong Motion Database, *Internet Website*: [http:// peer.berkeley. edu/smcat](http://peer.berkeley.edu/smcat).
- Rahim Labafzadeh, M.S. (2004), *Nonlinear Dynamic Behaviour of Structures Due to Near-Field Ground Motions*, Master's thesis, Amir Kabir University of Technology, Tehran, Iran.
- RAM International (2000), *RAM PERFORM-3D Version 1.15 user Guide*, Graham, H. Powell Inc.
- Somerville, P., Seismic Hazard Evaluation, *12th WCEE*, Auckland, New Zealand, No. 2833, 2000.
- Somerville, P., Graves, R. (1993), Condition that give rise to unusually large long period ground motion, *The structural Design of Tall Buildings*, 2, 211-232.
- Tagawa, H., MacRae, G.A. (2002), Near-Fault Shaking Effects on Inelastic Displacement Amplification Factor of SDOF Oscillators, *7th US NCEE*, Boston, Massachusetts, No. 0237.
- US-Japan Workshop Proceeding on Mitigation of Earthquake Damage in Near-Field Urban Area (1998), Hawaii.

ESTIMATION OF SEISMIC DEMAND OF MULTI-STORY ASYMMETRIC BUILDINGS WITH BI-DIRECTIONAL ECCENTRICITY

K. Fujii¹⁾, Y. Nakano²⁾, Y. Sanada³⁾, H. Sakata⁴⁾, and A. Wada⁵⁾

1) Post-doctoral Research Fellow, Center for Urban Earthquake Engineering, Tokyo Institute of Technology, Japan

2) Associate Professor, Institute of Industrial Science, University of Tokyo, Japan

3) Research Associate, Earthquake Research Institute, University of Tokyo, Japan

4) Associate Professor, Structural Engineering Research Center, Tokyo Institute of Technology, Japan

5) Professor, Structural Engineering Research Center, Tokyo Institute of Technology, Japan

kfujii@serc.titech.ac.jp, iisnak@iis.u-tokyo.ac.jp, ysanada@eri.u-tokyo.ac.jp,

hsakata@serc.titech.ac.jp, wada@serc.titech.ac.jp

Abstract: A simplified procedure for multi-story asymmetric buildings with bi-directional eccentricity and regular elevation subjected to bi-directional ground motion is proposed. In this procedure, their responses are predicted through a nonlinear static analysis of MDOF model considering the effect of bi-directional excitation and an estimation of seismic demand of equivalent SDOF model. The results are compared with those of the nonlinear dynamic analysis of MDOF models, and satisfactory prediction can be found in nonlinear response of asymmetric buildings.

1. INTRODUCTION

The estimation of nonlinear response of buildings subjected to a strong ground motion is a key issue for the rational seismic design of new buildings and the seismic evaluation of existing buildings (ATC-40, 1996). For this purpose, the nonlinear time-history analysis of Multi-Degree-Of-Freedom (MDOF) model might be one solution, but it is often too complicated whereas the results are not necessarily more reliable due to uncertainties involved in input data. To overcome such shortcomings, several researchers have developed simplified nonlinear analysis procedures (Saiidi and Sozen 1981, Fajfar and Fischinger 1988). This approach consists of a nonlinear static (pushover) analysis of MDOF model and a nonlinear dynamic analysis of the equivalent Single-Degree-Of-Freedom (SDOF) model, and it would be a promising candidate as long as buildings oscillate predominantly in the fundamental mode. Although these procedures have been more often applied to planar frame analyses, only a few investigations concerning the extension of them to asymmetric buildings have been made.

In this paper, a simplified procedure is for multi-story asymmetric building with by directional eccentricity and regular elevation subjected to bi-directional ground motion is proposed. In this procedure, the properties of the equivalent single-story model is determined from the pushover analyses of multi-story planar frames, as well as the procedure proposed by the authors for unidirectional excitation (Fujii et al. 2004a). The pushover analyses of equivalent single-story model are carried out to determine the equivalent SDOF models representing the first and second mode. The seismic demands of the equivalent SDOF model are determined independently for each direction. The pushover analyses of MDOF model are carried out considering the combination of bi-directional excitations. The results obtained by the proposed procedure are compared with the results obtained by the nonlinear dynamic analysis performed for simultaneous bi-directional ground motions.

2. DESCRIPTION OF SIMPLIFIED NONLINEAR ANALYSIS PROCEDURE

2.1 Model Assumption

The building model considered in this study is an idealized N -story asymmetric shear-building model with regular elevation as shown in Figure 1. In this paper, the following assumptions are made in the model: 1) each floor has the same configuration in plan and member location, 2) the center of mass of all floor diaphragms lie on the same vertical axis, 3) each floor has the same radius of gyration r about the center of mass as expressed in Equation (1), 4) all frames are oriented either in the X- or Y-direction that is mutually orthogonal, 5) each frame consists of column elements and wall elements, and their axial deformation is negligible, 6) the ratio of story stiffness and strength in X- and Y-direction is the same in all stories as expressed in Equations (2a) and (2b), 7) each frame has the same distribution of stiffness and strength along the story as expressed in Equations (3) and (4).

$$r = \sqrt{I_1/m_1} = \sqrt{I_2/m_2} = \dots = \sqrt{I_N/m_N} \quad (1)$$

$$\frac{\sum_l K_{Y1l}}{\sum_l K_{X1l}} = \frac{\sum_l K_{Y2l}}{\sum_l K_{X2l}} = \dots = \frac{\sum_l K_{YNl}}{\sum_l K_{XNl}} = \text{const.}, \frac{\sum_l Q_{yY1l}}{\sum_l Q_{yX1l}} = \frac{\sum_l Q_{yY2l}}{\sum_l Q_{yX2l}} = \dots = \frac{\sum_l Q_{yYNl}}{\sum_l Q_{yXNl}} = \text{const.} \quad (2a, b)$$

$$\frac{K_{Xil}}{K_{X11}} = \frac{K_{X12}}{K_{X12}} = \dots = \frac{K_{Xin_x}}{K_{X1n_x}} = \frac{K_{Yil}}{K_{Y11}} = \frac{K_{Y12}}{K_{Y12}} = \dots = \frac{K_{Yin_y}}{K_{Y1n_y}} = \text{const.} \quad (3)$$

$$\frac{Q_{yXil}}{Q_{yX11}} = \frac{Q_{yX12}}{Q_{yX12}} = \dots = \frac{Q_{yXin_x}}{Q_{yX1n_x}} = \frac{Q_{yYil}}{Q_{yY11}} = \frac{Q_{yY12}}{Q_{yY12}} = \dots = \frac{Q_{yYin_y}}{Q_{yY1n_y}} = \text{const.} \quad (4)$$

Where K_{Xil} and K_{Yil} are the stiffness of the l -th frame in i -th story oriented in X- and Y-direction, respectively, and Q_{yXil} and Q_{yYil} are the yield strength of the l -th frame in i -th story oriented in X- and Y-direction, respectively, and n_x and n_y are the number of frames oriented in X- and Y-direction, respectively. These assumptions described in 1) through 7) above lead to the result that the center of stiffness of all stories lie on the same vertical axis: the eccentricity ratio $E_X, E_Y (= e_X / r, e_Y / r, e_X, e_Y$: elastic eccentricity in X- and Y-direction, respectively) and the radius ratio of gyrations of story stiffness $J_X, J_Y (= j_X / r, j_Y / r, j_X, j_Y$: radius of gyration of story stiffness about the center of mass in X- and Y-direction, respectively) are the same in all stories. In this paper, the earthquake excitation is considered bi-directional in X-Y plane. Therefore $3N$ degrees of freedoms ($3N$ -DOFs) are oriented for the multi-story model studied herein. Another assumption is that the vertical distribution of displacement in all frames is invariant beyond the elastic range. Therefore the applicability of this procedure is limited to multi-story asymmetric buildings with regular elevation as in the previous study (Fujii et al, 2004a): the buildings with soft and/or weak stories are not considered in this study.

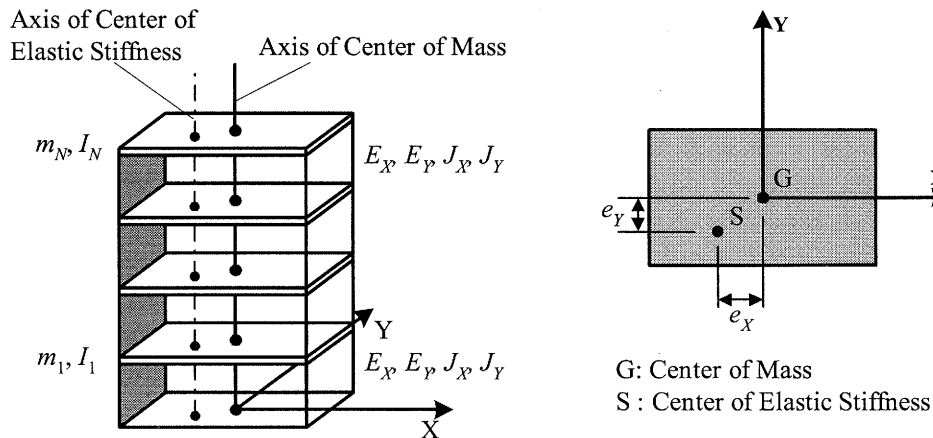


Figure 1 N -Story Asymmetric Shear-Building Model

2.2 Outlines of the Procedure

The outline of the proposed procedure is described as follows.

STEP 1: Pushover analysis of planar frames

STEP 2: Pushover analysis of equivalent single-story model (first mode)

STEP 3: Estimation of the seismic demand of equivalent SDOF model (first mode)

STEP 4: Pushover analysis of equivalent single-story model (second mode)

STEP 5: Estimation of the seismic demand of equivalent SDOF model (second mode)

STEP 6: Estimation of drift demand in each frame of equivalent single-story model

STEP 7: Estimation of drift demand in each story of planar frames

STEP 1: Pushover Analysis of Planar Frames

A pushover analysis of each planar frame is carried out to obtain its non-linear force-displacement relationship, assuming a vertical distribution of displacement $\Gamma_{S1}\phi_{S1}$ for all frames. The properties of the equivalent single-story model are determined from the results of these pushover analyses. The equivalent mass M_{T1}^* and the moment of inertia I_{T1}^* are determined from Equations (5a) and (5b), respectively, and the equivalent restoring force of each frame Q_{Xi}^* and Q_{Yi}^* , and the equivalent displacement of each frame d_{Xi}^* and d_{Yi}^* are determined from Equations (6a), (6b), (6c), and (6d) respectively.

$$M_{T1}^* = \Gamma_{S1}^2 \phi_{S1}^T \mathbf{M}_0 \phi_{S1}, I_{T1}^* = \Gamma_{S1}^2 \phi_{S1}^T \mathbf{I}_0 \phi_{S1} \quad (5a, b)$$

$$Q_{Xi}^* = \Gamma_{S1} \phi_{S1}^T \mathbf{f}_{RXi}, Q_{Yi}^* = \Gamma_{S1} \phi_{S1}^T \mathbf{f}_{RYi}, d_{Xi}^* = \Gamma_{S1} \phi_{S1}^T \mathbf{M}_0 \mathbf{d}_{Xi} / M_{T1}^*, d_{Yi}^* = \Gamma_{S1} \phi_{S1}^T \mathbf{M}_0 \mathbf{d}_{Yi} / M_{T1}^* \quad (6a, b, c, d)$$

$$\Gamma_{S1} = \frac{\phi_{S1}^T \mathbf{M}_0 \mathbf{a}_S}{\phi_{S1}^T \mathbf{M}_0 \phi_{S1}}, \phi_{S1} = \{\phi_{S1} \quad \dots \quad \phi_{SN}\}^T, \mathbf{a}_S = \{1 \quad \dots \quad 1\}^T \quad (7a, b, c)$$

$$\mathbf{f}_{RXi} = \{f_{RX1i} \quad \dots \quad f_{RXNi}\}^T, \mathbf{f}_{RYi} = \{f_{RY1i} \quad \dots \quad f_{RYNi}\}^T \quad (8a, b)$$

$$\mathbf{d}_{Xi} = \{d_{X1i} \quad \dots \quad d_{XNi}\}^T, \mathbf{d}_{Yi} = \{d_{Y1i} \quad \dots \quad d_{YNi}\}^T \quad (9a, b)$$

$$\mathbf{M}_0 = \begin{bmatrix} m_1 & & 0 \\ & \ddots & \\ 0 & & m_N \end{bmatrix}, \mathbf{I}_0 = \begin{bmatrix} I_1 & & 0 \\ & \ddots & \\ 0 & & I_N \end{bmatrix} = r^2 \mathbf{M}_0 \quad (10a, b)$$

Where \mathbf{f}_{RXi} , \mathbf{f}_{RYi} and \mathbf{d}_{Xi} , \mathbf{d}_{Yi} are the restoring force vector and displacement vector of each frame obtained by the pushover analysis, respectively.

STEP 2: Pushover Analysis of Equivalent Single-Story Model (First Mode)

The Equivalent SDOF model representing the first mode response is as shown in Figure 2. An eigenvalue analysis of an equivalent single-story model is carried out to obtain the mode shape in

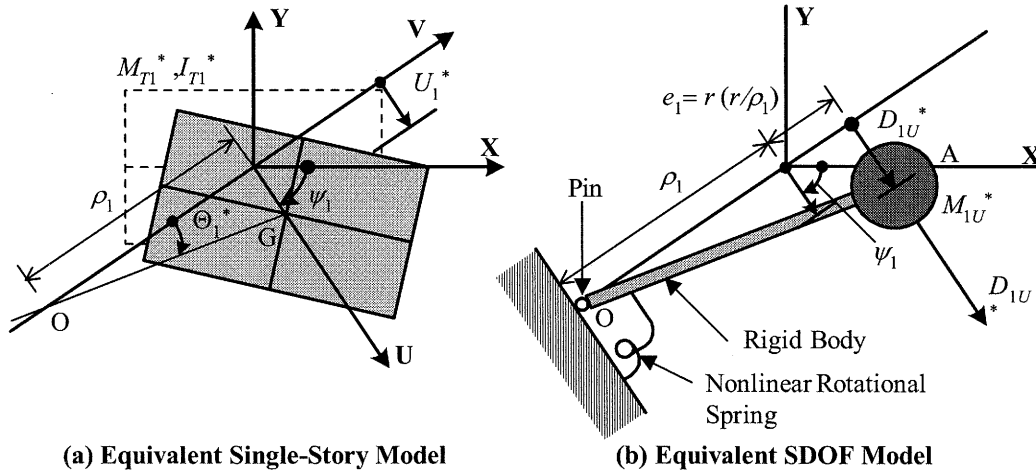


Figure 2 Equivalent SDOF Model Representing the First Mode Response

elastic range ϕ_{T1e} , ϕ_{T2e} and the direction of U-axis is determined as shown in Equation (12a, b).

$$\cos \psi_1 = \phi_{TX1e} / \sqrt{\phi_{TX1e}^2 + \phi_{TY1e}^2}, \sin \psi_1 = -\phi_{TY1e} / \sqrt{\phi_{TX1e}^2 + \phi_{TY1e}^2} \quad (12a, b)$$

$$\phi_{T1e} = \{\phi_{TX1e} \quad \phi_{TY1e} \quad \phi_{T\Theta1e}\}^T \quad (13)$$

Then a pushover analysis is carried out to obtain its force - displacement relationship representing the first mode response, considering the change in the first mode shape at each nonlinear stage. The numerical procedure of the pushover analysis can be found in the previous study developed by the authors (Fujii et al. 2004a). The property of the equivalent SDOF model is determined from the results of the pushover analysis. The equivalent acceleration A_{1U}^* and displacement D_{1U}^* of the equivalent SDOF model are determined by Equations (14a) and (14b), respectively. The $A_{1U}^* - D_{1U}^*$ relationship is referred to as capacity diagram.

$$A_{1U}^* = \Gamma_{T1U} \phi_{T1}^T \mathbf{f}_{RT} / M_{1U}^*, D_{1U}^* = \Gamma_{T1U} \phi_{T1}^T \mathbf{M}_T \mathbf{d}_T / M_{1U}^*, M_{1U}^* = \Gamma_{T1U} \phi_{T1}^T \mathbf{M}_T \mathbf{a}_{TU} \quad (14a, b, c)$$

$$\Gamma_{T1U} = \frac{\phi_{T1}^T \mathbf{M}_T \mathbf{a}_{TU}}{\phi_{T1}^T \mathbf{M}_T \phi_{T1}}, \phi_{T1} = \{\phi_{TX1} \quad \phi_{TY1} \quad \phi_{T\Theta1}\}^T, \mathbf{a}_{TU} = \{\cos \psi_1 \quad \sin \psi_1 \quad 0\}^T \quad (15a, b, c)$$

$$\mathbf{f}_{RT} = \{R_{X1}^* \quad R_{Y1}^* \quad M_{Z1}^*\}^T, \mathbf{d}_T = \{X_1^* \quad Y_1^* \quad \Theta_1^*\}^T \quad (16a, b)$$

$$\mathbf{M}_T = \begin{bmatrix} M_{T1}^* & 0 & 0 \\ 0 & M_{T1}^* & 0 \\ 0 & 0 & I_{T1}^* \end{bmatrix} \quad (17)$$

Where \mathbf{f}_{RT} , and \mathbf{d}_T are the restoring force vector and displacement vector of equivalent single-story model obtained by the pushover analysis, respectively.

STEP 3: Estimation of Seismic Demand of Equivalent SDOF Model (First Mode)

The seismic demand $D_{1U}^*_{MAX}$ and $A_{1U}^*_{MAX}$ of an equivalent SDOF model is obtained by the equivalent linearization procedure in this study (Otani, 2000). The equivalent period T_{eq} and equivalent damping ratio h_{eq} of the equivalent SDOF model at each nonlinear stage is calculated by Equations (18), (19), respectively. The response spectral acceleration and displacement are factored using F_h in Equation (20).

$$T_{eq} = 2\pi \sqrt{D_{1U}^* / A_{1U}^*} \quad (18)$$

$$h_{eq} = \sum_i h_{eqi} \cdot W_i / \sum_i W_i, h_{eqi} = 0.25(1 - 1/\sqrt{\mu_i}) + h_0, W_i = (1/2) \cdot Q_i^* \cdot d_i^* \quad (19)$$

$$F_h = 1.5 / (1 + 10h_{eq}) \quad (20)$$

Where h_{eqi} , W_i and μ_i are the equivalent damping ratio, potential energy, and ductility ratio of each element, respectively, and Q_i^* , d_i^* are the restoring force and displacement of each element, respectively, and h_0 is the initial damping ratio and assumed 0.03 in this study. The detail of the procedure can be found in elsewhere (Otani, 2000).

STEP 4: Pushover Analysis of Equivalent Single-Story Model (Second Mode)

The property of the equivalent SDOF model representing the second mode response is determined from the results of the pushover analysis as discussed in STEP 2. From the results of STEP 2 and 3, the first mode shape $\Gamma_{T1U} \phi_{T1}$ at $D_{1U}^*_{MAX}$ is obtained and the second mode shape $\Gamma_{T2V} \phi_{T2}$ is determined from Equations (21a), (21b) and (21c). Then another pushover analysis of an equivalent single-story model is carried out to obtain its force-displacement relationship representing the second mode response, applying the invariant force distribution \mathbf{P}_{T2} determined by Equation (22). The

equivalent acceleration A_{2V}^* and displacement D_{2V}^* of the equivalent SDOF model are determined by Equations (23a) and (23b), respectively.

$$\Phi_{T2} = \Phi_{T2e} - \frac{\Phi_{T2e}^T \mathbf{M}_T \Phi_{T1}}{\Phi_{T1}^T \mathbf{M}_T \Phi_{T1}} \cdot \Phi_{T1}, \Gamma_{T2V} = \frac{\Phi_{T2}^T \mathbf{M}_T \alpha_{TV}}{\Phi_{T2}^T \mathbf{M}_T \Phi_{T2}}, \alpha_{TV} = \{\sin \psi_1 \quad -\cos \psi_1 \quad 0\}^T \quad (21a, b, c)$$

$$\mathbf{P}_{T2} = \mathbf{M}_T (\Gamma_{T2V} \Phi_{T2}) \quad (22)$$

$$A_{2V}^* = \Gamma_{T2V} \Phi_{T2}^T \mathbf{f}_{RT} / M_{2V}^*, D_{2V}^* = \Gamma_{T2V} \Phi_{T2}^T \mathbf{M}_T \mathbf{d}_T / M_{2V}^*, M_{2V}^* = \Gamma_{T2V} \Phi_{T2}^T \mathbf{M}_T \alpha_{TV} \quad (23a, b, c)$$

STEP 5: Estimation of the Seismic Demand of Equivalent SDOF Model (Second Mode)

The seismic demand $D_{2V}^*_{MAX}$ and $A_{2V}^*_{MAX}$ of an equivalent SDOF model is obtained by the equivalent linearization procedure as discussed in STEP 3. For the estimation of the seismic demand of the second mode response, h_0 is also and assumed 0.03 in this study.

STEP 6: Estimation of Drift Demand in Each Frame of Equivalent Single-Story Model

The drift demand in each frame of equivalent single-story model is determined from the four pushover analyses results summarized below: 1) Determination of the four combined forces \mathbf{P}_U^+ , \mathbf{P}_U^- and \mathbf{P}_V^+ , \mathbf{P}_V^- from Equations (25) and (26). 2) Pushover analyses of equivalent single-story model using \mathbf{P}_U^+ and \mathbf{P}_U^- until the equivalent displacement D_U^* calculated by Equation (27a) reaches $D_{1U}^*_{MAX}$ obtained from STEP 3 (referred to as Pushover-1U and 2U, respectively). 3) Pushover Analyses using \mathbf{P}_V^+ and \mathbf{P}_V^- until the equivalent displacement D_V^* calculated by Equation (27b) reaches $D_{2V}^*_{MAX}$ obtained from STEP 5 (referred to as Pushover-1V and 2V, respectively). 4) Determination of the drift demand by envelope of (a) Pushover-1U and 2U obtained from 2) and (b) Pushover-1V and 2V obtained from 3).

$$\mathbf{P}_U^\pm = \mathbf{M}_T (\Gamma_{T1U} \Phi_{T1} \cdot A_{1U}^*_{MAX} \pm \gamma \cdot \Gamma_{T2V} \Phi_{T2} \cdot A_{2V}^*_{MAX}) \quad (25)$$

$$\mathbf{P}_V^\pm = \mathbf{M}_T (\pm \gamma \cdot \Gamma_{T1U} \Phi_{T1} \cdot A_{1U}^*_{MAX} + \Gamma_{T2V} \Phi_{T2} \cdot A_{2V}^*_{MAX}) \quad (26)$$

$$D_U^* = \Gamma_{T1U} \Phi_{T1}^T \mathbf{M}_T \mathbf{d}_T / M_{1U}^*, D_V^* = \Gamma_{T2V} \Phi_{T2}^T \mathbf{M}_T \mathbf{d}_T / M_{2V}^* \quad (27a, b)$$

where γ is the coefficient considering the combination of the first and second mode responses.

STEP 7: Estimation of Drift Demand in Each Story of Planar Frames

The drift demand in each story of the frame is determined from the results of STEP 1 and STEP 6. By substituting $d_{Xi}^*_{MAX}$ and $d_{Yi}^*_{MAX}$ obtained in STEP 6 into Equation (28a) and (28b), \mathbf{d}_{XiMAX} and \mathbf{d}_{YiMAX} and hence the drift demand in each story of the frame can be found.

$$\mathbf{d}_{XiMAX} = \Gamma_{S1} \Phi_{S1} \cdot d_{Xi}^*_{MAX}, \mathbf{d}_{YiMAX} = \Gamma_{S1} \Phi_{S1} \cdot d_{Yi}^*_{MAX} \quad (28a, b)$$

The value of γ is a key parameter to predict the drift at each frame. If A_{2V}^* equals to zero when $A_{1U}^*_{MAX}$ occurs, γ is taken as 0.0, while if $A_{1U}^*_{MAX}$ and $A_{2V}^*_{MAX}$ occurs simultaneously, γ is taken as 1.0. In this study, 11 cases are studied: γ is varied from 0.0 to 1.0 with interval of 0.1.

3. BUILDING AND GROUND MOTION DATA

3.1 Building Data

Buildings investigated in this paper are idealized four-story asymmetric shear-building models as shown in Figure 3. Their story height is assumed 3.60 m for all stories and the unit mass is assumed

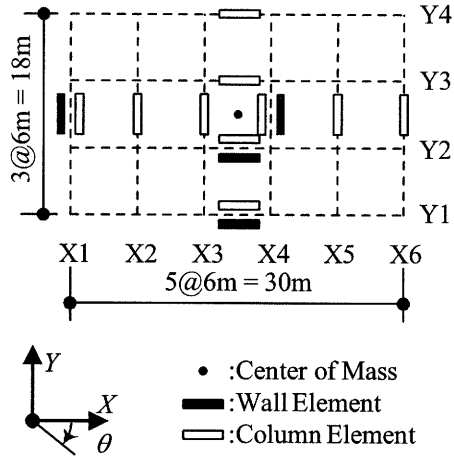


Figure 3 Plan of Model Building

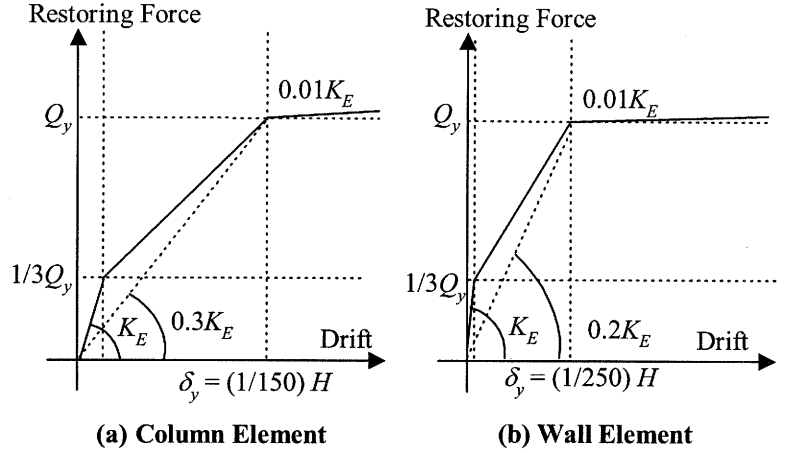


Figure 4 Envelope of Restoring Force-Drift Relationship

$1.2 \times 10^3 \text{ kg/m}^2$: the floor mass m_i and the radius of gyration r are $648 \times 10^3 \text{ kg}$ and 10.1 m , respectively. In each building model, the column element and wall element are placed in frames oriented in X- or Y-direction. The yield strength of i -th story in X- and Y-direction, Q_{yXi} and Q_{yYi} , respectively, are determined by Equation (29): the yield base shear in X- and Y-direction is assumed $1.0 \times W$ and $0.6 \times W$, respectively, where W is the total weight of the building model. The total yield strength of column and wall elements in X-directions are assumed $0.200 \times Q_{yXi}$ and $0.800 \times Q_{yXi}$, respectively, while those in Y-directions are assumed $0.333 \times Q_{yXi}$, $0.667 \times Q_{yXi}$, respectively.

$$Q_{yXi} = \frac{N+i}{N+1} \times 1.0 \times \sum_{j=i}^N w, Q_{yYi} = \frac{N+i}{N+1} \times 0.6 \times \sum_{j=i}^N w \quad (29)$$

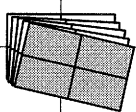
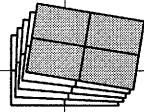
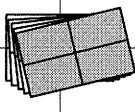
Figure 4 shows the envelope curve of restoring force-drift relationship of each element. The envelopes are assumed symmetric in both positive and negative loading directions. The Takeda hysteretic model (Takeda et al. 1970) is employed for both column and wall elements, assuming that they behave in a ductile manner. For column elements, the effect of bi-axial moment is neglected for the simplicity of the analysis. Figure 5 shows the mode shapes in elastic range of model building. The eccentricity ratios of the model E_X , E_Y are -0.495 and -0.270 , respectively, and the radius ratios of gyration of story stiffness about the center of mass of the model J_X , J_Y are 1.028 and 1.392 , respectively. Therefore, the model building can be classified as torsionally stiff (TS) buildings (Fajfar et al. 2002, Fujii et al. 2004b).

3.2 Ground Motion Data

In this study, the earthquake excitation is considered bi-directional in X-Y plane, and six sets of artificial ground motions are used. Target elastic spectrum with 5% of critical damping $S_A(T, 0.05)$ is determined by Equation (30):

$$S_A(T, 0.05) = \begin{cases} 4.8 + 45T & \text{m/s}^2 & T < 0.16\text{s} \\ 12.0 & & 0.16\text{s} \leq T < 0.864\text{s} \\ 12.0 \cdot (0.864/T) & & T \geq 0.864\text{s} \end{cases} \quad (30)$$

where T is the natural period of the SDOF model. The first 40.96 seconds ($2^{12} = 4096$ data, 0.01 second sampling) of two horizontal components of the following records are used to determine phase angles of the ground motion: El Centro 1940, Taft 1952, Hachinohe 1968, Tohoku University 1978, Kobe Meteorological Observatory 1995 and Fukiai 1995. Elastic acceleration response spectra of

1st Mode	2nd Mode	3rd Mode
		
$T_1 = 0.323s$ $\rho_1/r = 1.41$ $\psi_1 = 56.0\text{Deg.}$	$T_2 = 0.220s$ $\rho_2/r = 2.62$ $\psi_2 = -49.7\text{Deg.}$	$T_3 = 0.143s$ $\rho_3/r = 0.927$ $\psi_3 = 15.9\text{Deg.}$

Note: $\rho_i = \sqrt{\phi_{TXie}^2 + \phi_{TYie}^2} / \phi_{T\Theta ie}$, $\psi_i = \tan^{-1}(-\phi_{TYie} / \phi_{TXie})$

Figure 5 Mode Shape

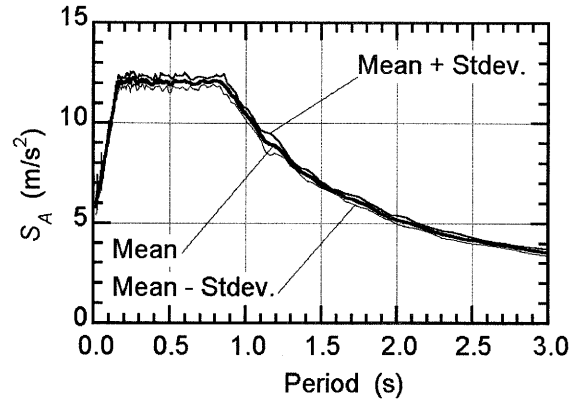


Figure 6 Elastic Acceleration Spectra

artificial ground motions with 5% of critical damping are shown in Figure 6. In this study the two horizontal components of those artificial ground motions are applied simultaneously and $6 \times 180 = 1080$ cases are numerically investigated: the direction of ground motion is varied from 0 to 180 degree with interval of 1 degree.

3.3 Numerical Analysis Procedure

In this study, the damping matrix is assumed proportional to the instant stiffness matrix and 3% of the critical damping for the first mode. Newmark- β method ($\beta = 1/4$) is applied in numerical integrations. The time increment for numerical integration is 0.005 sec. The unbalanced force due to stiffness change is corrected at a next time step during analysis.

4. ANALYSIS RESULTS

In this chapter, the results of time-history analysis of multi-story asymmetric building model (mean value of 1080 analyses, and mean \pm standard deviation) are compared with those of proposed procedure. Figure 7 shows the relationship of γ and the ratio of maximum roof displacement at frame X1, X6 Y1, and Y4 obtained by proposed procedure and mean of time-history analysis. As shown in this figure, the displacement at frame Y1 is underestimated in case of $\gamma = 0.0$ and $\gamma = 1.0$, while it is satisfactorily estimated in case of $\gamma = 0.5$. And those of frame X1, X6 and Y4 are satisfactorily estimated by the proposed procedure within the range of $\gamma = 0.0$ to 0.5 and overestimated in case of $\gamma = 1.0$. Therefore the proposed procedure with $\gamma = 0.5$ provides the most reasonable predictions in 11 cases. This result is consistent with the previous study (Fujii et al. 2004c).

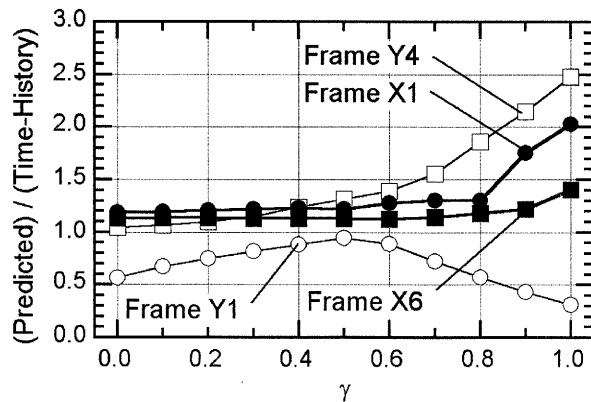


Figure 7 Relationship of γ and the Ratio of Predicted Results and Time-History Analyses

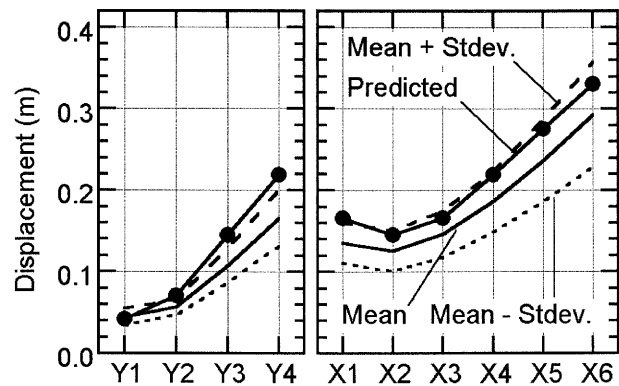


Figure 8 Prediction of Maximum Roof Displacement at Each Frame

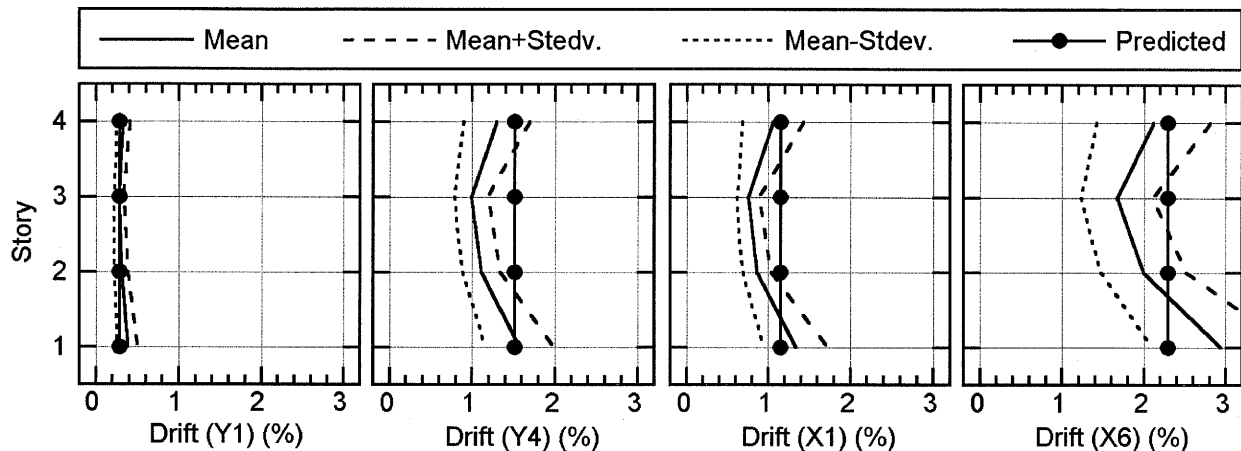


Figure 9 Prediction of Maximum Drift Angle at Frame X1, X6, Y1 and Y4

Figure 8 and 9 show the comparisons of the maximum roof displacement at each frame and the maximum drift angle obtained from time-history analysis and the proposed procedure ($\gamma = 0.5$). These figure show that the proposed procedure can successfully estimate the response of multi-story asymmetric building model.

5. CONCLUSIONS

In this paper, a simplified procedure for multi-story asymmetric buildings subjected to bi-directional ground motion is proposed, and the results obtained by the proposed procedure are compared with the results obtained by the nonlinear dynamic analysis. The results show that the nonlinear response of asymmetric buildings subjected to bi-directional ground motion can be satisfactorily estimated by the simplified procedure proposed in this study.

References:

- ATC-40 (1996), "Seismic Evaluation and Retrofit of Concrete Buildings", Vol. 1, ATC-40, Applied Technology Council.
- Saiidi M, Sozen MA. (1981), "Simple Nonlinear Seismic Analysis of R/C Structures," *Journal of the Structural Division*, ASCE, Vol. 107, ST5, 937-952.
- Fajfar P., Fischinger M. (1988), "N2-A Method for Non-Linear Seismic Analysis of Regular Buildings", *Proceedings of Ninth World Conference on Earthquake Engineering*, Vol. V, V-111-116.
- Fujii, K., Nakano, Y. and Sanada, Y. (2004a), "Simplified Nonlinear Analysis Procedure for Asymmetric Buildings", *Proceedings of 13th World Conference on Earthquake Engineering*, Paper Ref. 149.
- Fujii, K., Nakano, Y. and Sanada, Y. (2004b), "A Simplified Nonlinear Analysis Procedure for Single-Story Asymmetric Buildings", *Journal of Japan Association for Earthquake Engineering*, Vol. 4, No. 2, 1-20.
- Fajfar P., Kilar V., Marusic D., Perus I., Magliulo G. (2002), "The Extension of The N2 Method to Asymmetric Buildings", *Proceedings of the Fourth Forum on Implications of Recent Earthquakes on Seismic Risk*, TIT/EERG02-1, 291-308.
- Otani, S. (2000), "New Seismic Design Provision in Japan", *The Second U.S.-Japan Workshop on Performance-Based Earthquake Engineering Methodology for Reinforced Concrete Structures*, PEER Report 2000/10, 3-14.
- Takeda T, Sozen MA, Nielsen NN. (1970), "Reinforced Concrete Response to Simulated Earthquakes", *Journal of the Structural Division*, ASCE, Vol. 96, No. ST12, 2557-2573.
- Fujii, K., Nakano, Y. and Sanada, Y. (2004c), "Simplified Nonlinear Analysis Procedure for Single-Story Asymmetric Buildings Subjected to Bi-Directional Ground Motion", *First International Conference on Urban Earthquake Engineering*, CUEE, Tokyo Institute of Technology, 97-104.

Effects of Near-Field Vertical Ground Motions on Structural Response

M. Tehranizadeh¹, M.S. Rahim Labafzadeh²

1) Prof. Civil Engineering Department, Amir Kabir University of Technology, Tehran, Iran

2) PhD. candidate, International Institute of Earthquake Engineering and Seismology, Tehran, Iran
tehz@govir.ir, mosral@yahoo.com

Abstract: Vertical ground motion component is one of the near-field earthquake's characteristics. By increasing in epicentral distance, vertical acceleration component, decrease more than horizontal component. Therefore, in comparison with far-field regions this acceleration component is larger in near-field regions. This paper aims at studying the effects of vertical acceleration on structural response due to near-field excitations. To gain this objective, a 3-D steel building in 5, 13 stories, which were designed according to the Iran Building Code, were selected in this study. The sample buildings, subjected to 8 near-field ground motions recorded at Iran, Taiwan, US, With 3 far-field ground motions, categorized in two groups, horizontal component only, horizontal and vertical component simultaneously. Based on nonlinear analysis, story vertical acceleration and velocity, and base axial force have larger values in near-field in comparison with far-field. Studying on the characteristics of near-field vertical ground motions, such as PGV/PGA, PGD/PGV ratios, spectral velocity, duration of strong motion, ground input energy, duration and amplitude of pulses, shows that the demands increase in near-field regions. Although PGV/PGA ratio for horizontal component in near-field is more than the one in far-field but it is identified that this ratio for vertical component in near-field is visa versa. Studying on axial force in central and lateral columns in two exterior and middle frames, indicates that axial force in columns closer to central part of buildings is consequent of only vertical acceleration component, and the average ratio of axial force due to vertical ground motions to designed force, for building central column is about 1.65 for near-field excitations and 1.08 for far-field. In spite of this increase, vertical acceleration must be considered in structural design in near-field and both response spectra for vertical and horizontal acceleration must be intended in building codes.

Keywords: vertical ground motion, near-field, far-field, axial force, 3-D steel building, building code

1. INTRODUCTION

High vertical acceleration component is one of the near-field earthquake characteristics. By increasing the distance from the source of earthquake, the vertical acceleration decreases more severely than horizontal acceleration. So in near-field regions this component of acceleration is greater than far-field. Before recent great earthquakes, usually the vertical component acceleration was not considered in seismic design.

After Northridge and Kobe earthquakes, some researchers preformed extensive studies to distinguish the reasons for structural damages in these earthquakes and generally in earthquakes occurred near the seismic sources, in order to add new instructions to building codes. Previous investigations performed to study on the effects of vertical ground motion on structures include the following studies: Iyengra and Shinozuka (1972) examined the flounce of vertical component on vertical cantilever modes, Anderson and Bertero (1973) analyzed inelastic seismic response of steel frames subjected to both horizontal and vertical ground motions, Pan and Kelly (1984) examined seismic response of base-isolated structures with vertical-rocking coupling, Saadeghvaziri and

Foutch (1991) studied the effects of vertical motion on behavior of reinforced concrete (R/C) highway bridges, and Agbabian et al. (1994) investigated the effects of vertical component on shear resistance of R/C beam-column connections.

Niazi and Bozorgnia (1995, 1998) investigated on vertical ground motions of several earthquakes. They have shown that vertical ground motion is sensitive to site-to-source distance, and the ratio of vertical to horizontal response spectra depends on the distance and period of structures, and in the near-field region the ratio is higher at short periods, and can exceed the commonly assumed ratio of 2/3, however, it reduces to less than 2/3 at long periods. (Niazi et. al, 1998, Ambraseys, 2003)

The characteristics of free-field vertical ground motion have been studied by Niazi and Bozorgnia (1998), analyzing over 700 accelerogram of 12 earthquakes in Taiwan and Loma Prieta and 41 alluvial sites during the Northridge earthquake. They found that the main characteristics of the vertical to horizontal (V/H) spectral ratio are qualitatively similar for all these earthquakes. They obtained attenuation law for near field earthquakes. They also represent the vertical and horizontal response spectra for different distances from the fault in alluvial sites. They prepared a method to estimate the vertical response spectra from horizontal response spectra, which is very useful for engineering purposes. (Niazi et. al, 1998)

In the research executed by Kikuchi, Dan and Yashiro (2000) on a five-story reinforced concrete moment resistant frame, they understood that the columns did not yield by applying only the vertical ground motions to structure but it yielded by applying only the horizontal motions with lower PGA than vertical motion. Through their investigation on ductility ratios for both the vertical and horizontal motions and the horizontal motion only, they found that the vertical motion does not have considerable effects on demolition of structures.

In the research conducted by Chouw (1998) on a three-story steel frame, he understood that time coincidence for maximum amplitudes of ground in vertical and horizontal directions could have great effects on structure's responses. Also he expressed that when the greatest peak of the horizontal and vertical ground accelerations do not coincide in time, it can be expected that the maximum tension force in the column will be determined by the vertical excitation.

Andisheh (2003) in his research showed that the duration of strong ground motion in vertical direction relates inversely to the distance from site to seismic source.

This paper aims at studying the effects of vertical acceleration on structural response due to near-field excitations in order to find that how the effective parameters of near-field can affect vertical vibration of structures.

2. THE NATURE OF NEAR-FIELD EARTHQUAKES USED IN THIS RESEARCH

In this research it is attempted to use the near-field earthquakes of Iran and the world. So the earthquakes were selected according to the definition of near-field which is said by Mohras. (Naeim, 2001) The selected earthquakes were applied to the structure as a three component. The data base of Iranian near-field earthquakes is prepared from Iran Building and Housing Research Center (BHRC). In order to complete the information of Iranian earthquake data base, Landers and ChiChi earthquakes, are used. They are derived from PEER internet web site. (PEER, 2004) All the details are presented in table No.1.

In order to compare the behavior of structures in the near-field and far-field, according to IBC2000 (IBC, 2000) three far-field earthquakes which their epicentral distances are more than 50 km are used. They are derived from PEER site. The characteristics of these earthquakes are shown in table No.2. All the records in this research are scaled due to IBC2000 method.

Table 1 Characteristics of near-field records used in the research

Earthquake	Year	Station	Dir.	PGA cm/sec ²	PGV cm/sec	PGD cm	Dist. km	Soil Type*	Ms	T _d (sec)	PGV/PGA	PGD/PGV
Ghaen	1976	I	H1	132.435	10.595	3.012	10	I	6.4	19.57	0.080	0.284
			H2	187.371	7.426	2.099				19.51	0.040	0.283
			V	162.846	23.250	6.406				19.51	0.143	0.276
Naghan	1977	I	H1	716.130	61.509	12.361	5	I	6.1	20.99	0.086	0.201
			H2	459.108	54.053	12.165				16.71	0.118	0.225
			V	533.664	34.924	4.071				21.33	0.066	0.117
Tabas	1978	9101	H1	819.930	97.781	39.922	3	III	7.4	32.84	0.119	0.378
			H2	835.577	121.379	94.580				32.84	0.145	0.779
			V	675.416	45.560	17.038				32.84	0.067	0.374
Golbaf	1981	I	H1	209.934	22.759	5.964	13	III	7.0	59.33	0.108	0.262
			H2	258.003	14.126	5.876				59.19	0.055	0.416
			V	269.775	27.959	5.317				59.19	0.104	0.190
Meimand	1994	NM	H1	408.096	17.560	1.991	17	II	6.1	27.17	0.043	0.113
			H2	433.412	19.130	2.540				27.12	0.043	0.133
			V	161.865	10.202	2.335				27.13	0.063	0.229
Bam	2003	G B1	H1	623.444	59.675	20.773	<1	II	6.8	66.555	0.096	0.348
			H2	778.275	123.69	34.480				66.555	0.159	0.174
			V	979.554	39.634	8.610				66.555	0.040	0.217
Landers	1992	24 Lucerne	H1	769.890	31.873	16.415	1.1	I	7.4	48.125	0.041	0.515
			H2	707.070	97.603	70.311				48.125	0.138	0.720
			V	802.924	45.938	22.225				48.125	0.057	0.484
Chi Chi	1999	TCU068	H1	453.222	263.10	430.00	1.09	III	7.6	90.00	0.580	1.634
			H2	555.246	176.60	324.11				90.00	0.318	1.836
			V	476.766	187.30	266.55				90.00	0.392	1.423

* The classification is due to Iran code.

Table 2 Characteristics of far-field records used in the research

Earthquake	Year	Station	Dir.	PGA cm/sec ²	PGV cm/sec	PGD cm	Dist. km	Soil Type*	Ms	T _d (sec)	PGV/PGA	PGD/PGV
Tabas	1978	Ferdous 71	H1	85.347	5.7	4.61	94.40	I	7.4	40.00	0.812	0.066
			H2	105.948	8.6	9.69				40.00	1.127	0.081
			V	51.993	7.6	6.78				40.00	0.889	0.146
Landers	1992	12026 Indiana	H1	102.024	9.6	5.05	55.70	III	7.4	60.00	0.527	0.094
			H2	106.929	15.2	9.69				60.00	0.640	0.141
			V	41.202	6.6	3.99				60.00	0.601	0.162
Chi Chi	1999	CHY004	H1	97.119	20.00	17.51	50.89	IV	7.6	150.0	0.875	0.206
			H2	98.100	15.80	15.41				150.0	0.978	0.161
			V	40.221	6.50	5.34				150.0	0.824	0.161

* The classification is due to Iran code.

The figures No.1 and No.2 show the time history of vertical acceleration, velocity and displacement for some of the near-field and far field earthquakes which were used. It is obvious that vertical acceleration is severely higher in near-field earthquake than far-field.

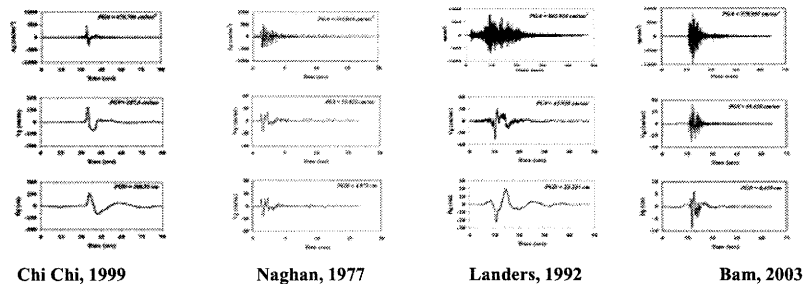


Figure 1 Vertical component time history for some of the near-field earthquakes

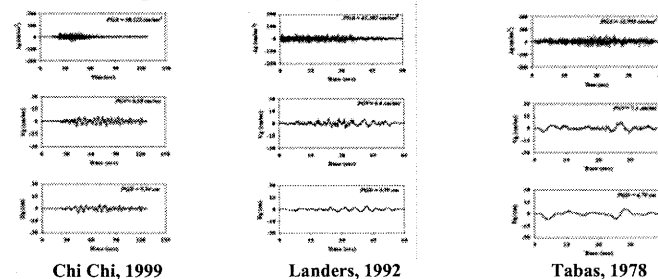


Figure 2 Vertical component time history for the far-field earthquakes

The directivity effect even causes single pulses with long periods in vertical component of near-field earthquakes' records. By investigation on existing records, it is understood that for near-field earthquake compared to far-field, usually the PGV/PGA and PGD/PGV for vertical component are lower, whereas the ratio of PGV/PGA for horizontal component in near-field earthquakes is higher than the far-field motions'. Table No.1 and No.2 shows the ratio of peaks ground motions.

To compute the duration of strong ground motion Page et al. and Bolt approach is used. (Naeim, 2001) Less distance to the source of earthquake, causes longer duration and increases input energy. (IBC, 2000) To remain the structure safe it must have the capacity to dissipate the ground energy. The input energy (E_i) is defined as $E_i = \int_{t_a}^{t_b} m \dot{u}^2 dt$ where t_a and t_b are the starting time and end time of strong ground motion respectively, m is the unit mass and \dot{u} is the ground velocity in the considered direction i . There is no unique method to define the duration of the pulse. The simplest way is to determine the pulse duration using the zero crossings of the pulse wave form. A more complicated way is the employment of an equivalent pulse width based on energy consideration (signal spectrum) and basic concepts from the signal processing theory. An alternative approach is the utilization of the peak value of the velocity response spectrum to indirectly define the pulse period. (Mavroeidis et. al, 2002) The peak ground velocity is considered as the amplitude of the pulse. Table No.3 shows the duration of strong ground motion, energy of earthquake, duration and amplitude of the pulse and spectral velocity for the vertical component of the selected earthquakes. By studying on this table, we understood that near the seismic source usually the duration of strong ground motion and respectively the released energy and also spectral velocity (S_v) are higher for sample structures than in far-field. As it is shown in figure No.3, the Fourier amplitude spectrum for vertical component of near-field in a very small range of frequencies or in another word in a specific frequency has its maximum value.

Table 3 T_s , E_i , T_p , and V_p for the vertical component of selected earthquake

Earthquake		Year	Station	T _S (sec)	E _i (J/kg)	T _P (sec)	S _V (cm/sec)	S _V (cm/sec)	
								T ₁ =1.471823	T ₁ =1.471822
Near-Field	Ghaen	1976	1	5.270	0.0357	2.50	23.250	21.58	18.07
	Naghan	1977	1	7.710	0.0380	0.45	34.924	71.21	28.30
	Tabas	1978	9101	28.120	0.2915	3.00	45.566	50.36	41.96
	Golbaf	1981	1	45.090	0.1710	0.60	27.959	46.03	45.66
	Meimand	1994	NM	6.975	0.0055	0.30	10.202	14.82	5.00
	Bam	2003	GB1	58.155	0.1146	1.00	39.634	23.84	63.84
	Landers	1992	24 Lucerne	33.535	0.1682	1.50	45.938	21.90	77.40
	Chi Chi	1999	TCU068	13.400	7.8727	8.00	187.280	40.91	88.12
Far-Field	Tabas	1978	Ferdous 71	8.120	0.0198	----	----	8.31	10.40
	Landers	1992	12026	0.000	0.0242	----	----	6.08	11.56
	Chi Chi	1999	CHY004	0.000	0.0638	----	----	5.13	7.37

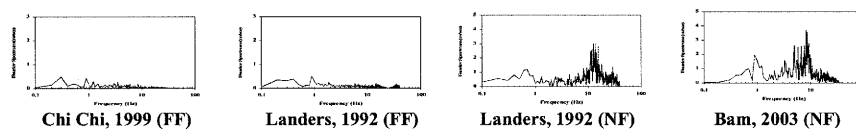
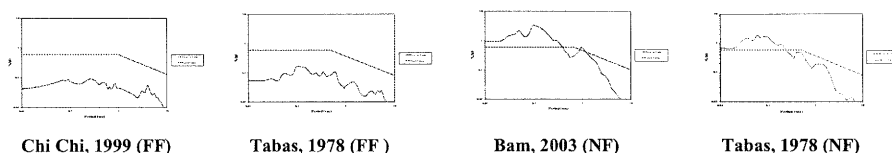


Figure 3 Fourier Amplitude Spectrum for the vertical component of some of the near-field (NF) and far-field (FF) earthquakes

Another characteristic of near-field earthquakes in comparison with the far-field motions is that, its response spectrum for vertical component usually has greater amounts than the design spectrum introduced by Iran Code. [16] The Figure No.5 shows the response spectrum prepared from some of the earthquakes separately and figure No.6 shows the comparison of near-field and far-field response spectra for vertical component, which will prove this subject.



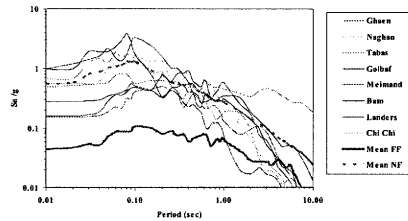


Figure 4 Response Spectra for vertical component of some of the near-field and far-field earthquakes and the comparison between them

3. MODELING AND ANALYZING OF STRUCTURES DUE TO NEAR-FIELD GROUND MOTIONS

The structures used in this research are steel ones with 5, 13 stories which their plans are shown in figure No.5. The spans are 6 m length and the height of each story is 3 m. The structure has braces in the lateral span of four exterior frames. Dead loads are 500 kg/m^2 for each story and 400 kg/m^2 for roof and live loads are 200 kg/m^2 and 150 kg/m^2 respectively for each story and roof. Sample structures are designed due to Iran Building code for high seismic activity regions and soil type II. (Iranian Code, 1999) In order to make models for nonlinear behavior of structures, tri-linear model was used for hinges. The characteristics of these hinges are selected due to FEMA 273. (FEMA, 1997) Their general behaviors are shown in figure No.6 were used. The nominal strength of each element is calculated due to AISC-LRFD code. (AISC, 1994) The damping of structure is assumed as classical damping (proportional to mass and stiffness), and the damping ratio is applied proportional to period of structure. Damping Ratio in linear case at $T_A = 0.33T_1$ and $T_B = T_1$ and for nonlinear case at $T_A = 0.33\sqrt{\mu} T_1$ and $T_B = \sqrt{\mu} T_1$ is 5%. (RAM International, 2000) T_1 is period of first mode, μ is ductility and here it is equal to 3.

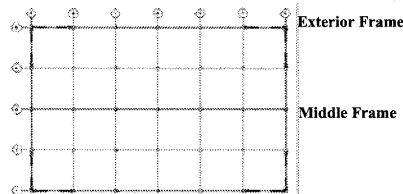


Figure 5 Plan of sample structures

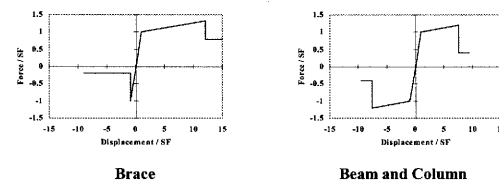


Figure 6 Hinges general behavior

4. EFFECTS OF VARIOUS PARAMETERS OF NEAR-FIELD ON SELECTED MODELS

After designing the structures, nonlinear and linear dynamic analysis are done through direct integration method for selected near-field and far field earthquakes in two groups, horizontal component only, horizontal and vertical components simultaneously. Relative Story velocity and absolute story acceleration in vertical direction, and base axial force are considered as the response of structures. In order to study the effects of near-field and far-field earthquakes on structures, the characteristics of these motions such as PGV/PGA, PGD/PGV, E_i , T_s , T/T_p and PGV are selected and the variation of the response of structures due to the changes of these characteristics are shown in future figures. Distribution of selected parameters over the height of structure for near-field earthquake and the average of far-field motions are shown in figures No.7. By comparing the results of near-field and far-field nonlinear analysis, significant differences can be seen obviously. The Sensitivity of the response of structures to selected earthquake characteristics can be effective for explaining the behavior of earthquakes. In figures No.8 the variation of base axial force, maximum story relative velocity and absolute acceleration due to different characteristics of

selected earthquakes are shown. To study the effects of vertical component of ground motions on structures in near-field and comparing it with far-field excitation, exterior and middle frames are selected and in each frame some of the lateral and central columns are intended. In figures No.9 and No.10 the average range of axial force and the average ratio of axial force stem from earthquakes to design force in some columns (P_E/P_D) are shown. For the 5-story structure the columns of the 1st, 3rd, and 5th stories and for the 13-story structure the columns of the 1st, 5th, 9th, and 13th stories, are chosen as the representative of structure's columns. (Rahim Labafzadeh, 2004)

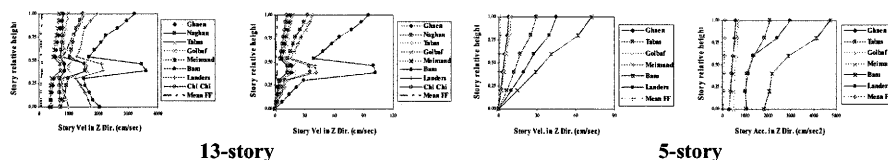


Figure 7 Distribution of response parameters over the height of structures

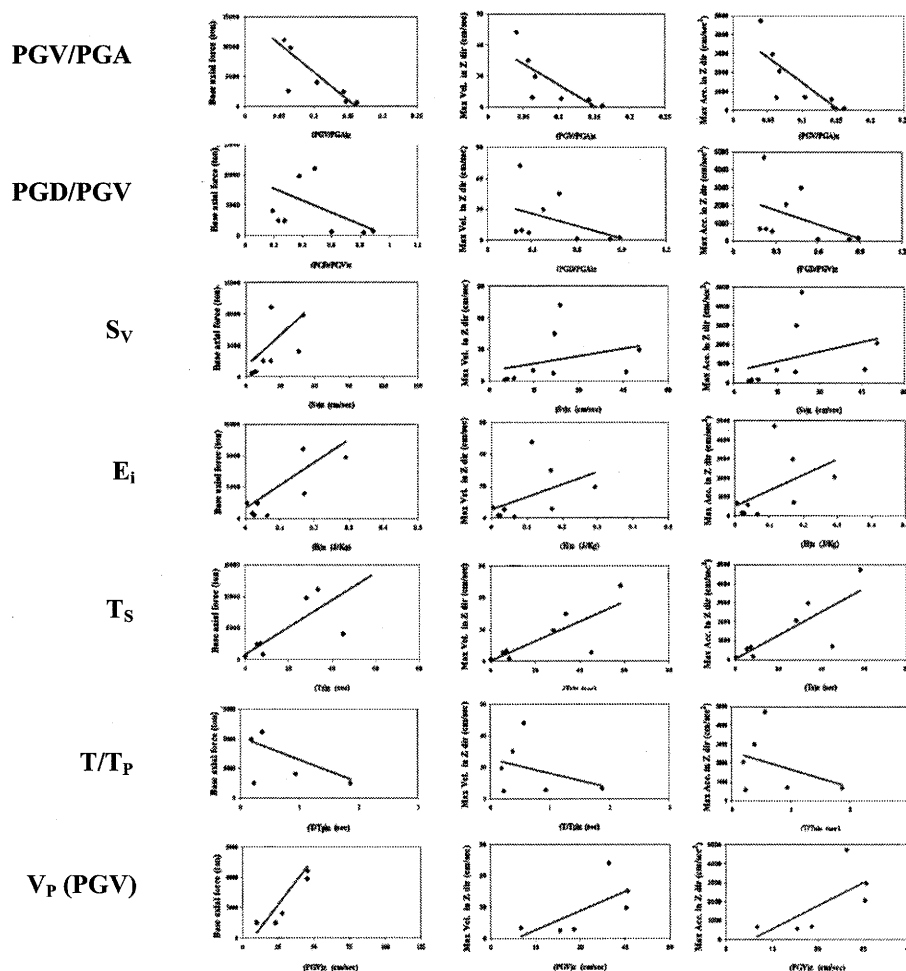
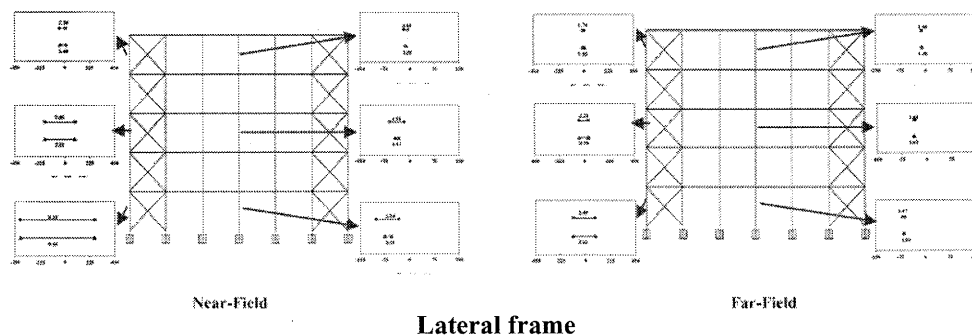


Figure 8 Variation of various response parameters versus earthquake parameters



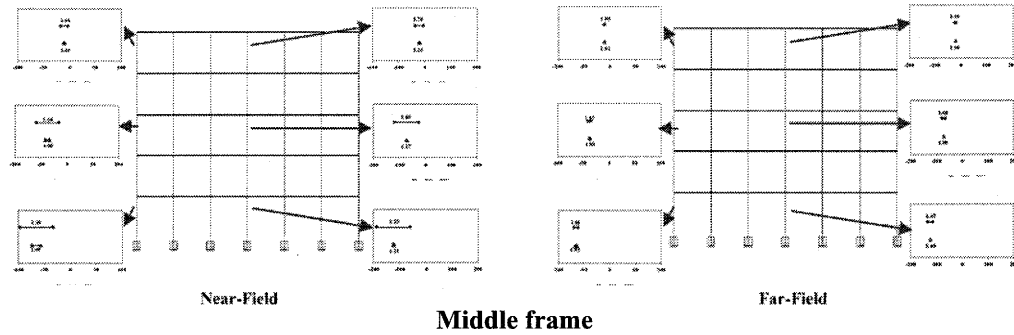


Figure 9 Average range of axial force and the average ratio P_E/P_D for lateral and middle frame of 5-story structure

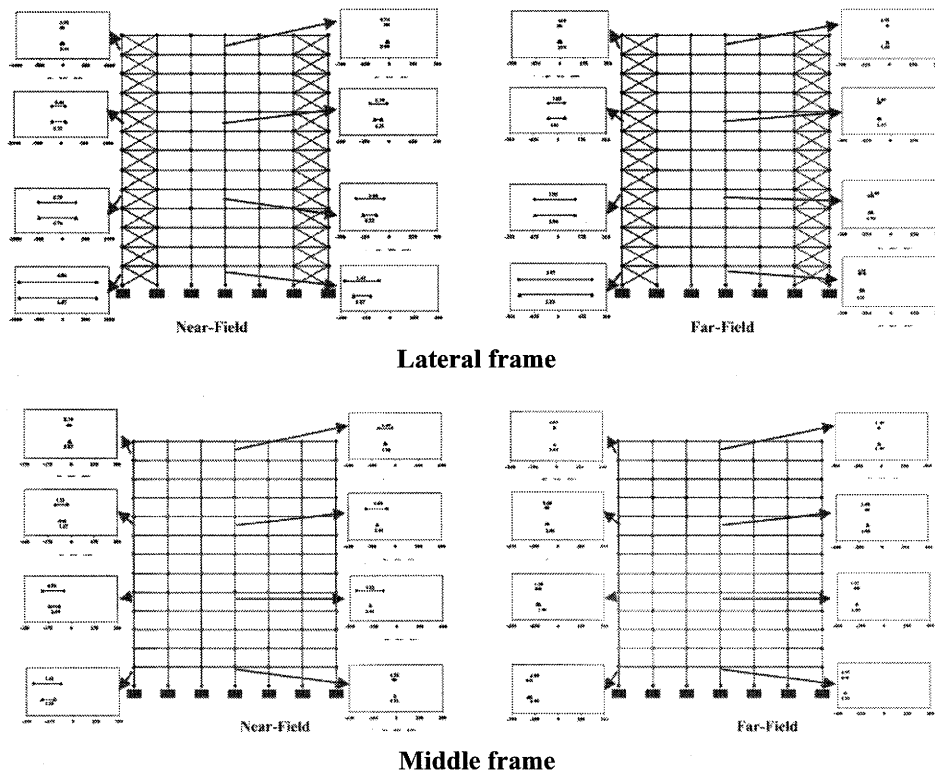


Figure 10 Average range of axial force and the average ratio P_E/P_D for lateral and middle frame of 13-story structure

5. CONCLUSION

The nonlinear dynamic response of 5 and 13 story steel structures due to Iran near-field earthquakes and Chi-Chi, Taiwan, and Landers, US earthquakes are compared with the response of three records of far-field earthquakes. The vertical components of near-field excitations used in this research have less PGV/PGA and PGD/PGV ratios and greater S_V , E_i , T_S than the far-field one, Whereas the ratio of PGV/PGA for horizontal component of near-field earthquakes is greater than this ratio for far-field. When a structure is exposed to near-field motions, because of higher vertical PGA in these regions, absolute story acceleration and story relative velocity have greater amounts. By studying the effects of the near-field effective parameters on structural responses, it was distinguished that if the PGV/PGA and PGD/PGV ratios of vertical component have lower values, and S_V , E_i , and T_S in vertical direction have higher amounts, the responses of the structures will increase. So with regard to the characteristics of near-field earthquakes, it can be concluded that the

response of structures in near-field regions is extremely greater than far-field one. Also, in those near-field earthquakes which have pulses with greater, amplitude (greater PGV) or greater duration of the pulse (less T/T_p) the response of the structure increases more. In order to study the effects of vertical near-field ground motions, the structures analyzed for two groups of earthquake, horizontal component only, and vertical and horizontal component simultaneously, in near-field and far-field. Study on lateral and central columns of selected frames show that the axial forces of columns which are closer to the central part of structure is consequent of vertical component much more than horizontal component. The average ratio of P_E/P_D in near-field regions is 1.65, whereas this ratio in far-field regions reduced to 1.08. This difference indicate that vertical acceleration must be considered in structural design in near-field and both response spectra for vertical and horizontal acceleration must be intended in building codes.

References

- Agabian, N. S., Higazy, E. M., Abdel-Jafar, A. N., Elnashai, A. S. (1994), Experimental observations on the seismic shear performance of R/C beam-column connections subjective to varying axial column force, *Earthquake engineering and Structural Dynamics*, 23, 859-876.
- AISC (1994), *Manual of Steel Construction, Load and Resistance Factor Design (LRFD)*, 2nd Edition, American Institute of Steel Construction, Illinois.
- Ambraseys N., Douglas J. (2003), Near-Field Horizontal and Vertical Earthquake Ground Motions, *Soil Dynamics and Earthquake Engineering*, 23, 1-18.
- Anderson, J. C., Bertero, V. V. (1973), Effects of gravity loads and vertical ground acceleration on the seismic response of multi-story frame, 5th WCEE, Rome, Proceeding, 2914-2923.
- Andishe K. (2003), *The Structural Design Criteria in Near-Field Regions*, Master's thesis, Science and Industry University, Tehran, Iran.
- Bozorgnia, Y., Mahin, S.A., Brady G. (1998), Vertical Response of Twelve Structures Recorded During the Northridge Earthquake, *Earthquake Spectra*, Vol. 14, No. 3, 411-432.
- Bozorgnia, Y., Niazi, M., Campbell K.W. (1995), Characteristics of Free-Field Vertical Ground Motion during the Northridge Earthquake", *Earthquake Spectra*, Vol. 11, No.4, 515-525.
- Chouw N. (1998), Effects of Strong Vertical Ground Motions on Structural Responses, 11th ECEE, Balkema, Rotterdam, Brook Field.
- FEMA (1997), *NEHRP Guidelines for the Seismic Rehabilitation of Buildings*, Building Seismic Safety Council for the Federal Emergency Management Agency (Report No. FEMA 273), Washington D.C.
- Iranian Code of Practice for Seismic Resistance Design of Buildings (1999), Standard No.2800, 2nd Edition, Building and Housing Research Centre.
- IBC (2000), International Building Code, ICBO Publisher.
- Iyengar, R. N., Shinozuka, M. (1972), Effect of self-weight and vertical acceleration on the behaviour of tall structures during earthquake, *Earthquake Engineering and Structural Dynamics*, 1, 69-78.
- Kikuchi M., Dan K., Yashiro K. (2000), Seismic Behavior of a Reinforced concrete Building Due to Large Vertical Ground Motions in Near-Source Regions, 12th WCEE, Auckland, New Zealand, No. 1876.
- Mavroeidis G.P., Papageorgiou A.S. (2002), Near-Source Strong Ground Motion: Characteristics and Design Issues, 7th US NCEE, Boston, No. 0240.
- Naeim F. (2001), *The Seismic Design Handbook*, 2nd edition, Kluwer Academic Publishers.
- Pacific Earthquake Engineering Research Center (2004), PEER Strong Motion Database, [http:// peer.berkeley.edu/smcat](http://peer.berkeley.edu/smcat), 2004.
- Pan, T. C., Kelly, j. N. (1984), Seismic response of base-isolated structures with vertical-rocking coupling, *Earthquake engineering and Structural Dynamics*, 12, 681-702.
- Rahim Labafzadeh M.S. (2004), *Nonlinear Dynamic Behaviour of Structures Due to Near-Field Ground Motions*, Master's thesis, Amir Kabir University of Technology, Tehran, Iran.
- RAM International (2000), *RAM PERFORM-3D Version 1.15 user Guide*, Graham H. Powell Inc.
- Saadeghvaziri, N. I., Foutch, E. A. (1991), Dynamic behavior of R/C highway bridges under the combined effect of vertical and horizontal earthquake motions, *Earthquake engineering and Structural Dynamics*, 20, 535-549.

SEISMIC RESPONSE CONTROL OF NONLINEAR ISOLATED BRIDGES WITH VARIABLE DAMPERS

T. Y. Lee¹⁾, and K. Kawashima²⁾

1) Graduate Student, Department of Civil Engineering, Tokyo Institute of Technology, Japan

2) Professor, Department of Civil Engineering, Tokyo Institute of Technology, Japan

tylee@cv.titech.ac.jp, kawasima@cv.titech.ac.jp

Abstract: The application and effectiveness of seismic response control with variable dampers for nonlinear isolated bridges, which exhibit inelastic responses at both the column and isolator, is studied. Active control system has been studied to mitigate the seismic response effectively as applied to the civil infrastructure. However, active systems may require large external power supply during extreme seismic events and their reliability is still the concerned issue. Semi-active control systems combine the features of active and passive control and have become popular recently. This study investigates the application of a semi-active control system utilizing variable viscous dampers to reduce the response of isolated bridges subjected to extreme earthquakes. Upon considering practical applications, the linear quadratic regulator (LQR) optimal control algorithm was used to command variable dampers. A typical viaduct was analyzed for evaluation. Through numerical simulation, the results show that variable dampers are effective for reducing the seismic response and can reach the similar performance of LQR active control using actuators.

1. INTRODUCTION

The isolator in bridge structure is effective to mitigate the induced seismic force by a shift of natural period. However, the deck displacement becomes excessively large when subjected to a ground motion with large intensity or unexpected characteristics. Even in a standard-size bridge a deck displacement reaches 0.5m under the ground motions developed in the 1999 Chi-Chi earthquake. Such a large displacement may result in the higher-than-expected seismic force due to the pounding effect of decks and the $P-\delta$ effects (Priestley et al. 1996). In the previous studies (e.g. Kawashima and Unjoh 1994, Yang et al. 1995, Symans and Kelly 1999, Loh et al. 2003), structural controls were studied to effectively reducing seismic responses of isolated bridges. However, the control effectiveness of the isolated bridges, which may exhibit high hysteretic behaviour on both columns and isolators when subjected to an extreme earthquake, has not been reported. Hence using seismic response control technology to reduce the deck displacement of isolated bridges with both the column and the isolator being nonlinear is emphasized in this study.

Although active control systems have been studied to mitigate the seismic response effectively as applied to the civil infrastructure, they may require large external power supply and their reliability is still the concerned issue. Semi-active control systems have the major advantages of the versatility and adaptability of active control systems, but without requiring large power or energy supply, and have the reliability of passive control systems. One means of achieving a semi-active control is to adopt a variable viscous damper, in which the damping coefficient can be regulated. Variable viscous dampers have been studied analytically and experimentally to effectively mitigate seismic response of bridges and buildings by, for example, Kawashima et al. (1994), Yang et al. (1995), Symans and Constantinou

(1997). This study focuses on the application of variable viscous dampers to reduce the seismic response of nonlinear isolated bridges subjected to extreme earthquakes. Upon considering practical applications, the linear quadratic regulator (LQR) optimal control algorithm, which is simple and reliable for on-line operations (Yang et al. 1994), will be used to command variable viscous dampers herein. A practical five-span viaduct with high-damping-rubber bearings is utilized for numerical simulation.

2. ANALYSIS MODEL FOR NONLINEAR ISOLATED BRIDGE

Assuming the deck of a typical isolated bridge is rigid in the longitudinal direction, a column with the effective deck mass on the top can be taken apart as a unit for seismic analysis, as shown in Fig. 1. For study of control effectiveness, the column-deck-isolator system may be idealized as a two degree of freedom lumped-mass system. A control device is set between the deck and the column where the isolator bearings are installed.

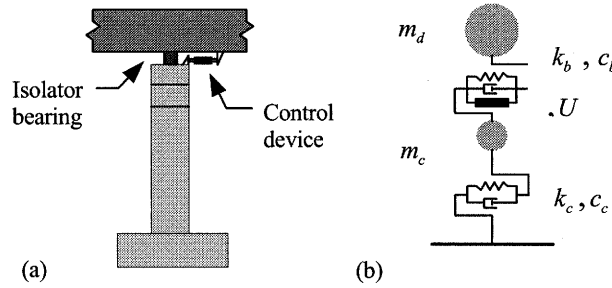


Figure 1 Analytical idealization: (a) analytical unit of column, and (b) 2DOF system..

The column and the isolator bearing are assumed here to be perfect elastoplastic and bilinear elastoplastic, respectively. The Bouc-Wen hysteretic model (Wen 1976) is used for the column and the bearing as.

$$F_{si}(t) = \alpha_i k_i x_i(t) + (1 - \alpha_i) k_i x_{yi} v_i(t) \quad (i = c \text{ and } b) \quad (1)$$

in which the subscripts c and b denote the column and the bearing, respectively, e.g. x_c = deformation of the column and x_b = deformation of the bearing; k_i = initial stiffness; α_i = ratio of the post-yielding to pre-yielding stiffness; x_{yi} = yield deformation; and v_i is a nondimensional variable introduced to describe the hysteretic component of the deformation with $|v_i| \leq 1$, where

$$\dot{v}_i = x_{yi}^{-1} \left[A_i \dot{x}_i - \beta_i |\dot{x}_i| |v_i|^{n_i-1} v_i - \gamma_i \dot{x}_i |v_i|^{n_i} \right] \quad (2)$$

in which parameters A_i , β_i and γ_i govern the scale and general shape of hysteresis loop, whereas the smoothness of force-deformation curve is determined by the parameter n_i . These parameters are considered time invariant herein.

The equations of motion of the isolated bridge system may be expressed as

$$\mathbf{M}\ddot{\mathbf{x}}(t) + \mathbf{C}\dot{\mathbf{x}}(t) + \mathbf{K}_e \mathbf{x}(t) + \mathbf{K}_l \mathbf{v}(t) = \boldsymbol{\eta} \ddot{x}_g(t) + \mathbf{H}U(t) \quad (3)$$

in which $\mathbf{x} = [x_c \ x_b]^T$ is a vector with the deformations of the column and the bearing; $\mathbf{v} = [v_c \ v_b]^T$ is a hysteretic vector; $\ddot{x}_g(t)$ is the absolute ground acceleration; $U(t)$ is the control force generated by the control device; \mathbf{M} , \mathbf{C} , \mathbf{K}_e and \mathbf{K}_l are mass, damping, elastic stiffness and hysteretic stiffness matrices, respectively; $\boldsymbol{\eta}$ and \mathbf{H} are the location matrices of the excitation and the control force, respectively. These matrices are given by

$$\mathbf{M} = \begin{bmatrix} m_c & 0 \\ m_d & m_d \end{bmatrix}; \quad \mathbf{C} = \begin{bmatrix} c_c & -c_b \\ 0 & c_b \end{bmatrix}; \quad \mathbf{K}_e = \begin{bmatrix} \alpha_c k_c & -\alpha_b k_b \\ 0 & \alpha_b k_b \end{bmatrix};$$

$$\mathbf{K}_l = \begin{bmatrix} (1-\alpha_c)k_c x_{yc} & -(1-\alpha_b)k_b x_{yb} \\ 0 & (1-\alpha_b)k_b x_{yb} \end{bmatrix}; \quad \boldsymbol{\eta} = \begin{bmatrix} -m_d \\ -m_c \end{bmatrix}; \quad \mathbf{H} = \begin{bmatrix} 1 \\ -1 \end{bmatrix} \quad (4)$$

where m_c and m_d are the masses of the column and the deck, respectively; c_c and c_d are the damping coefficients of the column and the bearing, respectively.

The equations of motion by Eq. (3) can be written as a state space formulation as follows:

$$\dot{\mathbf{Z}}(t) = \mathbf{g}[\mathbf{Z}(t), \mathbf{v}(t)] + \mathbf{B}U(t) + \mathbf{W}\ddot{x}_g(t) \quad (5)$$

where the space-state vector $\mathbf{Z}(t) = [\mathbf{x}(t) \quad \dot{\mathbf{x}}(t)]^T$; $\mathbf{g}[\mathbf{Z}(t), \mathbf{v}(t)]$ is a nonlinear function of $\mathbf{Z}(t)$ and $\mathbf{v}(t)$; \mathbf{B} and \mathbf{W} are the matrices of the control location and the excitation location, respectively. \mathbf{g} , \mathbf{B} and \mathbf{W} are defined as follows:

$$\mathbf{g}[\mathbf{Z}(t)] = \begin{bmatrix} \dot{\mathbf{x}} \\ -\mathbf{M}^{-1}[\mathbf{C}\dot{\mathbf{x}} + \mathbf{K}_e \mathbf{x} + \mathbf{K}_l \mathbf{v}] \end{bmatrix}; \quad \mathbf{B} = \begin{bmatrix} 0 \\ \mathbf{M}^{-1} \mathbf{H} \end{bmatrix}; \quad \mathbf{W} = \begin{bmatrix} 0 \\ \mathbf{M}^{-1} \boldsymbol{\eta} \end{bmatrix} \quad (6)$$

3. CONTROL ALGORITHM

The linear quadratic regulator (LQR) optimal control algorithm has been extensively used for active control and for semi-active control (e.g. Symans and Constantinou 1995) of structures. In this algorithm, the control force $U(t)$ in Eq. (3) is selected by minimizing, over the duration of the excitation, the following quadratic expression for the cost function:

$$J = \int_0^T [\mathbf{Z}^T(t) \mathbf{Q} \mathbf{Z}(t) + R U^2(t)] dt \quad (7)$$

in which \mathbf{Q} is a (4×4) symmetric positive semidefinite weighting matrix and R is a positive weighting scalar. The weighting values should be determined depending on the design performance goals and the constraints on the controller.

The optimal solution that minimizes the performance index, as shown in Eq. (7), is obtained under the constraint of the state equations of motion by Eq. (5) as follows (Yang et al. 1994)

$$U(t) = -0.5 R^{-1} \mathbf{B}^T \mathbf{P} \mathbf{Z}(t) \quad (8)$$

in which \mathbf{P} is the solution of Ricatti equation given by

$$\Lambda_0^T \mathbf{P} + \mathbf{P} \Lambda_0 - 0.5 \mathbf{P} \mathbf{B} R^{-1} \mathbf{B}^T \mathbf{P} = -2 \mathbf{Q} \quad (9)$$

where

$$\Lambda_0 = \partial \mathbf{g}(\mathbf{Z}) / \partial \mathbf{Z} |_{\mathbf{Z}=0} \quad (10)$$

Note that the constant Ricatti matrix \mathbf{P} in Eq. (9) is obtained by linearizing the structure at $\mathbf{Z} = 0$, as shown in Eq. (10), neglecting the earthquake excitation $\ddot{x}_g(t)$ and setting the transient part equal to zero, i.e. $\dot{\mathbf{P}} = 0$.

As variable viscous damper is used to apply control force to the isolated bridge, the force generated by the variable viscous damper cannot be commanded directly. Only damping coefficient of variable viscous dampers can be regulated by changing the opening of the valve. The control damping force $V(t)$ from the variable viscous damper is given by

$$V(t) = \xi_i(t)\dot{x}_i(t) \quad (11)$$

where $\xi_i(t)$ is the time-variant damping coefficient and $\dot{x}_i(t)$ is the relative velocity between the ends of damper i .

Since the capacity of variable damper is bounded by a minimum value and a maximum value, the damping coefficient $\xi_i(t)$ must be adjusted as

$$\xi_{i\min} \leq \xi_i(t) \leq \xi_{i\max} \quad (12)$$

When the variable viscous damper is expected to provide the demanded optimal control force $U(t)$ by Eq. (8), equaling Eq. (11) and Eq. (8) leads to

$$\xi_i^*(t)\dot{x}_i(t) = U(t) = -0.5R^{-1}BPZ(t) \quad (13)$$

By dividing Eq. (13) by $\dot{x}_i(t)$, the demanded damping coefficient $\xi_i^*(t)$ can be computed as

$$\xi_i^*(t) = \frac{U(t)}{\dot{x}_i(t)} = \frac{-0.5R^{-1}BPZ(t)}{\dot{x}_i(t)} \quad (14)$$

Note that the applied viscous damping coefficient $\xi_i(t)$ must be constrained by Eq. (12), namely

$$\xi_i(t) = \begin{cases} \xi_{i\max} & \xi_i^* \geq \xi_{i\max} \\ \xi_i^* & \xi_{i\min} < \xi_i^* < \xi_{i\max} \\ \xi_{i\min} & \xi_i^* \leq \xi_{i\min} \end{cases} \quad (15)$$

By doing so, the variable viscous damper not only can change the damping coefficient depending on measured structural responses to resemble an active system but also functions as a passive energy dissipater.

4. NUMERICAL SIMULATION

4.1 Target viaduct

In this study, a typical isolated bridge designed by Japan Design Specification of Highway Bridges, Part V Seismic Design (1996) was analyzed to investigate the performance of structural control presented in the previous section in terms of seismic displacement responses as shown in Fig. 2. The superstructure consists of a five-span continuous deck with a total deck length of $5 \times 40 \text{ m} = 200 \text{ m}$ and a width of 12 m. They are supported by short reinforced concrete columns. The longitudinal reinforcement ratio is 0.91% and the tie reinforcement ratio (volumetric ratio) is 0.53%. Five high-damping-rubber bearings with $112 \text{ mm} \times 600 \text{ mm} \times 600 \text{ mm}$ ($H \times B \times D$) are used per column.

The bridge is idealized as a two degree of freedom lumped-mass system. The effective mass of deck and column are 600T and 243.15T, respectively. As described earlier, the restoring forces of the columns and the isolators are perfect elastoplastic and bilinear elastoplastic, respectively. The parameters in Eqs. (1) and (2) are $k_c = 112.7 \text{ MN/m}$, $\alpha_c = 0$, $x_{yc} = 0.0309 \text{ m}$, $A_c = 1$, $\beta_c = \gamma_c = 0.5$ and $n_c = 95$ for the column, and $k_b = 47.6 \text{ MN/m}$, $\alpha_b = 0.1912$, $x_{yb} = 0.016 \text{ m}$, $A_b = 1$, $\beta_b = \gamma_b = 0.5$ and

$n_b=95$ for the isolators. The first and second natural periods of the isolated bridge with the initial elastic stiffness are 0.86 sec and 0.24 sec, respectively. The damping ratios of the system are assumed 2% for the both modes. In simulation, the isolated bridge is subjected to Sun-Moon Lake ground motion in the 1999 Chi-Chi, Taiwan earthquake, as shown in Fig. 3. In the uncontrolled system to the Sun-Moon Lake ground motion, the peak deck displacement reaches 0.55 m, presented in column 2 of Table 1. It is noted that the column has a residual displacement of 0.1 m. This results in the same magnitude of residual displacement in the deck.

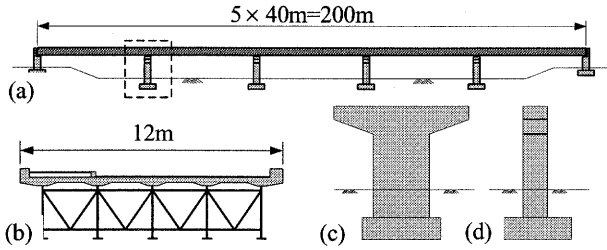


Figure 2 A continuous elevated highway bridge (a) elevation, (b) lateral view of superstructure, (c) lateral view of column, and (d) side view of column.

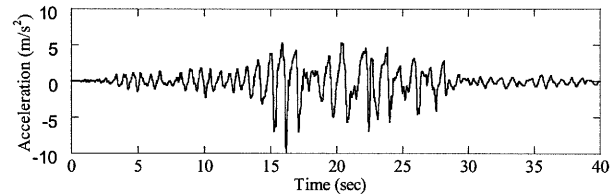


Figure 3 Sun-Moon Lake ground motion record

4.2 LQR optimum active control

Using LQR active control algorithm, the control force and the corresponding structural seismic response depend on the gain matrix by selecting weighting matrix \mathbf{Q} and \mathbf{R} in Eq. (9). A thorough parametric study showed that choosing \mathbf{Q} as $\text{diag}[1,1000,1,1]$ with off-diagonal elements to be zero achieves better performance in reducing the deck displacement. The columns 3 and 4 of Table 1 present the displacement responses under active controls with $\mathbf{Q}=\text{diag}[1,1000,1,1]$ and $\mathbf{R}=10^{-11}$ and $\mathbf{R}=3 \times 10^{-12}$, respectively. Observed from the results, larger weighting \mathbf{R} results in smaller control force. Both active control systems are effective in reducing the deck displacement, but larger control force does not render further decrease in deck displacement, even render almost the same column deformation as the uncontrolled system and larger control residual displacement. It can be attributed to that control force is effective for reducing isolator deformation while it is also effective for transmitting force from the deck to the column so that it increases the column deformation. Larger control force may hence cause column yielding, which in turn largely increases column deformation in inelastic range. Once the increase of the column deformation surpasses the decrease of the isolator deformation, larger control force inversely increases the deck displacement and results in an ineffective control. Therefore, saturation of control force is used to avoid large inelastic column deformation occurring and an ineffective control. The column 5 of Table 1 presents the displacement responses under active control with $\mathbf{R}=10^{-11}$ and the saturation of 15% of deck weight, i.e. 882 KN.

Table 1 Summary of peak control force and peak responses of the isolated bridge

Control method (1)	Uncontrolled (2)	Active $\mathbf{R}=10^{-11}$ (3)	Active $\mathbf{R}=3 \times 10^{-12}$ (4)	Active with saturation (5)	Semi-active damper (6)	Passive low damping (7)	Passive high damping (8)
Peak control force (KN)	-	1278	1947	882	882	468	1581
Peak deck displacement (m)	0.543	0.351	0.365	0.364	0.364	0.467	0.404
Peak isolator deformation (m)	0.406	0.261	0.181	0.282	0.290	0.380	0.272
Peak column deformation (m)	0.247	0.132	0.245	0.123	0.108	0.170	0.144
Column residual deformation (m)	0.105	0.092	0.204	0.035	0.027	0.043	0.105

It is observed that the saturated control achieves slightly less performance than the unsaturated control but especially the column residual displacement has been dramatically reduced.

4.3 Semi-active control

Variable viscous damper based on the LQR control algorithm is used to apply control force to the isolated bridge. The upper and lower bound of viscous coefficients of variable damper are 1000 KN/m/s and 250 KN/m/s, respectively. Fig. 4 shows the control force, the applied damping coefficient of variable viscous damper and the deck displacement response of the isolated bridge to Sun-Moon Lake ground motion for the following three cases: an uncontrolled system, a active control system, and a semi-active control system. In order to compare the control effect between active control and semi-active control, semi-active control uses the LQR control algorithm with $R=10^{-11}$ and the saturation of 15% of deck weight. As observed from Fig. 4, the control force generated by an actuator and a variable viscous damper is virtually similar to each other except at few time periods. The force difference between two devices can be attributed to two reasons. One is that variable viscous dampers are intrinsically energy dissipation devices and cannot add mechanical energy to the structural system while actuator can generate arbitrary force no matter when the control force dissipates or add energy. The other reason is that the damping coefficient of variable viscous dampers is bounded due to mechanics limitation. Although there is slight discrepancy, the variable viscous damper achieves close performance to the actuator. It implies that variable viscous dampers can provide most of required control forces based on LQR control algorithm. Under semi-active control, the peak deck displacement of the bridge reduces to 0.36 m and the residual displacement reduces to 0.03 m, which are almost the same as those under active control. The hysteretic loops of the isolator and the column are shown in Fig. 5 demonstrating that the column yields even in the controlled systems and that both

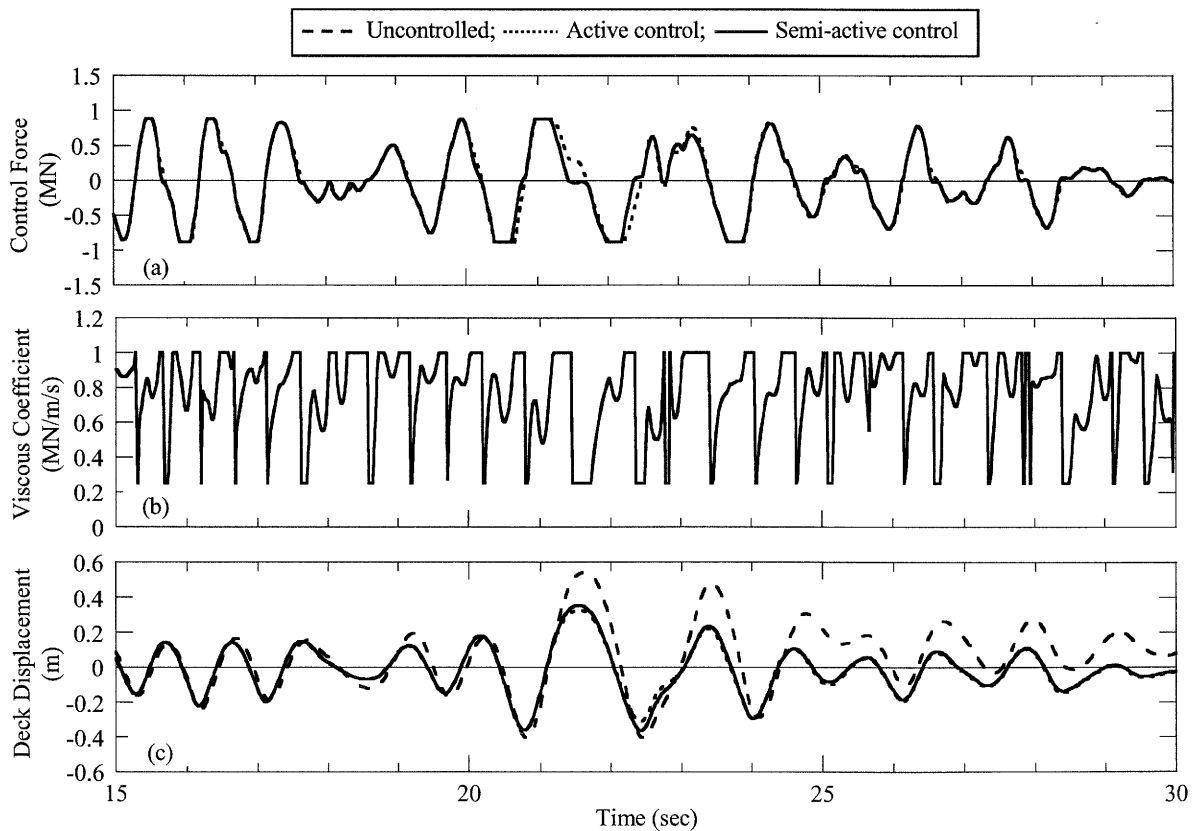


Figure 4 Comparison of the control force and the deck displacement (a) control force, (b) viscous coefficient of variable viscous damper, and (c) deck displacement.

active control and semi-active control have the similar hysteretic behaviour. Fig. 6 presents the hysteretic loops of control force and corresponding stroke. The hysteretic loops of active control and semi-active control are similar except some outer contours. The control force versus velocity of the control devices are shown in Fig. 7 demonstrating that the damping coefficient of variable viscous damper is confined, and that the actuator add energy into system in some time when exhibiting in the second and fourth quadrant, i.e. $U(t)\dot{x}_b(t) < 0$.

When the variable viscous damper with fixed damping coefficient, i.e. passive control, the control effects of low damping coefficient $\xi_{i\min}$ and high damping coefficient $\xi_{i\max}$ are shown in the columns 7 and 8 of Table 1. The results indicate semi-active control with variable damper present superior performance than passive control.

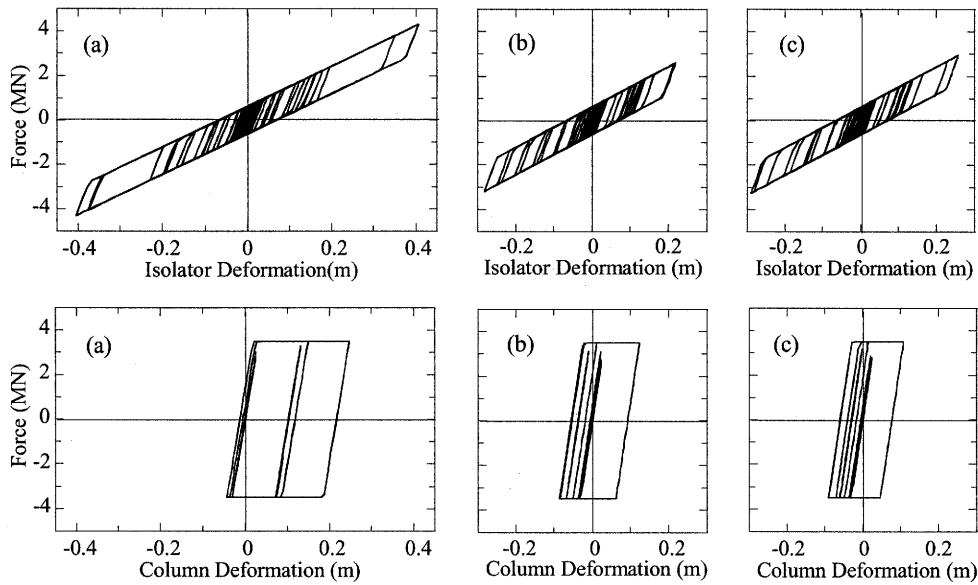


Figure 5 Hysteretic loops of the isolator and the column: (a) uncontrolled, (b) active control, and (c) semi-active control.

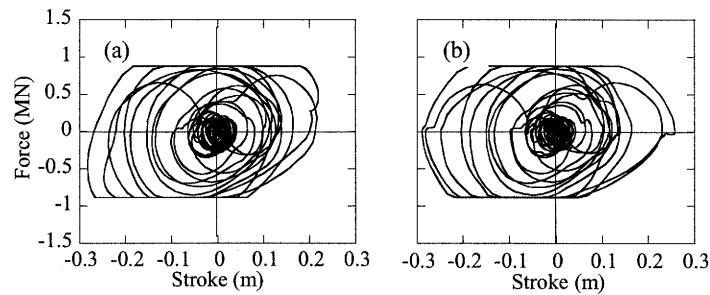


Figure 6 Hysteretic loops: (a) actuator, and (b) variable viscous damper

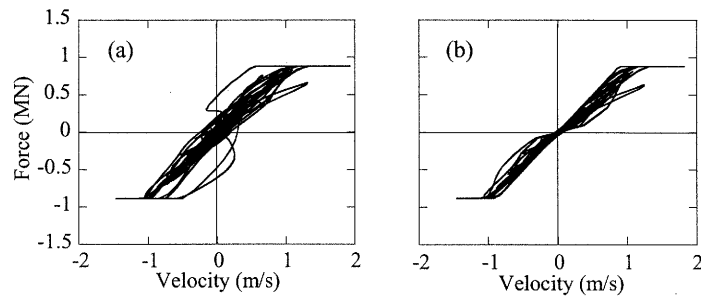


Figure 7 Control force vs. velocity: (a) actuator, and (b) variable viscous damper

5. CONCLUSIONS

The application and effectiveness of semi-active control for nonlinear isolated bridge, which exhibits inelastic response at both the column and the isolator, was studied numerically. The LQR control algorithm is used to command variable viscous dampers. Numerical simulations were carried out to investigate and compare the control performance of a practical five-span continuous highway elevated bridge equipped with high-damping-rubber bearings under active control, passive control and semi-active control. The results indicate the following:

- (a) The LQR optimal control is effective for reducing the deck displacement and isolator deformation at smaller control force. However, at larger control force level, although the isolator deformation further decreases, it potentially results in larger column yielding, which inversely increases the deck displacement. Such a situation may render an ineffective control on the deck displacement and larger residual displacement. It is preferable to apply the saturation of control force to prevent such an ineffective control.
- (b) Semi-active control with variable viscous dampers can be effective in reducing the seismic response and can reach the similar performance of LQR active control using actuators.
- (c) Semi-active control with variable viscous dampers presents superior performance than passive control with constant viscous coefficients of $\xi_{i\min}$ and $\xi_{i\max}$.

Acknowledgements:

The authors acknowledge support for the first author from the Center for Urban Earthquake Engineering (CUEE) in Tokyo Institute of Technology.

References:

- Japan Road Association (1996), "Design specification of highway bridges, part V seismic design", Tokyo: Maruzen.
- Kawashima, K. and Unjoh, S. (1994), "Seismic Response Control of Bridges by Variable dampers," *Journal of Structural Engineering*, American Society of Civil Engineers, **120**(9), 2583-2601.
- Loh, C. H., Wu, L. Y. and Lin, P. Y. (2003), "Displacement Control of Isolated structures with Semi-active Control Devices," *Journal of Structural Control*, **10**, 77-100.
- Priestley, M. J. N., Seible, F. and Calvi, G. M. (1996), "Seismic Design and Retrofit of Bridges", John Wiley & Sons, USA.
- Symans, M. D. and Constantinou, M. C. (1997), "Seismic Testing of a Building Structure with a Semi-active Fluid Damper Control System," *Earthquake Engineering and Structural Dynamics*, **26**(7), 759-777.
- Symans, M. D., Kelly, S.W. (1999), "Fuzzy Logic Control of Bridge Structures Using Intelligent Semi-active Seismic Isolation Systems," *Earthquake Engineering and Structural Dynamics*, **28**(1), 37-60.
- Wen, Y. K. (1976), "Method for Random Vibration of Hysteretic System," *Journal of Engineering Mechanics Division*, American Society of Civil Engineers, **102**(EM2), 249-263.
- Yang, J.N., Li, Z. and Vongchavallitkul, S. (1994), "A Generalization of Optimal Control Theory: Linear and Nonlinear Control," *Journal of Engineering Mechanics*, American Society of Civil Engineers, **120**(2), 266-283.
- Yang, J.N., Wu, J.C., Kawashima, K. and Unjoh, S. (1995), "Hybrid Control of Seismic-excited bridge structures," *Earthquake Engineering and Structural Dynamics*, **24**(11), 1437-1451.

A CONSTITUTIVE RULE FOR VISCOELASTIC MATERIAL CONSIDERING HEAT CONDUCTION AND HEAT TRANSFER

K. Kasai ¹⁾, and D. Sato ²⁾

1) Professor, Structural Engineering Research Center, Tokyo Institute of Technology, Japan

2) Graduate Student, Department of Built Environment, Tokyo Institute of Technology, Japan

kasai@serc.titech.ac.jp , daiki@enveng.titech.ac.jp

Abstract: This paper proposes a nonlinear model for VE damper subjected to a long duration cyclic load. The temperature rise and distribution of VE materials during cyclical loadings can be predicted by using a one dimensional heat transfer equation. Significant heat conduction and transfer, for some instance appears to influence the temperature rise, and this effect is included in the analytical model. The constitutive rule using fractional derivative considers VE material softening due to the temperature rise and sensitivity against excitation frequency. Excellent performance of proposed model is demonstrated through comparison with the long duration loading experimental results.

1. INTRODUCTION

It has been recognized that viscoelastic (VE) dampers have significant advantage of being effective against not only the wind but also the earthquake. First application of VE dampers to reduce building vibration was The World Trade Center in New York (Mahmoodi 1969). Since then, the VE dampers have been applied to buildings to reduce vibration due to earthquake and/or wind for many years (Nielsen et al. 1994).

It is known that VE materials have sensitivity against the frequency, temperature, and strain. The VE damper dissipates energy through shear deformation within the VE material during cycle loading, causing temperature-rise of the material. Consequently, the VE material becomes softer, and its energy dissipation capacity decreases during the loading. In order to simulate such nonlinear behavior, the temperature distribution of the VE material must be estimated accurately.

The nonlinear model was proposed earlier, by focusing on the effect of temperature-rise (Kasai et al. 1993, 2002, 2003). Since then, such model was adopted by Shen & Soong (1995), Huang et al. (2001). However, these models did not considered the heat conduction and heat transfer, which are still reasonable in case of short duration loading like a typical earthquake. However, in case of long duration loading such as long period earthquake or wind force, heat conduction and heat transfer must be considered.

In this paper, a nonlinear model for VE damper subjected to a long duration cyclic load is proposed. The constitutive rule of this model uses the fractional time-derivative of stresses and strain in order to accurately simulate sensitivities against the temperature and excitation frequency, and additionally considers VE material softening due to the temperature-rise. The present model also includes the effect of heat conduction and heat transfer using a one-dimensional heat transfer equation, and simulates the temperature distribution within the VE materials during cyclic loading. To validate performance of the proposed model, experiment applying sinusoidal displacement of almost one hour is conducted. Three-dimensional finite element analysis is also performed to demonstrate excellent accuracy of the proposed model

2. FRACTIONAL DERIVATIVE MODELS

2.1 Concept of Long Duration Fractional Derivative Model

Figures 1 and 2 contrasts the distributions of temperature, stiffness, and strain along thickness (Z-) direction of the VE damper, between the model for short duration loading like a typical earthquake and that for long duration loading such as long period earthquake or wind force. From now on, they will be called as "short duration model" and "long duration model", respectively.

The short duration model considers only the effect of temperature-rise caused by dissipation of energy. Due to the small heat conductivity of the VE material, heat conduction from VE material to steel plate and heat transfer to air are very slow, compared with the short duration of the loading. Therefore, the distributions of temperature, strain and stress are considered to be uniform within the VE material, and such a model has been found sufficiently accurate when typical earthquake loading is considered (Kasai et al. 1993).

In contrast, the long duration model considers one-dimensional heat conduction and transfer in the thickness direction. The area of VE material exposed to the air is small in comparison with such on area of steel plates that are bonded to the VE materials. Therefore, analysis assumes that the heat generated inside the VE material moves toward the steel plates, and finally transmitted to the air from the steel plates. Accordingly, strain and temperature are expressed by $\gamma(t, z)$ and $\theta(t, z)$, respectively, as the function of time "t" and in the thickness direction coordinate "z". Based on equilibrium, the VE material shear stress is assumed to be constant throughout the thickness.

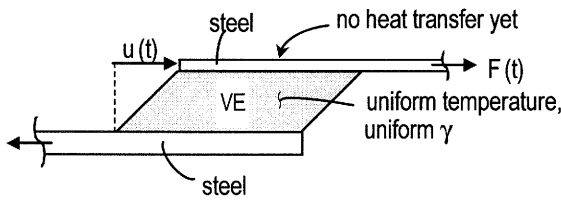


Figure 1 Short Duration Model

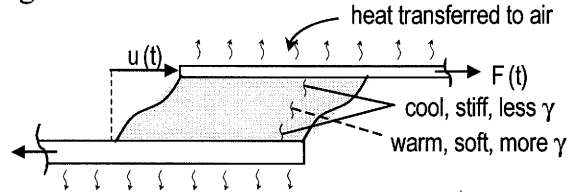


Figure 2 Long Duration Model

2.2 Short Duration Model (Past Fractional Derivative Model)

The shear stress $\tau(t)$ and strain $\gamma(t)$ of the VE damper are related to the force $F(t)$ and deformation $u(t)$ of the damper as follows:

$$\tau(t) = F(t)/A_s, \quad \gamma(t) = u(t)/d \quad (1)$$

where, A_s = shear area, and d = thickness of the VE damper.

From now on, we explain a method to obtain $F(t)$ for a given $u(t)$. Kasai et al. (1993) proposed the following shear stress–strain constitutive rule of the VE material as the short duration model.

$$\tau(t) + aD^\alpha \tau(t) = G[\gamma(t) + bD^\alpha \gamma(t)] \quad (2)$$

where $D^\alpha = d^\alpha/dt^\alpha$ = fractional derivative operator, α = order of the fractional derivative, a and b = parameters of constitutive rule, G = static shear modulus. Coefficients a and b are calculated by

$$a = a_{ref}\lambda^\alpha, \quad b = b_{ref}\lambda^\alpha, \quad \lambda = \exp[-p_1(\theta - \theta_{ref})/(p_2 + \theta - \theta_{ref})] \quad (3a-c)$$

where a_{ref} and b_{ref} = constants at reference temperature θ_{ref} , λ = shifting factor, and p_1 and p_2 = constants to model temperature-frequency equivalency of the VE material.

Numerical integration is used to simulate the stress – strain value at the n -th step of analysis (Eq.4).

$$\tau^{(n)} + \frac{a^{(n)}}{\Delta t^\alpha} \sum_{i=0}^N w^{(i)} \tau^{(n-i)} = G \left[\gamma^{(n)} + \frac{b^{(n)}}{\Delta t^\alpha} \sum_{i=0}^N w^{(i)} \gamma^{(n-i)} \right] \quad (4)$$

where, i = time step number, Δt = time step size, $w^{(i)}$ = weight function, and N = window size (Kasai et

al. 2001, 2002, 2003). Next step temperature $\theta^{(n+1)}$ is calculated from the every dissipated up to the n -th step as follows (Kasai et al. 1993):

$$\theta^{(n+1)} = \theta^{(n)} + \frac{(\tau^{(n)} + \tau^{(n-1)})(\gamma^{(n)} - \gamma^{(n-1)})}{2s\rho} \quad (5)$$

where, s = specific heat, ρ = mass density of the VE material.

2.3 Formulation of Long Duration Model

Under the long duration loading, temperature and strain inside the VE material depend on the location " z " and time " t ". Therefore, Eqs. (1) ~ (3) should be modified to Eqs. (6) ~ (8), respectively.

$$\tau(t) + a(z)D^\alpha \tau(t) = G[\gamma(z, t) + b(z)D^\alpha \gamma(z, t)] \quad (6)$$

$$a(z) = a_{ref}(\lambda(z))^\alpha, \quad b(z) = b_{ref}(\lambda(z))^\alpha \quad (7a, b)$$

$$\lambda(z) = \exp[-p_1(\theta(z, t) - \theta_{ref}) / (p_2 + \theta(z, t) - \theta_{ref})] \quad (8)$$

By integrating the fractional derivatives of Eq. (6), the shear stress $\tau^{(n)}$ and strain $\gamma_j^{(n)}$ can be obtained at n step,

$$\tau^{(n)} + \frac{a_j^{(n)}}{\Delta t^\alpha} \sum_{i=0}^N w^{(i)} \tau^{(n-i)} = G \left[\gamma_j^{(n)} + \frac{b_j^{(n)}}{\Delta t^\alpha} \sum_{i=0}^N w^{(i)} \gamma_j^{(n-i)} \right] \quad (9)$$

where j = the index denoting the location ($j = 0 \sim m$), and m = number of sampling points in the VE material in the thickness (Z direction).

By rearranging and manipulating about $\gamma_j^{(n)}$ of Eq. (9), $\gamma_j^{(n)}$ is written as

$$\gamma_j^{(n)} = \frac{\tau^{(n)}(\Delta t^\alpha + a_j^{(n)} w^{(0)}) + \tilde{A}_j^{(n)} - \tilde{B}_j^{(n)}}{G(\Delta t^\alpha + b_j^{(n)} w^{(0)})} \quad (10)$$

where,

$$\tilde{A}_j^{(n)} = a_j^{(n)} \sum_{i=1}^N w^{(i)} \tau^{(n-i)}, \quad \tilde{B}_j^{(n)} = G b_j^{(n)} \sum_{i=1}^N w^{(i)} \gamma_j^{(n-i)} \quad (11a, b)$$

As the length of per unit element divided into m is expressed by h_j ($= z_j - z_{j-1}$; See Figure 4) and when n step displacement of the damper $u_d^{(n)}$ is known, compatibility condition between $u_d^{(n)}$ and $\gamma_j^{(n)}$ can be given by Eq. (12).

$$u_d^{(n)} = \frac{1}{2} \left[\sum_{j=0}^{m-1} h_{j+1} \gamma_j^{(n)} + \sum_{j=1}^m h_j \gamma_j^{(n)} \right] \quad (12)$$

By substituting Eq. (10) into Eq. (12), then $\tau^{(n)}$ is expressed by Eq. (13).

$$\tau^{(n)} = \frac{2G u_d^{(n)} - \sum_{j=0}^{m-1} \frac{h_{j+1}(\tilde{A}_j^{(n)} - \tilde{B}_j^{(n)})}{\Delta t^\alpha + b_j^{(n)} w^{(0)}} - \sum_{j=1}^m \frac{h_j(\tilde{A}_j^{(n)} - \tilde{B}_j^{(n)})}{\Delta t^\alpha + b_j^{(n)} w^{(0)}}}{\sum_{j=0}^{m-1} \frac{h_{j+1}(\Delta t^\alpha + a_j^{(n)} w^{(0)})}{\Delta t^\alpha + b_j^{(n)} w^{(0)}} + \sum_{j=1}^m \frac{h_j(\Delta t^\alpha + a_j^{(n)} w^{(0)})}{\Delta t^\alpha + b_j^{(n)} w^{(0)}}} \quad (13)$$

After obtaining $\tau^{(n)}$, it can be re-substituted into Eq. (10) to determine $\gamma_j^{(n)}$ at any location j .

In order to predict the temperature distribution of VE damper, the following heat conduction

equation and initial temperature of next step $\bar{\theta}_j^{(n+1)}$ are expressed by Eq. (14) and (15) respectively. Where κ = heat conduction factor.

$$\frac{\partial \theta(z,t)}{\partial t} = \frac{\kappa}{s\rho} \frac{\partial^2 \theta(z,t)}{\partial z^2}, \quad \bar{\theta}_j^{(n+1)} = \theta_j^{(n)} + \frac{(\tau_j^{(n)} + \tau_j^{(n-1)})(\gamma_j^{(n)} - \gamma_j^{(n-1)})}{2s_j\rho_j} \quad (14),(15)$$

2.4 Heat Transfer Analysis

Since the VE damper is symmetrical with the inner steel plate in this study, the heat transfer analysis is carried out modeling to half of the VE damper as shown in Figure 3 and 4. In Figure 3, the position from "c" to "d" is the area of the VE material.

The temperature distribution of VE damper is calculated by Eq. (16).

$$\left(\frac{1}{\Delta t} [C] + \frac{1}{2} [K] \right) \{ \Theta(t + \Delta t) \} = \left(\frac{1}{\Delta t} [C] - \frac{1}{2} [K] \right) \{ \Theta(t) \} + \{ F(t) \} \quad (16)$$

Where,

$$[C] = \begin{bmatrix} c_{00} & c_{01} & & & & & & & & \\ c_{10} & c_{11} & c_{12} & & & & & & & \\ & c_{21} & c_{22} & c_{23} & & & & & & \\ & & c_{32} & c_{33} & c_{34} & & & & & \\ & & & \ddots & \ddots & \ddots & & & & \\ & & & & c_{g-1g-2} & c_{g-1g-1} & c_{g-1g} & & & \\ & & & & & c_{gg-1} & c_{gg} & & & \end{bmatrix}, \quad [K] = \begin{bmatrix} k_{00} & k_{01} & & & & & & & & \\ k_{10} & k_{11} & k_{12} & & & & & & & \\ & k_{21} & k_{22} & k_{23} & & & & & & \\ & & k_{32} & k_{33} & k_{34} & & & & & \\ & & & \ddots & \ddots & \ddots & & & & \\ & & & & k_{g-1g-2} & k_{g-1g-1} & k_{g-1g} & & & \\ & & & & & k_{gg-1} & k_{gg} & & & \end{bmatrix} \quad (17),(18)$$

$$\{ F(t) \} = \{ f_0(t) \quad 0 \quad 0 \quad 0 \quad \dots \quad 0 \quad f_g(t) \}^T \quad (19)$$

Here,

$$c_{00} = \frac{1}{3} s_1 \rho_1 h_1, \quad c_{ee} = \frac{1}{3} (s_e \rho_e h_e + s_{e+1} \rho_{e+1} h_{e+1}), \quad c_{gg} = \frac{1}{3} s_g \rho_g h_g \quad (e = 1 \sim g-1) \quad (20a \sim c)$$

$$c_{e \ e-1} = \frac{1}{6} s_e \rho_e h_e, \quad c_{e-1 \ e} = c_{e \ e-1} \quad (e = 1 \sim g) \quad (21a,b)$$

$$k_{00} = \kappa_1 / h_1, \quad k_{ee} = \kappa_e / h_e + \kappa_{e+1} / h_{e+1}, \quad k_{gg} = \kappa_g / h_g \quad (e = 1 \sim g-1) \quad (22a \sim c)$$

$$k_{e \ e-1} = \kappa_e / h_e, \quad k_{e-1 \ e} = k_{e \ e-1} \quad (e = 1 \sim g) \quad (23a,b)$$

$$f_0(t) = -q_0(t), \quad f_g(t) = -q_g(t) \quad (24a,b)$$

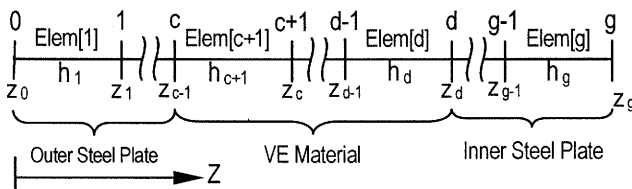


Figure 3 Element division for Long Duration Model

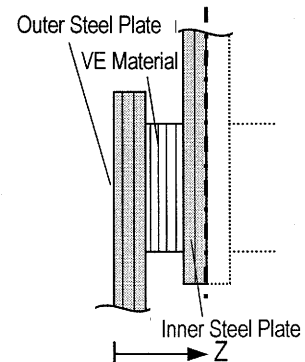


Figure 4 VE damper

3. LONG DURATION TEST AND ANALYSIS RESULTS

3.1 Test Piece Summary and Measurement Method

To understand characteristic of VE damper under the long duration loading and to validate about excellent performance of the long duration model, the long loading experiment of an individual VE damper is carried out. The damper is made of an acrylic polymer VE material (3M Corp., ISD 111). The two VE material laminations are bonded between outer steel plate and inner steel plate. The total area of two VE material laminations is 38.171 cm^2 , and the thickness of one lamination is 1.328 cm . The thickness of one steel plate is 0.476 cm .

Sinusoidal displacement of 0.664 cm peak amplitude $u_{d \max}$ (50% shear strain) and 3.0 seconds period are used in this study. The duration of sinusoidal wave is 3000 seconds (i.e., 1000 cycles). After the excitation, damper temperature decrease is monitored up to 5000 seconds. Ambient temperature is maintained at 24°C for 5000 seconds.

As shown in Figure 5, the temperature of VE damper is measured at the four locations; (A) air side of outer steel plate, (B) 1/4 thickness point of VE material, (C) 1/2 thickness point of VE material, and (D) center of inner steel plate.

The sampling frequency for measuring the damper deformation and damper force are 20 Hz. However, because of the capacity of the measuring instrument, it is impossible to measure for 3000 seconds continuously. Hence, the measurement duration of one time is 60 seconds, and that is repeated 13 times at 240 seconds interval.

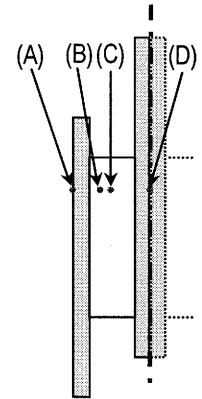


Figure 5
Measurement Points

3.2 Parameter of Long Duration Model

Parameters of the long duration model are indicated in Table 1. The heat transfer factors of the outer steel plate side $\alpha_{c,out}$ and the inner steel plate side $\alpha_{c,in}$ are $0.911 \text{ N / (sec cm } ^\circ\text{C)}$ and $0.613 \text{ N / (sec cm } ^\circ\text{C)}$ respectively. After the motion, convection factor of the inner steel plate side $\alpha_{c,in}$ is reduced to $0.438 \text{ N / (sec cm } ^\circ\text{C)}$ since the plate dose not move.

The analysis using the long duration model is done under the same conditions as experiment. From beginning to 3000 seconds, deformation of the sinusoidal wave whose period is 3.0 seconds and amplitude is 0.664 cm are given. After that, the only heat transfer analysis is done until 5000 seconds. External

temperature of the outer steel plate and the inner steel plate are 24°C always.

Table 1 Parameters of Long Duration Model

VE Material		Steel Plate	
$G \text{ (N/cm}^2\text{)}$	6.5158	$s \rho \text{ (N/cm}^2\text{ } ^\circ\text{C)}$	363.79
α	0.609	$\kappa \text{ (N/sec } ^\circ\text{C)}$	43.128
a_{ref}	0.0115	$\alpha_{c,out} \text{ (N/sec cm } ^\circ\text{C)}$	0.911
b_{ref}	21.157	$\alpha_{c,in} \text{ (N/sec cm } ^\circ\text{C)}$	0.613
$s \rho \text{ (N/cm}^2\text{ } ^\circ\text{C)}$	193.97		0.438
$\theta_{ref} \text{ (} ^\circ\text{C)}$	0.2	$H_s \text{ (Outer)}$	0.476
p_1	19.5	(cm)	(4Elem.)
p_2	80.2	$H_s \text{ (Inner)}$	0.238
$\kappa \text{ (N/sec } ^\circ\text{C)}$	0.188	(cm)	(2Elem.)
$A_d \text{ (cm}^2\text{)}$	38.171	$1 \text{ N / sec cm } ^\circ\text{C} = 100 \text{ W / m}^2\text{ } ^\circ\text{C}$	
$H_d \text{ (cm)}$	1.328 (12 Elem.)		

3.3 Comparison between Test Results and Analysis Results

Figure 6 shows that the time history of temperature at the each measurement point (See Figure 5) with the experimental and analytical results. The temperature distributions inside the VE damper obtained from experiment and analysis are shown in Figure 7. From test results in Figure 6 and 7, it is recognized that the change of temperature is different depending upon the position of the damper. Figure 6 shows that temperature rise becomes sluggish and temperature is constant at each measurement points after 1000 seconds. In case of under the long duration loading such as this study, as effect of the heat conduction to the steel plates, temperature of VE damper becomes the steady state at a certain time, and temperature does not continue to rise even if the VE damper have been vibrating.

After 3000 seconds when the vibration finished, temperature of each point rapidly decreases until 24 °C because the internal heat generation inside the VE materials stops.

Good agreements of temperature rise and distribution between test and analysis are shown in Figure 6 and 7, respectively.

Figure 8 shows the distribution of strain obtained from the analysis at a certain time when the peak strain of VE material at the center point occurs. The distortion strain at 0.75 seconds immediately after the starting almost is 50% at all positions of VE material. However, when analytical step have elapsed, the strain on this point increase because the temperature on this point increase (See Figure 7). So, the distributions inside the VE material under the long duration loading become uneven as shown in Figure 8.

Figure 9 shows the comparison of temperature rise between the results obtained from using the short duration model and using the long duration model. Since the short duration model is not considered the heat conduction and transfer, the temperature obtained from using the short duration model continues to increase when the duration time is long. Even if after the loading stops, the temperature of the short duration model not decreases like the long duration model.

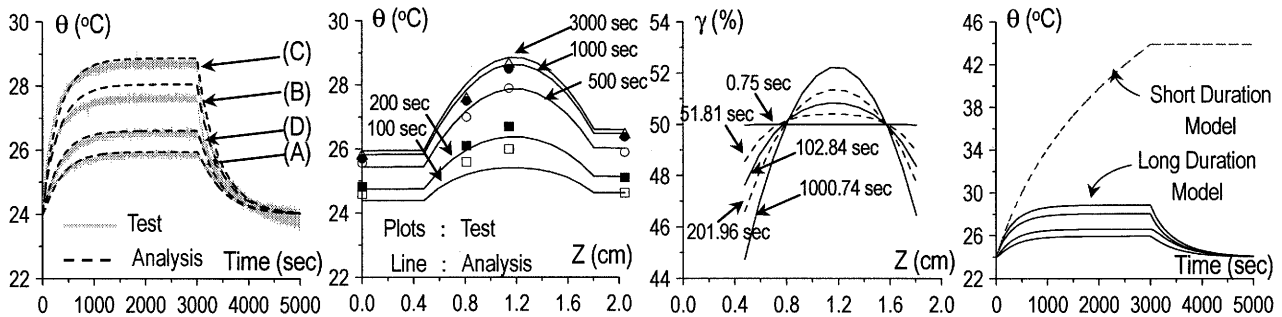


Figure 6 Temperature Time History Figure 7 Temperature Distribution Figure 8 Strain Distribution Figure 9 Temperature Time History

Figure 10 (a) shows the hysteresis obtained from the test result, and Figure 10 (b) and (c) express obtained from the analysis using the long duration model and the short duration model, respectively. Obviously, Figure 10 (b) shows good agreement with Figure 10 (a), but not Figure 10 (c) erroneously significant material softening due to the overestimated temperature (see Figure 9).

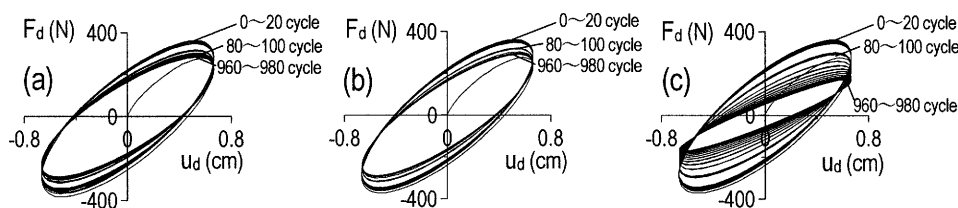


Figure 10 Comparison of Hysteresis Loop:
(a) Test, (b) Long Duration Model, and (c) Short Duration Model

4. THREE - DIMENSIONAL FINITE ELEMENT ANALYSIS OF VE DAMPER

4.1 Object of Three-Dimensional Finite Element Method Analysis and Analytical Technique

Because of convenience, the long duration model proposed in this study is done heat transfer analysis as one-dimensional problem of thickness direction. Object of this chapter is to examine one-dimensional problem, which is assumed in chapter 2, by comparing with results of the three-dimensional finite element method (3D-FEM) analysis.

3D-FEM done in this study is carried out alternately static analysis and heat transfer analysis without dynamic analysis. So, the variation of temperature and stiffness of VE damper having the

temperature dependency are simulated. This method is expressed as follows.

Firstly, initial temperature of VE damper is set. The Young's modulus of VE material E'_j is calculated from Eq. (25). Then G'_j in Eq. (26) is expressed by Eq. (26) (Kasai et al. 2001). Where, ν = Poisson's ratio.

$$E'_j = 2G'_j(1+\nu) \quad , \quad G'_j = G \frac{1+a_j b_j \omega^{2\alpha} + (a_j + b_j) \omega^\alpha \cos(\alpha\pi/2)}{1+a_j^2 \omega^{2\alpha} + 2a_j \omega^\alpha \cos(\alpha\pi/2)} \quad (25),(26)$$

As next step, the inner steel plate is moved the damper maximum deformation $u_{d \max}$, and static analysis is carried out

The dissipation energy $W_{d,j}$, which is dissipated by the element j of VE material in one cycle of steady state, is calculated from Eq. (27). In Eq. (28), η_j is expressed by Eq. (28). Where $W_{s,j}$ = strain energy of element j obtained from the static analysis results.

$$W_{d,j} = 2\pi\eta_j W_{s,j} \quad , \quad \eta_j = \frac{(-a_j + b_j) \omega^\alpha \sin(\alpha\pi/2)}{1+a_j b_j \omega^{2\alpha} + (a_j + b_j) \omega^\alpha \cos(\alpha\pi/2)} \quad (27),(28)$$

The heat generated per unit volume \dot{Q}_j is expressed by Eq. (29)

$$\dot{Q}_j = W_{d,j} / (T \cdot V_j) \quad (29)$$

Where, T = period of 1 cycle, V_j = volume of element j . The unsteady state heat transfer analysis is done for T seconds using the heat generated per unit volume in Eq. (28). After that, the Yong's modulus of each point is updated using temperature obtained from the heat transfer analysis results (Eq. (25)), and static analysis is done again.

The above process is repeated to simulate the temperature distribution inside the VE damper and the decrease of stiffness of VE material.

4.2 Three Dimensional Analytical Model

The 3D-FEM model is shown in Figure 11. This model is symmetric with on the center of inner plate, therefore in this study, 3D-FEM is carried out by using half of this model. Three dimensional coupled temperature – displacement elements (ABAQUS Ver. 6.4) are utilized in this model. The parameters for 3D-FEM are indicated in Table 2. The heat transfer factor of inner side of VE material and steel plate are $30 \text{ W} / \text{m}^2 \text{ } ^\circ\text{C}$, and outer side of VE and steel are $30 \text{ W} / \text{m}^2 \text{ } ^\circ\text{C}$. Because of the three dimensional effect, the heat transfer of 3D-FEM model become lower than the long duration model.

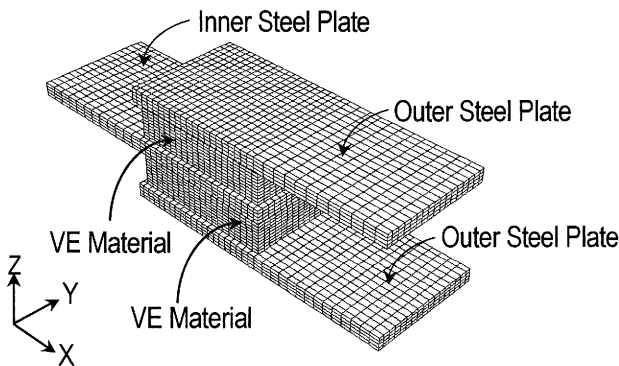


Figure 11 Three Dimensional FEM Model

Table 2 Parameters of 3D-FEM Model

VE Material		Steel Plate	
κ (W/m $^\circ\text{C}$)	0.188	κ (W/m $^\circ\text{C}$)	43.128
s (J/kg $^\circ\text{C}$)	1939.7	s (J/kg $^\circ\text{C}$)	466.3
ρ (kg/m ³)	1000	ρ (kg/m ³)	7801
$\alpha_{c,out}$ (W/m ² $^\circ\text{C}$)	20	$\alpha_{c,out}$ (W/m ² $^\circ\text{C}$)	20
$\alpha_{c,in}$ (W/m ² $^\circ\text{C}$)	30	$\alpha_{c,in}$ (W/m ² $^\circ\text{C}$)	30
ν	0.47	ν	0.3
		E (N/m ²)	2.05×10^{11}

4.3 Results of Three Dimensional Finite Element Method Analysis

The 3D-FEM analysis is carried out until 3000 seconds. The comparison between test results and 3D-FEM analysis results are shown in Figure 12 (a) temperature, (b) storage stiffness K'_d . FEM analysis results good agree with results of tests, so this method can express accurately temperature distribution inside the VE damper and the change of the stiffness of VE material.

The temperature distributions of VE damper obtained by 3D-FEM are shown in Figure 13 (a) ~ (c). The distribution of Z - axis have different temperature on each point, however, the temperature of X - axis and Y - axis are uniform distribution excluding the extremely portion of the surface. So, it is recognized that the assumption under the long duration model which temperature distribution inside the VE damper can be express by using one - dimensional problem.

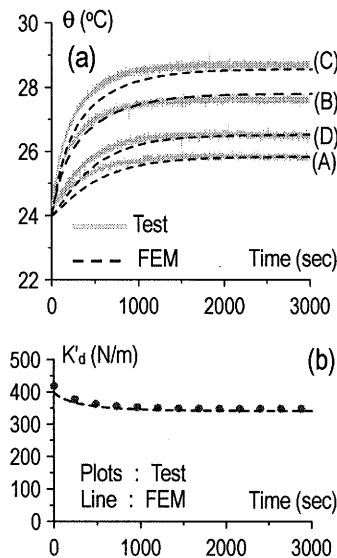


Figure 12 Comparison with Test and FEM:

(a) Temperature, and (b) K'_d

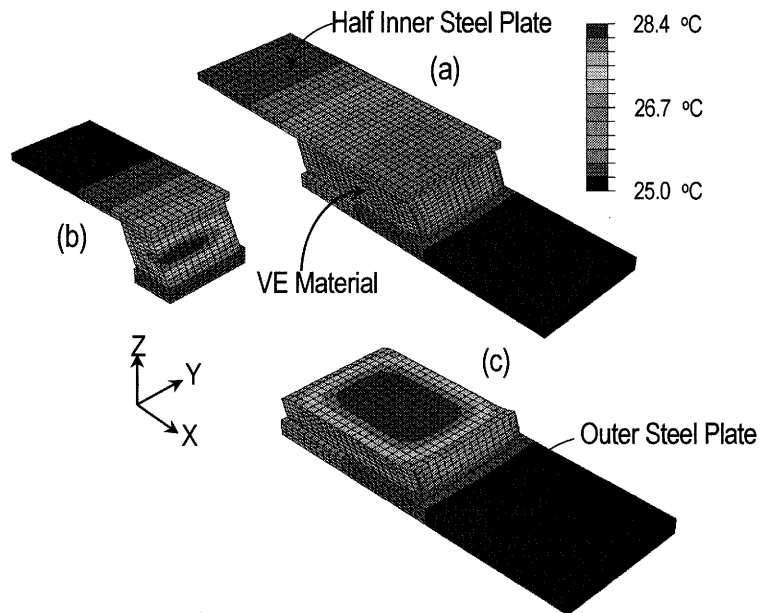


Figure 13 Results of 3D-FEM Analysis at 3000 seconds:
(a) Half VE damper, (b) Section of Measurement Points, and
(c) Section Point (C)

5. CONCLUSIONS

This paper has proposed a non-linear hysteresis model of VE damper considering heat conduction and heat transfer. In addition, the three dimensional finite element method analysis is carried out to validate about the assumption for the long duration model. This model may be used for design of the VE damper and / or the building having VE damper under the long period earthquake or wind force.

References:

- Mahmoodi, P. (1969), "Structural Dampers", *Journal of the Structural Division*, ASCE, Vol.95, No.ST8, pp.1661-1672
- Nielsen, F. J., Lai, M. L., and Maison, B. F. (1994), "Viscoelastic Damper Overview for Seismic and Wind Applications", *Proc. First World Conf. on Structural Control*, Vol.3, pp.FP/42-51
- Kasai, K., Munshi, J.A., Lai, M.-L., and Maison, B.F. (1993), "Viscoelastic Damper Hysteresis Model", *Theory, Experiment, and Application ATC17-1 Seminar*, Applied Technology Council, Vol.1.2, pp.521-532, Mar.
- Shen, K. L. and Soong, T.T. (1995), "Modeling of Viscoelastic Damper for Structural Applications", *ASCE Journal of Engineering Mechanics*, 121(6), pp.694-701
- Huang, Y., Wada, A., Iwata, A., Takeuchi, T., Okuma, K. (2001), "The Dynamic Mechanical Model of Viscoelastic Dampers Relying on the Frequency and Temperature", *Journal of Structural Engineering (Transactions of AIJ)*, Architectural Institute of Japan, No. 516, pp.91-98, Feb. (in Japanese)
- Kasai, K., Teramoto, M., Okuma, K., and Tokoro, K. (2001), "Constitutive Rule for Viscoelastic Materials Considering Temperature and Frequency Sensitivity (Part1: Linear Model with Temperature and Frequency Sensitivities)", *Journal of Structural and Construction Engineering (Transactions of AIJ)*, No. 543, pp. 77-86, May. (in Japanese)
- Kasai, K. and Tokoro, K. (2002), "Constitutive Rule for Viscoelastic Materials Considering Temperature and Frequency Sensitivity (Part2: Nonlinear Model Based on with Temperature-Rise, Strain, and Strain-Rate)", *Journal of Structural and Construction Engineering (Transactions of AIJ)*, No. 561, pp. 55-63, Nov. (in Japanese)
- Kasai, K., Ooki, Y., Amemiya, K., and Kimura, K. (2003), "A Constitutive Rule for Viscoelastic Materials Combining Iso- Butyrene and Styrene Polymers", *Journal of Structural and Construction Engineering (Transactions of AIJ)*, No. 569, pp. 47-54, Jul. (in Japanese)

SEISMIC PERFORMANCE OF REINFORCED CONCRETE BRIDGE COLUMNS UNDER BILATERAL EXCITATION

H. Ogimoto¹⁾, K. Kawashima²⁾, G. Watanabe³⁾, and S. Nagata¹⁾

1) Graduate Student, Department of Civil Engineering, Tokyo Institute of Technology, Japan

2) Professor, Department of Civil Engineering, Tokyo Institute of Technology, Japan

3) Research Associate, Department of Civil Engineering, Tokyo Institute of Technology, Japan
ogimoto@cv.titech.ac.jp, kawasima@cv.titech.ac.jp, gappo@cv.titech.ac.jp, nseiji@cv.titech.ac.jp

Abstract: This paper presents the effect of bilateral excitation on the seismic performance of reinforced concrete bridge columns based on a hybrid loading test. The loading test was conducted on 1350mm tall reinforced concrete columns with a cross section of 400 mm x 400 mm. Two ground motions were used and both unilateral and bilateral excitations were imposed to the columns. A fiber element analysis was conducted to correlate the experimental results. This paper presents an importance of considering bilateral excitation in the evaluation of flexural strength and ductility capacity of reinforced concrete columns..

1. INTRODUCTION

Although bridges are subjected to bilateral excitation, they are currently designed independently in the longitudinal and transverse directions. Combination of bilateral seismic effect has been sometimes considered, but it is limited in the elastic design. There is limited knowledge on how the plastic deformation of columns should be combined under the bilateral excitation.

Although various researches have been conducted for the bilateral excitation effects on columns and beam-column joints, most of them were for building columns. Because the elastic design had been used in bridges until recently, few studies have been conducted to bridge columns. However the bilateral excitation effect is more important in bridges than buildings since nonlinear response of bridges which have lesser degree of static indeterminate critically depends on the hysteretic behavior of the columns.

This paper presents a hybrid loading test and numerical correlation by the fiber element analysis on the effect of bilateral excitation on the seismic performance of rectangular reinforced concrete bridge columns.

2. EXPERIMENTAL NODEL AND TEST SETUP

A hybrid loading tests was conducted on four cantilevered reinforced concrete bridge columns shown in Figure 1. They had the same properties with the ones used for cyclic loading tests under unilateral and bilateral direction (Hayakawa et al 2004). They were designed and constructed based on the Japanese Design Specifications of Highway Bridges (Japan Road Association, 1996) assuming that the specimens were small prototype columns. They had a 400 mm x 400 mm square cross section with an effective height from the bottom to the loading point of 1350 mm. Sixteen 13 mm diameter

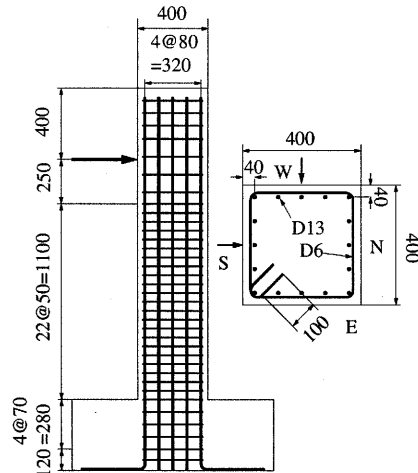


Figure 1 Test Specimen

Table 1 Test Cases and Concrete Strengths

Test Cases	Unilateral Loadings		Bilateral Loadings	
	40% Kobe	50% Sylmar	40% Kobe	50% Sylmar
Compression Strengths (MPa)	27.2	31.2	26.9	34.2

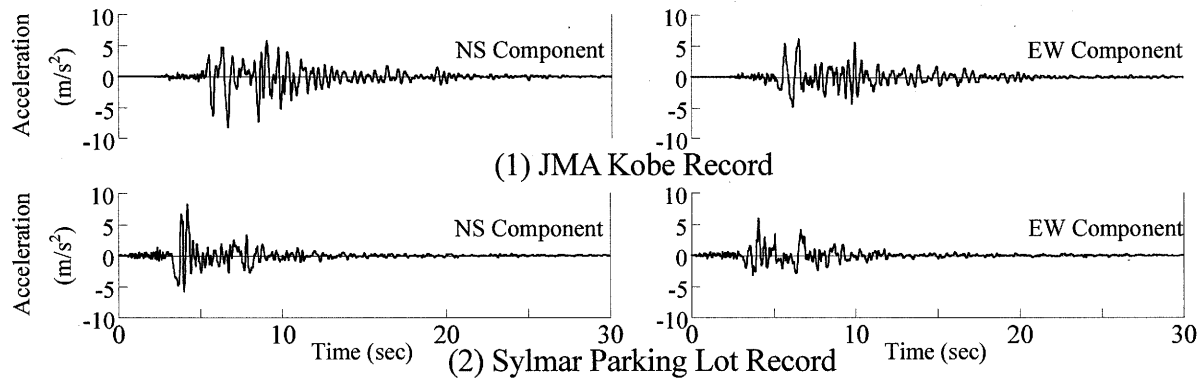


Figure 2 Ground Motions

deformed bars (D13, SD295A) were provided for longitudinal reinforcements. The nominal strength of the bar is 357 MPa. Longitudinal reinforcement ratio was 1.27%. Deformed bars with a 6 mm diameter (D6, SD295A) were provided at every 50 mm interval for tie reinforcements. The volumetric tie reinforcement ratio was 0.79%. The concrete strengths were 26.9-34.2 MPa as shown in Table 1.

The tests were conducted at the Earthquake Engineering Facility in Tokyo Institute of Technology. Unilateral and bilateral excitations were imposed to the columns under a constant vertical load of 160 kN which was equivalent to the design lateral force. The vertical load of 160 kN results in 1 MPa compression in the column, which is generally the case in Japanese RC bridge columns.

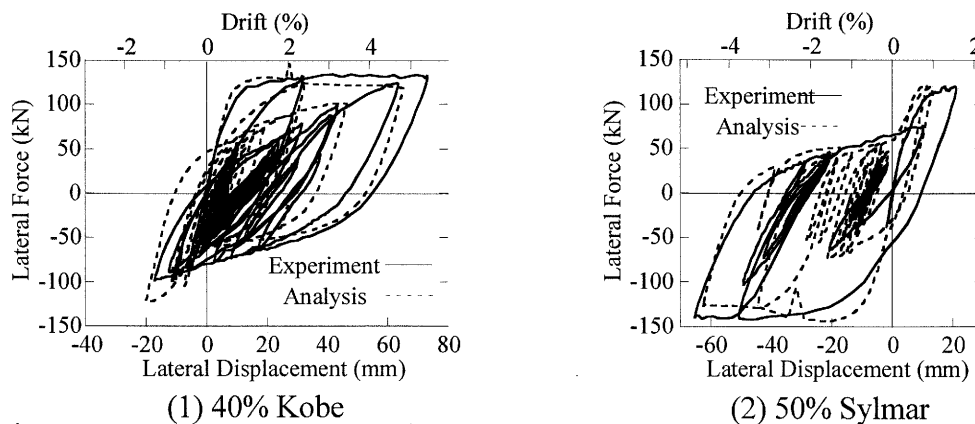
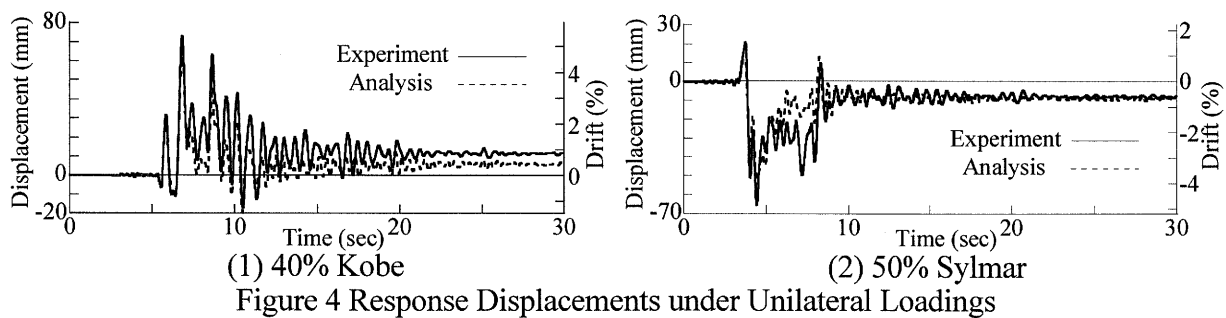
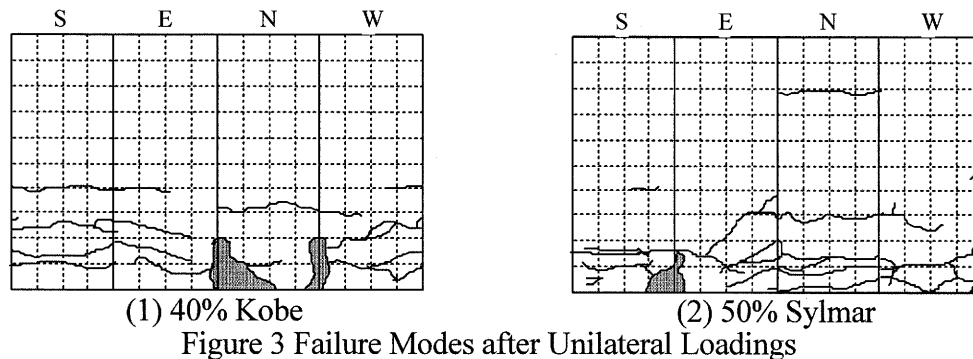
The ground motions recorded at JMA Kobe Observatory during 1995 Kobe, Japan earthquake and Sylmar Parking Lots during 1994 Northridge, USA earthquake, as shown Figure 2, were used. The lateral mass of the deck was assumed as 500 kN in the hybrid loading test so that the natural period of the column-deck system is in the range of about 0.5 sec. Since the deck mass assumed (500 kN) was about 3 times larger than the design lateral force (160 kN), the intensity of Kobe record was reduced to 40% of the original and the intensity of Sylmar record was reduced to 50% of the original. They are called hereinafter “40% Kobe record,” and “50% Sylmar record,” respectively. NS and EW components were applied to the columns in the longitudinal (NS) and transverse (EW) directions, respectively, in the bilateral loading, while NS component was applied to the columns in the longitudinal direction (NS) in the unilateral loading. A numerical integration scheme which avoids displacement overshooting using a displacement reduction factor was employed in the hybrid loading test (Shing et al., 1991). Damping ratio of 2% of critical was assumed in the numerical integration of

the equations of motion. The time increment for numerical integration was 0.01 sec. The loading velocity was about 1 mm/s.

3. EXPERIMENTAL PERFORMANCE OF THE COLUMNS

3.1 Unilateral Loading

Figure 3 shows the failure modes after the unilateral loading. The column suffered large flexural cracks and spalling-off covering concrete at the corner of E and N-surfaces under the 40% Kobe record and S and E-surfaces under the 50% Sylmar record. Figures 4 and 5 show the response displacements and lateral force vs. lateral displacement hysteresses at the loading point, respectively. The analytical results which will be described later are also presented here for comparison. The lateral drift of 5.4% was developed in the positive direction (N-side) under the 40% Kobe record. The flexural strength is 135.0 kN in the positive direction and 97.9 kN in the negative direction. On the other hand, the response displacement biased in the negative direction (S-side) under the 50% Sylmar record. The flexural strength in this side was 141.6 kN.



3.2 Bilateral Loading

Figure 6 shows the failure modes of the columns after bilateral loading. The damage under the bilateral excitation was more extensive than that under the unilateral loading. Not only the covering concrete but also a part of core concrete suffered damage at the corner of S and E-surfaces under the 50% Kobe ground motion. Local buckling of longitudinal bars occurred at this corner as well.

Figures 7 and 8 show the response displacements and the lateral force vs. lateral displacement hysteresses subjected to bilateral loadings, respectively. It is important to note that the peak lateral drift in the NS direction was 6.3% and 5.5% under 40% Kobe and 50% Sylmar bilateral loadings, respectively, which are 16.5% and 13.8% larger than those under the unilateral loadings. The peak drift in the EW component was 4.2% in the positive side (E-side) under 40% Kobe record and 5.0% in the negative side (W-side) under 50% Sylmar record.

The flexural strength in the NS direction was 118.6 kN and 123.7 kN under bilateral loading by Kobe and Sylmar records, respectively, which are 12.1% and 12.6% smaller than those under unilateral loadings. The flexural strength in the EW direction is 109.0 kN and 125.6 kN under Kobe and Sylmar records, respectively.

The residual drift was 0.42% in the NS direction and 0.33% in the EW direction under 40% Kobe record. On the other hand, it is -2.1% in the NS direction and -1.7% in the EW direction under 50% Sylmar record. The residual drift significantly depends on the ground motions.

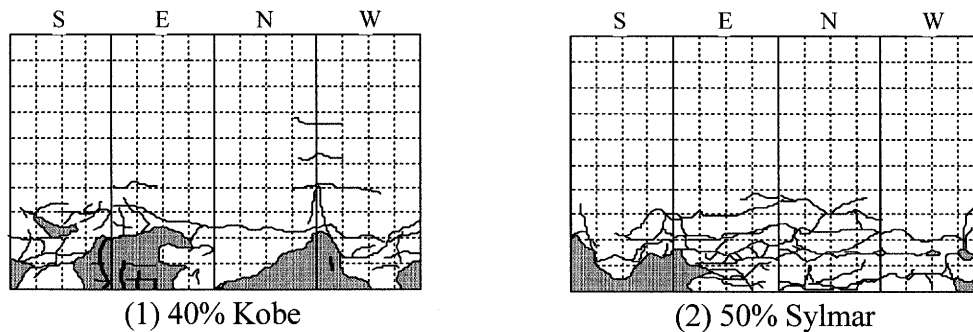


Figure 6 Failure Modes after Bilateral Loadings

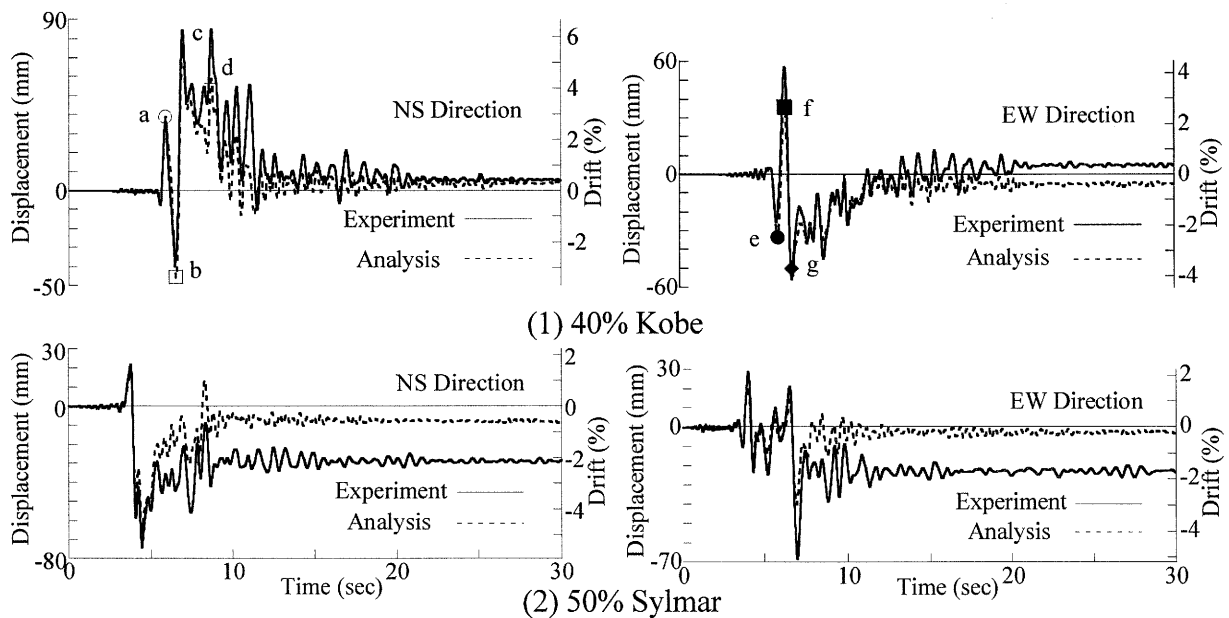


Figure 7 Response Displacements under Bilateral Loadings

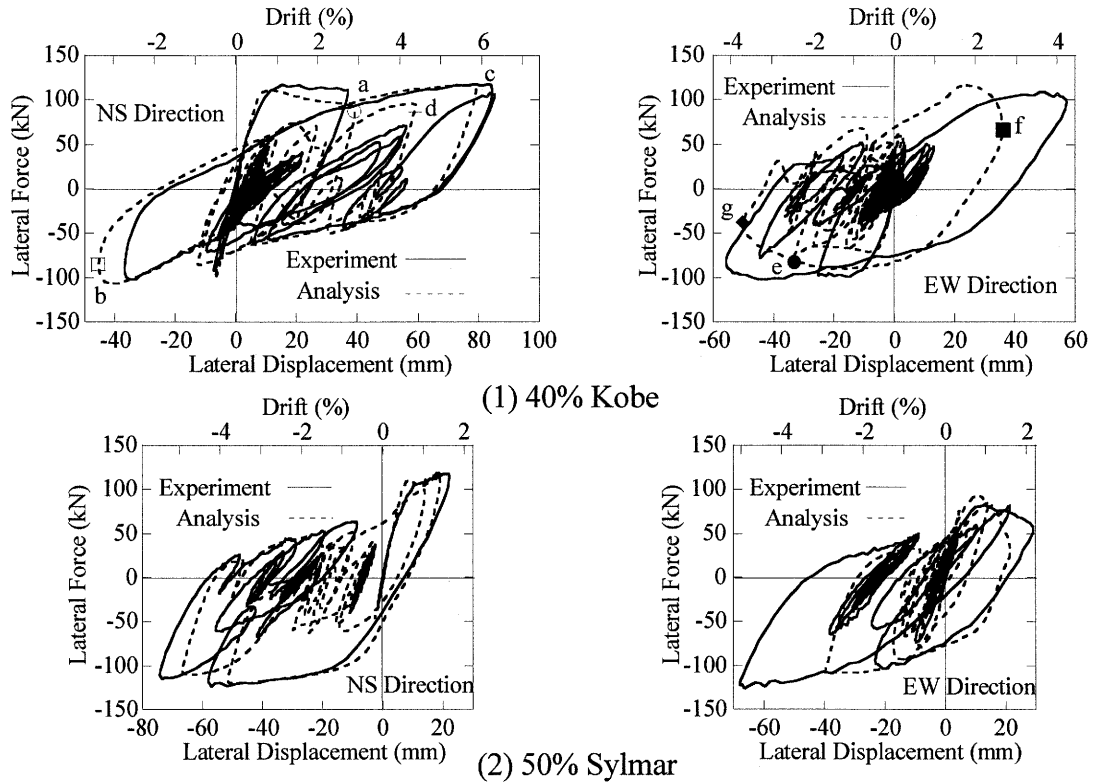


Figure 8 Lateral Force vs. Lateral Displacement Hystereses under Unilateral Loadings

4. FIBER ELEMENT ANALYSIS

4.1 Analytical Model

The columns were idealized as shown in Figure 9. The plastic hinge region was idealized by a fiber element. Deformation of the longitudinal bars in the footing contributes to the lateral displacement at the loading point. This effect was represented by a rotational spring at the bottom of the column. The stress vs. strain relation of the concrete was idealized by considering the lateral confinement (Hoshikuma et al, 1997). Unloading and reloading hystereses were idealized by Sakai and Kawashima model (Sakai and Kawashima, 2000). Menegotto-Pinto model (Menegotto and Pinto, 1973) was used to idealize the stress vs. strain hysteresis of longitudinal bars.

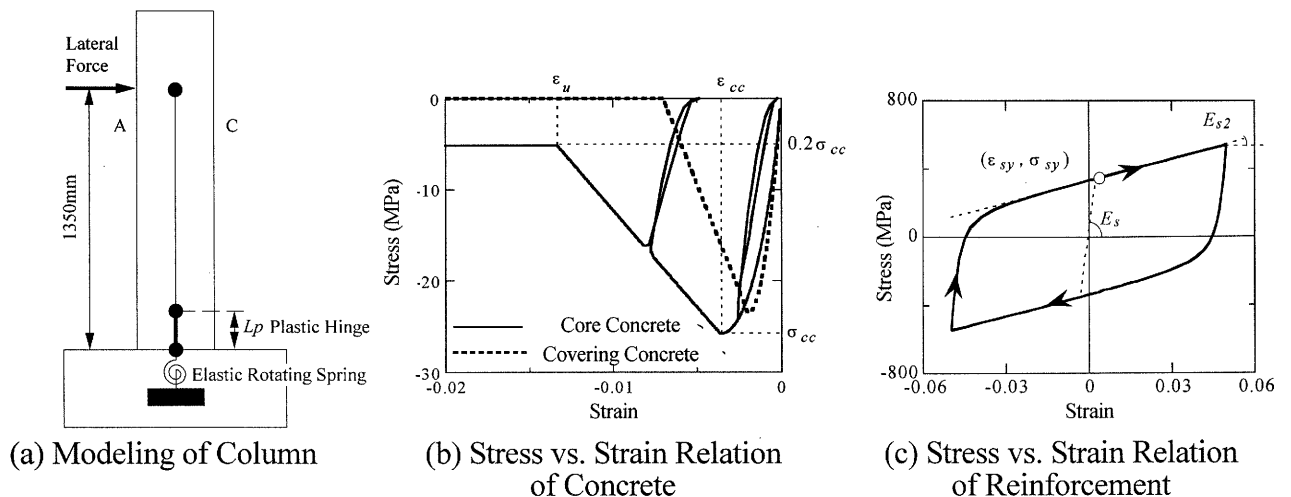


Figure 9 Analytical Model

4.2 Analytical Correlations

Analytical responses under the 40% Kobe and the 50% Sylmar unilateral excitations are presented in Figures 4 and 5. The computed response and hysteresis are close to the experimental results. In particular, the agreement of the analysis to experiment is satisfactory until the response started to decay after the peak.

The computed response displacements and lateral force vs. lateral displacement hysteresses are shown in Figures 7 and 8 for 40% Kobe and 50% Sylmar bilateral excitations. The response with larger displacement amplitude is well represented by analysis. However, the residual drift which becomes predominant after the peak response is underestimated in analysis. Because the residual drift is very sensitive to the post-peak stiffness (Kawashima et al 1998) and failure mode of the structures, the underestimation by analysis may be attributed to insufficient idealization of the fiber element on those issues. It is needed to accumulate more experience for the correlation on the hysteresis behavior with predominant residual drifts.

4.3 Stress vs Strain Relation by Fiber Element Analysis

Figures 10 and 11 show the computed stress vs. strain relations of core concrete and longitudinal bars, respectively, under 40% Kobe bilateral excitation. Because measured data on the stress vs. strain hysteresses of concrete and bars are not available in experiment, direct comparison of the computed relation with the test result cannot be presented. However the computed hysteresses provide useful information on the failure mechanism of the columns.

To correlate the stress vs. strain hysteresis with the displacement responses in Figure 7, notations from “a” to “g” are shown in Figures 7, 8, 10 and 11. At 5.87 sec (point “a”), the column displacement takes the first peak in the positive direction (N-side, refer to Figure 1). At this time, the stress at the center of core concrete on the N-surface has already exceeded the strength of concrete σ_{cc} and deteriorated to 5.77 MPa (10,500 μ in compression), which is 20% σ_{cc} . Because the core concrete at the other side (S-surface) is subjected to tension, stress is zero with a strain of 32,800 μ in tension. On the other hand, bars at the center on N-surface and S-surface experienced 10,000 μ in compression and 34,900 μ in tension, respectively. If we compare those strains with the ones under unilateral excitation shown in Figures 12 and 13, the strain of core concrete and bars under bilateral excitation is

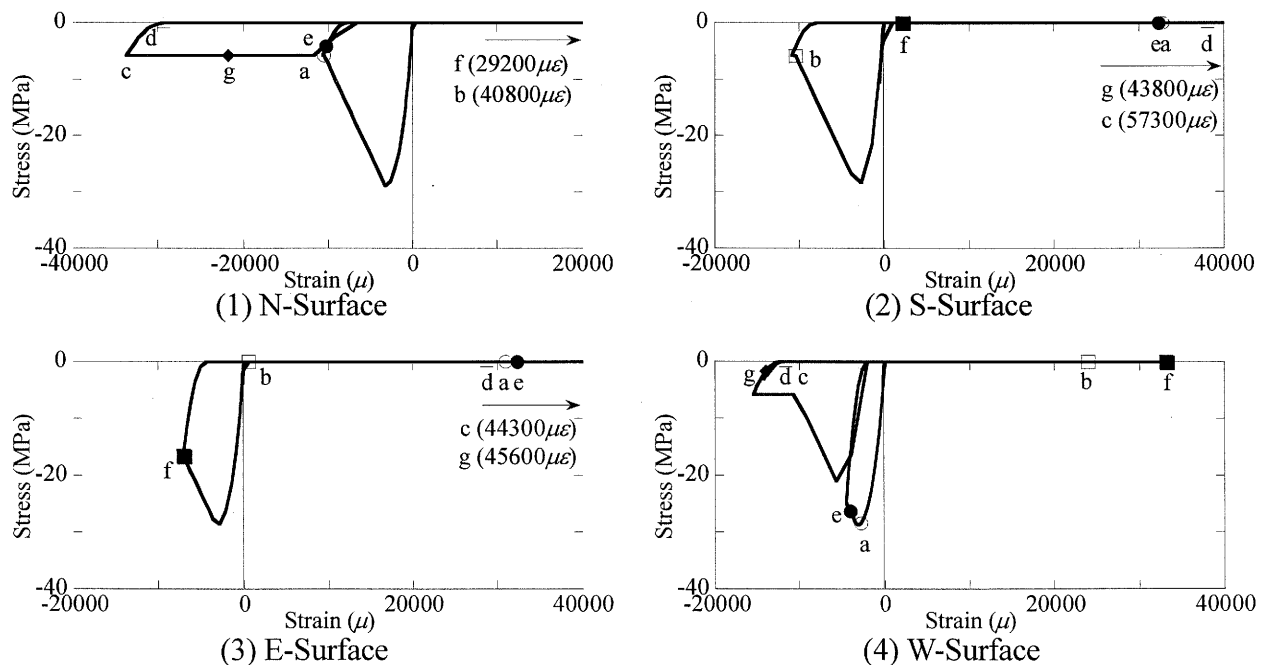


Figure 10 Stress vs. Strain Hystereses of Core Concrete under 40% Kobe Bilateral Loading

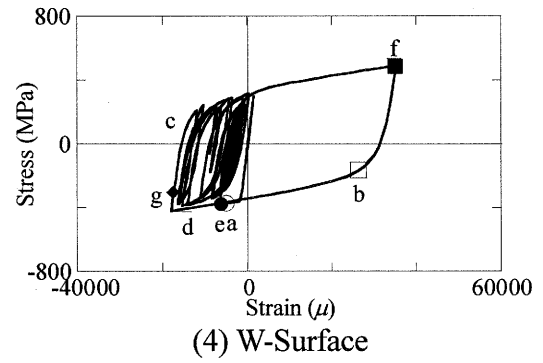
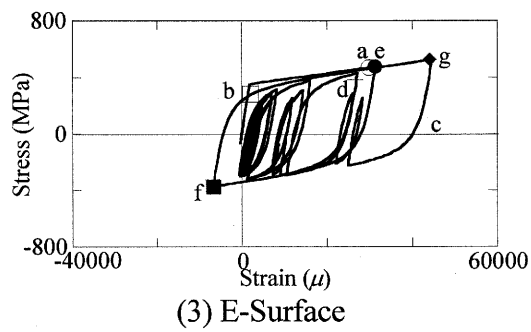
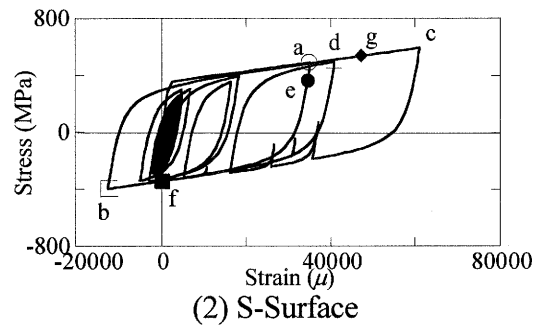
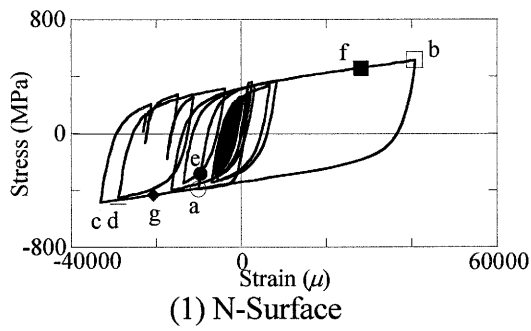


Figure 11 Stress vs. Strain Hystereses of Longitudinal Bars under 40% Kobe Bilateral Loading

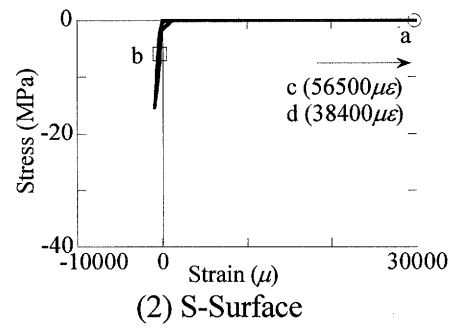
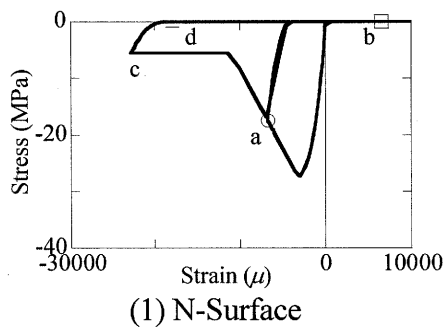


Figure 12 Stress vs. Strain Hystereses of Core Concrete under 40% Kobe Unilateral Loading

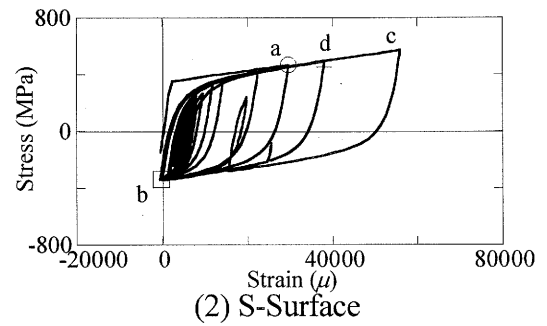
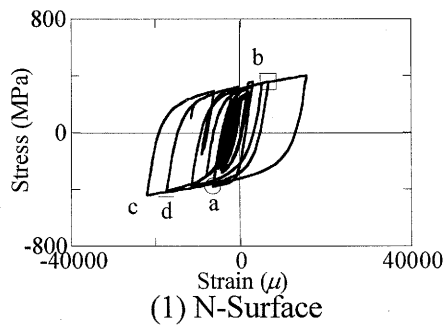


Figure 13 Stress vs. Strain Hystereses of Longitudinal Bars under 40% Kobe Unilateral Loading

54.4% and 53.8% larger than the respective strain under the unilateral excitation. This is consistent with the test results that the column deteriorated earlier under the bilateral excitation than the unilateral excitation.

In the same way, at the maximum response “c” (6.91 sec), strain of core concrete is $33,600 \mu$ in compression on N-surface and $57,300 \mu$ in tension on S-surface, and strains of longitudinal bars is $33,200 \mu$ in compression on N-surface and $61,000 \mu$ in tension on S-surface. In comparison with the strains under unilateral loading, the strain of core concrete on N surface and S-surface is 47.4% and 1.4% larger, respectively, and the strain of longitudinal bars on N-surface and S-surface is 48.9% and 9.1% larger, respectively.

5. CONCLUSIONS

To clarify the seismic performance of reinforced concrete single columns under bilateral excitation, a hybrid loading test and a fiber element analysis were conducted. Based on the results presented herein, the following conclusions may be deduced:

- 1) The bilateral excitation results in more extensive damage on the columns than unilateral excitation. The flexural strength under bilateral excitation is smaller than that under the unilateral excitation.
- 2) Deterioration of the flexural strength under the bilateral excitation results in larger deck displacements. Residual drifts after the excitation are also larger under the bilateral excitation.
- 3) The fiber element analysis provides a good correlation to the experimental response and hysteresis. However further improvement is required for the underestimation of response displacements where the displacement started to deteriorates.

Acknowledgements:

The authors express their sincere appreciation to Dr. Yabe, M., Chodai Consultants, for design of the model column. Extensive support was provided by Messrs. Nakamura, G., Fukuda, T., Ichikawa, Y., Miyaji, K. and Kijima, K. for constructing test specimens and conducting the tests.

References:

- Hayakawa, R., Kawashima, K. and Watanabe, G. (2004), “Effect of Bilateral Excitation on the Flexural Strength and Ductility Capacity of Reinforced Concrete Bridge Columns,” *Journal of Structural Mechanics and Earthquake Engineering*, Japan Society of Civil Engineers, 759/I-67, 79-98.
- Japan Road Association (1996), “Part V Seismic Design, Design Specifications of Highway Bridges,” Maruzen, Tokyo, Japan
- Shing, P. B., Vannan, M.T. and Cater, E. (1991), “Implicit Time Integration for Pseudodynamic Tests,” *Earthquake Engineering and Structural Dynamics*, Vol. 20, 551-576.
- Hoshikuma, J., Kawashima, K., Nagaya, K. and Taylor, A. W. (1997), “Stress-strain model for confined reinforced concrete in bridge piers,” *Journal of Structural Engineering*, American Society of Civil Engineers, 123(5), 624-633.
- Sakai, J., Kawashima, K. and Shoji, G. (2000), “A Stress-Strain Model for Unloading and Reloading of Concrete Confined by Tie Reinforcement,” *Journal of Structural Mechanics and Earthquake Engineering*, Japan Society of Civil Engineers, 654/I-52, 297-316.
- Menegotto, M. and Pinto, P.E. (1973), “Method of Analysis for Cyclically Loaded R.C. Plane Frames Force and Bending,” *Proc. of IABSE Symposium on Resistance and Ultimate Deformability of Structures Acted on by Well Defined Repeated Loads*, 15-22.
- Kawashima, K., MacRae, G.A., Hoshikuma, J. and Nagaya, K. (1998), “Residual Displacement Response Spectrum,” *Journal of Structural Engineering*, ASCE, 124(5), 523-530

SEISMIC PERFORMANCE EVALUATION OF BEAM-TO-COLUMN CONNECTIONS WITH FATIGUE RETROFITTING

A. Tanabe¹⁾, C. Miki²⁾, and E. Sasaki³⁾

1) Student, Department of Civil Engineering, Tokyo Institute of Technology, Japan

2) Professor, Department of Civil Engineering, Tokyo Institute of Technology, Japan

3) Assistant, Department of Civil Engineering, Tokyo Institute of Technology, Japan
tanabe@cv.titech.ac.jp, miki@cv.titech.ac.jp, esasaki@cv.titech.ac.jp

Abstract: Recently, many fatigue cracks were found at the beam-to-column connection of steel bridge bents. The evaluation of these fatigue cracks has been carried out, and some fatigue retrofitting methods were proposed: rib-installation, large-coring, etc. The effectiveness of these method were already examined, however, the effects for the seismic performance were not clear. On the other hand, the beam-to-column connection parts of actual frame piers were designed as thicker plate thickness region due to shear-lag stress. Therefore, there is high possibility of that the beam-to-column connections have enough seismic resistance, even if the gross section were reduced by modifications for fatigue retrofitting. This study aims to evaluate the effects of rib-installation and large-coring as fatigue retrofitting methods for the seismic performances. The seismic performances were evaluated by dynamic response analyses of actual pier models with/without fatigue retrofitting and cyclic loading tests of fatigue retrofitted beam-to-column connections. As a result, it was showed that fatigue retrofitted beam-to-column connections had enough seismic performance.

1. INTRODUCTION

In 2000, many fatigue cracks were found in the beam-to-column connection of the steel bridge bents of metropolitan express way bridges. These fatigue cracks were severe damage among the fatigue cracks which already reported (Fisher 1984). These fatigue cracks may cause bridge failure in both service conditions and earthquakes. Therefore, fatigue performance of beam-to-column connections were evaluated by fatigue test (Miki et al. 2002), and it was showed that the main causes of fatigue cracks were large defects in weld joints (Miki et al. 2003), which was named as “Delta-zone”, and high stress concentration at the corner of beam-to-column connection. From these reason, large-coring (Ono et al. 2004, Konishi et al. 2004), which is shown in Figure 1, and rib-installation (Tanabe et al. 2004), which is shown in Figure 2, were proposed to remove the delta-zones and to reduce the stress concentration respectively. The effectiveness of these methods for fatigue was already examined. However, the effects on the seismic performance of frame piers have not been made clear.

Figure 3 shows the distribution of the plate thickness of actual frame piers. By conventional design codes, the beam-to-column connection of steel bridge frame piers were designed as the thicker plate parts because of the high stresses due to shear-lag effects (Okumura and Ishizawa 1968). This fact indicates that beam-to-column connections may have higher seismic resistance than general member. The dynamic response analyses of some actual frame piers showed that

seismic damage occurred at the out of beam-to-column connections (Sasaki et al. 2004). This result means that the applied moment was limited up to the plastic moment of the general section. Therefore, beam-to-column connections may have higher moment resistance, even if the net section was reduced by the modification for fatigue retrofitting.

In this study, the seismic response of fatigue retrofitted frame piers is examined by FEM analyses, and then it is evaluated by cyclic loading test that the seismic resistance of fatigue retrofitted beam-to-column connections. The types of fatigue retrofitting method are considered as a main parameter; large-coring, rib-installation and both methods are considered.

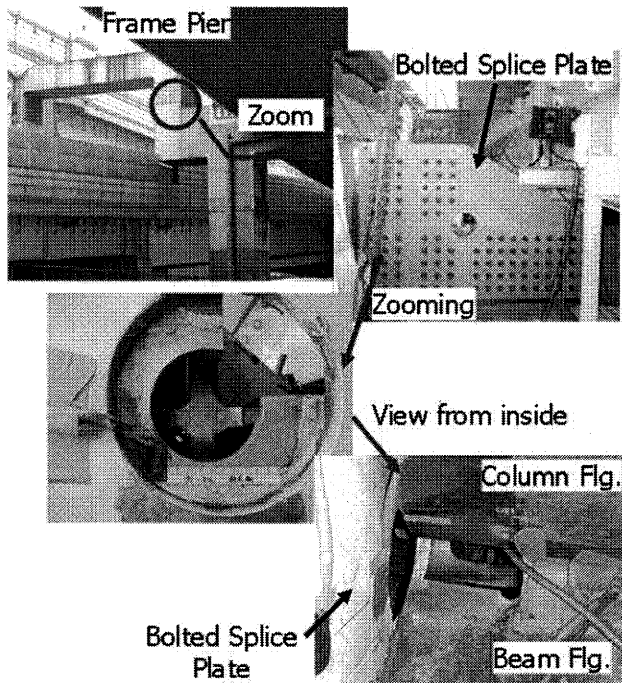


Figure 1 Large Coring

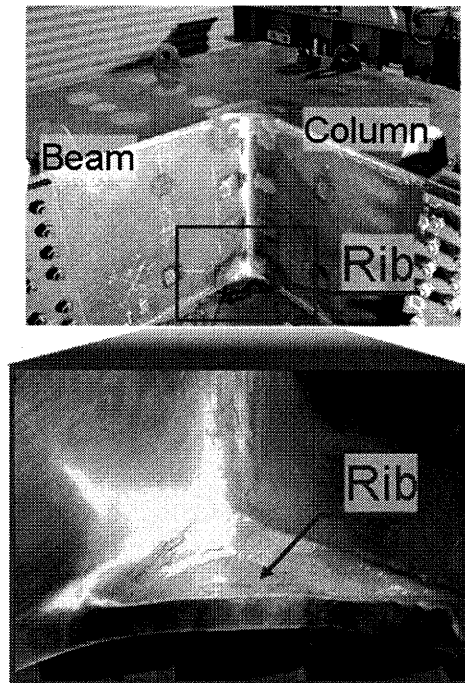


Figure 2 Rib-installation

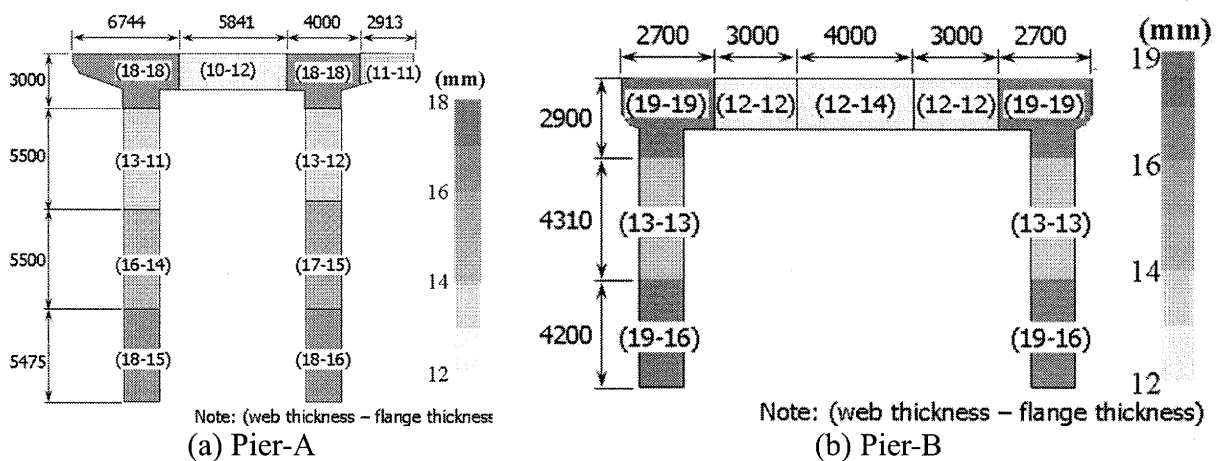


Figure 3 Plate Thickness Distribution of Actual Frame Piers

2. DYNAMIC RESPONSE ANALYSES OF FATIGUE RETROFITTED PIERS

In order to determine the effects of fatigue retrofitting for seismic response of frame piers, dynamic response analyses of frame piers with several fatigue retrofitting methods were carried out.

2.1 Analysis Cases and Conditions

Analysis cases were shown in Table 1. Figure 3 shows two target frame piers. Each target pier was selected as a common shape with the different aspect ratio of column height and beam length. In this paper, we mainly mention about Pier-A.

Target piers were modeled by shell element only. Mirror condition was used because the highway bridges have little deformation in longitudinal direction. The finite element model of each pier is shown in Figure 4. Figure 4 also shows the details of fatigue retrofitting at the corner of beam-to-column connections. Large-coring and large-coring + rib-installation were modeled by replacing the corner part of beam-to-column connection. The minimum mesh-size is less than plate thickness. The effective size of ribs for fatigue retrofit was already determined as the 10% size of beam height (Tanabe et al. 2004). According to this effective rib size, the 10% size of height was also used to these analyses. In case of large-coring + rib-installation model, it was used that the equivalent rib-width W' (see Figure 5) which is same as rib-width of typical rib-installed case. Superstructures were modeled as point masses on the top of beam flange.

The bases of piers were completely fixed and the earthquake motions were applied as inertial forces. The self-weight of piers and the dead-load of superstructures were also considered by vertical inertial forces. It was input that the east-west and up-down component of the acceleration records of the Kobe earthquake at the JR-Takatori and JMA-Kobe. The duration of analyses was 10 second.

Rayleigh-dumping was used in these analyses. Rayleigh-dumping is defined as Eq. (1). In order to determine the parameters in Eq. (1), the first and second angle frequencies were analyzed by the modal analyses.

$$\begin{aligned}
 [C] &= \alpha[M] + \beta[K] \\
 \alpha &= \frac{1\omega_1\omega_2(h_1\omega_2 - h_2\omega_1)}{\omega_2^2 - \omega_1^2} \\
 \beta &= \frac{2(h_2\omega_2 - h_1\omega_1)}{\omega_2^2 - \omega_1^2}
 \end{aligned} \tag{1}$$

Where, $[C]$ is Dumping matrix, $[M]$ is Mass matrix, $[K]$ is Stiffness matrix, ω_1, ω_2 are the angle frequency of each mode, and h_1, h_2 are dumping factors for each mode ($=0.02$).

Table 1 Analysis Cases

Analysis Case	Pier	Method	Input Wave
AN-T	A	None	Takatori
AN-K			Kobe
AC-T		Large Coring	Takatori
AC-K			Kobe
ACR-T		Large Coring + Rib Installation	Takatori
ACR-K			Kobe
BN-T	B	None	Takatori
BN-K			Kobe
BC-T		Large Coring	Takatori
BC-K			Kobe
BCR-T		Large Coring + Rib Installation	Takatori
BCR-K			Kobe

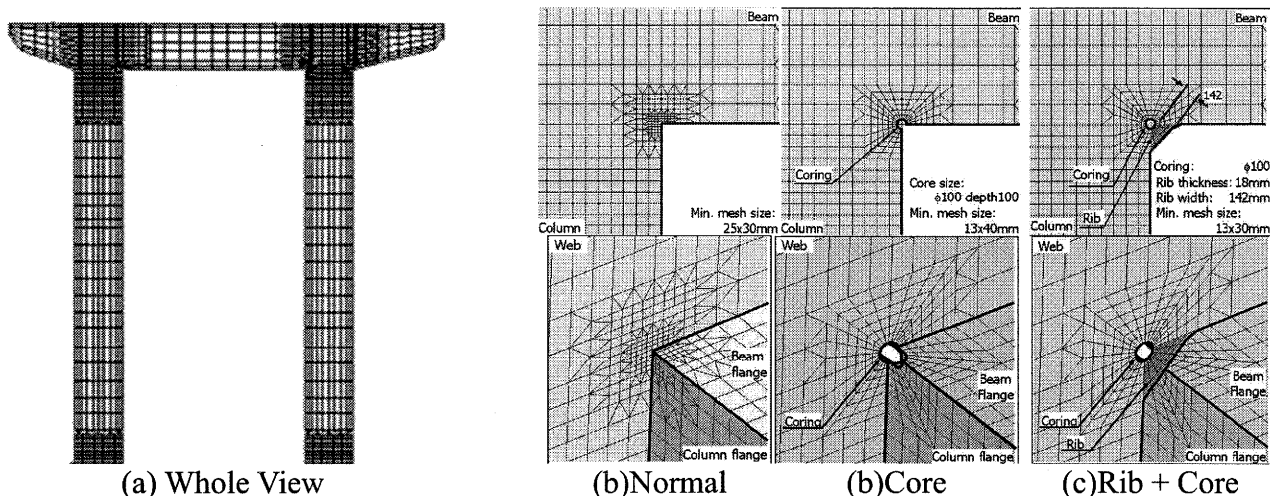


Figure 4 Finite Element Models

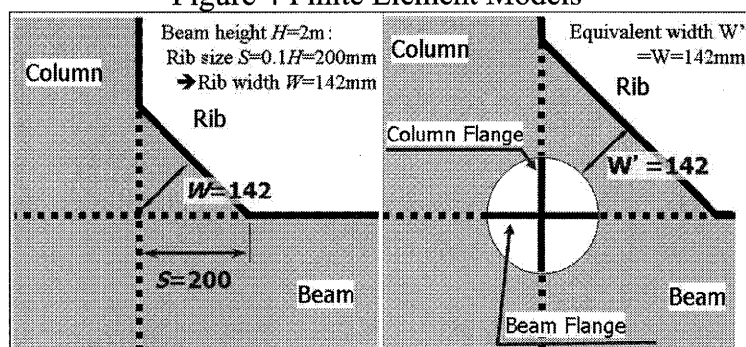


Figure 5 Equivalent Rib Width

2.2 Results and considerations

The results of modal analyses were shown in Figure 6 and Table 2. Figure 6 shows the deformation by first mode. Table 1 shows the angle frequencies and parameters for dumping. There are only small differences among the analyses cases, thus we may say that the fatigue retrofitting does not change the vibration modes of frame piers.

The results of the dynamic response analyses were shown in Figure 7 and Figure 8. Figure 7 shows the history of the displacement of the node at the center of upper flange. Figure 7 indicates that there is also no difference among the fatigue retrofitting. Figure 8 shows the deformation and plastic strain distribution when the maximum response was obtained. The local strain were different each other, however, the out of beam-to-column connection were mainly damaged.

From these results, we may say that the modification for fatigue retrofitting does not affect on the failure mode of frame piers because main damage occur at the out of beam-to-column connections, therefore, the resistance of frame piers may be kept if fatigue retrofitting was applied.

Table 2 Modal Analysis Results

FEM model	Natural frequency		Natural angle frequency		Factors	
	first	second	first	second	α	$\beta(\times 10^{-4})$
AN	1.236	5.149	7.77	32.4	0.251	9.97
AC	1.23	5.146	7.73	32.3	0.249	9.98
ACR	1.244	5.148	7.81	32.3	0.252	9.96
BN	1.938	5.279	12.2	33.2	0.356	8.82
BC	1.926	5.246	12.1	33	0.354	8.88
BCR	1.951	5.531	12.3	33.4	0.359	8.76

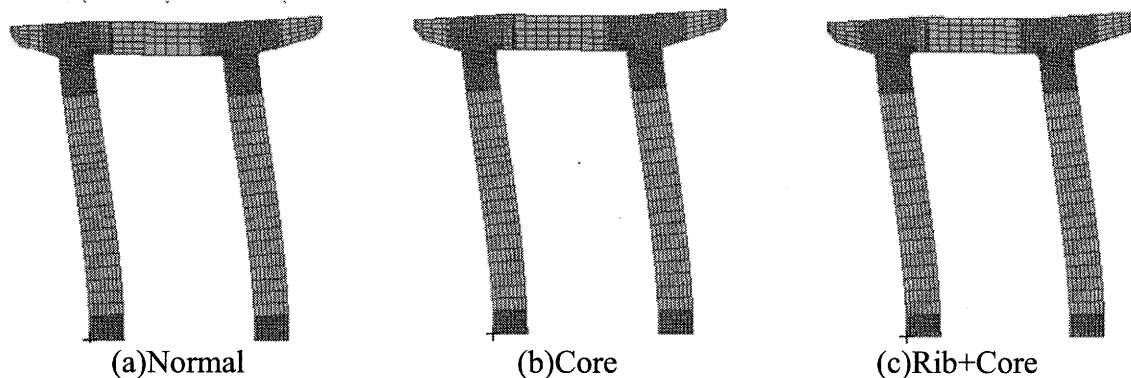


Figure 6 Results of Modal Analyses

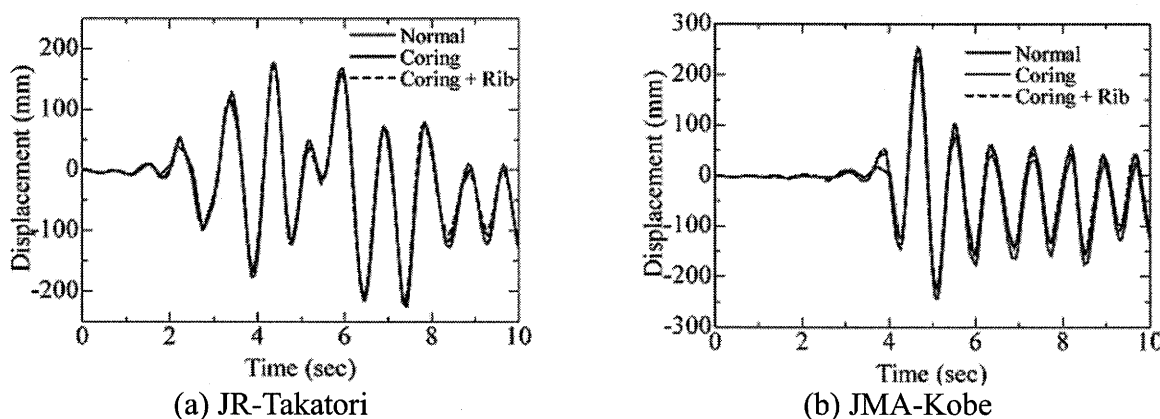


Figure 7 Time History of Displacement at the Center of Beam Upper Flange

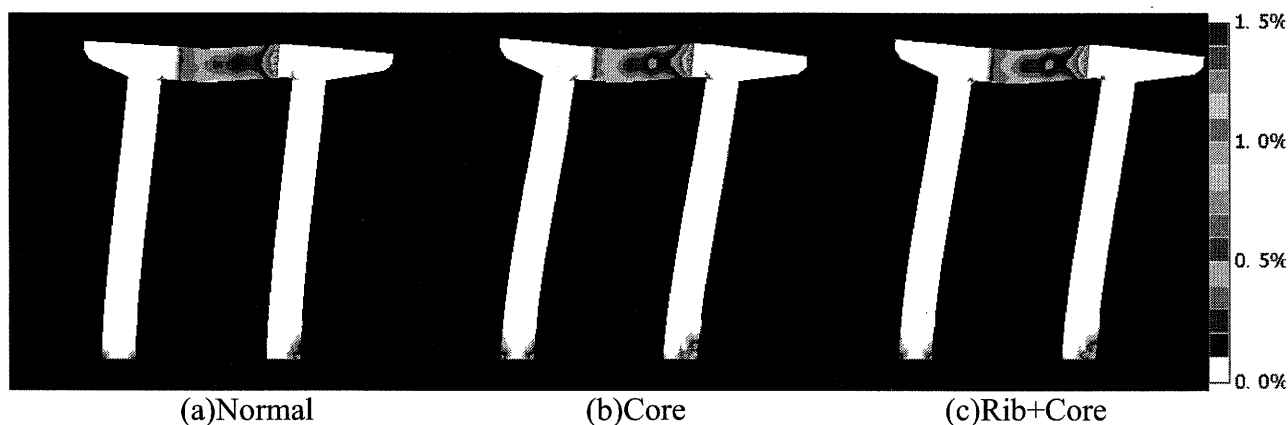


Figure 8 Deformation and Plastic Strain Distribution

2.3 Requirements for Beam-to-Column Connections

The time history of angle change between beam and column were evaluated. The definition of angle change θ_r is shown in Figure 9. When the angle is open, θ_r is plus, otherwise θ_r became minus.

Figure 10 shows the load-rotation relationship of the beam-to-column part (Pier-A). This figure indicates that yielding rotation angle θ_y of the Pier-A was ± 0.3 degree.

Figure 11 shows the angle change of Pier-A when the JR-Takatori earthquake motion was applied. This figure indicates that the both of opening and closing deformation were applied to beam-to-column connections, the magnitude of relative change is not so high, and that the relative angle change also did not effected by fatigue retrofitting.

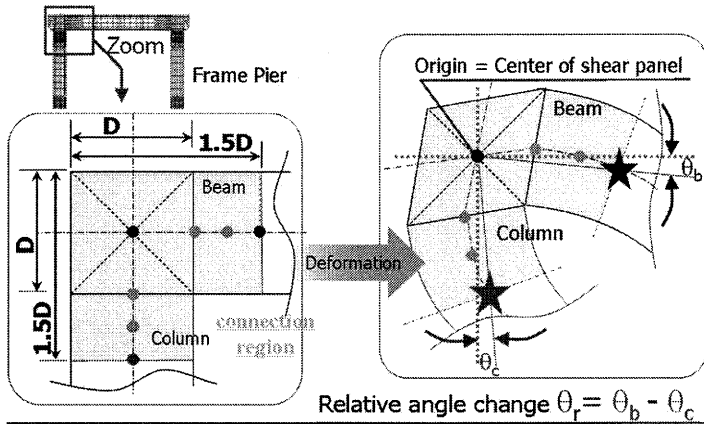


Figure 9 Definition of Angle Change

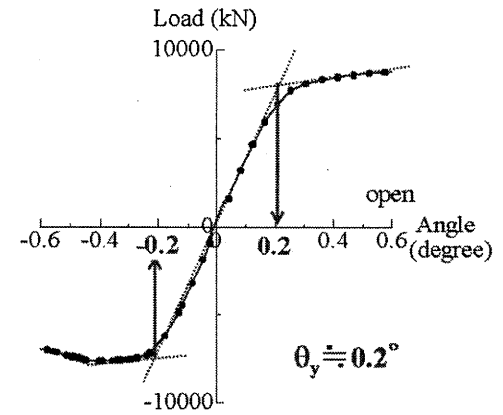


Figure 10 Yielding Rotation

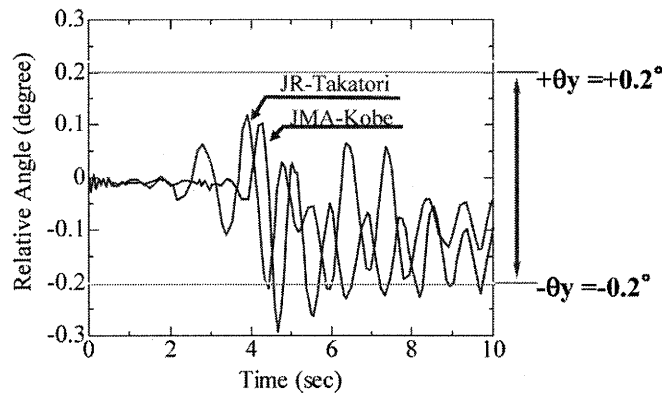


Figure 11 Angle Change

3. CYCLIC LOADING TESTS

The seismic resistance of fatigue retrofitted beam-to-column connection was evaluated by cyclic loading tests. The types of fatigue retrofitting and welding condition are considered as parameters.

3.1 Setup

The main parameter is the type of fatigue retrofit. Considered fatigue retrofitting types were basic type (as-built, no-retrofitting), large coring, rib-installation, large coring with rib-installation. Partially penetrated welding was used for assembling in order to simulate conditions in actual piers.

Figure 12 and Figure 13 show the geometry of specimens and test setup, respectively. In cyclic loading test, buckling behavior must be considered. The plate buckling was controlled by width-thickness ratio. Thus, the size of specimen was designed with a common width-thickness parameter R_R , which is defined in specifications of highway bridges (JRA 2002). The size of large coring was scale by the ratio of plate thickness because the local buckling related to the width-thickness ratio. The size of rib for the Rib specimen and Rib+Core specimen were determined by using the same concept of the FEM model of dynamic response analyses.

Common loading pattern was used for the test. Figure 14 shows the loading pattern for all of the specimens. In the loading condition, δ_y was defined by the kinking point of relationship of actuator's load-displacement relation of the Basic specimen. Same δ_y was used for other specimens even if the actual kinking point was different, because it has been showed that the fatigue retrofitting had ignorable changes for global response of frame system.

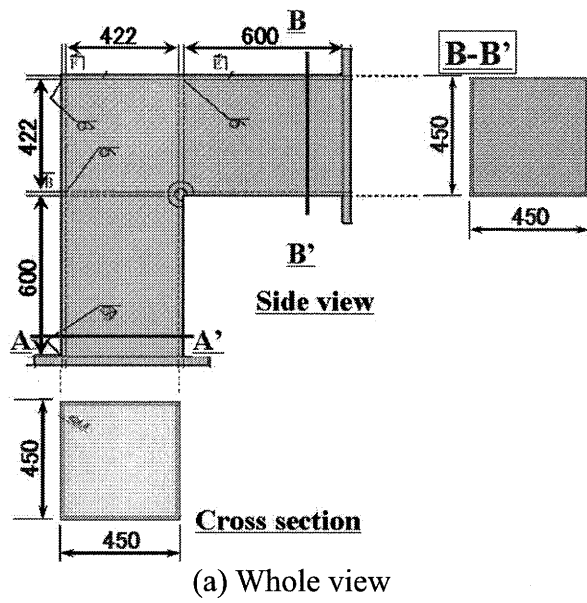


Figure 12 Geometry of Specimens

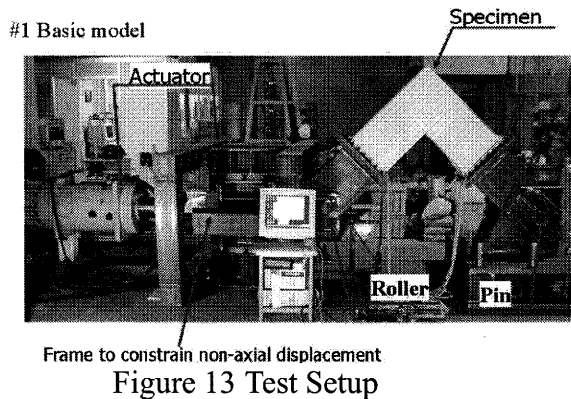


Figure 13 Test Setup

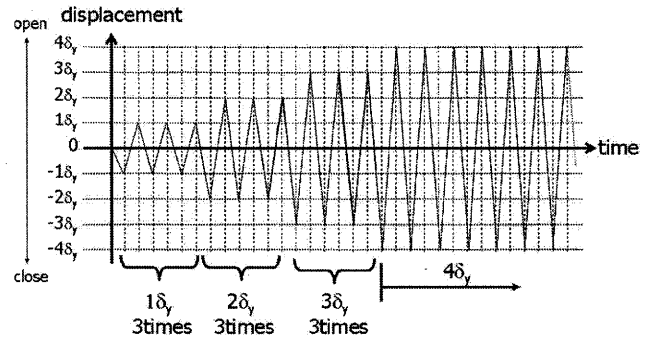


Figure 14 Loading Pattern

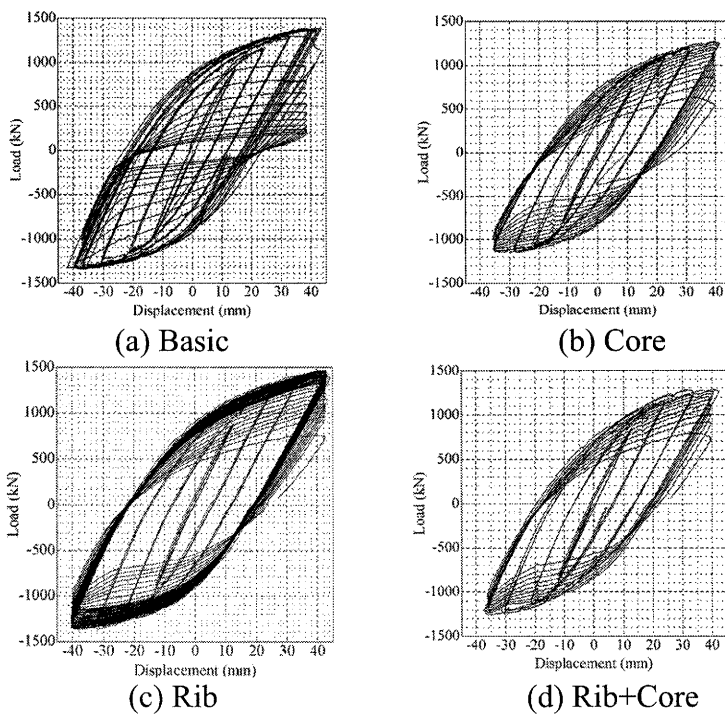


Figure 15 Load-displacement Relationships

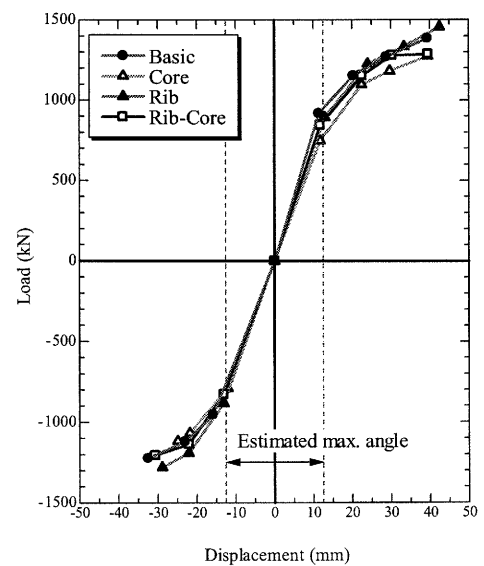


Figure 16 Skelton Curves

3.2 Test Results and Considerations

Figure 15 shows the Load-Displacement relationship of each specimen. The results of Load-Displacement relationship indicates that the all of the specimens had stable relationship, even in coring specimen

In order to compare the load-displacement relationships of all specimens, skeleton curves were used. Figure 16 shows skeleton curves of all specimens. The skeleton curve was made from the max and minimum peak of load-displacement relationships at the first cycle of each δ_y step. This figure indicates that all specimens had enough seismic resistance in spite of severe testing condition. Therefore, fatigue retrofitting did not reduce seismic performance of beam-to-column connection.

4. CONCLUSIONS

In this study, it was evaluated by dynamic response analyses and cyclic loading tests that the seismic resistance of fatigue retrofitted steel bridge frame piers. Following results were obtained by this study:

1. Fatigue retrofitting had ignorable effects for seismic response.
2. The fatigue retrofitted beam-to-column connections had enough seismic resistance.
3. Applied moment to beam-to-column connection was small. In this study, the maximum deformation was about $-1.5\theta_y$.

Therefore, we can say that the large-coring and rib-installation can be installed to the beam-to-column connection of existing steel bridge frame piers.

References:

- Hisashi Morikawa, Tetsuhiro Shimozato, Chitoshi Miki, and Atsushi Ichikawa (2002) "Study on fatigue cracking in steel bridge piers with box section and temporally repairing" *Journal of Structure Mechanics and Earthquake Engineering*, 703, 177–183
- Chitoshi Miki, Yasuaki Hirabayashi, Hideo Tokida, Takuyo Konishi, and Yasutoshi Yaginuma (2003) "Beam-column connection details of steel pier and their fatigue damage mode" *Journal of Structural Mechanics and Earthquake Engineering*, (745):105–119
- John W. Fisher (1984) "Fatigue and Fracture in Steel Bridges – Case Studies" Wiley-interscience
- Chitoshi Miki, Atsushi Ichikawa, Takuya Sakamoto, Atsushi Tanabe, Hideo Tokida, and Tetsuhiro Shimozato (2002) "Fatigue performance of beam-to-column connections with box sections in steel bridge frame piers" *Journal of Structure Mechanics and Earthquake Engineering*, 710:361–371,
- Shuichi Ono, Noboru Wakabayashi, Tetsuhiro Shimozato, Fumitaka Machida, and Chitoshi Miki (2004) "Full-size fatigue tests of beam-to-column connections for steel piers" *Proceedings of IIW Annual Assembly*, XIII-2019-04. International Institute of Welding
- Takuyo Konishi, Chitoshi Miki, Yasuaki Hirabayashi, and Tetsuhiro Shimozato (2004) "Inspection and repair of fatigue cracks in steel bridge piers" *Proceedings of IIW Annual Assembly*, XIII-2026-04. International Institute of Welding,
- Atsushi Tanabe, Chitoshi Miki, Atsushi Ichikawa, Eiichi Sasaki and Tetsuhiro Shimozato (2004) "Fatigue Strength Improvement of Beam-To-Column Connections with Box Section in Steel Bridge Frame Piers", *Journal of Structure Mechanics and Earthquake Engineering*, 773:137–148
- Toshie Okumura and Shigeo Ishizawa (1968) "The Design of Knee Joints for Rigid Steel Frames with Thin Walled Section", *Journal of Structural Mechanics and Earthquake Engineering*, 153: 1-18
- Japan Road Association (2002) "Specifications for Highway Bridges, Part V: Seismic design", Maruzen

ANALYSIS OF PASSIVE CONTROL SYSTEMS FOR EXISTING STEEL BRIDGES IN JAPAN

K. Kinoshita¹⁾

*1) Doctoral Student, Department of Civil Engineering, Tokyo Institute of Technology, Japan
kinoshita@cv.titech.ac.jp*

Abstract: In this study, two applications of passive control systems are evaluated as retrofit strategies for existing steel bridge structures: buckling restrained braces and steel dampers. The case-study structure is a box-section steel portal frame representative of many steel bridge pier frames found in densely developed urban areas of Japan. The design capacities of the damping elements were selected based upon a standard energy equivalence procedure aimed at limiting the core structural system response to slightly below the inelastic threshold. Inelastic, time-history analyses were used to evaluate the expected performance of the unretrofitted frame and the two retrofit designs. The results of the analyses indicate that the overall response of the unretrofitted frame exceeds the inelastic threshold. The results for both of the retrofit designs show satisfactory performance of overall elastic behavior. These preliminary results are being used as a basis for a more detailed evaluation of passive control retrofit applications for steel bridge frames.

1. INTRODUCTION

During the Great Hanshin Earthquake of 1995 near Kobe, Japan, several failures of steel bridge pier frames occurred. In the years immediately following the earthquake, a large number of research investigations were established to evaluate the seismic vulnerability of steel bridge pier frames. As a result of those investigations, several types of seismic retrofits were recommended and performed such as placing concrete in the piers (Imamura et al. 1999). Some studies indicate that even after such retrofitting, some steel frame bents could remain vulnerable to plastic deformation during shaking induced by large earthquakes (Nakai et al. 1993, Saizuka 1995).

In this research, by using analytical methods, two passive device systems for steel bridge bents were investigated: buckling restrained braces damper and shear damper system. At first, in order to determine the volume of damper, we calculated needed volume of damper from concept of energy equivalence of ductility. After that, we carried out push over analyses and dynamic analyses of each type of dampers.

2. DESIGN OF DAMPER

In this research, to determine damper size of steel bridge bents, the concept of absorbed energy equivalence was used: see for example Usami et al. (2003). Figure 1 shows energy absorption of structure. W_{Frame} indicates energy absorption of original frame. W_{Total} indicates energy absorption of original frame with installed damper system. Both W_{Frame} and W_{Total} are equivalent. From this concept, assuming elastic-perfectly plastic behavior, we can estimate the required yield strength of damper $H_{y Damper}$ as damper system for horizontal resistance. This concept assumes that K_{Damper} is known. Then we get the equation as Eq. (1) below:

$$H_{y \text{ Damper}} = K_{\text{Damper}} \delta_T - \sqrt{(K_{\text{Damper}} \delta_T)^2 - 2K_{\text{Damper}} (W_{\text{Frame}} - W)} \quad (1)$$

In the case of the buckling restrained braces, the horizontal structural stiffness imparted by the damper, K_{Damper} , depends upon the cross-sectional area of the of the core and so does the damper yield strength. In the case of the steel damper, the horizontal structural stiffness imparted by the damper, K_{Damper} , depends upon the total number of damper plates used and so does the damper yield strength. In this study, Eq. (1) was used to determine the core area of the buckling restrained braces and also to determine the total number of plates required in the steel damper. Design flow of damper system is shown in Figure 2.

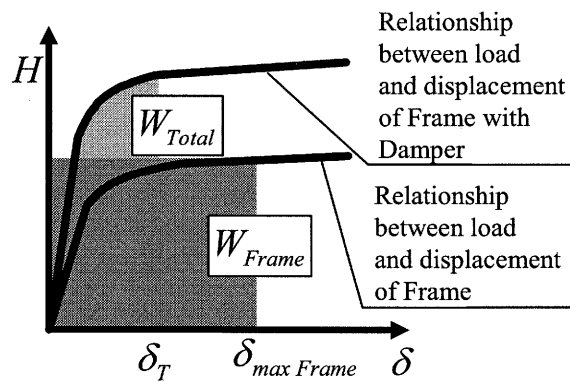


Figure 1 Energy Absorption

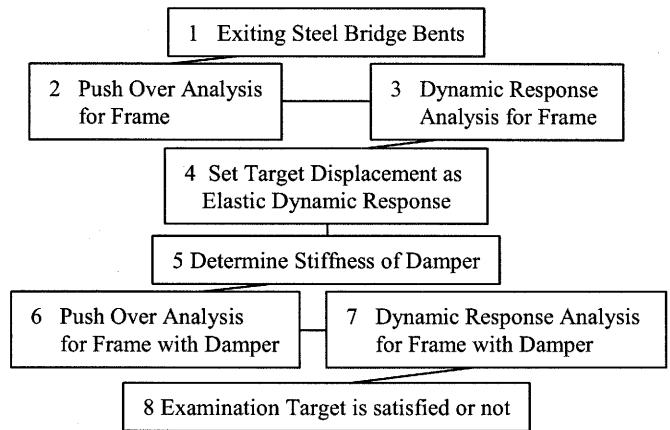


Figure 2 Design flow of Damper system

3. FEA OF TARGET EXISTING STEEL BRIDGE BENTS

As target steel bridge bents, typical type of steel bridge bents and its FEA mesh are shown in Figure 3. In this FEA model, weight of super structure was modeled by several mass elements. Column base modeled by beam element, other parts were modeled by shell elements. Also, column bases were fixed. Stress Strain curve of not only steel but also damper using in FEA model shown in Figure 4. For existing steel bridge bents, SS400 steel was used. Also, for buckling restrained braced damper, low yield point steel ($\sigma_y = 100\text{MPa}$) was used. In the dynamic analyses, seismic acceleration waves measured at JR Takatori station in the Great Hanshin Earthquake were used.

Figure 5 shows FEA cases. In this research, two type of damper system, buckling restrained damper type and steel shear beam type damper type were used. Figure 6 shows load distribution in existing steel bridge bents with each damper system. Normally, horizontal force of whole system with damper was express by horizontal force of original frame plus horizontal force of damper system. Buckling restrained braced dampers were modeled by truss element.

4. FEA RESULTS OF BUCKLING RESTRAINED TYPE

Figure 7 shows push over analysis results for the unretrofitted frame. Based upon the result from the original frame, a target maximum displacement of 60 mm was selected as the performance objective. Applying Equation 1 it was determined that the required core area of the buckling restrained braces is 0.015 m^2 . Figure 7 also shows the result of the pushover analysis for the frame retrofitted with buckling restrained braces. Both the stiffness and the strength are increased with the

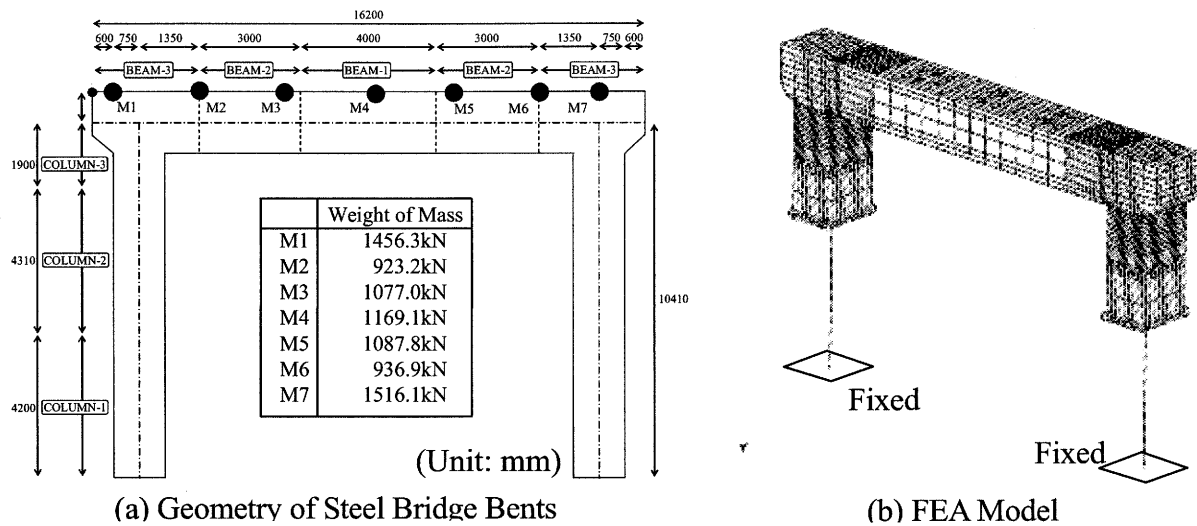


Figure 3 FEA Model of Exiting Steel Bridge Bent

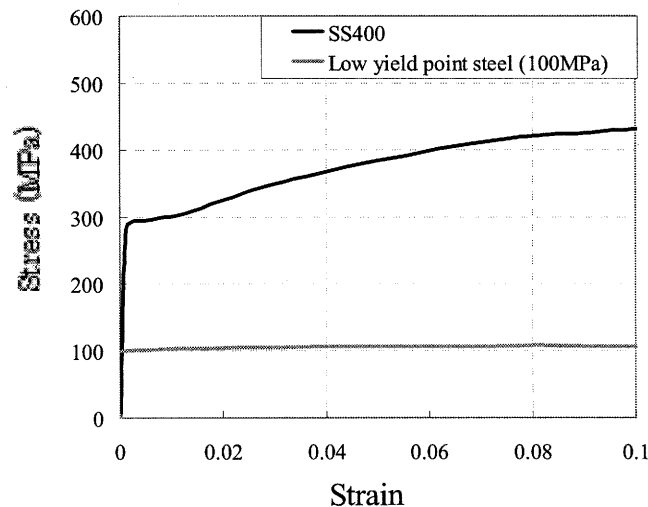


Figure 4 Stress-Strain Curve of Steel

addition of the braces. Dynamic analyses results show in Figure 8. Figure 8 shows time history of the horizontal displacement at center of beam. In these figures, symbol \bigcirc indicate maximum displacement $\delta_{\max \text{ Frame}}$, symbol \triangle indicate maximum displacement $\delta_{\max \text{ with Damper}}$ after installing damper system. From these results, due to installing each damper system, maximum response displacement during earthquake was reduced by 36 percent: from 75 mm to 47 mm. This result satisfies the performance objective of 60 mm with a factor of safety of approximately 1.3.

5. FEA RESULTS OF SHEAR DAMPER TYPE

There is several shear type of damper (Lee et al. 2002, Chen et al. 2004 and Kasai et al. 2004). In this study the shear damper is H shape made from SS400 steel. Figure 9 shows analysis results of hysteresis curve of steel damper. Again applying Equation 1, the required number of damper plates is 4 (see Figure 10). Figure 11 shows the result of the pushover analysis for the frame retrofitted with steel dampers. The result for the unretrofitted frame is also shown. Both the stiffness and the

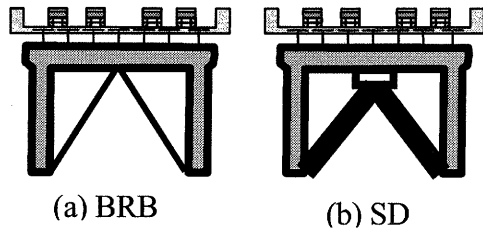


Figure 5 FEA Cases of Buckling Restrained

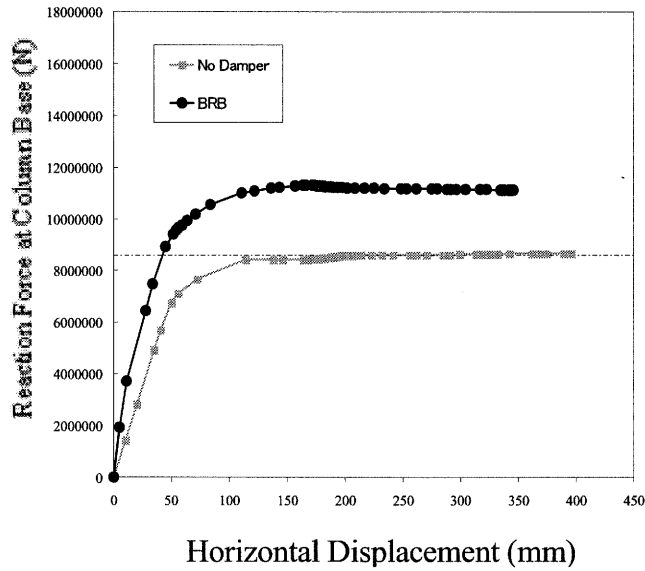


Figure 7 Push Over Analysis Results

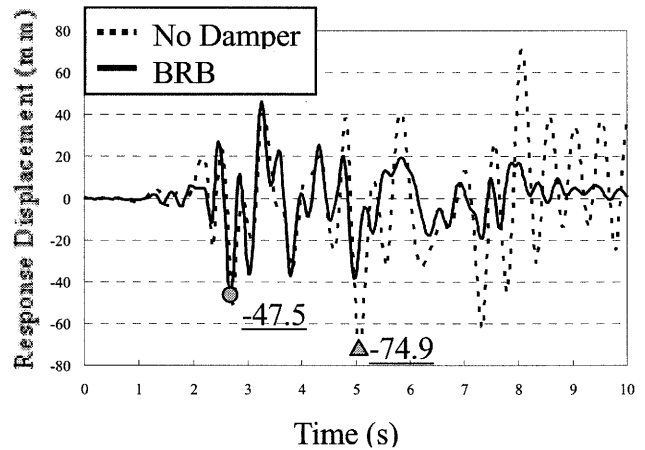
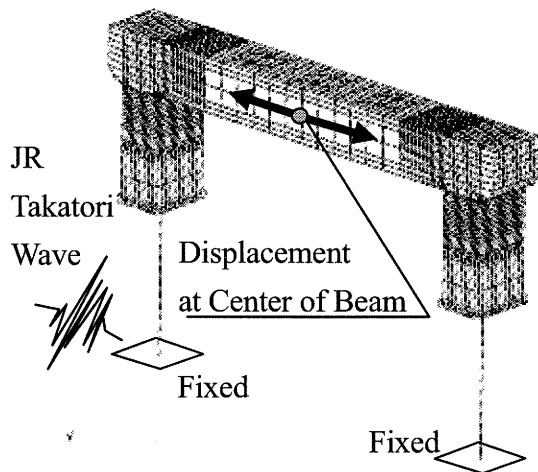


Figure 8 Time History of the Horizontal Displacement at the Center of Beam

strength are increased with the addition of the dampers. Dynamic analyses results are shown in Figure 12. Figure 12 shows time history of the horizontal displacement at center of beam. In these figures, symbol \bigcirc indicate maximum displacement $\delta_{\max \text{ Frame}}$, symbol \triangle indicate maximum displacement $\delta_{\max \text{ with Damper}}$ after installing damper system. From these results, due to installing each damper system, maximum response displacement during earthquake was reduced by 67 percent: from 75 mm to 25 mm. This result satisfies the performance objective of 60 mm with a factor of safety of approximately 2.4.

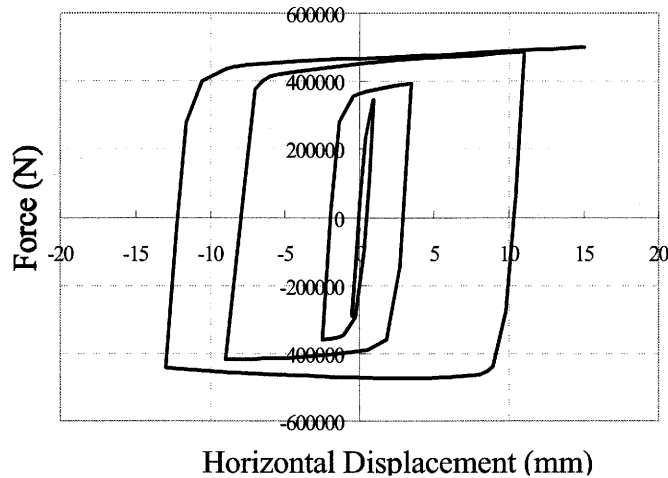


Figure 9 Hysteresis Curves of Steel Damper

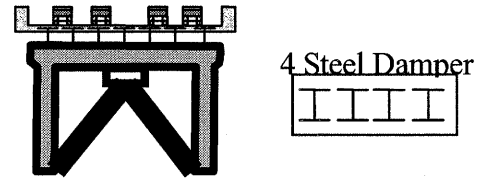


Figure 10 Number of Steel Dampers

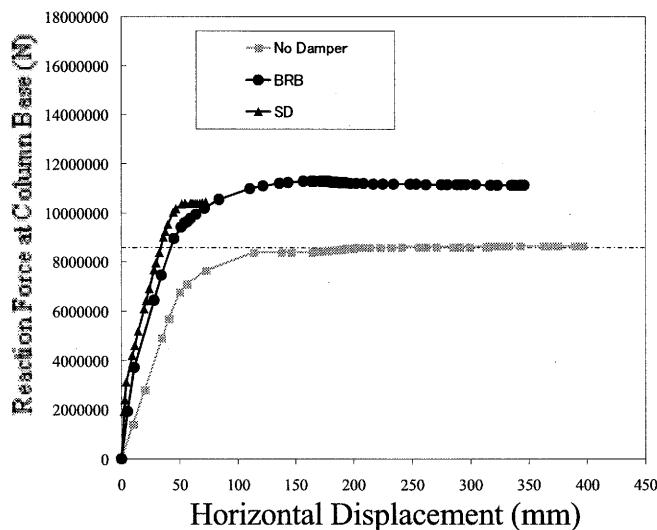


Figure 11 Push Over Analysis Results

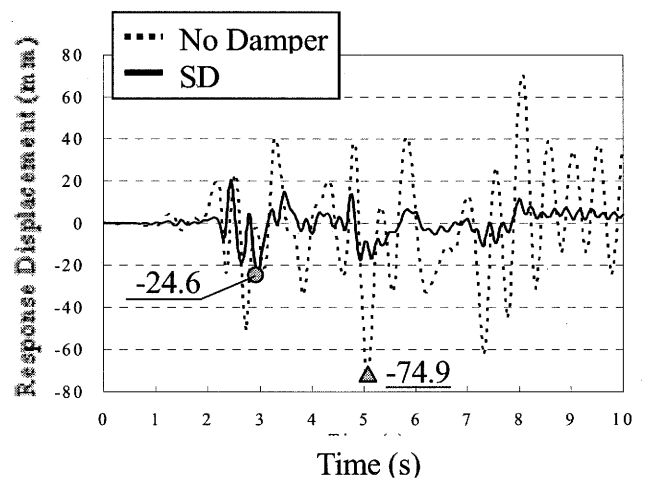


Figure 12 Time History of the Horizontal Displacement at the Center of Beam

6. CONCLUSIONS

The conclusion of this research can be summarized as follows.

1. Both types of damper system considered, buckling restrained damper system and shear damper system, are effective for improvement of seismic performance of existing steel bridge bents.
2. By using damper size designed by concept of equivalent energy the desired response displacement of existing steel bridge was achieved reliably.

7. FUTURE WORK

Although the damper systems described in this study were very effective, there are many situations where a concentrically braced frame cannot be installed within a steel bridge pier frame. Figure 13 shows an elevation view of the pier frame considered in this study. Also shown in Figure 13 is a dashed line that indicates an allowable clearance envelope that often must be maintained when

installing retrofit members. It is obvious that such clearance requirements severely constrain the problem of retrofitting a steel bridge pier frame. Ongoing and future research objectives are aimed at discovering effective means of retrofit to reduce the dynamic response of steel bridge pier frames that must maintain the clearances indicated in Figure 13.

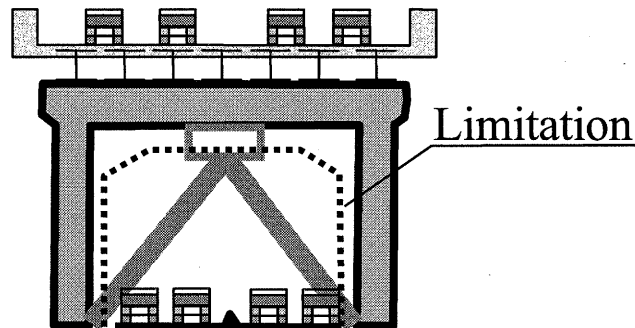


Figure 13 Clearance Requirement

Acknowledgements:

The author acknowledges support from Japan Ministry of Education, Culture, Sport, Science, and Technology (MEXT) for establishing the Center for Urban Earthquake Engineering (CUEE) in Tokyo Institute of Technology. The support has made possible this international conference, as well as international joint research projects and exchange programs with foreign universities. In addition, the author extends appreciation to Dr. Gary Fry, Visiting Associate Professor, Department of Civil Engineering, Tokyo Institute of Technology, for assistance with editing the manuscript.

References:

- Chen, S. and Kuo, C. (2004), "Experimental Study of Vierendeel Frames with LYP Steel Shear Panels," *International Journal of Steel Structures*, the Korean Society of Steel Construction, Vol. 4(4), 179-186.
- Imamura, K., and Takahashi, M. (1999), "Retrofitting of Existing Piers in Metropolitan Expressway," *Bridge and Foundation Engineering*, Vol. 33, 163-165.
- Kasai, K., Wada, A., Sakata, H., Ooki, Y., and Miyashita, T. (2004), "Passive Control for Mitigating Seismic Damage to Wood Houses Part 1 Behavior and Design of Joints, Damper, and System," *Passive Control Symposium 2004*, Structural Engineering Research Center Tokyo Institute of Technology, 169-184.
- Lee, M., Oh, S., Huh, C., Oh, Y., Yoon, M., and Moon, T. (2002), "Ultimate Energy Absorption Capacity of Steel Plate Slit Dampers Subjected to Shear Force," *International Journal of Steel Structures*, the Korean Society of Steel Construction, Vol. 2(2), 71-79.
- Morishita, K., Inoue, K., Kawashima, K., Abiru, H., Hirai, J., and Honda, M. (2004), "Experimental Verification on the Effectiveness of Damper Braces for Reducing Response of a Steel Model Bridge," *Journal of Structural Mechanics and Earthquake Engineering*, Japan Society of Civil Engineers, No.766/I-68, 277-290.
- Nakai, H., Kitada, T., Yoshikawa, O., Nakanishi, K., and Oyama, T. (1993), "Experimental Study on Ultimate Strength and Ductility of Concrete Filled Steel Box Columns," *Journal of Structural Engineering*, Japan Society of Civil Engineers, Vol.39, 1347-1360.
- Saizuka, K., Usami, T., Kiso, E., and Itoh, Y. (1995), "Pseudo-Dynamic Tests of Concrete-filled Steel Bridge Piers," *Journal of Structural Engineering*, Japan Society of Civil Engineers, Vol.41, 277-288.
- Usami, T., Kasai, A., and Itou, M., and Chushilp, P. (2003), "Fundamental Research of Simplified Design Method of Seismic Control Damper of Buckling Restrained Brace," *6th Bridge Seismic Design Based on the Ductility Symposium*, The Ductility Design Subcommittee, JSCE, 385-392.
- Usami, T., Ge, H., Hioki, K., Lu, Z., and Kono, T. (2004), "Seismic Performance Upgrading of Steel Arch Bridges using Structural Control Dampers against Transverse Directional Earthquake Motions," *Journal of Structural Mechanics and Earthquake Engineering*, Japan Society of Civil Engineers, No.766/I-68, 245-261.

ULTRASONIC DETECTION OF DEFECTS BY USING THE 3D ULTRASONIC PHASED ARRAY SYSTEM

N. Rattanasuwannachart¹⁾, M. Katsuyama²⁾, and C. Miki³⁾

1) Fellow, Center for Urban Earthquake Engineering, Tokyo Institute of Technology, Japan

2) Graduate Student, Department of Civil Engineering, Tokyo Institute of Technology, Japan

3) Professor, Department of Civil Engineering, Tokyo Institute of Technology, Japan

narong@cv.titech.ac.jp, katsuyama@cv.titech.ac.jp, miki@cv.titech.ac.jp

Abstract: In this research, the 3D ultrasonic flaw detection system with the planar phased array probe and the defect visualization system has been newly proposed and developed for improvement of ultrasonic inspection in terms of detectability, accuracy, and objectivity in three dimensions. The planar phased array probe was fabricated with 64 elements arranged in form of 8-by-8 matrix. This array probe has capability of steering and focusing incident waves arbitrarily in three dimensions. The detection of the artificial planar defect was performed for verification of the system. The result shows that the defect could be objectively visualized and information of the defect could be accurately obtained.

1. INTRODUCTION

In existing welded steel structures such as bridges and gas pipelines, it was found that weld defects and fatigue cracks exist in weld zones. Weld defects remain in weld joints during fabrication of structures (see Figure 1(a)). They are divided into 2 types consisting of planar defects and volumetric defects. In general, fatigue cracks start propagating from planar defects inside structures during service (see Figure 1(b)). When the structures with embedded fatigue cracks are subjected to strong or weak earthquakes, the brittle fracture of structures (see Figure 1(c)) will be the results and lead to tragic consequences.

Therefore, in order to prevent the brittle fracture of existing structures, the presence of fatigue cracks should be accurately known for replacement and retrofitting. In this aspect, the non-destructive evaluation (NDE) will play the main roles for inspection of existing structures. Recently ultrasonic testing is the most widely used method. Main objectives of ultrasonic testing are to detect cracks and defects inside weld joints and to give accurate information such as location, shape, size, and orientation.

In conventional ultrasonic testing, the single probe technique has been widely conducted (Krautkrämer and Krautkrämer 1983). However, the single probe technique lacks detectability of defects. In addition, results of ultrasonic testing have been presented in form of an unprocessed radio frequency (RF) signal or an A-scan as shown in Figure 2. The A-scan lacks recordability and objective evaluation, because it is only a plot of echoes on time axis shown on screen of the flaw detector and inspectors make judgment and evaluation of flaws and defects. Therefore, using the current ultrasonic testing system may lead to misjudgment and oversight of the presence of defects and fatigue cracks. As a result, new ultrasonic inspection systems with high detectability and accuracy are required.

Recently large amount of researches have been dedicated to develop new ultrasonic testing systems in order to improve detectability, accuracy, and reliability of ultrasonic inspections (Miki et al.

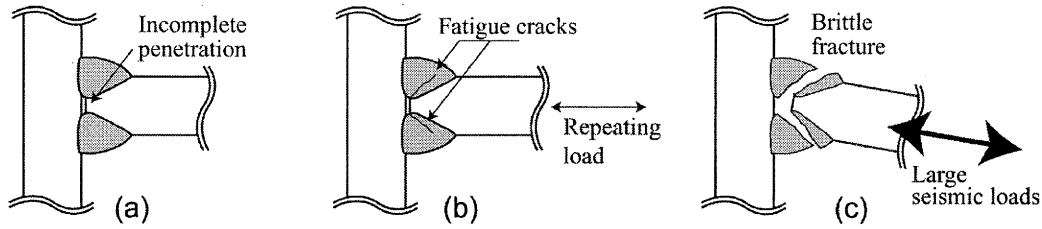


Figure 1 Damage Case of Structures: (a) Planar Defects in Weld Joints, (b) Propagation of Fatigue Cracks, and (c) Brittle Fracture due to Seismic Loads

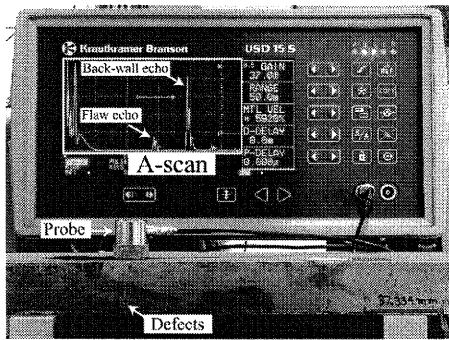


Figure 2 Current Presentation of Inspection Results by A-Scan

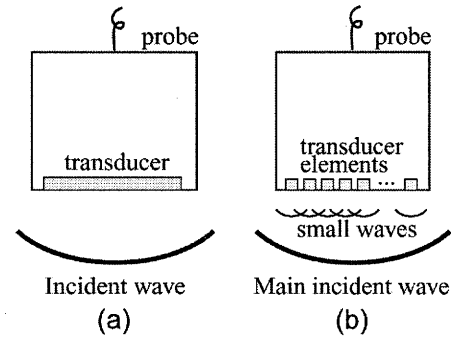


Figure 3 Transmission of Incident Waves: (a) Conventional Probes, and (b) Phased Array Probes

2000, Song et al. 2002, Fujiwara et al. 2003). Among those developments, the phased array system is known to be the most promising system due to flexibility of controlling directions of incident waves.

In general, phased array probes consist of many small elements of transducers, while conventional probes consist of only one big transducer as shown in Figure 3. Phased array probes can produce main incident waves by composing and integrating all small waves generated by many small elements. As a result, phased array probes can steer incident waves to arbitrary directions and can focus incident waves to arbitrary locations or points in test objects by applying time delays to transmitting pulses of each element.

Unfortunately, most of the recently developed systems perform only for 2D inspection, while defects and cracks are usually present with three-dimensional shape (Miki et al. 2001). The objective of this research is, therefore, to develop the 3D ultrasonic phased array system for efficient detection of defects in steel members with high detectability and accuracy in three dimensions.

2. NUMERICAL SIMULATION OF ULTRASONIC BEAM STEERING AND FOCUSING

2.1 Finite Element Model

In this research, two-dimensional finite element analyses were conducted in order to study the reflection behavior of steered and focused waves by a hole-like defect. Figure 4(a) is the finite element model of the steel with size of $15 \times 25 \text{ mm}^2$. The 2D rectangular solid elements with mesh size of 0.1 mm were used. The hole-like defect with diameter of 4 mm was included in the model. It was located at 4 mm from the bottom surface of this model.

In this analysis, the 16-elements linear phased array probe with element width of 0.55 mm and element pitch of 0.59 mm was simulated at the model top surface as shown in Figure 4(b). Two cases of analyses were carried out in order to observe the reflected waves when the wave was incident directly on target and out of target. In the first case (on-target case), the center location of the probe was located directly above the defect center. In the second case (out-of-target case), the center of the probe was located not directly above the defect but with horizontal distance of 2.36 mm to the left.

The displacement of 2-cycles sine wave (see Figure 4(c)) was applied to all nodes at top surface

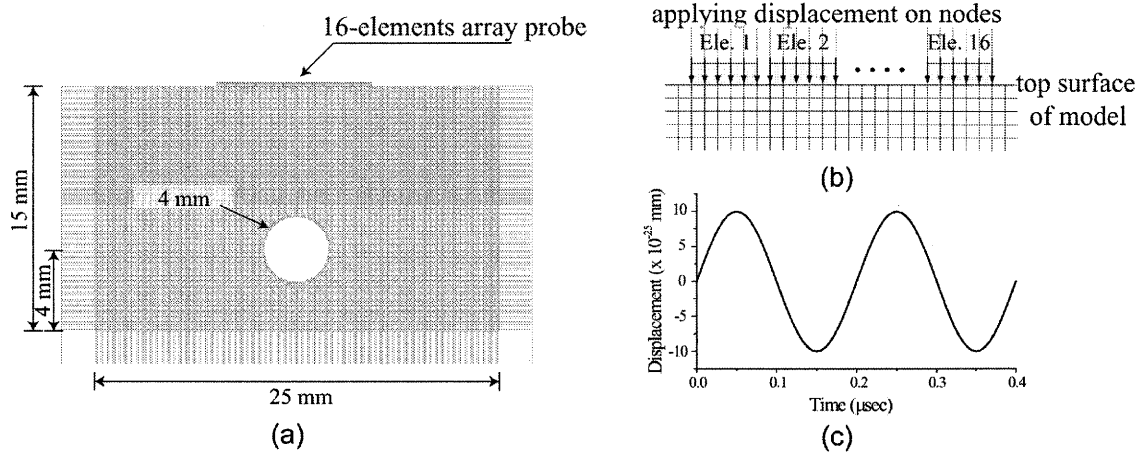


Figure 4 Details of FEM Analyses: (a) Finite Element Model, (b) Simulation of The Array Probe, and (c) Input Displacement

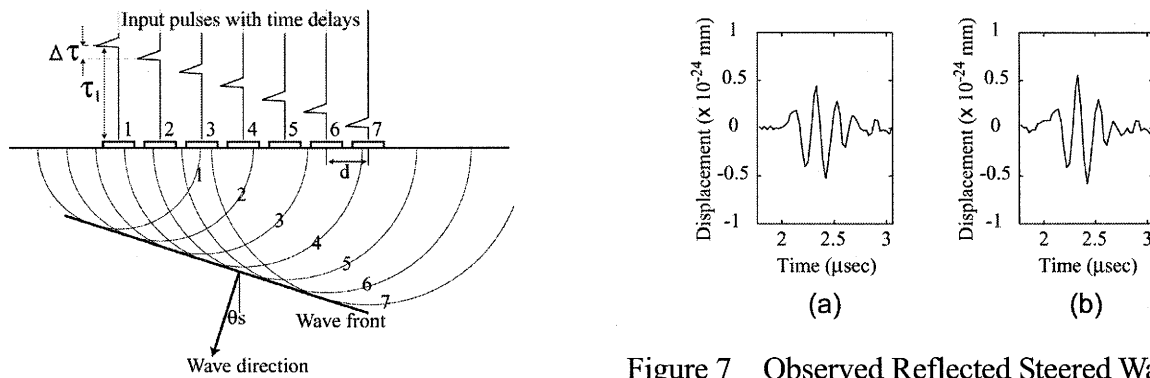


Figure 5 Theory of Ultrasonic Beam Steering

Figure 7 Observed Reflected Steered Waves: (a) On Target, and (b) Out of Target

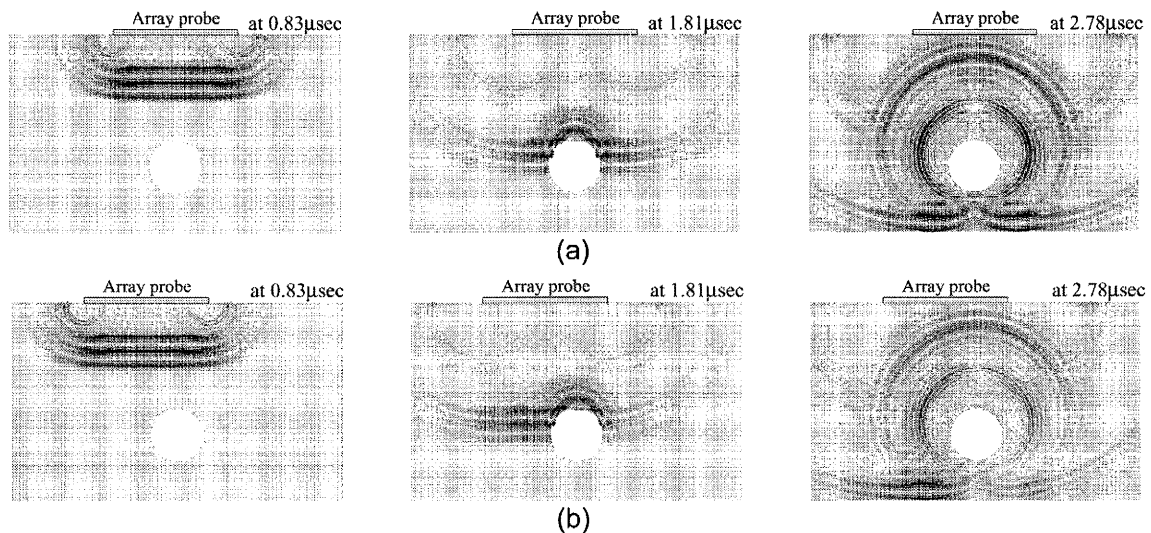


Figure 6 Snapshots of Behavior of Steered Waves: (a) On Target, and (b) Out of Target

of the model, which are directly beneath the elements of the phased array probe. In order to solve the dynamic problem, the direct integration method was conducted by using ABAQUS code. In the following, the input time delays of transmitting pulses of each element for forming the steered and focused waves were discussed.

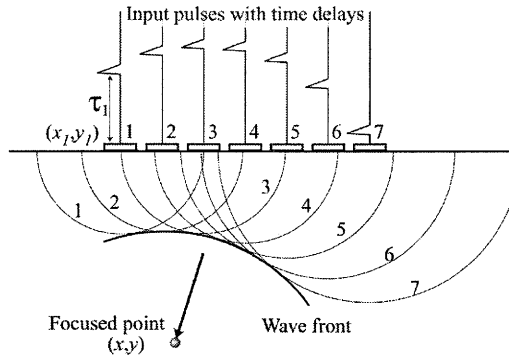


Figure 8 Theory of Ultrasonic Beam Focusing

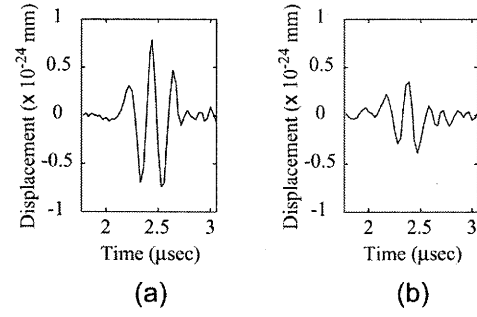


Figure 10 Observed Reflected Focused Waves:

(a) On Target, and (b) Out of Target

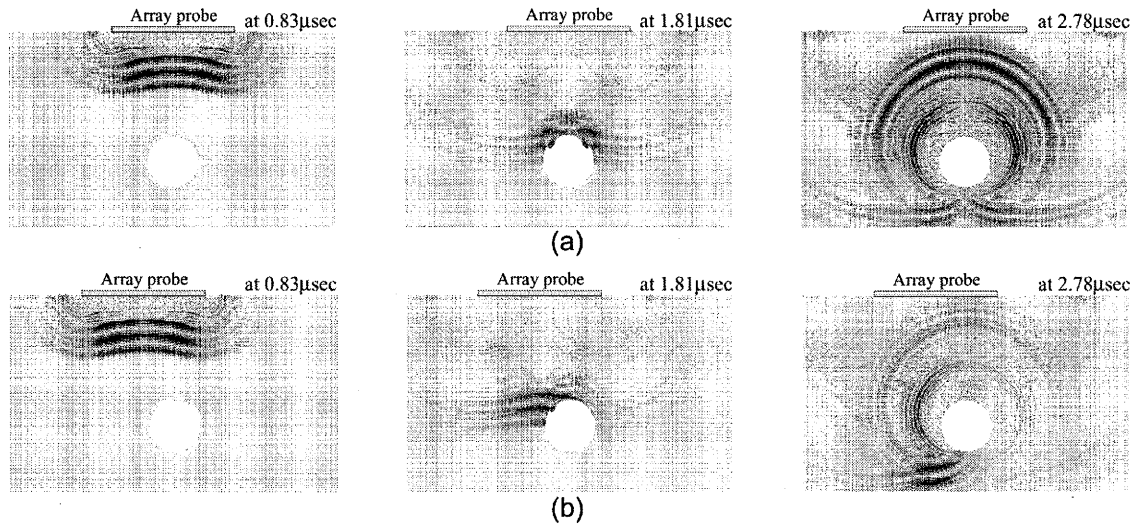


Figure 9 Snapshots of Behavior of Focused Waves: (a) On Target, and (b) Out of Target

2.2 Ultrasonic Beam Steering

The incident wave can be steered in the test object by applying the linear time delay to the transmitting pulses of all elements as shown in Figure 5. The increment of time delays for each element in the phased array probe can be calculated by using the following formula:

$$\Delta\tau = \frac{d \sin \theta_s}{c} \quad (1)$$

where $\Delta\tau$ is the increment of the time delay (sec), d is the element pitch (mm), θ_s is the steering angle, and c is the velocity of longitudinal waves (mm/sec). In this analysis, the incident wave was formed with $\theta_s = 0^\circ$ resulting in the normal-beam wave to propagate directly to the bottom surface of the model.

Figures 6(a) and (b), respectively, show the vector representations of the analyzed results of both the on-target and out-of-target cases at times = 0.83, 1.81, and 2.78 μ sec. The vector representations show propagation and reflection behavior of the formed incident wave. The reflected waves were observed at the center of the probe. Figures 7(a) and (b) are the reflected waves of the on-target and out-of-target cases. The result shows that the reflected waves of the same level could be obtained even though the center beam of the incident wave was not direct to the defect in the out-of-target case. This can be concluded to be the beam-spread effect of the steered incident wave.

2.3 Ultrasonic Beam Focusing

In case of beam focusing (see Figure 8), the calculation of time delays differs from that of the steered wave. Firstly, the distances from all elements to the target focused point (x, y) in the model will be determined in terms of the times of flight of the waves (t_i) using the following formula:

$$t_i = \frac{\sqrt{(x_i - x)^2 + (y_i - y)^2}}{c} \quad (2)$$

where x_i and y_i are the coordinates of phased array elements. Then, the time delays of each element (τ_i) will be determined as follows:

$$\tau_i = t_i - t_o \quad (3)$$

where t_o is the minimum value of t_i . In this analysis, the incident wave was focused to the point located under the probe center with vertical distance of 11 mm, which is the level of the hole center.

Figures 9(a) and (b) show the vector representations at times = 0.83, 1.81, and 2.78 μsec for the on-target and out-of-target cases, respectively. Figures 10(a) and (b) are the reflected waves of the on-target and out-of-target cases. The reflected wave was strong when the incident wave was directly focused to the hole, while it was comparatively weak when the incident wave was not directly focused to the hole.

Comparing the observed reflected waves by the beam focusing to those by the beam steering, it was found that the reflected focused wave was stronger than that of the steered wave in the on-target case. However, in the out-of-target case, the reflected focused wave was much weaker than that of the steered wave. That meant the focused wave is more effective for ultrasonic flaw detection, because it can produce very strong reflected waves when direct to the defect and produce very weak reflected waves when direct to the place where is no defect.

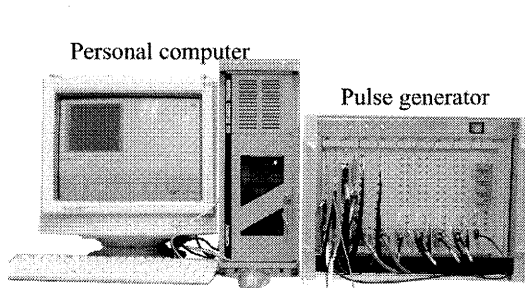


Figure 11 Ultrasonic Phased Array System

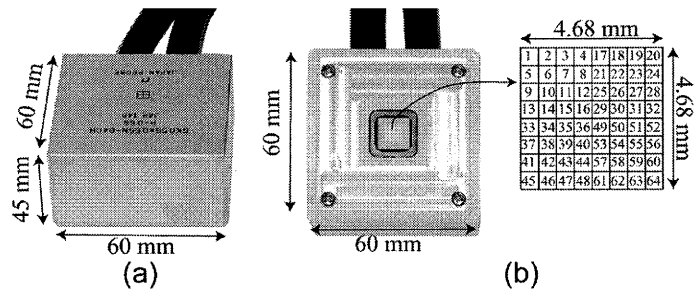


Figure 12 Details of The Planar Phased Array Probe:
(a) Size of Housing, and (b) Array Elements

3. ULTRASONIC PHASED ARRAY SYSTEM

3.1 Ultrasonic System

Ultrasonic system for phased array probes was developed. The system consists of the pulse generator and the personal computer as shown in Figure 11. In this system, the pulse generator has totally 64 channels. Among 64 channels, 16 channels can be selected to send or receive pulses at the same time. Therefore, we can produce incident waves with desired patterns by a group of 16 elements in the phased array probe.

The pulse generator will be controlled by the personal computer. At the computer, transmitting and receiving channels and corresponding time delays are input to match the desired patterns of the incident waves and the wave data can be recorded in form of the A-scan.

3.2 Planar Phased Array Probe

The planar phased array probe was newly developed. The geometry is shown in Figure 12. This planar phased array probe consists of 64 elements arranged in form of 8-by-8 matrix as shown in the figure. Each element has rectangular shape with element size of $0.55 \times 0.55 \text{ mm}^2$ and element pitch of 0.59 mm. All elements produce longitudinal waves with the central frequency of 5 MHz.

3.3 Detection Patterns

Detection of defects can be performed with 2 different detection patterns consisting of steering and focusing patterns. In case of the steering pattern (see Figure 13(a)), the beam center of the incident wave will be steered to many specific points at the plate bottom surface simulating the three-dimensional electrical scan in specimens. In case of the focusing pattern (see Figure 13(b)), the incident wave will be three-dimensionally focused to all points of the inspected volume in specimens. In this research, both of detection patterns will be performed for detection of defects in order to observe the accuracy of each pattern.

3.4 Visualization Systems

In order to improve reliability and objectivity of inspection results, the visualization systems were developed for visualizing defects in form of the reconstructed images based on the theory of synthetic aperture focusing technique (SAFT). Referring to Rattanasuwannachart et al. (2005) and Katsuyama (2005), the 3D SAFT algorithms were developed for both the wave data obtained from the steering and focusing patterns. The details of the 3D SAFT will not be mentioned in this manuscript.

4. DETECTION OF THE 3D ARTIFICIAL DEFECT

The steel specimen with the artificial defect is shown in Figure 14. This specimen has thickness of 12 mm and was machined on one surface making the three-dimensional cube-like defect with size of 4 mm x 4 mm x 2 mm (width x length x depth). The probe was mounted on the other surface, which is the opposite side to the machined surface.

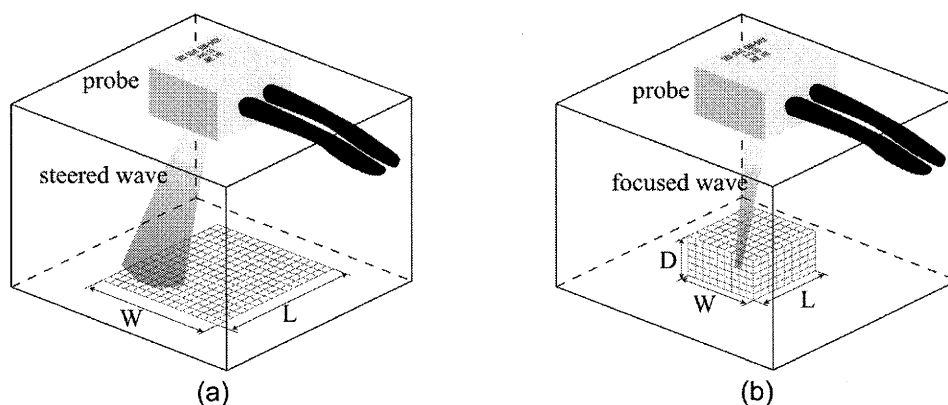


Figure 13 Detection Patterns: (a) Steering Pattern, and (b) Focusing Pattern

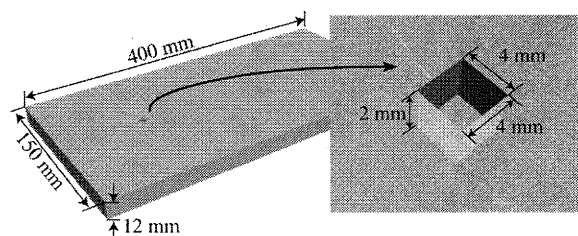


Figure 14 Details of Steel Specimen with 3D Artificial Defect

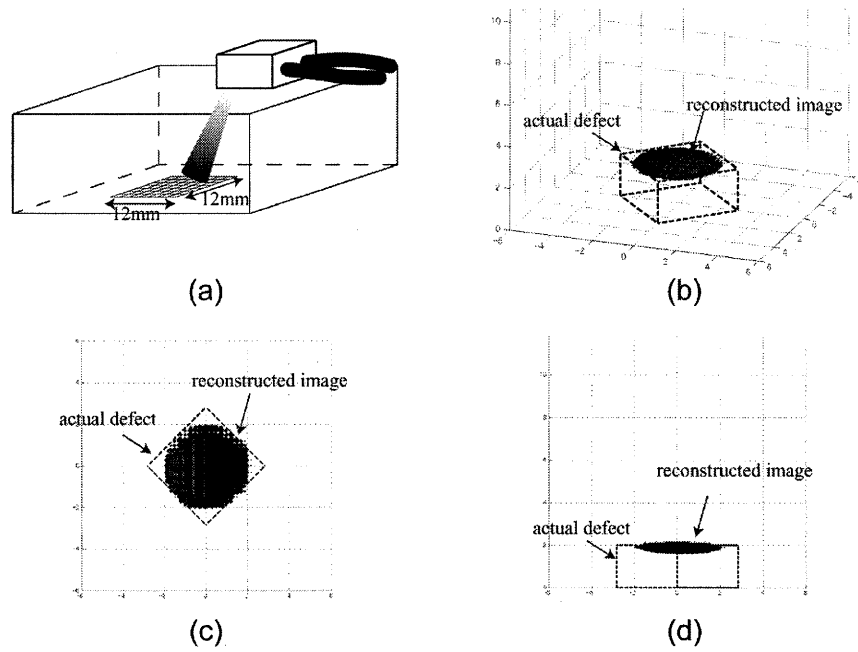


Figure 15 Detection Results of Steering Pattern: (a) Steering Range, (b) 3D View, (c) Plan View, and (d) Front View

4.1 Detection by Ultrasonic Beam Steering

The steering pattern was performed for detection. The specified group of points to which the beam center was steered is shown in Figure 15(a). The incident waves were steered to all points in the 12-by-12 mm² area at the bottom plate surface with 0.2 mm pitch resulting in the three-dimensional scan at approximately 1° pitch. A total of 3721 files of recorded wave data could be obtained for defect evaluation.

Applying the visualization system to manage and analyze the wave data gives the inspection result in the form of a three-dimensional image. Figures 15(b), (c), and (d) show the reconstructed image of the defect in 3D view, 2D plan view, and 2D front view, respectively. In the figures, exact location, shape, and size of the actual defect were additionally provided in order to observe accuracy of the detection. The result shows that the reconstructed image is in a very good agreement with the actual defect in terms of location and depth. However, the size of the reconstructed image appears smaller than that of the actual defect. It can be noticed that the reconstructed image accurately shows the center part of the actual defect, while the near-corner parts (all 4 corners) almost disappear. The size and shape of the actual defect are under-evaluated because the near-corner parts of the defect possess low reflection degree of the wave due to their small sizes.

4.2 Detection by Ultrasonic Beam Focusing

The focusing pattern was performed for detecting the defect. Since the rough location of the actual defect was known by the steering pattern, the points to be focused were designed to be slightly larger than the zone where the defect was present. The incident waves were directly focused to the points in the volume of 6 mm X 6 mm X 2 mm (width X length X depth) with focusing pitch of 0.2 mm (see Figure 16(a)). Therefore, the large amount of the wave data of 10571 files could be obtained.

Figures 16(b), (c), and (d) are the views of the reconstructed image of the defect in three dimensions, 2D plan view, and 2D front view, respectively. The result obtained from the focusing pattern is very accurate comparatively to that from the steering pattern. In Figure 16(c), the reconstructed image is almost perfectly the same with the actual defect in terms of shape, size, and location. The corner parts of the defect, which could not be detected by the steering pattern, could be

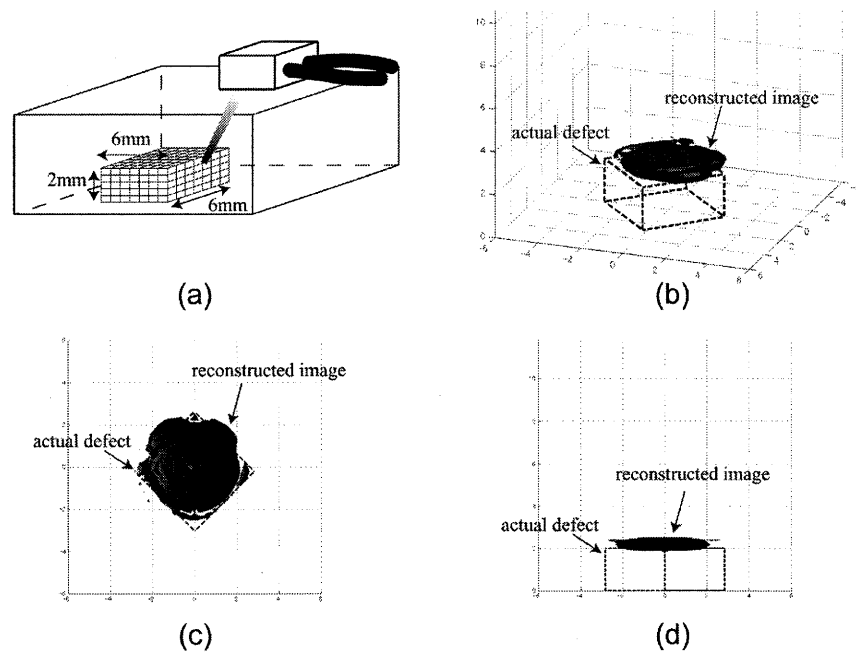


Figure 16 Detection Results of Focusing Pattern: (a) Focusing Volume, (b) 3D View, (c) Plan View, and (d) Front View

detected by the focusing pattern. This result shows very high detectability and accuracy of this system with the use of the focused waves.

5. CONCLUSIONS

In this research, the ultrasonic phased array system with the planar phased array probe was developed. The result showed that our developed system has very high detectability and accuracy for detection of defects in three dimensions.

Acknowledgements:

The authors acknowledge the support from the Center for Urban Earthquake Engineering (CUEE) in Tokyo Institute of Technology.

References:

- Fujiwara, M., Kimoto, K., and Hirose, S. (2003), "An Optimization Method for The Design Parameters of A Linear Phased Array Transducer Using Radiation Pattern of The Incident Field," *Japanese Journal of Applied Mechanics*, **6**, 1089-1096.
- Katsuyama, M. (2005), "Highly Accurate Ultrasonic Flaw Detection with Planar Phased Array and Three Dimensional Visualization," MS Thesis, Department of Civil Engineering, Tokyo Institute of Technology.
- Krautkrämer, J. and Krautkrämer, H. (1983), "Ultrasonic Testing of Materials," Springer-Verlag.
- Miki, C., Shirahata, H., Nishida, A., and Yaginuma, Y. (2000), "Nondestructive Evaluation of Butt Welded Joints by Tandem Array Transducer," *Structural Eng./Earthquake Eng. (proc. of JSCE)*, **654/I-52**, 131-142.
- Miki, C., Fahimuddin, F., and Anami, K. (2001), "Fatigue performance of butt-welded joints containing various embedded defects," *Structural Eng./Earthquake Eng. (proc. of JSCE)*, **18(1)**, 13s-25s.
- Song, S.J., Shin, H.J., and Jang, Y.H. (2002), "Development of An Ultrasonic Phased Array System for Nondestructive Tests of Nuclear Power Plant Components," *Nuclear Engineering and Design*, **214**, 151-161.
- Rattanasuwannachart, N., Takahashi, K., Miki, C., and Hirose, S. (2005), "Development of 3D flaw detection system with multi-channel planar array probes and 3D SAFT algorithms," *Structural Eng./Earthquake Eng. (proc. of JSCE)* (to be appeared).

EXPERIMENTAL ROCKING RESPONSE OF DIRECT FOUNDATIONS OF BRIDGES

D. Sakellarakis¹⁾, G. Watanabe²⁾, and K. Kawashima³⁾

1) Graduate Student, Department of Civil Engineering, Tokyo Institute of Technology, Japan

2) Research Associate, Department of Civil Engineering, Tokyo Institute of Technology, Japan

3) Professor, Department of Civil Engineering, Tokyo Institute of Technology, Japan

demis@cv.titech.ac.jp, gappo@cv.titech.ac.jp, kawasima@cv.titech.ac.jp

Abstract: In this paper a study on the rocking response of direct foundations of bridges based on shake table experiments is presented. An outline of the development of the experimental models and test procedure is described. The experimental response of two bridge models with same footing and column properties but different deck masses subjected to the JMA Kobe ground motion is compared with the results obtained by analysis.

1. INTRODUCTION

Traditionally direct bridge foundations have been designed by minimizing uplift from the underlying ground in order to prevent overturning of the bridge. Nevertheless during post earthquake inspection of piers cracks have been discovered on the ground surface along the edges of the footing indicating that rocking did take place during the earthquake. Analytical studies by Hosoi and Kawashima (2003) showed that rocking of footings has beneficial effect on the dynamic performance of piers by decreasing the deformation of the pier, therefore resulting in lower ductility demand.

This study presents the results obtained by experiments conducted on shaking table using models representing a footing-pier-deck system.

2. EXPERIMENTAL MODEL AND TEST PROCEDURE

The model idealized a footing-pier-deck system. The model consisted of steel top plates (deck), a column (pier), bottom plates (footing), and a rubber block (ground) as shown in Figure 1. Since it is not easy to satisfy the *similarity law* in a small model test, it was not exactly considered in the model test. The model was considered as a small prototype, and it was so designed and fabricated that it provides realistic response data which capture uplifts and contacts between the footing and the underlying ground. The experimental data can be used to verify the analytical model. Consequently it was not intended in any means that the seismic response of the prototype bridge is deduced from the experimental results based on the *similarity law*.

The deck mass and the column stiffness were so designed that the fundamental natural period is in the range of 0.3-1.2 s, which is easy to excite the model and measure the response data. The size of footing was designed so that the deck displacement resulted from rocking response of the footing is in

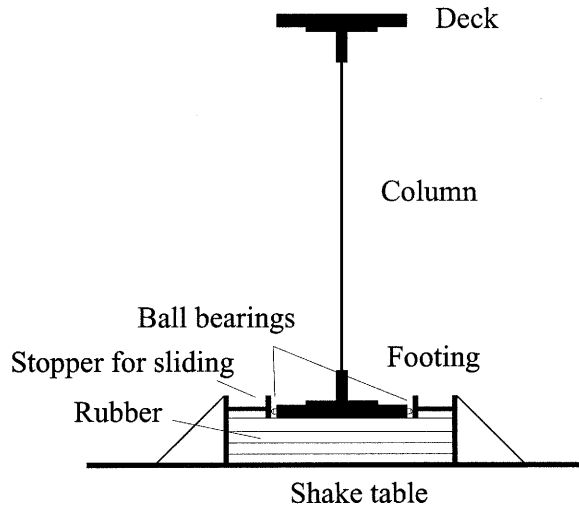


Figure 1 Specimen with top mass 21.2 kg

the range of 30-60% of the total deck displacement. Because the effect of plastic deformation of column at the plastic hinge was not the research target of this study, the column was designed and excited so that it remained in elastic response. Mild steel was used for the model because of easiness of fabrication. Because it was anticipated that damping ratio of the model was very small, putting dampers was once considered. However dampers were not put in the model because dominant energy dissipation by the dampers made the energy dissipation by the footing-soil interaction less significant.

The column was 840 mm tall with a width of 100 mm and a thickness of 6 mm. The deck was fabricated by 12mm and 30 mm thick square plates with a section of 300 mm. By using a 12mm thick plate and a 30 mm thick plate, the deck mass was varied as 8.5 kg and 21.2 kg. The footing was idealized by a 30 mm thick square bottom plate with a section of 300 mm.

Because poundings and contacts occur between the footing and the underlying ground, an elastic rubber block was used to idealize the ground. Because the radiation energy dissipation occurs when contact of the footing to the underlying ground occurs, a 100 mm thick square rubber block with a section of 500 mm was produced for the test. The nominal shear rigidity of the rubber block was 600 kN/m². Because clarification of effect of shear deformation and the amplification of ground motion in the underlying ground was not the purpose of this study, the lateral deformation of the rubber block was restricted.

The footing rested on the rubber block. If the footing is excited by allowing sway and rocking, various modes of structural response occur (Housner 1963, Ishiyama 1982). However, because direct foundations are generally embedded in ground, lateral sway is restricted by side soils. A special device was used to prevent sway motion of the footing with allowing only rocking response. Two small ball bearings which had very small friction force were attached at each side of the footing so that only rocking response was allowed to occur.

Free oscillation and shaking table test were conducted at the Earthquake Engineering Laboratory in Tokyo Institute of Technology. A one-dimensional shake table was used for the test. Used in the shake table tests were three near-field ground motions which were recorded at Japan Meteorological Agency Kobe Observatory (JMA Kobe) during the Kobe, Japan earthquake in 1995, near Bolu viaduct during the Duzce, Turkey earthquake in 1999, and Ojiya during the Niigata-chuetsu, Japan earthquake in 2004. Intensity of the ground motions were scaled down so that response amplitude of the model became in appropriate levels.

Vertical displacement of the footing at both ends as well as the lateral displacement and acceleration at the deck were measured. Accelerometers and LVDT were used to measure accelerations and displacements, respectively. It should be noted that accuracy of measurement on the

vertical displacements of the footing at both ends was not good because of some movement of the LVDT and insufficient resolution.

3. FREE OSCILLATION TESTS

It is obvious that the natural period of the model depends on the contact condition between the footing and the underlying rubber. Once the footing uplifts from the rubber block, it is well known that the natural period of a rocking rigid body depends on the amplitude of rocking response. Free oscillation test was conducted to provide experimental data on the amplitude dependence of the damping ratio of the model. Test was conducted on two conditions of the deck mass; 8.5 kg and 21.2 kg. The deck was laterally displaced by hand, and then smoothly released from the displaced position to have a free oscillation. The initial amplitude was varied in the range that the footing uplifted or did not uplift at the edges of the footing.

Figure 2 shows free oscillation response of the model with the deck mass of 8.5 kg and 21.2 kg. The natural period of the model with the deck mass of 8.5 kg is about 0.53 s at the small oscillation without uplift of the footing. Damping ratio which was obtained from the decay of the displacement amplitude is about 2%. However the natural period of the model increases when uplifts of the footing starts to occur. For example, the natural period of the model is 0.56s when the model was released from an initial deck displacement of 50 mm with an uplift of the footing at an edge of 6mm. However the natural period decreases from 0.56 s to 0.53 s and the damping ratio decreases from 2% to 1.2-1.9% as the oscillation amplitude decreases in the level that uplift no longer occurs.

This was the same on the model with deck mass of 21.2 kg. The natural period and the damping ratio of the model with small oscillation without uplift are 0.78s and 3%, respectively, while they change to 0.9s and 2% if the initial deck displacement is 100mm.

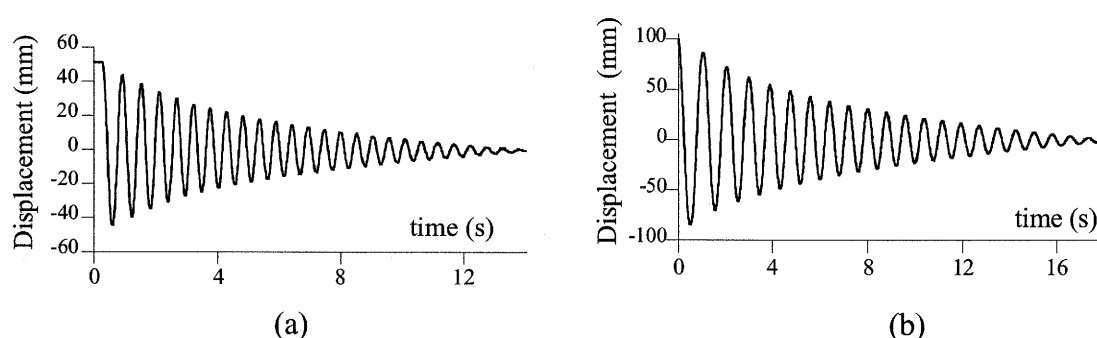


Figure 2 Horizontal displacement of the deck in free oscillation: (a) $m=8.5\text{kg}$ and (b) $m=21.2\text{kg}$

4. SHAKE TABLE TEST

Figure 3 shows response of the model bridge subjected to the JMA Kobe record with a 10% intensity of original (10% JMA Kobe). Because the excitation was small, uplift of the footing from the underlying rubber block did not take place. The peak displacement and acceleration at the deck are 17 mm and 0.3 g, respectively.

Figure 4 shows response of the model under the JMA Kobe record with 25% intensity of original (25% JMA Kobe). It is seen from the vertical response at the edges of the footing that the footing uplifted from the underlying rubber block with the peak uplift of 6 mm at both left and right edges. The peak displacement and acceleration at the deck are 45 mm and 0.6 g, respectively.

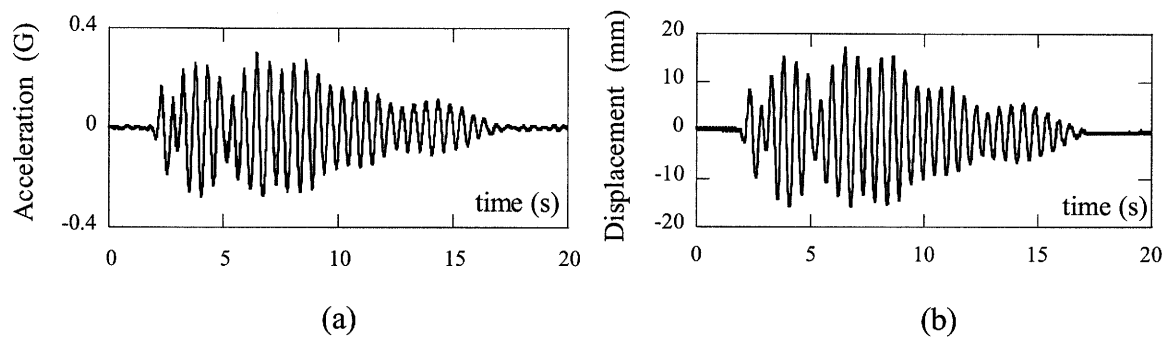


Figure 3 Bridge model with deck mass 8.5 kg subjected to 10% JMA Kobe ground motion: (a) horizontal acceleration at the deck and (b) horizontal displacement at the deck

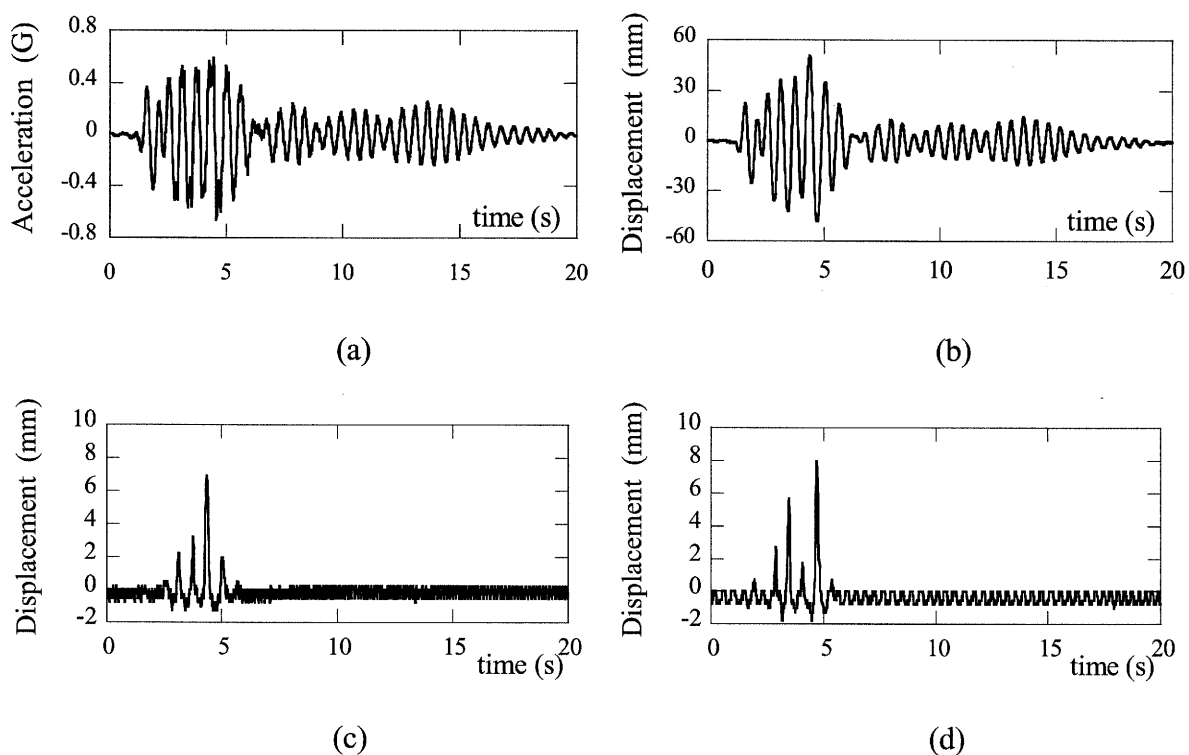


Figure 4 Bridge model with deck mass 8.5 kg subjected to 25% JMA Kobe ground motion: (a) horizontal deck acceleration (b) horizontal deck displacement (c) vertical footing displacement at the left edge and (d) vertical footing displacement at the right edge

5. ANALYTICAL CORRELATION

The seismic response of the model bridge was idealized by a discrete model as shown in Figure 5. The column was idealized by a linear beam element, and the deck mass was lumped at the top of the column. The footing was idealized by a linear beam element with a sufficiently high stiffness. The separation and contact between the footing and the rubber block were idealized by spring elements with the restoring force defined as

$$f_V = \begin{cases} k_S (\Delta v - \Delta v_{IS}) & \Delta v < \Delta v_{IS} \\ 0 & \Delta v \geq \Delta v_{IS} \end{cases} \quad (1)$$

where, k_S : stiffness of rubber block per area represented by a spring element, Δv_{IS} : initial settlement of the footing due to the dead weight of the model bridge, and Δv : relative displacement between the footing and the ground which is defined as

$$\Delta v = v_F - v_G \quad (2)$$

where v_F and v_G are vertical response displacement of the footing and the ground, respectively. The rubber stiffness was slightly modified so that the computed natural period of the bridge model became close to the measured natural period determined from the free oscillation test.

Damping ratio was assumed in the form of Rayleigh damping.

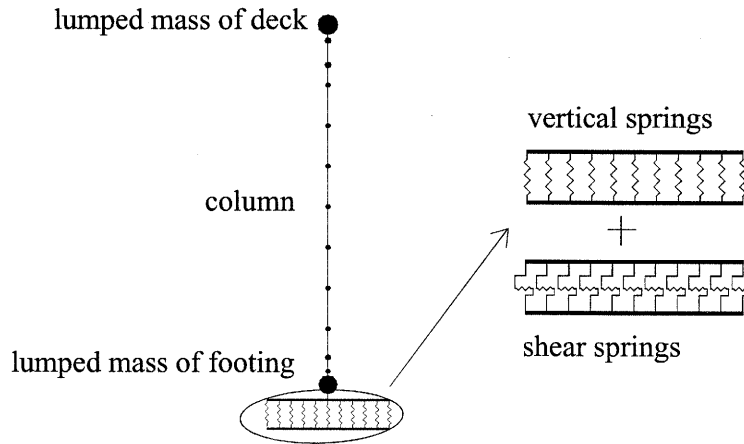


Figure 5 Model used for the analysis

Figure 6 shows the correlation on the seismic response of the model bridge with the deck mass of 8.5 kg under the 10% JMA Kobe ground motion. Damping ratio was assumed 2% here based on the result of free oscillation test.

The computed response is virtually the same with the measured responses until 12 s and after 17 s. However the computed response underestimates the experimental response by about 20% between 12s and 17 s. Therefore, the response was computed as shown in Figure7 by assuming damping ratio of 1%. The response between 12 s and 17 s is now improved, but the computed response after 17 s overestimates the experimental response by a factor of about 40%. Thus, it is apparent that the damping ratio depends on the oscillation amplitude even if uplift of the footing did not take place. Because response prediction of the model bridge at the higher response intensity is the major importance of the correlation analysis, the damping ratio is assumed 2% hereafter.

Figure 8 shows the correlation on the seismic response of the same model bridge subjected to 25% JMA Kobe ground motion. It should be reminded here that the accuracy of the measurement on the vertical displacement of the footing at both ends was not good. The computed responses are very close to the experimental responses at the deck. Uplifts of the footing at both ends are also well represented by analysis; however settlement (compression response) of the footing was overestimated. This has to be clarified later by correcting the measurement.

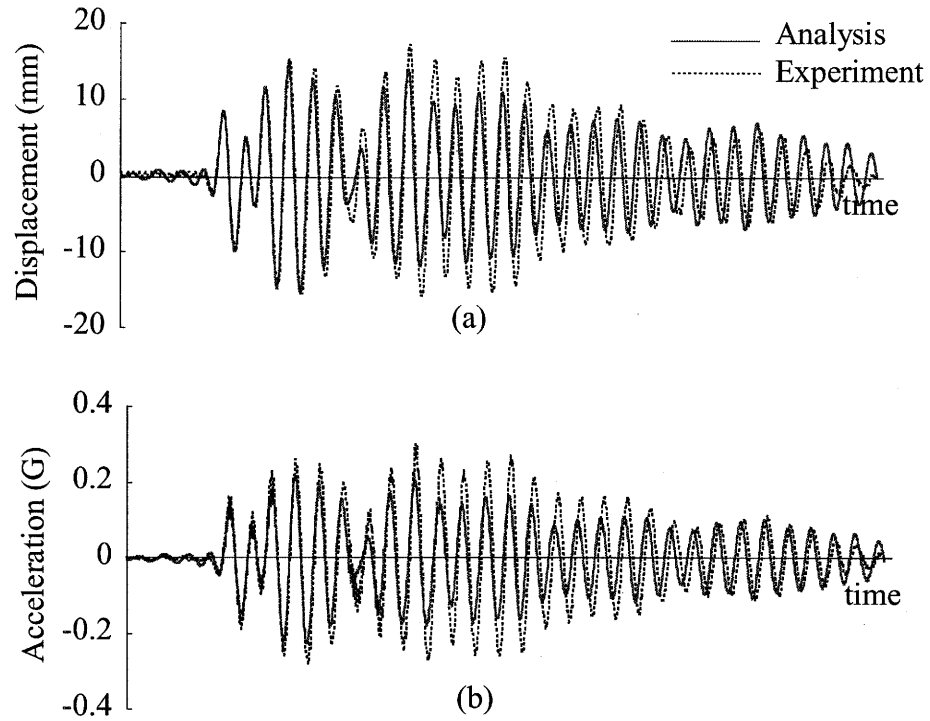


Figure 6 Correlation on the bridge model with deck mass 8.5 kg subjected to 10 % Kobe JMA ground motion with damping ratio 2%: (a) horizontal deck displacement and (b) horizontal deck acceleration

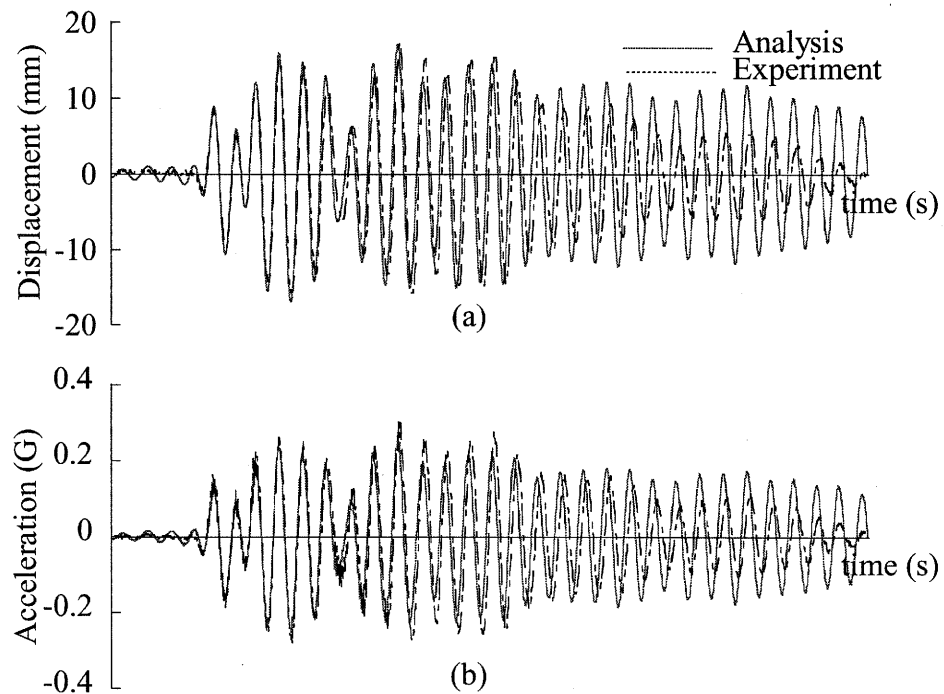


Figure 7 Correlation on the bridge model with deck mass 8.5 kg subjected to 10 % Kobe JMA ground motion with damping ratio 1%: (a) horizontal deck displacement and (b) horizontal deck acceleration

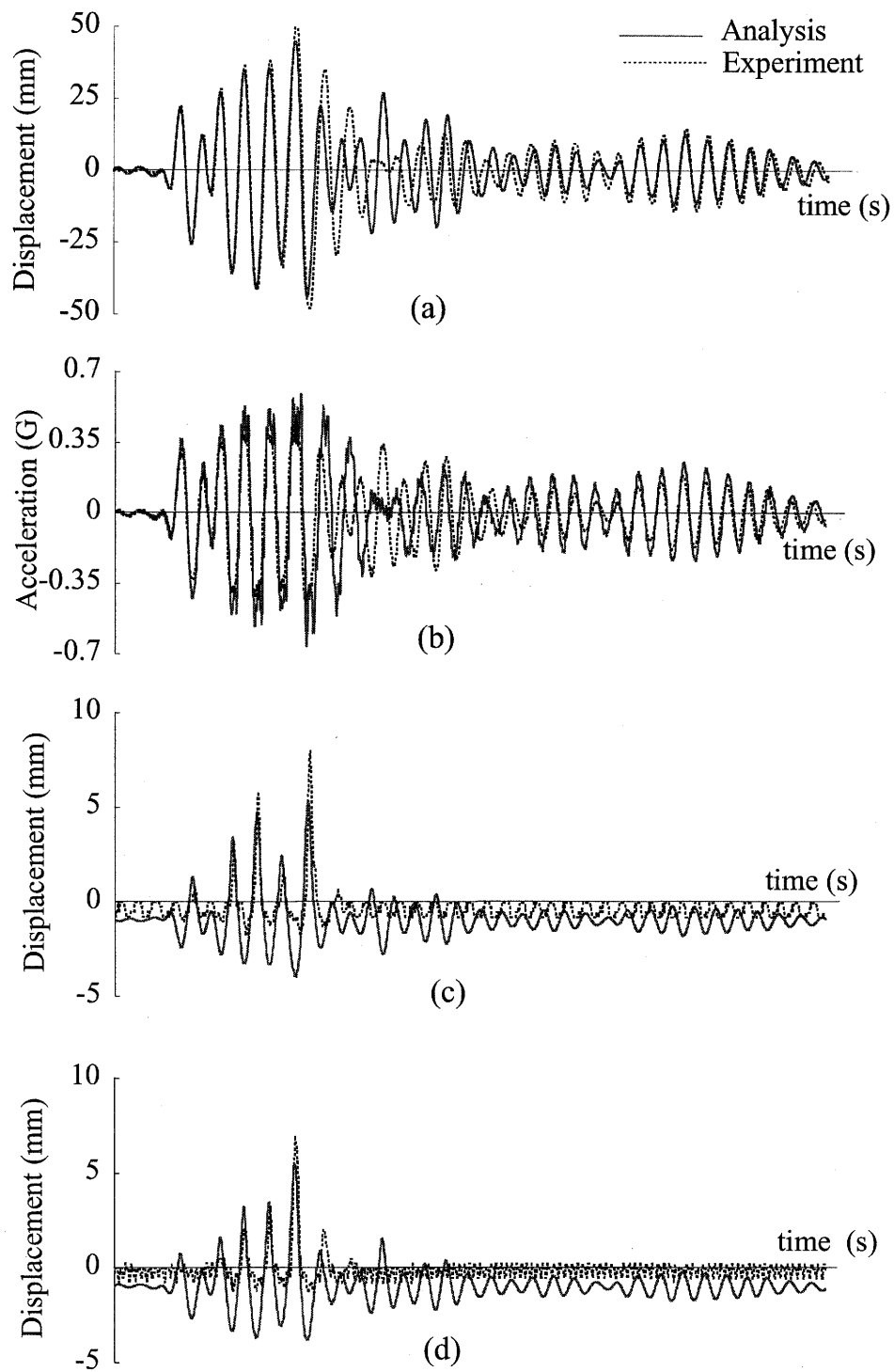


Figure 8 Correlation on the bridge model with deck mass of 8.5 kg and damping ratio 2% subjected to 25 % Kobe JMA ground motion (a) horizontal deck displacement (b) horizontal deck acceleration (c) vertical footing displacement at the left edge and (d) vertical footing displacement at the right edge

6. CONCLUSIONS

Seismic response of a foundation-pier-deck system with uplifts of the footing from the underlying ground was clarified based on a series of shake table test. A correlation analysis which represents the uplifts by contact spring elements with nonlinear stiffness was conducted. The following conclusions may be deduced from the results presented herein:

- 1) A peculiar oscillation response of the bridge model with and without uplifts of the footing from the underlying ground was obtained from the free oscillation and shake table tests. The experimental data provide realistic data on the effect of uplifts and contacts of the footing.
- 2) An analytical model of the model bridge was developed using contact spring elements with nonlinear stiffness in the separation and contact. The analytical model provides a good correlation on the experimental response.
- 3) The analytical model requires an improvement on the idealization of damping characteristics of the model bridge and the overestimation of the footing response in compression.

Acknowledgements:

The authors acknowledge support from Mr. T. Nagai, graduate student of the Tokyo Institute of Technology for conducting the shake table test.

References:

- Housner, G. W. (1963), "The Behavior of Inverted Pendulum Structures During Earthquakes," *Bulletin of the Seismic Society of America*, **53**(2), 403-417
- Ishiyama, Y. (1982), "Motions of Rigid Bodies and Criteria for Overturning by Earthquake Excitations," *Journal of Earthquake Engineering and Structural Dynamics*, Vol.10, 1982
- Kawashima, K. and Hosoi, K. (2003), "Rocking Response of Bridge Columns on Direct Foundations," *Proceedings FIB-Symposium, Concrete Structures in Seismic Region*, Paper No 118, CD-ROM, Athens 2003

**Center for Urban Earthquake Engineering (CUEE)
Tokyo Institute of Technology**

Suzukakedai Office ■

Department of Built Environment
Tokyo Institute of Technology
G3-11 4259 Nagatsuta-cho, Midori-ku, Yokohama, Japan 226-8502
Tel: +81-(0)45-924-5576 Fax: +81-(0)45-924-5199

O-okayama Office ■

Department of Architecture and Building Engineering
Tokyo Institute of Technology
M1-39 2-12-1 O-okayama, Meguro-ku, Tokyo, Japan 152-8552
Tel: +81-(0)3-5734-3200 Fax: +81-(0)3-5734-3200

Email:office@cuee.titech.ac.jp
URL:<http://www.cuee.titech.ac.jp>